Akhmediev and Kuznetsov–Ma rogue wave clusters of the higher-order nonlinear Schrödinger equation

Stanko N. Nikolić[1,2] · Najdan B. Aleksić[1,3] · Milivoj R. Belić[1,3]

© The Author(s), under exclusive licence to Springer Science+Business Media, LLC, part of Springer Nature 2024

Abstract

In this work, we analyze three types of rogue wave (RW) clusters for the quintic nonlinear Schrödinger equation (QNLSE) on a flat background. These exact QNLSE solutions, composed of higher-order Akhmediev breathers (ABs) and Kuznetsov–Ma solitons (KMSs), are generated using the Darboux transformation (DT) scheme. We analyze the dependence of their shapes and intensity profiles on the three real QNLSE parameters, eigenvalues, and evolution shifts in the DT scheme. The first type of RW clusters, characterized by the periodic array of peaks along the transverse or evolution axis, is obtained when the condition of commensurate frequencies of DT components is applied. The elliptical RW clusters are computed from the previous solution class when the first m evolution shifts in the DT scheme of order n are equal and nonzero. For both AB and KMS solutions a periodic structure is obtained with the central RW and m ellipses, containing the first-order maxima that encircle the central peak. We show that RW clusters built on KMSs are significantly more vulnerable to the application of high values of QNLSE parameters, in contrast to the AB case. We next present non-periodic long-tail KMS clusters, characterized by the rogue wave at the origin and n tails above and below the central point containing first-order KMSs. We finally show that the breather-to-soliton conversion, enabled by the QNLSE system, can transform the shape of RW clusters, by setting the real parts of DT eigenvalues to particular values, while keeping all other DT parameters intact.

Najdan B. Aleksić and Milivoj R. Belić contributed equally to this work.

✉ Stanko N. Nikolić
stankon@ipb.ac.rs

Najdan B. Aleksić
najdan@gmail.com

Milivoj R. Belić
milivoj.belic@qatar.tamu.edu

[1] Division of Arts and Sciences, Texas A &M University at Qatar, P.O. Box 23874, Doha, Qatar

[2] Institute of Physics Belgrade, University of Belgrade, Pregrevica 118, 11080 Belgrade, Serbia

[3] Serbian Academy of Nonlinear Sciences, Kneza Mihaila 36, Belgrade, Serbia

1 Introduction

One of the most useful partial differential equations in nonlinear sciences is the cubic nonlinear Schrödinger equation (NLSE) (Fibich 2015; Mirzazadeh et al. 2015; Biswas and Khalique 2011). We list here some branches of physics where the NLSE is found indispensable: nonlinear optics (Kivshar and Agrawal 2003; Dudley et al. 2014; Agrawal 2001; Dudley and Taylor 2010; Kibler et al. 2012), oceanography (Zakharov 1968; Osborne 2010), Bose−Einstein condensates (Bao 2007; Busch and Anglin 2001), and plasmas (Shukla and Eliasson 2010). However, the cubic NLSE is not fully comprehensive when it comes to determining the detailed dynamics of ultra-fast nonlinear systems (with processes in the order of a few femtoseconds); these problems necessitate the inclusion of higher-order dispersion and nonlinearity terms. To overcome this restriction, a group of researchers around Nail Akhmediev proposed a systematic extension of the cubic NLSE, known as the family of extended nonlinear Schrödinger equations (ENLSEs) that accomplished such a goal. In its full form, it contains an infinite number of additional operators that include precisely chosen higher-order dispersions and nonlinearity terms, as well as multiplicative parameters (Ankiewicz et al. 2016; Kedziora et al. 2015).

It should be noted that we speak of the NLSE in (1+1)-dimensions [(1+1)D], one spacial and one temporal. The solutions of higher-dimensional NLSEs, in (2+1)D and (3+1)D, generally develop problems with the instabilities and collapse (the critical and super-critical wave collapse, respectfully), which are very tough problems in soliton theory on their own. Therefore, we will not consider multidimensional solitons here.

So far, most attention was focused on calculating solutions of the Hirota equation (Ankiewicz et al. 2010; Nikolić et al. 2017; Wang et al. 2016) that includes two additional terms, the third-order transverse dispersion and the corresponding nonlinearity. The application of Hirota equation in describing the propagation of femtosecond solitons in inhomogeneous fiber was presented in Mani Rajan and Mahalingam (2015). Nowadays, even more complicated equations from the ENLSE family became an area of active research. Solutions of the quintic equation, comprising all dispersions and nonlinearities up to the fifth-order, were analyzed in Yang et al. (2015), Chowdury et al. (2015a), Nikolić et al. (2019a), Nikolić et al. (2019b). Recently, a paper on the nonlinear Schrödinger–Maxwell–Bloch system with the sextic terms was published in Shen et al. (2023), which could characterize the propagation of ultra-short optical pulses in an erbium-doped fiber.

There are other forms of NLSE, like the nonlocal nonlinear Schödinger equation, which can describe phenomena in nonlinear media where the index of refraction depends on the light intensity over a certain spatial area around the specific point in space. In recent years, various soliton solutions and their characteristics for such nonlocal systems have been reported (Sun et al. 2024; Shen et al. 2021, 2022; Song et al. 2020; Li et al. 2023; Yang et al. 2018). In addition, soliton solutions were reported for the higher-order Gerdjikov–Ivanov equation (Zou and Guo 2023) and the coupled Lakshmanan–Porsezian–Daniel equations in birefringent optical fibers (Li and Guo 2023).

The recursive procedure that is frequently used to derive exact analytical solutions of NLSE and ENLSE is the generalized Darboux transformation (DT) technique (Matveev and Salle 1991; Yang et al. 2015; Nikolić et al. 2019a). It uses the Lax pair formalism to calculate higher-order solutions, starting from some trivial zeroth-order ENLSE wave function. These higher-order solutions can be extremely complicated and lengthy, which makes it practically impossible to write in an exact analytical form. On the other hand, one can calculate the values of ENLSE solutions with an arbitrary precision at any point

of the spatio-temporal grid using a recursive numerical DT algorithm. Thus, the solution of a complicated partial differential equation is converted into a simple algebraic recursive numerical procedure. Here we underline that important solutions of both NLSE and ENLSE, such as Akhmediev breathers (ABs) (Akhmediev and Korneev 1986; Akhmediev et al. 1987) and solitons (Zakharov and Shabat 1972), can be derived using the DT scheme. The AB is characterized by an array of intensity maxima that are periodic in space and localized in time. The term soliton in general refers to a solitary wave packet that propagates without any shape distortion along some direction in the (x, t) plane. The Kuznetsov–Ma soliton (Zakharov and Shabat 1972; Kibler et al. 2012; Xiong et al. 2017; Dai and Wang 2015) resembles the AB wave function, except that it is periodic along the evolution axis and localized in space. The Peregrin soliton (Peregrine 1983; Kibler et al. 2010; Shrira and Geogjaev 2010) is the solution "in between" these two: it has a single intensity maximum localized at $(x, t) = (0, 0)$ and can be considered as the simplest rogue wave (RW).

The physics of rogue waves, as high-intensity narrow peaks that "appear from nowhere and disappear without a trace", is currently the hot area of research related to deep ocean waves (Osborne 2010; Garrett and Gemmrich 2009), nonlinear optics (Solli et al. 2008; Dudley et al. 2008), and Bose–Einstein condensates (Bludov et al. 2009). The investigation of the origin and nature of optical rogue waves for the NLSE is given in Akhmediev (2016); Belić et al. (2022); Chin et al. (2015). The examination of RWs is becoming even more popular since a new scheme for their excitation, via the electromagnetically induced transparency (Fleischhauer et al. 2005; Nikolić et al. 2013; Krmpot et al. 2009; Nikolić et al. 2015), was reported (Li et al. 2020).

In this paper, we present various formations of rogue waves, composed of the higher-order Akhmediev breathers and Kuznetsov–Ma solitons, for the quintic nonlinear Schrödinger equation (QNLSE). Our motivation was to generalize the periodic, multi-elliptic, and long-tail rogue wave clusters of the basic NLSE, that we reported in Nikolić et al. (2022), Alwashahi et al. (2023), on the more complex systems and geometries. We thus add new solutions of QNLSE to the previously described rogue wave triplets (Kedziora et al. 2011a), triangular cascades (Kedziora et al. 2012; Dubard et al. 2010; Ohta and Yang 2012), circular clusters (Kedziora et al. 2011b; Gaillard 2013; Ankiewicz and Akhmediev 2017; He et al. 2013), and general multi-RW structures (He et al. 2013; Kedziora et al. 2013; Akhmediev 2021) reported earlier for the cubic nonlinear Schrödinger equation.

We first show how an array of high-intensity narrow peaks can be constructed as a periodic rogue wave of the QNLSE on a flat background. This type of cluster solutions is obtained under the condition of commensurate frequencies in the n-th order DT scheme. The RW periodicity is achieved along the transverse (evolution) axis for the higher-order ABs of the QNLSE in the same way as for the NLSE. If we next set the first m evolution shifts to be nonzero and equal, while keeping the eigenvalues in the DT procedure unchanged, the periodic multi-elliptic rogue wave clusters are obtained. The novelty of this work is in exhibiting the shape of these solutions for more complex equations than NLSE and in analyzing how the three real quintic parameters affect the appearance and stability of RW clusters.

We also present long-tail RW clusters for the quintic equation, which are calculated when all imaginary parts of DT eigenvalues are increased by the same offset, to become higher than 1. These clusters are not periodic—they are characterized by KMSs of order $n - 2m$ at the coordinate center, from which n tails are spreading along both directions of the evolution axis. We also analyze how breather-to-soliton conversion, as an intrinsic feature of QNLSE (and not of NLSE) (Chowdury et al. 2015b), can significantly alter the shape of RW clusters with just a slight modification of the eigenvalues in the DT scheme.

2 The quintic nonlinear Schrödinger equation and the generalized Darboux transformation technique

The quintic nonlinear Schrödinger equation is written as follows:

$$i\psi_x + S[\psi(x,t)] - i\alpha H[\psi(x,t)] + \gamma P[\psi(x,t)] - i\delta Q[\psi(x,t)] = 0, \tag{1}$$

where $\psi \equiv \psi(x,t)$ is the slowly-varying wave envelope; α, γ, and δ are the quintic (real) parameters; and S, H, P, and Q are the operators arising in the systematic derivation of the infinite hierarchy of nonlinear Schrödinger equations (Kedziora et al. 2015; Ankiewicz et al. 2016), with increasing orders of dispersion and nonlinearity. The transverse (temporal) variable is denoted by t and the longitudinal (spatial) variable by x (the standard fiber-optics notation). Subscripts in Eq. (1) indicate partial derivatives.

Operator S includes the second-order dispersion and Kerr nonlinearity:

$$S[\psi(x,t)] = \frac{1}{2}\psi_{tt} + |\psi|^2\psi. \tag{2}$$

Equation (1) containing only the S term represents the standard cubic NLSE.

Hirota's operator H is characterized by the third-order dispersion and the corresponding nonlinearity (Ankiewicz et al. 2010):

$$H[\psi(x,t)] = \psi_{ttt} + 6|\psi|^2\psi_t. \tag{3}$$

It is used to describe the generation of supercontinuum (Dudley and Taylor 2010) and pulse-deforming phenomena (Anderson and Lisak 1983), among others.

Operator P, known as the Lakshmanan–Porsezian–Daniel (LPD) operator, encompasses the fourth-order dispersion and the corresponding nonlinearity, and may model Heisenberg spin chains (Chowdury et al. 2015b):

$$P[\psi(x,t)] = \psi_{tttt} + 8|\psi|^2\psi_{tt} + 6|\psi|^4\psi + 4|\psi_t|^2\psi \\ + 6\psi_t^2\psi^* + 2\psi^2\psi_{tt}^*. \tag{4}$$

The quintic operator Q includes the fifth-order dispersion and more complex nonlinearity terms:

$$Q[\psi(x,t)] = \psi_{ttttt} + 10|\psi|^2\psi_{ttt} + 30|\psi|^4\psi_t + 10\psi\psi_t\psi_{tt}^* \\ + 10\psi\psi_t^*\psi_{tt} + 20\psi^*\psi_t\psi_{tt} + 10\psi_t^2\psi_t^*. \tag{5}$$

The fifth-order dispersion has to be taken into account in experiments with laser pulses shorter than 20 fs (Backus et al. 1997). In this work we call Eq. (1) the *quintic* when the three parameters α, γ and δ are nonzero.

The exact n-th order breather solution of the quintic equation, denoted as $\psi_n(x,t)$, can be found using Darboux's transformation scheme. This technique, as applied to QNLSE, is described in detail in Nikolić et al. (2019a), so we here provide only a quick overview of the basic DT equations. The n-th order solution can be regarded as a nonlinear superposition of n first-order constituents, where each is defined by its complex eigenvalues $\lambda_p = r_p + iv_p$, real evolution shifts x_p, and real transverse shifts t_p ($1 \le p \le n$). The first step is to start from a simple plane-wave solution of QNLSE (the seed or zeroth-order wave function):

$$\psi_0 = e^{i(1+6\gamma)x}, \tag{6}$$

and then apply the recursive DT algorithm to compute a higher-order solution from the seed and a set of all free parameters (α, γ, δ, λ_p, x_p, and t_p). It is relatively easy to write down analytical expressions of the first-order Akhmediev breathers and Kuznetsov–Ma solitons (Yang et al. 2015; Nikolić et al. 2019a) from a plane wave seed [Eq. (6)], but for higher-order solutions the exact formulae become significantly more complex and extremely cumbersome. Results shown in this paper are for ABs or KMSs with precisely chosen eigenvalues and shifts for $n \geq 2$ or even larger n (denoted as ABn or KMSn), so we use the DT technique to *numerically* calculate wave function $\psi_n(x, t)$ over chosen xt-grid with *arbitrary* precision.

To accomplish this task we compute the following quantities for each eigenvalue λ_p:

$$
\begin{aligned}
\kappa_p &= 2\sqrt{1 + \lambda_p^2} \\
\chi_p &= \frac{1}{2} \arccos\left(\frac{\kappa_p}{2}\right) \\
\bar{d}_p &= 2(\alpha + 3\delta) + (1 + 4\gamma)\lambda_p - 4(\alpha + 2\delta)\lambda_p^2 - 8\gamma\lambda_p^3 + 16\delta\lambda_p^4,
\end{aligned} \tag{7}
$$

and then calculate the Lax pair functions $r_{1,p}(x, t)$ and $s_{1,p}(x, t)$:

$$
\begin{aligned}
r_{1,p}(x, t) &= 2i \sin\left[\frac{\kappa_p}{2}\left[\bar{d}_p\left(x - x_p\right) + \left(t - t_p\right)\right] + \chi_p - \frac{\pi}{4}\right] e^{-\frac{i}{2}(1+6\gamma)x} \\
s_{1,p}(x, t) &= 2 \cos\left[\frac{\kappa_p}{2}\left[\bar{d}_p\left(x - x_p\right) + \left(t - t_p\right)\right] - \chi_p - \frac{\pi}{4}\right] e^{\frac{i}{2}(1+6\gamma)x}.
\end{aligned} \tag{8}
$$

Next, we use recursive relations:

$$
\begin{aligned}
r_{n,j} =& [(\lambda_{n-1}^* - \lambda_{n-1})s_{n-1,1}^* r_{n-1,1} s_{n-1,j+1} \\
&+ (\lambda_{j+n-1} - \lambda_{n-1})|r_{n-1,1}|^2 r_{n-1,j+1} \\
&+ (\lambda_{j+n-1} - \lambda_{n-1}^*)|s_{n-1,1}|^2 r_{n-1,j+1}] \\
&/\left(|r_{n-1,1}|^2 + |s_{n-1,1}|^2\right), \\
s_{n,j} =& [(\lambda_{n-1}^* - \lambda_{n-1})s_{n-1,1} r_{n-1,1}^* r_{n-1,j+1} \\
&+ (\lambda_{j+n-1} - \lambda_{n-1})|s_{n-1,1}|^2 s_{n-1,j+1} \\
&+ (\lambda_{j+n-1} - \lambda_{n-1}^*)|r_{n-1,1}|^2 s_{n-1,j+1}] \\
&/\left(|r_{n-1,1}|^2 + |s_{n-1,1}|^2\right)
\end{aligned} \tag{9}
$$

to calculate higher-order $r_{n,1}(x, t)$ and $s_{n,1}(x, t)$. Finally, the n-th order DT wave function is computed using the following expression:

$$\psi_n(x, t) = \psi_{n-1}(x, t) + \frac{2(\lambda_n^* - \lambda_n)s_{n,1}(x, t)r_{n,1}^*(x, t)}{|r_{n,1}(x, t)|^2 + |s_{n,1}(x, t)|^2}. \tag{10}$$

3 Periodic rogue wave clusters on a flat background

First, we show the periodic rogue wave clusters composed of the higher-order ABs and KMSs, and investigate the influence of quintic parameters α, γ, and δ on their appearance and stability. We harness the fundamental characteristics of these solutions: the periodicity of ABs and KMSs along t and x axes. The main condition, as described in our previous work (Nikolić et al. 2019a, 2022; Alwashahi et al. 2023), is to keep the frequencies of all n DT building blocks commensurate, i.e. to start with some angular frequency $\omega_1 \equiv \omega$ for the first DT component, and calculate other frequencies as its higher harmonics:

$$\omega_p = p\omega \quad (p \geq 2).$$ (11)

We underline that all nondegenerate imaginary parts of DT eigenvalues have to be less/ greater than the ones for the AB/KMS case. Equation (11) ensures that the maxima of all building ABs or KMSs will coincide at some points along the t- or x-axis, producing periodic arrays of high-intensity narrow peaks. We stress that these clusters are built from a plane-wave seed, and should not be confused with the similarly called clusters on a dnoidal background, reported in Nikolić et al. (2019a).

In the AB case, we start from frequency ω of the first DT component (along the t-axis) and then determine imaginary parts ν_p of all eigenvalues, while keeping their real parts equal to zero. In Nikolić et al. (2022) we showed the connection between $\nu_1 \equiv \nu$ and ω ($\omega = 2\sqrt{1 - \nu^2}$) and also provided an appropriate expression, so that Eq. (11) is satisfied for higher-order Akhmediev breathers:

$$\nu_p = \sqrt{1 - \frac{p^2\omega^2}{4}} \quad (1 \leq p \leq n).$$ (12)

In the case of periodic rogue waves composed solely from Kuznetsov–Ma solitons, we slightly modified the starting step, to keep the commensurate condition along x-axis (Alwashahi et al. 2023); we define the imaginary part of the first eigenvalue, take into account the relation between ω and ν ($\omega = 2\nu\sqrt{\nu^2 - 1}$), and then compute the remaining imaginary parts using the following equation (the real parts are again set to zero):

$$\nu_p = \sqrt{\frac{1 + \sqrt{1 + 4p^2\nu^2(\nu^2 - 1)}}{2}} \quad (2 \leq p \leq n).$$ (13)

In Fig. 1, we show the periodic RW clusters made from the second-order Akhmediev breathers in the DT scheme. In nine panels, we display three intensity maxima (out of infinitely many) with sharp central peaks and the characteristic 2×2 lobe intensity patterns in peaks' vicinity. The results are obtained for $\omega = 2/3$. The eigenvalues in the DT scheme are obtained from Eq. (12). One can observe the influence of QNLSE parameters α, γ, and δ on the intensity distributions of the calculated wave function. In the top row, we varied only parameter α, while keeping $\gamma = 0$ and $\delta = 0$. The three breathers in the box are calculated for $\alpha = -0.07$ (left), $\alpha = 0$ (center), and $\alpha = 0.07$ (right). Analogously, in the middle row, we changed only γ values ($\alpha = 0$, $\delta = 0$): $\gamma = -0.07$ (left), $\gamma = 0$ (center), and $\gamma = 0.07$ (right). Finally, the three panels shown in the bottom row are the QNLSE solutions ($\alpha = 0$, $\gamma = 0$) for $\delta = -0.07$ (left), $\delta = 0$ (center), and $\delta = 0.07$ (right).

In agreement with our conclusions on the single-order quintic AB (Nikolić et al. 2019a), we state that the action of α and operator H introduces the skew of the breather
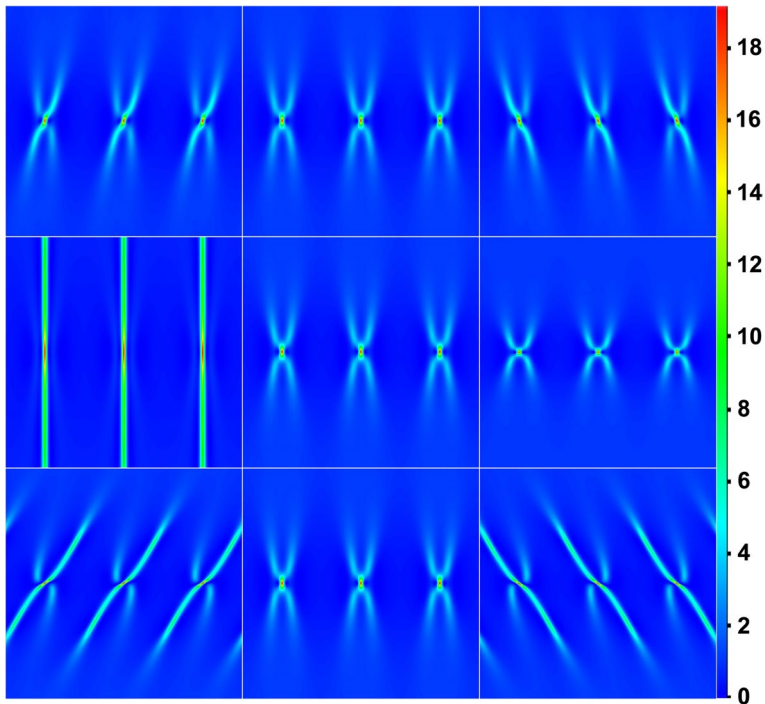
Fig. 1 Intensity distributions of the second-order Akhmediev breather in the (x, t) plane for different values of parameters α, γ, and δ. In each row, one parameter is varied and the other two are set to zero. Top row: $\gamma = 0$, $\delta = 0$, $\alpha = -0.07, 0, +0.07$, from left to right. Middle row: $\alpha = 0$, $\delta = 0$, $\gamma = -0.07, 0, +0.07$, from left to right. Bottom row: $\alpha = 0$, $\gamma = 0$, $\delta = -0.07, 0, +0.07$, from left to right. In each panel, the transverse axis (horizontal) spans from $t = -14.1$ to 14.1 and the evolution axis (vertical) from $x = -5$ to 5

whose tilt direction is determined by the sign of α. In addition, the larger the absolute value of α, the larger the tilt. On the contrary, parameter γ and operator P do not introduce the skew, but extend ($\gamma < 0$) or compress ($\gamma > 0$) the breather along the x-axis. For larger γ values, the change of the size is more prominent. Parameter δ and the quintic operator Q also skew the second-order AB, but significantly more strongly than the Hirota term. The quintic part of QNLSE also narrows the solution intensity profile. The stronger the absolute value of δ, the bigger the skew and the stretch of the solution. One can conclude that the Hirota and quintic operators (with odd-order t dispersion) tilt both the central maximum and the symmetric four lobes before and after the peak in the positive/negative t-direction for negative/positive α and δ values.

The intensity of RW at the center remains the same regardless of the values of α and δ, while the symmetric intensity distribution in four tails (lobes) is broken. For negative α or δ the lobes located top-right and bottom-left (with respect to AB2) are becoming stronger and stretched (especially for the δ case). The symmetry is broken in the opposite direction for positive α or δ values, as can be seen in Fig. 1. The P operator and γ (with even-order dispersion) extend or compress both the central RW and four lobes. Note that the central panels in all three rows of Fig. 1 are the same and correspond to the NLSE case ($\alpha = \gamma = \delta = 0$). They are placed centrally here, so that the reader can

see the influence of different terms in the QNLSE and compare it with the higher-order breathers of the cubic nonlinear Schrödinger equation.

In Fig. 2, we present the second-order Kuznetsov–Ma solitons of the QNLSE.

Analogously to Fig. 1, we plot two-dimensional intensity patterns in numerical boxes, where each contains five KMS peaks with two lobes on the left and right of their central maximum. The results are generated for $v = 1.1$, while v_2 is calculated using Eq. (13). One can observe the influence of α, γ, and δ on the KMS2 intensity distribution. In the top row, we fixed $\gamma = 0$ and $\delta = 0$, and varied only α. The three higher-order KM solitons are calculated for $\alpha = -0.002$ (left), $\alpha = 0$ (center), and $\alpha = 0.002$ (right). Similarly, in the middle row, we changed γ values ($\alpha = 0$, $\delta = 0$): $\gamma = -0.004$ (left), $\gamma = 0$ (center), and $\gamma = 0.004$ (right). In the bottom row, we depict pure quintic solutions for $\delta = -0.0005$ (left), $\delta = 0$ (center), and $\delta = 0.0005$ (right) ($\alpha = 0$, $\gamma = 0$).

The similarity of KMS2 results with AB2 solutions is observed when one compares Figs. 1 and 2. One can see that the effect of α and operator H is to introduce the skew of the soliton evolution direction. The tilt angle is determined by the sign of α, in the same way as for the AB2 case. Additionally, the larger the absolute α, the larger the tilt. Operator P extends (negative γ) or compresses (positive γ) the x-distance between the two adjacent
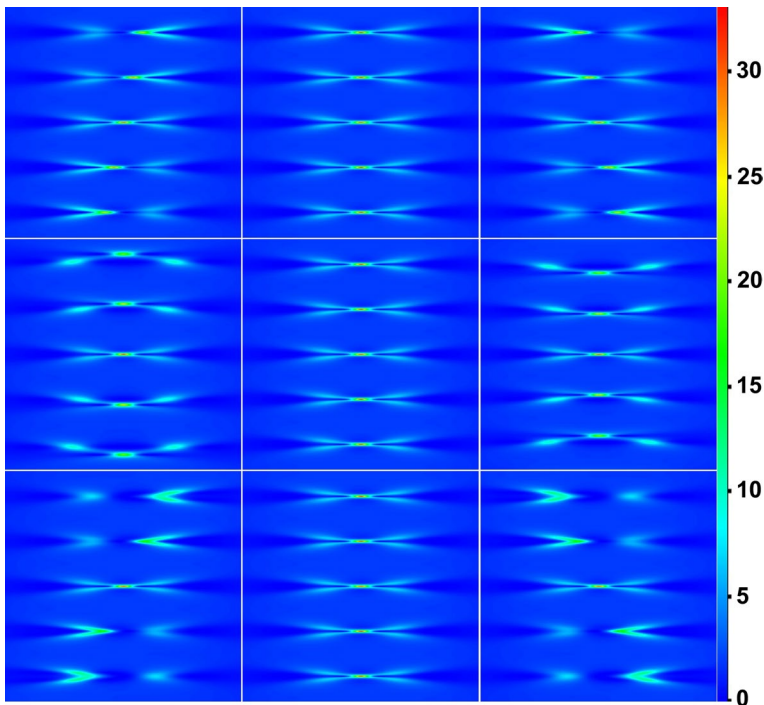

Fig. 2 Intensity distributions of the second-order Kuznetsov–Ma soliton in the (x, t) plane for different values of parameters α, γ, and δ. In each row, one parameter is varied and the other two are set to zero. Top row: $\gamma = 0$, $\delta = 0$, $\alpha = -0.002$, 0, $+0.002$, from left to right. The t-axis spans from -2.5 to 2.5 (horizontal), while the x-interval is from -16 to 16 (vertical). Middle row: $\alpha = 0$, $\delta = 0$, $\gamma = -0.004$, 0, $+0.004$, from left to right. The t- and x-intervals are $[-2.5, 2.5)$ and $[-20, 20)$, respectively. Bottom row: $\alpha = 0$, $\gamma = 0$, $\delta = -0.0005$, 0, $+0.0005$, from left to right. The t- and x-intervals are $[-2.5, 2.5)$ and $[-16, 16)$, respectively

KMS2 peaks. Parameter δ and the quintic operator Q skew the KMS2 (as for AB2), but stronger than the action of α and H.

Nonetheless, there are still differences, as compared to the AB2 case. The KMS2 peak at (0,0) is almost unchanged under the influence of higher-order terms in QNLSE. However, the action of αH, γP, and δQ at $x \neq 0$ destroys the periodic vertical maxima and the symmetry of four lobes. The peaks above RW at the coordinate center are more vulnerable to the deformation, as absolute x increases. For nonzero α, KMS2s are losing bigger portions of their intensities as x is getting larger, and so do the two lobes on the left. If x is more negative, the lobes (wings) on the right are stronger than their left counterparts. Also, with increasing $|x|$ the lobes on the left and right within the same KMS2 are getting more separated—see Fig. 2 (top-left). The same conclusion can be drawn for positive α, although the skew angle and deformation sides are in the opposite (Fig. 2 (top-right)). The disintegration of peaks and an asymmetric perturbation of the four lobes also happen under the action of LPD operator—see Fig. 2, middle-left and middle-right. One can observe that the overpowered lobes can be spotted above or below their disturbed maxima, depending on the sign of x and γ. Finally, the effect of the quintic term on the higher-order KMSs is the same as the amplified action of Hirota's term αH. That's the reason we show results for a smaller value of $|\delta| = 0.0005$, since it produces a bigger effect on intensity patterns compared to the case of $|\alpha| = 0.002$. As seen in Fig. 2, bottom-left and bottom-right, the central peaks completely vanish, and the lobes quickly deform, separate and weaken, as $|x|$ is getting larger. Note that the central panels in all three rows of Fig. 2 are identical. They correspond to the NLSE case ($\alpha = \gamma = \delta = 0$), so that one can compare directly the KMS2 of QNLSE and the cubic nonlinear Schrödinger equation.

4 Multi-elliptic rogue wave clusters of the quintic equation

Multi-elliptic rogue wave clusters (MERWCs) of the quintic equation, composed of higher-order Akhmediev breathers (AB MERWCs) or Kuznetsov–Ma solitons (KM MERWCs), can be computed using the same set of DT eigenvalues and evolution shifts, as for the NLSE (Nikolić et al. 2022; Alwashahi et al. 2023). Here we investigate the effect of higher-order terms of QNLSE on the cluster appearance and stability when building blocks in the DT procedure are ABs or KMSs.

The first requirement is to maintain commensurate frequencies of all DT constituents (Eq. 11). The second requirement is to set the first m shifts along the evolution axis to be nonzero and equal: $x_p \neq 0$ for $1 \leq p \leq m$, and the rest zero: $x_p = 0$ for $m < p \leq n$. Thus, as in the previous section, we keep all transverse shifts equal to zero. The expression used for calculating the x-shifts is borrowed from our AB and KM MERWC papers for the NLSE (Nikolić et al. 2022; Alwashahi et al. 2023):

$$x_p = \sum_{l=1}^{\infty} X_{pl}\omega^{2(l-1)} = X_{p1} + X_{p2}\omega^2 + X_{p3}\omega^4 + X_{p4}\omega^6 + \cdots . \tag{14}$$

The quantity ω is a number close to zero. Please note that ω is the main DT frequency in the AB MERWC case, while it is not in the case in the KM MERWC.

In general, both clusters are complex periodic structures, AB MERWC along the t and KM MERWC along the x-axis. In Fig. 3a, one segment of the AB MERWC is shown (out of infinitely many) for the pure Hirota equation ($\alpha = 0.07$, $\gamma = 0$, $\delta = 0$). The entire cluster is tilted to the left, since α is positive (the same effect as in AB2 of
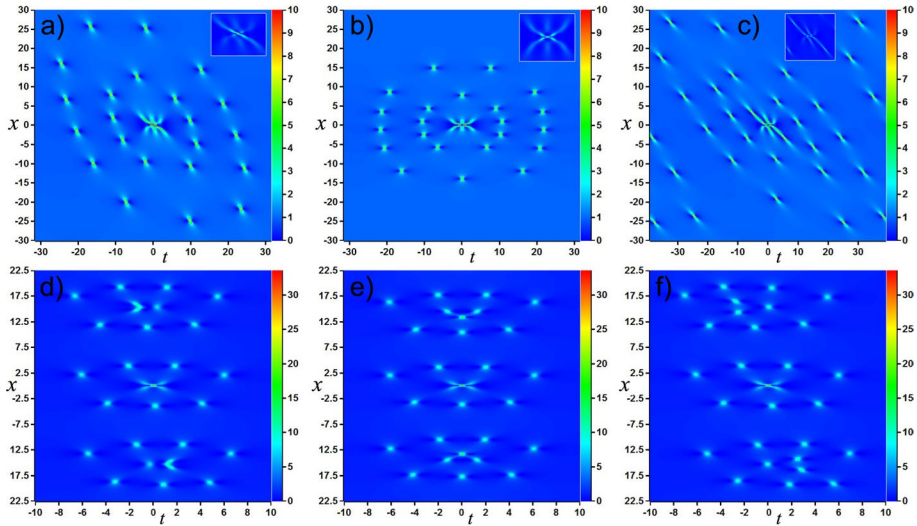
Fig. 3 Intensity distributions of the multi-elliptic rogue wave clusters built on the higher-order ABs and KMSs. AB MERWC is calculated from Eqs. (12) and (14) with $n = 7$, $m = 2$, $\omega = 0.1$, $x_1 = x_2 = 1$, and: **a** $\alpha = 0.07$, $\gamma = 0$, $\delta = 0$, **b** $\alpha = 0$, $\gamma = 0.07$, $\delta = 0$, and **c** $\alpha = 0$, $\gamma = 0$, $\delta = 0.035$. The insets show the actual appearance of the central RW. KM MERWC is computed from Eqs. (13) and (14) with $n = 4$, $m = 1$, $\nu_1 = 1.02$, $x_1 = 1$, and: **d** $\alpha = 0.006$, $\gamma = 0$, $\delta = 0$, **e** $\alpha = 0$, $\gamma = 0.006$, $\delta = 0$, and (f) $\alpha = 0$, $\gamma = 0$, $\delta = 0.002$

the previous section). When only the LPD operator is turned on ($\alpha = 0$, $\gamma = 0.07$, $\delta = 0$) the cluster is compressed from both vertical directions towards the center (Fig. 3b). For $\alpha = 0$, $\gamma = 0$, and $\delta = 0.035$ the AB MERWC is tilted even more towards the negative t-direction when compared to the Hirota case, as observed in Fig. 3c. These three instances were calculated for $n = 7$, $m = 2$, $\omega = 0.1$, and $x_1 = x_2 = 1$.

The general characteristic of AB MERWCs is that an Akhmediev breather of order $n - 2m$ (or $n - 2m$ order RW) is formed at the cluster center and is surrounded by m ellipses. The outer ellipse contains $2n - 1$ AB1, and each following one towards the center has 4 AB1 less. Our results confirm these claims; we see the third-order AB at the center and 2 elliptical rings with 13 and 9 AB1 on them, respectively. The AB MERWC is stable; the intensity of the central RW does not depend on α, γ, and δ, but solely on DT eigenvalues and shifts, and is equal to 44.45. The maximum of the pseudo-color scale bar is set to 10, to emphasize the AB1 structures around the ellipses. The insets in Figs. 3a-c depict the actual shape of the central RW.

The KM MERWC retains the outline of its characteristic NLSE shape (Alwashahi et al. 2023), but the disintegration of central rogue waves is becoming prominent for sufficiently large α, γ, and δ values. In Fig. 3d, three segments of the KM MERWC are depicted for $\alpha = 0.006$, $\gamma = 0$, and $\delta = 0$. As expected, the evolution direction of the cluster is tilted to the left, because of the positive α value. If only LPD operator is turned on ($\alpha = 0$, $\gamma = 0.006$, $\delta = 0$) the cluster is compressed from both vertical directions towards the center (Fig. 3e). In the purely quintic case ($\alpha = 0$, $\gamma = 0$, $\delta = 0.002$) the KM MERWC is again tilted more towards the left, since δQ is acting stronger on the wave function than the αH term (see Fig. 3f). The KM MERWC results were computed for $n = 4$, $m = 1$, $\nu_1 = 1.02$, and $x_1 = 1$.

The general characteristic of KM MERWCs is the same as for AB multi-elliptic clusters: a RW of order $n - 2m$ is formed at the cluster center, there are m surrounding elliptical rings with $2n - 1$ KMS1 on the outer one, and 4 KMS1 less on each following one towards the center. We show the $m = 1$ case, so only one ring is visible in Fig. 3d–f. However, the KM MERWC is not stable: the central rogue waves within single cluster segments decay for $|x| \neq 0$ and their 4 lobes are deformed, similarly to the KMS2 case of the previous section.

After presenting how quintic parameters solely affect the intensity profile of RW clusters, we now switch to the fully quintic case, having nonzero values of α, γ, and δ. In Fig. 4a we show one segment of the MERWC built from AB, for $\alpha = 0.09$, $\gamma = 0.03$, and $\delta = -0.02$. The DT parameters are $n = 6$, $m = 2$, $\omega = 0.1$, and $x_1 = x_2 = 1$. As expected, a second-order RW is formed with two ellipses around it. The opposite signs of α and δ cause the competing actions of Hirota and quintic terms on cluster's intensity pattern. In this particular case, the AB MERWC is slightly tilted to the positive direction of the t-axis, meaning that the δQ term overcomes the αH term, although $|\delta| < |\alpha|$. This is in agreement with the previous figures, where one could see a significantly stronger quintic effect, even for much lower δ.

In Fig. 4b, we depict three segments of the KM MERWC, for $\alpha = 0.003$, $\gamma = -0.0025$, and $\delta = -0.001$. The DT parameters are $n = 6$, $m = 2$, $v_1 = 1.02$, and $x_1 = x_2 = 1$. A KMS2 is formed at the center of each segment, with two surrounding elliptical rings. Although the quintic term surpasses the Hirota operator, it is difficult to determine the tilt of cluster's evolution line. Namely, the values of quintic parameters are sufficiently large to cause the disintegration of rogue waves inside the two segments that are above and below the central one. This is one more indication of the KM MERWC's vulnerability to the action of higher-order terms in the extended NLSE hierarchy.

5 Multi-elliptic and long-tail rogue wave clusters under the condition of breather-to-soliton conversion

The conversion of breathers to solitons is a rarely seen event. An exclusive feature of the QNLSE is exactly such a conversion, but it can take place only with carefully chosen parameters. The breather-to-soliton conversion takes place only when the quintic
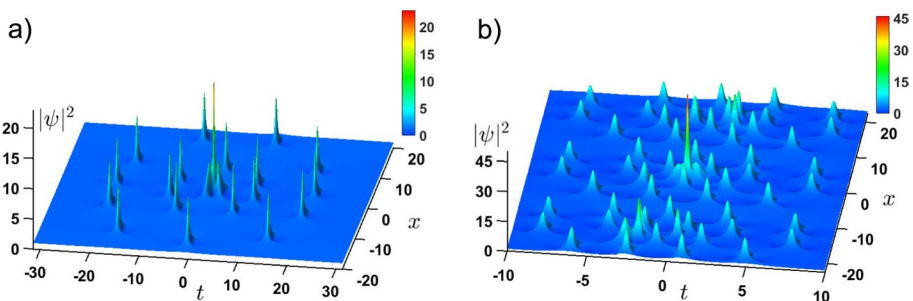

Fig. 4 Intensity distributions of the multi-elliptic rogue wave clusters for nonzero values of all quintic parameters: **a** AB MERWC for $n = 6$, $m = 2$, $\omega = 0.1$, $x_1 = x_2 = 1$, $\alpha = 0.09$, $\gamma = 0.03$, and $\delta = -0.02$, **b** KM MERWC for $n = 6$, $m = 2$, $v_1 = 1.02$, $x_1 = x_2 = 1$, $\alpha = 0.003$, $\gamma = -0.0025$, and $\delta = -0.001$

parameters, the real part r and the imaginary part v of an arbitrary DT eigenvalue satisfy the following expression (Nikolić et al. 2019a):

$$64\delta r^3 - 24\gamma r^2 - 8\left(\alpha + 2\delta + 8v^2\delta\right)r + 8\gamma v^2 + 4\gamma + 1 = 0. \tag{15}$$

For the origin of this expression, please consult the original reference. Note that it can be viewed as a cubic equation for the value of r.

The plan in converting an AB MERWC into a soliton is to keep all imaginary parts and evolution shifts of DT procedure and α, γ, and δ unchanged, and then to recalculate the real part of each DT eigenvalue using Eq. (15). In Fig. 5a, we depict an AB MERWC for $n = 6$, $m = 2$, $\omega = 0.1$, $x_1 = x_2 = 1$, $\alpha = 0.13$, $\gamma = 0.03$, and $\delta = -0.02$. The imaginary parts of n DT eigenvalues are computed using Eq. (12), while the real parts are set to zero. We recompute next the real parts r_p ($1 \leq p \leq n$) to be real solutions of Eq. (15) and obtain: $r_1 = 0.981945$, $r_2 = 0.979482$, $r_3 = 0.975373$, $r_4 = 0.969615$, $r_5 = 0.962199$, and $r_6 = 0.953116$. The DT procedure is applied again, and the converted AB MERWC cluster in the form of a multi-pulsed soliton is obtained, as shown in Fig. 5b. One can note that the fundamental breather periodicity along the t-axis and m elliptic rings have disappeared. The rogue wave at (0, 0) preserved its peak intensity of 22.98, but its shape is different in the converted case. The feature of the soliton solution is reflected in several straight diagonal traces flowing in and out from the central RW. It turns out that there are n straight lines of nearly uniform intensity and each is divided into two sublines. Note that maximal values of the pseudo-color scale bars in Fig. 5a, b are lower than the calculated peak maximum, to graphically emphasize solutions' lower intensity features.

The conversion of a KMS cluster into a soliton is presented in Fig. 6. In part (a) of the figure, we present the third type of the QNLSE RW solution—a long-tail KMS cluster that does not display a multi-elliptic form nor x-periodicity. This solution, already described in Alwashahi et al. (2023) for the NLSE, is characterized by the central KMS of order $n - 2m$ and n tails containing KMS1 that flow in and out from the RW at the solution center. Here, we observe the influence of QNLSE operators H, P,
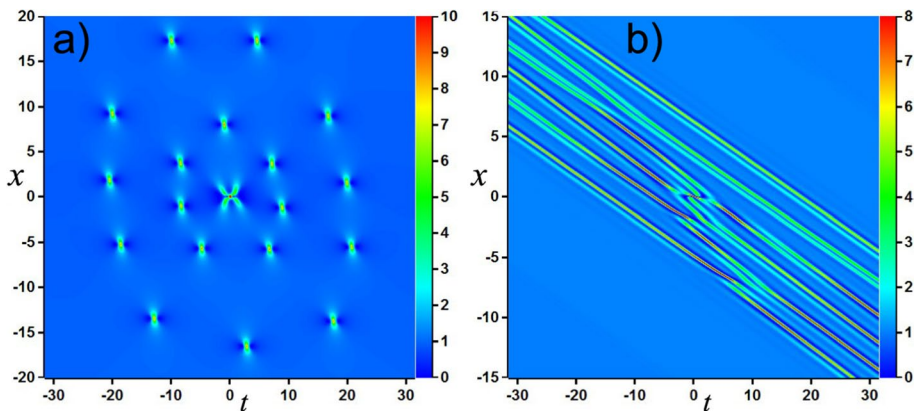

Fig. 5 **a** The AB MERWC for $n = 6$, $m = 2$, $\omega = 0.1$, $x_1 = x_2 = 1$, $\alpha = 0.13$, $\gamma = 0.03$, $\delta = -0.02$, and all real parts of DT eigenvalues set to zero. **b** The breather-to-soliton conversion of the AB MERWC from (**a**), for the same set of parameters, except for recalculated real parts of DT eigenvalues: $r_1 = 0.981945$, $r_2 = 0.979482$, $r_3 = 0.975373$, $r_4 = 0.969615$, $r_5 = 0.962199$, and $r_6 = 0.953116$
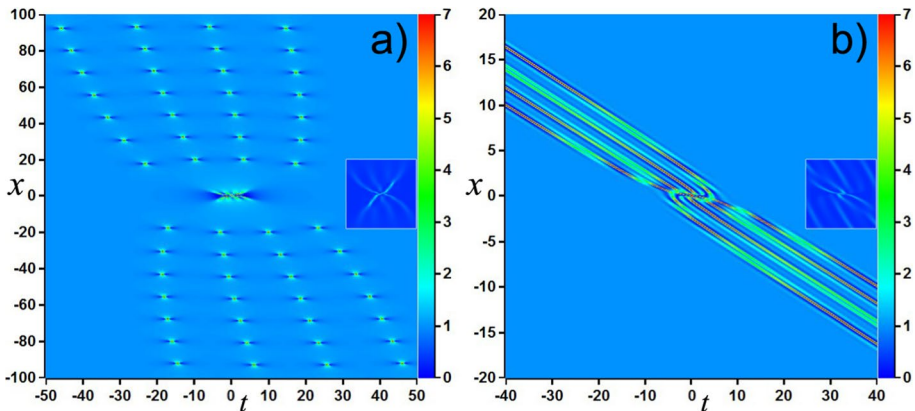
Fig. 6 a The KMS long-tail cluster for $n = 4$, $m = 0$, $\omega = 0.05$, $v_0 = 0.02$, $\alpha = 0.13$, $\gamma = 0.03$, $\delta = -0.02$, and all real parts of DT eigenvalues equal to zero. **b** The breather-to-soliton conversion of the long-tail RW cluster for the same set of parameters, except for recalculated real parts of DT eigenvalues: $r_1 = 0.995793$, $r_2 = 0.995168$, $r_3 = 0.994125$, and $r_4 = 0.992664$. The two insets show the actual intensity patterns of the central RWs

and Q on the intensity distribution. We briefly recall that this solution is obtained for the zero real parts of DT eigenvalues and the modified imaginary values:

$$v_p = v_0 + \sqrt{1 - \frac{1}{4}p^2\omega^2}. \tag{16}$$

The offset term v_0 from the last equation destroys the condition of commensurate frequencies and lifts all imaginary values above 1. The long-tail cluster in Fig. 6a is calculated for $n = 4$, $m = 0$, $\omega = 0.05$, $v_0 = 0.02$, $\alpha = 0.13$, $\gamma = 0.03$, and $\delta = -0.02$. It is characterized by the 4th-order KMS at the center. In contrast to the NLSE long-tail cluster, its QNLSE counterpart is tilted and so are the 4 lobes in the vicinity of the central RW .

Now, we recompute the real parts of DT eigenvalues, so that the Eq. (15) is satisfied. The new values are: $r_1 = 0.995793$, $r_2 = 0.995168$, $r_3 = 0.994125$, and $r_4 = 0.992664$. After reapplying the DT procedure, the long-tail KMS cluster is converted into a single multi-pulsed soliton—see Fig. 6b. The central RW remains with the same maximum intensity value of 83.56, as in Fig. 6a. The tails with KMS1 are transformed into diagonal intensity traces of nonuniform intensity, thus keeping the soliton nature of the new solution. The maximum values of the pseudo-color scale bars in Fig. 6a, b are lower than the central peak intensity, so that one can more easily spot the lower intensity features. The insets in both panels present the RW structure at (0, 0).

To the best of our knowledge, the three types of RW solutions, analyzed in this paper, are still not observed in the laboratory. We hope that substantial experimental progress could enable researchers to generate simple rogue waves during propagation of the ultrafast optical pulses in nonlinear media governed by the QNLSE. Achievement of this goal would be a step forward to experimental realization of more complex RW patterns, such as the multi-elliptic and long tail RW clusters.

6 Conclusion

In this work, we have analyzed the periodic, multi-elliptic, and long-tail rogue wave clusters of the quintic nonlinear Schrödinger equation. These clusters are built using the Darboux transformation scheme from the higher-order Akhmediev breathers and Kuznetsov–Ma solitons. We have analyzed in some detail the sole and combined effects of the Hirota, LPD, and quintic operators on the tilt, stretch, and compression of these cluster solutions. We displayed that the simple periodic and multi-elliptic rogue wave clusters can keep their basic shape under the action of higher-order operators, in the case when Akhmediev breathers are their building blocks. However, these clusters are much more vulnerable to the action of QNLSE operators if they are made from the Kuznetsov–Ma solitons. We also exhibited that rogue wave clusters of the quintic equation can be efficiently converted into multi-pulsed solitons for carefully chosen real parts of the eigenvalues. We believe the results presented in this article are just a small indicator of enormous possibilities and great richness of the analytical solutions of the extended family of nonlinear Schrödinger equations, enabled by the free choice of many parameters in the generalized Darboux transformation scheme.

Author Contributions SNN developed the theoretical and numerical model, wrote the text and programs, and generated the results. NBA helped with the results' analysis and image preparation. MRB provided funding, proposed the research, and revised the text. All authors contributed to the manuscript preparation.

Declarations

Conflict of interest The authors declare no competing interests.

References

Agrawal, G.P.: Applications of Nonlinear Fiber Optics. Academic Press, San Diego (2001)

Akhmediev, N., et al.: Roadmap on optical rogue waves and extreme events. J. Opt. **18**, 063001 (2016)

Akhmediev, N.: Waves that appear from nowhere: complex rogue wave structures and their elementary particles. Front. Phys. **8**, 612318 (2021)

Akhmediev, N.N., Korneev, V.I.: Modulation instability and periodic solutions of the nonlinear Schrödinger equation. Theor. Math. Phys. **69**, 1089 (1986)

Akhmediev, N., Eleonskii, V., Kulagin, N.: Exact first-order solutions of the nonlinear Schrödinger equation. Theor. Math. Phys. **72**, 809 (1987)

Alwashahi, S., Aleksić, N.B., Belić, M.R., Nikolić, S.N.: Kuznetsov–Ma rogue wave clusters of the nonlinear Schrödinger equation. Nonlinear Dyn. **111**, 12495–12509 (2023)

Anderson, D., Lisak, M.: Nonlinear asymmetric self-phase modulation and self-steepening of pulses in long optical waveguides. Phys. Rev. A **27**, 1393 (1983)

Ankiewicz, A., Akhmediev, N.: Multi-rogue waves and triangular numbers. Roman. Rep. Phys. **69**, 104 (2017)

Ankiewicz, A., Soto-Crespo, J.M., Akhmediev, N.: Rogue waves and rational solutions of the Hirota equation. Phys. Rev. E **81**, 046602 (2010)

Ankiewicz, A., Kedziora, D.J., Chowdury, A., Bandelow, U., Akhmediev, N.: Infinite hierarchy of nonlinear Schrödinger equations and their solutions. Phys. Rev. E **93**, 012206 (2016)

Backus, S., Durfee, C.G., III., Mourou, G., Kapteyn, H.C., Murnane, M.M.: 0.2-TW laser system at 1 kHz. Opt. Lett. **22**, 1256 (1997)

Bao, W.: The nonlinear Schrödinger equation and applications in Bose–Einstein condensation and plasma physics. In: Lecture Note Series, IMS, NUS, vol. **9** (2007)

Belić, M.R., Nikolić, S.N., Ashour, O.A., Aleksić, N.B.: On different aspects of the optical rogue waves nature. Nonlinear Dyn. **108**, 1655–1670 (2022)

Biswas, A., Khalique, C.M.: Stationary solutions for nonlinear dispersive Schrödinger equation. Nonlinear Dyn. **63**, 623–626 (2011)

Bludov, Y.V., Konotop, V.V., Akhmediev, N.: Matter rogue waves. Phys. Rev. A **80**, 033610 (2009)

Busch, T., Anglin, J.R.: Dark-bright solitons in inhomogeneous Bose–Einstein condensates. Phys. Rev. Lett. **87**, 010401 (2001)

Chin, S.A., Ashour, O.A., Belić, M.R.: Anatomy of the Akhmediev breather: cascading instability, first formation time, and Fermi–Pasta–Ulam recurrence. Phys. Rev. E **92**, 063202 (2015)

Chowdury, A., Kedziora, D.J., Ankiewicz, A., Akhmediev, N.: Breather solutions of the integrable nonlinear Schrödinger equation and their interactions. Phys. Rev. E **91**, 022919 (2015a)

Chowdury, A., Kedziora, D.J., Ankiewicz, A., Akhmediev, N.: Breather-to-soliton conversions described by the quintic equation of the nonlinear Schrödinger hierarchy. Phys. Rev. E **91**, 032928 (2015b)

Dai, C.Q., Wang, Y.Y.: Controllable combined Peregrine soliton and Kuznetsov-Ma soliton in PTPT-symmetric nonlinear couplers with gain and loss. Nonlinear Dyn. **80**, 715–721 (2015)

Dubard, P., Gaillard, P., Klein, C., Matveev, V.B.: On multi-rogue wave solutions of the NLS equation and positon solutions of the KdV equation. Eur. Phys. J. Spec. Top. **185**, 247 (2010)

Dudley, J.M., Taylor, J.M.: Supercontinuum Generation in Optical Fibers. Cambridge University Press, Cambridge (2010)

Dudley, J.M., Genty, G., Eggleton, B.J.: Harnessing and control of optical rogue waves in supercontinuum generation. Opt. Express **16**, 3644 (2008)

Dudley, J.M., Dias, F., Erkintalo, M., Genty, G.: Instabilities, breathers and rogue waves in optics. Nat. Photon. **8**, 755 (2014)

Fibich, G.: The Nonlinear Schrödinger Equation. Springer, Berlin (2015)

Fleischhauer, M., Imamoglu, A., Marangos, J.P.: Electromagnetically induced transparency: optics in coherent media. Rev. Mod. Phys. **77**, 633–673 (2005)

Gaillard, P.: Degenerate determinant representation of solutions of the nonlinear Schrödinger equation, higher order Peregrine breathers and multi-rogue waves. J. Math. Phys. **54**, 013504 (2013)

Garrett, C., Gemmrich, J.: Rogue waves. Phys. Today **62**, 62 (2009)

He, J.S., Zhang, H.R., Wang, L.H., Porsezian, K., Fokas, A.S.: Generating mechanism for higher-order rogue waves. Phys. Rev. E **87**, 052914 (2013)

Kedziora, D.J., Ankiewicz, A., Akhmediev, N.: Rogue wave triplets. Phys. Lett. A **375**, 2782 (2011a)

Kedziora, D.J., Ankiewicz, A., Akhmediev, N.: Circular rogue wave clusters. Phys. Rev. E **84**, 056611 (2011b)

Kedziora, D.J., Ankiewicz, A., Akhmediev, N.: Triangular rogue wave cascades. Phys. Rev. E **86**, 056602 (2012)

Kedziora, D.J., Ankiewicz, A., Akhmediev, N.: Classifying the hierarchy of nonlinear-Schödinger-equation rogue-wave solutions. Phys. Rev. E **88**, 013207 (2013)

Kedziora, D.J., Ankiewicz, A., Chowdury, A., Akhmediev, N.: Integrable equations of the infinite nonlinear Schrödinger equation hierarchy with time variable coefficients. Chaos **25**, 103114 (2015)

Kibler, B., Fatome, J., Finot, C., Millot, G., Dias, F., Genty, G., Akhmediev, N., Dudley, J.M.: The Peregrine soliton in nonlinear fibre optics. Nat. Phys. **6**, 790–795 (2010)

Kibler, B., Fatome, J., Finot, C., Millot, G., Genty, G., Wetzel, B., Akhmediev, N., Dias, F., Dudley, J.M.: Observation of Kuznetsov–Ma soliton dynamics in optical fibre. Sci. Rep. **2**, 463 (2012)

Kibler, B., Fatome, J., Finot, C., Millot, G., Dias, F., Genty, G., Akhmediev, N., Dudley, J.M.: Observation of Kuznetsov–Ma soliton dynamics in optical fibre. Sci. Rep. **6**, 463 (2012)

Kivshar, Y.S., Agrawal, G.P.: Optical Solitons. Academic Press, San Diego (2003)

Krmpot, A.J., Ćuk, S.M., Nikolić, S.N., Radonjić, M., Slavov, D.G., Jelenković, B.M.: Dark Hanle resonances from selected segments of the Gaussian laser beam cross-section. Opt. Express **17**, 22491–22498 (2009)

Li, X.-L., Guo, R.: Interactions of localized wave structures on periodic backgrounds for the coupled Lakshmanan–Porsezian–Daniel equations in birefringent optical fibers. Ann. Phys. **535**, 2200472 (2023)

Li, Z.-Y., Li, F.-F., Li, H.-J.: Exciting rogue waves, breathers, and solitons in coherent atomic media. Commun. Theor. Phys. **72**, 075003 (2020)

Li, J., Yang, Z.-J., Zhang, S.-M.: Periodic collision theory of multiple cosine-Hermite-Gaussian solitons in Schrödinger equation with nonlocal nonlinearity. Appl. Math. Lett. **140**, 108588 (2023)

Mani Rajan, M.S., Mahalingam, A.: Nonautonomous solitons in modified inhomogeneous Hirota equation: soliton control and soliton interaction. Nonlinear Dyn. **79**, 2469–2484 (2015)

Matveev, V.B., Salle, M.A.: Darboux Transformations and Solitons. Springer, Berlin (1991)

Mirzazadeh, M., Eslami, M., Zerrad, E., Mahmood, M.F., Biswas, A., Belić, M.: Optical solitons in nonlinear directional couplers by sine-cosine function method and Bernoulli's equation approach. Nonlinear Dyn. **81**, 1933–1349 (2015)

Nikolić, S.N., Radonjić, M., Krmpot, A.J., Lučić, N.M., Zlatković, B.V., Jelenković, B.M.: Effects of a laser beam profile on Zeeman electromagnetically induced transparency in the Rb buffer gas cell. J. Phys. B At. Mol. Opt. Phys. **46**, 075501 (2013)

Nikolić, S.N., Radonjić, M., Lučić, N.M., Krmpot, A.J., Jelenković, B.M.: Transient development of Zeeman electromagnetically induced transparency during propagation of Raman–Ramsey pulses through Rb buffer gas cell. J. Phys. B At. Mol. Opt. Phys. **48**, 045501 (2015)

Nikolić, S.N., Aleksić, N.B., Ashour, O.A., Belić, M.R., Chin, S.A.: Systematic generation of higher-order solitons and breathers of the Hirota equation on different backgrounds. Nonlinear Dyn. **89**, 1637–1649 (2017)

Nikolić, S.N., Aleksić, N.B., Ashour, O.A., Belić, M.R., Chin, S.A.: Breathers, solitons and rogue waves of the quintic nonlinear Schrödinger equation on various backgrounds. Nonlinear Dyn. **95**, 2855–2865 (2019)

Nikolić, S.N., Ashour, O.A., Aleksić, N.B., Zhang, Y., Belić, M.R., Chin, S.A.: Talbot carpets by rogue waves of extended nonlinear Schrödinger equations. Nonlinear Dyn. **97**, 1215 (2019)

Nikolić, S.N., Alwashahi, S., Ashour, O.A., Chin, S.A., Aleksić, N.B., Belić, M.R.: Multi-elliptic rogue wave clusters of the nonlinear Schrödinger equation on different backgrounds. Nonlinear Dyn. **108**, 479–490 (2022)

Ohta, Y., Yang, J.: General high-order rogue waves and their dynamics in the nonlinear Schrödinger equation. Proc. R. Soc. A **468**, 1716 (2012)

Osborne, A.: Nonlinear Ocean Waves and the Inverse Scattering Transform. Academic Press, Cambridge (2010)

Peregrine, D.H.: Water waves, nonlinear Schrödinger equations and their solutions. J. Austral. Math. Soc. B **25**, 16 (1983)

Shen, S., Yang, Z., Li, X., Zhang, S.: Periodic propagation of complex-valued hyperbolic-cosine-Gaussian solitons and breathers with complicated light field structure in strongly nonlocal nonlinear media. Commun. Nonlinear Sci. Numer. Simul. **103**, 106005 (2021)

Shen, S., Yang, Z.-J., Pang, Z.-G., Ge, Y.-R.: The complex-valued astigmatic cosine-Gaussian soliton solution of the nonlocal nonlinear Schrödinger equation and its transmission characteristics. Appl. Math. Lett. **125**, 107755 (2022)

Shen, Y., Tian, B., Zhou, T.Y., Cheng, C.D.: Localized waves of the higher-order nonlinear Schrödinger-Maxwell-Bloch system with the sextic terms in an erbium-doped fiber. Nonlinear Dyn. (2023). https://doi.org/10.1007/s11071-023-09005-5

Shrira, V.I., Geogjaev, V.V.: What makes the Peregrine soliton so special as a prototype of freak waves? J. Eng. Math. **67**, 11 (2010)

Shukla, P.K., Eliasson, B.: Nonlinear aspects of quantum plasma physics. Phys. Usp. **53**, 51 (2010)

Solli, D.R., Ropers, C., Jalali, B.: Active control of rogue waves for stimulated supercontinuum generation. Phys. Rev. Lett. **101**, 233902 (2008)

Song, L.-M., Yang, Z.-J., Li, X.-L., Zhang, S.-M.: Coherent superposition propagation of Laguerre–Gaussian and Hermite–Gaussian solitons. Appl. Math. Lett. **102**, 106114 (2020)

Sun, Z.-Y., Deng, D., Pang, Z.-G., Yang, Z.-J.: Nonlinear transmission dynamics of mutual transformation between array modes and hollow modes in elliptical sine-Gaussian cross-phase beams. Chaos Solitons Fractals **178**, 114398 (2024)

Wang, D.-S., Chen, F., Wen, X.-Y.: Darboux transformation of the general Hirota equation: multisoliton solutions, breather solutions and rogue wave solutions. Adv. Differ. Equ. **2016**, 67 (2016)

Xiong, H., Gan, J., Wu, Y.: Kuznetsov–Ma soliton dynamics based on the mechanical effect of light. Phys. Rev. Lett. **119**, 153901 (2017)

Yang, Y., Yan, Z., Malomed, B.A.: Rogue waves, rational solitons, and modulational instability in an integrable fifth-order nonlinear Schrödinger equation. Chaos **25**, 103112 (2015)

Yang, Z.-J., Zhang, S.-M., Li, X.-L., Pang, Z.-G., Bu, H.-X.: High-order revivable complex-valued hyperbolic-sine-Gaussian solitons and breathers in nonlinear media with a spatial nonlocality. Nonlinear Dyn. **94**, 2563–2573 (2018)

Zakharov, V.E.: Stability of periodic waves of finite amplitude on a surface of deep fluid. J. Appl. Mech. Tech. Phys. **9**, 15 (1968)

Zakharov, V.E., Shabat, A.B.: Exact theory of two-dimensional self-focusing and one-dimensional self-modulation of waves in nonlinear media. J. Exp. Theor. Phys. **34**, 62 (1972)

Zou, Z., Guo, R.: The Riemann–Hilbert approach for the higher-order Gerdjikov-Ivanov equation, soliton interactions and position shift. Commun. Nonlinear Sci. Numer. Simul. **124**, 107316 (2023)

WAVE AMPLIFICATION OUTSIDE OF
THE MODULATION INSTABILITY BAND

STANKO N. NIKOLIĆ[1,2,a], NAJDAN B. ALEKSIĆ[1,3,b], WIESLAV KROLIKOWSKI[1,4,c],
MILIVOJ R. BELIĆ[1,3,d], NAIL AKHMEDIEV[5,e]

[1]Division of Arts and Sciences, Texas A&M University at Qatar, P.O. Box 23874 Doha, Qatar
[2]Institute of Physics Belgrade, University of Belgrade, Pregrevica 118, 11080 Belgrade, Serbia
Corresponding author[a]: stankon@ipb.ac.rs
[3]Serbian Academy of Nonlinear Sciences, Kneza Mihaila 36, Belgrade, Serbia
E-mail [b]: najdan@gmail.com
E-mail [d]: milivoj.belic@qatar.tamu.edu
[4]Department of Quantum Science and Technology, Research School of Physics, Australian National
University, Canberra, ACT 2601, Australia
E-mail [c]: wieslaw.krolikowski@qatar.tamu.edu
[5]Department of Fundamental and Theoretical Physics, Research School of Physics, The Australian
National University, Canberra, ACT 2600, Australia
E-mail [e]: Nail.Akhmediev@anu.edu.au

Abstract. We show that linear stability analysis not only describes the effect of modulation instability of a plane wave in nonlinear media but it also predicts significant wave amplification outside of the standard instability band. As an example, we consider the classic MI in the case of the nonlinear Schrödinger equation. However, similar amplification may take place in many other nonlinear media that admit modulation instability.

Key words: Nonlinear Schrödinger equation, modulation instability.

1. INTRODUCTION

Modulation instability (MI) is one of the fundamental natural phenomena that is well known in optics [1], in hydrodynamics [2] and many other branches of nonlinear wave physics [3–7]. In simple terms, MI is the phenomenon of exponential growth of small periodic perturbations applied to a plane wave when the frequency of the perturbation lies within the instability band limited both from below and from above [8]. The lower limit is commonly zero frequency (long wave perturbations). The upper limit depends on a particular model of nonlinear medium. There are nonlinear media that admit several bands of instability. Here, we restrict ourselves with the case of a single instability band. This is the case for the most common model of waves described by the nonlinear Schrödinger equation (NLSE). It is also known that MI can cause appearance of rogue waves (RW) in systems described by the NLSE [9, 10]. This model is universal in the sense that it describes wide range of nonlinear

waves in physics. As we use the standard linear stability analysis for the description of modulations instability, our method can be easily applied to other models of nonlinear media.

It is commonly believed that beyond the upper limit of the MI band the plane wave is stable. In other words, small perturbations grow exponentially within the instability band and remain restricted outside of this band. This follows from the linear stability analysis of fixed points based on the ideas of nonlinear dynamics [11]. Indeed, the transition from the unstable region to the stable one is a switch from a saddle point to a centre in terms of nonlinear dynamics [12]. The saddle point is unstable with phase trajectories diverging from it, while the centre is stable with phase trajectories oscillating around it. However, in the recent works [13, 14], based on exact solutions of the NLSE, it was shown that the amplitude of small perturbations rises even outside the instability band. Periodic perturbations are amplified at 'stable' frequencies contrary to the predictions of linear stability analysis. This controversy suggests that the linear stability analysis has to be reconsidered or at least more careful analysis should be provided. Such careful analysis is given in the present work.

2. STANDARD LINEAR STABILITY ANALYSIS OF A PLANE WAVE IN A NONLINEAR MEDIUM

We begin our consideration with the standard linear stability analysis of a plane wave in a medium that is described by the nonlinear Schrödinger equation (NLSE) [15, 16]. In normalised form, the NLSE can be written as

$$i\frac{\partial \psi}{\partial t} + \frac{1}{2}\frac{\partial^2 \psi}{\partial x^2} + |\psi|^2 \psi = 0. \tag{1}$$

where $\psi(x,t)$ is an envelope of a wave, t is an evolution variable, and x is the 'tranverse' variable. The physical meaning of these variables depends on the particular physical problem under investigation. Solutions of the NLSE in the form (1) involve fast rotating phase. In order to switch from the fast rotating complex plane to a fixed one, we rewrite the wave function ψ as

$$\psi(x,t) = \overline{\psi}(x,t)e^{it}. \tag{2}$$

After the substitution of Eq. (2) into (1) we get:

$$i\frac{\partial \bar{\psi}}{\partial t} + \frac{1}{2}\frac{\partial^2 \bar{\psi}}{\partial x^2} + \left(|\bar{\psi}|^2 - 1\right)\bar{\psi} = 0. \tag{3}$$

The plane wave solution of Eq. (3) is $\bar{\psi} = 1$. We ignore the constant arbitrary phase of the wave.

Let us consider a small amplitude periodic perturbation applied to this plane

wave,

$$\bar{\psi}(x,t) = 1 + \varepsilon F(t)\cos\omega x. \tag{4}$$

where ϵ is a small real parameter, while ω is the angular frequency of the perturbation. Here, $F(t)$ is a complex function with real part $f(t)$ and imaginary part $g(t)$. Using this notation, $\bar{\psi}$ can be rewritten as:

$$\bar{\psi}(x,t) = 1 + \varepsilon f(t)\cos\omega x + i\varepsilon g(t)\cos\omega x. \tag{5}$$

Substitution of Eq. (5) into (3), in the first order in ϵ leads to:

$$-\varepsilon g'(t)\cos\omega x - \frac{1}{2}\varepsilon f(t)\omega^2\cos\omega x + 2\varepsilon f(t)\cos\omega x +$$
$$+ i\left(\varepsilon f'(t)\cos\omega x - \frac{1}{2}\varepsilon g(t)\omega^2\cos\omega x\right) = 0. \tag{6}$$

All terms ε^n of the order higher than $n \geq 2$ have been neglected. From Eq. (6) we get:

$$f' = \frac{1}{2}\omega^2 g \tag{7}$$

and

$$g' = \left(2 - \frac{\omega^2}{2}\right) f. \tag{8}$$

If we differentiate Eq. (7) and substitute g' from the expression (8) we get:

$$f''(t) - \frac{\omega^2}{4}\left(4 - \omega^2\right) f(t) = 0. \tag{9}$$

We obtain the second-order linear differential equation for $f(t)$. The function $g(t)$ satisfies the same equation:

$$g''(t) - \frac{\omega^2}{4}\left(4 - \omega^2\right) g(t) = 0. \tag{10}$$

The solutions of Eqs. (9) and (10) are:

$$f(t) = A_f e^{\lambda t} + B_f e^{-\lambda t} \tag{11}$$

$$g(t) = A_g e^{\lambda t} + B_g e^{-\lambda t}, \tag{12}$$

where

$$\lambda = \frac{\omega}{2}\sqrt{4 - \omega^2}. \tag{13}$$

Equation (13) is the well known expression for the growth rate of instability. Here λ is real within the interval of frequencies $\omega \in (0,2)$. This means that the small periodic perturbations of the plane wave grow within this interval due to the term with the exponential factor $e^{\lambda t}$ in the solution. The plot of $\lambda(\omega)$ is shown in Fig. 1 by the blue curve.
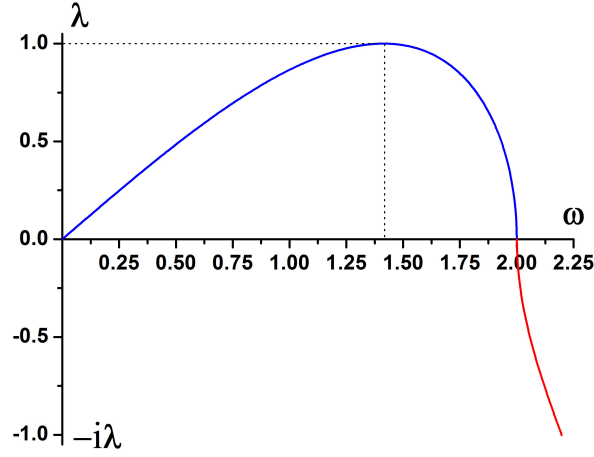
Fig. 1 – The modulation instability growth rate λ for $0 < \omega < 2$ (blue curve). The pure imaginary continuation of λ beyond $\omega > 2$ corresponds to the frequency of oscillations of the perturbation outside of the instability band. It is shown by the red curve.

The growth rate λ becomes imaginary above the threshold frequency $\omega > 2$:

$$\bar{\omega} = -i\lambda = \frac{\omega}{2}\sqrt{\omega^2 - 4}. \tag{14}$$

It is shown by the red curve in Fig. 1. Exponential solutions (11) and (12) are transformed into oscillating ones in this area with $\bar{\omega}$ being the frequency of these oscillations. This means that when $\omega > 2$, the perturbations of the plane wave do not grow. They oscillate in t keeping the plane wave stable. These are the common conclusions in the theory of modulation instability [1, 2].

However, this simple approach to modulation instability does not explain more complex phenomena of wave amplification beyond the instability band that have been found recently in Ref. [13]. Therefore, let us consider the linear stability analysis in more detail than it is commonly done.

3. LINEAR STABILITY ANALYSIS IN MORE DETAIL

According to the nonlinear dynamics theory, the plane wave solution of the NLSE is a fixed point in the phase space of the system. Linear stability analysis of the previous section provides us with phase trajectories around this fixed point. The set of these trajectories comprises the phase portrait of the system around the fixed point.

Examples of the phase portraits of the system within the instability band are shown in Fig. 2. For every perturbation frequency, the phase portrait is a saddle. This follows from Eqs. (11) and (12). However, the direction of the separatrices in a

saddle point changes with the frequency. The orientation of the separatrices is nearly vertical when ω is close to zero frequency. This case is shown in Fig. 2(a). The separatrices are located at 45 degrees to the real and imaginary axes of the complex plane when $\omega = \sqrt{2}$ and the growth rate of instability is maximal. This case is shown in Fig. 2(b). The orientation of separatrices becomes nearly horizontal close to the upper limiting frequency $\omega = 2$. This case is illustrated in Fig. 2(c).

These phase portraits provide us with the information about the phases of the perturbation and the direction of further evolution of the plane wave. The blue and red trajectories result in two qualitatively different orbits in the nonlinear evolution of the system. These differences have been elucidated in detail in Ref. [13]. The evolution along the separatrices results in the excitation of Akhmediev breathers. Thus, the choice of the initial phase of the perturbation relative to the plane wave results in variety of outcomes in the nonlinear stage of evolution.
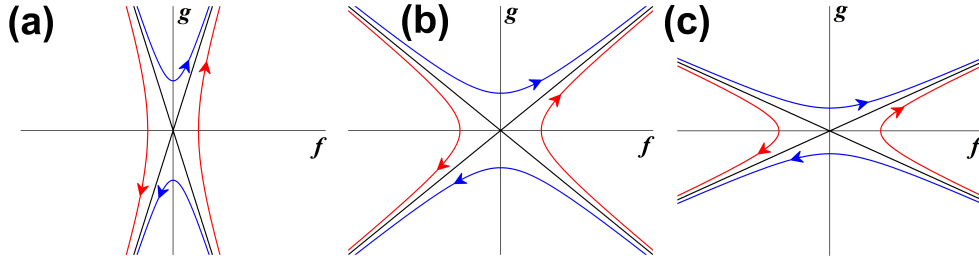
Fig. 2 – The phase portraits around the unperturbed plane wave solution within the instability band when the frequency changes from left to right: (a) $\omega = 0.5$, (b) $\omega = \sqrt{2}$, and (c) $\omega = 1.75$. In all cases, these are saddle points but with changed preferred directions of evolution. At the extreme points $\omega = 0$ and $\omega = 2.0$, the saddle point becomes vertical and horizontal respectively. At the point of maximum growth rate the saddle point is oriented at 45 degrees to the axes.

Now, let us turn to the 'stable' case when $\omega > 2$. Is the plane wave really stable here? In order to see the shape of the trajectories in this region, we divide Eq. (7) by (8):

$$\frac{df}{dg} = \frac{\frac{1}{2}g\omega^2}{\left(2 - \frac{\omega^2}{2}\right)f} \quad \Rightarrow \quad \frac{f\,df}{\omega^2} + \frac{g\,dg}{\omega^2 - 4} = 0. \tag{15}$$

Integration of Eq. (15), results in the equation for ellipses:

$$\frac{f^2}{\left(\omega\sqrt{C}\right)^2} + \frac{g^2}{\left(\sqrt{\omega^2 - 4}\sqrt{C}\right)^2} = 1, \tag{16}$$

where C is an integration constant. The fixed point $f = 0$ and $g = 0$ is the centre of the ellipses.

Examples of the phase portraits of the system outside the instability band are

shown in Fig. 3. For every frequency above the point $\omega = 2$, the fixed point is a centre. In all cases, trajectories around the fixed point are concentric ellipses with horizontal $a_\omega = \omega\sqrt{C}$ and vertical $b_\omega = \sqrt{(\omega^2 - 4)C}$ semi-axes. The ratio between the two semi-axes depends on ω:

$$\frac{b_\omega}{a_\omega} = \sqrt{1 - \frac{4}{\omega^2}}. \tag{17}$$

The ratio b_ω/a_ω tends to 0 when ω is slightly higher than 2 and the ellipses are elongated, as in Fig. 3(a) calculated for $\omega = 2.01$. Thus, right above the upper boundary of instability, $\omega = 2$, the ellipses are strongly elongated along the real axis. The elongation is the largest when ω is close to 2. This elongation is a natural continuation of elongated saddle at the left hand side of the special point $\omega = 2$. The practical outcome of this elongation is the growth of the modulation amplitude even beyond the instability band. Thus, small periodic perturbation on top of a plane wave will be amplified despite the plane wave at these frequencies is known to be 'stable'.

The ratio b_ω/a_ω is increasing as ω increases. Thus, the ellipses become less elongated. Figure 3(b) illustrates the case when $\omega = 2.04$. Consequently, the amplification becomes smaller further away from the point $\omega = 2.0$. When $\omega \to +\infty$, this ratio is approaching 1, thus, transforming the ellipses to circles. The case of higher $\omega = 2.5$ is illustrated in Fig. 3(c).
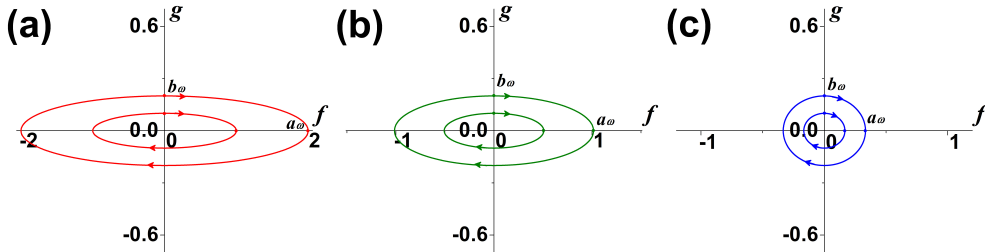

Fig. 3 – The phase portraits around the unperturbed plane wave solution outside the instability band when the frequency changes from left to right: (a) $\omega = 2.01$, (b) $\omega = 2.04$, and (c) $\omega = 2.5$. The fixed points are always centres with the elliptical phase trajectories around the fixed point. The ellipses are strongly elongated horizontally when the frequency is slightly above the limiting one $\omega = 2$.

One essential point is that the initial perturbation must be 90 degrees out of phase to the plane wave in order to be amplified. If the perturbation and the plane wave are in phase, the perturbation will decrease in amplitude as can be seen from Fig. 3(a).

One additional point here is that the perturbation despite being small must be finite in order to be amplified. This makes the distinction between the amplification in the stable region from the exponential growth of perturbation in the region of

instability. This fact is not a limitation, because in most of the practical applications and in experiments, perturbations are finite.

We should also mention that we are not considering chaotic perturbations here that consist of many frequencies. The latter is the case in natural conditions like for ocean waves, for example. We only consider perturbations at fixed frequencies that is the case for the lab experiments.

The amplification factor G of the modulation beyond the MI interval is

$$G = \frac{\left|\hat{\psi}\left(t = t_m\right)\right|}{\left|\hat{\psi}\left(t = 0\right)\right|} = \frac{a_\omega}{b_\omega}, \tag{18}$$

assuming that evolution starts from the point $(f,g) = (0, b_\omega)$. Note that $\hat{\psi}$ is the fundamental Fourier mode at frequency ω of the wave function $\bar{\psi}$, while time t_m is equal to one quarter of oscillation period:

$$t_m = \bar{T}/4 = \frac{\pi}{2\bar{\omega}} = \frac{\pi}{\omega\sqrt{\omega^2 - 4}}. \tag{19}$$

From Eqs. (17) and (18) we get the amplification factor in terms of the frequency:

$$G = \frac{1}{\sqrt{1 - \frac{4}{\omega^2}}}. \tag{20}$$

In order to check the amplification formula (20), we run the numerical simulations of NLSE with periodic boundary conditions, starting from the weak cosine perturbation

$$\psi\left(x, t = 0\right) = 1 + i\varepsilon\cos\omega x. \tag{21}$$

We take $\varepsilon = 10^{-4}$ to be small enough so the linear approximation holds during simulation time. The x-box size is chosen to be equal to exactly one spatial period $L = 2\pi/\omega$. The obtained intensity distribution $|\psi|^2$ in the xt-plane during numerical evolution is shown in Fig. 4 for the four cases: (a) $\omega = 2.001$, (b) $\omega = 2.01$, (c) $\omega = 2.05$, and (d) $\omega = 3.5$. One can see that no characteristic solutions of NLSE, such as Akhmediev breathers, were observed since we are in the region of stability ($\omega > 2$). However, we measure the $\left|\hat{\psi}\left(t = t_m\right)\right|$ and $\left|\hat{\psi}\left(t = 0\right)\right|$ from numerical data and calculate the numerical gain of the principal Fourier mode. The simulation results confirmed that maximal amplification occurs at t_m (Eq. (19)) and it is exactly equal to theoretical prediction. This can be seen in Fig. 5. The red curve corresponds to function from Eq. (20), while black squares indicate our numerical results. As it follows from Eq. (20), the amplification factor has an infinite limit when $\omega \to 2$. This may have practical applications.

We should also take into account that the period of oscillations $\bar{T} = 2\pi/\bar{\omega}$ is infinitely large close to the point $\omega = 2$ but becomes fixed at larger frequencies. This
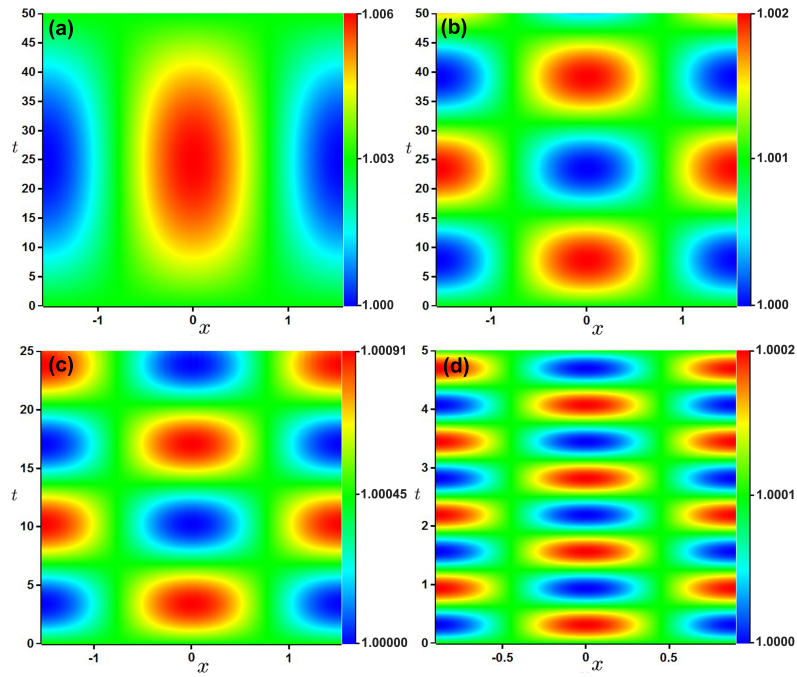
Fig. 4 – Numerical simulations of NLSE with initial conditions given by weak perturbation (amplitude 0.0001) with angular frequency: (a) $\omega = 2.001$, (b) $\omega = 2.01$, (c) $\omega = 2.05$, (d) $\omega = 3.5$.
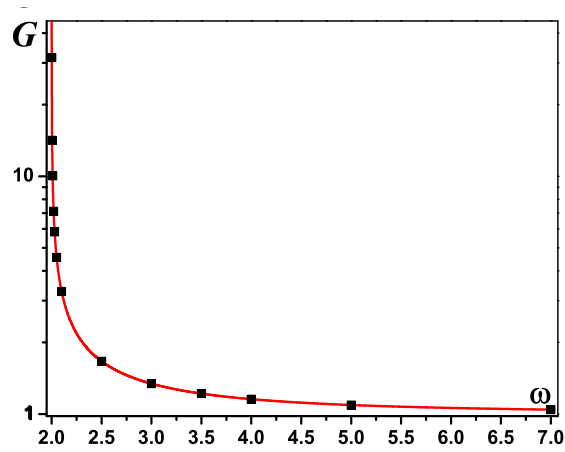

Fig. 5 – The theoretical gain G *versus* the frequency of perturbation ω from Eq. (20) (red curve). The black squares show simulation results.

means that the amplitude of the perturbation reaches it maximum value in a fixed time interval. This is in contrast to trajectories that start at saddle points. In the latter case,

the time of evolution is very sensitive to the choice of the initial conditions. This time becomes infinite when the initial point is located on the separatrix. The fixed time of evolution outside the instability band can be considered as an advantage when the effect is used in particular devices. This fact may increase the accuracy of the amplification.

4. CONCLUSIONS

The effect of wave amplification outside the instability band is one of the unexpected effects that may have far reaching consequences in optics and hydrodynamics. In order to demonstrate its existence, we considered here the nonlinear medium that can be described by the NLSE. The latter is well known and besides, it is integrable so that all its solutions can be presented in exact form [13] thus confirming the results of the linear stability analysis.

However, modulation instability is a much more common phenomenon in nature. Thus, a similar analysis can be applied to other nonlinear wave equations that are not necessarily integrable. In the latter case, the linear stability analysis can provide the first approach for solving the problem. Applying these ideas to other systems, may extend the range of technology devices build on new form of wave amplification [14].

For example, the systems described by Manakov equations may have several instability bands [17]. Each of them has limiting frequencies that are special points requiring more careful analysis than before. Some other systems may also have several instability bands. Among them, we can mention nonlocal nonlinear media [18]. They also deserve more careful analysis similar to the one given above.

Declaration of Competing interest

The authors declare that they have no known competing financial interests or personal relationships that could have appeared to influence the work reported in this paper.

Data Availability

All data generated or analyzed during this study are included in the published article.

REFERENCES

1. V.I. Bespalov and V.I. Talanov, Filamentary structure of light beams in nonlinear liquids, JETP Lett., **3**, 307 (1966).

2. T. B. Benjamin and J. E. Feir, The disintegration of wave trains on deep water. Part 1. Theory. J. Fluid Mechanics, **27**, 417 – 430 (1967).

3. S. Trillo and S. Wabnitz, Dynamics of the nonlinear modulational instability in optical fibers, Opt. Lett., **16**, 986 (1991),

4. C. M. de Sterke, Theory of modulational instability in fiber Bragg gratings, J. Opt. Soc. Am. B **15**, 2660 (1998).

5. G. Millot, Multiple four-wave mixing-induced modulational instability in highly birefringent fibers, Opt. Lett., **26**, 1391 (2001).

6. T. Tanemura and K. Kikuchi, Unified analysis of modulational instability induced by cross-phase modulation in optical fibers, J. Opt. Soc. Am. B **20**, 2502 (2003).

7. A. Armaroli and S. Trillo, Modulational instability due to cross-phase modulation *versus* multiple four-wave mixing: the normal dispersion regime, JOSA B **31**, 551 (2014).

8. G. P. Agrawal, Nonlinear Fiber Optics, 4-th edn., (Academic Press, NY, 2007).

9. N. Akhmediev *et al.*, Roadmap on optical rogue waves and extreme events. J. Opt. **18**, 063001 (2016)

10. M.R. Belić, S.N. Nikolić, O.A. Ashour, N.B. Aleksić, On different aspects of the optical rogue waves nature. Nonlinear Dyn. **108**, 1655–1670 (2022).

11. A. A. Andronov, A. A. Vitt, and S. E. Khaikin, (eds.), Theory of Oscillators, Pergamon Press Ltd, London, 1966.

12. E.M. Gromov, V.V. Tyutin, Stationary waves in a third-order nonlinear Schrödinger equation. Wave Motion **28**, 13-24 (1998).

13. M. Conforti, A. Mussot, A. Kudlinski, S. Trillo, and N. Akhmediev, Doubly periodic solutions of the focusing nonlinear Schrödinger equation: Recurrence, period doubling, and amplification outside the conventional modulation-instability band, Phys. Rev. A **101**, 023843 (2020).

14. G. Vanderhaegen, C. Naveau, P. Szriftgiser, A. Kudlinski, M. Conforti, A. Mussot, M. Onorato, S. Trillo, A. Chabchoub, and N. Akhmediev, "Extraordinary" modulation instability in optics and hydrodynamics, PNAS, **118**, e2019348118 (2021).

15. G. Fibich, The Nonlinear Schrödinger Equation. Springer, Berlin (2015).

16. B.E.A. Saleh, M.C. Teich, Fundamentals of Photonics. John Wiley & Sons, Inc. (1991).

17. Shao-Chun Chen, Chong Liu, and N. Akhmediev, Higher-order modulation instability and multi-Akhmediev breathers of Manakov equations: Frequency jumps over the stable gaps between the instability bands, Submitted to PRA, Manuscript AC12531.

18. W. Krolikowski, O. Bang, J. J. Rasmussen, and J. Wyller, Modulational instability in nonlocal nonlinear Kerr media, Phys. Rev. E **64**, 016612 (2001).

Mapping the Direction of Nucleocytoplasmic Transport of Glucocorticoid Receptor (GR) in Live Cells Using Two-Foci Cross-Correlation in Massively Parallel Fluorescence Correlation Spectroscopy (mpFCS)

Stanko N. Nikolić,[∥] Sho Oasa,[∥] Aleksandar J. Krmpot,[∥] Lars Terenius, Milivoj R. Belić, Rudolf Rigler,[⊥,#] and Vladana Vukojević*,[⊥]

ACCESS | 📊 Metrics & More | 📖 Article Recommendations | 🆂�🅸 Supporting Information

ABSTRACT: Nucleocytoplasmic transport of transcription factors is vital for normal cellular function, and its breakdown is a major contributing factor in many diseases. The glucocorticoid receptor (GR) is an evolutionarily conserved, ligand-dependent transcription factor that regulates homeostasis and response to stress and is an important target for therapeutics in inflammation and cancer. In unstimulated cells, the GR resides in the cytoplasm bound to other molecules in a large multiprotein complex. Upon stimulation with endogenous or synthetic ligands, GR translocation to the cell nucleus occurs, where the GR regulates the transcription of numerous genes by direct binding to glucocorticoid response elements or by physically associating with other transcription factors. While much is known about molecular mechanisms underlying GR function, the spatial organization of directionality of GR nucleocytoplasmic transport remains less well characterized, and it is not well understood how the bidirectional nucleocytoplasmic flow of GR is coordinated in stimulated cells. Here, we use two-foci cross-correlation in a massively parallel fluorescence correlation spectroscopy (mpFCS) system to map in live cells the directionality of GR translocation at different positions along the nuclear envelope. We show theoretically and experimentally that cross-correlation of signals from two nearby observation volume elements (OVEs) in an mpFCS setup presents a sharp peak when the OVEs are positioned along the trajectory of molecular motion and that the time position of the peak corresponds to the average time of flight of the molecule between the two OVEs. Hence, the direction and velocity of nucleocytoplasmic transport can be determined simultaneously at several locations along the nuclear envelope. We reveal that under ligand-induced GR translocation, nucleocytoplasmic import/export of GR proceeds simultaneously but at different locations in the cell nucleus. Our data show that mpFCS can characterize in detail the heterogeneity of directional nucleocytoplasmic transport in a live cell and may be invaluable for studies aiming to understand how the bidirectional flow of macromolecules through the nuclear pore complex (NPC) is coordinated to avoid intranuclear transcription factor accretion/abatement.
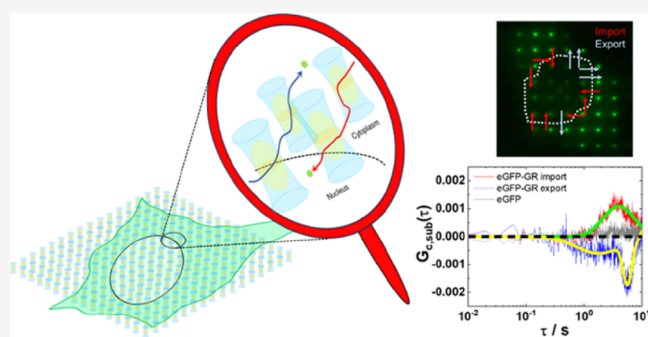
The concentration of transcription factors in the cell nucleus is a key determinant of the kinetics of gene transcription, through which cell identity and function are eventually conferred.[1,2] It is dynamically controlled in live cells by means of transcription factor import/export into/out of the cell nucleus via the nuclear pore complex (NPC), which is accomplished through two basic mechanisms: passive diffusion and active directional transport.[3,4] While our understanding of the energetics of the nucleocytoplasmic transport and the biochemical composition and overall organization of the NPC, which is the sole bidirectional gateway through which molecules pass in/out of the cell nucleus, is continuously improving,[5,6] the spatial organization of directionality of nucleocytoplasmic transport in a single cell remains less well characterized and it is not well

understood how the bidirectional nucleocytoplasmic flow of macromolecules is coordinated. The main obstacle to progress is the limited number of analytical methods that can quantitatively characterize the directionality of nucleocytoplasmic transport in live cells at multiple spots simultaneously.

To date, time-resolved fluorescence microscopy imaging and correlation spectroscopy techniques have been shown to be

well suited to address this problem in live cells. For example, fluorescence recovery after photobleaching (FRAP), Förster resonance energy transfer (FRET), single-molecule imaging/single particle tracking microscopy, and other related methods have been indispensable for this purpose, as they made it possible to quantify the dynamics of nucleocytoplasmic shuttling and characterize intranuclear reactions and retention.[7−13] Fluorescence correlation spectroscopy (FCS) and FCS-based methods have enabled us to simultaneously measure with single-molecule and particle sensitivity local translational diffusion coefficients and the local velocities and directions of transport. The value of conventional single-beam FCS for flow measurements was realized already at the inception of FCS when the theoretical background was developed, and a first successful application was demonstrated.[14] Subsequent studies have shown that conventional FCS is suitable even for more complex applications, such as hydrodynamic flow profiling in microchannel structures,[15] that the dynamic range of flow velocities that can be measured by FCS is wide, ranging over 4 orders of magnitude,[16] and that FCS is suitable for involved applications using microfluidic devices[17] or to characterize cerebral blood flow.[18] However, these studies have also revealed the limitations of conventional FCS for characterizing molecular transport, most notably the fact that it cannot determine the direction of flow. Hence, dual-focus FCS was developed to overcome this limitation and used to measure the velocity and direction of flow by cross-correlation analysis of signals in two foci.[19,20] In addition, more specialized FCS-based methods have also developed. For example, interferometric fluorescence cross-correlation spectroscopy (iFCCS) was applied to quantitatively characterize flow and diffusion transport in 2D and 3D;[21] and multipoint holographic FCS (MP-hFCS), where a spatial light modulator (SLM) was used to generate 8 independent foci, was applied in live cells to quantitatively characterize the nuclear import of the glucocorticoid (GR) receptor via cross-correlation analysis between two independent foci.[22] While these approaches were invaluable for measuring the velocity and direction of molecular transport, they provided this information for a limited region only. To overcome the limited overview and characterize molecular transport in a wider area, methods that use spatiotemporal correlation analysis of fluorescence fluctuations within an image/series of images were developed, such as two-photon image correlation and cross-correlation spectroscopy,[23] spatiotemporal image correlation spectroscopy (STICS),[24] and spatiotemporal image correlation of structured illumination microscopy data.[25] In addition, imaging FCS methods, such as imaging total internal reflection (ITIR)-FCS[26] and single-plane illumination microscopy-based FCS (SPIM-FCS),[27,28] were developed and used to characterize heterogeneity in diffusion and the direction and velocity of transport in multiple positions simultaneously. However, these methods also have some drawbacks that limit their suitability for characterizing the spatial heterogeneity of diffusion and the velocity and direction of transport in live cells. For example, the accuracy and precision of STICS-based methods depends, in addition to the dependence on the concentration and brightness of fluorescent molecules and the point spread function (PSF) of the microscope, on image settings in terms of scanning speed (pixel dwell time, time between the scan lines, and time between images), pixel size, the size of the region of interest (ROI) defined by the number of pixels that it contains, number of frames, and signal acquisition time,[29] and

averaging over a relatively large number of pixels (>64) is needed to allow an accurate characterization of diffusion/motion. This leads to averaging out of spatial heterogeneity of diffusion and the direction and velocity of transport. STICS-based methods also encounter problems when analyzing heterogeneous samples since the presence of bright speckles significantly deforms the autocorrelation curve (ACC). In imaging FCS methods, such as ITIR-FCS and SPIM-FCS, pixel binning and cross-correlation between distant, nonoverlapping pixel areas are necessary to avoid large errors that arise due to crosstalk when cross-correlating the signals from areas that overlap.[26]

We have recently developed massively parallel FCS (mpFCS) in which geometrically independent multiple excitation foci are formed in the specimen and demonstrated its value for quantitative scanning-free confocal fluorescence microscopy imaging and characterization of fast dynamic processes in live cells.[30,31] Here, we present how this new FCS-based imaging modality can be used to map the spatial organization of directionality of nucleocytoplasmic transport in live cells using, as a model system, live HEK cells expressing the GR fused at the N-terminal end with the enhanced green fluorescent protein (eGFP-GR). The GR is a hormone-dependent receptor that belongs to the nuclear receptor superfamily of transcriptional regulatory factors.[32] It is indispensable for maintaining homeostasis under normal physiology and under stress. In unstimulated cells, the GR resides in the cytoplasm, bound into a large multiprotein complex.[33,34] Upon stimulation with endogenous or synthetic ligands[35] and their binding to the cytoplasmic GR, ligand-induced GR translocation to the cell nucleus occurs. In the cell nucleus, GR regulates the transcription of numerous genes—it is estimated that glucocorticoid-responsive genes probably represent 3−10% of the human genome,[36] acting either as an activator or repressor of genes across the genome by direct binding of GR oligomeric forms (dimers or tetramers[37−42]) to glucocorticoid response elements (GREs) on the genome DNA and/or by physically associating with other transcription factors (e.g., NF-κB). The GR concentration in the cell nucleus is dynamically regulated through a complex, perpetually ongoing bidirectional nucleocytoplasmic shuttling of GR.[43] Despite being extensively studied,[10,11,44,45] little is known about how bidirectional flow of GR is spatially organized and coordinated in a live cell to avoid collision of inward/outward shuttling GR and its intranuclear accretion/abatement.

■ EXPERIMENTAL SECTION

Cell Culture and Pharmacological Treatment. HEK cells (ATCC) were grown in 25 mL cell culture flasks with filter caps (T-25, Sarstedt) in Dulbecco's modified Eagle medium (DMEM; Gibco) supplemented with 10% fetal bovine serum (FBS; Gibco) and 1% penicillin−streptomycin (Gibco), 100 U/mL final concentration penicillin, and 100 μg/mL streptomycin and maintained in a humidified atmosphere containing 5% CO_2 at 37 °C.

One day before transfection, HEK cells were seeded in Lab-Tek 8-well chambered coverglass (Thermo Fisher Scientific), with a seeding density of 1.0×10^4 cells per well (volume of 400 μL). The cells were transfected with 100 ng of peGFP-C1 or peGFP-GR-C1 plasmids for expression of the enhanced green fluorescent protein (eGFP) or wild-type human GR α fused with eGFP, respectively, using 0.2 μL of Lipofectamine 2000 (Thermo Fisher Scientific). Twenty-four hours after

transfection, the cell culture medium was replaced as described below, and the cells were subjected to further analysis.

To induce GR translocation into the nucleus, the synthetic ligand dexamethasone (Dex; Sigma-Aldrich) was used. For pharmacological treatment, a 2 mM Dex stock solution prepared by dissolving Dex in dimethyl sulfoxide (DMSO) was diluted to 500 nM in phenol red-free medium FluoroBrite DMEM (Gibco) and the cell culture medium was replaced. In control experiments, the phenol red-free medium FluoroBrite DMEM (Gibco) was used.

Chemicals. Yellow-green fluorescence (Ex/Em: 505/515) carboxylate-modified polystyrene nano/microspheres of different nominal diameters, $d = 100$ nm ($D_{fs,100} = 4.4 \times 10^{-12}$ m² s⁻¹) or 2.0 μm (FluoSpheres Size Kit #2), and carboxylate-functionalized quantum dot nanocrystals, $d = 20$ nm, with emission maxima at 525 nm (Qdot 525 ITK Carboxyl Quantum Dots; Molecular Probes, Life Technologies Corporation, USA) were used for mpFCS instrument calibration and performance characterization. Thirty min of sonication was applied to minimize the agglomeration of quantum dots/fluospheres.

For fFMI instrument alignment, a uniform thin layer of Rh6G was prepared by squeezing 1 μL of concentrated Rh6G solution in water between a microscopic slide and a cover glass (no. 1.5 thickness, 22 × 40 mm) and allowed to dry.

Confocal Laser Scanning Microscopy (CLSM) Imaging. Time-lapse CLSM imaging was performed using the LSM880 system (Carl Zeiss), equipped with the VIS-laser module comprising the Ar-ion laser (458, 488, and 514 nm), C-Apochromat 40×/1.2 N.A. W objective, and gallium arsenide phosphide (GaAsP) detector. eGFP was excited using a 488 nm Ar-ion laser line. Fluorescence was detected in the 493−630 nm range. Following treatment with 500 nM Dex, time-lapse confocal images were acquired at 1 min intervals for 35 min.

Optical Setup for Massively Parallel Fluorescence Correlation Spectroscopy (mpFCS). The optical setup for mpFCS is described in detail in our previous work[30,31] and the Supporting Information (Section SI1, Figure S1). Briefly, the instrument was built using an inverted epi-fluorescence microscope Axio Observer D1 frame equipped with a C-Apochromat 63×/1.2 W Corr objective lens (Carl Zeiss, Germany). A continuous wavelength (CW) 488 nm frequency-doubled diode laser Excelsior 488 (Spectra-Physics, France) was used as the excitation light source. A Diffractive Optical Element (DOE; Holoeye, Germany) was used to precisely create a spot-wise illumination pattern that matches the distribution of single-photon avalanche diodes (SPADs) on the Single Photon Counting SPC2 or the SPC3 camera (Micro Photon Devices MPD, Italy).[46] To enable fast sample localization, an 18.0 megapixel digital single-lens reflex (DSLR) camera EOS 600D (pixel size of 18.5 μm² and pixel pitch of 4.3 μm; Canon Inc., Japan) was coupled to the side port of the microscope opposite to the SPC2/SPC3 camera, and the light path between the two camera ports was manually switched.

mpFCS Data Acquisition. For mpFCS data acquisition in aqueous suspension of fluospheres or quantum dots, an instrumental setup comprising a 32 × 32 DOE and the SPC2 camera was used.[30] Here, the photosensitive area of the chip consists of 32 × 32 circular SPADs that are 20 μm in diameter, and the distance between adjacent diodes along a row/column, i.e., the pitch of the camera, is 100 μm. A total of

131,000 frames were acquired every 20.74 μs, yielding 1024 fluorescence intensity fluctuation traces recorded over 2.71 s. The data was stored in the internal memory of the SPC2 camera during signal acquisition and then transferred to a Dell Precision Fixed Workstation T5600 Xeon E5−2620 2 GHz equipped with an NVIDIA GeForce GTX 780 graphic card containing 2304 Compute Unified Device Architecture (CUDA) for fast data analysis by two-foci cross-correlation as described in Data Processing.

For mpFCS measurements in live cells, the more sensitive SPC3 camera with significantly reduced afterpulsing was used; here, the photosensitive area of the chip consists of 64 × 32 circular SPADs that are 30 μm in diameter, and the distance between adjacent diodes along a row/column, i.e., the pitch of the camera, is 150 μm. In addition, a spot-wise, 16 × 16 illumination was applied and every other SPAD in the centrally positioned 16 × 16 SPADs of the SPC3 camera was used for signal detection.[31] Fifteen minutes after treatment with 500 nM Dex, 1,048,570 frames were acquired at a temporal resolution of 100 μs/frame, yielding 256 fluorescence intensity fluctuation traces recorded over 104.85 s. During signal acquisition, the data was stored in the internal memory of the SPC3 camera and then transferred to a PC for further analysis using the Origin Data Analysis and Graphing software (OriginLab), as described in Data Processing.

Data Processing. To calculate the two-foci cross-correlation curve (tfCCC) for arbitrary pixels a and b of the SPAD camera, the following definition applies:

$$G_{ab}^{(2)}(\tau) = \frac{\langle F_a(t)F_b(t+\tau)\rangle}{\langle F_a(t)\rangle\langle F_b(t)\rangle} = \frac{\langle n_a(t)n_b(t+\tau)\rangle}{\langle n_a(t)\rangle\langle n_b(t)\rangle} \quad (1)$$

where $F_a(t)$ and $F_b(t)$ are fluorescence intensities that are directly proportional to the number of emitted photons $n_a(t)$ and $n_b(t)$ at time t for pixels a and b, respectively, the angular brackets indicate a time average, and τ is the lag time, also called correlation time. However, for the fast, real-time, and highly precise computation of the auto- and cross-correlation functions, a multitau algorithm was developed. Explanation of the multitau procedure can be found in the literature.[31,32,47,48]

For *in vitro* mpFCS measurements in dilute suspensions of fluospheres or quantum dots, the multitau algorithm was used to analyze the raw photon counts directly, and the following formula was used for the calculation of the tfCCCs:

$$G_{ab}^{(2)}(\tau_i) = \frac{\frac{1}{M-m}\sum_{k=1}^{M-m} n_a(k\Delta\tau_i)\cdot n_b(k\Delta\tau_i + m\Delta\tau_i)}{M_{a,dir}\cdot M_{b,del}} \quad (2)$$

Briefly, in eq 2, τ_i is the lag time and $\Delta\tau_i$ is the sampling time for channel i (ith value of the auto- or cross-correlation function). The bin width for the first group is $\Delta\tau_1 = 20.74$ μs. Numbers m and M are integers defined as $m = \tau_i/\Delta\tau_i$ and $M = T/\Delta\tau_i$, where T is the total measurement time. The number of photons counted over a time interval $[(k-1)\Delta\tau_i, k\Delta\tau_i]$ is denoted as $n(k\Delta\tau_i)$. One can see that the correlation analysis boils down to obtaining the sum of the products $n(k\Delta\tau_i)\cdot n(k\Delta\tau_i + m\Delta\tau_i)$ of the counted photons at time $k\Delta\tau_i$ and $m\Delta\tau_i$ later. In eq 1, $n_a(k\Delta\tau_i)$ and $n_b(k\Delta\tau_i)$ denote photon counts at time $k\Delta\tau_i$ for pixels indicated by the subscript, while $M_{a,dir}$ and $M_{b,del}$ are so-called direct and delayed monitor for pixels a and b, respectively. They are computed using the following equations:
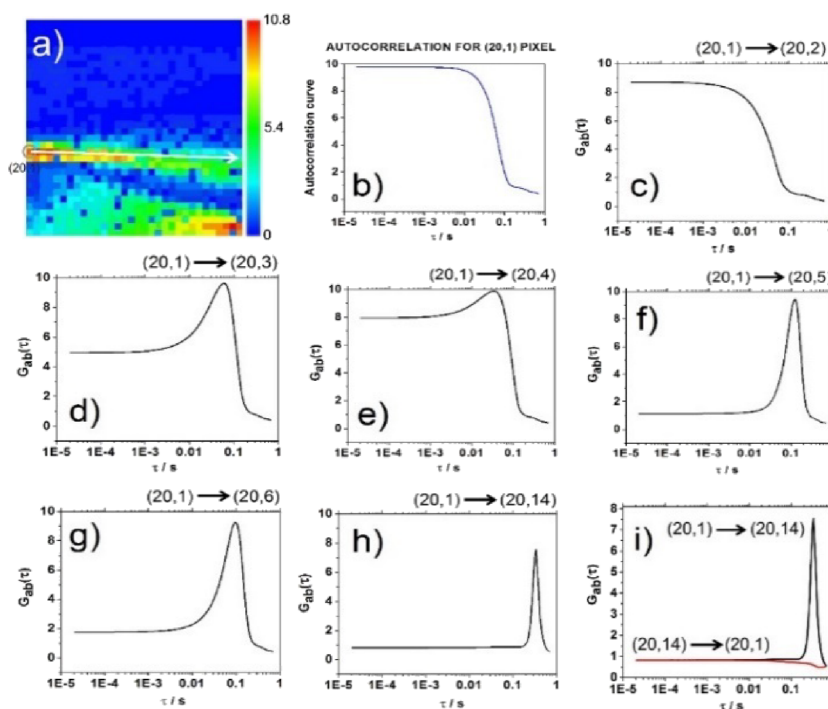
Figure 1. Two-foci cross-correlation analysis of directional particle motion in a diluted suspension of 2 μm fluospheres. (a) $G(0)$ map showing amplitudes of temporal ACCs at lag time $\tau = 20.74$ μs in the 32 × 32 SPAD array. The upper trail, starting at the referent SPAD $a = (20,1)$, is encircled. The white arrow indicates the path along which two-foci cross-correlation analysis is performed. (b) The two-foci ACC at the referent SPAD $a = (20,1)$ was calculated using eq 2 when $a = b$. (c−h) Two-foci cross-correlation curves (tfCCCs) between the referent pixel $a = (20,1)$ and pixels $b = (20,2)$ (c), $b = (20,3)$ (d), $b = (20,4)$ (e), $b = (20,5)$ (f), $b = (20,6)$ (g), and $b = (20,14)$ (h). (i) tfCCC$_{ab}$ between $a = (20,1)$ and $b = (20,14)$ (black; shown in panel h) and the corresponding tfCCC$_{ba}$ between $b = (20,14)$ and $a = (20,1)$ (red). The absence of a peak in tfCCC$_{ba}$ clearly indicates that the direction of particle motion is from (20,1) toward (20,14) and not from (20,14) toward (20,1).

$$M_{a,\text{dir}} = \frac{1}{M-m} \sum_{k=1}^{M-m} n_a(k\Delta\tau_i) \tag{3}$$

$$M_{b,\text{del}} = \frac{1}{M-m} \sum_{k=m}^{M} n_b(k\Delta\tau_i) \tag{4}$$

It is important to note that $G_{ab}^{(2)}(\tau_i) \neq G_{ba}^{(2)}(\tau_i)$. Thus, for each pair of pixels, there are two tfCCCs that are different in the case of directed molecular/particle motion, hence providing information about the direction of movement. Notably, a two-foci autocorrelation function is obtained when $a = b$ in eqs 1 and 2.

For measurements in live cells, Origin Data Analysis and Graphing software (OriginLab) was used to compute cross-correlation curves between foci in the cytoplasm and nucleus. As a first step, Origin Data Analysis and Graphing software (OriginLab) was used to post acquisition account for photobleaching in individual time series. To this aim, data compression was first applied by binning the data into 10 ms bins, and a fourth-order polynomial function was used to fit the fluorescence intensity traces that are decaying due to photobleaching:[49,50]

$$F_c(t) = \frac{F(t)}{\sqrt{\frac{f(t)}{f(0)}}} + f(0)\cdot\left(1 - \sqrt{\frac{f(t)}{f(0)}}\right) \tag{5}$$

Here, $F(t)$ and $F_c(t)$ are fluorescence intensities of raw and corrected data at time t, respectively, and $f(0)$ and $f(t)$ denote values of the fourth-order polynomial function at time 0 and t,

respectively. We then employed eq 2, substituting raw photon intensities (counts) with the fourth-order polynomial functions from eq 5. The forward, cytoplasm to nucleus, and backward, nucleus to cytoplasm, translocation cross-correlation curves are respectively defined as follows:

$$G_c^{\text{cyt,nuc}}(\tau) = \frac{\langle F_c^{\text{cyt}}(t)\cdot F_c^{\text{nuc}}(t+\tau)\rangle}{\langle F_c^{\text{cyt}}(t)\rangle\cdot\langle F_c^{\text{nuc}}(t)\rangle} \tag{6}$$

$$G_c^{\text{nuc,cyt}}(\tau) = \frac{\langle F_c^{\text{nuc}}(t)\cdot F_c^{\text{cyt}}(t+\tau)\rangle}{\langle F_c^{\text{nuc}}(t)\rangle\cdot\langle F_c^{\text{cyt}}(t)\rangle} \tag{7}$$

where $F_c^{\text{nuc}}(t)$ and $F_c^{\text{cyt}}(t)$ are photobleaching-corrected fluorescence intensity time series recorded in the selected pixels in the nucleus and cytoplasm, respectively.

To readily visualize the translocation direction between two foci, the tfCCC in the direction of nucleus to cytoplasm ($G_c^{\text{nuc,cyt}}(\tau)$) is subtracted from the tfCCC in the direction of cytoplasm to nucleus ($G_c^{\text{cyt,nuc}}(\tau)$):

$$G_{c,\text{sub}}(\tau) = G_c^{\text{cyt,nuc}}(\tau) - G_c^{\text{nuc,cyt}}(\tau) \tag{8}$$

In this way, a positive peak in $G_{c,\text{sub}}(\tau)$ signifies nuclear import, whereas a negative peak indicates nuclear export. We refer to $G_{c,\text{sub}}(\tau)$ as the subtracted cross-correlation curve.

■ RESULTS

Theoretical Results. Theoretical background and results of numerical simulations of fluorescent fluosphere motion are presented in the Supporting Information (Section SI2, Figures S2−S5).
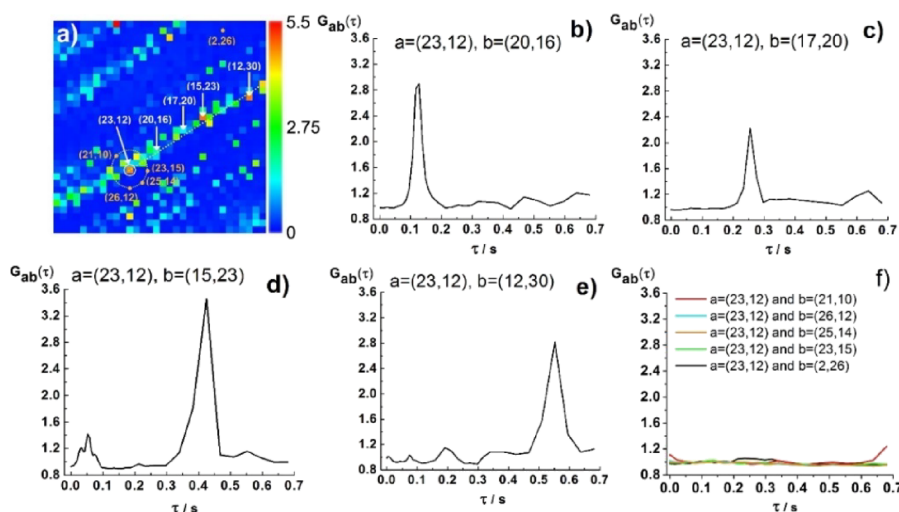
Figure 2. Two-foci cross-correlation analysis of directional particle motion in a 20 nM suspension of 100 nm fluospheres. (a) $G(0)$ map showing amplitudes of temporal ACCs at lag time $\tau = 20.74$ μs in the 32×32 SPAD array. To guide the eye, the trail of fluosphere motion, including the referent SPAD $a = (23,12)$, is highlighted (white dotted line). (b−e) tfCCCs between the referent SPAD $a = (23,12)$ and on-trajectory SPADs (white) $b = (20,16)$, $b = (17,20)$, $b = (15,23)$, or $b = (12,30)$. (f) tfCCCs between the referent SPAD $a = (23,12)$ and selected off-trajectory SPADs (orange-marked).

Proof-of-Concept Results Using Immobilized q-Dots and a Motorized Stage with Nanometer Positioning Precision. Results of proof-of-concept measurements using a precisely controllable motorized stage to move the sample are presented in the Supporting Information (Section SI3, Figures S6 and S7).

In Vitro Experimental Results. Here, we demonstrate using dilute suspensions of fluospheres of different diameters, $d = 2$ μm (Figure 1) and $d = 100$ nm (Figure 2), that the projection of particles' motion in the focal plane can be traced using two-foci cross-correlation analysis in mpFCS.

To begin with, a dilute suspension of large, $d = 2$ μm, and bright fluospheres is analyzed, where particle motion could readily be observed by temporal autocorrelation analysis of fluorescence intensity fluctuations acquired using the mpFCS system (Figure 1). As can be seen from the map of amplitudes of the temporal ACCs for lag time $\tau = 20.74$ μs, the so-called $G(0)$ map, high $G(0)$ values are observed along paths reflecting fluosphere movement (Figure 1a). To ascertain that these traces indeed reflect particle motion, two-foci cross-correlation analysis is performed between selected pixels along the upper trail (Figure 1a, white arrow), and the thus-obtained two-foci cross-correlation curves (tfCCCs) are shown in Figure 1b−i.

The ACC in pixel (20,1) shown in Figure 1b is calculated for the referent SPAD $a = (20,1)$ using eq 2 when $a = b$. The tfCCCs between two adjacent pixels $a = (20,1)$ and $b = (20,2)$ resemble the ACC shown in Figure 1b and lack the characteristic narrow peak that is characteristic of tfCCCs shown in Figure 1c−h. This is because of the large bead diameter, which exceeds the distance between the neighboring SPADs in the focal plane; the distance between the centers of two adjacent volume elements is $\Delta l = 1.6$ μm. Thus, fluorescence signals from the same particle are simultaneously measured in both SPADs. tfCCCs containing features of both the ACC and tfCCC features are observed for $b = (20,3)$ and $b = (20,4)$ (Figure 1d,e). When the distance between two pixels is sufficiently large (Figure 1f−h), a sharp peak is observed, as expected. Importantly, one can see that the greater the distance

between a and b, the longer the lag time of the cross-correlation peak. From the lag times of the cross-correlation peak, one can estimate the two-dimensional (2D) velocity. Projection of the three-dimensional (3D) fluosphere trajectory as it traverses the focal plane onto the 2D image plane divided by the lag time yields the 2D velocity. The 2D velocity at which the fluorescent particle is moving from pixel $a = (20,1)$ is first 50 μm/s, then increases to 80 μm/s, and then decreases to 60 μm/s. Given that we have neither controlled the direction nor the velocity of fluosphere motion but rather observed its movement under spontaneous, convection or pipet aspiration/dispensing-driven fluid flow, the observed difference could reflect local changes in fluosphere velocity due to heterogeneities in the fluid flow and/or apparent differences in fluosphere 2D velocity arising because 3D paths of different lengths may give the same 2D projection in the image plane. Finally, the direction of fluosphere motion in the focal plane could be determined (denoted by the white arrow in Figure 1a) from the results shown in Figure 2i. Here, a sharp peak is observed when the tfCCC is calculated in the direction from $a = (20,1)$ to $b = (20,14)$ (Figure 2i, black). However, when the calculation is performed in the opposite direction, from $b = (20,14)$ to $a = (20,1)$, the peak disappears (Figure 2i, red). This in turn means that the direction of fluosphere motion is from $a = (20,1)$ to $b = (20,14)$.

Sensitivity of the mpFCS instrument is further tested using a diluted suspension of small fluospheres, $d = 100$ nm (Figure 2).

As can be seen from the $G(0)$ map (Figure 2a) and the tfCCCs between the reference point $a = (23,12)$ and pixels $b = (20,16)$, $b = (17,20)$, $b = (15,23)$, or $b = (12,30)$, robust peaks can be observed in the tfCCCs, confirming that these points are on the trajectory and in the direction of 100 nm fluosphere movement (Figure 2b−e). The greater the distance between pixels a and b, the longer the lag time at which the peak in the tfCCC is observed (Figure 2b−e). As before (Figure 1i), tfCCCs calculated from b to a (data not shown) showed no peaks, confirming that the direction of 100 nm fluosphere motion is from point $a = (23,12)$ toward the set of white-

marked b points along the indicated trajectory (Figure 2a, white dotted line). Moreover, from the lag times of the peaks in the tfCCCs (Figure 2b−e), the projection of mean velocity in the focal plane could be estimated, yielding an approximate mean velocity of the directed motion of 30 μm/s between pixels (23,12) and (22,13) and 60 μm/s thereafter. We next prove that two-foci cross-correlation analysis can be used as a "radar" for detecting the direction of particle motion. In Figure 2a, we depict a circle centered at the reference pixel a = (23,12) with pixels (21,10), (26,12), (25,14), and (23,15) at its rim (Figure 2a, orange-marked). In addition, the distant pixel (2,26) is also included in this analysis as an off-trajectory example (Figure 2a, orange-marked). tfCCCs between a = (23,12) and these pixels, which are not positioned along the particle trajectory, clearly show no peaks (Figure 2f). Thus, this 360° sweeping procedure can discern the direction of the particle motion. To further corroborate this analysis, we show in the Supporting Information (Section SI4, Figures S8−S10) that two-foci cross-correlation analysis yields no tfCCCs when pure diffusion is observed (Figures S8 and S9) and that it is more powerful than classical temporal autocorrelation analysis for discerning free diffusion from directional motion when the flow is slow (Figure S10).

Nucleocytoplasmic Translocation of Glucocorticoid Receptor in the Live Cell. Finally, we applied our method to characterize in live cells the translocation of the glucocorticoid receptor tagged with enhanced green fluorescent protein (eGPFP-GR; Figure 3).

As can be seen, eGFP-GR is localized in the cytoplasm in untreated HEK cells (Figure 3a, top, 0 min). Dex (500 nM) treatment induced eGFP-GR relocation to the cell nucleus (Figure 3a, top, 30 min), whereas it did not change eGFP intracellular distribution (Figure 3a, bottom, 0 and 30 min). Over time, a 4-fold increase in nuclear fluorescence intensity following 500 nM Dex treatment was observed in eGFP-GR-expressing HEK cells (Figure 3b, dots), while no change was observed in the eGFP-expressing HEK cells (Figure 3b, circles). eGFP-GR nuclear translocation half time, defined as the time needed for fluorescence intensity in the cell nucleus to reach half of its highest value, was determined to be $t_{1/2}^{nuc}$ = 15 min (Figure 3b, red). Hence, mpFCS measurements of directional transport were performed in eGFP-GR-expressing HEK cells 15 min after the treatment with 500 nM Dex.

Nuclear/cytoplasmic positions of eGFP-GR in an untreated HEK cell expressing eGFP-GR are visualized using spot-wise illumination and the DSLR camera attached to the side-port of the mpFCS system (Figure 3c; nuclear localization is inside the white dotted contour). tfCCCs, $G_c^{cyt,nuc}(\tau)$ and $G_c^{nuc,cyt}(\tau)$, and corresponding $G_{c,sub}(\tau)$ are calculated at distinct positions along the nuclear envelope (Figure 3c, 1−13). Our data showed that the direction of nuclear import/export is location-specific, with nuclear import being observed at sites 1, 2, 3, 8, 9, 10, 12, and 13 (Figure 3c, red), whereas nuclear export was observed at sites 4, 5, 6, 7, and 11 (Figure 3c, faint blue).

Representative $G_{c,sub}(\tau)$, color-coded to indicate the direction of eGFP-GR nucleocytoplasmic transport, nuclear import (red) and nuclear export (blue), are shown in Figure 3d$_1$,d$_2$, respectively. $G_{c,sub}(\tau)$ for all 13 sites are shown in the Supporting Information (Section SI5, Figure S11a). Average $G_{c,sub}(\tau)$ for three different cells, showing similar results, are presented in Figure S11b$_1$−b$_3$.

We further computed the nucleocytoplasmic translocation times (Figure 3e$_1$) by fitting the $G_{c,sub}(\tau)$ by using a Gaussian
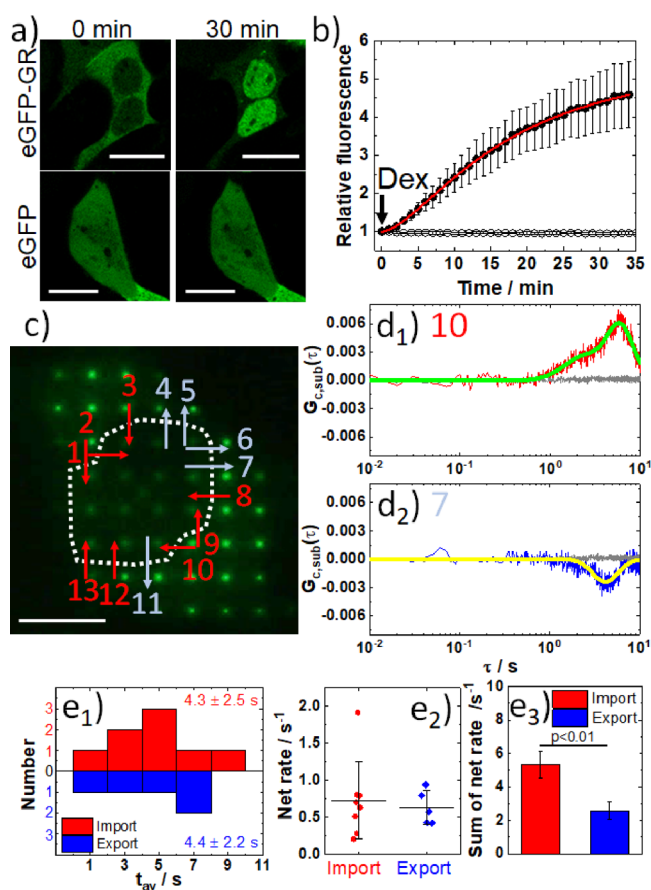

Figure 3. Spatial mapping of the direction and extent of nucleocytoplasmic transport of eGFP-GR in live cells using two-foci cross-correlation in mpFCS. (a) CLSM images of HEK cells expressing eGFP-GR (top) or eGFP (bottom; control) at 0 min (untreated) and 30 min after treatment with 500 nM Dex. Scale bars: 20 μm. (b) Relative change in nuclear fluorescence intensity over time following Dex treatment in cells expressing eGFP-GR (dots) or eGFP (circles). The arrow indicates the time of Dex addition to a concentration of 500 nM. Logistic function was used to fit the S-shaped relative fluorescence growth curve recorded in cells expressing eGFP-GR (red line). (c) Fluorescence image showing eGFP-GR distribution in an untreated cell acquired by using the DSRL Canon camera coupled to the side port of the mpFCS system. Arrows show the directions of eGFP-GR; nuclear translocation: import (red) and export (blue). Scale bar: 10 μm. (d$_1$, d$_2$) $G_{c,sub}(\tau)$ at an import-active (red, d$_1$) and export-active site (blue, d$_2$). Translocation time is determined by Gaussian distribution fitting to $G_{c,sub}(\tau)$ (green/yellow). (e$_1$) Histogram of import (red) and export (blue) translocation time. (e$_2$) Net rate of nucleocytoplasmic transport calculated as the ratio of the tfCCC amplitude over import/export time. (e$_3$) Sum net rate in a single cell. All values are shown as the average ± standard deviation (SD). SD was calculated from three independent measurements in three cells. Statistical significance was assessed using a two-tail Student's t test.

distribution function (Figure 3d$_1$,d$_2$, green and yellow, respectively). On the average, the nucleocytoplasmic translocation times were t_{av}^{imp} = (4.3 ± 2.5) s for nuclear import and t_{av}^{exp} = (4.4 ± 2.2) s for nuclear export (Figure 3e$_1$). By dividing the amplitude of the fitted Gaussian distribution function with the corresponding nucleocytoplasmic translocation time, the net rate of nucleocytoplasmic translocation could be estimated at independent sites (Figure 3e$_2$) and summed at all analyzed sites (Figure 3e$_3$).

This analysis, corroborated by theoretical calculations (Section SI5, Figures S12−S14), showed that on average, net rate of nucleocytoplasmic translocation at different sites along the nuclear envelope was not significantly different between nuclear import and export sites (Figure 3e$_2$). However, given that the number of sites at which nuclear import was observed is larger than the number of sites where nuclear export occurred, the total import net rate was twice the total export net rate (Figure 3e$_3$), consistent with the net eGFP-GR translocating into the cell nucleus.

DISCUSSION

In this work, we have theoretically and experimentally shown that two-foci cross-correlation analysis in mpFCS enables us to characterize the directional motion of fluospheres/molecules in solution/live cells. This is exemplified here for fluospheres of different sizes, $d = 2$ μm, which is larger than the distance between two adjacent pixels in the mpFCS instrument (Figure S1), and $d = 100$ nm, which is smaller, in dilute aqueous suspension (Figures 1 and 2 and Figures S2−S5), for immobilized q-dots precisely moved using a translation stage with nanometer step size (Figures S6 and S7), and for ligand-induced eGFP-GR nuclear translocation in live cells (Figure 3 and Figure S11).

Using dilute suspension of fluorescent particles, we demonstrated theoretically and experimentally that by calculating tfCCCs between a referent pixel and different adjacent pixels in the focal plane, we could identify the direction in which the particle is moving since a sharp peak is observed only in the tfCCC that is calculated along the projection of the 3D path of particle motion onto the 2D image plane as it traverses the focal plane and in the direction of particle movement from an earlier to a later particle position (Figures 1 and 2). Moreover, we showed that the tfCCC peak is observed at the lag time that corresponds to the transit time between the two foci positions, demonstrating that our technique can be used not only to trace the projection of the 3D particle trajectory onto the 2D image plane as the particle traverses the focal plane but also to map the forward/backward direction of its motion and the 2D velocity.

We further showed using ligand-induced eGFP-GR nuclear translocation as an example that two-foci cross-correlation analysis can characterize in live cells the cellular dynamics of fluorescently tagged proteins. Most notably, our study showed that by calculating tfCCCs, we could map the direction of ligand-induced eGFP-GR nucleocytoplasmic translocation along the nuclear envelope contour in the focal plane (Figure 3). This further revealed that eGFP-GR nuclear import and export occurred simultaneously at different locations along the nuclear envelope and with similar nucleocytoplasmic translocation times, $t_{av}^{imp} = (4.3 \pm 2.5)$ s for nuclear import and $t_{av}^{exp} = (4.4 \pm 2.2)$ s for nuclear export (Figure 3e$_1$), and that the net effect at the macroscopic level is determined by the number of sites through which import/export occurs (Figure 3e$_1$−e$_3$). We thus confirmed a previous finding by multipoint holographic fluorescence correlation spectroscopy (MP-hFCS)[22] showing that under ligand-induced eGFP-GR nuclear translocation, the actual passing through of nuclear pores is faster than the macroscopic change in fluorescence intensity that is observed by time-lapse confocal fluorescence microscopy imaging. We, however, took the understanding of mechanisms underlying acute, strong-binding ligand-induced eGFP-GR translocation one step further by showing that import/export processes occur simultaneously at different locations, which was not shown by MP-hFCS, and that the net change in eGFP-GR concentration at the macroscopic level is determined by the number of sites through which eGFP-GR import/export occurs and not by differences in the actual eGFP-GR translocation time (Figure 3e$_1$−e$_3$). Having said this, we underline here that this conclusion is valid only for acute, strong-binding ligand-induced eGFP-GR nuclear translocation at the time of the highest net change in eGFP-GR nuclear concentration and does not necessarily apply for other conditions, such as under stimulation with endogenous or synthetic weakly binding GR-specific ligands or upon withdrawal of GR ligand.[51−54]

In conclusion, two-foci cross-correlation in mpFCS is a versatile tool for characterization of both direction and 2D velocity of active transport in live cells and may be useful for understanding how the bidirectional traffic of macromolecules is spatially organized and coordinated in live cells to achieve controlled local accretion/abatement of molecules of interest. In addition, directional fluorescent particle motion in fluids can be characterized in detail, enabling us not only to characterize local heterogeneities in fluid flow but also to investigate the essential role of the fluid phase for long-range material transport and the emergence of large-scale synergy in biological systems.[55]

ASSOCIATED CONTENT

Supporting Information

The Supporting Information is available free of charge at https://pubs.acs.org/doi/10.1021/acs.analchem.3c01427.

> SI1: optical setup; SI2: theoretical background and numerical simulations of directional particle motion; SI3: proof-of-concept measurements using a piezo-based linear stage with nanometer positioning precision for controlled translation of immobilized quantum dots; SI4: comparison between auto- and two-foci cross-correlation analysis of diffusion and flow in dilute aqueous solution and nanoparticles in suspension; SI5: glucocorticoid receptor nucleocytoplasmic translocation in live cells (PDF)

AUTHOR INFORMATION

Corresponding Author

Vladana Vukojević − *Department of Clinical Neuroscience (CNS), Center for Molecular Medicine (CMM), Karolinska Institute, 17176 Stockholm, Sweden;* orcid.org/0000-0003-0873-5653; Email: Vladana.Vukojevic@ki.se

Authors

Stanko N. Nikolić − *Department of Clinical Neuroscience (CNS), Center for Molecular Medicine (CMM), Karolinska Institute, 17176 Stockholm, Sweden; Institute of Physics Belgrade, University of Belgrade, 11080 Belgrade, Serbia; Division of Arts and Sciences, Texas A&M University at Qatar, Doha, Qatar*

Sho Oasa − *Department of Clinical Neuroscience (CNS), Center for Molecular Medicine (CMM), Karolinska Institute, 17176 Stockholm, Sweden;* orcid.org/0000-0003-3800-590X

Aleksandar J. Krmpot − *Department of Clinical Neuroscience (CNS), Center for Molecular Medicine (CMM), Karolinska Institute, 17176 Stockholm, Sweden; Institute of Physics*

Belgrade, University of Belgrade, 11080 Belgrade, Serbia;
Division of Arts and Sciences, Texas A&M University at
Qatar, Doha, Qatar; orcid.org/0000-0003-2751-7395

Lars Terenius − *Department of Clinical Neuroscience (CNS),
Center for Molecular Medicine (CMM), Karolinska Institute,
17176 Stockholm, Sweden;* orcid.org/0000-0003-2880-
9576

Milivoj R. Belić − *Division of Arts and Sciences, Texas A&M
University at Qatar, Doha, Qatar*

Rudolf Rigler − *Department of Clinical Neuroscience (CNS),
Center for Molecular Medicine (CMM), Karolinska Institute,
17176 Stockholm, Sweden*

Complete contact information is available at:
https://pubs.acs.org/10.1021/acs.analchem.3c01427

Author Contributions

‖S.N.N., S.O., and A.J.K. contributed equally to this work.

Author Contributions

⊥R.R. and V.V. equally contributed to this work as senior
authors.

Author Contributions

#We regretfully inform that our esteemed colleague and FCS
pioneer R.R. has passed away on Oct 5th 2022.

Author Contributions

V.V. and R.R. designed the study. A.J.K. designed and built-up
the experimental setup, and performed the experiments with
S.O. S.N.N. wrote the mpFCS data acquisition, analysis, and
presentation program and performed numerical simulations.
M.R.B. supervised the numerical simulations. All authors
analyzed and interpreted the data, contributed to manuscript
writing, and have given approval to the final version of the
manuscript.

Notes

ACKNOWLEDGMENTS

REFERENCES

(1) Lambert, S. A.; Jolma, A.; Campitelli, L. F.; Das, P. K.; Yin, Y.; Albu, M.; Chen, X.; Taipale, J.; Hughes, T. R.; Weirauch, M. T. *Cell* **2018**, *172* (4), 650−665.

(2) Spitz, F.; Furlong, E. *Nat. Rev. Genet.* **2012**, *13* (9), 613−626.

(3) Bressloff, P. C.; Newby, J. M. *Rev. Mod. Phys.* **2013**, *85*, 135−196.

(4) Timney, B. L.; Raveh, B.; Mironska, R.; Trivedi, J. M.; Kim, S. J.; Russel, D.; Wente, S. R.; Sali, A.; Rout, M. P. *J. Cell. Biol.* **2016**, *215* (1), 57−76.

(5) Lin, D. H.; Hoelz, A. *Annu. Rev. Biochem.* **2019**, *88*, 725−783.

(6) Hampoelz, B.; Andres-Pons, A.; Kastritis, P.; Beck, M. *Annu. Rev. Biophys.* **2019**, *48*, 515−536.

(7) Qian, H.; Sheetz, M. P.; Elson, E. L. *Biophys. J.* **1991**, *60* (4), 910−921.

(8) Middeler, G.; Zerf, K.; Jenovai, S.; Thulig, A.; Tschödrich-Rotter, M.; Kubitscheck, U.; Peters, R. *Oncogene* **1997**, *14* (12), 1407−1417.

(9) Keminer, O.; Siebrasse, J. P.; Zerf, K.; Peters, R. *Proc. Natl. Acad. Sci. U.S.A.* **1999**, *96* (21), 11842−11847.

(10) Gebhardt, J. C. M.; Suter, D. M.; Roy, R.; Zhao, Z. W.; Chapman, A. R.; Basu, S.; Maniatis, T.; Xie, X. S.; et al. *Nat. Methods* **2013**, *10* (5), 421−426.

(11) Groeneweg, F. L.; van Royen, M. E.; Fenz, S.; Keizer, V. I. P.; Geverts, B.; Prins, J.; de Kloet, E. R.; Houtsmuller, A. B.; Schmidt, T. S.; Schaaf, M. J. M.; Tuckermann, J. P. *PLoS ONE* **2014**, *9*, 3e90532.

(12) Zhang, J.; Roggero, V. R.; Allison, L. A. *Vitam. Horm.* **2018**, *106*, 45−66.

(13) Sallaberry, I.; Luszczak, A.; Philipp, N.; Navarro, G. S. C.; Gabriel, M. V.; Gratton, E.; Gamarnik, A. V.; Estrada, L. C. *Sci. Rep.* **2021**, *11* (1), 24415.

(14) Magde, D.; Webb, W. W.; Elson, E. L. *Biopolymers* **1978**, *17* (2), 361−376.

(15) Gosch, M.; Blom, H.; Holm, J.; Heino, T.; Rigler, R. *Anal. Chem.* **2000**, *72* (14), 3260−3265.

(16) Brister, P. C.; Kuricheti, K. K.; Buschmann, V.; Weston, K. D. *Lab Chip* **2005**, *5* (7), 785−791.

(17) Kunst, B. H.; Schots, A.; Visser, A. J. W. G. *Anal. Chem.* **2002**, *74* (20), 5350−5357.

(18) Fu, X.; Sompol, P.; Brandon, J. A.; Norris, C. M.; Wilkop, T.; Johnson, L. A.; Richards, C. I. *Nano Lett.* **2020**, *20* (8), 6135−6141.

(19) Brinkmeier, M.; Dörre, K.; Riebeseel, K.; Rigler, R. *Biophys. Chem.* **1997**, *66* (2−3), 229−239.

(20) Brinkmeier, M.; Dörre, K.; Stephan, J.; Eigen, M. *Anal. Chem.* **1999**, *71* (3), 609−616.

(21) Saha, I.; Saffarian, S.; Abraham, T. *PLOS ONE* **2019**, *1412*, No. e0225797.

(22) Yamamoto, J.; Mikuni, S.; Kinjo, M. *Biomed. Opt. Express.* **2018**, *9* (12), 5881−5890.

(23) Wiseman, P. W.; Squier, J. A.; Ellisman, M. H.; Wilson, K. R. *J. Microsc.* **2000**, *200* (Pt 1), 14−25.

(24) Hebert, B.; Costantino, S.; Wiseman, P. W. *Biophys. J.* **2005**, *88* (5), 3601−3614.

(25) Ashdown, G. W.; Cope, A.; Wiseman, P. W.; Owen, D. M. *Biophys. J.* **2014**, *107* (9), L21−L23.

(26) Sankaran, J.; Manna, M.; Guo, L.; Kraut, R.; Wohland, T. *Biophys. J.* **2009**, *97* (9), 2630−2639.

(27) Wohland, T.; Shi, X.; Sankaran, J.; Stelzer, E. H. K. *Opt. Express* **2010**, *18* (10), 10627−10641.

(28) Sankaran, J.; Shi, X.; Ho, L. Y.; Stelzer, E. H. K.; Wohland, T. *Opt. Express* **2010**, *18* (25), 25468−25481.

(29) Longfils, M.; Smisdom, N.; Ameloot, M.; Rudemo, M.; Lemmens, V.; Fernández, G. S.; Röding, M.; Lorén, N.; Hendrix, J.; Särkkä, A. *Biophys. J.* **2019**, *117* (10), 1900−1914.

(30) Krmpot, A. J.; Nikolić, S. N.; Oasa, S.; Papadopoulos, D. K.; Vitali, M.; Oura, M.; Mikuni, S.; Thyberg, P.; Tisa, S.; Kinjo, M.; Nilsson, L.; Terenius, L.; Rigler, R.; Vukojević, V. *Anal. Chem.* **2019**, *91* (17), 11129−11137.

(31) Oasa, S.; Krmpot, A. J.; Nikolić, S. N.; Clayton, A. H. A.; Tsigelny, I. F.; Changeux, J. P.; Terenius, L.; Rigler, R.; Vukojević, V. *Anal. Chem.* **2021**, *93* (35), 12011−12021.

(32) Nicolaides, N. C.; Chrousos, G.; Kino, T. *Glucocorticoid Receptor. Comprehensive Free Online Endocrinology Book.* Feingold, K. R.; Anawalt, B.; Boyce, A. et al., Eds. MDText.com, Inc.: South Dartmouth (MA); 2000-. PMID: 25905394.

(33) Mazaira, G. I.; Echeverria, P. C.; Galigniana, M. D. *J. Cell Sci.* **2020**, *133* (12), jcs238873.

(34) Noddings, C. M.; Wang, R.Y-R.; Johnson, J. L.; Agard, D. A. *Nature* **2022**, *601* (7893), 465−469.

(35) Frew, A. J. Glucocorticoids. in *Clinical Immunology* (5ed.), Eds.: Robert R., Rich, Thomas A., Fleisher, William T., Shearer, Harry W., Schroeder, Anthony J., Frew, Cornelia M., Weyand, Elsevier, 2019, 1165−1175.e1 (ISBN 9780702068966).

(36) Nicolaides, N. C.; Chrousos, G.; Kino, T. *Glucocorticoid Receptor. Comprehensive Free Online Endocrinology Book.* Feingold, K. R.; Anawalt, B.; Boyce, A., et al. Eds. MDText.com, Inc.: South Dartmouth (MA); 2000-. https://www.ncbi.nlm.nih.gov/books/NBK279171/.

(37) Presman, D. M.; Ganguly, S.; Schiltz, R. L.; Johnson, T. A.; Karpova, T. S.; Hager, G. L. *Proc. Natl. Acad. Sci. U.S.A.* **2016**, *113* (29), 8236−8241.

(38) Presman, D. M.; Hager, G. L. *Transcription* **2017**, *8* (1), 32−39.

(39) Paakinaho, V.; Johnson, T. A.; Presman, D. M.; Hager, G. L. *Genome Res.* **2019**, *29* (8), 1223−1234.

(40) Johnson, T. A.; Paakinaho, V.; Kim, S.; Hager, G. L.; Presman, D. M. *Nat. Commun.* **2021**, *12* (1), 1987.

(41) Robertson, S.; Rohwer, J. M.; Hapgood, J. P.; Louw, A.; Chang, A. Y. W. *PLoS ONE* **2013**, *8*, 5e64831.

(42) Tiwari, M.; Oasa, S.; Yamamoto, J.; Mikuni, S.; Kinjo, M. *Sci. Rep.* **2017**, *7* (1), 4336.

(43) Mazaira, G. I.; Piwien Pilipuk, G.; Galigniana, M. D. *Trends in Endocrinol. Metabol.* **2021**, *32* (10), 827−838.

(44) McNally, J. G.; Müller, W. G.; Walker, D.; Wolford, R.; Hager, G. L. *Science* **2000**, *287* (5456), 1262−1265.

(45) Morisaki, T.; Müller, W. G.; Golob, N.; Mazza, D.; McNally, J. G. *Nat. Commun.* **2014**, *5*, 4456.

(46) Vitali, M.; Bronzi, D.; Krmpot, A. J.; Nikolic, S. N.; Schmitt, F.; Junghans, C.; Tisa, S.; Friedrich, T.; Vukojevic, V.; Terenius, L.; Zappa, F.; Rigler, R. *IEEE J. Sel. Top. Quantum Electron.* **2014**, *20* (6), 344−353.

(47) Wohland, T.; Rigler, R.; Vogel, H. *Biophys. J.* **2001**, *80* (6), 2987−2999.

(48) Brinkmeier, M.; Rigler, R. *Exp. Techn. Phys.* **1995**, *41*, 205−210.

(49) Ries, J.; Chiantia, S.; Schwille, P. *Biophys. J.* **2009**, *96* (5), 1999−2008.

(50) Macháň, R.; Foo, Y. H.; Wohland, T. *Biophys. J.* **2016**, *111* (1), 152−161.

(51) Robertson, S.; Hapgood, J. P.; Louw, A. *Steroids* **2013**, *78* (2), 182−194.

(52) Vandevyver, S.; Dejager, L.; Libert, C. *Traffic* **2012**, *13* (3), 364−374.

(53) Stavreva, D. A.; Wiench, M.; John, S.; Conway-Campbell, B. L.; McKenna, M. A.; Pooley, J. R.; Johnson, T. A.; Voss, T. C.; Lightman, S. L.; Hager, G. L. *Nat. Cell Biol.* **2009**, *11* (9), 1093−1102.

(54) Nicolaides, N. C.; Chrousos, G.; Kino, T.n[Updated 2020 Nov 21]. In: *Glucocorticoid Receptor*; Feingold, K. R.; Anawalt, B.; Blackman, M. R.; et al., Editors. Available from:https://www.ncbi.nlm.nih.gov/books/NBK279171/.

(55) Jingjing, F.; Zexin, Z.; Xiaodong, W.; Jianfeng, X.; Yan, He *iScience* **2019**, *22*, 123−132.

Supporting Information: Mapping the direction of nucleocytoplasmic transport of glucocorticoid receptor (GR) in live cells using two-foci cross-correlation in massively parallel Fluorescence Correlation Spectroscopy (mpFCS)

Stanko N. Nikolić[1,2,3,¶], Sho Oasa[1,¶], Aleksandar J. Krmpot[1,2,3,¶], Lars Terenius[1], Milivoj R. Belić[3], Rudolf Rigler[1,‡,†], Vladana Vukojević[1, ‡,*]

[1]Department of Clinical Neuroscience (CNS), Center for Molecular Medicine (CMM), Karolinska Institute, 17176 Stockholm, Sweden. [2]Institute of Physics Belgrade, University of Belgrade, 11080 Belgrade, Serbia. [3]Division of Arts and Sciences, Texas A&M University at Qatar, Doha, Qatar.

ABSTRACT: SI1: Optical setup. **SI2:** Theoretical background and numerical simulations of directional particle motion. **SI3:** Proof of concept measurements using a piezo-based linear stage with nanometre positioning precision for controlled translation of immobilized quantum dots. **SI4:** Comparison between auto- and two-foci cross-correlation analysis of diffusion and flow in dilute aqueous solution and nanoparticles in suspension. **SI5:** Glucocorticoid receptor nucleocytoplasmic translocation in live cells.

SI1: Optical setup.
Schematic drawing of the optical setup of the mpFCS system
is shown in Fig. S1.
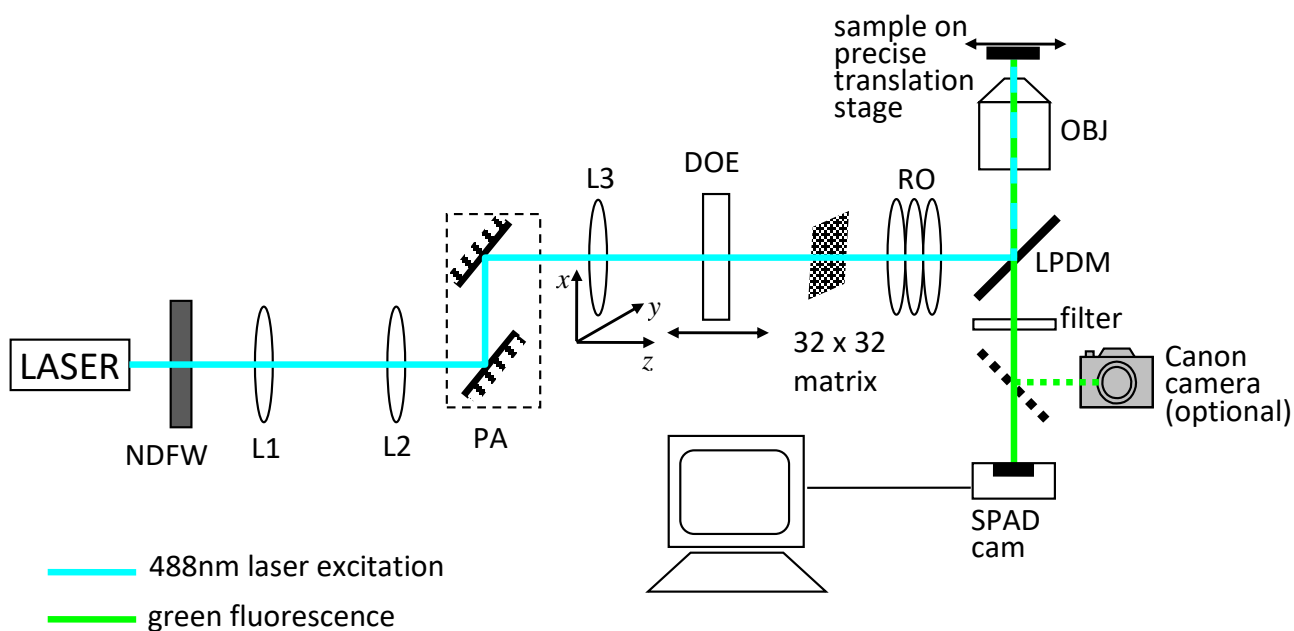
Figure S1. Optical setup for mpFCS. NDFW - neutral density filter wheel, L1 and L2 – beam expander lenses, PA – periscope assembly, L3 – focusing lens, DOE – diffractive optical element, RO – relay optics of the microscope, LPDM – long pass dichroic mirror, OBJ – microscope objective, SPAD cam – single photon avalanche photodiode camera. The laser beam passes through a double filter wheel of different optical density (OD 0.2-8.0) that can be adjusted in discrete steps for precise regulation of illumination intensity. Uniform filters are used rather than a variable one in order to avoid wave front distortion and thus preserve symmetrical light intensity distribution in the focus. The laser beam is than expanded about 10 times by a Keplerian telescope (L1 and L2). The expanded beam is focused by the plano-convex lens L3 through the diffractive optical element (DOE) designed to split a single laser beam into 32×32 beams. A 32×32 foci illumination matrix is formed at the rear port

image plane of the epi-fluorescence microscope Axio Observer D1. The relay optics of the rear port, dichroic mirror, and the C-Apochromat 63x/1.2 W Corr Objective transfer the illumination matrix image into the focal plane of the objective. Translation of L3 in x and y direction scans the incidence angle of the laser beam to the rear port of the microscope and tunes the illumination matrix lateral position in the object plane. Translation of L3 in z direction adjusts sureness of the matrix. The DOE can be translated along the beam propagation direction enabling the dimension *i.e.* the pitch of the illumination matrix to be adjusted in order to match the detector's matrix. The Zeiss Filter Set 38 HE for enhanced Green Fluorescent Protein (eGFP) consisting of an excitation band pass filter EX BP 470/40 nm (central wavelength/band width), long pass dichroic mirror with a cut-off wavelength of 495 nm, and an emission band pass filter EM BP 525/50 was used throughout. Fluorescence was detected using the SPC2 camera, containing a photosensitive chip and a 16-bit photon counter based on Field Programmable Gate Array (FPGA). The photosensitive area of the chip consists of 32×32 circular SPADs that are 20 μm in diameter. The distance between adjacent diodes in the same row/column is 100 μm. Further details on the SPC2 camera design and performance can be found in [36, 41-43]. Since the aperture of every SPAD in the SPC2 camera acts as a pinhole positioned in a conjugate focal plane with respect to the illumination matrix, confocal configuration is achieved for all 32×32 foci.

SI2: Theoretical background and numerical simulations of directional particle motion.

SI2a: Theoretical model.

To calculate the photon counts when a single particle (such as a fluosphere or a quantum dot) is travelling in the focal plane of the experimental setup, the particle motion is assumed to be two-dimensional. The frame duration in the model is taken to be the same as in the experiment: $dt = 20.74$ μs. For simplicity, the origin of the reference frame is placed at the centre of the first observation volume element (1,1). If we denote the distance between the centres of two adjacent volume elements with $\Delta l = 1.6$ μm, then the coordinates of the centre of element with indices (i,j) are: $y_{i,j} = (i-1)\Delta l$ and $x_{i,j} = (j-1)\Delta l$ $(1 \leq i,j \leq 32)$.

The laser radial intensity distribution of each volume element is Gaussian:

$$I = I_0 e^{-8r^2/D^2} \tag{S1}$$

where r corresponds to radial distance of an arbitrary point in the focal plane from the centre of the volume element *(i,j)* and D is a diameter of the beam (1/e^2 definition). Let the particle take initial position r_{0p} and velocity v, while its radius is $r_p = d/2$. Then, its coordinates at a given moment t are:

$$x_p = (r_{0p} + vt)e_x \tag{S2}$$

$$y_p = (r_{0p} + vt)e_y \tag{S3}$$

The number of photons $dN_{\text{photons}}(i,j,t)$ measured in the camera pixel corresponding to a volume element (i,j) during infinitesimally time interval $(t, t + dt)$ is calculated by using the following equation:

$$dN_{photons}(i,j,t) = \alpha dt \oiint I(r)\eta'(r,\varphi,x_p,y_p)d^2S \tag{S4}$$

Our assumption is that the number of photons is proportional to the: 1. incident laser intensity at particular point of the volume element with polar coordinates r and φ (in the second referential frame with origin in the center of (i,j)

element), 2. small area $d^2S = rdrd\varphi$ around that point, and 3. time interval dt. This applies if surface d^2S fully/partially overlaps with the particle. In addition, in the focal plane, the particle is considered as a circle of radius $r_p^2\pi$. Therefore, $\eta'(r,\varphi,x_p,y_p)$ indicates "overlapping" function: it is equal to one if a given point of a volume element (i,j) with coordinates (r, φ) is "inside" the particle at time t. Otherwise, $\eta'(r,\varphi,x_p,y_p)$ is zero. If we use η function defined as:

$$\eta(x) = 1 \; (x \geq 0)$$
$$\eta(x) = 0 \; (x < 0) \tag{S5}$$

we can write:

$$\eta'(r,\varphi,x_p,y_p) = \eta\left[r_p^2 - \left((j-1)\Delta l + r cos\varphi - x_p\right)^2 \right.$$
$$\left. - \left((i-1)\Delta l + r sin\varphi - y_p\right)^2\right] \tag{S6}$$

Finally, the eq. (S6) can be written as:

$$dN_{\text{photons}}(i,j,t) = \alpha I_0 \int_{r=0}^{\beta D/2} rdr \cdot \int_{\varphi=0}^{2\pi} d\varphi \cdot e^{\frac{-8r^2}{D^2}}$$
$$\cdot \eta\left[r_p^2 - \left((j-1)\Delta l + r cos\varphi - x_p\right)^2 \right.$$
$$\left. - \left((i-1)\Delta l + r sin\varphi - y_p\right)^2\right] \tag{S7}$$

In last equation, α is proportionality constant. We take additional parameter $\beta = 1.1$ to define the region of integration around the center of the volume element (i,j).

SI2b. Particle motion along the x-axis.

Setting overall simulation time (T), time step (Δt), and number of frames (N_{total}) to their experimental values: $T = 2.71$ s, $\Delta t = 20.74$ us, and $N_{total} = 2.71$ s/20.74 μs ~ 131000, we compute the photon counts $n_a(t)$ and $n_b(t)$ at two chosen pixels a and b, respectively, using eq. (S7). Then we calculate tfCCCs by placing $n_a(t)$ and $n_b(t)$ into eq. (2).

Here we provide results of numerical simulations when fluorescent particle is moving along the x-axis: $x_{0p} = y_{0p} = 0, v = 40$ μm/s $e_x, D = 560$ nm, $\Delta l = 1.6$ μm . We varied the size of the particle: $d = 100$ nm or $d = 2$ μm.

For a small particle with $d = 100$ nm, the calculated tfCCCs are shown in Fig. S2a-c. The volume element (1,1) is

fixed as pixel a. The partner pixel b for tfCCC calculation was varied as (1,2), (1,3) and (1,5), respectively.

The lag times of peaks in tfCCCs correspond to the travelling time of the 100 nm particle between two pixels. The average flight times are 0.04 s (for Δl), 0.08 s (for 2·Δl), and 0.16 s (for 4·Δl). The projection of the particle velocity in the focal plane is determined by the ratio of the distance between a and b to the position of the peak. From Fig. S2, $v = 1 \cdot \frac{\Delta l}{t_1} = 2 \cdot \frac{\Delta l}{t_2} = 4 \cdot \frac{\Delta l}{t_3} \sim 40 \ \mu m/s$. This is a theoretical proof that a particle velocity in the focal plane can be computed from tfCCC.

Next, we conducted numerical simulation when particle size (d = 2 μm) is larger than confocal volume element and pixel-to-pixel distance Δl (Fig. S2d-f). The tfCCCs computed in this case are also characterized by peaks appearing at particular time instants: 0.043 s, 0.083 s, and 0.17 s for Figs S2d-f, respectively. In contrast to a 100 nm fluosphere (Fig. S2a), the tfCCC in Fig. S2d is composed of a wider peak

standing on a high background before the peak has appeared. This high background is decreased (Fig. S2e), finally dropping to zero in Fig. S2f. When the particle radius is smaller, the photons are emitted from a single volume element at a time. This means that photon counts at different camera pixels are correlated only when time lag is equal to the time of flight. On the other hands, when diameter is large enough ($2r_p \geq \Delta l - D$), then particle can emit photons from different volume elements at the same time. The correlation then appears for time lags shorter than time of flight, which results in high cross-correlation values before the characteristic peak. In addition, the tfCCC peak is wider for larger particles (since it needs more time to pass through the entire volumes of two foci), making the velocity determination method from peak position less accurate.
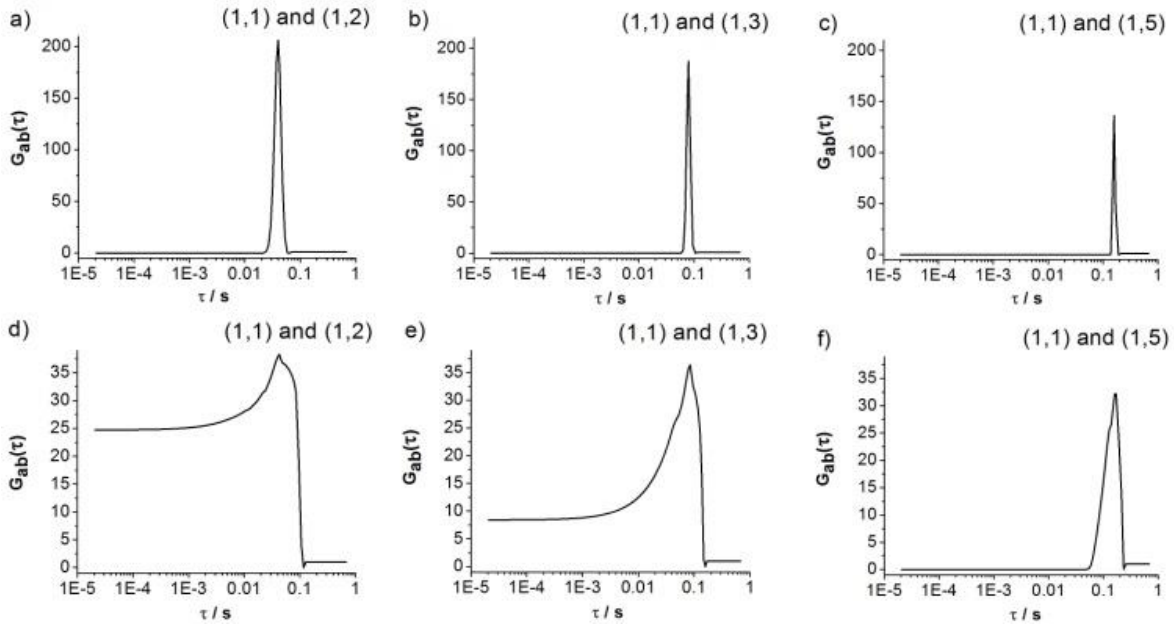

Figure S2. Theoretical simulation of particle movement. The two-foci cross-correlation curves (tfCCCs) corresponding to different pairs of volume elements that the 100 nm fluosphere **(a-c)** and 2 μm fluosphere **(d-f)** is passing through. The pixel pairs (a,b) are: a,d) (1,1) and (1,2), b,e) (1,1) and (1,3), c,f) (1,1) and (1,5). The particular peak in each graph indicates the time that a particle needs to arrive from pixel a and pixel b. **(a-c)** The peak positions on time axis are (a) t_1 = 0.04 s, (b) t_2 = 0.08 s, and (c) t_3 = 0.16 s for each pixel-pixel distances Δl, 2·Δl, and 4·Δl. Calculated velocity is 40 μm/s. **(d-f)** The peak positions on time axis are (d) t_1 = 0.043 s, (b) t_2 = 0.083 s, and (c) t_3 = 0.17 s for each pixel-pixel distances Δl, 2·Δl, and 4·Δl. Calculated velocity is 40 μm/s.

SI2c. The trajectory of particle motion at a non-zero angle with respect to the x-axis.

When the projection of particle velocity in the focal plane is oriented at a non-zero angle with respect to x-axis, then the speed can be determined from the tfCCC calculated between pixels that lie on a line which intercepts the x-axis under the same angle. To find the pixels pair for tfCCCs computation, the autocorrelation curves were determined first (Fig. S3).

For a d = 100 nm particle, single trace is obtained on the autocorrelation curves amplitude map. When 2 μm particle passes across the camera, its fluorescence signal is simultaneously detected in adjacent camera pixels leading to a "smeared" trace. The traces of particles in case of α = 30° angle between velocity vector and x-axis are shown in Figs S3a (d = 100 nm) and S3b (d = 2 μm). The results for α = 45° are shown in Figs S3c (d = 100 nm) and S3d (d = 2 μm).
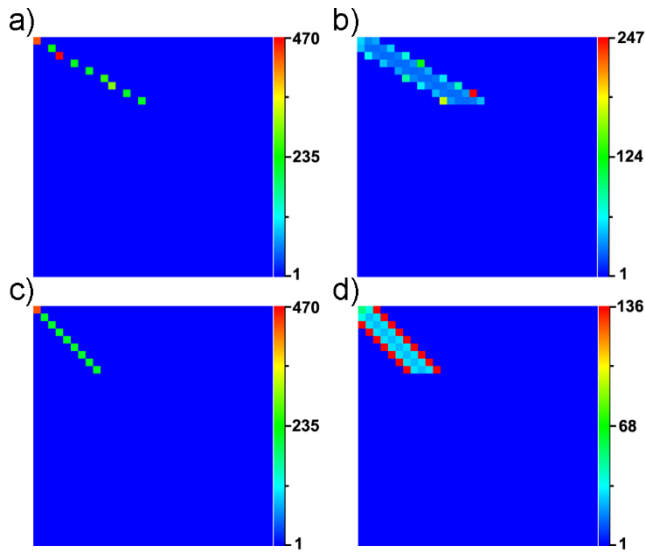
Figure S3. The amplitude of ACCs calculated up to the ninth row using theoretically obtained photons counts. Fluospheres diameter, d, and angle of motion (α) are: **(a)** d = 100 nm, α = 30°, **(b)** d = 2000 nm, α = 30°, **(c)** d = 100 nm, α = 45°, **(d)** d = 2000 nm, α = 45°.

The calculated tfCCCs for the angle α = 30° are shown in Fig. S4. Here, Figs S4a,b show data for a particle of diameter d = 100 nm and S4c,d for a particle d = 2 µm. The tfCCCs are calculated between the two volume elements (a,b) that a particle is passing through: a), c) (1,1) and (2,3), and b), d) (1,1) and (9,15). The positions of the peaks on the time axis are measured as: (a) 0.086 s, (b) 0.64 s, (c) 0.088 s, and (d) 0.61 s.
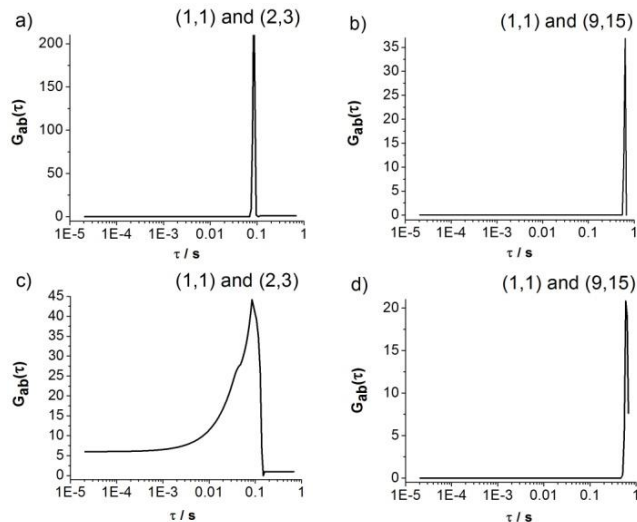
Figure S4. tfCCCs between the two volume elements *(a,b)*. **(a)** (1,1) and (2,3), **(b)** (1,1) and (9,15), **(c)** (1,1) and (2,3), and **(d)** (1,1) and (9,15). The angle between velocity projection in the focal plane and *x*-axis is α = 30°. Graphs shown in a) and b) correspond to particle of diameter d = 100 nm, while graphs shown in (c) and (d) correspond to particle diameter of d = 2 µm.

The theoretically preset velocity is exactly 40 µm/s, while the calculated values are: (a) 41.4 µm/s, (b) 40.2 µm/s, (c) 40.5 µm/s, and (d) 41.8 µm/s. The relative errors between exact and calculated speeds are less than 5 % which makes this method appropriate for measuring the velocity component along any direction in the focal plane.

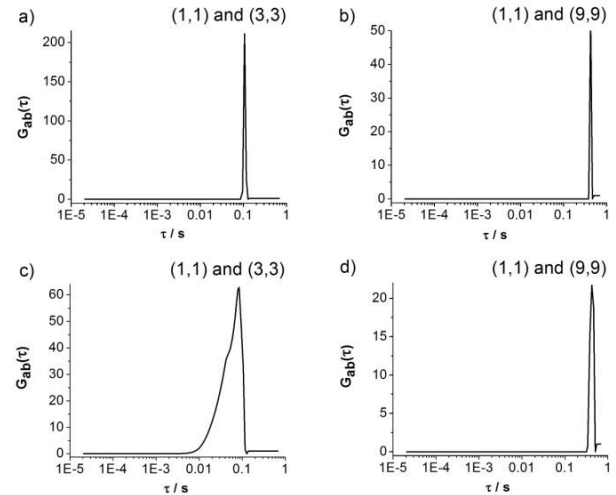We also show the tfCCCs when the angle of motion is α = 45° (Fig. S5).

Figure S5. tfCCCs between the two volume elements *(a,b)*. **(a)** (1,1) and (3,3), **(b)** (1,1) and (9,9), **(c)** (1,1) and (3,3), and **(d)** (1,1) and (9,9). The angle between velocity projection in the focal plane and *x*-axis is 45°. Figures (a) and (b) correspond to particle diameter of 100 nm, while figures (c) and (d) to particle diameter of 2 µm.

The tfCCCs were calculated between the two volume elements (a,b) that a particle is passing through: a), c) (1,1) and (3,3), and b), d) (1,1) and (9,9), for 100 nm and 2 µm particles. The peaks positions on time axis are measured as: (a) 0.11 s, (b) 0.42 s, (c) 0.084 s, and (d) 0.44 s. The exact velocity applied in a simulation is 40 µm/s, while the calculated values are: a) 41.9 µm/s, b) 42.8 µm/s, c) 53.5 µm/s, and d) 41.3 µm/s. The relative errors between exact and measured velocities are less than 5% for 100 nm particle (Figs S5a,b). However, the relative error was determined to 33% in case of 2 µm bead for a shorter pixel-to-pixel distance (Fig. S5c). The observed discrepancy could be explained in terms of very wide tfCCC maximum due to large particle diameter and a small pixel-to-pixel distance. This implicates that for certain angles and larger particles, the velocity should be calculated between the relatively distant pixels pairs.

S3: Proof-of-concept measurements using a piezo-based linear stage with nanometre positioning precision for controlled translation of immobilized quantum dots.

To validate the theoretical concepts under strictly controlled directional fluorescent particle motion, quantum dots (q-dots) immobilized on a glass surface were mounted

on a precise translation stage with a nanometer step size and the stage velocity was set to v_{stage} = 40 μm/s in the y-axis direction. The q-dot sample was translated over a specified distance and then rapidly, at a velocity v_{stage}^{return} >> 40 μm/s, brought back to the starting position. This procedure was repeated twice thereafter. Fluorescence intensity fluctuations collected using the SPC2 32×32 SPAD array camera were first analysed using temporal autocorrelation analysis (Fig. S6). Spatial mapping of the amplitudes of the auto-correlation curves (ACCs) at lag time τ = 20.74 μs, G(0), shows that the highest G(0) value was measured in pixel (7,29). The linear trajectory of the q-dot translation motion that started from pixel (7,29) is clearly visible across several rows in the 29th column (Fig. S6a). The actual ACC at pixel (7,29) is shown in Fig. S6b. The sharp peaks at long lag times reflect the moments when the same particle has entered pixel (7,29) for the second and the third time, respectively.
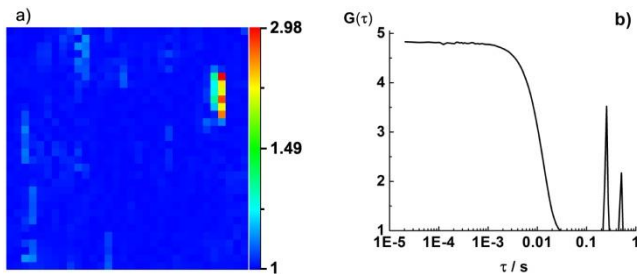

Figure S6. Autocorrelation measurements of immobilized q-dots translatory moved in the y-axis direction using a motorized stage. (a) The G(0) map showing amplitudes of temporal ACCs at lag time τ = 20.74 μs in the 32×32 SPAD array. **(b)** The ACC in pixel (7,29).

Of note, the characteristic decay time of the ACC in pixel (7,29), τ_c = 0.014 s, when multiplied with the pre-set velocity of the translational stage movement, v_{stage} = 40 μm/s, yields the diameter of the focal element: $d_F = v_{stage} \cdot \tau_c = 560$ nm. This value is in a good agreement with the focal diameter ω_{xy} = (510 ± 90) nm previously determined in mpFCS calibration experiments.[1]

Next, we calculated the tfCCCs corresponding to the different pairs of pixels along the trajectory generated by immobilized q-dots movement by stage translation along the y-axis. The results for pixel pairs (a,b) are presented in Fig. S7: a) (7,29) and (8,29), b) (7,29) and (9,29), c) (7,29) and (11,29), and d) (7,29) and (13,29). The lag times at which peaks in each tfCCC are observed indicates the q-dot arrival time to pixel b from pixel a. The first peak in figure a) corresponds to the travel time τ_1 of a particle between the i) first, ii) second, and iii) third subsequent arrivals in a and b. The second peak is measured at time τ_2, representing two events: i) the first arrival in a and the second arrival in b, and ii) the second arrival in a and the third arrival in b. Similarly, the third peak denotes the time interval between the

first arrival in a and the third arrival in b. Since fewer events are involved as time lag progresses, each subsequent peak has a lower amplitude. It should be noticed that all peaks are equidistant, $i.e.$, the time between adjacent peaks is Δτ = 0.255 s. The velocity of quantum dots is determined by the ratio of the distance between a and b to the position of the first peak. We have measured the velocity of q-dots in each graph a)-d), and the measured value agreed well with the value by which the translation stage was set to move.
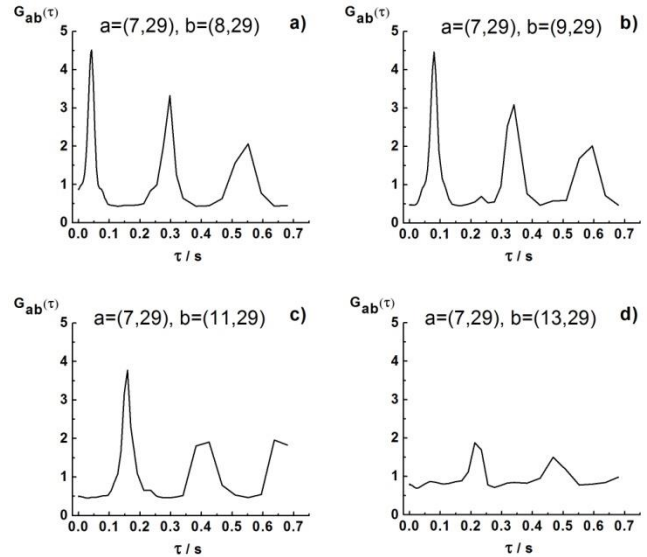

Figure S7. The tfCCCs between different pixels in case of translation motion of quantum dots. The pixel pairs (a,b) are: **(a)** (7,29) and (8,29), **(b)** (7,29) and (9,29), **(c)** (7,29) and (11,29), and **(d)** (7,29) and (13,29).

The velocity can be simply calculated from Fig. S7c): v = 4·1.59 μm / 0.158 s = 40 μm/s, as was adjusted at the translation stage. From Figs S7a to S7d, one can notice that if pixels a and b are at larger distance, the first peak is shifted on the time axis. This is expected since the particle will take longer time to reach b from a. Note that the time scales in all figures are linear, so the reader could easily observe equidistant peaks and thus the constant velocity of the q-dots, $i.e.$ stage, movement.

SI4: Comparison between auto- and two-foci cross-correlation analysis of diffusion and flow in dilute aqueous solution and nanoparticles in suspension
To verify the procedure for two foci cross-correlation, we show using dilute solution of eGFP, 100 base pairs double-stranded dual-colour labelled DNA (dc-DNA) and fluospheres (diameter, d = 20 nm) that tfCCCs for pure diffusion is zero (Fig.S8).
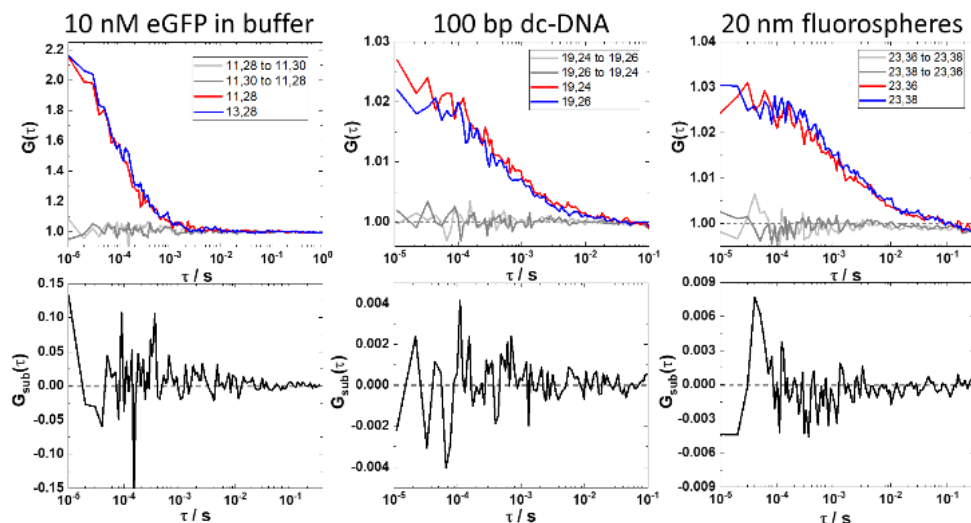
Figure S8. Spatial mapping of the direction and extent of transport in solution using two-foci cross-correlation in mpFCS. *Upper row:* Autocorrelation curves in individual pixels (red and blue) and corresponding cross-correlation curves calculated in opposite directions (light and dark grey) recorded in an aqueous buffer solution of eGFP (left), 100 bp ds-DNA (middle) and 20 nm fluospheres (right). *Lower row:* Corresponding $G_{c,sub}(\tau)$ obtained by subtracting the two-foci cross-correlation curve calculated in one direction, from the two-foci cross-correlation curve calculated in the opposite direction.

Moreover, we further corroborate the "360° sweeping procedure" by showing the results of two-foci cross-correlation analysis between all adjacent pixels for eGFP that undergoes free 3D diffusion only (Fig. S9).
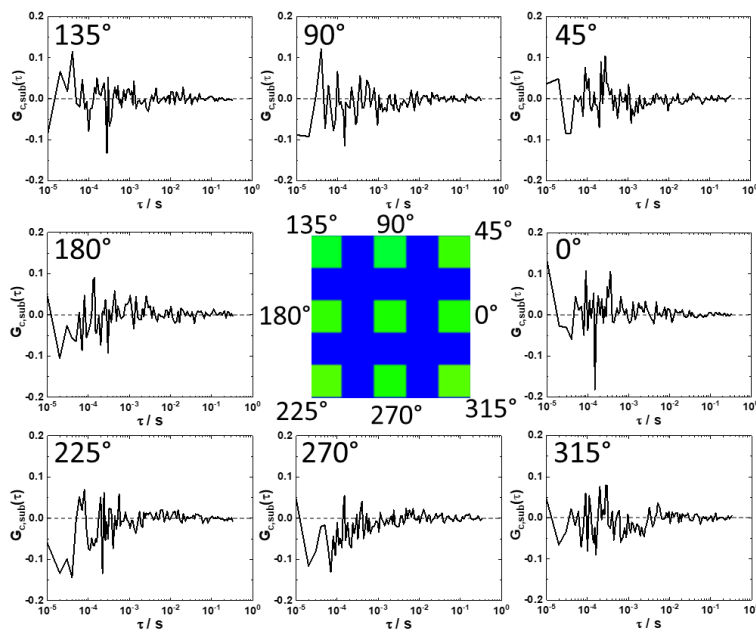

Figure S9. eGFP motion in a diluted aqueous solution assessed by two-foci cross-correlation analysis. Subtracted cross-correlation curves $G_{c,sub}(\tau)$ are calculated by subtracting one tfCCC calculated between two pixels from the other calculated in the opposite direction. For all lag time values, the amplitude of $G_{c,sub}(\tau)$ is close to zero, and the characteristic narrow peak that is typical when directed motion, *i.e.* flow is observed is not seen, as expected for free 3D diffusion of eGFP.

Finally, we show that while directed motion can also be observed in ACCs by residuals analysis, two-foci cross-correlation analysis is more powerful in this regard (Fig. S10).
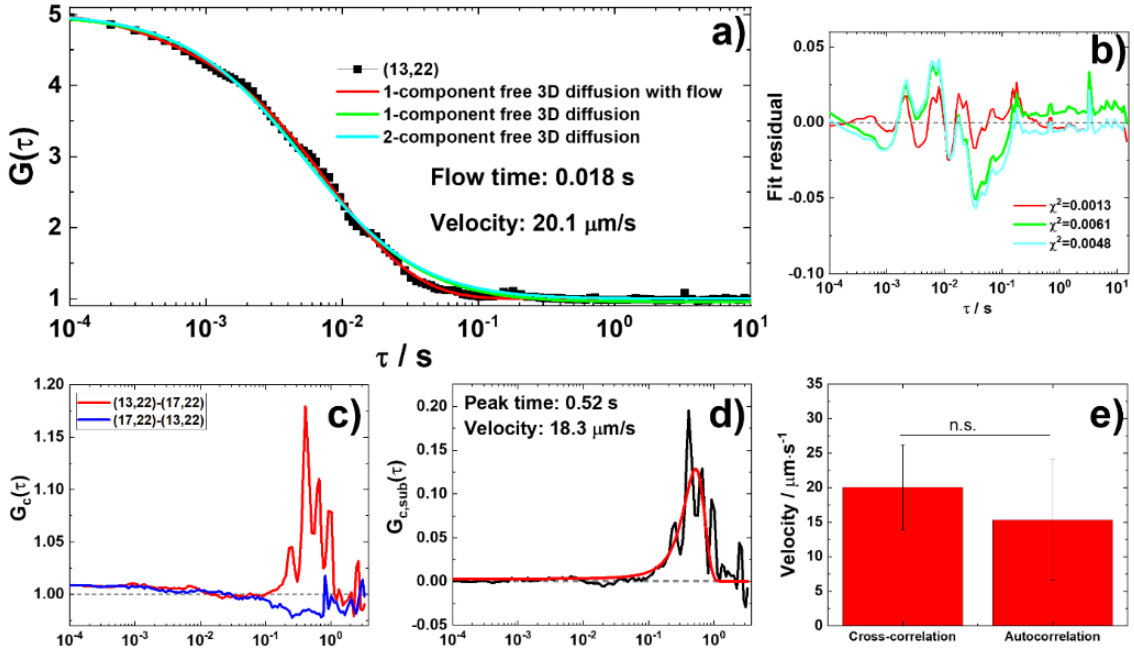
6

Figure S10. Autocorrelation and two-foci cross-correlation analysis of directional particle motion in a diluted suspension of 100 nm fluospheres. (a) Temporal autocorrelation curve in a single pixel (black) fitted to different model functions: free 3D diffusion of one component with flow (red), yielding a diffusion time τ_D = 5.5 ms and flow velocity of 20.1 µm/s; free 3D diffusion of one component without flow (green), yielding a diffusion time τ_D = 5.5 ms; and free 3D diffusion of two components (cyan), yielding two components with nearly equal contributions and roughly the same diffusion time τ_{D1} = 5.2 ms and τ_{D2} = 5.4 ms. **(b)** Unweighted fit residuals showing the difference between the experimental ACC and the values obtained by fitting different model functions indicated in a). The colour code is the same as in (a). Based on the analysis of fitting residuals, the best fit with the experimental ACC is obtained when using a model for free 3D diffusion with flow (red). **(c)** Two-foci cross-correlation curves (tfCCC) calculated in opposite directions, $G_{(13,22)\rightarrow(17,22)}(\tau)$ in the direction $(13,22) \rightarrow (17,22)$ (red) and $G_{(17,22)\rightarrow(13,22)}(\tau)$ in the direction $(17,22) \rightarrow (13,22)$ (blue). **(d)** The subtracted cross-correlation curve $G_{c,sub}(\tau)$ = $G_{(13,22)\rightarrow(17,22)}(\tau) - G_{(17,22)\rightarrow(13,22)}(\tau)$ obtained after subtracting the tfCCCs calculated for different directions of motion (black) fitted using a Gaussian distribution function (red), yielding a peak at the lag time τ_{Peak} = 0.52 s, which is also the transit time between the two foci. Consequently, the 2D flow velocity could be assessed, v_{flow} = 18.3 µm/s. **(e)** Flow velocities determined by tfCCC analysis agreed well with values estimated by temporal ACC fitting using the model function for free 3D diffusion of one component with flow.

In Fig. S10, the following analytical functions were fitted to the experimentally derived ACCs.

For free 3D diffusion of one or two components, eq. (S8) was used:

$$G(\tau) = G(\infty) + \frac{1}{N} \cdot \left[1 + \frac{T}{1-T} e^{-\frac{\tau}{\tau_T}}\right] \cdot$$

$$\cdot \left(\sum_{k=1}^{n} \frac{f_{D,k}}{\left(1 + \frac{\tau}{\tau_{D_k}}\right)\sqrt{1 + \frac{\omega_{xy}^2}{\omega_z^2} \cdot \frac{\tau}{\tau_{D_k}}}}\right) \quad (S8)$$

where, $G(\infty)$ denotes the value to which the autocorrelation curve converges at infinitely long measurement time; T is the fraction of molecules in the triplet state and τ_T is the average relaxation time of the triplet state (when not applicable, T = 0); n is the number of freely diffusing components

(n = 1 or 2); $f_{D,k}$ is the relative molar fraction of the k-th component (the sum of relative molar fractions is equal to 1); $\tau_{D,k}$ is the is the translational diffusion time of k-th component; ω_{xy} and ω_z are the $1/e^2$ radial and axial radii of the observation volume element (OVE), respectively. The ω_{xy} and ω_z are determined by mpFCS instrument calibration using a dilute suspension of 100 nm fluorospheres.

For free 3D diffusion of one component with flow. eq. (S9) was used:

$$G(\tau) = G(\infty) + \frac{1}{N} \cdot \left[1 + \frac{T}{1-T} e^{-\frac{\tau}{\tau_T}}\right] \cdot$$

$$\cdot \frac{1}{\left(1 + \frac{\tau}{\tau_D}\right)\sqrt{1 + \frac{\omega_{xy}^2}{\omega_z^2} \cdot \frac{\tau}{\tau_D}}} \cdot exp\left[-\frac{\left(\frac{\tau}{\tau_f}\right)^2}{1 + \frac{\tau}{\tau_D}}\right]$$

$$(S9)$$

where τ_f is the transport time; v_{flow}= ω_{xy}/τ_f is the flow velocity.

SI5: Glucocorticoid receptor nucleocytoplasmic translocation in live cells.

SI5a: Experimental data replicates and fitting

Fig. S11a shows 13 individual $G_{c,sub}(\tau)$ calculated at all positions shown in Fig. 3. Nuclear import (red) was observed at positions #1, 2, 3, 8, 9, 12 and 13, and nuclear export (blue) was observed at positions #4, 5, 6 and 11. In Fig. 11b, $G_{c,sub}^{av}(\tau)$ show average of nuclear import (red) and nuclear export (blue) in three different cells (Fig. 11b$_1$-b$_3$).
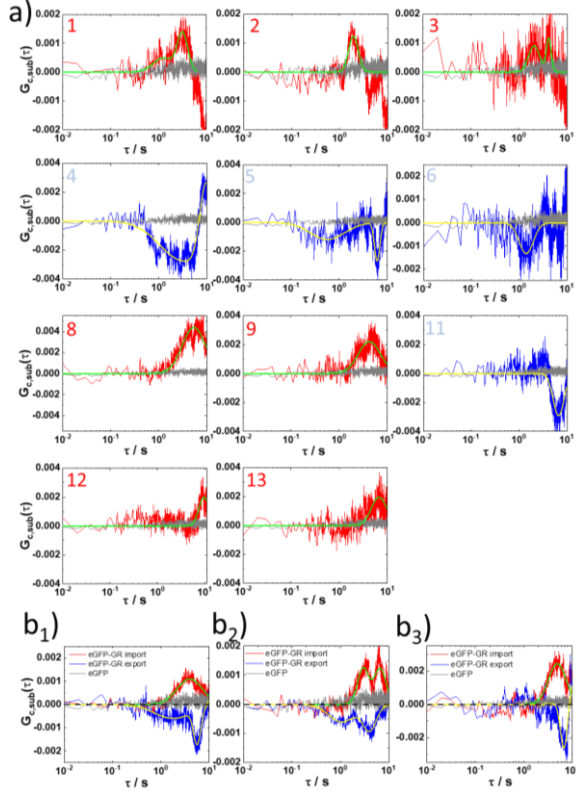

Figure S11. **Glucocorticoid receptor nucleoplasmic translocation in live cells. (a)** Individual $G_{c,sub}(\tau)$ showing nuclear import (red) and export (blue) at all sites shown in Fig. 3. Translocation time is determined by Gaussian distribution fitting to the $G_{c,sub}(\tau)$ (green/yellow). (**b$_1$-b$_3$**) $G_{c,sub}^{av}(\tau)$ show average of nuclear import (red) and export (blue) in three different cells. Data shown in b$_1$ correspond to data shown in Fig. 3.

The Origin Multiple Peak Fit tool was used to fit the peaks in $G_{c,sub}(\tau)$ with Gauss peak function:

$$G_{c,sub}(\tau) = G_0 + \sum_{k=1}^{n} \frac{S_k}{w_k \cdot \sqrt{\frac{\pi}{2}}} \cdot e^{\left(\frac{-2\cdot(\tau-t_k)^2}{w_k^2}\right)} \quad \text{(S10)}$$

In eq.(S10), $G(\infty)$ denotes the value to which the cross-correlation curve converges at infinitely long measurement time; S, w and t are the area, width, and peak time of the

fitted Gaussian model, respectively; n is the number of components, set as 1 or 2.

The average transporting time, t_{av} is computed when the subtracted cross-correlation shows multiple peaks:

$$t_{av} = \frac{s_1}{s_1+s_2} \cdot t_1 + \frac{s_2}{s_1+s_2} \cdot t_2 \quad \text{(S11)}$$

In case of single component, S_2 is equal to 0.
The translocation net rate, ψ_{net}, is calculated at each position in a live cell, as:

$$\psi_{net} = \frac{A_1}{t_1} + \frac{A_2}{t_2} \quad \text{(S12)}$$

In eq. (12), A_1 and A_2 are the amplitudes of the Gaussian distribution of each component. When a single peak was observed, A_2 is equal to 0.
The goodness of fit was assessed by residuals analysis (data not shown). When the residuals appeared to be ran-domly scattered around zero, we have regarded that the model describes the data well.

SI5b: Theoretical validation of net rate calculation

To corroborate the experimental analysis for net rate determination by $G_{c,sub}(\tau)$, numerical simulations were used to emulate the bidirectional movement of eGFP-GR into/out of the cell nucleus. As a first approximation, we have regarded in numerical simulations the passing of a molecule through the nuclear pore complex as a one-dimensional translation motion (Fig. S12).
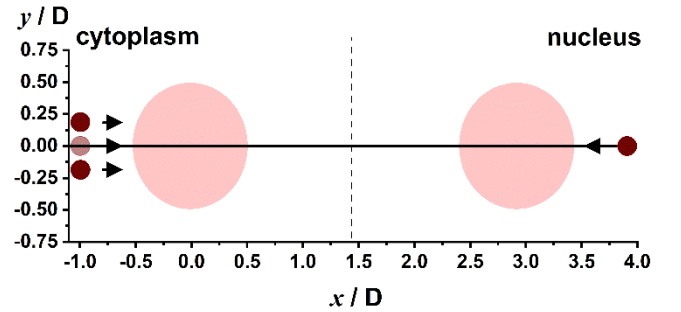

Figure S12. Schematic drawing of bidirectional translation of fluorescent particles along the *x*-axis through two adjacent observation volume elements (OVEs). The small wine circles represent fluorescent nanoparticles of diameter d = 100 nm. The large pink circles represent adjacent OVEs, the diameter of which was set in the numerical simulations to the experimentally determined value, D_{OVE} = 560 nm. The distance between OVE centres, Δl = 100 μm/63 = 1.59 μm, corresponds to real properties of our experimental setup – pitch distance between SPADs in the SPC^2 camera is 100μm and the microscope objective magnification is 63×. When simultaneous movement of two fluorescent particles is considered, their displacement from the central axis was D/10. The starting position of fluorescent particles from either side of the OVEs was arbitrarily set to Δl/6.
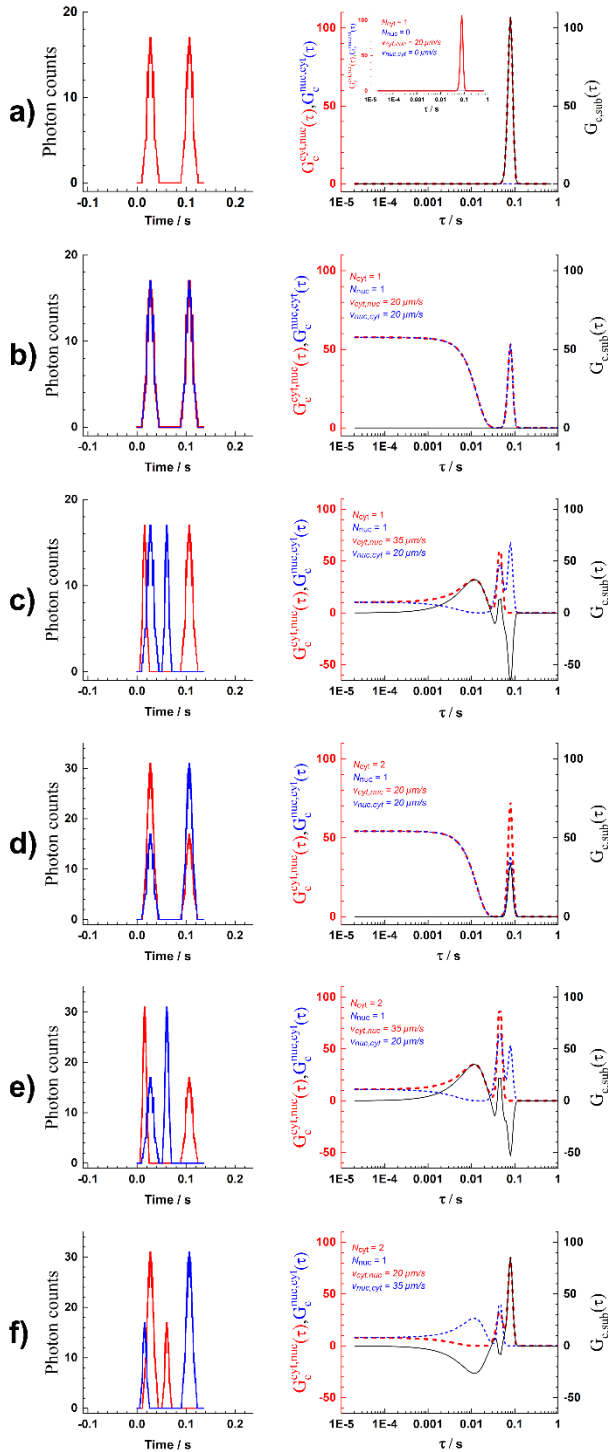
8

The results of numerical simulations are summarised in Fig. S13, with photon counts shown on the left and the corresponding tfCCCs to the right. In particular, the following distinct cases were considered: one fluorescent particle moving from the cytoplasm to the nucleus (Fig. S13 a); concomitant movement of two fluorescent particles, one from the cytoplasm and one from the nucleus, with the particles moving at the same (Fig. S13b) or different (Fig. S13c) speeds; and concomitant movement of three fluorescent particles, two fluorescent particles from the cytoplasm to the nucleus and one from the nucleus to the cytoplasm, with the particles moving at the same (Fig. S13d) or different (Fig. S13 e and f) speeds.

In the numerical simulations, photon counts distribution is emulated as the fluorescent particles (small, wine circles in Fig. S12) pass through the OVEs (large, shaded circles in Fig. S12). The excitation intensity distribution in the OVEs is Gaussian, and the fluorescence intensity, *i.e.*, photon count is zero when there is no fluorescent particle in the OVE (no background and no noise). The OVE diameter was set to the experimentally determined value, D_{OVE} = 560 nm, and the distance between the centres of the OVEs, Δl = 100 μm/63 = 1.59 μm, corresponds to real properties of our experimental setup – pitch distance between SPADs in the SPC² camera is 100μm and the microscope objective magnification is 63×. The time frame duration Δt = 20.74 μs, as in the real experiment. The fluorescent particle diameter was arbitrarily set to d = 100 nm. In cases when the movement of one or bidirectional motion of two fluorescent particles is considered, movement along the *x*-axis is simulated (Fig. S12, y/D = 0) and the obtained photon counts distributions are shown in Fig. S13 a, b and c, left panel. In cases when concomitant motion of three particles is considered, movement along a trajectory that is parallel to the *x*-axis (Fig. S12, y/D = 0.1) is simulated for the side from which two particles are moving and movement along the *x*-axis (Fig. S12, y/D = 0) is considered from the side from which one fluorescent particle is moving. The photon counts distributions for the latter case are shown in Fig. S13 d, e and f, left panel. The tfCCCs are calculated from the simulated photon counts distribution (Fig. S13, left panel) using eq. (2). Corresponding tfCCCs $G_c^{cyt,nuc}(\tau)$ and $G_c^{nuc,cyt}(\tau)$, as well as $G_{c,sub}(\tau)$, are shown in Fig. S13, right panel.

Of note, the results shown in Fig. S13 represent a small subset of many possible solutions of this complex problem. Nevertheless, they give us the first rough answers on how $G_{c,sub}(\tau)$ changes when the concentration of translocating molecules, their translation velocities, and the relative positions of nuclear pore complexes within the OVE are varied.

SI5c: Theoretical analysis of the effect of diffusion on the net rate of nuclear translocation

To emulate the effect of diffusion on the translation motion, we have numerically simulated the simplest case of combined translational and diffusion motion of a single fluorescent particle through two volume elements (Fig. S14).
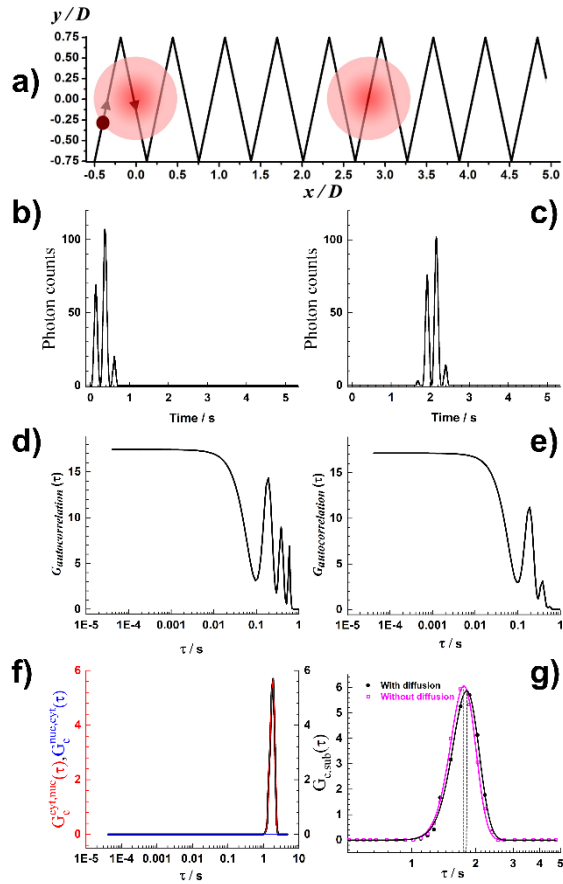
Figure S13. Numerical simulation of nuclear import/export. *Left panel*: Photon counts distribution in the cytoplasmic OVE (red) and the nuclear OVE (blue). *Right panel:* Corresponding tfCCCs $G_c^{cyt,nuc}(\tau)$ (red), $G_c^{nuc,cyt}(\tau)$ (blue), and $G_{c,sub}(\tau)$ (black). **(a)** N_{cyt} = 1, N_{nuc} = 0, $v_{cyt,nuc}$= 20 μm/s, $v_{nuc,cyt}$= 0 μm/s; **(b)** N_{cyt} = 1, N_{nuc} = 1, $v_{cyt,nuc}$ = 20 μm/s, $v_{nuc,cyt}$= 20 μm/s; **(c)** N_{cyt} = 1, N_{nuc} = 1, $v_{cyt,nuc}$= 35 μm/s, $v_{nuc,cyt}$= 20 μm/s; **(d)** N_{cyt} = 2, N_{nuc} = 1, $v_{cyt,nuc}$= 20 μm/s, $v_{nuc,cyt}$= 20 μm/s; **(e)** N_{cyt} = 2, N_{nuc} = 1, $v_{cyt,nuc}$= 35 μm/s, $v_{nuc,cyt}$= 20 μm/s; **(f)** N_{cyt} = 2, N_{nuc} = 1, $v_{cyt,nuc}$= 20 μm/s, $v_{nuc,cyt}$= 35 μm/s.

Figure S14. Emulating the effect of diffusion on the translation of molecules using tfCCC analysis. (a**)** Schematic drawing of the combined translational and diffusion motion of a single fluorescent particle (small wine circle) through two OVEs (large circles). **(b, c)** The simulated photon counts over time as the particle is passing through the OVE on the left (b) and right (c). **(d, e)** Autocorrelation curves reflecting fluorescent particle passage through the left and right OVE, $G_l(\tau)$ (d) and $G_r(\tau)$ (e), respectively. **(f)** The tfCCCs from left to right (red) and from right to left OVE (blue) and their difference, $G_{c,sub}(\tau)$ (black). **(g)** Diffusion broadens somewhat $G_{c,sub}(\tau)$, as reflected by $FWHM_m^{diff}$ = 0.65 s as compared to $FWHM_m$ = 0.59 s, and slightly changes the peak position towards longer lag times.

In the numerical simulations, the effect of diffusion on the directed motion was modelled as displacement in the y-axis direction – the translational velocity along x-axis is v_{transl} = 0.9 μm/s, and the y-component of the velocity changes over time the sign, but the magnitude of change is the same, v_{diff} = 4.3 μm/s (Fig. S14a). The fluorescent particle (Fig. S14a, wine circle) first passes through the left OVE, positioned in the cytoplasm, and after some time through the OVE on the right, positioned in the cell nucleus. The photon counts distribution over time reflecting fluorescent particle passage through the left, *i.e.*, cytoplasmic OVE, and the right, *i.e.*, nuclear OVE, are shown in FigS14 b and c, respectively. The corresponding ACCs $G_{cyt}(\tau)$ and $G_r(\tau)$ are presented in Fig. S14 d and e, respectively. The translational motion of the fluorescent particle can be clearly observed from the subtracted cross-correlation curve, $G_{c,sub}(\tau)$ = $G_{cyt,nuc}(\tau)$ - $G_{nuc,cyt}(\tau)$ (Fig. S14f). The $G_{c,sub}(\tau)$ peak is observed at a lag time τ_m^{diff} = 1.81 s, which corresponds to the time of flight between the two volume elements due to translational motion coupled with free diffusion. As expected, in the absence of diffusion, the $G_{c,sub}(\tau)$ peak is shifted towards slightly shorter lag times, τ_m = 1.75 s and a small peak broadening is noted in the presence of free diffusion, as reflected by the full width at half maximum, $FWHM_m^{diff}$ = 0.65 s as compared to $FWHM_m$ = 0.59 s (Fig. S14g).

References

[1] Krmpot, A.J.; Nikolić, S.N.; Oasa, S.; Papadopoulos, D.K.; Vitali, M.; Oura, M.; Mikuni, S.; Thyberg, P.; Tisa, S.; Kinjo, M.; Nilsson, L.; Terenius, L.; Rigler, R.; Vukojević, V. Functional Fluorescence Microscopy Imaging: Quantitative Scanning-Free Confocal Fluorescence Microscopy for the Characterization of Fast Dynamic Processes in Live Cells. Anal Chem. 2019, 91, 11129-11137.

Interactions of ultrashort laser pulses with hemoglobin: Photophysical aspects and potential applications

Mihajlo D. Radmilović [a], Ivana T. Drvenica [b], Mihailo D. Rabasović [a], Vesna Lj. Ilić [b],
Danica Pavlović [a], Sho Oasa [c], Vladana Vukojević [c], Mina Perić [d,e], Stanko N. Nikolić [a,f],
Aleksandar J. Krmpot [a,f,*]

[a] Institute of Physics Belgrade, University of Belgrade, Belgrade, Serbia
[b] Institute for Medical Research, National Institute of Republic of Serbia, University of Belgrade, Belgrade, Serbia
[c] Department of Clinical Neuroscience, Karolinska Institutet, Stockholm, Sweden
[d] Faculty of Biology, University of Belgrade, Belgrade, Serbia
[e] Institute of Molecular Genetics and Genetic Engineering, University of Belgrade, Belgrade, Serbia
[f] Division of Arts and Sciences, Texas A&M University at Qatar, Doha, Qatar

ABSTRACT

Hemoglobin (Hb), a life-sustaining and highly abundant erythrocyte protein, is not readily fluorescent. A few studies have already reported Two-Photon Excited Fluorescence (TPEF) of Hb, however, the mechanisms through which Hb becomes fluorescent upon interaction with ultrashort laser pulses are not completely understood. Here, we characterized photophysically this interaction on Hb thin film and erythrocytes using fluorescence spectroscopy upon single-photon/two-photon absorption, and UV-VIS single-photon absorption spectroscopy. A gradual increase of the fluorescence intensity, ending up with saturation, is observed upon prolonged exposure of Hb thin layer to ultrashort laser pulses at 730 nm. When compared to protoporphyrin IX (PpIX) and oxidized Hb by H_2O_2, TPEF spectra from a thin Hb film and erythrocytes showed good mutual agreement, broad peaking at 550 nm, supporting hemoglobin undergoes degradation and that same fluorescent specie(s) originating from the heme moiety are generated. The uniform square shaped patterns of the fluorescent photoproduct exhibited the same level of the fluorescence intensity even after 12 weeks from the formation, indicating high photoproduct stability. We finally demonstrated the full potential of the formed Hb photoproduct with TPEF scanning microscopy towards spatiotemporally controlled micropatterning in HTF and single human erythrocyte labelling and tracking in the whole blood.

1. Introduction

Human adult hemoglobin (Hb) is an iron-containing metalloprotein in erythrocytes, the primary function of which is to transport oxygen from the lungs to all other organs and tissues. It is made up of two α- and two β-polypeptide chains, each associated with one hem prosthetic group [1]. While the absorption spectrum of oxyhemoglobin (oxyHb) shows several bands, as the intense Soret or B band in the region of 370 nm - 450 nm and the so-called Q-band in the region of 500 nm – 650 nm in the porphyrin ring [2], the conventional single-photon excitation fluorescence (SPEF) of Hb is not or hardly detectable due to the fast non-radiative decay that dominates over spontaneous fluorescence emission [3–5]. In contrast, the intense two-photon absorptivity of Hb in the near-infrared range [6] followed by strong fluorescence emission, have made Two-Photon Excited Fluorescence (TPEF) imaging possible [4] and applicable in a number of studies: for erythrocytes imaging [7,8], analysis of residual Hb distribution in empty erythrocytes membranes (i. e., erythrocyte ghosts) [9], in vivo imaging of microvasculature [10–12], and even time-resolved diagnostic imaging [13]. Of note, Hb excitation through a two-photon absorption process, which is governed by significantly different selection rules than single photon absorption, is described in detail in [3,5], while the corresponding single and two photon absorption spectra are given in [6].

Due to high absorptivity of Hb in the VIS and near infrared (NIR) region, erythrocytes are also readily imaged using absorption-based techniques, such as photo-acoustic microscopy [14]. Photo-acoustic

---

microscopy is an imaging technique that leverages the non-radiative decay of Hb, which happens to be the most frequently used contrast agent for this modality [15–17]. Another type of label free imaging techniques, used for erythrocytes imaging is the nonlinear Third Harmonic Generation (THG) microscopy. This method has demonstrated efficacy in imaging erythrocytes contained within transfusion bags. [18].

The significance of photochemical manipulation of proteins is especially boosted by the discoveries of their optogenetics, photobiomodulation and bioimaging applications in recent years [19,20]. Understanding the photophysical and photochemical processes during the interaction of Hb with ultrashort laser pulses is of great importance for the development of functional imaging aimed for the assessment of erythrocytes functional status [21], where hemoglobin is the main intracellular protein of these cells. Besides, a better understanding of the interaction of Hb with ultrashort laser pulses could contribute to the development of new methods for the characterization and tracking of extracellular Hb presence. This implies extracellular Hb from endogenous sources due to hemolysis (in all diseases where in common feature is hemoglobinemia, such retinopathy, neuropathy, nephropathy and brain hemorrhages) [22], or exogenous sources, such in the cases of use of hemoglobin-based oxygen carriers [23] and hemoglobin-based drug delivery system, which have great potential in cancer therapy [22,24,25]. So far it was only shown that upon ultrashort laser pulses interaction with Hb, there is relation between TPEF spectra of heme and hemoglobin, as stated in [3].

However, despite already established, as well as emerging applications of Hb-based TPEF microscopy, the origin of generated fluorescence still needs to be completely understood. While it was initially proposed that the origin of the observed Soret fluorescence (420–460 nm) with a fluorescence emission peak at 438 nm originates from Hb [3], it was shown that TPEF does not directly originate from Hb, but rather from a photoproduct created upon the interaction of ultrashort laser pulses used in this nonlinear imaging technique with Hb [26]. This lack of basic understanding motivated us to deeper study ultrashort laser pulses interaction with Hb, with a particular focus on characterizing the durability of the Hb photoproduct and experimental conditions under which it is being formed. Since we efficiently demonstrated utility of TPEF microscopy to image the erythrocytes, the ultrashort laser pulses interaction with Hb was further photophysically characterized on thin Hb films using fluorescence spectroscopy upon two-photon absorption, UV-VIS single-photon absorption spectroscopy, and spectral fluorescent imaging. To examine whether degradation of the heme moiety occurs when ultrashort laser pulses used in TPEF microscopy imaging interact with Hb, spectroscopic properties of heme precursor protoporphyrin IX (PpIX), a heterocyclic organic compound that consists of four pyrrole rings, were analyzed. In addition, photophysical properties of the Hb photoproduct were compared to photophysical properties of compound (s) formed under Hb oxidation with hydrogen peroxide (H_2O_2) [27,28] to determine whether there are differences in the optical response of products formed under chemically induced Hb degradation. Finally, we examined the potential of the Hb photoproduct to be used for micro-patterning and single erythrocyte tracking.

2. Materials and methods

2.1. Sample collection and processing

Venous blood from healthy human volunteer was collected at the Institute for Transfusiology and Hemobiology, Military Medical Academy, Belgrade, Serbia. The protocol was approved by the Institutional Ethical Review Board (No 9/2021). In conformance with the World Medical Association Declaration of Helsinki, informed consent was obtained from potential participants. The blood was drawn using vacutainer tubes (10 mL plastic vacutainer (BD Vacutainer® EDTA Tubes) with BD Hemogard™ lavender closure containing 18 mg K2EDTA). To

prepare slides for direct TPEF microscopy imaging of erythrocytes, 10 μL of whole blood was diluted in isotonic saline solution (0.9 % NaCl, Natrii chloridi infundibile 9 g/L, Hemofarm, Serbia) in the volume: volume ratio 1:30. 3 μL of diluted whole blood sample was smeared onto a microscope slide, covered by a No. 1.5 coverslip and sealed.

2.2. Hb isolation

To isolate hemoglobin, human erythrocytes were precipitated by whole blood centrifugation. To this aim, 10 mL of whole blood was centrifuged at 1811 $\times g$ for 20 min at 4 °C (Megafuge 1.0R, Heraus centrifuge, Langenselbold, Germany). The supernatant, consisting of leucocytes in plasma, was carefully removed by aspiration and discarded. The precipitated erythrocytes were resuspended in isotonic saline solution (0.9 % NaCl, Natrii chloridi infundibile 9 g/L, Hemofarm, Serbia) in a volume:volume ratio of 1:4 and the suspension was homogenized by fine twisting the test tube. The remaining plasma proteins were removed by centrifugation of the erythrocyte suspension at 1257 $\times g$ for 10 min at 4 °C. These steps were repeated three times. Finally, the precipitated erythrocytes (packed) were resuspended in the isotonic phosphate buffered saline solution (PBS; 0.8 % saline buffered with 10 mM sodium phosphate, pH 7.2–7.4) in the volume: volume ratio of 1:4.

The hemolysis of erythrocytes suspension was performed using hypotonic 5 mM sodium phosphate buffer, pH 7.2, at 4 °C. Specifically, in 1 mL of erythrocytes suspension in PBS, 9 mL of 5 mM sodium phosphate buffer was added, and the tube was slightly mixed and then left at 4 °C for 1 h. The suspension was centrifuged at 3220 $\times g$ for 40 min at 4 °C. After centrifugation, the supernatant fluid containing released Hb molecules was collected, and the aliquots were filtered through 0.2 μm syringe filter. If not used immediately, the samples of Hb were aliquoted and stored at −20 °C for future use. Just before the experiment, a Hb aliquot would be thawed, and its concentration checked. Only one freeze-thaw cycle was allowed so the aliquots were discarded after experiment performed. All tests were done with Hb stored for less than two years from Hb isolation, since our previous results showed that it remains intact-undecomposed and non-aggregated under these storage conditions [29].

2.3. Hb thin film preparation for TPEF microscopy imaging

Thin Hb films were prepared by smearing 5 μL of Hb on the microscope slide, air-drying for 3 min and covered by No. 1.5 coverslip and sealed. The film thickness was <50 μm, as measured by confocal laser scanning microscopy, i.e., scanning along the *z*-axis. The smallest step of motorized the microscope stage stepper motor was 0.3 μm.

2.4. Protoporphyrin IX (PpIX) thin film preparation for TPEF microscopy imaging

Protoporphyrin IX (PpIX) in the form of a disodium salt was purchased from Sigma Aldrich (USA) and used without further purification. 20 μM stock solution of PpIX was prepared by dissolving 0.1 g of PpIX in 1 M HCl to the total volume of 50 mL. The stock solution was stored at 25 °C protected from light, to minimize photo-induced degradation of PpIX. To prepare slides for TPEF spectroscopy and spectral imaging, the PpIX stock solution was diluted in 1 × PBS (Sigma Aldrich, 140 mM NaCl, 10 mM phosphate buffer, and 3 mM KCl, pH 7.4) to the final concentration of 5 μM. 5 μL of this solution was placed on a microscope slide and treated in the same way as for Hb thin film preparation described above.

2.5. TPEF imaging of Hb treated with H_2O_2

The 22.5 M H_2O_2 was diluted using PBS (Sigma Aldrich, 140 mM NaCl, 10 mM phosphate buffer, and 3 mM KCl, pH 7.4) to a concentration of 250 μM. Further, 1 mL of Hb at a concentration of 22.3 g/L,

was incubated with 0.5 mL of 250 μM H_2O_2 for 30 min at room temperature (≈ 21 °C). After incubation, 5 μL of this mixture was placed on a microscope slide, smeared, dried, covered by a #1.5 coverslip and sealed.

2.6. TPEF scanning microscopy, micropatterning, and micro-spectroscopy

The experimental setup and home built TPEF microscope have been previously reported [30,31]. In this work, we upgraded it for micro-patterning and micro-spectroscopic experiments. Schematic drawing of the experimental setup is shown in Fig. 1. The Ti:Sapphire laser (Coherent, Mira 900-F), pumped by a frequency-doubled Nd:YVO4 laser (Coherent, Verdi V10), was used to generate ultrashort laser pulses with the repetition rate of 76 MHz and pulse duration of 160 fs. Galvo-scanning mirrors (Cambridge Technology) are used for raster scanning and micropatterning. Two microscope objectives were used in this study: EC Plan-NEOFLUAR 40× /1.3 N.A. oil (Carl Zeiss) for erythrocyte imaging and Plan-Apochromat 20× /0.8 N.A. air (Carl Zeiss) for Hb micropattering. The laser beam was expanded to fulfill the back aperture of the objective lens. A short-pass dichroic mirror was used to reflect the laser beam towards the objective lens and transmit the signal to the 15.1-megapixel digital single-lens reflex (DSLR) camera (Canon, EOS 50D) and the Photomultiplier Tube (PMT) (RCA, PF1006). The DSLR camera was used for taking bright-field images. We removed the infrared filter from the camera to see the back reflection of the laser beam from the cover glass for the purpose of system alignment and to facilitate axial positioning of the thin Hb layer. Band pass filters (VIS and/or 450 nm short pass) were placed in front of the PMT to collect Hb photoproduct fluorescence. A 700 nm long pass filter was used to remove parasitic laser lines shorter than 700 nm. A short pass 700 nm filter was placed in front of the PMT detector to additionally remove back scattered laser light. The Hb photoproduct formation and erythrocytes imaging were performed at 730 nm ultrashort laser pulses. This wavelength is chosen as optimal according to the optical setup and properties of Hb molecule, whilst details are given in our previous study [9].

In addition, we were able to record in situ TPEF emission spectra of the Hb photoproduct and erythrocytes using fiber-coupled, thermo-electrically (TE) cooled charge-coupled device (CCD) spectrometer with reduced thermal noise (Glacier X, BWTEK). To collect the TPEF emission from arbitrary chosen excitation point, the fiber was attached to the adapter plate (Thorlabs, S1SMA) mounted on the precise translation stage (Thorlabs, ST1XY-D/M). Henceforth, we refer to the in situ acquisition of TPEF emission spectra from an arbitrarily chosen point in
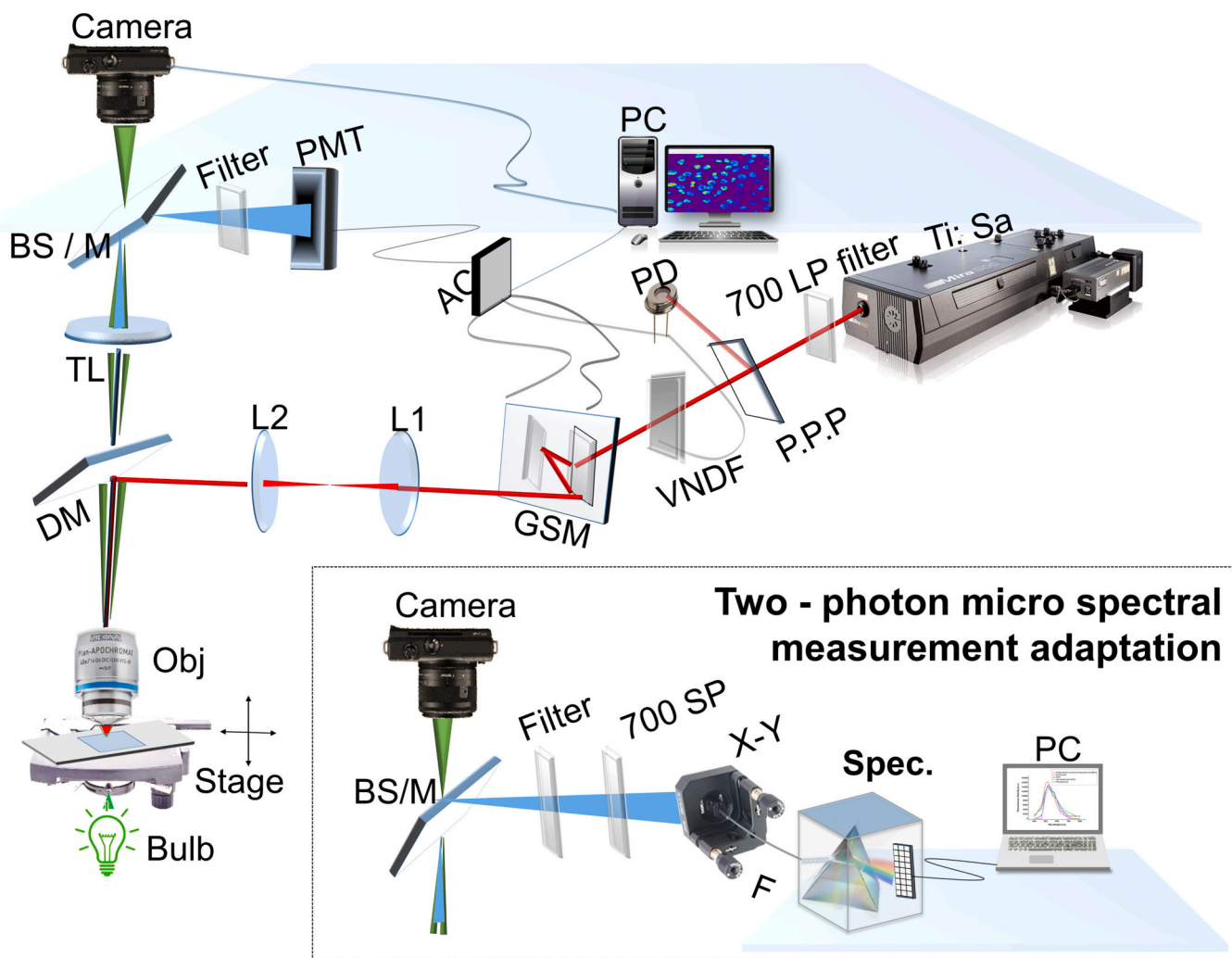

Fig. 1. Schematic 3D drawing of the home-built TPEF microscope with specific adaptations for in situ emission spectra measurement (inset). The TPEF microscope comprising: Ti:Sa, Ti:Sapphire laser; 700 LP filter, 700 nm long pass filter; P.P.P., plan parallel plate; PD, photo-diode; VNDF, variable neutral density filters; GSM, galvo scanning mirrors; L1 and L2 lenses; AC, acquisition card; DM, dichroic mirror (short pass); Bulb, bulb for bright-field imaging; TL, tube lens; BS/M, beam splitter or mirror; PMT, photomultiplier tube. Inset: The module for micro spectral measurements comprises: 700 SP filter, 700 nm short pass filter; X-Y F, functional X-Y stage controller, Spec, compact high-performance CCD spectrometer with TE cooling.

the sample as micro-spectroscopy. Square-shaped TPEF emission patterns were inscribed by raster-scanning of the sample, whereas arbitrary patterns were inscribed by scanning the beam along a corresponding line. The latter is enabled by a specially written program that recognizes arbitrary figures in both vector, and bitmap formats, and controls the dwell time, power and writing speed of the fs laser beam.

2.7. Single-photon excitation fluorescence (SPEF) and confocal laser scanning microscopy (CLSM)

Hb photoproduct lastingness was assessed by single-photon excitation fluorescence (SPEF) using a confocal laser scanning microscope (LSM 510, Carl Zeiss), equipped with an Ar multi-line (458 nm, 488 nm, and 514 nm) laser and a Plan Apochromat 40×1.3 N.A. oil-immersion objective (Carl Zeiss). Optical slice thickness was set to <4.3 μm, by choosing the pinhole diameter of 5.65 Airy units, to collect as much as possible fluorescence light from the photoproduct and to increase Signal to noise ratio (SNR). The best signal-to-noise-ratio in the SPEF images of the Hb photoproduct in the square-shaped patterns was at 488 nm excitation wavelength. Emission was collected using the main dichroic beam splitter, HFT 488 nm and long pass filter LP 505 nm.

2.8. Absorption spectra measurements

Absorption spectra of Hb and TPEF irradiated Hb in the intact thin film were measured using the Beckman Coulter DU700

spectrophotometer. A special aluminum holder was designed to hold the microscope slide with Hb specimen, to mimic a cuvette for the spectrophotometer. The dimensions of the holder were 45 mm × 10 mm × 10 mm. The mask with the round hole was placed over the cover glass with Hb layer and photoproduct square pattern. The hole matches the Hb photoproduct enabling the portion of incident light from the spectrophotometer to pass only through the region where the Hb photoproduct is. Prior to the absorption measurements, necessary calibration was performed for the overall transmission.

2.9. Spectral imaging

Spectral confocal Laser Scanning Microscopy (CLSM) imaging was performed using an LSM880 (Carl Zeiss) instrument, equipped with several lasers: three diode lasers (543 nm and 633 nm), and an Ar-ion laser (lines: 458 nm, 488 nm and 514 nm); objective lens (Plan-Apochromat 20×/0.8 N.A.); and gallium arsenide phosphide (GaAsP) spectral array detector. The pinhole size was adjusted to 33 μm (1 Airy unit at 488 nm). The fluorescence (single-photon excitation fluorescence (SPEF)) was spectrally split by a diffraction grating and detected in the 418 nm - 723 nm range with a 3 nm wavelength resolution using the GaAsP spectral array detector. For all wavelengths, the laser power was 9.4 μW at the objective lens. SPEF emission spectra are displayed only for wavelengths that are longer than the wavelength of the excitation laser.
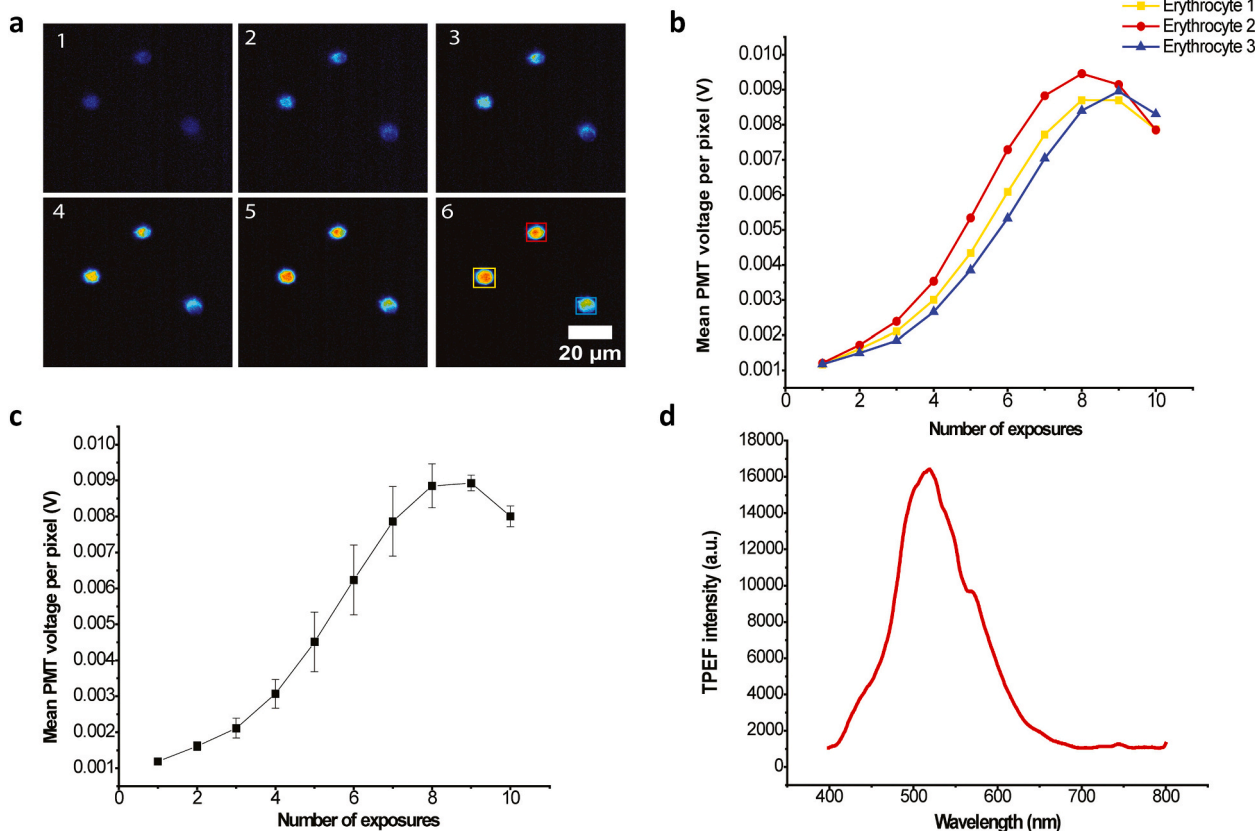

Fig. 2. TPEF microscopy enables both selective erythrocyte photolabeling and imagining in the whole blood. (a) Label-free TPEF microscopy images (6 out of 10) of erythrocytes. The image pixel size is 1024 × 1024 pixels; it is averaged out from 30 scans with the pixel dwell time is 8.53 e^{-4} s. In total, each image took 26.1 s to be recorded, which represents a single unit of exposure. The image intensity is represented by pseudocolor code of PMT voltage values for each pixel (dark blue – lowest TPEF signal, red – highest TPEF signal); (b) Mean pixel values of PMT voltage proportional to the TPEF intensity for each ROI (yellow, red and blue square box) shown in (a)), presented with the curve of the corresponding colour. Mean pixel values were calculated from region of interest (ROI), (yellow, red and blue squares) and for each image, the square size is 100 × 100 pixels; (c) Black curve is average of three erythrocytes shown in (b), standard error was presented for the ordinate (voltage); (d) TPEF spectrum recorded in an arbitrarily selected point in a single erythrocyte, using micro-spectral measurement adaptation. (For interpretation of the references to colour in this figure legend, the reader is referred to the web version of this article.)

3. Results and discussion

3.1. Photo-labeling of erythrocytes using TPEF microscopy and micro-spectroscopy analysis of erythrocytes fluorescence emission

To confirm already demonstrated feasibility of TPEF microscopy for erythrocytes imaging [8,9], we initially performed an analysis on diluted human whole blood. The blood was diluted in order to get sparse erythrocytes that are not stacked to each other and clearly distinguishable at the image. TPEF microscopy allowed us to selectively photo-label individual erythrocytes in a whole blood specimen. Here, photo-labeling refers to the process of rendering fluorescent individual erythrocytes using ultrashort 730 nm laser pulses. The gradual increase of TPEF from the irradiated erythrocytes as the laser beam scans over them is shown in Fig. 2a. This result was in accordance with the already demonstrated increase of the fluorescence intensity in the erythrocytes upon illumination with ultrashort laser pulses and formation of a so called Hb photoproduct [26]. Herein, the increase of TPEF signal has been proven through the PMT voltage dependence on the number of exposures (Fig. 2b), since PMT voltage is directly proportional to the fluorescence

intensity. The abscissa shows the number of exposures whereat one exposure refers to a series of 30 consecutive image frames acquired by raster laser scanning, the acquisition of which lasted ~26.1 s. The ordinate shows the mean PMT voltage *per* exposure per pixel of the rectangular regions given in the last image (no.6) at Fig. 2a. The average PMT voltage i.e., fluorescence intensity curve is presented in Fig. 2c. In addition, the TPEF emission spectrum was acquired (Fig. 2d) using a CCD array fiber optic spectrometer mounted on the nonlinear microscope (Fig. 1 inset).

3.2. Hb photoproduct formation using 730 nm ultrashort laser pulses

To ascertain that the observed increase in TPEF intensity comes solely from the Hb photoproduct that was formed upon erythrocytes illumination with ultrashort 730 nm laser pulses, but not from other molecules, we performed experiments using isolated Hb. To this aim, square-shaped patterns were inscribed in the thin Hb film in a spatio-temporally controlled manner: 1024×1024 pixels at average laser power of 20 mW (Fig. 3a). Both SPEF (Fig. 3b) and TPEF images (Fig. 3c) were acquired. The acquisition procedure was repeated 10 times
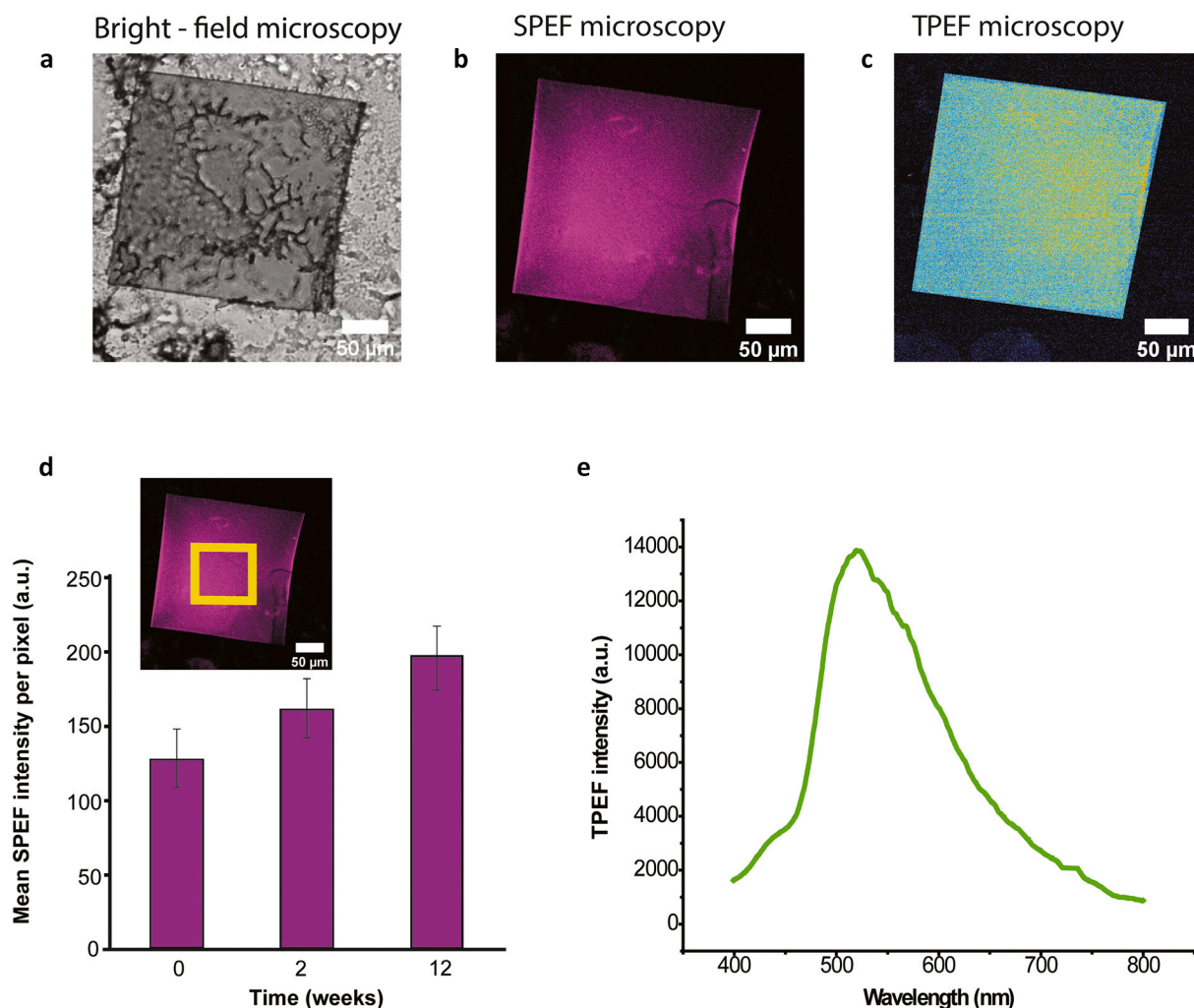

Fig. 3. SPEF spectra of the Hb photoproduct formed upon Hb thin film exposure to ultrashort 730 nm laser pulses. (a) Bright-field microscopy image of the specimen shown reveals that the Hb photoproduct (dark grey square) is less optically translucent than Hb (light grey surrounding); (b) Single-photon excitation fluorescence (SPEF) emission image of the specimen shown in (a) reveals that Hb photoproduct SPEF can be excited at 488 nm (plum square) whereas Hb cannot (black surrounding); (c) Representative TPEF microscopy image showing intense emission in the yellow-green square-shaped area where the Hb photoproduct was formed, in comparison to the non-fluorescent Hb in the surrounding (black); (d) The Hb photoproduct is lasting and its SPEF emission properties are preserved over extended time, as evident from the mean SPEF intensity per pixel (measured in the yellow rectangular area in the inset); (e) TPEF spectrum of the Hb photoproduct recorded in an arbitrarily selected point in the thin layer. (For interpretation of the references to colour in this figure legend, the reader is referred to the web version of this article.)

(number of exposures) after 8 scanning times the maximum TPEF intensity was reached, after that the TPEF intensity started to decrease due to photobleaching (see Fig. 2b). To demonstrate that strong TPEF emission is observed only from the region that was exposed to ultrashort 730 nm laser pulses, the field of view, i.e., the scanned region was expanded, the average laser power was lowered down to 2.5 mW and a TPEF image was acquired (Fig. 3c). In addition, bright field imaging clearly showed that transmission properties of the extensively illuminated square-shaped area have become less transparent (Fig. 3a). Finally, using single-photon excitation at 488 nm, we detected SPEF emission from the Hb photoproduct formed only in the region exposed to ultrashort 730 nm laser pulses, but not in the surrounding region (Fig. 3b, plum). Here, it is worth reminding that Hb is not naturally fluorescent [26], which is obvious from the dark region around the fluorescent square (Fig. 3a and c). The photoproduct formation depends on exposure time and laser average power, among other parameters that are fixed in our experiment (wavelength, repetition rate, pulse duration etc.). The fluorescence intensity signal starts to increase even after the first exposure. For Hb isolated as stated in previous Section 2.2, TPEF intensity of the Hb photoproduct becomes detectable at a laser excitation power of approximately 10 mW after the first exposure, which corresponds to the deposited energy of 261 mJ on the square area 62,500 μm^2.

Similarly, to erythrocytes, the increase in fluorescence intensity was gradual with the number of scanning times (i.e., number of exposures) across the square area which is proportional to the total absorbed dose/ energy (plot is equivalent to the plot shown in (Fig. 2b). This suggests that ultrashort laser pulses interact directly with Hb to form photoproduct in the erythrocyte. Longitudinal SPEF recordings showed that the Hb photoproduct is stable over a considerably long time (Fig. 3d). The TPEF spectrum of the Hb photoproduct in the thin film showed maximum at (550 ± 2) nm (Fig. 3e), the same to the TPEF emission spectrum recorded from a single erythrocyte (Fig. 2c). This observation suggests that ultrashort laser pulses interact solely with Hb in the erythrocytes from the whole blood, forming the same photoproduct. Or, at least, one could say that the interaction of the ultrashort laser pulses with other molecular species in erythrocytes is negligible, at the given conditions. The dynamic of Hb photoproduct formation is also the same in erythrocytes and Hb thin film: gradual increase of the fluorescence intensity with number of exposures that end up with saturation plateau. We might anticipate that interaction of ultrashort laser pulses with Hb is mainly followed up with an intensive Hb degradation, due to the increasing fluorescence intensity over time and the eventual saturation of the fluorescence when the majority of Hb in focal volume is degraded.

3.3. UV-VIS absorption spectroscopy of TPEF irradiated and non-irradiated thin Hb layer

To characterize the single-photon absorption spectra of Hb and the TPEF irradiated Hb in the intact thin film, measurements were performed outside and inside the illuminated square-shaped region (Fig. 3a-c), respectively. The term irradiated Hb was used because of the measurement procedure of the absorption spectra. Since photoproduct was formed in a thin layer of Hb film so that both Hb and the photoproduct are on the same optical path. In addition, some Hb remains unconverted into the photoproduct even in the treated volume. That's why the recorded absorption spectrum is not solely from the photoproduct, but from both, photoproduct and Hb together.

As expected, the UV-VIS absorption spectrum of Hb thin film showed spectral bands that are characteristic of oxyHb: an absorption band in the UV region with a maximum at $\lambda_{max}^{UV} \approx 275$ nm due to $\pi \to \pi^*$ transitions; and several absorption bands, such as the λ_{max}^{His} 350 nm attributed to the absorption of the non-covalent bond between iron and histidine in the Hb protein part; the Soret or B band λ_{max}^{Soret} at (410 ± 2) nm and the Q band with two transitions, the $\lambda_{max}^{Q\beta}\beta$ band at 539 nm and $\lambda_{max}^{Q\alpha}\alpha$ band at

577 nm [32] (Fig. 4, blue line). Similarly, the UV-VIS absorption spectrum of the TPEF irradiated Hb thin film showed the same bands, but clear differences in band intensity and/or peak position were noted (Fig. 4, red line). The observed differences and important relations between them are summarized in Table 1.

A 7 nm bathochromic shift of the Soret band was noted in the irradiated Hb with a significant decrease in Soret band intensity (Fig. 4, Table 1). The bands in the VIS part of the Hb absorption spectrum originate from the heme group, and changes in their positions and intensities are indicators of displacements along the normal coordinates of the porphyrin ring [33]. The ratio of $\Delta\alpha/\Delta\beta$ was <1 for both Hb and Hb after irradiation with fs laser pulses (Fig. 4, Table 1). Still, this ratio in irradiated Hb was significantly lower than untreated Hb indicating the degradation of Hb upon the interaction with fs laser pulses. The mentioned 7 nm bathochromic shift of the Soret peak in the irradiated Hb, indicates the transformation of oxygenated to oxidized Hb species [33–35]. Reduced ratio A_{max}^{Soret}/A_{560} ratios of irradiated Hb in comparison to intact Hb indicate free heme presence and breakdown of Hb molecule [33].

3.4. Single-photon excitation fluorescence (SPEF) emission spectra of thin film Hb photoproduct by confocal microscopy spectral imaging

The Hb photoproduct square shape patterns are imaged using single-photon excitation confocal microscopy (Fig. 5a), and square shape patterns (Fig. 5b) were formed previously by the exposure to the ultrashort laser pulses as explained in Section 2.9. SPEF emission spectra were recorded for different excitation wavelengths (Fig. 5c) from the Hb region of interest 1 (ROI1, dashed circle) and from the photoproduct region of interest (ROI 2, solid circle). Excitation efficiency dependence was constructed by extracting emission maxima at different excitation wavelengths (Fig. 5d). The SPEF emission spectrum acquired using the shortest excitation wavelength, $\lambda_{exc} = 458$ nm, showed a fluorescence emission maximum at $\lambda_{em} = 550$ nm and a broad emission band (red curve), being good agreement with TPEF emission spectrum (Fig. 3e). The emission spectra acquired using excitation wavelengths longer than 458 nm, $\lambda_{exc} > 458$ nm, showed emission maxima that are slightly red shifted to one another, possibly suggesting that the Hb photoproduct may comprise several spectrally distinct molecules. The existence of more than one molecular species is confirmed by the absorption spectroscopy (Section 3.3) and it is in accordance with the results given in
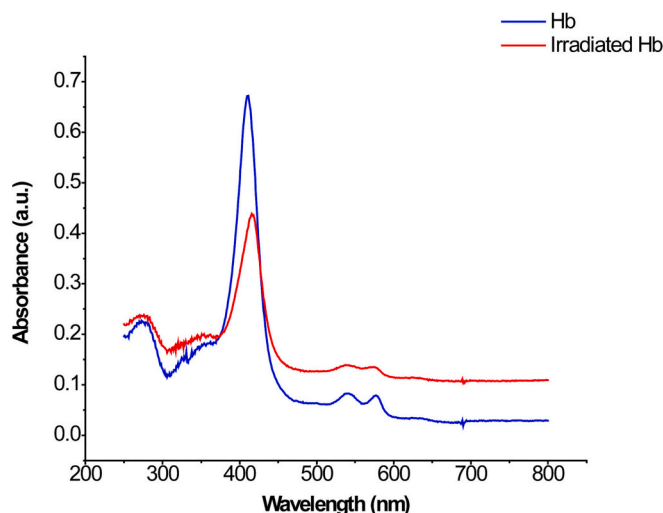

Fig. 4. Absorption spectra of Hb and the irradiated Hb thin layers. UV-VIS absorption spectra of intact Hb thin layer (blue) and irradiated Hb that contains the photoproduct (red line). All characteristics of absorption spectra are given in Table 1. (For interpretation of the references to colour in this figure legend, the reader is referred to the web version of this article.)

Table 1

Characteristics of Hb and Hb photoproduct UV-VIS absorption spectra. The mean and standard deviation of four separate absorbance measurements is represented.

Absorption band maximum position / intensity	Hb	Irradiated Hb region containing the photoproduct
λ_{max}^{UV} / nm	273 ± 2	272 ± 2
λ_{max}^{His} / nm	351 ± 2	351 ± 2
λ_{max}^{Soret} / nm	410 ± 2	417 ± 2
$\lambda_{max}^{Q\beta}$ / nm	539 ± 2	538 ± 2
$\lambda_{max}^{Q\alpha}$ / nm	577 ± 2	576 ± 2
A_{max}^{UV}	0.226 ± 0.003	0.237 ± 0.001
A_{max}^{His}	0.179 ± 0.008	0.200 ± 0.002
A_{max}^{Soret}	0.671 ± 0.002	0.438 ± 0.001
$A_{max}^{Q\beta}$	0.082 ± 0.007	0.139 ± 0.003
$A_{max}^{Q\alpha}$	0.079 ± 0.001	0.134 ± 0.003
A_{560}	0.063 ± 0.002	0.132 ± 0.005
$\Delta A_{Q\alpha}/\Delta A_{Q\beta}$ $= (A_{max}^{Q\alpha} - A_{560})/(A_{max}^{Q\beta} - A_{560})$	0.804 ± 0.027	0.371 ± 0.014
$A_{max}^{Soret} / A_{max}^{Q\alpha}$	8.506 ± 0.046	3.254 ± 0.007
$A_{max}^{Soret} / A_{max}^{UV}$	2.962 ± 0.042	1.848 ± 0.014

[33–35]. In addition, excited by the different wavelengths one molecular species would give just the change in the fluorescence intensity while keeping the position of the spectral maximum fixed.

3.5. TPEF emission of PpIX

To characterize the Hb iron ion role in Hb photoproduct formation, TPEF spectra of PpIX were investigated. The obtained TPEF emission spectrum of PpIX (Fig. 6a black line) shows both distinctions and similarities to TPEF spectrum of the Hb photoproduct (Fig. 3e). Most notably, unlike Hb, PpIX is easily excited and TPEF emission is readily observed even at low irradiation intensities (Fig. 6a, black curve). However, the TPEF emission observed at low irradiation intensities originated predominantly from unaltered PpIX molecules, as evident from previously published data [36]. When using higher laser power (e. g., 16.5 mW), the TPEF emission spectrum of PpIX is considerably changed: becoming broader and with a maximum peak around 550 nm (Fig. 6a, blue curve), resembling the TPEF emission spectrum of the Hb photoproduct (Fig. 3e). This, in turn, suggests that intense irradiation of PpIX leads to the generation of PpIX photoproduct that is similar to the Hb photoproduct, so that iron atom is not necessary for the formation of Hb photoproduct.

3.6. TPEF emission of Hb treated with H_2O_2

It has been shown that Hb treatment with H_2O_2 also leads to the formation of a fluorescent product [27,28]. To determine whether similar photoproducts are formed under Hb treatment with H_2O_2 as upon its interaction with 730 nm ultrashort laser pulses, we compared how the TPEF intensity changed when increasing the exposure time (Fig. 6b) and TPEF spectra (Fig. 6c). Unlike for Hb thin film, where increase of fluorescence intensity and saturation were eventually observed (Fig. 6b, light green squares), the fluorescence of the H_2O_2-treated Hb shows a high TPEF emission intensity immediately upon excitation, even at the first exposure (Fig. 6b, olive dots). The increase of fluorescence in Hb film (Fig. 6b, light green) has the same trend as in erythrocytes (Fig. 2b). The slight discrepancy is due to different number of graph points and concentration of Hb in erythrocytes and thin Hb film.

Moreover, the observed TPEF intensity was independent on the number of exposures, i.e., absorbed dose, of 730 nm ultrashort laser pulses. This confirms the hypothesis of the photodegradation of Hb involved in the photoproduct formation, since interaction between Hb and a 10 (or more) fold excess H_2O_2 leads to Hb degradation according to the [28]. Finally, the TPEF spectrum of H_2O_2-treated Hb thin film showed very good agreement with the TPEF spectra of Hb thin film treated with ultrashort laser pulses, the erythrocytes and the PpIX layer under high laser power, 16.5 mW (Fig. 6c).

Taken together, this suggests that upon Hb reaction with H_2O_2 and in the photochemical interaction of ultrashort laser pulses with Hb, the Hb photoproduct shows, at least with regard to TPEF emission, similar features. The overlap between the TPEF emission spectra of PpIX and Hb thin film suggests that heme, i.e., porphyrin rings photoexcitation playing a significant role in the Hb photoproduct formation. This could even include heme degradation, as already demonstrated within diseased so-called Köln erythrocytes', where observed fluorescence does not resemble that of porphyrins, chelated or otherwise, but does reveal some characteristics of dypirolic compound spectra [37]. Since dipyrrolic urinary pigments in patients with unstable hemoglobin disease are characterized and support the previous assumption regarding fluorescent Koln erythrocytes, it is more likely that under ultrashort laser pulses the heme's porphyrin ring breakage is enhanced. Importantly, fluorescent heme degradation products are already recognized as markers of red blood cell (RBC) oxidative stress [38], based on the original work of Nagababu and Rifkind, 1998, who have found that even small portion of the non-neutralized hydrogen peroxide in erythrocytes degrades the protoporphyrin and produce stable fluorescent heme degradation products. Nagababu and Rifkind 1998 reported two heme degradation products, one with an excitation wavelength of 321 nm and emission wavelength in the region of 465 nm and the second one with the excitation wavelength of 460 nm and emission wavelength in the region of 525 nm, based on the results that the same fluorescent bands were obtained after hydrogen peroxide treatment of heme or hemin. The broad emission spectra of a Hb photoproduct obtained in our study indicates that there are probably more than one Hb photoproduct species as well. The same authors [39] revealed that the mechanism for the generation of heme degradation products needs an initial reaction with hydrogen peroxide, producing Fe (IV) ferrylhemoglobin (ferrylHb) species, which further reacts with the second molecule of hydrogen peroxide producing superoxide radical, that can be retained longer in heme pocket than the superoxide formed during Hb autoxidation, and consequently initiating degradation of heme [28]. Namely, even in physiological conditions, RBCs are continuously exposed to both endogenous and exogenous sources of reactive oxygen species (ROS) (i.e., superoxide and hydrogen peroxide (H_2O_2)), which are mainly neutralized by the RBC antioxidant system. However, the autoxidation of Hb bound to the membrane is unavailable to the RBC antioxidant system which is mostly cytosolic. This process is especially pronounced when Hb is partially oxygenated, resulting in an increased rate of autoxidation and increased affinity for the RBC membrane, eventually affecting RBC deformability [38]. Even in fresh RBC samples heme degradation products can be found, and the amount of heme degradation increases in older RBCs [38]. Taking all these findings together, the interaction of ultrashort laser pulses with hemoglobin more likely accelerates the deoxygenation of hemoglobin and generation of superoxide radical, which affects heme, inducing the formation of stable fluorescent photoproduct.

3.7. Applications

3.7.1. Selective photo-labeling and live tracking of photo-labeled erythrocytes

Thanks to the high stability of the Hb photoproduct obtained upon interaction of the 730 nm ultrashort laser pulses with Hb molecules (Fig. 3d) and high spatiotemporal selectivity of our TPEF scanning microscope, we performed live tracking of individually labeled erythrocyte
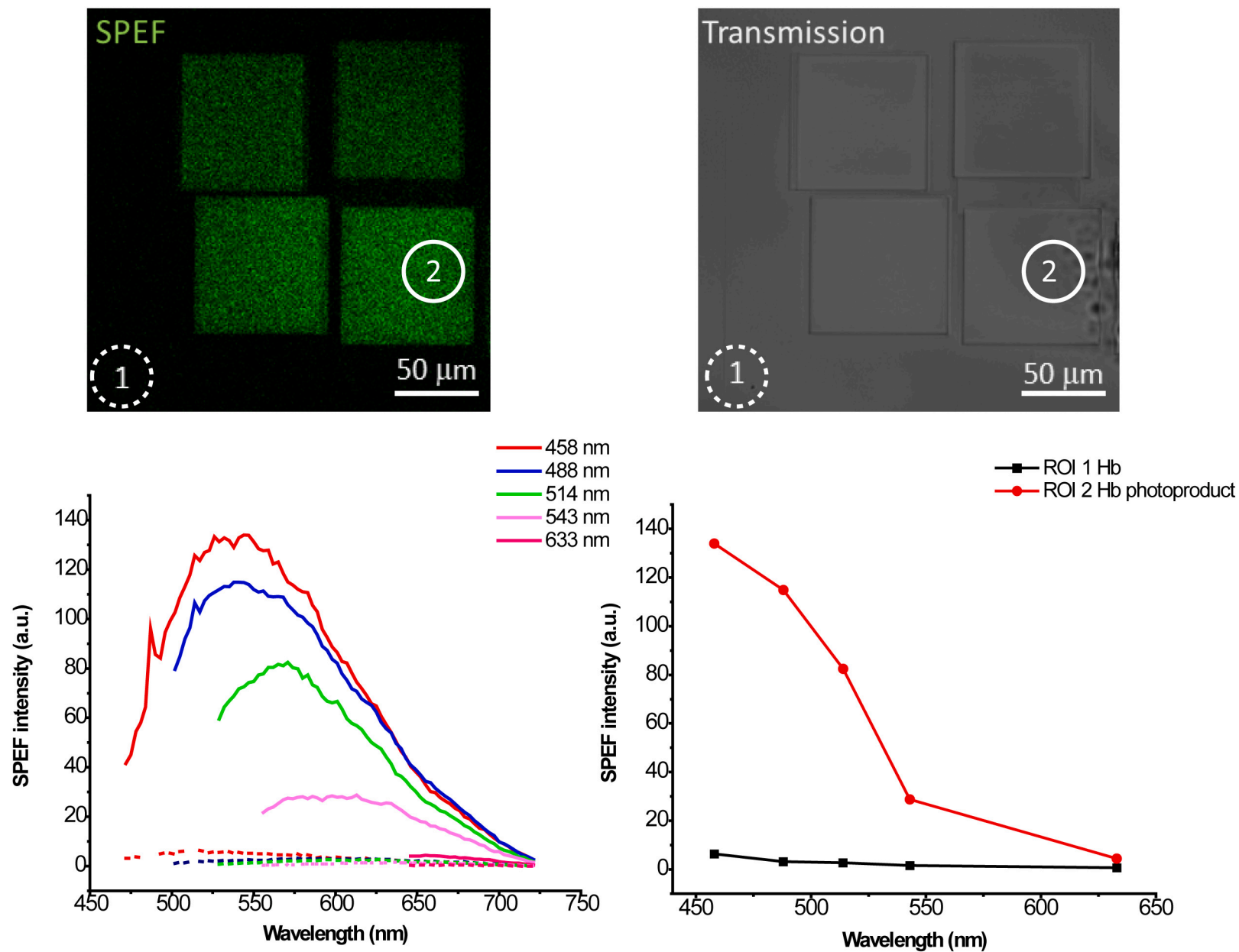
Fig. 5. Spectral imaging of Hb photoproduct patterns. (a) Single-photon excitation (SPEF) fluorescent image of the Hb photoproduct patterns recorded at 458 nm excitation, dashed circle represents region of interest (ROI 1) which is not irradiated by ultrashort pulsed laser beam under conditions needed for photoproduct formation, and solid circle represents ROI 2 which is irradiated by ultrashort pulsed laser beam, and it's clearly separate by photoproduct fluorescence emission, (b) Corresponding Bright-field image; (c) Single-photon excitation fluorescence spectra, read-out from ROI 1 (dashed line) for different excitation wavelengths and from ROI 2 (solid line); (d) Excitation efficiency: the emission intensity maxima at the different excitation wavelengths from ROI 1 Hb (untreated Hb) and ROI 2 (Hb photoproduct).
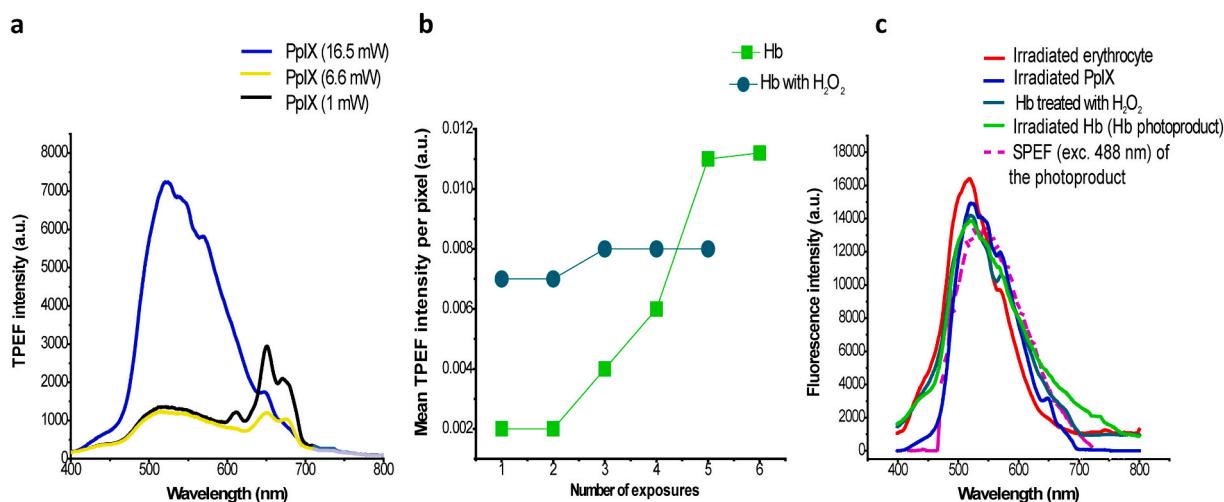
Fig. 6. TPEF spectra of PpIX and H_2O_2-treated Hb. (a) TPEF spectra of PpIX irradiated using different ultrashort pulsed laser powers (1.0 mW, black; 6.6 mW, yellow; 16.5 mW, dark blue); (b) Dependence of TPEF intensity vs. number of exposures in Hb thin film and H_2O_2-treated Hb thin film; (c) Overlapped TPEF spectra of Hb photoproduct (obtained in thin layer of Hb, green), the erythrocyte (red), thin layer PpIX under the laser power conditions (16.5 mW, blue), H_2O_2-treated Hb thin layer (cobalt blue) and Hb photoproduct SPEF spectrum (dashed purple). (For interpretation of the references to colour in this figure legend, the reader is referred to the web version of this article.)

(s) in vitro in the whole blood (Fig. 7 a-d). We present four timelapse images from the video (Supplemental Information) in which one erythrocyte is labeled by focused fs laser beam and then traced during its random motion. This was inspired by [11] where flow of the erythrocytes was shown in the vasculature of a whole, live animal but only with statical images, while we bring the dynamics of movement (Fig. 7 and corresponding video). Although the photo-labeling and tracking were performed in vitro, this method based on TPEF microscopy will enable to track with long-term period individual erythrocyte in a tissue [40] and blood vessel in laboratory animals, for instance in zebra fish [11] or even in mouse brain vasculature [41 – 43]. According to [41 – 43], where shadows of erythrocytes were traced in the blood flow in live animals through the cranial window using TPEF imaging, erythrocytes could be fluorescently activated by a fs laser beam and tracked through the vessels. In addition to selective photo-labeling of solely and deliberately chosen erythrocytes, that can be achieved by spatiotemporal control of the laser beam, but not by bulk H_2O_2 treatment, there are some more advantages of the presented method. Namely, treating the erythrocytes with H_2O_2 is rather uncontrollable in terms of targeted transformation of Hb only into the fluorescent molecule(s). H_2O_2 interact with other molecules in the erythrocytes' membrane and other structures which might be damaged or altered. Also, erythrocytes' morphology and related Hb distribution would be altered. Using the method of the laser photo-labeling presented in this work, only Hb molecules would be affected, and the erythrocytes would preserve their original morphology as well as its original Hb distribution which was already shown in [9]. The erythrocytes morphology and internal Hb distribution are one of key markers indicating the cell adaptation to physiological processes and their response to pathological conditions [9]. Eventually, the proposed method might have application for erythrocytes tracing in the blood vessels of the live animals even in imaging of highly bloodied and low transparent organs such as kidneys, since TPEF microscopy is extensively used nowadays for those purposes [41]. Prior investigations have unequivocally demonstrated that the morphology of erythrocytes can be studied using Two-Photon Excitation Fluorescence (TPEF) imaging, which enables examination of their oxygenation status [15], as well as distribution of Hb [9]. However, it is unclear whether the ultrashort laser pulses interferes with Hb's ability to perform its primary function of binding and releasing oxygen. In our present study, we establish that Hb undergoes alterations as a result of such interaction.

Having in mind the relationship of oxidative stress and hemoglobin, hemoglobin-based TPEF methodology is an emerging platform for the assessment of redox status of erythrocytes and their deformability under both physiological and pathophysiological conditions and even a broader spectrum of diseases that share the common feature of the appearance of extracellular hemoglobin or early cancer progression in means of neoangiogenesis. In this respect, photo acoustic microscopy can be employed for tracking of erythrocytes as suggested in [11] but with higher repetition rate lasers. Also, this technique can be used for investigation of oxygen saturation in the blood vessels [15].

3.7.2. Pattern inscription (micropatterning) in Hb layer

The long–term stability of the Hb photoproduct, its fluorescence and spatial precision of TPEF emission microscopy, enabled one more application – micro patterning of the Hb layer (Fig. 8). The inscribed patterns can stay fluorescent even for several months after being inscribed. In Fig. 8 a-d simple, spot-wise, patterns are presented in addition to the uniform square area. The spots were obtained from the diffraction limited focal volume and demonstrate the method limitation in terms of the spatial resolution. At each figure, a new spot-wise pattern was added, while the previous ones are still clearly visible. To demonstrate possibility and versatility of the method, as well as potential applications, we further wrote the letters "HEMMAGINERO" (dimensions 60 μm × 6 μm) in the Hb layer (Fig. 8e).

In terms of optical and spectroscopic response to the treatment with ultrashort laser pulses all mammalian [4,9,12,44,45] or even other vertebrates [46] Hb and erythrocytes are the same [47]. On the other hand, the slaughterhouses mammalian blood is a waste material from which Hb can be isolated in relatively low cost and relatively simple technological processes [48,49]. This might be a starting point for utilization of the Hb as the material for optical memories [50], hemoglobin-based therapeutics [51], intravital microscopy [52], conversion of micro fluorescent information into the document security or mass production of calibration samples in fluorescent microscopy [53–55]. Microscopic slides with fluorescent patterns are already commercially available [56] and broadly used for calibration and resolution measurements. While the fluorescence durability of the patterns in the existing materials remains unknown, we suggest Hb as a material for long lasting fluorescent patterns. In addition, the utilization of Hb from wasted slaughterhouse blood as the widely available material will be nature friendly since this material is considered to be severe pollutant [49].
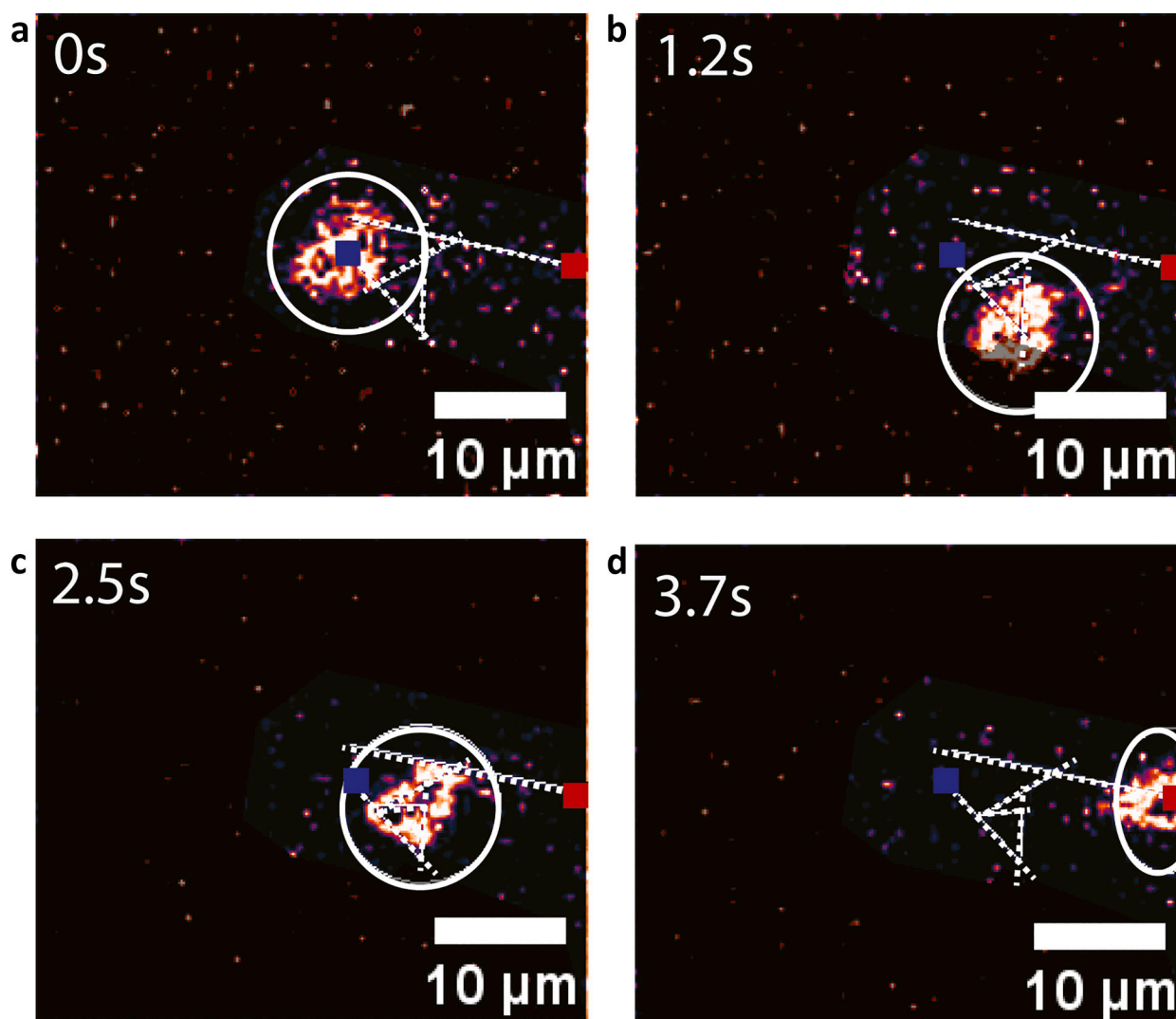
Fig. 7. Timelapse TPEF emission images of a single erythrocyte (encircled white). (a-d) Photo-labeled erythrocyte tracking in whole blood. The white dashed lines represent erythrocyte's trajectory with starting position (blue square) and final position (red square). (For interpretation of the references to colour in this figure legend, the reader is referred to the web version of this article.)

4. Conclusion

Using different spectroscopic techniques, in this study, we presented a novel insight into the photophysical properties of the fluorescent product emerged after exposure of Hb to 730 nm ultrashort laser pulses (hence Hb photoproduct) and its possible applications. We suggest that the interaction of the Hb with the ultrashort laser pulses in NIR region leads to the degradation of the Hb molecules and release of the iron, ending up with iron-free fluorescent species comparable to those emerged from the interaction of Hb with H_2O_2. Unlike the chemical interaction of Hb with H_2O_2 that occurs in bulk solution, using the tightly focused ultrashort pulsed laser beam the Hb photoproduct can be formed in spatiotemporal controllable manner without interaction with other molecules and erythrocytes structures (e.g. membrane). In other words, we can irradiate selected erythrocytes solely, and the laser pulses will alter primarily Hb, but not the other molecules. We inscribed submicrometer fluorescent patterns on a Hb thin film by the spatiotemporal control, of ultrashort pulsed laser beam. We have also induced the Hb photoproduct formation in a single human healthy erythrocyte making them fluorescent in the sample of whole blood and track their movement in space and time. The present study could contribute towards understanding photophysical properties of photoproduct, formed by the interaction of ultrashort laser pulses with Hb and erythrocytes, establishing a foundation for the future progress in the field of bio-derived biomaterials.

Supplementary data to this article can be found online at https://doi.org/10.1016/j.ijbiomac.2023.125312.

CRediT authorship contribution statement

M. Radmilović prepared the samples, performed TPEF imaging, TPEF spectra measurements and absorption spectra measurements, erythrocytes tracking, Hb micro-patterning, and prepared all the images; I. Drvenica prepared the samples and supervised Hb and erythrocytes isolation, managed the research; M. Rabasović constructed the TPEF experimental setup, supervised the TPEF imaging and spectra measurements, managed the research; V. Ilić supervised sample preparation, managed the research; D. Pavlović prepared the samples and imaged the erythrocytes by TPEF microscopy and measured absorption spectra; S. Oasa performed spectral imaging; V. Vukojević supervised spectral imaging; M. Perić performed confocal imaging; S. Nikolić maintained TPEF experimental setup and modified the imaging software; A. Krmpot constructed the TPEF experimental setup, supervised the measurements, managed the research. All the authors wrote and reviewed the
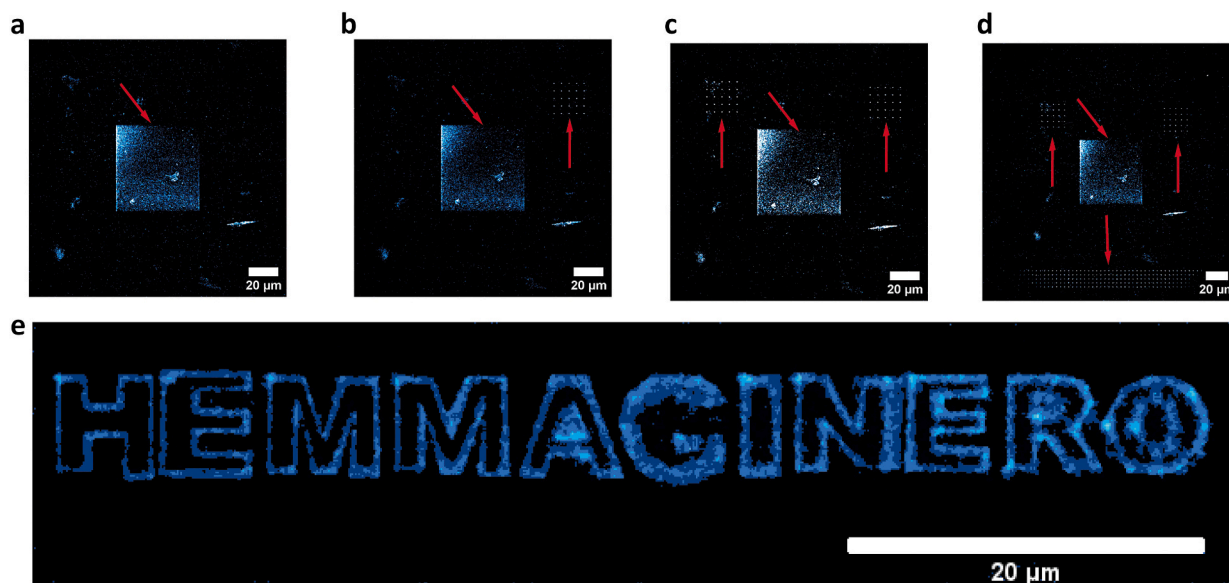
Fig. 8. Micropatterning in Hb layer by fs laser pulses. (a-d) Arbitrary uniform and spot-wise patterns (red arrow pointed) inscribed in the thin Hb film by ultrashort laser pulses. The patterns exhibit increased TPEF signal (marked by red arrows). (e) Fluorescent Hb photoproduct in the form of letters pattern. (For interpretation of the references to colour in this figure legend, the reader is referred to the web version of this article.)

manuscript. This article is a part of M. Radmilović's PhD thesis.

References

[1] L. Kiger, C. Vasseur, E. Domingues-Hamdi, G. Truan, M.C. Marden, V. Baudin-Creuza, Dynamics of α-Hb chain binding to its chaperone AHSP depends on heme coordination and redox state, Biochim. Biophys. Acta - Gen. Subj. 2014 (1840) 277–287, https://doi.org/10.1016/j.bbagen.2013.09.015.
[2] M. Weissbluth, Hemoglobin, Springer, Berlin, 1974, pp. 10–26.
[3] Q. Sun, W. Zheng, J. Wang, Y. Luo, J.Y. Qu, Mechanism of two-photon excited hemoglobin fluorescence emission, J. Biomed. Opt. 20 (2015) 105014, https://doi.org/10.1117/1.JBO.20.10.105014.
[4] W. Zheng, D. Li, Y. Zeng, Y. Luo, J.Y. Qu, W.R. Zipfel, R.M. Williams, R. Christie, A.Y. Nikitin, B.T. Hyman, W.W. Webb, Two-photon excited hemoglobin fluorescence, Biomed. Opt. Express 2 (2011) 71–79, https://doi.org/10.1364/BOE.2.000071.
[5] G.O. Clay, A.C. Millard, C.B. Schaffer, J. Aus-der-Au, P.S. Tsai, J.A. Squier, D. Kleinfeld, Spectroscopy of third-harmonic generation: evidence for resonances in model compounds and ligated hemoglobin, J. Opt. Soc. Am. B. 23 (2006) 932, https://doi.org/10.1364/josab.23.000932.
[6] G.O. Clay, C.B. Schaffer, D. Kleinfeld, Large two-photon absorptivity of hemoglobin in the infrared range of 780-880 nm, J. Chem. Phys. 126 (2007) 01B609, https://doi.org/10.1063/1.2404678.
[7] N.L. Garrett, A. Lalatsa, I. Uchegbu, A. Schätzlein, J. Moger, Exploring uptake mechanisms of oral nanomedicines using multimodal nonlinear optical microscopy, J. Biophotonics 5 (2012) 458–468, https://doi.org/10.1002/jbio.201200006.
[8] G.D. Vigil, S.S. Howard, Photophysical characterization of sickle cell disease hemoglobin by multi-photon microscopy, Biomed. Opt. Express 6 (2015) 4098–4104, https://doi.org/10.1364/boe.6.004098.
[9] K. Bukara, S.Z. Jovanić, I.T. Drvenica, A. Stančić, V. Ilić, M.D. Rabasović, D.V. Pantelić, B.M. Jelenković, B. Bugarski, A.J. Krmpot, Mapping of hemoglobin in erythrocytes and erythrocyte ghosts using two photon excitation fluorescence microscopy, J. Biomed. Opt. 22 (2017) 026003, https://doi.org/10.1117/1.jbo.22.2.026003.
[10] D. Li, W. Zheng, Y. Zeng, Y. Luo, J.Y. Qu, Two-photon excited hemoglobin fluorescence provides contrast mechanism for label-free imaging of microvasculature in vivo, Opt. Lett. 36 (2011) 834–836, https://doi.org/10.1364/OL.36.000834.
[11] Y. Zeng, J. Xu, D. Li, L. Li, Z. Wen, J.Y. Qu, Label-free in vivo flow cytometry in zebrafish using two-photon autofluorescence imaging, Opt. Lett. 37 (2012) 2490–2492, https://doi.org/10.1364/OL.37.002490.
[12] D. Li, W. Zheng, S.K. Teh, Y. Zeng, Y. Luo, J.Y. Qu, Time-resolved detection enables standard two-photon fluorescence microscopy for in vivo label-free imaging of microvasculature in tissue, Opt. Lett. 36 (2011) 2638–2640, https://doi.org/10.1364/OL.36.002638.
[13] R. Podlipec, J. Mur, J. Petelin, J. Štrancar, R. Petkovšek, Two-photon retinal theranostics by adaptive compact laser source, Appl. Phys. A Mater. Sci. Process. 126 (2020) 1–9, https://doi.org/10.1007/s00339-020-03587-2.
[14] R.L. Shelton, S.P. Mattison, B.E. Applegate, Volumetric imaging of erythrocytes using label-free multiphoton photoacoustic microscopy, J. Biophotonics 7 (2014) 834–840, https://doi.org/10.1002/jbio.201300059.
[15] Y. Wang, S. Hu, K. Maslov, Y. Zhang, Y. Xia, L.V. Wang, In vivo integrated photoacoustic and confocal microscopy of hemoglobin oxygen saturation and oxygen partial pressure, Opt. Lett. 36 (2011) 1029, https://doi.org/10.1364/ol.36.001029.
[16] J.J. Yao, L.V. Wang, Photoacoustic microscopy, Laser Photonics Rev. 7 (2013) 758–778.
[17] G.J. Tserevelakis, M. Pavlidis, A. Samaras, G.D. Barmparis, K.G. Mavrakis, I. Draganidis, A. Oikonomou, E. Fanouraki, G.P. Tsironis, G. Zacharakis, Hybrid confocal fluorescence and photoacoustic microscopy for the label-free investigation of melanin accumulation in fish scales, Sci. Rep. 12 (2022) 1–14, https://doi.org/10.1038/s41598-022-11262-0.
[18] I. Saytashev, R. Glenn, G.A. Murashova, S. Osseiran, D. Spence, C.L. Evans, M. Dantus, Multiphoton excited hemoglobin fluorescence and third harmonic generation for non-invasive microscopy of stored blood, Biomed. Opt. Express 7 (2016) 3449–3460, https://doi.org/10.1364/boe.7.003449.
[19] M.E. Reinhard, M.W. Mara, T. Kroll, H. Lim, R.G. Hadt, R. Alonso-Mori, M. Chollet, J.M. Glownia, S. Nelson, D. Sokaras, K. Kunnus, T.B. van Driel, R.W. Hartsock, K.S. Kjaer, C. Weninger, E. Biasin, L.B. Gee, K.O. Hodgson, B. Hedman, U. Bergmann,

E.I. Solomon, K.J. Gaffney, Short-lived metal-centered excited state initiates iron-methionine photodissociation in ferrous cytochrome c, Nat. Commun. 12 (2021) 1–8, https://doi.org/10.1038/s41467-021-21423-w.

[20] https://www.ncbi.nlm.nih.gov/pmc/articles/PMC3822757/.

[21] J.G. Mohanty, E. Nagababu, J.M. Rifkind, Red blood cell oxidative stress impairs oxygen delivery and induces red blood cell aging, Front. Physiol. 5 (2014) 1–6, https://doi.org/10.3389/fphys.2014.00084.

[22] S. Sun, A. Lv, S. Li, C. Zhao, Q. Chen, Z. Li, Y. Wang, A. Wu, H. Lin, Biomolecule-based stimuli-responsive nanohybrids for tumor-specific and cascade-enhanced synergistic therapy, Acta Biomater. 152 (2022) 484–494, https://doi.org/10.1016/j.actbio.2022.08.038.

[23] A.I. Alayash, Oxygen therapeutics: can we tame haemoglobin? Nat. Rev. Drug Discov. 3 (2004) 152–159, https://doi.org/10.1038/nrd1307.

[24] D. Chakraborty, S. Sarkar, P.K. Das, Blood dots: hemoglobin-derived carbon dots as hydrogen peroxide sensors and pro-drug activators, ACS Sustain. Chem. Eng. 6 (2018) 4661–4670, https://doi.org/10.1021/acssuschemeng.7b03691.

[25] S. Li, W. Sun, M. Ouyang, B. Yu, Y. Chen, Y. Wang, D. Zhou, Hemoglobin-related biomaterials and their applications, Adv. NanoBiomed Res. 2200103 (2022) 1–12, https://doi.org/10.1002/anbr.202200103.

[26] E.A. Shirshin, B.P. Yakimov, S.A. Rodionov, N.P. Omelyanenko, A.V. Priezzhev, V. V. Fadeev, M.E. Darvin, Formation of hemoglobin photoproduct is responsible for two-photon and single photon-excited fluorescence of red blood cells, Laser Phys. Lett. 15 (2018), 075604, https://doi.org/10.1088/1612-202X/aac003.

[27] E. Nagababu, J.M. Rifkind, Formation of fluorescent heme degradation products during the oxidation of hemoglobin by hydrogen peroxide, Biochem. Biophys. Res. Commun. 247 (1998) 592–596, https://doi.org/10.1006/bbrc.1998.8846.

[28] E. Nagababu, J.M. Rifkind, Reaction of hydrogen peroxide with ferrylhemoglobin: superoxide production and heme degradation, Biochemistry. 39 (2000) 12503–12511, https://doi.org/10.1021/bi992170y.

[29] A.Z. Stančić, I.T. Drvenica, H.N. Obradović, B.M. Bugarski, V.L. Ilić, D.S. Bugarski, Native bovine hemoglobin reduces differentiation capacity of mesenchymal stromal cells in vitro, Int. J. Biol. Macromol. 144 (2020) 909–920, https://doi.org/10.1016/j.ijbiomac.2019.09.167.

[30] M.D. Rabasović, D.V. Pantelić, B.M. Jelenković, S.B. Ćurčić, M.S. Rabasović, M. D. Vrbica, V.M. Lazović, B.P.M. Ćurčić, A.J. Krmpot, Nonlinear microscopy of chitin and chitinous structures: a case study of two cave-dwelling insects, J. Biomed. Opt. 20 (2015) 016010, https://doi.org/10.1117/1.jbo.20.1.016010.

[31] T. Lainović, J. Margueritat, Q. Martinet, X. Dagany, L. Blažić, D. Pantelić, M. D. Rabasović, A.J. Krmpot, T. Dehoux, Micromechanical imaging of dentin with Brillouin microscopy, Acta Biomater. 105 (2020) 214–222, https://doi.org/10.1016/j.actbio.2020.01.035.

[32] N.S. Selim, S.M. El-marakby, Radiation-induced changes in the optical properties of hemoglobin molecule, Spectrochim. Acta A Mol. Biomol. Spectrosc. 76 (2010) 56–61, https://doi.org/10.1016/j.saa.2010.02.046.

[33] E.K. Hanson, J. Ballantyne, A blue spectral shift of the hemoglobin soret band correlates with the age (time since deposition) of dried bloodstains, PLoS One 5 (2010) 1–11, https://doi.org/10.1371/journal.pone.0012830.

[34] I.T. Drvenica, A.Z. Stančić, A.M. Kalušević, S.B. Marković, J.J. Dragišić Maksimović, V.A. Nedović, B.M. Bugarski, V.L. Ilić, Maltose-mediated, long-term stabilization of freeze- and spray-dried forms of bovine and porcine hemoglobin, J. Serb. Chem. Soc. 84 (2019) 1105–1117, https://doi.org/10.2298/JSC190513067D.

[35] C. Bonaventura, R. Henkens, A.I. Alayash, S. Banerjee, A.L. Crumbliss, Molecular controls of the oxygenation and redox reactions of hemoglobin, Antioxid. Redox Signal. 18 (2013) 2298–2313, https://doi.org/10.1089/ars.2012.4947.

[36] H. Lu, F. Floris, M. Rensing, S. Andersson-Engels, Fluorescence spectroscopy study of protoporphyrin IX in optical tissue simulating liquid phantoms, Materials (Basel) 13 (2020) 7–16, https://doi.org/10.3390/ma13092105.

[37] S.M. Waugh, P.S. Low, Hemichrome binding to band 3: nucleation of Heinz bodies on the erythrocyte membrane, Biochemistry. 24 (1) (1985) 34–39, https://doi.org/10.1021/bi00322a006.

[38] J.G. Mohanty, E. Nagababu, J.M. Rifkind, Red blood cell oxidative stress impairs oxygen delivery and induces red blood cell aging, Front. Physiol. 5 (2014) 1–6, https://doi.org/10.3389/fphys.2014.00084.

[39] E. Nagababu, S. Ramasamy, J.M. Rifkind, Y. Jia, A.I. Alayash, Site-specific cross-linking of human and bovine hemoglobins differentially alters oxygen binding and redox side reactions producing rhombic heme and heme degradation, Biochemistry. 41 (2002) 7407–7415, https://doi.org/10.1021/bi0121048.

[40] U.N. Shroff, I.M. Schiessl, G. Gyarmati, A. Riquier-Brison, J. Peti-Peterdi, Novel fluorescence techniques to quantitate renal cell biology, Methods Cell Biol. 154 (2019) 85–107, https://doi.org/10.1016/bs.mcb.2019.04.013.

[41] D. Sardella, A.M. Kristensen, L. Bordoni, H. Kidmose, A. Shahrokhtash, D. S. Sutherland, S. Frische, I.M. Schiessl, Serial Intravital 2-photon Microscopy and Analysis of the Kidney Using Upright Microscopes, 2023, pp. 1–17, https://doi.org/10.3389/fphys.2023.1176409.

[42] E. Gutiérrez-jiménez, H. Angleys, P.M. Rasmussen, M.J. West, L. Catalini, N. K. Iversen, M.S. Jensen, S. Frische, L. Østergaard, Disturbances in the control of capillary flow in an aged APPswe/PS1ΔE9 model of Alzheimer's disease, Neurobiol. Aging 62 (2018) 82–94, https://doi.org/10.1016/j.neurobiolaging.2017.10.006.

[43] E. Gutiérrez-jiménez, C. Cai, I.K. Mikkelsen, P.M. Rasmussen, H. Angleys, M. Merrild, K. Mouridsen, S.N. Jespersen, J. Lee, N.K. Iversen, S. Sakadzic, L. Østergaard, Effect of electrical forepaw stimulation on capillary transit-time heterogeneity (CTH), J. Cereb. Blood Flow Metab. 36 (2016) 2072–2086, https://doi.org/10.1177/0271678X16631560.

[44] T. Wu, J. Liao, J. Yu, Y. Gao, H. Li, J. Wu, X. Xia, K. Shi, W. Zheng, In vivo label-free two-photon excitation autofluorescence microscopy of microvasculature using a 520 nm femtosecond fiber laser, Opt. Lett. 45 (2020) 2704–2707, https://doi.org/10.1364/OL.394242.

[45] S. He, C. Ye, Q. Sun, C.K.S. Leung, J.Y. Qu, Label-free nonlinear optical imaging of mouse retina, Biomed. Opt. Expr. 6 (2015) 2459–2465, https://doi.org/10.1364/BOE.6.001055.

[46] Y. Zeng, J. Xu, D. Li, L. Li, Z. Wen, J.Y. Qu, Label-free in vivo flow cytometry in zebrafish using two-photon autofluorescence imaging, Opt. Lett. 37 (2012) 2490–2492, https://doi.org/10.1364/OL.37.002490.

[47] J.F. Ortas, P. Mahou, S. Escot, C. Stringari, N.B. David, L. Bally-Cuif, N. Dray, M. Négrerie, W. Supatto, E. Beaurepaire, Label-free imaging of red blood cells and oxygenation with color third-order sum-frequency generation microscopy, Light Sci. Appl. 12 (2023), https://doi.org/10.1038/s41377-022-01064-4.

[48] I.T. Kostić, V.L. Ilić, V.B. Dordević, K.M. Bukara, S.B. Mojsilović, V.A. Nedović, D. S. Bugarski, D.N. Veljović, D.M. Mišić, B.M. Bugarski, Erythrocyte membranes from slaughterhouse blood as potential drug vehicles: isolation by gradual hypotonic hemolysis and biochemical and morphological characterization, Colloids Surf. B Biointerfaces. 122 (2014) 250–259, https://doi.org/10.1016/j.colsurfb.2014.06.043.

[49] C.S.F. Bah, A.E.D.A. Bekhit, A. Carne, M.A. Mcconnell, Slaughterhouse blood: an emerging source of bioactive compounds, Compr. Rev. Food Sci. Food Saf. 12 (2013) 314–331, https://doi.org/10.1111/1541-4337.12013.

[50] L.A. Frolova, Y. Furmansky, A.F. Shestakov, N.A. Emelianov, P.A. Liddell, D. Gust, I. Visoly-Fisher, P.A. Troshin, Advanced nonvolatile organic optical memory using self-assembled monolayers of porphyrin-fullerene dyads, ACS Appl. Mater. Interfaces 14 (2022) 15461–15467, https://doi.org/10.1021/acsami.1c24979.

[51] P. Charoenphol, K. Oswalt, C.J. Bishop, Therapeutics incorporating blood constituents, Acta Biomater. 73 (2018) 64–80, https://doi.org/10.1016/j.actbio.2018.03.046.

[52] W. Choe, A.P. Acharya, B.G. Keselowsky, B.S. Sorg, Intravital microscopy imaging of macrophage localization to immunogenic particles and co-localized tissue oxygen saturation, Acta Biomater. 6 (2010) 3491–3498, https://doi.org/10.1016/j.actbio.2010.03.006.

[53] I. Begemann, A. Viplav, C. Rasch, M. Galic, Stochastic micro-pattern for automated correlative fluorescence - scanning electron microscopy, Nat. Publ. Gr. (2015) 1–12, https://doi.org/10.1038/srep17973.

[54] L. Benedetti, E. Sogne, S. Rodighiero, D. Marchesi, P. Milani, M. Francolini, Customized patterned substrates for highly versatile correlative light-scanning electron microscopy, Sci. Rep. 4 (2014) 7033, https://doi.org/10.1038/srep07033.

[55] A.D. Corbett, M. Shaw, A. Yacoot, A. Jefferson, L. Schermelleh, T. Wilson, M. Booth, P.S. Salter, Microscope Calibration Using Laser Written Fluorescence 26, 2018, pp. 21887–21900, https://doi.org/10.1364/OE.26.021887.

[56] https://www.psfcheck.com/psfcheck-slides.

ORIGINAL PAPER

Kuznetsov–Ma rogue wave clusters of the nonlinear Schrödinger equation

**Sarah Alwashahi · Najdan B. Aleksić ·
Milivoj R. Belić · Stanko N. Nikolić**

Abstract In this work, we investigate rogue wave (RW) clusters of different shapes, composed of Kuznetsov–Ma solitons (KMSs) from the nonlinear Schrödinger equation (NLSE) with Kerr nonlinearity. We present three classes of exact higher-order solutions on uniform background that are calculated using the Darboux transformation (DT) scheme with precisely chosen parameters. The first solution class is characterized by strong intensity narrow peaks that are periodic along the evolution x-axis, when the eigenvalues in DT scheme generate KMSs with commensurate frequencies. The second solution class exhibits a form of elliptical rogue wave clusters; it is derived from the first solution class when the first m evolution shifts in the nth-order DT scheme are nonzero and equal. We show that the high-intensity peaks built on KMSs of order $n - 2m$ periodically appear along the x-axis. This structure, considered as the central rogue wave, is enclosed by m ellipses consisting of a certain num-
ber of the first-order KMSs determined by the ellipse index and the solution order. The third class of KMS clusters is obtained when purely imaginary DT eigenvalues tend to some preset offset value higher than one, while keeping the x-shifts unchanged. We show that the central rogue wave at $(0, 0)$ always retains its $n - 2m$ order. The n tails composed of the first-order KMSs are formed above and below the central maximum. When n is even, more complicated patterns are generated, with m and $m - 1$ loops above and below the central RW, respectively. Finally, we compute an additional solution class on a wavy background, defined by the Jacobi elliptic dnoidal function, which displays specific intensity patterns that are consistent with the background wavy perturbation. This work demonstrates an incredible power of the DT scheme in creating new solutions of the NLSE and a tremendous richness in form and function of those solutions.

S. Alwashahi
Faculty of Physics, University of Belgrade, Studentski trg 12, 11001 Belgrade, Serbia

Faculty of Science Al-Zawiya, University of Libya, Al Ajaylat, Libya

N. B. Aleksić · M. R. Belić · S. N. Nikolić
Division of Arts and Sciences, Texas A&M University at Qatar, P.O. Box 23874, Doha, Qatar

S. N. Nikolić (✉)
Institute of Physics Belgrade, University of Belgrade, Pregrevica 118, 11080 Belgrade, Serbia
e-mail: stankon@ipb.ac.rs

1 Introduction

In this paper, we present and analyze new solutions of the well-known partial differential equation, the nonlinear Schrödinger equation (NLSE) with Kerr nonlinearity. This equation is generally used for describing

various nonlinear phenomena in nature [1–3]:

$$i\psi_x + \frac{1}{2}\psi_{tt} + |\psi|^2\psi = 0, \tag{1.1}$$

where $\psi \equiv \psi(x, t)$ is the slowly varying envelope of the physical field under study and the nature of independent variables x and t depends on the nature of the problem considered. Here, we adopt the standard notation used in optical fibers, where t denotes the transverse spatial variable and x is the retarded time in the moving frame of reference. Another "standard" notation is used in the propagation problems of laser beams, in which x is the propagation distance, usually denoted by z, and t is the transverse spatial variable, denoted by x. We confine our attention to the localized optical waves generated on a constant intensity background that can be considered as high-order rogue waves.

Under certain approximations, NLSE can be used to describe the propagation of optical pulses in nonlinear dispersive media, i.e., in optical fibers and waveguides [4–7]. The usefulness of NLSE in photonics stems from the fact that it is formally equivalent to the paraxial wave equation in nonlinear optics. It is also used in plasma physics for describing the coupled dynamics of the electric field amplitude and the low-frequency density fluctuations of ions [8]. This equation also describes the interaction of the intra-molecular vibrations forming Davydov solitons with the acoustic disturbances in a molecular chain [8]. NLSE governs nonlinear optical modes in dilute Bose–Einstein condensates (BECs) [9], where it is known as the Gross–Pitaevskii equation. It also determines the evolution of an envelope that modulates long-crested surface gravity waves in deep water [10–12].

In recent times, an extended family of nonlinear Schrödinger equations (ENLSEs) has been proposed and investigated [13,14]. These equations consistently include any number of higher-order dispersion terms with the corresponding additional nonlinear terms that are conveniently grouped together in certain named equations of the hierarchy of NLSEs. The effort to derive and solve higher-order equations in the NLSE hierarchy comes from the need to understand and describe the propagation of ultrashort pulses through optical fibers [15,16]. Most attention so far was focused on the Hirota equation [17,18] (containing the third-order dispersion) and quintic equation (with dispersions up to the fifth-order) [19–22]. In general, the

entire family of extended NLSE offers a subtlety of possible forms for an additional shaping of basic NLSE solutions.

Nevertheless, the basic NLSE mentioned above remains a subject of broad interest, despite its relatively simple form (having only a cubic nonlinear term). Primarily, this is because of its complete integrability in one dimension. It contains infinitely many solutions, depending on the integration procedure and the form of solutions. The integrability feature has initiated a number of experimental and theoretical studies in many branches of physics, where the cubic NLSE can model the dynamics of various systems. In addition, the same mathematical procedure used for deriving the cubic NLSE solutions can be easily generalized and applied to the entire hierarchy of NLSEs. This implies that the features of the basic NLSE solutions are similar to those of the more complicated ENLSE family. Thus, by finding and analyzing the simple NLSE solutions, one can predict and describe the properties of similar solution classes of the extended family.

There are many methods for solving various partial differential equations (PDEs) with applications in nonlinear dynamics [23–26] and even in medicine [27,28]. The most basic is the inverse scattering method (ISM) [29], originating from the seminal work by Gardner, Greene, Kruskal, and Miura, in 1967 [30]. An extension of ISM, directly applicable to NLSE, was introduced by Zakharov and Shabat in 1972 [31] and later (1974) generalized by Ablowitz, Kaup, Newell, and Segur [32] to include other nonlinear PDEs into what is today known as the AKNS method. Other useful methods include the Bäcklund and Darboux transformations, based on the treatment of the Lax pair matrix operators [29]. Recently, the propagation of internal solitary waves in the ocean has been described by the solitary solutions of another PDE, called the generalized nonlinear Schrödinger equation, containing a third-order dispersion, in addition to the usual second-order [33].

Here, we are focused on the Darboux transformation (DT) technique [34], which is widely used to derive exact analytical solutions of both NLSE and ENLSEs [18,34,35]. Briefly, DT is based on the Lax pair eigenvalue problem and the resulting recursive relations, with the aim to calculate higher-order solutions starting from the trivial zeroth-order seed function that satisfies Eq. (1.1) (for more details, see Appendix). Different solution classes can be derived by selecting the DT order n, the zeroth seed, and a set of n complex eigen-

values, with arbitrary real shifts along the x- and t-axes. The major advantage of DT scheme is the straightforward algorithm for calculating infinitely many NLSE wave functions with incredible richness of solutions' patterns. The minor drawback of DT technique is that only specific analytical solutions can be computed that do not include the general NLSE evolution from arbitrary initial conditions. Also, by increasing the DT order n, the DT procedure becomes computationally expensive.

We also mention that the DT technique has similarity to other techniques of PDE integration, such as He's semi-inverse variational principle (HVP) [36]. In the HVP technique, the given PDE is transformed into ordinary differential equations (similar to the Lax pair in DT). Also, an ansatz is assumed, in parallel to the DT seed solution. The difference between HVP and DT schemes is the procedure for generating the final solution: In HVP, it is calculated using the variational formula and finding its stationary point, while in DT the algebraic recursive relations are employed (see Appendix).

The basic solutions of the cubic NLSE (and ENLSEs) that can be calculated using DT are the Akhmediev breathers (ABs) [37,38] (localized in x, but periodic along t-axis) and the Kuznetsov–Ma solitons (KMSs) [31,39–41] (localized in t, but periodic along x-axis). The Peregrine soliton (PS) (localized along both axes) can be considered as the limiting case of both ABs and KMSs when their corresponding periods go to infinity [42,43]. All these basic solutions ride on a background and can be considered as the prototype first-order RWs.

These solutions may also be considered as the fingerprints of NLSE—it is experimentally shown that such structures spontaneously appear during the NLSE evolution, even from the white noise [44]. Furthermore, the first-order ABs, PS, and KMSs are the building blocks for generating higher-order solutions of the NLSE. Such solutions, characterized by a narrow peak of high intensity, are considered as the true rogue waves. The simplest example of a RW is the PS [45]. The research on RWs is currently a hot topic, since these giant nonlinear waves can appear in nonlinear optics [46,47], deep ocean [12,48], quantum optics [49,50], and elsewhere. A recent paper proposed a new way for RW excitation [51], via the electromagnetically induced transparency (EIT) [52–55]. Significant effort has been expended to understand the nature and generating mechanisms of optical rogue waves [56,57]. The root of their appearance is related to the modulation instability [56,58]. A very recent paper succinctly summarizes the main characteristics of the RWs: They are nonlinear, deterministic, and physical in nature [59].

Our main objective in this paper is to present new analytical RW solutions of the cubic NLSE arising on the uniform background and indicate new intensity patterns in the nonlinear systems governed by the NLSE. To achieve this goal, we are using three different nonlinear superpositions of KMSs. The first class has the form of a periodic array of RW peaks along the evolution x-axis. It is calculated by applying the commensurate periods of KMSs in the DT scheme of order n. To calculate the second solution class, we introduce m nonzero DT shifts ($m < n$) along x-axis, to achieve the transformation of vertical (along evolution axis) RWs into multi-elliptic RW clusters composed of KMSs (KM MERWCs). The third solution class is obtained by breaking the proportionality relation among the DT constituents' frequencies, while retaining the evolution shifts. Imaginary parts of the eigenvalues are chosen to be slightly higher than 1 (i.e., to lie in close vicinity of 1), which could be approximately regarded as a degenerate DT problem. In this manner, we came up to cluster solutions characterized by a single high-order rogue wave in the center of the xt-plane, with n tails emanating before and after it, composed of the first-order (KMS1) solitons. We show that the parity of n determines whether the wave function contains the loops of the first-order KMSs around the $(0, 0)$ point.

The results presented here represent an extension and closure of our recent work [60], in which elliptic rogue wave clusters were obtained from the ABs of NLSE (AB MERWCs). We thus add new and complementary solutions to the previously described rogue wave triplets [61], triangular cascades [62–64], and circular clusters [35,65–67], but now based on the KMSs. The classification of multi-RW structures into different families was presented in a series of papers by Akhmediev's group [67–69]. We believe that the contribution of the three new KMS clusters, which were not presented before, represents a necessary symmetric closure on the possible higher-order RW clusters that can be obtained by the DT scheme. We also show that these solutions can be computed numerically on the elliptic dn background. Finally, the same sets of DT eigenvalues and shifts can be employed to all equations in the extended NLSE hierarchy, to generalize KMS rogue

wave clusters of more complex systems (not presented here).

The paper is organized as follows. In Sect. 2, we present the periodic array of RW peaks composed of higher-order KMSs. In Sect. 3, we display NLSE solutions in the form of multi-elliptic rogue wave clusters on a uniform background, built from KMSs. In Sect. 4, we analyze the third class of KMS clusters obtained when all imaginary parts of DT eigenvalues are higher than but close to 1. In Sect. 5, we exhibit the NLSE KMS cluster solutions on a nonuniform background, formed by the Jacobi elliptic dnoidal function. In Sect. 6, we summarize our results. A short introduction into the general DT scheme for NLSE is provided in Appendix.

2 Periodic arrays of RWs composed by KMSs

The expression that describes all first-order solutions, the AB, PS, and KMS on uniform background [37,38], is given by:

$$\psi(t, x) = \left[1 + \frac{2(1-2a)\cosh \lambda x + i\lambda \sinh \lambda x}{\sqrt{2a}\cos \omega t - \cosh \lambda x}\right] e^{ix}. \tag{2.1}$$

Here, parameter a determines the type of solution: If $a < 0.5$, one gets an AB that is periodic along the t-axis, with the period $L = \frac{\pi}{\sqrt{1-2a}}$. For $a = 0.5$, one obtains a single peak at the coordinate center, known as the Peregrine soliton. In this paper, we consider in detail the case $a > 0.5$, when Eq. (2.1) describes the Kuznetsov–Ma solitons. To analyze it further, we write the following expressions for the growth factor λ and the transverse frequency ω, present in (2.1):

$$\lambda = \sqrt{8a(1-2a)}, \tag{2.2}$$
$$\omega = 2\sqrt{1-2a}. \tag{2.3}$$

Note that the parameter a is closely related to the imaginary part ν of λ_{DT}:

$$\nu = \sqrt{2a}. \tag{2.4}$$

Therefore, we ignore the real parts of any DT eigenvalue λ_{DT} (assuming them equal to zero throughout this paper) and concentrate only on the imaginary parts. When $a > 0.5$, $\nu > 1$ and both λ and ω become imaginary numbers, so $\cosh \lambda x$ and $\sinh \lambda x$ in (2.1) turn into cos and sin functions, while $\cos \omega t$ transforms into hyperbolic cosine. This means that KMSs are periodic

along the evolution x-axis and localized along the transverse t-axis. The period T_x and frequency ω_x along x-axis are, respectively:

$$T_x = \frac{\pi}{\nu\sqrt{\nu^2 - 1}} \tag{2.5}$$

and

$$\omega_x = \frac{2\pi}{T_x} = 2\nu\sqrt{\nu^2 - 1}. \tag{2.6}$$

Our idea is to build the periodic rogue waves from the higher-order KMSs, using the DT scheme. The DT equations for conducting such a task for NLSE were presented in detail elsewhere [57], and a short description is provided in Appendix. The DT order n is also the order of RW peaks along the x-axis. In this scheme, we have n first-order KMSs (each defined by an imaginary eigenvalue $\lambda_j = i\nu_j$ ($\nu \equiv \nu_1$), with real vertical shifts x_j, and horizontal shifts t_j preset to zero) that are building blocks for a final solution. To produce a vertical array of high-intensity peaks, with a complex pattern in their vicinity, we employ the idea of commensurate KMS frequencies:

$$\omega_{xj} = j\omega_x, \tag{2.7}$$

where $\omega_x \equiv \omega_{x1}$ is the frequency of the first KMS in the DT scheme. This insures that all DT constituents will eventually collide at the same points along x-axis, thus producing periodic and strong intensity maxima. By combining last equations, one can easily obtain the DT eigenvalues needed to achieve the periodicity condition:

$$\nu_j = \sqrt{\frac{1 + \sqrt{1 + 4j^2\nu^2(\nu^2 - 1)}}{2}}. \tag{2.8}$$

We present analytical results when $\nu = 1.1$ for the second-order ($n = 2$) and third-order ($n = 3$) commensurate KMSs in Fig. 1a and b, respectively. Other eigenvalues in the DT scheme can be calculated using Eq. (2.8). One can clearly see the vertical periodic array of RWs having equal periods $T_x = 6.24$ along x-axis in both figures, which is in agreement with Eq. (2.5). The intensity I_{max} of each peak in the vertical array is even higher than in the case of higher-order Akhmediev breathers ($\nu < 1$). This can be simply explained by means of the peak-height formula (PHF) [70,71]:

$$|\psi(0, 0)|^2 = \left(1 + \sum_{j=1}^{n} 2\nu_j\right)^2. \tag{2.9}$$

By this equation, one can easily calculate the maximum intensity of higher-order ABs or KMSs, under the condition that all DT eigenvalues nonlinearly collide at the same point, say $(0, 0)$. When one builds higher-order ABs, all imaginary parts are less than one, while for the KMSs they are higher than 1. This is the reason why KMSs are characterized by higher peaks. For the KMS RW of order $n = 2$, we obtained $I_{max} = 33.06$, and for $n = 3$ the value is $I_{max} = 74.7$. This is in agreement with Eq. (2.8) and PHF for the starting value of $\nu = 1.1$.

We next performed numerical integration of these solutions, to check the influence of modulation instability (MI) on the dynamical generation of higher-order KMSs. The results are presented in Fig. 1c and d for the second-order and third-order KMSs, respectively. In both figures, one can see that higher Fourier modes arise quickly after the iteration onset, due to MI. This leads to the disintegration of the periodic array of RWs, in favor of the irregular growth of lower intensity peaks elsewhere in the (x, t) plane—in contrast to the desired dynamic generation of higher-order ABs. Namely, the Fourier transform (FT) in our split-step beam propagation method assumes periodicity along the transverse axis, which is characteristic of ABs. This enables the matching of constituent AB periods to the box size and neat generation of RWs along the t-axis, as analyzed in our previous papers [18,21,70]. Since KMSs are periodic along the evolution axis, it is impossible to match the periods of KMSs to the horizontal box, which is the reason why MI destroys RWs soon after the integration starts.

3 Multi-elliptic rogue wave clusters of Kuznetsov–Ma solitons

To generate KM MERWCs, we follow an analogous procedure to the one described in our previous paper for Akhmediev breathers [60]. The first condition is to keep commensurate frequencies of constituent first-order KMSs, as in the previous section (Eq. 2.7). The second requirement is to adjust the first m shifts along the evolution axis (x_j) to be nonzero and equal: $x_j \neq 0$ for $j \leq m$, and $x_j = 0$ when $m < j \leq n$. All transverse shifts are $t_j = 0$. Here, we use the same expression for calculating x-shifts from the AB MERWCs paper [60] (to keep close analogy with the Akhmediev breather

clusters):

$$x_j = \sum_{l=1}^{\infty} X_{jl}\omega^{2(l-1)} = X_{j1} + X_{j2}\omega^2$$
$$+ X_{j3}\omega^4 + X_{j4}\omega^6 + \cdots, \qquad (3.1)$$

in which ω denotes a number close to zero. Note that ω is a main DT frequency in the AB MERWCs case, but that is not the case for the KM MERWCs. The reader should not confuse $\omega \to 0$, which we retain for x_j calculation, with ω_x of the KMSs (Eq. (2.6)).

In Fig. 2, we present KM MERWCs on uniform background, having one ellipse around the central peak. The frequency ω in the expansion (Eq. (3.1)) is set to 10^{-1}, while $X_{j4} = 10^6$. This way, one gets evolution shift x_j in the order of 1. The imaginary part of the first eigenvalue is chosen as $\nu = 1.1$, while other ν_j values are calculated using Eq. (2.8). We set $m = 1$ and vary the value of n, to change the order of the central RW. For $n = 4$, one gets seven KMSs of order one (KMS1), situated on an ellipse around the second-order KMS (Fig. 2a). When $n = 5$, one obtains a third-order KMS, surrounded by 9 KMS1 distributed along a single ring (Fig. 2b).

The second example of KM MERWCs is shown in Fig. 3. Here, $m = 2$ so the two rings are formed around each central peak. Since m is increased compared to Fig. 2, we need to increase the solution order n. For $n = 6$, one obtains the second-order KMS at the center, with 11 and 7 KMS1 on the outer and inner ellipses, respectively (Fig. 3a). When $n = 7$, an array of the third-order KMSs is formed, with 13 and 9 KMS1 on two ellipses around each central RW peak (Fig. 3b). As for the $m = 1$ case, we left $\omega = 10^{-1}$ and $X_{j4} = 10^6$ unchanged. In both Figs. 2 and 3, one can easily observe the periodicity of the cluster along x-axis. The period T_x is calculated from Eq. (2.5) and is not perturbed by evolution shifts, meaning that the numerical value remains $T_x = 6.24$ in Fig. 2, since we did not change the ν value from Fig. 1. In Fig. 3, we set $\nu = 1.02$, to increase the T_x period according to equation (2.5). This was done to zoom in the three clusters in the selected numerical box, so the reader can clearly see the two rings around each RW at the center.

Our final conjecture is that the RW of $n - 2m$ order (denoted hereafter as KMS_{n-2m} or KMS $(n - 2m)$ or RW_{n-2m}) is obtained at $(0, 0)$, with m ellipses around the peak for $n \geq 2m + 2$. The outer ellipse contains $2n - 1$ KMS1, while each following ring toward the
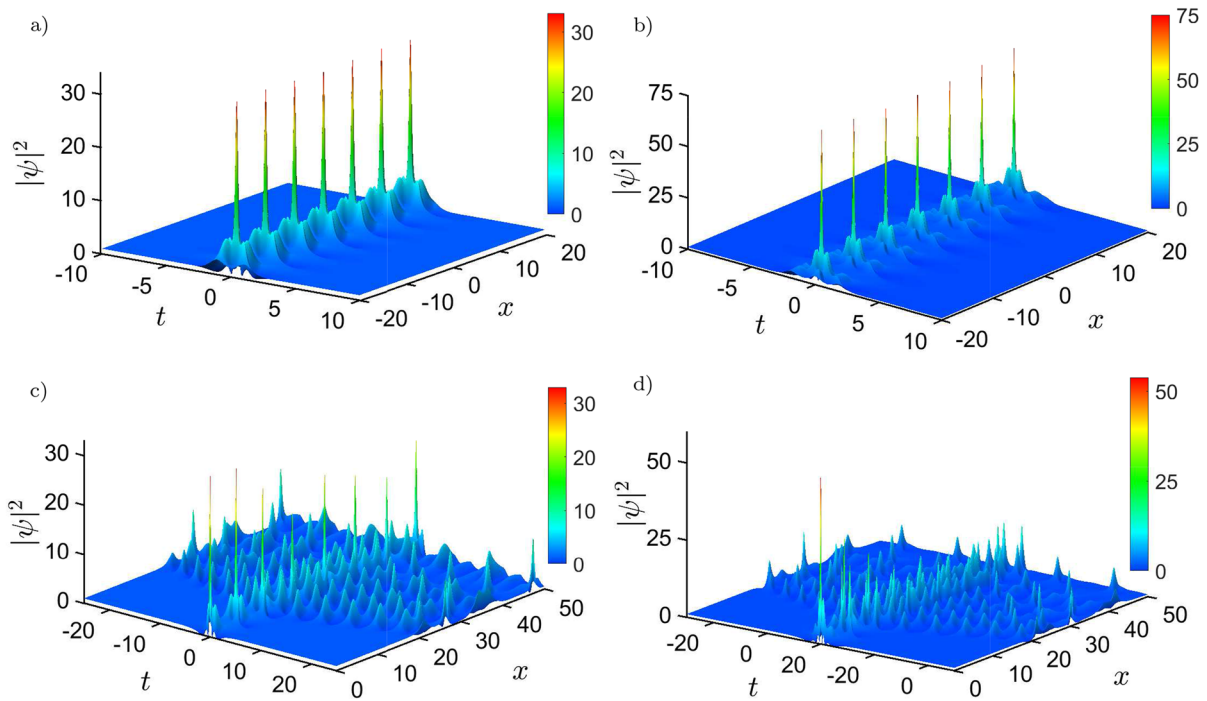
Fig. 1 3D color plots of higher-order Kuznetsov–Ma solitons with commensurate frequency components on a uniform background. **a** The second-order DT solution with eigenvalues $\nu = \nu_1 = 1.1$ and ν_2, calculated using Eq. (2.8). **b** The third-order DT solution with eigenvalues $\nu = \nu_1 = 1.1$, ν_2, and ν_3, calculated using Eq. (2.8). The modulation instability of higher-order KMSs is tested for (**c**) the second-order solution from figure (**a**)

and for (**d**) the third-order solution from figure (**b**), by executing the second-order beam propagation method from the analytical DT wave function at some fixed time x_0 between the two peaks. The modulation instability appearing soon after the iteration onset destroys the intensity distribution and periodicity of higher-order KMS peaks
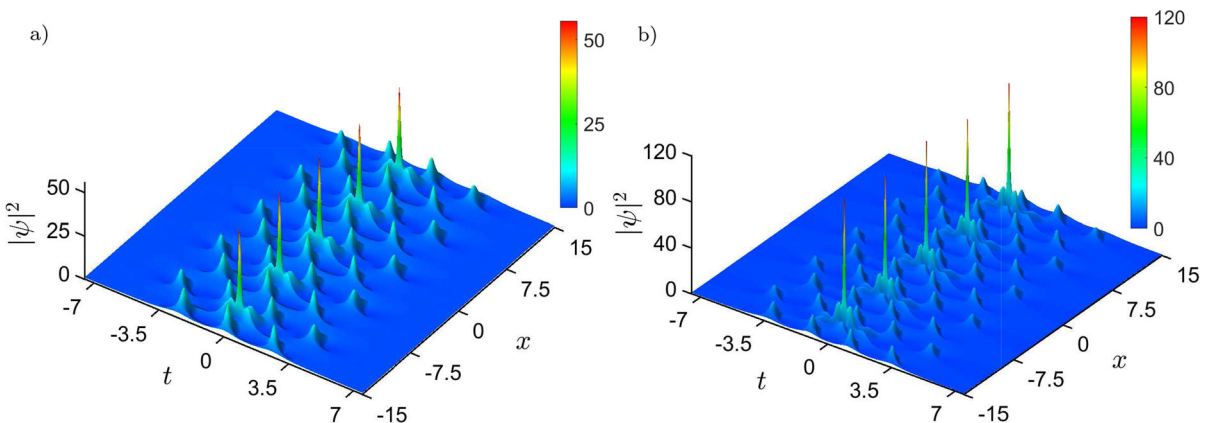
Fig. 2 3D color plots of KM MERWCs on the uniform background, having one ellipse ($m = 1$) around each $n - 2m$ order rogue wave. The clusters are formed periodically along the evolution x-axis. Shifts of the constituent DT components are obtained

for $X_{j4} = 10^6$. The orders of Darboux transformation and the high-intensity encircled peaks are, respectively: **a** $n = 4$ with the second-order rogue wave, and **b** $n = 5$ with the third-order rogue wave
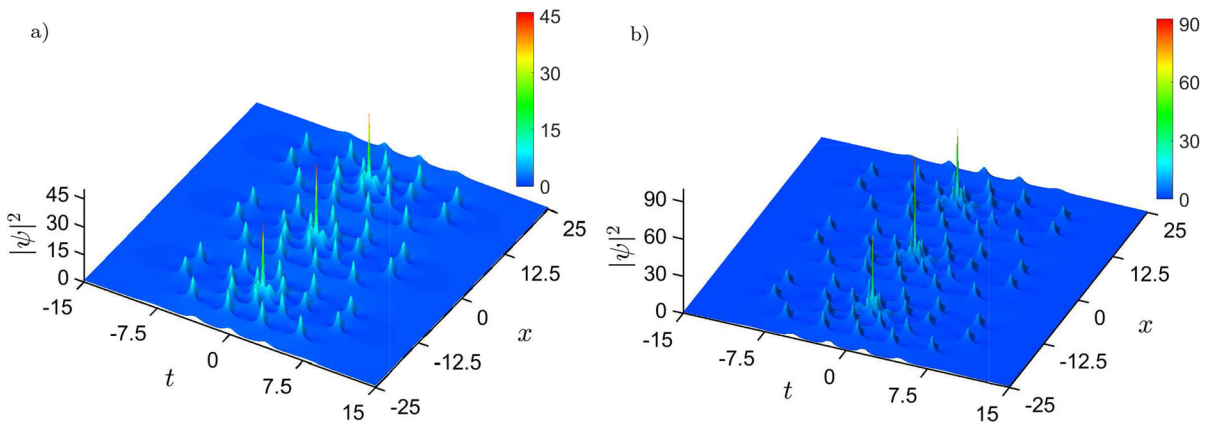
Fig. 3 3D color plots of KM MERWCs on the uniform background, having two ellipses ($m = 2$) around each $n - 2m$ order rogue wave. The clusters are formed periodically along the evolution x-axis. Shifts of the constituent DT components are obtained for $X_{j4} = 10^6$. The orders of Darboux transformation and the high-intensity encircled peaks are, respectively: **a** $n = 6$ with the second-order rogue wave, and **b** $n = 7$ with the third-order rogue wave

center has four KMS1 less. If the rings are indexed from 1 to m, going from outer to the inner one, the number of KMS1 on each ring is $c_i = 2n - 4i + 3$. This is the same conclusion as for the AB MERWCs [60,67,68]. The two differences are the lower intensity of AB MERWCs as compared to the KM MERWC case (due to PHF) and the direction of periodicity (AB MERWC is periodic along the $t-$axis).

The explanation of KMS cluster's appearance is similar to the AB case. If all x_j shifts are zero, the nonlinear superposition of all n DT components will take place at equidistant points along the x-axis (including coordinate origin), producing the periodic array of RWs, as shown in Fig. 1a and b. However, if one sets x-shifts to be nonzero for the first $m \geq 1$ DT components, the intensity distribution will decrease and split over the xt-plane. The understanding of why KM MERWC appears in such a way could be theoretically possible if one applies the mathematical analysis of exact analytical DT solutions. It is well known that deriving very complex DT expression for big n is extremely hard work with relatively little theoretical insight, so it was not performed anywhere before. Thus, we will not conduct that analysis here either.

4 Third solution class of nearly degenerate eigenvalues

Here, we present the third class of KMS cluster solutions that do not display a multi-elliptic form. This class is characterized by long-tail structure distributions, with loops of KMS1 in certain cases. We were motivated to explore new KMS patterns in order to compare them with the AB solutions obtained under similar computational conditions. Namely, the first requirement for generating AB MERWCs was to provide the proportionality condition for higher-order DT components ($\omega_j = j\omega$), which lead to the simple equation for the imaginary part of jth eigenvalue $v_j = \sqrt{1 - \frac{1}{4}j^2\omega^2}$, with $\omega \to 0$ [60]. For the KMS case, all v_j must be greater than one, so we slightly modified the last equation to:

$$v_j = v_0 + \sqrt{1 - \frac{1}{4}j^2\omega^2}, \tag{4.1}$$

where v_0 denotes the offset of KMS eigenvalues. Consequently, all v_j are close to the $1 + v_0$ value (in analogy to the AB case, when $v_j \to 1$). The difference, however, is significant: In the AB case, one retains the commensurate frequencies and AB MERWCs are obtained,

while for the KMS a new ν_j set destroys the proportionality of frequencies. In this section, we show the appearance of new KMS clusters under the condition of Eq. (4.1).

The algorithm for calculating long-tail KMS clusters is as follows: First, we set an offset ν_0 and some small value of ω. We choose values for n and m and calculate all x-shifts using Eq. (3.1). Next, we compute all eigenvalues in the DT scheme from Eq. (4.1) $(1 \le j \le n)$. Finally, we apply the DT procedure, to numerically calculate wave function $\psi(x, t)$ at all grid points with an arbitrary precision.

In Fig. 4, we show the intensity distribution for $n = 4$, $\nu_0 = 0.1$, and $\omega = 0.05$. When $m = 0$, a fourth-order peak is obtained at the origin $(0, 0)$, with a peak intensity of 95.67 (in agreement with the PHF). The intensity distribution is shown in Fig. 4a. One can easily discern the central RW and four tails containing the KMS1 solutions spreading below and above the peak. In Fig. 4b, we show the intensity distribution for $m = 1$. In this case, the second-order KMS peak is formed at the origin, with 28.97 maximal intensity. The one nonzero shift clearly moved apart constituent KMSs, producing a lower-order DT solution at the $(0, 0)$ point. Four KMS1 tails are also formed on both sides of the central RW, but are separated in groups of two in the lower half plane, for a given box. Further on, above the KMS2, a single loop consisting of KMS1 is formed, stretching out from $x = 0$ to $x \approx 43$. Note that the range of pseudo-color scales on both figures are set to $(0, 10)$ interval, to emphasize the central peak and KMS1 along the tails. We also display the insets, to show the central RW and its vicinity in more detail.

We next show the $n = 5$ case, for $m = 0$ (Fig. 5a), $m = 1$ (Fig. 5b), and $m = 2$ (Fig. 5c). The values of $\nu_0 = 0.1$ and $\omega = 0.05$ are left unchanged. When $m = 0$, RW5 is formed at the origin (peak intensity 143.17, in agreement with the PHF). Since n is changed, five symmetric KMS1 tails are observed on both sides of the central peak. For $m = 1$, one can see the RW3 at the $(0, 0)$ point (max. intensity 57.26, see the inset) and also five tails, but the outer two are not participating in the building of the central structure. If we set $m = 2$, no central RW emerges. Instead, a group of six KMS1 appears at the origin, while five tails are still preserved. The first clue of the solution structure can now be deduced from Figs. 4 and 5. The central peak at the origin, composed of the constituent KMS1 solitons, has the $n - 2m$ order, as expected for the KM

MERWCs. Next, the number of tails above and below the high-intensity peak is equal to the overall DT solution order n.

In Fig. 6, we present three long-tail KMS clusters for the $n = 6$ case, with $\nu_0 = 0.1$ and $\omega = 0.05$. The RW6 is formed at the origin, with the peak intensity of 199.83 (in agreement with the PHF), when $m = 0$ (Fig. 6a). Below and above the sharp RW peak (KMS of the sixth-order: KMS6), six symmetric tails can be observed. In Fig. 6b, the intensity distribution is presented for $m = 1$. One can observe the RW4 at $(0, 0)$ (max. intensity 94.95, see the inset) and six tails emerging from the origin, but the outer two are not contributing to the central RW4 structure. In the upper half plane, the tails are formed in three groups of two. Above the RW, one loop of KMS1 appears stretching out from $x = 0$ to $x \approx 69$. This solution has a similar form to the $n = 4$, $m = 1$ case shown in Fig. 4b. However, the loop is not present when $n = 5$. One may conclude that the loop is formed only for even values of n. This is supported by the next case of $n = 6$ and $m = 2$, when the second-order KMS is generated at the center, with two KMS1 loops above, one KMS1 loop below the RW, and six tails (Fig. 6c). The tails are divided into three groups of two, but only in the lower half of the plane.

Finally, we analyze the third class of solutions for even higher DT order: $n = 7$ ($\nu_0 = 0.1$ and $\omega = 0.05$) and $n = 8$ ($\nu_0 = 0.07$ and $\omega = 0.05$). When $n = 7$ and $m = 2$, the third-order KMS at $(0, 0)$, along with seven tails, is formed (Fig. 7a). No loop appears in this case. For $n = 7$ and $m = 3$, there is no RW at the center, only an AB-like cluster, since $n - 2m = 1$ (Fig. 7b). Again, seven tails are seen in both figures, but without KMS1 loops. The appearance of the cluster is different when $n = 8$. For $m = 2$, the KMS4 is found at the origin ($n - 2m = 4$), with eight tails on both sides of the peak. In the upper plane, the tails are formed in four groups of two. Two KMS1 loops are obtained above the peak and one loop is formed below the peak (Fig. 7c). When $n = 8$ and $m = 3$, one sees KMS2 at the xt-plane center and eight tails. Three/two KMS1 loops are generated above/below the RW (Fig. 7d).

From Figs. 4, 5, 6, and 7, we conclude the following: Kuznetsov–Ma solitons of order $n - 2m$ appear at the origin $(0, 0)$ when the overall solution order is n and when the first m nonzero and equal shifts in the DT scheme are used. Above and below the central RW, n tails are formed, each consisting of KMS1 solitons. For even values of n, the $m(m - 1)$ KMS1 loops
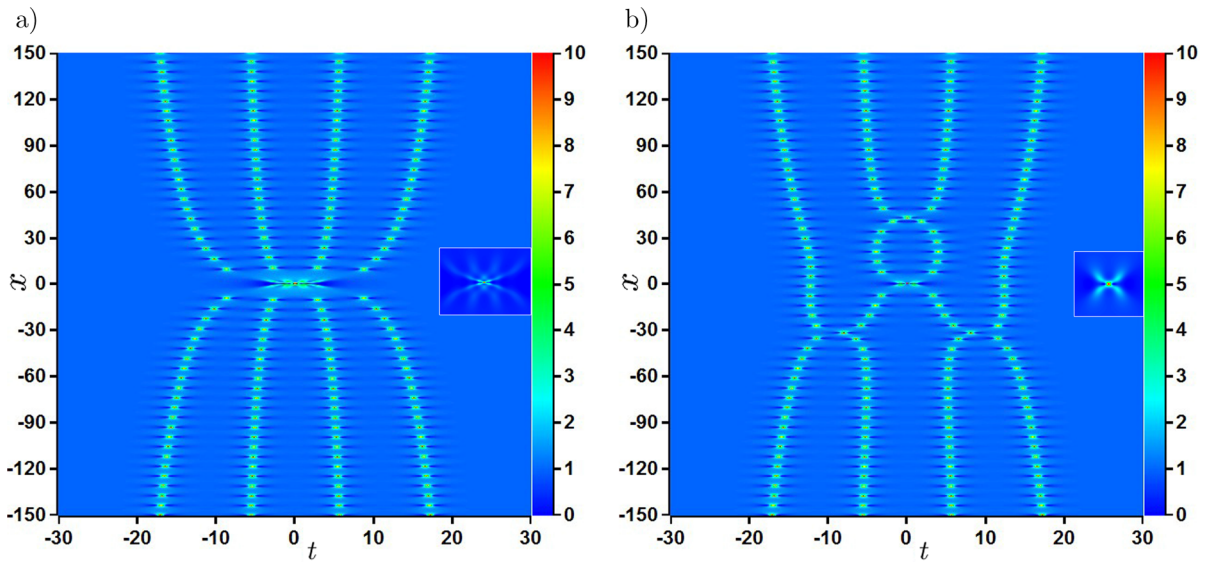
a)

b)

Fig. 4 2D color plots of the long-tail KMS clusters on the uniform background, having one rogue wave of the $n - 2m$ order formed at $(0, 0)$ of the (x, t) plane. The starting offset for cluster formation is $v_0 = 0.1$. DT shifts are obtained for $X_{j4} = 10^6$ and $\omega = 0.05$. The DT order is $n = 4$. The number of nonzero shifts

m and the order of high-intensity central peaks are, respectively: **a** $m = 0$ with the fourth-order rogue wave and **b** $m = 1$ with the second-order rogue wave. The insets in both images show the enlarged central RW and its vicinity

emerge above (below) the RW. We emphasize that if one changes the sign of x-shifts, the entire cluster simply flips about the $x = 0$ line (results not shown).

5 Long-tail KMS clusters on Jacobi elliptic dnoidal background

In this section, we show the long-tail KMS clusters computed on a wavy background, defined by the Jacobi elliptic dnoidal function dn. For this calculation, we use the modified DT scheme for the NLSE [72]. We start from the seed function $\psi_{\mathrm{dn}}(x, t) = \mathrm{dn}(t, g)e^{i(1-g^2/2)x}$, where the elliptic modulus is denoted by g ($0 < g < 1$) and the elliptic modulus squared is $m_{\mathrm{dn}} = g^2$. Although the choice of shifts and eigenvalues is the same as in the previous section, the procedure for calculating wave function is different. Namely, the exact analytical values of ψ can be obtained only when $t = 0$ [72]. We therefore use the fourth-order Runge–Kutta algorithm to calculate $\psi(x, t \neq 0)$ values in the grid along the t-line for the fixed x from the initial values of $\psi(x, t = 0)$.

In Fig. 8, we show the intensity distribution of the long-tail KMS cluster built on the dn background with

$m_{dn} = 0.4^2$. The order of DT solution is $n = 6$, and the number of nonzero shifts is $m = 2$. The computational parameters are: $v_0 = 0.1$, $\omega = 0.05$, and $X_{j4} = 10^6$. We report the formation of the second-order RW at the origin (clearly observable in the inset). Since n is even, we obtained two KMS1 loops above and one KMS1 loop below the central peak. The peak maximum is 28.61, but we set the maximum of pseudo-color scale to 10, to emphasize the fine vertical stripes representing the crests and troughs of the dnoidal background. Although the long-tail cluster is clearly visible, the tops of the two upper loops are blurred by the background wave.

6 Conclusion

In this paper, we presented the three classes of NLSE solutions built from Kuznetsov–Ma solitons in the DT scheme of order n. The first class is obtained for the commensurate frequencies of DT components, with all evolution shifts set to zero. These solutions have the form of vertically periodic arrays of RWs, composed of the nth-order KMSs. We discussed the difficulties in generating these solutions dynamically, since the
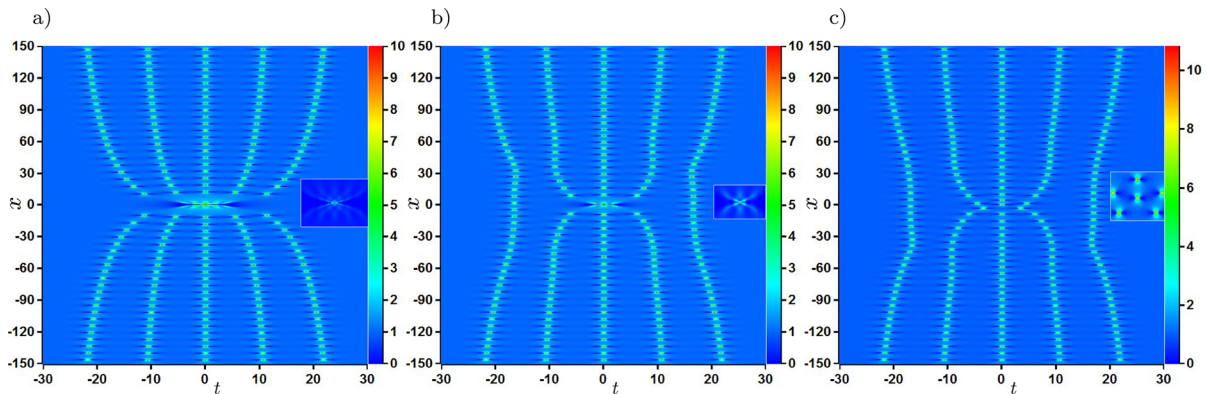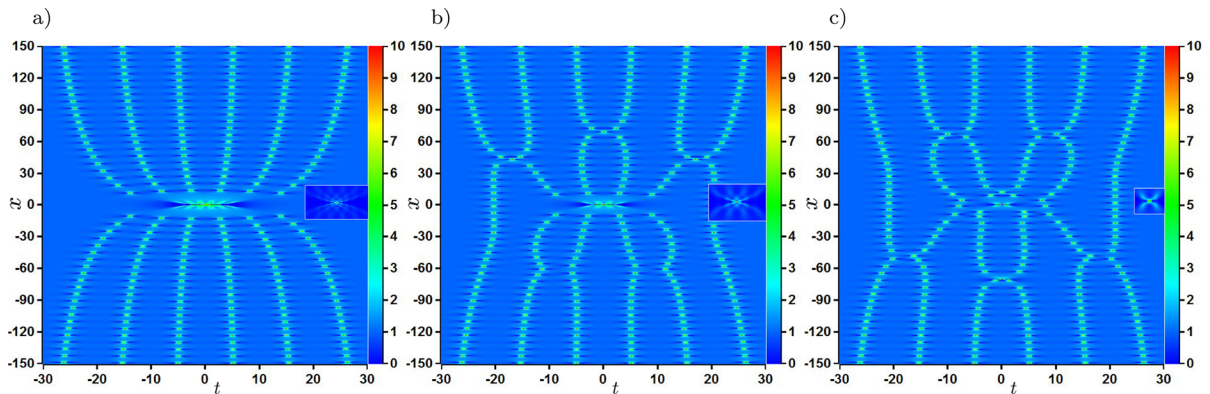
a)   b)   c)

Fig. 5 2D color plots of the long-tail KMS clusters on the uniform background. The rogue wave of $n - 2m$ order is conditionally formed at $(0, 0)$ of the (x, t) plane. The starting offset for cluster formation is $v_0 = 0.1$. Shifts in the DT scheme are calculated for $X_{j4} = 10^6$ and $\omega = 0.05$. The DT order is $n = 5$ and the number of nonzero shifts is m. **a** The fifth-order rogue wave for $m = 0$. **b** The third-order rogue wave for $m = 1$. **c** For $m = 2$, the central structure resembles a single Akhmediev breather, since $n - 2m = 1$. The insets in all images show the enlarged regions centered around $(0, 0)$

a)   b)   c)

Fig. 6 2D color plots of the long-tail KMS clusters on the uniform background. The rogue wave of $n - 2m$ order is conditionally formed at $(0, 0)$ of the (x, t) plane. The starting offset for cluster formation is $v_0 = 0.1$. Shifts in the DT scheme are calculated for $X_{j4} = 10^6$ and $\omega = 0.05$. The DT order is $n = 6$, and the number of nonzero shifts is m. **a** The sixth-order rogue wave is formed for $m = 0$. **b** The fourth-order rogue wave is formed for $m = 1$. **c** The second-order rogue wave is formed for $m = 2$. The insets on three images show the enlarged central RW and its vicinity

higher Fourier modes arise quickly after the simulation onset, due to the modulation instability, and lead to the disintegration of the periodic array of rogue waves.

Next, we showed the multi-elliptic KMS clusters, also periodic along the x-axis, computed using the same set of eigenvalues, but with the first m evolution shifts set to be equal and nonzero. The KMS of order $n - 2m$ (considered as the central rogue wave) is surrounded by m ellipses composed of KMS1 peaks. The number of KMS1 peaks on the outermost ellipse is $2n - 1$. On each following ring, we counted four KMS1 peaks less.

The third solution class are the long-tail KMS clusters. They are computed for a set of n nearly degenerate eigenvalues that are all close to some predefined value greater than one. The first m shifts were equal and zero, as for the second solution class. The computation was conducted to emphasize the analogy to multi-elliptic clusters of Akhmediev breathers. The central part of the KMS cluster consists of the $n - 2m$-order Kuznetsov–Ma soliton at the origin. Above and below this high-intensity narrow peak, the n tails composed of KMS1s are observed. For $m = 0$, the tails are perfectly symmet-
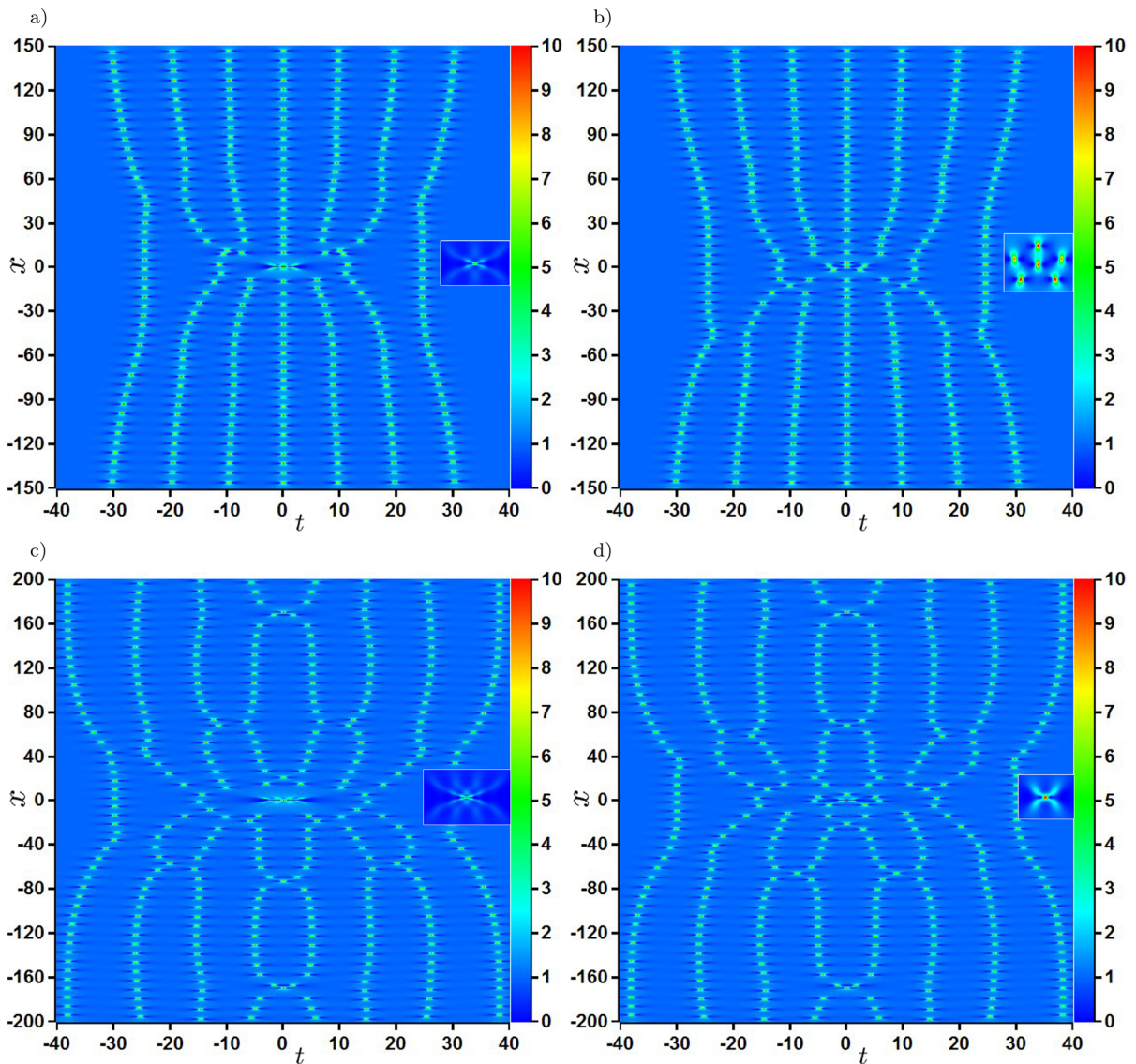
Fig. 7 2D color plots of the long-tail KMS clusters on the uniform background, for higher values of DT order n. The high-intensity central rogue wave is formed when $n - 2m > 1$. DT shifts are obtained for $X_{j4} = 10^6$ and $\omega = 0.05$. Values of n, nonzero shifts m, and the starting offset v_0 are, respectively: **a** $n = 7$, $m = 2$, $v_0 = 0.1$ (third-order RW at the center), **b** $n = 7$, $m = 3$, $v_0 = 0.1$ (single AB at the center), **c** $n = 8$, $m = 2$, $v_0 = 0.07$ (fourth-order RW at the center), and **d** $n = 8$, $m = 3$, $v_0 = 0.07$ (second-order RW at the center). The insets in all images show the enlarged regions centered around $(0, 0)$

ric. If $m \geq 1$, the symmetry is partially broken down, especially for even values of n. Namely, in this case ($n = 4$, $n = 6$, $n = 8$) one observes the loops consisting of the first-order KMSs around the peak. The numbers of loops above and below the RW are m and $m - 1$, respectively. Depending on the particular values of even n and m, the tails can be grouped in $n/2$ groups

by two, in the upper or lower half planes. Finally, these specific features are not observed for the odd n cases ($n = 5$ and $n = 7$).

We numerically built the long-tail KMS cluster on a periodic background, using the modified Darboux transformation scheme. The intensity of higher-order Kuznetsov–Ma solitons at the plane origin significantly
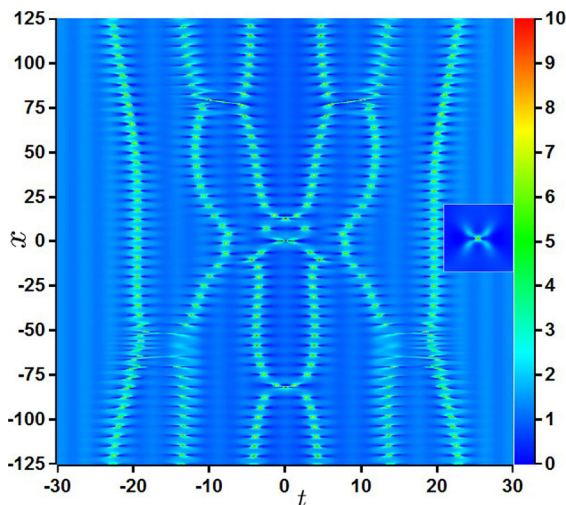
Fig. 8 2D color plot of the long-tail KMS cluster on the Jacobi elliptic dnoidal background, with elliptic modulus squared $m_{dn} = 0.4^2$. The starting offset is $\nu_0 = 0.1$, while DT shifts are obtained for $X_{j4} = 10^6$ and $\omega = 0.05$. The DT order value of $n = 6$ and the number of nonzero shifts $m = 2$ lead to generation of the second-order RW at $(x, t) = (0, 0)$. The inset shows the enlarged central RW and its vicinity

surpasses the amplitude of elliptic AB waves. However, we are still able to spot the weak background oscillations, on which the KMS cluster is constructed.

The results presented in this paper represent an extension and conclusion of our previous work on the multi-elliptic RW clusters composed of Akhmediev breathers. A perfect agreement with all facets of the complex DT analysis is demonstrated, often after complicated calculations. Nevertheless, our opinion is that even such complex investigation of various wave clusters can be of further research interest—after many years of NLSE research, new and interesting solutions emerge, due to the rich variety of parameters and possibilities in the Darboux transformation scheme. The research potential is increased even more if one considers the cluster solutions for the infinite hierarchy of extended nonlinear Schrödinger equations. The material presented in this paper can be a starting point to understand in more detail the rogue wave features in more complex physical systems that are governed by the extended nonlinear Schrödinger equations (Hirota, quintic, etc.)

Appendix: The general Darboux transformation scheme

The NLSE solution of order N is a nonlinear superposition of N independent components, where each one is determined by the complex eigenvalue λ_j ($1 \le j \le N$). The corresponding wave function is:

$$\psi_n = \psi_{n-1} + \frac{2\left(\lambda_n^* - \lambda_n\right) s_{n,1} r_{n,1}^*}{\left|r_{n,1}\right|^2 + \left|s_{n,1}\right|^2}. \tag{A.1}$$

The functions $r_{n,1}$ and $s_{n,1}$ are given by the recursive relations involving $r_{n,p}(x, t)$ and $s_{n,p}(x, t)$:

$$\begin{aligned}
r_{n,p} = \; & [\left(\lambda_{n-1}^* - \lambda_{n-1}\right) s_{n-1,1}^* r_{n-1,1} s_{n-1,p+1} \\
& + \left(\lambda_{p+n-1} - \lambda_{n-1}\right) \left|r_{n-1,1}\right|^2 r_{n-1,p+1} \\
& + \left(\lambda_{p+n-1} - \lambda_{n-1}^*\right) \left|s_{n-1,1}\right|^2 r_{n-1,p+1}] \\
& / \left(\left|r_{n-1,1}\right|^2 + \left|s_{n-1,1}\right|^2\right),
\end{aligned}$$

$$s_{n,p} = [\left(\lambda_{n-1}^* - \lambda_{n-1}\right) s_{n-1,1} r_{n-1,1}^* r_{n-1,p+1} \tag{A.2}$$

$$+ \left(\lambda_{p+n-1} - \lambda_{n-1} \right) \left| s_{n-1,1} \right|^2 s_{n-1,p+1}$$
$$+ \left(\lambda_{p+n-1} - \lambda_{n-1}^* \right) \left| r_{n-1,1} \right|^2 s_{n-1,p+1}]$$
$$/ \left(\left| r_{n-1,1} \right|^2 + \left| s_{n-1,1} \right|^2 \right).$$

Thus, all pairs $r_{n,p}$ and $s_{n,p}$ can be determined starting from $r_{1,j}$ and $s_{1,j}$. The functions $r_{1,j}(x,t)$ and $s_{1,j}(x,t)$, forming the Lax pair $R = \begin{pmatrix} r \\ s \end{pmatrix} \equiv \begin{pmatrix} r_{1,j} \\ s_{1,j} \end{pmatrix}$, are determined by the eigenvalue $\lambda \equiv \lambda_j$ and real shifts of the solution (x_j, t_j).

The Lax pair satisfies a system of linear differential equations

$$\frac{\partial R}{\partial t} = U \cdot R, \quad \frac{\partial R}{\partial x} = V \cdot R, \tag{A.3}$$

where matrices U and V for the NLSE are defined as ($\psi \equiv \psi_0$):

$$U = i \begin{bmatrix} \lambda & \psi(x,t)^* \\ \psi(x,t) & -\lambda \end{bmatrix},$$
$$V = \sum_{k=0}^{2} \lambda^k \cdot i \begin{bmatrix} A_k & B_k^* \\ B_k & -A_k \end{bmatrix}. \tag{A.4}$$

The coefficients A_k and B_k are given by:

$$A_0 = -\frac{1}{2} |\psi|^2, \tag{A.5}$$

$$B_0 = \frac{i}{2} \psi_t,$$
$$A_1 = 0,$$
$$B_1 = \psi,$$
$$A_2 = 1,$$
$$B_2 = 0.$$

We next define the following terms:

$$\kappa_j = 2\sqrt{1 + \lambda_j^2}$$
$$A_j = \frac{1}{2} \arccos \frac{\kappa_j}{2}$$
$$\quad + \frac{\kappa_j}{2} \left[(t - t_j) + \lambda_j (x - x_j) \right] - \frac{\pi}{4} \tag{A.6}$$
$$B_j = -\frac{1}{2} \arccos \frac{\kappa_j}{2}$$
$$\quad + \frac{\kappa_j}{2} \left[(t - t_j) + \lambda_j (x - x_j) \right] - \frac{\pi}{4}.$$

From Eqs. (A.3)–(A.6), one can calculate $r_{1,j}$ and $s_{1,j}$:

$$r_{1,j} = 2i e^{-ix/2} \sin A_j$$
$$s_{1,j} = 2 e^{ix/2} \cos B_j. \tag{A.7}$$

To emphasize again, $r_{n,1}$ and $s_{n,1}$ are calculated from $r_{1,j}$ and $r_{1,j}$, by applying Eq. (A.2) multiple times. Finally, the nth-order DT solution ψ_n is then calculated from $\psi_{n-1}, ..., \psi_0$ using Eq. (A.1).

References

1. Fibich, G.: The Nonlinear Schrödinger Equation. Springer, Berlin (2015)
2. Mirzazadeh, M., Eslami, M., Zerrad, E., Mahmood, M.F., Biswas, A., Belić, M.: Optical solitons in nonlinear directional couplers by sine-cosine function method and Bernoulli's equation approach. Nonlinear Dyn. **81**, 1933–1349 (2015)
3. Khalique, C.M.: Stationary solutions for nonlinear dispersive Schröödinger equation. Nonlinear Dyn. **63**, 623–626 (2011)
4. Saleh, B.E.A., Teich, M.C.: Fundamentals of Photonics. Wiley, Hoboken (1991)
5. Agrawal, G.P.: Applications of Nonlinear Fiber Optics. Academic Press, San Diego (2001)
6. Kivshar, Y.S., Agrawal, G.P.: Optical Solitons. Academic Press, San Diego (2003)
7. Kibler, B., Fatome, J., Finot, C., Millot, G., Dias, F., Genty, G., Akhmediev, N., Dudley, J.M.: Observation of Kuznetsov-Ma soliton dynamics in optical fibre. Sci. Rep. **6**, 463 (2012)
8. Bao, W.: The nonlinear Schrödinger equation and applications in Bose-Einstein condensation and plasma physics. In: Lecture Note Series, IMS, NUS, vol. **9** (2007)
9. Busch, T., Anglin, J.R.: Dark-bright solitons in inhomogeneous Bose-Einstein condensates. Phys. Rev. Lett. **87**, 010401 (2001)
10. Dudley, J.M., Genty, G., Mussot, A., Chabchoub, A., Dias, F.: Rogue waves and analogies in optics and oceanography. Nat. Rev. Phys. **1**, 675–689 (2019)
11. Zakharov, V.E.: Stability of periodic waves of finite amplitude on a surface of deep fluid. J. Appl. Mech. Tech. Phys. **9** (1968)
12. Osborne, A.: Nonlinear Ocean Waves and the Inverse Scattering Transform. Academic Press, London (2010)
13. Ankiewicz, A., Kedziora, D.J., Chowdury, A., Bandelow, U., Akhmediev, N.: Infinite hierarchy of nonlinear Schrödinger equations and their solutions. Phys. Rev. E **93**, 012206 (2016)
14. Kedziora, D.J., Ankiewicz, A., Chowdury, A., Akhmediev, N.: Integrable equations of the infinite nonlinear Schrödinger equation hierarchy with time variable coefficients. Chaos **25**, 103114 (2015)
15. Mani Rajan, M.S., Mahalingam, A.: Nonautonomous solitons in modified inhomogeneous Hirota equation: soliton control and soliton interaction. Nonlinear Dyn. **79**, 2469–2484 (2015)
16. Wang, D.-S., Chen, F., Wen, X.-Y.: Darboux transformation of the general Hirota equation: multisoliton solutions, breather solutions and rogue wave solutions. Adv. Differ. Equ. **2016**, 67 (2016)

17. Ankiewicz, A., Soto-Crespo, J.M., Akhmediev, N.: Rogue waves and rational solutions of the Hirota equation. Phys. Rev. E **81**, 046602 (2010)

18. Nikolić, S.N., Aleksić, N.B., Ashour, O.A., Belić, M.R., Chin, S.A.: Systematic generation of higher-order solitons and breathers of the Hirota equation on different backgrounds. Nonlinear Dyn. **89**, 1637–1649 (2017)

19. Chowdury, A., Kedziora, D.J., Ankiewicz, A., Akhmediev, N.: Breather solutions of the integrable nonlinear Schrödinger equation and their interactions. Phys. Rev. E **91**, 022919 (2015)

20. Yang, Y., Yan, Z., Malomed, B.A.: Rogue waves, rational solitons, and modulational instability in an integrable fifth-order nonlinear Schrödinger equation. Chaos **25**, 103112 (2015)

21. Nikolić, S.N., N.B., Aleksić, Ashour, O.A., Belić, M.R., Chin, S.A.: Breathers, solitons and rogue waves of the quintic nonlinear Schrödinger equation on various backgrounds. Nonlinear Dyn. **95**, 2855–2865 (2019)

22. Nikolić, S.N., Ashour, O.A., Aleksić, N.B., Zhang, Y., Belić, M.R., Chin, S.A.: Talbot carpets by rogue waves of extended nonlinear Schrödinger equations. Nonlinear Dyn. **97**, 1215 (2019)

23. Yin, Y.H., Lü, X., Ma, W.X.: Bäcklund transformation, exact solutions and diverse interaction phenomena to a (3+1)-dimensional nonlinear evolution equation. Nonlinear Dyn. **108**, 4181–4194 (2022)

24. Liu, B., Zhang, X.E., Wang, B., Lü, X.: Rogue waves based on the coupled nonlinear Schrödinger option pricing model with external potential. Modern Phys. Lett. B **36**, 2250057 (2022)

25. Lü, X., Chen, S.J.: Interaction solutions to nonlinear partial differential equations via Hirota bilinear forms: one-lump-multi-stripe and one-lump-multi-soliton types. Nonlinear Dyn. **103**, 947–977 (2021)

26. Zhao, Y.W., Xia, J.W., Lü, X.: The variable separation solution, fractal and chaos in an extended coupled (2+1)-dimensional Burgers system. Nonlinear Dyn. **108**, 4195–4205 (2022)

27. Yin, M.Z., Zhu, Q.W., Lü, X.: Parameter estimation of the incubation period of COVID-19 based on the doubly interval-censored data model. Nonlinear Dyn. **106**, 1347–1358 (2021)

28. Lü, X., Hui, H.W., Liu, F.F., Bai, Y.L.: Stability and optimal control strategies for a novel epidemic model of COVID-19. Nonlinear Dyn. **106**, 1491–1507 (2021)

29. Chaohao, G. (ed.): Soliton Theory and Its Applications. Springer-Verlag, Berlin, Heidelberg (1995)

30. Gardner, C.S., Greene, J.M., Kruskal, M.D., Miura, R.M.: Method for Solving the Korteweg-deVries Equation. Phys. Rev. Lett. **19**, 1095 (1967)

31. Zakharov, V.E., Shabat, A.B.: Exact theory of two-dimensional self-focusing and one-dimensional self-modulation of waves in nonlinear media. J. Exp. Theor. Phys. **34**, 62 (1972)

32. Ablowitz, M.J., Kaup, D.J., Newell, A.C., Segur, H.: The inverse scattering transform-Fourier analysis for nonlinear problems. Stud. Appl. Math. **53**, 249–315 (1974)

33. Liu, M.Z., Cao, X.Q., Zhu, X.Q., Liu, B.N., Peng, K.C.: Variational Principles and Solitary Wave Solutions of Generalized Nonlinear Schrödinger Equation in the Ocean. J. Appl. Comput. Mech. **7**(3), 1639–1648 (2021)

34. Matveev, V.B., Salle, M.A.: Darboux Transformations and Solitons. Springer, Berlin, Heidelberg (1991)

35. Kedziora, D.J., Ankiewicz, A., Akhmediev, N.: Circular rogue wave clusters. Phys. Rev. E **84**, 056611 (2011)

36. He, J.H.: Variational principles for some nonlinear partial differential equations with variable coefficients. Chaos Solitons Fractals **19**, 847–851 (2004)

37. Akhmediev, N.N., Korneev, V.I.: Modulation instability and periodic solutions of the nonlinear Schrödinger equation. Theor. Math. Phys. **69**, 1089 (1986)

38. Akhmediev, N., Eleonskii, V., Kulagin, N.: Exact first-order solutions of the nonlinear Schrödinger equation. Theor. Math. Phys. **72**, 809 (1987)

39. Kibler, B., Fatome, J., Finot, C., Millot, G., Genty, G., Wetzel, B., Akhmediev, N., Dias, F., Dudley, J.M.: Observation of Kuznetsov-Ma soliton dynamics in optical fibre. Sci. Rep. **2**, 463 (2012)

40. Xiong, H., Gan, J., Wu, Y.: Kuznetsov-Ma Soliton Dynamics Based on the Mechanical Effect of Light. Phys. Rev. Lett. **119**, 153901 (2017)

41. Dai, C.Q., Wang, Y.Y.: Controllable combined Peregrine soliton and Kuznetsov-Ma soliton in PTPT-symmetric nonlinear couplers with gain and loss. Nonlinear Dyn. **80**, 715–721 (2015)

42. Kibler, B., Fatome, J., Finot, C., Millot, G., Dias, F., Genty, G., Akhmediev, N., Dudley, J.M.: The Peregrine soliton in nonlinear fibre optics. Nature Phys. **6**, 790–795 (2010)

43. Shrira, V.I., Geogjaev, V.V.: What makes the Peregrine soliton so special as a prototype of freak waves? J. Eng. Math. **67**, 11 (2010)

44. Dudley, J.M., Dias, F., Erkintalo, M., Genty, G.: Instabilities, breathers and rogue waves in optics. Nature Phot. **8**, 755 (2014)

45. Peregrine, D.H.: Water waves, nonlinear Schrödinger equations and their solutions. J. Austral. Math. Soc. B **25**, 16 (1983)

46. Solli, D.R., Ropers, C., Jalali, B.: Active control of rogue waves for stimulated supercontinuum generation. Phys. Rev. Lett. **101**, 233902 (2008)

47. Dudley, J.M., Genty, G., Eggleton, B.J.: Harnessing and control of optical rogue waves in supercontinuum generation. Opt. Express **16**, 3644 (2008)

48. Garrett, C., Gemmrich, J.: Rogue waves. Phys. Today **62**, 62 (2009)

49. Ganshin, A.N., Efimov, V.B., Kolmakov, G.V., Mezhov-Deglin, L.P., McClintock, P.V.E.: Observation of an inverse energy cascade in developed acoustic turbulence in superfluid helium. Phys. Rev. Lett. **101**, 065303 (2008)

50. Bludov, Y.V., Konotop, V.V., Akhmediev, N.: Matter rogue waves. Phys. Rev. A **80**, 033610 (2009)

51. Li, Z.-Y., Li, F.-F., Li, H.-J.: Exciting rogue waves, breathers, and solitons in coherent atomic media. Commun. Theor. Phys. **72**, 075003 (2020)

52. Fleischhauer, M., Imamoglu, A., Marangos, J.P.: Electromagnetically induced transparency: optics in coherent media. Rev. Mod. Phys. **77**, 633–673 (2005)

53. Nikolić, S.N., Radonjić, M., Krmpot, A.J., Lučić, N.M., Zlatković, B.V., Jelenković, B.M.: Effects of a laser beam profile on Zeeman electromagnetically induced trans-

parency in the Rb buffer gas cell. J. Phys. B: At. Mol. Opt. Phys. **46**, 075501 (2013)

54. Krmpot, A.J., Ćuk, S.M., Nikolić, S.N., Radonjić, M., Slavov, D.G., Jelenković, B.M.: Dark Hanle resonances from selected segments of the Gaussian laser beam cross-section. Opt. Express **17**, 22491–22498 (2009)

55. Nikolić, S.N., Radonjić, M., Lučić, N.M., Krmpot, A.J., Jelenković, B.M.: Transient development of Zeeman electromagnetically induced transparency during propagation of Raman-Ramsey pulses through Rb buffer gas cell. J. Phys. B: At. Mol. Opt. Phys. **48**, 045501 (2015)

56. Akhmediev, N., et al.: Roadmap on optical rogue waves and extreme events. J. Opt. **18**, 063001 (2016)

57. Akhmediev, N., Soto-Crespo, J.M., Ankiewicz, A.: How to excite a rogue wave. Phys. Rev. A **80**, 043818 (2009)

58. Chin, S.A., Ashour, O.A., Belić, M.R.: Anatomy of the Akhmediev breather: cascading instability, first formation time, and Fermi-Pasta-Ulam recurrence. Phys. Rev. E **92**, 063202 (2015)

59. Belić, M.R., Nikolić, S.N., Ashour, O.A., Aleksić, N.B.: On different aspects of the optical rogue waves nature. Nonlinear Dyn. **108**, 1655–1670 (2022)

60. Nikolić, S.N., Alwashahi, S., Ashour, O.A., Chin, S.A., Aleksić, N.B., Belić, M.R.: Multi-elliptic rogue wave clusters of the nonlinear Schrödinger equation on different backgrounds. Nonlinear Dyn. **108**, 479–490 (2022)

61. Kedziora, D.J., Ankiewicz, A., Akhmediev, N.: Rogue wave triplets. Phys. Lett. A **375**, 2782 (2011)

62. Kedziora, D.J., Ankiewicz, A., Akhmediev, N.: Triangular rogue wave cascades. Phys. Rev. E **86**, 056602 (2012)

63. Dubard, P., Gaillard, P., Klein, C., Matveev, V.B.: On multi-rogue wave solutions of the NLS equation and positon solutions of the KdV equation. Eur. Phys. J. Special Topics **185**, 247 (2010)

64. Ohta, Y., Yang, J.: General high-order rogue waves and their dynamics in the nonlinear Schrödinger equation. Proc. R. Soc. A **468**, 1716 (2012)

65. Gaillard, P.: Degenerate determinant representation of solutions of the nonlinear Schrödinger equation, higher order Peregrine breathers and multi-rogue waves. J. Math. Phys. **54**, 013504 (2013)

66. Ankiewicz, A., Akhmediev, N.: Multi-rogue waves and triangular numbers. Romanian Rep. Phys. **69**, 104 (2017)

67. He, J.S., Zhang, H.R., Wang, L.H., Porsezian, K., Fokas, A.S.: Generating mechanism for higher-order rogue waves. Phys. Rev. E **87**, 052914 (2013)

68. Kedziora, D.J., Ankiewicz, A., Akhmediev, N.: Classifying the hierarchy of nonlinear-Schödinger-equation rogue-wave solutions. Phys. Rev. E **88**, 013207 (2013)

69. Akhmediev, N.: Waves that appear from nowhere: complex rogue wave structures and their elementary particles. Front. Phys. **8**, 612318 (2021)

70. Chin, S.A., Ashour, O.A., Nikolić, N.N., Belić, M.R.: Maximal intensity higher-order Akhmediev breathers of the nonlinear Schrödinger equation and their systematic generation. Phys. Lett. A **380**, 3625 (2016)

71. Chin, S.A., Ashour, O.A., Nikolić, S.N., Belić, M.R.: Peak-height formula for higher-order breathers of the nonlinear Schrödinger equation on nonuniform backgrounds. Phys. Rev. E **95**, 012211 (2017)

72. Kedziora, D.J., Ankiewicz, A., Akhmediev, N.: Rogue waves and solitons on a cnoidal background. Eur. Phys. J. Spec. Top. **223**, 43–62 (2014)

scientific reports

OPEN

Label-free third harmonic generation imaging and quantification of lipid droplets in live filamentous fungi

Tanja Pajić[1], Nataša V. Todorović[2], Miroslav Živić[1], Stanko N. Nikolić[3], Mihailo D. Rabasović[3], Andrew H. A. Clayton[4] & Aleksandar J. Krmpot [ID][3][✉]

We report the utilization of Third-Harmonic Generation microscopy for label-free live cell imaging of lipid droplets in the hypha of filamentous fungus *Phycomyces blakesleeanus*. THG microscopy images showed bright spherical features dispersed throughout the hypha cytoplasm in control conditions and a transient increase in the number of bright features after complete nitrogen starvation. Colocalization analysis of THG and lipid-counterstained images disclosed that the cytoplasmic particles were lipid droplets. Particle Size Analysis and Image Correlation Spectroscopy were used to quantify the number density and size of lipid droplets. The two analysis methods both revealed an increase from 16×10^{-3} to 23×10^{-3} lipid droplets/μm^2 after nitrogen starvation and a decrease in the average size of the droplets (range: 0.5–0.8 μm diameter). In conclusion, THG imaging, followed by PSA and ICS, can be reliably used for filamentous fungi for the in vivo quantification of lipid droplets without the need for labeling and/or fixation. In addition, it has been demonstrated that ICS is suitable for THG microscopy.

Third harmonic generation (THG) microscopy as a label-free nonlinear imaging technique is a powerful tool for visualization of various cells and tissue structures[1]. THG has been mainly applied to imaging animal cell structures[1–7] and tissues[1,4,6,12–14], as well as the dynamics of cellular processes (functional imaging)[1,6,15]. Also, THG microscopy has been used to study human and fossil vertebrate teeth[16], 3D engineered human adipose tissue[17], and small organisms (Drosophila melanogaster, zebrafish, Xenopus laevis, early mouse embryos[8,18–20] and C. elegans[21,22]). In addition to animal specimens, THG microscopy has also been applied to plants[11,23–27], algae[26,27] and yeast[2,28]. To the best of our knowledge, there is a paucity of THG studies on filamentous fungi.

The THG phenomenon is a nonlinear coherent scattering process induced by structures with specific properties. In THG, the joint energy of three photons is converted into one photon. As THG is a third-order process, ultra-short laser pulses with high peak power densities at the optical focus are required to ensure sufficient signal. Contrast in THG microscopy is generated at interfaces where there is a large change in refractive index or third-order non-linear susceptibility[29,30]. Due to higher index of refraction of lipids (R.I.(lipids) = 1.46–1.48 at 1100–480 nm)[31] with respect to the cytoplasm (R.I. = 1.360–1.390 at 633 nm)[32], the THG signal is efficiently produced at the interface between the aqueous phase and by lipid-rich structures[33–35]. These include cellular membranes and lipid droplets (LDs).

Lipid droplets are dynamic cellular organelles which play a key role in lipid homeostasis and energy in eukaryotic cells. Studies of lipid droplet physiology in fungi are still in their infancy but their quantitation has relevance to issues in biomedicine, agriculture, industrial waste and the energy crisis. As mentioned above, THG microscopy is a particularly suitable technique for lipid droplet physiology studies[11,35,36]. The advantages of THG microscopy are it is non-invasive, produces inherently confocal images, doesn't require fixation or external labelling-similar to Raman-based[37–42], differential interference contrast (DIC)[43] and light sheet microscopy[37], and is minimally phototoxic allowing for in vivo studies. A point of difference between Raman-based techniques and

[1]Faculty of Biology, Institute of Physiology and Biochemistry, University of Belgrade, Studentski trg 16, Belgrade 11158, Serbia. [2]Institute for Biological Research "Siniša Stanković", University of Belgrade, National Institute of the Republic of Serbia, Bulevar Despota Stefana 142, Belgrade 11000, Serbia. [3]Institute of Physics Belgrade, University of Belgrade, National Institute of the Republic of Serbia, Pregrevica 118, Belgrade 11080, Serbia. [4]Department of Physics and Astronomy, Optical Sciences Centre, School of Science, Computing and Engineering Technologies, Swinburne University of Technology, Melbourne, VIC 3122, Australia. ✉email: krmpot@ipb.ac.rs

THG microscopy is the simpler excitation scheme and minimal risk of aberration artefacts in THG microscopy. Combining THG with fluorescence microscopy is useful to identify the molecular source of the THG-generated signals (i.e. lipophilic fluorescent dyes to target LDs)[4,7,36]. Once THG-associated structures are identified they can be followed using THG microscopy in situ.

Quantitation of images containing LDs can be challenging. The desired parameters include LD number, density, size and morphology. Readily-available image analysis software and programming languages for this purpose are ImageJ, Cell Profiler, Imaris, AMIRA, Volocity, MATLAB, D programming, for both fluorescent images[44–47] and for lipid droplet images taken by label-free[11,17,20] techniques. Automated quantitation of lipid droplets uses either thresholding of the images (threshold-based) or watershed methods (morphology-based)[48], and are usually optimized for a specific cell line. It would be desirable to have a more general image analysis platform that does not require extensive cell-line specific thresholding. In this regard, Image Correlation Spectroscopy (ICS) is a promising method because it is based on measuring spatially-correlated fluctuations. ICS has been applied to confocal images where it measures the spatial variation of fluorescence intensity fluctuations, which can be further related to particle density and aggregation state[49]. On the other hand, ICS has been rarely used for nonlinear techniques, only for two photon excitation fluorescence (TPEF)[50] or recently for second harmonic generation imaging (SHG)[51].

The filamentous fungi[52] are ubiquitous organisms that contribute profoundly to a wide range of ecosystem processes, including decomposition of organic carbon, carbon storage and nutrient transfer. As an invisible and often overlooked part of carbon cycle, filamentous fungi as saprophytes and plant symbionts (mycorrhizal fungi) create a sink for plant organic carbon and distribute it to below-ground hyphal biomass[53]. The oleaginous filamentous fungi have the ability to accumulate large amount of carbon in the form of lipids, more than 20% of their biomass[54,55] under appropriate conditions. These lipids are considered to be a valuable alternative resource for various biotechnological applications (biodiesel production, high-value chemicals, food/feed additives, and efficient bioremediation of wastewaters)[56,57], in a bio-based economy. Additionally, the lipid accumulations have been implicated in the resistance of fungi to toxins[58] and virulence of pathogenic fungi[59]. Moreover, yeast cells modified to lack the lipid droplets entirely, are extremely vulnerable to a variety of stresses[60] altogether demonstrating that LD studies could potentially lead to novel antifungal treatments. We have chosen for the THG imaging study of LDs the well-known model species *Phycomyces blaekseneanus*, oleaginous fungi from the order Mucorales with very rapid growth (from the spores, through exponential growth phase, to stationary phase in under 36 h). The challenge of utilizing THG imaging for filamentous fungi is that the LDs in filamentous fungi are of rather small dimensions (< 1.5 μm) unlike e.g. in white adipocyte cells where LDs dimensions can reach 100 μm[61]. Our aim is to show that THG microscopy is highly suited for imaging the density and size of LDs in live filamentous fungi. To this end, we will use filamentous fungi in the baseline control condition, with sporadic and small LDs, corresponding to low lipid content conditions[62], and fungi with denser LDs brought upon by nitrogen starvation-induced autophagy response[63], the conserved cellular mechanism of molecular recycling[64]. In addition to label-free THG imaging of LDs in fungi, we also present two methods for LDs quantification and analysis. The first method is based on ImageJ/Fiji open source platform, particle analysis tool, which provides measurements of the size, shape and number of LDs. The second method is called Image Correlation Spectroscopy (ICS)[65], which provides measurements of density and size of particles through spatial autocorrelation analysis.

Our aim is to show that ICS is a good method for quantification of LDs in THG images.

Materials and methods

Filamentous fungus strain and growth conditions.   A wild-type strain of oleaginous Zygomycetous fungus *Phycomyces blakesleeanus* (Burgeff) [NRRL 1555(-)] was used as the model cell system in this study. For optimal growth of the mycelium, spores at concentration of the order 10^7 spores/ml were plated on 100 mm Petri dishes at 21–23 °C. Standard liquid minimal (SLM) medium for cultivation contained per liter: 20 g of D (+)-glucose (carbon source), 2 g of L-asparagine·H2O (nitrogen source), 5 g KH2PO4, 500 mg MgSO4·7H2O, and microelements/"trace stock" (28 mg CaCl2, 1 mg thiamine hydrochloride, 2 mg citric acid·H2O, 1.8 mg Fe(NO3)3·9H2O, 1 mg ZnSO4·7H2O, 300 μg MnSO4·H2O, 50 μg CuSO4·5H2O, and 50 μg Na2MoO4·2H2O). The glucose was autoclaved separately, and the final pH of the medium was 4.5. The osmolarity was about 200 mOsm.

For the nitrogen starvation experiments, the fungi were first grown in the SLM medium and after 22 h were divided into two groups. Group 1 was the control group and group 2 was the nitrogen starved group (N-starved). Fungi from control group 1 were collected by centrifugation (10 min) and resuspended in SLM medium. For group 2, fungal cells were centrifuged (10 min) and resuspended in nitrogen-free medium (SLM medium without L-asparagine) (Fig. 1). The age-matched fungal cultures were imaged at different time points after nitrogen starvation (3, 4.5, 6 h and > 6 h (up to 8.5 h)) at room temperature. All fungal cultures used for imaging were in exponential growth phase (total time from seeding was in the range 24–30.5 h). Data collected from the 6–8.5 h time-points were pooled and represented the group in prolonged nitrogen starvation (labelled 6 h on the graphs).

Lipid staining.   Live fungal cells were stained without chemical fixation. To stain the fungal cells, hyphae in exponential growth phase (26 h) were incubated with 40 ng/mL of Nile Red dye (Acros Organics) for 10 min at 20 °C.

Nonlinear laser scanning microscopy (NLSM) experimental setup and hyphae imaging.   The images of live unstained fungal cells were obtained using a bespoke nonlinear laser-scanning microscope, previously described in references[66,67], but modified for THG imaging (Fig. 2). For third harmonic generation (THG) imaging of hyphae the following experimental setup, based on significantly modified Zeiss Jenaval upright microscope, was used: Infrared femtosecond pulses were provided by a SESAM mode-locked Yb:KGW laser (Time-
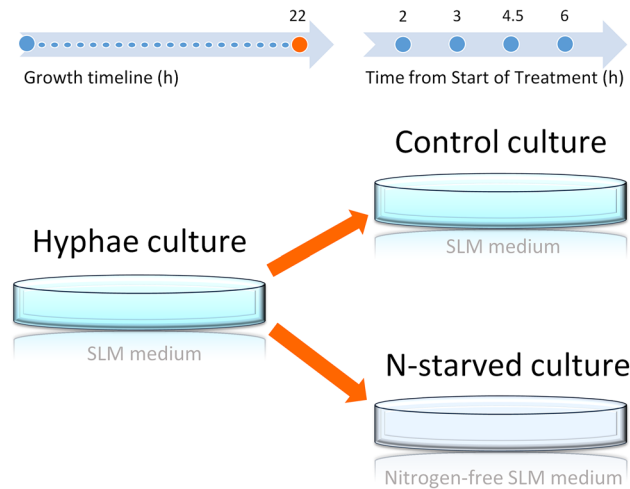
Figure 1. The outline of experimental design of nitrogen starvation. Hyphae cultures are grown in control conditions (Control culture) or in nitrogen-depleted medium (N-starved culture). Time points of sampling are marked as blue dots.
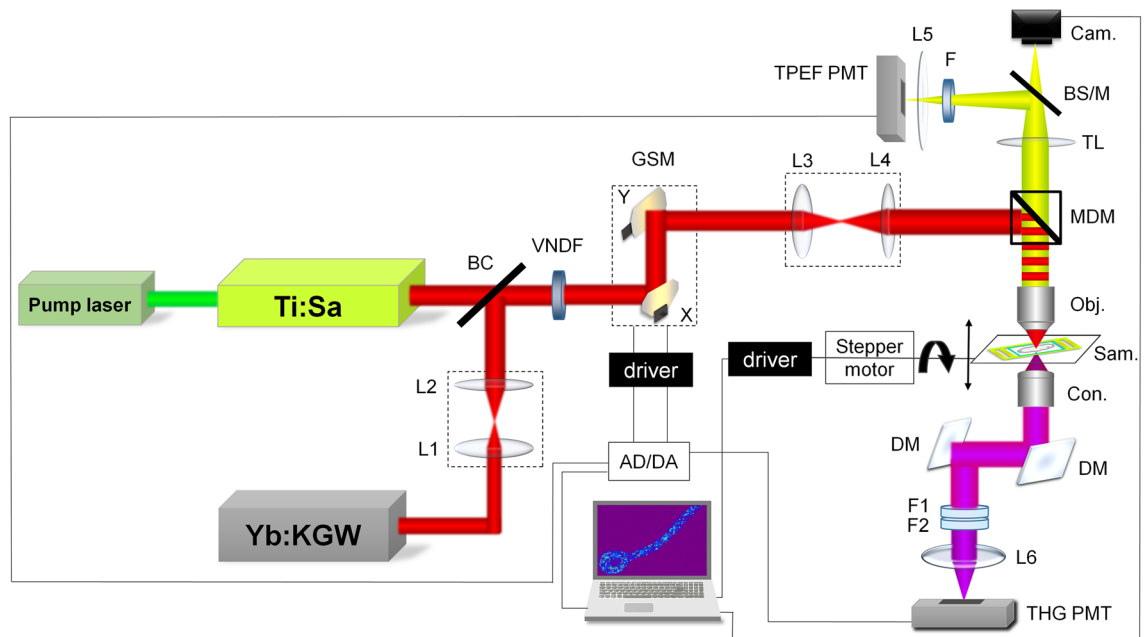

Figure 2. NLSM setup. Ti:Sa—laser for TPEF imaging, Yb:KGW—laser for TPEF and THG imaging, BC—beam combiner, L1 and L2—lenses of 1:1 beam expander for recollimation, VNDF—variable neutral density filter, GSM—galvanometer-scanning mirrors, L3 and L4—lenses of 1:3.75 beam expander for imaging, MDM—main dichroic mirror (cut-off 700 nm), Obj.—microscopic objective 40×1.3,   Sam.—sample, Con.—aspheric condenser lens, DM—dichroic mirrors reflective for THG (347 nm) and transmissive for Yb laser (1040 nm), F1—Hoya glass UV filter, peak transmission 340 nm, F2—bandpass filter 275–375 nm, L6—focusing lens, THG PMT—photomultiplier tube for THG signal, TL—tube lens, BS/M—beam splitter or mirror toggle, Cam.—camera, F—VIS filter 400–700 nm for autofluorescence or VIS + 570 nm long pass for Nile Red fluorescence, L5—focusing lens, TPEF PMT—photomultiplier tube for TPEF signal, AD/DA—acquisition card. The scheme was created in Microsoft Power Point 2016 (https://www.microsoft.com/en-us/microsoft-365/powerpoint).

Bandwidth Products AG, Time-Bandwidth Yb GLX; Zurich, Switzerland, wavelength 1040 nm, pulse duration 200 fs and repetition rate 83 MHz). The laser wavelength was chosen so that THG signal whose wavelength is 3 times shorter (347 nm) is still in the range of conventional air UV optics. The laser light was first passed through a collimating 1:1 beam expander (L1 and L2) for divergence compensation, and then combined (at BC) with the Ti: Sa laser beam used for TPEF imaging. After that, both beams pass the motorized variable neutral density filter (VNDF) for power regulation and the mechanical shutter. The beams were raster scanned over the sample

using two galvanometer mirrors (Cambridge Technologies, 6215H; Bedford, Massachusetts, USA) and a 1:3.75 beam expander (L3 and L4) was used to fill the back aperture of the objective lens and to achieve 4f. configuration. The beams were further directed onto the sample by a short-pass main dichroic mirror (MDM, cut-off at 700 nm) through the high numerical aperture (NA) oil immersion objective lens (Carl Zeiss, EC Plan-Neofluar 40X, NA 1.3). The THG signal was detected in the forward direction (transmission arm), parallel to the direction of laser propagation. First, the signal was collected by high NA aspheric lens (condenser). Then, it was reflected by two dichroic mirrors (DM) that reflect 347 nm but transmit 1040 nm to prevent the laser beam from reaching the detector. Further on, the signal was filtered out from the rest of the laser photons by a bandwidth filter 275–375 nm (Thorlabs FGUV11M) and a Hoya glass UV filter (Newport FSR-U340) with a maximum transmission at 340 nm. The THG signal was detected using a photomultiplier tube (PMT) (Hamamatsu, H7422, Japan), after being focused by a 50 mm focal length lens (L6) onto the entrance window of the PMT.

For the (auto)TPEF imaging a tunable (700–900 nm) Kerr lens mode locked Ti:Sa laser (Mira 900, Coherent Inc. CA, USA) was used, pumped by CW (continuous-wave) frequency doubled Nd:YVO4 laser at 532 nm (VERDI V10, Coherent Inc. CA, USA). The wavelength of the Ti:Sa laser was set to 730 nm for auto TPEF imaging since most of the endogenous fluorophores (NADH, flavins, etc.) can be excited at this wavelength[68] on the one hand, and because of the technical limitation (laser tunability range and dichroic mirror cut off) on the other hand. The fluorescent signal was collected in back reflection by the objective lens, passed the MDM, tube lens (TL) and filtered out by VIS (400–700 nm) band pass filter (Canon, taken from the camera EOS50D) for the detection of the autofluorescence excited by Ti:Sa laser. Additionally, 570 nm long pass filter (colored glass, unknown vendor) was used for Nile Red fluorescence which is excited by Yb: KGW laser and detected simultaneously by THG signal. TPEF signals were detected after being focused by 50 mm focal length lens (L5) onto the entrance window of the TPEF PMT.

The acquisition was performed by National Instrument card USB-6351 at the rate of 1.2 M sample/s. This enabled high enough frame rate at low resolution for live monitoring, for instance 3 frames per second at 256×256 pixels with 6 averages. For high resolution images, it takes 30 s for 1024×1024 image with 30 averages. The lateral and axial resolution of the microscope with 40×1.3 objective lens were estimated to be 300 nm and 1000 nm, respectively.

Bright field images were taken with a Canon EOS 50D digital camera (Tokyo, Japan) whose CMOS sensor was placed at the image plane of the tube lens. Toggle switch BS/M enables utilization either of camera for bright field or TPEF PMT for fluorescence imaging.

A specially designed sample holder was used, that enables hyphae with the growing medium to be placed between two coverslips in order meet the criteria for the best NA of the objective lens, but also to avoid losses of the UV THG signal by thick deck glass (Supplementary Figs. S1 and S2 show different imaging conditions of hyphae that were tested in order to find the best one). The #1.5 coverslips (170 µm thickness) were used. 20 µl of hyphae suspension was used to keep the hyphae alive. The holder was placed between objective lens and the aspheric condenser on the motorized table that can be translated in steps of 0.3 µm along the beam propagation direction (z axis) for optical slicing of the sample and 3D imaging.

In control versus N-starved group imaging, time points were gathered sequentially. Using a label-free imaging technique, such as THG, enabled us to take images of samples with minimal delay after taking fungi from the culture. The overall time a sample culture was kept under the microscope to acquire at least 3 THG images of live hypha was between 25 and 37 min. Effectively, time points for control and treatment were offset for 30–40 min on one experimental day and on the next day, offset in opposite direction to the other. The exact ranges of time of growth (mean and standard deviation) for all hypha included in experimental groups are collected in Supplemental Fig. S4.

Image analysis. THG image analysis of lipid droplets in 2D was performed using ImageJ (W. Rasband, National Institute of Health, Maryland, USA, http://imagej.nih.gov/ij/). Algorithms written in MATLAB (in-house-created code) and VolView software were used for 3D and 4D image processing. Two methods for image analysis were used to quantify LDs number and size, Particle Size Analysis (PSA) and Image Correlation Spectroscopy (ICS). Details of both procedures are in the Supplementary Information.

Statistics. For quantitative image analysis, images of individual hypha under control conditions (n = 44) and after nitrogen starvation (n = 17) were obtained from 6 independently grown cultures. GraphPad Prism was used for graphing and statistical comparisons. The boxes of the box and whisker plots are enclosed by the 25th and 75th percentile range with the line representing the median; the whiskers are extending to the minimal and maximal value, respectively. Histograms of number of LDs were generated from all LD diameters in each group with 0.3 µm binning and each bin value was divided with the sum of hypha areas in the group. Errors in histograms of Number of LDs/hypha area were calculated as: Relative Error (binned N/area) = Relative Error (Number of LDs/hypha area) + Relative Error (Area), and Relative Error (binned N/area) was multiplied by value of Number of LDs/hypha area for that bin. Two-way ANOVA with multiple comparisons and Holm-Sidac correction and unpaired two tailed t test with Welch's correction for unequal variances, were used for the calculation of statistical significances. Where appropriate, unpaired two-sided Mann–Whitney test with was used instead. Confidence level for statistical significance was: 0.05 (*), 0.01 (**), 0.005 (***), 0.0001 (****).

Results

THG images, one slice (2D) and 3D reconstruction, of unstained live *P. blakesleeanus* hyphae in exponential growth phase are shown in Fig. 3a,b, respectively. The THG signal at the cell circumference originates from chitinous cell wall and plasma membrane which follow the cell wall shape. In the cytoplasm, various entities that
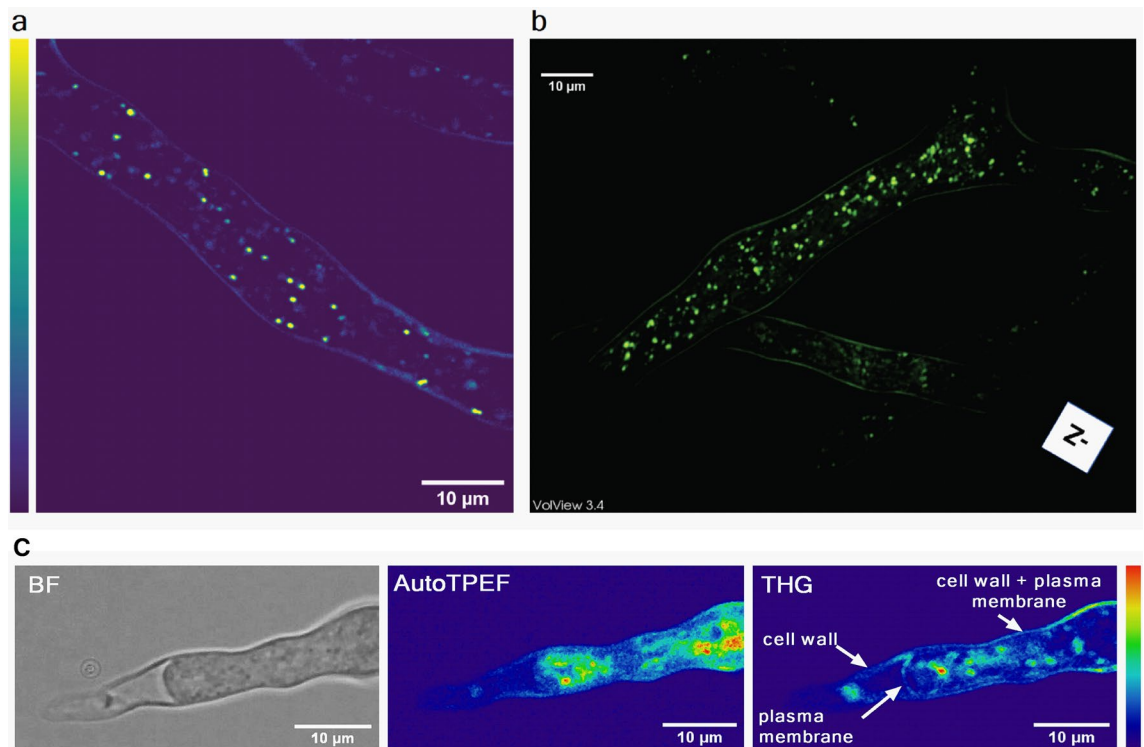
Figure 3. Label-free imaging of *Phycomyces blakesleeanus* hyphae from the exponential phase in SLM. (**a**) one THG slice; (**b**) 3D model built out of 23 THG slices 0.9 µm apart. The average laser power at sample plane was 23–26 mW. (**c**) Multimodal imaging: bright field (BF) (left), autoTPEF (middle) and THG (right) images of the same live unlabeled hypha. The hypha was plasmolyzed and the retracted plasma membrane is solely visible in the THG image. The average laser power at sample plane was 2.7 mW (TPEF) and 55 mW (THG). Color intensity bar for both, TPEF and THG signals: deep blue—the lowest signal, red the highest signal. All the images were taken with Zeiss 40 × 1.3 oil objective lens.

produce THG signal are visible. The hyphae were placed in the liquid growth medium between two coverslips. The high resolution of the microscopic system (diffraction limited), the thickness of the hyphae (ca 10 µm) and transparency of the medium make possible the whole hyphae to be optically sectioned and a 3D model to be reconstructed (Fig. 3b and Supplementary Video S1 in the Supplementary Information). It is obvious that strong THG signal features are prominent among all the entities in the cytoplasm. According to the literature these are most likely lipid droplets since they have a large index of refraction in comparison with the rest of cytoplasm. In addition, the power dependence of the THG signal originating from LDs is provided in Supplementary Material (Fig. S3).

The cell wall and plasma membrane are separated by a very small distance which is not resolvable in the images of native hyphae obtained by diffraction limited techniques (resolution of approximately 250 nm). To visualize the cell wall and the plasma membrane separately, we plasmolyzed the hyphae so the plasma membrane was retracted from the cell wall at a resolvable distance (Fig. 3c). The retracted cytoplasm is clearly visible in bright-field (Fig. 3c left) and autoTPEF images (Fig. 3c middle), but the plasma membrane can be solely distinguished only in the THG image (Fig. 3c right) since its refractive index is different from the cytoplasm.

There is no significant overlap of AutoTPEF and THG signal in the hyphae. While THG imaging is not necessarily specific for LDs, because the THG signal is produced by any refractive index change, LDs still produce significantly higher THG signal in comparison with other structures in the cytoplasm of a cell like *P. blakesleeanus*. This fact can be used to extract LDs in a cell, over a broad but still much lower signal range than other cytoplasm entities. As the very first step toward the confirmation that high THG signal features in unlabeled live *P. blakesleeanus* are LDs, we performed the imaging of the same hyphae by detecting auto fluorescence signal upon two photon excitation at 730 nm (Fig. 4a left). In order to ensure that high THG signal entities (Fig. 4a right) are not artifacts that might be caused by e.g. high laser intensity damage, we merged the two images, THG and autoTPEF (Fig. 4a middle) showing clearly there is no significant increase of TPEF signal at the same locations. The hyphae were in exponential growth phase, as in Fig. 3.

Colocalization of lipid droplets signal imaged by TPEF and THG. Whilst many label-free imaging studies on various biological samples have shown that strong THG contrast in the cytoplasm arises mostly from LDs[11,35,36], in the case of *Phycomyces blaekseneanus* THG imaging has never been applied to this type of organism.
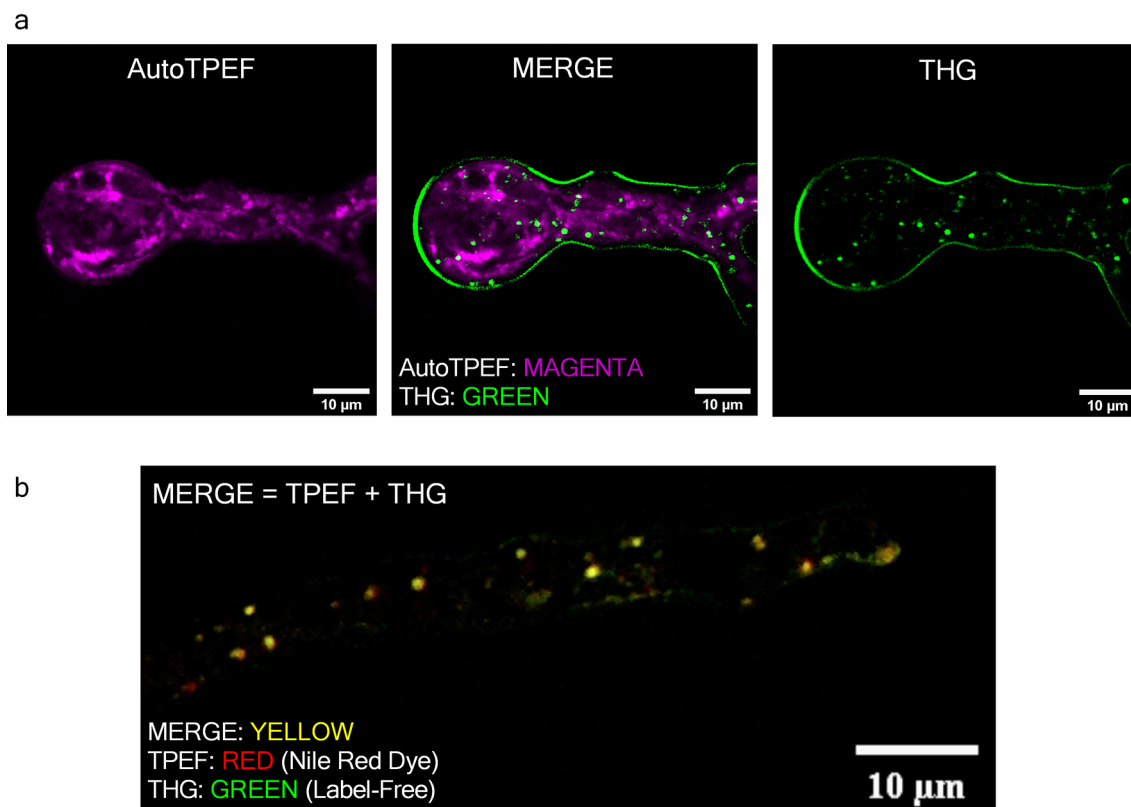
a

b

Figure 4. TPEF and THG images of *Phycomyces blakesleeanus* exponential growth phase hyphae in standard liquid medium show that the predominant source of spot wise THG signal are lipid droplets. (**a**) Merged autoTPEF and THG images of same unlabeled live hypha showing that there is no overlap of autoTPEF and THG signal. The average laser power at sample plane was 28 mW at 1040 nm (for THG) and 3.4 mW at 730 nm (autoTPEF). (**b**) In vivo colocalization of stained LDs imaged by TPEF and LDs imaged by THG modality. Average laser power at sample plane was 32 mW for both THG and TPEF at 1040 nm. Pearson's correlation coefficient $R_{total} = 0.844$ (ImageJ, The Colocalization Threshold plugin). All images were taken with Zeiss 40×1.3 oil objective lens.

To prove firmly that the cytoplasmic puncta in THG images of hyphae are LDs we performed colocalization experiments (Fig. 4b). The hyphae were stained by Nile Red dye which is considered as a standard for lipids[69]. The TPEF of Nile Red dye was excited by the same laser used for THG and the TPEF signal was collected through 400–700 nm band pass and 570 nm long pass filters, which effectively isolates the fluorescence signal to the 570–700 nm spectral region. The laser beam was focused with the Zeiss Plan Neofluar 40×1.3 objective lens, and both, TPEF and THG signals were detected simultaneously. Before the measurement, a very small volume of the sample (10 μl of fungi suspension) was added between two coverslips. This enables hyphae to stay alive during the imaging but also to be immobilized as close as possible to the coverslip thus achieving the best possible resolution.

The quantitative comparison of the TPEF and THG images (colocalization analysis) was performed based on Pearson's correlation coefficient and Image Cross-Correlation Spectroscopy (ICCS). Pearson's correlation coefficient was in the range $0.74 < R_{total} < 0.88$ (ImageJ, The Colocalization Threshold plugin). According to the ICCS analysis, the fraction of THG-detected clusters interacting with the TPEF-detected clusters was 0.89 indicating a high degree of spatial correlation between fluctuations generated from the lipid probe and THG signal. The degree of colocalization obtained in our work is in accordance or higher with those obtained in label-free imaging on live and in some fixed samples[7,70].

Based on the colocalization experiment (Fig. 4b) and the results shown in Fig. 4a one might consider that most round bright features in THG images of *Phycomyces blaekseneanus* are the lipid droplets.

THG image analysis and quantification of lipid droplets. For the quantification of LDs, we analyzed a small set of THG images by Particle Size Analysis and Image Correlation Spectroscopy (both available in ImageJ). To test and compare the two methods we used hyphae cultures grown in completely nitrogen-depleted media (N–starved) and their age-matched sister cultures from the same batch grown in standard media as a control. Nitrogen limitation is known to cause autophagy in filamentous fungi[71], leading to alterations in lipid metabolism and an increase in the number of LDs[72,73]. We performed THG imaging on hyphae in exponential growth phase, alternating between control (Fig. 5a) and N-starved (Fig. 5b) age matched hypha batches. From Fig. 5 it is obvious, even by the bare eye, that there is significant increase in LD number after nitrogen starvation
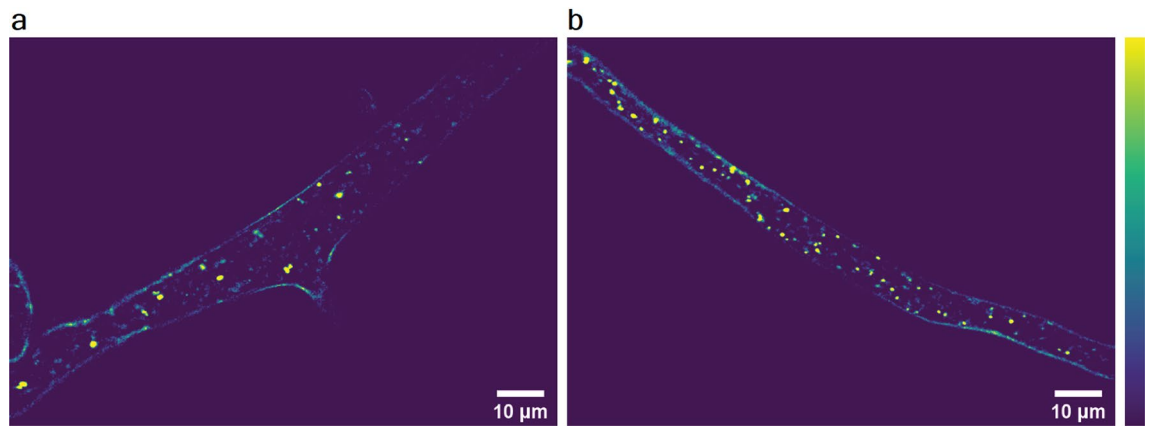
a   b

Figure 5. THG images of N-starved hyphae. (**a**) control hyphae; (**b**) N-starved (4.5 h duration of growth in nitrogen-depleted conditions). Both images were taken with Zeiss 40 × 1.3 objective lens whilst average laser power at sample plane was 24 mW (in A) and 20 mW (in B). Violet-lowest THG signal, yellow—highest THG signal.

for 4.5 h. Once we confirmed that we obtained the expected increase of LD number, we went ahead to test the two methods of quantification and the sensitivity of THG imaging for LDs detection.

For the PSA method (available in ImageJ as "Analyze particles") the raw THG image (Fig. 6a left) was thresholded and converted to an 8-bit mask, upon which the program automatically counted the number of "particles" representing LDs in images analyzed (Fig. 6a middle). In addition to the number of particles, the diameter and area were quantified as well.

Because of the thresholding and limited resolution of the image (pixel size), the PSA might be insensitive to very small or weak signal entities. As the result, some emerging LDs might be omitted and not shown in the final results. To resolve this issue, we performed ICS which extracts the information on particle properties (number and size) based on the spatial fluctuations of the signal intensity in the images. ICS is also applicable to images that are diffuse.

Due to the morphology of the hyphae, it was necessary to pre-process THG images before applying the ICS analysis. Cell wall of hyphae was removed from the image since it hinders the correlation analysis (producing the pedestal at the G curve) because of the sharp discontinuity in intensity at the periphery of the hyphae along the whole circumference. We applied multiple subtractions of the background (average pixel intensity of ROI outside the hypha) until the wall disappears[74]. The latter procedure is depicted in Fig. 6a right and it is obvious that the THG signal from the majority of LDs is much more intense than the signal from the wall (approx. > 10x).

After removal of the cell wall, image correlation procedure was performed in Image J. As the result one obtains a spatial autocorrelation image from which the G curve is extracted by taking an intensity profile through the center of the image. An example of a G curve is shown in Fig. 6b. The number of LDs was calculated using the following formula:

$$N_{LD} = \frac{N_{pix} \cdot N_{pix}}{r^2 \pi \cdot G(0)}$$

where N_{pix} is the pixel size of the $2^n \times 2^n$ image (where n is an integer), r is mean radius of LDs taken as half of the FWHM of the G curve, and G (0) is maximal value of the G curve. r and G (0) are extracted from the Lorentzian fit of the G curve (Fig. 6b insert). It should be noted that the morphology of the LDs differs substantially from the morphology of the clusters which are usually examined by ICS analysis. Thus, in our case, multiple subtractions of the background do not lead to the flattening of the curve G versus number of subtractions as might be expected[74]. The flattening of the G curve shown in the reference 74 is used as criterion how many times the background has to be subtracted before ICS is applied. Our criteria for the number of background subtraction were: (a) cessation of a significant reduction in the number of LDs after each subsequent subtraction (Fig. 6c, black squares), (b) approximate matching of the number of LDs per hyphae with PSA and (c) experience (the cell wall disappears from the image observed by the eye). Upon examination of tens of images, both control and treated hyphae, we concluded that, on average (depending on initial image quality), 20 consecutive subtractions were sufficient for reliable ICS analysis.

To check whether the extra removal of the cell wall would give different number of LDs, we performed manual removal of the cell wall solely. It was done by delineation and cropping prior to the multiple background subtractions. After 20 consecutive background subtractions, this method does not give substantially different results in the number of LDs compared to images where the cell wall was not manually cropped (illustrated by the graph in Fig. 6c).

LDs analysis by PSA and ICS.   A comparison of LD number and size obtained by ICS and PSA is in Table 1. The number of LDs per area of hyphae is approximately the same on average, but mean diameter obtained by ICS
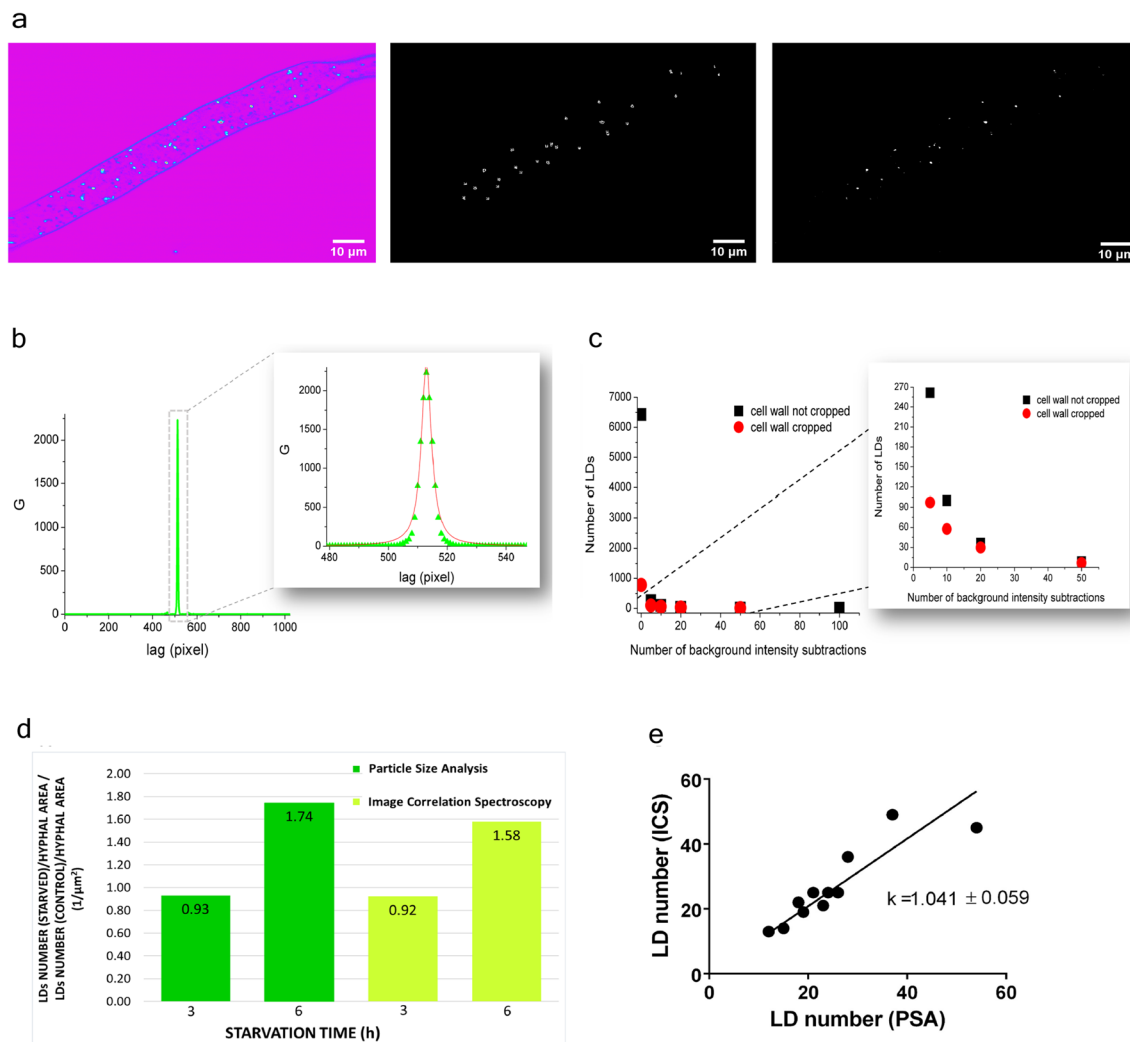
Figure 6. Image Correlation Spectroscopy (ICS) and Particle Size Analysis (PSA) on THG images. (**a**) Processing for PSA and ICS analysis of the same THG image. Left: The unprocessed THG image of *Phycomyces blakesleeanus* exponential growth phase hyphae in standard liquid medium; middle: 8-bit mask obtained in Particle size analysis; right: background subtracted image for ICS analysis. The image from left (unprocessed THG image) was processed by applying 20×background subtractions. Both images are displayed at full dynamic range (8 bits). THG image was taken with Zeiss 40×1.3 objective lens, while average laser power at sample plane was 27 mW. (**b**) ICS analysis: The autocorrelation function (G curve) taken as the plot through the center of intensity correlated THG image of a live and unlabeled hyphae. The autocorrelation curve was fit to a Lorentzian function to extract FWHM value as described in Methods section. (**c**) ICS analysis, the effect of the cell wall removal: The number of LDs obtained from the G curves after each background subtraction for the THG image where the cell wall was manually cropped (red circles) and for the same THG image where cell wall was not cropped prior to the background subtractions (black squares). (**d**) Comparison of ICS- and PSA—derived data obtained from the same set of THG images of cultures N-starved for 3 h and 6 h and their age-matched controls (n = 3 for each group). The ratio of the number of LDs per unit hyphal area, in N-starved hypha to the number of LDs per unit hypha area in age- matched controls. (**e**) The agreement of LD number quantification obtained by ICS and PSA. For each image, ICS-obtained LD number is plotted against PSA-obtained LD number for that image. Data for both graphs were obtained from label-free THG images, whose analysis is presented in Table 1.

is slightly lower. This discrepancy might be explained because of different definitions for the object size used in those two methods.

To estimate the change of LD number in treated hyphae, we calculated the ratio of LD number per area in treated hyphae in respect to control ones (Fig. 6d). The total number of LDs after 3 h of starvation shows no significant change. With longer starvation time the number of LDs increases by more than 50%.

Using ICS analysis, number of features counted was 80 ± 12% of the LD number that was found by visual inspection (n = 12) and in close correlation with the data obtained by PSA. When numbers of obtained LDs by both methods are plotted for each individual image as a separate point (Fig. 6e), the regression line has a slope close to 1, confirming that ICS is equally reliable as PSA method in detecting and counting LDs. The coefficient of regression R^2 was approximately 0.8.

Control/Treatment	Image correlation spectroscopy		Particles size analysis	
	Number of LDs/hyphae area (1/ μm^2) × 10^{-3} (mean ± SE)	Mean LDs diameter (μm) (mean ± SE)	Number of LDs/hyphae area (1/ μm^2) × 10^{-3} (mean ± SE)	Mean LDs diameter (μm) (mean ± SE)
Control cells for 3 h N-starvation	16 ± 1	0.56 ± 0.06	16 ± 2	0.74 ± 0.02
3 h N-starved cells	15 ± 5	0.60 ± 0.10	15 ± 6	0.74 ± 0.03
Control cells for 6 h N-starvation	15 ± 4	0.52 ± 0.08	13 ± 3	0.78 ± 0.02
6 h N-starved cells	24 ± 3	0.46 ± 0.02	22 ± 4	0.74 ± 0.04

Table 1. A comparison of the number and size of lipid droplets obtained by the quantification analysis of the two methods, ICS and PSA. n = 3 for each group presented.

Nitrogen starvation induced changes in lipid droplet number and size, as quantified from THG images. To fully use THG imaging (exposure time for an image takes maximum 30 s for 1024 × 1024 pixels image with 30 averages) and subsequent analysis as a LD assay, we performed a set of imaging and measurements across time, from filamentous fungi cultures, grown in nitrogen-depleted and control conditions. Fungi cultures were imaged after growing at least 2 h post start of the treatment (nitrogen starvation or control), precautionary step to avoid possible effects of manipulation during preparation for the start of treatment (e.g. centrifugation).

The number of LDs per unit cell area (Number of LDs/hypha area) in all imaged hypha in fungi cultures grown in nitrogen depleted media (N-starved) was significantly larger compared to the entire group of control culture hypha (Control) (Fig. 7a). To elucidate the time course of observed induction of increase in LD number, the Control and N-starved groups are broken down to duration-from-start-of-treatment groups each, and values of Number of LDs/hypha area plotted across time (Fig. 7b). The Number of LDs/hypha area in Controls remained almost the same during the time of observation, with the slight, not significant, trend of increase towards the later growth time points (Fig. 7b). N-starved had similar Number of LDs/hypha area to corresponding Control only at the 3 h of treatment time point. We detected twofold increase of Number of LDs/hypha area after 4.5 h treatment, compared to corresponding Control. Significant increase of Number of LDs/hypha area in N-starved hypha, compared to corresponding Control hypha, persisted at longer times of treatment (Fig. 7b).

The average diameter of LDs was significantly reduced in N-starved cultures, compared to controls, when entire groups were compared regardless of treatment time (Fig. 7c). As it can be seen from the time course graph (Fig. 7d), average LD diameters were approximately the same from the 2 h treatment time to the longest treatment time in Controls. They were also same in 3 h and 4.5 h N-starved hypha and their corresponding Controls. The effect of N-starvation on average LD size becomes clear only after 6 h or more of treatment (Fig. 7d).

The histograms of LD diameters, graphed as Number of LDs/hypha area (Fig. 7e) for the 4.5 h and 6 h time-of-treatment groups, reveal that LDs smaller than 1.6 μm are more numerous in N-starved groups than in corresponding Controls for 4.5 h time point, while at 6 h, only the number of LDs smaller than 1 μm is increased. LD average diameter change between 4.5 and 6 h N-starvation groups seems to be a result of significant loss of population of LDs larger than 0.6 μm during prolonged growth in N-starving conditions. To summarize, the overall change in LDs during growth without available nitrogen is found to be an increase in number of LDs between 3 and 4.5 h time point, followed with the loss of population of larger-than-average LDs during prolonged starvation.

Discussion

Once considered to be passive lipid storage agglomerations, lipid droplets are now recognized as dynamic cellular organelles, serving as ubiquitous central hubs of energy and lipid homeostasis in eukaryotic cells[75]. Studies of lipid droplet physiology in fungi, although still scarce[76], harbor promise of providing novel solutions for a number of important issues: mitigation and modulation of fungal resistance to fungicides and stress, securing the food safety, better understanding how to use fungi as a crucial component of sustainable organic waste reuse and conversion to energy source, to name a few. *Phycomyces blakesleeanus*, model fungus used in our study, belongs to *Mucormycota,* the phylogenetic group of fungi able of forming arbuscular mycorrhiza and other mutually beneficial symbiosis[77] with terrestrial plants[78]. During fungi-plant mutually beneficial interaction, a fungi transports nitrogen to a plant, and receives up to 30% of organic C compounds synthesized by a plant[78] in return. It is known that organic molecules sent from plant to fungi are lipids[79,80], and that lipid droplets form in large amounts in hypha adjacent to the area of contact with the plant[81]. Similar to *Phycomyces*, arbuscular mycorrhizal fungi can accumulate significant amount of acquired organic carbon in the form of lipid droplets[82]. THG imaging of LDs as described here is a method that could be directly applied to living mycorrhizal fungi related to *Phycomyces*, without the need for any modification of the protocol, or other staining.

The fungi culturing conditions used in our study resulted in a fairly modest accumulation of lipid droplets, as expected[62]. THG imaging analysis enabled us to watch and quantify changes in lipid droplet number, brought upon by complete removal of nitrogen, from such low density/diameter baseline. As expected, complete omission of nitrogen induced only a transient increase in number of lipid droplets, followed by lipid turnover[83]. THG imaging analysis detected the significant decline of lipid reserve at late stages of growth. Altogether, this shows the usefulness of THG imaging approach for broader exploration of LD in filamentous fungi under various living conditions.

Optical imaging techniques are commonly used to study lipid droplets in vivo, but lipids usually have to be labeled with various dyes. On the other hand, prolonged imaging using fluorescent dyes can be phototoxic to
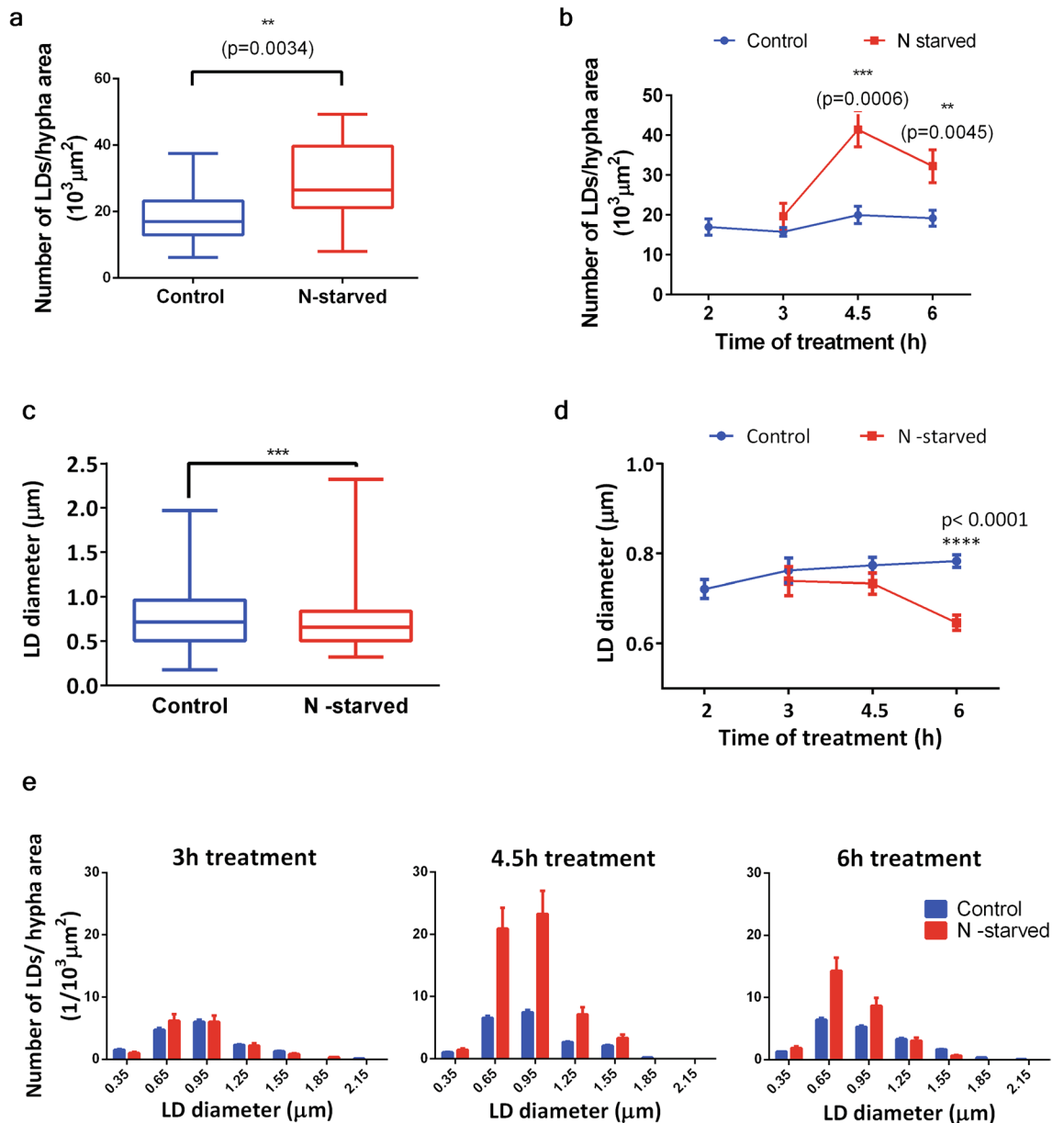
Figure 7. Quantification of LDs from THG images of *Phycomyces blaekseneanus* hypha. Hypha were cultured without nitrogen or in standard liquid media for 2–6 h (or longer up to 8 h) after the start of treatment. Obtained THG images of LDs were analyzed by PA. n = 6 independent cultures. (**a**) N-starvation increases number of LDs per unit area. LD number obtained from the individual hypha is normalized to hypha area (in 10^3 μm^2). Control (n = 44), N-starved group (n = 17). The box and whisker plots, enclosed by the 25th and 75th percentile range, median line with whiskers extending minimal to maximal value. Unpaired t test with Welch's correction, two tail, $p = 0.0038$. (**b**) Time course of LD number/unit area, showing that the increase of LD number by N-starvation is significant at 4.5 h ($p = p = 0.0006$) and later times ($p = 0.0045$), compared to corresponding control. Two-way ANOVA, with Holm-Sidac correction. Mean ± SE, n$_{(Control)}$ = 8; 7; 11; 21 for time points (in h), respectively: 2; 3; 4.5; 6. n$_{(N-starved)}$ = 6; 3; 7 for time points (in h), respectively: 3; 4.5; 6. (**c**) N-starvation decreases diameter of LDs. LD diameters from Control (n = 1205) and N-starved group (n = 431). The box and whisker plots, enclosed by the 25th and 75th percentile range, median line with whiskers extending minimal to maximal value. Mann–Whitney ($p = 0.0008$), two-tailed. (**d**) Time course of LD diameter changes, showing that the decrease by N-starvation is significant only at long starvation times. Two-way ANOVA, Holm-Sidac correction ($p < 0.0001$), compared to corresponding control. Mean ± SE, n$_{(Control)}$ = 176; 124; 302; 571 for time points (in h), respectively: 2; 3; 4.5; 6. n$_{(N-starved)}$ = 100; 118; 214 for time points (in h), respectively: 3; 4.5; 6. (**e**) Differential distribution of increased number of LDs after 4.5 h and 6 h N-starvation. The largest LDs are lost at longest starvation times. Histograms of LD diameter distributions, 0.3 μm binning, for Control and N-starved group. Number of LDs in each bin of the histogram is divided by sum of hypha area of the appropriate group. Errors are calculated as stated in Methods section. Numbers on x axes represent the upper bin limit.

cells and may perturb metabolic processes, including lipid metabolism. Hence, label-free imaging methods, are advantageous for the study of living cells[84–86].

THG imaging, a label-free method we have applied to live hyphae of oleaginous fungi *Phycomices blakesleeanus*, generated images with the characteristic spots of high THG signal intensity attributed to lipid droplets as the products of normal and stressed cellular physiology. Several lines of evidence support this attribution. First, the steep change of refractive index between lipids at the interface of lipid droplets and the rest of the cytoplasm generates high intensity THG signal, according to literature[11]. Second, to exclude possible laser-damaged spots that would produce high THG signal, we performed TPEF imaging of unstained hyphae showing that autoTPEF images are devoid of any prominent spots, present on a THG image of the same hypha. Third, we have performed colocalization experiments where the hyphae were stained with lipid specific dye and imaged by both, TPEF and THG method. The spots at the both images were mostly overlapped which verifies that the spots contained lipids. In addition, following the same logic of steep changes of refractive index, we have shown that the cell wall and the cell membrane in label-free hyphae can be imaged and distinguished by THG method.

There are a number of caveats to be discussed regarding the imaging of lipid stains. Because of the simultaneous detection of both (TPEF and THG) signals restricted number of dyes for live imaging could be used. In this study fixation was not a choice since it alters the structure of LDs[87]. The dye used in this study, Nile Red, might be not so specific for LDs and it can bind to other bodies and structures in the cell[88]. The signal originating from other structures than LDs can bleed into the detection band which eventually might affect the colocalization degree. In addition, the degree of colocalization is further deteriorated by the strong THG signal from the cell wall. The THG imaging requires significantly higher laser powers in comparison to the TPEF imaging. Because of that, one has to make a trade-off in terms of applied laser power when detecting both signals simultaneously. The price paid for this trade-off is the loss of some structures (e.g. small LDs, otherwise visible at higher laser powers) in THG images and appearance of weak, blurry TPEF signal from out of focus LDs (otherwise not visible at lower laser powers).

To extract quantitative data from THG images, two methods for image analysis were applied, Particle Size Analysis (PSA) and Image Correlation Spectroscopy (ICS). Both methods can quantify the number of lipid droplets and their average size (diameter). Since ICS was primarily developed for fluorescent images and cluster analysis and to the best of our knowledge it was not used so far for THG images, we have tested it by comparing the results to the PSA. The test was performed on the images of the hyphae under normal and stressed (nitrogen starvation) circumstances. The nitrogen starvation is known to cause increased number of lipid droplets[72,73] which was confirmed by both methods and the agreement between numbers obtained by both methods was good.

Overall, the proposed imaging method (THG) and the method of image analysis (ICS) was shown to be suitable for label-free in vivo studies of lipid droplets of oleaginous fungi. Application of THG method to future studies of lipid droplet dynamics in fungi could help to advance basic understanding of fungi cellular physiology, and then, of processes involved in the cycling of carbon in nature.

Data availability
The data available upon a reasonable request to the corresponding author.

References
 1. Weigelin, B., Bakker, G. J. & Friedl, P. Third harmonic generation microscopy of cells and tissue organization. *J. Cell Sci.* **129**, 245–255 (2016).
 2. Yelin, D. & Silberberg, Y. Laser scanning third-harmonic-generation microscopy in biology. *Opt. Express* **5**(8), 169–175 (1999).
 3. Barzda, V. *et al.* Visualization of mitochondria in cardiomyocytes. *Opt. Express* **13**, 8263 (2005).
 4. Witte, S. *et al.* Label-free live brain imaging and targeted patching with third-harmonic generation microscopy. *Proc. Natl. Acad. Sci. U. S. A.* **108**, 5970–5975 (2011).
 5. Tsai, C.-K. *et al.* Imaging granularity of leukocytes with third harmonic generation microscopy. *Biomed. Opt. Express* **3**, 2234 (2012).
 6. Weigelin, B., Bakker, G.-J. & Friedl, P. Intravital third harmonic generation microscopy of collective melanoma cell invasion. *IntraVital* **1**, 32–43 (2012).
 7. Gavgiotaki, E. *et al.* Third Harmonic Generation microscopy as a reliable diagnostic tool for evaluating lipid body modification during cell activation: The example of BV-2 microglia cells. *J. Struct. Biol.* **189**, 105–113 (2015).
 8. Oron, D. *et al.* Depth-resolved structural imaging by third-harmonic generation microscopy. *J. Struct. Biol.* **147**, 3–11 (2004).
 9. Sun, C.-K. *et al.* Multiharmonic-generation biopsy of skin. *Opt. Lett.* **28**, 2488 (2003).
 10. Aptel, F. *et al.* Multimodal nonlinear imaging of the human cornea. *Investig. Ophthalmol. Vis. Sci.* **51**, 2459–2465 (2010).
 11. Débarre, D. *et al.* Imaging lipid bodies in cells and tissues using third-harmonic generation microscopy. *Nat. Methods* **3**, 47–53 (2006).
 12. Farrar, M. J., Wise, F. W., Fetcho, J. R. & Schaffer, C. B. In vivo imaging of myelin in the vertebrate central nervous system using third harmonic generation microscopy. *Biophys. J.* **100**, 1362–1371 (2011).
 13. Genthial, R. *et al.* Label-free imaging of bone multiscale porosity and interfaces using third-harmonic generation microscopy. *Sci. Rep.* **7**, 1–16 (2017).
 14. Gavgiotaki, E. *et al.* Third Harmonic Generation microscopy distinguishes malignant cell grade in human breast tissue biopsies. *Sci. Rep.* **10**, 1–13 (2020).
 15. Canioni, L. *et al.* Imaging of Ca^{2+} intracellular dynamics with a third-harmonic generation microscope. *Opt. Lett.* **26**, 515–517 (2001).
 16. Chen, Y.-C. *et al.* Third-harmonic generation microscopy reveals dental anatomy in ancient fossils. *Opt. Lett.* **40**, 1354 (2015).
 17. Chang, T. *et al.* Non-invasive monitoring of cell metabolism and lipid production in 3D engineered human adipose tissues using label-free multiphoton microscopy. *Biomaterials* **34**, 8607–8616 (2013).
 18. Débarre, D. *et al.* Velocimetric third-harmonic generation microscopy: micrometer-scale quantification of morphogenetic movements in unstained embryos. *Opt. Lett.* **29**, 2881 (2004).

19. Sun, C. K. *et al.* Higher harmonic generation microscopy for developmental biology. *J. Struct. Biol.* **147**, 19–30 (2004).
20. Watanabe, T. *et al.* Characterisation of the dynamic behaviour of lipid droplets in the early mouse embryo using adaptive harmonic generation microscopy. *BMC Cell Biol.* **11**(1), 1–11 (2010).
21. Tserevelakis, G. J. *et al.* Imaging Caenorhabditis elegans embryogenesis by third-harmonic generation microscopy. *Micron* **41**, 444–447 (2010).
22. Aviles-Espinosa, R. *et al.* Cell division stage in C. elegans imaged using third harmonic generation microscopy. In *Biomedical Optics and 3-D Imaging (2010), Paper BTuD78 BTuD78* (The Optical Society, Washington, 2013).
23. Yu, M. M. L. *et al.* In situ analysis by microspectroscopy reveals triterpenoid compositional patterns within leaf cuticles of Prunus laurocerasus. *Planta* **227**, 823–834 (2008).
24. Prent, N. *et al.* Applications of nonlinear microscopy for studying the structure and dynamics in biological systems. *Photonic Appl. Nonlinear Opt. Nanophotonics Microw. Photonics* **5971**, 597106 (2005).
25. Tokarz, D. *et al.* Molecular organization of crystalline β-carotene in carrots determined with polarization-dependent second and third harmonic generation microscopy. *J. Phys. Chem. B* **118**, 3814–3822 (2014).
26. Cisek, R. *et al.* Optical microscopy in photosynthesis. *Photosynth. Res.* **102**, 111–141 (2009).
27. Barzda, V. *Non-Linear Contrast Mechanisms for Optical Microscopy* 35–54 (Springer, Dordrecht, 2008).
28. Segawa, H. *et al.* Label-free tetra-modal molecular imaging of living cells with CARS, SHG, THG and TSFG (coherent anti-Stokes Raman scattering, second harmonic generation, third harmonic generation and third-order sum frequency generation). *Opt. Express* **20**, 9551 (2012).
29. Barad, Y., Eisenberg, H., Horowitz, M. & Silberberg, Y. Nonlinear scanning laser microscopy by third harmonic generation. *Appl. Phys. Lett.* **70**, 922–924 (1997).
30. Boyd, R. W. *Nonlinear Optics* (Academic Press, New York, 2008).
31. Iy, Y., En, L. & Vv, T. Refractive index of adipose tissue and lipid droplet measured in wide spectral and temperature ranges. *Appl. Opt.* **57**, 4839 (2018).
32. Liu, P. Y. *et al.* Cell refractive index for cell biology and disease diagnosis: past, present and future. *Lab Chip* **16**, 634–644 (2016).
33. Chen, Y.-C., Hsu, H.-C., Lee, C.-M. & Sun, C.-K. Third-harmonic generation susceptibility spectroscopy in free fatty acids. *J. Biomed. Opt.* **20**, 095013 (2015).
34. Small, D. M. *et al.* Label-free imaging of atherosclerotic plaques using third-harmonic generation microscopy. *Biomed. Opt. Express* **9**, 214 (2018).
35. Bautista, G. *et al.* Polarized thg microscopy identifies compositionally different lipid droplets in mammalian cells. *Biophys. J.* **107**, 2230–2236 (2014).
36. Tserevelakis, G. J. *et al.* Label-free imaging of lipid depositions in C. elegans using third-harmonic generation microscopy. *PloS One* **9**(1), e84431 (2014).
37. Siddhanta, S., Paidi, S. K., Bushley, K., Prasad, R. & Barman, I. Exploring morphological and biochemical linkages in fungal growth with label-free light sheet microscopy and Raman spectroscopy. *ChemPhysChem* **18**, 72–78 (2017).
38. Zhang, C., Li, J., Lan, L. & Cheng, J.-X. Quantification of lipid metabolism in living cells through the dynamics of lipid droplets measured by stimulated Raman scattering imaging. *Anal. Chem.* **89**, 4502–4507 (2017).
39. Brackmann, C. *et al.* CARS microscopy of lipid stores in yeast: The impact of nutritional state and genetic background. *J. Raman Spectrosc.* **40**, 748–756 (2009).
40. Zhang, C. & Boppart, S. A. Dynamic signatures of lipid droplets as new markers to quantify cellular metabolic changes. *Anal. Chem.* **92**, 15943–15952 (2020).
41. Dong, P. T. *et al.* Polarization-sensitive stimulated Raman scattering imaging resolves amphotericin B orientation in Candida membrane. *Sci. Adv.* **7**, 1–11 (2021).
42. Yasuda, M., Takeshita, N. & Shigeto, S. Inhomogeneous molecular distributions and cytochrome types and redox states in fungal cells revealed by Raman hyperspectral imaging using multivariate curve resolution-alternating least squares. *Anal. Chem.* **91**, 12501–12508 (2019).
43. Kurian, S. M., Pietro, A. . Di. & Read, N. D. Live-cell imaging of conidial anastomosis tube fusion during colony initiation in Fusarium oxysporum. *PLoS One* **13**, e0195634 (2018).
44. Adomshick, V., Pu, Y. & Veiga-Lopez, A. Automated lipid droplet quantification system for phenotypic analysis of adipocytes using Cell Profiler. *Toxicol. Mech. Methods* **30**, 378–387 (2020).
45. Jüngst, C., Klein, M. & Zumbusch, A. Long-term live cell microscopy studies of lipid droplet fusion dynamics in adipocytes. *J. Lipid Res.* **54**, 3419–3429 (2013).
46. Exner, T. *et al.* Lipid droplet quantification based on iterative image processing. *J. Lipid Res.* **60**, 1333–1344 (2019).
47. Rambold, A. S., Cohen, S. & Lippincott-Schwartz, J. Fatty acid trafficking in starved cells: Regulation by lipid droplet lipolysis, autophagy, and mitochondrial fusion dynamics [Developmental Cell 32 (2015) 678–692]. *Dev. Cell* **32**, 678–692 (2015).
48. Dejgaard, S. Y. & Presley, J. F. New automated single-cell technique for segmentation and quantitation of lipid droplets. *J. Histochem. Cytochem.* **62**, 889–901 (2014).
49. Nohe, A. & Petersen, N. O. Image correlation spectroscopy. *Sci. STKE* **2007**, (2007).
50. Wiseman, P. W., Squier, J. A., Ellisman, M. H. & Wilson, K. R. Two-photo image correlation spectroscopy and image cross-correlation spectroscopy. *J. Microsc.* **200**, 14–25 (2000).
51. Slenders, E. *et al.* Image Correlation spectroscopy with second harmonic generating nanoparticles in suspension and in cells. *J. Phys. Chem. Lett.* **9**, 6112–6118 (2018).
52. Bahram, M. & Netherway, T. Fungi as mediators linking organisms and ecosystems. *FEMS Microbiol. Rev.* **46**, 1–16 (2022).
53. Parihar, M. *et al.* The potential of arbuscular mycorrhizal fungi in C cycling: A review. *Arch. Microbiol.* **202**, 1581–1596 (2020).
54. Ratledge, C. Regulation of lipid accumulation in oleaginous microorganisms. *Biochem. Soc. Trans.* **30**, A101–A101 (2002).
55. Cerdá-Olmeda, E. & Avalos, J. Oleaginous fungi: Carotene-rich from Phycomyces. *Prog. Lipid Res.* **33**, 185–192 (1994).
56. Passoth, V. Lipids of yeasts and filamentous fungi and their importance for biotechnology. *Biotechnol. Yeasts Filamentous Fungi* https://doi.org/10.1007/978-3-319-58829-2_6 (2017).
57. Mhlongo, S. I. *et al.* The potential of single-cell oils derived from filamentous fungi as alternative feedstock sources for biodiesel production. *Front. Microbiol.* **12**, 57 (2021).
58. Chang, W. *et al.* Trapping toxins within lipid droplets is a resistance mechanism in fungi. *Sci. Rep.* **51**(5), 1–11 (2015).
59. Liu, N. *et al.* Lipid droplet biogenesis regulated by the FgNem1/Spo7-FgPah1 phosphatase cascade plays critical roles in fungal development and virulence in Fusarium graminearum. *New Phytol.* **223**, 412–429 (2019).
60. Petschnigg, J. *et al.* Good fat, essential cellular requirements for triacylglycerol synthesis to maintain membrane homeostasis in yeast. *J. Biol. Chem.* **284**, 30981–30993 (2009).
61. Suzuki, M., Shinohara, Y., Ohsaki, Y. & Fujimoto, T. Lipid droplets: Size matters. *J. Electron Microsc.* **60**, S101–S116 (2011).
62. Nand, K. & Mohrotra, B. S. Mycological fat production in India. II. Effect of hydrogen-ion concentration on fat synthesis. *Sydowia* **24**, 144–152 (1971).
63. Pollack, J. K., Harris, S. D. & Marten, M. R. Autophagy in filamentous fungi. *Fungal Genet. Biol.* **46**, 1–8 (2009).
64. Jaishy, B. & Abel, E. D. Lipids, lysosomes, and autophagy. *J. Lipid Res.* **57**, 1619–1635 (2016).
65. Petersen, N. O., Höddelius, P. L., Wiseman, P. W., Seger, O. & Magnusson, K. E. Quantitation of membrane receptor distributions by image correlation spectroscopy: Concept and application. *Biophys. J.* **65**, 1135–1146 (1993).

66. Bukara, K. *et al.* Mapping of hemoglobin in erythrocytes and erythrocyte ghosts using two photon excitation fluorescence microscopy. *J. Biomed. Opt.* **22**, 026003 (2017).
67. Despotović, S. Z. *et al.* Altered organization of collagen fibers in the uninvolved human colon mucosa 10 cm and 20 cm away from the malignant Tumor. *Sci. Rep.* **101**(10), 1–11 (2020).
68. Huang, S., Heikal, A. A. & Webb, W. W. Two-photon fluorescence spectroscopy and microscopy of NAD (P) H and flavoprotein. *Biophys. J.* **82**(5), 2811–2825 (2002).
69. Greenspan, P., Mayer, E. P. & Fowler, S. D. Nile red: A selective fluorescent stain for intracellular lipid droplets. *J. Cell Biol.* **100**, 965 (1985).
70. Yi, Y.-H. *et al.* Lipid droplet pattern and nondroplet-like structure in two fat mutants of Caenorhabditis elegans revealed by coherent anti-Stokes Raman scattering microscopy. *J. Biomed. Opt.* **19**, 011011 (2013).
71. Chen, Y. *et al.* Nitrogen-starvation triggers cellular accumulation of triacylglycerol in Metarhizium robertsii. *Fungal Biol.* **122**, 410–419 (2018).
72. Weng, L. C. *et al.* Nitrogen deprivation induces lipid droplet accumulation and alters fatty acid metabolism in symbiotic dinoflagellates isolated from Aiptasia pulchella. *Sci. Rep.* **4**, 1–8 (2014).
73. Aguilar, L. R. *et al.* Lipid droplets accumulation and other biochemical changes induced in the fungal pathogen Ustilago maydis under nitrogen-starvation. *Arch. Microbiol.* **199**, 1195–1209 (2017).
74. Rocheleau, J. V., Wiseman, P. W. & Petersen, N. O. Isolation of bright aggregate fluctuations in a multipopulation image correlation spectroscopy system using intensity subtraction. *Biophys. J.* **84**, 4011–4022 (2003).
75. Olzmann, J. A. & Carvalho, P. (2018) Dynamics and functions of lipid droplets. *Nat. Rev. Mol. Cell Biol.* **203**(20), 137–155 (2018).
76. Yu, Y. *et al.* The role of lipid droplets in Mortierella alpina aging revealed by integrative subcellular and whole-cell proteome analysis. *Sci. Rep.* **71**(7), 1–12 (2017).
77. Bonfante, P. & Venice, F. Mucoromycota: going to the roots of plant-interacting fungi. *Fungal Biol. Rev.* **34**, 100–113 (2020).
78. Smith, S. & Read, D. *Mycorrhizal Symbiosis* (Academic Press, New York, 2008).
79. Luginbuehl, L. H. *et al.* Fatty acids in arbuscular mycorrhizal fungi are synthesized by the host plant. *Science* **356**, 1175–1178 (2017).
80. Jiang, Y. *et al.* Plants transfer lipids to sustain colonization by mutualistic mycorrhizal and parasitic fungi. *Science* **356**, 1172–1173 (2017).
81. Keymer, A. *et al.* Lipid transfer from plants to arbuscular mycorrhiza fungi. *Elife* **6**, e29107 (2017).
82. Deka, D., Sonowal, S., Chikkaputtaiah, C. & Velmurugan, N. Symbiotic associations: Key factors that determine physiology and lipid accumulation in oleaginous microorganisms. *Front. Microbiol.* **11**, 555312 (2020).
83. Athenaki, M. *et al.* Lipids from yeasts and fungi: Physiology, production and analytical considerations. *J. Appl. Microbiol.* **124**, 336–367 (2018).
84. Fujita, K. & Smith, N. I. Label-free molecular imaging of living cells. *Mol. Cells OS* 530–535 (2008).
85. Knaus, H., Blab, G. A., van Jerre Veluw, G., Gerritsen, H. C. & Wösten, H. A. B. Label-free fluorescence microscopy in fungi. *Fungal Biol. Rev.* **27**, 60–66 (2013).
86. Borile, G., Sandrin, D., Filippi, A., Anderson, K. I. & Romanato, F. Label-free multiphoton microscopy: Much more than fancy images. *Int. J. Mol. Sci.* **22**, 2657 (2021).
87. Martins, A. S., Martins, I. C. & Santos, N. C. Methods for lipid droplet biophysical characterization in flaviviridae infections. *Front. Microbiol.* **9**, 1951 (2018).
88. Nile Red. Available at: https://www.thermofisher.com/order/catalog/product/N1142.

Acknowledgements

Author contributions

T.P. conducted all the experiments, processed the images, and prepared the samples. N.T. designed the protocols and supervised the sample preparation and treatments. M.Ž. supervised the biological part of research. S.N. designed the acquisition and improved the software for imaging. M.R. designed the optical setup, supervised the imaging experiments and image analysis. A.C. supervised image processing, particularly LD quantification. A.K. designed the study, designed the optical setup, and supervised the experiments. All authors took participation in the manuscript preparation and revision.

Funding

Competing interests

The authors declare no competing interests.

Additional information

Supplementary Information The online version contains supplementary material available at https://doi.org/10.1038/s41598-022-23502-4.

Correspondence and requests for materials should be addressed to A.J.K.

Reprints and permissions information is available at www.nature.com/reprints.

Publisher's note Springer Nature remains neutral with regard to jurisdictional claims in published maps and institutional affiliations.

ORIGINAL PAPER

On different aspects of the optical rogue waves nature

Milivoj R. Belić · Stanko N. Nikolić · Omar A. Ashour · Najdan B. Aleksić

Abstract Rogue waves are giant nonlinear waves that suddenly appear and disappear in oceans and optics. We discuss the facts and fictions related to their strange nature, dynamic generation, ingrained instability, and potential applications. We present rogue wave solutions to the standard cubic nonlinear Schrödinger equation that models many propagation phenomena in nonlinear optics. We propose the method of mode pruning for suppressing the modulation instability of rogue waves. We demonstrate how to produce stable Talbot carpets—recurrent images of light and plasma waves—by rogue waves, for possible use in nanolithography. We point to instances when rogue waves appear as numerical artefacts, due to an inadequate numerical treatment of modulation instability and homoclinic chaos of rogue waves. Finally, we display how statistical analysis based on different numerical procedures

can lead to misleading conclusions on the nature of rogue waves.

1 Introduction

Analytical and numerical solutions of the nonlinear Schrödinger equation (NLSE) of different orders have been widely analyzed for their importance in a number of mathematical and physical systems [1–11]. In this work, we focus on the simple cubic one-dimensional NLSE arising in many fields of nonlinear and fiber optics. Our main concern are the NLSE solutions that are unstable due to the influence of modulation instability (MI). Although MI is usually recognized as the Benjamin–Feir instability, it already appeared in 1947, in the work of Bogoliubov on the uniform Bose gas [12], which introduced and discussed the MI of the cubic NLSE. In general, the modulation instability can be regarded as a nonlinear optical process where the power of the fundamental pump wave is attenuated and redistributed to a finite number of spectral sidebands. These higher-order modes are very weak at the onset of nonlinear evolution but their power increases exponentially during propagation [3,4,13]. The notion of MI is widely spread over several fields of physics. The NLSE-based study of nonlinear modulated waves and modulation instability in real electrical lattices was presented in

M. R. Belić · S. N. Nikolić (✉) · N. B. Aleksić
Science Program, Texas A&M University at Qatar, P.O. Box 23874, Doha, Qatar
e-mail: stankon@ipb.ac.rs

S. N. Nikolić
Institute of Physics Belgrade, University of Belgrade, Pregrevica 118, Belgrade 11080, Serbia

O. A. Ashour
Department of Physics, University of California, Berkeley, CA 94720, USA

N. B. Aleksić
Moscow State Technological University "STANKIN", Moscow, Russia

[14]. The properties of breathers and modulation instability in a discrete nonlinear lattice are investigated analytically in [15]. The issue of MI was also investigated in electronic wave packets in nonlinear chains modeled by the discrete NLSE [16].

Since MI is frequently indicated as the main cause of the rogue wave (RW) appearance in nonlinear optics [17], we are further motivated to investigate how this fundamental property of nonlinear systems affects various high-intensity NLSE solutions that can be regarded as rogue waves. This research is becoming more exciting since a new scheme for the excitation of rogue waves, via the electromagnetically induced transparency (EIT) [18–21], has been analyzed in [22].

In order to properly investigate the impact of MI on RWs, one needs to dynamically generate high-intensity peaks with narrow spatial profiles. We start from the well-known exact solution of the cubic NLSE, known as the higher-order Akhmediev breather (AB) [23–27]. A complication arises along the way, as these higher-order solutions also arise as the homoclinic orbits of unstable Stokes waves during the evolution of the system under NLSE [28–31]. Consequently, the long-time dynamics will become chaotic for ABs with two or more unstable modes. It is then questionable whether the chaotic behavior is intrinsic to the model equation or is induced by the numerical algorithm applied [28,29].

To address this question, we revisit our previous results [32] on the analytical and numerical NLSE solutions that are periodic both along the temporal and spatial axes, known as the Talbot self-images or carpets [25,33,34]. In optics, the Talbot effect is known as a near-field diffraction phenomenon, occurring when light beams undergo diffraction at some periodic structure and produce recurrent self-images at equidistant planes. The Talbot carpets refer to fractional and even fractal light patterns observed in-between the planes. Although Talbot effect is known for more than hundred years, it still finds applications in many fields, such as plasmonic nanolithography [35–37].

In reference [32], we presented a mode pruning procedure to mitigate the unavoidable impact of MI and obtain double-periodic solutions from Akhmediev breathers. Here, we briefly recap this effort: We calculate ABs of different orders using Darboux transformation (DT) technique and extract initial conditions in a wide box that is a multiple of the main breather period [38]. We next apply the mode pruning method combined with a chosen numerical NLSE integration

scheme to preserve the self-imaging recurrences for as long as possible. In this paper, we extend this analysis by taking into account different values of the main breather parameter a (Sect. 2.1) and initially having more breathers in the box. But, the central theme of this paper is concerned with the conflicting opinions formed about the nature of RWs: Are they linear or nonlinear; random or deterministic; numerical or physical? A short and in our opinion correct answer to these nagging questions is as follows.

Rogue waves are essentially nonlinear, because their cause is the modulation or Benjamin–Feir instability, which is one of the basic nonlinear optical processes. They are deterministic, because modulation instability leads to homoclinic chaos, which by its nature is deterministic; random phenomena are probabilistic and may look chaotic but are not deterministic. RWs are physical, because they are observed in many experiments and media, with similar statistics [39–41].

Now, there exist reservations to these facts, depending on how one generates and analyzes RWs. This especially holds if the work is numerical and statistical in nature. Nevertheless, even in this case, we will display how widely used beam propagation method can produce spurious RWs when inappropriately employed. We will also demonstrate how statistical analyses of exactly the same dynamical systems, but produced using different numerical algorithms, may lead to different statistics of RWs. We will address these reservations later in the paper.

2 Rogue wave solutions to the NLSE

To recap, we discuss the nature of optical rogue waves in the cubic NLSE, in view of conflicting opinions expressed in the literature. In particular, as already mentioned, we address three pairs of opposing suppositions on their nature: Linear versus nonlinear [3,5]; random versus deterministic [42,43]; and numerical versus physical [28,29]. A short answer to these suppositions is that rogue waves in optics are nonlinear, deterministic, and physical. To stress again, they are nonlinear because the major cause of rogue waves is the modulation or Benjamin–Feir instability. They are deterministic because modulation instability leads to deterministic chaos. They are physical because they appear in many experiments and media. Our opinion is supported by extensive numerical simulations of the

nonlinear Schrödinger equation in different regimes that touch upon the aspects of all three conflicting suppositions.

Disturbingly, in numerical simulations optical rogue waves may appear fictitiously, as numerical artefacts. One such published instance will be displayed below. Different numerical algorithms for exactly the same input may provide different evolution pictures and different statistics when modulation instability sets in and when numerical grid parameters are not set precisely. An example of different statistics of the probability density distributions, obtained by two different numerical algorithms applied to the same input, is also provided below. There, the standard beam propagation method (the split-step fast Fourier transform method), predominantly used in the literature, predicts the appearance of thousands of rogue waves, whereas the more precise symplectic algorithm of higher order predicts significantly fewer. Hence, owing to the vague definition of rogue waves, the way they are produced, and an exponential amplification of numerical errors, there are situations in which optical rogue waves may appear as linear, random, and numerical.

2.1 The influence and suppression of modulation instability

Before proceeding to these more subtle points, let us start by discussing the more standard behavior of RWs in the standard NLSE. We study double-periodic solutions of the simplest cubic nonlinear Schrödinger equation

$$i\psi_x + \frac{1}{2}\psi_{tt} + |\psi|^2\psi = 0. \tag{2.1}$$

The wave function $\psi \equiv \psi(x, t)$ corresponds to the slowly varying envelope that could be optical, plasmonic or other in nature. In a fiber optics notation, the transverse variable t is the retarded time in the frame that moves with a pulse group velocity. The evaluation variable x is considered as the distance along the fiber.

Let us consider the first-order AB solution, which is single-periodic along t-axis [24,25]:

$$\psi(t, x) = \left[1 + \frac{2(1-2a)\cosh\lambda x + i\lambda\sinh\lambda x}{\sqrt{2a}\cos\omega t - \cosh\lambda x}\right]e^{ix}. \tag{2.2}$$

The period L, angular frequency ω, and growth rate λ of an AB (first- or higher-order) are solely determined by parameter a, with $0 < a < 0.5$ [13]:

$$L = \frac{\pi}{\sqrt{1 - 2a}}, \tag{2.3}$$

$$\omega = 2\sqrt{1 - 2a}, \tag{2.4}$$

$$\lambda = \sqrt{8a(1 - 2a)}. \tag{2.5}$$

When $a = 0.5$, AB turns into the Peregrine RW, and for $a > 0.5$, it becomes the Kuznetsov–Ma (KM) soliton.

The procedure for dynamic generation of the first or higher-order Akhmediev breathers is explained in detail in Section 2 of [32]. Here, we briefly state that the initial condition for numerics is derived from an exact AB solution at a certain value x_0 of the evolution variable, using Darboux transformation [44]. To obtain double-periodic breathers resembling the Talbot carpets solutions, we need to adjust the size of the transverse interval to an integer multiple of the fundamental breather's period L, apply periodic boundary conditions and use the mode pruning method. Namely, when the box size is equal to the breather's fundamental period, the Fourier harmonics will form the set S_1 of N stable fundamental breather modes (N denotes the number of grid points along the transversal t-axis). If we extend the box to an integer multiple of the main period, the mode spacing will get smaller and a new set S_2 will be obtained. The way to generate nonlinear Talbot carpets is to suppress modulation instability caused by the exponential growth of unstable Fourier modes belonging to S_2 and not to S_1.

In Fig. 1a, we present the numerical evolution of the first-order Akhmediev breather ($a = 0.33$) when the box size is equal to five breather's periods. The intensity peaks at $x = 0$ are repeated along x-axis at the Talbot periods. This array is shifted for half-a-period along the t-axis during evolution, forming the secondary Talbot image at half the Talbot period. The corresponding Fourier spectrum is shown in Fig. 1b. This result is obtained when unstable subharmonics are eliminated after each iteration, leaving only those that form the fundamental AB, with indices 0, ±5, ±10, ±15, etc. This is in agreement with our previous work [32] showing the same behavior for $a = 0.36$. Our motivation to study this problem for NLSE also originates from the similarity of our results shown in Fig. 1 to those presented in [35] (their Fig. 2) and [36] (their Figs. 2, 3, and 4) which are related to the Talbot effect in lithography.
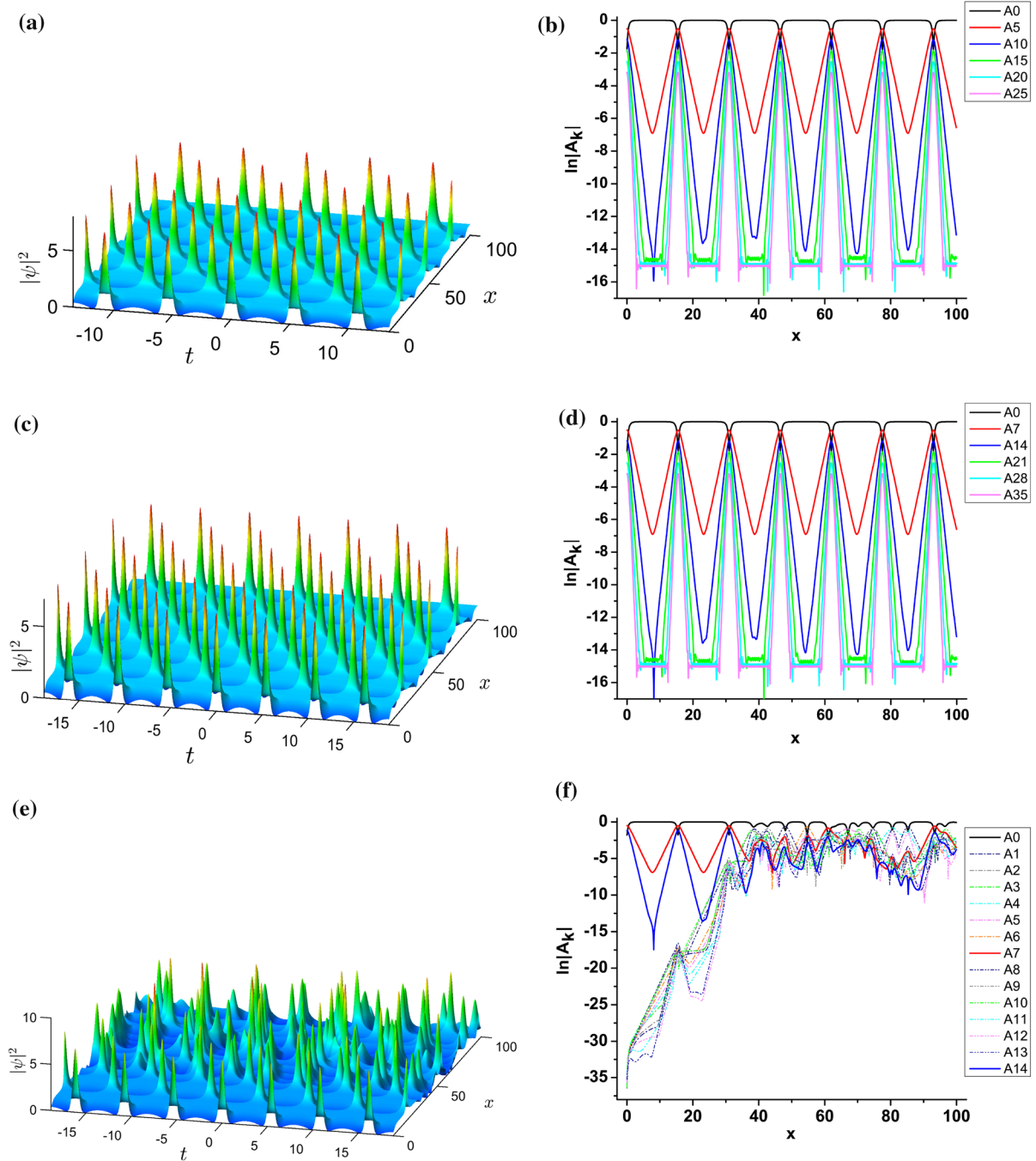
(a)

(b)

(c)

(d)

(e)

(f)

Fig. 1 Double-periodic numerical solutions, made of the first-order NLSE breathers, using the pruning procedure in FFT. The breather parameter is $a = 0.33$. **a** Five breathers in the box, with the pruning. **b** Its spectrum. **c** Seven breathers in the box, with the pruning. **d** The corresponding spectrum. **e** Seven breathers in the box, no pruning. **f** The corresponding spectrum

Next, we want to verify these results for even larger period, having seven breathers in the box. We apply the simple pruning algorithm to Fourier modes, setting all unstable mode amplitudes to zero except the modes indexed $0, \pm 7, \pm 14, \pm 21$, and so on. The result is an extended Talbot carpet with alternate shifting of intensity maxima along the x- and t-axes, as shown in Fig. 1c. The Fourier spectrum of the mode amplitudes is shown in Fig. 1d. If the pruning algorithm is not applied, the chaotic behavior ruins the carpet after three Talbot cycles, as shown in Fig. 1e. The unstable modes having the index not divisible by 7 grow exponentially due to MI, and prevent the homoclinic orbit from returning to itself after more than three cycles. The other view on the Talbot carpet disintegration is the irregular buildup of the Fourier modes spectrum, shown in Fig. 1f. As a result of the interaction or beating of different AB modes in the chaotic region, four second-order ABs are formed around $x = 41$, $x = 61$, and $x = 67$. We may consider these maxima as channels for the RW production through MI.

Another procedure to curb MI is the Gaussian pruning algorithm [32], in which the unstable modes are not eliminated completely but suppressed by a Gaussian factor. Thus, the unstable modes are multiplied by a number that depends on their strength: if the modes grow more, then the level of suppression is higher. In turn, the modes can grow only up to a certain value, determined by the Gaussian distribution, and cannot exceed the predefined value in the range of 10^{-11} to 10^{-9} (not shown).

To finalize, in Fig. 2, we present the nonlinear Talbot carpet consisting of the second-order breathers with higher intensities and narrower profiles. The box size is seven times the fundamental breather period, having $a = 0.41$. This is an additional analysis of our previous example in [32], but here with more breathers in the box and decreased spatial resolution. Figure 2a represents an unstable situation without pruning, while Fig. 2b is the stabilized carpet. The simple pruning algorithm was used, which left only each seventh Fourier mode intact.

In the end, one may wonder what such pruning procedures are worth for and how they can be utilized in the real world? After all, suppressing unstable Fourier modes numerically is a relatively simple task, but what its relevance might be in actual experiments is another matter. However, it is not difficult to envision situations in which it might be useful: for example, in experiments where signal transmission is interrupted periodically (and electronically) for data analysis. This typically happens when you have an experiment in an optical loop, where the beam circulates around. It also happens in long fiber experiments, when periodically you have to interrupt the propagation and ensure that it is still stable. The question for experimenters is then, how viable or advisable is to prune the data at the interruption, and inject back into the experiment, to force the beam and control the instability?

2.2 The influence of numerics on the dynamics and statistics of rogue waves

In this subsection, we address the questions pertaining to the numerics and statistics of RWs. But, before going to the details of numerics and statistics, let us briefly recap how we got to this point. To recall, the generating mechanism of optical rogue waves is the Benjamin–Feir or modulation instability. It is the basic nonlinear optical process in which a weak perturbation of the background pump wave produces an exponential growth of spectral sidebands that constructively interfere to build RWs. We have produced RWs in numerical simulations of the cubic nonlinear Schrödinger equation with inputs on the flat background determined by the DT. Optical RWs represent homoclinic orbits of unstable sideband modes that, due to MI, generate homoclinic chaos. The question is then whether the chaos seen belongs to the model itself or is induced by the numerical procedure applied. After all, even though the model is the same, different numerical algorithms for its solution represent different dynamical systems and may approach chaos differently.

As it will be discussed below, different numerical algorithms lead to similar values of the wave function once the evolution step in numerics dx for each algorithm is carefully chosen, but only up to a certain value x_{cr}. If the evolution is continued beyond x_{cr}, different dynamics will be generated using different numerical schemes, due to combined effects of finite numerical precision and modulation instability. It is common occurrence that in the region of instability and chaos different numerical methods offer different solutions to the same partial differential equation, under the same initial and boundary conditions. Sensitivity to small differences in initial conditions is one of the hallmarks of deterministic chaos.

Fig. 2 Double-periodic numerical solution of NLSE, made of the second-order breathers, having $a = 0.41$. The box contains seven breather periods. **a** The solution without pruning. **b** The solution with pruning
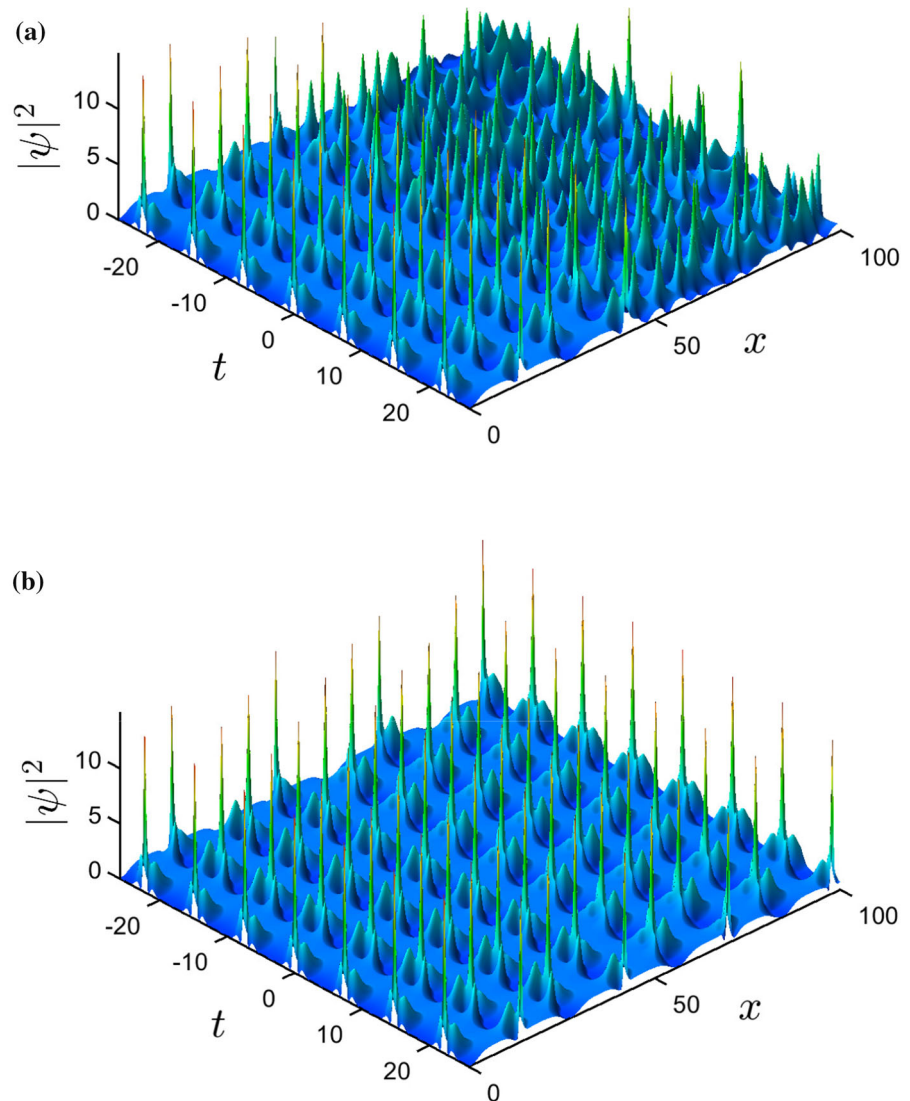
We present such an occurrence by simulating the same NLSE, with exactly the same parameters, inputs and boundary conditions, but using different numerical algorithms. We compare the standard second-order beam propagation method (BPM) with various higher-order symplectic algorithms. In our work, we prefer symplectic integrators for their utility in treating chaotic Hamiltonian systems that require long-time integration of noisy inputs. We demonstrate that distressingly, different algorithms may provide different evolutions and different statistics of the RW peaks, owing to homoclinic chaos and imprecise choice of the evolution step dx for each numerical procedure. Even

the same algorithms may provide different evolutions when the numerical step size is changed.

An appropriate example is the appearance of the third-order RW solution as a result of the collision of three ABs [45] for an initial condition given by $\psi(t, x = 0) = e^{i\pi t/10}[1 + 0.002 \cos(\pi t/10)]$. It is known that the collision of three localized pulses at the same point is unlikely to happen and difficult to observe, so we were intrigued by this finding in an otherwise excellent paper. Hence, we reproduced the same results by taking $dx = 10^{-4}$ (Fig. 3a). However, we discovered that just by taking half of the original numerical step size in the same numerical method, the third-order RW disappears (Fig. 3b). To check the

result, we recreated the solution using a fourth-order symplectic algorithm, which confirmed the disappearance of the RW ($dx = 10^{-4}$, Fig. 3c). It appears that the third-order RW in this example is just a numerical artefact.

When one solves the same equation by two numerical methods and finds different answers, an obvious question arises: Which of the two (if any) is correct? The question is especially relevant when one deals with the RWs in homoclinic chaos, because in chaos sooner or later all algorithms give different answers. Hence, the appropriate question to ask is not which solution is correct (because in chaos there exist no correct—meaning precise—solutions) but which algorithm is "more" correct. Then, the answer is obvious—the one that keeps to the presumed correct solution for longer (or conversely, the one shadowed by the correct solution for longer). Let us clarify this by presenting an example.

In Fig. 4, we analytically generate the fifth-order Akhmediev breather, represented by a very sharp and narrow peak at $x = 13$, using Darboux transformation. The main breather's frequency ω_1 is determined by parameter $a = 0.4850173$ (Eq. (2.4)). The remaining four higher-order modes ($i = 2, 3, 4, 5$) have harmonics with higher frequencies $\omega_i = i\omega_1$. We take the initial condition from DT at $x = 0$ (well before the peak) and numerically evolve the wave function, in order to see whether RW will appear at $x = 13$ and what happens after the peak. In the figure, we compare four different algorithms, by solving the cubic NLSE for the same initial condition around a highly unstable homoclinic orbit—the fifth-order RW. Such a RW, towering 81-times over the background intensity, is never seen in experiments and rarely even in numerical simulations.

One can see that all numerical algorithms correctly resolve the appearance of the RW, but afterward they all sooner or later give different answers. This happens because of the developing MI, which entails different evolutions in different algorithms. However, one can notice that the fourth-order and the sixth-order symplectic algorithms provide visually consistent solutions over the whole integration interval of 100 propagation units (10^5 integration steps!), while others do not. One may infer that these two numerical pseudo-orbits are shadowed by the true orbit over a longer distance. For this reason, in simulations that require long-distance integrations of noisy inputs that are necessary for the formation of statistics of RWs, we employ the fourth-order symplectic algorithm.

Here, it is worth mentioning that almost identical wave functions are observed up to some evolution point when running three different algorithms starting from the same initial condition, but with different integration steps: BPM for $dx = 0.00001$, sixth-order symplectic for $dx = 0.0002$, and eighth-order symplectic for $dx = 0.0005$. Quite expectedly, the lower-order algorithms require smaller steps for similar accuracy, whereas higher-order allow for larger steps. Nevertheless, as the evolution x-coordinate advances, the differences emerge due to both finite numerical precision and the intrinsic MI (not shown).

The fact that individual RWs may appear in different algorithms at different places and thus may represent fictitious structures or numerical artefacts is not the worst feature of dealing with RWs in homoclinic chaos. The more troublesome is the fact that the statistics of RWs obtained by different numerical methods may also be different, because by fiat, these statistics come from performing long-distance evolutions of a solution (or a class of solutions) to the NLSE, which are different for different numerical methods. It is desirable that they all provide the same statistics for the same underlying model, but this is not written in stone. As already mentioned, different numerical schemes represent different dynamical models. Worst of all, the long tail statistics of high intensity waves, i.e., the RWs, seems to be most affected by different numerical methods. Again, this is best explained by an example.

An example of two different evolution scenarios, starting from white noise with amplitude $A = 5\%$ around the background intensity $B = 1$, is shown in Fig. 5. We use two different methods: The second-order BPM (top) and the fourth-order symplectic (bottom). We intentionally use the same evolution step of $dx = 10^{-3}$ and the same transverse box $(-69.42, +69.42)$ (divided into $N = 2048$ intervals of the same width) for both figures, in order to spot the differences in the intensity graphs for identical initial conditions and numerical grids; the only difference is different algorithms. The evolution of intensity by the two algorithms appears consistent to about 100 longitudinal units (each unit is covered by 1000 numerical iterations), but after that the distributions become different. The wave function evolution is observed up to $x = 6500$, but for clarity the intensity is shown only from $x = 0$ to $x = 250$ in both figures. If certain regions of intensity maps are
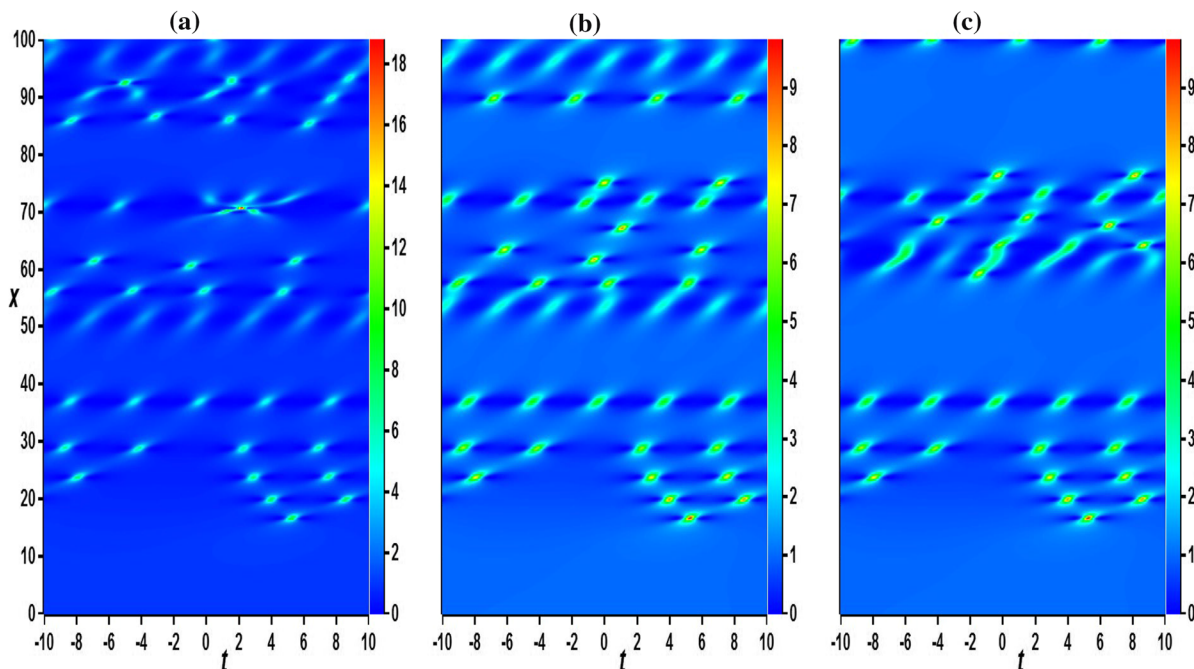
Fig. 3 Three solutions of the same equation, but obtained by two different algorithms and evolution steps dx. **a** second-order BPM, $dx = 10^{-4}$. **b** second-order BPM, $dx = 5 \times 10^{-5}$. **c**
fourth-order symplectic, $dx = 10^{-4}$. The prominent third-order RW in the left panel is a numerical artefact. It is absent in the other, more precise algorithm

enlarged, one can observe Akhmediev breathers of the first- and second order and long traces representing Kuznetsov–Ma solitons, as discussed in [3].

To settle a fine but important point that will become apparent later, we examine numerical evolution of the wave function $\psi(x, t)$, using the fourth-order symplectic algorithm, when the initial condition is chosen so that ψ is normalized at $x = 0$. The module of the wave function is

$$|\psi(x)|^2 = \int_{-L/2}^{L/2} |\psi(x, t)|^2 dt. \tag{2.6}$$

The last integral is approximated by numerical formula

$$|\psi(x = 0)|^2 = \sum_{i=1}^{N} |\psi(x = 0, t_i)|^2 \Delta t_i = \frac{L}{N} \sum_{i=1}^{N} |\psi_i|^2, \tag{2.7}$$

where L indicates the integration interval (box size), N is the number of points along the transverse t-axis, $\psi_i \equiv \psi(x = 0, t_i)$, and $\Delta t_i = \Delta t = L/N$. The initial wave function $\psi_{B=1,\,A=5\%}$ in Fig. 5 is not normalized and we can chose two different ways to set its module to one.

In the first case, one can divide all N initial complex numbers with $\sqrt{C}$, where $C = |\psi_{B=1,\,A=5\%}(x = 0)|^2$, so that $\psi_{norm1} = \psi_{B=1,\,A=5\%}/\sqrt{C}$. In the second case, one can hold these numbers unchanged and modify the grid size L so that the module is set to one according to Eq. (2.7): $\psi_{norm2} = \psi_{B=1,\,A=5\%}$ and $L' = L/C$. In the first case of lower intensity initial condition, the numerical evolution is very slow and the first structures that resemble Akhmediev breathers appear at $x \approx 800$ (Fig. 6a). The most similar structure appears at $t \approx -47$ and $x \approx 2450$, but evidently it is hugely extended along the evolution x-axis, with an approximate width of $\Delta x \approx 300$. This is far more stretched compared with the similar features obtained for non-normalized initial conditions, shown in Fig. 5b. In the second case, when the numerical $t-$box is significantly decreased (from $L \approx 140$ to $L' \approx 1$) the evolution gave us no char-

Fig. 4 Comparison of different numerical algorithms in resolving a fifth-order RW: **a** The standard BPM, **b** fourth-order symplectic, **c** sixth-order symplectic, and **d** eighth-order symplectic. Each panel extends transversely from -10 to 10 units and encompasses 100 longitudinal evolution units. For each figure, evolution step is the same: $dx = 0.0002$
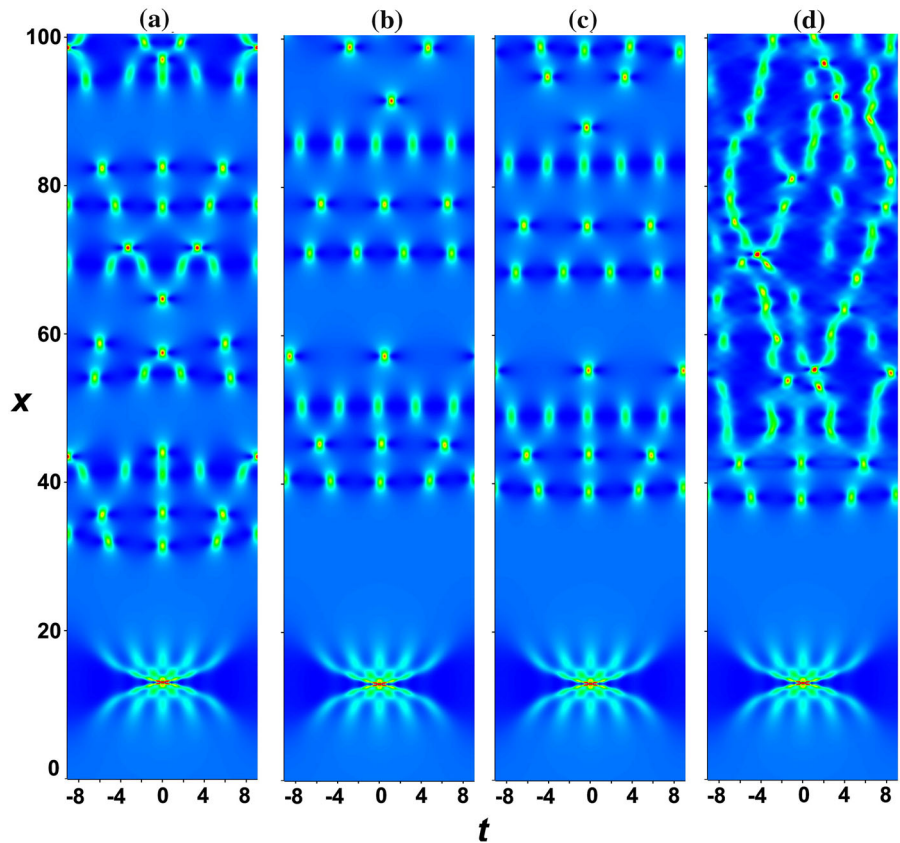
acteristic NLSE structures (Fig. 6b). One can easily spot the uniform intensity over the entire xt-grid with no vertical traces (Kuznetsov–Ma solitons) or localized maximums (Akhmediev breathers of the first or second order). Numerically, this is ill-advised.

What one can learn from these figures is that the ψ evolution is determined by the box size and the intensity of random wave function at the beginning of numerical iterations. Namely, the intrinsic modulation instability is the phenomenon that forms the characteristic NLSE structures during evolution. The amplitudes of higher Fourier modes that are very weak at $x = 0$ grow exponentially and produce KM solitons and ABs. If there are more unstable modes at beginning, then MI and NLSE features will appear sooner. The number of unstable modes N_{um} is related to the background noise level B and box size L via the following expression:

$$N_{um} = \frac{LB}{\pi}. \tag{2.8}$$

In case of low B and large L (see Fig. 6a, $B = 0.072$ and $L \approx 140$) we get $N_{um} = 3.2$. This means we have only a few unstable modes and MI is weak. That is the reason for obtaining very slow evolution and stretched NLSE features. In the second case, we have $B = 1$ and the small box $L' \approx 1$ and compute $N_{um} = 0.16$. This means that all Fourier modes are stable and the evolution is uniform without solitons and breathers formation, in agreement with Fig. 6b. We conclude that the normalization requirement imposes unacceptable conditions for noise background level and box size that adversely affect the dynamics of white noise under the NLSE model. Finally, we run the second-order BPM algorithm on the same initial condition and got the same results (not shown). The overall conclusion is that the integration with normalized ψ should be avoided, as it leads to different model behavior that is difficult to efficiently integrate.

We now go back to the case of non-normalized initial conditions ($B = 1$ and different values of A). We analyze the statistics of intensity maxima for evolutions obtained using the second-order BPM and the

Fig. 5 Evolution of the NLSE wave intensity seeded by white noise (5% amplitude) around the background intensity of 1. The wave evolution proceeds from 0 to 6500 propagation units, but only the first 250 are shown; the transverse box is approximately from -70 to 70 units. There are $6.5 \times 10^6 \times 2048$ grid points in overall. Top: Beam propagation method. Bottom: the fourth-order symplectic algorithm. For both algorithms the evolution step is $dx = 10^{-3}$
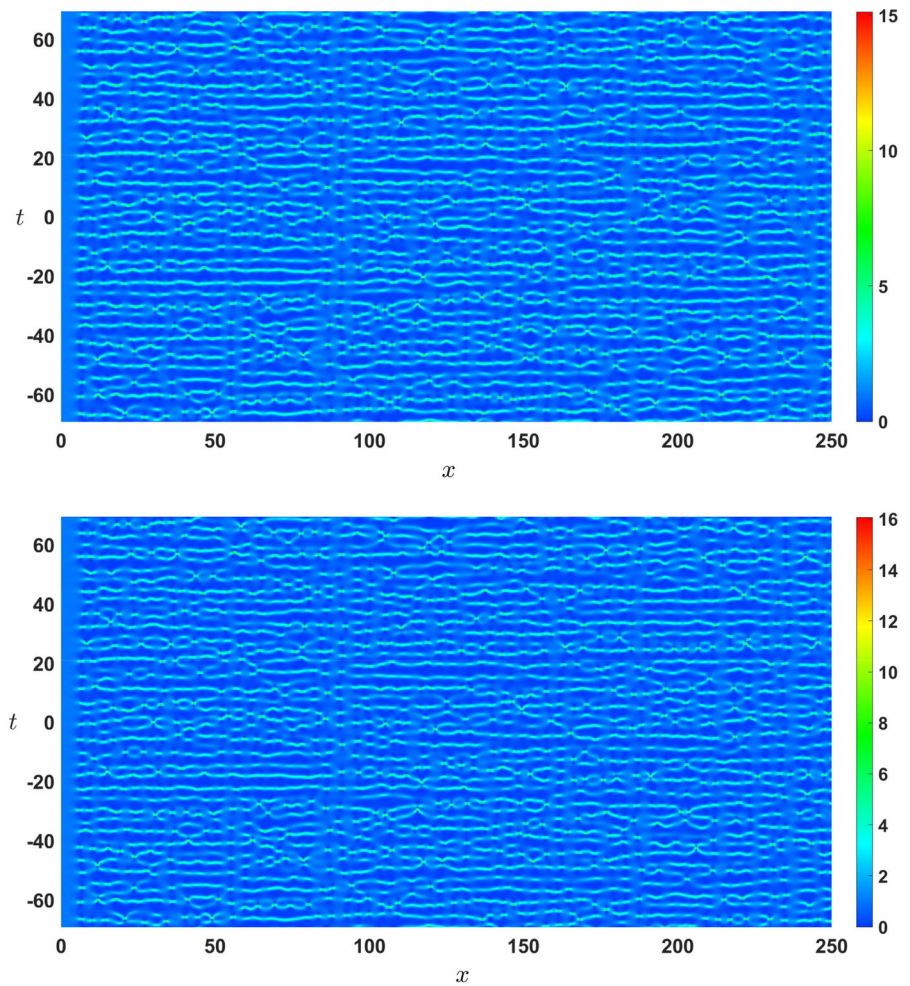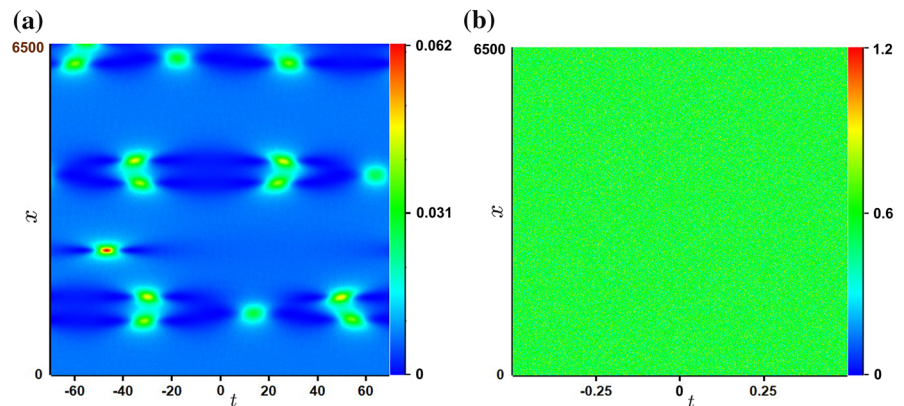

Fig. 6 Evolution from the white noise using fourth-order symplectic algorithm with wave function normalized at $x = 0$: **a** initial condition lowered ($B = 0.072$ and $A = 0.36\%$) within the large box ($L \approx 70$) and **b** initial condition remained the same ($B = 1$ and $A = 5\%$), but with box reduced ($L' \approx 1$)

fourth-order symplectic algorithms. During numerical integration, our software records intensity maxima $I_{i,j} = |\psi_{i,j}|^2$ at (x_i, t_j) point of the numerical grid, if this intensity is the highest value in the 8-connected neighborhood region. All maxima are being recorded in a file and then plotted in the histogram form, where each bin height corresponds to the number of maxima within the bin's intensity interval, divided by the total number of peaks. The additional requirement after each computational iteration is to eliminate the high-frequency Fourier modes forming the fast zig-zag glitches in the wave function ψ that are considered as false maxima. We should note that although our computational procedure appears to be rather stringent, it affects the chosen algorithms equally, so that the resulting differences are not caused by this feature.

First, we discuss the probability density of peaks' intensities from Fig. 5, where the white noise amplitude is $A = 5\%$. The results for BPM are presented in Fig. 7a, and for the fourth-order symplectic algorithm in Fig. 7b. It turns out that the results in general are different. Both distributions follow the familiar exponential decay of MI-driven systems, which may not be the case for the density of high-intensity peaks, forming RWs. At this point, we pose the question of what is the criterion for announcing an intensity peak as a rogue wave? Here we simultaneously adopt two criteria and make comparative analysis. The first is relatively simple: the peak with the intensity greater than that of the Peregrine soliton ($I \geq I_{PS} = 9$) is considered as a rogue wave. The second is statistical in nature and is widely adopted in the literature [46–50]: the intensity threshold I_{RW} above which one obtains a RW is a mean value of the largest third of intensity peaks multiplied by two (the same definition applies to the rogue wave amplitude in oceanography). Therefore, in Figs. 7 and 8, we indicate two vertical lines, dividing the intensity scale on RW and non-RW regions.

In Figs. 7a and 7b, there are millions of peaks and thousands of RWs (according to both definitions). The statistics are still similar, but the number of peaks, the maximum of intensity, and the slope of distributions, among other things, are different. Hence, in the chaos produced by MI, optical RWs and their statistics may appear as numerical artefacts and cannot be a priori counted as definite defining features of the RW phenomena. The exponential decay fit $y = ce^{-I/I_0}$ of the distributions in Figs. 7a and 7b is shown in Figs. 7c (with $c = 0.3339$, $I_0 = 1.2691$), and 7d

(with $c = 0.34151$, $I_0 = 1.25399$), respectively. Thus, while the distributions are well-described by exponentially decaying curves, in detail they differ most in the heavy-tailed region of higher intensities, where RWs reside.

The next relevant question is what is the influence of the white noise amplitude A (at $x = 0$) on the statistics of NLSE evolution? We therefore run six simulations using two algorithms (BPM and fourth-order symplectic) for three values of A. The corresponding histograms of intensity maxima are shown in Fig. 8a (BPM alg. and $A = 1\%$), 8b (4S alg. and $A = 1\%$), 8c (BPM alg. and $A = 2\%$), 8d (4S alg. and $A = 2\%$), 8e (BPM alg. and $A = 3.5\%$), and 8f (4S alg. and $A = 3.5\%$). Here, as in Fig. 5, we removed fast glitches from the wave function that present false maxima, by eliminating high-frequency Fourier modes. The statistics are similar to those obtained with 5% amplitudes, but the differences in the results between the two algorithms for the same value of A still persist.

All data for two algorithms and different amplitudes are summarized in Table 1. The first observation is that for the background level of $B = 1$, the statistical RW threshold I_{RW} is lower than $I_{PS} = 9$. Namely, the majority of intensity peaks are located at lower intensities for all eight histograms. Thus, the largest third of the peaks begins well below the Peregrine soliton intensity. Another conclusion is that the larger the amplitude A, the higher the statistical threshold I_{RW}. As for the overall intensity maximum I_{max} during numerical evolution, we observe that it depends on the algorithm and grid parameters.

We have also increased the value of the background level ($B = 1.5$) and realized that both I_{RW} and I_{max} increase significantly, so that $I_{RW} > 9$. However, once we magnify the breather structures in such an evolution, we realize that very high intensities at the breather's center do not correspond to the nth-order AB, as expected ($n \geq 3$), but retain the intensity distribution pattern characteristic of the second-order AB. Such dynamics can deceive the observer since it produces Akhmediev breathers of intrinsically larger intensity that could be generated through Darboux transformation using the seed function with modulus greater than one (which usually is not the case in literature). Therefore, one should stick to the $B = 1$ case.

The third conclusion is that the higher the noise amplitude A is, the larger is the total number of maxima N_{TP}. In Fig. 8, we also observe millions of peaks
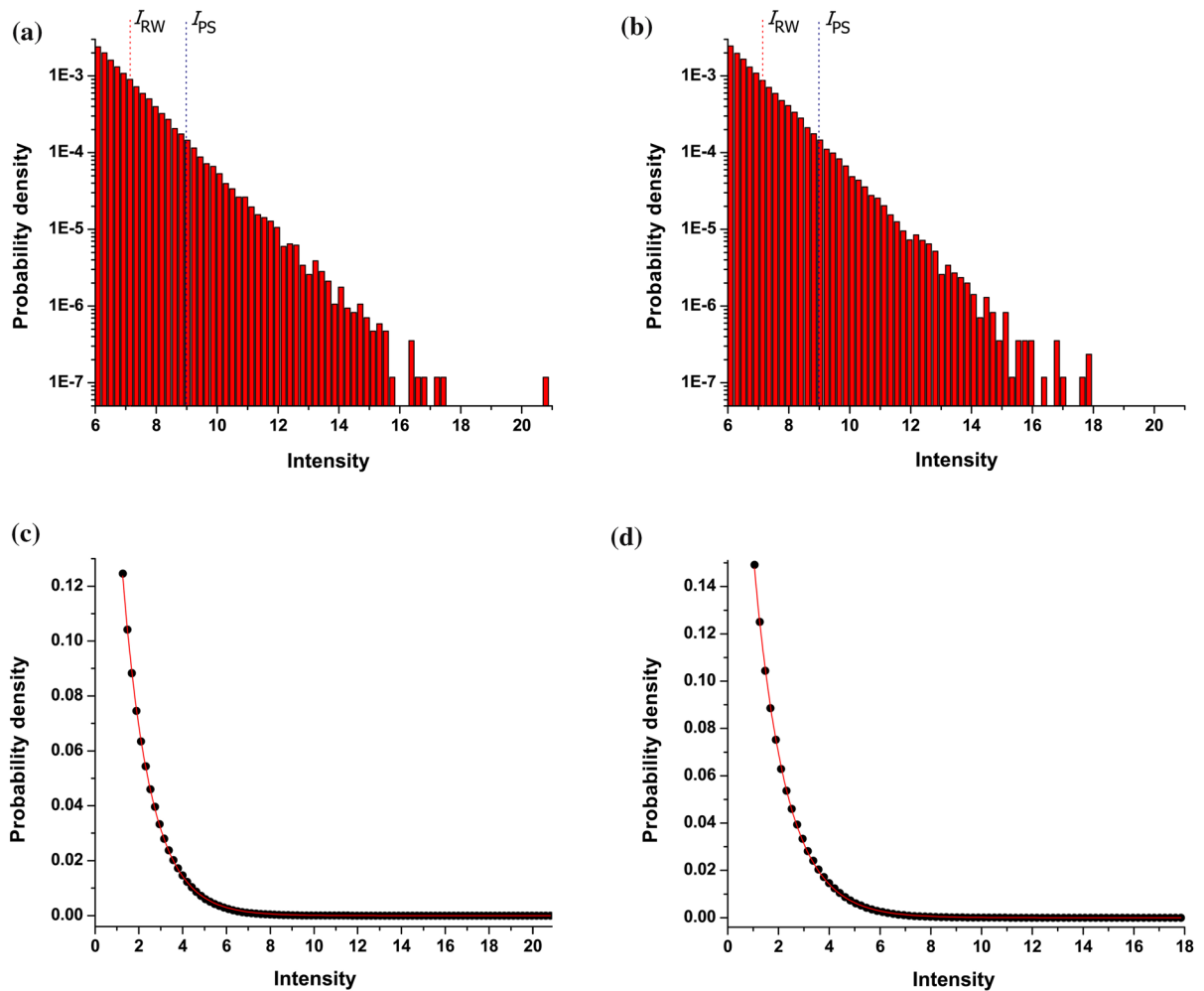
Fig. 7 Statistics of the intensity maxima, obtained from Fig. 5. The peak intensity histograms are derived from evolutions obtained by the execution of two different numerical algorithms: **a** The second-order beam propagation, and **b** the fourth-order symplectic method. Two vertical dashed lines indicate the Peregrine soliton intensity $I_{PS}=9$ and the statistical RW threshold I_{RW}. The exponential decay fits for Figs. **a** and **b** are presented in Figs. **c** and **d**, respectively

and thousands of RWs (N_{RW} and N_{PS}, according to the adopted RW definition). The fractions of peaks that can be considered as rogue waves (F_{RW} and F_{PS}) is considerably lower than 1% and relatively weekly depend on the algorithm and noise amplitude A.

Our final conclusion is that the most prominent difference between statistical results obtained by two algorithms for the same A value is observed at higher intensities. The second-order breathers that approach the limiting intensity value of 25 at its center arise in the collision of highly unstable modes during evolution. By switching from BPM to 4S algorithm one changes the way and the number of mathematical operations needed for the calculation of ψ values. This difference affects more the collision processes of highly unstable modes that then lead to high intensity maxima. Overall, these conclusions strengthen the claim that different numerical algorithms produce different statistics, especially in the long tail region of high intensities, where RWs exist.

We got similar results and confirmed our conclusions by using two times smaller evolution step ($dx = 0.0005$) or the transversal box size ($L/2 \approx 35$, instead of 70) (results not shown).
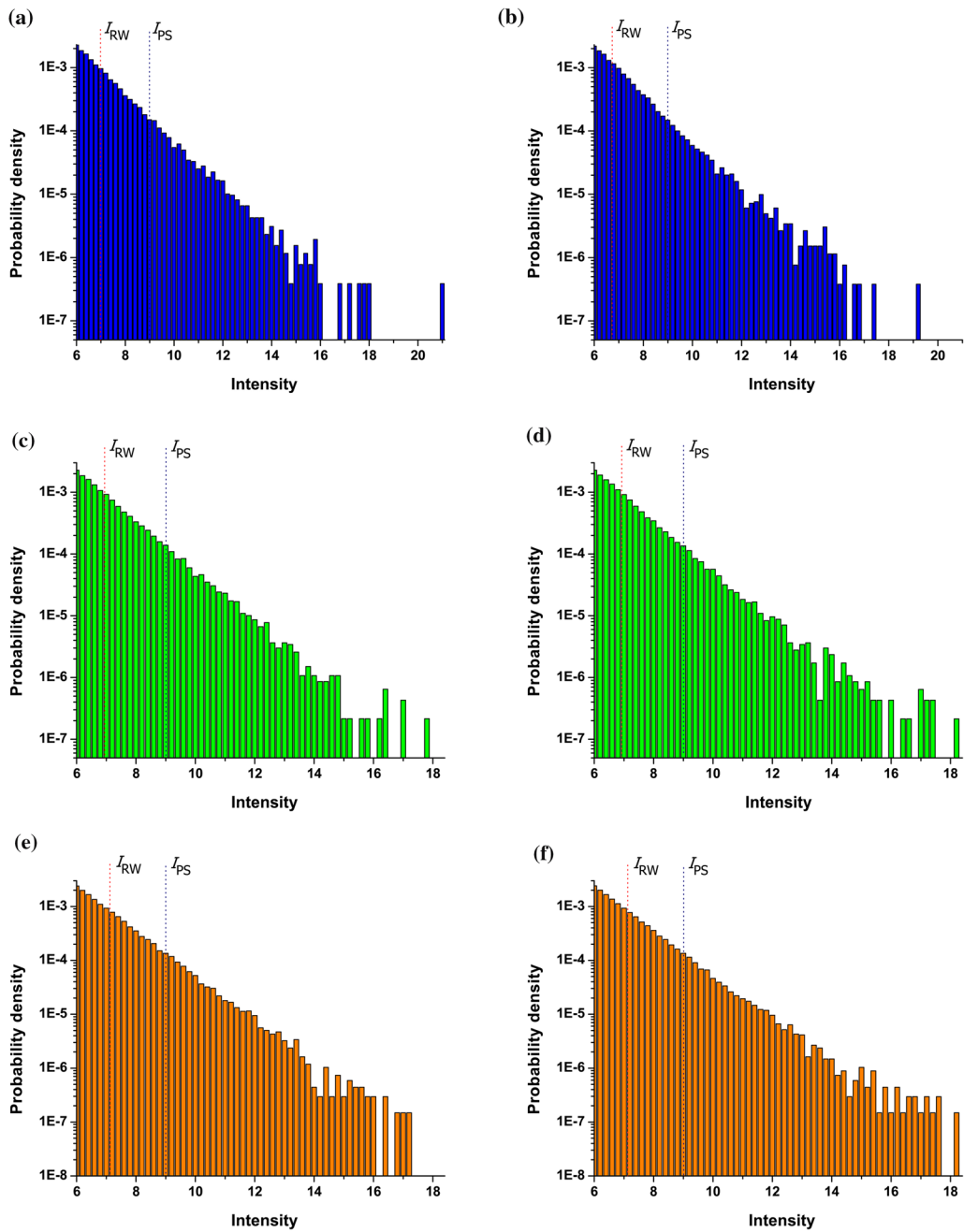
Fig. 8 Statistics of high intensity peaks obtained from evolution of the NLSE wave function, seeded by noises of different amplitude A around the background intensity of $B = 1$. The wave evolution proceeds from 0 to 6500 propagation units with evolution step $dx = 10^{-3}$; the transverse box is approximately from -70 to 70 units. There are $6.5 \times 10^6 \times 2048$ grid points. The algorithm used for numerical integration of wave function and amplitude A are: **a** BPM, $A = 1\%$, **b** the fourth-order symplectic method (4S), $A = 1\%$, **c** BPM, $A = 2\%$, **d** 4S, $A = 2\%$, **e** BPM, $A = 3.5\%$, and **f** 4S, $A = 3.5\%$. Two vertical dashed lines indicate the Peregrine soliton intensity and the statistical RW threshold

Table 1 Statistics of the wave function intensity maxima calculated during evolution with the white noise of amplitude A around the background value of $B = 1$

Alg.	$A\%$	I_{max}	N_{TP}	I_{RW}	N_{RW}	$F_{RW}\%$	N_{PS}	$F_{PS}\%$
2	1.0	21.05	2,585,329	6.86	16,865	0.652	2,616	0.102
4S	1.0	19.27	2,631,233	6.73	19,148	0.728	2,499	0.095
2	2.0	17.92	4,653,505	6.96	24,804	0.533	3.645	0.078
4S	2.0	18.21	4,662,564	6.93	25,380	0.544	3,610	0.078
2	3.5	17.35	6,777,188	7.12	32,104	0.474	5,261	0.078
4S	3.5	18.37	6,766,308	7.11	32,322	0.478	5,220	0.077
2	5.0	20.86	8,493,287	7.14	41,406	0.488	6,833	0.080
4S	5.0	18.03	8,494,281	7.15	40,996	0.483	6,992	0.082

Algorithms used for computations are the second-order beam propagation method (Alg. 2) and the fourth-order symplectic (Alg. 4S). The meaning of marks in the table top row are: I_{RW} - the maximum achieved intensity over the entire xt-grid, N_{TP} - the total number of peaks, I_{RW} - the RW intensity threshold, N_{RW} - the number of maxima having the intensity $I \geq I_{RW}$, $F_{RW} = N_{RW}/N_{TP}$, N_{PS} - the number of maxima exceeding the Peregrine soliton intensity ($I_{PS} = 9$), and $F_{PS} = N_{PS}/N_{TP}$

3 Conclusion

In conclusion, we have discussed the facts and fictions related to the strange nature, dynamic generation, ingrained instability, and potential applications of RWs.

We have proposed the method of mode pruning for suppressing the modulation instability of rogue waves. Using this procedure, we have computed and demonstrated the stable numerical Talbot carpets—the recurrent images of light and plasma waves—by rogue waves, for possible use in nanolithography. The pruning procedure was found indispensable in the production of stable recurring periodic images over wide but still finite windows.

We have also discussed the nature of optical rogue waves, in view of conflicting opinions expressed in the literature. In particular, we have addressed the three pairs of opposing suppositions on their nature: Linear versus nonlinear; random versus deterministic; and numerical versus physical. In summary, a correct answer to the three suppositions is that the rogue waves in optics are essentially nonlinear, deterministic, and physical. They are nonlinear because the major cause of rogue waves is the modulation or Benjamin–Feir instability, which by its nature is the basic nonlinear optical process. Rogue waves are deterministic because modulation instability leads to deterministic chaos; random phenomena are probabilistic and may look chaotic but are not deterministic. Rogue waves are physical because they appear in many experiments and media, with similar statistics.

Nevertheless, in numerical simulations optical rogue waves may appear fictitiously, as numerical artefacts. Different numerical algorithms for exactly the same inputs may provide different evolution pictures and—distressingly—different statistics of RWs, caused by imprecisely chosen integration steps and intrinsic modulation instability. An overall conclusion is that the numerical and statistical treatments of NLSE by different algorithms represent different dynamical systems that may introduce different long-time behaviors when they are unstable and under the influence of MI. Therefore, owing to a vague definition of rogue waves, different ways in which they are generated, and an exponential amplification of numerical errors in chaos, there are situations in which optical rogue waves may appear as linear, random, and numerical.

Data Availability Statement All data generated or analyzed during this study are included in the published article.

Declarations

Conflict of interest The authors declare that they have no conflict of interest.

References

1. Kivshar, Y.S., Agrawal, G.P.: Optical Solitons. Academic Press, San Diego (2003)
2. Fibich, G.: The Nonlinear Schrödinger Equation. Springer, Berlin (2015)
3. Dudley, J.M., Dias, F., Erkintalo, M., Genty, G.: Instabilities, breathers and rogue waves in optics. Nature Phot. **8**, 755 (2014)
4. Dudley, J.M., Taylor, J.M.: Supercontinuum Generation in Optical Fibers. Cambridge University Press, Cambridge (2010)
5. Solli, D.R., Ropers, C., Koonath, P., Jalali, B.: Optical rogue waves. Nature **450**, 1054 (2007)
6. Mirzazadeh, M., Eslami, M., Zerrad, E., Mahmood, M.F., Biswas, A., Belić, M.: Optical solitons in nonlinear directional couplers by sine-cosine function method and Bernoulli's equation approach. Nonlinear Dyn. **81**, 1933–1349 (2015)
7. Khalique, C.M.: Stationary solutions for nonlinear dispersive Schrödinger equation. Nonlinear Dyn. **63**, 623–626 (2011)
8. Ankiewicz, A., Kedziora, D.J., Chowdury, A., Bandelow, U., Akhmediev, N.: Infinite hierarchy of nonlinear Schrödinger equations and their solutions. Phys. Rev. E **93**, 012206 (2016)
9. Nikolić, S.N., Aleksić, N.B., Ashour, O.A., Belić, M.R., Chin, S.A.: Systematic generation of higher-order solitons and breathers of the Hirota equation on different backgrounds. Nonlinear Dyn. **89**, 1637–1649 (2017)
10. Nikolić, S.N., N.B., Aleksić, Ashour, O.A., Belić, M.R., Chin, S.A.: Breathers, solitons and rogue waves of the quintic nonlinear Schrödinger equation on various backgrounds. Nonlinear Dyn. **95**, 2855–2865 (2019)
11. Chin, S.A., Ashour, O.A., Nikolić, S.N., Belić, M.R.: Peak-height formula for higher-order breathers of the nonlinear Schrödinger equation on nonuniform backgrounds. Phys. Rev. E **95**, 012211 (2017)
12. Bogolubov, N.: On the theory of superfluidity. J. Phys. (USSR) **11**, 23 (1947)
13. Chin, S.A., Ashour, O.A., Belić, M.R.: Anatomy of the Akhmediev breather: cascading instability, first formation time, and Fermi-Pasta-Ulam recurrence. Phys. Rev. E **92**, 063202 (2015)
14. Marquié, P., Bilbault, J.M., Remoissenet, M.: Nonlinear Schrödinger models and modulational instability in real electrical lattices. Physica D **87**, 371–374 (1995)
15. Tang, B., Deng, K.: Discrete breathers and modulational instability in a discrete ϕ^4 nonlinear lattice with next-nearest-neighbor couplings. Nonlinear Dyn. **88**, 2417–2426 (2017)
16. Dias, W.S., Sousa, J.F.A., Lyra, M.L.: From modulational instability to self-trapping in nonlinear chains with power-law hopping amplitudes. Phys. A **532**, 121909 (2019)
17. Akhmediev, N., et al.: Roadmap on optical rogue waves and extreme events. J. Opt. **18**, 063001 (2016)
18. Fleischhauer, M., Imamoglu, A., Marangos, J.P.: Electromagnetically induced transparency: optics in coherent media. Rev. Mod. Phys. **77**, 633–673 (2005)
19. Nikolić, S.N., Radonjić, M., Krmpot, A.J., Lučić, N.M., Zlatković, B.V., Jelenković, B.M.: Effects of a laser beam profile on Zeeman electromagnetically induced transparency in the Rb buffer gas cell. J. Phys. B: At. Mol. Opt. Phys. **46**, 075501 (2013)
20. Krmpot, A.J., Ćuk, S.M., Nikolić, S.N., Radonjić, M., Slavov, D.G., Jelenković, B.M.: Dark Hanle resonances from selected segments of the Gaussian laser beam cross-section. Opt. Express **17**, 22491–22498 (2009)
21. Nikolić, S.N., Radonjić, M., Lučić, N.M., Krmpot, A.J., Jelenković, B.M.: Transient development of Zeeman electromagnetically induced transparency during propagation of Raman–Ramsey pulses through Rb buffer gas cell. J. Phys. B: At. Mol. Opt. Phys. **48**, 045501 (2015)
22. Li, Z.-Y., Li, F.-F., Li, H.-J.: Exciting rogue waves, breathers, and solitons in coherent atomic media. Commun. Theor. Phys. **72**, 075003 (2020)
23. Akhmediev, N., Soto-Crespo, J.M., Ankiewicz, A.: Extreme waves that appear from nowhere: on the nature of rogue waves. Phys. Lett. A **373**, 2137 (2009)
24. Akhmediev, N.N., Korneev, V.I.: Modulation instability and periodic solutions of the nonlinear Schrödinger equation. Theor. Math. Phys. **69**, 1089 (1986)
25. Akhmediev, N., Eleonskii, V., Kulagin, N.: Exact first-order solutions of the nonlinear Schrödinger equation. Theor. Math. Phys. **72**, 809 (1987)
26. Erkintalo, M., Hammani, K., Kibler, B., Finot, C., Akhmediev, N., Dudley, J.M., Genty, G.: Higher-order modulation instability in nonlinear fiber optics. Phys. Rev. Lett. **107**, 253901 (2011)
27. Chin, S.A., Ashour, O.A., Nikolić, N.N., Belić, M.R.: Maximal intensity higher-order Akhmediev breathers of the nonlinear Schrödinger equation and their systematic generation. Phys. Lett. A **380**, 3625 (2016)
28. Herbst, B.M., Ablowitz, M.J.: Numerically induced chaos in the nonlinear Schrödinger equation. Phys. Rev. Lett. **62**, 2065 (1989)

29. Ablowitz, M.J., Herbst, B.M.: On homoclinic structure and numerically induced chaos for the nonlinear Schrödinger equation. SIAM J. Appl. Math. **50**, 339 (1990)

30. Calini, A., Schober, C.M.: Homoclinic chaos increases likelihood of rogue wave formation. Phys. Lett. A **298**, 335 (2002)

31. Calini, A., Schober, C.M.: Dynamical criteria for rogue waves in nonlinear Schrödinger models. Nonlinearity **25**, R99 (2012)

32. Nikolić, S.N., Ashour, O.A., Aleksić, N.B., Zhang, Y., Belić, M.R., Chin, S.A.: Talbot carpets by rogue waves of extended nonlinear Schrödinger equations. Nonlinear Dyn. **97**, 1215 (2019)

33. Zhang, Y.Q., Belić, M.R., Zheng, H., Chen, H., Li, C., Song, J., Zhang, Y.P.: Nonlinear Talbot effect of rogue waves. Phys. Rev. E **89**, 032902 (2014)

34. Zhang, Y., Belić, M.R., Petrović, M.S., Zheng, H., Chen, H., Li, C., Lu, K., Zhang, Y.: Two-dimensional linear and nonlinear Talbot effect from rogue waves. Phys. Rev. E **91**, 032916 (2015)

35. Geints, Y.E., Minin, O.V., Minin, I.V., Zemlyanov, A.A.: Self-images contrast enhancement for displacement Talbot lithography by means of composite mesoscale amplitude-phase masks. J. Opt. **22**, 015002 (2020)

36. Chausse, P., Shields, P.: Spatial periodicities inside the Talbot effect: understanding, control and applications for lithography. Opt. Express **29**, 27628 (2021)

37. Shi, Z., Jefimovs, K., Romano, L., Stampanoni, M.: Optimization of displacement Talbot lithography for fabrication of uniform high aspect ratio gratings. Jpn. J. Appl. Phys. **60**(SCCA01), 1–4 (2021)

38. Ashour O.A.: Maximal intensity higher-order breathers of the nonlinear Schrödinger equation on different backgrounds. Undergraduate Research Scholars Thesis, Texas A&M University, USA (2017)

39. Onorato, M., Residori, S., Bortolozzo, U., Montina, A., Arecchi, F.T.: Rogue waves and their generating mechanisms in different physical contexts. Phys. Rep. **528**, 47–89 (2013)

40. Montina, A., Bortolozzo, U., Residori, S., Arecchi, F.T.: Non-gaussian statistics and extreme waves in a nonlinear optical cavity. Phys. Rev. Lett. **103**, 173901 (2009)

41. Randoux, S., Walczak, P., Onorato, M., Suret, P.: Intermittency in integrable turbulence. Phys. Rev. Lett. **113**, 113902 (2014)

42. Toenger, S., Godin, T., Billet, C., Dias, F., Erkintalo, M., Genty, G., Dudley, J.M.: Emergent rogue wave structures and statistics in spontaneous modulation instability. Sci. Rep. **5**, 10380 (2015)

43. Arecchi, F.T., Bortolozzo, U., Montina, A., Residori, S.: Granularity and inhomogeneity are the joint generators of optical rogue waves. Phys. Rev. Lett. **106**, 153901 (2011)

44. Kedziora, D.J., Ankiewicz, A., Akhmediev, N.: Circular rogue wave clusters. Phys. Rev. E **84**, 056611 (2011)

45. Akhmediev, N., Soto-Crespo, J.M., Ankiewicz, A.: How to excite a rogue wave. Phys. Rev. A **80**, 043818 (2009)

46. Kharif, C., Pelinovsky, E., Slunyaev, E.: Rogue Waves in the Ocean. Springer, Berlin (2009)

47. Dudley, J.M., Genty, G., Mussot, A., Chabchoub, A., Dias, F.: Rogue waves and analogies in optics and oceanography. Nat. Rev. Phys. **1**, 675–689 (2019)

48. Tlidi, M., Panajotov, K.: Two-dimensional dissipative rogue waves due to time-delayed feedback in cavity nonlinear optics. Chaos **27**, 013119 (2017)

49. Agafontsev, D.S., Zakharov, V.E.: Integrable turbulence and formation of rogue waves. Nonlinearity **28**, 2791–2821 (2015)

50. Bertola, M., El, G.A., Tovbis, A.: Rogue waves in multiphase solutions of the focusing nonlinear Schrödinger equation. Proc. R. Soc. A **472**, 20160340 (2016)

Higher-order breathers as quasi-rogue waves on a periodic background

Omar A. Ashour · **Siu A. Chin** ·
Stanko N. Nikolić · **Milivoj R. Belić**

Abstract We investigate higher-order breathers of the
cubic nonlinear Schrödinger equation on a periodic
elliptic background. We find that, beyond first order,
any arbitrarily constructed breather on a disordered
background generates a single-peaked solitary wave.
However, on the periodic backgrounds, the so-called
quasi-rogue waves are found more common. These
are the quasiperiodic breathers that feature distorted
side peaks. We construct such higher-order breathers
out of constituent first-order breathers with commen-
surate periods (i.e., as higher-order harmonic waves).
In addition to quasiperiodic, we also find fully peri-
odic breathers, when their wavenumbers are harmonic
multiples of the background and each other. But they
are truly rare, requiring finely tuned parameters. Thus,
on a periodic background, we arrive at the paradoxical
conclusion that the higher-order quasi-rogue waves are
rather common, while the truly periodic breathers are
exceedingly rare.

1 Introduction

The dimensionless cubic nonlinear Schrödinger (NLS)
equation [1], given by

$$i\frac{\partial \psi}{\partial x} + \frac{1}{2}\frac{\partial^2 \psi}{\partial t^2} + \psi\,|\psi|^2 = 0, \tag{1}$$

with t and x being the transverse and longitudinal
variables and $\psi \equiv \psi(x, t)$ the slowly varying wave
envelope, has been widely used in the field of nonlin-
ear optics and photonics to guide experimental real-
izations [2–4] and theoretical explorations [5–11] of
higher-order breathers and rogue waves (RWs) in opti-
cal fibers. For a recent review, see Ref. [12]. The physics
of RWs is getting more attention since a new scheme
to excite RWs, such as via electromagnetically induced
transparency (EIT) [13–15], is proposed [16].

While the study of breathers and RWs on a uniform
background, including those based on extended NLS
equations, has matured by now, with a vast body of ana-
lytical results [6,8,12,17–22], similar studies on peri-
odic backgrounds have started only recently [9,23–25].
For clarity, at this place we provide a short outlook on

O. A. Ashour (✉)
Department of Physics, University of California, Berkeley,
CA 94720, USA
e-mail: ashour@berkeley.edu

S. A. Chin
Department of Physics and Astronomy, Texas A&M
University, College Station, TX 77843, USA

S. N. Nikolić
Institute of Physics Belgrade, University of Belgrade,
Pregrevica 118, Belgrade 11080, Serbia

S. N. Nikolić · M. R. Belić
Science Program, Texas A&M University at Qatar, P.O. Box
23874, Doha, Qatar

the interconnection between different waveforms that
are encountered in the field thus far. Foremost, to see
interesting new waveforms, one needs a background.
Without background, at most one can observe bright
solitons [1,12]. Normally, breathers and RWs (higher-
order breathers) are generated when one seeds the back-
ground with proper initial wave conditions, based on
the Darboux transformation (DT). Such initial waves
also provide conditions for the breather-to-soliton con-
version, both bright and dark, which usually are dif-
ficult to observe in NLS equation without proper sys-
tem preparation. Thus, starting a numerical experiment
with uniform or randomly perturbed background and an
arbitrary collection of Stokes waves will only occasion-
ally, here and there, produce a second-order RW, almost
never higher-order RWs. For observing a full wealth of
different waveforms (breathers, solitons, RWs of dif-
ferent order, quasiperiodic and fully periodic RWs),
in general one needs specially prepared nonuniform
backgrounds and specially prepared initial waves. Pre-
viously, we considered backgrounds perturbed by the
Jacobi elliptic functions (JEFs) and initial waves com-
ing from Akhmediev breathers engineered using DT
[24,25]. The fine point in the numerical procedure is
how to prepare boundary conditions on the numerical
window.

In this work, we are specifically interested in
breathers of the simple cubic NLS equation on the
dnoidal Jacobi elliptic function (JEF) background,
which has the form:

$$\psi_0(x, t) = \mathrm{dn}(t; k)e^{ix(1-\frac{k^2}{2})}, \qquad (2)$$

where k is the elliptic *modulus* (not to be confused with
the elliptic *parameter*, k^2). As our analysis will show
below, at this time it is unlikely that one can derive
analytical expressions for our breathers; therefore, we
focus on studying solutions of (1) using a numerical
implementation of the analytical DT procedure [7–11].
In a nutshell, the procedure states that given a simple,
zeroth-order "seed" solution $\psi_0(x, t)$ of (1), such as (2),
one can generate an Nth-order solution recursively via:

$$\psi_N(x, t) = \psi_0(x, t) + \sum_{m=1}^{N} \frac{2i r_{m1} s_{m1}^* \left(\lambda_m - \lambda_m^*\right)}{|r_{m1}|^2 + |s_{m1}|^2}, \qquad (3)$$

where the sum goes over N constituent first-order
solutions of the Lax pair equation, characterized by

generally complex eigenvalues λ_m. The two functions
$r_{m1}(x, t)$ and $s_{m1}(x, t)$ are the Lax pair generating func-
tions for the mth first-order constituent breather. In this
work, we restrict ourselves to purely imaginary eigen-
values:

$$\lambda_m = i\nu_m, \quad \text{with} \quad 0 < \nu_m < 1, \qquad (4)$$

corresponding to Akhmediev-type breathers [26], rather
than Kuznetsov–Ma-type breathers [27,28]. As per the
peak height formula (PHF) [23], these solutions have
a peak height of

$$\psi_N(0, 0) = 1 + 2\sum_{m=1}^{N} \nu_m. \qquad (5)$$

In this work, we will concentrate on demonstrat-
ing the surprising finding mentioned in the abstract:
Beyond first order, any arbitrarily constructed breather
on an elliptic background looks very much like a rogue
wave. But, to generate quasiperiodic and fully periodic
RWs one needs to pay close attention how the periodici-
ties of constituent waves are arranged over the available
numerical window. We relegate all technical details on
the DT and PHF to the appendix.

The paper is structured as follows. In Sect. 2, we
demonstrate, by enforcing the reality of the wavenum-
ber, that in contrast to the uniform background case
[17,18], the first-order breathers on an elliptic back-
ground can at most be quasiperiodic in the t-direction
unless the matching condition (23) is obeyed. The con-
catenation of N such first-order breathers then gener-
ally results in an *aperiodic* Nth-order breather greatly
resembling a rogue wave (RW). In Sect. 3, we show that
if the periods of the constituent first-order breathers
are commensurate with one another, then one sees a
quasiperiodic Nth-order breather, where the repeating
side peaks are distorted by the background. In Sect.
4, we show that truly periodic Nth-order breathers are
produced if and only if the periods of the constituent
first-order breathers are all matched to that of the back-
ground. This requires restricting the parameters ν and k
to a special set of contours γ_q (Eq. 23) in the νk-plane.
Our conclusions are summarized in Sect. 5.

2 Aperiodic breathers on an elliptic background

For a breather to be periodic (along the t direction), its
wavenumber must be real [9]. Assuming purely imag-

inary eigenvalues $\lambda_m = i\nu_m$, the half-wavenumber is given by

$$\kappa_m = \sqrt{\left(\lambda_m - \frac{k^2}{4\lambda_m}\right)^2 + 1} = \sqrt{1 - \left(\nu_m + \frac{k^2}{4\nu_m}\right)^2}. \tag{6}$$

For κ_m to be real, we must have

$$\left(\nu_m + \frac{k^2}{4\nu_m}\right)^2 \leq 1 \implies k^2 \leq 4\nu_m(1 - \nu_m), \tag{7}$$

which restricts the range of ν_m to

$$\frac{1}{2} - \frac{1}{2}\sqrt{1 - k^2} \leq \nu_m \leq \frac{1}{2} + \frac{1}{2}\sqrt{1 - k^2}. \tag{8}$$

Alternatively, from (7) one sees that

$$k^2 \leq 4\left[\frac{1}{2} + \left(\nu_m - \frac{1}{2}\right)\right]\left[\frac{1}{2} - \left(\nu_m - \frac{1}{2}\right)\right], \tag{9}$$

or

$$k^2 + \frac{(\nu_m - \frac{1}{2})^2}{(1/2)^2} \leq 1, \tag{10}$$

which then restricts (ν_m, k) to half of an ellipse Γ, centered on (1/2,0), with the vertical semimajor axis being 1 and the horizontal semiminor axis 1/2. This is shown in Fig. 6 and summarized succinctly by

$$(\nu_m, k) \in \Gamma$$
$$:= \left\{(\nu_m, k) \in (0, 1) \times [0, 1] \,\bigg|\, k^2 + \frac{(\nu_m - \frac{1}{2})^2}{(1/2)^2} \leq 1\right\}. \tag{11}$$

In Fig. 1, we show the three periods of a first-order breather obeying the κ-reality condition (11). This breather is not periodic since the repeating side peaks are *not* identical to the central peak. Next, in Fig. 2, we show a set of higher-order breathers. Their eigenvalues ν_m obey (11), but are otherwise arbitrary. These higher-order breathers are even more aperiodic, with the repeating side peaks highly distorted and diminished in intensity, leaving only a central peak of great height intact. It is a matter of definition how one defines a rogue wave, but Fig. 2 clearly shows four solitary, high-intensity peaks amid an increasingly disordered background, each resembling more an oceanic rogue wave than a breather. We will refer to these unmatched solutions as *quasi-rogue waves* (QRWs). The phenomenon

of QRW has only come to light recently in the study of higher-order breathers on periodic backgrounds [25,29]. They are not apparent in the study of first-order breathers on a periodic background, nor are they mentioned in the study of RWs on a constant background.

3 Quasiperiodic breathers

We now match the periods of the constituent breathers of these higher-order structures to the fundamental breather, i.e.:

$$\kappa_m = m\kappa, \qquad m = 2, 3, \dots N, \tag{12}$$

where $\kappa \equiv \kappa_1$ is the period of the fundamental breather, characterized by $\nu \equiv \nu_1$. We choose the constituent breather wave numbers to be harmonics of each other, analogously to the uniform background case where these breathers would have been strictly periodic and of maximal peak height (at a given periodicity) [18]. Writing out (12) explicitly gives

$$m\sqrt{-\frac{k^4}{16\nu^2} - \frac{k^2}{2} - \nu^2 + 1}$$
$$= \sqrt{-\frac{k^4}{16\nu_m^2} - \frac{k^2}{2} - \nu_m^2 + 1}, \tag{13}$$

which leads to an expression for ν_m in terms of ν and k

$$\nu_m(k, \nu) = \frac{\sqrt{G_m(k, \nu) + \sqrt{[G_m(k, \nu)]^2 - 64k^4\nu^4}}}{4\sqrt{2}\nu}, \tag{14}$$

where

$$G_m(k, \nu) \equiv k^4 m^2 + 8\left(k^2 - 2\right)\left(m^2 - 1\right)\nu^2 + 16m^2\nu^4. \tag{15}$$

A plot of Eq. (14) for multiple values of m is shown in Fig. 3. Note that in Fig. 3, the curves $\nu_m(k)$, $\forall\, m \in \mathbb{Z}^+$, clearly intersect at a point $(\nu_{\max}, \nu_{\max})$ in the $\nu\nu_m$-plane, given by the upper limit of Eq. (8):

$$\nu_{\max}(k) = \frac{k'}{2} + \frac{1}{2}, \tag{16}$$

Fig. 1 First-order breather with $(\nu = 0.8602, k = 3/5) \in \Gamma$ (i.e., $\kappa \in \mathbb{R}$). The distortion of the side peaks is evident in the contour plot. In all contour plots that follow, maroon represents the background ($|\psi| = 1$), teal green is 0.25 *above* the background, while light orange is 0.2 *below* the background. The remaining colors denote other relevant low-$|\psi|$ features. The colormap is designed to showcase only the relevant low-$|\psi|$ features of the breathers, with a maximum height of 0.8 above the background
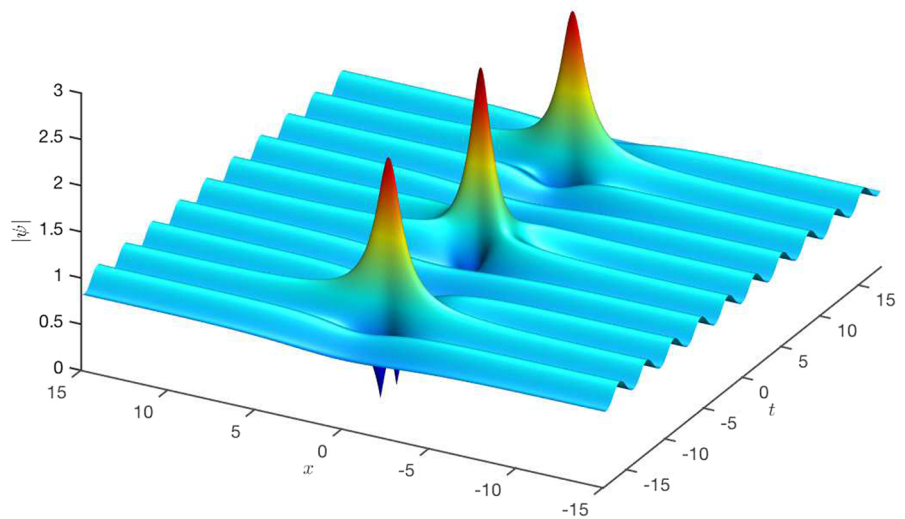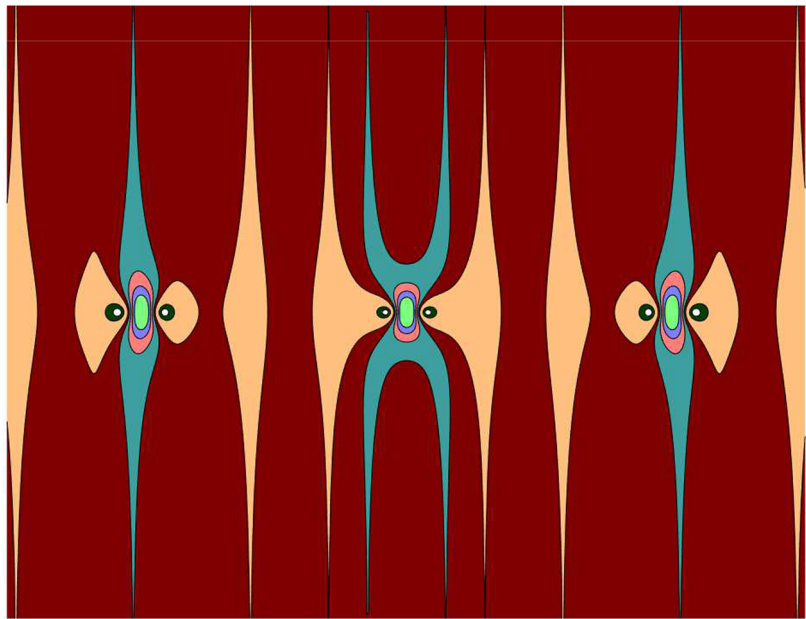
where $k' \equiv \sqrt{1 - k^2}$ is the complementary elliptic modulus. A first-order solution characterized by this value of ν is known as the concentrated cnoidal rogue wave (CCRW) [9] and was simply referred to as the "bright" rogue wave in Ref. [23]. This solution with $\kappa = 0$ is a single solitary peak on a periodic background and is considered the natural generalization of the Peregrine rogue wave on a constant background. However, higher-order rogue waves generated by multiple values of (16) have degeneracy problems and cannot be described by the DT [10]. By contrast, as shown

in Fig. 2, an arbitrary high-order QRW can be easily constructed using DT.

Figure 3, showing the plot of Eq. (14), implies that for a fixed m, there is some cutoff $\nu = \nu_m^*(k)$ such that $\nu_l(\nu = \nu_m^*, k) \notin \mathbb{R} \, \forall l > m$. Thus, to generate a breather of order at most N, one must have $\nu \in (\nu_N^*, \nu_{N+1}^*]$. The imaginary part of $\nu_m(k, \nu)$ will be nonzero if and only if the term under the inner square root in (14) is negative. Thus, to find ν_m^*, we need to solve:

$$\left[G_m(k, \nu = \nu_m^*) \right]^2 - 64k^4(\nu_m^*)^4 = 0 \,. \tag{17}$$
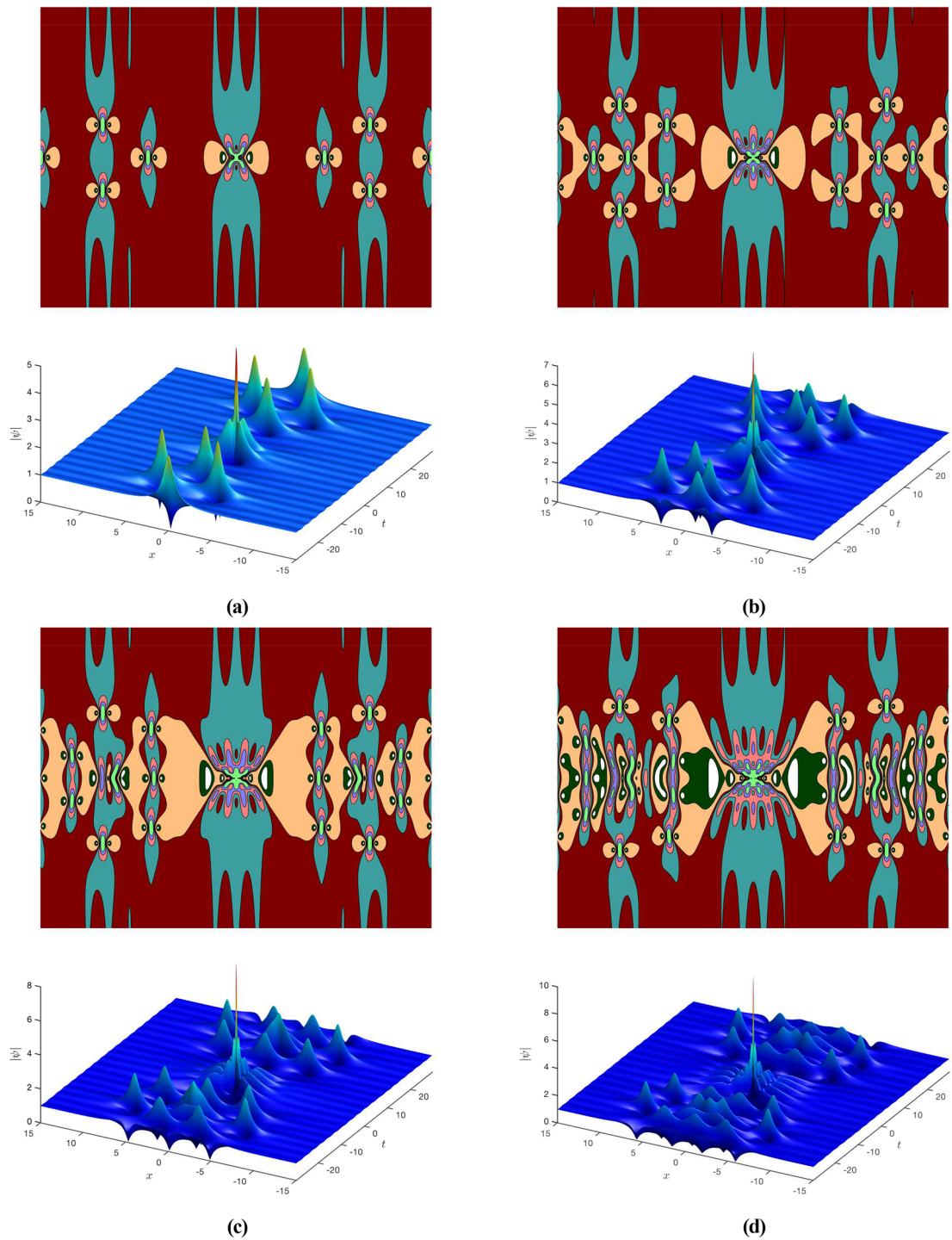
Fig. 2 Higher-order breathers on a dn background with $k = 1/4$ and $\kappa_m \in \mathbb{R}$. **a** Second-order, with $\{v_m\} = \{0.98, 0.91\}$. **b** Third-order, with $\{v_m\} = \{0.98, 0.91, 0.84\}$ **c** Fourth-order, with $\{v_m\} = \{0.98, 0.91, 0.84, 0.72\}$ **d** Fifth-order, with $\{v_m\} = \{0.98, 0.91, 0.84, 0.72, 0.51\}$. Inserts: Contour plots to emphasize the low-$|\psi|$ details

Fig. 3 Plot of the eigenvalues ν_m given by (14) as a function of ν, with $k = 2/5$. The dashed vertical lines represent the lower limit ν_m^* (Eq. 18), and the horizontal lines give the upper and lower limit on ν_m
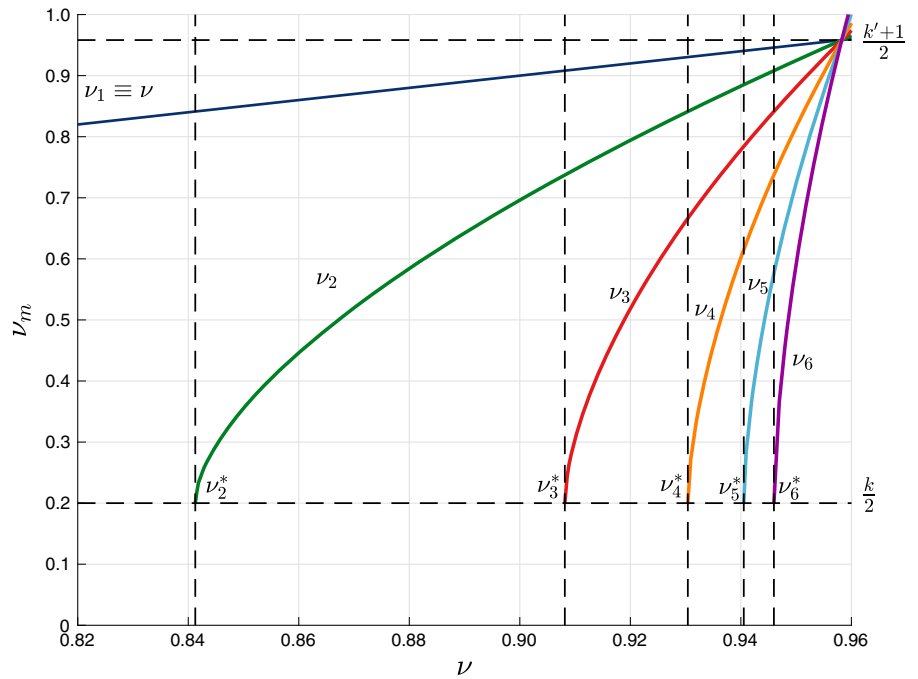
Fig. 4 Plot of the peak height formula (5) at $k = 1/2$ using the eigenvalues given by (14). The insert shows a zoomed-in version of the region between the peak heights of first- and second-order breathers, with a gap of $\Delta\psi(0, 0) = 1/2 = k$
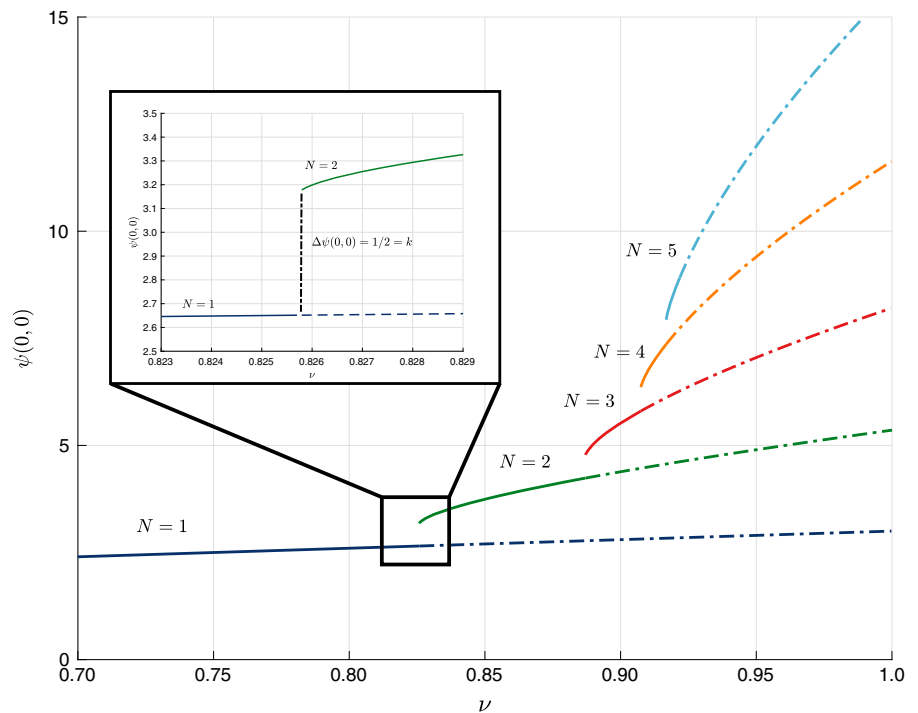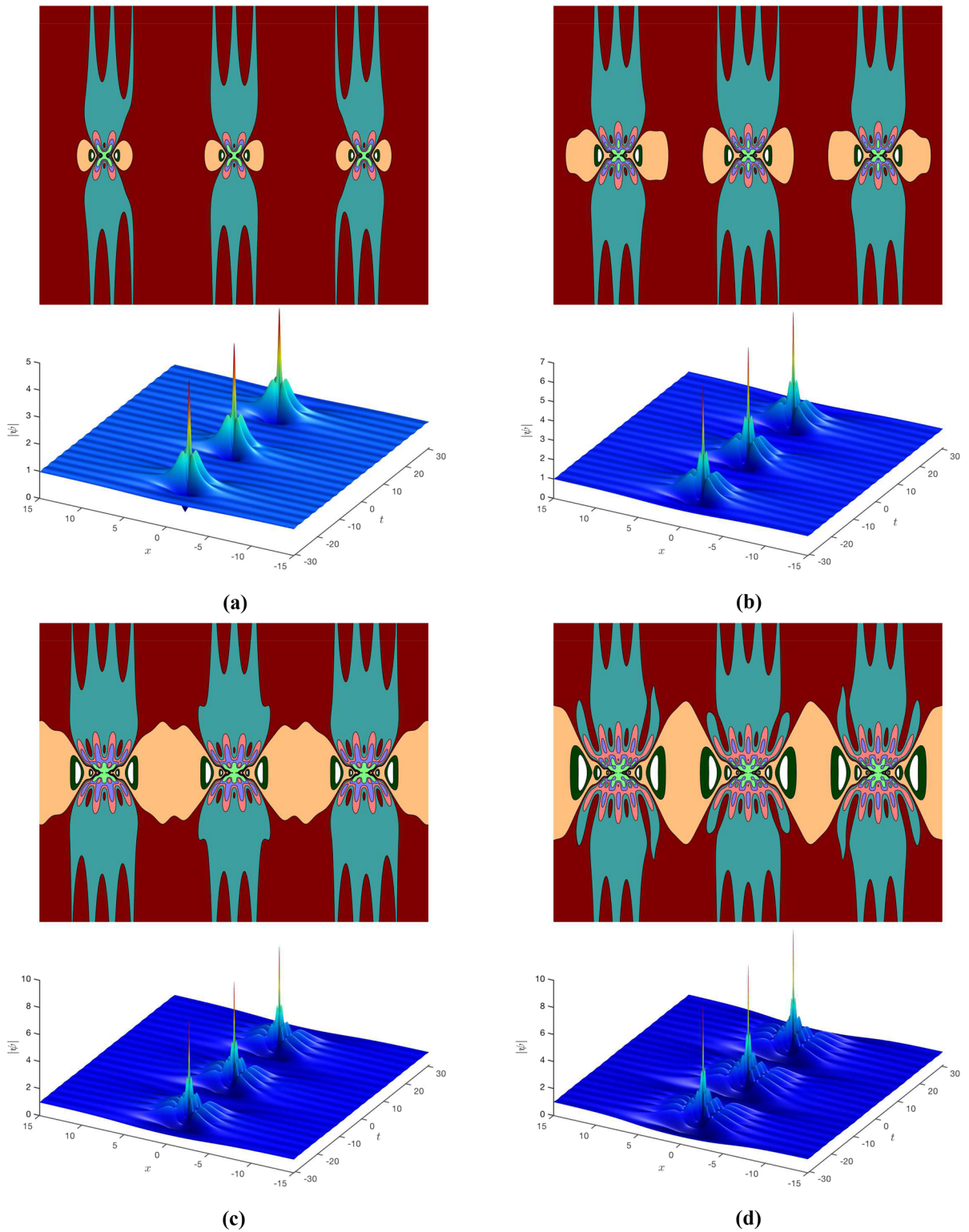
Fig. 5 Quasiperiodic higher-order breathers with ($\nu \approx 0.972$, $k = 1/4$), and higher-order ν_m computed via Eq. (14) **a** second order **b** third order **c** fourth order **d** fifth order. Inserts: contour plots to emphasize the low-$|\psi|$ details

Fig. 6 νk-plane, showing different regions of periodicity. The light blue shaded region is where κ is real, given by (11). The solid curves correspond to different values of q in (23)
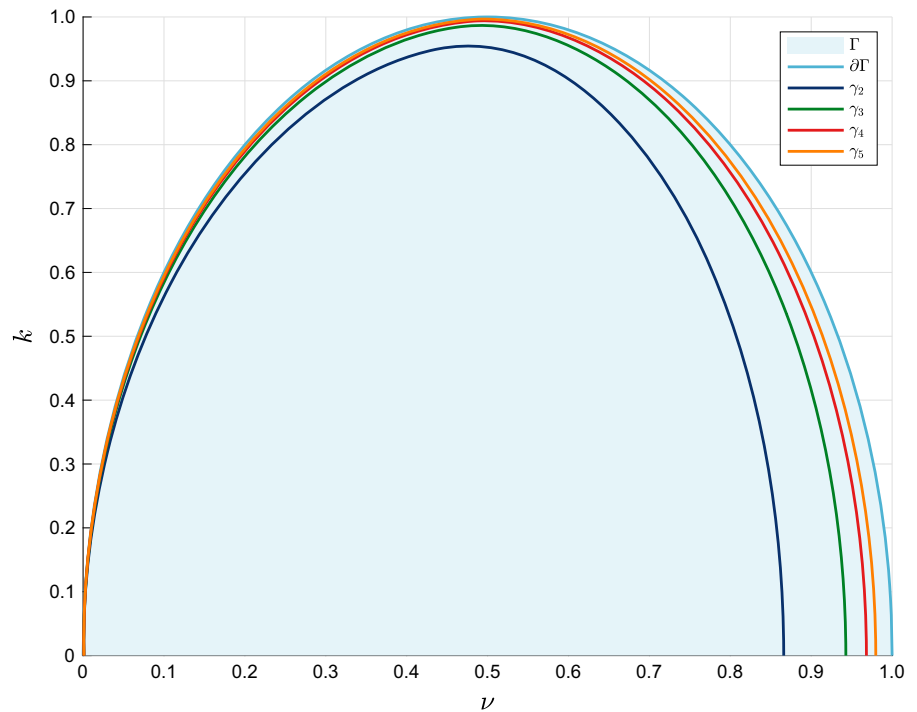
This gives:

$$\nu_m^*(k) = \frac{\sqrt{2C_m(k) + H_m(k)}}{2m}, \tag{18}$$

where

$$C_m(k) = \sqrt{(m^2 - 1)(k')^2 (m^2 - (k')^2)}, \\ H_m(k) = m^2 ((k')^2 + 1) - 2(k')^2. \tag{19}$$

Substituting (18) into (14), one obtains $\nu_m(\nu = \nu_m^*, k) = k/2$, $\forall m \in \mathbb{Z}^+$, independent of m. The importance of this result will be discussed in Appendix 1.

Consequently, each curve ν_m in the $\nu\nu_m$-plane starts from the point:

$$L_m(k) = \left(\nu_m^*(k), \frac{k}{2} \right), \quad m \geq 2. \tag{20}$$

This is a stricter condition on ν than the lower limit of Eq. (8), since $k > (1 - \sqrt{1-k^2}) \, \forall k \in (0, 1)$. Referring to the PHF (5), the lower limit (20) then implies that when transitioning from an Nth order to an $(N+1)$st order breather, the peak would instantly jump

by $2(k/2) = k$ and would not just increase smoothly as in the simpler constant background case [18]. This can be seen clearly in Fig. 4.

Figure 5 shows the three "quasi-periods" of higher-order breathers with ν_m obtained from Eq. (14), and ν and k selected arbitrarily. The effect of matching the constituent breathers' periods drastically improves the overall periodicity of the high-order breather, with seemingly repeating higher-order side peaks in the 3D plots. However, closer inspection of contour plots near the breather's base reveals remaining distortions in the side peaks. They are still not identical to the central peak. This distortion is reminiscent of the first-order case, as shown in Fig. 1. These higher-order breathers are all quasiperiodic. In the limit of $k \to 0$, $\nu_m \to \sqrt{m^2 - 1}/m$, (14) reproduces our previous results of $a_m = \nu_m^2/2 = (1 - 1/m^2)/2$ for breathers on a constant background in Ref. [18].

4 Fully periodic breathers

The period of the $\mathrm{dn}(t; k)$ background is given by

$$T_{\mathrm{dn}} = 2K(k) \tag{21}$$

Fig. 7 Fully periodic first-order breathers with $(\nu \approx 0.848, k = 3/5) \in \gamma_3$
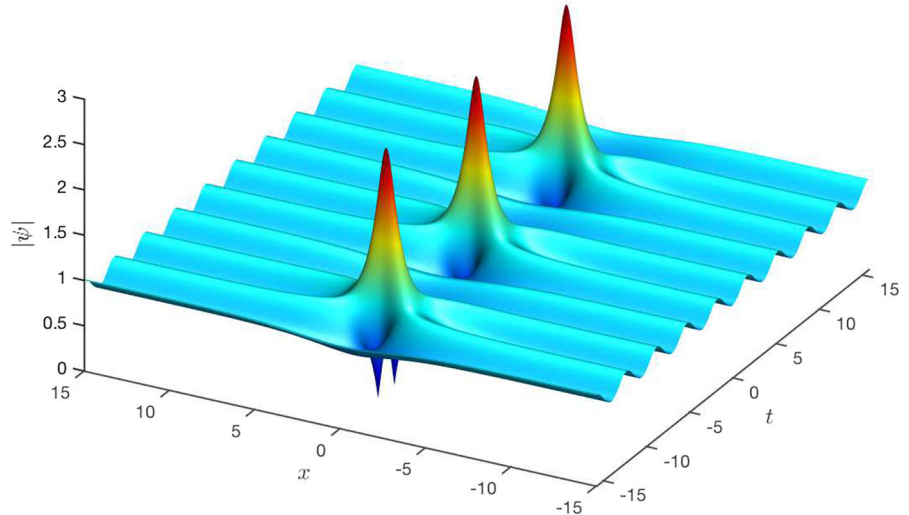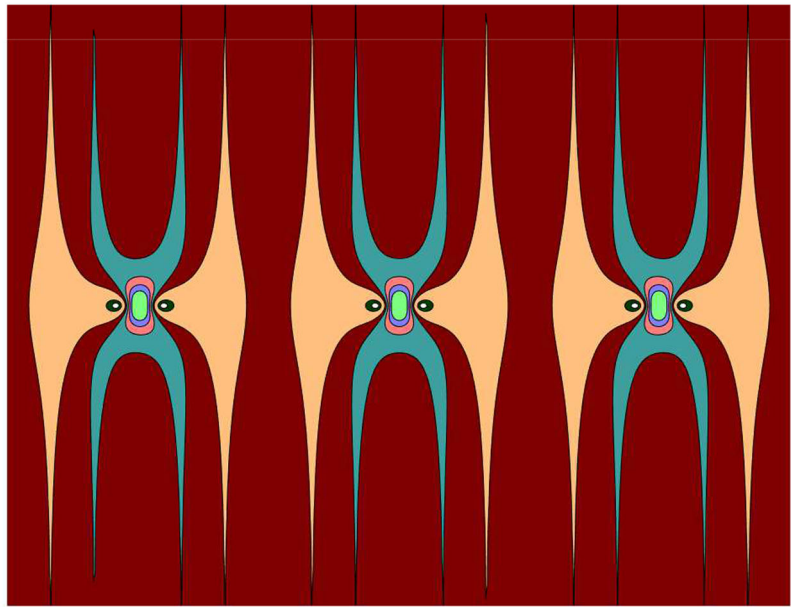
where $K(k) \equiv \int_0^{\frac{\pi}{2}} \frac{d\theta}{\sqrt{1-k^2 \sin^2 \theta}}$ is the complete elliptic integral of the first kind. Matching the period of the background (21) to the breather requires

$$T_{\mathrm{B}} = q T_{\mathrm{dn}}$$

where $T_{\mathrm{B}} = 2\pi/(2\kappa) = \pi/\kappa$ is the period of the fundamental breather and q is a positive integer. This leads to an expression for κ:

$$\kappa = \frac{\pi}{2q K(k)} . \tag{22}$$

Substituting back into (6), one obtains the condition for matching a breather to the background:

$$(\nu, k) \in \gamma_q := \left\{ (\nu, k) \in (0, 1) \times [0, 1] \,\middle|\, \left(\frac{\pi}{2q K(k)}\right)^2 + \frac{(k^2 + 4\nu^2)^2}{16\nu^2} = 1 \right\}. \tag{23}$$

Note that $\gamma_{q=1} = \varnothing$ (i.e., one cannot match to the breather so that its period is exactly equal to the background, it must be a periodic multiple). As shown in Fig. 6, it is clear that $\gamma_q \subset \Gamma \,\forall q \in \mathbb{Z}^+$, and $\gamma_{q \to \infty} =$
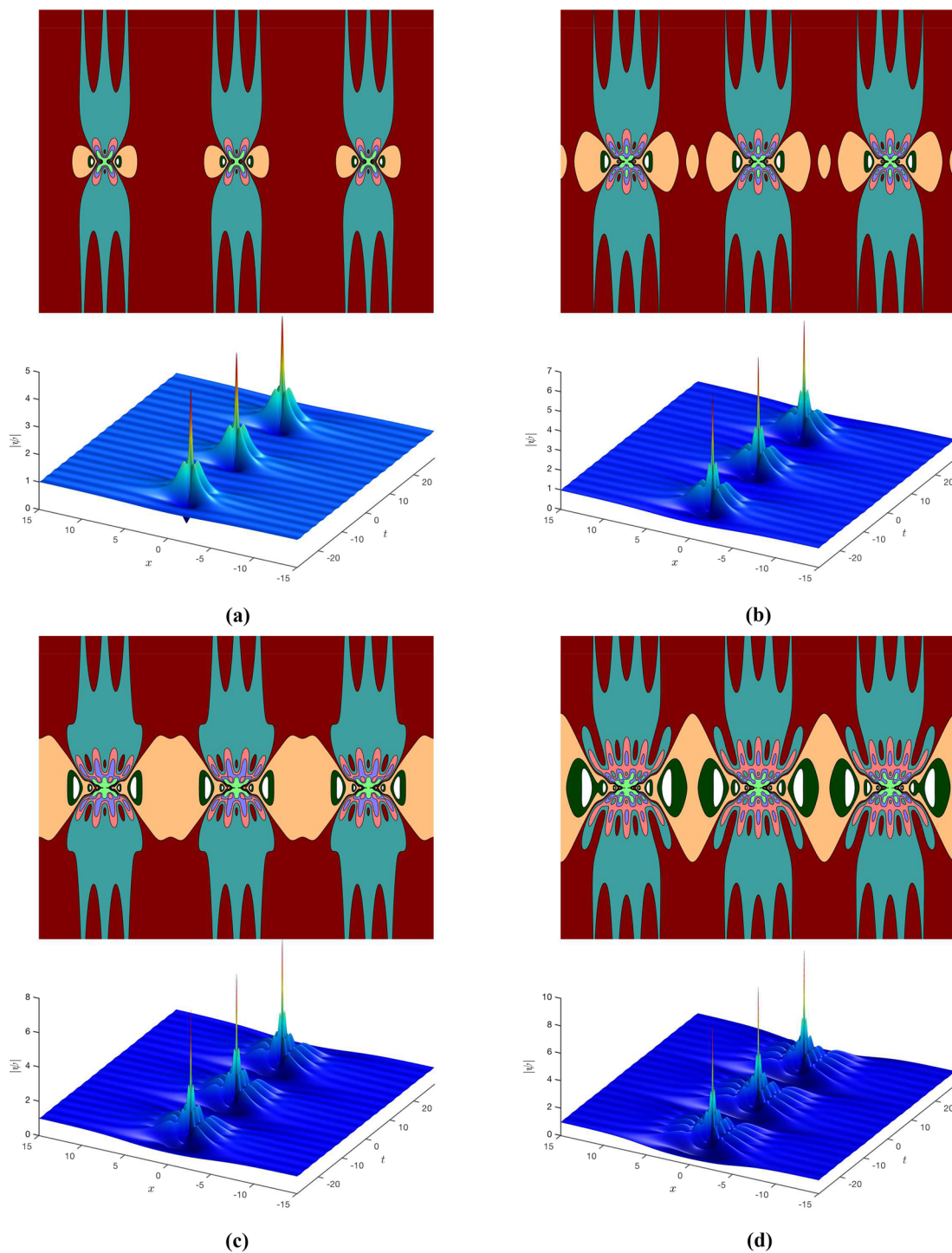
(a)

(b)

(c)

(d)

Fig. 8 Fully periodic higher-order breather with ($v \approx 0.9704, k = 1/4$) $\in \gamma_6$, and the higher v_m calculated via Eq. (14). **a** Second order. **b** Third order **c** Fourth order. **d** Fifth order.

Insert: Contour plots to emphasize the low-$|\psi|$ detail. The symmetry between the central and side peaks is apparent

Table 1 Necessary and sufficient conditions on the parameters for a fully periodic breather of order N

Condition	Equation	Explanation
$(v, k) \in \gamma_q, \ q = 2, 3, \ldots$	Eq. (23)	Matches a breather to the background
$v \equiv v_1 > v_N^*$	Eq. (18)	Ensures $v_m \in \mathbb{R}, \ m = 1, \ldots, N$
$v_m = v_m(v, k), \ m = 1, \ldots, N$	Eq. (14)	Matches the constituent breathers to each other

$\partial \Gamma$ (i.e., the boundary of Γ, Eq. (11)). Thus, any $(v, k) \in \gamma_q$ results in $\kappa \in \mathbb{R}$. Additionally, if a higher-order breather has matched constituents via Eq. (14), its period will be T_B, and thus one only needs $(v, k) \in \gamma_q$.

Figure 7 shows a fully periodic first-order breather. It is clear that selecting a set of parameters (v, k) satisfying Eq. (23) leads to a truly periodic structure. We additionally show several fully periodic higher-order breathers in Fig. 8, combining conditions (23) and (14). In general, the effect of matching to the background is subtle in 3D plots yet abundantly clear in the contour plots. The central breather's peak is centered at the origin, where $\psi_0(0, 0) = 1$. If the parameters $(v, k) \notin \gamma_q$ (i.e., $q \notin \mathbb{Z}$), the side peaks will then be displaced from the peak of ψ_0. On the other hand, when $(v, k) \in \gamma_q, \ q \in \mathbb{Z}^+$, all breather peaks lie precisely on top of the background crests, and we get perfect periodicity. We provide a video in this work's supplemental material, which visually demonstrates this process.

5 Discussion and conclusion

In this work, we have numerically solved for the higher-order breathers of the nonlinear Schrödinger equation on an elliptic background by iterating the Darboux transformation. We find that the periodic background exerts a much more profound impact on the higher-order breathers than previously thought. Because of the periodic background, any unmatched higher-order breather has only a single high-intensity peak, resembling a rogue wave. These QRWs have a far richer structure than the standard, monotonic Peregrine-like rational rogue waves.

The chaotic background shown in Fig. 2 is also of interest. It is well known that two-wave mixing can only result in quasiperiodic structures. This is the case of Fig. 1, the two waves being waves having the breather's period and that of the background. However, three and more wave mixing can lead to chaos. This is the resulting chaotic-looking background we see in Fig. 2.

Truly periodic higher-order breathers can only be recovered by matching all the constituent breathers' periods to each other and the background. Matching constituent breathers' periods to each other produces quasiperiodic with distorted side peaks. Further matching the breathers' periods to that of the background yields side peaks identical to the central peak, sitting precisely on top of the background's crests some periodic distance away. While a general breather of order N has an $N + 1$-dimensional parameter space, fully periodic breathers are constrained to a countably infinite set of contours in a 2D parameter space, thus being exceedingly rare. We have termed such a periodic higher-order breather the periodic rogue wave in Ref. [29]. Our findings are summarized in Table 1. This explains why, on a periodic background, the only common high peak structures that can occur are, paradoxically, the quasi-rogue waves of Fig. 2.

A The Darboux transformation and the peak height formula

The cubic NLSE (1) can be written as the compatibility condition of the following two equations [1]:

$$R_t = LR, \quad R_x = AR, \tag{24}$$

where

$$R = \begin{pmatrix} r \\ s \end{pmatrix} \equiv \begin{pmatrix} r_{1m} \\ s_{1m} \end{pmatrix}, \tag{25}$$

$$L = \begin{pmatrix} -i\lambda & \psi \\ -\psi^* & i\lambda \end{pmatrix},$$

$$A = \begin{pmatrix} -i\lambda^2 + i\frac{1}{2}|\psi|^2 & \lambda\psi + i\frac{1}{2}\psi_t \\ -\lambda\psi^* + i\frac{1}{2}\psi_t^* & i\lambda^2 - i\frac{1}{2}|\psi|^2 \end{pmatrix}. \tag{26}$$

The operators (matrices) L and A are known as the Lax pair of (1), and the functions $r(x, t)$ and $s(x, t)$ are the Lax pair generating functions. λ is generally a complex eigenvalue and is independent of the evolution variable x (so that the Lax pair is isospectral). The compatibility condition of (24) is known as the Lax equation or zero-curvature condition and gives rise to the cubic NLSE (1):

$$L_x - A_t - [A, L] = 0, \tag{27}$$

where $[A, L] \equiv AL - LA$ is the commutator.

Given an initial solution of (1), one can find a more complicated solution of order N via the Darboux transformation: [1,8,30,31]:

$$\psi_N = \psi_0 + \sum_{m=1}^{N} \frac{2ir_{m1}s_{m1}^* (\lambda_m - \lambda_m^*)}{|r_{m1}|^2 + |s_{m1}|^2}, \tag{28}$$

where the higher-order Lax-pair generating functions are computed recursively via [1,31]:

$$r_{mj} = [(l_{m-1}^* - l_{m-1})s_{m-1,1}^* r_{m-1,1} s_{m-1,j+1}$$
$$+ (l_{j+m-1} - l_{m-1})|r_{m-1,1}|^2 r_{m-1,j+1}$$
$$+ (l_{j+m-1} - l_{m-1}^*)|s_{m-1,1}|^2 r_{m-1,j+1}]$$
$$/(|r_{m-1,1}|^2 + |s_{m-1,1}|^2), \tag{29}$$
$$s_{mj} = [(l_{m-1}^* - l_{m-1})s_{m-1,1} r_{m-1,1}^* r_{m-1,j+1}$$
$$+ (l_{j+m-1} - l_{m-1})|s_{m-1,1}|^2 s_{m-1,j+1}$$
$$+ (l_{j+m-1} - l_{m-1}^*)|r_{m-1,1}|^2 s_{m-1,j+1}]$$

$$/(|r_{m-1,1}|^2 + |s_{m-1,1}|^2). \tag{30}$$

To find the starting functions of the recursion, i.e., r_{1m} and s_{1m}, we take the Ansätze:

$$r_{1m}(x, t) = a_{1m}(x, t)e^{\frac{ix}{4}(k^2-2)},$$
$$s_{1m}(x, t) = a_{1m}(x, t)e^{-\frac{ix}{4}(k^2-2)}, \tag{31}$$

and ψ as given in Eq. (2). Substituting in the Lax pair Eq. (24) and suppressing subscripts, one gets [9]

$$a_t = i\lambda a(x, t) + ib(x, t)\mathrm{dn}(t; k),$$
$$b_t = -i\lambda b(x, t) + ia(x, t)\mathrm{dn}(t; k),$$
$$a_x = \frac{1}{2}ia(x, t)\left(2\lambda^2 + k^2\left(\mathrm{sn}^2(t; k) - \frac{1}{2}\right)\right)$$
$$+ b(x, t)\left(i\lambda\mathrm{dn}(t; k) - \frac{k^2}{2}\mathrm{sn}(t; k)\mathrm{cn}(t; k)\right),$$
$$b_x = -\frac{1}{2}ib(x, t)\left(2\lambda^2 + k^2\left(\mathrm{sn}^2(t; k) - \frac{1}{2}\right)\right)$$
$$+ a(x, t)\left(i\lambda\mathrm{dn}(t; k) + \frac{k^2}{2}\mathrm{sn}(t; k)\mathrm{cn}(t; k)\right). \tag{32}$$

However, as noted in [9], the four coupled first-order differential Eq. (32) cannot be solved analytically. Nonetheless, one can solve for the profiles and derivatives at $t = 0$, given by [9]

$$a_{1m}|_{t=0} = Ae^{i(\chi_m + \kappa_m\lambda_m(x - x_m))}$$
$$- Be^{-i(\chi_m + \kappa_m\lambda_m(x - x_m))},$$
$$b_{1m}|_{t=0} = Ae^{i(-\chi_m + \kappa_m\lambda_m(x - x_m))}$$
$$+ Be^{-i(-\chi_m + \kappa_m\lambda_m(x - x_m))}, \tag{33}$$
$$a_{1m,t}|_{t=0} = i(\lambda_m a_{1m}|_{t=0} + b_{1m}|_{t=0}),$$
$$b_{1m,t}|_{t=0} = -i(\lambda_m b_{1m}|_{t=0} - a_{1m}|_{t=0}),$$

where

$$\kappa_m = \sqrt{\left(\lambda_m - \frac{k^2}{4\lambda_m}\right)^2 + 1} \tag{34}$$

is half the wavenumber of the mth constituent breather, $\chi_m = \arccos(\kappa_m)/2$ is the background-dependent phase, and A and B are two phase constants. One can then evolve Eq. (33) along the t-axis numerically. All

the results in this work employ a fourth-order Runge–Kutta method and sufficiently small grid spacing.

In previous works [18,23,24], using the DT, we derived the so-called peak height formula (PHF) for N^{th}-order solutions of nonlinear Schrödinger-type equations:

$$\psi_N(0, 0) = \psi_0(0, 0) + 2 \sum_{m=1}^{N} \nu_m \tag{35}$$

This requires the Lax pair generating functions to only differ by a phase at the origin [23]:

$$s_{1m}(0, 0) = e^{i\phi} r_{1m}(0, 0), \tag{36}$$

One can easily verify that equations (33), with proper choice of A and B, lead to $r(x, t)$ and $s(x, t)$ that obey the PHF condition (36) with $\phi = \pi/2$, leading to the PHF (5).

References

1. Akhmediev, N.N., Ankiewicz, A.: Solitons Nonlinear Pulses and Beams. Chapman & Hall, London (1997)
2. Solli, D.R., Ropers, C., Koonath, P., Jalali, B.: Optical rogue waves. Nature **450**(13), 1054–1057 (2007)
3. Frisquet, B., Kibler, B., Millot, G.: Collision of Akhmediev breathers in nonlinear fiber optics. Phys. Rev. X **3**(4), 041032 (2014)
4. Armaroli, A., Conti, C., Biancalana, F.: Rogue solitons in optical fibers: a dynamical process in a complex energy landscape? Optica **2**(5), 497 (2015)
5. Onorato, M., Residori, S., Bortolozzo, U., Montina, A., Arecchi, F.T.: Rogue waves and their generating mechanisms in different physical contexts. Phys. Rep. **528**(2), 47–89 (2013)
6. Akhmediev, N., Soto-Crespo, J.M., Ankiewicz, a: How to excite a rogue wave. Phys. Rev. A **80**(4), 043818 (2009)
7. Kedziora, D.J., Ankiewicz, A., Akhmediev, N.: Triangular rogue wave cascades. Phys. Rev. E **86**(5), 056602 (2012)
8. Kedziora, D.J., Ankiewicz, A., Akhmediev, N.: Circular rogue wave clusters. Phys. Rev. E **84**(056611), 056611 (2011)
9. Kedziora, D.J., Ankiewicz, A., Akhmediev, N.: Rogue waves and solitons on a cnoidal background. Eur. Phys. J. Spec. Top. **223**(1), 43–62 (2014)
10. Kedziora, D.J., Ankiewicz, A., Akhmediev, N.: Second-order nonlinear Schrödinger equation breather solutions in the degenerate and rogue wave limits. Phys. Rev. E **85**(6), 066614 (2012)
11. Akhmediev, N., Ankiewicz, A., Soto-Crespo, J.M.: Rogue waves and rational solutions of the nonlinear Schrödinger equation. Phys. Rev. E **80**(2), 026601 (2009)
12. Dudley, J.M., Dias, F., Erkintalo, M., Genty, G.: Instabilities, breathers and rogue waves in optics. Nat. Photonics **8**(September), 755–764 (2014)
13. Fleischhauer, M., Imamoglu, A., Marangos, J.P.: Electromagnetically induced transparency: optics in coherent media. Rev. Mod. Phys. **77**, 633–673 (2005)
14. Nikolić, S.N., Radonjić, M., Krmpot, A.J., Lučić, N.M., Zlatković, B.V., Jelenković, B.M.: Effects of a laser beam profile on Zeeman electromagnetically induced transparency in the Rb buffer gas cell. J. Phys. B At. Mol. Opt. Phys. **46**, 075501 (2013)
15. Krmpot, A.J., Ćuk, S.M., Nikolić, S.N., Radonjić, M., Slavov, D.G., Jelenković, B.M.: Dark Hanle resonances from selected segments of the Gaussian laser beam cross-section. Opt. Express **17**, 22491–22498 (2009)
16. Li, Z.-Y., Li, F.-F., Li, H.-J.: Exciting rogue waves, breathers, and solitons in coherent atomic media. Commun. Theor. Phys. **72**, 075003 (2020)
17. Chin, S.A., Ashour, O.A., Belić, M.R.: Anatomy of the Akhmediev breather: cascading instability, first formation time, and Fermi-Pasta-Ulam recurrence. Phys. Rev. E **92**(6), 063202 (2015)
18. Chin, S.A., Ashour, O.A., Nikolić, S.N., Belić, M.R.: Maximal intensity higher-order Akhmediev breathers of the nonlinear Schrödinger equation and their systematic generation. Phys. Lett. A **380**(43), 3625–3629 (2016)
19. Ankiewicz, A., Kedziora, D.J., Akhmediev, N.: Rogue wave triplets. Phys. Lett. A **375**(28–29), 2782–2785 (2011)
20. Chowdury, A., Kedziora, D.J., Ankiewicz, A., Akhmediev, N.: Breather-to-soliton conversions described by the quintic equation of the nonlinear Schrödinger hierarchy. Phys. Rev. E **91**(3), 032928 (2015)
21. Ankiewicz, A., Kedziora, D.J., Chowdury, A., Bandelow, U., Akhmediev, N.: Infinite hierarchy of nonlinear Schrödinger equations and their solutions. Phys. Rev. E **93**(1), 012206 (2016)
22. Kedziora, D.J., Ankiewicz, A., Chowdury, A., Akhmediev, N.: Integrable equations of the infinite nonlinear Schrödinger equation hierarchy with time variable coefficients. Chaos **25**(10), 17105 (2015)
23. Chin, S.A., Ashour, O.A., Nikolić, S.N., Belić, M.R.: Peak-height formula for higher-order breathers of the nonlinear Schrödinger equation on non-uniform backgrounds. Phys. Rev. E **95**, 012211 (2017)
24. Nikolić, S.N., Aleksić, N.B., Ashour, O.A., Belić, M.R., Chin, S.A.: Systematic generation of higher-order solitons and breathers of the Hirota equation on different backgrounds. Nonlinear Dyn. **89**(3), 1637–1649 (2017)
25. Ashour, O.A.: Maximal Intensity Higher-Order Breathers of the Nonlinear Schrödinger Equation on Different Backgrounds. Undergraduate Research Scholars Thesis, Texas A&M University (2017)
26. Akhmediev, N.N., Korneev, V.I.: Modulation instability and periodic solutions of the nonlinear Schrödinger equation. Teor. i. Mat. Fiz. **69**(2), 189–194 (1987)
27. Kuznetsov, E.: Solitons in a parametrically unstable plasma. Akad. Nauk SSSR Dokl. **236**, 575–577 (1977)
28. Ma, Y.C.: The perturbed plane-wave solutions of the Cubic Schrödinger equation. Stud. Appl. Math. **60**(1), 43–58 (1979)

29. Nikolić, S.N., Ashour, O.A., Aleksić, N.B., Belić, M.R., Chin, S.A.: Breathers, solitons and rogue waves of the quintic nonlinear Schrödinger equation on various backgrounds. Nonlinear Dyn. **95**, 2855–2865 (2019)

30. Akhmediev, N., Soto-crespo, J.M., Ankiewicz, A.: Extreme waves that appear from nowhere: on the nature of rogue waves. Phys. Lett. A **373**(25), 2137–2145 (2009)

31. Matveev, V.B., Salle, M.A.: Darboux Transformations and Solitons. Springer-Verlag, Heidelberg (1991)

Multi-elliptic rogue wave clusters of the nonlinear Schrödinger equation on different backgrounds

Stanko N. Nikolić⬤ · **Sarah Alwashahi** ·
Omar A. Ashour · **Siu A. Chin** ·
Najdan B. Aleksić · **Milivoj R. Belić**

Abstract   In this work, we analyze the multi-elliptic rogue wave clusters of the nonlinear Schrödinger equation (NLSE) in order to understand more thoroughly the origin and appearance of optical rogue waves in this system. Such structures are obtained on uniform backgrounds by using the Darboux transformation scheme for finding analytical solutions of the NLSE under various conditions. In particular, we solve the eigenvalue problem of the Lax pair of order n in which the first m evolution shifts are equal, nonzero, and eigenvalue dependent, while the imaginary parts of all eigenvalues tend to one. We show that an Akhmediev breather of order $n - 2m$ appears at the origin of the (x, t) plane and can be considered as the central rogue wave of the so-formed cluster. We show that the high-intensity narrow peak, with the characteristic intensity distribution in its vicinity, is enclosed by m ellipses consisting of the first-order Akhmediev breathers. The number of maxima on each ellipse is determined by its index and the solution order. Since rogue waves in nature usually appear on a wavy background, we utilize the modified Darboux transformation scheme to build such solutions on a Jacobi elliptic dnoidal background. We analyze the vertical semi-axis of all ellipses in a cluster as a function of an absolute evolution shift. We show that the cluster radial symmetry in the (x, t) plane is broken when the shift value is increased above a threshold. We apply the same analysis on the Hirota equation, to examine the influence of a real parameter and Hirota's operator on the cluster appearance. The same analysis can be applied to the infinite hierarchy of extended NLSEs. The main outcomes of this paper are the new multi-rogue wave solutions of the nonlinear Schrödinger equation and its extended family on uniform and elliptic backgrounds.

S. N. Nikolić (✉)
Science Program, Texas A&M University at Qatar, P.O.
Box 23874, Doha, Qatar
e-mail: stankon@ipb.ac.rs

S. N. Nikolić
Institute of Physics Belgrade, University of Belgrade,
Pregrevica 118, Belgrade 11080, Serbia

S. Alwashahi
Faculty of Physics, University of Belgrade, Studentski trg
12, Belgrade 11001, Serbia

S. Alwashahi
Faculty of Science Al-Zawiya, University of Libya, Al
Ajaylat, Libya

O. A. Ashour
Department of Physics, University of California, Berkeley,
CA 94720, USA

S. A. Chin
Department of Physics and Astronomy, Texas A&M
University, College Station, TX 77843, USA

N. B. Aleksić
Moscow State Technological University "STANKIN",
Moscow, Russia

N. B. Aleksić · M. R. Belić
Science Program, Texas A&M University at Qatar, P.O. Box
23874, Doha, Qatar

1 Introduction

The cubic nonlinear Schrödinger equation (NLSE) [1–3] is one of the most studied partial differential equations in nonlinear sciences since it was first introduced in 1960s. The extensive research on NLSE solutions and their dynamical stability is still being conducted, due to its huge importance in various fields of physics, such as nonlinear optics [4–8], Bose−Einstein condensates [9,10], oceanography [11,12], and plasmas [13]. The NLSE is a general equation for the nonlinear wave propagation that can describe a variety of phenomena in nonlinear regimes of different physical systems. However, due to its simple form, it cannot be used for more accurate explanation of some higher-order effects in nonlinear optics. To this end, in recent times an extended family of nonlinear Schrödinger equations (ENLSEs) that may include an arbitrary number of higher-order dispersion terms with additional nonlinearities, has been proposed and investigated in [14,15]. The extension of NLSE to the hierarchy of higher-order equations originated from the need to explain the propagation of ultrashort pulses through optical fibers [16,17]. So far, attention was mostly focused on the Hirota [18,19] (with the third-order dispersion) and quintic equations (containing the dispersions up to the fifth-order) [20–23].

Although NLSE is a well-known equation, it remains a subject of broad interest for several reasons. First, both NLSE and its extended variants are completely integrable in one dimension. The possibility of deriving exact analytical NLSE solutions has motivated a number of experimental studies in many branches of physics where NLSE appears. Second, the same mathematical procedure used for deriving NLSE solutions can be applied to the ENLSE as well. Finally, the characteristics of NLSE solutions are similar to those of the more complicated equations emanating from the ENLSE. Therefore, one can analyze the simpler NLSE solutions and still predict the properties of the same solution class of the extended family.

The one-dimensional NLSE that will be mostly considered in this work has the form

$$i\psi_x + \frac{1}{2}\psi_{tt} + |\psi|^2\psi = 0. \tag{1.1}$$

The transverse spatial variable is denoted by t, the retarded time in the moving frame by x, while the slowly varying envelope of the electric field corresponds to the wave function $\psi \equiv \psi(x, t)$. This form of NLSE is appropriate for the propagation of light pulses in fibers. However, if pulses are very short, additional operators have to be introduced that add finer details to the basic NLSE solutions. Thus, in this work we will also deal with the Hirota equation, comprising of a new operator (with a third-order dispersion along t-axis and additional nonlinearities) added to the basic NLSE, multiplied by a real parameter α:

$$i\frac{\partial\psi}{\partial x} + \frac{1}{2}\frac{\partial^2\psi}{\partial t^2} + |\psi|^2\psi$$
$$-i\alpha\left(\frac{\partial^3\psi}{\partial t^3} + 6|\psi|^2\frac{\partial\psi}{\partial t}\right) = 0. \tag{1.2}$$

Both the NLSE and its extended variants exhibit similar classes of localized solutions, among which the most important seem to be Akhmediev breathers (ABs) [24,25] and different solitons [26]. An AB consists of a series of intensity maxima on a finite background that are localized in time and periodic in space. The term soliton in general describes a solitary wave packet that propagates in some direction in the (x, t) plane on a zero background, without any distortion in its shape. The technique that is often used to derive exact analytical solutions is the Darboux transformation (DT) [27]. It utilizes the Lax pair formalism and recursive relations to calculate higher-order solutions of the NLSE, starting from the trivial zeroth-order seed function which satisfies Eq. (1.1).

The importance of DT for this work is its ability to provide higher-order Akhmediev breathers on uniform [28] and periodic backgrounds [29,30]. The breather emerges as a high-intensity narrow peak with a complex intensity distribution at its base. Such structures can be considered as rogue waves (RWs), which "appear from nowhere and disappear without a trace." The RW is localized both in space and time and is defined by one dominant peak. The simplest example of a RW is the Peregrine soliton [31]. The notion of rogue waves is now widely spread around, in studies of deep ocean waves [12,32], nonlinear optics [33,34], superfluidity [35], Bose–Einstein condensates [36], and others. The current hot topic in the nonlinear science is to investigate the cause and nature of optical rogue waves [37].

The root of their appearance is related to the homoclinic chaos theory and modulation instability [37,38]. The understanding of chaos theory is also important for other fields, such as medicine [39–45] or finance. The RW research is attracting more attention because a new scheme for RWs excitation, via the electromagnetically induced transparency (EIT) [46–48], was described recently [49].

In this paper, we add new results to the field of RWs by investigating the special multi-elliptic rogue wave clusters of the NLSE. These solutions are also periodic along t-axis and throughout the paper we consider intensity distributions within a single transverse period. They consist of a rogue wave peak (ABs of the second order or higher), surrounded by the first-order ABs positioned on a number of concentric ellipses centered on the peak (see Fig. 1). We obtain these structures on uniform and Jacobi elliptic dnoidal backgrounds, by using the DT of order n, having the first m evolution shifts equal, nonzero, and eigenvalue dependent. We show that the order of the central rogue wave and the number of ellipses are determined by the two mode numbers, n and m.

Various multi-rogue wave solutions have been previously analyzed as triplets [50], triangular cascades [51–53], and circular clusters [28,54–56]. The classification of various hierarchies of multi-RW structures into different families was presented in [57,58]. Although our results are similar to those in [56], where the authors used the determinant representation of DT, we believe that the first important contribution of our study is the simple method for generating elliptical clusters by using the evolution shifts in the Darboux transformation scheme. The second novelty in our results is the analysis of semi-axes of ellipses as functions of the evolution shifts and an estimate when the radial symmetry of the cluster will break up. Our third contribution to the field is the generation of elliptic RW clusters on a dn background, which was not presented before, to the best of our knowledge. Finally, the significance of our work is also the determination of new solutions of the Hirota equation in the form of elliptic RW clusters. We also point to ways how to generalize this analysis to the infinite hierarchy of NLSEs.

We stress out that the solutions presented in this paper are in the form of two-dimensional (2D) or three-dimensional (3D) color plots. The clusters on the uniform background are calculated by using the exact analytical DT procedure. However, the mathematical expressions of higher-order DT solutions are extremely lengthy and complicated, and would require many journal pages to be written down. We therefore omit the derivation of such expressions. In turn, we pick the convenient grid and calculate the numerical values at each point with infinite accuracy (that is, up to the machine precision limit).

To ensure the correctness of our calculations, our DT method has been extensively validated by: (1) comparing it to directly solved NLSE, verified by the conservation of energy [38], (2) showing that our DT algorithm exactly satisfied the Peak-height formula [30], and (3) always halving the grid-size when doing the DT iterations and confirming that the results are stable and unchanged.

The paper is organized as follows. In Sect. 2, we briefly discuss the main properties of higher-order Akhmediev breathers. In Sect. 3, we present various NLSE solutions in the form of multi-elliptic rogue wave clusters on a uniform background. In Sect. 4, we analyze the properties of such clusters, in particular the lengths of semi-axes of elliptical rings, by going up to the four ellipses in a cluster. In Sect. 5, we exhibit the NLSE cluster solutions on a Jacobi elliptic dnoidal background. In Sect. 6, we generalize our findings to the Hirota equation that includes the third-order dispersion and additional nonlinearities. In Sect. Conclusion, we summarize our results.

2 Higher-order Akhmediev breathers

Here, we briefly describe Akhmediev breathers of the NLSE and how to use DT scheme to generate higher-order RW solutions. The first-order AB is a single-periodic function along the t-axis [24,25]:

$$\psi(t, x) = \left[1 + \frac{2(1-2a)\cosh \lambda x + i\lambda \sinh \lambda x}{\sqrt{2a}\cos \omega t - \cosh \lambda x}\right]e^{ix} \tag{2.1}$$

that rides on a finite background and is localized along the x-axis. The period L and the angular frequency ω of an AB of any order are determined by a single parameter a, with $0 < a < 0.5$ [38]:

$$L = \frac{\pi}{\sqrt{1-2a}}, \tag{2.2}$$

$$\omega = 2\sqrt{1-2a}. \tag{2.3}$$

AB turns into the Peregrine RW at $a = 0.5$ and becomes the Kuznetsov–Ma soliton when $a > 0.5$. An

arbitrary AB can be derived using DT, starting from the seed solution $\psi_0 = e^{ix}$. The n-th-order AB (its wave function $\psi_n(x, t)$) turns out to be a nonlinear superposition of n first-order ABs, each characterized by the complex eigenvalue $\lambda_j = r_j + i v_j$ and the evolution x_j, and spatial shifts t_j $(j = 1, \ldots, n)$. The existence of such abundance of relevant parameters offers an incredible variety of possible RW solutions.

The Lax pair procedure and the recursive relations in the DT scheme that are used to calculate $\psi_n(x, t)$ from ψ_0 are described in details in [28]. Here, we briefly mention that computational complexity for calculating the n-th-order DT solution exhibits a quadratic growth ($\approx O(n^2)$). Therefore, by increasing n, the number of iterations and the complexity of analytical expressions rise significantly. For this reason, we do not write down these expressions explicitly here, but only represent them graphically.

It is important to note that the imaginary part v of an AB is simply related to the parameter a: $v = \sqrt{2a}$. By taking into account relation (2.3), one can see that the imaginary part of AB's eigenvalue is completely determined by its angular frequency: $v = \sqrt{1 - \omega^2/4}$.

3 Multi-elliptic rogue wave clusters on uniform background

To generate multi-elliptic RW clusters, we require that the frequencies of constituent single-order breathers are all different, but close to zero. This goal can be achieved by defining them as harmonics of $\omega_1 = \omega \to 0$, so that $\omega_j = j\omega$, where $j \geq 2$ [28]. In this work, we take the simplest possibility that all real parts are zero: $r_j = 0$. The n ABs are thus formed by using their imaginary parts calculated from the corresponding frequencies:

$$v_j = \sqrt{1 - \frac{j^2\omega^2}{4}} \quad (1 \leq j \leq n). \tag{3.1}$$

It is easy to see that all v_j tend to 1. Having set the eigenfrequencies, it remains to choose the evolution and spatial shifts. Different choices lead to very different solutions. We introduce a slight modification with respect to [28]: The first m evolution shifts x_j are set to be equal, nonzero, and eigenvalue dependent. We assume them to be given via an expansion

$$x_j = \sum_{l=1}^{\infty} X_{jl}\omega^{2(l-1)}$$

$$= X_{j1} + X_{j2}\omega^2 + X_{j3}\omega^4 + X_{j4}\omega^6 + \cdots \tag{3.2}$$

for $j \leq m$, and $x_j = 0$ for $j > m$. In addition, we simply set all t_j shifts to be zero. We also assume that all $X_{jl} = 0$ except one particular value that is explicitly stated in the text. Although seemingly an oversimplification, this choice of parameters nonetheless leads to an interesting family of new RW clusters. And, as mentioned, all this is provided for by an incredible richness in the choice of four sets of parameters.

It turns out that such an n-th-order Darboux solution with m nonzero shifts x_j is characterized by a single Akhmediev breather of order $n - 2m$ placed at the origin $(0, 0)$ (a central rogue wave, labeled as RW_{n-2m}) and m ellipses (rings) around the RW. The outer ellipse contains $2n - 1$ ABs of order 1 (AB1), and each following ring toward the center has four AB1s less, as analyzed in [56,57]. We term this Darboux solution as the multi-RW cluster.

This remarkable intensity pattern can be described as follows. If all x_j shifts are zero, the nonlinear superposition of all n DT components will arise at the origin of (x, t) plane, forming an Akhmediev breather of order n. If only one shift is applied, say $x_1 \neq 0$, the central AB of lower order and intensity will remain, but it will partially break up and a ring structure of $2n - 1$ rational solutions centered at $(0, 0)$ will be displayed [28]. The minimal n value for this picture is $n = 3$. As mentioned above, if one chooses $m > 1$ components shifts to be nonzero, they will split and decrease the intensity of the central structure even more and produce more rings. The exact splitting mechanism could be understood if one applies the mathematical analysis of exact analytical DT expression. However, deriving and analyzing such complex expressions for big n is a very tedious job that offers little insight and was not performed anywhere before; hence, it will not be performed here either.

In Fig. 1, we present the multi-rogue wave cluster on uniform background having 2 ellipses. Hence, we set $m = 2$ and vary the value of n in order to change the order of the central RW. The main frequency ω is set to 10^{-1} so that the imaginary part v is getting close to one, according to Eq. (3.1). Also, we choose $X_{j4} = 10^6$, to set evolution shift x_j in the order of 1 (Eq. 3.2). In Fig. 1a, we set $n = 6$ and obtain the second-order RW at the center. The outer and inner ellipses consist of $c_1 = 11$ and $c_2 = 7$ AB1s, respectively. In Fig. 1b, we set $n = 7$ to get a third-order RW. The number of AB1s on two
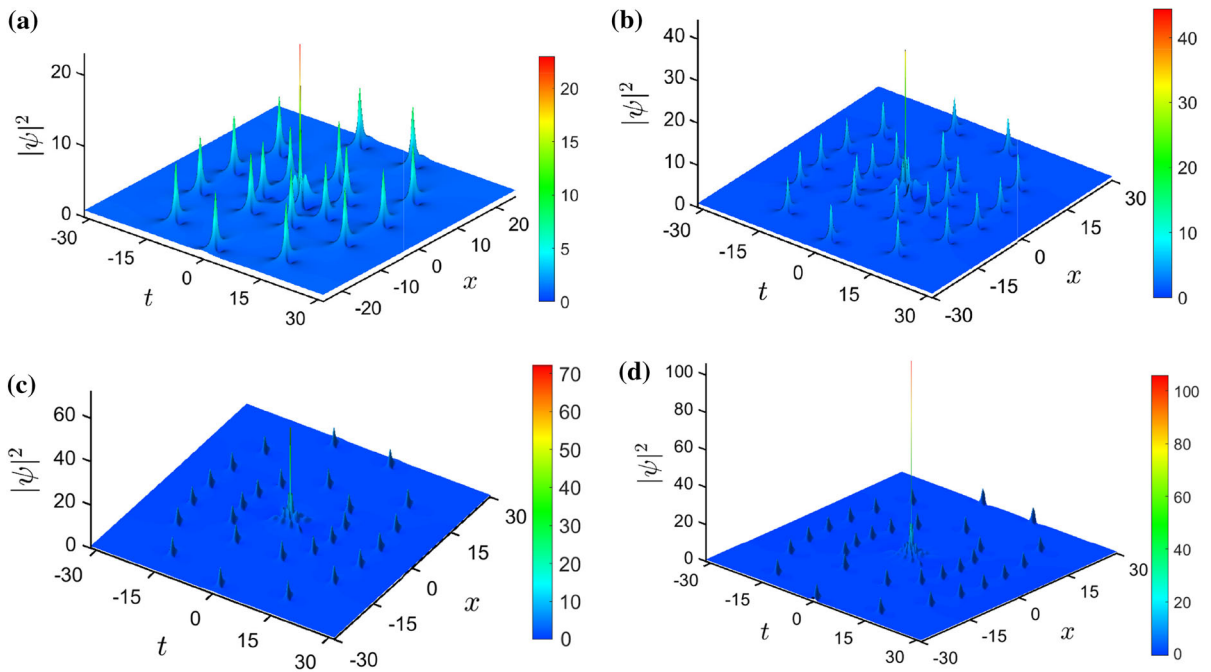
Fig. 1 3D color plots of double-elliptic rogue wave clusters ($m = 2$) on the uniform background. The rogue wave of order $n - 2m$ is formed at the origin $(0, 0)$ of the (x, t) plane. The shifts are calculated for $X_{j4} = 10^6$. The orders of Darboux transformation and the Akhmediev breather representing the high-intensity central peak are: **a** $n = 6$ with the second-order rogue wave, **b** $n = 7$ with the third-order rogue wave, **c** $n = 8$ with the fourth-order rogue wave, and **d** $n = 9$ with the fifth-order rogue wave

ellipses is $c_1 = 13$ and $c_2 = 9$. One can further increase n to get higher-order RWs that are rarely or never seen before. For $n = 8$, the RW4 is obtained with $c_1 = 15$ and $c_2 = 11$ (Fig. 1c). For $n = 9$, the RW5 is formed with $c_1 = 17$ and $c_2 = 13$ (Fig. 1d). It is seen that higher the order of the central RW, the narrower and stronger the RW peak at $(0, 0)$. The highest intensities in Fig. 1a–d are, respectively: 22.98, 44.45, 77.26, and 105.81. We have also computed solutions with other frequencies, for instance $\omega = 0.05$. The appearance of this RW cluster was very similar to the 10^{-1} case (not shown), so we proceeded with the 0.1 value.

In Fig. 2, we show the elliptic rogue wave cluster with 3 ellipses. Thus, we take $m = 3$ and change the n value. In Fig. 2a, we set $n = 8$ and obtain the second-order RW at $(0, 0)$. The outer, middle, and inner ellipses consists of $c_1 = 15$, $c_2 = 11$, and $c_3 = 7$ AB1s, respectively. In Fig. 2b, $n = 9$ and a RW3 was observed with $c_1 = 17$, $c_2 = 13$, and $c_3 = 9$. The RW4 with $c_1 = 19$, $c_2 = 15$, and $c_3 = 11$ is computed for $n = 10$ (Fig. 2c).

We last show the results for $m = 4$. The analysis is analogous to the previous two cases. When $n = 10$, we get RW2 and 4 rings surrounding the central peak. The number of AB1 on four ellipses, from outer to the inner, is $c_1 = 19$, $c_2 = 15$, $c_3 = 11$, and $c_4 = 7$, respectively (Fig. 3a). Next, we take $n = 11$ and obtain RW3 with $c_1 = 21$, $c_2 = 17$, $c_3 = 13$, and $c_4 = 9$ (Fig. 3b).

In general, under the conditions for DT computation presented in this section, our conjecture is that the RW of $n - 2m$ order is obtained at $(0, 0)$ with m ellipses around the peak for $n \geq 2m + 2$. If we index the rings from 1 to m, going from the outer to the inner one, then the number of AB1 on each ring is $c_i = 2n - 4i + 3$.

4 The semi-axes of ellipses in clusters

In paper [28], dealing with a single circular rogue wave cluster, the authors proposed a formula for the radius of the ring depending on Darboux shifts along the x- and t-axes. Having ellipses at hand, we present how the length of the vertical semi-axis depends on an absolute
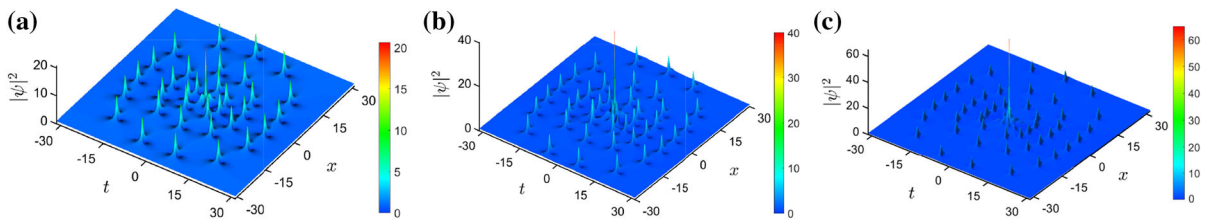
(a)

(b)

(c)

Fig. 2 3D color plots of triple-elliptic rogue wave clusters ($m = 3$) on the uniform background ($X_{j4} = 10^6$). The rogue wave of order $n - 2m$ is formed at the origin $(0, 0)$ of the (x, t) plane. The orders of Darboux transformation and the Akhmediev breather representing the high-intensity central peak are: **a** $n = 8$ with the second-order rogue wave, **b** $n = 9$ with the third-order rogue wave, and **c** $n = 10$ with the fourth-order rogue wave
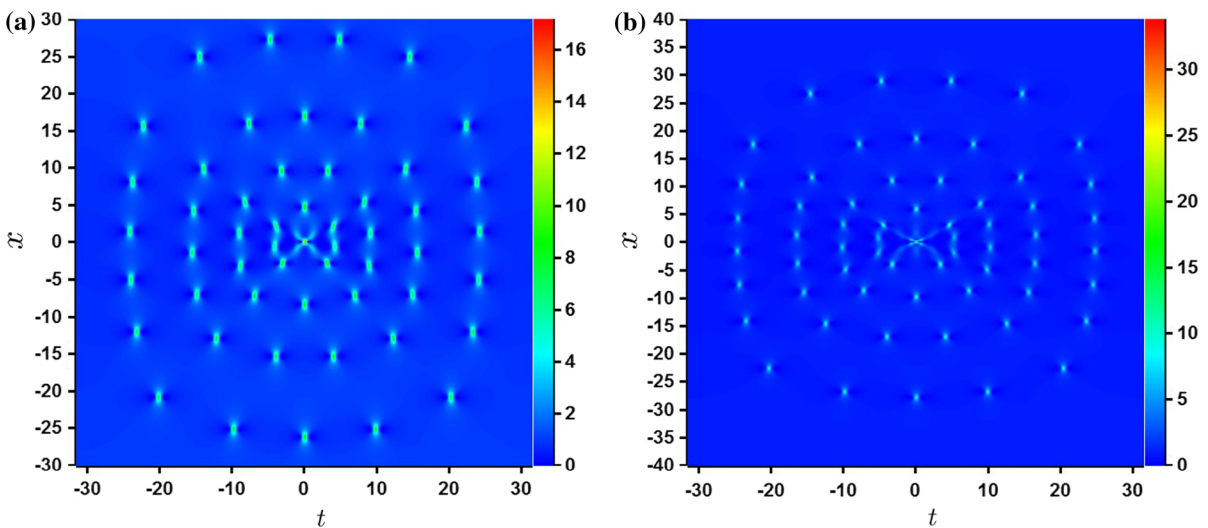
(a)

(b)

Fig. 3 2D color plots of rogue wave clusters on the uniform background having four ellipses ($m = 4$) around $n - 2m$ order rogue wave, formed at the origin $(0, 0)$ of the (x, t) plane. Shifts are obtained for $X_{j4} = 10^6$. The orders of Darboux transformation and the Akhmediev breather representing the high-intensity central peak are: **a** $n = 10$ with the second-order rogue wave, and **b** $n = 11$ with the third-order rogue wave

evolution shift for all ellipses, up to four rings ($m = 4$) in the cluster. In Fig. 4, we show the $n = 10$ and $m = 4$ case and indicate the AB1s on an i-th ellipse with numbers $i = 1$ to $i = 4$ (from the inner-most toward the outer-most ring). It turns out that all rings, for any m, have AB1s at $t = 0$ with alternating positions along this vertical line: the inner-most AB1 is positioned above the central RW. The next AB1 with index 2 is below the maximum at (0,0), the AB1 marked 3 is in the upper half of the (x, t) plane, and so on. We therefore define the length of the vertical semi-axis R_{xi} as the distance between the central RW at the origin and AB1 indexed with i. Since the higher-order DT solution is expressed by a very complicated and cumber-

some analytical expression, which is difficult to write and analyze, we applied the numerical calculation of AB1 positions along the $t = 0$ line.

In Fig. 5a, we show the R_x dependence on $x_{shift} = x_1 = \dots = x_m$ for two rings surrounding RW2 at the center ($n = 6$, $m = 2$) at two main frequencies: $\omega = 0.1$ and $\omega = 0.05$. We see that the position of AB1 at the first ring is increasing as the evolution shift becomes larger, in contrast to AB1's x-coordinate on the outer ring, which first increases but then saturates and finally starts to decline slowly. Therefore, one can differ two regions in the (x, t) plane: the first one (I) is roughly estimated as the half-plane before the interception of R_{x1} and R_{x2} curves. In this region, the cluster has a

Fig. 4 2D color plots of the quadruple-elliptic rogue wave cluster, obtained for $n = 10$ and $m = 4$, with numbers 1, 2, 3, and 4 indicating the single-order Akhmediev breathers located at $t = 0$ on each ellipse. The distance along x-axis between the RW center at $(0, 0)$ and the maximum of the breather labeled with i corresponds to the vertical semi-axis R_{xi} of the i-th ellipse
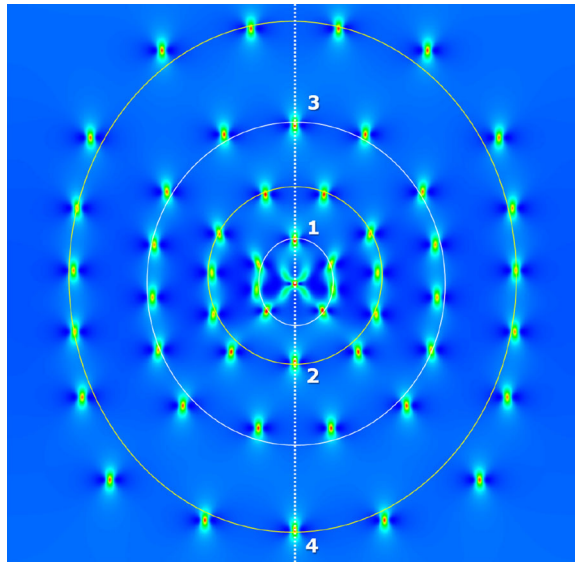
regular "concentric ellipses" - like shape. For $\omega = 0.1$, the region I is determined by $x_{\text{shift}} < 11.7$. When $\omega = 0.05$, the region I is given by $x_{\text{shift}} < 23$. The example of a RW cluster in the second region (II) is shown in Fig. 5b. It is clearly seen that the two rings are deformed and thus no longer elliptical in the shape. In Fig. 5c and 5d, the R_{x1} and R_{x2} dependence is shown for the case of RW2 and RW3 at the center, respectively, only in the region I, where the radial symmetry is preserved.

In Fig. 6a, we plot the graph of R_x as a function of x_{shift} in the case of three rings around a RW2 cluster ($n = 8$ and $m = 3$). We see that the vertical semi-axis of the first and third ellipses is an increasing function of the evolution shift, in contrast to R_{x2}. In Fig. 6b, the RW2 with four rings is analyzed ($n = 10$ and $m = 4$). Graphs in both figures are computed in region I. Our conclusion is that the x position of AB1 (with $t = 0$) on odd-labeled ellipses (1, 3) grows constantly with the increasing shift, while R_x of even indexed rings (2, 4) first increases, then saturates and finally slowly declines until the symmetry is broken.

5 Multi-elliptic rogue wave clusters on Jacobi elliptic dnoidal background

In this section, we demonstrate that multi-elliptic RW clusters can be obtained on a periodic background defined by Jacobi elliptic dnoidal function dn, by using the modified DT scheme for the NLSE [29]. The seed

function used here is $\psi_{\text{dn}}(x, t) = \text{dn}(t, g)e^{i(1-g^2/2)x}$, where g is the elliptic modulus and $m_{\text{dn}} = g^2$ is the elliptic modulus squared. The choice of eigenvalues and shifts is the same as described in previous sections, but the procedure for calculating $\psi(x, t)$ of order n is different. As explained in [29], the exact analytical values of wave function can be obtained only when $t = 0$. In order to compute $\psi(x, t \neq 0)$ over the entire (x, t) grid, the numerical calculation is required. In this work, we use the fourth-order Runge–Kutta algorithm. We manage to obtain a two-ring cluster around RW2 ($n = 6$ and $m = 2$) on an elliptic background ($m_{\text{dn}} = 0.4^2$) using this numerical procedure. The result is shown in Fig. 7a. We also present the 2-elliptic cluster around RW3 ($n = 7$, $m = 2$, $m_{\text{dn}} = 0.4^2$) in Fig. 7b. By a careful look at both 3D plots, one can observe the low-amplitude background waves on which the AB1 structures and high-intensity AB2/AB3 peaks are generated.

6 Multi-elliptic rogue wave clusters for extended NLSE family

Finally, we generalize our results to Hirota equation, which is a first member of the extended family of nonlinear Schrödinger equations [14,15]. It is important to note that the DT technique retains the same recursive relations for the Lax pair and higher-order ψ functions as before. We therefore can generate solitons and
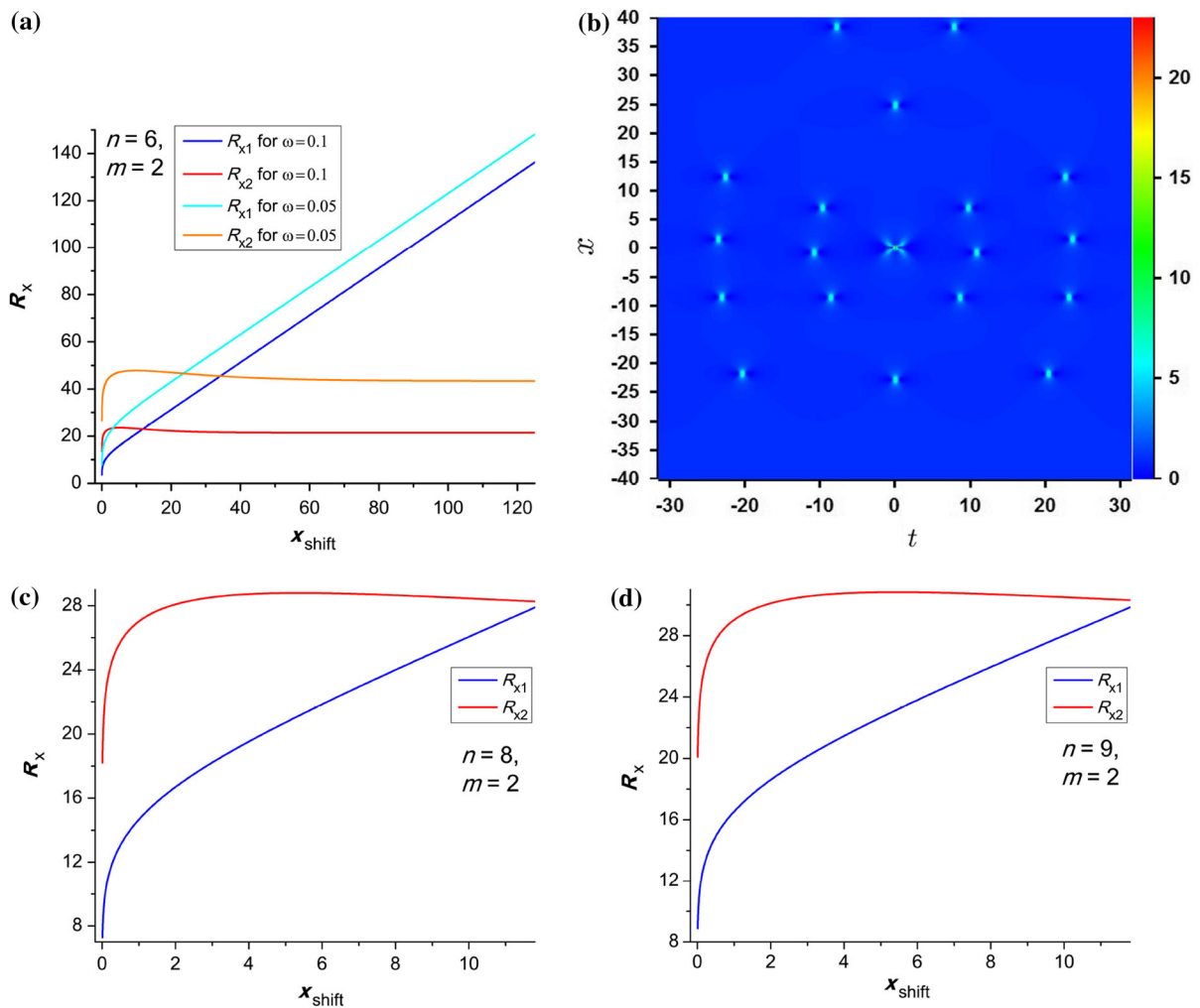
Fig. 5 Dependencies of the vertical semi-axes R_{x1} and R_{x2} on the absolute shift x_{shift} of the first two components in the Darboux transformation scheme for two ellipses in the RW cluster ($m = 2$). **a** The graphs of R_{x1} and R_{x2} as functions of x_{shift} for $n = 6$ and two main frequencies: $\omega = 0.1$ and $\omega = 0.05$. The region in which two ellipses in a cluster are deformed roughly begins at x_{shift} coordinate where R_{x2} saturates and decrease to R_{x1} value (here, $x_{shift} \approx 11.7$ for $\omega = 0.1$, and $x_{shift} \approx 23$ for $\omega = 0.05$). **b** The deformed double-elliptic cluster obtained for $n = 6$ and $x_{shift} = 13.5$. **c** The R_{x1} and R_{x2} as functions of x_{shift} for $n = 8$ in the region of undeformed elliptic cluster. **d** The R_{x1} and R_{x2} as functions of x_{shift} for $n = 9$ in the region of undeformed elliptic cluster

breathers of any order using the sets of eigenvalues and transverse/evolution shifts as explained above. The intensity distribution of such solutions will differ from the simple cubic NLSE, due to free parameters in the extended families and a bunch of additional dispersion and nonlinear terms, but the procedure for their analytical buildup remains the same. In other words, one can utilize the same algorithm and take identical sets of shifts to compute multi-elliptic RW clusters for any equation from the extended NLSE hierarchy.

The only difference in the DT scheme between NLSE and Hirota equation is in analytical expressions for the Lax pair functions r and s, but all recursive relations remain the same, as stated above. The Hirota DT scheme is presented in detail in [19]. Here, we generate the multi-elliptic RW cluster on a uniform background with $\psi_0 = e^{ix}$ as the seed. Our main goal is to investi-

Fig. 6 Dependencies of the vertical semi-axes R_{xi} on the absolute shift x_{shift} of the first m components in the Darboux transformation scheme of order n for **a** three ellipses in the RW cluster ($n = 8$ and $m = 3$), and **b** four ellipses in the RW cluster ($n = 10$ and $m = 4$)
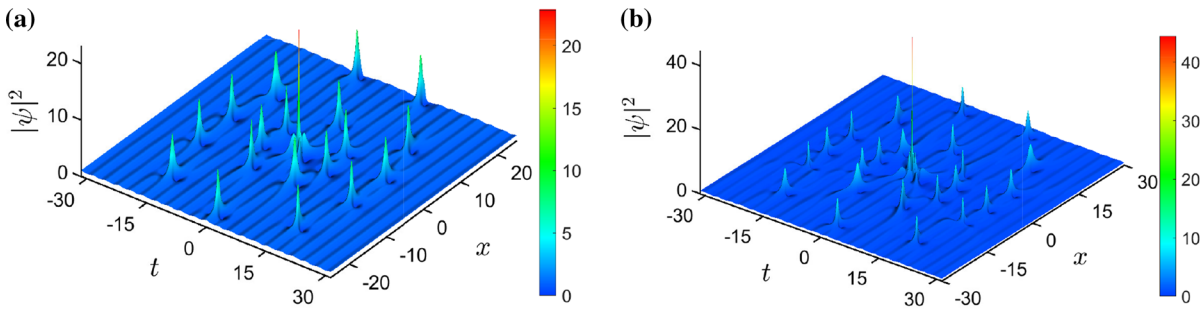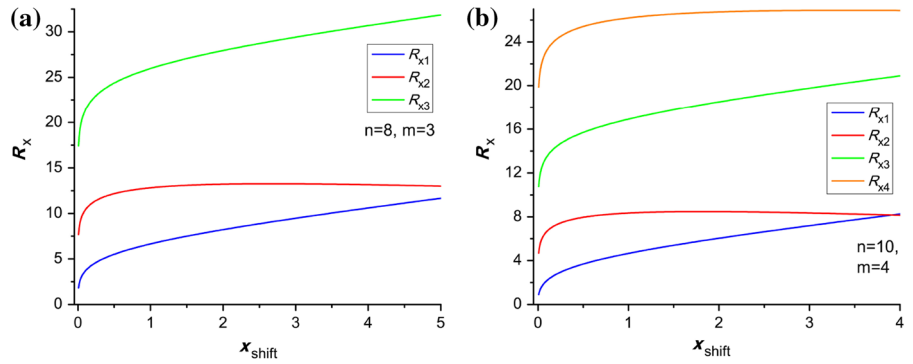

Fig. 7 3D color plots of the rogue wave clusters on the Jacobi elliptic dnoidal background. The rogue wave of $n - 2m$ order is formed at the origin of the (x, t) plane and is encircled by two ellipses ($m = 2$). The shifts are computed for $X_{j4} = 10^6$. The elliptic modulus squared is $m_{dn} = 0.4^2$. The orders of Darboux transformation and Akhmediev breather representing the high-intensity central peak are: **a** $n = 6$ with the second-order rogue wave, and **b** $n = 7$ with the third-order rogue wave
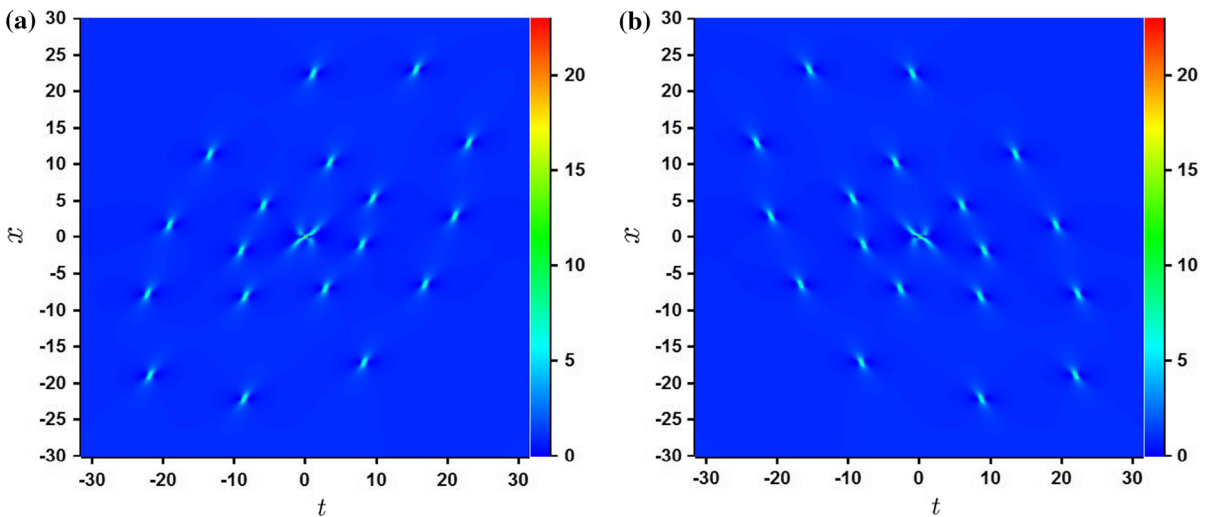

Fig. 8 3D color plots of double-elliptic rogue wave clusters ($m = 2$), formed on the uniform background around the second-order RW peak ($n = 6$) at $(0, 0)$ for Hirota equation. The shifts are calculated for $X_{j4} = 10^6$. The free parameter is: **a** $\alpha = -0.07$ and **b** $\alpha = 0.07$

gate the cluster appearance when Hirota operator (the term in Eq. 1.2 multiplied by α) sets in. For this purpose, we take $\alpha = \pm 0.07$ and build two clusters having RW2 at the (x, t) center, surrounded by two rings ($n = 6$ and $m = 2$). When α is negative, the entire cluster is tilted toward the positive direction of t-axis. In addition, the radial symmetry of the central RW2 is broken, since the local maxima in the vicinity of RW2 are more pronounced in the tilted direction.

The intensity distribution for $\alpha = -0.07$ is shown in Fig. 8a. If one changes the sign of α then the skew angle (between the vertical axis of the cluster and x-axis) will just change the sign. The results for $\alpha = 0.07$ are shown in Fig. 8b. The measured skew angle for $\alpha = \pm 0.07$ is $\theta \approx \mp 18.6°$. In addition, both ellipses are stretched for nonzero α, since the distances between AB1s on inner and outer rings (marked in Fig. 4 with 1 and 2) and the central RW2 are bigger than in the NLSE case. For the cubic NLSE ($\alpha = 0$: Fig. 1a) the semi-axis lengths are $R_{x1} = 10.1$ and $R_{x2} = 22$. In the Hirota case, shown in Fig. 8, the semi-axis lengths are $R_1 = 10.76$ and $R_2 = 23.7$. Here we claim that larger the α, the bigger the skew angle and the amount of cluster stretching (results not shown).

The analysis can be further applied on even higher-order equations of the extended NLSE hierarchy using the same procedure—with similar results. The subject of ongoing research is the influence of higher-order dispersions, additional nonlinearities, and real parameters on the overall shape of multi-elliptic RW clusters for this highly nonlinear systems. The limitation of this study is the complication for producing the rogue wave clusters dynamically. Even using the single period box and appropriate initial conditions from DT, the modulation instability sets in during numerical integration, decreasing the AB1 intensities on the rings and introducing additional peaks. The challenge for obtaining RW clusters numerically for NLSE and ENLSE remains the topic for the next research. In addition, the verification and analysis of the conservation laws of such numerical solutions using different methods, such as structure-preserving method [59–64] could be considered.

7 Conclusion

In this paper, we have presented the multi-elliptic rogue wave clusters of the nonlinear Schrödinger equation on uniform and nonuniform (Jacobi elliptic dnoidal) backgrounds. We showed that the Darboux transformation scheme of an arbitrary order n (up to $n = 11$) with m equal and nonzero evolution shifts, can produce Akhmediev breathers of $n - 2m$ order positioned at the origin of the (x, t) plane. We showed that this high-intensity narrow peak, a central rogue wave, is encircled by m concentric elliptical rings of the first-order Akhmediev breathers. The number of AB1s on each ring depends on the ring index and the solution order.

In order to better understand the cluster geometry, we have numerically investigated the lengths of semi-axes of all rings around the central RW. We provided the graphs where distances from RW at $(0, 0)$ to AB1 on the vertical $t = 0$ line at each ellipse were plotted as functions of the absolute evolution shift. Our results suggest that the radial symmetry is destroyed for large evolution shifts.

We next used the modified Darboux transformation scheme to numerically build RW clusters on a periodic background. Although the intensity of higher-order Akhmediev breather at the center significantly surpasses the amplitude of elliptic waves, we were able to observe the weak background oscillations on which the cluster is constructed.

We concluded our analysis by applying the Darboux transformation scheme on the Hirota equation. We exhibited that the Hirota operator introduces the titling and stretching of the entire cluster in a direction determined by the sign of the single real Hirota parameter.

We believe that further research of multi-rogue wave clusters on the cubic NLSEs is warranted in the future, owing to many degrees of freedom offered by the Darboux transformation scheme (the choice of eigenvalues and the spatial and temporal shifts). Research possibilities grow even more if one considers the cluster solutions for the infinite hierarchy of extended nonlinear Schrödinger equations. The analysis and results presented in this paper could be used to understand better the origin and generation of rogue waves in physical systems governed by cubic and extended nonlinear Schrödinger equations.

Data availability All data generated or analyzed during this study are included in the published article.

Declarations

Conflict of interest The authors declare that they have no conflict of interest.

References

1. Fibich, G.: The Nonlinear Schrödinger Equation. Springer, Berlin (2015)
2. Mirzazadeh, M., Eslami, M., Zerrad, E., Mahmood, M.F., Biswas, A., Belić, M.: Optical solitons in nonlinear directional couplers by sine-cosine function method and Bernoulli's equation approach. Nonlinear Dyn. **81**, 1933–1949 (2015)
3. Khalique, C.M.: Stationary solutions for nonlinear dispersive Schrödinger equation. Nonlinear Dyn. **63**, 623–626 (2011)
4. Agrawal, G.P.: Applications of nonlinear fiber optics. Academic Press, San Diego (2001)
5. Kivshar, Y.S., Agrawal, G.P.: Optical Solitons. Academic Press, San Diego (2003)
6. Dudley, J.M., Dias, F., Erkintalo, M., Genty, G.: Instabilities, breathers and rogue waves in optics. Nature Phot. **8**, 755 (2014)
7. Dudley, J.M., Taylor, J.M.: Supercontinuum Generation in Optical Fibers. Cambridge University Press, Cambridge (2010)
8. Kibler, B., Fatome, J., Finot, C., Millot, G., Dias, F., Genty, G., Akhmediev, N., Dudley, J.M.: Observation of Kuznetsov-Ma soliton dynamics in optical fibre. Sci. Rep. **6**, 463 (2012)
9. Bao, W.: The nonlinear Schrödinger equation and applications in Bose-Einstein condensation and plasma physics. In: Lecture Note Series, IMS, NUS, vol. **9** (2007)
10. Busch, T., Anglin, J.R.: Dark-bright solitons in inhomogeneous Bose-Einstein condensates. Phys. Rev. Lett. **87**, 010401 (2001)
11. Zakharov, V.E.: Stability of periodic waves of finite amplitude on a surface of deep fluid. J. Appl. Mech. Tech. Phys. **9**, (1968)
12. Osborne, A.: Nonlinear ocean waves and the inverse scattering transform. Academic Press, Cambridge (2010)
13. Shukla, P.K., Eliasson, B.: Nonlinear aspects of quantum plasma physics. Phys. Usp. **53**, 51 (2010)
14. Ankiewicz, A., Kedziora, D.J., Chowdury, A., Bandelow, U., Akhmediev, N.: Infinite hierarchy of nonlinear Schrödinger equations and their solutions. Phys. Rev. E **93**, 012206 (2016)
15. Kedziora, D.J., Ankiewicz, A., Chowdury, A., Akhmediev, N.: Integrable equations of the infinite nonlinear Schrödinger equation hierarchy with time variable coefficients. Chaos **25**, 103114 (2015)
16. Mani Rajan, M.S., Mahalingam, A.: Nonautonomous solitons in modified inhomogeneous Hirota equation: soliton control and soliton interaction. Nonlinear Dyn. **79**, 2469–2484 (2015)
17. Wang, D.-S., Chen, F., Wen, X.-Y.: Darboux transformation of the general Hirota equation: multisoliton solutions, breather solutions and rogue wave solutions. Adv. Differ. Equ. **2016**, 67 (2016)
18. Ankiewicz, A., Soto-Crespo, J.M., Akhmediev, N.: Rogue waves and rational solutions of the Hirota equation. Phys. Rev. E **81**, 046602 (2010)
19. Nikolić, S.N., Aleksić, N.B., Ashour, O.A., Belić, M.R., Chin, S.A.: Systematic generation of higher-order solitons and breathers of the Hirota equation on different backgrounds. Nonlinear Dyn. **89**, 1637–1649 (2017)
20. Chowdury, A., Kedziora, D.J., Ankiewicz, A., Akhmediev, N.: Breather solutions of the integrable nonlinear Schrödinger equation and their interactions. Phys. Rev. E **91**, 022919 (2015)
21. Yang, Y., Yan, Z., Malomed, B.A.: Rogue waves, rational solitons, and modulational instability in an integrable fifth-order nonlinear Schrödinger equation. Chaos **25**, 103112 (2015)
22. Nikolić, S.N., Aleksić, N.B., Ashour, O.A., Belić, M.R., Chin, S.A.: Breathers, solitons and rogue waves of the quintic nonlinear Schrödinger equation on various backgrounds. Nonlinear Dyn. **95**, 2855–2865 (2019)
23. Nikolić, S.N., Ashour, O.A., Aleksić, N.B., Zhang, Y., Belić, M.R., Chin, S.A.: Talbot carpets by rogue waves of extended nonlinear Schrödinger equations. Nonlinear Dyn. **97**, 1215 (2019)
24. Akhmediev, N.N., Korneev, V.I.: Modulation instability and periodic solutions of the nonlinear Schrödinger equation. Theor. Math. Phys. **69**, 1089 (1986)
25. Akhmediev, N., Eleonskii, V., Kulagin, N.: Exact first-order solutions of the nonlinear Schrödinger equation. Theor. Math. Phys. **72**, 809 (1987)
26. Zakharov, V.E., Shabat, A.B.: Exact theory of two-dimensional self-focusing and one-dimensional self-modulation of waves in nonlinear media. J. Exp. Theor. Phys. **34**, 62 (1972)
27. Matveev, V.B., Salle, M.A.: Darboux Transformations and Solitons. Springer, Berlin-Heidelberg (1991)
28. Kedziora, D.J., Ankiewicz, A., Akhmediev, N.: Circular rogue wave clusters. Phys. Rev. E **84**, 056611 (2011)
29. Kedziora, D.J., Ankiewicz, A., Akhmediev, N.: Rogue waves and solitons on a cnoidal background. Eur. Phys. J. Special Topics **223**, 43–62 (2014)
30. Chin, S.A., Ashour, O.A., Nikolić, S.N., Belić, M.R.: Peak-height formula for higher-order breathers of the nonlinear Schrödinger equation on nonuniform backgrounds. Phys. Rev. E **95**, 012211 (2017)
31. Peregrine, D.H.: Water waves, nonlinear Schrödinger equations and their solutions. J. Austral. Math. Soc. B **25**, 16 (1983)
32. Garrett, C., Gemmrich, J.: Rogue waves. Phys. Today. **62**, 62 (2009)

33. Solli, D.R., Ropers, C., Jalali, B.: Active Control of Rogue Waves for Stimulated Supercontinuum Generation. Phys. Rev. Lett. **101**, 233902 (2008)

34. Dudley, J.M., Genty, G., Eggleton, B.J.: Harnessing and control of optical rogue waves in supercontinuum generation. Opt. Express **16**, 3644 (2008)

35. Ganshin, A.N., Efimov, V.B., Kolmakov, G.V., Mezhov-Deglin, L.P., McClintock, P.V.E.: Observation of an Inverse Energy Cascade in Developed Acoustic Turbulence in Superfluid Helium. Phys. Rev. Lett. **101**, 065303 (2008)

36. Bludov, Y.V., Konotop, V.V., Akhmediev, N.: Matter rogue waves. Phys. Rev. A **80**, 033610 (2009)

37. Akhmediev, N., et al.: Roadmap on optical rogue waves and extreme events. J. Opt. **18**, 063001 (2016)

38. Chin, S.A., Ashour, O.A., Belić, M.R.: Anatomy of the Akhmediev breather: cascading instability, first formation time, and Fermi-Pasta-Ulam recurrence. Phys. Rev. E **92**, 063202 (2015)

39. Zhu, Q., Lin, F., Li, H., Hao, R.: Human-autonomous devices for weak signal detection method based on multimedia chaos theory. J. Ambient Intell. Human. Comput (2020). https://doi.org/10.1007/s12652-020-02270-x

40. Gupta, V., Mittal, M.: QRS Complex Detection Using STFT, Chaos Analysis, and PCA in Standard and Real-Time ECG Databases. J. Inst. Eng. India Ser. B **100**, 489–497 (2019)

41. Gupta, V., Mittal, M., Mittal, V.: R-peak detection based chaos analysis of ECG signal. Analog Integr. Circ. Sig. Process **102**, 479–490 (2020)

42. Gupta, V., Mittal, M.: A novel method of cardiac arrhythmia detection in electrocardiogram signal. Int. J. Med. Eng. Inf. **12**, (5) (2020)

43. Gupta, V., Mittal, M., Mittal, V.: R-Peak Detection Using Chaos Analysis in Standard and Real Time ECG Databases. IRBM **40**, 341–354 (2019)

44. Gupta, V., Mittal, M., Mittal, V., Saxena, N.K.: BP signal analysis using emerging techniques and its validation using ECG Signal. Sens. Imag. **22**, 25 (2021)

45. Gupta, V., Mittal, M., Mittal, V.: Chaos theory and ARTFA: emerging tools for interpreting ECG signals to diagnose cardiac arrhythmias. Wireless Pers. Commun. **118**, 3615–3646 (2021)

46. Fleischhauer, M., Imamoglu, A., Marangos, J.P.: Electromagnetically induced transparency: optics in coherent media. Rev. Mod. Phys. **77**, 633–673 (2005)

47. Nikolić, S.N., Radonjić, M., Krmpot, A.J., Lučić, N.M., Zlatković, B.V., Jelenković, B.M.: Effects of a laser beam profile on Zeeman electromagnetically induced transparency in the Rb buffer gas cell. J. Phys. B: At. Mol. Opt. Phys. **46**, 075501 (2013)

48. Krmpot, A.J., Ćuk, S.M., Nikolić, S.N., Radonjić, M., Slavov, D.G., Jelenković, B.M.: Dark Hanle resonances from selected segments of the Gaussian laser beam cross-section. Opt. Express **17**, 22491–22498 (2009)

49. Li, Z.-Y., Li, F.-F., Li, H.-J.: Exciting rogue waves, breathers, and solitons in coherent atomic media. Commun. Theor. Phys. **72**, 075003 (2020)

50. Kedziora, D.J., Ankiewicz, A., Akhmediev, N.: Rogue wave triplets. Phys. Lett. A **375**, 2782 (2011)

51. Kedziora, D.J., Ankiewicz, A., Akhmediev, N.: Triangular rogue wave cascades. Phys. Rev. E **86**, 056602 (2012)

52. Dubard, P., Gaillard, P., Klein, C., Matveev, V.B.: On multi-rogue wave solutions of the NLS equation and positon solutions of the KdV equation. Eur. Phys. J. Special Topics **185**, 247 (2010)

53. Ohta, Y., Yang, J.: General high-order rogue waves and their dynamics in the nonlinear Schrödinger equation. Proc. R. Soc. A **468**, 1716 (2012)

54. Gaillard, P.: Degenerate determinant representation of solutions of the nonlinear Schrödinger equation, higher order Peregrine breathers and multi-rogue waves. J. Math. Phys. **54**, 013504 (2013)

55. Ankiewicz, A., Akhmediev, N.: Multi-rogue waves and triangular numbers. Roman. Rep. Phys. **69**, 104 (2017)

56. He, J.S., Zhang, H.R., Wang, L.H., Porsezian, K., Fokas, A.S.: Generating mechanism for higher-order rogue waves. Phys. Rev. E **87**, 052914 (2013)

57. Kedziora, D.J., Ankiewicz, A., Akhmediev, N.: Classifying the hierarchy of nonlinear-Schrödinger-equation rogue-wave solutions. Phys. Rev. E **88**, 013207 (2013)

58. Akhmediev, N.: Waves that appear from nowhere: complex rogue wave structures and their elementary particles. Front. Phys. **8**, 612318 (2021)

59. Hu, W., Wang, Z., Zhao, Y., Deng, Z.: Symmetry breaking of infinite-dimensional dynamic system. Appl. Math. Letts. **103**, 106207 (2020)

60. Hu, W., Huai, Y., Xu, M., Feng, X., Jiang, R., Zheng, Y., Deng, Z.: Mechanoelectrical flexible hub-beam model of ionic-type solvent-free nanofluids. Mech. Syst. Signal Process. **159**, 107833 (2021)

61. Hu, W., Xu, M., Song, J., Gao, Q., Deng, Z.: Coupling dynamic behaviors of flexible stretching hub-beam system. Mech. Syst. Signal Process. **151**, 107389 (2021)

62. Hu, W., Zhang, C., Deng, Z.: Vibration and elastic wave propagation in spatial flexible damping panel attached to four special springs. Commun. Nonlinear. Sci. Numer. Simulat. **84**, 105199 (2020)

63. Hu, W., Ye, J., Deng, Z.: Internal resonance of a flexible beam in a spatial tethered system. J. Sound Vib. **45**, 115286 (2020)

64. Hu, W., Xu, M., Jiang, R., Zhang, C., Deng, Z.: Wave propagation in non-homogeneous asymmetric circular plate. Int. J. Mech. Mater. Des. (2021). https://doi.org/10.1007/s10999-021-09556-8

Article

Dynamic Cellular Cartography: Mapping the Local Determinants of Oligodendrocyte Transcription Factor 2 (OLIG2) Function in Live Cells Using Massively Parallel Fluorescence Correlation Spectroscopy Integrated with Fluorescence Lifetime Imaging Microscopy (mpFCS/FLIM)

Sho Oasa,[¶] Aleksandar J. Krmpot,[¶] Stanko N. Nikolić,[¶] Andrew H. A. Clayton, Igor F. Tsigelny, Jean-Pierre Changeux, Lars Terenius, Rudolf Rigler,* and Vladana Vukojević*

Read Online

ACCESS | Metrics & More | Article Recommendations | SI Supporting Information

ABSTRACT: Compartmentalization and integration of molecular processes through diffusion are basic mechanisms through which cells perform biological functions. To characterize these mechanisms in live cells, quantitative and ultrasensitive analytical methods with high spatial and temporal resolution are needed. Here, we present quantitative scanning-free confocal microscopy with single-molecule sensitivity, high temporal resolution ($\sim$10 μs/frame), and fluorescence lifetime imaging capacity, developed by integrating massively parallel fluorescence correlation spectroscopy with fluorescence lifetime imaging microscopy (mpFCS/FLIM); we validate the method, use it to map in live cell location-specific variations in the concentration, diffusion, homodimerization, DNA binding, and local environment of the oligodendrocyte transcription factor 2 fused with the enhanced Green Fluorescent Protein (OLIG2-eGFP), and characterize the effects of an allosteric inhibitor of OLIG2 dimerization on these determinants of OLIG2 function. In particular, we show that cytoplasmic OLIG2-eGFP is largely monomeric and freely diffusing, with the fraction of freely diffusing OLIG2-eGFP molecules being $f_{D,free}^{cyt} = (0.75 \pm 0.10)$ and the diffusion time $\tau_{D,free}^{cyt} = (0.5 \pm 0.3)$ ms. In contrast, OLIG2-eGFP homodimers are abundant in the cell nucleus, constituting $\sim$25% of the nuclear pool, some $f_{D,bound}^{nuc} = (0.65 \pm 0.10)$ of nuclear OLIG2-eGFP is bound to chromatin DNA, whereas freely moving OLIG2-eGFP molecules diffuse at the same rate as those in the cytoplasm, as evident from the lateral diffusion times $\tau_{D,free}^{nuc} = \tau_{D,free}^{cyt} = (0.5 \pm 0.3)$ ms. OLIG2-eGFP interactions with chromatin DNA, revealed through their influence on the apparent diffusion behavior of OLIG2-eGFP, $\tau_{D,bound}^{nuc}$ (850 $\pm$ 500) ms, are characterized by an apparent dissociation constant $K_{d,app}^{OLIG2-DNA} = (45 \pm 30)$ nM. The apparent dissociation constant of OLIG2-eGFP homodimers was estimated to be $K_{d,app}^{(OLIG2-eGFP)2} \approx 560$ nM. The allosteric inhibitor of OLIG2 dimerization, compound NSC 50467, neither affects OLIG2-eGFP properties in the cytoplasm nor does it alter the overall cytoplasmic environment. In contrast, it significantly impedes OLIG2-eGFP homodimerization in the cell nucleus, increasing five-fold the apparent dissociation constant, $K_{d,app,NSC50467}^{(OLIG2-eGFP)2} \approx 3$ μM, thus reducing homodimer levels to below 7% and effectively abolishing OLIG2-eGFP specific binding to chromatin DNA. The mpFCS/FLIM methodology has a myriad of applications in biomedical research and pharmaceutical industry. For example, it is indispensable for understanding how biological functions emerge through the dynamic integration of location-specific molecular processes and invaluable for drug development, as it allows us to quantitatively characterize the interactions of drugs with drug targets in live cells.
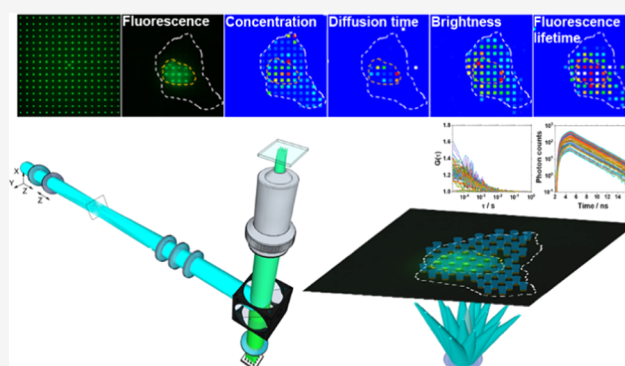
T he intracellular environment is a complex and crowded, spatially heterogeneous medium the organization of which is bestowed and dynamically maintained through innumerable reaction-diffusion processes.[1,2] While strong interactions (bond dissociation energies $D_0 > 20$ kJ/mol) are important determinants of cellular physiology as they confer specificity and selectivity,[3] it is well established that weak, nonspecific interactions ($D_0 < 20$ kJ/mol), such as hydrogen bonding and interactions between permanent and transient

dipoles, are equally important despite being so weak that they can be broken with energies that are within the range of thermal fluctuations. At the molecular level, weak interactions define macromolecular configuration and conformation, and hence, their function.[4] At the cellular level, they are critical determinants of the overall organization of the cellular interior and significantly contribute to compartmentalization, i.e., the formation of distinct local environments (often called membrane-less organelles), where particular interactions between relevant biomolecules are enabled to efficiently proceed.[5−7] The evolution of mechanisms that harness weak cooperative interactions was recently shown to render living organisms more capable of robustly undergoing evolutionary changes, and it appears that such mechanisms have been repeatedly positively selected during the evolution of increasingly complex organisms.[8] The quest to deploy weak cooperative interactions is also of relevance for designing new drugs, in particular for the development of so-called allosteric drugs.[9−11] Allosteric drugs exploit a fundamental mechanism, initially identified in multisubunit/multimeric proteins,[12−14] which was later observed also in monomeric, intrinsically disordered proteins.[15] They bind to a distant binding site, inducing rearrangements in the network of weak cooperative interactions that propagate across comparatively long distances, eventually rendering the active site more/less amenable for orthosteric ligand/drug binding.[16] Efforts to develop allosteric drugs focus on understanding the function of natural molecules that act as allosteric modulators,[17] rely on the use of computational approaches to identify allosteric binding sites that can be specifically targeted,[18,19] and are inseparable from the advancement of experimental techniques to understand detailed molecular mechanisms that underlie allostery[20] and to characterize the effects of prospective allosteric drug candidates.[21] Experimental techniques designed to probe these processes in the cellular milieu need to be sensitive over a range of timescales (nanoseconds-to-seconds) and length scales (nanometers to microns).

Fluorescence correlation spectroscopy (FCS) and its dual-color variant fluorescence cross-correlation spectroscopy (FCCS) are the only presently available techniques that can nondestructively measure the concentration, diffusion, and binding of fluorescent/fluorescently labeled molecules in live cells with single-molecule sensitivity and high, sub-micro-second, temporal resolution.[22] However, the same feature of FCS/FCCS that enables the ultimate, single-molecule sensitivity—the possibility to probe a minute observation volume element, thereby significantly reducing the background and improving the signal-to-background-ratio, confers also a serious limitation. Thus, conventional FCS/FCCS is of limited overview, i.e., measurements are restricted to a single-point location, probing in the cell a tiny volume of $(0.2-2) \times 10^{-15}$ l.[23−26] To overcome this limitation, FCS was "amalgamated" with imaging-based methods, yielding new experimental techniques, such as temporal image correlation spectroscopy (TICS)[27] and raster image correlation spectroscopy (RICS),[28,29] which rely on raster scanning of the laser beam to illuminate a larger area; and single-plane illumination microscopy-based FCS (SPIM-FCS)[30−33] and massively parallel FCS (mpFCS),[34−36] which deploy different illumination strategies to cover a larger area. While these new techniques enable location-specific mapping of molecular concentration and diffusion in cells, they also entail some limitations. For example, the temporal and spatial resolution of

TICS are inversely related and one is improved at the expense of the other—spatial resolution of TICS increases when the temporal resolution is in the millisecond range, due to long image plane acquisition time by raster scanning. This renders TICS either ill-suited for the study of fast processes or confers low spatial resolution.[27] Similarly, RICS sacrifices spatial resolution to determine the diffusion and the number of molecules,[28,29,37] as averaging over a relatively large number of pixels (>64) is needed to allow an accurate spatial correlation analysis. It also has significant problems when analyzing heterogeneous samples since the presence of bright speckles significantly deforms the autocorrelation curve. SPIM-FCS, which relies on the use of light-sheet illumination and a 2D camera to examine larger areas, can achieve high temporal resolution—recently reaching 6 μs for a reasonably short ($\approx$100 s) measurement duration using the Swiss single-photon avalanche diode array (CHSPAD) camera.[32,38] SPIM-FCS is, however, inherently hampered by the nonuniform thickness of the light sheet, which widens toward the edges, thus forming larger observation volume elements. Furthermore, scattering of the light sheet in heterogeneous environments and the presence of opaque compounds within the specimen alter the light-sheet intensity and can even completely block the incident light, which is recognized by the appearance of dark stripes in SPIM images. In SPIM-FCS, this translates to nonuniform illumination and hence a nonuniform signal-to-noise (SNR) ratio across the image. mpFCS relies on the spatial modulation of the incident laser beam by a diffractive optical element (DOE) to generate a large number of illumination spots, and a matching SPAD camera to detect in a confocal arrangement of the fluorescence intensity fluctuations from a large number (1024 in a 32 × 32 arrangement) of observation volume elements, providing single-molecule sensitivity and high spatial (~250 nm) and temporal (21 μs) resolution.[34,35,39,40] mpFCS was shown to be widely applicable, for the analysis of fast diffusion processes of eGFP-fused functional biomolecules in live cells[35] and in live tissue *ex vivo*.[39] The broad applicability of the mpFCS for functional fluorescence microscopy imaging (fFMI) was a motivation for us to go a step further and develop a new fFMI modality, mpFCS integrated with fluorescence lifetime imaging microscopy (mpFCS/FLIM). The fluorescence lifetime of a fluorophore or a fluorescently labeled macromolecule provides information on the environment local to the fluorophore (e.g., refractive index, polarity, pH, PO_2, Ca^{2+}). It can provide complementary insights into nanoscale (1−10 nm) macro-molecular interactions or conformations via Förster resonance energy transfer (FRET) and dynamic quenching on the nanosecond timescale.

Here, we present an integrated massively parallel FCS and FLIM system (mpFCS/FLIM) on the same microscope frame. This enables massively parallel measurements to quantitatively characterize the location-specific concentration, mobility and interactions (via FCS), and local properties of the immediate surrounding of biomolecules (via fluorescence lifetime). We demonstrate the capabilities of mpFCS/FLIM for quantitative live cell biochemistry and cellular pharmacology by character-izing the effect of test compound NSC 50467 on oligodendrocyte transcriptional factor 2 (OLIG2) dimeriza-tion. OLIG2, a basic helix−loop−helix transcription factor in the central nervous system, plays an important role in neuronal cell differentiation during development,[41] adult neurogenesis,[42] and glioblastoma development.[43] Substances that target
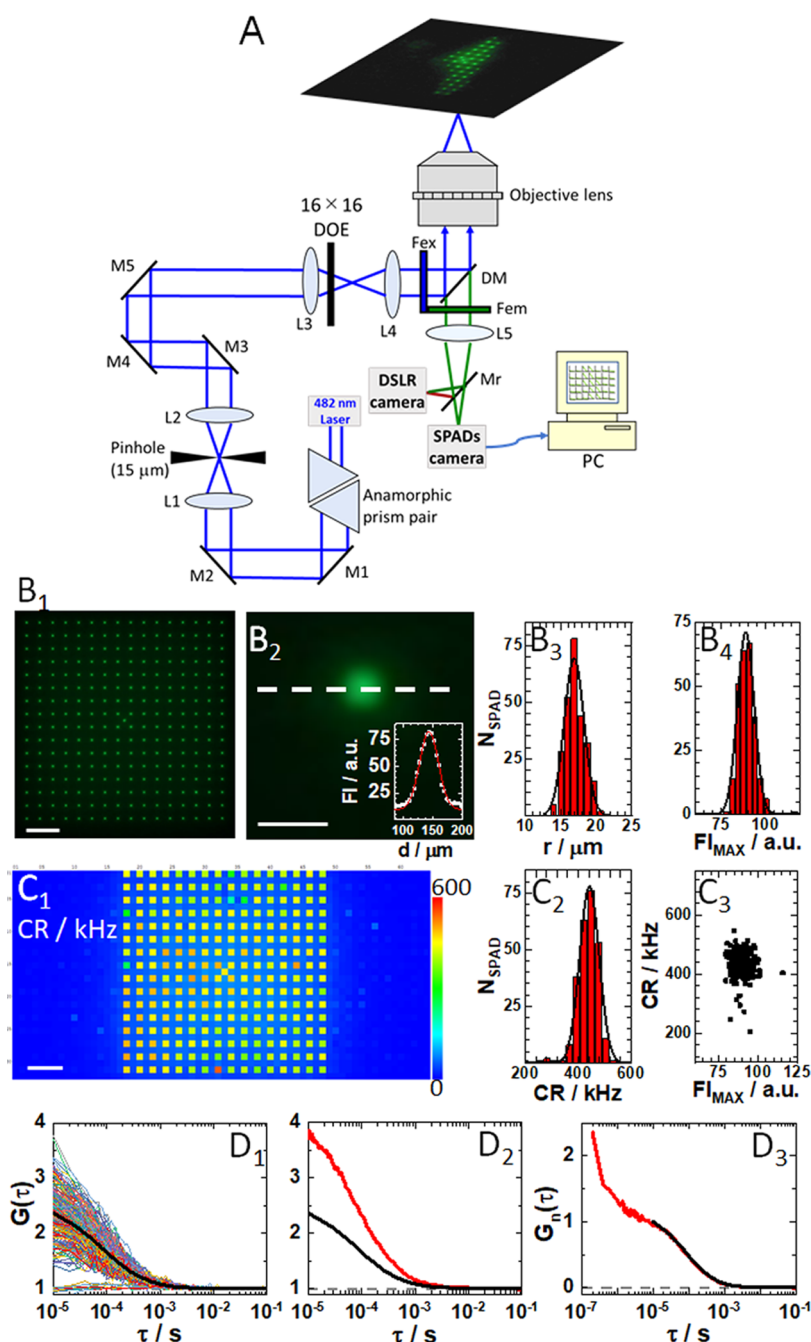
Figure 1. Optical setup for mpFCS/FLIM. (A) Schematic drawing of the mpFCS/FLIM optical setup. The 482 nm laser beam with elliptical cross-section is transformed into a circular beam using an anamorphic prism pair and expanded using a Kepler telescope setup (L1 and L2) with a pinhole in its focus. The expanded circular laser beam is focused by the focusing lens (L3) mounted on an *xyz* translation stage, which is positioned in front of the diffractive optical element (DOE) that can be translated along and rotated around the *z*-axis. The illumination matrix consisting of 16 × 16 (256) spots, which are generated in the image plane of the back port of the microscope, is imaged by the microscope relay optics (L4) and the objective lens to the object plane. Fluorescence is detected by a single-photon avalanche diode (SPAD) camera that can be translated along the *z*-axis and tilted at two angles (pitch and yaw) or a digital single-lens reflex (DSLR) camera. (B$_1$) Image of the illumination matrix visualized by the DSLR camera using a thin fluorescence layer as a specimen. (B$_2$) Enlarged image of a single illumination spot shown in (B$_1$). Inset: Fluorescence intensity (FI) distribution through the center of the spot (white dashed line) and the best-fit Gaussian curve (red solid line). Spot roundness, assessed by measuring the spot radius in different directions: horizontal (0°; white dashed line), 45, 90, and 135°, showed that the ratio of spot radius over the spot radius at 0° was 1.00, 1.02, 0.96, and 1.04, respectively. (B$_3$) Histogram of spot radii for all 256 spots in the confocal image of the illumination matrix is shown in (B$_1$). The average spot radius, $r_{spot} = (17 \pm 2)$ μm, was determined from a half of the full width at half-maximum (FWHM) of the best-fit Gaussian curve. (B$_4$) Histogram of peak fluorescence intensity for all spots in the confocal image of the illumination matrix is shown in (B$_1$). The average peak fluorescence intensity, $FI_{MAX} = (90 \pm 5)$ au. (C$_1$) Scanning-free confocal image of the same specimen as in (B$_1$) acquired using the SPC^3 SPAD camera. Here, each SPAD in addition to being a photodetector also acts as a 30 nm pinhole. Of note, every other SPAD in the centrally positioned 32 × 32 SPADs of the 64 × 32 SPC^3 SPAD camera was used. Unilluminated SPADs (dark blue), on the sides and in-between the illuminated ones (yellow−red ones), are clearly distinguishable by fluorescence intensity. (C$_2$) Histogram of fluorescence intensity, i.e., photon count rates (CR) measured in all illuminated SPADs shown in (C$_1$). The average fluorescence intensity was

Figure 1. continued

determined, CR = (440 ± 35) kHz. (C_3) Scatter plot showing spot peak intensity measured using the SPC^3 SPAD camera (C_1) as compared to the spot intensity measured using the DSLR camera (B_1). While a unimodal distribution is observed, six SPADs with disparate values were identified. (D_1) 256 single-SPAD autocorrelation curves (ACCs) recorded in an aqueous buffer solution of eGFP, c_{eGFP} = 4 nM, with the corresponding average ACC (black). (D_2) ACCs acquired in the same solution as in D_1 by mpFCS (black; same as in D_1) and spFCS ACC (red). The dashed gray line shows $G(\tau)$ = 1. (D_3) ACCs shown in D_2 normalized to the same amplitude, $G(10\ \mu s)$ = 1 at τ = 10 μs, acquired using the spFCS (red) and the mpFCS (black) systems. The dashed gray line shows $G_n(\tau)$ = 0. In all images, scale bar is 10 μm.

OLIG2 are attractive candidates for the development of therapeutic agents for glioblastoma.[44] However, identification of such molecules is not trivial due to the large and complex surface through which OLIG2 interacts with itself and other partners, which is uncharacteristic and with no hydrophobic pockets.[18,19] The NSC 50467 compound was identified *in silico* using the so-called "combined pharmacophore approach" and was predicted to act as an allosteric inhibitor of OLIG2 homodimerization[45−47] thus impeding OLIG2 homodimer binding to the enhancer box (E-box), which is the canonical bHLH transcription factor binding site.[45−47]

EXPERIMENTAL SECTION

Optical Setup for Massively Parallel Fluorescence Correlation Spectroscopy Integrated with Fluorescence Lifetime Imaging Microscopy (mpFCS/FLIM). The optical design of the mpFCS/FLIM system and important features are shown in Figure 1A−C_3. Information about optical alignment, calibration, data acquisition, analysis, image rendering, and fitting of temporal autocorrelation curves (ACCs) using eq S1 is provided in the Supporting Information (Section S1, Figures S1−S5).

Software for mpFCS/FLIM. mpFCS/FLIM data acquisition, analysis, and graphical presentation were carried out using our own software, into which the Micro Photon Device (MPD) software for running the 2D SPAD array was integrated. The software was written in Embarcadero C++ Builder 10.2 (Embarcadero Technologies). Detailed information about data acquisition, analysis, and image rendering are given for mpFCS in Section S1b and for FLIM in Section S1c. Phasor plot analysis is presented in Section S1d.

Cell Culture and Transfection. Procedures for cell culturing and transfection for mpFCS/FLIM measurements (Section S2a), pharmacological treatment of cells (Section S2b), and cell culture for FRET-FLIM measurements (Section S2c) can be found in the indicated sections in the Supporting Information.

Dissociation Constant Assessment. Procedures for calculating the apparent dissociation constants of OLIG2-eGFP dimers (Section S3) and Olig2-eGFP−DNA complexes (Section S4) can be found in the indicated sections in the Supporting Information.

Standard Solutions for mpFCS/FLIM Calibration. Relevant information about standard solutions used for mpFCS/FLIM system calibration can be found in Section S5.

Statistical Analysis. All values are presented as mean ± standard deviation (SD). Two-tailed Student's t-test was used to compare two groups. The correlation analyses were reported using the probability value (p-value). Differences between two groups were considered to be significant when $p < 0.05$. Pearson's sample correlation coefficient r was used to assess the strength of a linear association between two variables. Statistical analysis was performed using the Origin 2018 program for interactive scientific graphing and data analysis

and/or Excel. During data analysis, data from a few pixels (<5%) were disregarded due to the extremely high background in these SPADs. The results were replicated in three independent experiments, starting from cell transfection, culturing, treatment, and measurement. Similar trends were observed in all three experiments. Figures show representative data acquired in a single cell.

RESULTS

Validation of mpFCS/FLIM System Performance for FCS. The sensitivity and temporal resolution of the mpFCS/FLIM system are unprecedented, enabling us to perform measurements in a buffered aqueous solution of the enhanced Green Fluorescent Protein (eGFP; Figure 1D_1−D_3). Of note, the amplitude of the average ACC acquired by mpFCS is half the amplitude of the ACC acquired using conventional single-point FCS (spFCS), largely due to a higher background in the mpFCS system than in the spFCS system (Figure 1D_2). In contrast, normalized autocorrelation curves nicely overlap (Figure 1D_3), revealing that the observation volume elements (OVEs) in the mpFCS and the spFCS systems are of similar size. We also show that the ACC can be fitted with the acceptable signal to noise using eq S1, α = 1, i = 1, T = 0 (Figure S4A,B) and that the axial ratio is not diverging ($s = \omega_z/\omega_{xy}$ = 4.6), which indicates that the assumption of a 3D-ellipsoidal Gaussian OVE is applicable. Finally, we show by z-stack imaging that the fluorescence intensity profile in the axial direction is Gaussian with a half width at half-maximum, HWHM = (1.15 ± 0.09) μm (Figure S4C).

Validation of mpFCS/FLIM System Performance for FLIM. To characterize the performance of the mpFCS/FLIM system for fluorescence lifetime (τ_f) measurements, the instrument response function (IRF) was measured and single-exponential decay fitting of FLIM curves was compared to convolution fitting with the IRF (Figure S6); effects of the gate width and the step size between gates on τ_f were examined (Figure S7); the precision with which τ_f of pure species can be determined was assessed using solutions of molecules with known fluorescence lifetimes (Figures 2 and S8); and the ability of our system to resolve two lifetimes using measurements at a single frequency was evaluated using a series of two-component solutions with different relative contributions of the two component (Figures 2 and S9). The most important results are summarized in Figure 2.

Briefly, Figure 2A_1 shows 256 simultaneously recorded fluorescence decay curves in a phosphate buffer solution of eGFP. Analysis using the single-exponential decay model (eq S2) yielded a histogram of fluorescence lifetimes from which eGFP fluorescence lifetime was determined, $\tau_{f,eGFP}$ = (2.5 ± 0.02) ns (Figure 2A_2). This value agrees well (i.e., to within 10%) with the values obtained in other laboratories.[48−50]

Using a 2.0 ns gate width and a 0.2 ns gate step time, τ_f was measured for several standards in solution, covering a τ_f range from 1 to 10 ns (Figure 2B_1,B_2). The agreement between
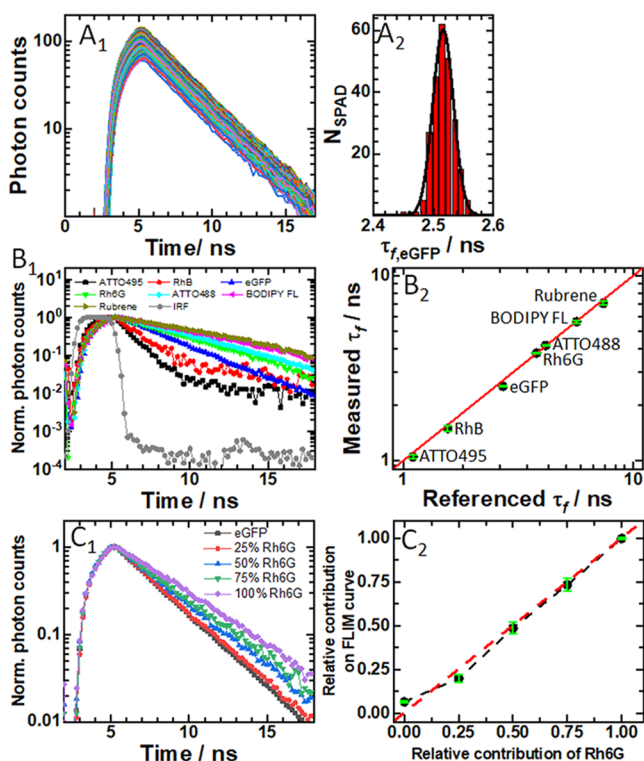
Figure 2. Fluorescence lifetime imaging microscopy (FLIM) using the integrated mpFCS/FLIM system. (A_1) 256 simultaneously recorded eGFP fluorescence decay curves in aqueous phosphate buffer. (A_2) Corresponding histogram of fluorescence lifetimes obtained using a one-component exponential decay model to fit the fluorescence decay curves. From a best-fit Gaussian curve, the fluorescence lifetime was determined, $\tau_{f,eGFP} = (2.50 \pm 0.02)$ ns. (B_1) Fluorescence decay curves recorded in aqueous solutions of different fluorescent dyes: ATTO495 (black), Rhodamine B (RhB; red), eGFP (blue), Rhodamine 6G (Rh6G; green), ATTO488 (cyan), BODIPY FL (magenta), Rubrene (dark yellow), and the Instrumental Response Function (IRF; gray), all acquired using the same SPAD in the SPC3 camera. (B_2) Comparison of fluorescence lifetimes measured using the mpFCS/FLIM system with literature values. Pearson's correlation indicated that there was a significant positive association between the measured and literature values ($r(7) = 0.999$, $p < 0.001$). The red line indicates perfect agreement. (C_1) Normalized fluorescence decay curves for Rh6G, eGFP, and their mixtures made so that a specified number of photons originates from Rh6G, e.g., 50% Rh6G indicates that 50% of photons are from Rh6G: eGFP (0% Rh6G; dark gray), 25% Rh6G (red), 50% Rh6G (blue), 75% Rh6G (green), and 100% Rh6G (violet). (C_2) Comparison of the relative contribution of Rh6G, as determined from fluorescence lifetime measurements using a two-component exponential decay fitting model with fixed fluorescence lifetimes: $\tau_{f,eGFP} = 2.5$ ns and $\tau_{f,Rh6G} = 3.8$ ns (black dots), with its actual concentration in a two-component mixture. Pearson's correlation indicated that there was a significant positive association between the measured τ_f and values found in the literature ($r(5) = 0.995$, $p < 0.01$).

expected and measured fluorescence lifetimes, which can be gleaned from Figure 2B_2, is excellent ($r = 0.999$, $p < 0.001$).

Given that τ_f can be considered a "molecular fingerprint," allowing detection and discrimination between multiple species that emit fluorescence over the same spectral window, we tested the capability of our instrument to distinguish fluorophores that emit in the same spectral region and have discernible lifetimes, Rhodamine 6G (Rh6G), $\tau_{f,Rh6G} = (3.80 \pm 0.04)$ ns, and eGFP, $\tau_{f,eGFP} = (2.50 \pm 0.02)$ ns. To this aim, we

mixed Rh6G and eGFP solutions at different proportions (Figure 2C_1,C_2). As expected, the total τ_f increased as the proportion of the species with the longer τ_f (here Rh6G) was increased (Figure 2C_1). A fit of the data to an exponential decay function by two processes (eq S3; with τ_f for eGFP and Rh6G fixed and amplitudes floated) yielded relative amplitudes that matched well the calculated relative contribution of the components in the mixture (Figure 2C_2).

Since attempts to fit the data with a two-component-exponential decay model with free-floating τ_f and their relative contributions did not lead to extraction of the correct component lifetimes and their relative amounts (Figure S9A_1,A_2), phasor analysis[51−53] was used to analyze the simultaneously acquired fluorescence decay curves, assuming that two lifetime components were common to all of the curves. By deploying phasor analysis, which uses the Fourier transform to decompose experimentally measured fluorescence decay curves into complex-valued functions of the modulus (m) and the phase angle (θ_{tot}) (eqs S4−S21), global analysis of a two-component system is reduced to algebraic calculations in the phasor space (Figure S9B_3). Following calibration experiments (Figure S8), we computed by phasor analysis τ_f and components' fractions with dramatically improved accuracy and precision (Figure S9B_1,B_2).

Spatial Mapping of Fluorescence Lifetime in a Fixed Specimen. To demonstrate spatial mapping of τ_f a fixed plant specimen, the acridine orange stained section through the rhizome of the lily of the valley (*Convallaria majalis*) was used (Figure 3).

Fluorescence images acquired using a spot-wise, 16×16, illumination and the DSLR camera (Figure 3A,B_1) show cells in the central parenchyma made visible owing to the fluorescence signal from the cell wall. The fluorescence image of the same cell as in Figure 3B_1 acquired using the SPC³ SPAD camera is shown in Figure 3B_2. Fluorescence decay curves simultaneously recorded in 256 individual SPADs (Figure S10), exemplified in Figure 3C, when fitted using a two-component exponential decay model (Figure 3D_1), yielded a short, $\tau_{f,wall1} = (0.6 \pm 0.1)$ ns (Figure 3D_2) and a long fluorescence lifetime component, $\tau_{f,wall2} = (2.9 \pm 0.2)$ ns (Figure 3D_3). Importantly, the thus determined τ_f provided significant image contrast (Figure 3E_1,E_2), and even a "ratiometric" image could be obtained revealing the relative contribution of the component with the short fluorescence lifetime (Figure 3E_3).

Spatial Mapping of Concentration, Diffusion, and Fluorescence Lifetime in Live Cells. To demonstrate spatial mapping of the concentration, diffusion, and lifetime in live cells (Figure S11), we first performed measurements on fluorescent proteins, eGFP (Figures 4 and S12) or eGFP tetramer (eGFP$_{tet}$; Figures S13 and S14), as nonreactive molecular probes.

Our data show that for similar eGFP concentrations in the cell, $c_{eGFP} \approx 20$ nM, and in the aqueous buffer solution, $c_{eGFP} \approx 4$ nM, the mean diffusion time of eGFP was about 2.5 times longer in the cell than in the aqueous buffer, $\tau_{D,eGFP,cell} = (260 \pm 60)$ μs vs $\tau_{D,eGFP,buffer} = (110 \pm 10)$ μs, consistent with previous studies,[54] whereas the molecular brightness and fluorescence lifetimes were similar CPSM$_{eGFP,cell} = (1.0 \pm 0.3)$ kHz and CPSM$_{eGFP,buffer} = (1.0 \pm 0.2)$ kHz, $\tau_{f,eGFP,cell} = (2.50 \pm 0.05)$ ns and $\tau_{f,eGFP,buffer} = (2.50 \pm 0.02)$ ns. However, the relative standard deviations (RSD) of all measured variables were higher in the living cell (Figure 4B_2,C_2,D_2,E_2) than those
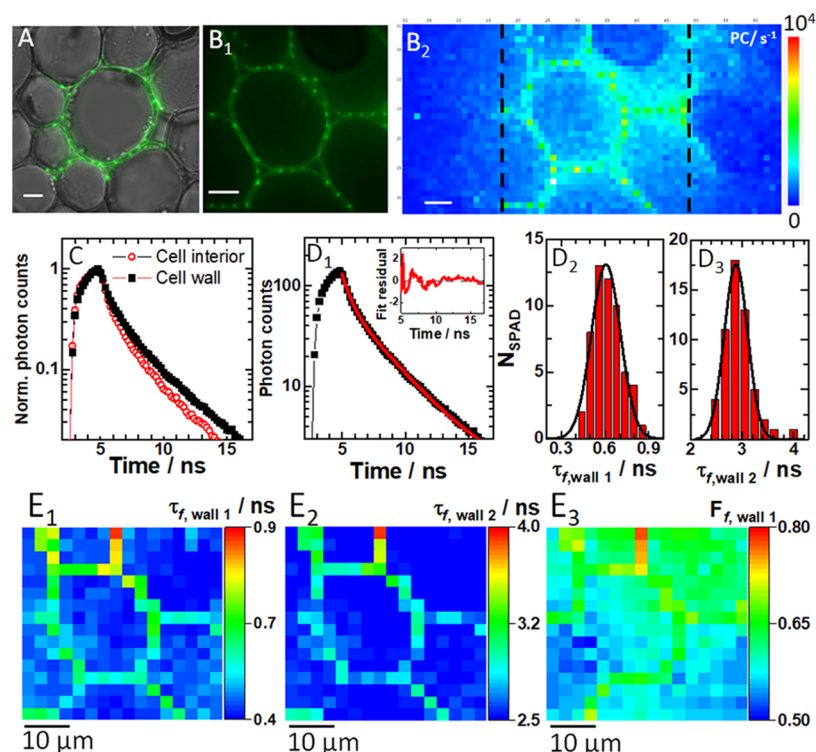
Figure 3. Spatial distribution of fluorescence lifetime in a fixed section of the rhizome of lily of the valley (*C. majalis*). (A) Fluorescence image of a spot-wise, 16 × 16, illuminated cell (green) overlaid on a wide-field transmission image (gray) of a region in the central parenchyma recorded using the DSLR camera. (B_1) Zoomed fluorescence image of a spot-wise illuminated cell in the central parenchyma recorded using the DSLR camera. (B_2) Fluorescence image of the same cell as in (B_1) acquired using the SPC[3] SPAD camera. Fluorescence intensity is given in photon counts (PC), exposure time 46 ms. (C) Fluorescence decay curves recorded in individual SPADs at distinct intracellular locations: cell wall (black squares) and inside the cell (red circles). All fluorescence decay curves are shown in Figure S10. (D_1) A fluorescence decay curve recorded in an individual SPAD at the cell wall (black squares) fitted using a two-component exponential decay model (eq S3, red line). Inset: Corresponding residuals. (D_2) Histogram of the short fluorescence lifetime component in the plasma membrane and the best-fit Gaussian curve yield $\tau_{f,wall1} = (0.6 \pm 0.1)$ ns. (D_3) Histogram of the long fluorescence lifetime component in the plasma membrane and the best-fit Gaussian curve yield $\tau_{f,wall2} = (2.9 \pm 0.2)$ ns. (E_{1-3}) FLIM images of the cell in (B_2) rendered visible by mapping the: short (E_1) and long (E_2) fluorescence lifetime component and the relative contribution of the short component (E_3). In all images, the scale bar is 10 μm.

in the homogenous solution (Figure S3B−E), indicating that the cell environment presents a spatial variation in local concentration, local diffusion processes (Figure S15), and local excited-state decay (environment). Correlation maps (Figure S16) showed that no correlation was observed between the concentration (number of eGFP), molecular brightness, and lifetime, ruling out any spatially dependent concentration quenching in the fluorescence lifetime and absence of diffusion-influenced lifetime quenching. Taken together, these results are largely consistent with the view of eGFP being a biochemically inert, monomeric protein, able to roam largely unimpeded inside the cellular milieu. The broadened distribution functions observed here (relative to homogenous aqueous buffer) reveal that the cellular interior is not uniform and that eGFP is not totally confined to the cytosol but is also found in cytoplasmic organelles.

In contrast to eGFP, which can access the entire cell, a fluorescence image of a HEK cell-expressing eGFP$_{tet}$ reveals distinctive fluorescence intensities in the cytoplasm and the cell nucleus (Figures S11B and S13A). Furthermore, the large RSD of the diffusion time for eGFP$_{tet}$ in the cytoplasm is of particular note, as it is ten-fold larger than the corresponding value for the monomeric eGFP in the cytoplasm. Because the eGFP$_{tet}$ is 4 times larger than eGFP (4 nm long axis dimension), this suggests that obstacles in the size range of 10 nm or more in the cellular environment affect eGFP$_{tet}$

dynamics, as revealed using the anomalous diffusion model (eq S1, $\alpha \neq 1$)[55−57] to fit the experimentally derived ACCs and determine the anomalous diffusion exponent (α; Figure S15B). Furthermore, and in contrast to the diffusion time, the fluorescence lifetime was homogeneous in cells expressing eGFP$_{tet}$ (Figure S13E$_1$). FLIM curves in the nucleus showed lower photon counts but revealed similar decay rates (Figure S14C$_{1-3}$). The histogram of fluorescence lifetime quantified $\tau_{f,eGFPtet} = (2.4 \pm 0.05)$ ns in the cytoplasm and similarly in the nucleus (Figure S13E$_2$).

Spatial Mapping of Transcription Factor OLIG2-eGFP in Live Cells Before and After Treatment with Compound NSC 50467: an Allosteric Inhibitor of OLIG2 Dimerization. To demonstrate spatial mapping of the concentration, diffusion, and lifetime of interacting molecules in live cells, intracellular localization and dynamics of OLIG2 was characterized (Figures 5, S11C,D, and S17−S25).

OLIG2 is known to bind as a homodimer to the enhancer box (E-box), the canonical bHLH transcription factor binding site.[45−47] It is predominantly localized in the cell nucleus (Figures 5A$_1$ and S11C), but is known to shuttle between the nucleus and the cytoplasm (Figure S11D), with the actual localization pattern emerging from a dynamic equilibrium that is predominantly governed by the nuclear export signal.[58] Spatial mapping of the number of OLIG2-eGFP in untreated
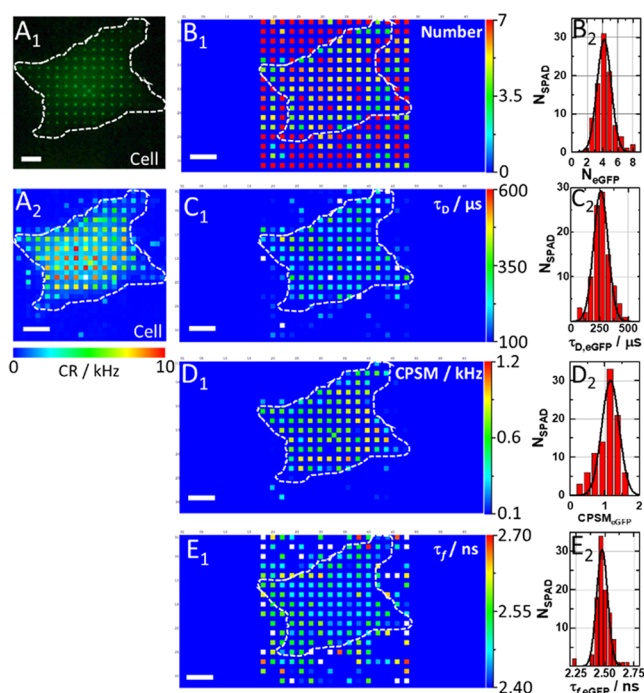
Figure 4. Spatial map of eGFP concentration, diffusion, brightness, and fluorescence lifetime in a live HEK cell. (A_1) Fluorescence image of an eGFP-expressing HEK cell acquired using a spot-wise, 16×16, illumination and a DSLR camera. The hand-drawn dashed line highlights the cell border visualized by transmission light imaging. (A_2) Count rate map. Corresponding ACCs and FLIM curves are shown in Figure S12. (B_1) Spatial map of the average N_{eGFP} in the OVE. Of note, the apparently high average number of molecules in the cell surrounding is an artifact of the near-zero amplitude of the ACCs in the cell culture medium (see Figure S12A_2). (B_2) Histogram corresponding to B_1. The best-fit Gaussian curve yields $N_{eGFP} = (4.22 \pm 0.92)$, corresponding to $c_{eGFP} \approx 20$ nM. (C_1) Spatial map of $\tau_{D,eGFP}$. (C_2) Histogram corresponding to (C_1) yields the average eGFP diffusion time, $\tau_{D,eGFP} = (260 \pm 60)$ μs. (D_1) Spatial map of eGFP brightness as reflected by counts per second per molecule (CPSM). (D_2) Histogram corresponding to (D_1) yields average $CPSM_{eGFP} = (1.0 \pm 0.3)$ kHz. (E_1) Spatial map of eGFP fluorescence lifetimes. (E_2) Histogram corresponding to (E_1) yields the average eGFP fluorescence lifetime, $\tau_{f,eGFP} = (2.50 \pm 0.05)$ ns.

cells revealed that the concentration of OLIG2-eGFP in the cell nucleus is higher than in the cytoplasm (Figure 5A_2); the diffusion time, determined from the full width of the ACC at half maximum, is significantly longer in the cell nucleus than in the cytoplasm, $\tau_D^{nuc} = (250 \pm 300)$ ms vs $\tau_D^{cyt} = (0.9 \pm 1.5)$ ms (Figure 5A_3,E), and the fluorescence lifetime map revealed a significantly longer lifetime states in the cell nucleus, fluorescence lifetime, $\tau_{f,OLIG2\text{-}eGFP}^{nuc} = (3.0 \pm 0.3)$ ns vs $\tau_{f,OLIG2\text{-}eGFP}^{cyt} = (2.7 \pm 0.2)$ ns (Figure 5F), reflecting differences in the local environment surrounding the eGFP probe of OLIG2-eGFP in these cellular locations (Figure 5A_4). Given the unexpectedly large experimental errors for diffusion times, we further examined ACCs. This analysis revealed two characteristic decay times in both, the cytoplasm (Figures 5C_1 and S18B_1,C_1) and the cell nucleus (Figures 5C_2 and S18B_2,C_2), with the fast-decaying components being, within the experimental error, indistinguishable between these compartments, $\tau_{D,free}^{cyt} = \tau_{D,free}^{nuc} = (0.5 \pm 0.3)$ ms, while the relative amplitude and the diffusion time of the second component were larger and much longer in the cell nucleus

than in the cytoplasm, $f_{D,bound}^{nuc} = (0.65 \pm 0.10)$ vs $f_{D,bound}^{cyt} = (0.25 \pm 0.10)$ and $\tau_{D,bound}^{nuc} = (850 \pm 500)$ ms vs $\tau_{D,bound}^{cyt} = (60 \pm 30)$ ms, respectively. (Of note, fluorescence intensity time series (Figure S18A_1,A_2) show that the signal intensity is unchanged over time and is not distorted by photobleaching. Rather, the ACCs recorded in the cell nucleus do not settle at 1 because the decay time of the second component is comparable to the signal acquisition time length (20 s).) Finally, OLIG2-eGFP molecular brightness in the cytoplasm, $CPSM_{OLIG2\text{-}eGFP}^{cyt} = (1.0 \pm 0.7)$ kHz (Figure 5G), was within the experimental error indistinguishable from that of eGFP in live cells, $CPSM_{eGFP} = (1.0 \pm 0.3)$ kHz, measured under the same conditions, suggesting that OLIG2-eGFP is monomeric in the cytoplasm. In the nucleus, average molecular brightness is higher, $CPSM_{OLIG2\text{-}eGFP}^{nuc} = (1.4 \pm 0.7)$ kHz (Figure 5G and Table S1), suggesting that a dynamic equilibrium between OLIG2-eGFP monomers and dimers exists.

Treatment with the allosteric inhibitor of OLIG2 dimerization did neither change the concentration, nor the diffusion time, nor the fluorescence lifetime, and nor the molecular brightness of OLIG2-eGFP residing in the cytoplasm; $p > 0.05$ for all measurements (Figures 5C_1, D–G, S17A_{1-3} and S19A_{1-4}). However, it significantly perturbed the motions and the local environment of OLIG2-eGFP in the cell nucleus, causing, on the average, a decrease in the diffusion time by 4 times (from 850 to 200 ms; Figures 5C_2,E and S19B_2, $p = 5 \times 10^{-3}$), and reduced the fluorescence lifetime (Figure 5F, $p = 1.5 \times 10^{-8}$) and the molecular brightness (Figures 5G, S17B_3 and S19B_4, $p = 7 \times 10^{-3}$), while leaving the overall OLIG2-eGFP concentration unchanged, as reflected by the number of OLIG2-eGFP molecules (Figures 5D and S17B_1, $p > 0.05$). Moreover, the positive correlation between local OLIG2-eGFP molecular brightness and the local diffusion, which was strong in the cell nuclei of untreated cells, was significantly reduced (Figure S19$B_{2-2,3-2}$).

Finally, mpFCS measurements enabled us to assess the value of the apparent dissociation constants for OLIG2-eGFP binding to chromatin DNA before, $K_{d,app}^{OLIG2\text{-}DNA} = (45 \pm 30)$ nM, and after treatment, $K_{d,NSC50467}^{OLIG2\text{-}DNA} = (130 \pm 40)$ nM (Figure S19C_{1-3}). Also, mpFCS measurement of OLIG2-eGFP concentration and molecular brightness revealed that in untreated cells about 25% of OLIG2-eGFP molecules are homodimers and that treatment with NSC 50467 effectively reduced OLIG2-eGFP homodimer levels to below 7% (Table S1). This, in turn, enabled us also to infer apparent OLIG2-eGFP homodimer dissociation constants in untreated cells $K_{d,app}^{(OLIG2\text{-}eGFP)2} \approx 560$ nM, which upon treatment becomes $K_{d,app,NSC50467}^{(OLIG2\text{-}eGFP)2} \approx 3$ μM.

Taken together, the mpFCS data indicate that treatment with the allosteric modulator NSC 50467 does not significantly alter OLIG2-eGFP properties in the cytoplasm, whereas in the cell nucleus OLIG2-eGFP dimers are not efficiently formed in the presence of NSC 50467 and OLIG2-eGFP binding to chromatin DNA is significantly abolished.

We then used Förster resonance energy transfer (FRET) via FLIM (FRET-FLIM), to further characterize NSC 50467 effects on OLIG2-eGFP dimer formation. To this aim, cells expressing OLIG2-eGFP, with eGFP acting as a FRET donor, and dark yellow fluorescent protein ShadowY tagged OLIG2 molecules (OLIG2-ShY), with ShY acting as FRET acceptor, were used. For a positive FRET control, a tandem dimer of eGFP and ShadowY (eGFP-ShY) was transfected into cells. As expected, robust FRET was observed with the positive FRET
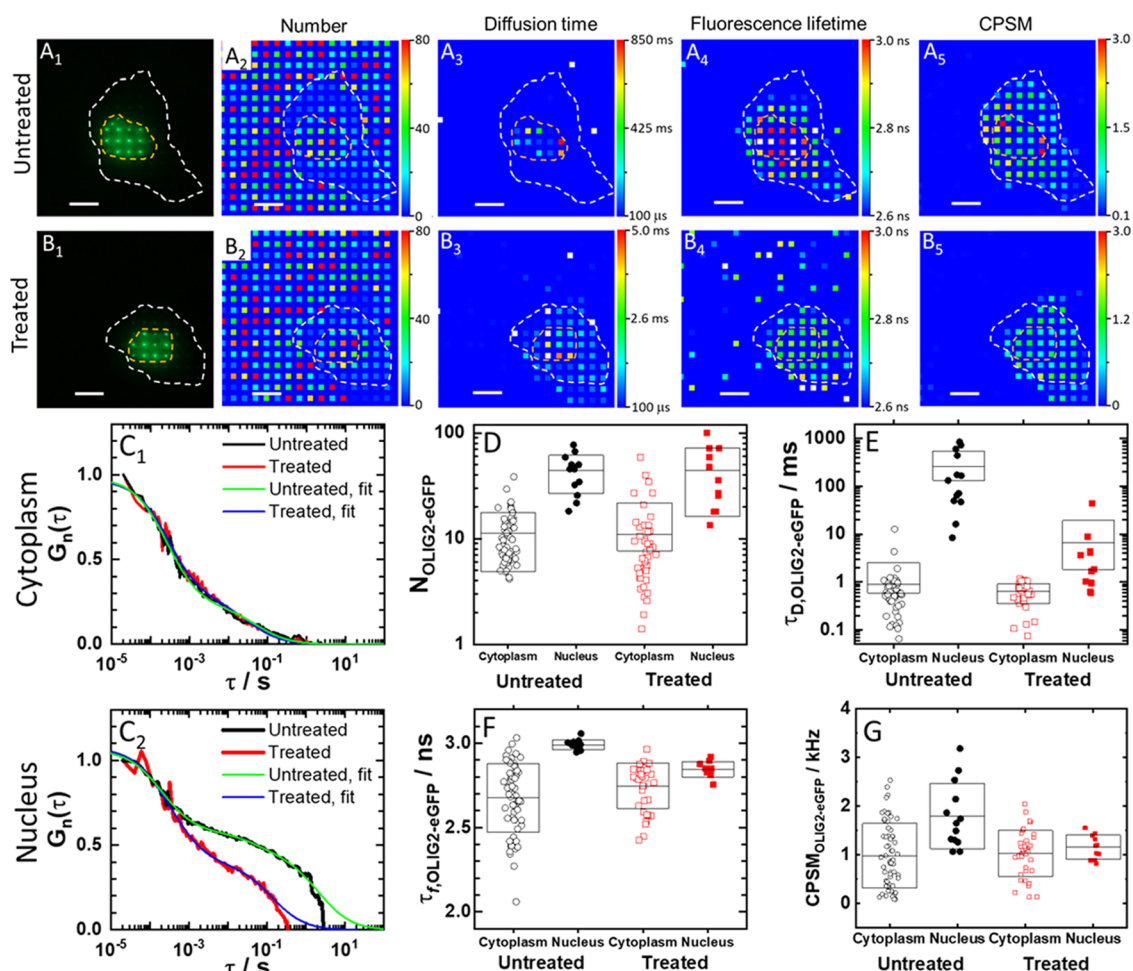
Figure 5. Spatial map of OLIG2-eGFP concentration, diffusion, brightness, and fluorescence lifetime in a live HEK cell before and after treatment with NSC 50467. (A_1, B_1) Fluorescence images of an untreated (A_1) and a treated (B_1) HEK cell-expressing OLIG2-eGFP, acquired using a spot-wise, 16×16, illumination and a DSLR camera. The hand-drawn dashed lines that highlight the cell border (white) and the cell nucleus (orange) were visualized by transmission light microscopy. Corresponding fluorescence intensity fluctuation time series and ACCs are shown in Figure S18. (A_2, B_2) Spatial map of the average number of OLIG2-eGFP molecules in an OVE, recorded in an untreated (A_2) and a treated (B_2) cell. (A_3, B_3) Spatial map of OLIG2-eGFP diffusion times recorded in an untreated (A_3) and a treated (B_3) cell. (A_4, B_4) Spatial map of fluorescence lifetimes recorded in an untreated (A_4) and a treated (B_4) cell. Corresponding FLIM curves are shown in Figure S18. (A_5, B_5) Spatial map of OLIG2-eGFP brightness (CPSM) recorded in an untreated (A_5) and a treated (B_5) cell. (C_1, C_2) Single-pixel ACCs normalized to the same amplitude, $G(20\ \mu s)$ = 1 at $\tau = 20\ \mu s$, recorded in the same pixel in the cytoplasm (C_1) and the same pixel in the cell nucleus (C_2) before (black) and after (red) treatment. Two-component 3D free diffusion model fitting to the ACCs recorded in the cell nucleus and the cytoplasm in the untreated (green) and the treated (blue) cell. (D−G) Effect of treatment on the number of molecules (D), diffusion time (E), average fluorescence lifetime (F), and average molecular brightness (G).

control probe, with a FRET efficiency of 55% (as determined by phasor analysis of the FLIM data, Figure S20). Phasor plots recorded in cells expressing OLIG2-eGFP and OLIG2-ShadowY showed evidence of emission from a mixture of FRET and non-FRET states including the FRET contribution from the OLIG2 dimer (Figure S21A). In the context of a FRET/non-FRET state model (involving donor, acceptor, and FRET states), our analysis delivered an amplitude fraction of FRET to be (0.3 ± 0.1) in the absence of allosteric inhibitor, which decreased to (0.07 ± 0.06) upon treatment with the inhibitory compound, also observable at other cells (Figure S21B,E,F). As expected, the decrease in the FRET fraction was accompanied by an increase in the contribution of non-FRET states. This data provides evidence for the efficient inhibition of OLIG2 dimer formation by the inhibitory compound. Since the RSD of the amplitude of the FRET fraction of OLIG2 without compound is larger than that of the tandem dimer of

fluorescent proteins (eGFP-ShY), we can conclude that OLIG2 dimerization in the nucleus was in addition to OLIG2 dimerization inhibition also affected by the nuclear environment (e.g., genome DNA structure).

■ DISCUSSION

In this work, we present two important achievements, the development of a new functional fluorescence microscopy imaging (fFMI) modality attained by integrating massively parallel fluorescence correlation spectroscopy with fluorescence lifetime imaging microscopy (mpFCS/FLIM) and demonstrate its use to characterize the action of a compound with potential therapeutic effects that target OLIG2.

Our instrument is a quantitative scanning-free confocal fluorescence microscope with single-molecule sensitivity; it has similar confocal volume elements with single-point FCS and 10 μs/frame temporal resolution and can map fluorescence

lifetimes from 1 to 10 ns. The instrument builds on our previous work,[35] but we have now improved to longer signal acquisition duration, ~10 s from previous 2.7 s, with a higher temporal resolution, ~10 μs/frame from previous ~21 μs/frame, toward tracking faster dynamic processes. In addition, the SNR was dramatically improved. In particular, the number of particles ratio against spFCS reduced 10 times, from 50 to 5 for fluorospheres ($d = 100$ nm). Also, single-pixel autocorrelation curves in eGFP and QD525 in water agree to within 10% with spFCS. Importantly, the system integrated with FLIM enabled us to perform mpFCS and FLIM at the same position in the cell. This is a significant improvement compared to current practice, where considerable time lags are introduced when moving the specimen from one microscope to the other. At the same time, the time needed for finding the same cell after moving the specimen from one microscope to the other is entirely abolished. Our dedicated software provides mono- and two-component exponential decay fitting for all 256 SPADs nearly instantly, rendering a fluorescence lifetime image in a few seconds. Implementation of phasor analysis makes multicomponent analysis in FLIM easily achieved without the need to fit multicomponent exponential decay curves.

In comparison with other presently available 2D FCS instruments, such as FCS based on total internal reflection (TIR-FCS[59−62]) and single plane illumination microscopy (SPIM-FCS[30−33]), our approach is more versatile. The main limitation of TIR-FCS is its restriction to an investigation of processes at the basal plasma membrane. SPIM-FCS, on the other hand, enables us to visualize the inside of cells and perform measurements there, but it is hampered by an inhomogeneous illumination and is characterized by a relatively larger observation volume ($\sim 1 \times 10^{-15}$ l). Advantages of our approach are optical sectioning, homogenous illumination and detection, and small confocal volume elements ($\sim 0.35 \times 10^{-15}$ l), which is particularly important since larger observation volume elements average local differences in concentration, mobility, and intermediate surrounding of molecules in a live cell. Thus, the integrated mpFCS/FLIM system uniquely enables us to map with great precision the molecular numbers and mobility via mpFCS and characterize the local environment immediately surrounding fluorescent/fluorescently labeled molecules via FLIM. Instrument performance was stringently assessed in a series of validation experiments using well-characterized samples. Most notably, we have demonstrated that we could measure the concentration and diffusion of eGFP in a dilute aqueous solution ($c_{eGFP} = 4$ nM, Figure 1D$_1$−D$_3$) and showed that it is uniform (Figures S3 and S15). We have also shown that noninteracting molecules smaller than 5 nm, e.g., eGFP, diffuse without significant hindrance through the entire cell (Figures 4 and S15), while molecules/molecular complexes that are larger than 10 nm, such as eGFP$_{tet}$, largely reside in the cytoplasm where their diffusion is hindered by internal membranes in the cytoplasm (Figures S13 and S15). These findings are in line with experimental findings reported in the literature and with theoretical findings showing that the cytoplasm behaves to a very large extent as a liquid phase for length scales shorter than 100 nm and as a dynamically structured macromolecular matrix for longer length scales.[63] They are also important for the validation of our instrument performance.

Importantly, the integrated mpFCS/FLIM system enabled us to characterize in live cells the heterogeneous reaction-diffusion landscape of transcription factor OLIG2-eGFP and provided important new insights into its intracellular organization. It also enabled us to characterize in great detail the effects of the allosteric inhibitor NSC 50467 on OLIG2-eGFP homodimerization and interactions with chromatin DNA. The possibility to quantitatively characterize in live cells location-specific differences in transcription factor concentration, homodimerization, and DNA binding and the effect of pharmacological agents on these determinants of transcription factor function opens transcription factors to experimental therapeutics. Here, we have shown that the therapeutic compound NSC 50467 targeting OLIG2 homodimerization efficiently abolishes OLIG2-eGFP binding to chromatin DNA. We have also shown that this compound does not affect OLIG2-eGFP levels in the cytoplasm and its distribution in cytoplasmic organelles/membrane-less microdomains. The possibility to perform such detailed, previously intractable measurements may significantly facilitate new therapeutic discoveries.

In conclusion, the methodology presented here is a versatile tool with myriads of applications in biomedical research. In its current realization with 256 (16 × 16) OVEs, simultaneous sampling in cellular organelles is limited to a handful of locations. This, however, can be improved using another DOE (e.g., (32 × 32), as we have previously shown[35,39]). Also, while we have demonstrated the application of our method for studies in live tissue *ex vivo*,[35,39] our approach is better suited for studies in cell cultures, where the background from scattered fluorescence is lower than in tissues/small organisms. Despite these limitations, the strength of our approach lies in the user-friendly instrument design and the capacity of our methods to characterize both, compartmentalization of molecular processes, by measuring local excited-state decay via FLIM, and their dynamic integration, by measuring diffusion/active transport using mpFCS. Compartmentalization and dynamic integration of molecular processes are opposed yet coexisting and intertwined principles essential for normal cellular physiology as they enable location-specific processing of information and integral whole-cell response. Our methodology is thus paving the way to better understanding how biological functions emerge from underlying spatially confined chemical processes.

■ ASSOCIATED CONTENT

Ⓢ Supporting Information

The Supporting Information is available free of charge at https://pubs.acs.org/doi/10.1021/acs.analchem.1c02144.

> S1: Optical setup for mpFCS/FLIM, data analysis, and image rendering; S2: Cell culture and transfection procedures; S3: Determining the apparent dissociation constant of OLIG2-eGFP homodimers; S4: Determining the apparent dissociation constant for OLIG2-eGFP binding to chromatin DNA by FCS; and S5: Standard solutions for mpFCS/FLIM system calibration (PDF)

■ AUTHOR INFORMATION

Corresponding Authors

Rudolf Rigler − *Department of Medical Biochemistry and Biophysics (MBB), Karolinska Institutet, 17177 Stockholm, Sweden; Department of Clinical Neuroscience (CNS), Center for Molecular Medicine (CMM), Karolinska Institutet, 17176 Stockholm, Sweden;* Email: Rudolf.Rigler@ki.se

Vladana Vukojević − *Department of Clinical Neuroscience (CNS), Center for Molecular Medicine (CMM), Karolinska Institutet, 17176 Stockholm, Sweden;* orcid.org/0000-0003-0873-5653; Email: Vladana.Vukojevic@ki.se

Authors

Sho Oasa − *Department of Clinical Neuroscience (CNS), Center for Molecular Medicine (CMM), Karolinska Institutet, 17176 Stockholm, Sweden;* orcid.org/0000-0003-3800-590X

Aleksandar J. Krmpot − *Institute of Physics Belgrade, University of Belgrade, 11080 Belgrade, Serbia; Department of Clinical Neuroscience (CNS), Center for Molecular Medicine (CMM), Karolinska Institutet, 17176 Stockholm, Sweden*

Stanko N. Nikolić − *Institute of Physics Belgrade, University of Belgrade, 11080 Belgrade, Serbia; Department of Clinical Neuroscience (CNS), Center for Molecular Medicine (CMM), Karolinska Institutet, 17176 Stockholm, Sweden*

Andrew H. A. Clayton − *Optical Sciences Centre, Department of Physics and Astronomy, School of Science, Swinburne University of Technology, Melbourne, Victoria 3122, Australia;* orcid.org/0000-0002-6182-3049

Igor F. Tsigelny − *Department of Neurosciences, University of California San Diego, La Jolla, California 92093-0819, United States*

Jean-Pierre Changeux − *Department of Neuroscience, Unité Neurobiologie Intégrative des Systèmes Cholinergiques, Institut Pasteur, F-75724 Paris 15, France*

Lars Terenius − *Department of Clinical Neuroscience (CNS), Center for Molecular Medicine (CMM), Karolinska Institutet, 17176 Stockholm, Sweden*

Complete contact information is available at:
https://pubs.acs.org/10.1021/acs.analchem.1c02144

Author Contributions

¶S.O., A.J.K., and S.N.N. contributed equally. The manuscript was written through the contributions of all authors. All authors have given approval to the final version of the manuscript.

Notes

The authors declare no competing financial interest.

■ ACKNOWLEDGMENTS

■ REFERENCES

(1) Rivas, G.; Minton, A. P. *Trends Biochem. Sci.* **2016**, *41*, 970−981.
(2) Baum, M.; Erdel, F.; Wachsmuth, M.; Rippe, K. *Nat. Commun.* **2014**, *5*, No. 4494.
(3) Helm, C. A.; Knoll, W.; Israelachvili, J. N. *Proc. Natl. Acad. Sci. U.S.A.* **1991**, *88*, 8169−8173.
(4) Johnson, E. R.; Keinan, S.; Mori-Sánchez, P.; Contreras-García, J.; Cohen, A. J.; Yang, W. *J. Am. Chem. Soc.* **2010**, *132*, 6498−6506.
(5) Alberti, S.; Gladfelter, A.; Mittag, T. *Cell* **2019**, *176*, 419−434.
(6) Wheeler, R. J.; Hyman, A. A. *Philos. Trans. R. Soc. B* **2018**, *373*, No. 20170193.
(7) Hyman, A. A.; Weber, C. A.; Jülicher, F. *Annu. Rev. Cell Dev. Biol.* **2014**, *30*, 39−58.
(8) Gao, A.; Shrinivas, K.; Lepeudry, P.; Suzuki, H. I.; Sharp, P. A.; Chakraborty, A. K. *Proc. Natl. Acad. Sci. U.S.A.* **2018**, *115*, E11053−E11060.
(9) Nussinov, R.; Tsai, C. J. *Curr. Pharm. Des.* **2012**, *18*, 1311−1316.
(10) Amor, B. R.; Schaub, M. T.; Yaliraki, S. N.; Barahona, M. *Nat. Commun.* **2016**, *7*, No. 12477.
(11) Huang, W.; Nussinov, R.; Zhang, J. *Methods Mol. Biol.* **2017**, *1529*, 439−446.
(12) Monod, J.; Wyman, J.; Changeux, J. P. *J. Mol. Biol.* **1965**, *12*, 88−118.
(13) Koshland, D. E., Jr.; Némethy, G.; Filmer, D. *Biochemistry* **1966**, *5*, 365−385.
(14) Kirschner, K.; Eigen, M.; Bittman, R.; Voigt, B. *Proc. Natl. Acad. Sci. U.S.A.* **1966**, *56*, 1661−1667.
(15) Gunasekaran, K.; Ma, B.; Nussinov, R. *Proteins* **2004**, *57*, 433−443.
(16) Cui, Q.; Karplus, M. *Protein Sci.* **2008**, *17*, 1295−1307.
(17) Bruder, M.; Polo, G.; Trivella, D. B. B. *Nat. Prod. Rep.* **2020**, *37*, 488−514.
(18) Tsigelny, I. F.; Mukthavaram, R.; Kouznetsova, V. L.; Chao, Y.; Babic, I.; Nurmemmedov, E.; Pastorino, S.; Jiang, P.; Calligaris, D.; Agar, N.; Scadeng, M.; Pingle, S. C.; Wrasidlo, W.; Makale, M. T.; Kesari, S. *Oncotarget* **2017**, *8*, 22370−22384.
(19) Wodak, S. J.; Paci, E.; Dokholyan, N. V.; Berezovsky, I. N.; Horovitz, A.; Li, J.; Hilser, V. J.; Bahar, I.; Karanicolas, J.; Stock, G.; Hamm, P.; Stote, R. H.; Eberhardt, J.; Chebaro, Y.; Dejaegere, A.; Cecchini, M.; Changeux, J. P.; Bolhuis, P. G.; Vreede, J.; Faccioli, P.; Orioli, S.; Ravasio, R.; Yan, L.; Brito, C.; Wyart, M.; Gkeka, P.; Rivalta, I.; Palermo, G.; McCammon, J. A.; Panecka-Hofman, J.; Wade, R. C.; Di Pizio, A.; Niv, M. Y.; Nussinov, R.; Tsai, C. J.; Jang, H.; Padhorny, D.; Kozakov, D.; McLeish, T. *Structure* **2019**, *27*, 566−578.
(20) Motlagh, H. N.; Wrabl, J. O.; Li, J.; Hilser, V. J. *Nature* **2014**, *508*, 331−339.
(21) Oasa, S.; Vukojević, V.; Rigler, R.; Tsigelny, I. F.; Changeux, J. P.; Terenius, L. *Proc. Natl. Acad. Sci. U.S.A.* **2020**, *117*, 2683−2686.
(22) Rigler, R.; Elson, E. S. Fluorescence Correlation Spectroscopy. In *Theory and Applications*; Springer: Berlin, 2001; Vol. *65*.
(23) Vukojević, V.; Papadopoulos, D. K.; Terenius, L.; Gehring, W. J.; Rigler, R. *Proc. Natl. Acad. Sci. U.S.A.* **2010**, *107*, 4093−4098.
(24) Mikuni, S.; Pack, C.; Tamura, M.; Kinjo, M. *Exp. Mol. Pathol.* **2007**, *82*, 163−168.
(25) Ries, J.; Schwille, P. *BioEssays* **2012**, *34*, 361−368.

(26) Tiwari, M.; Oasa, S.; Yamamoto, J.; Mikuni, S.; Kinjo, M. *Sci. Rep.* **2017**, *7*, No. 4336.

(27) Kolin, D. L.; Costantino, S.; Wiseman, P. W. *Biophys. J.* **2006**, *90*, 628−639.

(28) Hendrix, J.; Dekens, T.; Schrimpf, W.; Lamb, D. C. *Biophys. J.* **2016**, *111*, 1785−1796.

(29) Brown, C. M.; Dalal, R. B.; Hebert, B.; Digman, M. A.; Horwitz, A. R.; Gratton, E. *J. Microsc.* **2008**, *229*, 78−91.

(30) Wohland, T.; Shi, X.; Sankaran, J.; Stelzer, E. H. *Opt. Express* **2010**, *18*, 10627−10641.

(31) Ng, X. W.; Teh, C.; Korzh, V.; Wohland, T. *Biophys. J.* **2016**, *111*, 418−429.

(32) Buchholz, J.; Krieger, J.; Bruschini, C.; Burri, S.; Ardelean, A.; Charbon, E.; Langowski, J. *Biophys. J.* **2018**, *114*, 2455−2464.

(33) Singh, A. P.; Galland, R.; Finch-Edmondson, M. L.; Grenci, G.; Sibarita, J. B.; Studer, V.; Viasnoff, V.; Saunders, T. E. *Biophys. J.* **2017**, *112*, 133−142.

(34) Vitali, M.; Bronzi, D.; Krmpot, A. J.; Nikolić, S. N.; Schmitt, F.; Junghans, C.; Tisa, S.; Friedrich, T.; Vukojević, V.; Terenius, L.; Zappa, F.; Rigler, R. *IEEE J. Sel. Top. Quantum Electron.* **2014**, *20*, 344−353.

(35) Krmpot, A. J.; Nikolić, S. N.; Oasa, S.; Papadopoulos, D. K.; Vitali, M.; Oura, M.; Mikuni, S.; Thyberg, P.; Tisa, S.; Kinjo, M.; Nilsson, L.; Terenius, L.; Rigler, R.; Vukojević, V. *Anal. Chem.* **2019**, *91*, 11129−11137.

(36) Gösch, M.; Serov, A.; Anhut, T.; Lasser, T.; Rochas, A.; Besse, P. A.; Popovic, R. S.; Blom, H.; Rigler, R. *J. Biomed. Opt.* **2004**, *9*, 913−921.

(37) Scipioni, L.; Di Bona, M.; Vicidomini, G.; Diaspro, A.; Lanzanò, L. *Commun. Biol.* **2018**, *1*, No. 10.

(38) Buchholz, J. Evaluation of Single Photon Avalanche Diode Arrays for Imaging Fluorescence Correlation Spectroscopy: FPGA-Based Data Readout and Fast Correlation Analysis on CPUs, GPUs and FPGAs. Dissertation, Heidelberg University, 2015.

(39) Papadopoulos, D. K.; Krmpot, A. J.; Nikolić, S. N.; Krautz, R.; Terenius, L.; Tomancak, P.; Rigler, R.; Gehring, W. J.; Vukojević, V. *Mech. Dev.* **2015**, *138*, 218−225.

(40) Krmpot, A. J.; Nikolic, S. N.; Vitali, M.; Papadopoulos, D. K.; Oasa, S.; Thyberg, P.; Tisa, S.; Kinjo, M.; Nilsson, L.; Gehring, W. J.; Terenius, L.; Rigler, R.; Vukojevic, V. In *Quantitative Confocal Fluorescence Microscopy of Dynamic Processes by Multifocal Fluorescence Correlation Spectroscopy*, Advanced Microscopy Techniques IV; and Neurophotonics II SPIE Proceedings, Optical Society of America, 2015; p 953600.

(41) Dennis, D. J.; Han, S.; Schuurmans, C. *Brain Res.* **2019**, *1705*, 48−65.

(42) Buffo, A.; Vosko, M. R.; Ertürk, D.; Hamann, G. F.; Jucker, M.; Rowitch, D.; Götz, M. *Proc. Natl. Acad. Sci. U.S.A.* **2005**, *102*, 18183−18188.

(43) Franceschi, E.; Minichillo, S.; Brandes, A. A. *CNS Drugs* **2017**, *31*, 675−684.

(44) Kosty, J.; Lu, F.; Kupp, R.; Mehta, S.; Lu, Q. R. *Cell Cycle* **2017**, *16*, 1654−1660.

(45) Edwards, A. L.; Meijer, D. H.; Guerra, R. M.; Molenaar, R. J.; Alberta, J. A.; Bernal, F.; Bird, G. H.; Stiles, C. D.; Walensky, L. D. *ACS Chem. Biol.* **2016**, *11*, 3146−3153.

(46) Meijer, D. H.; Kane, M. F.; Mehta, S.; Liu, H.; Harrington, E.; Taylor, C. M.; Stiles, C. D.; Rowitch, D. H. *Nat. Rev. Neurosci.* **2012**, *13*, 819−831.

(47) Sagner, A.; Gaber, Z. B.; Delile, J.; Kong, J. H.; Rousso, D. L.; Pearson, C. A.; Weicksel, S. E.; Melchionda, M.; Mousavy Gharavy, S. N.; Briscoe, J.; Novitch, B. G. *PLoS Biol.* **2018**, *16*, No. e2003127.

(48) Pepperkok, R.; Squire, A.; Geley, S.; Bastiaens, P. I. *Curr. Biol.* **1999**, *9*, 269−272.

(49) Sarkisyan, K. S.; Goryashchenko, A. S.; Lidsky, P. V.; Gorbachev, D. A.; Bozhanova, N. G.; Gorokhovatsky, A. Y.; Pereverzeva, A. R.; Ryumina, A. P.; Zherdeva, V. V.; Savitsky, A. P.; Solntsev, K. M.; Bommarius, A. S.; Sharonov, G. V.; Lindquist, J. R.;

Drobizhev, M.; Hughes, T. E.; Rebane, A.; Lukyanov, K. A.; Mishin, A. S. *Biophys. J.* **2015**, *109*, 380−389.

(50) Boens, N.; Qin, W.; Basaric, N.; Hofkens, J.; Ameloot, M.; Pouget, J.; Lefevre, J. P.; Valeur, B.; Gratton, E.; vandeVen, M.; Silva, N. D., Jr.; Engelborghs, Y.; Willaert, K.; Sillen, A.; Rumbles, G.; Phillips, D.; Visser, A. J.; van Hoek, A.; Lakowicz, J. R.; Malak, H.; Gryczynski, I.; Szabo, A. G.; Krajcarski, D. T.; Tamai, N.; Miura, A. *Anal. Chem.* **2007**, *79*, 2137−2149.

(51) Vallmitjana, A.; Dvornikov, A.; Torrado, B.; Jameson, D. M.; Ranjit, S.; Gratton, E. *Methods Appl. Fluoresc.* **2020**, *8*, No. 035001.

(52) Clayton, A. H.; Hanley, Q. S.; Verveer, P. J. *J. Microsc.* **2004**, *213*, 1−5.

(53) Weber, G. *J. Phys. Chem. A* **1981**, *85*, 949−953.

(54) Dauty, E.; Verkman, A. S. *J. Mol. Recognit.* **2004**, *17*, 441−447.

(55) Feder, T. J.; Brust-Mascher, I.; Slattery, J. P.; Baird, B.; Webb, W. W. *Biophys. J.* **1996**, *70*, 2767−2773.

(56) Weiss, M.; Hashimoto, H.; Nilsson, T. *Biophys. J.* **2003**, *84*, 4043−4052.

(57) Schwille, P.; Haustein, E. Fluorescence Correlation Spectroscopy: An Introduction to its Concepts and Applications. https://pages.jh.edu/~iic/resources/ewExternalFiles/FCS-Schwille.pdf (accessed May 17, 2019).

(58) Setoguchi, T.; Kondo, T. *J. Cell Biol.* **2004**, *166*, 963−968.

(59) Thompson, N. L.; Burghardt, T. P.; Axelrod, D. *Biophys. J.* **1981**, *33*, 435−454.

(60) Ohsugi, Y.; Kinjo, M. *J. Biomed. Opt.* **2009**, *14*, No. 014030.

(61) Hassler, K.; Leutenegger, M.; Rigler, P.; Rao, R.; Rigler, R.; Gosch, M.; Lasser, T. *Opt. Express* **2005**, *13*, 7415−7423.

(62) Veerapathiran, S.; Wohland, T. *Methods* **2018**, *140−141*, 140−150.

(63) Kwapiszewska, K.; Szczepański, K.; Kalwarczyk, T.; Michalska, B.; Patalas-Krawczyk, P.; Szymański, J.; Andryszewski, T.; Iwan, M.; Duszyński, J.; Hołyst, R. *J. Phys. Chem. Lett.* **2020**, *11*, 6914−6920.

Supporting Information: Dynamic Cellular Cartography: Mapping the local determinants of oligodendrocyte transcription factor 2 (OLIG2) function in live cells using massively parallel Fluorescence Correlation Spectroscopy integrated with Fluorescence Lifetime Imaging Microscopy (mpFCS/FLIM)

Sho Oasa[1,‡], Aleksandar J. Krmpot[1,2,‡], Stanko N. Nikolić[1,2,‡], Andrew H. A. Clayton[3], Igor F. Tsigelny[4], Jean-Pierre Changeux[5], Lars Terenius[1], Rudolf Rigler[1,6,*], Vladana Vukojević[1,*]

[1]Department of Clinical Neuroscience (CNS), Center for Molecular Medicine (CMM), Karolinska Institutet, 17176 Stockholm, Sweden. [2]Institute of Physics Belgrade, University of Belgrade, 11080 Belgrade, Serbia. [3]Optical Sciences Centre, Department of Physics and Astronomy, School of Science, Swinburne University of Technology, Melbourne, Victoria 3122, Australia. [4]Department of Neurosciences, University of California San Diego, La Jolla, California 92093-0819. [5]Department of Neuroscience, Unité Neurobiologie Intégrative des Systemes Cholinergiques, Institut Pasteur, F-75724 Paris 15, France. [6]Department of Medical Biochemistry and Biophysics (MBB), Karolinska Institutet, 17177 Stockholm, Sweden.

SUMMARY: (S1) Optical setup for mpFCS/FLIM, data analysis and image rendering. S1a: Optical setup and alignment; S1b: mpFCS data acquisition, analysis and instrument calibration; S1c: FLIM measurement, data analysis and image rendering; S1d: Phasor analysis of FLIM; S1e: FLIM in complex sample. (S2) Cell culture. S2a: Imaging; S2b: Pharmacological treatment; S2c: FLIM-FRET. (S3) Determining the concentration of OLIG2-eGFP homodimers based on molecular brightness. (S4) Determining the apparent dissociation constant for OLIG2-eGFP binding to chromatin DNA. (S5) Standard solutions for calibration.

S1. OPTICAL SETUP FOR MASSIVELY PARALLEL FLUORESCENCE CORRELATION SPECTROSCOPY INTEGRATED WITH FLUORESCENCE LIFETIME IMAGING MICROSCOPY (mpFCS/FLIM), DATA ANALYISIS AND IMAGE RENDERING

S1a: mpFCS/FLIM instrumental setup. Principal components that comprise the mpFCS/FLIM system shown in Fig. 1A in the main text are: (1) a directly current-modulated picosecond 482 nm laser switchable between continuous wavelength (CW) or pulsed mode (Laser Diode Head LDH-D-C-485 driven using the Picosecond Pulsed Diode Laser Driver PDL 800-D for Pulsed and CW operation, PicoQuant, Germany); (2) a 16×16 Diffractive Optical Element (DOE; Holoeye Photonics AG, Germany); (3) a photon-counting camera based on a 64×32 Single-Photon Avalanche Diode (SPAD) array (SPC[3] Single Photon Counting Camera, Micro Photon Devices MPD, Italy), where the photosensitive area of the chip consists of 64×32 circular SPADs that are 30 μm in diameter and the distance between adjacent diodes along a row/column, *i.e.*, the pitch of the camera is 150 μm; and (4) an objective (C-Apochromat 63×/1.2 W Corr) mounted on an inverted epi-fluorescence microscope Axio Observer Z1 equipped with a high efficiency filter set (Filter Set 38 HE) for enhanced Green Fluorescent Protein (eGFP) that consists of an excitation bandpass filter EX BP 470/40 nm (central wavelength/ bandwidth), long pass dichroic mirror with a cutoff wavelength of 495 nm, and an emission band pass filter EM BP 525/50 (all from Carl Zeiss, Germany). These components are assembled on an optical table with active vibration damping (Thorlabs Inc., USA) and connected using standard opto-mechanical components (Newport Corporation, USA, and Thorlabs Inc., USA). An anamorphic antireflection coated prism pair (PS879-A, Thorlabs Inc., USA) is used to correct the intrinsic ellipticity of the laser beam, (3:1 ratio of major to minor axis); and the laser beam is further shaped and expanded by a Kepler telescope setup (L1 and L2) with a 15 μm pinhole in its focus to obtain a laser beam with a circular cross-section (15 mm) and a Gaussian intensity distribution profile. The expanded Gaussian laser beam is focused by a focusing lens (L3) and diffracted by the DOE to generate 16×16 foci in the image plane of the back port of the microscope. The illumination matrix is imaged by the microscope relay optics (schematically presented by L4) and the objective lens to the object plane. Fluorescence is collected with the same objective lens and imaged either using a Complementary Metal Oxide Semiconductor (CMOS) 18.0 Megapixel Digital Single-Lens Reflex (DSLR) camera Canon EOS 100D, pixel size 18.5 μm[2] and pixel pitch of 4.3 μm (Canon Inc., Japan), used to enable fast sample localization, or the 64×32 SPC[3] SPAD camera used for time-resolved measurements. The light path between the two camera ports was manually switched.

A uniform thin fluorescence layer deposited on the coverslips surface by a highlighter marker was used for checking daily the optical alignment of the mpFCS/FLIM system.

S1b: mpFCS measurement, data analysis and image rendering. Raw mpFCS data, *i.e.* photon counts, were acquired using the so-called free-running operating mode of the SPC[3] camera; stored on the camera's internal memory and then transferred to an SSD storage unit in a HP Workstation Z440-Xeon E5-1620 3.5 GHz using the high-speed USB 3.0 computer interface that the SPC[3] camera is equipped with. Fast data analysis by auto- and cross-correlation was performed using an NVIDIA GeForce GTX 780 graphic card containing 2304 Compute Unified Device Architecture (CUDA) cores as describe in detail in Krmpot *et al.*[1].

For mpFCS measurements in solution, fluorescence intensity fluctuations were acquired for 10 s with a temporal resolution of 10 µs *per* frame. mpFCS measurements in live cells lasted 20 s, with a temporal resolution of 20 µs *per* frame. To map the concentration, the amplitude of the autocorrelation curves (ACCs) simultaneously recorded in 16×16 observation volume elements (OVEs) was estimated from the value of G(τ) at lag time τ = 10 µs, G(10 µs), for measurements in solution and G(τ) at lag time τ = 20 µs, G(20 µs), for measurements in live cells. The average number of molecules in the OVE calculated from the autocorrelation amplitude as N = 1/(G(10 µs) − 1) or N = 1/(G(20 µs) − 1). To render diffusion time (τ_D) maps, the characteristic decay time of the ACCs was determined from its full width at half maximum. If not otherwise indicated, the full width of the ACC at half maximum is plotted in the fFMI images to show the spatial distribution of average translational diffusion times (τ_D), respectively. ACCs were fitted using the analytical function for three-dimensional (3D) diffusion of one (*i* = 1) or two (*i* = 2) components and, where appropriate, triplet formation:

$$G(\tau) = 1 + \frac{1}{N} \cdot \left[1 + \frac{T}{1-T} e^{-\frac{\tau}{\tau_T}} \right]$$

$$\cdot \left(\sum_{i=1}^{n} \frac{f_{D,i}}{\left(1 + \left(\frac{\tau}{\tau_{D_i}} \right)^{\alpha} \right) \sqrt{1 + \frac{\omega_{xy}^2}{\omega_z^2} \left(\frac{\tau}{\tau_{D_i}} \right)^{\alpha}}} \right) \quad \text{(S1)}$$

In equation (S1), N is the average number of molecules in the OVE; T is the average equilibrium fraction of molecules in the triplet state (when not applicable, $T = 0$); and τ_T is the triplet correlation time, related to the rate constants for intersystem crossing and the triplet decay; f_i is the relative amplitude of the *i*-th component and the sum of all relative amplitudes is equal to 1, $\sum_{i=1}^{n} f_{D,i} = 1$; τ_{Di} is the translational diffusion time of the *i*-th component; ω_{xy} and ω_z are the $1/e^2$ radial and axial radii of the observation volume element (OVE), respectively; α is the anomalous diffusion exponent: $\alpha = 1$, for free 3D diffusion; $\alpha < 1$ for sub-diffusion, *e.g.* as a result of molecular crowding – the smaller α, the greater the crowding; or $\alpha > 1$ for super-diffusion, *e.g.* as a result of active cellular transport. The diffusion coefficient D was determined from the diffusion time using the relationship $\tau_D = \omega_{xy}^2/D$. Offline ACCs fitting was performed using the Origin Data Analysis and Graphing Software (OriginLab Corporation, USA).

The local molar concentration was determined as $c_{local\,(l,m)} = N_{l,m}/(N_A \cdot V_{l,m})$, where N_A is the Avogadro's number (6.02×10^{23} mol^{-1}), $N_{l,m}$ is the average number of molecules in the individual (*l,m*) OVE determined by fitting the corresponding experimental ACC, and $V_{l,m}$ is the volume of the (*l,m*) observation volume element (OVE).
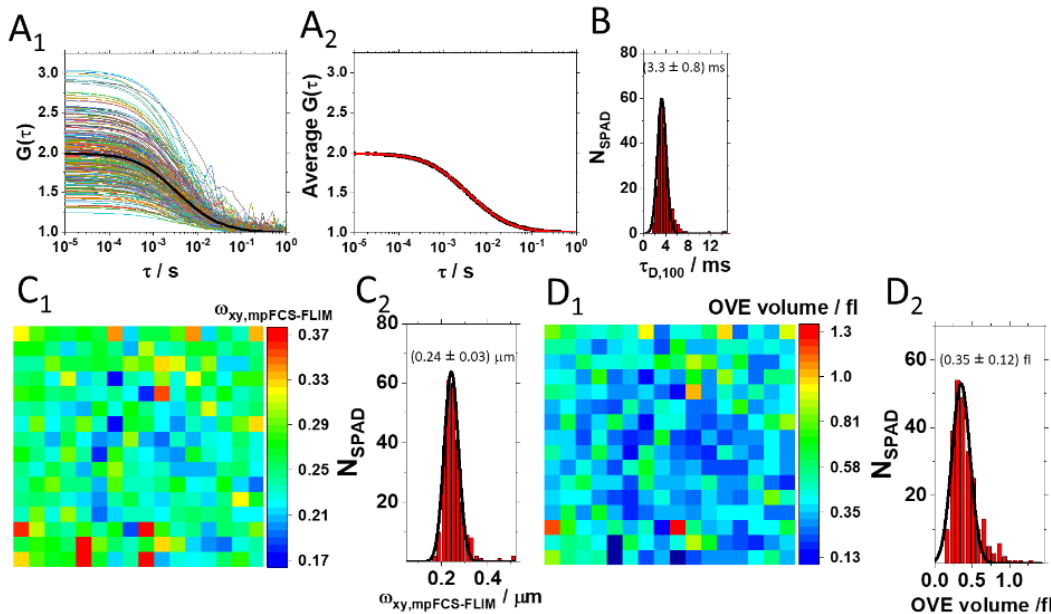

Fig. S1. Characterizing the Observation Volume Element (OVE) size in the integrated mpFCS/FLIM system using 100 nm fluospheres. (A₁) 256 single-SPAD autocorrelation curves (ACCs) recorded in an aqueous suspension of 100 nm fluospheres, c = 2 nM (by spFCS), with the corresponding average ACC (black). **(A₂)** Fitting the analytical function for three-dimensional (3D) diffusion of one component (red) to the average ACC shown in (A₁; black). The average structure parameter was determined to be s = 4.6. **(B)** Histogram of diffusion times determined from the full width at half-maximum of the ACCs shown in (A₁). From the best-fit Gaussian curve (black), the average diffusion time was determined, $\tau_{D,100}$ = (3.3 ± 0.8) ms. **(C₁)** Spatial map of OVE waist radius ($\omega_{xy,mpFCS-FLIM}$) derived from the diffusion times in (B) and the diffusion constant of 100 nm fluospheres, D_{100} = 4.4 µm²/s, using equation: $\tau_D = \omega_{xy}^2/4D$. **(C₂)** Corresponding histogram of OVE waist radius. From the best-fit Gaussian curve (black), the average OVE waist radius was determined, $\omega_{xy,mpFCS-FLIM}$ = (0.24 ± 0.03) µm. **(D₁)** Spatial map of the effective OVE volume ($V_{OVE,mpFCS-FLIM}$), derived from the waist radius in (C₁) and the average structure parameter s = 4.6, using equation: $V_{OVE} = \pi^{3/2} \omega_{xy}^3 s$. **(D₂)** From the best-fit Gaussian curve (black), the average effective OVE volume was determined to be $V_{OVE,mpFCS-FLIM}$ = (0.35 ± 0.12) fl. Data on mpFCS/FLIM system calibration for mpFCS measurements are shown in Figs S1-S5.

To begin with, the observation volume element (OVE) size was measured using 100 nm fluospheres (diameter d = 100 nm; diffusion coefficient D_{100} = 4.4 µm² s⁻¹)² (Fig. S1).

Single-SPAD autocorrelation curves (ACCs) acquired in a 2 nM aqueous suspension of fluospheres, the concentration of which was determined using the reference single point FCS (spFCS) system, are shown in Fig. S1A₁. By fitting the average ACC using a theoretically derived equation for free 3D diffusion of a single component (eq. (S1), α = 1, i = 1, T = 0; Fig. S1A₂, red), the average diffusion time (τ_D), $\tau_{D,100}$ = (3.3 ± 0.8) ms (Fig. S1B); the average structure parameter s = 4.6; and the average OVE waist radius $\omega_{xy,mpFCS/FLIM}$ = (0.24 ± 0.03) µm (Fig. S1C), were determined. The $\omega_{xy,mpFCS/FLIM}$ value is similar to the OVE radius measured in the reference spFCS system, $\omega_{xy,spFCS}$ = (0.25 ± 0.04) µm, determined using a dilute solution of ATTO488 (data not shown). Using the experimentally determined average structure parameter (Fig. S1A₂) and the OVE waist radius (Fig. S1C), the effective volume, $V_{OVE,mpFCS-FLIM}$ = (0.35 ± 0.12)×10⁻¹⁸ m³ and the average axial radius of the OVEs was determined, $\omega_{z,mpFCS/FLIM}$ = $\omega_{xy,mpFCS/FLIM} \cdot s$ = 0.24 µm · 4.6 = (1.1 ± 0.2) µm.

The mpFCS/FLIM system calibration was further verified using an aqueous suspension of quantum dots (Fig. S2).
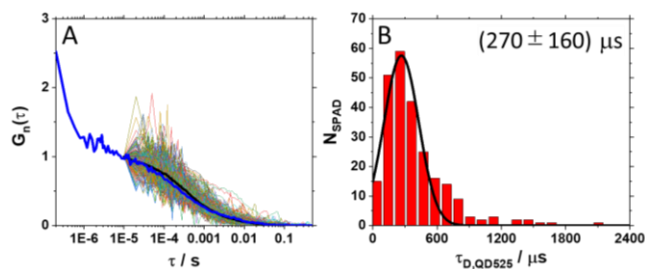

Fig. S2. Performance of the integrated mpFCS/FLIM system compared to the conventional spFCS system using an aqueous suspension of quantum dots. (A) 256 single-SPAD autocorrelation curves (ACCs) normalized to the same amplitude, G(τ) = 1 at lag time τ = 10 µs, recorded in an aqueous suspension of quantum dots (QD525), c_{QD525} = 7 nM, and the corresponding average ACC determined by mpFCS (black). ACC recorded in the same suspension using the conventional single-point FCS (spFCS) used as a reference (blue). (B) Histogram of diffusion times determined from the full width at half-maximum of the ACCs shown in (A). From the best-fit Gaussian curve, the average diffusion time was determined, $\tau_{D,QD525}$ = (270 ± 160) µs. In some pixels, significantly longer diffusion times, 600 µs – 2 ms, were measured likely to be due to the formation of QD525 agglomerates.

A 4 nM buffered aqueous solution of the enhanced Green Fluorescent Protein (eGFP) was used to confirm single-molecule sensitivity of the mpFCS/FLIM system (Fig. S3) and assess whether possible artifacts are arising due to deviations of the OVE shape from a 3D-ellipsoidal Gaussian (Fig. S4A and S4B). To this aim, goodness of fitting the average ACC recorded in the aqueous buffer solution of eGFP (c_{eGFP} = 4 nM) using the equation for a one-component free 3D diffusion in a Gaussian OVE (eq. (S1), α = 1, i = 1, T = 0) was examined[3]. As can be seen (Fig. S4A and S4B), a poor fit with large fitting residuals at long time scales and a divergent axial ratio, which are indications of a non-Gaussian observation volume, were not observed, indicating that the assumption of a Gaussian observation profile is valid.
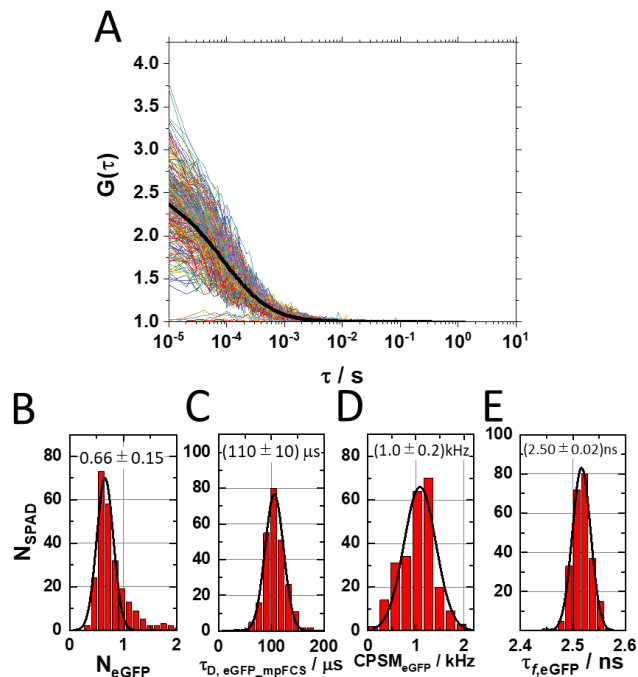

Fig. S3. Measuring with single-molecule sensitivity the concentration, diffusion, brightness and fluorescence lifetime of eGFP in an aqueous phosphate buffer solution using the integrated mpFCS/FLIM system. (A) 256 single-SPAD autocorrelation curves (ACCs) recorded in an aqueous buffer solution of eGFP, c_{eGFP} = 4 nM, with the corresponding average ACC (black). (B) Histogram of number of eGFP molecules, determined from the ACCs shown in (A). From the best-fit Gaussian curve (black), the average ACC amplitude was determined, N_{eGFP} = (0.66 ± 0.15). (C) Histogram of diffusion times determined from the full width at half-maximum of the ACCs shown in (A). From the best-fit Gaussian curve (black), the average diffusion time was determined, $\tau_{D,eGFP,mpFCS}$ = (110 ± 10) µs. (D) Histogram of eGFP brightness (CPSM). From the best-fit Gaussian curve (black), the average eGFP brightness was determined, $CPSM_{eGFP}$ = (1.0 ± 0.2) kHz. (E) Histogram of eGFP fluorescence lifetimes. From the best-fit Gaussian curve (black), the average eGFP fluorescence lifetime was determined, $\tau_{f,eGFP}$ = (2.50 ± 0.02) ns.

Finally, the axial resolution (Fig. S4C) and sensitivity of the integrated mpFCS/FLIM system were characterized (Fig. S5).

The axial resolution of the mpFCS/FLIM system was assessed in two ways, from FCS calibration experiments using a 2 nM aqueous suspension of fluospheres (Fig. S1), and z-stack imaging of a thin fluorescence layer deposited on the coverslip surface by a highlighter marker (Fig. S4C, black symbols). As described above, FCS calibration experiments yielded the axial radius $\omega_{z,mpFCS/FLIM}$ = (1.1 ± 0.2) µm, in good agreement with the value derived from z-stack imaging, for which the best-fit Gaussian curve of the fluorescence intensity profile as a function of distance from the focal plane yielded the half width at half maximum, HWHM = (1.15 ± 0.09) µm (Fig. S4C, red solid line).
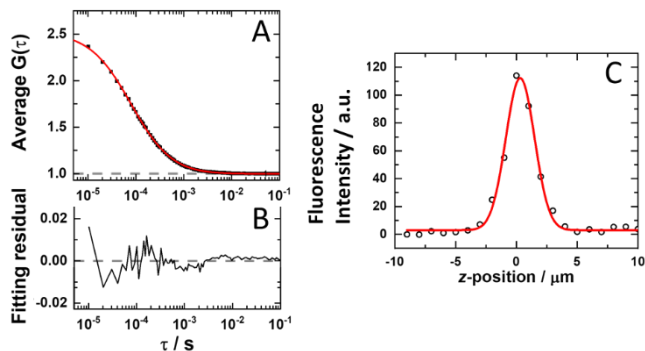
Figure S4. Assessing possible deviation of the observation volume element (OVE) shape from a 3D-ellipsoidal Gaussian and the Axial resolution of the mpFCS/FLIM system. (A) Average ACC recorded in an aqueous buffer solution of eGFP, c_{eGFP} = 4 nM (black symbols; same data as shown in Fig. 1D$_1$ and Fig. S3A) fitted using a one-component free 3D diffusion model in a Gaussian OVE (eq. (S1); α = 1, i = 1, T = 0). **(B)** Residuals corresponding to data shown in (A). **(C)** Fluorescence intensity as a function of distance from the focal plane.

The sensitivity of the integrated mpFCS/FLIM system was characterized using standard dilution series (Fig. S5).
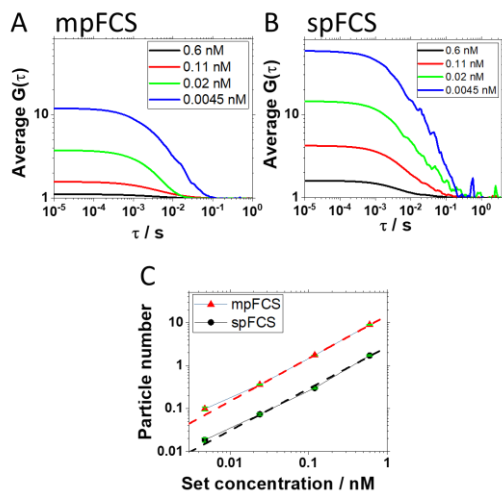

Figure S5. Sensitivity of the integrated mpFCS/FLIM system compared to that of the conventional spFCS system assessed using a dilution series of 100 nm fluospheres in aqueous suspensions. (A) Average autocorrelation curves (ACCs) recorded by the integrated mpFCS/FLIM system in a series of diluted suspensions of 100 nm fluospheres in water. The indicated nominal concentrations, calculated from the concentration of the original solution as provided by the manufacturer, were: 0.6 nM (black), 0.11nM (red), 0.02 nM (green) and 0.0045 nM (blue). **(B)** Average ACCs acquired on the same samples as in (A) using the reference spFCS system. **(C)** Particle number determined by mpFCS (red) and spFCS (black) as a function of the nominal concentration of the fluospheres in a suspension. Linear regression analysis revealed that the average particle concentration determined by mpFCS was 5-fold higher than the concentration determined by spFCS. SDs are shown as yellow and green error bars.

S1c: FLIM measurement, data analysis and image rendering using the integrated mpFCS/FLIM system. For fluorescence

lifetime measurements, the so-called time-gating operating mode of the SPC[3] camera was used[1, 4]. To this aim, the laser is operated in the pulsed mode, pulse repetition rate 50 MHz, with a pulse being triggered by the SPAD camera, after which the gate is opened. The gate width (smallest available value 220 ps) and step duration (smallest available value 20 ps) were adjusted to provide optimal trade-off between signal-to-noise; fluorescence lifetime accuracy, taking into account the convolution of the Instrumental Response Function (IRF) with the intensity measured at the first time gate (Fig. S6), and signal acquisition time. The number of steps was adjusted to match the time frame of the 20 ns internal clock following instructions provided in the MPD SPC[3] User Manual (http://www.micro-photon-evices.com/MPD/media/User Manuals/SPC3_usermanual.pdf).
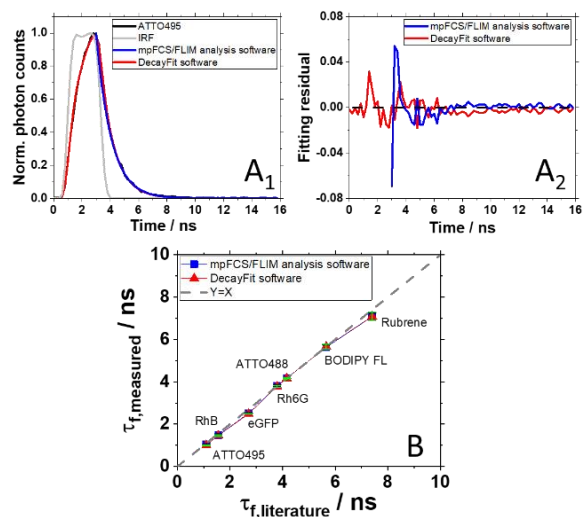

Figure S6. Effect of Instrumental Response Function (IRF) on fluorescence lifetime measurement using the integrated mpFCS/FLIM system. (A$_1$) Single-SPAD FLIM curve recorded in an aqueous solution of ATTO495, $c_{ATTO495}$ = 100 nM (black). Fluorescence lifetime of ATTO495 is $\tau_{f,ATTO495,literature}$ = 1.10 ns. Fitting of one-component exponential decay function to this FLIM curve using our mpFCS/FLIM software (blue), yields $\tau_{f,ATTO495}$ = 1.05 ns. Convolution fitting with IRF (red) using the freely available DecayFit software (http://www.fluortools.com/software/decayfit), yields $\tau_{f,ATTO495}$ = 1.00 ns. **(A$_2$)** Residuals between observed and fitted photon counts. Both models had similar residuals plot at times longer than 1 ns from the excitation pulse, but the convolution fit (red) exhibited fluctuations at earlier times than the simple mono-exponential decay fit without IRF deconvolution (blue). **(B)** Comparison between fluorescence lifetimes of several standard dyes, 1.0 ns $\leq \tau_f \leq$ 8 ns, measured using the integrated mpFCS/FLIM system and determined by fitting a simple mono-exponential decay curve (blue symbols) to the FLIM fluorescence decay curve or by using the convolution fit with IRF (red symbols). The dashed grey line shows the perfect correlation between experimental and literature values. SDs are shown as green error bars.

To optimize the gate width and step duration, ATTO488 in aqueous buffer solution was used as a fluorescence lifetime standard, $\tau_{f,ATTO488}$ = 4.16 ns. Gate widths and step durations were chosen based on the appearance of the fluorescence decay curves (Fig. S7) and the accuracy and precision of the measured lifetimes relative to the lifetime standard (Fig. S6). (Of note, curves that were noisy or had spurious fluctuations, *e.g.* Fig. S7A, black, were rejected.)
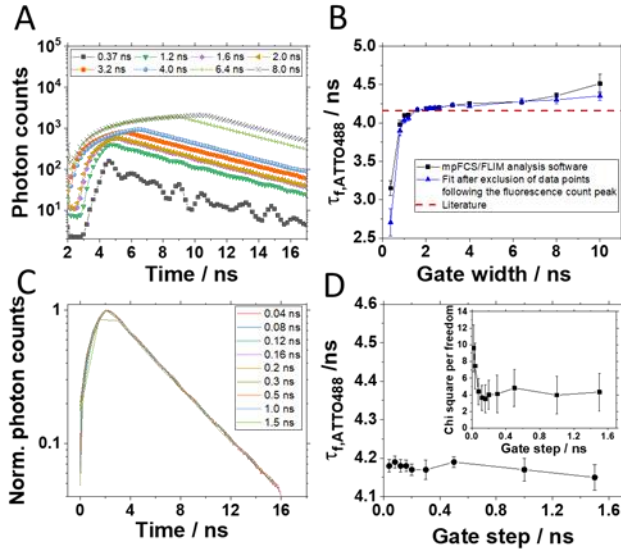
Figure S7. Effect of gate width and gate step time on measured fluorescence lifetimes. (A) Single-SPAD FLIM curves recorded in an aqueous solution of ATTO488, $c_{ATTO488} = 100$ nM, acquired using different gate widths, 0.37 ns – 10 ns. Note the similarity in the intensity decays for gate widths 1.2 ns – 4 ns. **(B)** Effect of gate width on the extracted fluorescence lifetime. The mpFCS/FLIM data analysis software performs fitting starting from the 3rd data point after the photon count peak. Extracted fluorescence lifetimes increased for increasing gate widths, because the IRF effect prolonged to longer times for longer gate widths. To verify this interpretation, single-exponential decay fitting was performed after excluding more and more data points from the photon counts peak as the gate width was increased. While the agreement between measured and literature findings was thereby somewhat improved for longer gate widths (8.0 ns and 10 ns), the agreement was not satisfactory. Results obtained using gate widths of 1.6 ns and 2.0 ns agreed best with literature findings, and the results obtained using a gate width of 2.0 ns were less noisy as the number of collected photons was higher than when 1.6 ns gate width was used. Therefore, 2.0 ns gate width is recommended for precise FLIM measurement. **(C)** Single-SPAD FLIM curves acquired in the same solution as in (A) using different gate step times, 0.04 ns – 1.5 ns. While similar FLIM curves were obtained for all gate step times tested, the maximum photon counts peak in the FLIM curve was missed when the 1.5 ns gate step time was used. **(D)** Fluorescence lifetime values as a function of gate step times. While similar values were obtained for all gate step times tested, the average fitting chi-square per degree of freedom decreased to a plateau for gate step times longer than 0.1 ns (inlet). Therefore, gate step time in the interval 0.12 ns – 1.0 ns is recommended for precise FLIM measurement.

Based on these criteria, we have selected to use a 2 ns gate width, a 0.2 ns step size and a total sampling of 80 steps. Thus, an individual FLIM curve, *i.e.* a fluorescence decay curve recorded by a single SPAD in the SPAD camera, consists of an array of integer photon counts (8 or 16 bits unsigned integer type data), representing the fluorescence decay curve over one FLIM period. A single value of index k in a FLIM measurement is equal to the total number of photons counted through a short gate window of 2 ns duration, $\Delta t_{gate} = 2$ ns, starting at time $t_k = t_s + (k-1) \cdot \Delta t_{shift}$ (measured from the onset of the excitation laser pulse). The entire FLIM curve is thus recorded by shifting this window by $\Delta t_{shift} = 0.2$ ns time steps, where the first window begins at $t_s = 2$ ns start

shift, the second at 2.2 ns, and so on. Eighty measurement points were recorded in total for each FLIM curve, extending over a 2-18 ns sub-period during a single 20 ns FLIM measurement time.

In order to minimize the noise and improve the precision of fluorescence lifetime measurements, mpFLIM data were acquired for 10 min (averaging over 180 FLIM curves). The single-SPAD FLIM curves acquired for all 256 SPADs, with each single-SPAD curve being an average of 180 FLIM fluorescence decay curves, are stored in a single binary file, the so-called ".spcf" file, which comprises a header and acquisition metadata followed by raw image data, which is created by the MPD Software Development Kit (SDK) functions incorporated in our program. The file format is described in the MPD SPC[3] User Manual (http://www.micro-photon-evices.com/MPD/media/User Manuals/SPC3_usermanual.pdf).

Our dedicated mpFLIM data analysis software includes several options. The first option enables the user to load and graphically display any individually recorded FLIM curves for each selected pixel (i, j), where $1 \le i \le 32$ and $1 \le j \le 64$. If several FLIM measurements are acquired consecutively, the software can also calculate the arithmetic average of all FLIM curves for a given pixel, yielding an individual average FLIM curve for each pixel.

The second option enables the user to fit a mono-component exponential decay function to the experimentally derived FLIM curves:

$$y_{fit1} = y_0 + A exp\left(-\frac{(t-t_0)}{\tau}\right) \qquad (S2)$$

or to fit an exponential decay function with two characteristic times, so-called two-component exponential decay function, to the experimentally derived FLIM curves:

$$y_{fit2} = y_0 + A_1 exp\left(-\frac{(t-t_{0_1})}{\tau_1}\right)$$
$$+ A_2 exp\left(-\frac{(t-t_{0_2})}{\tau_2}\right) \qquad (S3)$$

Irrespective of which fitting function is chosen, the software automatically makes initial guesses for the fitting parameters for each individual average FLIM curve. In the case of function y_{fit1}, equation (S2), the initial amplitude value A is set to the difference between the maximum and the minimum of the individual averaged FLIM curve. The time shift t_0 is simply equal to the time position of the fluorescence intensity peak, while the fluorescence lifetime τ is estimated as the time when the photon count drops e times, *i.e.* decreases to $1/e$ of its maximal value (measured from the FLIM peak). Offset y_0 is set to be equal to the minimal fluorescence intensity value in a FLIM curve. As for the two-component exponential decay case, the procedure for guessing the initial parameter values is similar to the one for one-component exponential decay analysis, with the exception of a procedure for guessing the fractional contribution of each process to the total fluorescence, *i.e.* for guessing the relative amplitudes A_1 and A_2 in equation (S3), for which the program assumes that: $A_1 = A_2 = A/2$.

FLIM data are further processed using the Levenberg–Marquardt's method for nonlinear least squares curve-fitting, as described in the *mrqmin* nonlinear least-squares fit, Marquardt's method, Chapter 15, Numerical Recipes 2nd ed. ANSI C Files (https://www.aquila.infn.it/pierleoni/LFC/ROUTINES/Chap15.pdf). Using our software, all fitting functions are calculated within a few seconds, which significantly increases the efficiency of the experiment. If, for any reason, the fit diverges for a particular FLIM curve, the user can select that FLIM curve, enter the initial

parameter values manually and repeat the algorithm just for the selected dataset.

S1d: Phasor analysis of FLIM data. In the phasor analysis of FLIM data, Fourier transform of FLIM fluorescence decay curves is calculated and the resulting complex number is presented in a 2D polar coordinate system where the abscissa represents the real part and the ordinate the imaginary part of the complex number[5-10]. In this way, a phase vector, so-called phasor, is obtained, for which the distance from the pole and the polar angle are uniquely defined by the fluorescence lifetime. Phasors follow the normal vector algebra and their coordinates can be added/subtracted. This allows multi-component analysis of FLIM data without the need to fit multi-component exponential decay functions to FLIM fluorescence decay curves and reduces to vector algebra the analysis of complex fluorescence intensity decays by two or more processes expected in situations where there are multiple fluorophores in a mixture or when Förster Resonance Energy Transfer (FRET) occurs between the fluorophores[5-10]. We have developed the routine for phasor analysis of FLIM data in Excel (Microsoft Office, Microsoft, Seattle, WA), using the add-in program Solver to find optimal solutions for the fitting parameters.

As a first step, Fourier transformation of the normalized FLIM fluorescence decay curve is calculated using the following equations:

$$mcos(\theta_{tot}) = \frac{\sum_0^\infty [F(t) - BG] \cdot \cos(2\pi\omega t)}{\sum_0^\infty F(t) - BG} \quad (S4)$$

$$msin(\theta_{tot}) = \frac{\sum_0^\infty [F(t) - BG] \cdot \sin(2\pi\omega t)}{\sum_0^\infty F(t) - BG} \quad (S5)$$

In equations (S4) and (S5), shown by Fereidouni *et al.*[11] to be valid for a number of time-gates that is > 16 (80 in our experiments), $F(t)$ is detected fluorescence intensity, *i.e.* photon counts at time t, BG is the background fluorescence intensity, m is the modulus, θ_{tot} is the phase angle and ω is the phasor frequency that is related in time-domain fluorescence lifetime measurements with the FLIM measurement time (T), $\omega = 1/T$. Usually, the FLIM curve acquisition time is defined by the laser repetition frequency (here 50 MHz, yielding for a single FLIM curve a maximum measurement time of 20 ns), and a phasor frequency is conventionally chosen that matches the excitation laser repetition frequency of the pulsed laser. However, the Instrument Response Function (IRF) and the gating process effectively shorten the FLIM curve acquisition time (the actual FLIM curve acquisition time in our experiments was 13.6 ns) and alter the shape of the recorded fluorescence intensity decay curve, which manifests itself in phasor analysis through rescaling of the theoretical modulus and phasor rotating by a fixed value. To account for instrument phase delay and instrument demodulation of the signal, a series of fluorescence lifetime standards were used to determine the correction factors according to the following equations:

$$mcos(\theta_{tot})_{corr} = \frac{M_t}{M_e} \cdot [mcos(\theta_{tot}) \cdot cos(\theta_t - \theta_e) \\ - msin(\theta_{tot}) \cdot sin(\theta_t - \theta_e)] \quad (S6)$$

$$msin(\theta_{tot})_{corr} = \frac{M_t}{M_e} \cdot [msin(\theta_{tot}) \cdot cos(\theta_t - \theta_e) \\ - mcos(\theta_{tot}) \cdot sin(\theta_t - \theta_e)] \quad (S7)$$

In equations (S6) and (S7), M is the modulation, θ is the phase angle and the subscripts t and e denote the theoretical and the experimentally measured values, respectively. Using six different fluorescent dyes with known fluorescence lifetimes (Fig. S8A), the instrumental demodulation correction ratio, M_t/M_e, and the instrumental phase shift correction, $\theta_t - \theta_e$, were determined $M_t/M_e = 1.006$ and $\theta_t - \theta_e = 0.035$ rad for $\omega = 77$ MHz (corresponding to the actual FLIM curve acquisition time of ~13 ns).
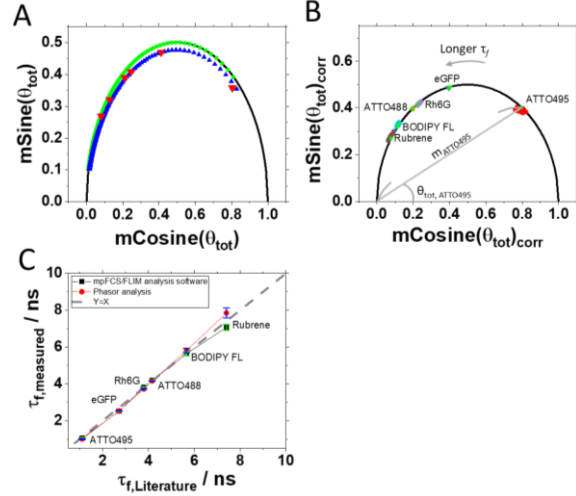

Figure S8. Phasor plot calibration and fluorescence lifetimes. **(A)** Phasor plot showing the universal circle (black). Phasors calculated using equations (S4) and (S5) to analyze theoretical mono-exponential decay functions with decay times from 1 ns – 20 ns (blue). Phasors calculated using equations (S11) and (S12), the phasor frequency $\omega = 77$ MHz and fluorescence lifetime values, 1 ns ≤ τ_f ≤ 20 ns with $F_2 = 0$ (green). Experimentally measured uncorrected phasors (red). **(B)**. Corrected fluorescence lifetime values calculated using equations (S6), (S7) and (S8) to determine the displacement of the phasor positions. **(C)** Comparison of fluorescence lifetimes determined using single exponential fit (black rectangles) to the intensity decay data with that of the phasor approach (red circles). Dashed grey line indicates perfect agreement between the fluorescence lifetime values derived using mono-exponential fit to the FLIM fluorescence decay curves (black symbols) and the phasor analysis approach (red symbols) against literature values. SDs are shown as green error bars.

After correction, the apparent fluorescence lifetime was calculated:

$$\langle\tau\rangle = \frac{msin(\theta_{tot})_{corr}}{mcos(\theta_{tot})_{corr}} \cdot \frac{1}{2\pi\omega} \quad (S8)$$

and the phasor plot was drawn (Fig. S8B). Comparison of fluorescence lifetimes determined using one-exponential fit to the intensity decay data acquired using the phasor approach are shown in (Fig. S8C).

In a two-component mixture containing two species with different fluorescence lifetimes or in a solution of one species where fluorescence lifetime decays by two parallel processes with different half-lives, FLIM fluorescence decay curves can be described using a two-component exponential decay function:

$$F(t) = A_1 \exp\left(-\frac{t}{\tau_1}\right) + A_2 \exp\left(-\frac{t}{\tau_2}\right) \quad (S9)$$

$$f_1 = \frac{A_1}{A_1 + A_2}, \quad f_2 = \frac{A_2}{A_1 + A_2} \quad (S10)$$

where the pre-exponential factors A_1 and A_2 are amplitudes, τ_1 and τ_2 are fluorescence lifetimes, and f_1 and f_2 are the fractional contributions of species 1 and 2, respectively, to the total fluorescence.

Phasor analysis in this case yields the total phasor, which is the vector sum of the two component phasors weighted by their fractional intensity contributions. The cosine and sine components of the total phasor depend on the fractional contribution of component 1 (F_1), the lifetime of component 1 (τ_1), the lifetime of component 2 (τ_2) and the phasor frequency (ω):

$$mcos(\theta_{tot})_{corr} = \frac{F_1}{1 + (2\pi\omega)^2\tau_1^2} + \frac{F_2}{1 + (2\pi\omega)^2\tau_2^2} \quad \text{(S11)}$$

$$msin(\theta_{tot})_{corr} = \frac{2\pi F_1 \omega \tau_1}{1 + (2\pi\omega)^2\tau_1^2} + \frac{2\pi F_2 \omega \tau_2}{1 + (2\pi\omega)^2\tau_2^2} \quad \text{(S12)}$$

$$F_1 = \frac{A_1\tau_1}{A_1\tau_1 + A_2\tau_2}, \quad F_2 = 1 - F_1 \quad \text{(S13)}$$

To extract from FLIM fluorescence decay curves the values of these parameters, the Excel add-in program Solver was used to find optimal values along with a minimization of the chi-square value of photon counts by varying two lifetimes (τ_1 and τ_2) and the fractional contribution of component 1 (F_1):

$$\chi^2 = \frac{1}{L - p - 1} \quad \text{(S14)}$$

In equation (S14), L denotes total number of gates in the FLIM curve (in our experiments $L = 80$); p is a parameter number; F_k is photon counts at the k-th gate in the amplitude-normalized FLIM curve, and $F_{k,phas}$ is photon counts at the k-th gate in FLIM curve re-constructed by phasor parameters.

For a two-component exponential decay, the phasor lies inside the semicircle (Fig. S9B₃). However, the phasor of the two-component mixture must be positioned between the phasors of the two individual components, which lie on the semicircle. The relative distance of the phasor for the mixed state from the individual components reflects the fractional intensity contribution of each component. From this, the molar fractions of the two-component mixture can be inferred.
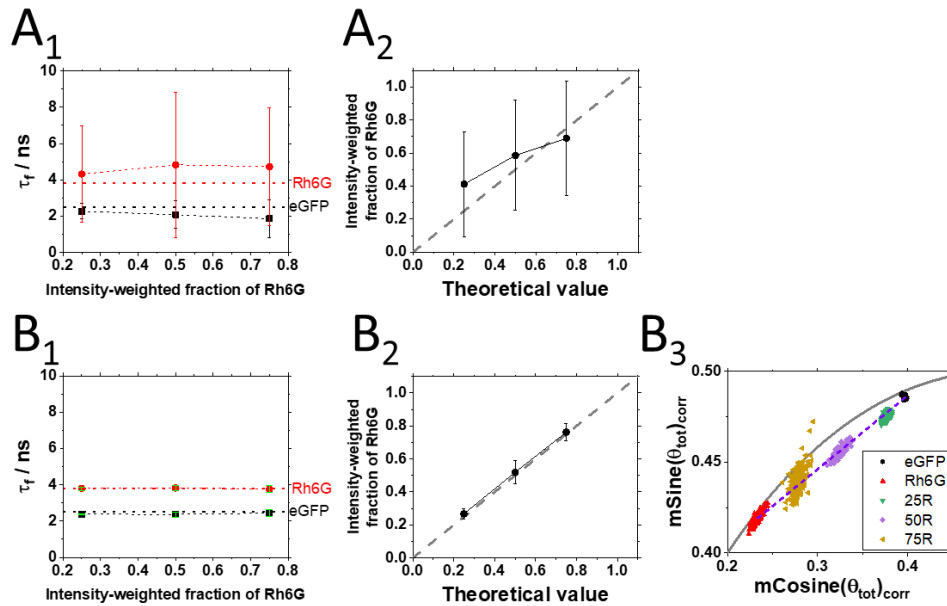

Figure S9. Fluorescence lifetime measurement in a mixture of Rh6G and eGFP, and mixture composition determination *via* mpFLIM. Comparison of results obtained by exponential decay fitting (A₁ and A₂) and phasor analysis (B₁₋₃). (A₁) Fluorescence lifetimes of Rh6G and eGFP determined using a two-component exponential decay fitting with all parameters in equation (S9) being allowed to freely vary. **(A₂)** Intensity-weighted fractions of Rh6G in mixtures with different Rh6G/eGFP content determined using equations (S9) and (S10) for fitting the experimentally measured mpFLIM fluorescence decay curves shown in Fig. 2C₁. For fitting, fluorescence lifetimes of eGFP and Rh6G were fixed to the values obtained by analysing mpFLIM fluorescence decay curves shown in Fig. 2C₁ (black and violet, respectively) and the intensity-weighted fraction was varied. The dashed grey line shows perfect correlation between measured and actual values. **(B₁)** Fluorescence lifetimes of Rh6G and eGFP determined using two-component phasor analysis, equations (S11)-(S13). SDs are shown as yellow and green error bars. **(B₂)** Intensity-weighted fraction of Rh6G in mixtures with different Rh6G/eGFP content determined using two-component phasor analysis, equations (S11)-(S13). The dashed grey line shows perfect correlation between measured and actual values. **(B₃)** Phasors in pure eGFP (black) and Rh6G (red) solutions and their mixtures containing different amounts of these components expressed as intensity-weighted fractions: Rh6G:eGFP = 0.25:0.75 (green), 0.5:0.5 (lilac), 0.75:0.25 (ochre). Of note, phasor values measured in the mixtures are distributed along the dashed blue line connecting the eGFP (black) and Rh6G (red) phasor positions.

Finally, we have also developed a three-component phasor analysis procedure to allow characterization of OLIG2 dimerization by FLIM-FRET using eGFP and ShadowY (ShY) as FRET donor and acceptor, respectively. eGFP and ShY constitute a suitable donor-acceptor pair with a Förster radius equal to 6.2 nm[12]. However, both eGFP and ShY are efficiently excited with the 488 nm laser line (molar absorption coefficient: ε_{eGFP} = 55 900 M^{-1}cm^{-1} [13] and ε_{ShY} = 136 000 M^{-1}cm^{-1} [12]) and emit in the region detected by our instrumental set-up, even though ShY emission is comparatively lower due to its small fluorescence quantum yield (QY$_{ShY}$= 0.01[12], QY$_{eGFP}$ = 0.6[13]). Since only a fraction of OLIG2 molecules will dimerize, there will be three characteristic decay times in cells expressing OLIG2-eGFP and OLIG2-ShY: for OLIG2-eGFP molecules that do not undergo dimerization and the eGFP donor is therefore not subject to FRET ($\tau_{feGFP, \, donor \, only}$), for OLIG2-eGFP molecules undergoing dimerization and hence likely FRET ($\tau_{feGFP, \, FRET}$) and for the acceptor (directly excited or indirectly excited via FRET, $\tau_{fShY, \, acceptor \, only}$). To describe this situation, a three-component phasor analysis routine was developed, with fixed phasor positions of the donor (x_D, y_D) and the acceptor (x_A, y_A), determined in HEK cells expressing OLIG2 labelled with the donor or the acceptor alone, and varying along the x-axis the phasor position of the FRET component (x_F):

$$x_{tot,corr} = F_D \cdot x_D + F_A \cdot x_A + F_F \cdot x_F \qquad (S15)$$

$$y_{tot,corr} = F_D \cdot y_D + F_A \cdot y_A + F_F \cdot y_F \qquad (S16)$$

$$F_D + F_A + F_F = 1 \qquad (S17)$$

$$\left(x_F - \frac{1}{2}\right)^2 + y_F^2 = \frac{1}{4} \qquad (S18)$$

where, $x = m\cos(\theta)$ and $y = m\sin(\theta)$ denote phasor position for donor (D), acceptor (A) and FRET component (F). F is an intensity-weighted fraction of donor, acceptor and FRET component. The intensity-weighted fraction is defined by area of triangles:

$$F_D = \frac{S_D}{S_D + S_A + S_F} \qquad (S19)$$

$$F_A = \frac{S_A}{S_D + S_A + S_F} \qquad (S20)$$

$$F_F = \frac{S_F}{S_D + S_A + S_F} \qquad (S21)$$

where, S is the area of a triangle at each diagonal position of vertices. For example, S_D is the area made by three vertexes, phasor positions of donor, acceptor and measurement in which area is defined by these phasor positions. The add-in program Solver was used to find optimal solutions for the fitting parameters along with the minimization of chi-square value as shown in equation (S14). Further information is given below in section (S2c): Positive and negative controls for phasor analysis of FRET.

S1e: FLIM in a fixed acridine orange stained section through the rhizome of the lily of the valley (Convallaria majalis). Single SPAD fluorescence intensity decay curves recorded in the fixed acridine orange stained section through the rhizome of the lily of the valley (Convallaria majalis; Fig. S10).
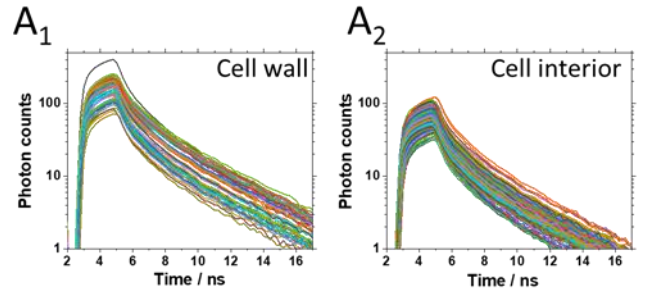

Figure S10. Single-SPAD fluorescence intensity decay curves recorded in a fixed acridine orange stained section through the rhizome of the lily of the valley (Convallaria majalis). (A$_1$) Single-SPAD FLIM curves recorded in the cell wall of a single cell in the central parenchyma. (A$_2$) Single-SPAD FLIM curves recorded in the interior of the same cell. Results of FLIM curve analysis are given in the main text (Fig. 3).

S2: CELL CULTURE AND PHARMACOLOGICAL TREATMENT

S2a: Cell culture and fluorescent proteins expression. HEK cells (American Type Culture Collection (ATCC)) were maintained in a humidified atmosphere containing 5 % CO$_2$ at 37 °C in Dulbecco's Modified Eagle Medium (Gibco Life Technologies) supplemented with 10 % fetal bovine serum (Gibco), 1 % penicillin-streptomycin (Gibco; final conc. 100 U/mL of penicillin and 100 µg/ mL streptomycin).

Expression vectors encoding the enhanced Green Fluorescent Protein (peGFP-N1), eGFP-fused OLIG2 (pOLIG2-eGFP-N1) or eGFP tetramer (peGFP$_{tet}$-C1) were transiently transfected into HEK cells [1, 14] (Figs S11-S19).
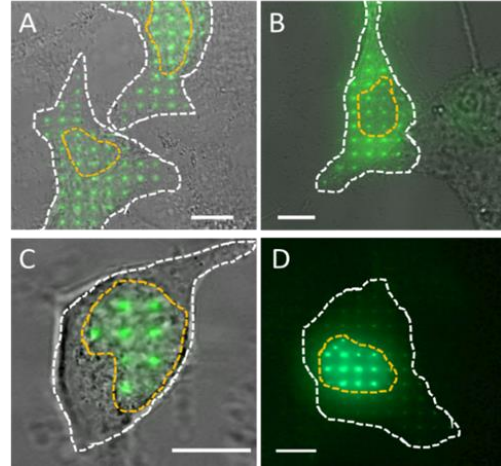

Figure S11. Fluorescence images of spot-wise (16×16) illuminated cells expressing eGFP-tagged molecules of interest (green) overlaid on a wide-field transmission image (grey) recorded using the DSLR camera. (A) Live HEK cells expressing monomeric eGFP showing its uniform distribution inside the cell. (B) Live HEK cells expressing the eGFP tetramer (eGFP$_{tet}$), showing preferential eGFP$_{tet}$ localization in the cytoplasm. (C) Live HEK cell expressing OLIG2-eGFP showing a nuclear localization of the eGFP tagged OLIG2 transcription factor. (D) Fluorescence image of a live HEK cell expressing OLIG2-eGFP contrasted after image acquisition to render visible the cytoplasmic pool of OLIG2-eGFP. In all images, the hand-drawn dashed lines highlight the border of the cell (white) and the cell nucleus (orange). Scale bar: 10 µm.
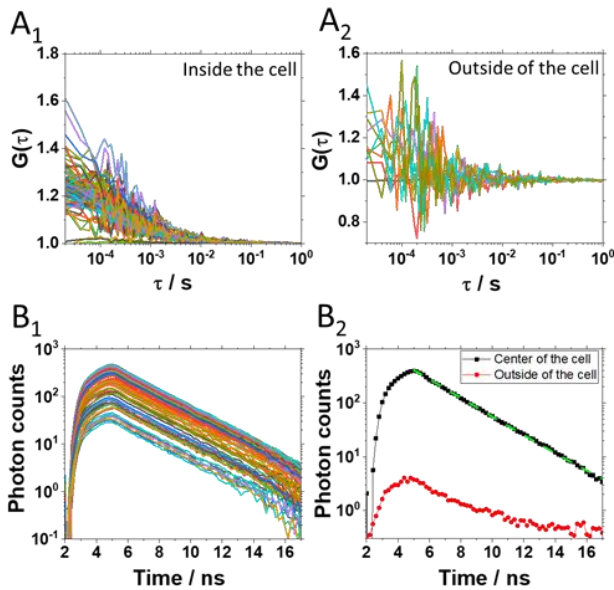
Figure S12. Single-SPAD autocorrelation curves (ACCs) and mpFLIM curves of eGFP fluorescence in a live eGFP expressing HEK cell. (A₁) Single-SPAD ACCs recorded inside the cell. **(A₂)** Single-SPAD ACCs recorded outside of the cell, in the immediately surrounding cell culture medium. **(B₁)** Single-SPAD FLIM curves recorded inside the cell. **(B₂)** A typical single-SPAD FLIM curve recorded inside the cell (black symbols) as compared to a single-SPAD FLIM curve recorded outside of the cell (red symbols), in the immediately surrounding cell culture medium. The dashed green line shows a one-exponential decay function fitted to the FLIM data recorded inside the cell.
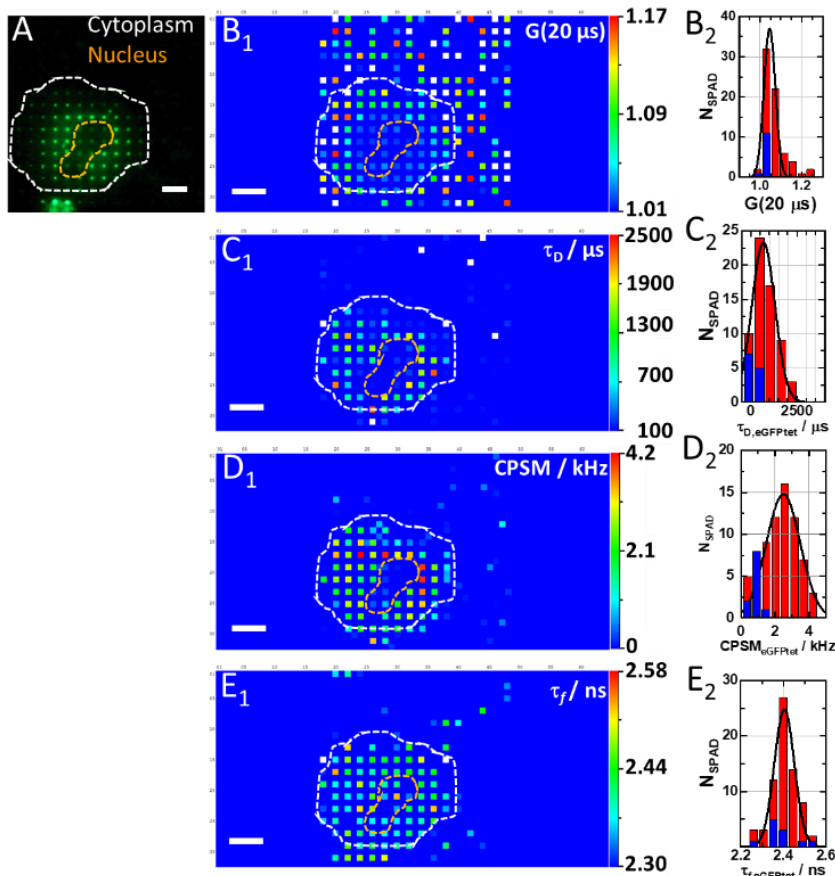

Figure S13. Spatial map of the autocorrelation amplitudes, diffusion times and fluorescence lifetimes of tetrameric eGFP (eGFP_tet) in a live HEK cell. (A) Fluorescence image of a HEK cell expressing eGFP_tet acquired using a spot-wise, 16×16, illumination and a DSLR camera. The hand-drawn dashed lines that highlight the cell border (white) and the cell nucleus (orange), were visualized by transmission light microscopy. Corresponding ACCs and FLIM curves are shown in Fig. S14. **(B₁)** Spatial map of the autocorrelation amplitude at lag time $\tau = 20$ μs (G(20 μs)), which is inversely proportional to the average number of eGFP tetramers in the OVE. **(B₂)** Histograms corresponding to the data in B₁, showing the distribution of autocorrelation amplitudes in the cytoplasm (red) and the nucleus (blue). From the best-fit Gaussian curve (black), the average amplitude in the cytoplasm was determined G(20 μs)_cyt = (1.05 ± 0.03), corresponding to an average concentration of eGFP_tet, $c_{eGFPtet,cyt} \approx 100$ nM. For ACCs recorded in the cell nucleus, please see explanation in the main text. **(C₁)** Spatial map of eGFP_tet diffusion times. **(C₂)** Histograms corresponding to the data in C₁, showing the distribution of diffusion times in the cytoplasm (red) and the nucleus (blue). From the best-fit Gaussian curve (black), the average eGFP_tet diffusion time in the cytoplasm was determined to be $\tau_{D,eGFPtet,cyt} = (700 ± 600)$ μs and $\tau_{D,eGFPtet,nuc} = (160 ± 80)$ μs. **(D₁)** Spatial map of eGFP_tet brightness (CPSM). **(D₂)** Histograms corresponding to the data in D₁, showing the distribution of eGFP_tet brightness in the cytoplasm (red) and the nucleus (blue). From the best-fit Gaussian curve (black), the average eGFP_tet brightness was determined to be CPSM_eGFPtet,cyt = (2.5 ± 1.0) kHz in the cytoplasm and CPSM_eGFPtet,nuc = (0.8 ± 0.2) kHz in the nucleus. **(E₁)** Spatial map of eGFP_tet fluorescence lifetimes. **(E₂)** Histograms corresponding to the data in E₁, showing the distribution of fluorescence lifetimes in the cytoplasm (red) and the nucleus (blue). From the best-fit Gaussian curve (black), the average eGFP_tet fluorescence lifetime was determined to be $\tau_{f,eGFPtet,cyt} = (2.4 ± 0.1)$ ns in the cytoplasm and $\tau_{f,eGFPtet,nuc} = (2.4 ± 0.1)$ ns in the nucleus. Scale bar: 10 μm.
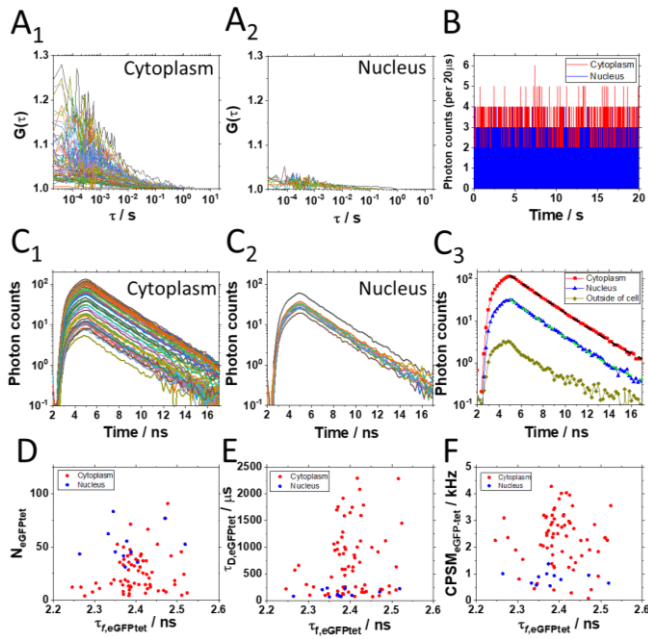
Figure S14. Single-SPAD autocorrelation curves (ACCs) and mpFLIM curves of eGFP tetramer in a live HEK cell. (**A₁**) Single-SPAD ACCs in the cytoplasm. (**A₂**) Single-SPAD ACCs recorded in the cell nucleus. (**B**) Typical photon counts in the cytoplasm (red) and the nucleus (blue). Due to the lower fluorescence intensity in the cell nucleus, the SNR is lower for FCS measurements in the cell nucleus. Subsequently, the amplitude of the ACCs recorded in the nucleus is lower as a consequence of the high background. (**C₁**) Single-SPAD FLIM curves recorded in the cytoplasm. (**C₂**) Single-SPAD FLIM curves recorded in the cell nucleus. (**C₃**) A typical single-SPAD FLIM curve recorded in the cytoplasm (red symbols), cell nucleus (blue symbols) and outside the cell, in the immediately surrounding cell culture medium (ochre symbols). The dashed navy and green lines show a one-exponential decay function fitted to the FLIM data recorded in the cytoplasm and the nucleus, respectively. (**D**) The number of eGFP$_{tet}$ in the cytoplasm (red) and the nucleus (blue) against the fluorescence lifetime. (**E**) The diffusion time recorded in the cytoplasm (red) and the nucleus (blue) against the fluorescence lifetime. (**F**) The molecular brightness recorded in the cytoplasm (red) and the nucleus (blue) against the fluorescence lifetime.
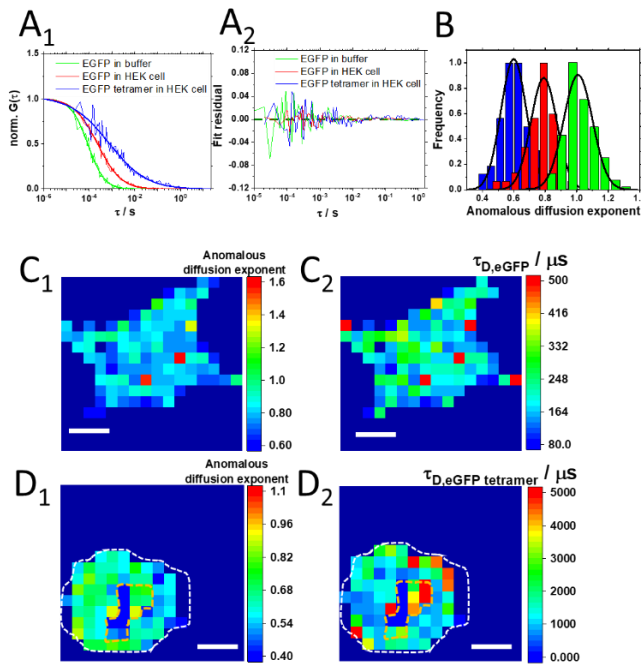

Figure S15. Anomalous diffusion analysis of eGFP and eGFP tetramer (eGFP$_{tet}$) in live HEK cells. (**A₁**) Typical autocorrelation curves of eGFP in phosphate buffer (green), eGFP in a live HEK cell (red), and eGFP$_{tet}$ in a live HEK cell (blue). (**A₂**) Residuals between the experimental ACCs and the fitted theoretical functions for 3D diffusion (equation (S1)) show excellent agreement (chi-square values ranging from $10^{-6} – 10^{-4}$). (**B**) Histograms of the anomalous diffusion exponent distribution and average values determined from the best-fit Gaussian curves (black): $\alpha_{eGFP,buffer} = 1.00 \pm 0.09$ (green), $\alpha_{eGFP,cell} = 0.80 \pm 0.08$ (red), and $\alpha_{eGFPtet,cell} = 0.60 \pm 0.08$ (blue). (**C₁**) Spatial map of the anomalous diffusion exponent for eGFP in a live HEK cell. The anomalous diffusion exponent in the cytoplasm is not statistically significantly different from the value measured in the cell nucleus, $p > 0.05$. (**C₂**) Spatial map of the diffusion time of eGFP in a live HEK cell. (**D₁**) Spatial map of the anomalous diffusion exponent for eGFP$_{tet}$ in a live HEK cell. The anomalous diffusion exponent in the cytoplasm, $\alpha_{eGFP_{tet}}^{cyt} = 0.6 \pm 0.1$, is statistically significantly different from the value measured in the cell nucleus, $\alpha_{eGFP_{tet}}^{nuc} = 0.5 \pm 0.3$, $p = 0.027$. (**D₂**) Spatial map of the diffusion time of eGFP$_{tet}$ in a live HEK cell. Dashed lines show nuclear region (orange) and the cell (white). Scale bar: 10 μm.
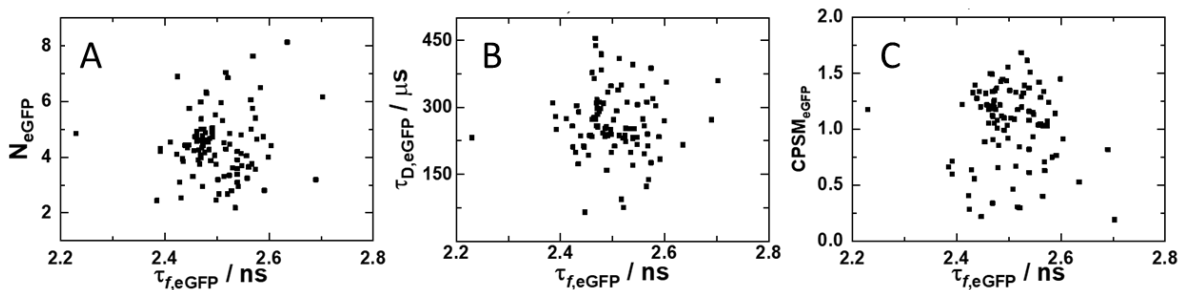

Figure S16. Scatter plots derived from spatial maps of eGFP concentration, diffusion and brightness as a function of fluorescence lifetime in a live HEK cell. (**A**) Scatter plots of number of eGFP against fluorescence lifetime of eGFP. (**B**) Scatter plots of eGFP diffusion time against fluorescence lifetime. (**C**) Scatter plots of eGFP CPSM against fluorescence lifetime.

S2b: Pharmacological treatment. After transfection, HEK cells were cultured for 24 h in the 8-well chambered cover glass. Thereafter, the cell culture medium was replaced either with a phenol red free medium (untreated cells) or with a phenol red free medium containing 1 µM 5-chloro-N1,N3-bis[3(4,5-dihydro-1H-imidazol-2yl)phenyl]benzene-1,3-dicarboxamide, dihydrochloride (compound NSC 50467; treated cells). Detailed information on the NSC 50467 compound pound and its preparation can be found in[14]. Briefly, the NSC 50467 compound was dissolved in Dime-

thyl sulfoxide (DMSO) yielding a stock solution (mM concentration) that was stored at 4 °C for future use. On the day of treatment, an aliquot was taken from the stock solution, allowed to warm up to room temperature and an adequate volume was pipetted-out and diluted with the phenol red free medium to a final concentration of 1 µM NSC 50467. After 1 h incubation, all measurements were performed at room temperature. The results are shown in Figs S17-S19.
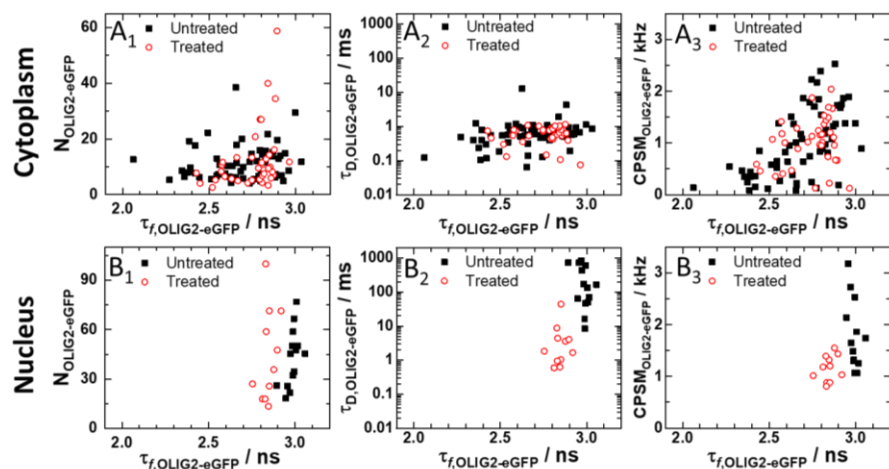

Figure S17. Relationship between number, diffusion times or brightness and fluorescence lifetime in live OLIG2-eGFP expressing HEK cells following the treatment with 1 µM NSC 50467, the allosteric inhibitor of OLIG2 homodimerization. (A1-3) Relationship between the number (A1), diffusion time (A2) and molecular brightness (A3) against fluorescence lifetime in the cytoplasm of untreated (black) and treated (red) cells. (B1-3) Relationship between the number (B1), diffusion time (B2) and molecular brightness (B3) against fluorescence lifetime in the nucleus of untreated (black) and treated (red) cells.
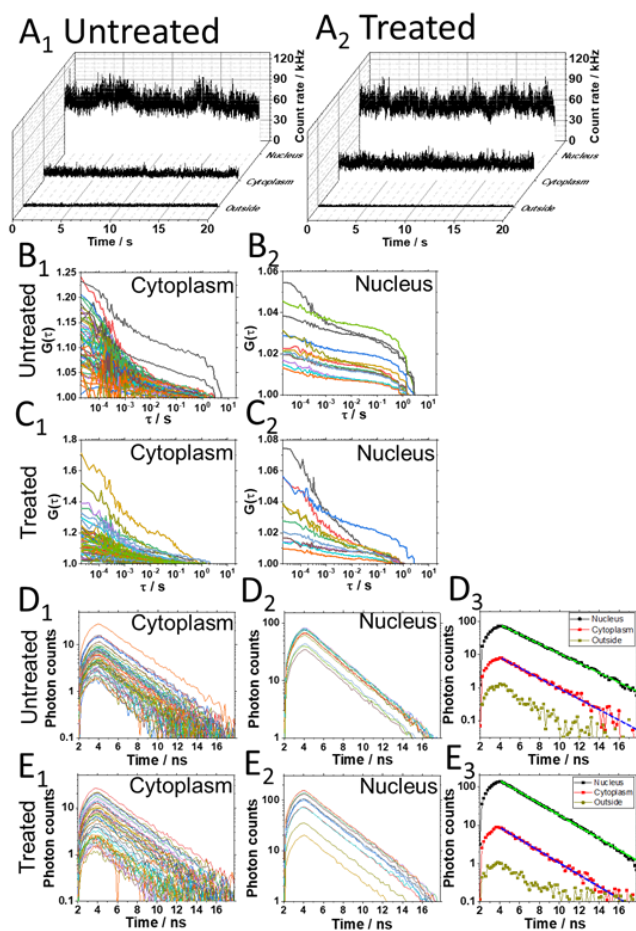

Figure S18. Single-SPAD autocorrelation curves (ACCs) and mpFLIM curves of OLIG2-eGFP in a live HEK cell before and after treatment with the allosteric inhibitor of OLIG2 homodimerization NSC 50467. (A1) Photon counts recorded in the cytoplasm, nucleus and outside of the cell before treatment. (A2) Photon counts recorded in the cytoplasm, nucleus and outside of the cell after treatment with the allosteric inhibitor of OLIG2 dimerization NSC 50467. (B1) Single-SPAD ACCs recorded in the cytoplasm of an untreated cell. (B2) Single-SPAD ACCs recorded in the nucleus of the same cell. (C1) Single-SPAD ACCs recorded in the cytoplasm of the same cell following 1 h treatment with 1 µM NSC 50467. (C2) Single-SPAD ACCs recorded in the nucleus of the same cell, following treatment with NSC 50467. (D1) Single-SPAD FLIM curves recorded in the cytoplasm of an untreated cell. (D2) Single-SPAD FLIM curves recorded in the nucleus of the same cell as in D1. (D3) Typical single-SPAD FLIM curves recorded in the nucleus (black symbols) and cytoplasm (red symbols) of an untreated cell and outside the cell, in its immediate surroundings (ochre symbols), together with corresponding fitted curves (dashed lines). (E1) Single-SPAD FLIM curves recorded in the cytoplasm of the same cell as in (D1) following a 1 h treatment with 1 µM NSC 50467. (E2) Single-SPAD FLIM curves recorded in the nucleus of the same cell as in D1 following treatment. (E3) Typical single-SPAD FLIM curves recorded in the nucleus (black symbols) and cytoplasm (red symbols) of a treated cell and outside the cell, in its immediate surroundings (ochre symbols), together with corresponding fitted curves (dashed lines).
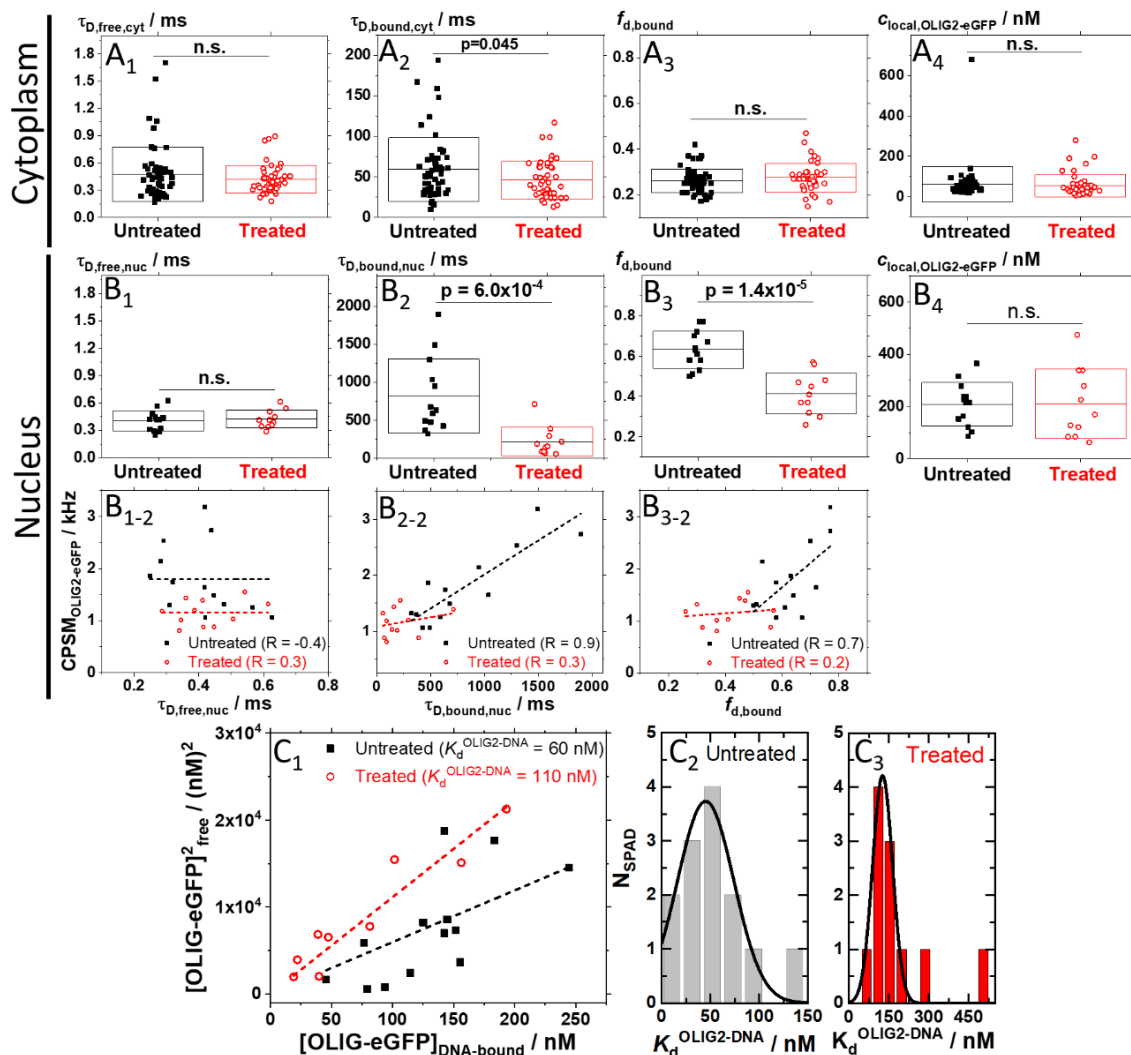
Figure S19. Determination of the apparent dissociation constant of OLIG2-eGFP binding to chromatin DNA in a live HEK cell before and after treatment with the allosteric inhibitor of OLIG2 homodimerization NSC 50467. (A$_{1-4}$) Cytoplasm: Diffusion time of free (A$_1$) and bound (A$_2$) OLIG2-eGFP, the mole fraction of bound OLIG2-eGFP (A$_3$) and OLIG2-eGFP local concentration in individual OVEs (A$_4$), before (black) and after (red) treatment. **(B$_{1-4}$)** Nucleus: Diffusion time of free (B$_1$) and bound (B$_2$) OLIG2-eGFP, the mole fraction of bound OLIG2-eGFP (B$_3$) and OLIG2-eGFP local concentration in individual OVEs (B$_4$), before (black) and after (red) treatment. **(B$_{i-2}$)** Molecular brightness in the nucleus, as reflected by counts *per* second and molecule (CPSM) measured in a single-SPAD, as a function of: the diffusion time of the free OLIG2-eGFP fraction (B$_{1-2}$), the diffusion time of the DNA-bound OLIG2-eGFP fraction (B$_{2-2}$) and the mole fraction of the DNA-bound OLIG2-eGFP (B$_{3-2}$) before (black) and after (red) treatment. **(C$_{1-3}$)** Apparent dissociation constant of OLIG2-eGFP binding to chromatin DNA determined from linear-regression analysis of $[OLIG2\text{-}eGFP]^2_{free} = f([OLIG2\text{-}eGFP]_{DNA\text{-}bound})$ (C$_1$) and from Gaussian curve fitting to the histograms of apparent dissociation constant distribution before (C$_2$) and after treatment (C$_3$).

S2c: FLIM-FRET. For FLIM-FRET experiments, the expression plasmids of ShadowY (ShY) and tandem dimer of eGFP-ShY on pCPCI3 vector were kindly provided by Dr. Hideji Murakoshi, National Institute for Physiological Sciences, Aichi Japan[12]. Expression plasmids of pShY-CPCI3 and peGFP-N1 were transfected into HEK cells as a negative control, eGFP-ShY as a positive control in FRET experiments. Expression plasmid of OLIG2-ShY was constructed as previously described[14]. Briefly, OLIG2 sequence was amplified from pGEM-OLIG2 using forward primer with NheI site and reverse primer with AgeI site[15], ligating into pShY-CPCI3 vector.

One day before the transfection, HEK cells were split and transferred to 8-well chambered coverglass with 1.0×10^4 (cells/mL in each chamber). HEK cells on the 8-well chamber were transfected with 100 ng plasmid DNA and 0.2 μL Lipofectamine 2000 (Thermo Fisher Scientific) in each well. After the transfection, HEK cells were cultured for 24 h in a humidified atmosphere containing 5 % CO_2 at 37 °C. The medium was replaced to phenol red free medium, FluoroBrite™ DMEM (Gibco) just before the experiments (Figs S20 and S21).
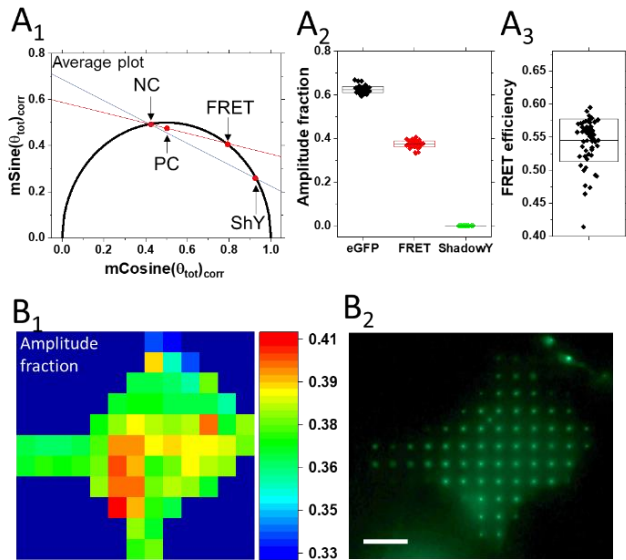
Figure S20. Positive and negative controls for phasor analysis of FRET between the eGFP donor and the ShadowY (ShY) acceptor. Negative control (NC), live HEK cells co-expressing eGFP and ShY. Positive control (PC), live HEK cells expressing the fusion protein eGFP-ShY linked *via* a peptide SGLRSG. (A$_1$) Average fluorescence lifetimes presented in a phasor plot. Fluorescence lifetime measured in the NC is virtually indistinguishable from the fluorescence lifetime of the eGFP donor (phasor positions for NC: $(x,y) = (0.4253, 0.4923)$ and eGFP: $(x,y)=(0.4333, 0.4895)$), the phasor of which is located on the semicircle, suggesting that neither FRET nor direct ShY excitation affect eGFP lifetime and its measurement in the NC cells. In contrast, the PC phasor exhibited a shift with respect to the eGFP donor, indicating a FRET contribution. (A$_2$) Amplitude of the FRET state fraction, 0.38 ± 0.02. (A$_3$) FRET efficiency in the FRET population is 0.55 ± 0.03. (B$_1$) Spatial mapping of the amplitude fraction in a PC cell shows a homogenous, tight distribution of amplitude fraction of FRET component (range: 0.33-0.41), with slightly higher amplitude fraction in some pixels. (B$_2$) Fluorescence images of a spot-wise (16×16) illuminated PC cell recorded using the DSLR camera.
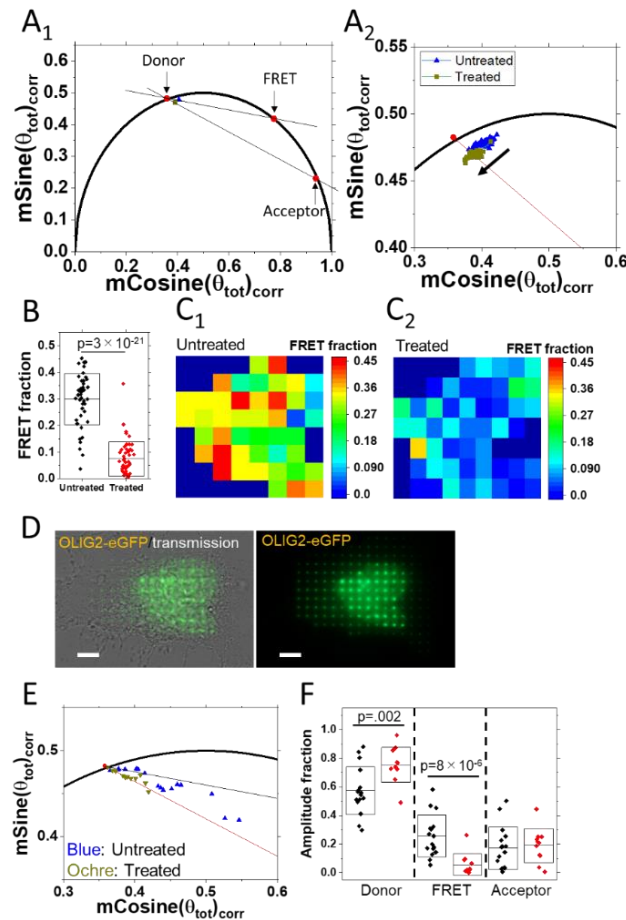

Figure S21. The effect of treatment with the allosteric inhibitor NSC 50467 on OLIG2 homodimerzation in live HEK cells co-expressing OLIG2 constructs genetically fused with the eGFP (donor) or the ShY (acceptor) characterized using the multicomponent FLIM-FRET phasor analysis approach. (A$_1$) Phasor positions in untreated cells (blue) and cells treated with NSC 50467 (ochre) localize inside the universal circle, indicative of donor fluorescence quenching due to FRET. (A$_2$) Magnified detail of the phasor plot in (A$_1$) reveals that 1 h treatment with 1 µM NSC 50467 causes the phasor to move counter-clockwise, indicating less quenching due to FRET. (B) Amplitude fraction of the FRET component in untreated cells (0.3 ± 0.1) was reduced to (0.07 ± 0.06) upon treatment with NSC 50467, suggesting that OLIG2 dimerization is significantly reduced. (C$_1$) Spatial mapping of the amplitude fraction of FRET in untreated cells. (C$_2$) Spatial mapping of the amplitude fraction of FRET in cells treated with the inhibitory NSC 50467 compound. (D) *Left:* Fluorescence image of a spot-wise (16×16) illuminated HEK cell expressing OLIG2-eGFP and OLIG2-ShY (green) overlaid on a widefield transmission image (grey) recorded using the DSLR camera. *Right:* The same fluorescence image shown on its own to better visualize the nuclear localization of OLIG2. (E) Positions of average phasors acquired in untreated (ochre) and treated (blue) cells. Each phasor point is an average over a single cell. The black solid line links the donor and the FRET component (FRET trajectory). The red solid line links the donor with the acceptor. Phasor plots in the absence of inhibitory compound were distributed in-between the red and black lines, suggesting OLIG2 dimer formation. On the other hand, phasor plots in the presence of inhibitory compound were shifted onto the red line, reducing FRET. (F) Box and whisker plot showing the amplitude fraction of each component measured in untreated (black) and treated (red) cells, suggest that the FRET fraction was significantly reduced, while the donor fraction was significantly increased, suggesting OLIG2 dimer dissociation or perturbation by inhibitory compound.

S3. DETERMINING THE CONCENTRATION OF OLIG2-EGFP HOMODIMERS BASED ON MOLECULAR BRIGHTNESS ANALYSIS BY FCS.

To determine the fraction of OLIG2-eGFP homodimers based on molecular brightness analysis, the procedure described by Oasa *et al.*[16] is applied. Briefly, the mole fraction of OLIG2-eGFP monomers ($F_{monomer}$) and ho-

modimers ($F_{homodimer}$), the sum of which is equal to one ($F_{monomer} + F_{homodimer} = 1$), were calculated using equations (S22) and (S23):

$$F_{monomer} = \frac{4 - 2CPSM_n}{3 - CPSM_n} \qquad (S22)$$

$$F_{homodimer} = \frac{CPSM_n - 1}{3 - CPSM_n} \qquad (S23)$$

where OLIG2-eGFP molecular brightness is reflected by counts *per* second and molecule (CPSM) and:

$$CPSM_n = \frac{CPSM_{OLIG2\text{-}eGFP,nuc}}{CPSM_{eGFP, cell}} . \qquad (S24)$$

The concentration of OLIG2-eGFP monomers ($c_{monomer}$) and homodimers ($c_{homodimer}$) in the cell nucleus is the product of the corresponding mole fraction and the total concentration as measured by FCS ($c_{monomer} = F_{monomer} \cdot c_{tot}$ and $c_{homodimer} = F_{homodimer} \cdot c_{tot}$), and the apparent dissociation constant of OLIG2-eGFP homodimers was determined as:

$$K_{d,app}^{(OLIG2\text{-}eGFP)2} = \frac{c_{monomer}^2}{c_{homodimer}} . \qquad (S25)$$

The results of this analysis are summarized in Table S1.

Table S1. OLIG2-eGFP brightness analysis and determination of the apparent average dissociation constant of OLIG2-eGFP homodimers.

	Cytoplasm		Nucleus	
	Untreated	Treated	Untreated	Treated
CPSM / kHz	1.0 ± 0.7	1.0 ± 0.5	1.4 ± 0.7	1.1 ± 0.3
$CPSM_n$	1.0	1.0	1.4	1.1
$F_{monomer}$	1	1	0.77	0.94
$F_{homodimer}$	0	0	0.23	0.06
c_{tot} / nM	50 ± 20	50 ± 40	210 ± 80	210 ± 130
$c_{monomer}$ / nM	50 ± 20	50 ± 40	160	197
$c_{homodimer}$ / nM	0	0	47	13
$K_{d,apparent}^{(OLIG2\text{-}eGFP)2}$ / nM	*	*	560	3000

CPSM: Average OLIG2-eGFP molecular brightness determined by mpFCS. The bright pixels with CPSM > 2 were not included in this analysis.

$CPSM_n$: Molecular brightness of OLIG2-eGFP against average molecular brightness of eGFP in live cell (Fig. 4, main text).

F: Mole fraction

c: Concentration

$K_{d,apparent}^{(OLIG2\text{-}eGFP)2}$: Apparent dissociation constant of OLIG2-eGFP homodimers

S4. DETERMINING THE APPARENT DISSOCIATION CONSTANT FOR OLIG2-EGFP BINDING TO CHROMATIN DNA BY FCS.

By fitting the theoretically derived equation for free 3D diffusion of two components to the ACCs recorded in the cell nucleus, (Fig. 5C$_2$, Fig.S18B$_2$ and C$_2$) the mole fraction of free, f_{free}^{nuc} and DNA-bound, f_{bound}^{nuc}, OLIG2-eGFP were determined.

The concentration of free, [OLIG2-eGFP]$_{free}$, and bound, [OLIG2-eGFP]$_{DNA\text{-}bound}$, is the product of the corresponding mole fraction and the total OLIG2-eFFP concentration as measured by FCS, and the average apparent dissociation constant for OLIG2-eGFP binding to chromatin DNA was determined as:

$$K_{d,apparent}^{OLIG2\text{-}DNA} = \frac{[OLIG2\text{-}eGFP]_{free}^2}{[OLIG2\text{-}eGFP]_{DNA\text{-}bound}} . \qquad (S26)$$

To this aim, linear-regression analysis of $[OLIG2\text{-}eGFP]_{free}^2 = f$ ($[OLIG2\text{-}eGFP]_{DNA\text{-}bound}$) was used to assess $K_{d,apparent}^{OLIG2\text{-}DNA}$ from the slope (Fig. S19C$_1$). Gaussian curve fitting to the histograms of apparent dissociation constant distribution is shown for measurements in the same cell before (Fig. S19C$_2$) and after treatment (Fig. S19C$_3$).

To examine the possible effects of slow processes and/or photobleaching on assessing the dissociation constants, we note that for processes with characteristic times that are very long, *i.e.* comparable with the signal acquisition time length, an apparently abrupt decay in the amplitude of the ACC is observed that arises because a small number of data points is collected at such long time scales (Fig. S5C$_2$). While longer measurements would make it possible to collect more data points at long time scales, they would also increase the risk of photobleaching. Hence, there is a tradeoff between optimization of photobleaching and the signal acquisition length. To assess whether the ACCs could be fit satisfactorily with acceptable signal to noise using eq. (S1), $\alpha = 1$, $i = 2$, $T = 0$, we performed the chi-square test for goodness of fit. This analysis yielded chi-square (χ^2) values $\chi_{nuc}^2 = 2.7 \times 10^{-4}$ and $\chi_{cyt}^2 = 5.0 \times 10^{-5}$ in untreated OLIG2-eGFP expressing cells. For monomeric eGFP in live cells the goodness of fit using eq. (S1), $\alpha = 1$, $i = 1$, $T = 0$, yielded $\chi_{eGFP,cell}^2 = 3.2 \times 10^{-5}$ and for eGFP in buffer solution $\chi_{eGFP,sol}^2 = 2.4 \times 10^{-5}$. We therefore regard that ACCs reflecting OLIG2-eGFP diffusion and binding could be fit satisfactorily with acceptable signal to noise using eq. (S1), $\alpha = 1$, $i = 2$, $T = 0$.

In order to assess to what extent data points for which very long decay times were observed (such as data shown in Fig. S22, curves A-C) affect our analysis, we have compared the

relative fraction of bound OLIG2-eGFP in the cell nucleus ($f_{D,bound}^{nuc}$); the apparent diffusion behavior of OLIG2-eGFP in the cell nucleus affected by DNA binding, ($\tau_{D,bound}^{nuc}$) and the apparent dissociation constant of OLIG2-eGFP—DNA complexes ($K_{d,app}^{OLIG2-DNA}$) when including/excluding these data points.
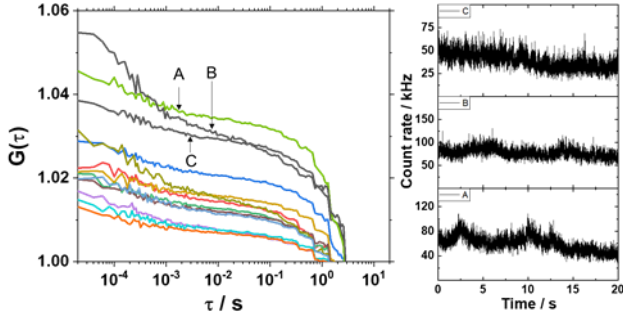

Figure S22 Fluorescence intensity fluctuation with very long characteristic times. Autocorrelation curves A-C are corresponding to fluorescence intensity fluctuation time series A-C in the right graph.

This analysis showed that while exclusion of data points with CPSM that are larger than twice the CPSM$_{eGFP}$, which are characterized by very long decay times (ACCs denoted A-C in Fig.S22) changes somewhat the actual values of the assessed variables: from $f_{D,bound}^{nuc}$ = (0.65 ± 0.10) to $f_{D,bound}^{nuc}$ = (0.60 ± 0.10); from $\tau_{D,bound}^{nuc}$ = (850 ± 500) ms to $\tau_{D,bound}^{nuc}$ = (600 ± 200) ms and from $K_{d,app}^{OLIG2-DNA}$ = (45 ± 30) nM to $K_{d,app}^{OLIG2-DNA}$ = (60 ± 21) nM, the overall conclusions remain.

Moreover, we have tested whether adoption of different fitting models affects the interpretation of our data. In particular, the following models were tested: the two-component free diffusion model (eq. (S1), α = 1, T = 0, i = 2; Fig. S23, red), the two-component anomalous diffusion model (eq. (S1), α ≠ 1, T = 0, i = 2; Fig. S23, green); the two-component diffusion model with anomalous first diffusion component and free second diffusion component (eq. (S1), $α_1$ ≠ 1, $α_2$ = 1 T = 0, i = 2; Fig. S23, blue); the one-component free diffusion model with binding (eq. (S27))[17], α = 1, T = 0, i = 1; Fig. S23, dark yellow) or the one-component anomalous diffusion model with binding (eq. (S27))[17], α ≠ 1, T = 0, i = 1; Fig. S23, dark blue). In eq. (S27)[17]:

$$G(\tau) = 1 + \frac{1}{N} \cdot \left[1 + \frac{T}{1-T} e^{-\frac{\tau}{\tau_T}} \right]$$

$$\cdot \left(\frac{f_D}{\left(1 + \left(\frac{\tau}{\tau_{D_i}}\right)^\alpha\right)\sqrt{1 + \frac{w_{xy}^2}{w_z^2}\left(\frac{\tau}{\tau_{D_i}}\right)^\alpha}} + (1-f_D)e^{-k_{off}\cdot\tau} \right) \quad \text{(S27)}$$

k_{off} denotes the dissociation rate constant, while all other parameters are the same as in eq. (S1).
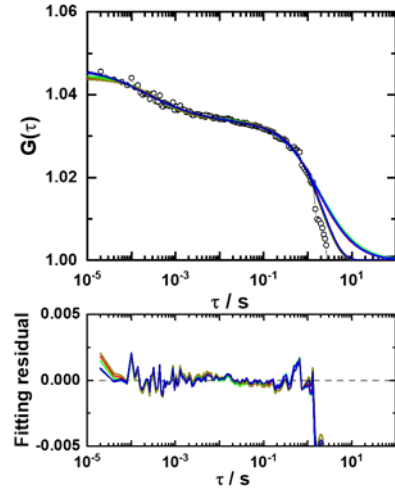

Figure S23: Analysis of OLIG2-eGFP diffusion and binding in the cell nucleus using different free and/or anomalous diffusion models with/without binding. *Upper*: Single-pixel autocorrelation curve (open circles) fitted using the two-component free diffusion model (red), the two-component anomalous diffusion model (green), the two-component anomalous (first component) and free (second component) diffusion model (blue), the one-component free diffusion model with binding (dark yellow), or the one-component anomalous diffusion model with binding (dark blue). *Bottom*: Corresponding fitting residuals.

As can be seen from the residuals analysis, all models can fit the ACC with similar chi-square values per degree of freedom: $\chi^2_{free,2c}$ = 4.0 ×10^{-6}, $\chi^2_{anom,2c}$ = 4.4 ×10^{-6}, $\chi^2_{free+anom,2c}$ = 4.1 ×10^{-6}, $\chi^2_{free+binding,2c}$ = 2.0 ×10^{-6} and $\chi^2_{free+binding,2c}$ = 2.0 ×10^{-6}. Moreover, the number of molecules (N), diffusion time of free OLIG2-eGFP (τ_{D1}) and the relative fraction of the second/binding component (*f*) are similar between all models: N$_{free,2c}$ = 22.6, N$_{anom,2c}$ = 22.3, N$_{free+anom,2c}$ = 21.6, N$_{free+binding,2c}$ = 22.7 and N$_{anom+binding,2c}$ = 21.2; $\tau_{D1}^{free,2c}$ = 390 µs, $\tau_{D1}^{anom,2c}$ = 340 µs, $\tau_{D1}^{free+anom,2c}$ = 270 µs, $\tau_{D1}^{free+binding,2c}$ = 450 µs, $\tau_{D1}^{anom+binding,2c}$ = 240 µs; $\tau_{D2}^{free,2c}$ = 1.7 s, $\tau_{D2}^{anom,2c}$ = 1.8 s, $\tau_{D2}^{free+anom,2c}$ = 1.8 s, $\tau_{Binding}^{free+binding,2c}$ = 2 s (k_{off} = 0.49 s^{-1}), $\tau_{Binding}^{anom+binding,2c}$ = 2.2 s (k_{off} = 0.46 s^{-1}); $f_2^{free,2c}$ = 0.77, $f_2^{anom,2c}$ = 0.76, $f_2^{free+anom,2c}$ = 0.73, $f_{binding}^{free+binding,2c}$ = 0.77 and $f_{binding}^{anom+binding,2c}$ = 0.71; for $\alpha^{free,2c}$ = 1, $\alpha^{anom,2c}$ = 0.95, $\alpha^{free+anom,2c}$ = 0.75, $\alpha^{free+binding,2c}$ = 1 and $\alpha^{anom+binding,2c}$ = 0.65. Interestingly, the anomalous diffusion exponent (α) was close to free diffusion (α ≈ 1) when the two-component anomalous diffusion model was applied, whereas the diffusion model with anomalous diffusion of the first component and free diffusion of the second component yielded α = 0.75, a value that is in-between values of α for eGFP monomer and tetramer.

Importantly, all diffusion models tested yielded congruent results and similar values for the apparent dissociation constant of OLIG2-eGFP–DNA-complexes, whereas a principal difference arises by adopting the diffusion and binding model (eq. (S27)), which yields the OLIG2-eGFP dissociation rate constant (k_{off}) instead of $\tau_{D,bound}^{nuc}$. According to this model, the mean life of the OLIG2-eGFP–DNA complex (1/k_{off}) is esti-

mated to be ≈ 2 s. While further studies are needed to establish which model correctly interprets the ACCs, it was previously shown that eGFP fluorescence is not changing upon eGFP-tagged transcription factor binding to DNA[18, 19], favoring our original interpretation.

For OLIG2-eGFP behavior in the cytoplasm, residuals- analysis showed that three different diffusion models: one-component anomalous diffusion (Fig. S24, green), two-component free diffusion model (Fig. S24, blue) and a two-component anomalous diffusion model (Fig. S24, red). could fit the ACC with similar chi-square values per degree of freedom: $\chi^2_{anom,1c} = 2.8 \times 10^{-5}$, $\chi^2_{free} = 2.5 \times 10^{-5}$ and $\chi^2_{anom,2c} = 2.0 \times 10^{-5}$: yielding $N_{anom,1c} = 1.9$, $N_{free} = 5.5$ and $N_{anom,2c} = 5.2$; $\tau_D^{anom,1c} = 17$ µs, $\tau_{D1}^{free} = 560$ µs and $\tau_{D1}^{anom} = 350$ µs; $\tau_{D2}^{free} = 70$ ms and $\tau_{D2}^{anom} = 40$ ms; $f_2^{free} = 0.26$ and $f_2^{anom} = 0.26$; for $\alpha^{anom,1c} = 0.34$, $\alpha^{free} = 1$ and $\alpha^{anom,2c} = 0.66$.

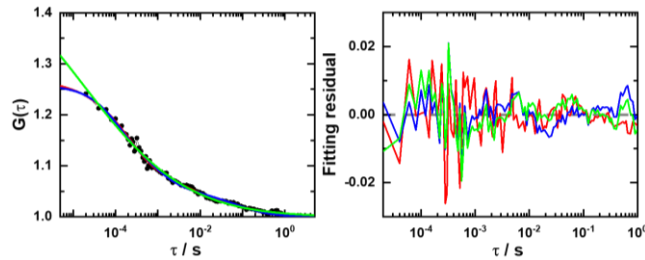**Figure S24. Two-component free *versus* anomalous diffusion model analysis of OLIG2-eGFP dynamics in the cytoplasm.** *Left*: Single-pixel autocorrelation curve (black symbols) fitted using a one-component anomalous diffusion model (green), two-component free diffusion model (blue) or a two-component anomalous diffusion model (red). ***Right***: Corresponding residuals.

However, the one-component anomalous diffusion model yields a very short diffusion time value, $\tau_D^{anom,1c} = 17$ µs, that is inconsistent with protein diffusion. This model is therefore not applicable.

Finally, we show (Fig. S25) that similar results were obtained in different cells from three independently replicated experiments.
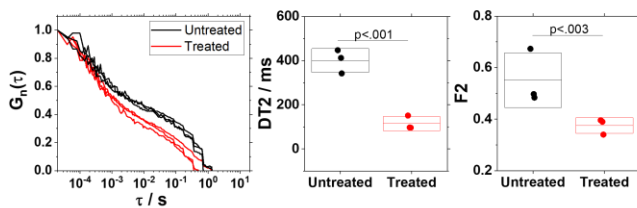

Figure S25: Effect of treatment with NSC 50467 on OLIG2-eGFP diffusion and binding in different cells. *Left:* Average autocorrelation curves (ACCs) reflecting OLIG2-eGFP diffusion and binding in the nucleus of untreated (black) and treated (red) cells. Measurements were taken in three independent experiments, starting from cell transfection, culturing, treatment and measurement. *Middle:* Diffusion time of bound OLIG2-eGFP (τ_{D2}) derived by fitting the ACCs shown to the left using a two-component free diffusion model. ***Right:*** Relative contribution of bound OLIG2-eGFP (f_2).

S5. STANDARD SOLUTIONS FOR mpFCS/FLIM CALIBRATION

Dilute aqueous suspension of 100 nm fluospheres (Fluo Spheres® Size Kit #2; Ex/Em: 505/515, Molecular Probes, Life Technologies Corporation, USA; $D_{100} = 4.4$ µm^2/s [2]) was used for the daily calibration of the mpFCS system. Occasionally, dilute aqueous suspension of quantum dots 525 (Qdot® 525 ITK™ Carboxyl Quantum Dots, Molecular Probes, Life Technologies Corporation, USA) and eGFP (purified by His-tag from E. coli) in 200 mM Phosphate buffer pH7.4, were used as secondary mpFCS calibration standards. For this purpose, the fluospheres and quantum dots were suspended in water and sonicated for 30 min before use. The standard solutions for mpFCS calibration were freshly prepared on the day of use and their concentration was measured by spFCS.

Single point Fluorescence Correlation Spectroscopy (spFCS) was performed using an uniquely modified ConfoCor3 system built on an LSM510 META platform, consisting of an inverted microscope for transmitted light and epifluorescence (Axiovert 200 M), the VIS-laser module comprising the Ar-ion (458, 477, 488 and 514 nm), HeNe 543 nm and the HeNe 633 nm lasers, the C-Apochromat 40×/1.2 N. A. W objective and silicon avalanche photodiodes (SPCM-AQR-1X; PerkinElmer) (Carl Zeiss MicroImaging GmbH, Jena, Germany)[20]. Dilute aqueous solution of ATTO488 (Sigma-Aldrich; $D_{ATTO488} = 400$ µm^2/s [2]) was used for the daily calibration of the spFCS system. spFCS data were analyzed using the program for FCS data analysis that is part of the ConfoCor3 running software package.

For fluorescence lifetime (τ_f) measurements, the following standards were used: ATTO495 (Sigma-Aldrich: $\tau_{f,ATTO495} = 1.1$ ns[21]), Rhodamine B (RhB; Sigma-Aldrich: $\tau_{f,RhB} = 1.56$ ns[22]), enhanced Green Fluorescent Protein (eGFP: $\tau_{f,eGFP} = 2.4$ ns and 2.6 ns[23, 24]), Rhodamine 6G (Rh6G; Sigma-Aldrich: $\tau_{f,Rh6G} = 3.79$ ns[25]), ATTO488 (Sigma-Aldrich: $\tau_{f,ATTO488} = 4.2$ ns and 4.16 ns[26, 27], BODIPY FL (Thermo Fisher Scientific: $\tau_{f,BODIPY}$ FL = 5.66 ns[28]), Rubrene (Sigma-Aldrich: $\tau_{f,Rubrene} = 7.4$ ns[29, 30]). These substances were suspended in Dimethyl sulfoxide (DMSO) at a concentration of 10 µM, aliquoted and stored at -20 °C. For actual measurements, the fluorescence standards were thawed and, after reaching room temperature, diluted 100 - 1000 times using as a solvent: water for ATTO488, ATTO495, BODIPY FL, Rhodamine B and Rhodamine 6G; 200 mM Phosphate buffer pH7.4 for eGFP; and methanol for Rubrene.

For all measurements, in solution and in live cells, 8-well chambered cover glass (Nunc® Lab-Tek® II, Thermo Fisher Scientific) were used.

SUPPORTING REFERENCES

1. Krmpot, A. J.; Nikolić, S. N.; Oasa, S.; Papadopoulos, D. K.; Vitali, M.; Oura, M.; Mikuni, S.; Thyberg, P.; Tisa, S.; Kinjo, M.; Nilsson, L.; Terenius, L.; Rigler, R.; Vukojević, V., Functional Fluorescence Microscopy Imaging: Quantitative Scanning-Free Confocal Fluorescence Microscopy for the Characterization of Fast Dynamic Processes in Live Cells. Anal Chem 2019, 91 (17), 11129-11137.
2. Kapusta, P., Absolute Diffusion Coefficients: Compilation of Reference Data for FCS Calibration. Application Note (PicoQuant) Available at

https://www.picoquant.com/images/uploads/page/files/7353/appnote_diffusioncoefficients.pdf 2010.

3. Hess, S. T.; Webb, W. W., Focal volume optics and experimental artifacts in confocal fluorescence correlation spectroscopy. Biophys J 2002, 83 (4), 2300-17.

4. Vitali, M.; Bronzi, D.; Krmpot, A. J.; Nikolić, S. N.; Schmitt, F.; Junghans, C.; Tisa, S.; Friedrich, T.; Vukojević, V.; Terenius, L.; Zappa, F.; Rigler, R., A Single-Photon Avalanche Camera for Fluorescence Lifetime Imaging Microscopy and Correlation Spectroscopy. IEEE Journal of Selected Topics in Quantum Electronics 2014, 20 (6), 344-353.

5. Vallmitjana, A.; Dvornikov, A.; Torrado, B.; Jameson, D. M.; Ranjit, S.; Gratton, E., Resolution of 4 components in the same pixel in FLIM images using the phasor approach. Methods Appl Fluoresc 2020, 8 (3), 035001.

6. Digman, M. A.; Caiolfa, V. R.; Zamai, M.; Gratton, E., The phasor approach to fluorescence lifetime imaging analysis. Biophys J 2008, 94 (2), L14-L16.

7. Hanley, Q. S.; Clayton, A. H., AB-plot assisted determination of fluorophore mixtures in a fluorescence lifetime microscope using spectra or quenchers. J Microsc 2005, 218 (Pt 1), 62-7.

8. Clayton, A. H.; Hanley, Q. S.; Verveer, P. J., Graphical representation and multicomponent analysis of single-frequency fluorescence lifetime imaging microscopy data. J Microsc 2004, 213 (1), 1-5.

9. Weber, G., Resolution of the fluorescence lifetimes in a heterogeneous system by phase and modulation measurements. The Journal of Physical Chemistry 1981, 85 (8), 949-953.

10. Chen, S. J.; Sinsuebphon, N.; Rudkouskaya, A.; Barroso, M.; Intes, X.; Michalet, X., In vitro and in vivo phasor analysis of stoichiometry and pharmacokinetics using short-lifetime near-infrared dyes and time-gated imaging. J Biophotonics 2019, 12 (3), e201800185.

11. Fereidouni, F.; Esposito, A.; Blab, G. A.; Gerritsen, H. C., A modified phasor approach for analyzing time-gated fluorescence lifetime images. J Microsc 2011, 244 (3), 248-58.

12. Murakoshi, H.; Shibata, A. C. E., ShadowY: a dark yellow fluorescent protein for FLIM-based FRET measurement. Sci Rep 2017, 7 (1), 6791.

13. Lambert, T. J., FPbase: a community-editable fluorescent protein database. Nat Methods 2019, 16 (4), 277-278.

14. Oasa, S.; Vukojević, V.; Rigler, R.; Tsigelny, I. F.; Changeux, J. P.; Terenius, L., A strategy for designing allosteric modulators of transcription factor dimerization. Proc Natl Acad Sci U S A 2020, 117 (5), 2683-2686.

15. Tabu, K.; Ohnishi, A.; Sunden, Y.; Suzuki, T.; Tsuda, M.; Tanaka, S.; Sakai, T.; Nagashima, K.; Sawa, H., A novel function of OLIG2 to suppress human glial tumor cell growth via p27Kip1 transactivation. J Cell Sci 2006, 119 (Pt 7), 1433-41.

16. Oasa, S.; Mikuni, S.; Yamamoto, J.; Kurosaki, T.; Yamashita, D.; Kinjo, M., Relationship Between Homodimeric Glucocorticoid Receptor and Transcriptional Regulation Assessed via an In Vitro Fluorescence Correlation Spectroscopy-Microwell System. Sci Rep 2018, 8 (1), 7488.

17. Zhao, Z. W.; White, M. D.; Alvarez, Y. D.; Zenker, J.; Bissiere, S.; Plachta, N., Quantifying transcription factor–DNA binding in single cells in vivo with photoactivatable fluorescence correlation spectroscopy. Nature Protocols 2017, 12 (7), 1458-1471.

18. Vukojević, V.; Papadopoulos, D. K.; Terenius, L.; Gehring, W. J.; Rigler, R., Quantitative study of synthetic Hox transcription factor-DNA interactions in live cells. Proc Natl Acad Sci U S A 2010, 107 (9), 4093-8.

19. Papadopoulos, D. K.; Skouloudaki, K.; Engstrom, Y.; Terenius, L.; Rigler, R.; Zechner, C.; Vukojević, V.; Tomancak, P., Control of Hox transcription factor concentration and cell-to-cell variability by an auto-regulatory switch. Development 2019, 146 (12).

20. Vukojević, V.; Heidkamp, M.; Ming, Y.; Johansson, B.; Terenius, L.; Rigler, R., Quantitative single-molecule imaging by confocal laser scanning microscopy. Proc Natl Acad Sci U S A 2008, 105 (47), 18176-81.

21. Karedla, N.; Enderlein, J.; Gregor, I.; Chizhik, A. I., Absolute Photoluminescence Quantum Yield Measurement in a Complex Nanoscopic System with Multiple Overlapping States. J Phys Chem Lett 2014, 5 (7), 1198-202.

22. Mercadé-Prieto, R.; Rodriguez-Rivera, L.; Chen, X. D., Fluorescence lifetime of Rhodamine B in aqueous solutions of polysaccharides and proteins as a function of viscosity and temperature. Photochem Photobiol Sci 2017, 16 (11), 1727-1734.

23. Pepperkok, R.; Squire, A.; Geley, S.; Bastiaens, P. I., Simultaneous detection of multiple green fluorescent proteins in live cells by fluorescence lifetime imaging microscopy. Curr Biol 1999, 9 (5), 269-72.

24. Sarkisyan, K. S.; Goryashchenko, A. S.; Lidsky, P. V.; Gorbachev, D. A.; Bozhanova, N. G.; Gorokhovatsky, A. Y.; Pereverzeva, A. R.; Ryumina, A. P.; Zherdeva, V. V.; Savitsky, A. P.; Solntsev, K. M.; Bommarius, A. S.; Sharonov, G. V.; Lindquist, J. R.; Drobizhev, M.; Hughes, T. E.; Rebane, A.; Lukyanov, K. A.; Mishin, A. S., Green fluorescent protein with anionic tryptophan-based chromophore and long fluorescence lifetime. Biophys J 2015, 109 (2), 380-9.

25. Zander, C.; Sauer, M.; Drexhage, K. H.; Ko, D. S.; Schulz, A.; Wolfrum, J.; Brand, L.; Eggeling, C.; Seidel, C. A. M., Detection and characterization of single molecules in aqueous solution. Applied Physics B 1996, 63 (5), 517-523.

26. Urban, N. T.; Foreman, M. R.; Hell, S. W.; Sivan, Y., Nanoparticle-Assisted STED Nanoscopy with Gold Nanospheres. ACS Photonics 2018, 5 (7), 2574-2583.

27. Niehörster, T.; Löschberger, A.; Gregor, I.; Krämer, B.; Rahn, H. J.; Patting, M.; Koberling, F.; Enderlein, J.; Sauer, M., Multi-target spectrally resolved fluorescence lifetime imaging microscopy. Nat Methods 2016, 13 (3), 257-62.

28. Terpetschnig, E.; Jameson, D. M., Fluorescence Lifetime. ISS Technical note Available at http://www.iss.com/resources/pdf/technotes/Fluorescence_Lifetime.pdf 2005.

29. Boens, N.; Qin, W.; Basaric, N.; Hofkens, J.; Ameloot, M.; Pouget, J.; Lefevre, J. P.; Valeur, B.; Gratton, E.; vandeVen, M.; Silva, N. D., Jr.; Engelborghs, Y.; Willaert, K.; Sillen, A.; Rumbles, G.; Phillips, D.; Visser, A. J.; van Hoek, A.; Lakowicz, J. R.; Malak, H.; Gryczynski, I.; Szabo, A. G.; Krajcarski, D. T.; Tamai, N.; Miura, A., Fluorescence lifetime standards for time and frequency domain fluorescence spectroscopy. Anal Chem 2007, 79 (5), 2137-49.

30. Desportes, S.; Yatabe, Z.; Baumlin, S.; Génot, V.; Lefèvre, J.-P.; Ushiki, H.; Delaire, J. A.; Pansu, R. B., Fluorescence lifetime imaging microscopy for in situ observation of the nanocrystallization of rubrene in a microfluidic set-up. Chemical Physics Letters 2007, 446 (1), 212-216.

S17

Functional Fluorescence Microscopy Imaging: Quantitative Scanning-Free Confocal Fluorescence Microscopy for the Characterization of Fast Dynamic Processes in Live Cells

Aleksandar J. Krmpot,◆,‡ Stanko N. Nikolić,◆,‡ Sho Oasa,◆ Dimitrios K. Papadopoulos,§,† Marco Vitali,‖ Makoto Oura,⊥ Shintaro Mikuni,⊥ Per Thyberg,# Simone Tisa,¶ Masataka Kinjo,⊥ Lennart Nilsson,▽ Lars Terenius,◆ Rudolf Rigler,*,◆,○ and Vladana Vukojević*,◆

◆Department of Clinical Neuroscience (CNS), Center for Molecular Medicine (CMM), Karolinska Institutet, Stockholm 17176, Sweden

‡Institute of Physics Belgrade, University of Belgrade, Belgrade 11080, Serbia

§Max-Planck Institute for Molecular Cell Biology and Genetics, Dresden 01307, Germany

‖Sicoya GmbH, Berlin 12489, Germany

⊥Laboratory of Molecular Cell Dynamics, Faculty of Advanced Life Science, Hokkaido University, Sapporo, Hokkaido 001-0021, Japan

#Department of Applied Physics, AlbaNova University Center, Royal Institute of Technology, Stockholm 10691, Sweden

¶Micro Photon Devices (MPD), Bolzano 39100, Italy

▽Department of Biosciences and Nutrition, Karolinska Institutet, Huddinge 14183, Sweden

○Department of Medical Biochemistry and Biophysics (MBB), Karolinska Institutet, Stockholm 17177, Sweden

S *Supporting Information*

ABSTRACT: Functional fluorescence microscopy imaging (fFMI), a time-resolved (21 μs/frame) confocal fluorescence microscopy imaging technique without scanning, is developed for quantitative characterization of fast reaction-transport processes in solution and in live cells. The method is based on massively parallel fluorescence correlation spectroscopy (FCS). Simultaneous excitation of fluorescent molecules in multiple spots in the focal plane is achieved using a diffractive optical element (DOE). Fluorescence from the DOE-generated 1024 illuminated spots is detected in a confocal arrangement by a matching matrix detector comprising 32 × 32 single-photon avalanche photodiodes (SPADs). Software for data acquisition and fast auto- and cross-correlation analysis by parallel signal processing using a graphic processing unit (GPU) allows temporal autocorrelation across all pixels in the image frame in 4 s and cross-correlation between first- and second-order neighbor pixels in 45 s. We present here this quantitative, time-resolved imaging method with single-molecule sensitivity and demonstrate its usefulness for mapping in live cell location-specific differences in the concentration and translational diffusion of molecules in different subcellular compartments. In particular, we show that molecules without a specific biological function, e.g., the enhanced green fluorescent protein (eGFP), exhibit uniform diffusion. In contrast, molecules that perform specialized biological functions and bind specifically to their molecular targets show location-specific differences in their concentration and diffusion, exemplified here for two transcription factor molecules, the glucocorticoid receptor (GR) before and after nuclear translocation and the Sex combs reduced (Scr) transcription factor in the salivary gland of *Drosophila* ex vivo.
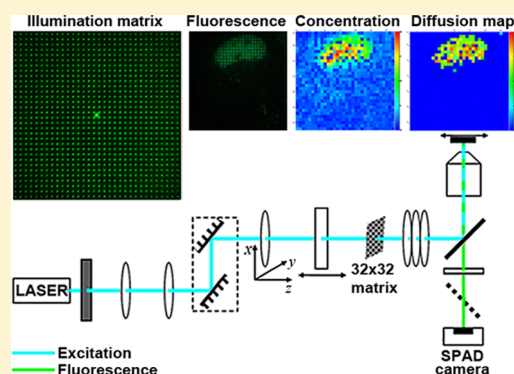
The living cell is a complex dynamic system where local concentrations and spatial distribution of molecules are perpetually changing. Living cells control the concentration and spatial distribution of biological molecules through molecular interactions and transport processes. Through reaction-transport processes, biomolecules are integrated over space and time into dynamical self-regulatory networks and perform complex, life-sustaining functions, such as gene transcription and signal transduction. To understand how these complex biological functions emerge through random motion and molecular collisions, the concentration and mobility of biological molecules need to be quantitatively characterized in live cells.[1,2]

So far, fluorescence microscopy techniques, confocal laser scanning microscopy (CLSM)[3−10] and fluorescence correlation spectroscopy (FCS)[11−16] in particular, have proven to be indispensable for such studies. However, despite their great versatility, CLSM and FCS also have limitations. Most notably, CLSM imaging is not directly quantitative; while fluorescence is inherently quantitative and fluorescence intensity is proportional to the number of molecules, involved calibration experiments are needed to relate the signal intensity measured using a CLSM system to the number of molecules.[17] Moreover, because of the heterogeneous chemical composition inside different subcellular compartments or because of different conditions in different cells (e.g., pH, oxidative stress, crowding), fluorescent molecules are not necessarily in the same local environment. Hence, their brightness may be different.[18] Under such circumstances, the difference in fluorescence intensity need not necessarily reflect differences in molecular numbers but may rather reflect differences in molecular brightness due to local differences in environmental conditions.

In addition, the temporal resolution of CLSM is low. In CLSM, the acquisition at the level of individual pixels is fast, in the order of microseconds, but the acquisition of an image frame is slow, lasting more than a quarter of a second for a 512×512 pixels image. On top of this, the signals in a CLSM image are not acquired at the same point in time, and there is always a time lag between the signals acquired in individual pixels. The temporal resolution of CLSM can be improved by scaling down the number of pixels, i.e., by reducing the area from which the signal is acquired. This, however, results in loss of overview. Classical single-point FCS (spFCS) is also hampered by limited overview, providing quantitative information in a minute observation volume element (OVE) that is typically 0.2−2.0 fl (μm^3). Hence, to acquire quantitative information from several locations in a cell using the conventional spFCS setup, spFCS measurements need to be performed successively, which is not suitable for the study of fast dynamical processes.

To overcome these limitations, specific illumination techniques are used to irradiate a larger area in the sample and the signal is simultaneously recorded from different locations using array detectors. Following the pioneering work at the beginning of this millennium,[19−22] several different experimental realizations of multiplexed FCS have been reported.[23−36] These inventions have significantly advanced our capacity to characterize the spatiotemporal dynamics of complex biological transformations and approach challenging biological problems from the holistic point of view.[24,26,28,33,35,37−45] However, further improvements are needed in order to develop instrumentation with better temporal resolution and with data acquisition and analysis software that are sufficiently robust for reliable routine application in biomedical research.

We present here a setup for quantitative, time-resolved confocal fluorescence microscopy imaging without scanning that is based on massively parallel FCS (mpFCS) measurements, where a diffractive optical element (DOE) and a matching matrix single-photon avalanche photodiode (SPAD) camera are used to achieve massively parallel confocal arrangement.[32,34,38] We show that this approach can map the local concentration and translational diffusion coefficients of molecules in live cells. Since these properties are tightly linked to biomolecular activity at functional sites and are crucial for understanding their mechanisms of action, we call this method functional fluorescence microscopy imaging (fFMI).

■ MATERIALS AND METHODS

fFMI Instrumental Setup. The fFMI system consists of an inverted epi-fluorescence microscope Axio Observer D1 equipped with a C-Apochromat 63×/1.2 W Corr objective and a high efficiency filter set (Filter Set 38 HE) for enhanced green fluorescent protein (eGFP) consisting of an excitation bandpass filter EX BP 470/40 nm (central wavelength/bandwidth), long pass dichroic mirror with a cutoff wavelength of 495 nm, and an emission band pass filter EM BP 525/50 (all from Carl Zeiss, Germany); a continuous wave (CW) 488 nm frequency-doubled diode laser Excelsior 488 (Spectra-Physics, France); a telescopic laser beam expander; a double filter wheel with 10 (5 + 5) uniform neutral density filters of different optical density (OD) to enable a wide range of attenuation (OD 0.2−8.0) in discrete steps (Thorlabs Inc., USA); a diffractive optical element (DOE) specially designed to split the single laser beam into 32×32 beams (Holoeye, Germany); a Single Photon Counting Camera SPC[2] that enables parallel single photon counting by means of a monolithic 32×32 array (Micro Photon Devices MPD, Italy).[32] These elements were assembled on an optical table with active vibration damping (Technical Manufacturing Corporation TMC, USA) using standard opto-mechanical components (Newport Corporation, USA, and Thorlabs Inc., USA). To enable fast sample localization, an 18.0 megapixel digital single-lens reflex (DSLR) camera Canon EOS 600D (Canon Inc., Japan) with a pixel size of 18.5 μm^2 and a pixel pitch of 4.3 μm (http://snapsort.com/compare/Canon-600d-vs-Canon_EOS_550D/specs) was coupled to the side port opposite to the SPAD camera, and the light path between the two camera ports was manually switched.

Raw data, i.e., photon counts, acquired by the SPAD camera were transferred to a Dell Precision Fixed Workstation T5600-Xeon E5-2620 2 GHz equipped with an NVIDIA GeForce GTX 780 graphic card containing 2304 compute unified device architecture (CUDA) cores that were used for fast data analysis by auto- and cross-correlation.

LSM 510 ConfoCor 3 System. An individually modified ConfoCor 3 instrument (Carl Zeiss, Germany) for laser scanning fluorescence microscopy imaging and for spFCS was used as a reference.[46] spFCS data were analyzed using the program for data analysis in the running software package and the scientific graphing and data analysis software Origin (OriginLab).

Software for fFMI. The software for data acquisition and analysis was written in Embaracadero C++ Builder XE7 (Embarcadero Technologies, USA).

■ RESULTS

Instrumental Design. Key elements of the instrumental design, highlighted in Figure 1a and insets a₁−a₃, describe the underlying working principle. Briefly, collimated light from the single-beam CW laser is expanded and led to an achromatic doublet lens (focal length $f = 150$ mm) mounted on a precise $x−y−z$ translation stage (Figure 1a, focusing lens), which focuses the expanded and collimated laser beam on the DOE mounted on a single-axis precise translation stage (Figure 1a, DOE). By filling the aperture of the DOE, the diffraction pattern consisting of 32×32 well-separated illumination spots and the zeroth-order diffraction maximum in the center is formed in the focal plane of the focusing lens that coincides with the image plane of the rear port of the inverted epi-fluorescence microscope (Figure 1a, rear port image plane). Formation of the spot-wise
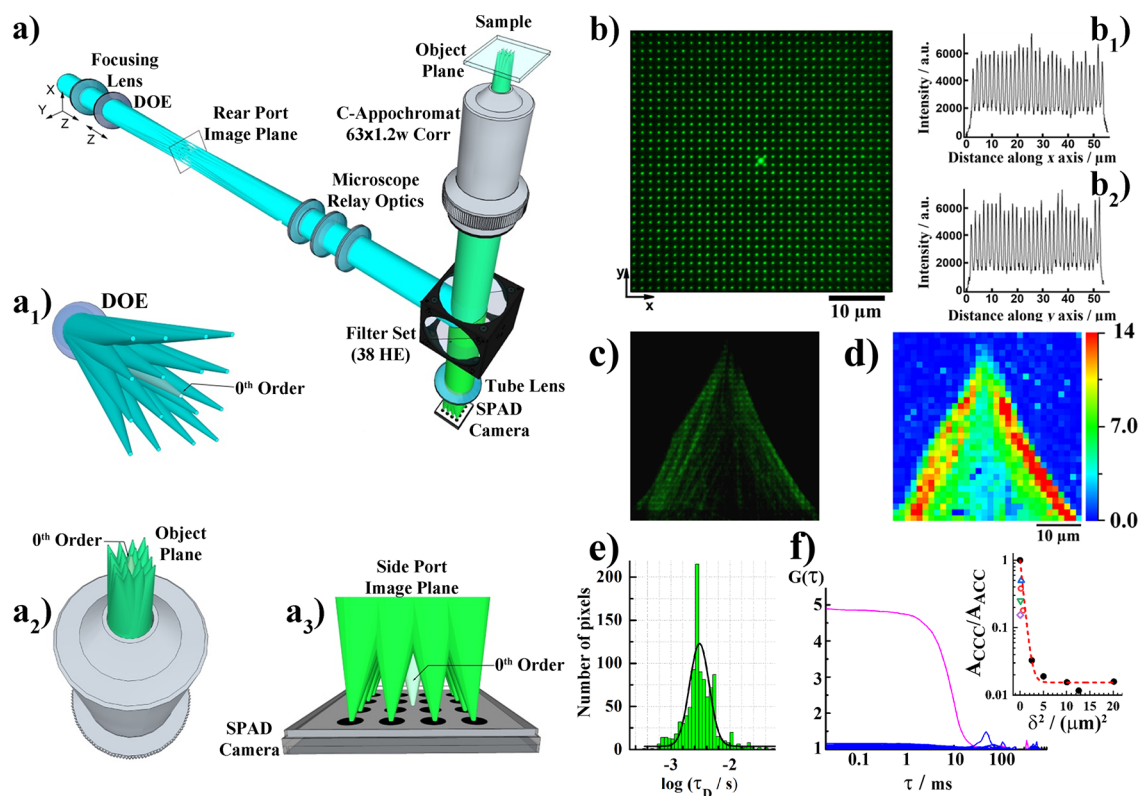
Figure 1. Instrumental setup for functional fluorescence microscopy imaging (fFMI). (a) Schematic presentation of the optical arrangement in the fFMI instrument. The expanded single laser beam is focused by the focusing lens on the diffractive optical element (DOE). The illumination matrix of 32 × 32 laser beam spots (here depicted as a 4 × 4 matrix for simplicity) is formed at the image plane of the rear port of the microscope. Inset: Formation of the ordered spotty pattern at three characteristic planes: (a$_1$) in the rear port image plane, (a$_2$) in the object plane, and (a$_3$) in the side port image plane. Of note, the zeroth-order diffraction peak falls exactly between 4 central pixels of the SPAD camera when the fFMI system is fully aligned and is therefore not detected by the SPAD camera. (b) Image of the illumination matrix generated in the focal plane of the microscope objective. A thin layer formed by drying of a concentrated Rhodamine 6G (Rh6G) solution was used as the sample, and the image was acquired by the 18.0 megapixel digital single-lens reflex (DSLR) camera. The zeroth-order diffraction peak is readily visible when using the pixel-dense DSLR camera. Inset: Fluorescence intensity profiles along (b$_1$) the x-axis and (b$_2$) the y-axis show that the sample is illuminated in a distinct pattern of 32 × 32 spots. The pitch (the shortest distance between two adjacent spots) of the illumination matrix in the sample plane is 1.587 μm. (c) Image of filamentous actin in fixed muntjac skin fibroblast cells acquired under spot-wise illumination using the 18.0 megapixel DSLR camera. (d) Image of the sample described in (c) acquired by the SPAD camera. Signal acquisition time = 1 ms. Fluorescence intensities ranged from 0 (dark blue) to ≥13 700 photons per second (red). The scale bar is 10 μm. (e) Distribution of diffusion times in a dilute aqueous suspension of fluospheres, d = 100 nm, recorded by the fFMI system. The average diffusion time was determined to be τ_D = (3 ± 2) ms. (f) ACC recorded in an individual pixel, i.e., by an individual SPAD in the SPAD matrix detector (magenta). Cross-correlation curves (CCCs) derived by cross-correlating the signals recorded in this particular SPAD and its first- and second-order neighbors (blue). Inset: (f$_1$) Amplitude of the CCCs (blue) normalized to the amplitude of the ACC (magenta), A_{CCC}/A_{ACC}, as a function of the squared distance between neighboring OVEs (δ). As expected, the amplitudes of the CCCs decay exponentially with the distance between neighboring OVEs squared,[47] and the data from this study (black dots) agree well with results reported in the literature: Buchholz, PhD Thesis (CCC1 and CCC2, Figure 6.4; red circles),[48] Dertinger et al. (Figure 6; blue triangle),[47] Ries and Schwille (Figure 4; green inverted triangle),[49] and Ries et al. (Figure 2d; lilac diamond).[50] The relative amplitude A_{CCC}/A_{ACC} = 1 at OVE distance δ = 0 corresponds to cross-correlation of fluorescence intensity fluctuations in the reference pixel to itself. The fitted single-exponential decay curve (red, dashed) shows that the amplitude of the CCC decays exponentially with δ^2.[47]

illumination pattern is schematically depicted in Figure 1, inset a$_1$, featuring for the sake of clarity an array of 4 × 4 spots with the clearly indicated zeroth-order diffraction maximum. The relay optics of the rear port of the microscope (Figure 1a, microscope relay optics), the dichroic mirror (integrated in the Filter Set 38 HE), and the objective lens project the illumination matrix from the rear port into the focal plane of the objective (Figure 1a, object plane; Figure 1, inset a$_2$). A uniform thin layer of dried Rh6G was used to visualize the illumination matrix. The image acquired using the pixel-dense DSLR camera shows that the sample is illuminated in a distinct spot-wise array of 32 × 32 well-separated points of similar intensity, except for the zeroth-order diffraction spot visible in the center (Figure 1b). Corresponding fluorescence intensity distribution profiles

along the x and y axes are shown in Figure 1, insets b$_1$ and b$_2$, respectively.

After passing through the dichroic mirror and the emission filter integrated in the Filter Set 38 HE, the spot-wise fluorescence matrix is imaged by the objective and the tube lenses onto the SPAD camera (Figure 1a and inset a$_3$). The SPAD camera is attached to one of the two side ports of the microscope, with the DSLR camera being attached to the other side and used for fast sample localization using standard wide-field imaging. The SPAD camera contains a photosensitive chip and a 16-bit photon counter based on a field programmable gate array (FPGA). The photosensitive area of the chip consists of 32 × 32 circular SPADs that are 20 μm in diameter. The distance between adjacent diodes along a row/column, i.e., the pitch of
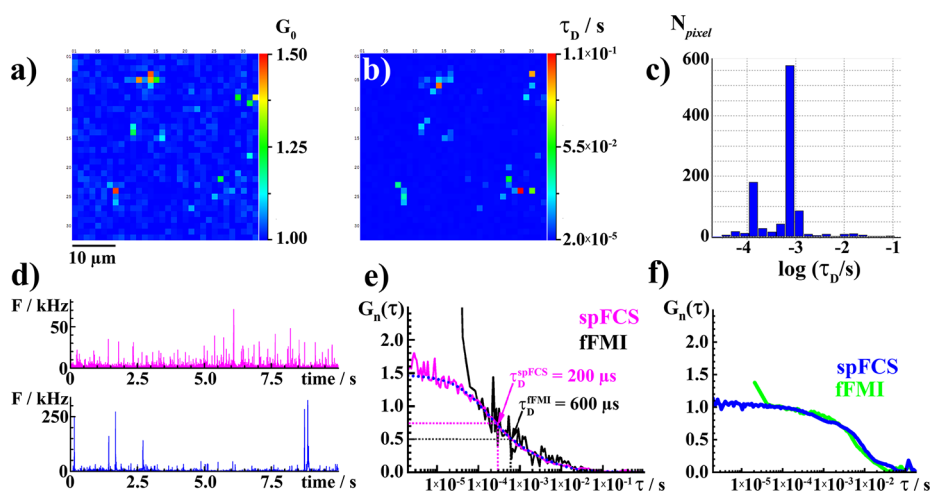
Figure 2. fFMI instrument calibration and performance characterization using a dilute aqueous suspension of quantum dots. (a) Spatial map of amplitudes (G_0) of individual ACCs at the lag time $\tau = 103.7$ μs, acquired by fFMI. Fluorescence intensity fluctuations were recorded in a single measurement lasting 2.7 s. (b) Corresponding spatial map of translational diffusion times (τ_D). (c) Diffusion time distribution histogram corresponding to the data shown in (b). (d) Fluorescence intensity fluctuations recorded in the same sample as in (a−c) acquired using a conventional spFCS system. Fluorescence intensity bursts of different intensities (note the different scales on the ordinates) reveal that the dilute quantum dot suspension is polydisperse, containing single quantum dots (magenta) and a significantly lower amount of very bright quantum dot agglomerates that were sporadically observed (blue trace). (e) ACCs normalized to the same amplitude, $G_n(\tau) = 1$ at lag time $\tau = 103.7$ μs, obtained by temporal autocorrelation analysis of fluorescence intensity fluctuations reflecting diffusion of single quantum dots. The ACCs were acquired by fFMI (black) and spFCS (magenta). The black ACC is an average ACC acquired from 10 consecutive fFMI recordings of fluorescence intensity fluctuations in a single SPAD, i.e., in a single OVE/single pixel, each measurement lasting 2.7 s. The magenta ACC is acquired from the fluorescence intensity fluctuation time series of 10 s. The dotted blue line shows fitting of the magenta ACC. (f) ACCs normalized to the same amplitude, $G_n(\tau) = 1$ at lag time $\tau = 103.7$ μs, reflecting diffusion of sparse quantum dot agglomerates, acquired by fFMI in a single pixel and in a 2.7 s measurement (blue) and by spFCS (green).

the camera, is 100 μm. Further details on the SPAD camera design and performance can be found in refs 32 and 51−53. Since the aperture of every SPAD is a pinhole positioned in the conjugate focal plane with respect to the illumination matrix, confocal configuration is achieved for all 32 × 32 foci.

By imaging the complex spatial distribution of filamentous actin in fixed muntjac skin fibroblast cells, we could verify that there is no significant loss of information due to interspaced sampling (Figure 1c,d). Images acquired by the pixel-dense DSLR camera (Figure 1c) and the SPAD camera (Figure 1d) clearly show that the SPAD camera veritably reflects the spatial distribution of actin filaments over long distances.

In a well-aligned fFMI system, similar values for the translational diffusion time are obtained in the majority of pixels, and the distribution of diffusion times across the whole matrix is narrow, exemplified here for a measurement performed in a dilute aqueous suspension of 100 nm fluospheres (Figure 1e). The measured diffusion time, $\tau_D = (3 \pm 2)$ ms (Figure 1e), is in good agreement with the value obtained using the reference spFCS system, $\tau_D = (2.5 \pm 0.5)$ ms (see fFMI Instrument Calibration and Performance Characterization for details on instrument calibration).

Finally, cross-correlation of signals recorded in a reference pixel with the signal recorded in its first- and second-order neighbors showed that there is virtually no cross-talk between neighboring SPADs, as is evident from the relatively small amplitude of the CCCs (Figure 1f, blue) that is less than 4% of the amplitude of the ACC (Figure 1f, magenta). The Supporting Information contains details of the software for data analysis, the calculation of auto- and cross-correlation curves, and image rendering (Section S1), cell culture (Section S2), instrument alignment (Section S3, Figure S1), OVE size determination

(Section S4, Figure S2), and accuracy, precision, and sensitivity (Section S5, Figure S3).

fFMI Instrument Calibration and Performance Characterization. A dilute aqueous suspension of carboxylate functionalized quantum dots (2 nM) was used to compare the fFMI instrument performance with respect to the conventional spFCS system used as a reference. For this purpose, fFMI and conventional spFCS measurements were performed on the same sample (Figure 2a−f). To have similar conditions in both experiments, the illumination intensity in the conventional spFCS instrument was set to 14.8 μW at the microscope objective lens, in order to match the intensity in individual foci of the fFMI instrument, which was estimated to be 1/1024 of the intensity measured at the microscope objective (18.9 mW) reduced by 20% to account for the intensity of the zeroth-order diffraction peak.

Both fFMI and spFCS revealed that, despite prolonged sonication, the quantum dots suspension is polydisperse, being made up of individual quantum dots present in large excess (Figure 2a,b (blue pixels), Figure 2d (top), and corresponding ACCs in Figure 2e) but also containing a small amount of very bright quantum dot agglomerates of different sizes (Figure 2a,b (green-red pixels), Figure 2d (bottom), and corresponding ACCs in Figure 2f). In measurements using the conventional spFCS instrument, the presence of sparse agglomerates could be readily revealed in some but not all recordings (Figure 2d, the magenta time series exemplifies a measurement where quantum dot agglomerates were not observed), whereas fFMI revealed in a single shot that the quantum dot suspension is polydisperse and provided the spatial localization of agglomerates at the moment of measurement, as is evident from the map of ACC amplitudes, G_0, (Figure 2a, green-red pixels), the translational
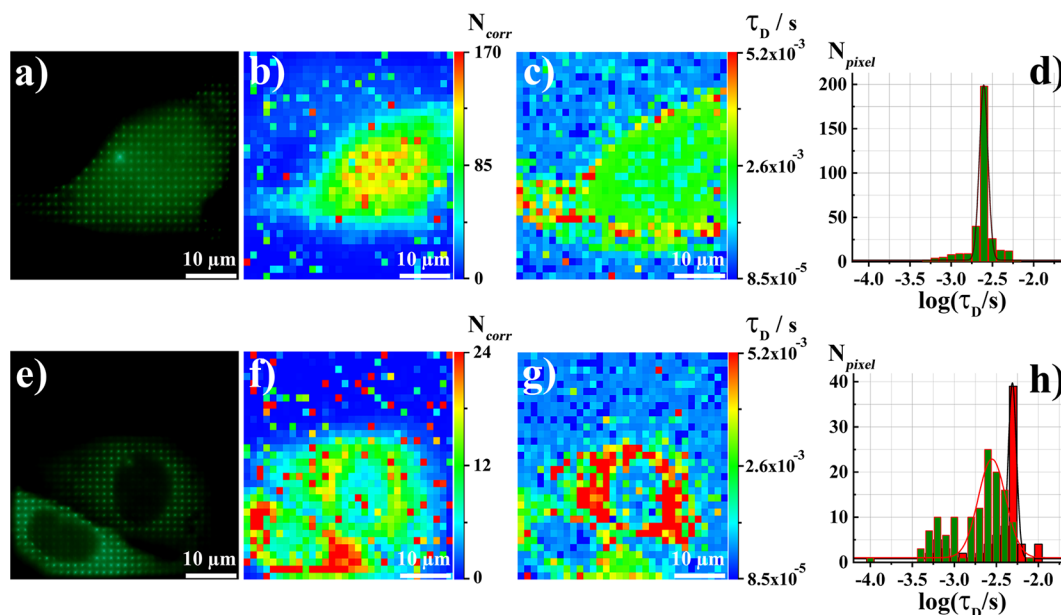
Figure 3. Spatial distribution of molecular numbers and diffusion time maps in live U-2 OS cells expressing monomeric or tetrameric eGFP. (a) 18.0 megapixel DSLR image of a spot-wise illuminated U-2 OS cell expressing monomeric eGFP. (b) Spatial distribution of molecular numbers (N_{corr}) across an optical section in the cell, with slight eGFP accumulation in the nucleus. (c) eGFP diffusion times (τ_D) across the same section as in (b). (d) The corresponding τ_D distribution histogram shows that eGFP mobility inside the cell is rather uniform, $\tau_D = (2.5 \pm 0.5)$ ms. (e) DSLR image of two cells expressing eGFP$_4$, acquired as described in (a). (f) Molecular numbers (N_{corr}) map reveals eGFP$_4$ prevalence in the cytoplasm. (g) eGFP$_4$ diffusion time map in two adjacent cells. In the upper cell, the average diffusion time, $\tau_D = (5.0 \pm 0.8)$ ms, is two times longer than the diffusion time measured for eGFP in (d). This is in agreement, within the experimental error, with the expected theoretical difference of 1.6 times. In the lower cell, where eGFP$_4$ degradation was observed, the average nuclear concentration was higher than in the upper cell, $N_{corr}^{lcell} \approx 12$ versus $N_{corr}^{lcell} \approx 6$; τ_D was the same as in cells expressing monomeric eGFP, and a wider distribution of diffusion times ((h), green histogram, versus (d)) was observed. (h) Diffusion time distribution histograms in the upper (red) and the lower (green) cell shown in (g).

diffusion time, τ_D, map (Figure 2b, green-red pixels), and the distribution of diffusion times (Figure 2c).

Both, the conventional spFCS and the fFMI system, showed marked differences in diffusion times between single quantum dots, $\tau_{D,sqd}^{spFCS} = (200 \pm 50)$ μs (Figure 2e), and quantum dot agglomerates, $\tau_{D,qda}^{spFCS} = (7 \pm 2)$ ms (Figure 2f). Importantly, the characteristic decay times of ACC obtained using the fFMI instrument and the conventional spFCS setup concurred, as is evident from the overlap of the ACCs normalized to the same amplitude, $G_n(\tau) = 1$ at $\tau = 103.7$ μs, for individual quantum dots (Figure 2e) and for quantum dot agglomerates (Figure 2f). This observation is in line with calibration measurements showing that the OVEs in the fFMI system are similar in size to that in the conventional spFCS instrument.

Of note, the average diffusion time for single quantum dots estimated from the diffusion time histogram, $\tau_{D,sqd}^{hist} = (600 \pm 100)$ μs (Figure 2c), is evidently longer than the value determined by fitting spFCS data, $\tau_{D,sqd}^{spFCS} = (200 \pm 50)$ μs (Figure 2e, magenta). This discrepancy, which is particularly pronounced for molecules/particles with short diffusion times, arises because of the comparatively low temporal resolution of the matrix SPAD detector, due to which plateauing of the ACC cannot be observed (Figure 2e). Consequently, the translational diffusion time, estimated from the full width of the ACC at its half-maximum (Figure 2e, black), will appear to be somewhat longer than what it really is (Figure 2e, magenta). Using fluospheres of different size, we could demonstrate that, the longer the translational diffusion time, the less pronounced will be this difference, and the diffusion coefficient could be correctly determined (as shown in Section S5, Figure S2).

Small Differences in Translational Diffusion Time between eGFP Monomers and Tetramers Could Be Measured in Live Cells by fFMI. In order to assess the precision of the fFMI system, its capacity to measure small differences in translational diffusion time was probed using live U-2 OS cells expressing monomeric or tetrameric eGFP, eGFP, or eGFP$_4$, respectively (Figure 3).

fFMI could also measure subtle differences in the translational diffusion between eGFP (Figure 3c,d) and eGFP$_4$ (Figure 3g,h, red pixels and bars). It showed that translational diffusion of eGFP monomers in U-2 OS cells is rather uniform across the cell, with an average diffusion time $\tau_{D,eGFP} = (2.5 \pm 0.5)$ ms (Figure 3c,d), whereas the translational diffusion time of eGFP$_4$ is about two times longer, $\tau_{D,eGFP4} = (5.0 \pm 0.8)$ ms (Figure 3g, upper cell; Figure 3h, red histogram). This difference, derived from measurements in 10 cells in each group, is in agreement with the theoretically expected value of 1.6 times.

fFMI also indicated cells where oligomeric forms containing less than four eGFP molecules prevail. Such cells (Figure 3g, lower cell) are identifiable through the shorter translational diffusion time (Figure 3h, green histogram (lower cell) versus the red histogram (upper cell)), higher average nuclear concentration of fluorescent molecules, $N_{corr}^{lcell} \approx 12$ versus $N_{corr}^{ucell} \approx 6$ (Figure 3f), and wider distribution of diffusion times (Figure 3h, green histogram, versus Figure 3d). Lower size oligomers can occur due to degradation processes. While eGFP is not efficiently degraded by proteinases, the flexible linker is, due to the specific construction of the plasmid where each eGFP sequence is preceded by an ATG start codon.

Mapping the Heterogeneous Distribution and Dynamics of Molecules in Live Cells by fFMI. Having
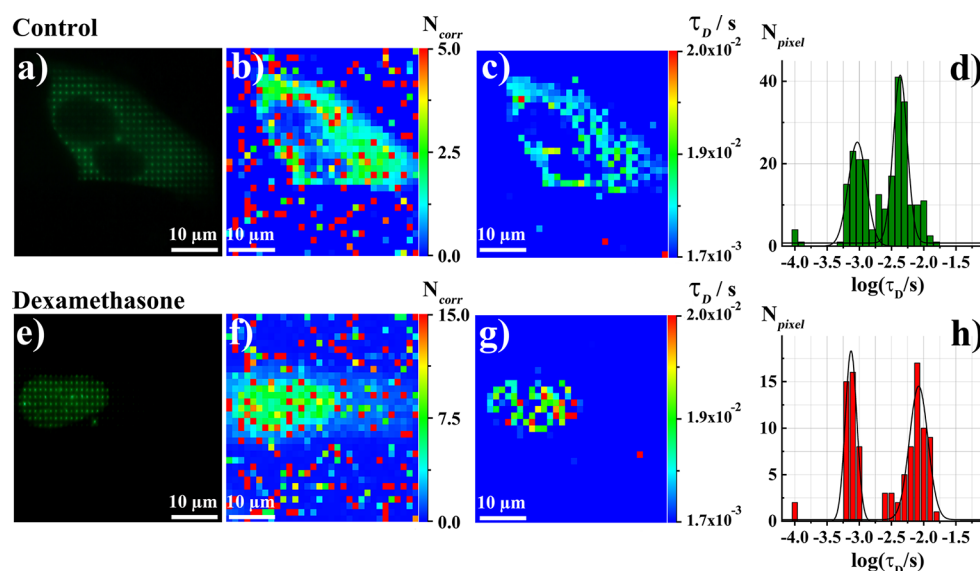
Figure 4. Spatial distribution of molecular numbers and diffusion time maps of glucocorticoid receptors (GR) before and upon ligand-induced nuclear translocation in live U-2 OS cells. (a) DSLR image of a spot-wise illuminated unstimulated U-2 OS cell expressing eGFP-GR$_{wt}$. (b) fFMI reveals the spatial distribution of eGFP-GR$_{wt}$ numbers (N_{corr}) across an optical section in the cell with their accumulation in the cytoplasm. (c) Spatial distribution of translational diffusion times (τ_D) across the same section as in (b). (d) Diffusion time distribution histogram in the cytoplasm of cells shown in (c). (e) DSLR image showing eGFP-GR$_{wt}$ translocation to the cell nucleus after stimulation with dexamethasone. (f) Spatial distribution of molecular numbers (N_{corr}) reveals eGFP-GR$_{wt}$ translocation from the cytoplasm to the cell nucleus. (g) fFMI map of eGFP-GR$_{wt}$ diffusion times (τ_D), reflecting a patchy distribution due to differences in eGFP-GR$_{wt}$ interactions with the surrounding molecules. (h) Diffusion time distribution histogram in the cell nucleus shown in (g).

established that fFMI can measure small differences in translational diffusion between cells that express uniformly diffusing molecules of different size, we assessed its capacity to map the heterogeneous distribution and nonuniform dynamic behavior of a molecule in the same cell (Figure 4). We have therefore chosen the glucocorticoid receptor (GR), a transcription factor for which the heterogeneous distribution and complex intracellular dynamics are well established and characterized by conventional spFCS.[54−56]

fFMI readily revealed the nonuniform distribution and uneven diffusion of fluorescently tagged wild type glucocorticoid receptors (eGFP-GR$_{wt}$) in the cytoplasm of untreated U-2 OS cells (Figure 4a−d), showing that eGFP-GR$_{wt}$ concentration in the periphery is lower, $N_{avg}^{pnr} \approx 1.25$, and its diffusion time is shorter, $\tau_D^{per} = \approx (0.8 \pm 0.2)$ ms, than in the perinuclear region that is enriched in intracellular membranes, $N_{avg}^{pnr} \approx 2.5$ and $\tau_D^{pnr} = (4.0 \pm 0.5)$ ms.

As expected, treatment of U-2 OS cells with the GR agonist dexamethasone (100 nM Dex) induced eGFP-GR$_{wt}$ translocation from the cytoplasm to the cell nucleus (Figure 4). In the nucleus (Figure 4e−h), eGFP-GR$_{wt}$ partitioned into different domains, showing both an uneven distribution of molecular numbers (Figure 4f) and "patchy" diffusion behavior (Figure 4g), revealing domains where eGFP-GR$_{wt}$ motility is fast and interactions with other molecules are scarce and/or nonspecific, characterized by short diffusion times, as opposed to regions where binding with higher affinities is observed; eGFP-GR$_{wt}$ motion is therefore stalled, and diffusion times are longer.

Mapping Dynamic Processes in the Plasma Membrane of Live Cells by fFMI. The capacity of the fFMI system was tested for quantitative characterization of dynamic processes in the plasma membrane. For this purpose, PC12 cells stably transformed to express a G protein-coupled receptor (GPCR), the wild type μ-opioid receptor fused at the N-terminal end with eGFP (eGFP-MOP), were used to map in live cells its spatial

surface density and lateral diffusion in the plasma membrane (Figure 5). As can be seen, the plasma membrane and the perinuclear region, enriched with membranous structures of the endoplasmic reticulum and the Golgi complex, could be easily distinguished from the remaining cellular compartments and the surroundings by fluorescence intensity imaging using the DSLR camera under spot-wise illumination (Figure 5a). While the map of the average number of molecules in the OVE (N_{corr}) was noisy due to low expression levels of eGFP-MOP (Figure 5b), the translational diffusion time maps could be readily acquired, rendering the plasma membrane and the membranous structures in the perinuclear region clearly visible (Figure 5c). fFMI revealed that the eGFP-MOP diffusion in the plasma membrane (Figure 5 d, red) and in membranous structures in the perinuclear region (Figure 5d, blue) is complex, and two principal decay times were identified: $\tau_{D1} = (1.0 \pm 0.5)$ ms and $\tau_{D2} = (100 \pm 20)$ ms (Figure 5d).

Mapping ex Vivo the Heterogeneous Distribution and Dynamics of Molecules in Thick Tissue Specimen by fFMI. While we have established that crosstalk between pixels is not an issue for quantitative characterization of concentration and diffusion in dilute solutions/suspensions (Figure 1f), it is well-known that the main challenge for quantitative fluorescence microscopy imaging of a thick specimen using multifocal optical arrangement arises because out-of-focus light that originates from bright structures in remote focal planes above/below the sample plane can pass through adjacent pinholes. This increases the background signal, i.e., reduces the SNR, and gives rise to hazy images where the details that are normally observed in confocal laser scanning microscopy are obscured in spinning disk confocal microscopy.[57] In order to probe the capacity of the fFMI system to characterize dynamical processes in thick samples, the concentration and nuclear dynamics of the mCitrine-tagged Sex combs reduced (Scr) dimeric transcription factor (mCitrine-(Scr)$_2$) were investigated in salivary glands
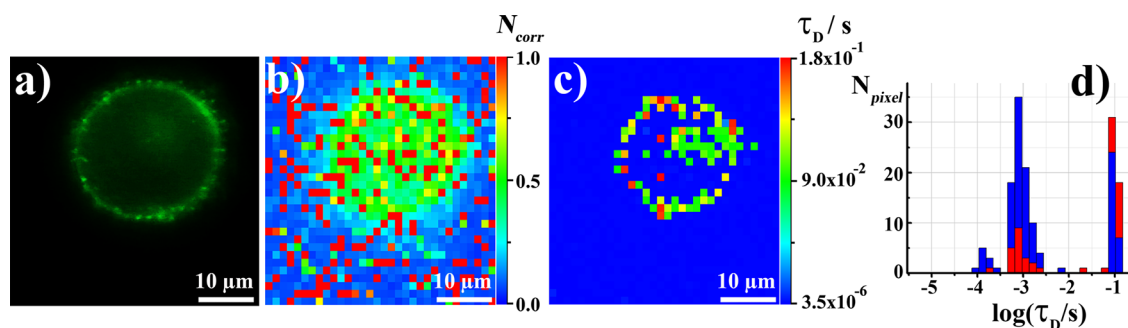
Figure 5. Dynamic lateral organization of mu-opioid receptor in the plasma membrane. (a) DSLR image of a spot-wise illuminated PC12 cell expressing eGFP-MOP. (b) Spatial distribution of eGFP-MOP numbers (N_{corr}) across an optical section in the cell. (c) Spatial distribution of diffusion times (τ_D) across the same section as in (b). (d) Corresponding diffusion time distribution histograms inside the cell (blue) and in the plasma membrane (red).

from *Drosophila* third instar larvae bearing in the genome a multimeric specific binding site of Scr ($fkh250^{con}$; see Section S2 and ref 38 for details). The results are presented in Section S6 and Figure S4.

■ DISCUSSION

Spatial filtering of fluorescence, which is at the heart of CLSM, is achieved by conjugate focal plane arrangement of optical elements and obstruction of out-of-focus light by detection through a pinhole. This significantly improves the SNR of fluorescence microscopy, enabling optical sectioning and fluorescence imaging with high spatiotemporal resolution and single-molecule sensitivity. Advantages for biomedical research and diagnostics brought about by confocal imaging are so numerous that it has been stated that "...confocal technology is proving to be one of the most important advances ever achieved in optical microscopy."[58] Confocal configuration was also shown to be critical for FCS;[59,60] by reducing the size of the OVE, a significantly smaller number of solvent molecules was observed, which efficiently reduced the background and enhanced the signal-to-noise ratio. This, in turn, has enabled single-molecule detection and short measurement time. The possibility to have multiplexed confocal arrangements of excitation and detection pathways is therefore essential for quantitative studies of fast dynamic processes in live cells that require high spatiotemporal resolution and single-molecule sensitivity.

Presently available state-of-the-art instruments for massively parallel FCS measurements, such as the systems described in refs 29 and 31, rely on the use of light sheet illumination and point-wise detection via an electron multiplying charge coupled device (EMCCD) camera[29] or a SPAD matrix detector.[31,36] In these arrangements, a selected plane in the sample is illuminated at a defined *z*-position by a micrometer-thin light sheet that is perpendicular to the optical axis of the detection objective lens. The advantage of light sheet illumination over a confocal arrangement comes from the specific illumination of an area that is significantly larger than the cross sectional area of the confocal volume element. The disadvantage of light sheet illumination as compared to multiplexed confocal arrangement comes from the nonuniformity of the light sheet over longer distances, which means that the area over which OVEs of the same size are obtained is restricted. In addition, structures in the specimen that absorb/scatter the excitation light distort the light sheet, and the size of the OVEs is not uniform across heterogeneous samples.[29,31] To circumvent these problems in light sheet based microscopy imaging, the sample needs to be repositioned and

precisely rotated, which is a limiting factor for the study of fast dynamical processes. It also complicates sample preparation and mounting, and sample preparation procedures are considerably more complex for light sheet microscopy than for confocal imaging.[61] Such restrictions do not exist for fFMI. Here, the limit in number of focal spots is set by the intensity of the single-beam laser and the dark count of individual SPADs that comprise the matrix detector.

The advantage of the SPAD matrix detectors over EMCCD cameras primarily lies in the temporal resolution, which is inherently low in EMCCD cameras because of the slow readout and frame-transfer processes. At present, the temporal resolution of EMCCDs is in the millisecond range, at best, whereas the temporal resolution of SPADs is easily in the microsecond and even submicrosecond range. Thus, SPAD matrices hold the promise to significantly improve the temporal resolution of fluorescence microscopy imaging, allowing a 100- to 1000-times better temporal resolution. Furthermore, no analogue measurement of voltage or current is needed for SPADs, so no additional noise is added by the readout process. Finally, the SPAD detector is typically less sensitive than EMCCD to electromagnetic interference due to electromagnetic radiation generated by other equipment.

The disadvantage of SPAD matrix detectors over an EMCCD stems mainly from the variability in dark count rates between individual detectors, which gives a nonuniform SNR over an image frame (Figure 1f). This, however, is not too big a problem for fFMI; while differences in dark count rates affect the signal intensity, the outcome of temporal autocorrelation analysis is not significantly affected and the average number of molecules in the OVE and the diffusion time could still be accurately determined by autocorrelation analysis even though the SNR is not exactly the same in all foci. Of course, this is only possible when the SNR is sufficiently high in all foci. If this is not the case, the amplitude of the autocorrelation curve becomes unreliable.

Another well-known limitation associated with SPADs is related to afterpulsing.[32,62,63] In the present camera, afterpulsing is observed in the ACCs as a prominent and fast-decaying peak at lag times, $\tau < 100 \, \mu s$ (Figure 2e, black; Figure 2f, green; Section S6, Figure S4g, blue). Afterpulsing is more prominently observed in measurements where low signal intensities were measured, e.g., individual quantum dots (Figure 2e, black) versus bright quantum dot agglomerates (Figure 2f, green). However, afterpulsing-related distortion of ACCs may be circumvented by cross-correlating the signals between two detectors,[32,62] by subtracting the contribution of afterpulsing from the ACCs,[63] and by SPAD design.[64]

Despite the limitations of currently available technologies for massive production of SPADs, which restrain the temporal resolution and affect quantitative characterization in live cells as discussed above, the data presented here compellingly show that it is possible to achieve a massively parallel confocal arrangement and quantitative confocal imaging with single-molecule sensitivity without scanning via massively parallel FCS. This yields quantitative confocal imaging with an unprecedented temporal resolution, which in the present setup is 21 μs/frame. We have demonstrated that massively parallel analysis of fluorescence intensity fluctuations by temporal autocorrelation and spatiotemporal cross-correlation analyses can be achieved, yielding 1024 ACCs in about 4 s and about 24 000 CCCs in 45 s. The use of the graphic processing unit (GPU) is a major advantage for the calculation of CCCs, since the number of CCCs is much larger than the number of ACCs. The FPGA approach described in ref 30 calculates ACCs in real time, but the memory constraints would not allow the calculation of CCCs as well. Hence, a combination of these two approaches will likely be the best for future applications.

CONCLUDING REMARKS

The quantitative, time-resolved confocal fluorescence microscopy imaging approach developed here retains the capacity to perform optical sectioning and is empowered by the abolishment of scanning, thus allowing simultaneous data acquisition in all points in an image frame with a submillisecond temporal resolution (here 21 μs/frame). It provides, with diffraction limited spatial resolution, quantitative information about location-specific differences in the concentration and mobility of the molecules, which cannot be otherwise deduced. The possibility to characterize the fast cellular dynamics of molecules: quantitatively, nondestructively, with the ultimate sensitivity and with unprecedented temporal resolution, enables us to address how biomolecules are integrated via chemical reactions and transport processes into dynamical self-regulated networks through which emergent properties, such as gene transcription and signal transduction, arise at the higher level of organization and at longer spatio-temporal scales.

ASSOCIATED CONTENT

ⓢ Supporting Information

The Supporting Information is available free of charge on the ACS Publications website at DOI: 10.1021/acs.analchem.9b01813.

> Details of software for data analysis and calculation of auto- and cross-correlation curves, image rendering, cell culture, and instrument alignment along with imaging in a thick tissue specimen (PDF)

AUTHOR INFORMATION

Corresponding Authors

*E-mail: Vladana.Vukojevic@ki.se.

*E-mail: Rudolf.Rigler@ki.se.

ORCID ⓞ

Aleksandar J. Krmpot: 0000-0003-2751-7395

Sho Oasa: 0000-0003-3800-590X

Dimitrios K. Papadopoulos: 0000-0003-0914-3051

Lennart Nilsson: 0000-0002-5067-6397

Lars Terenius: 0000-0003-2880-9576

Rudolf Rigler: 0000-0003-4742-0857

Vladana Vukojević: 0000-0003-0873-5653

Present Address

[†]D.K.P.: MRC Human Genetics Unit, Institute of Genetics and Molecular Medicine, University of Edinburgh, Edinburgh EH4 2XU, UK.

Author Contributions

The manuscript was written through contributions of all authors. All authors have given approval to the final version of the manuscript.

Notes

The funding agencies had no influence on the study design, methods, data collection, analyses, or the manuscript writing. The authors declare no competing financial interest.

ACKNOWLEDGMENTS

REFERENCES

(1) Qian, H. *J. Stat. Phys.* **2010**, *141* (6), 990−1013.

(2) Qian, H.; Ge, H. *Mol. Cell. Biomech.* **2012**, *9* (1), 1−30.

(3) Claridge, S. A.; Schwartz, J. J.; Weiss, P. S. *ACS Nano* **2011**, *5* (2), 693−729.

(4) Diekmann, S.; Hoischen, C. *Physics of life reviews* **2014**, *11* (1), 1−30.

(5) Lock, J. G.; Stromblad, S. *Exp. Cell Res.* **2010**, *316* (8), 1438−44.

(6) Mavrakis, M.; Pourquie, O.; Lecuit, T. *Development* **2010**, *137* (3), 373−87.

(7) Owen, D. M.; Williamson, D.; Rentero, C.; Gaus, K. *Traffic* **2009**, *10* (8), 962−71.

(8) Petibois, C. *Anal. Bioanal. Chem.* **2010**, *397* (6), 2051−65.

(9) Requejo-Isidro, J. *Journal of chemical biology* **2013**, *6* (3), 97−120.

(10) Weigert, R.; Porat-Shliom, N.; Amornphimoltham, P. *J. Cell Biol.* **2013**, *201* (7), 969−79.

(11) Ries, J.; Schwille, P. *BioEssays* **2012**, *34* (5), 361−8.

(12) Elson, E. L. *Biophys. J.* **2011**, *101* (12), 2855−70.

(13) Fitzpatrick, J. A.; Lillemeier, B. F. *Curr. Opin. Struct. Biol.* **2011**, *21* (5), 650−60.

(14) Digman, M. A.; Gratton, E. *Annu. Rev. Phys. Chem.* **2011**, *62*, 645−68.

(15) Tian, Y.; Martinez, M. M.; Pappas, D. *Appl. Spectrosc.* **2011**, *65* (4), 115A−124A.

(16) Elson, E. L. *Methods* **2018**, *140−141*, 3−9.

(17) Kedziora, K. M.; Prehn, J. H.; Dobrucki, J.; Bernas, T. *J. Microsc.* **2011**, *244* (1), 101−11.

(18) Morikawa, T. J.; Fujita, H.; Kitamura, A.; Horio, T.; Yamamoto, J.; Kinjo, M.; Sasaki, A.; Machiyama, H.; Yoshizawa, K.; Ichimura, T.; Imada, K.; Nagai, T.; Watanabe, T. M. *Sci. Rep.* **2016**, *6*, 22342.

(19) Blom, H.; Johansson, M.; Hedman, A. S.; Lundberg, L.; Hanning, A.; Hard, S.; Rigler, R. *Appl. Opt.* **2002**, *41* (16), 3336−42.

(20) Blom, H.; Johansson, M.; Gosch, M.; Sigmundsson, T.; Holm, J.; Hard, S.; Rigler, R. *Appl. Opt.* **2002**, *41* (31), 6614−20.

(21) Gosch, M.; Serov, A.; Anhut, T.; Lasser, T.; Rochas, A.; Besse, P. A.; Popovic, R. S.; Blom, H.; Rigler, R. *J. Biomed. Opt.* **2004**, *9* (5), 913−21.

(22) Gosch, M.; Blom, H.; Anderegg, S.; Korn, K.; Thyberg, P.; Wells, M.; Lasser, T.; Rigler, R.; Magnusson, A.; Hard, S. *J. Biomed. Opt.* **2005**, *10* (5), 054008.

(23) Michalet, X.; Colyer, R. A.; Antelman, J.; Siegmund, O. H.; Tremsin, A.; Vallerga, J. V.; Weiss, S. *Curr. Pharm. Biotechnol.* **2009**, *10* (5), 543−58.

(24) Needleman, D. J.; Xu, Y.; Mitchison, T. J. *Biophys. J.* **2009**, *96* (12), 5050−9.

(25) Colyer, R. A.; Scalia, G.; Rech, I.; Gulinatti, A.; Ghioni, M.; Cova, S.; Weiss, S.; Michalet, X. *Biomed. Opt. Express* **2010**, *1* (5), 1408−1431.

(26) Capoulade, J.; Wachsmuth, M.; Hufnagel, L.; Knop, M. *Nat. Biotechnol.* **2011**, *29* (9), 835−9.

(27) Colyer, R. A.; Scalia, G.; Villa, F. A.; Guerrieri, F.; Tisa, S.; Zappa, F.; Cova, S.; Weiss, S.; Michalet, X. *Proc. SPIE* **2011**, *7905*, 790503.

(28) Oh, D.; Zidovska, A.; Xu, Y.; Needleman, D. J. *Biophys. J.* **2011**, *101* (6), 1546−54.

(29) Bag, N.; Sankaran, J.; Paul, A.; Kraut, R. S.; Wohland, T. *ChemPhysChem* **2012**, *13* (11), 2784−94.

(30) Buchholz, J.; Krieger, J. W.; Mocsar, G.; Kreith, B.; Charbon, E.; Vamosi, G.; Kebschull, U.; Langowski, J. *Opt. Express* **2012**, *20* (16), 17767−82.

(31) Singh, A. P.; Krieger, J. W.; Buchholz, J.; Charbon, E.; Langowski, J.; Wohland, T. *Opt. Express* **2013**, *21* (7), 8652−68.

(32) Vitali, M.; Bronzi, D.; Krmpot, A. J.; Nikolic, S. N.; Schmitt, F. J.; Junghans, C.; Tisa, S.; Friedrich, T.; Vukojevic, V.; Terenius, L.; Zappa, F.; Rigler, R. *IEEE J. Sel. Top. Quantum Electron.* **2014**, *20* (6), 344.

(33) Krieger, J. W.; Singh, A. P.; Bag, N.; Garbe, C. S.; Saunders, T. E.; Langowski, J.; Wohland, T. *Nat. Protoc.* **2015**, *10* (12), 1948−74.

(34) Krmpot, A. J.; Nikolic, S. N.; Vitali, M.; Papadopoulos, D. K.; Oasa, S.; Thyberg, P.; Tisa, S.; Kinjo, M.; Nilsson, L.; Gehring, W. J.; Terenius, L.; Rigler, R.; Vukojevic, V. *SPIE Proc.* **2015**, *9536*, 95360O.

(35) Singh, A. P.; Galland, R.; Finch-Edmondson, M. L.; Grenci, G.; Sibarita, J. B.; Studer, V.; Viasnoff, V.; Saunders, T. E. *Biophys. J.* **2017**, *112* (1), 133−142.

(36) Buchholz, J.; Krieger, J.; Bruschini, C.; Burri, S.; Ardelean, A.; Charbon, E.; Langowski, J. *Biophys. J.* **2018**, *114* (10), 2455−2464.

(37) Brugues, J.; Needleman, D. *Proc. Natl. Acad. Sci. U. S. A.* **2014**, *111* (52), 18496−500.

(38) Papadopoulos, D. K.; Krmpot, A. J.; Nikolic, S. N.; Krautz, R.; Terenius, L.; Tomancak, P.; Rigler, R.; Gehring, W. J.; Vukojevic, V. *Mech. Dev.* **2015**, *138*, 218.

(39) Bag, N.; Ng, X. W.; Sankaran, J.; Wohland, T. *Methods Appl. Fluoresc.* **2016**, *4* (3), 034003.

(40) Sezgin, E.; Azbazdar, Y.; Ng, X. W.; Teh, C.; Simons, K.; Weidinger, G.; Wohland, T.; Eggeling, C.; Ozhan, G. *FEBS J.* **2017**, *284* (15), 2513−2526.

(41) Huang, S.; Lim, S. Y.; Gupta, A.; Bag, N.; Wohland, T. *Biochim. Biophys. Acta, Biomembr.* **2017**, *1859* (9 Pt A), 1483−1492.

(42) Hanley, M. L.; Yoo, T. Y.; Sonnett, M.; Needleman, D. J.; Mitchison, T. J. *Mol. Biol. Cell* **2017**, *28* (11), 1444−1456.

(43) Ng, X. W.; Teh, C.; Korzh, V.; Wohland, T. *Biophys. J.* **2016**, *111* (2), 418−429.

(44) Oh, D.; Yu, C. H.; Needleman, D. J. *Proc. Natl. Acad. Sci. U. S. A.* **2016**, *113* (31), 8729−34.

(45) Langowski, J. *Methods* **2017**, *123*, 3−10.

(46) Vukojevic, V.; Heidkamp, M.; Ming, Y.; Johansson, B.; Terenius, L.; Rigler, R. *Proc. Natl. Acad. Sci. U. S. A.* **2008**, *105* (47), 18176−81.

(47) Dertinger, T.; Pacheco, V.; von der Hocht, I.; Hartmann, R.; Gregor, I.; Enderlein, J. *ChemPhysChem* **2007**, *8* (3), 433−443.

(48) Buchholz, J. *Evaluation of single photon avalanche diode arrays for imaging fluorescence correlation spectroscopy: FPGA-based data readout and fast correlation analysis on CPUs, GPUs and FPGAs*; German Cancer Research Center (DKFZ), Helmholtz Association of National Research Centers: Heidelberg, Germany, 2015.

(49) Ries, J.; Schwille, P. *Biophys. J.* **2006**, *91* (5), 1915−1924.

(50) Ries, J.; Petrášek, Z.; García-Sáez, A. J.; Schwille, P. *New J. Phys.* **2010**, *12*, 113009.

(51) Michalet, X.; Siegmund, O. H.; Vallerga, J. V.; Jelinsky, P.; Millaud, J. E.; Weiss, S. *J. Mod. Opt.* **2007**, *54* (2−3), 239.

(52) Michalet, X.; Colyer, R. A.; Scalia, G.; Weiss, S.; Siegmund, O. H.; Tremsin, A. S.; Vallerga, J. V.; Villa, F.; Guerrieri, F.; Rech, I.; Gulinatti, A.; Tisa, S.; Zappa, F.; Ghioni, M.; Cova, S. *Proc. SPIE* **2011**, *8033*, 803316.

(53) Michalet, X.; Colyer, R. A.; Scalia, G.; Ingargiola, A.; Lin, R.; Millaud, J. E.; Weiss, S.; Siegmund, O. H.; Tremsin, A. S.; Vallerga, J. V.; Cheng, A.; Levi, M.; Aharoni, D.; Arisaka, K.; Villa, F.; Guerrieri, F.; Panzeri, F.; Rech, I.; Gulinatti, A.; Zappa, F.; Ghioni, M.; Cova, S. *Philos. Trans. R. Soc., B* **2013**, *368* (1611), 20120035.

(54) Mikuni, S.; Pack, C.; Tamura, M.; Kinjo, M. *Exp. Mol. Pathol.* **2007**, *82* (2), 163−8.

(55) Stortz, M.; Presman, D. M.; Bruno, L.; Annibale, P.; Dansey, M. V.; Burton, G.; Gratton, E.; Pecci, A.; Levi, V. *Sci. Rep.* **2017**, *7* (1), 6219.

(56) Mikuni, S.; Tamura, M.; Kinjo, M. *FEBS Lett.* **2007**, *581* (3), 389−93.

(57) Shimozawa, T.; Yamagata, K.; Kondo, T.; Hayashi, S.; Shitamukai, A.; Konno, D.; Matsuzaki, F.; Takayama, J.; Onami, S.; Nakayama, H.; Kosugi, Y.; Watanabe, T. M.; Fujita, K.; Mimori-Kiyosue, Y. *Proc. Natl. Acad. Sci. U. S. A.* **2013**, *110* (9), 3399−404.

(58) Claxton, N. S.; Fellers, T. J.; Davidson, M. W. Microscopy, confocal. In *Encyclopedia of medical devices and instrumentation*, Webster, J. G., Ed. John Wiley & Sons: Hoboken, NJ; 2006, 449−477.

(59) Rigler, R.; Mets, U.; Widengren, J.; Kask, P. *Eur. Biophys. J.* **1993**, *22* (3), 169−175.

(60) Eigen, M.; Rigler, R. *Proc. Natl. Acad. Sci. U. S. A.* **1994**, *91* (13), 5740−5747.

(61) Reynaud, E. G.; Krzic, U.; Greger, K.; Stelzer, E. H. K. *HFSP J.* **2008**, *2* (5), 266−275.

(62) Overbeck, E.; Sinn, C.; Flammer, I.; Ricka, J. *Rev. Sci. Instrum.* **1998**, *69* (10), 3515−3523.

(63) Zhao, M.; Jin, L.; Chen, B.; Ding, Y.; Ma, H.; Chen, D. Y. *Appl. Opt.* **2003**, *42* (19), 4031−4036.

(64) Ziarkash, A. W.; Joshi, S. K.; Stipcevic, M.; Ursin, R. *Sci. Rep.* **2018**, *8* (1), 5076.

Supporting Information: Functional Fluorescence Microscopy Imaging. Quantitative Scanning-Free Confocal Fluorescence Microscopy for the Characterization of Fast Dynamic Processes in Live Cells

Aleksandar J. Krmpot[1,2], Stanko N. Nikolić[1,2], Sho Oasa[1], Dimitrios K. Papadopoulos[3,†], Marco Vitali[4], Makoto Oura[5], Shintaro Mikuni[5], Per Thyberg[6], Simone Tisa[7], Masataka Kinjo[5], Lennart Nilsson[8], Lars Terenius[1], Rudolf Rigler[1,9,*], Vladana Vukojević[1,*]

[1]Department of Clinical Neuroscience (CNS), Center for Molecular Medicine (CMM), Karolinska Institutet, 17176 Stockholm, Sweden; [2]Institute of Physics Belgrade, University of Belgrade, 11080 Belgrade, Serbia; [3]Max-Planck Institute for Molecular Cell Biology and Genetics, 01307 Dresden, Germany; [4]Sicoya GmbH, 12489 Berlin, Germany; [5]Laboratory of Molecular Cell Dynamics, Faculty of Advanced Life Science, Hokkaido University, Sapporo, 001-0021, Japan; [6]AlbaNova University Center, Royal Institute of Technology, Department of Applied Physics, 10691 Stockholm, Sweden; [7]Micro Photon Devices (MPD), 39100 Bolzano, Italy; [8]Department of Biosciences and Nutrition, Karolinska Institutet, 14183 Huddinge, Sweden; [9]Department of Medical Biochemistry and Biophysics (MBB), Karolinska Institutet, 17177 Stockholm, Sweden

SUMMARY: Description of the software for data analysis, calculation of auto- and cross-correlation curves and image rendering (S1); standard solutions, auxiliary slides for instrument calibration, alignment, and cell culture (S2); optical alignment of the fFMI system (S3); observation volume element size determination (S4); accuracy, precision and single-molecule detection sensitivity of the fFMI system(S5) are given in the Supporting Information (S1-S5) together with the results obtained by imaging in thick specimen the transcription factor Sex Combs Reduced (Scr) in live salivary glands of *Drosophila ex vivo* (S6).

S1. SOFTWARE FOR DATA ANALYSIS

Auto-correlation and cross-correlation analysis. Raw data collected by the SPAD camera, consisting of 131000 frames acquired every 20.74 μs that yield 1024 fluorescence intensity fluctuation traces recorded over 2.7 s, were stored in the camera's internal memory, transferred to the computer and subjected to correlation analysis to yield auto- and first- and second-order cross-correlation curves (ACC and CCC, respectively) for all 32×32 pixels in an image frame. For this purpose, the so-called multi-tau algorithm was used, described in detail elsewhere[1, 2]. Briefly, in the multi-tau algorithm values of the second order correlation function $G^{(2)}(\tau)$ are determined on a quasi-logarithmic time scale. Each lag time (τ) for which the $G^{(2)}(\tau)$ value is calculated, is called a channel. The channel is thus characterized by an individual sampling time (the bin width) and the lag time τ (the delay from the measurement at time 0). The first sixteen channels form the first group, while all other groups consist of eight consecutive channels. The bin width for the first group is determined by the shortest counting interval of the detector, which is 20.74 μs for the SPAD camera used. The following group has an individual sampling time that is twice as long, while for the

other channels it is equal to the accumulated sampling time of all preceding channels plus the bin width of its group. Two additional variables are introduced: the so-called delayed monitor M_{del} defined for each channel and the direct monitor M_{dir} defined for each group. The purpose of M_{del} is to accumulate all counts sampled in its channel, while M_{dir} accumulates all counts without delay time at a particular sampling time.

The ACCs, M_{del} and M_{dir} are calculated according to the following formulas:

$$G^{(2)}(\tau_i) = \frac{\dfrac{1}{M-m}\sum_{k=1}^{M-m} n(k\Delta\tau_i)\cdot n(k\Delta\tau_i + m\Delta\tau_i)}{M_{del}\cdot M_{dir}}, \qquad (1)$$

$$M_{del} = \frac{1}{M-m}\sum_{k=m}^{M} n(k\Delta\tau_i) \qquad (2)$$

$$M_{dir} = \frac{1}{M-m}\sum_{k=1}^{M-m} n(k\Delta\tau_i) \qquad (3)$$

Here, τ_i is the lag time and $\Delta\tau_i = 2^{i-1}\Delta\tau_1$ is the sampling time for channel *i*. Bin width for the first group is $\Delta\tau_1 = 20.74\,\mu s$.

m and M are integers defined as $m = \tau_i / \Delta\tau_i$ and $M = T / \Delta\tau_i$, where T is the total measurement time. The number of photons counted over a time interval $[(k-1)\Delta\tau_i, k\Delta\tau_i]$ is denoted as $n(k\Delta\tau_i)$. In essence, the correlation analysis boils down to obtaining the sum of the products $n(k\Delta\tau_i) \cdot n(k\Delta\tau_i + m\Delta\tau_i)$ of the counted photons at time $k\Delta\tau_i$ and $m\Delta\tau_i$ later, as described by Wohland et al. [3].

The CCCs are calculated for two SPADs of the camera designated as the "first" or "second" order neighbors of the reference pixel. For example, if the row and column of pixels a and b are denoted as $row(a)$, $col(a)$, $row(b)$ and $col(b)$, respectively, then pixels a and b are said to be "first" order neighbors if relationships (1) or (2) apply: (1) $|row(a) - row(b)| = 1$ and $|col(a) - col(b)| \leq 1$ or (2) $|col(a) - col(b)| = 1$ and $|row(a) - row(b)| = 0$. Similarly, for "second" order neighbors: (1) $|row(a) - row(b)| = 2$ and $|col(a) - col(b)| \leq 2$ or (2) $|col(a) - col(b)| = 2$ and $|row(a) - row(b)| \leq 1$.

The following formula was used for the calculation of CCCs:

$$G_{ab}^{(2)}(\tau_i) = \frac{\frac{1}{M-m}\sum_{k=1}^{M-m} n_a(k\Delta\tau_i) \cdot n_b(k\Delta\tau_i + m\Delta\tau_i)}{M_{a,dir}M_{b,del}} , \qquad (4)$$

where $n_a(k\Delta\tau_i)$ and $n_b(k\Delta\tau_i)$ denote photon counts at time $k\Delta\tau_i$ for pixels a and b, respectively. $M_{a,del}$ and $M_{a,dir}$ are calculated according to (2) and (3) by taking the photon counts n_a of pixel a. In analogy, $M_{b,del}$ and $M_{b,dir}$ were calculated by taking the photon counts n_b of pixel b. It is important to note that, in general, $G_{ab}^{(2)}(\tau_i) \neq G_{ba}^{(2)}(\tau_i)$, since the symmetry relation $G_{ab}^{(2)}(\tau_i) = G_{ba}^{(2)}(\tau_i)$ only holds in the absence of directed motion. Thus, for each pair of pixels there are two cross-correlation curves, which may be different in case of directed molecular movement i.e. flow[4].

Massively parallel calculations of ACC and CCC using the graphics processing unit (GPU). Since fluorescence intensity fluctuations are independently recorded by SPADs that constitute the SPC² camera, parallel computing could be used to speed up data analysis by auto- and cross-correlation. For this purpose, the NVIDIA GeForce GTX 780 graphic card was used that contains 2304 Compute Unified Device Architecture (CUDA) cores that can run tens of thousands of independent tasks (threads) simultaneously. By running as many threads in parallel as possible, the CUDA platform enabled us to use the processing power of the GPU to massively parallelize data analysis. Using one thread to calculate the $G^{(2)}(\tau)$ value of one channel for one particular pixel, the CUDA program executed two groups of threads for ACCs calculation and forty groups of threads for CCCs calculation, where each group runs 64000 threads in parallel on the GPU. This decreased the time required for computation of 1024 ACCs by a central processing unit (CPU) from $\approx$ 210 s to $\approx$ 4 s by a GPU, and from $\approx$ 77 minutes (CPU) to $\approx$ 45 s (GPU) for the calculation of CCCs.

fFMI image rendering. An ACC was calculated for each pixel. The amplitude of the ACC was estimated from the value of $G(\tau)$ at $\tau = 103.7$ µs, chosen because the contribution of afterpulsing, which decays quickly, was determined to be negligible for lag times longer than 100 µs. The average number of molecules in the observation volume element (OVE) was calculated as $N = 1/(G(103.7) - 1)$), and then corrected, $N_{corr} = N/f_{corr}$, where the correction factor $f_{corr} = 48.1$ was determined from calibration experiments described in subsection 3.4. The characteristic decay time of the ACC, which is equal to the average translational diffusion time (τ_D), was determined from its full width at half maximum. If not otherwise indicated, these values are plotted in fFMI images to show the spatial distribution of molecular numbers (N_{corr}) and translational diffusion times (τ_D).

For measurements by conventional, spFCS, the experimental ACCs were fitted using the analytical function for free three-dimensional (3D) diffusion of a single chemical species and, where appropriate (e.g. Rh6G), triplet formation:

$$G(\tau) = 1 + \frac{G_0}{\left(1 + \frac{\tau}{\tau_D}\right) \cdot \sqrt{1 + \frac{\omega_{xy}^2}{\omega_z^2}\frac{\tau}{\tau_D}}}$$
$$\cdot \left(1 + \frac{T}{1-T}exp\left(-\frac{\tau}{\tau_T}\right)\right) =$$
$$= 1 + \frac{1}{N} \cdot \frac{1}{\left(1 + \frac{\tau}{\tau_D}\right)\sqrt{1 + \frac{\omega_{xy}^2}{\omega_z^2}\frac{\tau}{\tau_D}}} \cdot \left(1 + \frac{T}{1-T}exp\left(-\frac{\tau}{\tau_T}\right)\right). \qquad (5)$$

In eq. (5), G_0 is the zero lag time amplitude of the ACC; N is the average number of molecules in the OVE; τ_D is the average diffusion time; ω_{xy} and ω_z are the radial and the axial radius of the OVE, respectively, where the excitation intensity reaches $1/e^2$ of its value at the center; T is the average equilibrium fraction of molecules in the triplet state (when not applicable, $T = 0$); and τ_T is the triplet correlation time, related to the rate constants for intersystem crossing and the triplet decay. The diffusion coefficient D was determined from the diffusion time using the relationship $\tau_D = \omega_{xy}^2/4D$.

S2. STANDARD SOLUTIONS, AUXILIARY SLIDES FOR INSTRUMENT CALIBRATION, ALIGNMENT, AND CELL CULTURE.

Laser grade Rhodamine 6G (Rh6G), dye content 99 % (Sigma-Aldrich), $D_{Rh6G} = 4.14 \times 10^{-10}$ m² s^{-1}, was used to prepare standard solutions for spFCS instrument calibration. Dilute aqueous suspension of yellow-green fluorescent carboxylate-modified polystyrene nano/microspheres of different diameter: $d = 20$ nm, 100 nm ($D_{fs100} = 4.4 \times 10^{-12}$ m² s^{-1},), 200 nm, 500 nm, 1.0 µm and 2.0 µm (FluoSpheres® Size Kit #2; Ex/Em: 505/515) and carboxylate functionalized quantum dot nano-

crystals, $d = 20$ nm, emission maxima at 525 nm (Qdot® 525 ITK™ Carboxyl Quantum Dots), Molecular Probes, Life Technologies Corporation, USA, were used for fFMI instrument calibration and performance characterization. For this purpose quantum dots/fluospheres suspension were freshly prepared and sonicated in an ultrasonic bath for 30 min before use.

For fFMI instrument alignment, a uniform thin layer of Rh6G was prepared by squeezing 1 µL of concentrated Rh6G solution in water between a microscopic slide and a cover glass (#1.5 thickness, 22×40 mm) and allowed to dry.

Preparation of fixed muntjac skin fibroblast cells with filamentous actin stained using Alexa Fluor® 488 phalloidin (FluoCells® Prepared Slide #6; Muntjac cells with Mouse Anti-OxPhos Complex V Inhibitor Protein, Alexa Fluor® 555 Goat Anti-Mouse IgG, Alexa Fluor® 488 Phalloidin, and TO-PRO®-3) was purchased from Molecular Probes, Life Technologies Corporation, USA and used for fFMI performance characterization.

Live salivary glands ex vivo. Third instar wandering *Drosophila* larvae expressing dimers of the Hox transcription factor Sex combs reduced (Scr) coupled to the mCitrine fluorescent protein and a multimer Scr-binding site of the fork-head enhancer (*fkh250^{con}*), as previously described[5-7], were dissected in phosphate buffered saline (PBS, pH = 7.4) at room temperature. The salivary glands were transferred to 8-well chambered cover glass (Nunc® Lab-Tek® II, Thermo Fisher Scientific, USA) containing 200 µL of PBS for imaging.

Cell culture. PC12 and U-2 OS cells were purchased from the American Type Culture Collection (ATCC). PC12 cells were stably transformed to express the µ-opioid receptor genetically fused with the enhanced Green Fluorescent Protein at the C terminus (eGFP-MOP)[8, 9]. U-2 OS cells were transiently transformed to express the eGFP monomer (eGFP), eGFP tetramer (eGFP$_4$) consisting of four eGFP molecules covalently bound *via* a flexible linker, or the glucocorticoid receptor tagged with eGFP at the N terminus (eGFP-GR$_{wt}$)[10].

For multiplication purposes PC12 cells were cultured in collagen-coated flasks using RPMI 1640 medium supplemented with 5 % fetal bovine serum (FBS), 10 % heat-inactivated horse serum, 100 U/ml penicillin and 100 µg/ml streptomycin; whereas U-2 OS cells were grown in the Dulbecco's modified Eagle's medium (DMEM) supplemented with 10 % FBS. All cell culture reagents were from Invitrogen, Sweden. The cells were maintained at 37 °C in a humidified 5 % CO$_2$ atmosphere and sub-cultured every 3-4 days. For FCS experiments, PC12 cells were plated in 8-well chambered cover glass (Nunc® Lab-Tek® II, Thermo Fisher Scientific, USA) 2-3 days before the FCS experiment and grown in phenol-red free RPMI cell culture medium.

The U-2 OS cells were plated in the 8-well chambered cover glass at a cell density of ~10,000 cells *per* well one day before transfection. The cells were transfected with 300 ng plasmid DNAs for transient expression of eGFP-GR$_{wt}$, eGFP monomer or eGFP$_4$ tetramer using 2.6 µL Lipofectamine 2000. Three hours after transfection, the cell culture medium was replaced by a fresh medium supplemented with 10 % FBS. The trans-

fected U-2 OS cells were then cultured for 21 hours and subjected to FCS measurements. All FCS experiments were performed at room temperature.

In order to induce eGFP-GR$_{wt}$ nuclear translocation, U-2 OS cells were treated with 100 nM Dexamethasone (Dex), purchased from Sigma (St.Louis, MO, USA).

S3. OPTICAL ALIGNMENT OF THE fFMI SYSTEM

To align the illumination and detection matrices, the dried Rh6G sample was illuminated and the spot-wise image was recorded using the DSLR camera. The pitch of the illumination matrix was adjusted by translating the DOE along the beam axis (Fig. 1 a). Thereafter, light was directed to the SPAD camera attached to the other side port of the microscope. Photon counts were observed in all SPADs in real time using a software routine specially designed for this purpose. By moving the focusing lens (Fig. 1 a) in the plane perpendicular to the laser beam the lateral position of the illumination matrix was adjusted until the signal was maximized in all SPADs simultaneously, indicating that the system is well aligned (Fig. S1 a).
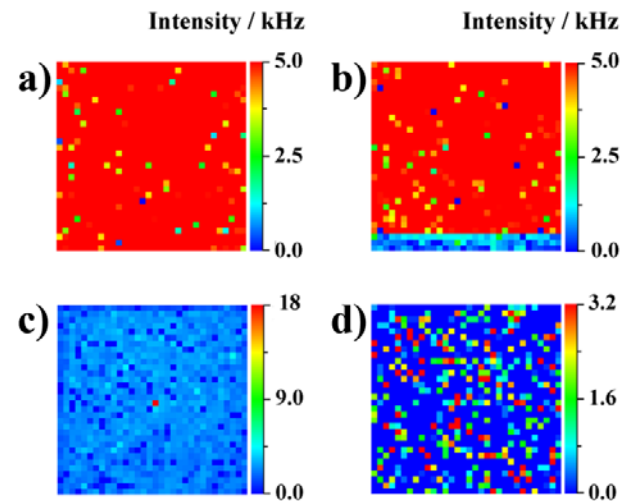

Figure S1. Optical alignment of the fFMI system. a) Image of dried Rh6G obtained using the SPAD matrix detector when the fFMI system is well aligned. **b)** Image of dried Rh6G obtained using a deliberately misaligned fFMI system, where the illumination and detection matrices are shifted three rows between one another. **c)** Image of dried Rh6G acquired using a deliberately misaligned fFMI system, where individual illumination spots fall between individual SPADs and the 0th-order maximum, which in a well aligned system is not visible as it falls between the central pixels, is captured in the red pixel (17,16). **d)** Dark count rate distribution in the SPAD camera.

In order to verify that the illumination and detection matrices overlap, we show here two examples of deliberate misalignment: (1) when there is a mismatch of three rows between the illumination and detection matrices (Fig. S1 b); and (2) when the zero-order diffraction spot, which normally is not visible as it falls between the central SPADs on the SPAD matrix detector, is deliberately visualized in pixel (17, 16) (Fig. S1 c, red pixel). Since all illumination spots in the latter case fall

between the SPADs, the signal recorded in all other SPADs is very low (Fig. S1 c, blue) and the measured intensity is at the level of the detector dark count (Fig. S1 d).

S4. OBSERVATION VOLUME ELEMENT SIZE

To determine the OVE size, a suspension of fluospheres, $d =$ 100 nm, with a known diffusion coefficient (D = 4.4×10^{-12} $m^2 s^{-1}$)[11], was used as a calibration standard. The spatial distribution of diffusion times was mapped (Fig. S2 a), and the corresponding histogram of diffusion time distribution was obtained (Fig. S2, b), yielding an average diffusion time $\tau_D =$ (3.7 ± 1.1) ms.
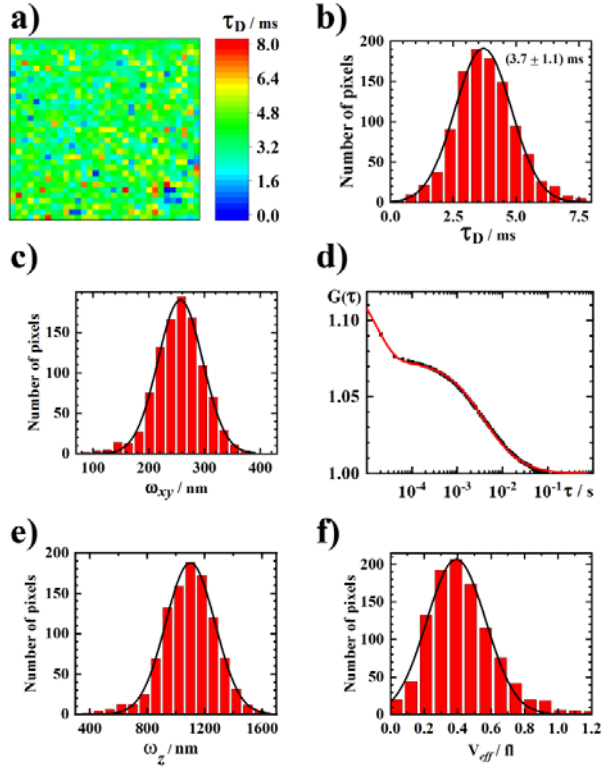

Figure S2. Observation volume element size. a) Diffusion time map recorded in an aqueous suspension of fluospheres, d = 100 nm. **b)** Corresponding histogram of diffusion times distribution. The average diffusion time was determined to be τ_D = (3.7 ± 1.1) ms. **c)** Histogram of lateral radius size distribution, ω_{xy} = (255 ± 40) nm. **d)** Average ACC across all pixels (black squares) and the fitted ACC (red). **e)** Histogram of axial radius size distribution, ω_z = (1.1 ± 0.2) μm. **f)** Histogram of effective volume size distribution, V_{eff} = $(0.36 \pm 0.17) \times 10^{-15}$ l.

The lateral radius size was then calculated for each OVE using the relationship $\tau_D = \omega_{xy}^2/4D$, i.e. $\omega_{xy}^2 = 4 \cdot D \cdot \tau_D$, yielding a map of lateral radii size (data not shown) and the average size of the lateral radius was determined from the histogram of lateral radius size distribution, $\omega_{xy} = (255 \pm 40)$ nm (Fig. S2 c).

To determine the axial radius, an average ACC across the SPAD matrix was generated (Fig. S2 d, black squares) and fitted using a theoretical equation that is analogous to equation (5), where detector afterpulsing visible at lag times $\tau_D < 40$ μs

was represented by an exponential decay term (Fig. S2 d, red curve). Fitting yielded the diffusion time, $\tau_D = (3.7 \pm 1.1)$ ms and the axial to lateral structure parameter ratio, $\omega_z/\omega_{xy} =$ 4.28. Using this value and the average lateral radius size, the axial radius size was determined to be $\omega_z = (1.1 \pm 0.2)$ μm (Fig. S2 e).

Finally, the effective volume was calculated $V_{eff} =$ $\pi^{3/2} \cdot \omega_{xy}^2 \cdot \omega_z$ for each pixel (data not shown), and the average effective volume of the OVE was determined from the histogram of effective volume size distribution, $V_{eff} = (0.36 \pm 0.17) \times 10^{-15}$ l (Fig. S2 f).

S5. ACCURACY, PRECISION AND SINGLE-MOLECULE DETECTION SENSITIVITY OF THE fFMI SYSTEM

While diffusion times can be determined with great precision and the diffusion coefficients obtained by fFMI agreed well with values determined by spFCS and with theoretically calculated values (Fig. S3 a), the distribution of diffusion times measured in the suspension of fluospheres is somewhat broad (Fig. 1 e) for several reasons. Most notably, the fluospheres suspension contains, despite prolonged sonication, not only individual fluospheres but also some agglomerates, which are now more readily detected since we examine 1024 OVEs simultaneously. Furthermore, the intensity of the incident light in individual foci is rather weak, estimated to be 1/1024 of the intensity measured at the microscope objective (18.9 mW) reduced by 20 % to account for the intensity of the zero-order diffraction peak. Consequently, the autocorrelation curves are somewhat noisier. Finally, the diffusion time is determined by reading out the full width at half-maximum from the experimentally derived ACCs, which are noisy, rather than from the fitted theoretical ACCs.

In comparison to diffusion times, the amplitude of the autocorrelation curve determined by the fFMI and the spFCS differed considerably (Fig. S3 b).

The difference in the amplitudes of ACCs arises primarily due to differences in the signal-to-noise-ratio (SNR) between the fFMI and the spFCS systems. The primary contributor to lower SNR ratio in the fFMI system is the dark count rate of individual SPADs, which for most SPADs comprising the matrix detector was over 1000 counts *per* second for individual SPAD (Fig. S1 d). and less than 250 photons *per* second in the conventional spFCS system used as a reference[12].

Another important contributing factor is the so-called pinhole cross-talk, *i.e.* increase in the background signal arising due to inadvertent transmission of out-of-focus light through neighboring detectors. Finally, when 1024 ACCs are simultaneously recorded, the signal acquisition time length in the fFMI system is limited to 2.7 s by the internal memory of the matrix SPAD camera, which may restrain the underlying statistical analysis resulting in noisy ACCs. By improving these features, the concentration and diffusion of eGFP molecules in water could be characterized (Fig. S3 c–f). Here, the amplitude of the average ACC recorded by the fFMI system, $G_{0,fFMI} =$ 1.05 ± 0.01 (Fig. S3 d, black), differed from the value measured by
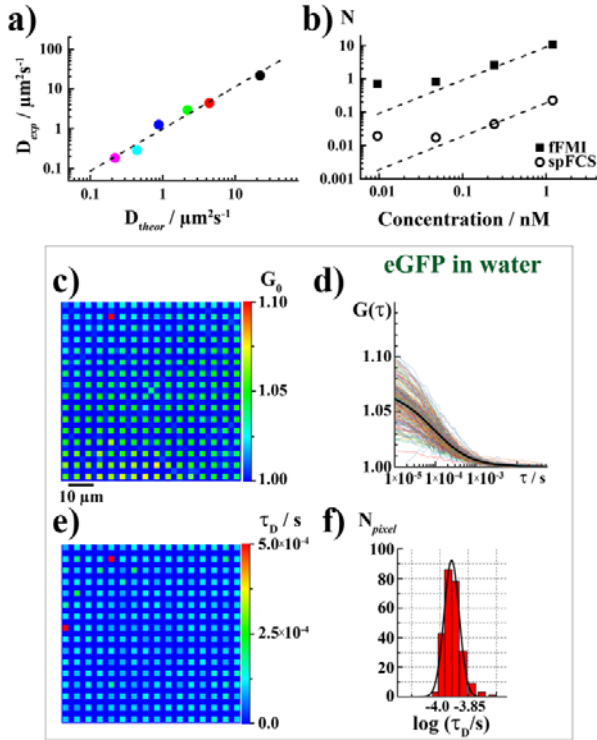
Figure S3. Accuracy, precision and single-molecule detection sensitivity of the ffmi system. a) Diffusion coefficient of fluospheres of different diameter: $d = 0.02$ μm (black), $d = 0.1$ μm (red), $d = 0.2$ μm (green), $d = 0.5$ μm (blue), $d = 1.0$ μm (cyan) and $d = 2.0$ μm (pink), experimentally measured by fFMI, with respect to theoretically expected values. **b)** Amplitudes of ACCs measured in a dilute suspension of fluospheres, $d = 100$ nm, by fFMI (squares) and spFCS (open circles). For all concentrations tested, the amplitude measured by spFCS was 48.1 times larger than the amplitude by fFMI, as determined from the ratio of slopes of the regression equations: $y = (0.189 \pm 0.005) \cdot x$, for fFMI, and $y = (9.1 \pm 0.4) \cdot x$, for spFCS, yielding the correction factor $f_{corr} = 9.1/0.189 = 48.1$. The fFMI and spFCS measurements were performed at comparable excitation intensities (14.8 μW at the microscope objective lens in spFCS). Background correction was not applied. ***Box***: **c)** Spatial map of amplitudes (G_0) acquired by fFMI in a (18.5 ± 0.4) nM solution of eGFP in water (eGFP concentration was determined by the spFCS system). **d)** Individual ACCs acquired by fFMI in the same sample described in i). The amplitude G_0 of the average ACC (solid black) was $G_{0,fFMI} = (1.05 \pm 0.01)$. **e)** Spatial map of translational diffusion times acquired by fFMI in the same sample described in c). **f)** Corresponding histogram of translation diffusion time distribution. Gaussian fitting yields translational diffusion time for eGFP in water, $\tau_{D,eGFP} = (110 \pm 30)$ μs. In c)–f), the inter-pixel distance was increased using a 16×16 DOE and every other detector on the next generation SPAD camera. Signal acquisition time was four times longer, as the number of simultaneously acquired ACCs was reduced from 1024 to 256.

spFCS, $G_{0,spFCS} = 1.26 \pm 0.01$, 4.9 times ($f_{corr} = 4.9$). Similarly, the translational diffusion times, $\tau_{D,fFMI} = (120 \pm 30)$ μs and $\tau_{D,spFCS} = (85 \pm 3)$ μs, yield, after correction for differences in

the observation volume area size ($\omega^2_{xy,spFCS} = 0.042$ μm^2 and $\omega^2_{xy,fFMI} = 0.054$ μm^2), diffusion coefficient values that agree within the experimental error ($D_{spFCS} = (1.2 \pm 0.1) \times 10^{-10}$ m^{2}s^{-1} and $D_{fFMI} = (1.1 \pm 0.1) \times 10^{-10}$ m^{2}s^{-1}). Importantly, these values agree also with literature values, $D_{eGFP} = 0.95 \times 10^{-10}$ m^{2}s^{-1} [13].

S6. IMAGING THICK SPECIMEN USING fFMI

While we have established that crosstalk between pixels is not an issue for quantitative characterization of concentration and diffusion in dilute solutions/suspensions (Fig. 1 f), it is well known that the main challenge for quantitative fluorescence microscopy imaging of thick specimen using multi-focal optical arrangement arises because out-of-focus light that originates from bright structures in remote focal planes above/below the sample plane can pass through adjacent pinholes. This increases the background signal, *i.e.* reduces the SNR, and gives rise to hazy images where details that are normally observed in confocal laser scanning microscopy are obscured in spinning disk confocal microscopy [14]. In order to probe the capacity of the fFMI system to characterize dynamical processes in thick samples, the concentration and nuclear dynamics of the mCitrine-tagged Sex combs reduced (Scr) dimeric transcription factor (mCitrine-(Scr)$_2$) was investigated in salivary glands from *Drosophila* third instar larvae bearing in the genome a multimeric specific binding site of Scr (*fkh250^{con}*; see Materials and Methods and [15] for details). The obtained results are presented in Fig. S4.

Fluorescence intensity imaging of a polytene nucleus acquired by the DSLR camera is shown in Fig. S4 a. The spatial map of the average number of mCitrine-(Scr)$_2$, calculated by extrapolating to zero lag time the virtually noise-free G(τ) values at lag time τ = 5 ms, is shown in Fig. S4 b, and the corresponding spatial map of diffusion times in Fig. S1 c. The histogram reflecting the distribution of diffusion times inside the cell nucleus is shown in Fig. S4 d. Fluorescence intensity fluctuations simultaneously recorded at several different positions in the cell nucleus (Fig. S4 e, yellow, blue and magenta) and in the cytoplasm (Fig. S4 e, black), show that the average signal intensity is unchanged during the signal acquisition time (2.7 s), indicating that the signal is not distorted by extensive photobleaching. Individual ACCs acquired in different pixels in the cell nucleus are shown in Fig. S4 f.

fFMI maps of the average number of mCitrine-(Scr)$_2$ molecules (Fig. S4 b) and their translational diffusion time (Fig. S4 c), clearly show that the mCitrine-(Scr)$_2$ transcription factor is predominantly located in the cell nucleus (Fig. S4 b), and that nuclear diffusion is rather slow (Fig. S4 c and d), presumably due to interactions with the multimeric specific binding site of Scr. Furthermore, fFMI shows that the investigated protein is not uniformly distributed in the cell nucleus, and that domains with different mCitrine-(Scr)$_2$ concentration and diffusion exist. This is expected, since polytene cell nuclei contain 2^{10} chromosomal copies associated together in giant polytene chromosomes. In the nucleoplasm, where there is no chromatin, the diffusion of unbound mCitrine-(Scr)$_2$ is faster because its movement is not deterred by interactions with the DNA [5, 6].
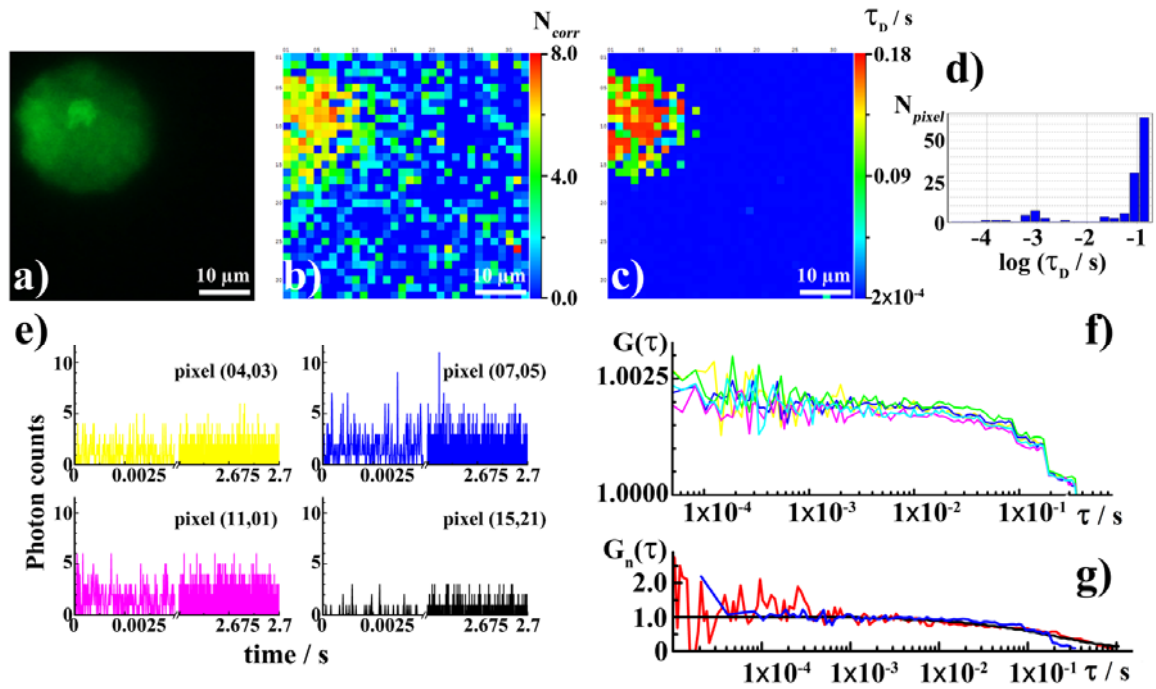
Figure S4. Spatial distribution of molecular numbers and diffusion time maps of transcription factor dimers in live salivary glands of *Drosophila*. a) DSLR image of a polytene cell nucleus in a live salivary gland dissected from a third instar larva of the fruit fly *Drosophila melanogaster* genetically engineered to express a mCitrine-tagged dimeric Sex Combs Reduced (Scr) transcription factor mCitrine-(Scr)$_2$. Note that only the cell nucleus is unambiguously visible in the images, while the fluorescence intensity in the cytoplasm was at the level of background. b) Spatial map of molecular numbers (N_{corr}) in the nucleus shown in a) (slightly shifted due to differences in the position of the images), shows uneven transcription factor distribution. c) Spatial map of diffusion times (τ_D) reveals that transcription factor dynamic behavior is non-uniform, showing domains where fast or slow diffusion prevails. Regions where slow diffusion is observed reflect transcription factor binding to chromatin, *i.e.* putative sites of transcriptional activity. d) Corresponding diffusion time histogram (pixels in rows 3-16 and columns 1-10). e) Fluorescence intensity fluctuations (photon counts *per* 20.74 µs) recorded in selected pixels in the cell nucleus (yellow, blue and magenta) and the cytoplasm (black). Time series collected during 2.7 s show that significant photobleaching was not observed during signal acquisition. f) Corresponding ACCs recorded in the selected pixels in the cell nucleus, generated by temporal autocorrelation analysis of fluorescence intensity fluctuations shown in e). g) ACCs normalized to the same amplitude (G(τ) = 1 at τ =103.7 µs) recorded by fFMI (blue) and conventional FCS instrument used as a reference (red). The black line represents the fitting using an autocorrelation function derived for a model for free three-dimensional diffusion (eq. (5)). The overlap between ACCs shows that optical properties of the newly developed instrument are of high quality and that the observation volume element size is similar in both setups.

On the average, the amplitudes of ACCs acquired by fFMI were estimated to be about 50-60 times smaller than the amplitudes of ACCs acquired spFCS. (As it was not always possible to perform measurements on exactly the same cell using both systems, the difference in amplitudes was estimated at the population level from measurements on 10 cells in the same salivary gland.) This value is somewhat larger than the value determined for in solution measurements, f_{corr} = 48.1, suggesting that the SNR is lower. However, the decay times of the ACCs acquired by fFMI (Fig. S4 g, blue) and by conventional spFCS (Fig. S4 g, red), agreed well, as can be seen from the overlap of ACC normalized to the same amplitude (Fig. S4 g),

and ACCs acquired by fFMI showed similar value for the translational diffusion time, $\tau_{D,fFMI} \approx \tau_{D,FCS}$ = 25 ms, as was obtained by fitting the ACCs obtained by spFCS using eq. 5 (Fig. S4 g, black). This is expected for FCS measurements in thick samples. Here, the amplitudes of ACCs change due to the uncorrelated crosstalk from deeper tissue sections, which increases the background and reduces the amplitude of the ACCs. However, the decay time of the ACCs is not influenced, and the diffusion time can be correctly determined.

REFERENCES

1. Schatzel, K.; Drewel, M.; Stimac, S., Photon-Correlation Measurements at Large Lag Times - Improving Statistical Accuracy. *J Mod Optic* **1988,** *35* (4), 711-718.

2. Schatzel, K., Accuracy of Photon-Correlation Measurements on Nonergodic Samples. *Appl Optics* **1993,** *32* (21), 3880-3885.

3. Wohland, T.; Rigler, R.; Vogel, H., The standard deviation in fluorescence correlation spectroscopy. *Biophys J* **2001,** *80* (6), 2987-2999.

4. Magde, D.; Webb, W. W.; Elson, E. L., Fluorescence Correlation Spectroscopy .3. Uniform Translation and Laminar-Flow. *Biopolymers* **1978,** *17* (2), 361-376.

5. Vukojevic, V.; Papadopoulos, D. K.; Terenius, L.; Gehring, W. J.; Rigler, R., Quantitative study of synthetic Hox transcription factor-DNA interactions in live cells. *Proceedings of the National Academy of Sciences of the United States of America* **2010,** *107* (9), 4093-8.

6. Papadopoulos, D. K.; Vukojevic, V.; Adachi, Y.; Terenius, L.; Rigler, R.; Gehring, W. J., Function and specificity of synthetic Hox transcription factors in vivo. *Proceedings of the National Academy of Sciences of the United States of America* **2010,** *107* (9), 4087-92.

7. Papadopoulos, D. K.; Skouloudaki, K.; Adachi, Y.; Samakovlis, C.; Gehring, W. J., Dimer formation via the homeodomain is required for function and specificity of Sex combs reduced in Drosophila. *Developmental biology* **2012,** *367* (1), 78-89.

8. Rogacki, M. K.; Golfetto, O.; Tobin, S. J.; Li, T.; Biswas, S.; Jorand, R.; Zhang, H.; Radoi, V.; Ming, Y.; Svenningsson, P.; Ganjali, D.; Wakefield, D. L.; Sideris, A.; Small, A. R.; Terenius, L.; Jovanovic-Talisman, T.; Vukojevic, V., Dynamic lateral organization of opioid receptors (kappa, muwt and muN40D) in the plasma membrane at the nanoscale level. *Traffic* **2018,** *19* (9), 690-709.

9. Tobin, S. J.; Wakefield, D. L.; Terenius, L.; Vukojevic, V.; Jovanovic-Talisman, T., Ethanol and Naltrexone Have Distinct Effects on the Lateral Nano-organization of Mu and Kappa Opioid Receptors in the Plasma Membrane. *ACS chemical neuroscience* **2019,** *10* (1), 667-676.

10. Mikuni, S.; Pack, C.; Tamura, M.; Kinjo, M., Diffusion analysis of glucocorticoid receptor and antagonist effect in living cell nucleus. *Experimental and molecular pathology* **2007,** *82* (2), 163-8.

11. Kapusta, P. Absolute Diffusion Coefficients: Compilation of Reference Data for FCS Calibration. *Application Note* [Online], 2010.

12. Vukojevic, V.; Heidkamp, M.; Ming, Y.; Johansson, B.; Terenius, L.; Rigler, R., Quantitative single-molecule imaging by confocal laser scanning microscopy. *Proceedings of the National Academy of Sciences of the United States of America* **2008,** *105* (47), 18176-81.

13. Petrasek, Z.; Schwille, P., Precise measurement of diffusion coefficients using scanning fluorescence correlation spectroscopy. *Biophys J* **2008,** *94* (4), 1437-48.

14. Shimozawa, T.; Yamagata, K.; Kondo, T.; Hayashi, S.; Shitamukai, A.; Konno, D.; Matsuzaki, F.; Takayama, J.; Onami, S.; Nakayama, H.; Kosugi, Y.; Watanabe, T. M.; Fujita, K.; Mimori-Kiyosue, Y., Improving spinning disk confocal microscopy by preventing pinhole cross-talk for intravital imaging. *Proceedings of the National Academy of Sciences of the United States of America* **2013,** *110* (9), 3399-404.

15. Papadopoulos, D. K.; Krmpot, A. J.; Nikolic, S. N.; Krautz, R.; Terenius, L.; Tomancak, P.; Rigler, R.; Gehring, W. J.; Vukojevic, V., Probing the kinetic landscape of Hox transcription factor-DNA binding in live cells by massively parallel Fluorescence Correlation Spectroscopy. *Mechanisms of development* **2015,** *138 Pt 2*, 218-225.

ORIGINAL PAPER

Talbot carpets by rogue waves of extended nonlinear Schrödinger equations

Stanko N. Nikolić · **Omar A. Ashour** · **Najdan B. Aleksić** ·
Yiqi Zhang · **Milivoj R. Belić** · **Siu A. Chin**

Abstract We present analytical and numerical double-periodic solutions of the one-dimensional nonlinear Schrödinger equation and its extended versions in the form of Talbot carpets. The breathers and rogue waves of different orders are obtained using numerical simulations, starting from the initial conditions calculated by the Darboux transformation. To suppress undesirable aspects of modulation instability leading to homoclinic chaos, Fourier mode pruning procedures are invented to preserve and maintain the twofold periodicity of carpets. The novelty of this paper is analytical Talbot carpets for Hirota–quintic equation and ability to obtain them dynamically by controlling the growth of the Fourier modes. In addition, the new period-matching procedure is also described for periodic rogue waves that can be utilized to produce Talbot carpets without mode pruning. Tablot carpets may find future utility in optoplasmonic nanolithography.

Keywords Quintic equation · Talbot carpet · Rogue waves

S. N. Nikolić (✉) · N. B. Aleksić · M. R. Belić
Science Program, Texas A&M University at Qatar,
P.O. Box 23874, Doha, Qatar
e-mail: stankon@ipb.ac.rs

S. N. Nikolić · N. B. Aleksić
Institute of Physics Belgrade, University of Belgrade,
Pregrevica 118, Belgrade 11080, Serbia

O. A. Ashour
Department of Physics, University of California, Berkeley,
Berkeley, CA 94720, USA

Y. Q. Zhang
Department of Applied Physics, School of Science, Xi'an
Jiaotong University, Xi'an 710049, China

S. A. Chin
Department of Physics and Astronomy, Texas A&M University,
College Station, TX 77843, USA

1 Introduction

Nonlinear Schrödinger equations (NLSEs) of different orders continue to elicit acute attention of numerous research groups around the world, for their utility in various branches of mathematics and physics [1–8]. Here, our attention is focused on the one-dimensional NLSEs arising in the extension of the basic cubic NLSE up to the fifth-order in nonlinearity and dispersions, of utility in nonlinear fiber optics. In particular, we are interested in the unstable solutions of these models when the modulation instability sets in.

Modulation instability (MI) is the basic nonlinear optical process in which a weak periodic perturbation of the fundamental pump wave produces an exponential growth of a finite number of spectral sidebands locked to and growing at the expense of the pump [4,5,9]. Although commonly known as the Benjamin–Feir instability of Stokes waves, that appeared in the 1960s, the MI of the cubic NLSE debuted already in 1947, in the Bogoliubov's work on the uniform Bose gas [10]. It is widely believed that MI is the root cause of the appearance of rogue waves (RWs) in nonlinear optics. The problem is, how to systematically incorpo-

rate the process of MI into the dynamics of generation and observation of RWs in the NLSEs of different types.

A convenient handle in this process is provided by the existence of a family of exact solutions to the basic cubic NLSE in the form of Akhmediev breathers (ABs), Kuznetsov–Ma (KM) solitons, and the Peregrine soliton, which may be regarded as the elementary solutions on a finite background from which higher-order RW solutions can be formed. In this sense, ABs seem to be especially relevant [11,12], which can be generalized to the doubly periodic solutions (as well as to the extended NLSEs). They allow for an easy systematic buildup of higher-order breathers that can be regarded as prototype RWs [13,14].

The complication is that these basic and higher-order solutions represent homoclinic orbits of unstable Stokes waves in the dynamics of cubic NLSE [15–18]. The generic long-time dynamics of modulated Stokes waves, for example, ABs with two or more unstable modes, is chaotic. Once the system, for a range of relevant parameters and initial and boundary conditions, enters homoclinic chaos, the predictive power of the model diminishes. The question has even been raised whether the chaos seen belongs to the model itself or is induced by the numerical procedure applied [15,16].

For these reasons, a school of thought has emerged which holds that it is not important to follow exact dynamics of individual members of the family of exact solutions, but to look at the statistics of RWs in the chaotic regime [4,6,13,19,20]. Optical RWs are rare extreme events in the fluctuation of optical fields; therefore, their statistical features, such as long-tailed probability distributions, should be considered as their defining features. Thus, one should proceed with the numerical solution of different NLSEs with appropriate initial conditions seeded with noise of various types, and after many runs compare the associated statistics of the resulting field distributions with the available experimental data.

In this paper, we adopt a different approach. It is our belief that for specific applications, one still must perform carefully designed numerical simulations of individual well-defined RW solutions, even when it leads to following their dynamics deep in the chaotic region. The general idea is to discern order from chaos. The specific goal is to investigate the possibility of producing Talbot carpets out of ABs of different orders, with an eye on possible applications in nanolithography. Such an investigation requires launching an exact

breather and following its repeated self-imaging recurrences for as long as possible.

Thus, we examine how AB and RW solutions may be obtained for the NLSE and its extensions, the Hirota and quintic equation, and used to accomplish the goal stated. To this end, of immense importance are the analytical solutions to the NLSE that are periodic both along the spatial and temporal axes, and can be viewed as Talbot self-images, introduced in [12]. This study was extended in [21,22], where the nonlinear Talbot carpets of rogue waves were reported for the first time. These solutions are associated with the Talbot effect, first described in the nineteenth century [23], about the same time the solitary waves were discovered. An interesting feature of the nonlinear Talbot effect is that it only displays the primary and secondary images.

The Talbot effect is a near-field diffraction effect, observed when light beams diffract at some periodic structure (such as gratings) and produce recurrent self-images at equidistant planes. In-between the planes, fractional and even fractal images are observed, leading to intricate light patterns that are called the Talbot carpets. Later, the self-imaging phenomena have been reported in many areas of physics, such as atomic [24,25] and quantum [26] optics, waveguide arrays [27], Bose–Einstein condensates [28,29], photonic lattices [30], and X-ray imaging [31]. Talbot self-images can even be regarded as an example of Fermi–Pasta–Ulam recurrence [9]. Nonlinear Talbot effect from nonlinear photonic crystals was experimentally demonstrated in [32]. An overview of the recent advances of Talbot effect in modern science is presented in [33].

The major advances in this paper can be stated as follows. We present the dynamical generation of breathers and rogue waves in Talbot carpet-like arrangements, for the NLSE and its extensions. We calculate the first- and higher-order breathers using Darboux transformation (DT) and extract initial conditions in a wide box that is a multiple of the main breather's period [34]. We invent two pruning procedures for Fourier modes, to suppress modulation instability that ruins the double-periodic pattern of high-intensity peaks. We generalize the NLSE solution formula from [12] and obtain exact solutions for the Hirota–quintic equation. We display a new class of solutions and analyze different mode pruning algorithms for their dynamical stabilization. We introduce a novel way for generating Talbot carpets for the quintic equation on nonuniform backgrounds,

based on specific ratios of the breather and elliptic background periods on which the breathers ride.

The paper is organized in the following fashion. In Sect. 2, we introduce the model of generalized NLSEs and analyze a numerical algorithm for generating nonlinear Talbot carpets from their solutions that may or may not require mode pruning. In Sect. 3, we provide exact solutions of the Hirota–quintic equation and exhibit dynamical procedure for producing Talbot carpets for this specific extended NLSE. In Sect. 4, we build double-periodic RWs on a dnoidal background for the quintic equation and arrange them also in the form of Talbot carpets. In Sect. 5, we summarize our results.

2 Dynamical double-periodic solutions of the extended NLSE

In this paper, we study double-periodic solutions of the extended nonlinear Schrödinger equation, called the quintic NLS equation (QNLSE)

$$i\psi_x + S[\psi(x,t)] - i\alpha H[\psi(x,t)] + \gamma P[\psi(x,t)] - i\delta Q[\psi(x,t)] = 0. \tag{1}$$

Here, the transverse variable is denoted by t and the longitudinal variable by x, while α, γ and δ are arbitrary real numbers used to introduce higher-order terms. The wave function $\psi \equiv \psi(x,t)$ represents the slowly varying envelope that could be optical, plasmonic or other in nature. A distinct value of Eq. (1) is that it represents a general extension of the NLS equation to the quintic order that includes in a consistent manner various dispersive and nonlinear contributions of relevance to the propagation of pulses in fibers.

Operators S, H, P, and Q comprise the nonlinearity terms and higher-order spatial dispersions. They arise in an infinite hierarchy of NLSEs [7,8,35]. Their expressions are as follows:

$$S[\psi(x,t)] = \frac{1}{2}\psi_{tt} + |\psi|^2\psi, \tag{2}$$

$$H[\psi(x,t)] = \psi_{ttt} + 6|\psi|^2\psi_t, \tag{3}$$

$$P[\psi(x,t)] = \psi_{tttt} + 8|\psi|^2\psi_{tt} + 6|\psi|^4\psi + 4|\psi_t|^2\psi + 6\psi_t^2\psi^* + 2\psi^2\psi_{tt}^*, \tag{4}$$

$$Q[\psi(x,t)] = \psi_{ttttt} + 10|\psi|^2\psi_{ttt} + 30|\psi|^4\psi_t + 10\psi\psi_t\psi_{tt}^* + 10\psi\psi_t^*\psi_{tt} + 20\psi^*\psi_t\psi_{tt} + 10\psi_t^2\psi_t^*, \tag{5}$$

where the subscripts t [and x in Eq. (1)] represent the partial derivatives. Additional terms of higher-order dispersion and nonlinearity are required for the description of ultrashort pulse propagation through optical fibers [2,36–39].

The third-order term (Hirota) is used to explain the generation of supercontinuum [5] and pulse-deforming phenomena in fibers [40]. The fourth-order (Lakshmanan–Porsezian–Daniel) operator appears in the analysis of Heisenberg spin chains [35]. The fifth-order dispersion (quintic) is noticeable in laser experiments with ultrashort pulse duration (below 20 fs) [41].

When $\alpha = \gamma = \delta = 0$, Eq. (1) reduces to the well-known cubic NLSE, which is the fundamental equation of nonlinear optics [4,9,20,42,43]. If only $\alpha \neq 0$, we deal with the Hirota equation [44–47]. In case of nonzero α and δ with $\gamma = 0$, we talk about Hirota–quintic equation.

Various solutions of the QNLSE, such as solitons [48,49], breathers [49,50], and RWs [51], have been discussed in the literature. It is well known that breathers and solitons of arbitrary order can be obtained analytically using the DT technique. These solutions are single periodic: breathers along t, and solitons along x direction. Single-periodic NLSE solutions, such as ABs, can be utilized to dynamically construct nonlinear Talbot carpets, which are also intimately connected with the double-periodic solutions of NLSE.

The period of an AB (first order or higher order) is determined by the single parameter $a < 0.5$ of the solution [9]:

$$L = \frac{\pi}{\sqrt{1-2a}}. \tag{6}$$

The initial condition for dynamical generation is derived from exact AB solutions at a certain value of the evolution variable $x = x_0$, using Darboux transformation [52]. Here, it is essential to adjust the size of the transverse box (t_1, t_2) to an integer multiple M of the fundamental breather's period and apply periodic boundary conditions,

$$\Delta T = t_2 - t_1 = ML. \tag{7}$$
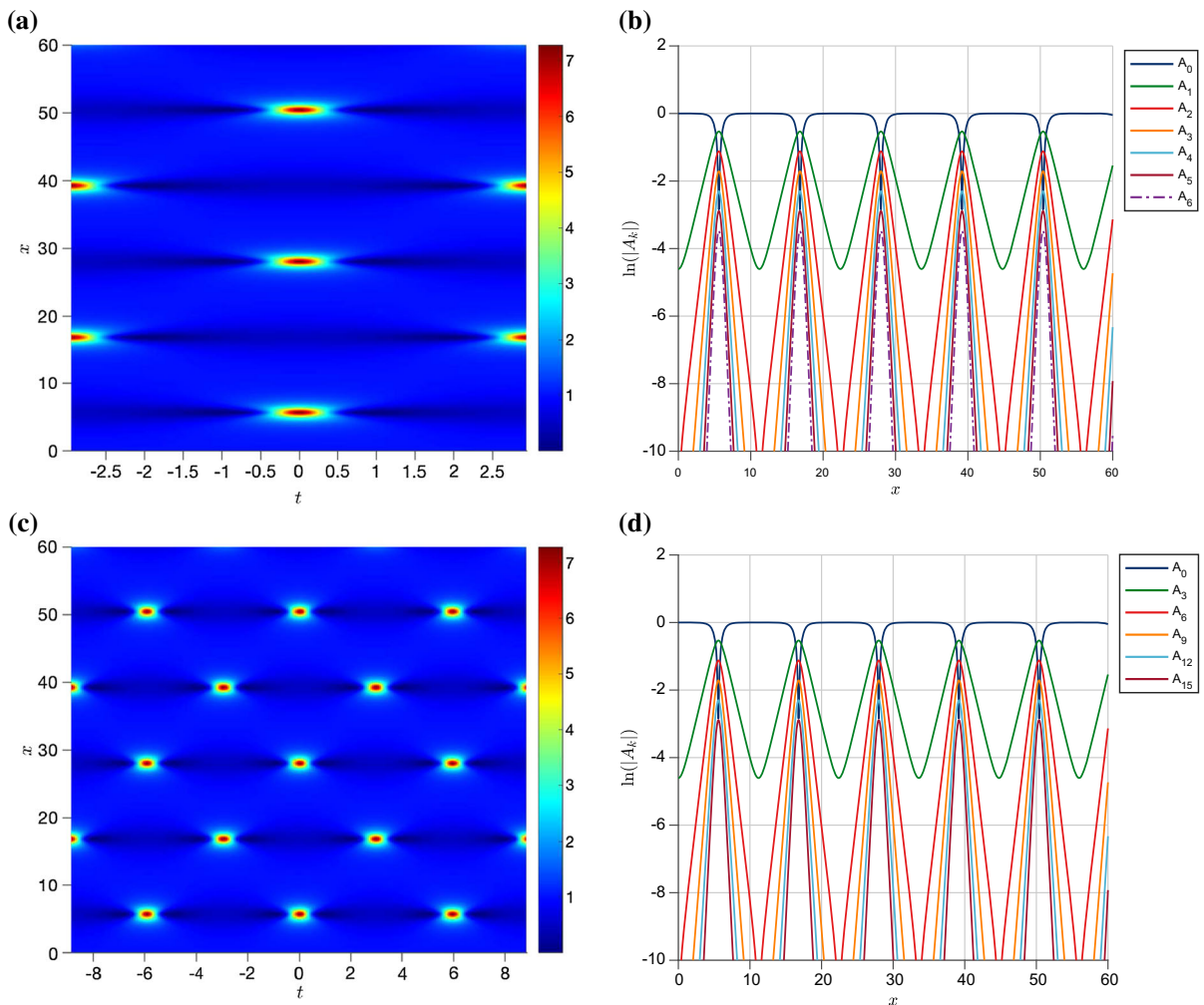
(a)

(b)

(c)

(d)

Fig. 1 Double-periodic numerical solutions, made of the first-order NLSE breathers ($\alpha = \gamma = \delta = 0$), using the pruning procedure in FFT. The breather parameter is $a = 0.36$. **a** One breather in the box, no pruning. **b** Its spectrum. **c** Three breathers (3 periods) in the box, with the pruning. **d** The corresponding spectrum

Numerical solutions of NLSEs in this paper are obtained using the second-order split-step fast Fourier transform (FFT) method. When the box size is exactly equal to the breather's fundamental period L, the Fourier harmonics form the basic set of spatial frequencies

$$S_1 = \left\{ \omega_j = j\Omega; \, | \, 0 \leq j < N \right\}, \qquad (8)$$

where $\Omega = 2\pi/L$ is the mode spacing and N the total number of modes. The mode growing out of this basic set will be the stable fundamental breather mode. However, if the box is larger ($M > 1$), the fundamental

mode and mode spacings are smaller $\Omega_M = \Omega/M$, and Fourier modes form a new set S_M with a larger number of modes (NM). All modes from S_M that are not elements of S_1 exponentially grow from infinitesimal amplitudes, owing to modulation instability. Now, the modes from S_1 are also under MI and grow exponentially, but they interfere constructively and only form the fundamental AB mode.

The key point in generating nonlinear Talbot carpets is to suppress the undesirable unstable Fourier modes. This can be achieved in different ways. In the simplest, after each numerical iteration one simply eliminates the unstable subharmonics, leaving only the ones responsi-
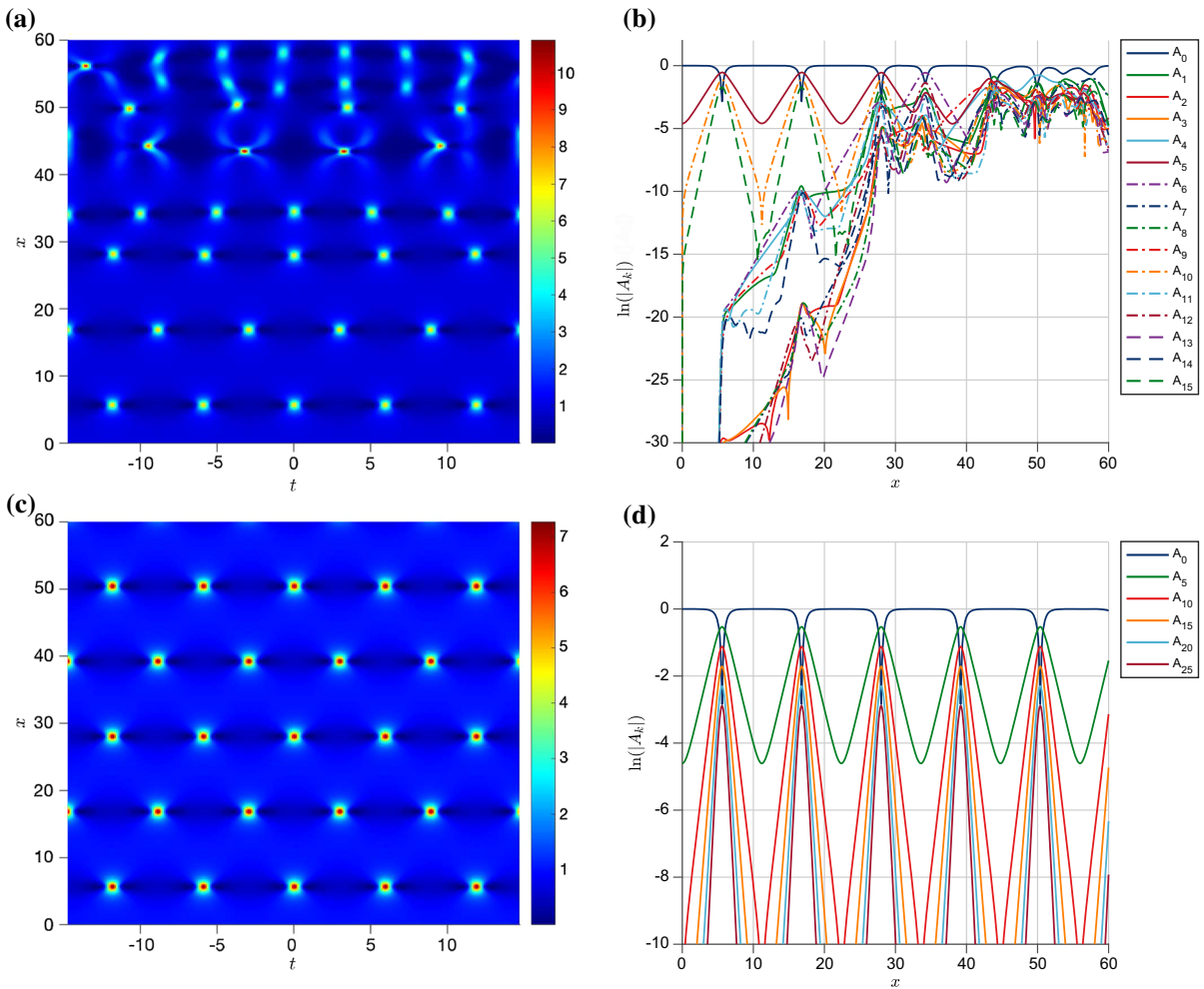
(a)

(b)

(c)

(d)

Fig. 2 Dynamical generation of Talbot carpet from the first-order breathers using a DT initial condition, with $a = 0.36$ and $M = 5$. **a** A failed attempt, due to MI. **b** The corresponding Fourier spectrum, displaying loss of Talbot periodicity due to the exponential growth of non-quintuplet modes. **c** Successful generation of the Talbot carpet using the pruning procedure. **d** Fourier spectrum after the pruning is applied

ble for the formation of the fundamental AB (labeled as $0, \pm M, \pm 2M, \pm 3M$, etc). It effectively eliminates MI. The procedure is illustrated in Fig. 1. Although quite drastic, it apparently works. The other ways include suppressing the unstable modes selectively and to a degree.

In Fig. 1a, we show numerical evolution of the first-order Akhmediev breather ($a = 0.36$) when the box size is equal to the breather's period ($M = 1$). One can see that the intensity peak at $t = 0$ is repeated along x-axis at the Talbot periods, forming a stable mode. This peak is consecutively shifted for half a period along t-axis, forming the secondary Talbot image at half the Talbot period. The corresponding Fourier spectrum is shown in Fig. 1b. Next, we calculate the same breather over three periods ($M = 3$). We apply the simple pruning algorithm to Fourier modes, setting all unstable mode amplitudes to zero except the triplet modes, indexed as $0, \pm 3, \pm 6, \pm 9$, and so on. The result is an extended Talbot carpet with alternate shifting of intensity maxima along x- and t-axes, as presented in Fig. 1c. The spectrum of the triplet mode amplitudes is shown in Fig. 1d.

In Fig. 2, we display how the simple pruning technique actually works. We again choose the first-order breather with $a = 0.36$ and set the numerical box to
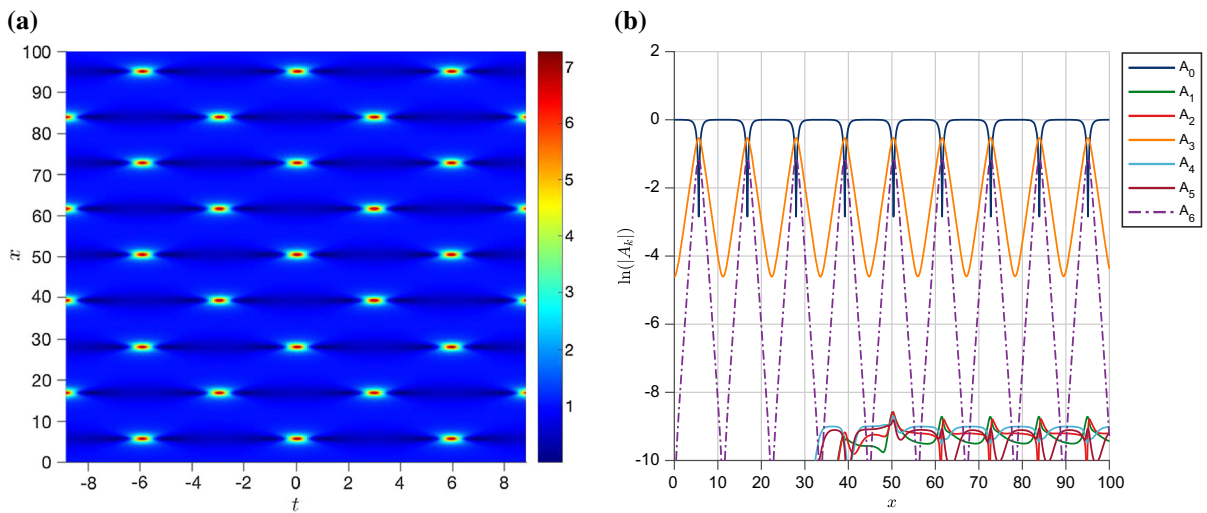
(a)

(b)

Fig. 3 Same as Fig. 1 but with Gaussian pruning. **a** The carpet. **b** Its spectrum. The modes at the bottom are the suppressed unstable modes

be exactly five times the breather's period: $M = 5$. In this case, the AB will be formed by the modes $A_0, A_5, A_{10}, \ldots, A_{5m}$. If the pruning algorithm is not applied, the chaotic behavior ruins the carpet after just one full Talbot cycle, as shown in Fig. 2a. This is the MI in action: The unstable modes grow exponentially and prevent the homoclinic orbit (the initial AB mode) from returning to itself after more than one cycle. This is clearly observed in the buildup of Fourier spectrum of all modes (Fig. 2b), which destroys the spatial Talbot periodicity. Note that after the full cycle, another displaced AB appears but not at half-cycle, interacting
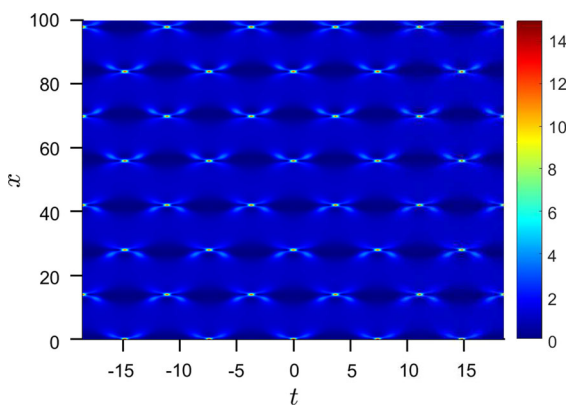
with the full mode. As a result of this interaction, or beating of the two modes, two second-order ABs (that can be regarded as the second-order RWs) are formed around $x = 45$, which constitutes the normal channel for the production of RWs through MI. However, when the pruning procedure is applied, all non-quintuplet modes are killed after each iteration. Effectively, the procedure prevents the orbit to wander in the homoclinic tangle, forcing it to stick to itself and return back to the starting point. The result is the perfect nonlinear Talbot carpet (Fig. 2c), with the perfect Fourier spectrum (Fig. 2d).

In Fig. 3, we illustrate the Gaussian pruning algorithm, in which the unstable modes are not eliminated completely but suppressed by a Gaussian factor. Thus, the unstable modes are multiplied by a Gaussian factor that depends on their strength: When weak, they are allowed to grow; but the more they grow the more they are suppressed. Effectively, they can grow only up to a certain level, determined by the Gaussian distribution. In Fig. 3b, the unstable modes, visible at the bottom of the figure, cannot grow above the level of approximately 10^{-9}.

In Fig. 4, we present the nonlinear Talbot carpet consisting of the second-order breathers with consequently higher peak intensity. It can be regarded as a carpet composed of rogue waves. The box size is five times the fundamental breather period, having $a = 0.41$. This breather contains two unstable modes. Initial con-

Fig. 4 Double-periodic numerical solution of NLSE, made of the second-order breathers, having $a = 0.41$. The box contains 5 breather's periods. The solution is obtained using the pruning procedure

ditions were derived from DT along a line passing through the breather's maximum. As in the previous figures, the simple pruning algorithm was used, which left only the quintuplet Fourier modes intact.

Obtaining Talbot carpets composed of the third-order ABs required tedious mode elimination procedure, due to inherent instability of such solutions and low probability of the triple collisions of breather's constituents in the xt-plane. No effective pruning algorithm could be devised yet, although different mode pruning techniques produced nonuniform carpets of extended stability. We are actively engaged in this investigation, and hope to resolve the issues in a future publication.

3 Talbot carpets for the Hirota and Hirota–quintic equation

A family of double-periodic solutions of NLSE that include Jacobi elliptic functions (JEFs) is presented in [12] and in Eq. (6) of [21]. Here, we report the generalization of this expression to the exact solution of the Hirota–quintic equation:

$$
\begin{aligned}
&\psi(x, t) \\
&= \frac{k}{\sqrt{2}} \frac{A(x, t) \cdot \mathrm{dn}\left(\frac{kx}{2}, g = \frac{1}{k}\right) + \frac{i}{k}\mathrm{sn}\left(\frac{kx}{2}, g = \frac{1}{k}\right)}{1 - A(x, t) \cdot \mathrm{cn}\left(\frac{kx}{2}, g = \frac{1}{k}\right)} \cdot \\
&\quad \cdot e^{ix/2},
\end{aligned}
\tag{9}
$$

where

$$
\begin{aligned}
&A(x, t) \\
&= \frac{\mathrm{cn}\left(\sqrt{k}\left(t + 2\alpha x + \left(4 - \frac{1}{2}k^2\right)\delta x\right), g = \sqrt{\frac{k-1}{2k}}\right)}{\sqrt{1 + k}}
\end{aligned}
\tag{10}
$$

g is the elliptic modulus, $m = g^2$ is the elliptic modulus squared, and k is a positive real constant. The JEF functions $\mathrm{sn}(x, g)$, $\mathrm{cn}(x, g)$, and $\mathrm{dn}(x, g)$ are all periodic, with the periods $4K$, $4K$, and $2K$, respectively, where $K(m) = \int_0^{\pi/2} d\theta/\sqrt{1 - g^2\sin^2\theta}$ is the complete elliptic integral of the first kind. Therefore, solutions described in Eq. (9) are periodic in both t and x directions for any $k > 0$. They allow the formation of Talbot carpets for the extended NLSE, up to the fifth-order dispersion.

We use analytical solution from Eq. (9) to dynamically generate Talbot carpets for the Hirota equation ($\alpha \neq 0$, $\gamma = \delta = 0$). We calculate initial conditions for numerics at some particular x value using Eq. (9). However, the numerical algorithm is different from the basic NLS equation. Since we have $6|\psi|^2\psi_t$ terms in the H operator, comprising both dispersion and nonlinearity in a single term, it is not convenient to use FFT. Instead, we use a finite difference method to calculate derivatives and the fourth-order explicit Runge–Kutta method for the evolution of the wave function.

In Fig. 5a, we show a failed attempt to dynamically generate Hirota Talbot carpet ($\alpha = 0.2712$, $\gamma = \delta = 0$, and $k = 1.7286$). The box is exactly equal to 10 periods along the t-axis. At $x \approx 25$, modulation instability starts to ruin the carpet, leading to chaotic behavior of the modes. The intensity peaks are smeared and of lower intensity, since the unstable modes increase their amplitudes during evolution. To overcome the influence of MI, after each few iterations we perform the FFT of $\psi(x, t)$ and then set the amplitudes of all modes to zero, except for the modes with indices 0, ± 10, ± 20, ± 30, etc. In this manner, modulation instability is suppressed and Talbot carpet produced, as shown in Fig. 5b. The numerical solution obtained in this way is equal to the analytical one, all the way to the total calculation time ($x = 60$).

In the next example, we exhibit analytical Talbot carpets of the Hirota–quintic equation, having $\gamma = 0$ and $k = 1.772$. No pruning is needed here. In Fig. 6a, we show Talbot carpet obtained for $\alpha = -0.2712$ and $\delta = -0.1$. In general, the breathers are tilted. One can infer that the tilt of each breather-like structure to the right is caused by the negative signs of quintic parameters. If signs of α and δ are changed, identical intensity patterns will be produced, but with the tilt in the opposite direction (Fig. 6b). If α and δ have different signs, then Hirota and quintic terms will tend to tilt and stretch intensity maxima in different directions. For the given values of α and δ, one can balance the action of H and Q operators, and obtain a solution that satisfies both the NLSE and Hirota–quintic equations. This condition is met when the coefficient which multiplies x in Eq. (10) is set to zero: $2\alpha + (4 - k^2/2)\delta = 0$. From this expression, for $\alpha = -0.2712$ and $k = 1.772$, one can calculate $\delta = -4\alpha/(8 - k^2) = 0.2232$. The solution so found is straight Talbot carpet, as shown in Fig. 6c.
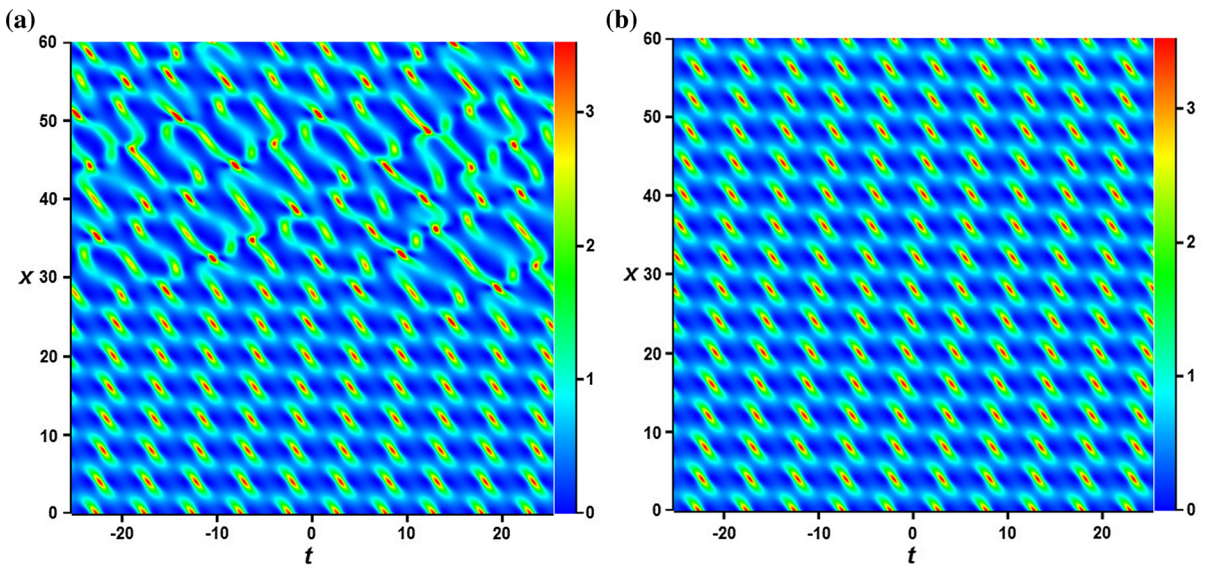
(a)

(b)

Fig. 5 Hirota Talbot carpet (numerical evolution) with 10 periods in a box. Initial conditions are given by analytical expression (9), with $\alpha = 0.2712$, $\gamma = \delta = 0$ and $k = 1.7286$. **a** Normal evolution of the initial breather, with MI included. **b** Talbot carpet, with the pruning procedure applied
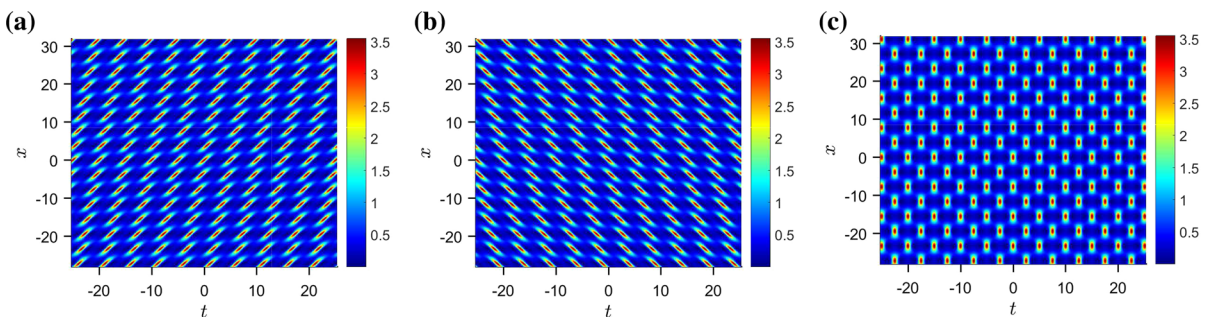
(a)

(b)

(c)

Fig. 6 Talbot carpet of Hirota–quintic equation ($\gamma = 0$ and $k = 1.772$). Parameters are: **a** $\alpha = -0.2712$ and $\delta = -0.1$, **b** $\alpha = 0.2712$ and $\delta = 0.1$, **c** $\alpha = -0.2712$ and $\delta = -\frac{4\alpha}{8-k^2} = 0.2232$

(a)

(b)
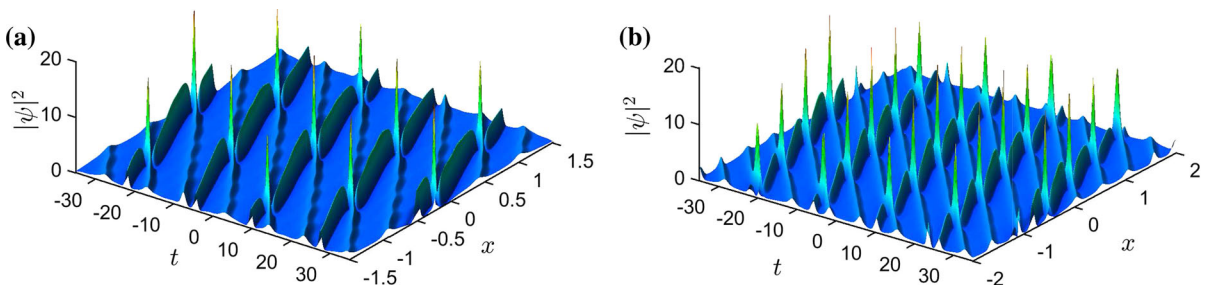
Fig. 7 Quintic Talbot carpet made of the second-order breathers that are matched mutually and to the dn background wave. Parameters: $c = 1$, $\alpha = -0.03$, $\gamma = -0.0614$, $\delta = 0.7$: **a** $m = 0.1192$, $\nu_1 = 0.92$, $\nu_2 = 0.83$, $q = 9$. **b** $m = 0.0505$, $\nu_1 = 0.92$, $\nu_2 = 0.8104$, $q = 8$

4 Double-periodic rogue waves of the quintic equation using period-matching procedure

In this section, we discuss the numerical procedure for generating double-periodic RW solutions of the quintic equation ($\alpha \neq 0$, $\gamma \neq 0$, $\delta \neq 0$). These are basically higher-order breathers obtained by the Darboux transformation technique, when one sets JEFs as the starting seed solutions $\psi_0(x, t)$. Being doubly periodic, they can appear in the form of Talbot carpets. Hence, no pruning procedure is necessary, owing to the extensive and very precise period matching that ensures constructive nonlinear interference of modes and prevents the growth of unstable sidebands. Only the fundamental double-periodic RW mode can grow. This is similar to the generation of the stable AB in Fig. 1, where also no pruning was necessary.

The discussion here leans a lot on the results obtained in [53]. We choose the dn function as the background [7,8,53]:

$$\psi_0(x, t) = c e^{i\phi x} \mathrm{dn}\left(ct + vx, m\right), \qquad (11)$$

with $\phi = \frac{1}{2}(2 - m)c^2 + \gamma c^4\left(6 - 6m + m^2\right)$ and $v = (2 - m)\alpha c^3 + \delta c^5\left(6 - 6m + m^2\right)$. Next, we calculate an arbitrary-order breather on the elliptic background, using the procedure described in detail in [53].

As shown in Sect. 5 of [53], the matching of the higher-order breather period T_B to the period of the dn background T_{dn} may lead to the appearance of periodic RWs. This means that the ratio of periods $q = T_B/T_{dn}$ should be a positive integer. In addition, it is also needed to match the periods T_{B1}, ..., T_{BK} of the DT constituents that form a Kth-order breather ($T_{Bj} = T_{B1}/j$, for $j = 2, \ldots, K$) with the background. An intricate period-matching procedure ensues, which leads to a Talbot carpet of periodic RWs that requires no pruning.

Two examples of the quintic Talbot carpets, consisting of the second-order breathers, are shown in Fig. 7. We take $c = 1$, $\alpha = -0.03$, $\gamma = -0.0614$, and $\delta = 0.7$. We use expressions from [53] to calculate $m = 0.1192$, $v_1 = 0.92$, and $v_2 = 0.83$, leading to $q = 9$ and $T_{B2} = T_{B1}/2$. Here, v_1 and v_2 are the eigenvalues of the first two unstable modes, according to the DT. We get the double-periodic rogue wave shown in Fig. 7a. Similarly, we take the second set of values: $m = 0.0505$, $v_1 = 0.92$, and $v_2 = 0.8104$, and obtain

$q = 8$. The result is another quintic Talbot carpet, seen in Fig. 7b.

5 Conclusion

In this paper, we have presented dynamical procedure for generating Talbot carpets from the solutions of generalized NLSEs, consisting of the first- and second-order breathers. We have shown that to this end, it is necessary to calculate the initial wave for numerics using DT, and to set the transverse box size equal to an integer number of breather periods.

We have introduced two pruning algorithms, by which unstable Fourier modes that produce modulation instability and may ruin the carpet are eliminated or suppressed (except the ones building the fundamental breather).

We have next displayed new exact Talbot carpet solutions of the Hirota–quintic equation, which is a generalization of the NLSE resulting from a consistent Taylor expansion of dispersive and nonlinear terms. We have analyzed how the three parameters in the equation affect intensity distributions in the carpet. We pointed out that for particular combination of the parameter values, common solutions of both NLSE and Hirota–quintic equation can be obtained.

In the end, we applied the analysis from our previous work to generate doubly periodic rogue waves of the quintic equation. We used an extensive period matching of higher-order breathers and an elliptic background on which the breather is constructed, to produce rare periodic RWs which obliviate the need for using the pruning procedure to suppress MI.

We believe that various Talbot carpet solutions of extended nonlinear Schrödinger equations (up to the fifth-order dispersion) can find applications within the broad class of self-imaging phenomena and possibly for nano-photonic lithography. An interesting extension of this work is to invent pruning techniques that are amenable to experimental generation of modes in fibers, in which only the adverse effects of MI are suppressed.

References

1. Kivshar, Y.S., Agrawal, G.P.: Optical Solitons. Academic Press, San Diego (2003)
2. Agrawal, G.P.: Applications of Nonlinear Fiber Optics. Academic Press, San Diego (2001)
3. Fibich, G.: The Nonlinear Schrödinger Equation. Springer, Berlin (2015)
4. Dudley, J.M., Dias, F., Erkintalo, M., Genty, G.: Instabilities, breathers and rogue waves in optics. Nat. Photon. **8**, 755 (2014)
5. Dudley, J.M., Taylor, J.M.: Supercontinuum Generation in Optical Fibers. Cambridge University Press, Cambridge (2010)
6. Solli, D.R., Ropers, C., Koonath, P., Jalali, B.: Optical rogue waves. Nature **450**, 1054 (2007)
7. Ankiewicz, A., Kedziora, D.J., Chowdury, A., Bandelow, U., Akhmediev, N.: Infinite hierarchy of nonlinear Schrödinger equations and their solutions. Phys. Rev. E **93**, 012206 (2016)
8. Kedziora, D.J., Ankiewicz, A., Chowdury, A., Akhmediev, N.: Integrable equations of the infinite nonlinear Schrödinger equation hierarchy with time variable coefficients. Chaos **25**, 103114 (2015)
9. Chin, S.A., Ashour, O.A., Belić, M.R.: Anatomy of the Akhmediev breather: cascading instability, first formation time, and Fermi–Pasta–Ulam recurrence. Phys. Rev. E **92**, 063202 (2015)
10. Bogolubov, N.: On the theory of superfluidity. J. Phys. (USSR) **11**, 23 (1947)
11. Akhmediev, N.N., Korneev, V.I.: Modulation instability and periodic solutions of the nonlinear Schrödinger equation. Theor. Math. Phys. **69**, 1089 (1986)
12. Akhmediev, N., Eleonskii, V., Kulagin, N.: Exact first-order solutions of the nonlinear Schrödinger equation. Theor. Math. Phys. **72**, 809 (1987)
13. Erkintalo, M., Hammani, K., Kibler, B., Finot, C., Akhmediev, N., Dudley, J.M., Genty, G.: Higher-order modulation instability in nonlinear fiber optics. Phys. Rev. Lett. **107**, 253901 (2011)
14. Chin, S.A., Ashour, O.A., Nikolić, S.N., Belić, M.R.: Maximal intensity higher-order Akhmediev breathers of the nonlinear Schrödinger equation and their systematic generation. Phys. Lett. A **380**, 3625 (2016)
15. Herbst, B.M., Ablowitz, M.J.: Numerically induced chaos in the nonlinear Schrödinger equation. Phys. Rev. Lett. **62**, 2065 (1989)
16. Ablowitz, M.J., Herbst, B.M.: On homoclinic structure and numerically induced chaos for the nonlinear Schrödinger equation. SIAM J. Appl. Math. **50**, 339 (1990)
17. Calini, A., Schober, C.M.: Homoclinic chaos increases likelihood of rogue wave formation. Phys. Lett. A **298**, 335 (2002)
18. Calini, A., Schober, C.M.: Dynamical criteria for rogue waves in nonlinear Schrödinger models. Nonlinearity **25**, R99 (2012)
19. Toenger, S., Godin, T., Billet, C., Dias, F., Erkintalo, M., Genty, G., Dudley, J.M.: Emergent rogue wave structures and statistics in spontaneous modulation instability. Sci. Rep. **5**, 10380 (2015)
20. Akhmediev, N., et al.: Roadmap on optical rogue waves and extreme events. J. Opt. **18**, 063001 (2016)
21. Zhang, Y.Q., Belić, M.R., Zheng, H., Chen, H., Li, C., Song, J., Zhang, Y.P.: Nonlinear Talbot effect of rogue waves. Phys. Rev. E **89**, 032902 (2014)
22. Zhang, Y., Belić, M.R., Petrović, M.S., Zheng, H., Chen, H., Li, C., Lu, K., Zhang, Y.: Two-dimensional linear and nonlinear Talbot effect from rogue waves. Phys. Rev. E **91**, 032916 (2015)
23. Talbot, H.F.: Facts relating to optical science. Philos. Mag. **9**, 401 (1836)
24. Wen, J., Du, S., Chen, H., Xiao, M.: Electromagnetically induced Talbot effect. Appl. Phys. Lett. **98**, 081108 (2011)
25. Zhang, Y.Q., Yao, X., Yuan, C.Z., Li, P.Y., Yuan, J.M., Feng, W.K., Jia, S.Q., Zhang, Y.P.: Controllable multiwave mixing Talbot effect. IEEE Photon. J. **4**, 2057 (2012)
26. Song, X.-B., Wang, H.-B., Xiong, J., Wang, K., Zhang, X., Luo, K.-H., Wu, L.-A.: Experimental observation of quantum Talbot effects. Phys. Rev. Lett. **107**, 033902 (2011)
27. Iwanow, R., May-Arrioja, D.A., Christodoulides, D.N., Stegeman, G.I., Min, Y., Sohler, W.: Discrete Talbot effect in waveguide arrays. Phys. Rev. Lett. **95**, 053902 (2005)
28. Deng, L., Hagley, E.W., Denschlag, J., Simsarian, J.E., Edwards, M., Clack, C.W., Helmerson, K., Rolston, S.L., Phillips, W.D.: Temporal, matter-wave-dispersion Talbot effect. Phys. Rev. Lett. **83**, 5407 (1999)
29. Ryu, C., Andersen, M.F., Vaziri, A., d'Arcy, M.B., Grossman, J.M., Helmerson, K., Phillips, W.D.: High-order quantum resonances observed in a periodically kicked Bose–Einstein condensate. Phys. Rev. Lett. **96**, 160403 (2006)
30. Ramezani, H., Christodoulides, D.N., Kovanis, V., Vitebskiy, I., Kottos, T.: PT-symmetric Talbot effects. Phys. Rev. Lett. **109**, 033902 (2012)
31. Pfeiffer, F., Bech, M., Bunk, O., Kraft, P., Eikenberry, E.F., Brönnimann, C., Grünzweig, C., David, C.: Hard-X-ray dark-field imaging using a grating interferometer. Nat. Mater. **7**, 134 (2008)
32. Zhang, Y., Wen, J., Zhu, S.N., Xiao, M.: Nonlinear Talbot effect. Phys. Rev. Lett. **104**, 183901 (2010)
33. Wen, J., Zhang, Y., Xiao, M.: The Talbot effect: recent advances in classical optics, nonlinear optics, and quantum optics. Adv. Opt. Photon. **5**, 83 (2013)
34. Ashour O.A.: Maximal Intensity Higher-Order Breathers of the Nonlinear Schrödinger Equation on Different Back-

grounds. Undergraduate Research Scholars Thesis, Texas A&M University, USA (2017)

35. Chowdury, A., Kedziora, D.J., Ankiewicz, A., Akhmediev, N.: Breather-to-soliton conversions described by the quintic equation of the nonlinear Schrödinger hierarchy. Phys. Rev. E **91**, 032928 (2015)

36. Trippenbach, M., Band, Y.B.: Effects of self-steepening and self-frequency shifting on short-pulse splitting in dispersive nonlinear media. Phys. Rev. A **57**, 4791 (1998)

37. Wang, D.-S., Chen, F., Wen, X.-Y.: Darboux transformation of the general Hirota equation: multisoliton solutions, breather solutions and rogue wave solutions. Adv. Differ. Equ. **2016**, 67 (2016)

38. Guo, R., Hao, H.Q.: Breathers and multi-solitons solutions for the higher-order generalized nonlinear Schrödinger equation. Commun. Nonlinear Sci. Numer. Simul. **18**, 2426–2435 (2013)

39. Mani Rajan, M.S., Mahalingam, A.: Nonautonomous solitons in modified inhomogeneous Hirota equation: soliton control and soliton interaction. Nonlinear Dyn. **79**, 2469–2484 (2015)

40. Anderson, D., Lisak, M.: Nonlinear asymmetric self-phase modulation and self-steepening of pulses in long optical waveguides. Phys. Rev. A **27**, 1393 (1983)

41. Backus, S., Durfee III, C.G., Mourou, G., Kapteyn, H.C., Murnane, M.M.: 0.2-TW laser system at 1 kHz. Opt. Lett. **22**, 1256 (1997)

42. Mirzazadeh, M., Eslami, M., Zerrad, E., Mahmood, M.F., Biswas, A., Belić, M.: Optical solitons in nonlinear directional couplers by sine-cosine function method and Bernoulli's equation approach. Nonlinear Dyn. **81**, 1933–1349 (2015)

43. Biswas, A., Khalique, C.M.: Stationary solutions for nonlinear dispersive Schroödinger equation. Nonlinear Dyn. **63**, 623–626 (2011)

44. Hirota, R.: Exact envelope-soliton solutions of a nonlinear wave equation. J. Math. Phys. **14**, 805–809 (1973)

45. Tao, Y., He, J.: Multisolitons, breathers, and rogue waves for the Hirota equation generated by the Darboux transformation. Phys. Rev. E **85**, 026601 (2012)

46. Guo, R., Zhao, X.-J.: Discrete Hirota equation: discrete Darboux transformation and new discrete soliton solutions. Nonlinear Dyn. **84**, 1901–1907 (2016)

47. Nikolić, S.N., Aleksić, N.B., Ashour, O.A., Belić, M.R., Chin, S.A.: Systematic generation of higher-order solitons and breathers of the Hirota equation on different backgrounds. Nonlinear Dyn. **89**, 1637–1649 (2017)

48. Chowdury, A., Kedziora, D.J., Ankiewicz, A., Akhmediev, N.: Soliton solutions of an integrable nonlinear Schrödinger equation with quintic terms. Phys. Rev. E **90**, 032922 (2014)

49. Lan, Z., Gao, B.: Solitons, breather and bound waves for a generalized higher-order nonlinear Schrödinger equation in an optical fiber or a planar waveguide. Eur. Phys. J. Plus **132**, 512 (2017)

50. Chowdury, A., Kedziora, D.J., Ankiewicz, A., Akhmediev, N.: Breather solutions of the integrable nonlinear Schrödinger equation and their interactions. Phys. Rev. E **91**, 022919 (2015)

51. Yang, Y., Yan, Z., Malomed, B.A.: Rogue waves, rational solitons, and modulational instability in an integrable fifth-order nonlinear Schrödinger equation. Chaos **25**, 103112 (2015)

52. Kedziora, D.J., Ankiewicz, A., Akhmediev, N.: Circular rogue wave clusters. Phys. Rev. E **84**, 056611 (2011)

53. Nikolić, S.N., Ashour, O.A., Aleksić, N.B., Belić, M.R., Chin, S.A: Breathers, solitons and rogue waves of the quintic nonlinear Schrödinger equation on various backgrounds. Nonlinear Dyn. **95**, 2855–2865 (2019)

CrossMark

ORIGINAL PAPER

Breathers, solitons and rogue waves of the quintic nonlinear Schrödinger equation on various backgrounds

Stanko N. Nikolić · Omar A. Ashour · Najdan B. Aleksić · Milivoj R. Belić · Siu A. Chin

Abstract We investigate the generation of breathers, solitons, and rogue waves of the quintic nonlinear Schrödinger equation (QNLSE) on uniform and elliptical backgrounds. The QNLSE is the general nonlinear Schrödinger equation that includes all terms up to the fifth-order dispersion. We use Darboux transformation to construct initial conditions for the dynamical generation of localized high-intensity optical waves. The condition for the breather-to-soliton conversion is provided with the analysis of soliton intensity profiles. We discover a new class of higher-order solutions in which Jacobi elliptic functions are set as background seed solutions of the QNLSE. We also introduce a method for generating a new class of rogue waves—the periodic rogue waves—based on the matching of the periodicity of higher-order breathers with the periodicity of the background dnoidal wave.

S. N. Nikolić (✉) · N. B. Aleksić
Institute of Physics Belgrade, University of Belgrade,
Pregrevica 118, Belgrade 11080, Serbia
e-mail: stankon@ipb.ac.rs

S. N. Nikolić · N. B. Aleksić · O. A. Ashour · M. R. Belić
Science program, Texas A&M University at Qatar,
23874 Doha, Qatar

O. A. Ashour · S. A. Chin
Department of Physics and Astronomy, Texas A&M
University, College Station, TX 77843, USA

O. A. Ashour
Department of Physics, University of California, Berkeley,
CA 94720, USA

1 Introduction

Current research on various nonlinear Schrödinger equations (NLSEs) with different dispersion and nonlinearity terms is incredibly rich and very intense, owing to their widespread use as mathematical models for physical systems in diverse fields, such as plasmas, Bose–Einstein condensates, nonlinear optics, and solid state physics [1–6]. Solitons, the solutions of NLSEs that keep their shapes during propagation and mutual interactions, as a result of balance between dispersive and nonlinear terms, are of special interest [4,6–10]. The properties revealed by the propagation and interaction of solitons play a vital role in developing many applications [11,12]. Therefore, it is important to find new soliton solutions to different physical models based on NLSEs and to study their properties.

In this paper, we study breathers, solitons, and rogue waves of the extended nonlinear Schrödinger equation, called the quintic equation

$$
\begin{aligned}
& i\psi_x + S[\psi(x,t)] - i\alpha H[\psi(x,t)] \\
& \quad + \gamma P[\psi(x,t)] - i\delta Q[\psi(x,t)] = 0,
\end{aligned}
\tag{1.1}
$$

where S, H, P, and Q are the specific operators arising in the systematic derivation of the infinite hierarchy of nonlinear Schrödinger equations [9,10]. They act on the optical slowly-varying wave envelope, denoted

by $\psi \equiv \psi(x, t)$, and systematically take into account increasing orders of dispersion and nonlinearity. As it is customary in the field of fiber optics, the transverse (temporal) variable is denoted by t and the longitudinal (spatial) variable by x.

The nonlinear Schrödinger operator S includes the basic second-order dispersion and Kerr nonlinearity:

$$S[\psi(x, t)] = \frac{1}{2}\psi_{tt} + |\psi|^2\psi. \qquad (1.2)$$

The NLSE with only these terms present is the fundamental equation of nonlinear optics [13], on which the whole edifice of higher-order NLSEs and various physical models are built. The Hirota operator H encompasses the third-order dispersion and the corresponding nonlinearity [14]:

$$H[\psi(x, t)] = \psi_{ttt} + 6|\psi|^2\psi_t. \qquad (1.3)$$

It is of importance in the generation of supercontinuum [8] and in pulse-deforming phenomena [15]. Operator P is called the Lakshmanan–Porsezian–Daniel (LPD) operator and it encloses the fourth-order dispersion and nonlinearity:

$$\begin{aligned} P[\psi(x, t)] = {} & \psi_{tttt} + 8|\psi|^2\psi_{tt} + 6|\psi|^4\psi + 4|\psi_t|^2\psi \\ & + 6\psi_t^2\psi^* + 2\psi^2\psi_{tt}^*. \end{aligned} \qquad (1.4)$$

It arises in the analysis of Heisenberg spin chains [16]. The quintic operator Q includes the fifth-order terms:

$$\begin{aligned} Q[\psi(x, t)] = {} & \psi_{ttttt} + 10|\psi|^2\psi_{ttt} + 30|\psi|^4\psi_t + 10\psi\psi_t\psi_{tt}^* \\ & + 10\psi\psi_t^*\psi_{tt} + 20\psi^*\psi_t\psi_{tt} + 10\psi_t^2\psi_t^*. \end{aligned} \qquad (1.5)$$

The fifth-order dispersion cannot be neglected in laser experiments producing ultrashort pulses, where the pulse duration reaches below 20 fs [17].

In Eq. (1.1), we follow the convention adopted in [16], calling the equation *quintic* and assuming that all three real parameters: α, γ and δ are in general nonzero (this is a slight change in notation as compared to [16], in which the term "quintic" is reserved for the case of $\alpha = \gamma = 0$ and $\delta \neq 0$). Also, this equation is slightly different from Eq. (1) in [18] having the same name, but including the $|\psi|^4\psi$ term with the second-order dispersion, rather than the fourth.

By setting all three parameters α, γ, and δ in Eq. (1.1) to zero, the QNLSE reduces to the basic NLSE, on which there exists a wealth of results [4,7,12,19–21]. By extending the NLSE to a more complex equation with variable coefficients, several novel optical solitary waves have been found [22]. Additional higher-order dispersion and nonlinearity terms in the NLSE are required to describe the propagation of ultrashort pulses through optical fibers [5,23–28].

Different solutions of the QNLSE, such as breathers [29,30], solitons [29,31], and rogue waves (RWs) [32], have been found and discussed in the literature. While higher-order dispersion terms are needed for a more accurate description of various propagation waves, the H, P, and Q operators (which contain more than just dispersion terms) were introduced based on the paramount concern of integrability. How best to choose the values α, γ and δ for a better, yet integral, description of any physical system remains an on-going process [9,16]. The aim of this work is to explore the impact of these higher-order nonlinear operators on breathers, solitons and rogue waves. The current work is an initial mathematical investigation rather than a final physical modeling. But, now that extensive numerical computations of these higher-order terms are available, we are in position to help experimenters in determining the optimal values of α, γ and δ for any physical system of interest.

The primary contributions of this work can be summarized as follows: (1) We presented the procedure for dynamical generation of high-intensity breathers and RWs on uniform background, based on the Darboux transformation (DT) method applied to QNLSE. (2) We provided conditions for the breather-to-soliton conversion in QNLSE and examined the transverse intensity profiles of such solitons when α, γ, and δ are nonzero. (3) We obtained new solutions of the QNLSE, when Jacobi elliptic functions (JEFs) are used as the seed waves in the DT scheme. (4) We discovered a new class of RWs, the periodic rogue waves. (5) We confirmed that the peak-height formula, introduced in [33], gives the correct peak value for all the higher-order solutions of QNLSE.

Some comments on the prior work are in order. Previously, the QNLSE has been analyzed as a specific member in the infinite NLSE hierarchy of equations [9,10]. There, new families of exact solutions have been presented that included the dnoidal/cnoidal JEFs (for an elementary introduction to JEFs, see [34]). The conversion of the breather to a soliton was analyzed in [16], but for the specific case of $\alpha = \gamma = 0$ and $\delta > 0$. Following similar lines to our combined analytical-numerical procedure for the Hirota and NLSE [35–37], here we

were able to find new solutions of QNLSE, when the dn JEF is taken as the seed wave function in the DT scheme. The algorithm is essentially the same as the one introduced in [33,35] for the Hirota equation, but the complexity of QNLSE required a more extensive and intricate numerical procedure to attain the stated goals. To this end, we extracted initial wave functions from the DT applied to the QNLSE and then propagated these functions to obtain dynamical propagating RW solutions at an arbitrary x.

In the end, we demonstrated a method for generating recurring high-intensity structures of the QNLSE on an elliptical background, which we call, paradoxically, the "periodic rogue waves". This is clearly explained in Sect. 5. Our work generalizes the procedure previously applied to the NLSE, as described in details in [38]. The new insight we bring to this work is the realization that *any* breather constructed on a periodic background will, in general, no longer be periodic. This is because the period of the breather will generally be incommensurate with the period of the background. For higher-order breathers, with more than two periods, the resulting disorder from more than two-wave mixing will destroy any periodicity, and they will therefore appear as solitary peaks on a noisy background—that is, as commonly understood RWs. However, by painstakingly matching the periods of the breathers to the background, one can resurrect the hidden periodic peaks obliterated by the background. Therefore, a new class of RWs will be produced, the *periodic* rogue waves.

This paper is organized as follows. In Sect. 2, we analyze the basic solutions of the QNLSE and show how higher-order breathers can be obtained numerically from the initial DT wave function. In Sect. 3, we provide the condition for the breather-to-soliton conversion. In Sect. 4, we present the procedure for calculating breathers and RWs on an elliptical background. In Sect. 5, we show how to build periodic RWs on a dnoidal background. In Sect. 6, we summarize our results. The general DT scheme for QNLSE is provided in "Appendix".

2 Breather solutions of the quintic equation on a uniform background

In this work, we evolve QNLSE numerically with a precisely determined initial wave function so that its intrinsic modulation instability focuses the initial wave function into breathers and RWs of different orders. The goal is to demonstrate that by adjusting the parameters of QNLSE to match realistic fiber propagation properties, the initial wave functions determined appropriately might be utilized in real experiments to produce higher-order RW structures physically. To this end, carefully chosen initial waves $\psi(x_0, t)$ at a particular value of the propagation variable $x = x_0$ are required, which can be derived by specific procedures coming from the inverse scattering theory, such as the DT. Then, the RWs are generated dynamically, by employing convenient numerical algorithms to evolve the wave function ψ over the entire (x, t) grid.

Exact first-order solutions of the infinite NLSE hierarchy are calculated in [9,10]. Here, we are interested in the more realistic case of QNLSE (1.1) and higher-order solutions. Thus, all the coefficients in the infinite hierarchy multiplying the sixth and higher-order dispersions will be set to zero, while the initial waves will be carefully chosen, so as to generate solutions of different orders. The solution procedure is as follows.

According to the inverse scattering theory of NLSE, the first-order breather solution $\psi_1(x, t)$, characterized by the complex eigenvalue

$$\lambda = r + i\nu, \tag{2.1}$$

is obtained from the DT scheme having the $\psi_0 = e^{i(1+6\gamma)x}$ plane-wave seed. It is of the form:

$$\psi_1(x, t) = \left(1 + 2\nu \frac{G_1 + iH_1}{D_1}\right) e^{i(1+6\gamma)x}. \tag{2.2}$$

Here:

$$
\begin{aligned}
G_1 &= \cos(\kappa_r t + d_r x)\cosh(2\chi_i) \\
&\quad - \cosh(\kappa_i t + d_i x)\sin(2\chi_r), \\
H_1 &= \sinh(\kappa_i t + d_i x)\cos(2\chi_r) \\
&\quad + \sin(\kappa_r t + d_r x)\sinh(2\chi_i), \\
D_1 &= \cosh(\kappa_i t + d_i x)\cosh(2\chi_i) \\
&\quad - \cos(\kappa_r t + d_r x)\sin(2\chi_r),
\end{aligned}
\tag{2.3}
$$

where the wavenumbers, frequencies and other parameters are:

$$
\begin{aligned}
\kappa &= 2\sqrt{1 + \lambda^2} = \kappa_r + i\kappa_i \\
\chi &= \frac{1}{2}\arccos\left(\frac{\kappa}{2}\right) = \chi_r + i\chi_i \\
\bar{d} &= 2(\alpha + 3\delta) + (1 + 4\gamma)\lambda - 4(\alpha + 2\delta)\lambda^2 \\
&\quad - 8\gamma\lambda^3 + 16\delta\lambda^4 \quad (\bar{d} = \bar{d}_r + i\bar{d}_i) \\
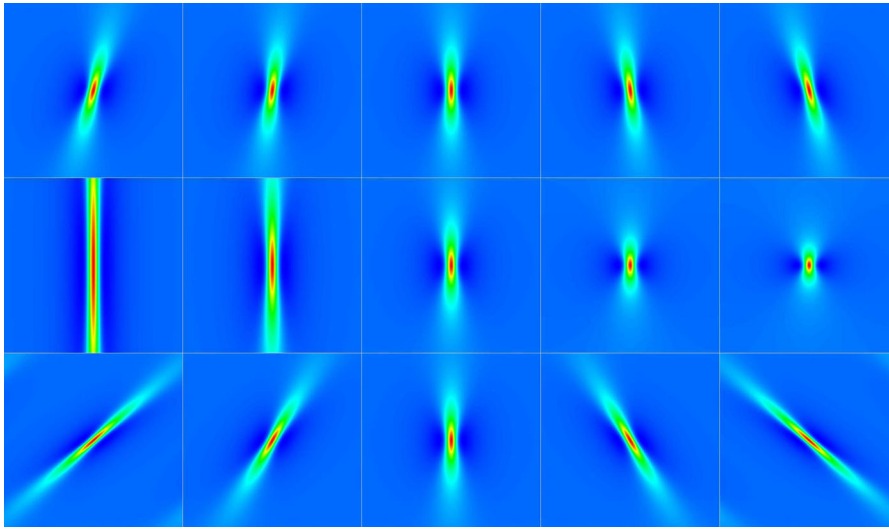d &= \kappa\bar{d} = d_r + id_i.
\end{aligned}
\tag{2.4}
$$

Fig. 1 First-order breather intensity distribution in the (x, t) plane for different values of parameters α, γ and δ. The eigenvalue is $\lambda \approx 0.97i$. In each row, one parameter is varied and the other two are set to zero. Top row: $\gamma = 0$, $\delta = 0$, $\alpha = -0.10, -0.05, 0, +0.05, +0.10$, from left to right. Middle row: $\alpha = 0$, $\delta = 0$, $\gamma = -0.10, -0.05, 0, +0.05, +0.10$, from left to right. Bottom row: $\alpha = 0$, $\gamma = 0$, $\delta = -0.10, -0.05, 0, +0.05, +0.10$, from left to right. In each panel, the transverse axis (horizontal) spans from $t = -6.3$ to 6.3 and the propagation axis (vertical) from $x = -2.5$ to 2.5

One can see that ψ_1 is periodic in the transverse direction (with the imaginary part of the eigenvalue $0 < \nu < 1$), i.e., it represents a breather. The frequency ω and the period L are solely determined by the imaginary part of the eigenvalue:

$$\omega = 2\sqrt{1 - \nu^2}, \quad L = \frac{\pi}{\sqrt{1 - \nu^2}}. \quad (2.5)$$

In Fig. 1, we show the first-order breathers with purely imaginary eigenvalues, to depict the influence of the QNLSE parameters α, γ and δ on the intensity distribution of ψ_1 in the (x, t) plane. In the top row, we varied parameter α from -0.1 to $+0.1$, keeping $\gamma = 0$ and $\delta = 0$. Analogously, in the middle (bottom) row, we changed only γ (δ) value. One can see that the larger absolute value of α introduces the bigger skew of the breather, while the sign of α determines to which side the breather is tilted. The parameter γ does not introduce the skew, but extends ($\gamma < 0$) or compresses ($\gamma > 0$) the breather along the evolution x-axis. As for δ, it also skews the breather (but stronger than α) and narrows its intensity profile. These observations also hold for the breathers on nonuniform backgrounds and for higher-order breathers (i.e., RWs) that will be covered in the next sections. These, as it will be seen, can

be calculated via a recursive DT scheme using the same seed for a given set of eigenvalues.

In order to create the Nth-order QNLSE breather dynamically, we have to preserve the fundamental periodicity of ψ_1 and thus choose periodic boundary conditions in numerics. The details of the procedure are given in [33,35]. Now, there are N eigenvalues, and we assume that initially each of these eigenvalues is purely imaginary $\lambda_j = i\nu_j$. We choose the eigenvalues such that the higher-order frequencies are equal to the integer multiples of the first-order frequency: $\omega_j = j\omega$ ($\nu_1 \equiv \nu$, $\omega_1 \equiv \omega$). It follows:

$$\lambda_j = i\nu_j = i\sqrt{j^2\nu^2 - (j^2 - 1)} \quad \text{for} \quad 2 \leq j \leq N. \quad (2.6)$$

The procedure is to take the initial ν, calculate other eigenvalues using the last equation and apply the DT, to calculate the appropriate initial wave condition across the transverse t-axis. That wave is then evolved numerically, starting from some value of x before the desired peak of the rogue wave and ending well past the peak. For numerical integration, we use a finite difference method, to calculate the derivatives up to fifth-order and the fourth-order explicit Runge–Kutta method for the evolution of the wave function. Due to the complexity and high nonlinearity of the quintic equation,
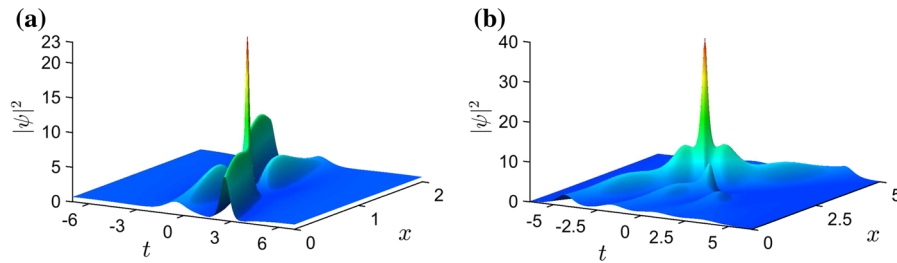
(a)

(b)

Fig. 2 Dynamically generated higher-order breathers of QNLSE on a uniform background. Initial wave functions are extracted from the DT solutions and then numerically evolved along coordinate x. The values of ν_1 are set at the beginning of the procedure, while other imaginary parts are calculated using Eq. (2.6). **a** The second-order breather: $\nu_1 = \sqrt{0.95}$, $\alpha = 0.0625$, $\gamma = 0.053$, $\delta = 0.043$. **b** The fourth-order breather: $\nu_1 = \sqrt{0.9384}$, $\alpha = -0.1625$, $\gamma = 0.017$, $\delta = 0.006$

derivatives are calculated with $O(h^{12})$ accuracy, where h is the step size along the t-axis.

In Fig. 2, we demonstrate the second- and fourth-order breathers obtained dynamically. In Fig. 2a, we choose $\nu_1 = \sqrt{0.95}$ for the first constituent breather and calculate ν_2 using Eq. (2.6). The parameters are: $\alpha = 0.0625$, $\gamma = 0.053$, and $\delta = 0.043$. In Fig. 2b, it is $\nu_1 = \sqrt{0.9384}$, $\alpha = -0.1625$, $\gamma = 0.017$, and $\delta = 0.006$. As explained before, the tilt and the stretching of breathers are caused by the QNLSE parameters. We also confirm that the peak intensities ($|\psi|^2_{\max} = 22.453$ in Fig. 2a and $|\psi|^2_{\max} = 39.029$ in Fig. 2b) are determined solely by the imaginary parts of eigenvalues, independent of α, γ, δ, in agreement with the peak-height formula derived in our previous work [33,35]. In fact, the same conclusion holds for the infinite hierarchy of NLSEs.

3 Breather-to-soliton conversion in the quintic equation

Usually, solitons cannot be obtained from breathers. However, in QNLSE, for the specific values of α, γ, and δ, the solitons can be directly obtained from the breather solutions. The breather-to-soliton conversion happens when the extrema of trigonometric and hyperbolic functions in Eq. (2.3) are located along the same straight lines in the (x,t) plane [16]. From Eq. (2.3), one can write:

$$\frac{d_r}{\kappa_r} = \frac{d_i}{\kappa_i}. \tag{3.1}$$

From this equation and Eq. (2.4), it follows:

$$\bar{d}_i = 0. \tag{3.2}$$

Assuming a general complex eigenvalue $\lambda = r + i\nu$, we use Eqs. (2.3) and (3.2) to derive a relation between α, γ, δ, and ν for which the breather-to-soliton conversion emerges:

$$8r\left(8r^2\delta - 3r\gamma - \alpha - 2\delta\right)$$
$$+ 8\nu^2(\gamma - 8r\delta) + 4\gamma + 1 = 0. \tag{3.3}$$

The soliton obtained in this manner is characterized by oscillatory tails at both sides of the central maximum. If we analyze the transverse soliton profile at $x = 0$, we see from Eq. (2.3) that the modulus of the wave function ψ is determined by the ratio of $\cos(\kappa_r t)$ to $\cosh(\kappa_i t)$. It follows that the number of side fringes depends on the quantity κ_r/κ_i. Similar "multi-peak" and W-shaped solitons were reported for the LPD equation, that is, Eq. (1.1) with $\alpha = \delta = 0$ [39,40].

In Fig. 3, we show two breather-to-soliton conversions under the condition of Eq. (3.3). One chooses the real and imaginary parts of eigenvalue λ and of the two quintic parameters. The remaining parameter is then computed by Eq. (3.3). The soliton in Fig. 3a is formed for $\lambda = 0.75 + 0.9i$, $\alpha = 0.75$, $\gamma = -0.12$, $\delta = -0.13139$. For the soliton in Fig. 3b, we have $\lambda = 0.057 + 0.85i$, $\alpha = \frac{1}{12}$, $\gamma \approx -0.08397$, $\delta = \frac{1}{24}$. In the first case, one sees one fringe at both sides of the soliton maximum, due to the low $k_r/k_i \approx 1.7$ ratio. In the second case, several fringes are seen, since $\kappa_r/\kappa_i \approx 6$.

4 Solutions of the quintic equation on an elliptical background

Rogue waves in nature never appear on a flat background. There is always a wavy background, on which
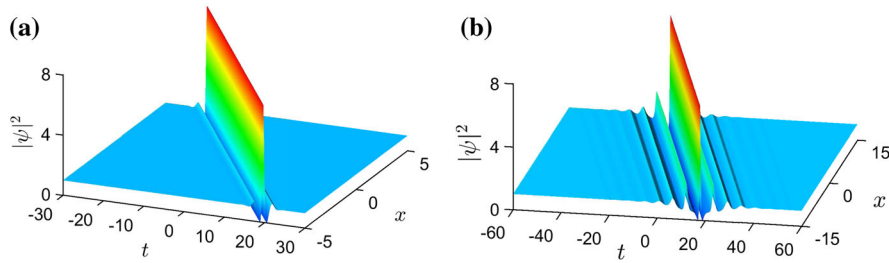
(a)

(b)

Fig. 3 Conversion of the first-order breather of QNLSE to a soliton: **a** $\lambda = 0.75 + 0.9i$, $\alpha = 0.75$, $\gamma = -0.12$, $\delta = -0.13139$ and $\kappa_r/\kappa_i \approx 1.7$, **b** $\lambda = 0.057 + 0.85i$, $\alpha = \frac{1}{12}$, $\gamma \approx -0.08397$, $\delta = \frac{1}{24}$ and $\kappa_r/\kappa_i \approx 6$

under certain circumstances suddenly giant waves appear. Therefore, of particular interest are localized solutions that grow on nonuniform backgrounds [35]. It is shown in [37] that the general form of NLSE solution on an elliptical background can include only two JEFs, cn or dn. We generalize this finding to the QNLSE.

Exact solutions of the QNLSE that include JEFs are presented in [9,10]:

$$\psi_{dn}(x, t) = ce^{i\phi x} dn (ct + vx, m),\tag{4.1}$$

$$\psi_{cn}(x, t) = \frac{c}{\sqrt{2}}\sqrt{s + 1}e^{i\phi x}$$
$$\cdot cn\left(\sqrt{s}ct + \sqrt{s}vx, m = \frac{1}{2} + \frac{1}{2s}\right).\tag{4.2}$$

Here we produce analogous solutions dynamically. With $m = g^2$ we denote the elliptic modulus squared, c is an arbitrary constant, while ϕ and v are quantities determined by α, γ, δ, m, and c, as specified below. We can use any of these functions as a seed in the DT scheme to calculate the Nth-order breathers on elliptical backgrounds. The matrices U and V, necessary for the DT scheme of the quintic NLSE, are given in "Appendix".

Note that all results obtained for the Hirota equation and presented in [35], can be obtained by the method of this section, when $\gamma = \delta = 0$ is chosen. However, here we aim at obtaining more general solutions of the QNLSE.

4.1 Applying the DT scheme to $\psi_0 = \psi_{dn}$

We now apply the DT procedure, as described in "Appendix". We first examine the case when the seed function ψ_0 is given by Eq. (4.1), with $\phi = \frac{1}{2}(2 - m)c^2 + \gamma c^4(6 - 6m + m^2)$ and $v = (2 - m)$

$\alpha c^3 + \delta c^5(6 - 6m + m^2)$ [10]. To solve a system of four coupled linear differential equations for Lax pairs r_t, s_t, r_x and s_x (subscripts indicate partial derivatives), we use the traveling wave variable u

$$u = ct + vx,\tag{4.3}$$

and replace the t-derivatives with the u-derivatives. Having in mind the form of equations, we try the solutions of the form:

$$r(x, u) = g(x, u)e^{-i\phi x/2}, \quad s(x, u) = h(x, u)e^{+i\phi x/2}.\tag{4.4}$$

We skip the derivation details, which can be found in [35]. First, one finds the u-derivatives of g and h:

$$g_u = i\frac{\lambda}{c}g + i \cdot dn(u)h,\tag{4.5}$$

$$h_u = i \cdot dn(u)g - i\frac{\lambda}{c}h.\tag{4.6}$$

Next, one provides the constants A and B for the quintic case (cf. "Appendix"):

$$A = \left(4\lambda^2 - mc^2\right)\left(\frac{1}{4} - \alpha\lambda\right)$$
$$+ (\gamma - 2\delta\lambda)\left[4\lambda^2\left(c^2 - 2\lambda^2\right) - \frac{1}{2}mc^4(2 - m)\right],\tag{4.7}$$

$$B = c\lambda\left[(1 - 4\alpha\lambda) + 2(\gamma - 2\delta\lambda)\left[(2 - m)c^2 - 4\lambda^2\right]\right].\tag{4.8}$$

The solution for the Lax pair generating functions, with the eigenvalues λ_j and x-shifts x_{0j} ($1 \leq j \leq N$) is:

$$r_{1j}(x, u = 0) = 2ie^{-i\phi(x - x_{0j})/2}$$
$$\cdot \sin[+\chi_j + \kappa_j\lambda_j(x - x_{0j}) - \pi/4],\tag{4.9}$$

$$s_{1j}(x, u = 0) = 2e^{+i\phi(x - x_{0j})/2}$$
$$\cdot \cos[-\chi_j + \kappa_j\lambda_j(x - x_{0j}) - \pi/4],\tag{4.10}$$

where:

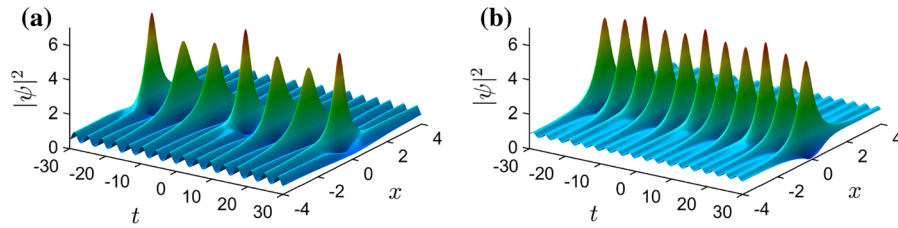$$\kappa_j = \frac{\sqrt{A_j^2 + B_j^2}}{\lambda_j},\tag{4.11}$$

Fig. 4 First-order breathers on the dn background. The parameters are: $c = 1$, $\lambda = 0.75i$, $\alpha = 0.13$, $\gamma = 0.1$, $\delta = -0.07$: **a** $m = 0.75^2$ and **b** $m = 0.5^2$. As m decreases, the breather appears more periodic

$$\chi_j = \frac{1}{2} \arccos \frac{\kappa_j \lambda_j}{B_j}. \tag{4.12}$$

Constants A and B (and thus κ and χ) are labeled with the j index and are calculated for each $\lambda \equiv \lambda_j$.

Now, we need to calculate $r_{1,j}$ and $s_{1,j}$ for any u. The evolution equations are given by expressions (4.5) and (4.6). We can solve them numerically, using the fourth-order Runge–Kutta method. We write $u = ct + v(x - x_0) = 0$ and get $t = -\frac{v}{c}(x - x_0)$. Starting from this value of t and by numerically evolving $du = cdt$ (at a given x in the grid), one can calculate $r_{1,j}(x, u)$ and $s_{1,j}(x, u)$. Next, we shift these values to the entire (x, t) plane, to get $r(x, t)$ and $s(x, t)$. Finally, one employs Eqs. (A 1) and (A 2) to calculate the Nth-order solution $\psi_N(x, t)$.

In Fig. 4, we show the first-order breather ($\lambda = 0.75i$) on an oscillatory dn background, for different values of m. The parameters are: $c = 1$, $\alpha = 0.13$, $\gamma = 0.1$, and $\delta = -0.07$. For (a) $m = 0.75^2$ and for (b) $m = 0.5^2$. Whereas breathers on a constant background are strictly periodic, except at $\lambda = i$, when one obtains the Peregrine soliton, the peaks here are aperiodic. This is easily understandable because we now have two periods, that of the breather, and that of the background. When the two periods are incommensurate, no overall periodicity is possible. We thus see the quasi-periodic oscillation of the peaks with increasing value of m. The spacing between the peaks can also be understood as the beat phenomenon associated with having two periods. As shown, there are only 7 peaks for $m = 0.75^2$ but 11 for $m = 0.5^2$. In the limit of $m \to 0$, one recovers the constant background case. For this case of first-order breathers, having two periods only changes periodicity to quasi-periodicity. As we will see in Sect. 5, for higher-order breathers involving more than two periods, the changes will be more dramatic.

4.2 Applying the DT scheme to $\psi_0 = \psi_{\text{cn}}$

The seed function ψ_0 is now given by Eq. (4.2), where $\phi = \frac{1}{2}c^2 + \frac{1}{2}\gamma c^4(3 - s^2)$ and $v = \alpha c^3 + \frac{1}{2}\delta c^5(3 - s^2)$. We again consider the traveling wave variable u and continue working in the xu-grid:

$$u = \sqrt{s}\,(ct + vx). \tag{4.13}$$

Following the procedure from the previous subsection, we get for the values of A and B:

$$A = \left[\lambda^2 - \frac{c^2}{4(2m-1)}\right]$$
$$\cdot [1 - 4\alpha\lambda + 2(\gamma - 2\delta\lambda)(c^2 - 4\lambda^2)], \tag{4.14}$$

$$B = c\lambda\sqrt{\frac{m}{2m-1}}[1 - 4\alpha\lambda$$
$$+ 2(\gamma - 2\delta\lambda)(c^2 - 4\lambda^2)]. \tag{4.15}$$

The Lax pair generating functions $r_{1j}(x, u = 0)$ and $s_{1j}(x, u = 0)$, as well as κ_j and χ_j, all have the same *general* form as for the dn seedings—Eqs. (4.9) to (4.12). However, κ_j and χ_j differ in the two cases, due to different A and B for the dn/cn seeds, and therefore r, s and the final solution $\psi_N(x, t)$ will differ too.

5 Periodic rogue waves

In this section, we show that the appearance of RW solutions in the QNLSE is determined by the interaction of the periods of a higher-order breather with that of the dn background.

In Fig. 5a, we show a second-order breather generated with $\nu_1 = 0.92$, $\nu_2 = 0.81$, and quintic parameters $c = 1$, $m = 0.1049$, $\alpha = 0.05$, $\gamma = -0.003$ and $\delta = 0.5$. Similar to the first-order breather case of Fig. 4, the peaks are not periodic. For the second and higher-order breathers, the mixing of three or more modes generally leads to chaos, and the periodicity
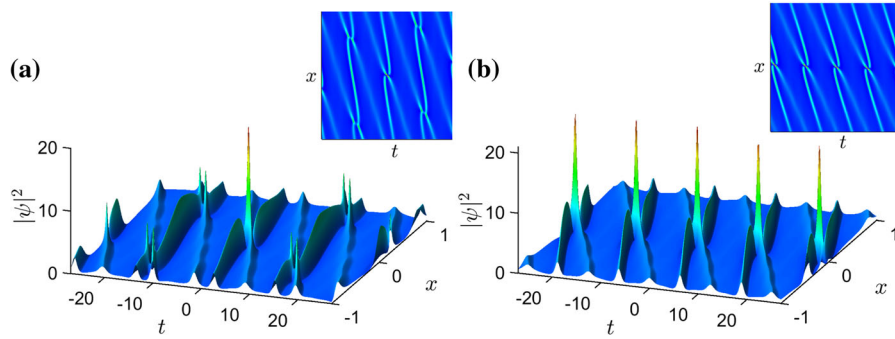
Fig. 5 Second-order breather on a dn background. Parameters: $c = 1$, $m = 0.1049$, $\alpha = 0.05$, $\gamma = -0.003$, $\delta = 0.5$. **a** Unmatched case, when only the central RW peak is generated: $\nu_1 = 0.92$, $\nu_2 = 0.81$, $q = 3.17$. **b** Periodic rogue wave. Constituent breathers are matched mutually and to the dn background wave: $\nu_1 = 0.94$, $\nu_2 = 0.8345$, $q = 4$. Insets in both figures show the 2D-intensity distributions, depicting high-intensity peaks imposed on the elliptic background. Note the appearance of the slanted secondary RW peaks in (**a**), suggesting the possibility of building a Talbot carpet out of RWs

is destroyed. Therefore, one sees in Fig. 5a, only a solitary peak on a noisy background. *Thus, higher-order breathers on a periodic background are generally rogue waves*. On a periodic background, there is therefore a radical distinction between first-order breathers and all higher-order breathers.

What happens now if one insists that the higher-order breather's period matches that of the background?

The period of the dnoidal part of the DT seed function [Eq. (4.1) with $c = 1$] is given by:

$$T_{dn} = 2K(m) = 2 \int_0^{\pi/2} \frac{d\theta}{\sqrt{1 - m \sin^2 \theta}}, \qquad (5.1)$$

where $K(m)$ is the complete elliptic integral of the first kind. On the other hand, from the exact solution of the Lax pair along the $u = 0$ line (Sect. 4), one can write the characteristic breather period as:

$$T_B = \frac{\pi}{\kappa_r}. \qquad (5.2)$$

Here $\kappa = \kappa(\alpha, \gamma, \delta, \nu, m) = \kappa_r + i\kappa_i$ is given by Eq. (4.11). In order for the breather's period to be commensurate with that of the *dn* function, one must match

$$\frac{\pi}{\kappa_r} = 2q K(m) \Rightarrow \kappa_r = \frac{\pi}{2q K(m)}, \qquad (5.3)$$

for some positive integer q. This matching requires two steps. (1) After some values of α, γ, δ and ν_1 are chosen, one writes the general expression for κ_1 and the breather period T_{B1} using Eqs. (4.7), (4.8), (4.11) and (5.2). Then, one numerically solves Eq. (5.3) to find m for given ν and q (note that this procedure can be inverted, i.e. one can calculate ν_1 for the given m). (2)

One matches the periods of all constituent breathers by numerically solving the set of $N - 1$ equations:

$$T_{Bj} = T_{B1}/j, \quad \text{where} \quad j = 2, \ldots, N. \qquad (5.4)$$

In this way, one calculates $\nu_2, \ldots, \nu_N$. Having the complete set of breather frequencies, the wave function $\psi_N(x, t)$ can be calculated using DT (see Sect. 4.1).

For the same set of quintic parameters as used in Fig. 5a, we now take $\nu_1 = 0.94$, giving $q = 4$, meaning that the period of the first constituent breather is four times larger than the period of the dn seed function (4.1). Next, we determine ν_2 of the second constituent breather from $T_{B2} = T_{B1}/2$ to be $\nu_2 = 0.8345$. Now both breather's periods are commensurate to the background and to each other. The resulting second-order breather is shown Fig. 5b. One now sees a periodic series of peaks of nearly equal height as that of Fig. 5a. Clearly, if Fig. 5a is a rogue wave, then Fig. 5b is a *periodic rogue wave*.

We repeat the procedure for a third-order breather, keeping the same values of c, m, α, γ, δ and ν_1 as in the previous figure. The results are depicted in Fig. 6. Again, if we just take $\nu_2 = 0.81$ and $\nu_3 = 0.61$, with periods unmatched to the background, one obtains a RW shown in Fig. 6a. However, if one takes $\nu_2 = 0.8345$ and $\nu_3 = 0.625$, matching the background period, then one obtains the periodic RW of Fig. 6b. Note that the peaks are lying along a skewed line in the (x, t) plane, not along the t-axis.

If one changes the elliptic modulus squared m sufficiently, while keeping the breather's eigenvalues intact, the RW periodicities would also be disturbed (not
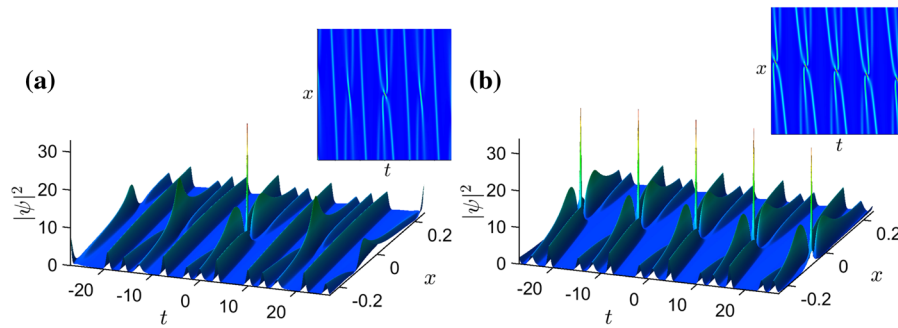
Fig. 6 Third-order breather on a dn background. Parameters: $c = 1$, $m = 0.1049$, $\alpha = 0.05$, $\gamma = -0.003$, $\delta = 0.5$. **a** An unmatched case when only the central RW peak is generated: $\nu_1 = 0.92$, $\nu_2 = 0.81$, $\nu_3 = 0.61$, $q = 3.17$. **b** Periodic RW. The constituent breathers are matched mutually and to the dn background wave: $\nu_1 = 0.94$, $\nu_2 = 0.8345$, $\nu_3 = 0.625$, $q = 4$. Insets in both figures show the 2D-intensity distributions, depicting high-intensity peaks imposed on the elliptical background

shown). We stress the fact that the third-order periodic RWs are harder to obtain and are more vulnerable to the mismatch of the frequencies, when compared to the second-order breathers. Also, the possibility of building Talbot carpets with the third-order periodic RWs appears more remote. Namely, the modulation instability of the third-order solutions is greater and the probability of three different modes constructively interfering in the (x, t) plane is significantly lower.

We also confirm the validity of the peak-height formula for the dn background (Figs. 4, 5, 6), since it exactly reproduces the maximum intensity of the central peak at $(0, 0)$ (not shown). This further points to the universal validity of the peak-height formula for all members of the infinite hierarchy of NLSEs.

6 Conclusion

In this paper, we have presented a procedure for the dynamical generation of breathers and RWs of the QNLSE on uniform and elliptical backgrounds. We have derived the condition for the breather-to-soliton conversion of QNLSE for nonzero α, γ, and δ parameters, and provided an analysis of intensity profiles of a converted soliton.

We have obtained various intense solitary or periodic peaks for the highly nonlinear and computationally demanding QNLSE. In many aspects, our procedure can be termed as an exact procedure for obtaining numerical RWs of the QNLSE. In this way, one can construct and analyze unstable higher-order solutions due to the modulation instability. They could be of impor-

tance for the production of exotic solutions in physical systems modeled by the QNLSE.

But most importantly, we have pointed out a radical distinction between the first-order breathers and all higher-order breathers on a periodic background. The first-order breathers can at most be quasi-periodic, whereas all higher-order breathers are generally RWs. By matching the period of the breather to that of the background, which requires exceedingly fine tuning, one can generate a new and even more rare kind of RWs, which, paradoxically, are *periodic*.

Compliance with ethical standards

Conflict of interest The authors declare that they have no conflict of interest.

Appendix A: The general Darboux transformation scheme

The quintic solution of order N is a nonlinear superposition of N independent simple solutions, where each is determined by the complex eigenvalue λ_j ($1 \leq j \leq$

N). The corresponding wave function is:

$$\psi_n = \psi_{n-1} + \frac{2\left(\lambda_n^* - \lambda_n\right) s_{n,1} r_{n,1}^*}{\left|r_{n,1}\right|^2 + \left|s_{n,1}\right|^2}. \tag{A 1}$$

The Lax pair functions $r_{n,1}$ and $s_{n,1}$ are given by recursive relations involving $r_{n,p}(x,t)$ and $s_{n,p}(x,t)$:

$$
\begin{aligned}
r_{n,p} &= \Big[\left(\lambda_{n-1}^* - \lambda_{n-1}\right) s_{n-1,1}^* r_{n-1,1} s_{n-1,p+1} \\
&\quad + \left(\lambda_{p+n-1} - \lambda_{n-1}\right)\left|r_{n-1,1}\right|^2 r_{n-1,p+1} \\
&\quad + \left(\lambda_{p+n-1} - \lambda_{n-1}^*\right)\left|s_{n-1,1}\right|^2 r_{n-1,p+1}\Big] \\
&\quad \Big/ \left(\left|r_{n-1,1}\right|^2 + \left|s_{n-1,1}\right|^2\right), \\
s_{n,p} &= \Big[\left(\lambda_{n-1}^* - \lambda_{n-1}\right) s_{n-1,1} r_{n-1,1}^* r_{n-1,p+1} \\
&\quad + \left(\lambda_{p+n-1} - \lambda_{n-1}\right)\left|s_{n-1,1}\right|^2 s_{n-1,p+1} \\
&\quad + \left(\lambda_{p+n-1} - \lambda_{n-1}^*\right)\left|r_{n-1,1}\right|^2 s_{n-1,p+1}\Big] \\
&\quad \Big/ \left(\left|r_{n-1,1}\right|^2 + \left|s_{n-1,1}\right|^2\right).
\end{aligned}
\tag{A 2}
$$

Thus, all pairs $r_{n,p}$ and $s_{n,p}$ can be determined starting from $r_{1,j}$ and $s_{1,j}$. The functions $r_{1,j}(x,t)$ and $s_{1,j}(x,t)$, forming the Lax pair $R = \begin{pmatrix} r \\ s \end{pmatrix} \equiv \begin{pmatrix} r_{1,j} \\ s_{1,j} \end{pmatrix}$, are determined by the eigenvalue $\lambda \equiv \lambda_j$ and an embedded arbitrary center of the solution (x_{0j}, t_{0j}). The Lax pair satisfies a system of linear differential equations:

$$\frac{\partial R}{\partial t} = U \cdot R, \quad \frac{\partial R}{\partial x} = V \cdot R. \tag{A 3}$$

For the quintic NLSE, matrices U and V are defined as $(\psi \equiv \psi_0)$ [31]:

$$
U = i \begin{bmatrix} \lambda & \psi(x,t)^* \\ \psi(x,t) & -\lambda \end{bmatrix},
$$
$$
V = \sum_{k=0}^{5} \lambda^k \cdot i \begin{bmatrix} A_k & B_k^* \\ B_k & -A_k \end{bmatrix}. \tag{A 4}
$$

The coefficients A_k and B_k are given by:

$$
\begin{aligned}
A_0 &= -\frac{1}{2}|\psi|^2 - 3\gamma|\psi|^4 - i\alpha\left(\psi_t^*\psi - \psi_t\psi^*\right) \\
&\quad - \gamma\left(\psi_{tt}^*\psi - |\psi_t|^2 + \psi_{tt}\psi^*\right) \\
&\quad - i\delta\left(\psi_{ttt}^*\psi - \psi_{tt}^*\psi_t + \psi_{tt}\psi_t^* - \psi_{ttt}\psi^*\right) \\
&\quad - 6i\delta\left(\psi_t^*\psi - \psi_t\psi^*\right)|\psi|^2, \\
B_0 &= 2\alpha|\psi|^2\psi + 6\delta|\psi|^4\psi + i\frac{1}{2}\psi_t + 6i\gamma|\psi|^2\psi_t \\
&\quad + \alpha\psi_{tt} + 2\delta\psi_{tt}^*\psi^2 + 4\delta|\psi_t|^2\psi + 6\delta(\psi_t)^2\psi^* \\
&\quad + 8\delta\psi_{tt}|\psi|^2 + i\gamma\psi_{ttt} + \delta\psi_{tttt},
\end{aligned}
$$

$$
\begin{aligned}
A_1 &= 2\alpha|\psi|^2 + 6\delta|\psi|^4 - 2i\gamma\left(\psi_t^*\psi - \psi_t\psi^*\right) \\
&\quad + 2\delta\left(\psi_{tt}^*\psi - |\psi_t|^2 + \psi_{tt}\psi^*\right), \tag{A 5} \\
B_1 &= \psi + 4\gamma|\psi|^2\psi - 2i\alpha\psi_t - 12i\delta|\psi|^2\psi_t \\
&\quad + 2\gamma\psi_{tt} - 2i\delta\psi_{ttt}, \\
A_2 &= 1 + 4\gamma|\psi|^2 + 4i\delta\left(\psi_t^*\psi - \psi_t\psi^*\right), \\
B_2 &= -4\alpha\psi - 8\delta|\psi|^2\psi - 4i\gamma\psi_t - 4\delta\psi_{tt}, \\
A_3 &= -4\alpha - 8\delta|\psi|^2, \\
B_3 &= -8\gamma\psi + 8i\delta\psi_t, \\
A_4 &= -8\gamma, \\
B_4 &= 16\delta\psi, \\
A_5 &= 16\delta, \\
B_5 &= 0. \tag{A 6}
\end{aligned}
$$

The solutions of Lax pair equations are further pursued in the text.

References

1. Bao, W.: The nonlinear Schrödinger equation and applications in Bose–Einstein condensation and plasma physics. In: Lecture Note Series, IMS, NUS, vol. 9 (2007)
2. Shukla, P.K., Eliasson, B.: Nonlinear aspects of quantum plasma physics. Phys. Usp. **53**, 51 (2010)
3. Busch, T., Anglin, J.R.: Dark–bright solitons in inhomogeneous Bose–Einstein condensates. Phys. Rev. Lett. **87**, 010401 (2001)
4. Dudley, J.M., Dias, F., Erkintalo, M., Genty, G.: Instabilities, breathers and rogue waves in optics. Nature Photon. **8**, 755 (2014)
5. Agrawal, G.P.: Applications of Nonlinear Fiber Optics. Academic Press, San Diego (2001)
6. Kibler, B., Fatome, J., Finot, C., Millot, G., Dias, F., Genty, G., Akhmediev, N., Dudley, J.M.: Observation of Kuznetsov-Ma soliton dynamics in optical fibre. Sci. Rep. **6**, 463 (2012)
7. Osborne, A.S.: Nonlinear Ocean Waves and the Inverse Scattering Transform. Academic Press, New York (2010)
8. Dudley, J.M., Taylor, J.M.: Supercontinuum Generation in Optical Fibers. Cambridge University Press, Cambridge (2010)
9. Kedziora, D.J., Ankiewicz, A., Chowdury, A., Akhmediev, N.: Integrable equations of the infinite nonlinear Schrödinger equation hierarchy with time variable coefficients. Chaos **25**, 103114 (2015)
10. Ankiewicz, A., Kedziora, D.J., Chowdury, A., Bandelow, U., Akhmediev, N.: Infinite hierarchy of nonlinear Schrödinger equations and their solutions. Phys. Rev. E **93**, 012206 (2016)
11. Serkin, V.N., Hasegawa, A.: Novel soliton solutions of the nonlinear Schrödinger equation model. Phys. Rev. Lett. **85**, 4502 (2000)

12. Akhmediev, N., et al.: Roadmap on optical rogue waves and extreme events. J. Opt. **18**, 063001 (2016)

13. Sulem, C., Sulem, P.-L.: The Nonlinear Schrödinger Equation. Springer, New York (1999)

14. Ankiewicz, A., Soto-Crespo, J.M., Akhmediev, N.: Rogue waves and rational solutions of the Hirota equation. Phys. Rev. E **81**, 046602 (2010)

15. Anderson, D., Lisak, M.: Nonlinear asymmetric self-phase modulation and self-steepening of pulses in long optical waveguides. Phys. Rev. A **27**, 1393 (1983)

16. Chowdury, A., Kedziora, D.J., Ankiewicz, A., Akhmediev, N.: Breather-to-soliton conversions described by the quintic equation of the nonlinear Schrödinger hierarchy. Phys. Rev. E **91**, 032928 (2015); Chowdury, A., Krolikowski, W.: Breather-to-soliton transformation rules in the hierarchy of nonlinear Schrödinger equations. Phys. Rev. E **95**, 062226 (2017)

17. Backus, S., Durfee III, C.G., Mourou, G., Kapteyn, H.C., Murnane, M.M.: 0.2-TW laser system at 1 kHz. Opt. Lett. **22**, 1256 (1997)

18. Xu, S.-L., Petrović, N., Belić, M.R.: Exact solutions of the (2 + 1)-dimensional quintic nonlinear Schrödinger equation with variable coefficients. Nonlinear Dyn. **80**, 583–589 (2015)

19. Mirzazadeh, M., Eslami, M., Zerrad, E., Mahmood, M.F., Biswas, A., Belić, M.: Optical solitons in nonlinear directional couplers by sine-cosine function method and Bernoulli's equation approach. Nonlinear Dyn. **81**, 1933–1349 (2015)

20. Biswas, A., Khalique, C.M.: Stationary solutions for nonlinear dispersive Schrödinger equation. Nonlinear Dyn. **63**, 623–626 (2011)

21. Chin, S.A., Ashour, O.A., Belić, M.R.: Anatomy of the Akhmediev breather: cascading instability, first formation time, and Fermi-Pasta-Ulam recurrence. Phys. Rev. E **92**, 063202 (2015)

22. Wu, X.-F., Hua, G.-S., Ma, Z.-Y.: Evolution of optical solitary waves in a generalized nonlinear Schrödinger equation with variable coefficients. Nonlinear Dyn. **70**, 2259–2267 (2012)

23. Trippenbach, M., Band, Y.B.: Effects of self-steepening and self-frequency shifting on short-pulse splitting in dispersive nonlinear media. Phys. Rev. A **57**, 4791 (1998)

24. Potasek, M.J., Tabor, M.: Exact solutions for an extended nonlinear Schrödinger equation. Phys. Lett. A **154**, 449 (1991)

25. Cavalcanti, S.B., Cressoni, J.C., da Cruz, H.R., Gouveia-Neto, A.S.: Modulation instability in the region of minimum group-velocity dispersion of single-mode optical fibers via an extended nonlinear Schrödinger equation. Phys. Rev. A **43**, 6162 (1991)

26. Wang, D.-S., Chen, F., Wen, X.-Y.: Darboux transformation of the general Hirota equation: multisoliton solutions, breather solutions and rogue wave solutions. Adv. Differ. Equ. **2016**, 67 (2016)

27. Guo, R., Hao, H.Q.: Breathers and multi-solitons solutions for the higher-order generalized nonlinear Schrödinger equation. Commun. Nonlinear Sci. Numer. Simul. **18**, 2426–2435 (2013)

28. Mani Rajan, M.S., Mahalingam, A.: Nonautonomous solitons in modified inhomogeneous Hirota equation: soliton control and soliton interaction. Nonlinear Dyn. **79**, 2469–2484 (2015)

29. Lan, Z., Gao, B.: Solitons, breather and bound waves for a generalized higher-order nonlinear Schrödinger equation in an optical fiber or a planar waveguide. Eur. Phys. J. Plus **132**, 512 (2017)

30. Chowdury, A., Kedziora, D.J., Ankiewicz, A., Akhmediev, N.: Breather solutions of the integrable nonlinear Schrödinger equation and their interactions. Phys. Rev. E **91**, 022919 (2015)

31. Chowdury, A., Kedziora, D.J., Ankiewicz, A., Akhmediev, N.: Soliton solutions of an integrable nonlinear Schrödinger equation with quintic terms. Phys. Rev. E **90**, 032922 (2014)

32. Yang, Y., Yan, Z., Malomed, B.A.: Rogue waves, rational solitons, and modulational instability in an integrable fifth-order nonlinear Schrödinger equation. Chaos **25**, 103112 (2015)

33. Chin, S.A., Ashour, O.A., Nikolić, S.N., Belić, M.R.: Maximal intensity higher-order Akhmediev breathers of the nonlinear Schrödinger equation and their systematic generation. Phys. Lett. A **380**, 3625–3629 (2016)

34. Schwalm, W.A.: Lectures on selected topics in mathematical physics: elliptic functions and elliptic integrals. Morgan & Claypool publication as part of IOP Concise Physics, vol. 68, San Rafael, CA, USA. (2015)

35. Nikolić, S.N., Aleksić, N.B., Ashour, O.A., Belić, M.R., Chin, S.A.: Systematic generation of higher-order solitons and breathers of the Hirota equation on different backgrounds. Nonlinear Dyn. **89**, 1637–1649 (2017)

36. Kedziora, D.J., Ankiewicz, A., Akhmediev, N.: Rogue waves and solitons on a cnoidal background. Eur. Phys. J. Spec. Top. **223**, 43–62 (2014)

37. Chin, S.A., Ashour, O.A., Nikolić, S.N., Belić, M.R.: Peak-height formula for higher-order breathers of the nonlinear Schrödinger equation on nonuniform backgrounds. Phys. Rev. E **95**, 012211 (2017)

38. Ashour O.A.: Maximal intensity higher-order breathers of the nonlinear Schrödinger equation on different backgrounds. In: Undergraduate Research Scholars Thesis, Texas A&M University, USA (2017)

39. Wang, L., Zhang, J.-H., Wang, Z.-Q., Liu, C., Li, M., Qi, F.-H., Guo, R.: Breather-to-soliton transitions, nonlinear wave interactions, and modulational instability in a higher-order generalized nonlinear Schrödinger equation. Phys. Rev. E **93**, 012214 (2016)

40. Zhang, J.-H., Wang, L., Liu, C.: Superregular breathers, characteristics of nonlinear stage of modulation instability induced by higher-order effects. Proc. R. Soc. A **473**, 20160681 (2017)

CrossMark

ORIGINAL PAPER

Systematic generation of higher-order solitons and breathers of the Hirota equation on different backgrounds

**Stanko N. Nikolić · Najdan B. Aleksić ·
Omar A. Ashour · Milivoj R. Belić · Siu A. Chin**

Abstract We investigate the systematic generation of higher-order solitons and breathers of the Hirota equation on different backgrounds. The Darboux transformation is used to construct proper initial conditions for dynamical generation of high-intensity solitons and breathers of different orders on a uniform background. We provide expressions for the Lax pair generating functions and the procedure for calculating higher-order solutions when Jacobi elliptic functions are the background seed solutions of the Hirota equation. We confirm that the peak height of each soliton or breather in the nonlinear Darboux superposition adds linearly, to form the intensity maximum of the final solution.

Keywords Hirota equation · Darboux transformation · Higher-order solitons · Breathers and rogue waves

S. N. Nikolić (✉)· N. B. Aleksić · O. A. Ashour ·
M. R. Belić
Science Program, Texas A&M University at Qatar,
P.O. Box 23874 Doha, Qatar
e-mail: stankon@ipb.ac.rs

S. N. Nikolić · N. B. Aleksić
Institute of Physics Belgrade, University of Belgrade,
Pregrevica 118, Belgrade 11080, Serbia

O. A. Ashour · S. A. Chin
Department of Physics and Astronomy, Texas A&M University,
College Station, TX 77843, USA

1 Introduction

In this work, we study the solitons and breathers of the Hirota equation (HE) [1–3]

$$i\frac{\partial \psi}{\partial x} + \frac{1}{2}\frac{\partial^2 \psi}{\partial t^2} + |\psi|^2\psi - i\alpha\left(\frac{\partial^3 \psi}{\partial t^3} + 6|\psi|^2\frac{\partial \psi}{\partial t}\right) = 0 \tag{1.1}$$

on various backgrounds. Here, x and t are the retarded time in the moving frame and the transverse spatial variable, respectively, while ψ denotes the slowly varying wave envelope.

The fundamental solutions of HE are of great importance in many fields dealing with nonlinear propagating waves, ranging from oceanography to fiber-optics [4]. HE contains only one real parameter α, related to the transverse velocity of the wave. Setting $\alpha = 0$ reduces HE to the nonlinear Schrödinger equation (NLSE) [5–8]. The necessity of extending the NLSE to the HE and other higher-order members of the NLS hierarchy of equations arises from the need to understand propagation of ultrashort pulses through optical fibers [9,10]. A more accurate description of the real physical systems requires additional terms, to account for self-steepening, self-frequency shift, and third-order dispersion [11–15]. It was shown that these third-order terms are of significant importance in pulse-deforming phenomena [16] and supercontinuum generation [17].

In this work, we show that the solitons and breathers of high intensity can be *dynamically* generated on zero and constant backgrounds by a direct numerical inte-

gration of an initial wave function extracted from the Darboux transformation (DT), with appropriate boundary conditions. We also find new Hirota solutions, derived by DT on an elliptic background. In all the cases, we demonstrate that the peak height formula [(PHF—Eq. (4.1)] gives the correct peak value of a higher-order solution of HE, as a linear sum of peak heights of its DT constituents [18].

Solitons, breathers and rational solutions of HE have been previously studied using DT in Refs. [2,19–22]. Additional interest in NLSE and Hirota breathers arises from their relationship with the rogue waves (RWs) [23–27] that can be modeled by higher-order breathers concatenated from the first-order ones via DT iterations [24,27–29]. An interesting finding in Hirota [30] and quintic NLSE [31] is the breather-to-soliton conversion, obtained for specific values of the breather eigenvalues—a feature not possible in the ordinary cubic NLSE. The study of NLSE breathers on a Jacobi elliptic function (JEF, see [32]) background was previously done in Refs. [33,34]. A recent discovery of an infinite hierarchy of extended nonlinear Schrödinger equations [35–38] has also revealed that they may only have dnoidal and cnoidal backgrounds in their solutions. To the extent that HE can better describe light propagation in an optical fiber, this work should also contribute to a better understanding of optical RW generation.

The paper is organized as follows: In Sect. 2, we analyze the basic Hirota solutions and show the usefulness of DT for numerical simulations. In Sect. 3, we provide a derivation of the Lax pair generating functions and higher-order solutions when cnoidal and dnoidal functions are taken as seed solutions in DT. In Sect. 4, the PHF for HE is presented. In Sect. 5, we present analytical and numerical results concerning higher-order solitons and breathers on different backgrounds, utilizing the periodicity of ABs and breather-to-soliton conversion. In Sect. 6, we summarize the findings and importance of our results. The general DT scheme is provided in "Appendix."

2 Solitons and breathers of the Hirota equation

Darboux transformation can be used to obtain higher-order soliton/breather and rogue wave solutions of the Hirota equation on different backgrounds. The key steps in obtaining these nonlinear structures *dynam-*

ically, for discretized x and t intervals, are: 1. use DT to calculate the initial wave function at a particular value of the propagation variable $x = x_0$, i.e., to find $\psi(x_0, t)$, 2. analyze the wave function values at the edges of the t-interval in order to pick appropriate boundary conditions, and 3. apply a convenient numerical algorithm to calculate the wave function over the entire xt-grid (in this case, the fourth-order Runge–Kutta method).

To numerically generate higher-order solitons, we calculate the initial wave function from a zero seed: $\psi_0 = 0$. The appropriate boundary condition can be found from the first-order DT solution, characterized by a pure imaginary eigenvalue $\lambda = i\nu$ (without loss of generality, we can assume zero shifts along the x and t axes),

$$\psi(x, t) = \frac{2\nu e^{2i\nu^2 x}}{\cosh\left[2\nu\left(t + 4\alpha\nu^2 x\right)\right]}. \tag{2.1}$$

From (2.1), it follows that the first-order soliton has a single peak with the amplitude $|\psi(0, 0)| = 2\nu$, and its intensity decays exponentially, following the cosh function. Consequently, the Neumann boundary condition $\frac{\partial \psi}{\partial t} = 0$ can be used in numerical evaluations of higher-order Hirota solitons. It should be noted that the Hirota coefficient α appears only in the denominator, giving a tilt to the soliton propagation.

A higher-order Akhmediev breather (AB) of HE is constructed by DT when a plane-wave seed, $\psi_0 = e^{ix}$, is utilized. The first-order AB is given by [19]

$$\psi(x, t) = \left[\frac{2(1 - 2a)\cosh(\beta x) + i\beta\sinh(\beta x)}{\cosh(\beta x) - \sqrt{2a}\cos\left[\omega(t + vx)\right]} - 1\right]e^{ix}, \tag{2.2}$$

where a is an arbitrary parameter in the range $0 < a < 1/2$. The frequency ω, the growth factor β, and the parameter v determining the tilt of the breather in the xt-plane are given solely in terms of a:

$$\omega = 2\sqrt{1 - 2a}, \quad \beta = \omega\sqrt{2a}, \quad v = 2\alpha(1 + 4a). \tag{2.3}$$

The difference between NLSE and Hirota breathers originates only from the parameter v. NLSE solutions are obtained when $v = 0$ ($\alpha = 0$).

From Eq. (2.2), one can see that Hirota's AB is periodic along t-axis, with the period

$$L = \frac{2\pi}{\omega} = \frac{\pi}{\sqrt{1-2a}}. \qquad (2.4)$$

Consequently, in contrast to solitons, periodic boundary conditions are required for dynamical generation of higher-order ABs. Briefly, one assumes that each of N eigenvalues is purely imaginary $\lambda_j = i v_j$. The parameter a_j of each breather constituent is connected to the imaginary part of its eigenvalue via the relation

$$v_j = \sqrt{2a_j}. \qquad (2.5)$$

Due to periodicity, it is natural to choose higher-order breathers that retain the same periodic length L of the first-order breather, having $\omega_j = j\omega$ ($a_1 \equiv a$, $\omega_1 \equiv \omega$). From Eqs. (2.3) to (2.5), it follows

$$\lambda_j = i\sqrt{2\left(j^2 a - \frac{j^2-1}{2}\right)}. \qquad (2.6)$$

If, for any j, ω_j is not an integer multiple of ω, then the periodicity of the original breather is destroyed. For more details, see [18]. The procedure for generating higher-order ABs is to take an initial a, calculate other eigenvalues according to Eq. (2.6), and apply the DT.

3 New solutions of the Hirota equation on dnoidal/cnoidal backgrounds

In recent articles [35,36], new exact solutions of HE that include JEFs are presented:

$$\psi_{\mathrm{dn}}(x, t) = c e^{i\phi x} \mathrm{dn}\left(ct + vx, m\right), \qquad (3.1)$$

$$\psi_{\mathrm{cn}}(x, t) = \frac{c}{\sqrt{2}}\sqrt{s+1} e^{i\phi x} \cdot$$

$$\cdot \mathrm{cn}\left(\sqrt{s}ct + \sqrt{s}vx, m = \frac{1}{2} + \frac{1}{2s}\right). \qquad (3.2)$$

Here, m is the elliptic modulus squared, c, s, ϕ are constants, and v is the speed of the wave that depends on α. By setting $c = 2v$ and $m = 1$, we reproduce the soliton solution of Eq. (2.1). Any of these functions may be used as a seed for the Darboux transformation. This motivated us to examine how higher-order solutions can be obtained on dnoidal/cnoidal backgrounds. All results in this section are derived using the general Darboux transformation scheme for Hirota equation given in "Appendix."

3.1 Derivation of the DT Lax pair generating functions and higher-order solutions for $\psi_0 = \psi_{\mathrm{dn}}$

Here the seed function ψ_0 is given by Eq. (3.1) with $\phi = \left(1 - \frac{m}{2}\right)c^2$ and $v = (2 - m)\alpha c^3$ [35]. The Lax pair equations consist of a system of four coupled linear differential equations for r_t, s_t, r_x, and s_x. Here, the subscripts stand for partial derivatives. To solve these equations, we introduce the traveling variable

$$u = ct + xv \qquad (3.3)$$

and continue the analysis with x and u. Now, the t-derivatives are replaced by the u-derivatives: $\frac{\partial \psi}{\partial t} = c^2 e^{i\phi x}\frac{\partial dn(u)}{\partial u}$ and $\frac{\partial^2 \psi}{\partial t^2} = c^3 e^{i\phi x}\frac{\partial^2 dn(u)}{\partial u^2}$. We take the ansatz:

$$r(x, u) = g(x, u)e^{-i\phi x/2} \text{ and}$$

$$s(x, u) = h(x, u)e^{+i\phi x/2}. \qquad (3.4)$$

The matrix elements of U and V from Eq. (7.4) in "Appendix" can be calculated by substituting ψ_0 into Eq. (7.5). From Eq. (7.4), the u-evolutions are obtained

$$g_u = i\frac{\lambda}{c}g + i \cdot \mathrm{dn}(u)h, \qquad (3.5)$$

$$h_u = i \cdot \mathrm{dn}(u)g - i\frac{\lambda}{c}h. \qquad (3.6)$$

The equations for the x-derivative are a bit more complicated, but actually not needed for numerical calculations. It is only necessary to obtain the x-derivative at $u = 0$, to initiate the numerical integration of r and s. Evolution along the x-axis at $u = 0$ follows from Eq. (7.3)

$$g_x = iAg + iBh, \qquad (3.7)$$

$$h_x = iBg - iAh, \qquad (3.8)$$

where constants A and B are

$$A = \left(\lambda^2 - \frac{mc^2}{4}\right)(1 - 4\alpha\lambda), \qquad (3.9)$$

$$B = c\lambda(1 - 4\alpha\lambda). \qquad (3.10)$$

By differentiating and combining Eqs. (3.7) and (3.8) one obtains:

$$g_{xx} = -(A^2 + B^2)g \qquad (3.11)$$

and

$$h_{xx} = -(A^2 + B^2)h. \qquad (3.12)$$

Thus, the exact solution for g or h is $h(x, u = 0) = C_1 e^{i\kappa\lambda x} + C_2 e^{-i\kappa\lambda x}$. Here, $\kappa = \frac{\sqrt{A^2 + B^2}}{\lambda}$, while C_1 and C_2 are arbitrary constants. We can embed the phase shift of $\pi/4$ into $h(x, u = 0)$, to center the solution at the origin. Next, we take $C_1 = e^{-i\pi/4 - i\chi}$ and $C_2 = e^{+i\pi/4 + i\chi}$. Therefore: $h(x, u = 0) = 2\cos(-\chi + \kappa\lambda x - \pi/4)$. If we substitute $h(x, u = 0)$ in (3.8), we will get the solution $g(x, u = 0) = 2i\sin(-\chi + \kappa\lambda x - \pi/4 + \varphi)$. The idea is to make the solutions for g and h symmetrical and in agreement with the published articles [27,28,33]. We can choose $-\chi + \varphi = +\chi$, and therefore $\chi = \frac{1}{2}\varphi = \frac{1}{2}\arccos\frac{\kappa\lambda}{B}$. The solution for g is $g(x, u = 0) = 2i\sin(+\chi + \kappa\lambda x - \pi/4)$.

Now, we go back to the Lax pair generating functions, introducing N eigenvalues and x-shifts (t-axis shifts are ignored since they provide negligible advance in the understanding, alongside with numerical complications). The quantities κ and χ are labeled with the j index. Hence, the Lax pair generating functions for eigenvalue λ_j and shift x_{0j} ($1 \leq j \leq n$) are:

$$r_{1j}(x, u = 0)$$
$$= 2i e^{-i\phi x/2} \sin[+\chi_j + \kappa_j\lambda_j(x - x_{0j}) - \pi/4] \tag{3.13}$$

$$s_{1j}(x, u = 0)$$
$$= 2 e^{+i\phi x/2} \cos[-\chi_j + \kappa_j\lambda_j(x - x_{0j}) - \pi/4], \tag{3.14}$$

where

$$\kappa_j = (1 - 4\alpha\lambda_j)\sqrt{c^2 + \left(\lambda_j - \frac{mc^2}{4\lambda_j}\right)^2} \tag{3.15}$$

$$\chi_j = \frac{1}{2}\arccos\frac{\kappa_j}{c(1 - 4\alpha\lambda_j)}. \tag{3.16}$$

The remaining task is to find the $r_{1,j}$ and $s_{1,j}$ functions for any u. The evolution equations are given by expressions (3.5) and (3.6). We can solve them only numerically, for instance using the fourth-order Runge–Kutta method. We write $u = ct + xv = 0$ and for a given x, we find $t = -\frac{v}{c}x$. We start from this t value and numerically evolve $du = cdt$ (in both directions) to find $r_{1,j}(x, u)$ and $s_{1,j}(x, u)$. Next, we shift these values from the (x, u) to the (x, t) frame, to get all values on the grid: $r(x, t)$ and $s(x, t)$. Finally, by employing the well-known recursive relations in Eq. (7.2) and iterative relations in Eq. (7.1), the Nth-order

solution, $\psi_N(x, t)$, can be calculated. In the special case of $\alpha = 0$ and $c = 1$, the Hirota Lax pair generating functions and the final Nth-order wave function are equivalent to the NLSE solutions described in Section 2.2 of [33].

3.2 Derivation of the DT Lax pair generating functions and higher-order solutions for $\psi_0 = \psi_{cn}$

The analysis is analogous to the previous case. The seed function ψ_0 is given by Eq. (3.2), where $\phi = \frac{1}{2}c^2$ and $v = \alpha c^3$. The substitution

$$u = \sqrt{s}\,(ct + xv) \tag{3.17}$$

gives $\frac{\partial\psi}{\partial t} = c^2\sqrt{\frac{s(s+1)}{2}}e^{i\phi x}\frac{\partial \text{cn}(u)}{\partial u}$ and $\frac{\partial^2\psi}{\partial t^2} = c^3 s\sqrt{\frac{s+1}{2}}e^{i\phi x}\frac{\partial^2 \text{cn}(u)}{\partial u^2}$. The ansatz is now:

$$r(x, u) = g(x, u)e^{-i\phi x/2} \text{ and}$$
$$s(x, u) = h(x, u)e^{+i\phi x/2}. \tag{3.18}$$

The evolution along u-axis (from the U matrix) is

$$g_u = \frac{i\lambda}{c\sqrt{s}}g + \frac{i\sqrt{s+1}}{\sqrt{2s}}\text{cn}(u)h, \tag{3.19}$$

$$h_u = \frac{i\sqrt{s+1}}{\sqrt{2s}}\text{cn}(u)g - \frac{i\lambda}{c\sqrt{s}}h. \tag{3.20}$$

Again, we restrict further analysis only to $u = 0$. The evolution along the x-axis is:

$$g_x = iAg + iBh, \tag{3.21}$$
$$h_x = iBg - iAh, \tag{3.22}$$

where

$$A = (1 - 4\alpha\lambda)\left(\lambda^2 - \frac{1}{4}c^2 s\right), \tag{3.23}$$

$$B = \frac{c\lambda\sqrt{m}}{\sqrt{2m - 1}}(1 - 4\alpha\lambda). \tag{3.24}$$

By differentiating the last two equations, one gets

$$g_{xx} = -(A^2 + B^2)g, \tag{3.25}$$
$$h_{xx} = -(A^2 + B^2)h. \tag{3.26}$$

The exact solution for h is $h(x, u = 0) = C_1 e^{i\kappa\lambda x} + C_2 e^{-i\kappa\lambda x}$, with $\kappa = \frac{\sqrt{A^2 + B^2}}{\lambda}$. We choose C_1 and C_2 constants as in the previous case. The final solution for Lax pair generating functions is obtained

after the complete sets of eigenvalues and x-shifts are introduced,

$$
\begin{aligned}
&r_{1j}(x, u = 0) \\
&\quad = 2ie^{-i\phi x/2} \sin[+\chi_j + \kappa_j \lambda_j (x - x_{0j}) - \pi/4],
\end{aligned}
\tag{3.27}
$$

$$
\begin{aligned}
&s_{1j}(x, u = 0) \\
&\quad = 2e^{+i\phi x/2} \cos[-\chi_j + \kappa_j \lambda_j (x - x_{0j}) - \pi/4],
\end{aligned}
\tag{3.28}
$$

where

$$
\kappa_j = \left(1 - 4\alpha\lambda_j\right) \cdot
$$
$$
\cdot \sqrt{m} \sqrt{\frac{c^2}{2m-1} + \frac{1}{m}\left(\lambda - \frac{c^2}{2m-1} \cdot \frac{1}{4\lambda}\right)^2},
\tag{3.29}
$$

$$
\chi_j = \frac{1}{2} \arccos \frac{\kappa_j \sqrt{2m-1}}{c\sqrt{m}\left(1 - 4\alpha\lambda_j\right)}.
\tag{3.30}
$$

The Lax pairs generating functions for both dn and cn seedings have the same form. However, parameters κ_j and χ_j differ in the two cases, so the r and s functions and the final solutions differ too. An equivalent numerical scheme, proposed in the previous subsection, can be used to calculate r and s functions for any x and u, and then over the entire xt-grid. Again, in the special case of $\alpha = 0$ and $c = \sqrt{2m-1}$, the Hirota Lax pair generating functions and the final Nth-order solution are equivalent to the NLSE solutions described in Section 2.3 of [33].

4 Peak height formula for the Hirota equation

We have stated that the maximum amplitude of the Nth order DT solution is just a *linear* sum of peak heights of the individual solitons or breathers in the *nonlinear* superposition. In [34], we have proven that the peak height formula (PHF) holds regardless of the choice of the seed function in DT,

$$
\psi_N(0, 0) = \psi_0(0, 0) + \sum_{n=1}^{N} 2\nu_n.
\tag{4.1}
$$

Again, the assumption is that all N eigenvalues are purely imaginary $\lambda_j = i\nu_j$ (the real part would not change the PHF). It is proven in [18] that PHF holds when the Lax pair generating functions satisfy the following equation, assuming zero x and t shifts for all eigenvalues:

$$
s_{1,j}(0, 0) = ir_{1,j}(0, 0).
\tag{4.2}
$$

In Table 1, explicit expressions for the seed and Lax pair generating functions of HE are given. For brevity, we omit "j" index in N eigenvalues.

It is easy to check that the relation in Eq. (4.2) applies to all cases given in Table 1.

For the potential applications of soliton propagation in optical fibers modeled by HE, a high soliton intensity is an advantage. As explained in detail in [30], a breather can be converted to a soliton for a specific value of the real part $\Re\{\lambda_j\}$ of all eigenvalues,

$$
\Re\{\lambda_j\} = \frac{1}{8\alpha}.
\tag{4.3}
$$

According to the PHF, this means that such a "converted" soliton (single or higher order) would have greater amplitude compared to the one obtained with zero seed, having the same set of eigenvalues.

Table 1 Seed solutions for Hirota equation and the corresponding Lax pair generating functions ($r_{1,j} \equiv r$ and $s_{1,j} \equiv s$)

Seed function $\psi_0(x, t)$	Lax pair generating functions	PHF
0	$r(x, t) = e^{i\left[\lambda t - \lambda^2(4\alpha\lambda - 1)x - \pi/4\right]}$ $s(x, t) = e^{-i\left[\lambda t - \lambda^2(4\alpha\lambda - 1)x - \pi/4\right]}$	$\psi_N(0, 0) = \sum_{n=1}^{N} 2\nu_n$
e^{ix}	$r(x, t) = 2ie^{-ix/2} \sin\left(\chi + \frac{1}{2}\kappa t + \frac{1}{2}dx - \pi/4\right)$ $s(x, t) = 2e^{+ix/2} \cos\left(-\chi + \frac{1}{2}\kappa t + \frac{1}{2}dx - \pi/4\right)$	$\psi_N(0, 0) = 1 + \sum_{n=1}^{N} 2\nu_n$
$\psi_{\text{dn}}(x, t)$	$r(0, 0) = 2i \sin(+\chi - \pi/4)$ $s(0, 0) = 2 \cos(-\chi - \pi/4)$	$\psi_N(0, 0) = c + \sum_{n=1}^{N} 2\nu_n$
$\psi_{\text{cn}}(x, t)$	$r(0, 0) = 2i \sin(+\chi - \pi/4)$ $s(0, 0) = 2 \cos(-\chi - \pi/4)$	$\psi_N(0, 0) = c\sqrt{\frac{m}{2m-1}} + \sum_{n=1}^{N} 2\nu_n$

5 Numerical verification

Here we present numerical simulations of higher-order solitons and breathers on uniform and nonuniform backgrounds and introduce a simple criterion to estimate the solution peak value using the PHF.

5.1 Solutions of Hirota equation on uniform backgrounds

First, we show that the single-soliton solutions, obtained by DT (Fig. 1a) and by dynamical integration (Fig. 1b), are in excellent agreement if one chooses the Neumann boundary conditions. The maximum intensity in both figures is 7.84, in agreement with PHF ($\lambda = 1 + 0.9i$), $7.84 = (0 + 2 \cdot 0.9)^2$. The second-

order soliton is shown in Fig. 1c (DT) and 1d (direct integration). It is generated from the two single solitons, characterized by eigenvalues $\lambda_1 = 1 + 0.9i$ and $\lambda_2 = 1 + i$. The maximum intensity in this case is $14.44 = (0 + 2 \cdot 0.9 + 2 \cdot 1)^2$. The tilt in the soliton propagation in all figures mainly comes from the Hirota parameter $\alpha = 1/8$, but also from the real part of eigenvalues.

In Fig. 2, we demonstrate that higher-order breathers can numerically evolve from an initial DT wave function by applying a periodic boundary condition. First, we choose $a_1 = a = 0.464$ for the first AB in a nonlinear superposition and calculate its eigenvalue according to Eq. (2.5). As stated in Sect. 2, the second- and third-order breathers should have their frequencies exactly two and three times higher than the fre-
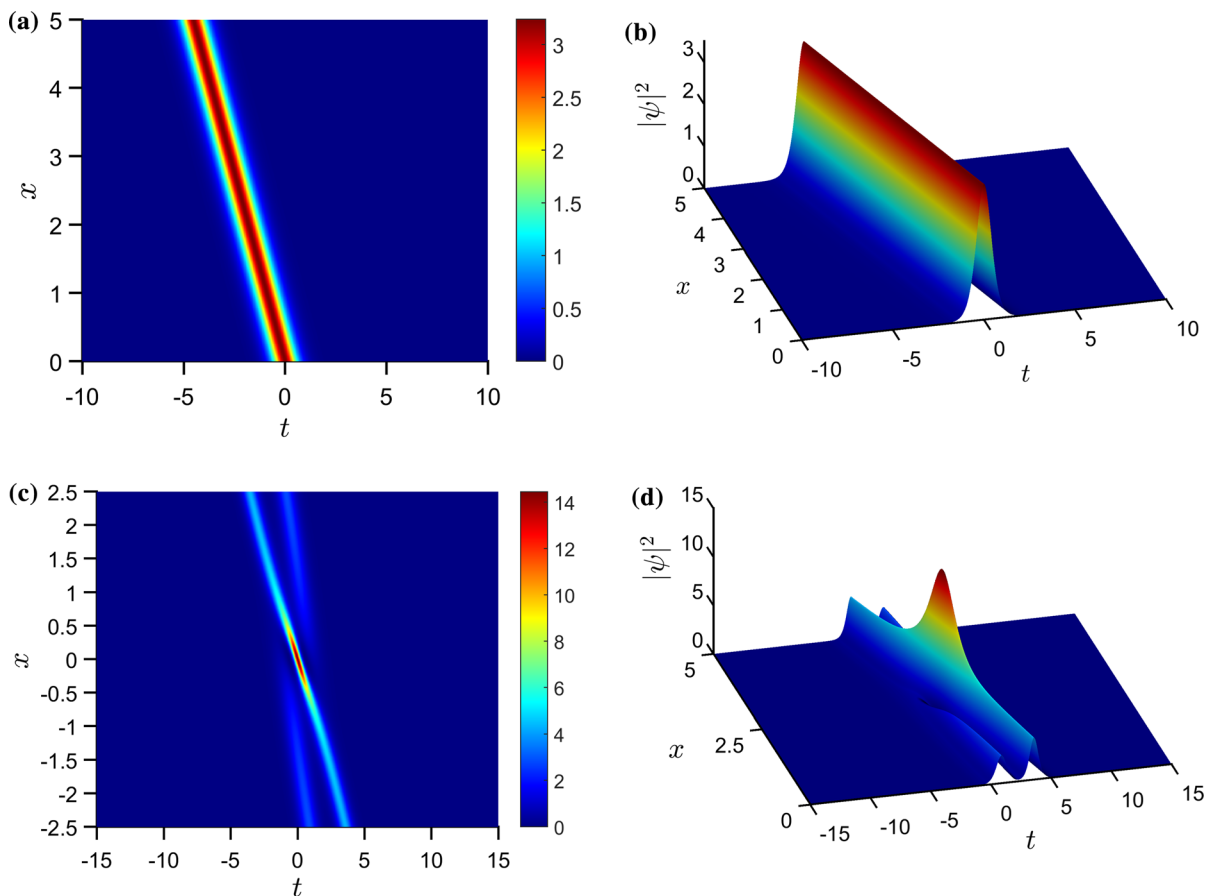
Fig. 1 Propagation of the soliton with $\alpha = 1/8$: **a** 2D intensity plot of the first-order DT solution with $\psi_0 = 0$ and $\lambda = 1 + 0.9i$; **b** numerical evolution of the initial condition taken at $x = 0$ from (**a**); **c** 2D intensity plot of the second-order DT solution with $\psi_0 = 0$, $\lambda_1 = 1 + 0.9i$, and $\lambda_2 = 1 + i$; and **d** numerical evolution of the initial condition taken at $x = -2.5$ from (**c**). Maximum intensity value $|\psi|^2$ is 3.24 in (**a**) and (**b**), and 14.44 in (**c**) and (**d**), in agreement with PHF

(a)

(b)
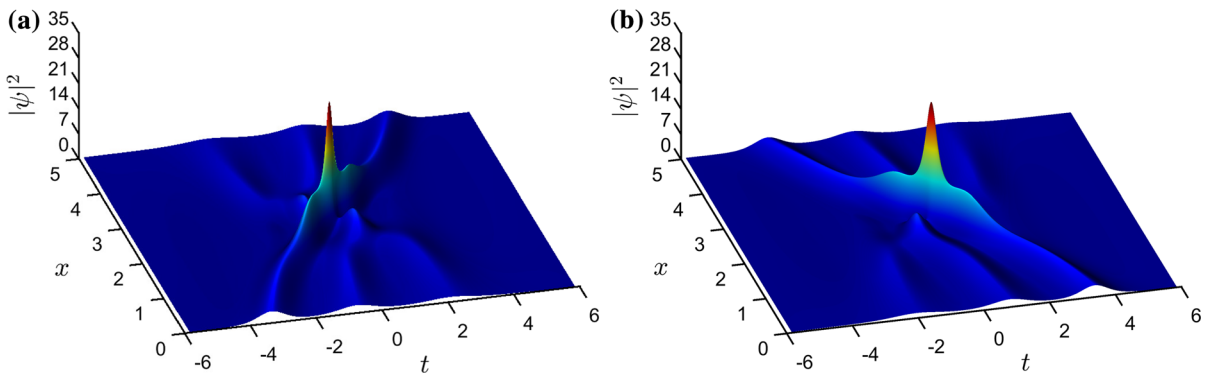
Fig. 2 Dynamically generated third-order breathers. Initial wave function is extracted from DT solution, having a plane-wave seed, at $x = -2.5$. The fundamental period is characterized by $a = 0.464$ from Eq. (2.3). Pure imaginary eigenvalues λ_j, with $1 \leq j \leq 3$, are calculated using Eq. (2.6). The peak intensity is $|\psi|^2_{\max} = 33.64$, in agreement with PHF. **a** $\alpha = -0.1$, **b** $\alpha = +0.1$
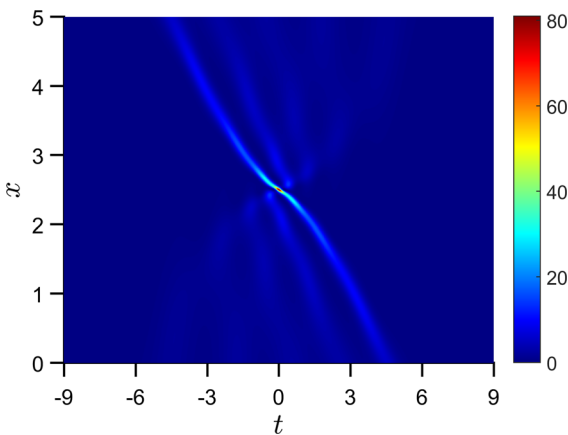
Fig. 3 2D intensity plot of dynamically generated fifth-order breather. Initial wave function is extracted from the DT solution, having a plane-wave seed, at $x = -2.5$. The fundamental period is characterized by $a = 0.485$ from Eq. (2.3). Pure imaginary eigenvalues λ_j, with $1 \leq j \leq 5$, are calculated using Eq. (2.6). The peak intensity is $|\psi|^2_{\max} = 81$, in agreement with PHF. Hirota parameter is $\alpha = 0.1$

quency of the first-order one. We show the third-order breather in Fig. 2a for $\alpha = -0.1$, and in Fig. 2b for $\alpha = 0.1$. The tilt and a slight stretching of the solution are determined by the parameter α solely. The PHF holds: $|\psi|^2_{\max} = 33.64 = (1 + 2\nu_1 + 2\nu_2 + 2\nu_3)^2$.

In Fig. 3, we show a fifth-order breather, numerically obtained in the same way as the third-order breather from the previous figure. We start from $a_1 = a = 0.485$, calculate other eigenvalues accordingly (Eq. 2.6), and set the domain for numerics assuming

periodic boundary conditions. The peak intensity is $|\psi|^2_{\max} = 81 = (1 + 2\nu_1 + 2\nu_2 + 2\nu_3 + 2\nu_4 + 2\nu_5)^2$.

Next, we utilize a breather-to-soliton conversion of HE, to further exemplify the utility of PHF. Even when the plane-wave seeding is used to generate breathers, the solitons of arbitrary orders are generated under the condition given by Eq. (4.3). One can immediately see the benefits of PHF: The "converted" soliton will have the amplitude maximum of $1 + \sum_i 2\nu_i$, instead of $\sum_i 2\nu_i$, obtained from the usual zero seed. We demonstrate this by using the same eigenvalues as in Fig. 1, but having real parts equal to $\frac{1}{8\alpha}$. The intensity peak heights of single and double converted solitons are 7.84 and 23.04, respectively, which are higher than those of the solitons of the same shape shown in Fig. 1. Real and imaginary parts of the wave function have a discontinuity at the edges of the t interval. Furthermore, $\lim_{t \to \pm\infty} |\psi|^2 = 1$ and $\lim_{t \to \pm\infty} \frac{\partial \psi}{\partial t} = 0$, so the Neumann boundary condition can still be applied in this case (Fig. 4).

5.2 Solutions of Hirota equation on nonuniform backgrounds

We now switch to the solutions generated by the DT when the seed is taken from dn or cn family of JEFs, given by Eqs. (3.1) and (3.2). First, we examine if the breather-to-soliton conversion holds for nonuniform backgrounds. In Fig. 5a, b, we show the first-order converted solitons, differing only in the parameter c of Eq. (3.1). For $c = 1$, the background oscillations have
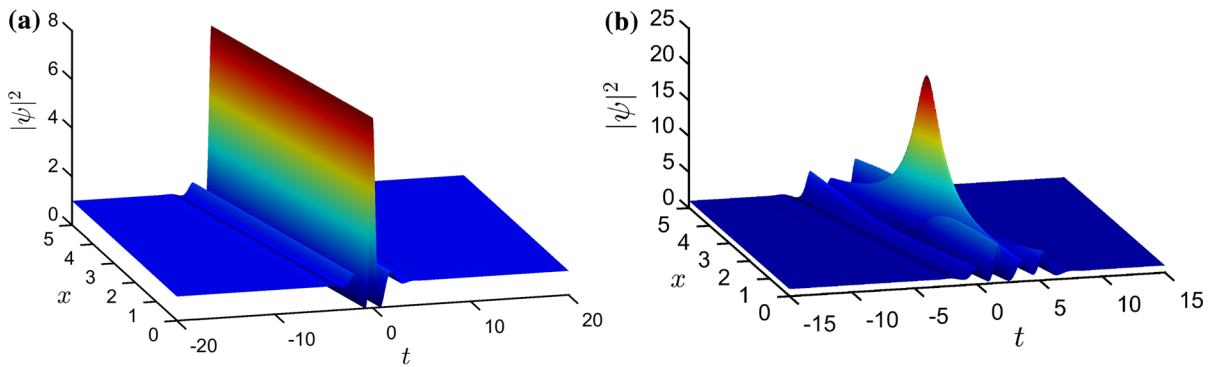
Fig. 4 Dynamically generated soliton solutions of the **a** first and **b** second order, for $\alpha = 1/8$. A breather-to-soliton conversion in Hirota equation is utilized to obtain higher-intensity solitons. Initial wave functions are extracted from the DT solutions having a plane-wave seed. The real parts of all eigen-values satisfy Eq. (4.3). Parameters are: **a** $\lambda_1 = 1 + 0.9i$, $|\psi|^2_{\max} = (1 + 2 \cdot 0.9)^2 = 7.84$, and **b** $\lambda_1 = 1 + 0.9i$, $\lambda_2 = 1 + i$, $|\psi|^2_{\max} = (1 + 2 \cdot 0.9 + 2 \cdot 1)^2 = 23.04$, both in agreement with the PHF for breathers
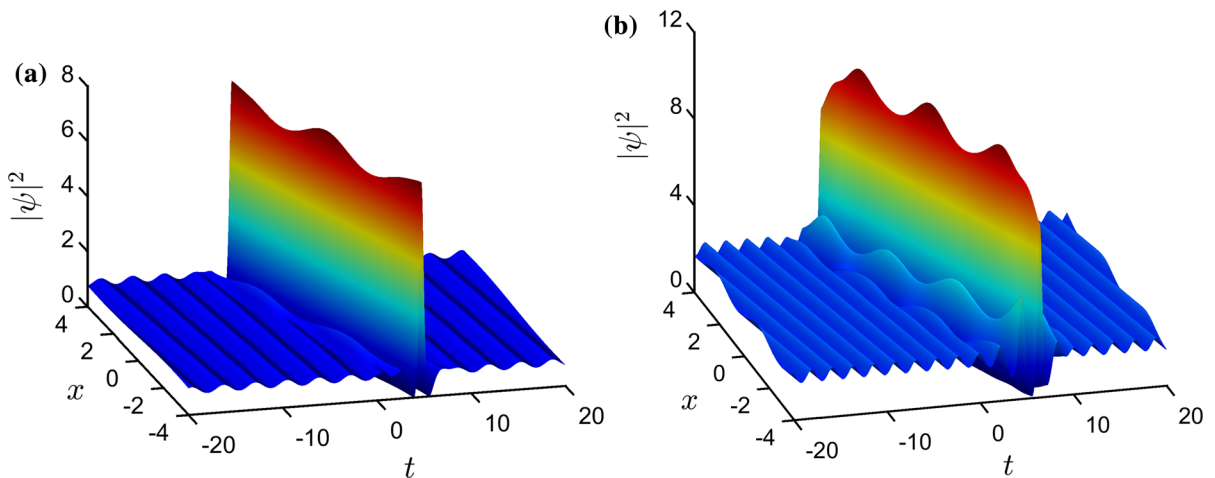
Fig. 5 Breather-to-soliton conversion of the Hirota equation on dnoidal background. Wave functions are calculated using the DT with the seed given by Eq. (3.1). Parameters are: $\alpha = 1/6$, $m = 0.5^2$, $\lambda = 0.75 + 0.9i$, with **a** $c = 1$ and **b** $c = 1.5$

longer periods and smaller amplitudes, as compared to the $c = 1.5$ case. We conclude that a weaker oscillation causes less perturbation in the soliton propagation. Therefore, the converted soliton is slightly affected, as shown in Fig. 5a, while in Fig. 5b a considerable distortion is observed.

Akhmediev breathers and Kuznetsov–Ma solitons of HE can be also produced on elliptic backgrounds. Similar to the NLSE case, ABs are produced when the imaginary part of an eigenvalue is $\nu < 1$, while the KM solitons are obtained in the $\nu > 1$ case. It was shown in [33] that the NLSE ABs are stretching out and KM solitons are compressing, as the elliptic modulus $\sqrt{m}$ or ν is increasing. Our calculations for Hirota equation produced the same results (not shown). Here we examine the influence of parameter c in the seed function ψ_{dn} on the period of ABs and KM solitons. We set $\alpha = 1/6$, $m = 0.5^2$, and $\lambda = 0.75i$ for AB, and $\alpha = 0.03$, $m = 0.5^2$, and $\lambda = 1.25i$ for KM soliton. When $c = 1$ (Fig. 6a), five peaks are visible, compared to seven in the $c = 1.2$ case (Fig. 6b). Results differ when the KM soliton is produced: More crests are visible for lower c, as shown in Fig. 6c, d. It is clear that a higher c
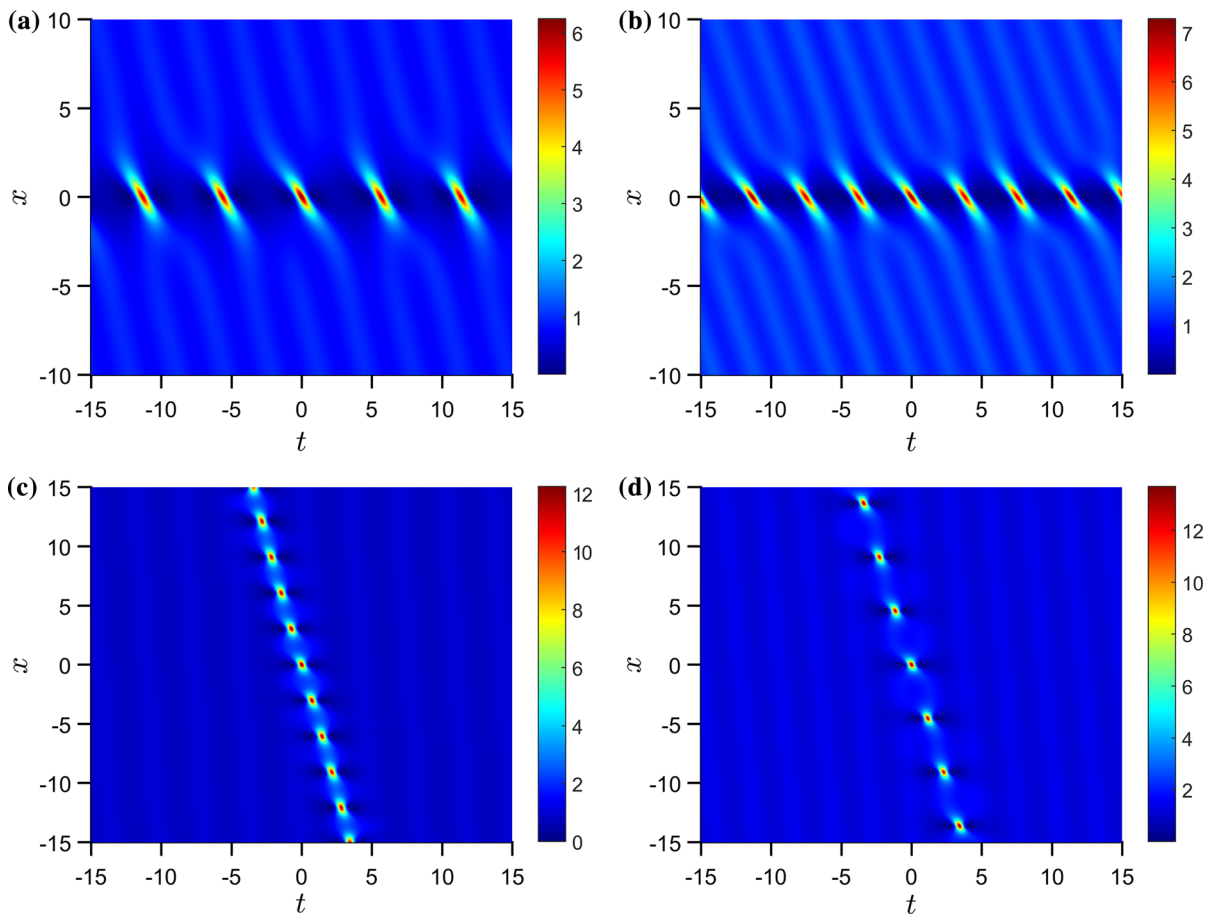
Fig. 6 First-order Akhmediev breathers obtained by the DT, with dnoidal seed from Eq. (3.1). Parameters are: $\alpha = 1/6$ and $m = 0.5^2$. The eigenvalue is $\lambda = 0.75i$, with **a** $c = 1$ and **b** $c = $ 1.2. Kuznetsov–Ma soliton is obtained for $\alpha = 0.03$, $m = 0.5^2$, and $\lambda = 1.25i$, with **c** $c = 1$ and **d** $c = 1.2$

yields shorter periods of ABs and longer periods of KM solitons.

Next, we generate the first-order breathers, denoted as the dim and bright RWs, on a dnoidal background ($c = 1$). These results are similar to those in [33] and [34]. In general, the dim RW is obtained when $\nu \approx \frac{1}{2} - \frac{1}{2}\sqrt{1-m}$, while the bright RW is generated for $\nu \approx \frac{1}{2} + \frac{1}{2}\sqrt{1-m}$. In Fig. 7a, b, the dim and bright RWs are shown, respectively, for $\alpha = 0.3$ and $m = 0.5$. The intensities of dim (bright) RWs are 1.6716 (7.3284). These two RWs can be combined into a second-order solution using DT, as shown in Fig. 7c. Its intensity is always 9 (in agreement with PHF), independent of the background parametrized by m. In the special case of $m = 0.5$, the inten-

sity of this second-order rogue wave is equal to the sum of intensities of the dim and bright RWs. In this manner, we have generated a "Pythagorean triplet" of rogue waves for the Hirota equation. A comparison of these results with the same solutions of NLSE (Figs. 3, 4, and 5 in [34]) reveals a similar structure, except for the tilt introduced by the parameter α.

In Fig. 8a, b, we show the third-order breathers generated by DT for both dnoidal and cnoidal seeds. The backgrounds differ in the two cases, showing distorted oscillatory patterns. However, very sharp and strong central peaks appear similarly in both figures, suggesting that these maxima can be recognized as RWs of HE on nonuniform backgrounds.
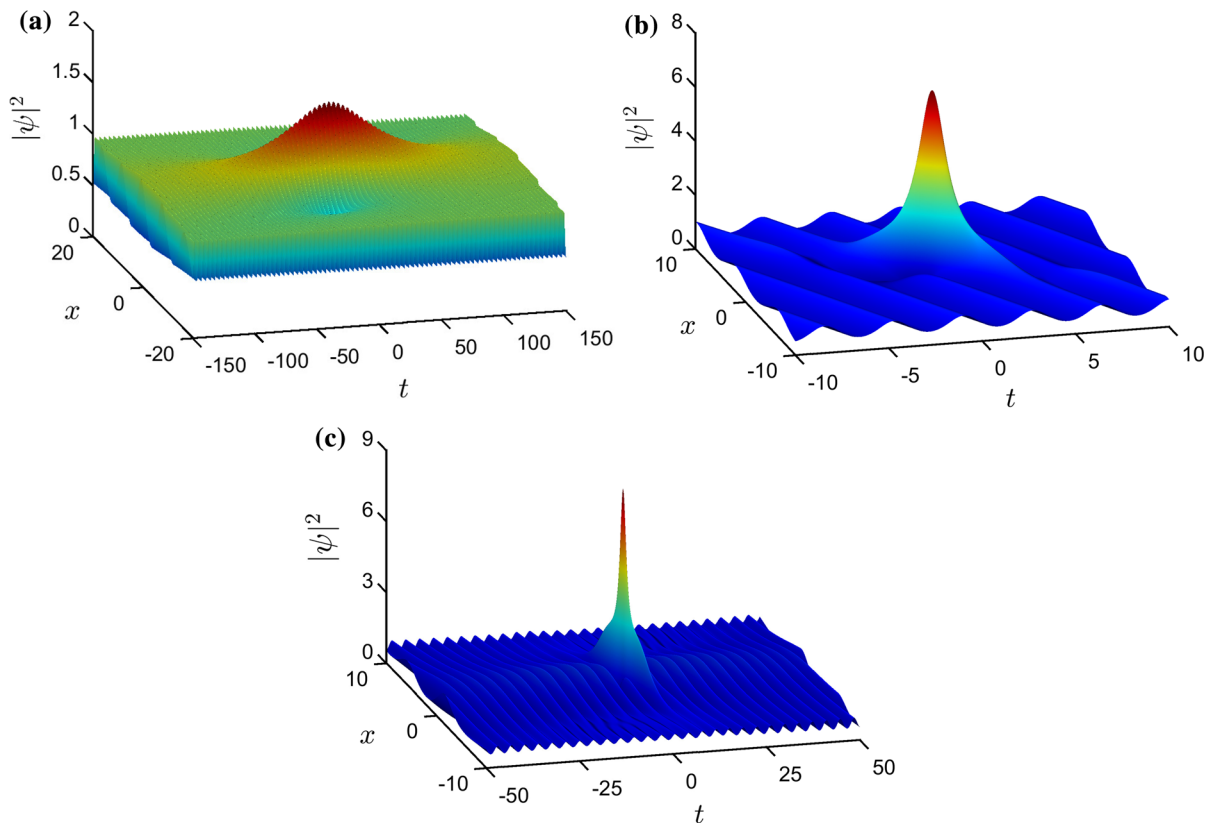
Fig. 7 a The dim and **b** the bright rogue waves obtained for $\alpha = 0.3$, $m = 0.5$, and $\nu \approx \frac{1}{2} \mp \frac{1}{2}\sqrt{1-m}$. **c** The second-order solution formed by the DT from RWs of (**a**) and (**b**). The peak intensity is 9, precisely equal to the sum of its constituents' intensities
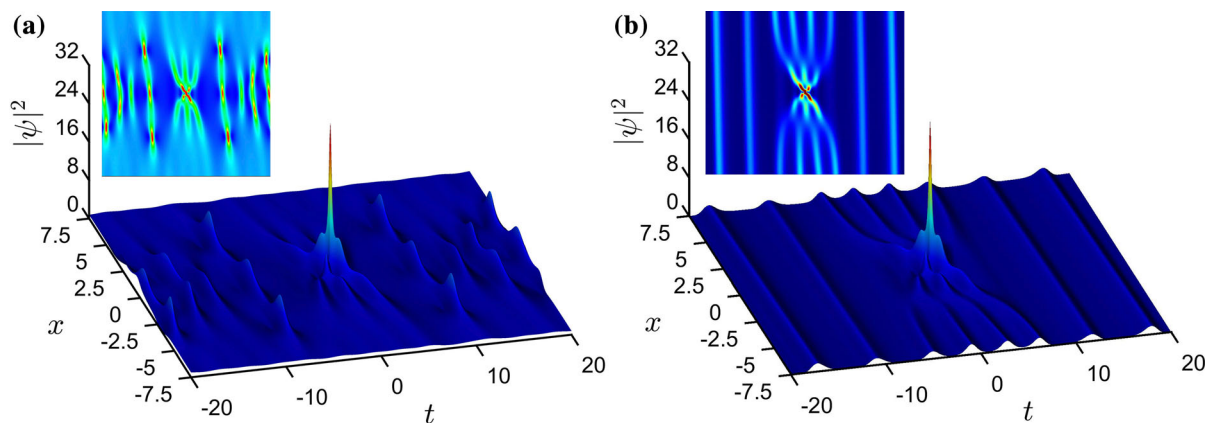
Fig. 8 Third-order breathers calculated using the DT on a nonuniform background. Parameters are $\lambda_1 = 0.91i$, $\lambda_2 = 0.81i$, $\lambda_3 = 0.61i$, and $\alpha = 0.05$. Seed functions: **a** $\psi_0 = \psi_{\mathrm{dn}}$, $m = 1/9$, $c = 1$, and **b** $\psi_0 = \psi_{\mathrm{cn}}$, $m = 0.98^2$, $c = \sqrt{2m-1}$. Both intensity maxima are in agreement with the PHF: **a** $|\psi|^2_{\max} = 32.036 = [c + 2(0.91 + 0.81 + 0.61)]^2$ and

b $|\psi|^2_{\max} = 31.810 = \left[c\sqrt{\frac{m}{2m-1}} + 2(0.91 + 0.81 + 0.61)\right]^2$. Insets in both figures show 2D intensity distributions, in order to depict strong and sharp central peaks imposed on irregular oscillatory patterns of the background

6 Conclusion

In this work, we have presented a procedure for dynamical generation of higher-order solitons and breathers of the Hirota equation on uniform background, using the Darboux transformation. Once the wave function at a particular value of the evolution variable is found using DT, it can be used as an initial condition for numerical evaluation, with appropriate boundary conditions. This dynamical evolution toward higher-order solitons and breathers is important in the situations when the existence of such solutions is questionable in the presence of modulation instability. Thus, the DT may provide analytical higher-order solutions that might not exist, owing to modulation instability, which—as a rule—exists in these solutions. We have shown that the breather-to-soliton conversion can be used to produce solitons of higher amplitude and that the periodicity of Akhmediev breathers can be utilized for dynamical generation of rogue waves.

We also presented a derivation of the Lax pair generating functions and a procedure for calculating higher-order solutions of Hirota equation when dnoidal and cnoidal JEFs are used as seed solutions for the DT. We demonstrated that higher-order ABs and Kuznetsov–Ma solitons can be generated on these nonuniform backgrounds. For particular sets of parameters, we found that the higher-order DT solutions can be treated as rogue waves of the Hirota equation.

Finally, we generalized our peak height formula for the Hirota equation, proving that the peak height of a higher-order solution is a simple linear sum of the constituent peak heights. This formula may be useful in guiding the design and production of breathers of maximal intensity in physical systems modeled by the Hirota equation.

7 Appendix: The general Darboux transformation scheme

A higher-order soliton (breather) solution of the Nth order is a nonlinear superposition of N independent solitons (breathers), each determined by a complex eigenvalue λ_j, where $1 \leq j \leq N$ (the real part of the eigenvalue determines the angle between the localized solution and x-axis, while the imaginary part characterizes the periodic modulation frequency [27]). The Nth-order wave function given by the DT is:

$$\psi_n = \psi_{n-1} + \frac{2\left(\lambda_n^* - \lambda_n\right) s_{n,1} r_{n,1}^*}{\left|r_{n,1}\right|^2 + \left|s_{n,1}\right|^2}. \tag{7.1}$$

In order to find $r_{n,1}$ and $s_{n,1}$, one has to analyze recursive relations between $r_{n,p}(x,t)$ and $s_{n,p}(x,t)$ functions of the Lax pair equations in the general form:

$$\begin{aligned}
r_{n,p} &= [\left(\lambda_{n-1}^* - \lambda_{n-1}\right) s_{n-1,1}^* r_{n-1,1} s_{n-1,p+1} \\
&\quad + \left(\lambda_{p+n-1} - \lambda_{n-1}\right) \left|r_{n-1,1}\right|^2 r_{n-1,p+1} \\
&\quad + \left(\lambda_{p+n-1} - \lambda_{n-1}^*\right) \left|s_{n-1,1}\right|^2 r_{n-1,p+1}] \\
&\quad \Big/ \left(\left|r_{n-1,1}\right|^2 + \left|s_{n-1,1}\right|^2\right) \\
s_{n,p} &= [\left(\lambda_{n-1}^* - \lambda_{n-1}\right) s_{n-1,1} r_{n-1,1}^* r_{n-1,p+1} \\
&\quad + \left(\lambda_{p+n-1} - \lambda_{n-1}\right) \left|s_{n-1,1}\right|^2 s_{n-1,p+1} \\
&\quad + \left(\lambda_{p+n-1} - \lambda_{n-1}^*\right) \left|r_{n-1,1}\right|^2 s_{n-1,p+1}] \\
&\quad \Big/ \left(\left|r_{n-1,1}\right|^2 + \left|s_{n-1,1}\right|^2\right).
\end{aligned} \tag{7.2}$$

From the last equation, it can be deduced that all $r_{n,p}$ and $s_{n,p}$ can be calculated just from $r_{1,j}$ and $s_{1,j}$, with $1 \leq j \leq N$. The functions $r_{1,j}(x,t)$ and $s_{1,j}(x,t)$, forming the Lax pair $R = \begin{pmatrix} r \\ s \end{pmatrix} \equiv \begin{pmatrix} r_{1,j} \\ s_{1,j} \end{pmatrix}$, are determined by the eigenvalue $\lambda \equiv \lambda_j$, an embedded arbitrary center of the solution $\left(x_{0j}, t_{0j}\right)$, and a system of linear differential equations:

$$\frac{\partial R}{\partial t} = U \cdot R, \quad \frac{\partial R}{\partial x} = V \cdot R. \tag{7.3}$$

Particularly for the Hirota equation, matrices U and V are defined as ($\psi \equiv \psi_0$) [30]:

$$U = i \begin{bmatrix} \lambda & \psi(x,t)^* \\ \psi(x,t) & -\lambda \end{bmatrix},$$

$$V = \sum_{k=0}^{3} \lambda^k \cdot i \begin{bmatrix} A_k & B_k^* \\ B_k & -A_k \end{bmatrix}, \qquad (7.4)$$

where the coefficients A_k and B_k are

$$A_0 = -\frac{1}{2}|\psi|^2 - i\alpha \left(\psi_t^* \psi - \psi_t \psi^* \right),$$

$$B_0 = 2\alpha|\psi|^2\psi + \frac{1}{2}i\psi_t + \alpha\psi_{tt},$$

$$A_1 = 2\alpha|\psi|^2, \quad B_1 = \psi - 2i\alpha\psi_t$$

$$A_2 = 1, \quad B_2 = -4\alpha\psi, \quad A_3 = -4\alpha, \quad B_3 = 0.$$

$$(7.5)$$

References

1. Hirota, R.: Exact envelope-soliton solutions of a nonlinear wave equation. J. Math. Phys. **14**, 805–809 (1973)
2. Tao, Y., He, J.: Multisolitons, breathers, and rogue waves for the Hirota equation generated by the Darboux transformation. Phys. Rev. E **85**, 026601 (2012)
3. Guo, R., Zhao, X.-J.: Discrete Hirota equation: discrete Darboux transformation and new discrete soliton solutions. Nonlinear Dyn. **84**, 1901–1907 (2016)
4. Dudley, J.M., Dias, F., Erkintalo, M., Genty, G.: Instabilities, breathers and rogue waves in optics. Nat. Photon. **8**, 755 (2014)
5. Osborne, A.S.: Nonlinear Ocean Waves and the Inverse Scattering Transform. Academic Press, New York (2010)
6. Biswas, A., Khalique, C.M.: Stationary solutions for nonlinear dispersive Schröödinger equation. Nonlinear Dyn. **63**, 623–626 (2011)
7. Mirzazadeh, M., Eslami, M., Zerrad, E., Mahmood, M.F., Biswas, A., Belić, M.: Optical solitons in nonlinear directional couplers by sine-cosine function method and Bernoulli's equation approach. Nonlinear Dyn. **81**, 1933–1349 (2015)
8. Chin, S.A., Ashour, O.A., Belić, M.R.: Anatomy of the Akhmediev breather: cascading instability, first formation time, and Fermi-Pasta-Ulam recurrence. Phys. Rev. E **92**, 063202 (2015)
9. Mani Rajan, M.S., Mahalingam, A.: Nonautonomous solitons in modified inhomogeneous Hirota equation: soliton control and soliton interaction. Nonlinear Dyn. **79**, 2469–2484 (2015)
10. Wang, D.-S., Chen, F., Wen, X.-Y.: Darboux transformation of the general Hirota equation: multisoliton solutions, breather solutions and rogue wave solutions. Adv. Differ. Equ. **2016**, 67 (2016)
11. Agrawal, G.P.: Applications of Nonlinear Fiber Optics. Academic Press, San Diego (2001)
12. Guo, R., Hao, H.Q.: Breathers and multi-solitons solutions for the higher-order generalized nonlinear Schrödinger equation. Commun. Nonlinear. Sci. Numer. Simul. **18**, 2426–2435 (2013)
13. Potasek, M.J., Tabor, M.: Exact solutions for an extended nonlinear Schrödinger equation. Phys. Lett. A **154**, 449 (1991)
14. Cavalcanti, S.B., Cressoni, J.C., da Cruz, H.R., Gouveia-Neto, A.S.: Modulation instability in the region of minimum group-velocity dispersion of single-mode optical fibers via an extended nonlinear Schrödinger equation. Phys. Rev. A **43**, 6162 (1991)
15. Trippenbach, M., Band, Y.B.: Effects of self-steepening and self-frequency shifting on short-pulse splitting in dispersive nonlinear media. Phys. Rev. A **57**, 4791 (1998)
16. Anderson, D., Lisak, M.: Nonlinear asymmetric self-phase modulation and self-steepening of pulses in long optical waveguides. Phys. Rev. A **27**, 1393 (1983)
17. Dudley, J.M., Taylor, J.M.: Supercontinuum Generation in Optical Fibers. Cambridge University Press, Cambridge (2010)
18. Chin, S.A., Ashour, O.A., Nikolić, S.N., Belić, M.R.: Maximal intensity higher-order Akhmediev breathers of the nonlinear Schrödinger equation and their systematic generation. Phys. Lett. A **380**, 3625–3629 (2016)
19. Ankiewicz, A., Soto-Crespo, J.M., Akhmediev, N.: Rogue waves and solutions of the Hirota equation. Phys. Rev. E **81**, 046602 (2010)
20. Guo, B., Ling, L., Liu, Q.P.: Nonlinear Schrödinger equation: generalized Darboux transformation and rogue wave solutions. Phys. Rev. E **85**, 026607 (2012)
21. Mu, G., Qin, Z., Chow, K.W., Ee, B.K.: Localized modes of the Hirota equation: Nth order rogue wave and a separation of variable technique. Commun. Nonlinear Sci. Numer. Simul. **39**, 118–133 (2016)
22. Yang, Y., Yan, Z., Malomed, B.A.: Rogue waves, rational solitons, and modulational instability in an integrable fifth-order nonlinear Schrödinger equation. Chaos **25**, 103112 (2015)
23. Akhmediev, N., Ankiewicz, A., Soto-Crespo, J.M.: Rogue waves and rational solutions of the nonlinear Schrödinger equation. Phys. Rev. E **80**, 026601 (2009)
24. Kedziora, D.J., Ankiewicz, A., Akhmediev, N.: Circular rogue wave clusters. Phys. Rev. E **84**, 056611 (2011)
25. Kedziora, D.J., Ankiewicz, A., Akhmediev, N.: Triangular rogue wave clusters. Phys. Rev. E **86**, 056602 (2012)
26. Akhmediev, N., et al.: Roadmap on optical rogue waves and extreme events. J. Opt. **18**, 063001 (2016)
27. Akhmediev, N., Soto-Crespo, J.M., Ankiewicz, A.: Extreme waves that appear from nowhere: on the nature of rogue waves. Phys. Lett. A **373**, 2137–2145 (2009)
28. Akhmediev, N., Eleonskii, V.M., Kulagin, N.E.: N-modulation signals in a single-mode optical waveguide under nonlinear conditions. Zh. Eksp. Teor. Fiz. **94**, 159–170 (1988). [Sov. Phys. JETP **67**, 89-95 (1988)]
29. Geng, X.G., Lv, Y.Y.: Darboux transformation for an integrable generalization of the nonlinear Schrödinger equation. Nonlinear Dyn. **69**, 1621–1630 (2012)
30. Chowdury, A., Ankiewicz, A., Akhmediev, N.: Moving breathers and breather-to-soliton conversion for the Hirota equation. Proc. R. Soc. A **471**, 20150130 (2015)
31. Chowdury, A., Kedziora, D.J., Ankiewicz, A., Akhmediev, N.: Breather-to-soliton conversions described by the quintic equation of the nonlinear Schrödinger hierarchy. Phys. Rev. E **91**, 032928 (2015)

32. Schwalm, W.A.: Lectures on Selected Topics in Mathematical Physics: Elliptic Function-sand Elliptic Integrals, vol. 68. Morgan & Claypool publication as part of IOP Concise Physics, San Rafael (2015)

33. Kedziora, D.J., Ankiewicz, A., Akhmediev, N.: Rogue waves and solitons on a cnoidal background. Eur. Phys. J. Spec. Top. **223**, 43–62 (2014)

34. Chin, S.A., Ashour, O.A., Nikolić, S.N., Belić, M.R.: Peak-height formula for higher-order breathers of the nonlinear Schrödinger equation on nonuniform backgrounds. Phys. Rev. E **95**, 012211 (2017)

35. Ankiewicz, A., Kedziora, D.J., Chowdury, A., Bandelow, U., Akhmediev, N.: Infinite hierarchy of nonlinear Schrödinger equations and their solutions. Phys. Rev. E **93**, 012206 (2016)

36. Kedziora, D.J., Ankiewicz, A., Chowdury, A., Akhmediev, N.: Integrable equations of the infinite nonlinear Schrödinger equation hierarchy with time variable coefficients. Chaos **25**, 103114 (2015)

37. Ankiewicz, A., Wang, Y., Wabnitz, S., Akhmediev, N.: Extended nonlinear Schrödinger equation with higher-oder odd and even terms and its rogue wave solutions. Phys. Rev. E **89**, 012907 (2014)

38. Yang, Y., Wang, X., Yan, Z.: Optical temporal rogue waves in the generalized inhomogeneous nonlinear Schrödinger equation with varying higher-order even and odd terms. Nonlinear Dyn. **81**, 833–842 (2015)

Peak-height formula for higher-order breathers of the nonlinear Schrödinger equation on nonuniform backgrounds

Siu A. Chin,[1] Omar A. Ashour,[1,2] Stanko N. Nikolić,[2,3] and Milivoj R. Belić[2]

[1]*Department of Physics and Astronomy, Texas A&M University, College Station, Texas 77843, USA*
[2]*Science Program, Texas A&M University at Qatar, P.O. Box 23874 Doha, Qatar*
[3]*Institute of Physics, University of Belgrade, Pregrevica 118, 11080 Belgrade, Serbia*

Given any background (or seed) solution of the nonlinear Schrödinger equation, the Darboux transformation can be used to generate higher-order breathers with much greater peak intensities. In this work, we use the Darboux transformation to prove, in a unified manner and without knowing the analytical form of the background solution, that the peak height of a high-order breather is just a sum of peak heights of first-order breathers plus that of the background, *irrespective* of the specific choice of the background. Detailed results are verified for breathers on a cnoidal background. Generalizations to more extended nonlinear Schrödinger equations, such as the Hirota equation, are indicated.

I. INTRODUCTION

The study of high-intensity optical solitons and breathers of the cubic nonlinear Schrödinger (NLS) equation, has became a cornerstone of modern nonlinear physics and is of special importance in modern nonlinear photonics. For a comprehensive review of optical solitons and breathers, see the work by Dudley *et al.* [1].

While the inverse scattering [2] and the direct method [3] have been used in the past to study solitons of the NLS equation, many of the recent advances in understanding breathers [4] and rogue waves [5,6] are based on using the Darboux transformation (DT) [7]. Given any background (or seed) solution of the NLS equation, the Darboux transformation can be used to generate a high-order solution on top of that background with either greater peak intensity [4–6], or greater shape complexity [8,9].

The Darboux transformation is generic in that by iterating a pair of generating solutions of the Lax-pair [10] equation containing the background as an input function, it provides a systematic procedure for creating new solutions. The Darboux transformation itself knows nothing about the evolution equation it is transforming, or the background wave function it is using. The Darboux iterations are therefore the same for the cubic NLS equation, the Hirota equation [11–13], and other extended NLS equations [14–16], regardless of the choice of the background. Variants in the evolution equation and the background solution are only reflected in the initial generating solutions of the Lax-pair equation. Different evolution equations have different Lax-pair equations and therefore different generating solutions. The same Lax-pair equation with different background solutions will also have different generating solutions.

In this work, we first prove in Sec. II a remarkable generic result for DT. If the initial generating functions of DT satisfy a simple phase condition (7) below, then the peak-height formula (6) follows. This formula states that the peak height of a high-order soliton or breather is just a sum of its constituent first-order soliton or breather peak heights plus that of the background. Thus, as long as (7) is true, regardless of the choice of evolution equation or the background wave function,

one has the peak-height formula (6). Hence, Eq. (7) guarantees the peak-height formula for the cubic NLS equation, the Hirota equation [11–13], and any other extended NLS equation [14–16] that evolves according to the Lax-pair equation [10]. This then greatly generalizes the peak-height formula first stated for solitons [17] and more recently proved for Akhmediev breathers [18]. We recall that in Ref. [18], we have shown that the peak-height formula on a constant background is essential for determining what first-order breathers are necessary for producing a higher-order breather of a given intensity. One can then extract an initial profile of the light pulse, with the correct Fourier components, so that when such a pulse is initiated in an optical fiber (assuming that its propagation is well described by the NLS equation), it will be compressed into a breather of the required intensity. Such an initial light pulse can be produced in experiments similar to those described in Refs. [19,20], particularly via the latter reference's frequency comb. By proving a more general peak-height formula here, we hope to pave the way for a possible future practical realization of these more general NLS equations.

The phase condition (7), however, is simply a relative phase between the two generating functions of the Lax equation, and can always be conveniently so chosen in the soliton case of $\psi_0 = 0$. This is also shown in Sec. II. Thus, the peak-height formula holds for solitons of all the NLS equations mentioned above.

Furthermore, when $\psi_0 \neq 0$, the background generates a nontrivial phase for the two generating functions of the Lax equation. We prove in Sec. III that for the cubic NLS equation, and without knowing the analytical form of the background wave function, Eq. (7) remains true despite the added background phase. That is, the peak-height formula (6) for the cubic NLS equation is true regardless of the choice of the background solution: vanishing, uniform, or varying. In this manner, the proof of the peak-height formula for the cubic NLS equation is made complete.

For the Hirota and other extended NLS equations on a uniform background, others [11–16] have shown that (7) is true and therefore the peak-height formula also holds. However, for a nonuniform background, the Lax-pair equations for these

extended equations are more complex and it is difficult and beyond the scope of this work to prove (7) for the extended equations on a general background.

Finally, in Sec. IV we show that for the cubic NLS equation, the only nonuniform background that can support Akhmediev-type breathers is the Jacobi elliptic function $dn(t,k)$, which forms a "dnoidal" background. In the end, in Sec. V we verify our theoretical results with numerical calculations and summarize our conclusions in Sec. VI.

II. BASIC RESULT FOR THE DARBOUX TRANSFORMATION

The Nth-order DT wave function of any nonlinear evolution equation, such as the cubic nonlinear Schrödinger equation

$$i\frac{\partial\psi}{\partial x} + \frac{1}{2}\frac{\partial^2\psi}{\partial t^2} + |\psi|^2\psi = 0, \qquad (1)$$

is given by [7]

$$\psi_N(x,t) = \psi_0(x,t) + \sum_{n=1}^{N}\frac{2(l_n^* - l_n)s_{n1}r_{n1}^*}{|r_{n1}|^2 + |s_{n1}|^2}, \qquad (2)$$

where $\psi_0(x,t)$ is the background solution and the sum goes over N constituent soliton or breather solutions, each characterized by an eigenvalue

$$l_n = i\nu_n, \qquad \text{with} \qquad \nu_n > 0.$$

Here, x and t are the conventional propagation distance and transverse variable of fiber optics. At a given n, the functions $r_{n1}(x,t)$ and $s_{n1}(x,t)$ depend recursively on all the lower n functions via [7]

$$
\begin{aligned}
r_{nj} = {}& [(l_{n-1}^* - l_{n-1})s_{n-1,1}^*r_{n-1,1}s_{n-1,j+1} \\
& + (l_{j+n-1} - l_{n-1})|r_{n-1,1}|^2 r_{n-1,j+1} \\
& + (l_{j+n-1} - l_{n-1}^*)|s_{n-1,1}|^2 r_{n-1,j+1}]/(|r_{n-1,1}|^2 \\
& + |s_{n-1,1}|^2),
\end{aligned}
\qquad (3)
$$

$$
\begin{aligned}
s_{nj} = {}& [(l_{n-1}^* - l_{n-1})s_{n-1,1}r_{n-1,1}^*r_{n-1,j+1} \\
& + (l_{j+n-1} - l_{n-1})|s_{n-1,1}|^2 s_{n-1,j+1} \\
& + (l_{j+n-1} - l_{n-1}^*)|r_{n-1,1}|^2 s_{n-1,j+1}]/(|r_{n-1,1}|^2 \\
& + |s_{n-1,1}|^2).
\end{aligned}
\qquad (4)
$$

These DT iterations are "generic" in that they are of the same form for all NLS or extended equations they are designed to solve. The knowledge of a particular nonlinear equation or a background solution is encoded only in the initial solutions $r_{1j}(x,t)$ and $s_{1j}(x,t)$ of the Lax-pair equation (to be described below), which kick-start the iterations of (3) and (4).

For the general wave function $\psi_N(x,t)$, iterations (3) and (4) are recursively too complex to be written down analytically beyond the lowest few orders. However, we can prove a fundamental result on the basis of (3) and (4) alone, that if for all $1 \leqslant n \leqslant N$, $s_{n1}(0,0)$ and $r_{n1}(0,0)$ only differ by an arbitrary phase ϕ,

$$s_{n1}(0,0) = e^{i\phi}r_{n1}(0,0), \qquad (5)$$

then

$$
\begin{aligned}
\psi_N(0,0) &= \psi_0(0,0) + \sum_{n=1}^{N}(-ie^{i\phi})2\nu_n \\
&= \psi_0(0,0) + \sum_{n=1}^{N}2\nu_n.
\end{aligned}
\qquad (6)
$$

This *peak-height formula* (6) follows from (5) by simply evaluating (2) at the origin $x = t = 0$ with the choice of the phase

$$\phi = \frac{\pi}{2}.$$

Note that (6) gives the wave function itself, not its modulus. Since one can always center the soliton or breather at the origin, this formula gives the peak height of the Nth-order soliton or breather as a *linear* sum of peak heights of individual solitons or breathers plus the height of the background solution. The choice of the phase $e^{i\phi} = i$ is natural, in that the resulting peak height is real and positive.

We will now prove that (5) is true if the initial Lax solutions also satisfy the phase condition

$$s_{1j}(0,0) = e^{i\phi}r_{1j}(0,0), \qquad (7)$$

for each j-constituent soliton or breather. We defer the proof of (7) to the next section, since these initial Lax solutions require knowledge of the specific equation and the background.

To prove (5) on the basis of (7), we apply iterations (3) and (4) at $x = t = 0$ and suppress the notation $(0,0)$. Starting from (7), which is $s_{1j} = e^{i\phi}r_{1j}$ for $1 \leqslant j \leqslant N$, one can prove successively that $s_{2j} = e^{i\phi}r_{2j}$ for $1 \leqslant j \leqslant N-1$, $s_{3j} = e^{i\phi}r_{3j}$ for $1 \leqslant j \leqslant N-2$, etc. Therefore, given $s_{n-1,j} = e^{i\phi}r_{n-1,j}$, (3) and (4) read as

$$r_{nj} = -(ie^{-i\phi})\nu_{n-1}s_{n-1,j+1} + i\nu_{j+n-1}r_{n-1,j+1},$$

$$s_{nj} = (-ie^{i\phi})\nu_{n-1}r_{n-1,j+1} + i\nu_{j+n-1}s_{n-1,j+1},$$

which means that

$$
\begin{aligned}
e^{i\phi}r_{nj} &= -i\nu_{n-1}s_{n-1,j+1} + i\nu_{j+n-1}(e^{i\phi}r_{n-1,j+1}) \\
&= (-ie^{i\phi})\nu_{n-1}r_{n-1,j+1} + i\nu_{j+n-1}s_{n-1,j+1} \\
&= s_{nj}.
\end{aligned}
$$

Thus, the proof by induction is complete. Note that we only need the above equality to evaluate (2) for the peak height; we *do not* need the actual analytical expression for r_{nj} and s_{nj}. This is why the peak height can be evaluated simply, circumventing the full nonlinear complexity of DT.

In the case of the cubic NLS equation, the initial functions $s_{1j}(x,t)$, $r_{1j}(x,t)$ are solutions to the following set of four Lax-pair partial differential equations [5] (subscripts dropped for clarity):

$$r_t = i\psi_0^*s + ilr, \qquad (8)$$

$$s_t = i\psi_0 r - ils, \qquad (9)$$

$$r_x = \left(il^2 - \frac{i}{2}|\psi_0|^2\right)r + \left(il\psi_0^* + \frac{1}{2}(\psi_0^*)_t\right)s, \qquad (10)$$

$$s_x = \left(-il^2 + \frac{i}{2}|\psi_0|^2\right)s + \left(il\psi_0 - \frac{1}{2}(\psi_0)_t\right)r, \quad (11)$$

whose compatibility condition requires ψ_0 to be a solution of the NLS equation. For more extended NLS equations, the Lax-pair equations remain linear, but are more complex, and can be found in Refs. [14–16]. Since (8)–(11) is a set of four *linear* equations, the solutions $s_{1j}(x,t)$ and $r_{1j}(x,t)$ will contain four constants of integration. As the DT wave function (2) is unaffected by a common phase (or a common scale factor) of $s_{1j}(x,t)$ and $r_{1j}(x,t)$, one constant can be used to normalize both to unit modulus. Two constants can be used to shift the solution peak to x_0 and t_0 and the last constant can be chosen to fix the relative phase, so that (7) is true. Such a relative phase then guarantees a positive wave function peak height. This argument suggests that (7) is always possible (when $x_0 = t_0 = 0$) by simply choosing

$$r_{1j}(0,0) = e^{-i\pi/4} \quad \text{and} \quad s_{1j}(0,0) = e^{i\phi}r_{1j}(0,0) = e^{i\pi/4}. \quad (12)$$

This is indeed the case for solitons based on the background $\psi_0 = 0$. For example, integrating (8)–(11) with $\psi_0 = 0$ gives

$$r_{1j}(x,t) = \exp[-\nu_j(t - t_0) - i\nu_j^2(x - x_0) - i\pi/4], \quad (13)$$

$$s_{1j}(x,t) = \exp[\nu_j(t - t_0) + i\nu_j^2(x - x_0) + i\pi/4], \quad (14)$$

which produces a first-order soliton (when setting $x_0 = t_0 = 0$)

$$\begin{aligned}
\psi_1(x,t) &= \psi_0 + \frac{2(l_1^* - l_1)r_{11}^* s_{11}}{|r_{11}|^2 + |s_{11}|^2} \\
&= \frac{2(-2i\nu_1)\exp\left(i2\nu_1^2 x + i\pi/2\right)}{\exp(-2\nu_1 t) + \exp(2\nu_1 t)} \\
&= \frac{2\nu_1 \exp\left(i2\nu_1^2 x\right)}{\cosh(2\nu_1 t)}
\end{aligned}$$

with a positive peak height at the origin

$$\psi_1(0,0) = 2\nu_1. \quad (15)$$

Since (13) and (14) satisfy (7) when $x_0 = t_0 = 0$, the peak height of an Nth-order soliton is given by (6), with $\psi_0(0,0) = 0$. This result has been stated without a proof some time ago [17], but with a different relative phase between $r_{1j}(x,t)$ and $s_{1j}(x,t)$. Result (12) remains true for $\psi_0 = 0$ in the more extended NLS equations, including the Hirota and the Lakshmanan-Porsezian-Daniel operators (see Ref. [14]). Thus, the peak-height formula holds for solitons in all extended NLS equations.

When $\psi_0 \neq 0$, as we shall see below, the background will generate an additional phase on the initial Lax solutions, and one must show that (7) remains true in spite of the added phase.

III. GENERAL BACKGROUND WAVE FUNCTIONS

For solutions of the NLS equation with a nonuniform background of the form

$$\psi_0(x,t) = AF(t)e^{iBx}, \quad (16)$$

where $A \neq 0$ and $F(t)$ is real, we will show that Eq. (7) remains true, but now *requires* that $\phi = \pi/2$. For $\psi_0(0,0)$ to be the peak, we assume that $F(t)$ is normalized such that

$$F(0) = 1 \quad \text{and} \quad F_t(0) = 0. \quad (17)$$

This is all that we need to prove (7); we do not need to know the analytic form of $F(t)$. [We also do not need to require $F_{tt}(0) < 0$; the case of $F_{tt}(0) > 0$ is covered by taking $A < 0$.]

For $F(t)$ not constant, one cannot solve all four Lax-pair equations. However, one can still solve (10) and (11) by invoking (16) and (17). Fixing $t = 0$ with $l = i\nu$, the last two Lax-pair equations read [suppressing the subscripts and $(x,0)$ dependence]

$$r_x = -i\left(\nu^2 + \tfrac{1}{2}A^2\right)r - \nu A e^{-iBx}s,$$

$$s_x = i\left(\nu^2 + \tfrac{1}{2}A^2\right)s - \nu A e^{iBx}r.$$

Letting

$$r = a e^{-iBx/2} \quad \text{and} \quad s = b e^{iBx/2}$$

gives

$$a_x = -iUa - \nu Ab, \quad (18)$$

$$b_x = iUb - \nu Aa, \quad (19)$$

where $U = \nu^2 + \tfrac{1}{2}(A^2 - B)$. It follows that

$$b_{xx} = (\nu^2 A^2 - U^2)b = \nu^2\omega^2 b \quad (20)$$

with

$$\omega = \sqrt{B - \nu^2 - \left(\frac{A^2 - B}{2\nu}\right)^2}, \quad (21)$$

and hence the solution is

$$b = Ce^{\nu\omega x} + De^{-\nu\omega x}.$$

In this work, we focus on the breathers with real ω, thus restricting

$$B - \nu^2 - \frac{1}{\nu^2}\left(\frac{A^2 - B}{2}\right)^2 \geqslant 0. \quad (22)$$

The boundary value of this equation defines the rogue wave limit of $\omega = 0$. When ω is imaginary, one has Kuznetsov-Ma-type solutions periodic in x [21,22].

For breathers, the solution for a follows from (19),

$$\begin{aligned}
a &= \frac{1}{\nu A}(iUb - b_x) = D\left(\frac{\nu\omega + iU}{\nu A}\right)e^{-\nu\omega x} \\
&\quad - C\left(\frac{\nu\omega - iU}{\nu A}\right)e^{\nu\omega x}.
\end{aligned}$$

From (20), the parentheses are just pure phases,

$$a = De^{i2\chi - \nu\omega x} - Ce^{-i2\chi + \nu\omega x},$$

given by

$$\cos(2\chi) = \omega/A \quad \text{and} \quad \sin(2\chi) = U/(\nu A). \quad (23)$$

To make a and b symmetrical, we can choose

$$D = e^{-i\chi - i\delta} \quad \text{and} \quad C = e^{i\chi + i\gamma},$$

with phases δ and γ yet to be determined. This then gives, restoring all subscripts,

$$r_{1j}(0,0) = e^{i\chi_j - i\delta} - e^{-i\chi_j + i\gamma} = e^{i\chi_j - i\delta} + e^{-i\chi_j + i\gamma - i\pi},$$

$$s_{1j}(0,0) = e^{i\chi_j + i\gamma} + e^{-i\chi_j - i\delta}.$$

The above will satisfy (7) if the phase ϕ is given by

$$\phi = \delta + \gamma = \frac{\pi}{2}.$$

Note that only the sum $\delta + \gamma$ is fixed to be $\pi/2$; however, the symmetrical choice of $\delta = \gamma = \pi/4$ is universally adopted in the literature [6,7,23]. Thus, for the above choice of ϕ, (7) remains true *independent of the phase χ_j generated by the background*. Therefore, the peak-height formula (6) for breathers is true regardless of the choice of the background.

To verify that $2\nu_1$ is indeed the peak height of the first-order DT wave function, we compute directly

$$\psi_1(x,0) = \psi_0(x,0) + \frac{2(l_1^* - l_1)s_{1j}r_{11}^*}{|r_{11}|^2 + |s_{11}|^2} = \left(A + \frac{2\nu_1[1 - \sin(2\chi_1)\cosh(2\nu_1\omega_1 x) + i\,\cos(2\chi_1)\sinh(2\nu_1\omega_1 x)]}{\cosh(2\nu_1\omega_1 x) - \sin(2\chi_1)} \right)e^{iBx}. \quad (24)$$

At $x \to \pm\infty$, we have intensity

$$|\psi_1(\pm\infty,0)|^2 = [A - 2\nu_1\sin(2\chi_1)]^2 + [2\nu_1\cos(2\chi_1)]^2 = A^2 - 4A\nu_1\sin(2\chi_1) + 4\nu_1^2 = A^2 - 4U + 4\nu_1^2 = 2B - A^2, \quad (25)$$

provided that $\omega \neq 0$. For Akhmediev breathers on a uniform background $\psi_0 = e^{ix}$ with $A = B = 1$, the above reproduces the background intensity $|\psi_1(x \to \pm\infty, 0)|^2 = 1$, as compared to the peak height $\psi_1(0,0) = 1 + 2\nu_1$.

Breathers of the Hirota and extended NLS equations on the uniform background have initial Lax solutions satisfying (7) [13,16]. Therefore, these breathers obey the same peak-height formula as the Akhmediev breathers.

IV. CNOIDAL BACKGROUND BREATHERS

For solutions of the cubic NLS equation with nonuniform backgrounds, we substitute (16) into (1), to find

$$\frac{d^2 F}{dt^2} = 2BF - 2A^2 F^3.$$

Comparing this to the equation satisfied by any of the 12 Jacobi elliptic functions [24] $zn(t,k)$

$$\frac{d^2 zn}{dt^2} = \beta zn + 2\alpha zn^3,$$

we must have $\alpha = -A^2$ and $\beta = 2B$. Among the 12 elliptic functions, only four have α negative [24], given by

(1) $F(t) = \text{cn}(t,k)$ with $A = k, B = k^2 - 1/2$,

(2) $F(t) = \text{dn}(t,k)$ with $A = 1, B = 1 - k^2/2$,

(3) $F(t) = \text{nd}(t,k)$ with $A = \sqrt{1-k^2}, B = 1 - k^2/2$,

(4) $F(t) = \text{sd}(t,k)$ with $A = k\sqrt{1-k^2}, B = k^2 - 1/2$,

where k is the modulus of the elliptic function. For cases (1) and (2), $t = 0$ is the peak of $\text{cn}(t,k)$ and $\text{dn}(t,k)$. However, for cases (3) and (4) the peaks are at $\text{nd}(K,k)$ and $\text{sd}(K,k)$, where K is the quarter-period of cn. Therefore, for these to peak at $t = 0$, one must set $F(t) = \text{nd}(t + K,k)$ and $F(t) = \text{sd}(t + K,k)$. For case (3) this means

$$AF(t) = \sqrt{1-k^2}\,\text{nd}(t + K,k) = \frac{\sqrt{1-k^2}}{\text{dn}(t + K,k)} = \text{dn}(t,k),$$

which is identical to case (2). For case (4), one has

$$AF(t) = k\sqrt{1-k^2}\,\text{sd}(t + K,k) = k\sqrt{1-k^2}\,\frac{\text{sn}(t + K,k)}{\text{dn}(t + K,k)}$$

$$= k\,\text{dn}(t,k)\frac{\text{cn}(t,k)}{\text{dn}(t,k)} = k\,\text{cn}(t,k),$$

which is identical to case (1). There are therefore only two cnoidal background solutions, (1) and (2). For these two cases, respectively, our general formula (23) for the background phase,

$$\cos(2\chi_j) = \sqrt{1 - \frac{1}{k^2}\left(\nu_j + \frac{1}{4\nu_j}\right)^2},$$

$$\cos(2\chi_j) = \sqrt{1 - \left(\nu_j + \frac{k^2}{4\nu_j}\right)^2},$$

agrees with the results of Ref. [23].

For the cn background, the restriction (22) for breathers gives

$$k^2 \geqslant \left(\nu + \frac{1}{4\nu}\right)^2 \geqslant 1,$$

since the right-hand side has a minimum of 1. There is therefore no breather except possibly at $k = 1$. However, at $k = 1$, $\text{cn}(t,1) = \text{sech}(t)$, which is the same as the dn case at $k = 1$, described below. Thus, all breathers are contained in the dn case and the cn background only supports the Kuznetsov-Ma-type [21,22] breathers.

For the dn background, the breather condition (22) gives

$$\left(\nu + \frac{k^2}{4\nu}\right)^2 \leqslant 1 \quad \to \quad k^2 \leqslant 4\nu(1 - \nu),$$

which restricts the range of ν to

$$\tfrac{1}{2} - \tfrac{1}{2}\sqrt{1-k^2} \leqslant \nu \leqslant \tfrac{1}{2} + \tfrac{1}{2}\sqrt{1-k^2}. \quad (26)$$

As k ranges from 0 to 1, the range of ν narrows from [0,1] to [1/2,1/2]. In contrast to the Akhmediev breather case, where there is only a single rogue wave at $\nu = 1$, corresponding to the Peregrine breather, here, at each value of k, there are *two* rogue waves, corresponding to the lower and upper boundary values of (26). (These are called the DCRW and CCRW, respectively,
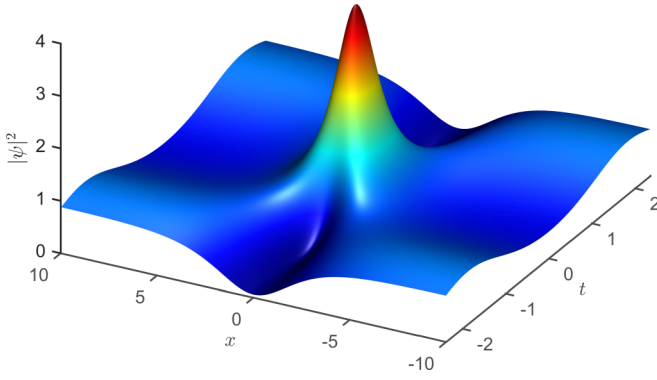
FIG. 1. A breather on the $dn(t)$ elliptic function background, with $v = 1/2$ and $k^2 = 1/2$. The peak intensity is 4.

in Ref. [23]). The peak intensity of the brighter rogue wave is

$$|\psi_1(0,0)|^2 = (2 + \sqrt{1-k^2})^2, \tag{27}$$

to be compared to the background intensity from (25):

$$|\psi_1(x \to \pm\infty, 0)|^2 = 1 - k^2. \tag{28}$$

While the absolute peak intensity (27) is less than that of the Peregrine breather, its ratio with respect to the background intensity (28) is always greater than 9, with increasing k.

V. NUMERICAL VERIFICATION

We have implemented the Darboux transformation on cnoidal backgrounds with the same initial conditions as used by Kedziora *et al.* [23].

In Fig. 1, we show a breather on the $dn(t)$ elliptic function background at $v = 1/2$ and $k^2 = 1/2$. The peak intensity is precisely 4, in agreement with the peak-height formula. While the evolution of $|\psi(x,0)|^2$ given in Fig. 2 only reaches a single
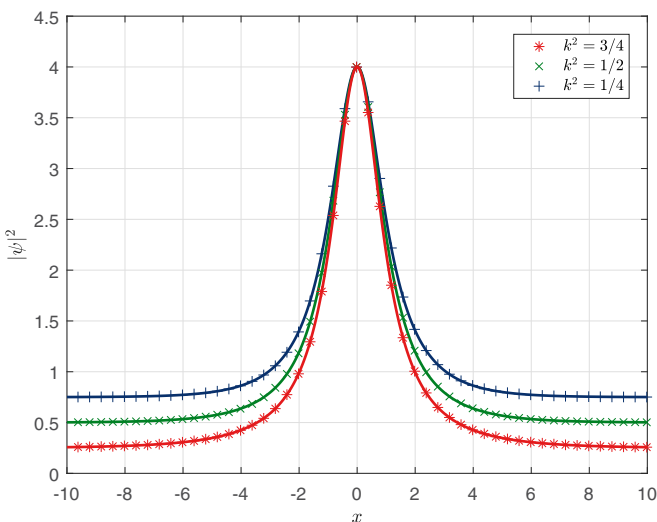
FIG. 2. Comparing the DT evolution of $|\psi(x,0)|^2$ (symbols) with prediction (24) (lines) at $v = 1/2$ and at three values of $k^2 = 1/4, 1/2, 3/4$. The peak intensity at the origin is 4 for all three cases, but the background intensities given by (28) are respectively $3/4$, $1/2$, and $1/4$.
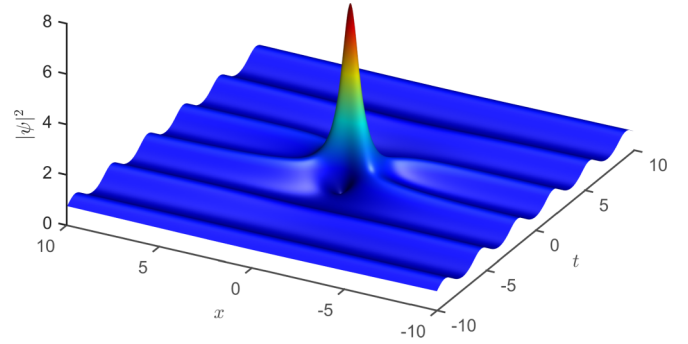
FIG. 3. The bright rogue wave at $k^2 = 1/2$ and $v = \frac{1}{2} + \frac{1}{2}\sqrt{1-k^2}$. The numerical peak intensity is 7.3284; the peak-height formula intensity is $4 + 1/2 + 2\sqrt{2} = 7.3284$.

peak, its variation in the t direction is modulated by the periodic elliptic function background.

In Fig. 2, the DT profile $|\psi(x,0)|^2$ is compared to the general theoretical result (24) at $v = 1/2$, but at three values of $k^2 = 1/4, 1/2, 3/4$. Since the peak height only depends on v, all three cases have the same peak intensity of 4. However, the background intensity changes according to k^2, as given by (28). The agreement between numerical DT simulations and theoretical predictions is perfect.

For the case of $k^2 = 1/2$, the bright rogue wave is at $v = \frac{1}{2} + \frac{1}{2}\sqrt{1-k^2}$, with peak intensity $(1 + 2v)^2 = 7.3284$. This is shown in Fig. 3. Rogue waves on a uniform background reach their peaks monotonically in both the x and t directions. Rogue waves on a cnoidal background arise out of a background periodic in the t direction.

In Fig. 4, we show the dim rogue wave with $v = \frac{1}{2} - \frac{1}{2}\sqrt{1-k^2}$ at the same value of $k^2 = 1/2$. The intensity is more than a factor of 4 dimmer and with much shorter wavelength oscillations in the t direction, due to the smaller v. This intensity profile is similar to Fig. 8(a) of Ref. [23].

Using DT, one can form a second-order rogue wave by combining the two v-values of the bright and dim rogue waves. This rogue wave is special in that, since the plus and minus terms in v cancel, i.e., from (6),

$$|\psi(0,0)|^2 = (1 + 2v_1 + 2v_2)^2$$
$$= (1 + 1 + \sqrt{1-k^2} + 1 - \sqrt{1-k^2})^2 = 9,$$
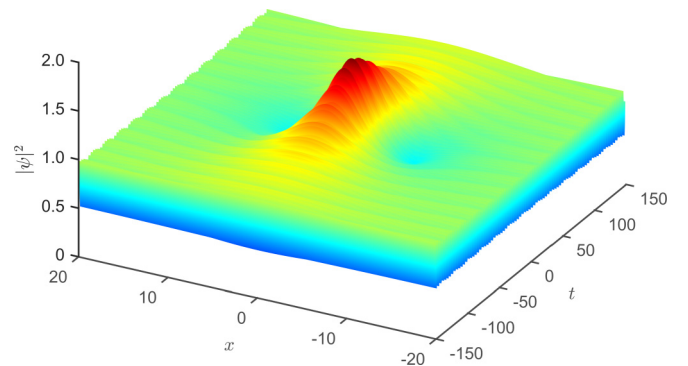
FIG. 4. The dim rogue wave at $k^2 = 1/2$ and $v = \frac{1}{2} - \frac{1}{2}\sqrt{1-k^2}$. The numerical peak intensity is 1.6716; the peak-height formula intensity is $4 + 1/2 - 2\sqrt{2} = 1.6716$.
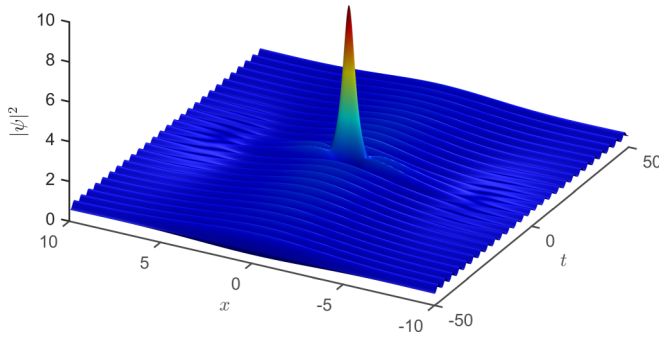
FIG. 5. Second-order rogue wave at $k^2 = 1/2$ formed by the bright and dim rogue waves of Figs. 3 and 4. The peak intensity of 9 here is precisely the sum of those two figures' intensities.
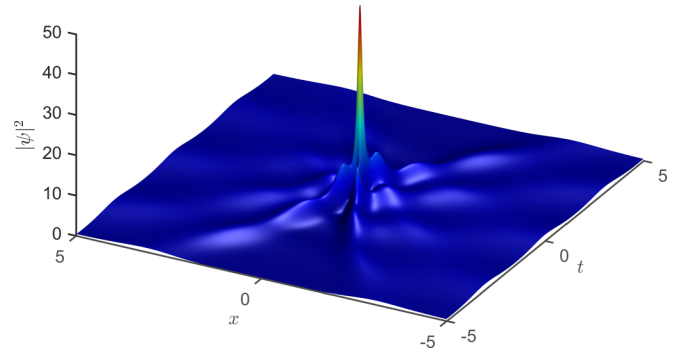

FIG. 6. Fifth-order breather at $k^2 = 1/2$, with five values of $v_i = 0.4, 0.5, 0.6, 0.7, 0.8$. The numerical DT peak intensity is 49. The peak-height formula intensity is also 49.

its intensity is always 9 *independent* of the background parametrized by k. Its intensity is exactly at the border between first- and second-order breathers. This is shown in Fig. 5. Such a rogue wave was originally suggested, but not computed, by Kedziora *et al.* [23]. What is even more remarkable is that the intensity of this second-order rogue wave is exactly the sum of the intensities of the previous two first-order rogue waves. We have therefore found a "Pythagorean triplet" of rogue waves, in the sense that the sum of squares of two wave function peaks is equal to the square of a third wave function peak. Such a result would seem inexplicable and unexpected without having an analytical form for the wave function peak. The power of our peak-height formula is that, in order for the sum of two squares of wave function peaks to satisfy

$$(2 - \sqrt{1 - k^2})^2 + (2 + \sqrt{1 - k^2})^2 = 9,$$

the two first-order rogue waves must reside on a background of $k^2 = 1/2$. Thus our peak-height formula makes it easy to see that among all possible rogue waves given by (26), this Pythagorean triplet is unique to the background of $k^2 = 1/2$. There are no such rogue wave triplets on other backgrounds.

A fifth-order breather is shown in Fig. 6. Such a high-order breather is very concentrated and one has to zero-in on the origin, to see the extremely high, yet narrow, peak. Our peak-height formula perfectly predicted the peak height of this high-order breather.

VI. CONCLUSIONS

In this work, we have shown that for the NLS equation, the peak-height formula (6) is true for all proper choices of the background solution—vanishing, uniform, or varying.

More generally, we have also shown that, since the DT iterations are generic, as long as (7) is true, the peak-height formula (6) is true for all extended NLS equations. Such a peak-height formula will be useful in guiding the design and production of maximal-intensity breathers in physical systems that can be modeled by the NLS equation [18] and its extended variants. Also, while there is no direct generalization of DT to higher spatial dimensions for the NLS equation, the one-dimensional (1D) solution of the NLS can be embedded into the three-dimensional (3D) solution via similarity reductions [25,26] in the study of Bose-Einstein condensates. The resulting 3D solution is then basically the 1D solution multiplied by some prefactors. Our peak-height formula will be useful in determining the peak density of the condensate by evaluating those prefactors.

Finally, our peak-height formula provided insights into relating all breathers generated by DT. For example, it can be used to prove the uniqueness of the Pythagorean triplet of rogue waves. It also provides a simple check on the accuracy of any numerical solution of the NLS equation. This is especially useful when solving extended NLS equations with complex higher-order terms.

[1] J. M. Dudley, F. Dias, M. Erkintalo, and G. Genty, Instabilities, breathers and rogue waves in optics, Nat. Photonics **8**, 755 (2014).

[2] V. E. Zakharov and A. B. Shabat, Exact theory of two-dimensional self-focusing and one-dimensional self-modulation of waves in nonlinear media, Zh. Eksp. Teor. Fiz. **61**, 118 (1972) [Sov. Phys. JETP **34**, 62 (1972)].

[3] R. Hirota, *The Direct Method in Soliton Theory* (Cambridge University Press, Cambridge, UK, 2004).

[4] N. Akhmediev and V. Korneev, Modulation instability and periodic solutions of the nonlinear Schrödinger equation, Theor. Math. Phys. **69**, 1089 (1986).

[5] N. Akhmediev, A. Ankiewicz, and J. M. Soto-Crespo, Rogue waves and rational solutions of the nonlinear Schrödinger equation, Phys. Rev. E **80**, 026601 (2009).

[6] N. Akhmediev, J. M. Soto-Crespo, and A. Ankiewicz, Extreme waves that appear from nowhere: On the nature of rogue waves, Phys. Lett. A **373**, 2137 (2009).

[7] N. N. Akhmediev, V. I. Korneev, and N. V. Mitskevich, *N*-modulation signals in a single-mode optical waveguide under nonlinear conditions, Zh. Eksp. Teor. Fiz. **94**, 159 (1988) [Sov. Phys. JETP **67**, 89 (1988)].

[8] D. J. Kedziora, A. Ankiewicz, and N. Akhmediev, Circular rogue wave clusters, Phys. Rev. E **84**, 056611 (2011).

[9] D. J. Kedziora, A. Ankiewicz, and N. Akhmediev, Classifying the hierarchy of nonlinear-Schrödinger-equation rogue-wave solutions, Phys. Rev. E **88**, 013207 (2013).

[10] P. Lax, Integrals of nonlinear equations of evolution and solitary waves, Commun. Pure Appl. Math. **21**, 467 (1968).

[11] R. Hirota, Exact envelope-soliton solutions of a nonlinear wave equation, J. Math. Phys. **14**, 805 (1973).

[12] A. Ankiewicz, J. M. Soto-Crespo, and N. Akhmediev, Rogue waves and rational solutions of the Hirota equation, Phys. Rev. E **81**, 046602 (2010).

[13] A. Chowdury, A. Ankiewicz, and N. Akhmediev, Moving breathers and breather-to-soliton conversions for the Hirota equation, Proc. R. Soc. London, Ser. A **471**, 20150130 (2015).

[14] A. Ankiewicz and N. Akhmediev, Higher-order integrable evolution equation and its soliton solutions, Phys. Lett. A **378**, 358 (2014).

[15] A. Chowdury, D. J. Kedziora, A. Ankiewicz, and N. Akhmediev, Soliton solutions of an integrable nonlinear Schrödinger equation with quintic terms, Phys. Rev. E **90**, 032922 (2014).

[16] A. Chowdury, D. J. Kedziora, A. Ankiewicz, and N. Akhmediev, Breather-to-soliton conversions described by the quintic equation of the nonlinear Schrödinger hierarchy, Phys. Rev. E **91**, 032928 (2015).

[17] N. N. Akhmediev and N. V. Mitzkevich, Extremely high degree of N-soliton pulse compression in an optical fiber, IEEE J. Quantum Electron. **27**, 849 (1991).

[18] S. A. Chin, O. A. Ashour, S. N. Nikolic, and M. R. Belic, Maximal intensity higher-order Akhmediev breathers of the nonlinear Schrödinger equation and their systematic generation, Phys. Lett. A **380**, 3625 (2016).

[19] M. Erkintalo, K. Hammani, B. Kibler, C. Finot, N. Akhmediev, J. M. Dudley, and G. Genty, Higher-Order Modulation Instability in Nonlinear Fiber Optics, Phys. Rev. Lett. **107**, 253901 (2011).

[20] B. Frisquet, A. Chabchoub, J. Fatome, C. Finot, B. Kibler, and G. Millot, Two-stage linear-nonlinear shaping of an optical frequency comb as rogue nonlinear-Schrödinger-equation-solution generator, Phys. Rev. A **89**, 023821 (2014).

[21] E. A. Kuznetsov, Solitons in a parametrically unstable plasma, Sov. Phys. Dokl. **22**, 507 (1977).

[22] Y. C. Ma, The perturbed plane-wave solution of the cubic Schrödinger equation, Stud. Appl. Math. **60**, 43 (1979).

[23] D. J. Kedziora, A. Ankiewicz, and N. Akhmediev, Rogue waves and solitons on a cnoidal background, Eur. Phys. J. Spec. Top. **223**, 43 (2014).

[24] W. A. Schwalm, *Lectures on Selected Topics in Mathematical Physics: Elliptic Functions and Elliptic Integrals*, Morgan and Claypool publication as part of IOP Concise, Physics (IOP Publishing, Bristol, UK, 2015), Table 1.1.

[25] Z. Yan, V. V. Konotop, and N. Akhmediev, Three-dimensional rogue waves in nonstationary parabolic potentials, Phys. Rev. E **82**, 036610 (2010).

[26] F.-D. Zong, Y.-S. Yan, and S.-T. Shen, Higher-order modes of modulation instability in Bose-Einstein condensates with a time-dependent three-dimensional parabolic potential, J. Phys. Soc. Jpn. **83**, 104002 (2014).

Maximal intensity higher-order Akhmediev breathers of the nonlinear Schrödinger equation and their systematic generation

Siu A. Chin [a,*], Omar A. Ashour [a,b], Stanko N. Nikolić [b,c], Milivoj R. Belić [b]

[a] *Department of Physics and Astronomy, Texas A&M University, College Station, TX 77843, USA*
[b] *Science Program, Texas A&M University at Qatar, P.O. Box 23874 Doha, Qatar*
[c] *Institute of Physics, University of Belgrade, Pregrevica 118, 11080 Belgrade, Serbia*

A B S T R A C T

It is well known that Akhmediev breathers of the nonlinear cubic Schrödinger equation can be superposed nonlinearly via the Darboux transformation to yield breathers of higher order. Surprisingly, we find that the peak height of each Akhmediev breather only adds *linearly* to form the peak height of the final breather. Using this peak-height formula, we show that at any given periodicity, there exists a unique high-order breather of maximal intensity. Moreover, these high-order breathers form a continuous hierarchy, growing in intensity with increasing periodicity. For any such higher-order breather, a simple initial wave function can be extracted from the Darboux transformation to dynamically generate that breather from the nonlinear Schrödinger equation.

© 2016 Elsevier B.V. All rights reserved.

The study of high-intensity optical solitons on a finite background, known as "breathers" (and "rogue waves"), is of growing importance in modern nonlinear photonics. For a comprehensive reference of recent works, see the review by Dudley et al. [1]. One way of achieving high intensity is to create higher-order versions of these breathers. (We regard rogue waves as special cases of breathers with infinite period [2].) While it has been known for a long time [3] that these higher-order breathers can be composed from first-order breathers via the Darboux transformation (DT), the recursive complexity of the transformation [3–7] has obscured insights into the working of DT's nonlinear superposition. In this work, we find analytically that, despite the nonlinear superposition, the peak heights of the breathers only add *linearly*. From this key result, one can prove that: I) At each periodicity, there is a unique higher order breather of *maximal* peak intensity. II) With increasing periodicity, these higher-order breathers form a continuous hierarchy of single-peak solitary waves with monotonically rising intensity. III) In the limit of an infinite period, these higher-order breathers morph smoothly into rational rogue waves of the same order. IV) From the breather's numerical wave function produced by DT, an initial wave function in the form of a cosine series can be extracted, so that when the latter is inputted into the non-

linear Schrödinger equation (NLSE), the breather can be generated *dynamically*. Since the NLSE is an excellent model for propagating light pulses in an optical fiber, our results strongly suggest that breathers of extreme intensity and short duration can be systematically produced in optical fibers.

Let's first summarize some well-known properties of first-order Akhmediev breathers (ABs) [8,9]. The breather's wave function

$$\psi(t, x) = \left[1 + \frac{2(1-2a)\cosh(\lambda t) + i\lambda \sinh(\lambda t)}{\sqrt{2a}\cos(\Omega x) - \cosh(\lambda t)} \right] e^{it}, \tag{1}$$

is an exact solution to the cubic NLSE

$$i\frac{\partial \psi}{\partial t} + \frac{1}{2}\frac{\partial^2 \psi}{\partial x^2} + |\psi|^2 \psi = 0, \tag{2}$$

on a finite background: $|\psi(t \to \pm\infty, x)| \to 1$. Its most fundamental characteristic is that it is *periodic* over a length L parametrized by the modulation parameter a:

$$L = \pi / \sqrt{1-2a}.$$

Only in the singular limit of $a \to 1/2$, $L \to \infty$, does it become the non-periodic, Peregrine soliton [10].

At a given a, because of this basic periodicity, the allowed Fourier modes can only have wave numbers

$$k_m = m\Omega \quad \text{for} \quad m = 0, \pm 1, \pm 2, \cdots, \tag{3}$$

where Ω is the interval's fundamental wave number:

$$\Omega = 2\pi/L = 2\sqrt{1-2a}. \tag{4}$$

The growth factor $\lambda = \sqrt{8a(1-2a)} = \Omega\sqrt{1-(\Omega/2)^2}$ is due to the instability of this fundamental mode, as determined by the Bogoliubov spectrum [11–13] or by the Benjamin–Feir [14] instability. This growth factor, when real, implies that all modes with $|k_m| < 2$ are unstable. Specifically, the first nonzero $|m|$ harmonic modes are unstable for $|m|\Omega < 2$, or at the parameter values [15]

$$a > a_m^* \equiv \frac{1}{2}\left(1 - \frac{1}{m^2}\right). \tag{5}$$

If a were negative, then (4) implies that $\Omega > 2$ and all modes are stable. A negative a will therefore not result in an AB, but only in stable Bogoliubov excitation modes [13].

The AB wave function (1) peaks at $t = 0$, with profile

$$\psi(0,x) = 1 + \frac{2(1-2a)}{\sqrt{2a}\cos(\Omega x) - 1}. \tag{6}$$

The maximum peak height is at $x = 0$,

$$|\psi|_{max} = 1 + 2\sqrt{2a}. \tag{7}$$

As a increases from 0 to 1/2, this peak height increases from the background height of 1 and smoothly matches the Peregrine's [10] peak height of 3.

By using DT, an nth-order breather can be constructed from n ABs with an arbitrary set of real modulation parameters

$$a_1 > a_2 > a_3 > \cdots a_n > 0. \tag{8}$$

(All t- and x-shift parameters [6] are set to zero.) However, such a construction would overlook the importance of periodicity. Given an initial AB with $a_1 = a$, it is periodic over a length of $L_1 = L$. For any $a_k < a_1$, the resulting Ω_k, if incommensurate with Ω, would completely destroy the periodicity of the original AB. Even if Ω_k were commensurate with Ω, unless Ω_k is just a multiple of Ω, the periodic length L must be enlarged to accommodate both wave numbers. While there is no logical argument forbidding such an arbitrary a_k construction, it is reasonable to insist that the higher-order breather retains the same periodic length L as the initial AB. In this case, one must choose $\Omega_k = k\Omega$, resulting in the following set of modulation parameters:

$$a_k = k^2\left(a - \frac{1}{2}\right) + \frac{1}{2}. \tag{9}$$

This set of a_k as a function of a is plotted in Fig. 1. Note that $a_k > 0$ only when $a > a_k^*$. Let's denote the region $a_n^* < a < a_{n+1}^*$ as R_n; then in each region R_n there are exactly n values of (8) that can be combined by DT to form an nth-order breather. We will show below that such a breather has the highest peak intensity at any given periodic length parametrized by a.

The Darboux transformation gives

$$\psi_n(t,x) = \psi_{n-1}(t,x) + \delta\psi(t,x), \tag{10}$$

where $\delta\psi(t,x)$ depends *recursively* on all the previous-order wave functions [3–6]. This is classic nonlinear superposition. However, we will prove in the Appendix that for an nth-order AB, the maximum peak height at $t=0$ and $x=0$ only adds *linearly*, given by

$$|\psi|_{max} = 1 + 2\sum_{k=1}^{n}\sqrt{2a_k}. \tag{11}$$

This is one key finding of this work, valid for an arbitrary set of real a_k.
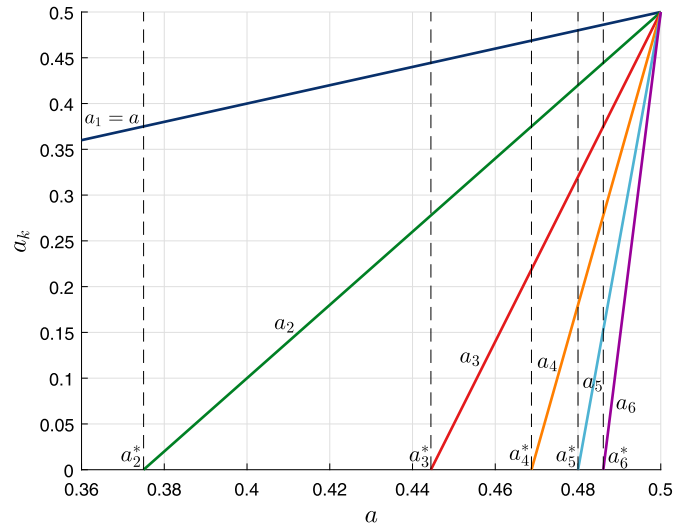

Fig. 1. Modulation parameters a_k of (9) as functions of a. Vertical broken lines indicate the locations of a_m^*.

The peak height of $|\psi(0,0)|$ has been studied previously. In an early work of Akhmediev and Mitzkevich [16], a formula similar to (11) was stated without proof for solitons, in terms of the imaginary parts of DT eigenvalues. (For an AB, the corresponding imaginary part is $\sqrt{2a}$.) More recently, Kedziora, Ankiewicz and Akhmediev [17] have found *numerically* that the peak amplitude of a fused n-order rogue wave is one plus twice the imaginary part times n, corresponding to (11) with all a_k equal. Later in Ref. [18], a case (their Fig. 8) with three different imaginary parts is also found to be true, numerically. However, in all these cases, the term with the imaginary part was never explicitly identified as the peak-height of the constituent breather or soliton.

For the special set of a_k given by (9), we can further deduce that: 1) In each region of R_n there is a unique nth-order AB with peak height given by (11). This peak height is maximal because it is a sum over all available and possible a_k's of a given periodic length. 2) In regions lower than R_n, this nth-order AB does not exist because some of the required a_k are not positive. 3) In regions higher than R_n, this nth-order AB retains the highest peak height among all nth-order ABs. For example, in R_3, we have $a_1 > a_2 > a_3 > 0$. Clearly, from Fig. 1 and (11), the second-order AB formed from a_1 and a_2 will have the greater peak height than the AB2 formed from a_1 and a_3 or a_2 and a_3. The last case also illustrates that the peak height of an AB2 formed from any two a values having commensurate wave numbers will always be lower than that formed from wave numbers k_1 and k_2 over the *same* periodic interval. Therefore, by (11), the nth-order AB formed from the first n values of (9) has peak intensity greater than any other AB having the same periodic length.

The peak heights of these maximal higher-order ABs are plotted in Fig. 2. In each R_n region, the maximal intensity breather is indicated as a solid line. These solid lines can be joined continuously over each region, forming a single hierarchy of maximal intensity breathers. In higher R_n regions, the lower-order ABs remain maximal for their order and are denoted by broken lines. As $a \to 1/2$, (11) smoothly yields $|\psi|_{max} = 1 + 2n$, which are the peak heights of nth-order *rational* rogue waves (RWs) [2]. Thus, RWs are the natural end points of our periodic ABs. Although RWs have the highest intensity at each order, their intensities are discrete, with ever-growing gaps between successive orders. By contrast, the intensity of our hierarchy of periodic ABn, as shown in Fig. 2, can be continuously chosen by changing the periodic length via the modulation parameter a.
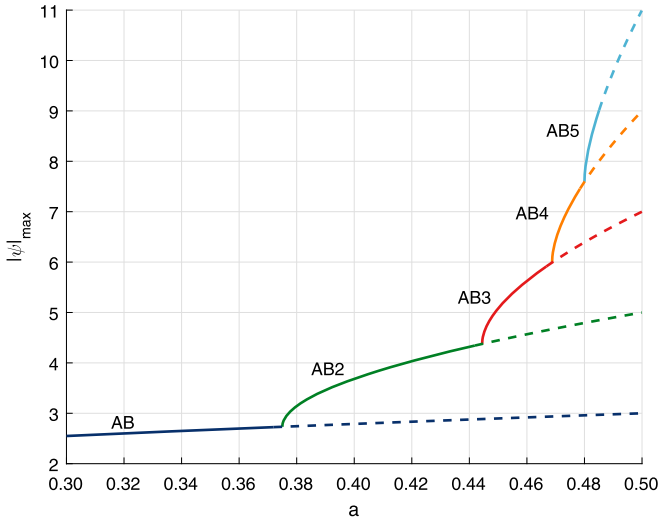
Fig. 2. Peak heights of maximal intensity nth-order Akhmediev breathers at any spatial periodic length parametrized by the modulation parameter a.

Now that we have shown that this hierarchy of high-order ABs is of maximal intensity, the next step is to find ways of producing them *systematically*. Currently, only breathers up to the second-order have been observed in optical fibers [19–21]. While third-order breathers have been seen in random field searches [1,22], the analytical initial wave functions used for exciting a second-order RW optically [20], or a third-order RW theoretically [23], were essentially obtained by trial and error.

Recall that the AB wave function at $t=0$, (6), is an *even* function of x. Since the NLSE preserves the symmetry of the wave function, the full wave function must remain spatially symmetric [8], in the form of

$$\psi(t,x) = A_0(t) + 2\sum_{m=1}^{\infty} A_m(t)\cos(m\Omega x), \qquad (12)$$

with complex amplitudes $A_m(t)$. As shown in Ref. [24], the instability of the fundamental mode $A_1(t)$ induces a cascading instability of all the $|m|>1$ modes, causing all to grow exponentially in locked-step with $A_1(t)$, as $|A_m(t)| \sim |A_1(t)|^{|m|}$. Therefore, at a long time *before* the AB peak, all higher-mode amplitudes are exponentially small, as compared to $A_1(t)$, and the wave function must be of the form

$$\psi_0(x) = A_0 + 2A_1\cos(\Omega x), \qquad (13)$$

with complex amplitudes $A_0 \sim 1$ and $A_1 \sim 0$. Similarly, for an nth-order AB, with n unstable modes, the wave function at a long time before the peak must be of the form

$$\psi_0(x) = A_0 + 2\sum_{m=1}^{n} A_m\cos(m\Omega x), \qquad (14)$$

with n complex coefficients A_m shaping the growth of the n unstable modes into a single nth-order AB. Clearly, any trial and error, or grid-search method would be impractical for determining more than two A_m coefficients.

Here, we propose an extremely simple, yet systematic way of determining these coefficients. The method is to use the Darboux transformation to generate a numerical nth-order AB wave function at a sufficiently long time before the peak and extract the n coefficients A_m by *fitting* it with the functional form (14). (The constant A_0 is fixed by normalization.)

Figs. 3 and 4 show the resulting second-order AB at $a = 0.43$, produced from the NLSE with the $n = 2$ initial wave function (14).
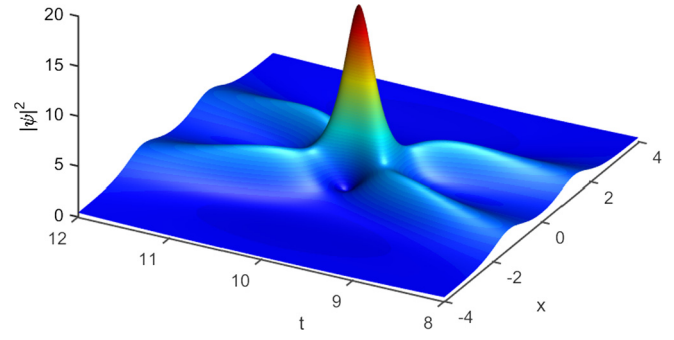
Fig. 3. (Color online.) Second-order Akhmediev breather at $a = 0.43$, generated from the nonlinear Schrödinger equation using initial wave function (14). Coefficients are fitted from the Darboux transformation at $t = 10$ before the peak; $A_1 = (0.532+1.32i)10^{-3}$, $A_2 = (-7.56-6.54i)10^{-5}$, $|\psi|_{max}^2 = 17.48$ (17.48). The value in parentheses gives the maximum intensity according to Eq. (11).
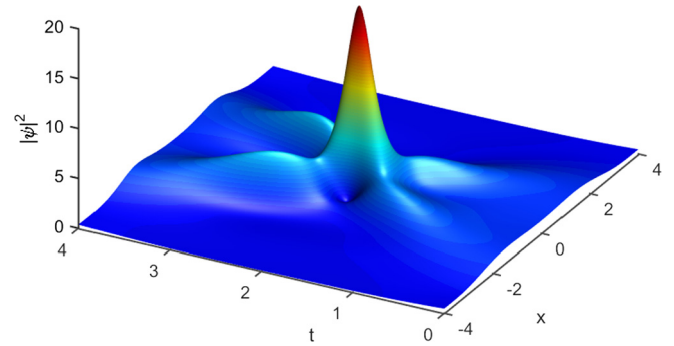
Fig. 4. (Color online.) Same as Fig. 3, but with coefficients fitted at $t = 2$ before the peak, with only two decimal places, $A_1 = 0.18+0.28i$, $A_2 = -0.11-0.03i$, $|\psi|_{max}^2 = 18.61$ (17.48). This second-order AB is asymmetric.

The NLSE was solved numerically using a second-order splitting fast Fourier transform method with time step $\Delta t = 0.0001$ and double-checked using a fourth-order symplectic splitting scheme [25]. We extracted the coefficients by fitting (14) to the DT wave function at $t = -2$ and at $t = -10$. (Therefore, when solving the NLSE numerically, the peak appears at $t = 2$ and $t = 10$ simulation time.) Since an overall phase is irrelevant, we subtract the phase of A_0 from all coefficients, so that A_0 is real and we renormalize it, to obtain $A_0 = \sqrt{1-2|A_1|^2-2|A_2|^2}$. Thus, only two complex numbers for A_1 and A_2 suffice.

The fitted coefficients from $t = -10$ generate a nearly-perfect reproduction of the AB2 generated from DT, with symmetric two-lobes before and after the peak. The spectral "fingerprint" shown in Fig. 5 is indistinguishable from the exact DT spectrum. The fit at $t = -2$ yields larger coefficients and produces a rather distorted/asymmetric two-lobe structure in Fig. 4 and an asymmetric spectral fingerprint in Fig. 6. Yet, despite such a distortion, the latter AB2 has slightly higher peak intensity than predicted by (11).

The use of DT to analyze numerical simulations and experiments has been done by Erkintalo et al. [15] at the same value of $a = 0.43$ (see their Fig. 1). However, they used the t-shift parameter in DT to displace the two AB, so that they only get a 1-2 peak structure, rather than an AB2. One *cannot* reproduce an AB2, unless one uses the initial wave function of the form (14).

In Fig. 7 we show the resulting AB3 at $a = 0.464$, a value used in the experiment of Ref. [15]. It is a relatively poor approximation to an exact AB3, similar to Fig. 4. In Figs. 8 and 9, we show intensities of AB4 and AB5, obtained in a much better approximation. For these two breathers, one must fit (14) at $t = -8$ and $t = -13$ respectively, yielding rather small but accurate coefficients.

Since an nth-order AB is composed of n ABs with wave numbers Ω, 2Ω, $\cdots$ $n\Omega$, each having 1, 2, 3, $\cdots$ n peaks respectively,
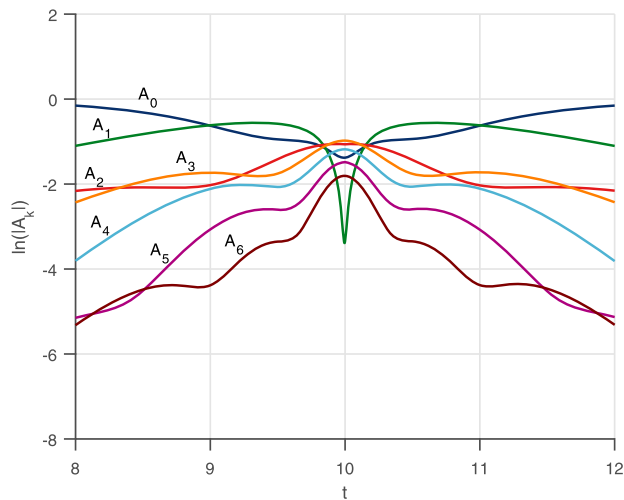
Fig. 5. (Color online.) The spectral "fingerprint" of Fig. 3, with coefficients fitted at $t=10$ before the peak. The amplitudes are perfectly symmetric before and after the peak.
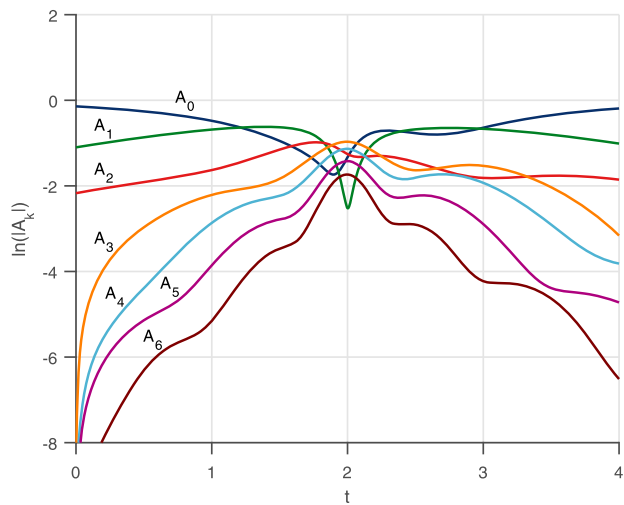

Fig. 6. (Color online.) The spectral "fingerprint" of Fig. 4, with coefficients fitted at $t=2$ before the peak. This is a poor, asymmetric imitation of Fig. 5, but the resulting AB still has comparable (actually, slightly higher) peak intensity.
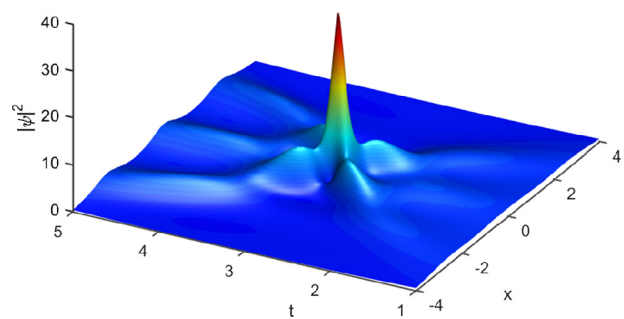

Fig. 7. (Color online.) Third-order AB at $a = 0.464$ from the initial wave function (14). Coefficients are fitted at $t = 3$ before the peak: $A_1 = 0.17 + 0.32i$, $A_2 = -0.14 + 0.004i$, $A_3 = 0.04 + 0.001i$, $|\psi|^2_{max} = 35.21$ (33.65). The pre-peak 3 lobes are much reduced.

it is equivalent to $1 + 2 + \cdots n = n(n+1)/2$ single-peak ABs. This is also the observation of Ref. [5,6] on rogue waves. This composition can be seen in the evolving intensity of all nth-order ABs in each region R_n, not just in rational RWs [6]. The nth-order AB will emerge from the background with n lobes, then $(n-1)$ lobes, $(n-2)$ lobes, etc., until the intensity converges into a narrow sin-
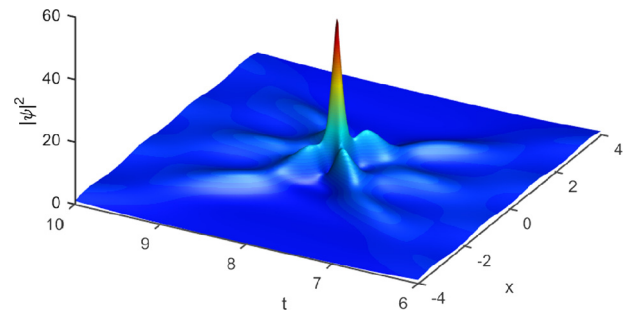
Fig. 8. (Color online.) Fourth-order AB at $a = 0.47395$ from the initial wave function (14). Coefficients are fitted at $t = 8$ before the peak; $A_1 = 0.016563 + 0.067661i$, $A_2 = -0.005927 - 0.005156i$, $A_3 = 0.002951 + 0.001122i$, $A_4 = -0.008055 - 0.003309i$, $|\psi|^2_{max} = 48.57$ (49). Outer 4 lobes are at $t < 6$.
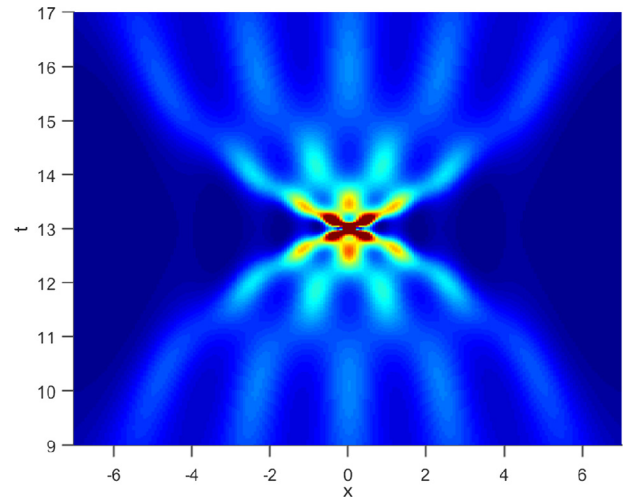
Fig. 9. (Color online.) Fifth-order AB at $a=0.4850173$ from initial wave function (14). Coefficients are fitted at $t = 13$ before the peak; $A_1 = (0.64382 + 3.6195i)10^{-2}$, $A_2 = (-1.2676 - 1.3896i)10^{-3}$, $A_3 = (1.7862 + 1.5434i)10^{-4}$, $A_4 = (-6.6953 - 4.4011i)10^{-5}$, $A_5 = (1.2706 + 0.6913i)10^{-4}$. Peak intensity is $|\psi|^2_{max} = 80$ (81), but only the base with $|\psi|^2 < 10$ is plotted to show the time-symmetric 5-4-3-2-1-lobe structure.

gle peak. It then decays in a time-symmetric manner back into 2 lobes, 3 lobes, $\cdots n$ lobes, and fades back into the background. In Fig. 9, we only plot the intensity near the base of the AB, to better show the evolving lobe structure described above.

Since the NLSE can model well the propagation of light pulses in an optical fiber, the above dynamical generation of high order ABs strongly suggests that they can also be produced in experiments similar to those described in Refs. [15,21]. The latter's frequency-comb can basically produce all the initial wave functions given above.

Acknowledgements

Appendix. Proof of (11)

We follow the Darboux iteration in the Appendix of Ref. [6], with zero x- and t-shift parameters. The wave function at $x = 0$ and $t = 0$ can be evaluated starting from their Eq. (A4),

$$r_{1j} = 2i \sin(A_{jr}), \quad s_{1j} = 2\cos(B_{jr}),$$

$$A_{jr} = \frac{1}{2}\arccos(\frac{\Omega_j}{2}) - \frac{\pi}{4}, \quad B_{jr} = -\frac{1}{2}\arccos(\frac{\Omega_j}{2}) - \frac{\pi}{4},$$

with $\Omega_j = 2\sqrt{1 - 2a_j^2}$. Therefore,

$$s_{1j} = 2\cos(B_{jr}) = 2\cos(A_{jr} + \frac{\pi}{2}) = -2\sin(A_{jr})$$
$$= ir_{1j}. \tag{15}$$

Equation (15) is the only result we needed to prove our formula. It follows that for all $j \geq 1$

$$|s_{1j}|^2 = |r_{1j}|^2. \tag{16}$$

From Ref. [6]'s Eq. (A6),

$$|\psi|_{max} = 1 + \frac{2(l_1^* - l_1)s_{11}r_{11}^*}{|r_{11}|^2 + |s_{11}|^2} = 1 + \frac{2(l_1^* - l_1)i|r_{11}|^2}{|r_{11}|^2 + |s_{11}|^2}$$
$$= 1 + (l_1^* - l_1)i = 1 + (-i\sqrt{2a_1} - i\sqrt{2a_1})i$$
$$= 1 + 2\sqrt{2a_1}, \tag{17}$$

where $l_n = i\sqrt{2a_n}$. Note that we only need to know (15) and (16) to arrive at (17); we do not need to know the *explicit* forms of s_{11} and r_{11}.

We now prove by induction that (15) generalizes to all $n \geq 1$, for $j \geq 1$:

$$s_{nj} = ir_{nj}. \tag{18}$$

Assuming that $s_{n-1,k} = ir_{n-1,k}$ for all k, specifically $k = 1$, then Ref. [6]'s Eq. (A7) gives,

$$r_{nj} = -\sqrt{2a_{n-1}}\,s_{n-1,j+1} + i\sqrt{2a_{j+n-1}}\,r_{n-1,j+1},$$
$$s_{nj} = \sqrt{2a_{n-1}}\,r_{n-1,j+1} + i\sqrt{2a_{j+n-1}}\,s_{n-1,j+1}.$$

Now invoking $s_{n-1,k} = ir_{n-1,k}$ for $k = j+1$ then gives

$$ir_{nj} = -i\sqrt{2a_{n-1}}\,s_{n-1,j+1} - \sqrt{2a_{j+n-1}}\,r_{n-1,j+1}$$
$$= \sqrt{2a_{n-1}}\,r_{n-1,j+1} + i\sqrt{2a_{j+n-1}}\,s_{n-1,j+1}$$
$$= s_{nj}. \tag{19}$$

From Ref. [6]'s Eq. (A8), each a_n will only contribute a factor $2\sqrt{2a_n}$ to the maximum peak height by applying $s_{n1} = ir_{n1}$, as done similarly in (17).

References

[1] J.M. Dudley, F. Dias, M. Erkintalo, G. Genty, Instabilities, breathers and rogue waves in optics, Nat. Photonics 8 (2014) 755.

[2] Nail Akhmediev, Adrian Ankiewicz, J.M. Soto-Crespo, Rogue waves and rational solutions of the nonlinear Schrödinger equation, Phys. Rev. E 80 (2009) 026601.

[3] N. Akhmediev, V.M. Eleonskii, N.E. Kulagin, N-modulation signals in a single-mode optical waveguide under nonlinear conditions, Zh. Eksp. Teor. Fiz. 94 (1988) 159–170, Sov. Phys. JETP 67 (1988) 89–95.

[4] N. Akhmediev, J.M. Soto-Crespo, A. Ankiewicz, Extreme waves that appear from nowhere: on the nature of rogue waves, Phys. Lett. A 373 (2009) 2137–2145.

[5] Adrian Ankiewicz, David J. Kedziora, Nail Akhmediev, Rogue wave triplets, Phys. Lett. A 375 (2011) 2782–2785.

[6] David J. Kedziora, Adrian Ankiewicz, Nail Akhmediev, Circular rogue wave clusters, Phys. Rev. E 84 (2011) 056611.

[7] David J. Kedziora, Adrian Ankiewicz, Nail Akhmediev, Second-order nonlinear Schrödinger equation breather solutions in the degenerate and rogue wave limits, Phys. Rev. E 85 (2012) 066601.

[8] N. Akhmediev, V. Korneev, Modulation instability and periodic solutions of the nonlinear Schrödinger equation, Theor. Math. Phys. 69 (1986) 1089–1093.

[9] N. Akhmediev, V. Eleonskii, N. Kulagin, Exact first-order solutions of the nonlinear Schrödinger equation, Theor. Math. Phys. 72 (1987) 809–818.

[10] D.H. Peregrine, Water waves, nonlinear Schrödinger equations and their solutions, J. Aust. Math. Soc. B 25 (1983) 16.

[11] N.N. Bogoliubov, On the theory of superfluidity, J. Phys. (USSR) 11 (1947) 23; Reprinted in: D. Pine, The Many-Body Problem, Benjamin, New York, 1961, p. 292.

[12] A.L. Fetter, J.D. Walecka, Quantum Theory of Many-Particle Systems, McGraw-Hill, New York, 1971, pp. 317, 493–496.

[13] C.J. Pethick, H. Smith, Bose–Einstein Condensation in Dilute Gases, Cambridge University Press, Cambridge, 2002, pp. 174–177.

[14] T.B. Benjamin, J. Feir, The disintegration of wave trains on deep water, part 1. Theory, J. Fluid Mech. 27 (1967) 417–430.

[15] M. Erkintalo, K. Hammani, B. Kibler, C. Finot, N. Akhmediev, J.M. Dudley, G. Genty, Higher-order modulation instability in nonlinear fiber optics, Phys. Rev. Lett. 107 (2011) 253901.

[16] Nail N. Akhmediev, Nina V. Mitzkevich, Extremely high degree of N-soliton pulse compression in an optical fiber, IEEE J. Quantum Electron. 21 (1991) 849–857.

[17] D.J. Kedziora, A. Ankiewicz, N. Akhmediev, Rogue waves and solitons on a cnoidal background, Eur. Phys. J. Spec. Top. 223 (2014) 43–62.

[18] A. Chowdury, D.J. Kedziora, A. Ankiewicz, N. Akhmediev, Breather-to-soliton conversions described by the quintic equation of the nonlinear Schrödinger hierarchy, Phys. Rev. E 91 (2015) 032928.

[19] B. Kibler, J. Fatome, C. Finot, G. Millot, F. Dias, G. Genty, N. Akhmediev, J. Dudley, The Peregrine soliton in nonlinear fibre optics, Nat. Phys. 6 (10) (2010) 790–795.

[20] B. Frisquet, B. Kibler, G. Millot, Collision of Akhmediev breathers in nonlinear fiber optics, Phys. Rev. X 3 (2013) 041032.

[21] B. Frisquet, A. Chabchoub, J. Fatome, C. Finot, B. Kibler, G. Millot, G. Genty, Two-stage linear–nonlinear shaping of an optical frequency comb as rogue nonlinear-Schrödinger-equation-solution generator, Phys. Rev. A 89 (2014) 023821.

[22] S. Toenger, T. Godin, C. Billet, F. Dias, M. Erkintalo, G. Genty, J.M. Dudley, Emergent rogue wave structures and statistics in spontaneous modulation instability, Sci. Rep. 5 (2015) 10380.

[23] N. Akhmediev, J.M. Soto-Crespo, A. Ankiewicz, How to excite a rogue wave, Phys. Rev. A 80 (2009) 043818.

[24] Siu A. Chin, Omar A. Ashour, Milivoj R. Belić, Anatomy of the Akhmediev breather: cascading instability, first formation time, and Fermi–Pasta–Ulam recurrence, Phys. Rev. E 92 (2015) 063202.

[25] H. Yoshida, Construction of higher order symplectic integrators, Phys. Lett. A 150 (1990) 262–268.

CrossMark

Probing the kinetic landscape of Hox transcription factor–DNA binding in live cells by massively parallel Fluorescence Correlation Spectroscopy

Dimitrios K. Papadopoulos [a],[*],[1], Aleksandar J. Krmpot [b],[c],[1], Stanko N. Nikolić [b],[c], Robert Krautz [d], Lars Terenius [b], Pavel Tomancak [a], Rudolf Rigler [e],[f], Walter J. Gehring [g],[2], Vladana Vukojević [b],[*]

[a] Max-Planck Institute for Molecular Cell Biology and Genetics, 01307 Dresden, Germany
[b] Department of Clinical Neuroscience (CNS), Center for Molecular Medicine (CMM), Karolinska Institutet, 17176 Stockholm, Sweden
[c] Institute of Physics, University of Belgrade, 11080 Belgrade, Serbia
[d] Department of Molecular Biosciences, The Wenner-Gren Institute, Stockholm University, 10691 Stockholm, Sweden
[e] Department of Medical Biochemistry and Biophysics, Karolinska Institutet, 17177 Stockholm, Sweden
[f] Laboratory of Biomedical Optics, Swiss Federal Institute of Technology, 1015 Lausanne, Switzerland
[g] Department of Cell Biology, Biozentrum, University of Basel, 4056 Basel, Switzerland

ARTICLE INFO

ABSTRACT

Hox genes encode transcription factors that control the formation of body structures, segment-specifically along the anterior–posterior axis of metazoans. Hox transcription factors bind nuclear DNA pervasively and regulate a plethora of target genes, deploying various molecular mechanisms that depend on the developmental and cellular context. To analyze quantitatively the dynamics of their DNA-binding behavior we have used confocal laser scanning microscopy (CLSM), single-point fluorescence correlation spectroscopy (FCS), fluorescence cross-correlation spectroscopy (FCCS) and bimolecular fluorescence complementation (BiFC). We show that the Hox transcription factor Sex combs reduced (Scr) forms dimers that strongly associate with its specific *fork head* binding site (*fkh250*) in live salivary gland cell nuclei. In contrast, dimers of a constitutively inactive, phospho-mimicking variant of Scr show weak, non-specific DNA-binding. Our studies reveal that nuclear dynamics of Scr is complex, exhibiting a changing landscape of interactions that is difficult to characterize by probing one point at a time. Therefore, we also provide mechanistic evidence using massively parallel FCS (mpFCS). We found that Scr dimers are predominantly formed on the DNA and are equally abundant at the chromosomes and an introduced multimeric *fkh250* binding-site, indicating different mobilities, presumably reflecting transient binding with different affinities on the DNA. Our proof-of-principle results emphasize the advantages of mpFCS for quantitative characterization of fast dynamic processes in live cells.

© 2015 Elsevier Ireland Ltd. All rights reserved.

1. Introduction

Hox transcription factors specify segmental identity in animals by launching the developmental programs required for morphological diversification of segments, such as the formation of body appendages and the acquisition of specialized functions (Gehring, 1987; Lewis, 1978; McGinnis and Krumlauf, 1992). However, despite the wealth of knowledge on their biological function, we still lack detailed mechanistic insight into how they achieve their complex function *in vivo*, at the molecular level.

The DNA-binding properties of Hox transcription factors in large metazoan genomes, and the mechanisms deployed thereby to control the regulation of their target genes, remain open questions in developmental biology. The dynamic behavior of Hox transcription factors in the nucleus can be viewed in its entirety as the problem of Hox specificity, namely how Hox transcription factors, that are structurally very similar in their DNA-binding preferences and bind in a widespread manner in the genome, regulate apparently dissimilar morphogenetic programs, such as the formation of body appendages, as diverse as a fly wing and an antenna. In *Drosophila*, a wealth of studies has approached the problem of Hox specificity, either structurally or functionally.

Structural studies of homeodomain–DNA binding are exemplified in the context of Scr (Joshi et al., 2007), Ultrabithorax (Ubx) (Passner et al., 1999) and Antennapedia (Antp) (Muller et al., 1988; Otting et al., 1990; Otting et al., 1988; Qian et al., 1989), for which the corresponding DNA-bound structures have been resolved by X-ray crystallography or NMR, respectively. In these structures, DNA binding topologies have been

mapped to the third helix of the homeodomain (major DNA groove contacts), as well as its N-terminal arm sequences (minor DNA groove contacts). Careful examination of these structures, as in the case of Antp, has identified important roles of the N-terminal arm of the homeodomain (Qian et al., 1994) and the linker between the YPWM motif (also termed the hexapeptide motif) and the homeodomain (Qian et al., 1992) in DNA-binding affinities. In fact, both the YPWM motif and the N-terminal arm of the homeodomain have been found to play a major role in specificity (Papadopoulos et al., 2011; Papadopoulos et al., 2012; Papadopoulos et al., 2010). Such specificity, as in the cases of Scr and Antp, is required for paralog specific functions (Furukubo-Tokunaga et al., 1993; Gibson et al., 1990; Zeng et al., 1993), although the structure of the *cis*-binding site (the structure of the DNA minor groove itself) is equally important for target recognition, at least in the cases of Scr and Deformed (Dfd) (Joshi et al., 2007; Joshi et al., 2010).

Functional studies on the specificity of Hox proteins have led to the identification of cofactors, which physically interact with Hox transcription factors and allow the binding of Hox complexes with higher stringency on the DNA. For example, Extradenticle (Exd) binds DNA together with Hox proteins, interacts physically with them *via* the YPWM motif and functions as a generic Hox cofactor (Mann and Chan, 1996). The contribution of Exd in Hox function can be appreciated, for instance, in the case of determination of antennal and leg identities (Casares and Mann, 1998), or salivary gland morphogenesis (Rieckhof et al., 1997), which depends on the regulation of the *fkh* gene, and which, in turn, represents one of the extensively characterized *bona fide* targets of Scr (Ryoo and Mann, 1999). Moreover, the YPWM motif and its interaction with cofactors have been remarkably conserved in evolution, emphasizing their importance in Hox functionality (Chang et al., 1995; Knoepfler and Kamps, 1995; Lu et al., 1995).

Notwithstanding the validity of such studies in elucidating the function and specificity of Hox factors, little quantitative information has been gained. We still do not know how much transcription factor is contained in cells, how often and how strongly it binds to the DNA, how long it stays on the DNA, as well as how other transcription factors/cofactors/interacting proteins are embedded into Hox reaction–diffusion networks to control the dynamics and kinetics of DNA-binding and, thereby, gene regulation. As with most biomolecules, the temporal evolution and spatial distribution of transcription factors in live cell nuclei are the most important determinants of their kinetic behavior. Despite this, comprehensive quantitative information on the cellular dynamics of molecules in these processes is still lacking. The importance of the kinetics of Hox–DNA binding has been appreciated already in early studies (Affolter et al., 1990). To date, technological advances have allowed the quantification of transcription factors with high precision, at least *ex vivo* (Simicevic et al., 2013). Few attempts have been made to dissect the dynamics of Hox–DNA binding behavior using methods that allow the quantification of concentration and molecular mobility in live cells, such as single-point FCS (Gehring, 2011; Vukojevic et al., 2010). These studies outlined the importance of the measurement of transcription factor behavior in live cells, but could not study this behavior simultaneously in a heterogeneous system, such as a whole cell nucleus or cells in a larger tissue.

In this paper we utilize a prototype instrument for mpFCS measurements that is developed in our laboratory (Vitali et al., 2014 and Krmpot et al., in preparation) to study *in vivo* the integration of Scr transcription factor molecules into reaction–diffusion networks in the nuclei of giant salivary gland polytene cells, a tissue that is normally specified by Scr during development.

Scr is expressed in the labial and prothoracic segments of the embryo (Kuroiwa et al., 1985; LeMotte et al., 1989; Martinez-Arias et al., 1987), the central nervous system and subesophageal ganglia (Mahaffey and Kaufman, 1987), as well as predominantly in the prothoracic, among the larval, imaginal discs (Glicksman et al., 1987). In these primordia, Scr specifies prothoracic leg development, while being – at least in part – responsible for repression of prothoracic wing formation (Rogers et al., 1997), a function conserved across extant insects (Hrycaj et al., 2010). Scr has been functionally preserved in evolution, which is best demonstrated by the ability of its mouse ortholog to induce Scr-specific homeotic transformations in flies (Zhao et al., 1993; Zhao et al., 1996). Finally, Scr plays a pivotal role in the specification of salivary gland development (Andrew et al., 1994; Panzer et al., 1992; Zhou et al., 2001).

Here, we make use of flies expressing wild-type or constitutively inactive Scr variants. They also carry a 50mer of the *fkh250* specific binding site (Ryoo and Mann, 1999), to which Scr dimers bind strongly and accumulate in salivary gland cells (Papadopoulos et al., 2012). Our experimental setup allows us to quantitatively characterize the spatial distribution of Scr molecules and measure differences in their local diffusion properties across the whole cell nucleus.

2. Materials and methods

2.1. Microscopic setups

The ConfoCor 3 instrument and a prototype microscopic setup for mpFCS, have been used in this study.

The uniquely modified ConfoCor3 instrument (Carl Zeiss, Jena, Germany) consisting of an inverted microscope for transmitted light and epifluorescence (Axiovert 200 M); a vis–laser module comprising the Ar/ArKr (458, 477, 488 and 514 nm), HeNe 543 nm and HeNe 633 nm lasers; and the scanning module LSM 510 META was used for single-point measurements. The instrument is modified to enable detection using silicon Avalanche Photo Detectors (SPCM-AQR-1X; PerkinElmer, USA) for imaging, which allows confocal fluorescence microscopy imaging with single-molecule sensitivity (Vukojevic et al., 2008). Images were recorded at a 512×512 pixel resolution. The C-Apochromat $40\times/1.2$ W UV-VIS-IR objective was used throughout. Fluorescence intensity fluctuations were recorded in arrays of 10–30 consecutive measurements, each measurement lasting 5–10 s. Averaged curves were analyzed using the software for online data analysis or exported and fitted offline using the OriginPro 8 data analysis software (OriginLab Corporation, Northampton, MA). In either case, the nonlinear least square fitting of the autocorrelation curve was performed using the Levenberg–Marquardt algorithm. Quality of the fitting was evaluated by visual inspection and by residuals analysis.

The specific design and construction of the mpFCS setup is described elsewhere (Vitali et al., 2014 and Krmpot et al., in preparation). Briefly, simultaneous excitation of fluorescent molecules across the specimen is achieved by passing a single laser beam through a diffractive optical element (DOE), which transforms it into a rectangular illumination matrix that consists of 32×32 spots. Fluorescence from 1024 illuminated spots is detected in a confocal arrangement by a matching matrix detector consisting of the same number of single-photon avalanche photodiodes (SPADs). Dedicated software was developed for data acquisition and fast auto- and cross-correlation analysis by parallel signal processing using a graphic processing unit (GPU). This approach enables quantitative characterization of physiological processes in live cells/tissue with a sub-millisecond temporal resolution, presently 21 µs/frame. The prototype setup also allows single-molecule sensitivity, but for long signal acquisition times. Due to technical limitations, such measurements are presently feasible only if the number of pixels is being reduced.

2.2. Expression of Scr transcription factors in Drosophila salivary glands

Expression of UAS-mCitrine-Scr(wt) alone, or of combinations of UAS-mCitrine-Scr(wt) and UAS-mCherry-Scr(wt), as well as UAS-mCitrine-Scr(DD) and UAS-mRFP1-Scr(DD), has been induced by *dpp*-blk-Gal4 (Staehling-Hampton et al., 1994), or *sgs3*-Gal4 (obtained from the Bloomington Stock Center, stock number 6870). The 50mer of

fkh250 binding sites is bound by Scr homodimers and has been previously described (Papadopoulos et al., 2012). Fluorescent balancers (Le et al., 2006) and examination of salivary gland fluorescence through the larval cuticle have been used for selection of genotype.

2.3. Expression of Scr dimers by bimolecular fluorescence complementation (BiFC) in Drosophila salivary glands

Flies expressing synthetic UAS-V_C-Scr and UAS-V_N-Scr constructs, as wild-type or constitutively inactive variants, have been used in this study, as previously described (Papadopoulos et al., 2012; Papadopoulos et al., 2010). The synthetic Scr constructs are comprised of the homeodomain, YPWM motif and C-terminus, tagged to the C (V_C) or N (V_N) terminus of the Venus fluorescent protein and they successfully recapitulate the Scr homeotic function to a great extent (Papadopoulos et al., 2012). Expression has been induced using the *sgs3*-Gal4 driver. Fluorescent balancers (Le et al., 2006) and examination of salivary gland fluorescence through the larval cuticle have been used for selection of genotype.

2.4. Preparation of salivary glands for live measurements

Salivary glands of third instar larvae have been dissected in phosphate buffered saline (PBS) at room temperature and transferred to 8-well chambered cover glass (Nunc® Lab-Tek® II, Thermo Fisher Scientific, USA) containing 200 μL of PBS. Salivary glands were then used directly for measurements.

3. Results

We have previously used single-point FCS to quantitatively characterize the complex Scr DNA-binding in live salivary gland cell nuclei (Vukojevic et al., 2010). However, the transcription factor molecules are not uniformly distributed in polytene nuclei (Fig. 1). They undergo free-diffusion in the nucleoplasm (Fig. 1A, *blue circle*), bind to chromosomal DNA, both specifically and non-specifically (Fig. 1A, *green circle*), and form sites of accumulation on the DNA (Fig. 1A, *red circle*). This suggests that Scr participates in different types of interactions in the nucleus at different locations. In classical, single-point FCS, fluorescence intensity fluctuations in a stationary observation volume element (OVE) are recorded over time, using detectors with single-photon

sensitivity, and subjected to autocorrelation analysis, which provides information about the average number of fluorescent molecules in the OVE and their mobility. (For an overview of FCS methodology, refer to Vukojevic et al., 2005). FCS measurements on the aforementioned nuclear locations reveal differences in mobility between the nucleoplasm and the polytene chromosomes (Fig. 1B). These are evident from the shift of the autocorrelation curve (ACC) recorded in the nucleoplasm towards shorter decay times, as compared to the ACC recorded on the polytene chromosomes and at the site of accumulation, where longer decay time is observed, indicating binding to the DNA (Fig. 1B, blue *versus* red ACCs). However, little – if any – difference in molecular mobility is observed between the sites of high Scr concentration and its binding elsewhere on the chromosomes (Fig. 1B, compare green and red FCS curves). Moreover, the strong fluorescence intensity observed at Scr binding sites in the nucleus suggests that, in addition to Scr accumulation, higher order complexes are formed on the DNA.

We have previously established that Scr forms homodimers, which are required for a great portion of its homeotic function in flies (Papadopoulos et al., 2012). Here, we have sought to characterize the DNA binding behavior of these dimers using the BiFC system (Hu et al., 2002) and FCS.

In BiFC, proteins that are hypothesized to interact are tagged to the N- and C-terminal portions (V_N and V_C, respectively) of the Venus fluorescent protein. While the two halves of Venus do not fluoresce on their own, when the two interacting partners bring them together, fluorescence is being reconstituted. BiFC has been successfully used in many systems, including flies, for monitoring protein–protein interactions, as in the case of Hox transcription factors and their interacting partners (Boube et al., 2014; Duffraisse et al., 2014; Hudry et al., 2014; Hudry et al., 2011; Papadopoulos et al., 2012; Sambrani et al., 2013).

By CLSM, we have observed that Scr dimers reside overwhelmingly on the DNA (Fig. 2A) and accumulate on chromosomal regions of decondensed chromatin (polytene chromosome interbands). In contrast, a constitutively inactive phosphomimicking variant of Scr, where threonine 6 and serine 7 of the homeodomain have been substituted by aspartates [Scr(DD)] (Berry and Gehring, 2000), and which has limited homeotic function in flies (Berry and Gehring, 2000; Papadopoulos et al., 2012; Papadopoulos et al., 2010; Vukojevic et al., 2010), shows limited dimerization, despite being expressed in similar amounts as compared to Scr(wt) (Papadopoulos et al., 2012). Moreover, Scr(DD) dimers are largely excluded from the DNA (Fig. 2A). FCS measurements on
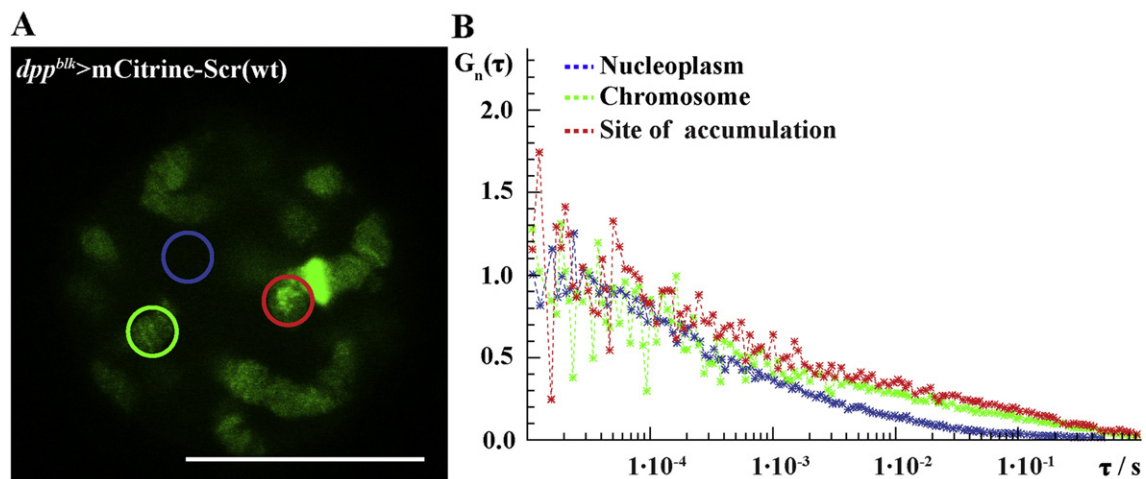

Fig. 1. Scr(wt) distribution and DNA-binding in polytene nuclei, visualized by confocal laser scanning microscopy (CLSM) and characterized by classical, single-point FCS. (A) mCitrine-Scr(wt) distribution in the salivary gland cell nucleus is non-uniform. In the nucleoplasm (*blue circle*) its concentration is low, on the chromosomes (*green circle*) it preferentially associates with sites of loose chromatin conformation, and it also forms sites of accumulation (red circle). (B) Autocorrelation curves (ACCs) normalized to the same amplitude ($G_n(\tau) = 1$ at $\tau = 1 \times 10^{-5}$ s) recorded in the areas indicated in (A) reveal fast movement of Scr(wt) in the nucleoplasm (blue ACC), as compared to the chromosome (green ACC) and the site of Scr(wt) accumulation (red ACC). The latter two indicate binding to the DNA (autocorrelation curves shifted towards longer characteristic times), but the differences between Scr(wt)–DNA binding on the chromosomes and the site of accumulation is not easily discernible. Due to bleaching, which may be extensive for FCS measurements on the chromatin, signal acquisition time on the chromosome and the site of accumulation was shorter (10 s) than for measurements in the lumen, which allow longer signal acquisition time (100 s). Scale bar is 20 μm.
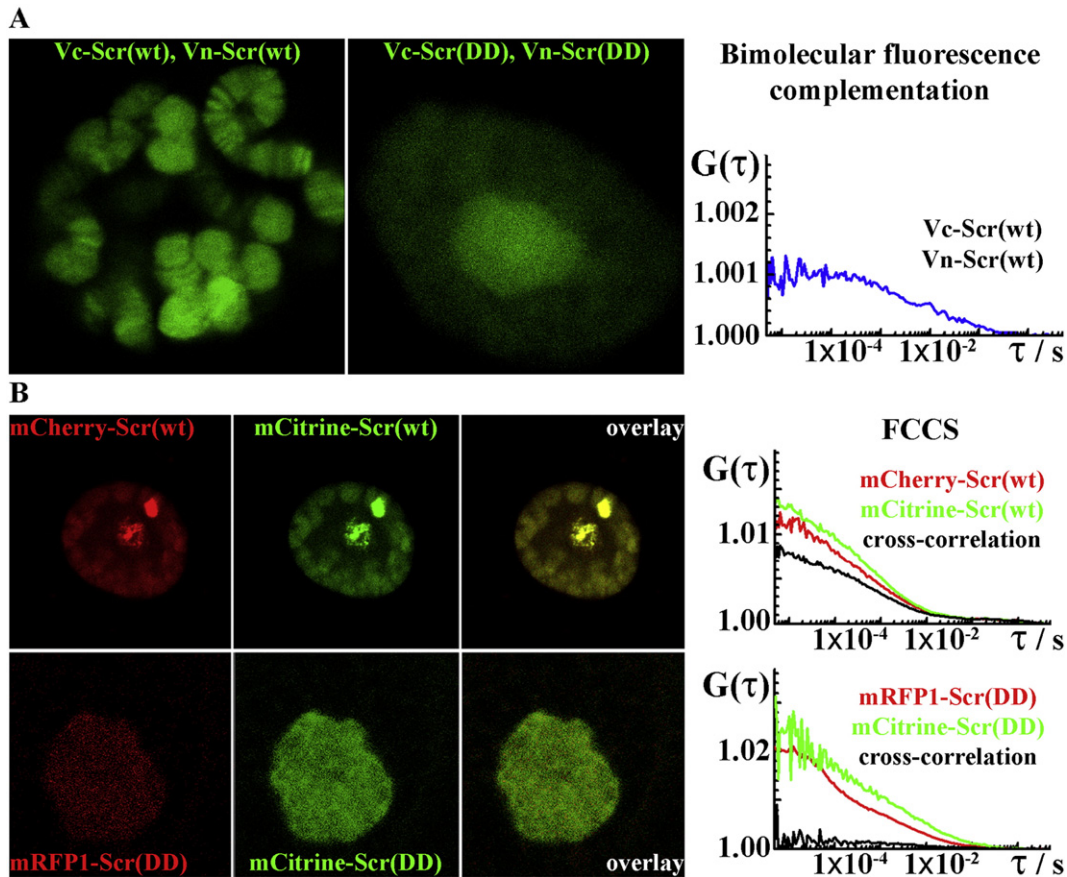
Fig. 2. Study of Scr(wt) and Scr(DD) dimer formation, visualized by CLSM and characterized by BiFC, FCS and FCCS. (A) CLSM images of Scr(wt) and Scr(DD) dimers in live salivary gland cells, visualized by BiFC. Scr(wt) dimers exhibit widespread association with chromosomal DNA, they accumulate on polytene interbands (regions of loose chromatin compaction and hence higher transcriptional activity) and are mostly excluded from the nucleoplasm. In contrast, Scr(DD) dimers show less DNA-binding activity and some accumulation at the chromocenter, but reside mostly in the nucleoplasm. Note the lower abundance of Scr(DD) dimers as compared to Scr(wt), despite their similar levels of expression. FCS measurements on Scr(wt) binding on the chromosome reveal a pronounced fraction of slowly diffusing Scr dimers, $\tau_D > 5 \times 10^{-4}$ s, and a higher contribution of components characterized with decay times $\tau_D > 1 \times 10^{-2}$ s. (B) Study of monomeric and dimeric Scr(wt) and Scr(DD) dynamics by FCCS, using dually-labeled (red and green) Scr molecules. Scr(wt) monomers (*upper panel*) reside on the DNA and accumulate on the giant *fkh250* binding site (and the chromocenter). Co-localization of red and green transcription factor molecules on both the *fkh250* binding site and the residual chromatin is very pronounced in this case. FCCS analysis reveals strong interaction between red and green Scr(wt) molecules (black ACC) with a relatively higher fraction of slowly diffusing molecules characterized by longer diffusion times, as compared to the individual monomers. In the case of Scr(DD) (*lower panel*), little, if any, binding to the DNA is observed in both the green and the red channels, and Scr is mostly excluded from chromatin [similar to (A)] and resides predominantly in the nucleoplasm. Co-localization is not observed for Scr(DD). FCCS analysis reveals little dimer formation in this case, as evidenced by the absence of significant cross-correlation (black autocorrelation curve).

Scr(wt) dimers visualized by BiFC showed multiple characteristic decay times, $\tau_D > 5 \times 10^{-4}$ s, that indicate predominantly slow diffusion. These results are corroborated by FCCS analysis, using dually labeled Scr molecules (Fig. 2B). Salivary gland nuclei of flies expressing UAS-mCherry-Scr(wt) and UAS-mCitrine-Scr(wt), as well as bearing a multimeric *fkh250* binding site [as previously described (Papadopoulos et al., 2012)], show widespread co-localization of green and red Scr monomers (Fig. 2B, upper panel), reminiscent of the binding pattern of Scr(wt) dimers tagged in the BiFC system (Fig. 2A, left). Scr(wt) dimers reside mostly on polytene chromosomes and accumulate on the introduced giant binding site (as well as the chromocenter, which contains mostly heterochromatic regions). FCCS measurements corroborated the finding that Scr(wt) forms dimers characterized by diverse mobilities, as evident from the bimodal cross-correlation curve (CCC) with at least two characteristic decay times (Fig. 2B, black). In contrast, the constitutively inactive variant Scr(DD) dimerizes to a much lower extent (compare the black CCC for Scr(wt) with the corresponding one for Scr(DD) in Fig. 2B). Moreover, Scr(DD) does not accumulate on the *fkh250* binding site or elsewhere on the chromosomes and appears to reside mostly in the nucleoplasmic space.

As evidenced by fluorescent imaging, FCS and FCCS analyses presented above, the Scr interaction pattern across the nucleus is complex. It bears various modes of residence, depending on Scr–DNA and Scr–Scr interactions and involves three-dimensional diffusion in the nucleoplasm, specific and non-specific binding along chromosomes, as well as homodimerization on specific binding sites, but also elsewhere on the DNA. This dynamic behavior is challenging to characterize using single-point FCS measurements, which, in turn, emphasizes the need for methodology that would allow recording of molecular movement and numbers in a larger area, where spatial information is concurrently obtained. To this end, we resided to mpFCS analysis, using a prototype experimental setup that has recently been developed in our laboratory (Vitali et al., 2014 and Krmpot et al., in preparation). In mpFCS, fluorescence intensity fluctuations are recorded simultaneously using a multiplexed confocal arrangement of the illumination matrix, comprised of 1024 points, and a matrix of 1024 SPADs, thus allowing the concomitant study of molecular numbers and motion in a wider area.

We have applied this methodology to characterize the molecular distribution and dynamics of Scr(wt) and Scr(DD) dimers, tagged in the BiFC system (Fig. 3). Fig. 3A shows a salivary gland nucleus expressing V_C-Scr(wt) and V_N-Scr(wt) and bearing the *fkh250* binding site. In accordance with results obtained by CLSM and classical FCS, mpFCS analysis of the concentration and mobility of Scr(wt) dimers revealed high concentration of Scr(wt) dimers in the nucleus, as compared to the cytoplasm, where the protein is produced prior to its translocation
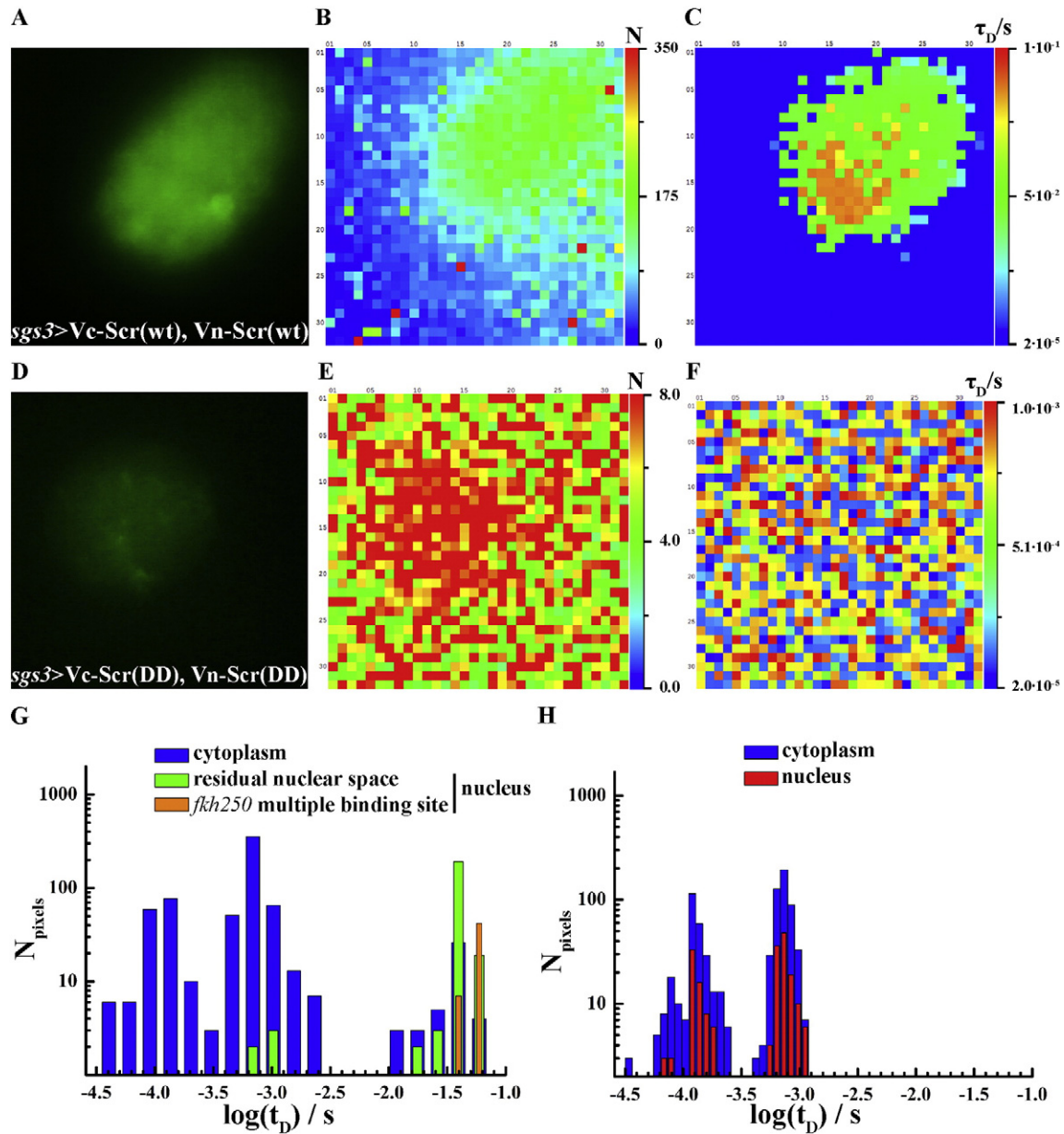
Fig. 3. Spatial distribution of molecular numbers and mobility of wild-type and constitutively inactive Scr transcription factor by mpFCS. (A) Scr(wt) dimers, visualized by BiFC and captured by the 18.0 megapixel digital single-lens reflex (DSLR) camera Canon EOS 600D (Canon Inc., Japan), associate strongly with polytene chromosomes and accumulate on the multimeric *fkh250* binding site. (B) Distribution of average molecular numbers per OVE shows high concentration of dimers in the nucleus and low concentration in the cytoplasm, the site of Scr(wt) synthesis (and possible post-translational modifications). The synthetic binding site cannot be discerned and the average number of molecules appears to be similar across the nucleus. However, the nucleus is enriched roughly 100-fold in transcription factor concentration over the cytoplasm. (C) Distribution of diffusion times in the same cell as in (A) and (B) shows different mobility of Scr(wt) molecules in the *fkh250* binding site, the residual nuclear space and the cytoplasm. Two- to three-fold differences in diffusion times are discernible between different nuclear compartments. (D) Salivary gland nuclei overexpressing Scr(DD), tagged in the BiFC system, are populated by a much lower amount of dimers, despite comparable expression levels to Scr(wt). Scr(DD) dimers do not bind significantly to the DNA and reside in the nucleoplasmic space, where they occasionally form aggregates. (E) Average molecular number distribution of Scr(DD) in the same cell as in (D) shows higher concentration of the dimers in the nucleus, as compared to the cytoplasm, but roughly 10-fold lower concentrations compared to Scr(wt) in (B). (F) The distribution of diffusion times in Scr(DD) expressing nuclei indicates that all molecules move fast. As their movement is not impeded by interactions with nuclear DNA, their movement in the nucleus is as fast as in the cytoplasm. Therefore, in the map of diffusion times the nucleus is not detectable. (G–H) Histogram of the distribution of diffusion times in Scr(wt) (G) and Scr(DD) (H) expressing nuclei. In the case of Scr(wt), the diffusion times of cytoplasmic molecules are lower than the ones in the nucleus. Within the nucleus, most of the molecules move slowly, but it is possible to discern differences in diffusion, which may reflect differences in interactions with the DNA. Scr(DD) molecules show a narrower distribution of fast diffusion times. In this case, there is barely any differences observed between nucleus and cytoplasm.

to the nucleoplasm. Concentration of Scr(wt) dimers in the nucleus was estimated to be in the micromolar range, but obvious differences in the distribution of molecular numbers were not observed (Fig. 3B). However, we observed differences in the mobility of Scr(wt) dimers between the nucleus and the cytoplasm, as well as locally within the nucleus (Fig. 3C and G). Their distribution in the nucleus is overall characterized by slow diffusion, but local differences in their mobility between the

fkh250 binding site and elsewhere on the chromosomes were observed (Fig. 3C and G). This suggests that interactions between Scr(wt) dimers and the chromatin are slow but not uniform. They are of different strength at different nuclear locations, which is reflected as differences in mobility.

In contrast, dimers of the inactive variant Scr(DD) show a very different behavior. Since they bind DNA to a lower extent, they reside
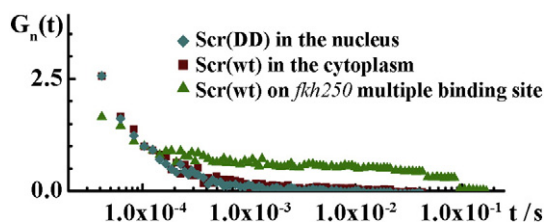
Fig. 4. Average ACCs from selected pixels (refer to Fig. S1) in nuclei expressing Scr(wt) and Scr(DD) normalized to the same amplitude ($G_n(\tau) = 1$ at $\tau = 1 \times 10^{-4}$ s). Scr(DD) molecules in the nucleus (blue diamonds) show overlapping dynamics with cytoplasmic Scr(wt) transcription factor (wine squares), which does not bind DNA. Scr(wt) molecules in the nucleus (green triangles) show significantly slower dynamics, due to interaction with the DNA.

mostly in the nucleoplasm, in between chromosomes, where they rather form aggregates (Fig. 3D). Moreover, the *fkh250* binding site is not populated by Scr(DD) dimers. mpFCS analysis of Scr(DD) dimers revealed a ten-fold lower concentration than Scr(wt) (Fig. 3E, as compared to Fig. 3B), with the nucleus being barely distinguishable over the cytoplasm in the plot of molecular numbers (Fig. 3E). The diffusion times were distributed indiscriminately between the nucleus and cytoplasm (Fig. 3F and H, as compared to Fig. 3C and G), indicating fast molecular movement and limited association with the DNA.

FCS measurements on Scr(wt)- and Scr(DD)-expressing cells showed similar dynamics between Scr(DD) and the cytoplasmic fraction of Scr(wt), which is not binding to the DNA, but a clear shift to longer characteristic times could be observed in the case of nuclear Scr(wt) dimers, suggesting strong binding to the DNA (Fig. 4).

3.1. Discussion and conclusions

The problem of how the dynamic behavior of transcription factors is linked to their function is a central question in developmental biology. This question becomes even more interesting (and challenging to answer) for transcription factors that bind DNA in a relatively indiscriminate, widespread manner, such as Hox transcription factors. Most studies involving Hox transcription factors to date have focused on understanding specific and context-dependent developmental processes, such as the regulation of specific downstream genes involved in morphogenesis. The major reason for this is presumably methodological, namely the lack of technology that could allow the study of the dynamic behavior of these proteins in live cells, such as DNA-binding, target identification, complex formation with cofactors and kinetic behavior. However, it is precisely this knowledge that would allow us to gain a holistic view of the problem of specificity that lies in the core of Hox biology. In order to do this, live cell experimentation is primarily a requirement, as fast, dynamic processes, such as transcription factor–DNA interactions, are far more than a snapshot of transcription factor nuclear distribution, which can be investigated in a fixed cell. Second, two important questions need to be answered in order to understand how biological molecules are integrated in reaction–diffusion networks, namely how many transcription factor molecules the nucleus contains (concentration) and how fast they are moving (molecular mobility). Such information can be best gained using FCS. Moreover, since the gene expression landscape is not static, but rather dynamic, it is beneficial to be able to acquire quantitative information about the local concentration and mobility of transcription factors simultaneously across the cell nucleus. This is because the temporal changes in transcription factor–DNA occupancy, mobility, interaction with other proteins and kinetics within a small fraction of nuclear volume can be influenced by local factors outside of this volume, such as global changes in chromatin conformation and dynamics, local cofactor abundance or the presence of other regulatory molecules, which can influence transcription factor concentration and DNA-binding.

In this paper, we have taken initial steps in this direction using mpFCS measurements of Scr in giant salivary gland nuclei. By classical FCS we could not simultaneously study Scr-DNA binding on sites of accumulation *versus* elsewhere in the nucleus, but mpFCS allowed us to concurrently record with high spatial resolution differences in diffusion and concentration of Scr between different cellular and even nuclear compartments. mpFCS indicated that the transcription factor is rather uniformly distributed across the nucleus, but at the multimeric *fkh250* binding site Scr(wt) dimer mobility is slower compared to its diffusion in the surrounding (Fig. 3C). We attribute this to the high local concentration of specific binding sites to which Scr(wt) dimers bind. This is reflected in FCS as longer diffusion times, which indicate transcription factor "stalling" due to interactions with the binding sites.

We have also observed that mobility of Scr(wt) in the residual nuclear volume (away from the binding site) is variable (Fig. 3G), which lends evidence for the existence of diverse target sites in the genome to which Scr binds with different affinities. Possible reasons why this is so could be, apart from the binding sequence itself, also the variability in region-specific abundance of cofactors, the existence of distinct chromatin states, or the variation in the chemical properties among different nuclear compartments. In fact, the notion of high and low affinity binding of Hox transcription factors is just starting to be explored and has recently been characterized in the context of Ubx–Exd binding on enhancers of the shavenbaby (svb) gene, where clustered, low-affinity binding of Ubx–Exd complexes are required for robustness of expression (Crocker et al., 2015). Our experiments point towards the existence of such binding sites also for Scr. However, whether this observation has a functional meaning also in this case, and which regulatory sequences are bound weakly and which strongly by Scr, are questions that remain to be investigated.

BiFC, FCS, FCCS and mpFCS experiments all indicate that Scr(wt) forms dimers to a much greater extent than the functionally impaired Scr(DD) (Figs 2 and 3). Artificially induced dimerization in BiFC due to high concentration and molecular crowding of transcription factor molecules bound to neighboring sites on the DNA (S. Merabet, personal communication), is not supported by our FCCS analysis and by our previous studies of Scr homodimerization in coimmunoprecipitation experiments (Papadopoulos et al., 2012).

We observed that Scr(wt) dimers localize predominantly on and strongly interact with nuclear DNA, whereas Scr(DD) dimers are more nucleoplasmic and less abundant on chromatin. This difference between the two variants, Scr(wt) and Scr(DD), together with the requirement of Scr dimer formation for homeotic function *in vivo* (Papadopoulos et al., 2012), make it possible that phosphorylation/dephosphorylation of Scr buffers its DNA-binding capacity not only through repulsion of the flexible N-terminal arm of the homeodomain, but also by controlling its ability to homodimerize.

Finally, we observed that Scr(DD) dimers to some extent form aggregates in the nucleoplasm of salivary gland cells. We attribute this to the high molecular crowding of these variants, due to the limited free space in between polytene chromosomes in these cells.

The results reported in this study agree well with our previously published results (Papadopoulos et al., 2012; Vukojevic et al., 2010) and clearly demonstrate the potential of the newly developed methodology for quantitative characterization of fast dynamical processes in live cells. Despite these positive achievements, the results of this study should be also viewed in the light of several limitations. The first and most important limitation of the current study lies in the sensitivity of the instrumental setup. The dark count of SPADs that comprise the detector is relatively high, according to the producer's specification it is 4 kHz on the average and 2 kHz at best, which gives rise to a lower signal-to-noise ratio (SNR) than in a conventional single-point FCS instrument, where the dark count of the single detector is less than 200 Hz. Another limitation, which arises due to technical reasons, is that it is at present not possible to perform measurements that are longer than 2.7 s using the full matrix detector array. In FCS, fluorescence

intensity fluctuations are recorded over a certain period of time and statistical methods of analysis are applied to detect non-randomness in the data. The longer the measurement time, the better the statistical analysis and the less noisy the resulting ACC. However, since we could not extend the signal acquisition time beyond 2.7 s using the full size of the array, this precludes direct quantitative characterization with single-molecule sensitivity and gives rise to an experimental error in the determination of molecular numbers. Comparison between single-point FCS and mpFCS measurements obtained in a dilute aqueous suspension of quantum dots, which was used as a calibration standard (Fig. S2), shows that the amplitude measured by mpFCS is much smaller than the amplitude measured by single-point FCS (Fig. S2 and F), in line with what is expected given the high dark count of SPAD detectors comprising the matrix array. However, the diffusion time measured by both setups was largely the same, both for individual quantum dots and for quantum dot agglomerates, as evident from the overlap of ACCs normalized to the same amplitude (Fig. S2) which indicates that the size of the OVE is the same in both, the conventional single-point FCS setup and the mpFCS instrument. In order to achieve direct quantitative confocal fluorescence microscopy imaging with single-molecule sensitivity and microsecond temporal resolution, the sensitivity of the detector needs to be significantly improved. At present such technology is emerging, but it is still too rare and expensive for massive parallelization.

Finally, we should also note that imaging without scanning does not allow continuous sampling across the specimen, as there are areas between the stationary focal spots from which the signal is not collected. In the present study, the pitch of the illumination matrix in the object plane is 1.5 μm. Hence, adjacent observation volume elements in the same row/column from which the signal is recorded are separated by one OVE from which the signal is not recorded. Such arrangement was deliberately used in the current setup in order to minimize cross-talk between adjacent OVE.

Previous experimental setups have demonstrated the ability to perform FCS in a larger area by means of scanning (Balaji and Maiti, 2005; Levi et al., 2003; Vukojevic et al., 2008). Such approaches underlined the importance of obtaining quantitative information across larger areas of the same sample. However, a major concern in any scanning approach is the inability to obtain information from distant locations simultaneously. For example, in raster scanning approaches signal acquisition at the level of an individual pixel is fast, in the order of microseconds, but the acquisition of an image frame is slow, lasting more than a quarter of a second for an image frame of 512×512 pixels. Therefore the information acquired in the first and the last pixel in an image frame acquired by scanning does not reflect the same state of a fast changing dynamical system. Furthermore, transcription factors exhibit complex spatio-temporal dynamics, where molecular motion reflects diffusion in the nucleoplasm, non-specific binding with the DNA during its "search" for target sites and specific binding with presumably various affinities on the DNA. Such a complex behavior is difficult to "capture" by scanning, but the ability to perform a high number of concurrent FCS measurements holds the promise to overcome such constrains.

In spite of the limitations of currently available technologies for massive production of highly sensitive SPADs, which restrain the temporal resolution and affect the quantitative analysis in live cells, as mentioned above and detailed out in Krmpot et al., in preparation, the data presented here compellingly show that it is possible to achieve quantitative confocal imaging without scanning *via* mpFCS. This approach retains all advantages of confocal microscopy, including the ability to control depth of field, improved SNR by elimination of out-of-focus light and the capability to produce 3D reconstruction of the specimen by optical sectioning. Abolishment of scanning allows confocal microscopy imaging with significantly improved temporal resolution, being 21 μs/ frame in the prototype instrument used in this study. The underlying FCS analysis provides quantitative information about the spatial distribution of molecular numbers and the mobility of molecules across the specimen. This information, which cannot be deduced from classical

fluorescence microscopy imaging, is essential for understanding how molecular interactions, which take place in a small, very well defined location, are integrated *via* molecular diffusion and transporting processes into dynamic regulatory networks.

This dataset indicates that mpFCS is a suitable method for the simultaneous recording of molecular mobility and concentration over a larger area. Therefore, it is possible to study differences in these parameters in live cells with high spatiotemporal resolution. mpFCS holds the promise of facilitating the analysis of protein interactions (and other cellular components) in heterogeneous systems, such as the precise quantification of cell-to-cell variations in protein concentration and gradients (*e.g.* during morphogenesis). Moreover, the high temporal resolution of mpFCS is expected to allow quantification and dynamics of faster processes, such as calcium signaling and neuronal transmission, simultaneously and across larger areas. Finally, the existing technologies of precise gene-editing methodologies and a further improvement of detector sensitivity (as discussed above) are anticipated to permit the study of protein dynamic behavior in a larger area and at endogenous levels in live cells.

Supplementary data to this article can be found online at http://dx.doi.org/10.1016/j.mod.2015.09.004.

Acknowledgments

References

Affolter, M., Percival-Smith, A., Muller, M., Leupin, W., Gehring, W.J., 1990. DNA binding properties of the purified Antennapedia homeodomain. Proc. Natl. Acad. Sci. U. S. A. 87, 4093–4097.

Andrew, D.J., Horner, M.A., Petitt, M.G., Smolik, S.M., Scott, M.P., 1994. Setting limits on homeotic gene function: restraint of Sex combs reduced activity by teashirt and other homeotic genes. EMBO J. 13, 1132–1144.

Balaji, J., Maiti, S., 2005. Quantitative measurement of the resolution and sensitivity of confocal microscopes using line-scanning fluorescence correlation spectroscopy. Microsc. Res. Tech. 66, 198–202.

Berry, M., Gehring, W., 2000. Phosphorylation status of the SCR homeodomain determines its functional activity: essential role for protein phosphatase 2A,B'. EMBO J. 19, 2946–2957.

Boube, M., Hudry, B., Immarigeon, C., Carrier, Y., Bernat-Fabre, S., Merabet, S., Graba, Y., Bourbon, H.M., Cribbs, D.L., 2014. *Drosophila melanogaster* Hox transcription factors access the RNA polymerase II machinery through direct homeodomain binding to a conserved motif of mediator subunit Med19. PLoS Genet. 10, e1004303.

Casares, F., Mann, R.S., 1998. Control of antennal versus leg development in *Drosophila*. Nature 392, 723–726.

Chang, C.P., Shen, W.F., Rozenfeld, S., Lawrence, H.J., Largman, C., Cleary, M.L., 1995. Pbx proteins display hexapeptide-dependent cooperative DNA binding with a subset of Hox proteins. Genes Dev. 9, 663–674.

Crocker, J., Abe, N., Rinaldi, L., McGregor, A.P., Frankel, N., Wang, S., Alsawadi, A., Valenti, P., Plaza, S., Payre, F., Mann, R.S., Stern, D.L., 2015. Low affinity binding site clusters confer hox specificity and regulatory robustness. Cell 160, 191–203.

Duffraisse, M., Hudry, B., Merabet, S., 2014. Bimolecular fluorescence complementation (BiFC) in live *Drosophila* embryos. Methods Mol. Biol. 1196, 307–318.

Furukubo-Tokunaga, K., Flister, S., Gehring, W.J., 1993. Functional specificity of the Antennapedia homeodomain. Proc. Natl. Acad. Sci. U. S. A. 90, 6360–6364.

Gehring, W.J., 1987. Homeo boxes in the study of development. Science 236, 1245–1252.

Gehring, W.J., 2011. How do Hox transcription factors find their target genes in the nucleus of living cells? Biol Aujourdhui 205, 75–85.

Gibson, G., Schier, A., LeMotte, P., Gehring, W.J., 1990. The specificities of Sex combs reduced and Antennapedia are defined by a distinct portion of each protein that includes the homeodomain. Cell 62, 1087–1103.

Glicksman, M.A., Soppet, D., Willard, M.B., 1987. Posttranslational modification of neuro-filament polypeptides in rabbit retina. J. Neurobiol. 18, 167–196.

Hrycaj, S., Chesebro, J., Popadic, A., 2010. Functional analysis of Scr during embryonic and post-embryonic development in the cockroach, Periplaneta americana. Dev. Biol. 341, 324–334.

Hu, C.D., Chinenov, Y., Kerppola, T.K., 2002. Visualization of interactions among bZIP and Rel family proteins in living cells using bimolecular fluorescence complementation. Mol. Cell 9, 789–798.

Hudry, B., Thomas-Chollier, M., Volovik, Y., Duffraisse, M., Dard, A., Frank, D., Technau, U., Merabet, S., 2014. Molecular insights into the origin of the Hox-TALE patterning system. Elife 3, e01939.

Hudry, B., Viala, S., Graba, Y., Merabet, S., 2011. Visualization of protein interactions in living Drosophila embryos by the bimolecular fluorescence complementation assay. BMC Biol. 9, 5.

Joshi, R., Passner, J.M., Rohs, R., Jain, R., Sosinsky, A., Crickmore, M.A., Jacob, V., Aggarwal, A.K., Honig, B., Mann, R.S., 2007. Functional specificity of a Hox protein mediated by the recognition of minor groove structure. Cell 131, 530–543.

Joshi, R., Sun, L., Mann, R., 2010. Dissecting the functional specificities of two Hox proteins. Genes Dev. 24, 1533–1545.

Knoepfler, P.S., Kamps, M.P., 1995. The pentapeptide motif of Hox proteins is required for cooperative DNA binding with Pbx1, physically contacts Pbx1, and enhances DNA binding by Pbx1. Mol. Cell. Biol. 15, 5811–5819.

Kuroiwa, A., Kloter, U., Baumgartner, P., Gehring, W.J., 1985. Cloning of the homeotic Sex combs reduced gene in Drosophila and in situ localization of its transcripts. EMBO J. 4, 3757–3764.

Le, T., Liang, Z., Patel, H., Yu, M.H., Sivasubramaniam, G., Slovitt, M., Tanentzapf, G., Mohanty, N., Paul, S.M., Wu, V.M., Beitel, G.J., 2006. A new family of Drosophila balancer chromosomes with a w-dfd-GMR yellow fluorescent protein marker. Genetics 174, 2255–2257.

LeMotte, P.K., Kuroiwa, A., Fessler, L.I., Gehring, W.J., 1989. The homeotic gene Sex Combs Reduced of Drosophila: gene structure and embryonic expression. EMBO J. 8, 219–227.

Levi, V., Ruan, Q., Kis-Petikova, K., Gratton, E., 2003. Scanning FCS, a novel method for three-dimensional particle tracking. Biochem. Soc. Trans. 31, 997–1000.

Lewis, E.B., 1978. A gene complex controlling segmentation in Drosophila. Nature 276, 565–570.

Lu, Q., Knoepfler, P.S., Scheele, J., Wright, D.D., Kamps, M.P., 1995. Both Pbx1 and E2A-Pbx1 bind the DNA motif ATCAATCAA cooperatively with the products of multiple murine Hox genes, some of which are themselves oncogenes. Mol. Cell. Biol. 15, 3786–3795.

Mahaffey, J.W., Kaufman, T.C., 1987. Distribution of the Sex combs reduced gene products in Drosophila melanogaster. Genetics 117, 51–60.

Mann, R.S., Chan, S.K., 1996. Extra specificity from extradenticle: the partnership between HOX and PBX/EXD homeodomain proteins. Trends Genet. 12, 258–262.

Martinez-Arias, A., Ingham, P.W., Scott, M.P., Akam, M.E., 1987. The spatial and temporal deployment of Dfd and Scr transcripts throughout development of Drosophila. Development 100, 673–683.

McGinnis, W., Krumlauf, R., 1992. Homeobox genes and axial patterning. Cell 68, 283–302.

Muller, M., Affolter, M., Leupin, W., Otting, G., Wuthrich, K., Gehring, W.J., 1988. Isolation and sequence-specific DNA binding of the Antennapedia homeodomain. EMBO J. 7, 4299–4304.

Otting, G., Qian, Y.Q., Billeter, M., Muller, M., Affolter, M., Gehring, W.J., Wuthrich, K., 1990. Protein–DNA contacts in the structure of a homeodomain–DNA complex determined by nuclear magnetic resonance spectroscopy in solution. EMBO J. 9, 3085–3092.

Otting, G., Qian, Y.Q., Muller, M., Affolter, M., Gehring, W., Wuthrich, K., 1988. Secondary structure determination for the Antennapedia homeodomain by nuclear magnetic resonance and evidence for a helix–turn–helix motif. EMBO J. 7, 4305–4309.

Panzer, S., Weigel, D., Beckendorf, S.K., 1992. Organogenesis in Drosophila melanogaster: embryonic salivary gland determination is controlled by homeotic and dorsoventral patterning genes. Development 114, 49–57.

Papadopoulos, D.K., Resendez-Perez, D., Cardenas-Chavez, D.L., Villanueva-Segura, K., Canales-del-Castillo, R., Felix, D.A., Funfschilling, R., Gehring, W.J., 2011. Functional synthetic Antennapedia genes and the dual roles of YPWM motif and linker size in

transcriptional activation and repression. Proc. Natl. Acad. Sci. U. S. A. 108, 11959–11964.

Papadopoulos, D.K., Skouloudaki, K., Adachi, Y., Samakovlis, C., Gehring, W.J., 2012. Dimer formation via the homeodomain is required for function and specificity of Sex combs reduced in Drosophila. Dev. Biol. 367, 78–89.

Papadopoulos, D.K., Vukojevic, V., Adachi, Y., Terenius, L., Rigler, R., Gehring, W.J., 2010. Function and specificity of synthetic Hox transcription factors in vivo. Proc. Natl. Acad. Sci. U. S. A. 107, 4087–4092.

Passner, J.M., Ryoo, H.D., Shen, L., Mann, R.S., Aggarwal, A.K., 1999. Structure of a DNA-bound ultrabithorax–extradenticle homeodomain complex. Nature 397, 714–719.

Qian, Y.Q., Billeter, M., Otting, G., Muller, M., Gehring, W.J., Wuthrich, K., 1989. The structure of the Antennapedia homeodomain determined by NMR spectroscopy in solution: comparison with prokaryotic repressors. Cell 59, 573–580.

Qian, Y.Q., Otting, G., Furukubo-Tokunaga, K., Affolter, M., Gehring, W.J., Wuthrich, K., 1992. NMR structure determination reveals that the homeodomain is connected through a flexible linker to the main body in the Drosophila Antennapedia protein. Proc. Natl. Acad. Sci. U. S. A. 89, 10738–10742.

Qian, Y.Q., Resendez-Perez, D., Gehring, W.J., Wuthrich, K., 1994. The des(1–6)antennapedia homeodomain: comparison of the NMR solution structure and the DNA-binding affinity with the intact Antennapedia homeodomain. Proc. Natl. Acad. Sci. U. S. A. 91, 4091–4095.

Rieckhof, G.E., Casares, F., Ryoo, H.D., Abu-Shaar, M., Mann, R.S., 1997. Nuclear translocation of extradenticle requires homothorax, which encodes an extradenticle-related homeodomain protein. Cell 91, 171–183.

Rogers, B.T., Peterson, M.D., Kaufman, T.C., 1997. Evolution of the insect body plan as revealed by the Sex combs reduced expression pattern. Development 124, 149–157.

Ryoo, H.D., Mann, R.S., 1999. The control of trunk Hox specificity and activity by Extradenticle. Genes Dev. 13, 1704–1716.

Sambrani, N., Hudry, B., Maurel-Zaffran, C., Zouaz, A., Mishra, R., Merabet, S., Graba, Y., 2013. Distinct molecular strategies for Hox-mediated limb suppression in Drosophila: from cooperativity to dispensability/antagonism in TALE partnership. PLoS Genet. 9, e1003307.

Simicevic, J., Schmid, A.W., Gilardoni, P.A., Zoller, B., Raghav, S.K., Krier, I., Gubelmann, C., Lisacek, F., Naef, F., Moniatte, M., Deplancke, B., 2013. Absolute quantification of transcription factors during cellular differentiation using multiplexed targeted proteomics. Nat. Methods 10, 570–576.

Staehling-Hampton, K., Jackson, P.D., Clark, M.J., Brand, A.H., Hoffmann, F.M., 1994. Specificity of bone morphogenetic protein-related factors: cell fate and gene expression changes in Drosophila embryos induced by decapentaplegic but not 60A. Cell Growth Differ. 5, 585–593.

Vitali, M., Bronzi, D., Krmpot, A.J., Nikolić, S., Schmitt, F.-J., Junghans, C., Tisa, S., Friedrich, T., Vukojević, V., Terenius, L., Zappa, F., Rigler, R., 2014. A single-photon avalanche camera for fluorescence lifetime imaging microscopy and correlation spectroscopy. IEEE J. Sel. Top. Quantum Electron. 20, 344–353.

Vukojevic, V., Heidkamp, M., Ming, Y., Johansson, B., Terenius, L., Rigler, R., 2008. Quantitative single-molecule imaging by confocal laser scanning microscopy. Proc. Natl. Acad. Sci. U. S. A. 105, 18176–18181.

Vukojevic, V., Papadopoulos, D.K., Terenius, L., Gehring, W.J., Rigler, R., 2010. Quantitative study of synthetic Hox transcription factor–DNA interactions in live cells. Proc. Natl. Acad. Sci. U. S. A. 107, 4093–4098.

Vukojevic, V., Pramanik, A., Yakovleva, T., Rigler, R., Terenius, L., Bakalkin, G., 2005. Study of molecular events in cells by fluorescence correlation spectroscopy. Cell. Mol. Life Sci. 62, 535–550.

Zeng, W., Andrew, D.J., Mathies, L.D., Horner, M.A., Scott, M.P., 1993. Ectopic expression and function of the Antp and Scr homeotic genes: the N terminus of the homeodomain is critical to functional specificity. Development 118, 339–352.

Zhao, J.J., Lazzarini, R.A., Pick, L., 1993. The mouse Hox-1.3 gene is functionally equivalent to the Drosophila Sex combs reduced gene. Genes Dev. 7, 343–354.

Zhao, J.J., Lazzarini, R.A., Pick, L., 1996. Functional dissection of the mouse Hox-a5 gene. EMBO J. 15, 1313–1322.

Zhou, B., Bagri, A., Beckendorf, S.K., 2001. Salivary gland determination in Drosophila: a salivary-specific, fork head enhancer integrates spatial pattern and allows fork head autoregulation. Dev. Biol. 237, 54–67.

Quantitative confocal fluorescence microscopy of dynamic processes by multifocal fluorescence correlation spectroscopy

Aleksandar J. Krmpot[a,b], Stanko N. Nikolić[a,b], Marco Vitali[c,d], Dimitrios K. Papadopoulos[e], Sho Oasa[f], Per Thyberg[g], Simone Tisa[h], Masataka Kinjo[f], Lennart Nilsson[i], Walter J. Gehring[†j], Lars Terenius[a], Rudolf Rigler*[a,k], Vladana Vukojević*[a]

[a]Department of Clinical Neuroscience (CNS), Center for Molecular Medicine (CMM), Karolinska Institutet, 17176 Stockholm, Sweden; [b]Institute of Physics, University of Belgrade, 11080 Belgrade, Serbia; [c]Department of Chemistry, Berlin Institute of Technology, 10623 Berlin, Germany; [d]Omicron Energy Solutions GmbH, 12099 Berlin, Germany; [e]Max-Planck Institute for Molecular Cell Biology and Genetics, 01307 Dresden, Germany; [f]Laboratory of Molecular Cell Dynamics, Faculty of Advanced Life Science, Hokkaido University, Sapporo, 001-0021, Japan; [g]AlbaNova University Center, Royal Institute of Technology, Department of Applied Physics, 106 91 Stockholm, Sweden; [h]Micro Photon Devices (MPD), 39100 Bolzano, Italy; [i]Department of Biosciences and Nutrition, Karolinska Institutet, 14183 Huddinge, Sweden; [j]Department of Cell Biology, Biozentrum, University of Basel, 4056 Basel, Switzerland; [k]Department of Medical Biochemistry and Biophysics (MBB), Karolinska Institutet, 17177 Stockholm, Sweden

[†]We are deeply saddened by the sudden loss of our colleague Prof. Walter J. Gehring, a visionary scientist whose work will continue to educate and inspire many generations to come.

[*]Corresponding authors: vladana.vukojevic@ki.se and rudolf.rigler@ki.se

ABSTRACT

Quantitative confocal fluorescence microscopy imaging without scanning is developed for the study of fast dynamical processes. The method relies on the use of massively parallel Fluorescence Correlation Spectroscopy (mpFCS). Simultaneous excitation of fluorescent molecules across the specimen is achieved by passing a single laser beam through a Diffractive Optical Element (DOE) to generate a quadratic illumination matrix of 32×32 light sources. Fluorescence from 1024 illuminated spots is detected in a confocal arrangement by a matching matrix detector consisting of the same number of single-photon avalanche photodiodes (SPADs). Software was developed for data acquisition and fast auto- and cross-correlation analysis by parallel signal processing using a Graphic Processing Unit (GPU). Instrumental performance was assessed using a conventional single-beam FCS instrument as a reference. Versatility of the approach for application in biomedical research was evaluated using *ex vivo* salivary glands from Drosophila third instar larvae expressing a fluorescently-tagged transcription factor Sex Combs Reduced (Scr) and live PC12 cells stably expressing the fluorescently tagged mu-opioid receptor (MOP$_{eGFP}$). We show that quantitative mapping of local concentration and mobility of transcription factor molecules across the specimen can be achieved using this approach, which paves the way for future quantitative characterization of dynamical reaction-diffusion landscapes across live cells/tissue with a sub-millisecond temporal resolution (presently 21 μs/frame) and single-molecule sensitivity.

Keywords: Quantitative confocal microscopy without scanning, Functional fluorescence microscopy imaging (fFMI), Dynamical reaction-diffusion landscapes, Transcription factor, G protein-coupled receptor (GPCR).

1. INTRODUCTION

The living cell is a complex dynamical system, where local concentrations and spatial distribution of molecules are perpetually changing. Living cells control the concentration, spatial distribution and temporal dynamics of biological molecules through molecular interactions and transporting processes. Through reaction-diffusion processes biomolecules are integrated in specific dynamical networks, *i.e.* pathways, and perform specialized cellular functions. To understand detailed molecular mechanisms underlying the function of complex biological pathways, the concentration and mobility of interacting molecules need to be quantitatively characterized in live cells.

We present here a setup for quantitative confocal fluorescence microscopy imaging without scanning *via* massively parallel FCS measurements, where a Diffractive Optical Element (DOE) and a matrix single-photon avalanche photodiode (SPAD) camera are used to achieve massively parallel confocal arrangement.[1] This approach holds the potential to map the landscape of biomolecules activity and quantitatively characterize the concentration and dynamics of molecules in live cells/tissue. We therefore name this approach functional Fluorescence Microscopy Imaging (fFMI).

2. INSTRUMENTAL DESIGN

The setup for fFMI is schematically depicted in Figure 1. The light beam generated by the continuous wave (CW) 488 nm frequency-doubled diode laser was guided through a double filter wheel for intensity regulation. The double filter wheel consists of 5+5 uniform neutral density filters of different optical density (OD) enabling wide range of attenuation (OD 0.2-8.0) in discrete steps. Uniform rather than variable filters were used in order to avoid wave front distortion and thus preserve symmetrical light intensity distribution in the focus. The laser beam is then expanded about 10 times by lenses L1 and L2 arranged in a Keplerian telescope configuration. The beam path is deflected by two steering mirrors M1 and M2 and the periscope assembly (PA) in order to match the height and lateral position of the back port of the microscope. The expanded beam is focused by the plano-convex lens L3 through the diffractive optical element (DOE) designed to split the single laser beam into 32×32 beams. Using a lens with 150 mm focal distance (L3 in Fig. 1) and positioning the DOE to a focal plane distance of 130 mm, a 32×32 foci illumination matrix was formed at the rear port image plane of the microscope. (The halogen lamp and the light guide for transmitted light through the rear port were previously removed.) The relay optics of the rear port, dichroic mirror, and the C-Apochromat 63×/1.2 W Corr objective transfer the illumination matrix image into the focal plane of the objective. The lateral position of the illumination matrix and its sharpness can be adjusted by moving the steering mirrors M1 and M2 and/or lens L3, which is mounted on a precise *x-y-z* translation stage. The DOE is mounted on a single-axis precise translation stage, and the pitch of the illumination matrix could be adjusted to match the detector matrix by moving the DOE along the beam axis (*z*-axis).

The Zeiss Filter Set 38 HE for enhanced Green Fluorescent Protein (eGFP) consisting of an excitation band pass filter EX BP 470/40 nm (central wavelength/bandwidth), long pass dichroic mirror with a cut-off wavelength of 495 nm, and an emission band pas filter EM BP 525/50 was used throughout.

Fluorescence was detected using the SPAD camera, containing a photosensitive chip and a 16-bit photon counter based on a Field Programmable Gate Array (FPGA). The photo sensitive area of the chip consists of 32×32 circular SPADs that are 20 μm in diameter. The distance between adjacent SPADs in the same row/column is 100 μm.[1-4] Since the aperture of every SPAD in the camera acts as a pinhole positioned in a conjugate focal plane with respect to the illumination matrix, confocal configuration is achieved for all 32×32 foci.
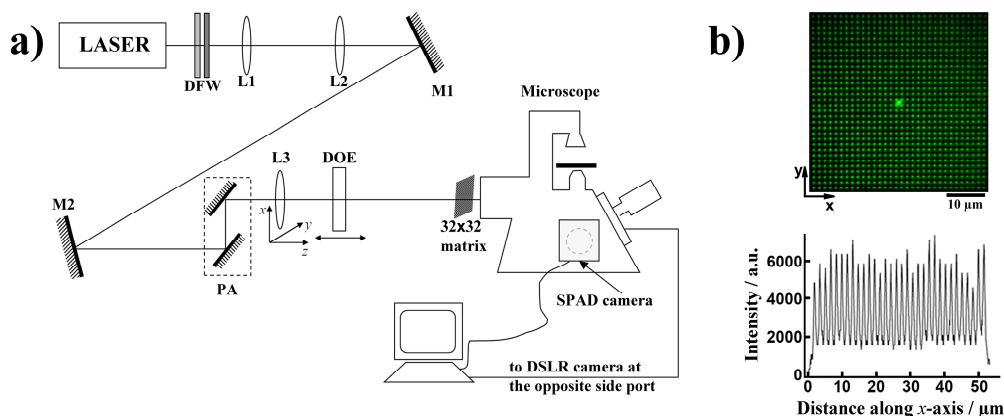

Figure 1. Schematic representation of the instrumental setup for functional Fluorescence Microscopy Imaging (fFMI). **a)** DFW – double filter wheel, L1, L2, and L3 – lenses, M1 and M2 mirrors, PA – periscope assembly, DOE – diffractive optical element, DSLR – 18.0 megapixel digital single-lens reflex camera. The illumination matrix of 32×32 laser beam spots is formed at the image plane of the rear port of the microscope by passing a single-laser beam through the DOE and L3. **b)** Top: Image of the illumination matrix generated in the focal plane of the microscopic objective after passing the single laser beam through the DOE and L3. A thin layer of concentrated Rh 6G solution in water was used as a sample. The image was acquired by the DSLR camera. Bottom: Fluorescence intensity (in arbitrary units, a.u.) along the *x*-axis. The pitch of the illumination matrix in the sample plane (the shortest distance between two adjacent spots) is 1.587 μm.

Data analysis

Raw data collected by the SPAD camera, consisting of 131000 frames acquired every 20.74 µs that yield 1024 fluorescence intensity fluctuation traces recorded over 2.7 s, were stored in the camera's internal memory, transferred to the computer and subjected to correlation analysis to yield auto- and first- and second-order cross-correlation curves (ACC and CCC, respectively) for all 32×32 pixels in an image frame. For this purpose, the so-called multi-tau algorithm was used.[5,6] Briefly, in the multi-tau algorithm values of the second order correlation function $G^{(2)}(\tau)$ are determined on a quasi-logarithmic time scale. Each lag time (τ) for which the $G^{(2)}(\tau)$ value is calculated, is called a channel. The channel is thus characterized by an individual sampling time (the bin width) and the lag time τ (the delay from the measurement at time 0). The first sixteen channels form the first group, while all other groups consist of eight consecutive channels. The bin width for the first group is determined by the shortest counting interval of the detector, which is 20.74 µs for the SPAD camera used. The following group has an individual sampling time that is twice as long, while for the other channels it is equal to the accumulated sampling time of all preceding channels plus the bin width of its group. Two additional variables are introduced: the so-called delayed monitor M_{del} defined for each channel and the direct monitor M_{dir} defined for each group. The purpose of M_{del} is to accumulate all counts sampled in its channel, while M_{dir} accumulates all counts without delay time at a particular sampling time.

The ACCs, M_{del} and M_{dir} are calculated according to the following formulas:

$$G^{(2)}(\tau_i) = \frac{\frac{1}{M-m}\sum_{k=1}^{M-m} n(k\Delta\tau_i)\cdot n(k\Delta\tau_i + m\Delta\tau_i)}{M_{del}\cdot M_{dir}}, \tag{1}$$

$$M_{del} = \frac{1}{M-m}\sum_{k=m}^{M} n(k\Delta\tau_i) \tag{2}$$

and

$$M_{dir} = \frac{1}{M-m}\sum_{k=1}^{M-m} n(k\Delta\tau_i) \cdot \tag{3}$$

Here, τ_i is the lag time and $\Delta\tau_i = 2^{i-1}\Delta\tau_1$ is the sampling time for channel i. Bin width for the first group is $\Delta\tau_1 = 20.74\,\mu s$. m and M are integers defined as $m = \tau_i/\Delta\tau_i$ and $M = T/\Delta\tau_i$, where T is the total measurement time. The number of photons counted over a time interval $[(k-1)\Delta\tau_i, k\Delta\tau_i]$ is denoted as $n(k\Delta\tau_i)$. In essence, the correlation analysis boils down to obtaining the sum of the products $n(k\Delta\tau_i)\cdot n(k\Delta\tau_i + m\Delta\tau_i)$ of the counted photons at time $k\Delta\tau_i$ and $m\Delta\tau_i$ later.[7]

The CCCs are calculated for two SPADs of the camera designated as the "first" or "second" order neighbors of the reference pixel. For example, if the row and column of pixels a and b are denoted as $row(a)$, $col(a)$, $row(b)$ and $col(b)$, respectively, then pixels a and b are said to be "first" order neighbors if relationships (1) or (2) apply: (1) $|row(a) - row(b)| = 1$ and $|col(a) - col(b)| \leq 1$ or (2) $|col(a) - col(b)| = 1$ and $|row(a) - row(b)| = 0$. Similarly, for "second" order neighbors: (1) $|row(a) - row(b)| = 2$ and $|col(a) - col(b)| \leq 2$ or (2) $|col(a) - col(b)| = 2$ and $|row(a) - row(b)| \leq 1$.

The following formula was used for the calculation of CCCs:

$$G_{ab}^{(2)}(\tau_i) = \frac{\frac{1}{M-m}\sum_{k=1}^{M-m} n_a(k\Delta\tau_i)\cdot n_b(k\Delta\tau_i + m\Delta\tau_i)}{M_{a,dir}M_{b,del}}, \tag{4}$$

where $n_a(k\Delta\tau_i)$ and $n_b(k\Delta\tau_i)$ denote photon counts at time $k\Delta\tau_i$ for pixels a and b, respectively. $M_{a,del}$ and $M_{a,dir}$ are

calculated according to (2) and (3) by taking the photon counts n_a of pixel a. In analogy, $M_{b,del}$ and $M_{b,dir}$ were calculated by taking the photon counts n_b of pixel b. It is important to note that, in general, $G_{ab}^{(2)}(\tau_i) \neq G_{ba}^{(2)}(\tau_i)$, and that the symmetry relation $G_{ab}^{(2)}(\tau_i) = G_{ba}^{(2)}(\tau_i)$ only holds in the absence of directed motion. Thus, for each pair of pixels there are two cross-correlation curves, which may be different in case of directed molecular movement *i.e.* flow.[8]

Since fluorescence intensity fluctuations are independently recorded by SPADs that constitute the SPC[2] camera, parallel computing could be used to speed up data analysis by auto and cross-correlation. For this purpose, the NVIDIA GeForce GTX 780 graphic card was used that contains 2304 Compute Unified Device Architecture (CUDA) cores that can run tens of thousands of independent tasks (threads) simultaneously. By running as many threads in parallel as possible, the CUDA platform enabled us to use the processing power of the GPU to massively parallelize data analysis. Using one thread to calculate the $G^{(2)}(\tau)$ value of one channel for one particular pixel, the CUDA program executed two groups of threads for ACCs calculation and forty groups of threads for CCCs calculation, where each group runs 64000 threads in parallel on the GPU. This decreased the time required for computation of 1024 ACCs by a central processing unit (CPU) from ≈ 210 s to ≈ 4 s by a GPU, and from ≈ 77 minutes (CPU) to ≈ 45 s (GPU) for the calculation of CCCs.

fFMI image rendering

An ACC was calculated for each pixel. The amplitude of the ACC was estimated from the value of $G(\tau)$ at $\tau = 103.7$ µs, and the characteristic decay time of the ACC from its full width at half maximum. If not otherwise indicated, these values are plotted in fFMI images to show the spatial distribution of ACC amplitudes and decay times across the sample.

3. RESULTS AND DISCUSSION

Quantum dots dynamics in dilute aqueous suspension

A dilute suspension of carboxylate functionalized quantum dots in water was used to evaluate the potential of the fFMI setup for single-particle studies. For this purpose, fFMI and conventional FCS measurements were performed on the same sample (Fig. 2). fFMI was performed in a single-run experiment, with signal acquisition lasting 2.7 s (Fig. 2a-c and Fig. 2g), and in a series of 10 consecutive measurements, with each measurement lasting 2.7 s (Fig. 2d-f and Fig. 2h). Diffusion time histograms (Fig. 2c and f) show two characteristic values, $\tau_{diff} = (0.6 \pm 0.2)$ ms and $\tau_{diff} = (10 \pm 5)$ ms.

Fluctuations in fluorescence intensity recorded by conventional FCS (Fig. 2i) and corresponding autocorrelation curves (Fig. 2j), show that the quantum dots suspension is polydisperse, containing single quantum dots and a small amount of bright quantum dot agglomerates. The concentration of single quantum dots was ≈ 2 nM (Fig. 2j, magenta ACC) and the apparent brightness, estimated as counts per molecule and second (CPMS), was CPMS = 7.4 kHz. The agglomerate concentration was ≈ 0.7 nM (Fig. 2j, blue ACC) and the apparent brightness CPMS = 42.0 kHz. Single quantum dots and agglomerates differ also in diffusion, as evident from different characteristic decay times of the corresponding ACCs normalized to the same amplitude (Fig. 2k, magenta *vs* blue ACCs).

For a single time series acquisition of 2.7 s, temporal autocorrelation analysis yielded smooth ACCs for bright quantum dot clusters, as shown for several selected pixels in Fig. 2g, whereas ACCs for individual quantum dots were rather noisy (data not shown). As expected, acquisition of multiple time series (Fig. 2d-f), significantly improved the statistical analysis yielding smoother ACCs (Fig. 2h). From these measurements even diffusion properties of individual quantum dots could be assessed (Fig. 2k, black line).

Decay times measured using the fFMI instrument and the conventional FCS setup agree well, as evident from the overlap of ACCs normalized to the same amplitude for both, individual quantum dots (Fig. 2k, magenta and black) and quantum dot clusters (Fig. 2k, green and blue), indicating that the observation volume element (OVE) size in individual fFMI pixels was similar to that in the conventional FCS setup. In some measurements signals from individual quantum dots and quantum dot clusters were observed, yielding biphasic ACCs with two characteristic decay times (Fig. 2l, violet). Again, the ACC determined by fFMI (Fig. 2l, violet) overlaps with the ACC obtained by the conventional FCS setup (Fig. 2l, olive).
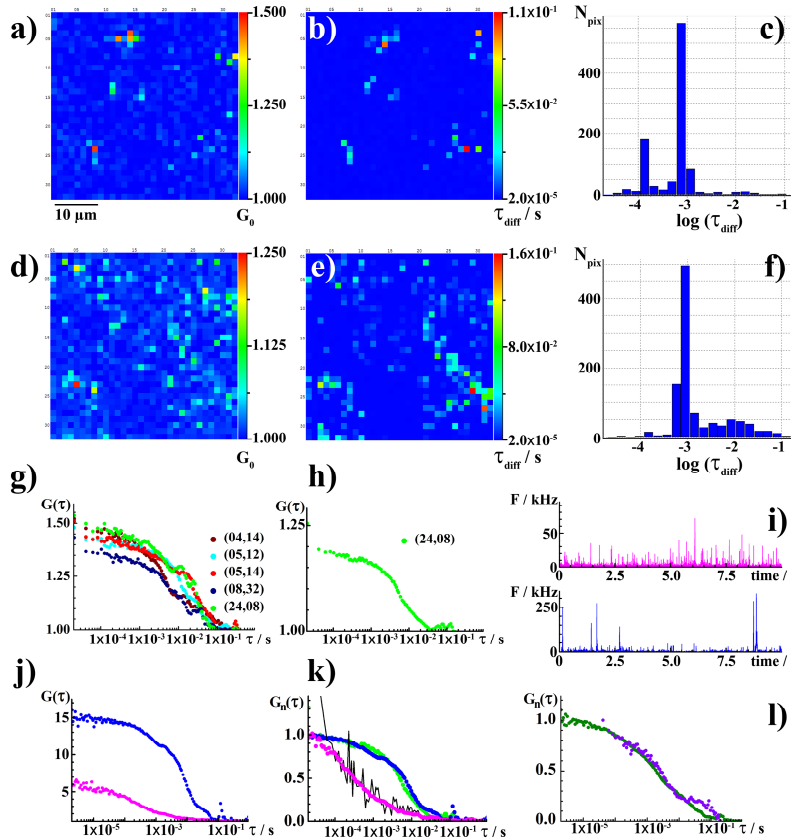
Figure 2. fFMI of quantum dots dynamics in dilute aqueous suspension. **a)** Spatial map of G_0 values, denoting the amplitude of individual ACCs at the lag time $\tau = 100$ µs, acquired in a single measurement lasting 2.7 s. **b)** Corresponding map of estimated diffusion times, τ_{diff}. **c)** Diffusion time histogram corresponding to the data shown in b). **d)** Spatial map of G_0 values for the same sample as in a), acquired as an average of 10 consecutive measurements, each individual measurement lasting 2.7 s. **e)** Map of estimated diffusion times, $\tau_{diff.}$, corresponding to measurements shown in d). **f)** Diffusion time histogram corresponding to the data shown in e). **g)** ACCs for selected pixels from the image frame shown in a), acquired during a single run (signal acquisition 2.7 s). **h)** An average ACC for a selected pixel from the image frame shown in d), obtained from 10 consecutive measurements, each measurement lasting 2.7 s. **i)** Fluorescence intensity fluctuations recorded in the same sample using conventional FCS confirm that the suspension is polydisperse, showing the presence of single quantum dots (magenta trace) and quantum dots agglomerates (blue trace). **j)** Corresponding ACCs, obtained by temporal autocorrelation analysis of fluorescence intensity fluctuations presented in i). Autocorrelation analysis (pink ACC) showed that the concentration of individual quantum dots is ≈ 2 nM and the diffusion time $\tau_{diff} = (400 \pm 100)$ µs; the apparent brightness of individual quantum dots was estimated to be CPM = 7.4 kHz. As compared to individual quantum dots, the concentration of quantum dot clusters was lower, $c \approx 0.7$ nM, the diffusion time was longer, $\tau_{diff} = (6 \pm 5)$ ms and they are brighter, CPM = 42 kHz (blue ACC). **k)** ACCs derived from 10 consecutive measurements and normalized to the same amplitude reflect the diffusion properties of individual quantum dots characterized by fFMI (black) and conventional FCS (pink), and of quantum dot clusters characterized by fFMI (green) and conventional FCS (blue). **l)** ACCs normalized to the same amplitude recorded in a mixture of individual quantum dots with quantum dot clusters, acquired by fFMI (violet) and conventional FCS (olive). fFMI and single-point FCS measurements were performed at comparable excitation intensities (14.8 µW at the microscope objective lens in single-point FCS). The illumination intensity in individual foci (estimated to be 1/1024 of the intensity measured at the fFMI microscope objective (18.9 mW) reduced by 20 % to account for the zeroth order) was roughly the same as in the conventional set-up (14.8 µW at the microscope objective lens).

As evident from the data presented in Fig. 2, quantum dots in dilute suspension could be visualized and characterized using the fFMI setup. Diffusion times measured by fFMI and conventional FCS agreed well, indicating that the OVE in individual pixels in the fFMI setup is similar in size in both setups. However, the amplitude of the ACCs acquired by fFMI was, at best, 10 times smaller than the amplitude of ACCs acquired by the conventional FCS setup. This suggests that the signal-to-noise (SNR) in the fFMI setup is at best ~ 3 times lower than in the conventional FCS system. The difference in SNR between the fFMI and conventional FCS system arises primarily due to differences in dark-count rates

of SPADs, which for most SPADs comprising the matrix detector was over 1000 photons *per* second, and about 250 photons *per* second in the conventional system. Due to the low SNR, concentration could be correctly determined by the fFMI system only when very bright fluospheres were used (data not shown). For the quantum dots, a linear relationship between the ACC amplitudes measured by fFMI and conventional FCS was determined in a concentration range of $0.1 - 100$ nM, making it possible to measure the concentration of quantum dots using a calibration curve (data not shown).

Transcription factor dynamics in live salivary glands

The fFMI instrument was used to characterize under *ex vivo* conditions the nuclear dynamics of a synthetic transcription factor that interacts with chromosomal DNA (Fig. 3). For this purpose we have used salivary glands from *Drosophila* third instar larvae expressing an mCitrine-tagged Sex combs reduced (Scr) dimeric transcription factor (mCitrine-(Scr)$_2$) and bearing a multimeric specific binding site of Scr (*fkh250^{con}*) in the genome.
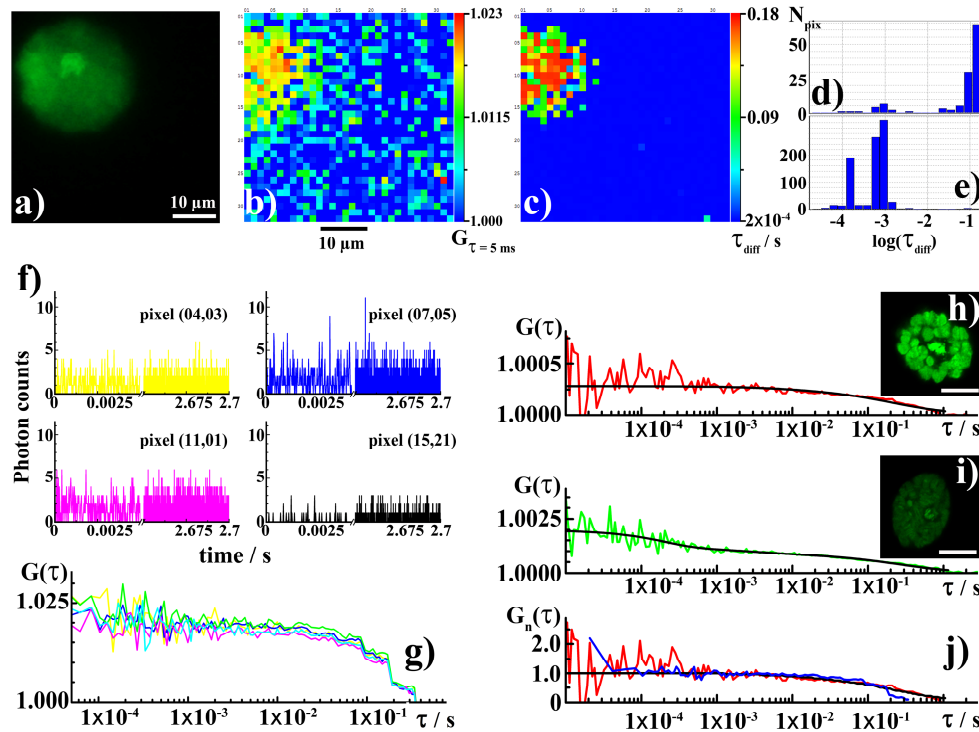
Figure 3. Functional Fluorescence Microscopy Imaging (fFMI) of transcription factor dynamics in live salivary glands of *Drosophila*. **a)** Fluorescence image of a polytene cellnucleus of a live salivary gland dissected from a third instar larva of the fruit fly *Drosophila melanogaster* genetically engineered to express a mCitrine-tagged dimeric Sex Combs Reduced (Scr) transcription factor mCitrine-(Scr)$_2$. The image was acquired using a digital single-lens reflex camera. **b)** Spatial map of G_0 values, reflecting the amplitude of auto-correlation curves (ACC) at the lag time $\tau = 5$ ms. The blue-cyan background reflects regions in the cytoplasm where uncorrelated signal is observed. Green-yellow-red pixels show transcription factor molecules sparsely distributed in the cytoplasm and their accumulation in the cell nucleus. **c)** Map of estimated diffusion times, τ_{diff}. In the cytoplasm, the diffusion time of molecules is shorter than 2 ms (dark blue pixels). Diffusion in the cell nucleus is non-uniform, showing domains where fast or slow diffusion prevails. Regions where slow diffusion is observed reflect transcription factor binding to chromatine, *i.e.* putative sites of transcriptional activity. **d)** Diffusion time histogram reflecting diffusion time distribution in the cell nucleus (pixels in rows 3-16 and columns 1-10). **e)** Diffusion time histogram reflecting mCitrine-(Scr)$_2$ diffusion in the cytoplasm (all pixels except the ones analyzed in d). **f)** Fluorescence intensity fluctuations recorded in selected pixels in the cell nucleus (yellow, blue and magenta traces) and the cytoplasm (black trace). The traces, collected during 2.7 s, show that little photobleaching was observed during signal acquisition. **g)** ACCs recorded in the cell nucleus, generated by temporal autocorrelation analysis of fluorescence intensity fluctuations shown in f). **h)** and **i)** ACCs recorded by conventional single-point FCS in two different nuclei in the same salivary gland as in a). Black lines represent curves generated by fitting a model for free three-dimensional diffusion of two components. Images of cell nuclei acquired by CLSM are shown in the insets. **j)** ACCs normalized to the same amplitude recorded by fFMI (blue) and conventional FCS instrument used as a reference (red). The overlap between ACCs shows that optical properties of the newly developed instrument are of high quality and that the observation volume element size is similar in both set-ups.

Fluorescence image of a polytene nucleus acquired by the DSLR camera is shown in Fig. 3a. The spatial map of $G(\tau)$ values at lag time $\tau = 5$ ms is shown in Fig. 3b, and the spatial map of diffusion times in Fig. 3c. Corresponding histograms, reflecting the distribution of diffusion times inside the cell nucleus (Fig. 3d) as compared to the distribution of diffusion times in the cytoplasm (Fig. 3e), are also shown. Fluorescence intensity fluctuations simultaneously recorded at several different positions in the cell nucleus (Fig. 3f, yellow, blue and magenta) and in the cytoplasm (Fig. 3f, black), show that the average signal intensity is rather even during the signal acquisition time (2.7 s) and that photobleaching is not extensive. ACCs acquired in selected pixels in the cell nucleus (pixels (04,03), (07,05) and (11,01)) are shown in Fig. 3g).

fFMI measurements (Fig. 3b and c), clearly show that mCitrine-$(Scr)_2$ is predominantly located in the cell nucleus (Fig. 3b), and that nuclear diffusion is significantly slower than its diffusion in the cytoplasm (Fig. 3c). Furthermore, fFMI shows that the investigated protein is not uniformly distributed in the cell nucleus, and that domains with different mCitrine-$(Scr)_2$ concentration and diffusion exist. This is expected, since polytene cell nuclei contain 2^{10} chromosomal copies associated together in giant polytene chromosomes. In the nucleoplasm, where there is no chromatin, the diffusion of unbound mCitrine-$(Scr)_2$ is faster because its movement is not deterred by interactions with DNA.[9,10] Fast and slow diffusion of mCitrine-$(Scr)_2$ was also observed by conventional FCS, as evident from the biphasic ACC in Fig. 3i, which shows two characteristic decay times. Likewise, the concentration of mCitrine-$(Scr)_2$ in the nuclear lumen is typically smaller than on the chromosome arms, where it readily accumulates.

Results of conventional FCS analysis performed on the polytene chromosome in two different nuclei are shown in Fig. 3h and i), with corresponding CLSM images shown in the insert. Again, the characteristic decay times of the ACCs obtained by fFMI and conventional FCS agree well, $\tau_{D,fFMI} \approx \tau_{D,FCS} = 25$ ms, as can be seen from the overlap of ACCs normalized to the same amplitude (Fig. 3j).

Amplitudes of ACCs measured by fFMI and conventional FCS cannot be compared since the measurements were performed in different cell nuclei. The concentration of the investigated molecule may be different in different cell nuclei, as evident from conventional FCS (Fig. 3h and i). It is reasonable to expect that the SNR is low, as discussed in the previous section, likely affecting the amplitude of the autocorrelation function. Still, one should note that the amplitude of ACCs recorded in the cytoplasm is larger than that of ACCs recorded in the nucleus and that the correlation decay time is shorter in the cytoplasm than in the cell nucleus, showing the concentration of mCitrine-$(Scr)_2$ is lower and molecular movement is faster in the cytoplasm than in the nucleus.

Preliminary data on mu-opioid receptor lateral organization in live PC12 cells

A particular challenge in biomedical research is to characterize the dynamic lateral organization of cell surface receptors in the plasma membrane and investigate how it is altered in signal transduction. We present here first proof-of-principle results showing mu-opioid receptor dynamics across an optical section in live PC12 cell (Fig.4). Further characterization of MOP$_{eGFP}$ dynamics using pharmacological substances is ongoing.
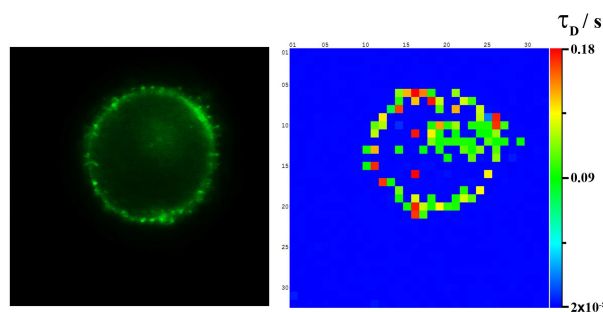

Figure 4. Left: Fluorescence image of a PC12 cell stably expressing the mu-opioid receptor fused with the enhanced Green Fluorescence Protein (MOP$_{eGFP}$) acquired using the fFMI instrument and the 18.0 megapixel digital single-lens reflex camera. Right: Diffusion time (τ_D) map shows that MOP-eGFP localizes in the plasma membrane and the endoplasmic reticulum. Lateral mobility in the plasma membrane and the endoplasmic reticulum is slow, 8 ms $< \tau_D <$ 180 ms.

4. CONCLUDING REMARKS

Data presented here show that it is possible to achieve a massively parallel confocal arrangement and quantitative confocal imaging without scanning *via* multiplexed FCS. This yields quantitative confocal imaging at an unprecedented temporal resolution, which in our set-up is 21 μs/frame. We showed that massively parallel analysis of fluorescence intensity fluctuations by temporal autocorrelation and spatio-temporal cross-correlation analyses can be achieved, yielding 1024 ACCs in about 4 s and about 24000 CCCs in 45 s. The possibility to have multiplexed confocal arrangements of excitation and detection pathways is therefore essential for quantitative studies of fast dynamical processes. By combining multi-spot illumination with single photon counting avalanche photodiode arrays, [1,11-14] it is possible to retain all advantages of confocal microscopy, including the ability to control depth of field, improved SNR by elimination of out-of-focus light and the capability to produce 3D reconstruction of specimen by optical sectioning. In addition, this allows for the abolishment of scanning, bringing about a 100-fold and in the future even a 1000-fold improvement in temporal resolution of confocal microscopy. The underlying FCS analysis provides quantitative information about the local concentration and the mobility of molecules across the specimen, which cannot be deduced from classical fluorescence imaging by CLSM. The possibility to measure local concentrations and mobility of biomolecules is essential for understanding the spatio-temporal integration of molecular interactions in live cells/tissues. This approach is therefore of particular interest for biomedical research applications, as it holds the capacity to map the dynamic landscape of biomolecules activity in live cells/tissue with single-molecule sensitivity and sub-millisecond temporal resolution.

REFERENCES

[1] Vitali, M., Bronzi, D., Krmpot, A. J., Nikolić, S. N., Schmitt, F-J., Junghans, C., Tisa, S., Friedrich, T., Vukojević V., Terenius, L., Zappa, F. and Rigler, R., "A single-photon avalanche camera for fluorescence lifetime imaging microscopy and correlation spectroscopy" IEEE J. Sel. Top. Quantum Electron. 20(6), 344-353 (2014).

[2] Michalet, X., Siegmund, O. H., Vallerga, J. V., Jelinsky, P., Millaud, J.E. and Weiss, S., "Detectors for single-molecule fluorescence imaging and spectroscopy." J. Mod. Opt. 54(2-3), 239-281 (2007).

[3] Michalet, X., Colyer, R. A., Scalia, G., Weiss, S., Siegmund, H. W. O., Tremsin, A. S., Vallerga, J. V., Villa, F., Guerrieri, F., Rech, I., Gulinatti, A., Tisa, S., Zappa, F., Ghioni, M. and Cova, S. "New photon-counting detectors for single-molecule fluorescence spectroscopy and imaging." Proc. of SPIE 8033, 803316 (2011).

[4] Michalet, X., Colyer, R. A., Scalia, G., Ingargiola, A., Lin, R., Millaud, J. E., Weiss, S., Siegmund, O. H., Tremsin, A. S., Vallerga, J. V., Cheng, A., Levi, M., Aharoni, D., Arisaka, K., Villa, F., Guerrieri, F., Panzeri, F., Rech, I., Gulinatti, A., Zappa, F., Ghioni, M. and Cova, S., "Development of new photon-counting detectors for single-molecule fluorescence microscopy." Philos Trans R Soc Lond B Biol Sci. 368, 20120035 (2012).

[5] Schätzel, K., Drewel, M. and Stimac, S., "Photon correlation measurements at large lag times: improving statistical accuracy." J Mod Opt 35, 711–718 (1988).

[6] Schätzel, K., "Accuracy of photon correlation measurements on nonergodic samples." Applied Optics 32, 3880-3885 (1993).

[7] Wohland, T., Rigler, R. and Vogel, H., "The Standard Deviation in Fluorescence Correlation Spectroscopy." Biophys J. 80, 2987–2999 (2001).

[8] Magde, D., Webb, W. W. and Elson, E. L., "Fluorescence correlation spectroscopy. III. Uniform translation and laminar flow." Biopolymers. 17, 361–376 (1978).

[9] Vukojević, V., Papadopoulos, D. K., Terenius, L., Gehring, W. J. and Rigler R., "Quantitative study of synthetic Hox transcription factor-DNA interactions in live cells." Proc Natl Acad Sci U S A. 107:4093-4098 (2010).

[10] Papadopoulos, D. K., Skouloudaki, K., Adachi, Y., Samakovlis, C. and Gehring, W. J. "Dimer formation via the homeodomain is required for function and specificity of Sex combs reduced in Drosophila." Dev Biol. 367, 78-89 (2012).

[11] Blom, H., Johansson, M., Hedman, A. S., Lundberg, L., Hanning, A., Hård, S. and Rigler, R. "Parallel fluorescence detection of single biomolecules in microarrays by a diffractive-optical-designed 2 x 2 fan-out element." Appl Opt. 41, 3336-3342 (2002).

[12] Blom, H., Johansson, M., Gösch, M., Sigmundsson, T., Holm, J., Hård, S. and Rigler R., "Parallel flow measurements in microstructures by use of a multifocal 4 x 1 diffractive optical fan-out element." Appl Opt. 41, 6614-6620 (2002).

[13] Gösch, M., Serov, A., Anhut, T., Lasser, T., Rochas, A., Besse, P. A., Popovic, R. S., Blom, H. and Rigler R., "Parallel single molecule detection with a fully integrated single-photon 2x2 CMOS detector array." J Biomed Opt. 9, 913-921 (2004).

[14] Gösch, M., Blom, H., Anderegg, S., Korn, K., Thyberg, P., Wells, M., Lasser, T., Rigler, R., Magnusson, A. and Hård, S., "Parallel dual-color fluorescence cross-correlation spectroscopy using diffractive optical elements." J Biomed Opt. 10, 054008 (2005).

Transient development of Zeeman electromagnetically induced transparency during propagation of Raman–Ramsey pulses through Rb buffer gas cell

Transient development of Zeeman electromagnetically induced transparency during propagation of Raman–Ramsey pulses through Rb buffer gas cell

S N Nikolić, M Radonjić, N M Lučić, A J Krmpot and B M Jelenković

Institute of Physics, University of Belgrade, Pregrevica 118, 11080 Belgrade, Serbia

E-mail: stankon@ipb.ac.rs

CrossMark

Abstract

We investigate, experimentally and theoretically, time development of Zeeman electromagnetically induced transparency (EIT) during propagation of two time separated polarization laser pulses, preparatory and probe, through Rb vapour. The pulses were produced by modifying laser intensity and degree of elliptical polarization. The frequency of the single laser beam is locked to the hyperfine $F_g = 2 \rightarrow F_e = 1$ transition of the D_1 line in ^{87}Rb. Transients in the intensity of σ^- component of the transmitted light are measured or calculated at different values of the external magnetic field, during both preparatory and probe pulse. Zeeman EIT resonances at particular time instants of the pulse propagation are reconstructed by appropriate sampling of the transients. We observe how laser intensity, Ramsey sequence and the Rb cell temperature affect the time dependence of EIT line shapes, amplitudes and linewidths. We show that at early times of the probe pulse propagation, several Ramsey fringes are present in EIT resonances, while at later moments a single narrow peak prevails. Time development of EIT amplitudes are determined by the transmitted intensity of the σ^- component during the pulse propagation.

(Some figures may appear in colour only in the online journal)

1. Introduction

Electromagnetically induced transparency (EIT) [1–3] is a quantum interference phenomenon which is manifestated as a narrow spectral resonance observed in transmitted laser light through otherwise opaque vapour of, typically, alkali metals. EIT is attained when two light fields couple two atomic ground levels to a common excited level (so-called Λ-scheme). Within the spectral bandwidth of the EIT there is a strong dispersion of the index of refraction, resulting in a slow light and storage of light phenomena in EIT medium [4, 5]. EIT is demonstrated as a coherent technique for controlling the propagation of classical light pulses and other nonlinear optics applications [4]. A review of EIT in various atomic schemes is given in [6].

Studies of pulse propagation through EIT medium is a mature field. Measurements of transient fluorescence [7], of transient gains of the probe pulse [8], and of non-resonant (for both preparation and probe beams) transients [9] were done. Also, transient effects in adiabatic [10] and non-adiabatic [11] regimes, depending if the rise time of the pulse is slow or fast compared to the Rabi period and relaxation times, were analyzed. Transients of transmission of the probe pulse were studied for cases when the pump beam is turned off [9] or on [11], when the probe itself is turned on, and when pump and probe fields are suddenly detuned from the resonance [8, 12]. Detailed theoretical investigation of EIT and features of the space-time dependent probe field in Λ-, V-, and cascade-type schemes are presented in [13]. The same authors performed a time-dependent analysis of the four-wave mixing process

(FWM) in a double-Λ system, showing that generated FWM field can acquire ultraslow group velocity [14].

It was shown that the pulse strength of the laser, the pulse switching rate, and the magnetic field determine the rate at which transmitted pulse reaches a new steady state. These parameters also determine transient behavior of the probe transmission with or without free induction decay [15]. Stepwise Raman detuning of circularly polarized pump and probe beams resulted in the oscillatory behavior of the transient signal, with the period of oscillations depending on the Raman detuning [16]. Dependence of decay rates of the amplitudes of the signal oscillations on the cell temperature and laser power was studied in [12]. Behavior of transmission of lasers inducing Zeeman EIT, when magnetic field is suddenly turned off and on, was studied both experimentally and theoretically [17]. Transients in coherent population trapping (CPT) can be also induced by ac magnetic field as calculated in [18, 19]. Transient response of an EIT media to a phase-modulated pump was examined in [20].

Propagation of a probe pulse through EIT medium is closely related to temporal evolution of EIT resonance. However, the transient development of EIT was much less studied than transmission of the laser pulse. In [21], the build up of EIT was observed after sudden two-photon detuning from EIT. It was found that the Zeeman EIT width decreases inversely with the interaction time and approaches an asymptotic value determined by the preparatory laser intensity [21].

Various models of transient effects were developed to predict, or to explain, the propagation of the laser pulse through EIT medium. Typically, analytical solutions of equations for density matrix describing a three-state model is used [15]. In [22] the authors compared transients for the dressed-atom and bare-atom pictures. The calculations of temporal evolution of EIT were also studied [23]. The transient response of atomic system was calculated when the laser is suddenly turned on in the presence of external magnetic field [24].

The Ramsey method of separated oscillatory fields [25] was applied to alkali atoms contained in the glass cell in order to narrow resonance linewidth. Application of two or more successive laser pulses leads to the appearance of high contrast and narrow (~100 Hz) CPT and EIT fringes [26–30]. Calculations have also shown that quantum interference, driven by two identical pulses, results in Ramsey-like fringes [31]. Two-photon free-induction decay in a three-level Λ system used to obtain EIT was reported in [32]. Ramsey interference effect appears after pulsed excitation, with fringes observed as time-domain oscillations in the transmission amplitude of a long attenuated query pulse [33]. Transient of Raman–Ramsey fringes (RRF) and EIT have been measured in sodium vapour in the hyperfine Λ system [34]. Ramsey fringes induced by Zeeman coherence in various Rb cells for both spatially and temporally separated laser fields were reported in [35]. Ramsey-like measurements of Zeeman decoherence that determine the dumping rate of such oscillations are presented in [36]. One application of Ramsey interference is frequency selective magnetometer based on light-pulse atom interferometry, as described in [37]. Implementation of a compact atomic clock based on Ramsey–CPT interference is proposed in [38].

This work extends previous studies of laser pulse propagation through EIT medium by observing transient development of Zeeman EIT during the pulse propagation. Experimentally and theoretically, we monitor intensity of the σ^- component during propagation of two time separated elliptically polarized laser pulses. The laser is locked to the D_1 line of ^{87}Rb. Zeeman EIT curves are reconstructed from transients of σ^- intensity at different external magnetic fields. We investigate transient behavior of the EIT line shapes, amplitudes and linewidths from the moments when laser pulses enter the Rb buffer gas cell. In particular, we investigated the case when pulses are highly elliptical (maximum relative optical power of σ^- component is only 15%), since several slow and stored light experiments typically use this level of ellipticity [4, 39]. We explore the effects of Ramsey sequences by comparing the behavior of EIT during the preparatory and the probe pulse by varying the length of the dark time between them. The Zeeman EIT resonances are then expected to exhibit the oscillation of transmission in magnetic field caused by Larmor precession during the dark time. The motivation of this work was in part to investigate the properties of the foreseen Ramsey oscillation with respect to pulse intensities and Rb density. Experimentally observed developments of the Zeeman EIT are compared with corresponding theoretical results. Our theoretical model based on time dependent Maxwell–Bloch equations qualitatively reproduces experimental observations. We are not aware of previous publications that show the time evolution of Zeeman EIT and Ramsey effect on this evolution when fast developing pulse propagates through Rb cell with buffer gas.

The detection of Raman–Ramsey oscillations on EIT line shapes presented in this work can find application in high precision magnetic field measurements and in determining the atomic decoherence rates.

2. Theory

2.1. Description of the model

The evolution of Rb atoms contained in a buffer-gas cell is calculated using time dependent optical Bloch equations for Rb density matrix $\hat{\rho}$

$$\frac{\partial \hat{\rho}}{\partial t} = D \nabla^2 \hat{\rho} - \frac{i}{\hbar} \Big[\hat{H}_{\text{atom}}(B) + \hat{V}_{\text{int}}(r, t), \hat{\rho} \Big] + \left(\frac{\partial \hat{\rho}}{\partial t} \right)_{\text{SE}} + \left(\frac{\partial \hat{\rho}}{\partial t} \right)_{\text{coll}}, \qquad (1)$$

where $\hat{H}_{\text{atom}}(B)$ is the atomic Hamiltonian in the external longitudinal magnetic field, $\hat{V}_{\text{int}}(r, t)$ describes laser-atom interaction and the term with subscript SE corresponds to spontaneous emission. The hyperfine levels either coupled to the laser light or populated due to spontaneous emission are shown in the energy level diagram in figure 1.

Collisions with the buffer-gas affect the atomic evolution in several ways. First, Rb atoms acquire diffusive motion within the cell, as described by the first term at the right-hand
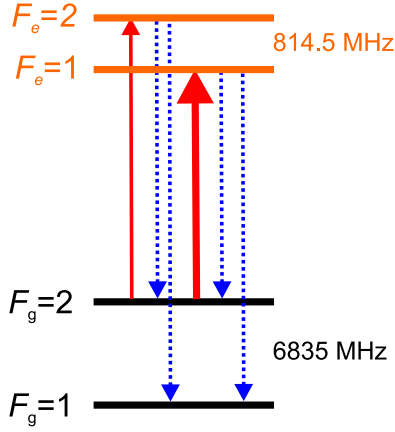
Figure 1. Energy level diagram for D_1 line transitions considered in the theoretical model. Solid lines represent transitions induced by the laser, while dotted lines correspond to possible spontaneous emission channels from excited levels. Frequency differences between adjacent hyperfine levels are shown.

side of (1) with D as the diffusion coefficient. Second, within each excited state manifold the populations of Zeeman sub-levels are equalized, while the coherences are destroyed due to total collisional depolarization of the excited state [40, 41]. The collisions with the buffer gas also broaden the optical transition and together with the Rb–Rb collisions lead to the relaxation of the ground state populations and coherences. These effects correspond to the last term at the right-hand side of (1). For the buffer gas pressure of 30 Torr the collisional broadening of $\approx$300–400 MHz is comparable with the Doppler width, so that we use the approximation of the motionless atoms in the direction of the laser beam propagation. Detailed exposition of the theoretical model is given in [42]. The present experimental configuration requires some additions concerning time dependent features. Contrary to the steady state calculations in [42], here we are solving (1) in cylindrical coordinates (r, z) and *in time*. The effects of propagation of slowly varying envelopes (SVEs) of the laser electric field $\mathcal{E}$ and the polarization $\mathcal{P}$ of the Rb vapour are also incorporated via

$$\frac{1}{c}\frac{\partial \mathcal{E}(r, z, t; B)}{\partial t} + \frac{\partial \mathcal{E}(r, z, t; B)}{\partial z} = \frac{\mathrm{i}\omega}{2\epsilon_0 c}\mathcal{P}(r, z, t; B), \quad (2)$$

where ϵ_0 is the vacuum dielectric constant, c is vacuum speed of light and ω is the laser frequency. The time dependence of these SVEs originates from the time dependent boundary condition for the electric field at the entrance to the Rb cell $\mathcal{E}(r, z = 0, t; B) = \mathcal{E}_{\mathrm{in}}(r, t)$. In the frequency domain the propagation equation is

$$\mathrm{i}\frac{\nu}{c}\mathcal{E}(r, z, \nu; B) + \frac{\partial \mathcal{E}(r, z, \nu; B)}{\partial z} = \frac{\mathrm{i}\omega}{2\epsilon_0 c}\mathcal{P}(r, z, \nu; B). \quad (3)$$

The frequencies for which $\mathcal{E}_{\mathrm{in}}(r, \nu)$ is significant satisfy

$$\left|\frac{\nu}{c}\mathcal{E}(r, z, \nu; B)\right| \ll \left|\frac{\partial \mathcal{E}(r, z, \nu; B)}{\partial z}\right| \sim \left|\frac{\mathcal{E}_{\mathrm{in}}(r, \nu)}{L}\right|, \quad (4)$$

where L is the cell length, so that we can safely drop the first term from (2). This leads to

$$\frac{\partial \mathcal{E}(r, z, t; B)}{\partial z} = \frac{\mathrm{i}\omega}{2\epsilon_0 c}\mathcal{P}(r, z, t; B), \quad (5)$$

which is used, in conjunction with (1), for calculation of the transmitted electric field at $z = L$ and Zeeman EIT resonances at particular time instants. The normalized σ^- transmission corresponds to the ratio $I_{\mathrm{tr}}^-/I_{\mathrm{in}}^-$, where I_{tr}^- and I_{in}^- denote intensities of the σ^- component of a laser beam, after propagation through and before entering into the Rb cell, respectively. Numerical calculations are performed using the DOLFIN finite element library [43] (part of the FEniCS project [44]) and CBC.PDESys package [45].

2.2. Theoretical results

The EIT resonances were determined from calculated σ^- transmissions at a given time instant after the σ^- pulse is launched into the Rb cell, at various magnetic fields. The cell temperature is 67 °C. The period between the two pulses, when the laser beam was turned off, was set to 60 μs. Overall laser intensities during the first (preparatory) and the second (probe) pulse were 4.9 and 0.9 mW cm^{-2}, respectively. Both pulses were elliptically polarized with 15% of photons carrying the σ^- polarization. Calculated EIT curves at $t = 6, 16, 100,$ and 328 μs from the beginning of the probe pulse are shown in figures 2(a)–(d), respectively.

From the calculated transmission signals, the amplitudes and the linewidths of Zeeman EIT resonances evolving in time were extracted and shown in figures 3(a) and (b), respectively. These results show that the central peak has higher amplitude and wider line shape soon after the start of the probe pulse.

3. Experiment

3.1. Description of the experiment

Propagation of the polarization laser pulses and temporal evolution of Zeeman EIT resonances are experimentally realized in the Hanle configuration. A schematic of the experiment is given in figure 4(a).

The external cavity diode laser is frequency locked to the hyperfine $F_g = 2 \rightarrow F_e = 1$ transition of the D_1 line in ^{87}Rb using the Doppler-free dichroic atomic vapour laser lock method [46, 47]. Gaussian profile for the laser beam is obtained by the short single mode optical fiber. In order to apply the Ramsey method of repeated interactions of a laser light with Rb atoms, the power of the first order diffracted beam from the AOM is modulated and transmitted through the cell. The linear polarization of the laser light is assured by the high quality polarizer. The Pockels cell and the $\lambda/4$ plate are used to generate laser pulses with elliptical polarization: pure σ^+ circular polarization is obtained when no voltage is applied to the cell, while 15% of the σ^- light is produced

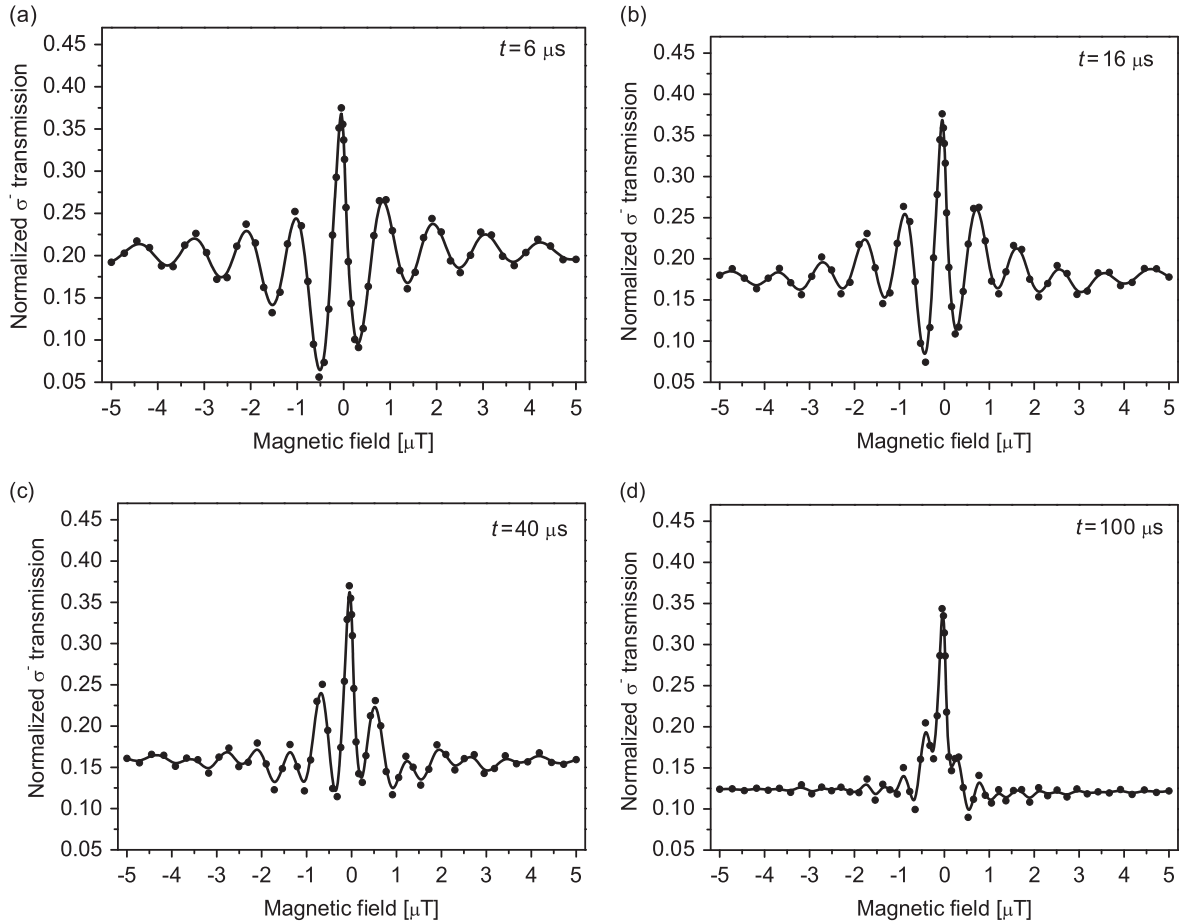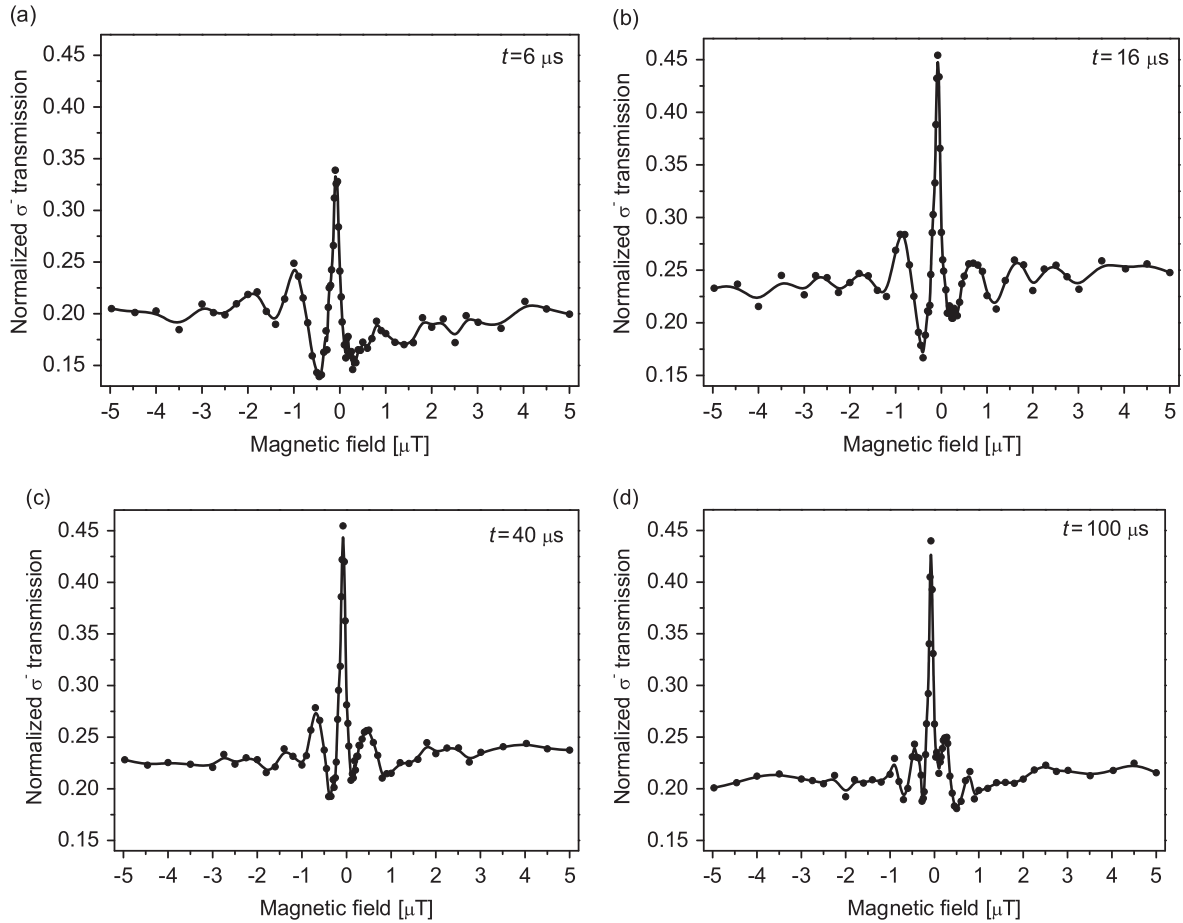**Figure 2.** Time evolution of calculated Zeeman EIT resonances during the probe pulse with overall laser beam intensity of $I_2 = 0.9 \, \mathrm{mW \, cm^{-2}}$. The overall laser beam intensity during the preparatory pulse is $I_1 = 4.9 \, \mathrm{mW \, cm^{-2}}$. The dark period is $T_D = 60 \, \mu\mathrm{s}$. The resonances are reconstructed and normalized from σ^- transmission signals at four different times: (a) $t = 6 \, \mu\mathrm{s}$, (b) $t = 16 \, \mu\mathrm{s}$, (c) $t = 40 \, \mu\mathrm{s}$, and (d) $t = 100 \, \mu\mathrm{s}$. The cell temperature is 67 °C.
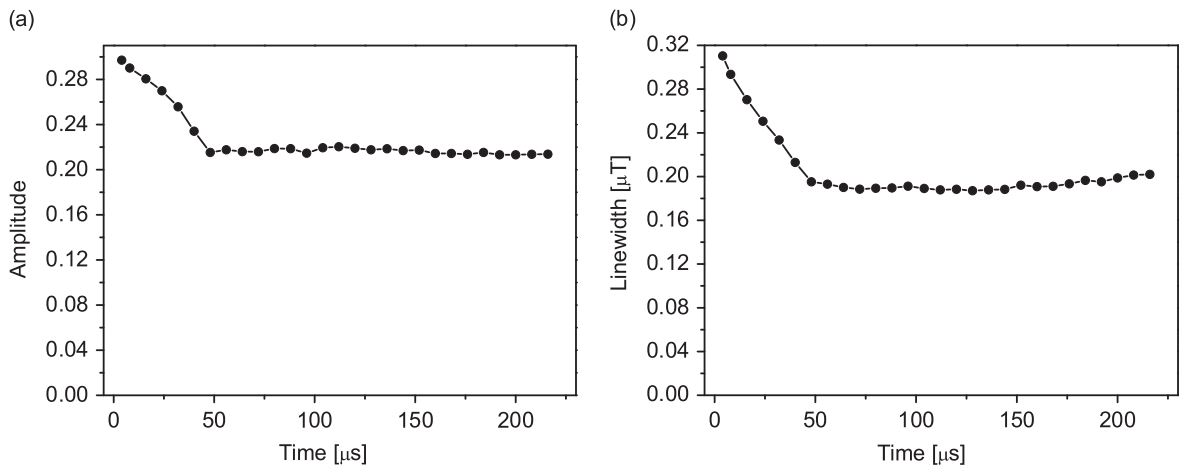
Figure 3. Theoretically obtained time evolution of Zeeman EIT (a) amplitudes and (b) linewidths of the central fringe during the probe pulse, for overall laser beam intensity of $I_2 = 0.9 \, \mathrm{mW \, cm^{-2}}$. The overall laser beam intensity during the preparatory pulse is $I_1 = 4.9 \, \mathrm{mW \, cm^{-2}}$. The dark period is $T_D = 60 \, \mu\mathrm{s}$. The cell temperature is 67 °C.

otherwise. The Rb cell containing 30 Torr of Ne buffer gas is 8 cm long and has 2.5 cm in diameter. The Rb cell was heated by using hot air circulating around the cell. Measurements were done at 67 °C and 85 °C. The Rb cell is shielded from stray magnetic fields by the triple μ-metal layers which reduce stray magnetic fields below 10 nT. In order to obey two-photon detuning, long solenoid placed around the Rb cell produces controllable longitudinal magnetic field in the range
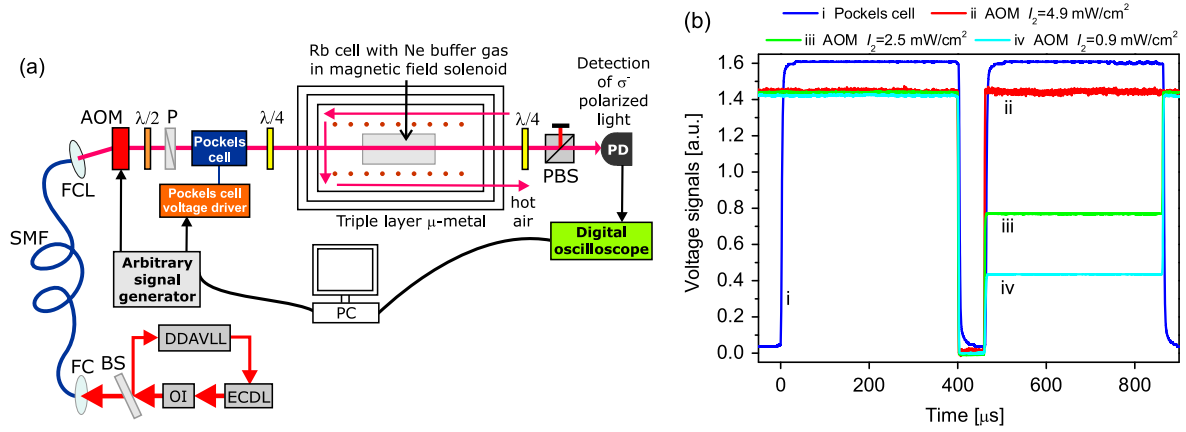
Figure 4. (a) Experimental setup: ECDL—external cavity diode laser; OI—optical insulator; DDAVLL—Doppler-free dichroic atomic vapour laser lock; BS—beam splitter; FC—fiber coupler; SMF—single-mode fiber; FCL—fiber collimator; AOM—acousto-optic modulator; P—polarizer; PBS—polarizing beam splitter; PD—photodetector. Hot air is used for heating the cell. (b) Pockels cell and AOM signals used in the experiment.
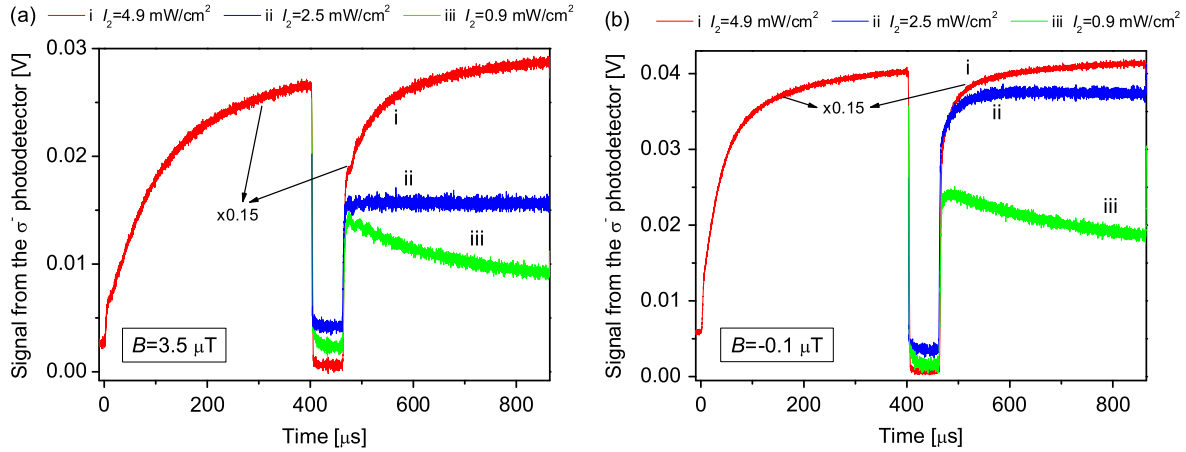
Figure 5. Measured σ^- transmission signals during preparatory and probe polarization laser pulse for magnetic field (a) 3.5 μT and (b) -0.1 μT. The curves in both figures correspond to the probe pulse overall intensity of (i) $I_2 = 4.9$ mW cm^{-2}, (ii) $I_2 = 2.5$ mW cm^{-2}, and (iii) $I_2 = 0.9$ mW cm^{-2}. The overall laser beam intensity during the preparatory pulse is $I_1 = 4.9$ mW cm^{-2}. The cell temperature is 67 °C.
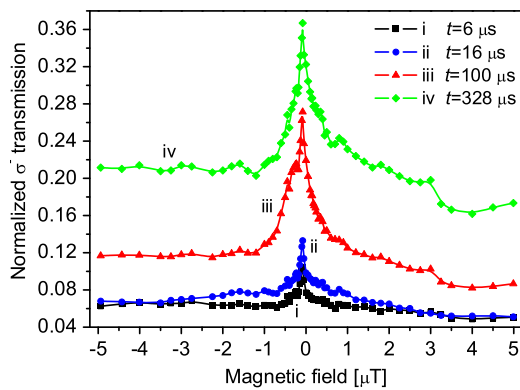
Figure 6. Time evolution of Zeeman EIT resonances during the preparatory pulse with overall laser beam intensity of $I_1 = 4.9$ mW cm^{-2}. The resonances are reconstructed and normalized from the σ^- transmission signals at four different times: $t = 6$ μs (curve i), $t = 16$ μs (curve ii), (c) $t = 100$ μs (curve iii), and (d) $t = 328$ μs (curve iv). The cell temperature is 67 °C.

of ± 10 μT. The σ^- light is extracted from the transmitted laser beam with the $\lambda/4$ plate and the PBS. Transmitted σ^- laser intensity over time, for a given magnetic field, is measured by the photodetector and recorded by the digital storage oscilloscope.

Laser pulses are produced after applying voltage pulses to the AOM and the Pockels cell as shown in figure 4(b). Note that the laser pulse here refers to the temporal change of a laser beam polarization. That is, polarization changes from σ^+ before the pulse, to elliptical polarization with 15% of σ^- relative optical power during the pulse. The first voltage pulse to the Pockels cell (signal (i)) is preparatory pulse that prepares Rb atoms into the dark state. Then, the voltages on the Pockels cell and the AOM are synchronously turned off for a certain period of dark time. During the dark time, Zeeman coherence makes a Larmor precession if the external magnetic field is not zero. After the dark time, the voltage pulses are again applied to AOM and Pockels cell and the second (probe) pulse, with the same polarization but intensity that can

Figure 7. Time evolution of Zeeman EIT resonances during the probe pulse with overall laser beam intensity of $I_2 = 0.9$ mW cm^{-2}. The overall laser intensity during the preparatory pulse is $I_1 = 4.9$ mW cm^{-2}. The dark period is $T_D = 60\,\mu$s. The resonances are reconstructed and normalized from the σ^- transmission signals at four different times (from top to bottom): $t = 6\,\mu$s, $t = 16\,\mu$s, $t = 40\,\mu$s, and $t = 100\,\mu$s. The cell temperature is 67 °C.
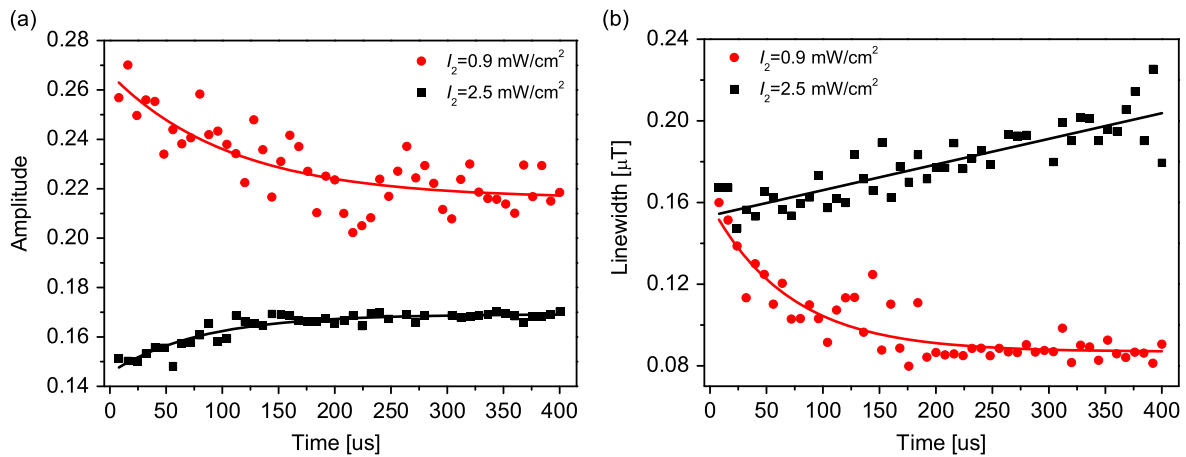

Figure 8. Experimentally obtained time evolution of Zeeman EIT (a) amplitude and (b) linewidth during the probe pulse. The overall intensities of the probe pulse are $I_2 = 0.9$ mW cm^{-2} or $I_2 = 2.5$ mW cm^{-2}. The overall laser intensity during the preparatory pulse is $I_1 = 4.9$ mW cm^{-2}. The dark period is $T_D = 60\,\mu$s. The cell temperature is 67 °C. Solid lines are to guide the eye.

be different than the preparatory pulse, is created to probe the atomic coherences. At the end of the probe pulse, we return to a strong σ^+ polarization for several ms to repump atoms back to the Zeeman sublevels of the ground state before the next Ramsey sequence of pulses. Note that all the time we measure

only the σ^- component of the elliptically polarized laser beam. We denote by I_1 and I_2 overall intensities of a laser beam during the preparatory (duration T_1) and probe pulse (duration T_2), respectively. Two synchronous voltage signals, controlling the AOM and the Pockels cell with fully
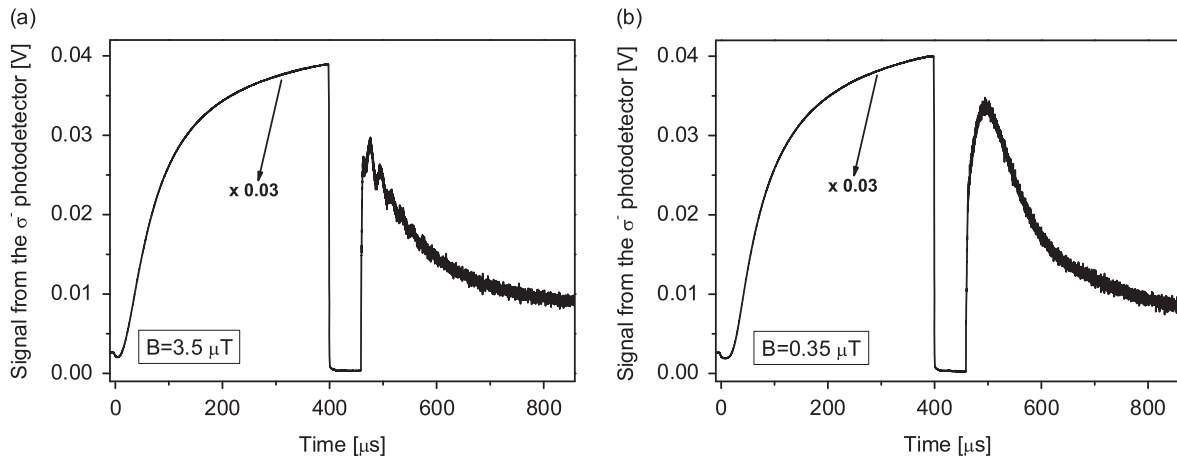
Figure 9. Measured σ^- transmission signals during preparatory and probe polarization laser pulse for magnetic field (a) 3.5 μT and (b) 0.35 μT. The curves in both figures correspond to the probe pulse overall intensity of $I_2 = 4.8$ mW cm^{-2}. The overall laser beam intensity during the preparatory pulse is $I_1 = 49$ mW cm^{-2}. The cell temperature is 85 °C.

adjustable amplitudes and durations, were generated by field-programmable gate array based signal generator and oscilloscope, as described in [48].

Development of Zeeman EIT for cell temperature of 67 °C, corresponding to Rb density of 5×10^{11} cm^{-3} [49], was measured with the following sequence of pulses: $I_1 = 4.9$ mW cm^{-2}, $T_1 = 400$ μs; $T_D = 60$ μs and $T_D = 160$ μs; $T_2 = 400$ μs. We varied the overall laser intensity during the probe pulse: $I_2 = 4.9$ mW cm^{-2} (AOM signal (ii)), $I_2 = 2.5$ mW cm^{-2} (AOM signal (iii)), and $I_2 = 0.9$ mW cm^{-2} (AOM signal (iv)) in order to measure the intensity dependencies of the: (1) σ^- transmission and (2) Zeeman EIT temporal development. The same Ramsey sequence was used for the cell temperature of 85 °C (Rb density of 1.4×10^{12} cm^{-3} [49]), except the higher laser intensity was required during the two pulses due to increased residual absorption: $I_1 = 49$ mW cm^{-2} and $I_2 = 4.8$ mW cm^{-2}.

3.2. Experimental results

In this section we show effects of the probe pulse intensity, the Ramsey sequences of successive excitation pulses, the external magnetic field and the cell temperature on propagation of pulses and development of EIT.

Measured transmissions of the σ^- component of a laser beam, during the preparatory and the probe pulse are shown in figure 5. The Rb cell temperature is 67 °C. Presented results are obtained for three values of the overall laser intensities during the probe pulse, and for the two values of magnetic field. The intensity and duration of the preparatory pulse are always $I = 4.9$ mW cm^{-2} and $T_1 = 400$ μs, so that during this pulse ^{87}Rb atoms are efficiently prepared into the dark state.

Transient behavior of the probe pulse depends on the laser intensity, duration of the dark time, and magnetic field. We show in figure 5 propagation of preparatory and probe pulse for two values of magnetic field, 3.5 and -0.1 μT, for three values of the probe pulse intensity, and for dark time of 60 μs. For the preparatory pulse intensity of 4.9 mW cm^{-2}, transmission of the probe pulse can be quite different

depending on its intensity. At high intensity of the probe pulse (4.9 mW cm^{-2}), probe transmission increases with time due to optical pumping. When probe intensity is decreased to 2.5 mW cm^{-2}, transmission is constant in time. For the lowest probe intensity of 0.9 mW cm^{-2}, the probe pulse probes the coherences without significantly contributing to atomic evolution and optical pumping. The signal then decays due to decoherence and relaxation. At low magnetic field, the transmission of the probe is higher compared to transmission at higher magnetic fields (compare figures 5(a) and (b)), because more atoms are coherently prepared into the dark state by the preparatory pulse.

Due to Larmor precession of atomic polarization during the dark time, oscillations in the measured intensity of the probe pulse can be seen in figure 5(a), when intensity is low and magnetic field is different from zero. Frequency of observed fringes depends on the magnetic field, while their amplitudes depend on the amount of coherence between Zeeman sublevels. These results are in agreement with [35, 36]. The fringes on the transmission signal disappear when the σ^+ polarized laser beam is kept on between the preparatory and probe pulse (not shown), providing the evidence that observed fringes are indeed due to interference between coherently prepared atoms and the probe light.

From the transient curves of the σ^- transmission, like those in figure 5, taken at 70 different values of the longitudinal magnetic field, we have reconstructed Zeeman EIT resonances at different times during the development of preparatory and probe pulse. We first show Zeeman EIT resonances developing during the preparatory pulse (see curves (i)–(iv) in figure 6). As time progresses, EIT resonances keep the similar shape and only have higher amplitude since more atoms undergo dark state preparation.

Development of EIT during the probe pulse, when dark time is $T_D = 60$ μs is shown in figure 7. The overall laser beam intensities during the preparatory and the probe pulses were $I_1 = 4.9$ mW cm^{-2} and $I_2 = 0.9$ mW cm^{-2}. Characteristically, EIT resonance has central peak and fringes due to interference between atomic coherence precessing in the
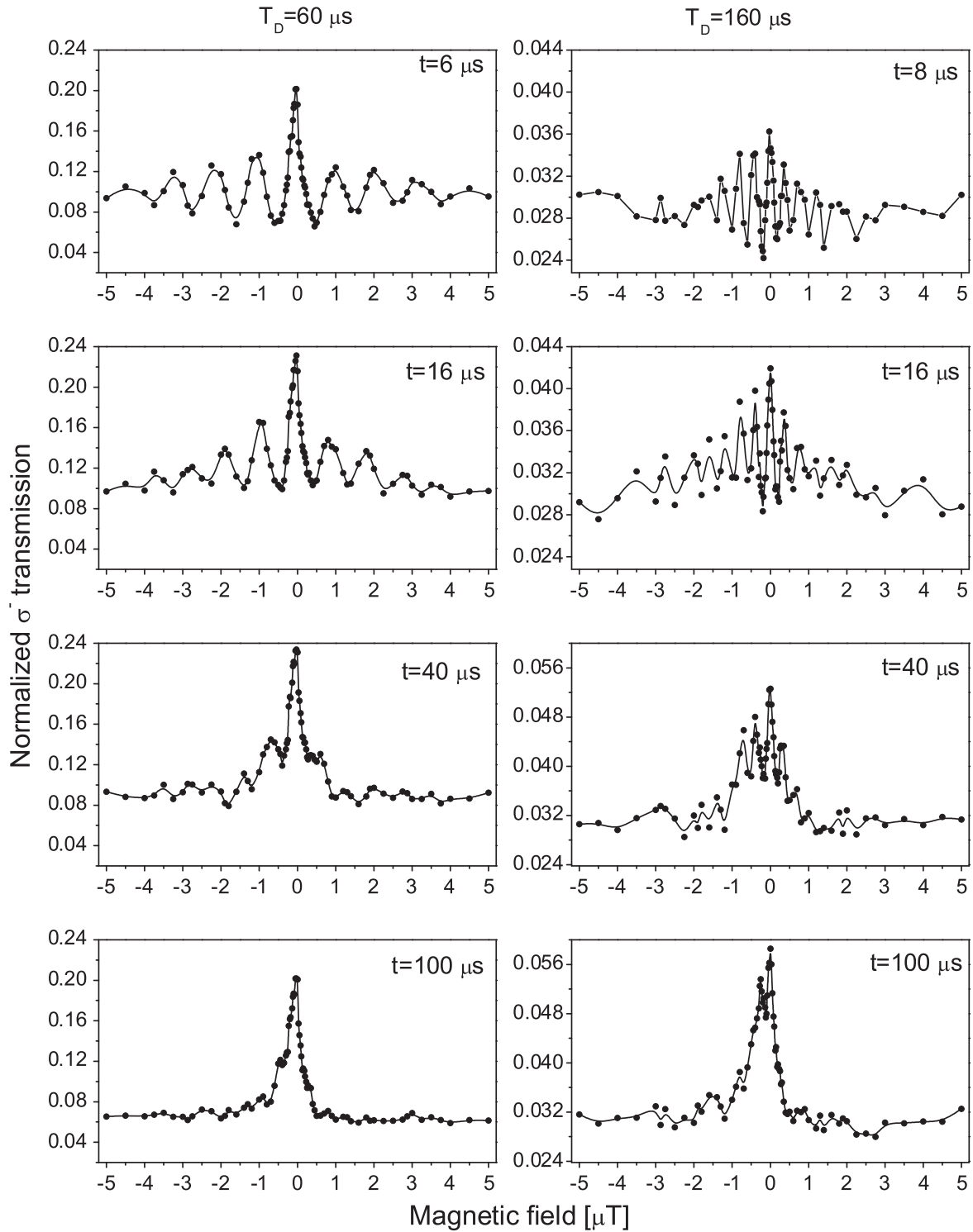
Figure 10. Time evolution of Zeeman EIT resonances during the probe pulse with overall laser beam intensity of $I_2 = 4.8$ mW cm^{-2}. The overall laser intensity during the preparatory pulse is $I_1 = 49$ mW cm^{-2}. The dark period is $T_D = 60\,\mu$s (left column) and $T_D = 160\,\mu$s (right column). The resonances are reconstructed and normalized from σ^- transmission signals at four different times (from top to bottom): $t = 6$ or $8\,\mu$s, $t = 16\,\mu$s, $t = 40\,\mu$s, and $t = 100\,\mu$s. The cell temperature is 85 °C.

magnetic field and probe electric field (at $t = 6\,\mu$s and $t = 16\,\mu$s). The frequency width of the fringes decreases with time of precession. At about $40\,\mu$s since the beginning of the probe pulse only first order fringes are visible. At longer time they start merging with the central peak ($t = 100\,\mu$s), and at even longer time only central peak remains.

Experimental waveforms of EIT are in qualitative agreement with theoretical curves shown in figure 2, which are calculated under the same experimental conditions. We also found similar transition from EIT with fringes to EIT with only central peak at higher pulse intensity, except this transition is during shorter time.
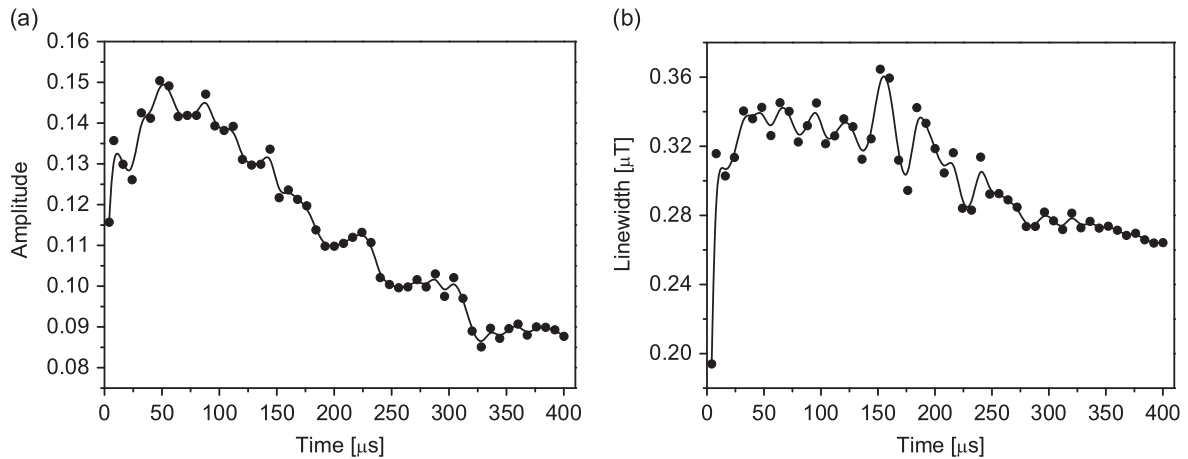
Figure 11. Experimentally obtained time evolution of Zeeman EIT (a) amplitude and (b) linewidth during the probe pulse. The overall intensities of the laser beam during preparatory and probe pulse are $I_1 = 49$ mW cm^{-2} and $I_2 = 4.8$ mW cm^{-2}, respectively. The dark period is $T_D = 60$ μs. The cell temperature is 85 °C.

Time dependencies of Zeeman EIT amplitudes and linewidths are shown in figures 8(a) and (b), respectively, for dark time of 60 μs and two values of probe intensity, 0.9 and 2.5 mW cm^{-2}. One can see that more contrasted and narrower resonances are obtained when the probe pulse intensity is lower. Amplitudes of EIT behave differently at different pulse intensities. Similar to time dependence of transmitted probe intensity in figure 5, amplitudes of EIT resonances increase (decrease) with time for high (lower) probe intensity. When the pulse intensity is higher there is prevalent influence of power broadening. High intensity of the probe pulse also affects time evolution of Zeeman EIT. At high intensities (black squares at figure 8(b)) the strong electric field slows the precession, causing merging of the fringes with the central peak and broadening of the peak. However, at the beginning of the pulse, the EIT width is independent on the pulse intensity. It remains the same even when two pulses have very different intensities, as seen in figure 8. The significance of this finding is that EIT width will not vary with variations of intensities of the probe pulse as long as the pulse is shorter then a few μs. The width of the central peak is not sensitive to the intensity/power but to the absorbed energy of the laser light. The measured amplitudes agree well with calculated data shown in figure 3(a). However, the calculated linewidths (figure 3(b)) are somewhat larger than experimental ones.

In the investigation of the development of EIT when Raman detuning is achieved by modulating laser frequency at constant magnetic field, Yoshida *et al* have distinguished between the Raman–Ramsey and the hyperfine EIT spectra depending on the time gating within excitation pulse [34]. RRF were obtained at the pulse beginning while the EIT spectrum was obtained at its end. Due to variable magnetic field in our experiment, reconstructed σ^- transmission curve at each time instant consists of both Raman–Ramsey and EIT spectra.

Dependence of the transient development of Zeeman EIT resonances on Rb density and on the length of the dark time is studied by measuring signal pulse waveforms for Rb cell temperature of 85 °C and for two dark times: 60 μs and 160 μs. Similarly, σ^- transmission signal was measured at different magnetic fields during the preparatory and the probe pulse.

For investigations of transient behavior of EIT resonances, the intensities of preparatory and probe pulse were 49 and 4.8 mW cm^{-2}, respectively. At higher Rb density we needed to increase incident intensities in order to obtain signal from the transmitted σ^- component, that is high enough for good visibility of reconstructed EIT fringes. Measured transmissions of the σ^- component of the laser beam, during the preparatory and the probe pulse, are shown in figure 9 for two values of external magnetic field. As seen from figure 9(b), transmission of the σ^- component at very low magnetic field increases once the probe pulse has been established, and reaches the maximal value at some instant. After that moment, transmission starts to decay. This could be explained in terms that the probe pulse has enough optical power to further pump the atoms into the dark state, but at later times decoherence prevails and transmission drops. In the case of higher magnetic field, transmission drops right after the pulse is generated because of the higher value of two-photon detuning.

The reconstructed EIT curves for two dark times of 60 and 160 μs, are shown in figure 10.

RRF are observed at 6 and 8 μs after the beginning of the probe pulse. The fringes get narrower and weaker with precession time due to Zeeman decoherence, leading to a single EIT peak at later time instants. In classical Ramsey effect, the frequency width of the central Ramsey fringe is $1/(2 \cdot T_D)$. We have found that for dark times of 60 and 160 μs, the ratio of widths of the first order Ramsey fringes is in agreement with $1/(2 \cdot T_D)$ dependence. At these density and laser intensities fringes decay faster comparing to lower intensities (case with 67 °C cell temperature) because precession of the dark state is affected by electric field. The central peak is at each time instant also narrower when the dark time is 160 μs. Its narrowing could be explained by the work from [36]

where authors have shown the increase of Zeeman decoherence rate because of the Rb–Rb spin-exchange collisions.

Measured time dependencies of EIT amplitudes and linewidths during the probe pulse when dark time is 60 μs and temperature is 85 °C are shown in figures 11(a) and (b), respectively. The amplitudes increase at the beginning of the probe pulse and decay later. This is in qualitative agreement with the σ^- transmission time dependence as presented in figure 9(b). The linewidths of EIT resonances are wider at higher density (85 °C versus 67 °C) due to the power broadening caused by higher laser beam intensity. At high pulse intensities needed for this Rb vapour density, the precession of the Zeeman coherences is slowed in the laser electric field and fringes start to merge with the central peak, thus broadening the resonance at earlier times.

4. Conclusion

We presented experimental and theoretical study of the transient response of EIT medium to propagation of laser polarization pulses resonant to EIT transition. Through observed time development of the σ^- pulse transmission at different magnetic fields, we reconstructed Zeeman EIT resonances corresponding to various time instants during pulse propagation. The EIT resonances during the probe pulse have characteristic Ramsey fringes at early times and a narrow central peak at later moments. Ramsey fringes or oscillations of probe transmission during pulse propagation in magnetic field are caused by Larmor precession during the dark time. The disappearance of fringes is faster for larger probe pulse intensities due to incoherent pumping and effects of electric field on precession of atomic coherences. The behavior of amplitudes and linewidths of the EIT central peak depends on the probe intensity and Rb density. At very low probe intensity they both monotonically decay if Rb density is low, while at higher density amplitudes and widths they first increase and then decay.

We have studied transients of the polarization laser pulses for the system that is often used in slow light and storage of light experiments. Thus, better knowledge of polarization pulse transmission and time development of EIT resonances is valuable.

Acknowledgments

References

[1] Boller K J, Imamoğlu A and Harris S E 1991 *Phys. Rev. Lett.* **66** 2593

[2] Field J E, Hahn K H and Harris S E 1991 *Phys. Rev. Lett.* **67** 3062

[3] Arimondo E 1996 *Prog. Opt.* **35** 257

[4] Phillips D F, Fleischhauer A, Mair A, Walsworth D F and Lukin M D 2001 *Phys. Rev. Lett.* **86** 783

[5] Klein M J 2009 Slow and stored light in atomic vapor cells *PhD Thesis* Harvard University

[6] Fleischhauer M, Imamoğlu A and Marangos J P 2005 *Rev. Mod. Phys.* **77** 633

[7] Bai Y S, Mossberg T W, Lu N and Berman P R 1986 *Phys. Rev. Lett.* **57** 1692

[8] Fry E S, Li X, Nikonov D, Padmabandu G G, Scully M O, Smith A V, Tittel F K, Wang C, Wilkinson S R and Zhu S Y 1993 *Phys. Rev. Lett.* **70** 3235

[9] Greentree A D, Smith T B, Echaniz S R, Durrant A V, Marangos J P, Segal D M and Vaccaro J A 2002 *Phys. Rev. A* **65** 053802

[10] Harris S E and Luo Z-F 1995 *Phys. Rev. A* **52** R928

[11] Chen H X, Durrant A V, Marangos J P and Vaccaro J A 1998 *Phys. Rev. A* **58** 1545

[12] Park S J, Cho H, Kwon T Y and Lee H S 2004 *Phys. Rev. A* **69** 023806

[13] Wu Y and Yang X 2005 *Phys. Rev. A* **71** 053806

[14] Wu Y and Yang X 2004 *Phys. Rev. A* **70** 053818

[15] Meinert F, Basler C, Lambrecht A, Welte S and Helm H 2012 *Phys. Rev. A* **85** 013820

[16] Vanier J, Godone A and Levi F 1998 *Phys. Rev. A* **58** 2345

[17] Valente P, Failache H and Lezama A 2002 *Phys. Rev. A* **65** 023814

[18] Margalit L, Rosenbluh M and Wilson-Gordon A D 2012 *Phys. Rev. A* **85** 063809

[19] Margalit L, Rosenbluh M and Wilson-Gordon A D 2013 *Phys. Rev. A* **88** 023827

[20] Shwa D and Katz N 2014 *Phys. Rev. A* **90** 023858

[21] Valente P, Failache H and Lezama A 2003 *Phys. Rev. A* **67** 013806

[22] Berman P R and Salomaa R 1982 *Phys. Rev. A* **25** 2667

[23] Li Y Q and Xiao M 1995 *Opt. Lett.* **20** 1489

[24] Dimitrijević J, Arsenović D and Jelenković B M 2011 *New J. Phys.* **13** 033010

[25] Ramsey N F 1956 *Molecular Beams* (New York: Oxord University Press)

[26] Zanon T, Guérandel S, Clercq de E, Holleville D, Dimarcq N and Clairon A 2005 *Phys. Rev. Lett.* **94** 193002

[27] Zanon T, Trémine S, Guérandel S, Clercq de E, Holleville D, Dimarcq N and Clairon A 2005 *IEEE Trans. Instrum. Meas.* **54** 776

[28] Liu X, Mérolla J-M, Guérandel S, Clercq de E and Boudot R 2013 *Opt. Express* **21** 12451

[29] Chen X, Yang G-Q, Wang J and Zhan M-S 2010 *Chin. Phys. Lett.* **27** 113201

[30] Yisheng M, Jianliao D, Zhengfeng H, Huijuan H and Yuzhu W 2013 *Chin. Opt. Lett.* **11** 032701

[31] Supplee J M 2010 *J. Opt. Soc. Am. B* **27** 1543

[32] Chen J F, Lu W, Wang S, Loy M M T, Wong G K L and Du S 2010 *Opt. Lett.* **35** 1923

[33] Pati G S, Fatemi F K and Shahriar M S 2011 *Opt. Express* **19** 22388

[34] Yoshida I, Hayashi N, Fujita K, Taniguchi S, Hoshina Y and Mitsunaga M 2013 *Phys. Rev. A* **87** 023836

[35] Zibrov A S and Matsko A B 2001 *Phys. Rev. A* **65** 013814

[36] Shuker M, Firstenberg O, Sagi Y, Ben-kish A, Davidson N and Ron A 2008 *Phys. Rev. A* **78** 063818

[37] Braje D A, DeSavage S A, Adler C L, Davis J P and Narducci F A 2014 *J. Mod. Opt.* **61** 61

[38] Yang J, Tian Y, Tan B, Yun P and Gu S 2014 *J. Appl. Phys.* **115** 093109

[39] Mair A, Hager J, Phillips D F, Walsworth R L and Lukin M D 2002 *Phys. Rev. A* **65** 031802(R)

J. Phys. B: At. Mol. Opt. Phys. **48** (2015) 045501

S N Nikolić *et al*

[40] Taichenachev A V, Yudin V I, Wynands R, Stahler M, Kitching J and Hollberg L 2003 *Phys. Rev.* A **67** 033810

[41] Failache H, Valente P, Ban G, Lorent V and Lezama A 2003 *Phys. Rev.* A **67** 043810

[42] Nikolić S N, Radonjić M, Krmpot A J, Lučić N M, Zlatković B V and Jelenković B M 2013 *J. Phys. B: At. Mol. Opt. Phys.* **46** 075501

[43] Anders L and Garth W 2010 *ACM Trans. Math. Softw.* **37** 20:1–20:28

[44] Logg A, Mardal K-A and Wells G N 2012 *Automated Solution of Differential equations by the Finite Element Method* (*Lecture Notes in Computational Science and Engineering* vol 84) (Berlin: Springer)

[45] Mortensen M, Langtangen H P and Wells G N 2011 *Adv. Water Resour.* **34** 1082

[46] Wasik G, Gawlik W, Zachorowski J and Zawadzki W 2002 *Appl. Phys.* B **75** 613

[47] Petelski T, Fattori M, Lamporesi G, Stuhler J and Tino G M 2003 *Eur. Phys. J.* D **22** 279

[48] Nikolić S N, Batić V, Panić B and Jelenković B M 2013 *Rev. Sci. Instrum.* **84** 063108

[49] Steck D A 2008 *Rubidium 87 D Line Data* (http://steck.us/alkalidata)

A Single-Photon Avalanche Camera for Fluorescence Lifetime Imaging Microscopy and Correlation Spectroscopy

Marco Vitali, Danilo Bronzi, *Student Member, IEEE*, Aleksandar J. Krmpot, Stanko N. Nikolić, Franz-Josef Schmitt, Cornelia Junghans, Simone Tisa, Thomas Friedrich, Vladana Vukojević, Lars Terenius, Franco Zappa, *Senior Member, IEEE*, and Rudolf Rigler

Abstract—Confocal laser scanning microscopy (CLSM) is commonly used to observe molecules of biological relevance in their native environment, the live cell, and study their spatial distribution and interactions nondestructively. CLSM can be easily extended to measure the lifetime of the excited state, the concentration and the diffusion properties of fluorescently labeled molecules, using fluorescence lifetime imaging microscopy (FLIM) and fluorescence correlation spectroscopy (FCS), respectively, in order to provide information about the local environment and the kinetics of molecular interaction in live cells. However, these parameters cannot be measured simultaneously using conventional CLSM due to damaging effects that are associated with strong illumination, including phototoxicity, photobleaching, and saturation of the fluorescence signal. To overcome these limitations, we have developed a new camera consisting of 1024 single-photon avalanche diodes that is optimized for multifocal microscopy, FLIM and FCS. We show proof-of-principle measurements of fluorescence intensity distribution and lifetime of the enhanced green fluorescent protein expressed in live cells and measurement of quantum dot diffusion in solution by FCS using the same detector.

Index Terms—Single photon avalanche diode array, multifocal microscopy, fluorescence lifetime imaging microscopy, fluorescence correlation spectroscopy.

I. INTRODUCTION

CONFOCAL laser scanning microscopy (CLSM) is universally used in biomedical research to investigate molecular mechanisms underlying vital biological functions. CLSM primarily owes its widespread use to its capacity to produce sharp images of structures *in vivo*. This is achieved through a special arrangement of optical elements, which focus the laser beam in a diffraction-limited volume of about 1 fL, depending on the excitation wavelength, and detect fluorescence from an even smaller volume by filtering the emitted light through a pinhole, a circular aperture of few tens of micrometers in diameter that is placed in front of the detector. Through this special optical arrangement, a fluorescence signal is detected only from molecules that are confined in this small, so-called confocal volume. Fluorescence emission from outer molecules is strongly attenuated by the pinhole, thus enabling the selective observation of a subset of fluorophores at a high signal-to-noise ratio [1].

An important feature of confocal microscopy is the possibility to visualize the three-dimensional spatial distribution of molecules of interest within the investigated specimen. This is achieved by raster-scanning the confocal volume either by steering the laser beam using fast galvanometric scanners and acousto-optic deflectors, or by moving the sample using nanopositioning piezoelectric microscope stages.

Confocal laser scanning microscopes achieve image acquisitions at rates of about 30 frames per second (fps) or more in fast scanning modes [2]. Under these operating conditions, a relatively high illumination intensity is needed since the dwell time per pixel is 10^4 to 10^6 times shorter than the acquisition time required for a single frame. Acquisitions at higher frame-rates are possible with the currently available instrumentation, but the intensity of the excitation beam has to be strongly increased to facilitate signal acquisition at very short times. For this reason, photobleaching of the observed fluorophore and induced phototoxicity to the investigated biosystems might be fostered by nonlinear processes [3]. In addition, absorption might even reach saturation levels, and further increase in the illumination intensity does not significantly improve the signal but rather increases the optical background noise.

These limitations were overcome by constructing multifocal microscopes, where multiple confocal volumes are simultaneously scanned over the sample. Indeed, the use of massively parallel confocal arrangements permits to acquire a full frame at the acquisition time of a single pixel in classical CLSM. Hence, fast acquisition rates are achieved without increasing the

illumination power as a result of the longer dwell times per pixel. Line-scanning and spinning disk confocal systems achieve up to 1000 fps [1], [4] and two-dimensional detector arrays such as electron-multiplying CCD cameras or CMOS sensors are commonly used to measure the fluorescence signal. Fast frame-rate microscopy techniques have a huge potential for biological investigations. An improvement of the frame acquisition speed up to 10–100 kfps would allow the characterization of molecular diffusion processes.

A standard tool to investigate the mobility of molecules in living cells is fluorescence correlation spectroscopy (FCS). In FCS, temporal autocorrelation analysis is applied to detect non-randomness in the fluctuations of the fluorescence signal. This technique is therefore able to monitor all processes that lead to fluorescence intensity fluctuations at the temporal scale between few tens of nanoseconds up to seconds or longer e.g. formation of triplet and dark states, Brownian motion, protein-protein interactions and liquid flow [5]. On the other hand, classical FCS experimental setups are mostly limited to the observation of a single confocal volume and they cannot investigate simultaneously multiple regions in the sample. The construction of a multifocal microscopy setup which is capable of fast frame-rates above 10 kfps is, therefore, of major scientific interest. Not only the intensity of the fluorescence emission signal would be observed, but also its fast fluctuations as a function of the position within the sample, enabling parallel FCS studies across a cell.

The design of suitable bidimensional photodetectors plays a key role for the implementation of the described multifocal system. The acquisition speed is not the only important parameter, but also the photon detection efficiency (PDE), dark signal and saturation levels are limiting factors. High-gain solid-state detectors as the single photon avalanche photodiode (SPAD) have all these properties. A fair PDE above 40% and few thousands dark counts per second (cps) are commonly specified [6]–[8]. Saturation rates in the order of many millions of photons per second are possible [7]. Additionally, SPADs are not affected by any read-out noise, in contrast to CCD or CMOS sensors, which is a major advantage for combining high frame-rate imaging and FCS. In fact, the frames acquired at 10 to 100 kfps, which are required for FCS, can be binned over time, e.g. few milliseconds, to visualize the spatial distribution of the measured fluorophores. This binning operation, which is performed during post-processing of the data, does not degrade the signal-to-noise ratio due to the absence of read-out noise.

Several pioneering works investigated the use of multifocal FCS experimental setups more than 10 years ago [9]–[11]. The number of SPADs and confocal volumes was not sufficiently large to allow for the reconstruction of images, although the main experimental concepts were already developed. More recent works used the next generation SPAD imagers featuring 1024 photodetectors on the same silicon chip [12]–[15].

We present a new 32×32 SPAD camera which fulfills all the requirements indicated above, which makes it suitable for a multifocal FCS experimental setup. This device implements additionally a fast time-gating control, which enables the pixel electronics for short time periods down to 1.5 ns and at delay steps below 100 ps. This camera is therefore capable of measuring not only the fluctuations of the fluorescence intensity at very high frame-rates (50 to 100 kHz) but also the decay kinetics of fluorophores after illumination by a pulsed laser. Combined with a multifocal optical setup, this system is readily extended into a time-gated fluorescence lifetime imaging microscopy (FLIM) [16]–[18] experimental setup. The measurement of fluorescence decay kinetics by each SPAD allows the monitoring of ultra-fast photophysical processes as Förster resonance energy transfer (FRET) and to identify multiple fluorescence sources. In summary, the multifocal FLIM/FCS setup combines three of the most important microscopy techniques in a single system. We validated the proposed camera using several model experiments such as the measurement of the diffusion time of single quantum dots (QD) in solution and the fluorescence decay kinetics of genetically encoded enhanced Green Fluorescent Protein (eGFP) expressed in live cells.

II. CAMERA DESIGN

The camera design optimized for multifocal microscopy was based on an array of 1024 independent SPADs produced in standard CMOS technology [7], [19], [20]. The detectors were organized in a 32×32 array of smart pixels, featuring both photodetection circuitry and pre-processing electronics Fig. 1(a). The physical dimension of the pixel was $100 \times 100 \ \mu$m, while the circular active area had a diameter of $20 \ \mu$m.

The SPAD [21] is a reverse-biased p-n junction, which is operated well above its breakdown voltage. Under this biasing condition the absorption of a single photon, causes the generation of an electron-hole pair, which is accelerated by the electric field across the junction. The energy of the charge carriers is eventually sufficient to trigger a self-sustained macroscopic avalanche current of few milliamperes through the device.

A quenching circuit based on a time-varying active load (variable-load quenching circuit, VLQC) [22] has been integrated for sensing the SPAD ignition, quenching the avalanche and resetting the detector to its initial condition. Compared to quenching circuits based on passive loads, the VLQC has the major advantage of speeding up the quenching action, thus minimizing the charge amount which flows through the SPAD after ignition. Moreover, a fixed dead-time, i.e. the minimum time interval between two detection events, of several tens of nanoseconds is externally set.

The use of SPADs as photodetectors has major advantages for imaging applications concerning the signal-to-noise ratio. No analog measurement of voltage or current is needed, since the detectors act as a digital Geiger-like counter. Hence, no read-out noise is added to the measurement process. This is a very important advantage for high-frame rate microscopy imaging, since the probability of detecting a single photon per frame and per pixel is usually low ($\ll 1$). A second major advantage of the presented pixel structure concerns the short dead-time, which has a lower limit of about 50 ns. This rises the maximum number of photons which are processed per second.

The dominant noise processes for the described pixels were dark counts generation and afterpulsing [19]. The former was below 4000 cps for more than 75% of the total number of pixels at room temperature and at +5 V excess bias. The remaining ones showed values between tens to several hundredths thousands CPSs.
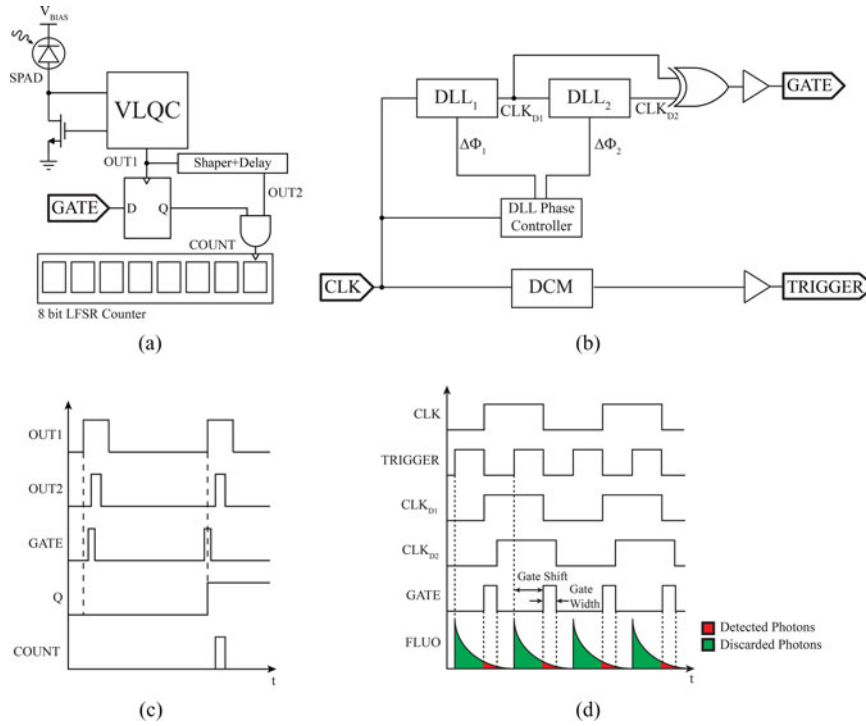
Fig. 1. (a) Scheme of the smart pixel architecture. (b) Timing signals within the pixel architecture. (c) Architecture for the generation of the fast gate signal by a Spartan 6 FPGA devices. (d) Scheme of the time-gated FLIM experiment.

Afterpulsing depends strongly on the overvoltage and dead-time values. In this study, the dead time was set to 200 ns, and the afterpulsing probability achieved a maximum of 5% over the whole array. It increased above 20% if the dead-time was set to 50 ns, which is the lower limit for the current hardware design. On the other hand, the PDE at the defined overvoltage was above 40% at 450 nm, and it decreased to about 27% at 550 nm.

Fig. 1(a) provides a schematic view of the pixel architecture. The VLQC output, which is synchronous with the avalanche sensing, triggers the processing electronics and an 8-bit Linear-Feedback Shift-Register (LFSR) counts the detection events. Routing electronics is then implemented on the same chip to read-out the counter values and to transfer them to the off-chip electronics. This design allows the measurements of 50 000 to 100 000 fps. The presented architecture additionally allows gating of the LFSR counters for a very short time between 1.5 and 20 ns. Hence, the trigger signal by the VLQC circuit increments the LFSR counter only when the signal GATE is asserted (logic level '1'). Otherwise, the detected photons are not counted (logic level '0'). To reach gated photon counting within each pixel, the output pulse from the quenching circuit (OUT1) is used to clock a D-Flip-Flop (D-FF), which samples the signal GATE generated by the camera electronics. OUT1 is additionally delayed, reshaped and sent to an AND gate to properly drive the counter. Fig. 1(c) shows the timing diagram of the counting circuitry when the fast gate signal is applied.

In order to keep the architecture as flexible as possible, the generation of the GATE signal was performed by an external Field Programmable Gate Array (FPGA) (Spartan 6, XC6SLX45-2FGG484 Xilinx, San Jose, CA, USA). A Xem6010 (Opal Kelly, Portland, OR, USA) development board, which incorporates both the Spartan 6 FPGA and a high speed USB 2.0 interface, was used to control the read-out of the chip and to transfer the measured images to the host computer.

Fig. 1(b) shows the architecture based on the internal delay locked loops (DLLs) of the FPGA device, which were used to generate fast gate signals. FPGA devices require DLLs to de-skew the internal digital paths and to fine-tune the sampling time of fast serial communication lines. They are designed to produce a precise phase shift between 10 and 40 ps, which can be dynamically controlled during operation. The update of the DLL shift requires few tens of clock cycles in the worst case, i.e. few microseconds depending on the used FPGA family. This dynamic phase shift is, therefore, well suited to generate periodic sequences of pulses. Fig. 1(d) shows how de-phased clock signals are combined to generate pulses of variable width. The 50 to 100 MHz board clock (CLK), which is used to synchronize and control the camera operations, is sent to DLL_1 and shifted of a fixed delay $\Delta\Phi_1$. This clock signal, CLK_{D1}, is sent to a second DLL (DLL_2) which creates an additional phase shifted clock ($\Delta\Phi_2$, CLK_{D2}). The XOR between CLK_{D1} and CLK_{D2} creates short pulses of variable width and at a repetition rate which is twice the clock frequency (GATE). The phase difference between CLK and CLK_{D1} will be referred to in the text as *gate shift* while the phase between CLK_{D1} and CLK_{D2} will be denoted *gate width*. Both *gate shift* and *gate width* are dynamically adjusted during data acquisition.

This logic design was implemented to set up a time-gated FLIM detection system [18]. The board clock is frequency doubled by a digital clock manager (DCM) and used as a trigger signal for a pulsed laser diode (TRIGGER) [Fig. 1(b) and
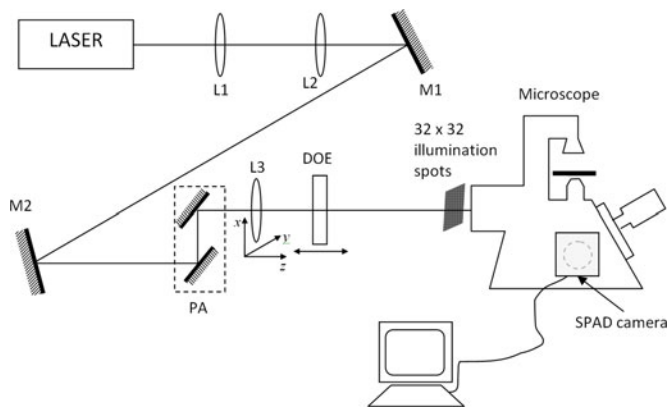
Fig. 2. Scheme of the optical setup used for the creation of the 32×32 confocal volumes. Lenses L1, L2, and L3, mirrors M1 and M2 and PA. The DOE and lens L3 were used to project an illumination array at the image plane of the microscope.

(d)]. The generated laser pulses are coupled to a wide-field fluorescence microscope, as described in Section V-A, and used to illuminate the sample. The laser radiation is absorbed by fluorescent molecules which are electronically excited. During relaxation into the ground state, the molecules emit fluorescence photons with a certain probability, which are then measured by the camera. The GATE signal activates the LFSR counters after the generation of the laser pulse for the time defined by *gate width* (Fig. 1(c), red color). Accordingly, the fluorescence decay kinetics is measured by changing *gate shift* over time. Both *gate shift* and *gate width* have optimal values depending on the lifetime of the excited state of the fluorescent molecules and on the imaging frame-rate [23], [24]. For simplicity, we used a constant *gate width* and incremented *gate shift* by fixed steps between 100 and 500 ps.

In summary, the presented camera architecture is a tradeoff between accurate time measurements on the timescale of few nanoseconds and fast processing of the measured signals up to the limit of millions of photons per second and pixel. Any detector that is suitable for both FLIM and FCS experiments must fulfill these requirements.

III. MULTIFOCAL MICROSCOPY SETUP

The multifocal FLIM/FCS setup was built on a standard Axio Observer D1 inverted microscope (Zeiss, Jena, Germany) equipped with a C-Apochromat $63\times/1.2$ W. Corr. objective (Zeiss, Jena, Germany). The filter setting for eGFP (Ex. band-pass 470/40, beam splitter FT 495, Em. band-pass 525/50) was used. The optical pathway scheme is shown in Fig. 2. Two laser sources were used for the experiments. For FCS measurement, a CW diode laser (Excelsior 488, Newport-Spectra Physics, Darmstadt, Germany) was used. Its fundamental emission wavelength at 976 nm was frequency doubled at 488 nm and a beam quality factor smaller than 1.1 at a power of 80 mW was obtained. For lifetime imaging microscopy, a pulsed laser diode (LDH-475, Picoquant, Berlin, Germany) with pulses shorter than 100 ps FWHM, a repetition rate of 50 MHz and total average power of about 1 mW was used. The laser beam was firstly attenuated by neutral density filters and then expanded by a factor of 10 using a telescope (L1 and L2). The beam height

from the optical table was adjusted by a periscope assembly (PA) to enter the back illumination port of the microscope. The expanded beam was then re-focused by lens L3 (focal length 150 mm). Immediately after, the beam passed through a diffractive optical element (DOE) (Holoeye, Berlin, Germany) in order to create an array of 32×32 spots with a pitch of 100 μm and a diameter of 12.5 μm at the image plane.

The DOE is a glass hologram designed to diffract a single laser beam into 1024 beams at different angles. The diffraction angles and the intensity of the zeroth order diffraction (transmitted beam) depends on the incident wavelength. The zero order beam, although not negligible, did not affect the performance of the system.

The sharpness of the spots projected on the image plane was adjusted by moving lens L3 along the optical axis. Other two micrometer stages were used to center the position of the array perpendicularly to the optical axis. The distance between the DOE position and the lens L3 was fine-tuned to match the pitch of the illumination spots and the active areas of the SPAD camera. The small diameter of the SPAD acts as a spatial filter and no additional pinholes are required in front of the detectors, in contrast with standard confocal microscopes. The previously described 32×32 SPAD camera (Micro-Photon-Devices, Bolzano, Italy) was connected to the side port of the microscope by a standard C-mount adapter. The acquired images were then transferred to the processing computer via a high-speed USB 2.0 interface. FCS imaging was performed using Visual SPC^2 acquisition software (Micro-Photon-Devices, Bolzano, Italy) and the frame-rate was set to values between 50 to 100 kHz.

The acquisition of FLIM images required the optimization of the camera firmware to generate fast gate signals and the synchronization pulses to trigger the laser diode.

IV. ANALYSIS OF THE DATA

The analysis of FLIM data acquired by time-gated techniques has been a subject of several works [25], [26] and more recently of a specialized review focusing on solid-state imaging sensors [24]. The data analysis method depends strongly on the gating scheme used, i.e. the selected values of *gate shift* and *gate width* as a function of the lifetime of the excited state of the observed fluorophores. The method described in [26] provides results close to the optimum for the gating scheme described in Section II. Indeed, it is a maximum likelihood (ML) approach and it provides an unbiased estimation of the model parameter even for very low numbers of photons per pixel. Compared to other approaches like the least square technique, ML estimation is both more precise and accurate, as experimentally verified by Maus *et al.* [27]. This approach has only one drawback. It does not account for the uncorrelated noise present in the decay traces, e.g. due to room light or dark counts of the SPAD detectors. Therefore, background subtraction has to be applied before estimating the lifetimes.

The adopted method searches for the lifetime value τ which is the solution of the implicit equation

$$\frac{\sum_{i=1}^{k} i * x[i]}{\sum_{i=1}^{k} x[i]} = \frac{1}{\exp(T/\tau) - 1} - \frac{k}{\exp(k * T/\tau) - 1} + 1$$

(1)

where x_i are the number of detected photons in the ith gate channel, T is the constant duration of the time channel, 0.18 ns for the described experiments, and m is the total number of channels. The estimated τ represents the average lifetime, when the observed fluorophores decay according to multiexponential models ($m(t)$).

$$m(t) = \sum_{i=1}^{N_c} a_i \exp\left(t/\tau_i\right) \qquad (2)$$

$$<\tau> \; = \sum_{i=1}^{N_c} a_i \tau_i^2 \qquad (3)$$

where a_i are the pre-exponential factors and τ_i the set of lifetimes.

While eq. (1) can be solved in less than 1 s for a whole FLIM image using MATLAB (The MathWorks Inc., Natick, MA, USA), the FCS data analysis requires more optimized computational methods to be executed within few seconds. The standard algorithm to calculate the autocorrelation curves (ACCs), which is usually known as Multi-τ algorithm or Schätzel method [28], [29], is computationally expensive. Indeed, millions of multiplications are needed to construct the ACC for each single pixel. The ACC, G(τ), is calculated from eq. (4)

$$G(\tau) = \frac{< F(t)F(t+\tau) >}{< F(t) >^2} \qquad (4)$$

where $F(t)$ is the measured time-dependent fluorescence intensity, and $< >$ denotes averaging over time [30].

Eq. (4) can be solved analytically for simple geometries and processes as the translational motion of freely diffusing fluorophores in solution [31]. The solution for this special case yields the autocorrelation function (ACF):

$$G(\tau) = \; G(0) \left(1 + \frac{\tau}{\tau_D}\right)^{-1} \left[1 + \left(\frac{s}{u}\right)^2 \frac{\tau}{\tau_D}\right]^{-1/2}$$

$$\tau_D = \; \frac{s^2}{4D} \qquad (5)$$

where G(0) is the amplitude at $\tau = 0$, τ_D is the diffusion time, s and u are the radii of the confocal volume measured perpendicular to, and along the optical axis where the excitation intensity reaches e^{-2} of its value at the center of the confocal volume, and D is the diffusion constant of the investigated molecules in solution.

We developed dedicated software both to communicate efficiently with the camera and to calculate the ACC for each pixel from sets of 130 000 images by massive parallelization of the calculation using a NVIDIA GeForce GTX 780 (NVIDIA corporation, Santa Clara, CA, USA) Graphical Processing Unit (GPU). This GPU board supports the CUDA parallel computing platform and it is capable of running tens of thousands of threads concurrently. Thereby, the computational time of the calculation of 1024 complete ACCs decreased to about 4 s, compared to the about 200 s execution time that was needed when using a single CPU. The parameters of the ACF [eq. (5)] were calculated for each pixel. G_0 and τ_D were estimated by the

value of the ACC at 41.4 μs and its full width at half maximum respectively.

It has been shown that both the estimation of lifetimes and the processing required for FCS data analysis can be embedded in the acquisition electronics [13], [32], [33]. These methods, thought excellent, are absolutely needed for real-time and high throughput applications, which are outside the scope of the current work. Future developments will focus on implementing similar algorithms for the described SPAD array architecture.

V. Experimental Results

We applied the multifocal microscope in several model experiments to show the performance of the system. The results are divided in three sections concerning the microscopy setup, FLIM and FCS.

A. Microscopy Setup

A first important test was to measure the uniformity of the field of view after illumination by the DOE and detection using the SPAD camera. The uniformity of the experimental setup was measured by imaging an aqueous solution of quantum dots (QD, 525 ITK$^{\text{TM}}$ Molecular Probes, Darmstadt Germany). The selected QDs emit around 525 nm after excitation at 488 nm, and the diameter of the nanocrystals is approximately 20 nm according to the manufacturer's specifications.

Several parameters influenced the uniformity of the detected signal over the field of view, which depend both on the optical coupling of the laser to the microscope, the alignment of the detectors, and the variation of the detection efficiency of the SPADs of the matrix. This parameter is, therefore, the product between the uniformity of the excitation intensity obtained by the DOE, the coupling efficiency between the excitation volumes and the SPAD, and the PDE of the SPADs. Fig. 3 shows the measured uniformity of the system normalized by its mean value after dark counts subtraction. More than 70% of the pixels have a uniformity within 15% of the mean value. The largest deviations of about 30%, which were caused by an uneven illumination of the DOE by the Gaussian laser beam, were obtained at the outer rim of the array. The measured overall uniformity was sufficient for the proposed applications.

Additionally, we tested the linearity of the *gate width* (Fig. 4), i.e. how precisely *gate width* could be set by the FPGA device. A stabilized LED was placed in front of the sensor, and image sequences at variable *gate widths* between 1 and 20 ns were acquired. Considering that the illumination intensity was constant, a signal dependent on the width of the gate was measured. Fig. 4 shows the estimated *gate width* as a function of the expected value programmed by the control software. One can observe that the width of the gate is well approximated by a linear model over a large temporal range. Below 1.5 ns and above 18 ns, deviations from linearity were observed. Indeed, the gate pulses become too short to efficiently enable and disable the LFSR counters. The obtained *gate width* range is definitely sufficient for most FLIM experiments.
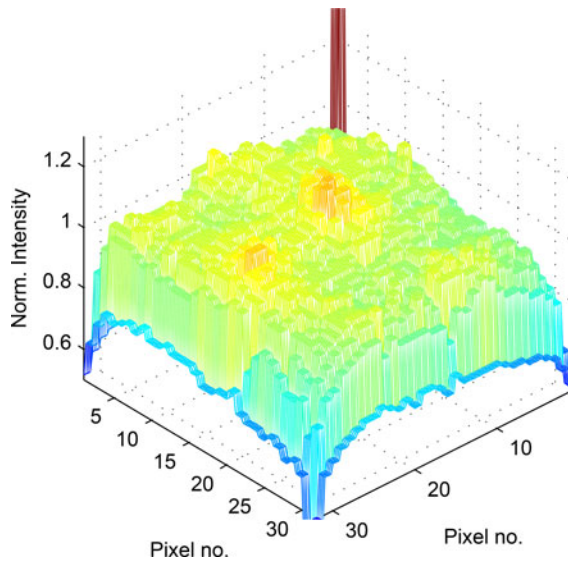
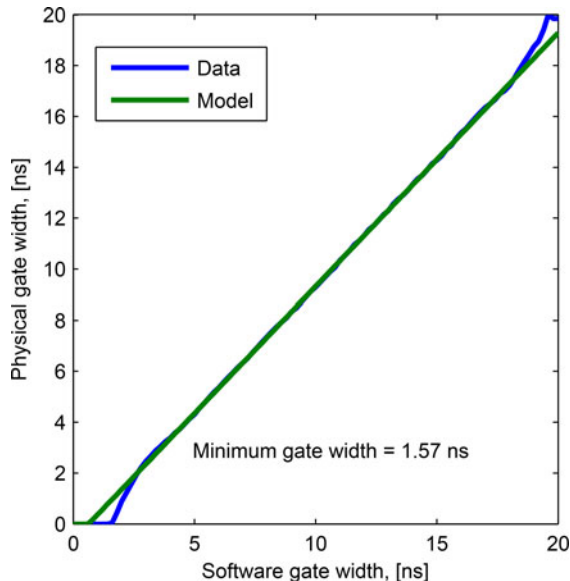Fig. 3.   Illumination uniformity over the whole 32×32 SPAD array.

Fig. 4.   Linearity of the gate width as a function of the camera setting. Uncorrelated light from a stabilized LED was used to generate a constant light signal.

B. Fluorescence Lifetime Imaging Microscopy

The multifocal FLIM-FCS setup was applied to measure the lifetime of known fluorophores both in solution and in live cells and compared to previously published values. In order to estimate the lifetime [τ, eq. (3)] precisely, *gate width* was set to the minimum value of about 1.5 ns and shifted by steps of 180 ps. The exposure time of the camera for each gate shift was about 100 ms, and a total acquisition time per FLIM image of 10 s was obtained. Before each image acquisition, a dark frame at exactly the same camera setting was acquired to perform reliable background subtraction. The laser intensity on the object plane was set to values between 5 and $500\,\mathrm{mW/cm^2}$ depending on the brightness of the sample. Rhodamine 6 G was dissolved

in water at the concentration of 10 μM, and excited by pulsed laser light at 473 nm. A gradient in the illumination intensity [Fig. 5(a)] was artificially generated to measure a variable number of photons per pixel over the field of view. A subset of the images was selected and the fit algorithm based on eq. (1) was applied to each pixel. A systematic deviation of the measured fluorescence intensity was present for less than 10% of the array detectors, which showed the highest dark counts levels. In fact, the background subtraction becomes less accurate for these pixels due to the detector saturation.

The measured average lifetime over all the pixels was 3.8 ns $\pm$ 0.3 ns. This value is consistent with previously published results [34]. The distribution of the average lifetime over the field of view is uniform Fig. 5(b) even though the illumination field is uneven [Fig. 5(a)]. This is expected because the estimated lifetimes must be independent from the number of detected photons per pixel.

Afterwards, we investigated living Human Embryonal Kidney HEK293-T cells expressing the eGFP [35]. The cells were plated in 35 mm petri dishes with a 150 μm glass bottom (Ibidi, Munich, Germany), cultured in Dulbecco's modified Eagle's medium without phenol red, supplemented with 10% fetal calf serum, 2 mM L-glutamine and 100 μ/ml penicillin/streptomycin and grown to about 70% confluence at 37 °C in a cell culture incubator at 5% CO_2 in water-saturated air. Subsequently, cells were transfected with eGFP cDNA in plasmid vector pEGFP-N1 (Clontech, Saint-Germain-en-Laye, France) using Lipofectamine 2000 (Life Technologies, Darmstadt, Germany) as transfection reagent according to the manufacturer's instructions. Transfected cells were used for microscopy within 48 h. Fig. 5(c) shows the intensity image of two HEK293-T cells at variable expression levels of the protein. The decay dynamics of eGFP is known to be multi-exponential both when expressed in living systems and in solutions of the isolated protein [36], [37], depending e.g. on pH or the refractive index of the solvent. Precise modeling of the fluorescence decay kinetic of this type of fluorescent molecules requires time-correlated single photon counting instrumentation with a temporal resolution of few tens of picoseconds. The fluorophore exists, indeed, in a protonated form which decays with a time constant of 250 ps [36]. Despite that, it is still possible to measure the average lifetime of eGFP using time-gated techniques, even though the shortest gate achievable is above one nanosecond [38]. The average and standard deviation of the estimated lifetimes for both cells in Fig. 5(c) and (d) was 2.4 $\pm$ 0.13 ns, which is very similar to the results from previous investigations [36]. The deviation of the measured lifetimes around the mean value is due to statistical fluctuations of the detected photons and not by a heterogeneity of the observed sample. It must be observed that the acquisition time of the FLIM images were limited by the available laser power and by the used gate settings rather than by the performance of the camera. The presented camera is capable of collecting two-gate FLIM images within 25 to 50 μs, depending on the clock frequency. This exposure time is calculated as twice the shortest acquisition time for the single frame (10.37 to 20.74 μs) and the update time of the DLLs inside the FPGA. However, reliable FLIM experiments under this operating condition would require an optimization of the gate intervals, the
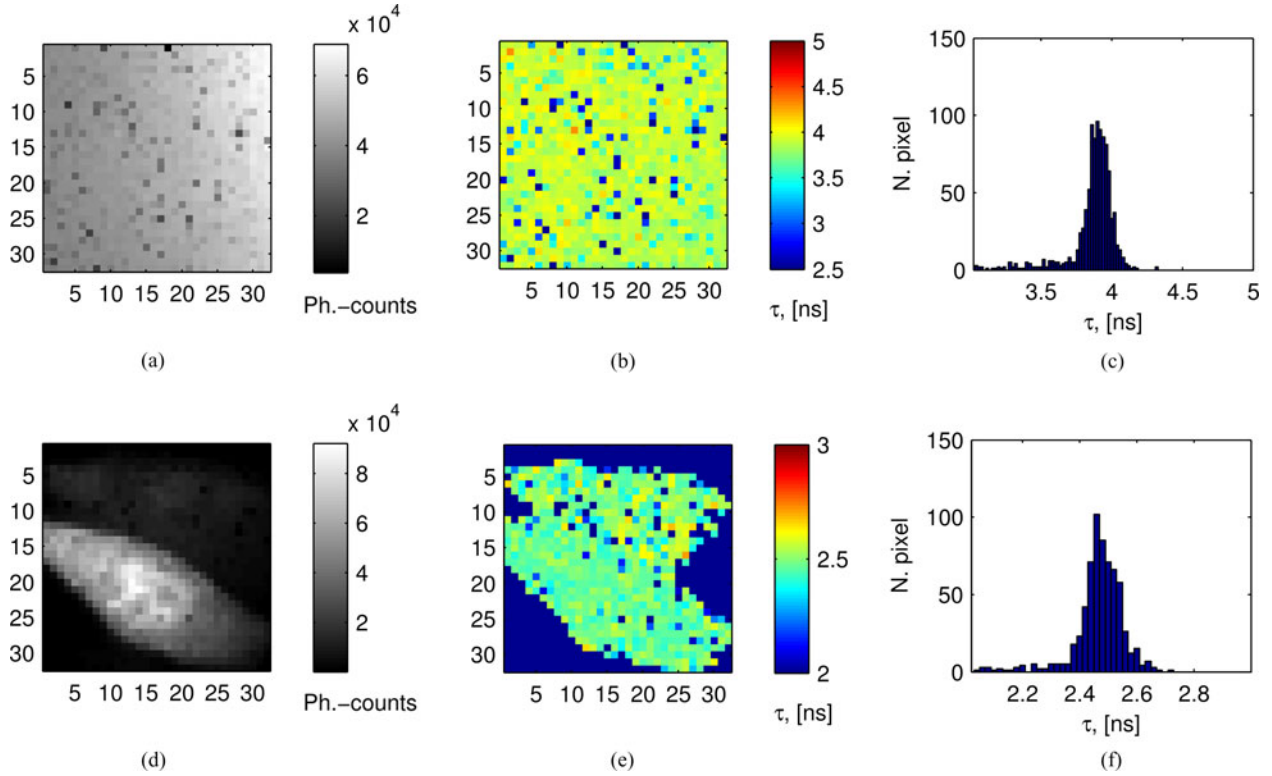
Fig. 5. (a) Fluorescence emission of Rhodamine 6G under gradient illumination. (b) FLIM image and (c) histogram of the estimated average lifetimes of the same Rhodamine solution. (d) Fluorescence emission of two HEK293-T cells with different eGFP expression levels. (e) FLIM image and (f) histogram of the estimated average lifetimes of the same cells.

repetition rate and power of the pulsed laser source which are outside the scope of the current work. Compared with standard FLIM techniques, Time correlated single photon counting experiments, both based on point detectors or coded-anode photomultipliers, outperform the presented camera in term of the accuracy and resolution of the measured lifetimes. But the presented system is capable of measuring FCS in 1024 regions of the sample, additionally to the lifetime of the fluorophores, in a single experiment.

C. Fluorescence Correlation Spectroscopy

The multifocal microscope was applied to measure the diffusion of single fluorophores in solution. We have chosen QD because of their brighter emission and slower diffusion time compared to Rhodamine 6G, which is typically used for the calibration of FCS setups. The probe was prepared as described in section V-A. The sample was illuminated by an average laser power of about 25 μW per excitation volume. Raw FCS data collected by the camera consisted of 130 000 frames acquired every 20.74 μs, yielding 1024 fluorescence intensity fluctuation traces recorded over 2.7 s. The average count-rate per pixel was about 30 kcps.

The concentration of the fluorophores in various runs was slightly different, but always between 0.05 nM and 2 nM, as verified by FCS using a conventional instrument (ConfoCor 3, Zeiss, Jena, Germany).

Fig. 6(a) and (b) show the values of the estimated τ_D and G_0 for each pixel respectively. These images appear to be noisy because they have contribution from fluctuations generated by single QDs movement, characterized by a diffusion time $\tau_D \approx 600 \mu$s, and QD agglomerates that are slowly diffusing, $\tau_D \approx 3 - 30$ ms, and are readily visualized because of their relatively higher brightness. This is evident from the diffusion time distribution histogram in Fig. 6(d), which shows a bimodal distribution that is characteristic of the presence of fast and slowly moving fluorophores. The measured values are similar to those reported by other groups [39].

Fig. 6(c) shows the ACC curves of selected pixels. The green and blue traces show the typical ACC of freely diffusing fluorophores in solution. The measured ACC do not substantially differ from those measured by the commercial ConfoCor 3 microscope, although the shortest lag time for the SPAD camera has a much longer duration [Fig. 6(f)]. One should observe that all the ACC of Fig. 6(b) have a peak at lag times below 100 μs. These peaks are due to a long-afterpulsing process, which is present for SPADs produced by the used standard CMOS process, and which generates correlated detection events on the microsecond time scale. The ACC of one of the selected pixels [red trace, Fig. 6(b)] shows a dominant afterpulsing contribution. The presence of afterpulsing was verified by cross-correlating the measured signal of neighboring pixels after uniform illumination of the camera. While the ACC show the peak for short lag-times, the cross-correlation curve was statistically spread around one (data not shown). The autocorrelation peak present in Fig. 6(c) would be removed by implementing more advanced correlation techniques as fluorescence cross-correlation spectroscopy. This would however require the parallel
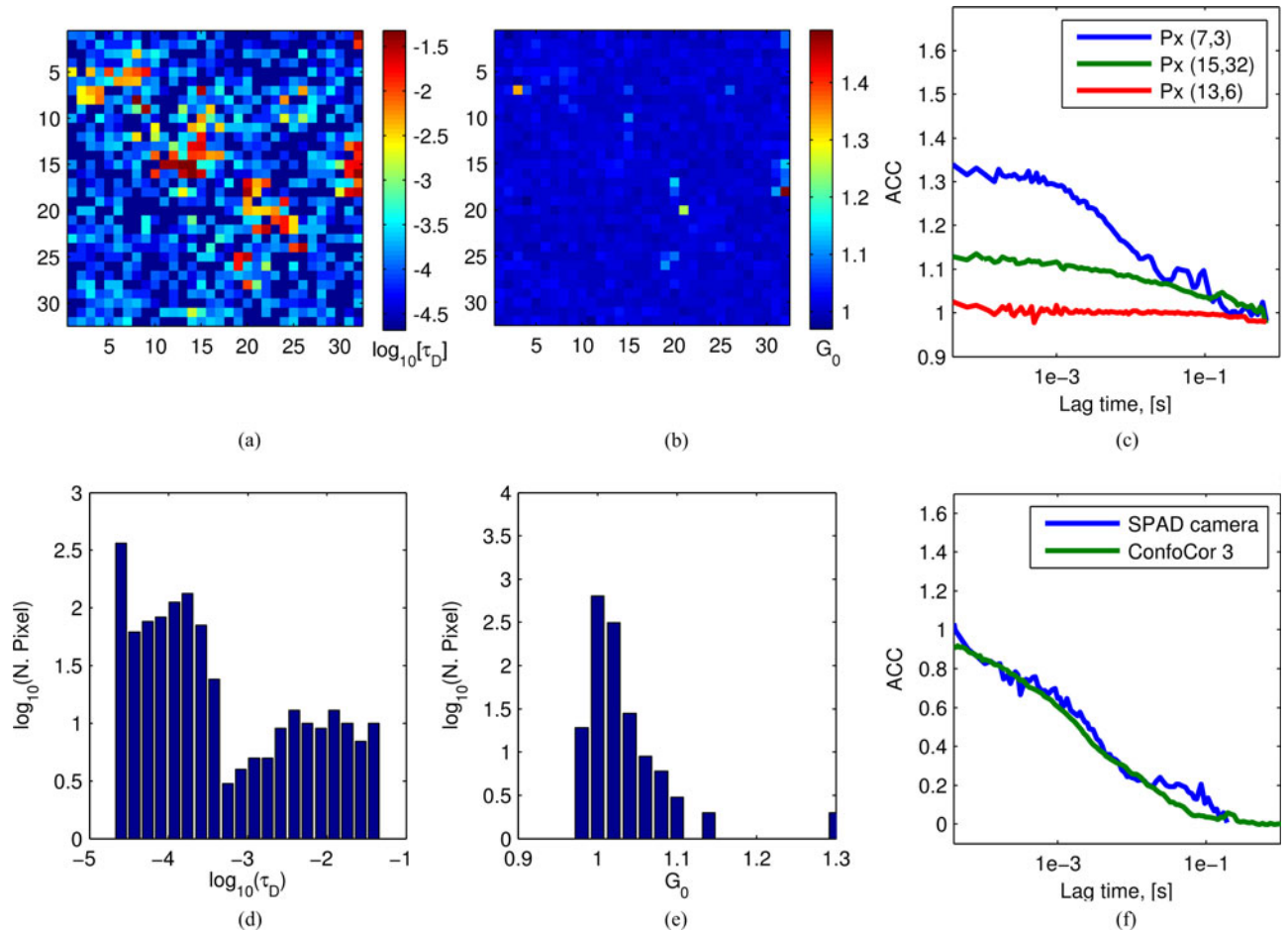
Fig. 6. Plot of the estimated τ_D (a) and G_0 (b) values over the whole field of view and corresponding histograms (d) and (e). (c) Measured ACC of selected pixels. (f) Comparison of ACC obtained by the SPAD camera (blue) and the reference microscope (ConfoCor 3, green).

acquisition of the fluorescence emission signal by two identical SPAD cameras.

At present, the dominant noise sources in the FCS measurements shown in Fig. 6 are the afterpulsing and dark-counts generation processes, which systematically affect the absolute value of G_0 and, therefore, perturbs the quantitative analysis. However, since most of the afterpulsing contribution vanishes within 1 μs [19], the effect of afterpulsing on diffusion times of individual QDs and QD agglomerates, which are in the order of 600 μs and 3–30 ms, respectively, is not significant.

VI. CONCLUSION

We presented a 32×32 SPAD based camera which is suitable for multifocal microscopy. This device has not only a very high frame rate, short dead-time and single photon sensitivity, but also a fast gating unit, which activates the counting of the photons in individual pixels for short intervals down to 1.5 ns. Both FCS, FLIM and standard confocal imaging are possible on the same multifocal microscope. The device has been used to accurately measure the translational diffusion time of QD in solution and the fluorescence decay kinetics of eGFP in living HEK293-T cells.

Future improvements of the current experimental setup will focus on the observation of single molecules in solutions and in live cells, and on the real-time processing of FCS and FLIM data by the acquisition electronics. Additionally, further investigations are required to improve the photodetectors by reducing the dark-count rate and afterpulsing probability.

REFERENCES

[1] J. Pawley, *Handbook of Biological Confocal Microscopy*, 3rd ed. New York, NY, USA: Plenum Press, 2006.
[2] G. Y. Fan, H. Fujisaki, A. Miyawaki, R. K. Tsay, R. Y. Tsien, and M. H. Ellisman, "Video-rate scanning two-photon excitation fluorescence microscopy and ratio imaging with Cameleons," *Biophys. J*, vol. 76, no. 5, pp. 2412–2420, 1999.
[3] L. Greenbaum, C. Rothmann, R. Lavie, and Z. Malik, "Green fluorescent protein photobleaching: A model for protein damage by endogenous and exogenous singlet oxygen," *Biol. Chem.*, vol. 381, no. 12, pp. 1251–1258, Dec. 2000.

[4] E. Wang, C. M. Babbey, and K. W. Dunn, "Performance comparison between the high-speed Yokogawa spinning disc confocal system and single-point scanning confocal systems," *J. Microsc.*, vol. 218, no. 2, pp. 148–159, 2005.

[5] R. Rigler, *FCS in Single Molecule Analysis. Nobel Symposium on Single Molecule Spectroscopy in Chemistry, Physics and Biology*. New York, NY, USA: Springer, 2010.

[6] A. Rochas, M. Gosch, A. Serov, P. Besse, R. Popovic, T. Lasser, and R. Rigler, "First fully integrated 2-D array of single-photon detectors in standard CMOS technology," *IEEE Photon. Technol. Lett.*, vol. 15, no. 7, pp. 963–965, Jul. 2003.

[7] F. Guerrieri, S. Tisa, A. Tosi, and F. Zappa, "Two-dimensional SPAD imaging camera for photon counting," *IEEE Photon. J.*, vol. 2, no. 5, pp. 759–774, Oct. 2010.

[8] M. Gersbach, J. Richardson, E. Mazaleyrat, S. Hardillier, C. Niclass, R. Henderson, L. Grant, and E. Charbon, "A low-noise single-photon detector implemented in a 130 nm CMOS imaging process," *Solid-State Electron.*, vol. 53, no. 7, pp. 803–808, 2009.

[9] H. Blom, M. Johansson, A.-S. Hedman, L. Lundberg, A. Hanning, S. Hård, and R. Rigler, "Parallel fluorescence detection of single biomolecules in microarrays by a diffractive-optical-designed 2×2 fan-out element," *Appl. Opt.*, vol. 41, no. 16, pp. 3336–3342, 2002.

[10] H. Blom, M. Johansson, M. Gösch, T. Sigmundsson, J. Holm, S. Hård, and R. Rigler, "Parallel flow measurements in microstructures by use of a multifocal 4×1 diffractive optical fan-out element," *Appl. Opt.*, vol. 41, no. 31, pp. 6614–6620, 2002.

[11] M. Gösch, A. Serov, T. Anhut, T. Lasser, A. Rochas, R. S. Popovic, H. Blom, and R. Rigler, "Parallel single molecule detection with a fully integrated single-photon 2×2 CMOS detector array," *J. Biomed. Opt.*, vol. 9, no. 5, pp. 913–921, 2004.

[12] X. Michalet, R. A. Colyer, G. Scalia, T. Kim, M. Levi, D. Aharoni, A. Cheng, F. Guerrieri, K. Arisaka, J. Millaud, I. Rech, D. Resnati, S. Marangoni, A. Gulinatti, M. Ghioni, S. Tisa, F. Zappa, S. Cova, and S. Weiss, "High-throughput single-molecule fluorescence spectroscopy using parallel detection," presented at the SPIE Photon. West Conf. Proc., San Jose, CA, USA, vol. 7608, no. 76082D, 2010.

[13] J. Buchholz, J. W. Krieger, G. Mocsár, B. Kreith, E. Charbon, G. Vámosi, U. Kebschull, and J. Langowski, "FPGA implementation of a 32×32 autocorrelator array for analysis of fast image series," *Opt. Exp.*, vol. 20, no. 16 pp. 17 767–17 782, 2012.

[14] X. Michalet, R. A. Colyer, G. Scalia, A. Ingargiola, R. Lin, J. E. Millaud, S. Weiss, O. H. W. Siegmund, A. S. Tremsin, J. V. Vallerga, A. Cheng, M. Levi, D. Aharoni, K. Arisaka, F. Villa, F. Guerrieri, F. Panzeri, I. Rech, A. Gulinatti, F. Zappa, M. Ghioni, and S. Cova, "Development of new photon-counting detectors for single-molecule fluorescence microscopy," *Philos. Trans. Royal Soc. Lond. B Biol. Sci.*, vol. 368, no. 1611, p. 20120035, 2013.

[15] M. Kloster-Landsberg, D. Tyndall, I. Wang, R. Walker, J. Richardson, R. Henderson, and A. Delon, "Note: Multi-confocal fluorescence correlation spectroscopy in living cells using a complementary metal oxide semiconductor-single photon avalanche diode array," *Rev. Sci. Instrum.*, vol. 84, no. 7, p. 076105, 2013.

[16] A. Draaijer, R. Sanders, and H. C. Gerritsen, "Fluorescence lifetime imaging, a new tool in confocal microscopy," in *Handbook of Biological Confocal Microscopy*. New York, NY, USA: Springer, 1995, pp. 491–505.

[17] C. J. de Grauw and H. C. Gerritsen, "Multiple time-gate module for fluorescence lifetime imaging," *Appl. Spectrosc.*, vol. 55, no. 6, pp. 670–678, Jun. 2001.

[18] T. W. J. Gadella, Ed., *FRET and FLIM Techniques*, vol. 33. Amsterdam, The Netherlands: Elsevier Science, 2008.

[19] S. Tisa, A. Tosi, and F. Zappa, "Fully-integrated CMOS single photon counter," *Opt. Exp.*, vol. 15, no. 6, pp. 2873–2887, 2007.

[20] F. Guerrieri, S. Tisa, and F. Zappa, "Fast single-photon imager acquires 1024 pixels at 100 kframe/s," *Proc. SPIE*, vol. 7249, p. 72490U, Jan. 27, 2009.

[21] S. Cova, M. Ghioni, A. Lacaita, C. Samori, and F. Zappa, "Avalanche photodiodes and quenching circuits for single-photon detection," *Appl. Opt.*, vol. 35, no. 12, pp. 1956–1976, 1996.

[22] S. Tisa, F. Guerrieri, and F. Zappa, "Variable-load quenching circuit for single-photon avalanche diodes," *Opt. Exp.*, vol. 16, no. 3, pp. 2232–2244, 2008.

[23] S. P. Chan, Z. J. Fuller, J. N. Demas, and B. A. DeGraff, "Optimized gating scheme for rapid lifetime determinations of single-exponential luminescence lifetimes," *Anal. Chem.*, vol. 73, no. 18, pp. 4486–4490, 2001.

[24] D. D.-U. Li, S. Ameer-Beg, J. Arlt, D. Tyndall, R. Walker, D. R. Matthews, V. Visitkul, J. Richardson, and R. K. Henderson, "Time-domain fluorescence lifetime imaging techniques suitable for solid-state imaging sensor arrays," *Sensors*, vol. 12, no. 5, pp. 5650–5669, 2012.

[25] P. Hall and B. Selinger, "Better estimates of exponential decay parameters," *J. Phys. Chem.*, vol. 85, no. 20, pp. 2941–2946, 1981.

[26] J. Tellinghuisen and C. W. Wilkerson, "Bias and precision in the estimation of exponential decay parameters from sparse data," *Anal. Chem.*, vol. 65, no. 9, pp. 1240–1246, 1993.

[27] M. Maus, M. Cotlet, J. Hofkens, T. Gensch, F. C. de Schryver, J. Schaffer, and C. A. Seidel, "An experimental comparison of the maximum likelihood estimation and nonlinear least-squares fluorescence lifetime analysis of single molecules," *Anal. Chem.*, vol. 73, no. 9, pp. 2078–2086, 2001.

[28] K. Schätzel, M. Drewel, and S. Stimac, "Photon correlation measurements at large lag times: Improving statistical accuracy," *J. Mod. Opt.*, vol. 35, no. 4, pp. 711–718, 1988.

[29] T. Wohland, R. Rigler, and H. Vogel, "The standard deviation in fluorescence correlation spectroscopy," *Biophys. J.*, vol. 80, no. 6, pp. 2987–2999, 2001.

[30] J. R. Lakowicz, *Principles of Fluorescence Spectroscopy.*, 3rd ed. New York, NY, USA: Springer, 2006.

[31] S. R. Aragon and R. Pecora, "Fluorescence correlation spectroscopy as a probe of molecular dynamics," *J. Chem. Phys.*, vol. 64, no. 4, pp. 1791–1803, 1976.

[32] D.-U. Li, E. Bonnist, D. Renshaw, and R. Henderson, "On-chip, time-correlated, fluorescence lifetime extraction algorithms and error analysis," *J. Opt. Soc. Amer. A Opt. Image Sci. Vis.*, vol. 25, no. 5, pp. 1190–1198, 2008.

[33] D.-U. Li, J. Arlt, J. Richardson, R. Walker, A. Buts, D. Stoppa, E. Charbon, and R. Henderson, "Real-time fluorescence lifetime imaging system with a 32×32 0.13 μm CMOS low dark-count single-photon avalanche diode array," *Opt. Exp.*, vol. 18, no. 10 pp. 10 257–10 269, 2010.

[34] R. Reisfeld, R. Zusman, Y. Cohen, and M. Eyal, "The spectroscopic behaviour of rhodamine 6G in polar and non-polar solvents and in thin glass and PMMA films," *Chem. Phys. Lett.*, vol. 147, no. 2, pp. 142–147, 1988.

[35] G. Zhang, V. Gurtu, and S. R. Kain, "An enhanced green fluorescent protein allows sensitive detection of gene transfer in mammalian cells," *Biochem. Biophys. Res. Commun.*, vol. 227, no. 3, pp. 707–711, 1996.

[36] M. Cotlet, J. Hofkens, M. Maus, T. Gensch, M. van der Auweraer, J. Michiels, G. Dirix, M. van Guyse, J. Vanderleyden, A. J. W. G. Visser, and F. de Schryver, "Excited-state dynamics in the enhanced green fluorescent protein mutant probed by picosecond time-resolved single photon counting spectroscopy," *J. Phys. Chem. B*, vol. 105, no. 21, pp. 4999–5006, 2001.

[37] M. Vitali, F. Picazo, Y. Prokazov, A. Duci, E. Turbin, C. Götze, J. Llopis, R. Hartig, A. J. W. G. Visser, and W. Zuschratter, "Wide-field multi-parameter FLIM: Long-term minimal invasive observation of proteins in living cells," *PloS One*, vol. 6, no. 2, p. e15820, 2011.

[38] H. C. Gerritsen, M. A. H. Asselbergs, A. V. Agronskaia, and W. G. J. H. M. van Sark, "Fluorescence lifetime imaging in scanning microscopes: acquisition speed, photon economy and lifetime resolution," *J. Microsc.*, vol. 206, no. 3, pp. 218–224, 2002.

[39] Y. Han, J. Lee, Y. Lee, and S. W. Kim, "Measurement of the diffusion coefficients of fluorescence beads and quantum dots by using fluorescence correlation spectroscopy," *J. Korean Phys. Soc.*, vol. 59, no. 5, pp. 3177–3181, 2011.

Marco Vitali received the M.Sc. degree in electronic engineering from Politecnico di Milano in 2006, and the Ph.D. degree (*summa cum laude*) from the Berlin Institute of Technology in 2011. His main research interests are fluorescence lifetime imaging microscopy of living cells and the development of bidimensional single photon timing detectors as position-sensitive photomultipliers and SPAD arrays. He is currently working as a Hardware Engineer at Omicron Energy Solutions GmbH, Berlin, Germany.

Danilo Bronzi (S'13) received the B.Sc. degree (*cum laude*) in biomedical engineering and the M.Sc. degree (*cum laude*) in electronic engineering from Politecnico di Milano, Italy, in 2008 and July 2011, respectively. Since October 2011, he has been enrolled in the Ph.D. program in the Department of Electronics, Information and Bioengineering, Politecnico di Milano. His current research activity focuses on the design and development of novel CMOS single-photon sensors for 2-D and 3-D imaging applications.

Aleksandar J. Krmpot received the Ph.D. degree in quantum optics from the University of Belgrade, Serbia, in 2010. He is a Research Associate at the Institute of Physics, University of Belgrade. During M.Sc. and Ph.D studies, he was investigating the evolution of the coherently prepared atoms traversing different laser beams profiles. His main research activities are quantum optics and biophotonics. His current research activities are development and application of nonlinear microscopy for biohotonics structures studies in Institute of physics, Belgrade, Serbia and multifocal correlation microscopy for studies of molecular diffusion dynamics at Karolinska Institute, Stockholm, Sweden.

Stanko N. Nikolić received the B.Sc. degree in experimental physics from the Faculty of Physics, University of Belgrade, in 2007, and the M.Sc. degree in quantum optics from the same institution in 2008. Since 2007, he has been working at the Institute of Physics as a Research Assistant in the field of experimental quantum optics. Since November 2008, he has been enrolled in the Ph.D. program at Faculty of Physics, University of Belgrade, in the field of electromagnetically induced transparency and slow light in Rb buffer gas cells. He is also an external collaborator at Karolinska Institute, Stockholm, Sweden, with activities focused on laboratory software development.

Franz-Josef Schmitt has been a Postdoctoral Researcher at the Institute of Physical Chemistry, Berlin Institute of Technology since 2011, where he finished his doctoral thesis in physics. His research focuses on the spectroscopy of pigment–pigment and pigment–protein interactions in photosynthesis and molecular biology. He published about 40 peer-reviewed articles. He is currently substitutional management committee member of COST action MP 1205.

Cornelia Junghans received the Diploma degree in physics from the Berlin Institute of Technology in 2011. Since September 2011, she has been working toward the Ph.D. degree at the Department of Biophysical Chemistry of the same university. Her main research interests are fluorescence spectroscopy of genetically-encoded photoswitchable fluorophores and microscopy techniques such as confocal microscopy, fluorescence recovery after photobleaching, and lifetime imaging microscopy.

Simone Tisa was born in Milano, Italy, in 1977. He received the M.Sc. degree in electronic engineering from Politecnico di Milano in 2001, and the Ph.D. degree from the same university in 2006. He is currently a Product R&D Manager for electronics design and system integration at Micro Photon Devices. In 2008, he pioneered the first monolithic 2-D SPAD imager of 32×32 pixels. His main research interests are in the field of single-photon imaging and single-photon timing of fast phenomena, by means of fully integrated arrays of SPADs and associated microelectronics.

Thomas Friedrich was born in 1965. He received the Diploma degree in physics from the University of Heidelberg in 1992, and the Ph.D. degree in biochemistry from the University of Frankfurt/Main in 1997. After two postdoctoral positions at the Center of Molecular Neurobiology in Hamburg and the Max-Planck-Institute of Biophysics, he became the Head of the Junior Research Group Microfluidics and Biosensors at the Technical University of Ilmenau/Thuringia. Since 2006, he has been a full professor of physical chemistry at the Berlin Institute of Technology. His research deals with electrophysiological investigations of ion transporters or ion channels in cellular membranes and fluorescence lifetime imaging microscopy to analyze bioenergetic processes. He is coauthor of more than 66 papers, published in peer-reviewed journals of the biophysics and biochemistry field.

Vladana Vukojević was born in Belgrade, Serbia, in 1965. She commenced her research career at the H. C. Ørsted Institute, Copenhagen, Denmark, in 1989, and her academic career at the Faculty of Physical Chemistry, University of Belgrade, Serbia, where she was an Associate Professor of biophysical chemistry until 2005. Since 2011, she has been an Associate Professor of biochemistry at the Karolinska Institute, Stockholm, Sweden. Her research focuses on self-organization of dynamical systems. She uses fluorescence microscopy imaging and correlation spectroscopy to identify and quantitatively characterize in live cells self-regulatory mechanisms underlying vital biological functions such as gene transcription and cellular signaling. She is coauthor of more than 50 papers published in peer-reviewed journals.

Lars Terenius was born in Örebro, Sweden, in 1940. He was appointed as a Professor in pharmacology at Uppsala University in 1976 and resigned in 1988 for a visiting scientist scholarship at the National Institutes of Health in Bethesda, MD, USA. He was appointed a Professor at the Karolinska Institutet in 1989. His research is focused on molecular mechanisms of pathology ranging from cancer to chronic pain and drug/alcohol dependence. He is also the Founding Director of Center for Molecular Medicine (CMM), a research center at the Karolinska University Hospital with over 300 scientists. His recent work in collaboration with Prof. R. Rigler is imaging of molecules in the living cell using fluorescence correlation spectroscopy. This research has required modification or new constructions of apparatus, to acquire single molecule sensitivity and high temporal and spatial resolution. He has published more than 500 papers in peer-reviewed periodicals.

Franco Zappa (M'00–SM'07) was born in Milano, Italy, in 1965. Since 2011, he has been a Full Professor of electronics at Politecnico di Milano. His research deals with microelectronic circuitry for single-photon detectors (SPAD) and CMOS SPAD imagers, for high-sensitivity time-resolved measurements, 2-D imaging and 3-D depth ranging. He is a coauthor of more than 130 papers, published in peer-reviewed journals and in conference proceedings, and nine text books on Electronic Design and Electronic Systems. He is a coauthor of four international patents. In 2004, he cofounded "Micro Photon Devices" focused on the production of SPAD modules for single photon-counting and photon-timing.

Rudolf Rigler was born in Franfurt/Main, Germany, in 1936. He received the M.D. degree from the University Graz, Austria, in 1960, the Ph.D. degree from Karolinska Institute, Stockholm, Sweden, in 1966. He was a Postdoctoral Fellow with Manfred Eigen (Nobel laureate in chemistry) from 1967 to 1970. He was a Professor in molecular and medical biophysics at the Karolinska Institutet from 1976 to 2001. He was an invited Professor at the Swiss Federal Institute of Technology Lausanne (EPFL) from 2001 to 2011. He is a Member of the Nobel Assembly of the Karolinska Institutet. He is a Member of the Royal Swedish Acedemy of Sciences (KVA) and the Royal Engineering Science Academy (IVA). In his laboratory, Fluorescence Correlation Spectroscopy, Confocal Single Molecule Detection, and Wide Field Imaging were developed. He has published more than 200 scientific papers. He is an inventor of 40 patents and Cofounder of Evotec AG, in Germany and Gnothis AG and Biophos AG, both in Switzerland.

Optical Ramsey fringes observed during temporal evolution of Zeeman coherences in Rb buffer gas cell

S N Nikolić, M Radonjić, N M Lučić, A J Krmpot and B M Jelenković

Institute of Physics, University of Belgrade, Pregrevica 118, 11080 Belgrade, Serbia

E-mail: stankon@ipb.ac.rs

Abstract

We experimentally studied the temporal evolution of Zeeman electromagnetically induced transparency (EIT) resonances induced by the laser resonant to hyperfine transition $F_g = 2 \rightarrow F_e = 1$ of ^{87}Rb in a rubidium buffer gas cell. We simultaneously modulated the laser beam intensity and polarization to achieve the repeated interaction of the laser beam with coherently prepared atoms. Our cell was placed in a homogenous magnetic field to obtain the Larmor precession of the phase of coherences. The weak laser beam was used to probe the atoms at the end of the Ramsey sequence. We measured the transparency of the probe pulse at different magnetic fields for a given excitation pulse and the period of free evolution of Zeeman coherences in the dark. From these data, we reconstructed the temporal evolution of EIT resonances. The Ramsey fringes that appeared on the EIT curves at the beginning of the second probing pulse disappeared at later moments due to various decay processes.

(Some figures may appear in colour only in the online journal)

1. Introduction

Electromagnetically induced transparency (EIT) is a phenomenon characterized by a narrow transparency resonance of a laser field through coherent media, such as alkali atomic vapor [1]. This effect is of special interest because it allows for fine control of pulse propagation. EIT-based slow and stored light observations [2] may benefit telecommunications and quantum memories.

EIT resonance in Hanle configuration is based on Zeeman coherences between magnetic sublevels of a given hyperfine state of an alkali atom electronic ground state. When such an atom is exposed to the external magnetic field, its magnetic dipole moment rotates around the field direction with a Larmor frequency. This allows the possibility for a Ramsey method of separated oscillatory fields [3]. For instance, in the interaction of an atom with a first light field, coherence between atomic levels is created. Under the influence of the magnetic field, the phase of the rotation of the magnetic dipole moment defines the coherence phase. The second light field, which can be either spatially or temporally separated from the first field, probes the coherence [4]. The result is an interferometric picture with Ramsey fringes in the probe transparency signal, due to the phase differences between the coherence and the probe field.

Ramsey-like measurements of Zeeman decoherence that determine the dumping rate of the oscillations are presented in [5]. The effects of Ramsey narrowing of EIT resonances due to atomic diffusion in and out from the interaction region were discussed in [6, 7]. High contrast Ramsey fringes in a double Λ atomic scheme were obtained in [8]. Raman-Ramsey fringes are also shown in vacuum Rb cells using time-delayed optical pulses [9] and a probe beam that was spatially enclosed by the pump beam [10].

In this work, we present the experimental study of the temporal evolution of the Zeeman EIT resonances based on repeated interaction of coherently prepared atoms with the laser beam. The obtained transparency of the σ^- probe at
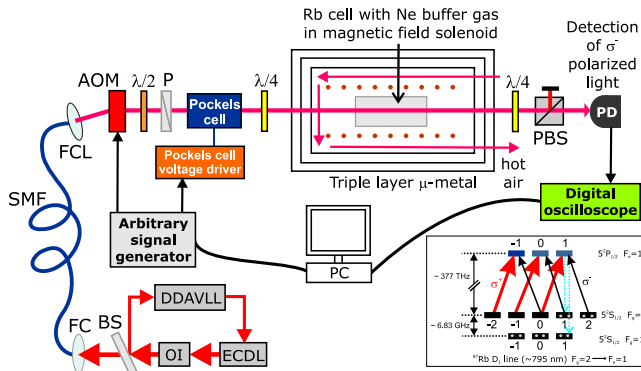
Figure 1. Experimental setup and atomic transition [15] used in the experiment. ECDL—external cavity diode laser; OI—optical insulator; DDAVLL—Doppler-free dichroic atomic vapor laser lock; BS—beam splitter; FC—fiber coupler; SMF—single-mode fiber; FCL—fiber collimator; AOM—acousto-optic modulator; P—polarizer; PBS—polarizing beam splitter; PD—photodetector. Hot air is used to heat the cell.

different magnetic fields was used to reconstruct the EIT resonances at different moments from the beginning of the probe pulse. The studies of dark states temporal behavior [11] and transient effects of EIT phenomenon [12–14] have been previously shown. In our work, the evolutions of (i) damped Ramsey fringes on the probe transparency and (ii) reconstructed EIT resonances during the probe propagation allowed for unique observation of the development and decay of Zeeman coherences.

2. Experimental setup

The experimental setup is shown in figure 1. The external cavity diode laser is frequency locked to the hyperfine $F_g = 2 \rightarrow F_e = 1$ transition of the D_1 line in ^{87}Rb in vacuum cell using the Doppler-free dichroic atomic vapor laser lock (DDAVLL) method [16, 17]. Gaussian distribution of radial laser intensity is obtained using the single-mode optical fiber. To achieve the repeated interaction of the laser light with Rb atoms, the power of the acousto-optical modulator (AOM) first-order diffracted beam is modulated and transmitted through the cell. The linear polarization of the laser light is assured by the high-quality linear polarizer. The Pockels cell and the $\lambda/4$ plate are used to modulate the polarization of the laser beam, so that pure σ^+ circular polarization is obtained when no voltage is applied to the cell and some percent of the σ^- light is produced otherwise. The arbitrary signal generator is programmed by the computer, whereas its two synchronized outputs control the AOM and the Pockels cell. The Rb cell containing 30 Torr of Ne buffer gas is 8 cm long and 25 mm in diameter. The difference between the $F_g = 2 \rightarrow F_e = 1$ transition frequencies in a vacuum and our buffer gas cell is approximately −20 MHz [18], which in total gives one photon detuning of −90 MHz in the experiment, due to −110 MHz AOM frequency shift in the first diffraction maximum. The Rb cell was heated using hot air circulating around the cell. The Rb vapor is shielded from external

magnetic fields by the triple μ-metal layers, which reduce stray magnetic fields below 10 nT. To obey two-photon detuning, a long solenoid placed around the Rb cell produces a controllable longitudinal magnetic field in the range of $\pm$ 40 μT. The estimated magnetic field error is on the order of 10 nT. The transmitted σ^- laser light is extracted with $\lambda/4$ plate and polarizing beam splitter (PBS). The σ^- laser intensity as a function of applied magnetic field is measured by the photodetector and recorded by the storage oscilloscope. The intensities of polarization pulses were 4.9 and 0.95 mW cm^{-2} and the cell temperature was set to 67 ° C.

The signals applied to the AOM and the Pockels cell are shown in figure 2(a). We first generate a 400 μs pulse, in which 15% of the optical power is carried by σ^- polarized photons. Two coherent light fields (strong σ^+ and weak σ^-) pump the Rb atoms into the nonabsorbing dark state. After completion, the voltage on the Pockels cell is set back to zero and the AOM is synchronously turned off for 60 μs. During this dark interval, Zeeman coherence makes a Larmor precession in the external magnetic field. After this dark interval, the Pockels cell again generates the same elliptically polarized pulse and the AOM is turned back on to produce five times weaker light. This second pulse, with 400 μs duration, probes the previously created Zeeman coherences. Finally, we return the full beam power and set circular σ^+ polarization during 5 ms to reset atoms back in the ground state before the next pulse train. In this way, we produced Ramsey-like measurements with two temporally separated polarization pulses.

3. Results and discussions

The σ^- transparency signals measured for three different values of the external magnetic field are shown in figure 2(b). As expected, in the case of zero magnetic field, we see no Ramsey fringes in the transparency curve. We measured the linear dependence of fringes' frequency on the applied magnetic field with a slope close to magnetic sublevels energy splitting factor of ^{87}Rb hyperfine state $5^2S_{1/2}$ $F_g = 2$ (not shown). Due to decoherence processes, the oscillations are dumped.

The noise in figure 2(b) comes from the low transparency of the σ^- signal and the photo detector's electronic noise. The measured value of signal to noise ratio is 12 dB in the 21 MHz bandwidth of the entire data acquisition system. From these data, we were able to reconstruct the EIT resonances at different times during the probe pulse propagation. First, we set $t = 0$ at the beginning of the second polarization pulse. Next, we take the values of the σ^- transparency at a particular time instant t for all magnetic field values and plot this data set using the B-spline routine. EIT resonances obtained this way, as shown in figure 3(a), show clean oscillations because the reconstruction process takes one transparency value at a time and therefore eliminates the noise itself. However, because of measurement uncertainty, these oscillations are not perfect, i.e., fringes of the same order have slightly different amplitudes. The reconstructed EIT resonances are shown in figure 3 for the Rb density of $\sim 4.5 \cdot 10^{11}$
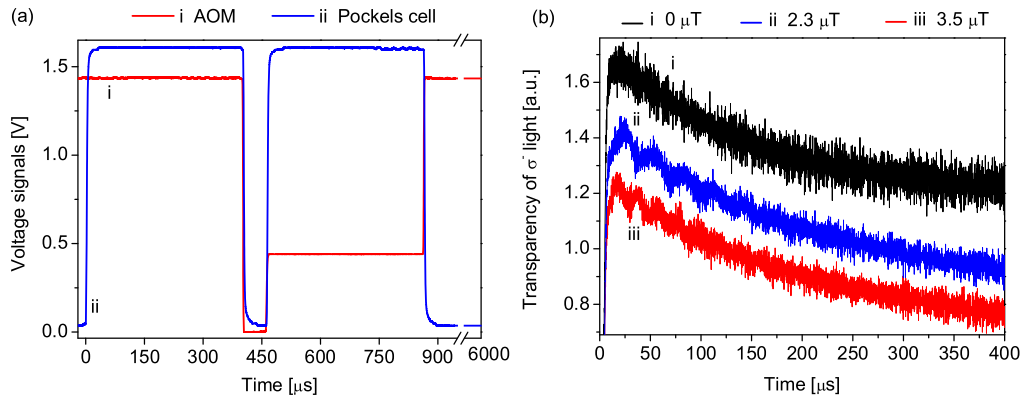
Figure 2. (a) The signals used in the experiment: AOM (i) and Pockels cell (ii). (b) Transparency of the σ^- light measured during the second probing pulse for various magnetic fields: $0\,\mu$T (i), $2.3\,\mu$T (ii), and $3.5\,\mu$T (iii).
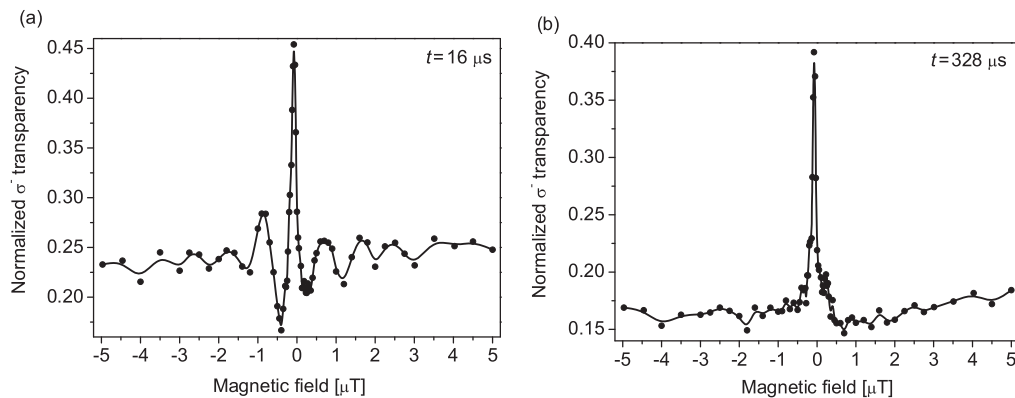

Figure 3. Reconstructed Zeeman EIT resonances from the σ^- transparency signal at different time moments t from the beginning of the second polarization pulse: (a) $t = 16\,\mu$s and (b) $t = 328\,\mu$s.

cm^{-3} and the laser beam diameter of 1.3 mm. Ramsey fringes were observed at EIT resonances for $t \lesssim 196\,\mu$s and vanish at later moments due to the finite lifetime of Zeeman coherence. The decay rate of Zeeman coherences γ_2 was obtained by fitting the σ^- transparency signal (ii) from figure 2(b) to function $\ \ y = A_1 e^{-\gamma_1 t} + A_2 e^{-\gamma_2 t} \sin(\omega t + \varphi_0)$ (not shown). The measured γ_2 value is on the order of $\sim 9000\,\text{s}^{-1}$. In figure 3(a), an EIT resonance with oscillation pattern at $t = 16\,\mu$s is shown. In figure 3(b), an EIT curve at $t = 328\,\mu$s with no fringes is presented.

4. Conclusion

We experimentally studied the Zeeman coherence using Ramsey fringes obtained at the transparency signal of the probe σ^- laser field in the presence of the external magnetic field. Temporal evolution of Zeeman EIT resonances in Rb buffer gas cell were also presented. The first polarization pulse containing weak σ^- and strong σ^+ fields was used to create Zeeman coherences in Rb atoms. The subsequent weaker probe pulse with the same polarization state was produced to probe these coherences. The laser beam was completely turned off between the pulses to enable free evolution of the dark state in the magnetic field. The oscillatory pattern on the reconstructed EIT curves obtained soon

after the second pulse generation disappeared at later times because of the various decoherence processes.

References

[1] Fleischhauer M, Imamoglu A and Marangos J P 2005 Electromagnetically induced transparency: optics in coherent media *Rev. Mod. Phys.* **77** 633–73
[2] Phillips D F, Fleischhauer A, Mair A, Walsworth R L and Lukin M D 2001 Storage of light in atomic vapor *Phys. Rev. Lett.* **86** 783–6
[3] Ramsey N F 1956 *Molecular Beams* (Oxford: Oxford University Press)
[4] Zibrov A S and Matsko A B 2001 Optical Ramsey fringes induced by Zeeman coherence *Phys. Rev.* A **65** 013814

[5] Shuker M, Firstenberg O, Sagi Y, Ben-kish A, Davidson N and Ron A 2008 Ramsey-like measurement of the decoherence rate between Zeeman sublevels *Phys. Rev.* A **78** 063818

[6] Xiao Y, Novikova I, Phillips D F and Walsworth R L 2006 Diffusion-induced Ramsey narrowing *Phys. Rev. Lett.* **96** 043601

[7] Xiao Y, Novikova I, Phillips D F and Walsworth R L 2008 Repeated interaction model for diffusion-induced Ramsey narrowing *Opt. Express* **16** 14128

[8] Zanon T, Guerandel S, Clercq de E, Holleville D, Dimarcq N and Clairon A 2005 High contrast Ramsey fringes with coherent-population-trapping pulses in a double lambda atomic system *Phys. Rev. Lett.* **94** 193002

[9] Pati G S, Salit K, Tripathi R and Shahriar M S 2008 Demonstration of Raman Ramsey fringes using time delayed optical pulses in rubidium vapor *Opt. Comm.* **281** 4676–80

[10] Grujić Z D, Mijailović M, Arsenović D, Kovačević A, Nikolić M and Jelenković B M 2008 Dark Raman resonances due to Ramsey interference in vacuum vapor cells *Phys. Rev.* A **78** 063816

[11] Valente P, Failache H and Lezama A 2003 Temporal buildup of electromagnetically induced transparency and absorption resonances in degenerate two-level transitions *Phys. Rev.* A **67** 013806

[12] Meinert F, Basler C, Lambrecht A, Welte S and Helm H 2012 Quantitative analysis of the transient response of the refractive index to conditions of electromagnetically induced transparency *Phys. Rev.* A **85** 013820

[13] Park S J, Cho H, Kwon T Y and Lee H S 2004 Transient coherence oscillation induced by a detuned Raman field in a rubidium Λ system *Phys. Rev.* A **69** 023806

[14] Greentree A D, Smith T B, Echaniz de S R, Durrant A V, Marangos J P, Segal D M and Vaccaro J A 2002 Resonant and off-resonant transients in electromagnetically induced transparency: Turn-on and turn-off dynamics *Phys. Rev.* A **65** 053802

[15] Steck D A 2008 *Rubidium 87 D Line Data* (http://steck.us/ alkalidata/rubidium87numbers.pdf)

[16] Wasik G, Gawlik W, Zachorowski J and Zawadzki W 2002 Laser frequency stabilization by Doppler-free magnetic dichroism *Appl. Phys.* B **75** 613–9

[17] Petelski T, Fattori M, Lamporesi G, Stuhler J and Tino G M 2003 Doppler-free spectroscopy using magnetically induced dichroism of atomic vapor: a new scheme for laser frequency locking *Eur. Phys. J.* D **22** 279–83

[18] Demtröder W 2002 Laser spectroscopy *Basic Concept and Instrumentation* (Werlag Berlin Heidelberg New York: Springer)

Effects of laser beam diameter on electromagnetically induced transparency due to Zeeman

coherences in Rb vapor

Effects of laser beam diameter on electromagnetically induced transparency due to Zeeman coherences in Rb vapor

S N Nikolić, A J Krmpot, N M Lučić, B V Zlatković, M Radonjić and B M Jelenković

Institute of Physics, University of Belgrade, Pregrevica 118, 11080 Belgrade, Serbia

E-mail: stankon@ipb.ac.rs

Abstract

We experimentally studied the effects of laser beam diameter on electromagnetically induced transparency (EIT) due to Zeeman coherences induced by a laser resonant with the hyperfine transition $F_g = 2 \rightarrow F_e = 1$ of ^{87}Rb in a rubidium buffer gas cell. We use two laser beams of Gaussian intensity radial profile for laser beam diameters of 6.5 and 1.3 mm, laser intensities in the range of 0.1–35 mW cm^{-2} and cell temperatures between 60 and 82 °C. The results show that the amplitude of the normalized EIT resonance has a maximum at a laser intensity which depends on laser beam diameter and cell temperature. The laser intensity corresponding to the maximum EIT amplitude is higher for a smaller laser beam and higher cell temperature. The linewidth of Zeeman EIT resonance varies nearly linearly with laser intensity, almost independent of cell temperature and laser beam diameter.

PACS numbers: 03.65.Fd, 03.65.Sq

(Some figures may appear in colour only in the online journal)

1. Introduction

Electromagnetically induced transparency (EIT) is a coherence phenomenon characterized by narrow transmission resonance of a laser beam through alkali atom vapor [1]. It is essential for fields such as slow and stored light [2], lasing without inversion [3], frequency mixing [4], etc. Important devices such as atomic frequency standards [5] and magnetometers [6] are based on EIT. The optimization of all these processes and devices is therefore directly conditioned on achieving better EIT properties.

The average time-of-flight of an atom through the laser beam limits the EIT amplitudes and linewidths. In order to prolong interaction time and thus the dark states lifetime, an inert buffer gas is added to atomic vapor to slow down the diffusion of the coherently prepared atoms through the laser beam. The linewidth, governed by the ground state relaxation and laser power, is reduced by several orders of magnitude due to the Dicke effect [7]. Linewidths as narrow as 30 Hz are obtained [8].

Hyperfine EIT resonance is formed as a coherent superposition of two ground hyperfine levels while EIT resonance in the Hanle configuration is based on Zeeman coherences between magnetic sublevels of a given hyperfine state of the alkali atom electronic ground state. Cell temperature affects differently hyperfine coherences than Zeeman coherences. For the former, it is found that linewidths vary inversely with density [9, 10]. The linewidth is a linear function of laser intensity and the slope of the linear curve decreases as the cell temperature increases. At lower temperatures than in [9, 10], in the range 30–60 °C, linewidth can be independent on cell temperature, as shown in [11]. On the other hand, EIT resonances due to Zeeman coherence are nearly independent of cell temperature [10]. In addition, the behavior of EIT as a function of laser beam diameter [12], optical depth [13], laser intensity [14, 15] and laser beam profile [16, 17] was investigated.

In this paper, we analyze the properties of Zeeman EIT resonances under different parameters in order to obtain optimum EIT contrast and linewidths, which is essential
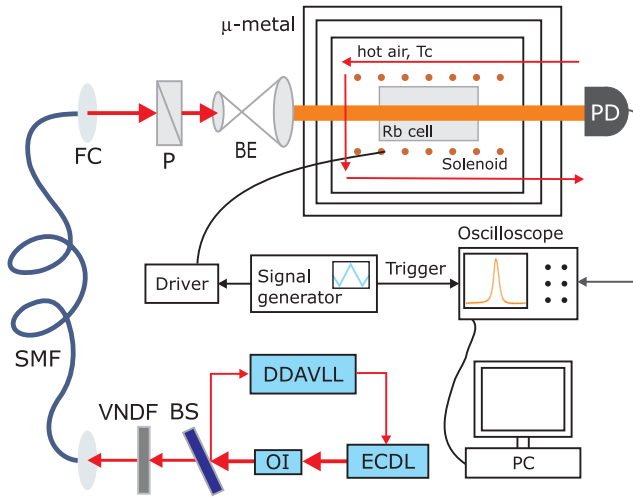
Figure 1. Experimental setup: ECDL—external cavity diode laser; OI—optical insulator; DDAVLL—Doppler-free dichroic atomic vapor laser lock; BS—beam splitter; VNDF—variable neutral density filter; SMF—single-mode fiber; FC—fiber coupler; P—polarizer; BE—beam expander; PD—large-area photodiode. Hot air is used for heating the cell.

for application of Zeeman coherences, like efficient slowing down of light pulses in the cell [18] as well as their storage. Zeeman coherences were induced by the laser locked to the $F_g = 2 \rightarrow F_e = 1$ transition in ^{87}Rb, contained in the cell with 30 Torr of Ne. We analyze EIT for two laser beam diameters and a wide range of laser intensity and cell temperature. Unlike the hyperfine EIT, there are no detailed studies on the behavior of Zeeman EIT when the main experimental parameters vary.

2. Experimental setup

The experimental setup is shown in figure 1. The external cavity diode laser is frequency locked to the hyperfine $F_g = 2 \rightarrow F_e = 1$ transition of the D_1 line in ^{87}Rb by using the Doppler-free dichroic atomic vapor laser lock method [19, 20]. Gaussian distribution of laser intensity radial dependence is achieved by the single-mode optical fiber. For adjusting the laser beam diameter, a beam expander is used. The linear polarization of laser light is ensured by a high-quality polarizer. Laser beam intensity is controlled by the variable neutral density filter. A Rb cell with 30 Torr of Ne as the buffer gas is 8 cm long and 25 mm in diameter. The Rb vapor is shielded from external magnetic fields by the triple layer of μ-metal which reduces stray magnetic fields below 10 nT. In order to obey two-photon detuning in the Hanle experiment, a long solenoid placed around the Rb cell produces a controllable longitudinal magnetic field in the range of $\pm 20\,\mu$T. The intensity of transmitted laser light as a function of applied magnetic field was monitored by the photodiode and recorded by the storage oscilloscope. The Rb cell was heated up to a certain temperature by using circulating hot air around the cell. The advantage of this system in comparison with electrical heating is avoiding the stray magnetic field inside the μ-metal that is inevitably introduced by heating current.
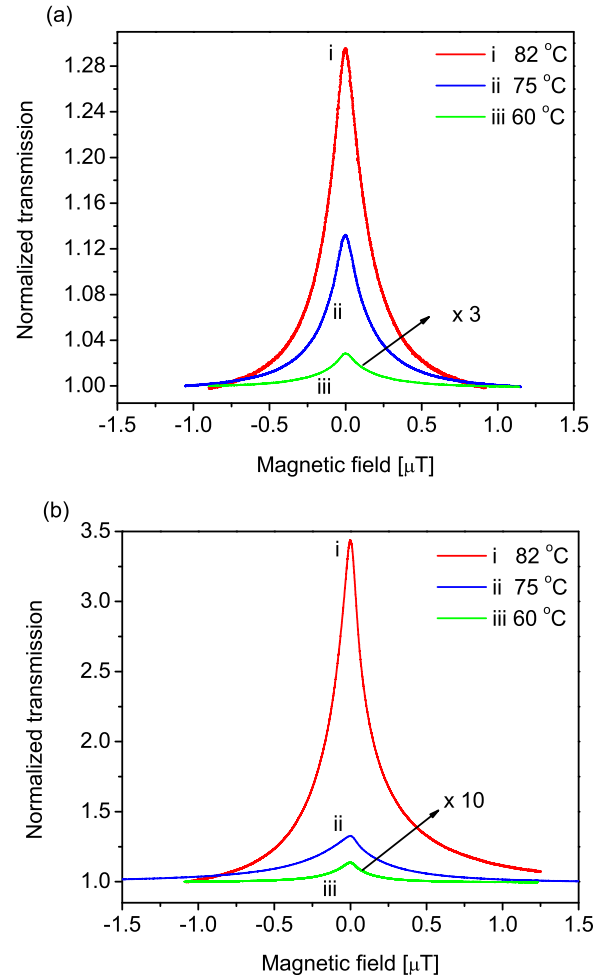

Figure 2. Measured EIT resonances for Gaussian laser beams of diameter (a) $D = 6.5$ mm and (b) $D = 1.3$ mm. Resonances are measured for an overall laser beam intensity of 3.3 mW cm^{-2} at temperatures of 60, 75 and 82 °C.

3. Results and discussions

We present measured EIT resonances in the Hanle configuration obtained with laser beams of Gaussian radial intensity profile for cell temperatures of 60, 75 and 82 °C and laser beam diameters of 1.3 and 6.5 mm. The intensity range covered in the experiment was 0.1–10 mW cm^{-2} for wide and 0.1–35 mW cm^{-2} for narrow laser beams. EIT resonances presented in this paper are obtained after normalizing measured resonances to the transmission signal away from Raman resonance. Examples of experimentally obtained EIT resonances for wide and narrow Gaussian laser beams at three temperatures are given in figure 2.

As can be seen in figure 2, the amplitudes of Zeeman EIT increase with cell temperature, and this effect is particularly strong for narrower laser beams.

The EIT amplitude dependence on overall laser beam intensity measured at different temperatures, for wide and narrow laser beams, is shown in figures 3(a) and (b), respectively. As can be seen, the highest cell temperature with the smaller laser beam diameter gives the strongest EIT resonances. Higher temperatures mean larger atomic density and number of atoms coherently prepared in the dark state. As the laser beam diameter gets smaller, the contribution of wings
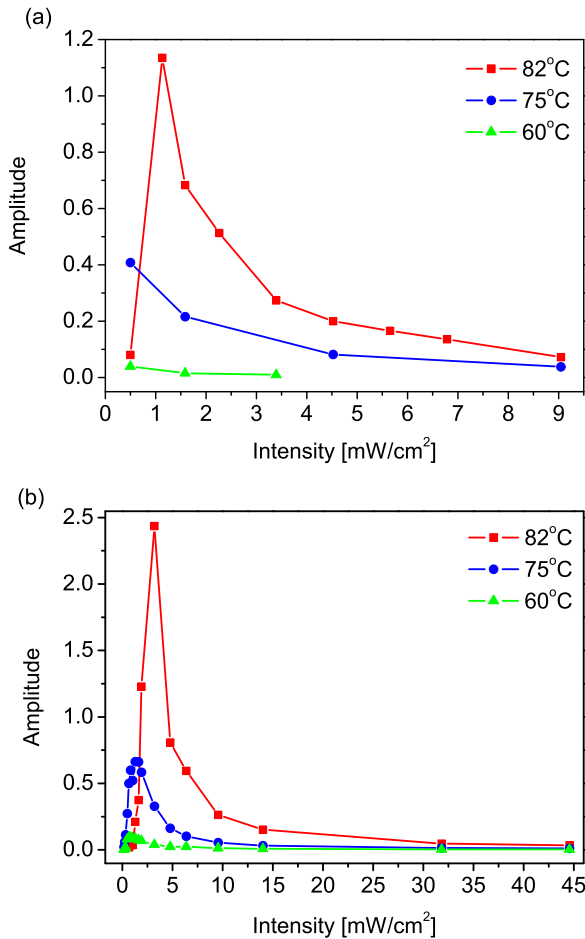
Figure 3. Experimental dependences of EIT amplitudes on overall light intensity for Gaussian laser beams of diameter (a) 6.5 mm and (b) 1.3 mm at temperatures of 60, 75 and 82 °C.
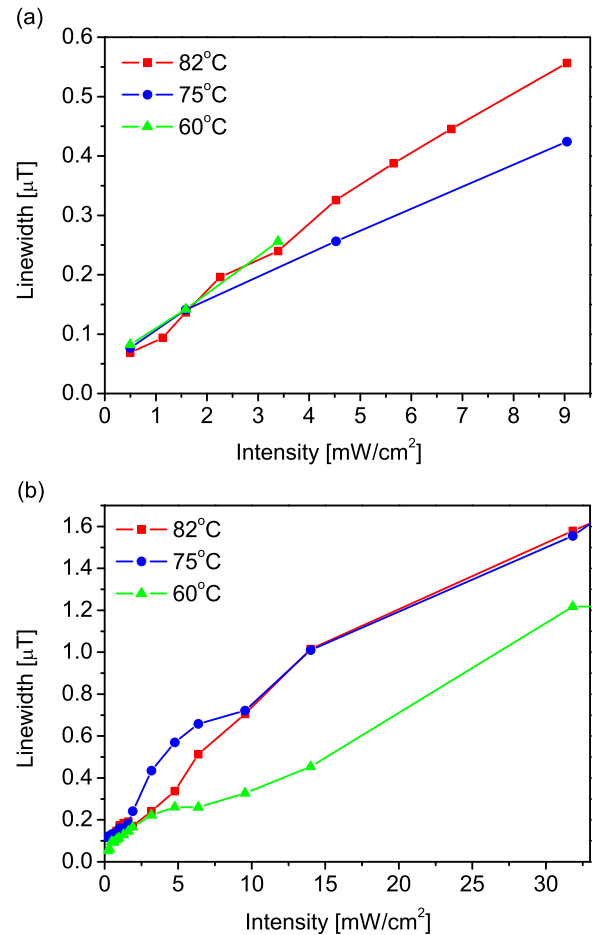

Figure 4. Experimental dependences of EIT linewidth on overall laser beam intensity for Gaussian laser beams of diameter (a) 6.5 mm and (b) 1.3 mm at three different temperatures.

of the Gaussian laser beam to two-photon type resonance like EIT is enhanced.

In figure 4 the EIT linewidth as a function of laser intensity at three different cell temperatures is shown for two Gaussian laser beam diameters. The dependence of EIT linewidths on laser intensity, for either wide or narrower laser beams, is apparently independent of cell temperature. Such behavior of Zeeman EIT with cell temperature is shown in the pump–probe laser configuration in [10]. Ultra narrow Zeeman EIT resonances with linewidths below 100 nT were achieved because of careful elimination of stray magnetic fields inside the triple antimagnetic shielding surrounding the Rb buffer gas cell.

4. Summary

We carried out an experimental study of the behavior of EIT resonances due to Zeeman coherences among sublevels of the ^{87}Rb hyperfine state $F_g = 2$ in a Rb buffer gas cell of 8 cm length, 25 mm diameter and 30 Torr of Ne buffer gas. The dependence of EIT on laser beam diameter (6.5 and 1.3 mm), laser intensity (0.1–35 mW cm^{-2}) and Rb cell temperature (60–82 °C) reveals that the highest contrast and amplitude to linewidth ratios are obtained with the narrower laser beam at about 5 mW cm^{-2}.

References

[1] Fleischhauer M, Imamoglu A and Marangos J P 2005 *Rev. Mod. Phys.* **77** 633–73
[2] Phillips D F, Fleischhauer A, Mair A, Walsworth R L and Lukin M D 2001 *Phys. Rev. Lett.* **86** 783–6
[3] Scully M O, Zhu S and Gavrielides A 1989 *Phys. Rev. Lett.* **62** 2813–6
[4] Harris S E, Field J E and Imamoğlu A 1990 *Phys. Rev. Lett.* **64** 1107–10
[5] Knappe S, Shah V, Schwindt P D, Holberg L, Kitching J, Liew L A and Moreland J 2004 *Appl. Phys. Lett.* **85** 1460–2
[6] Fleischhauer M, Matsko A V and Scully M O 2000 *Phys. Rev.* A **62** 013808
[7] Dicke R H 1953 *Phys. Rev.* **89** 472–3
[8] Erhard M and Helm H 2001 *Phys. Rev.* A **63** 043813
[9] Sautenkov V A, Kash M M, Velichansky V L and Welch G R 1999 *Laser Phys.* **9** 889–93
[10] Figueroa E, Vewinger F, Appel J and Lvovsky A L 2006 *Opt. Lett.* **31** 2625–7
[11] Deng J L, Hu Z F, He H J and Wang Y Z 2006 *Chin. Phys. Lett.* **23** 1745–8
[12] Li L, Peng X, Liu C, Guo H and Chen X 2004 *J. Phys. B: At. Mol. Opt. Phys.* **37** 1873–8

[13] Pack M V, Camacho R M and Howell J C 2007 *Phys. Rev. A* **76** 013801

[14] Javan A, Kocharovskaya O, Lee H and Scully M O 2002 *Phys. Rev. A* **66** 013805

[15] Ye C Y and Zibrov A S 2002 *Phys. Rev. A* **65** 023806

[16] Taichenachev A V, Tumaikin A M, Yudin V I, Stahler M, Wynands R, Kitching J and Hollberg L 2004 *Phys. Rev. A* **69** 024501

[17] Radonjić M, Arsenović D, Grujić Z and Jelenković B M 2009 *Phys. Rev. A* **79** 023805

[18] Nikolić S N, Djokic V, Lučić N M, Krmpot A J, Ćuk S M, Radonjić M and Jelenković B M 2012 *Phys. Scr.* **T149** 014009

[19] Wasik G, Gawlik W, Zachorowski J and Zawadzki W 2002 *Appl. Phys.* B **75** 613–9

[20] Petelski T, Fattori M, Lamporesi G, Stuhler J and Tino G M 2003 *Eur. Phys. J.* D **22** 279–83

Influence of a laser beam radial intensity distribution on Zeeman electromagnetically induced

transparency line-shapes in the vacuum Rb cell

Influence of a laser beam radial intensity distribution on Zeeman electromagnetically induced

transparency line-shapes in the vacuum Rb cell

Influence of a laser beam radial intensity distribution on Zeeman electromagnetically induced transparency line-shapes in the vacuum Rb cell

S M Ćuk, A J Krmpot, M Radonjić, S N Nikolić and B M Jelenković

Institute of Physics, University of Belgrade, Pregrevica 118, 11080 Belgrade, Serbia

E-mail: krmpot@ipb.ac.rs

Abstract
Experimental and theoretical analyses show the effect of laser beam radial intensity distribution on line-shapes and line-widths of the electromagnetically induced transparency (EIT). We used Gaussian and Π (flat top) laser beam profiles, coupling the D_1 transition of ^{87}Rb atoms in the vacuum cell in the Hanle experimental configuration. We obtained non-Lorentzian EIT line-shapes for a Gaussian laser beam, while line-shapes for a Π laser beam profile are very well approximated with Lorentzian. EIT line-widths, lower for Gaussian than for Π, show nonlinear dependence on laser intensity for both laser beam profiles. EIT amplitudes have similar values and dependence on laser intensity for both laser beams, showing the maximum at around 0.8 mW cm^{-2}. Differences between the EIT line-shapes for the two profiles are mainly due to distinct physical processes governing atomic evolution in the rim of the laser beam, as suggested from the EIT obtained from the various segments of the laser beam cross-section.

(Some figures may appear in colour only in the online journal)

1. Introduction

Electromagnetically induced transparency (EIT) [1–3], an effect causing the narrow coherent resonance in a laser transmission through the atomic vapour media, is essential for subjects like slow light and storage of light [4], lasing without inversion [5], frequency mixing [6], Kerr nonlinearities [7], etc. The importance of EIT has become evident after several recent applications, including the development of atomic frequency standards [8, 9] and magnetometers [10, 11]. Prior to EIT, magneto-optical effects, like the ground-state Hanle effect and nonlinear Faraday effect, were studied and their possible application in extremely low magnetic field measurements was shown [12–15]. EIT resonance line-shape and line-width are of interest for many EIT applications. EIT line-shape in alkali vapours contained in gas cells is altered from the fundamental Lorentzian shape of atomic resonances by several factors. In

addition to power broadening, thermal motion of atoms in vacuum cells affects the shape of EIT resonance through a transient evolution of the state of the atoms passing through the laser beam [16–18]. The investigation of the temporal evolution of the optical pumping into a dark state in an atomic beam, with special attention given to the influence of the weak external magnetic field, has been performed in [19]. Studies of EIT dependence on laser beam radius [20], laser intensity [21, 22] and radial profile of the laser intensity [16, 23–26] were performed. Recent experiments have shown effects of different laser modes i.e. a Laguerre–Gaussian laser beam gave narrower EIT than a Gaussian laser beam [27]. In buffer gas cells, filled with a mixture of alkali atoms and inert gas at several Torr, EIT line-shapes are influenced by diffusion of the alkali atoms in and out of a laser beam. Such repeated interaction effectively enables Ramsey-induced narrowing and non-Lorentzian EIT line-shape in media where Doppler
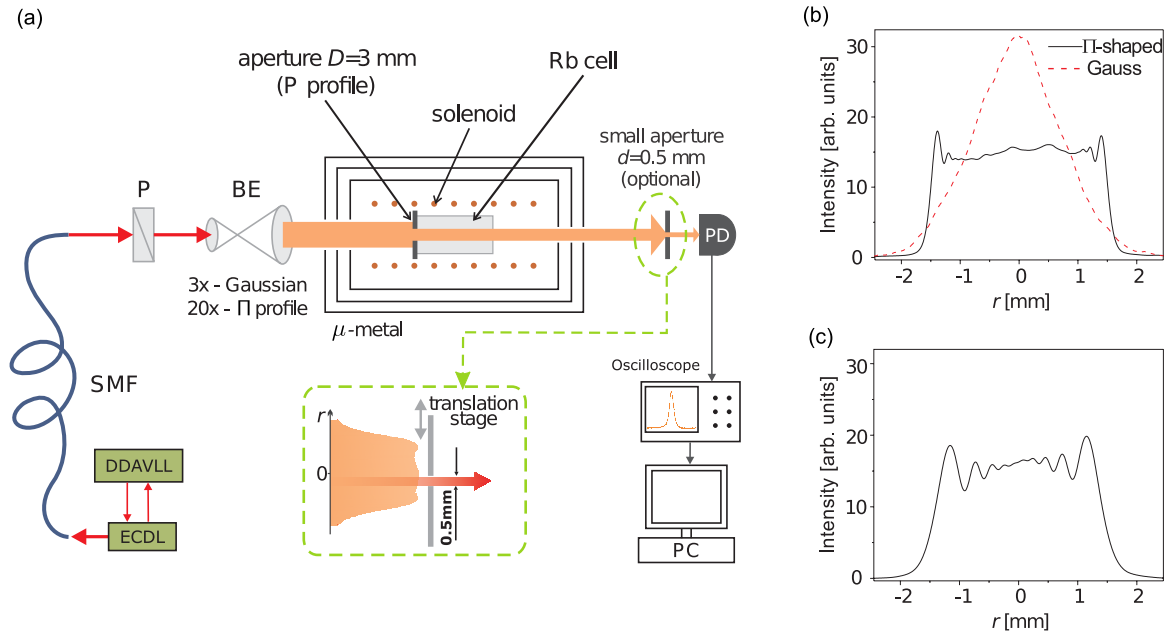
Figure 1. (a) Experimental setup: ECDL—external cavity diode laser; DDAVLL—Doppler-free dichroic atomic vapour laser lock; SMF—single-mode fiber; P—polarizer; BE—beam expander; PD—large area photo diode. For certain measurements the small aperture on the translation stage is placed in the laser beam allowing only a selected part of the laser beam cross-section to reach the detector, while the rest of the laser beam is blocked. Π-shaped beam profiles were recorded by a beam profiler placed at 3 cm (b) and 30 cm (c) from the 3 mm circular aperture. (b) The dashed (red) curve is the profile of the Gaussian laser beam of the same power and diameter as the Π-shaped beam. Note that, in order to have the same overall power of the two laser beams, the peak of the Gaussian beam in the present graph has to have double the value of the flat region of the Π-shaped beam if the diameter of the Gaussian beam is measured at $1/e^2$ of the peak intensity.

broadening is not influential (see [28, 29] and references therein).

Theoretical studies of EIT line-shapes in vacuum cells were mainly carried out assuming a Π (flat top) function for the radial intensity distribution of the laser radiation (see [21] and references therein). Measurements of the EIT line-width as a function of the laser intensity [22], performed with the Gaussian laser beam, show different EIT behaviour with laser intensity than theory [21]— theory predicts wider EIT resonances than experiment, with the discrepancy increasing with the laser intensity. The importance of the laser beam profile on the EIT was indeed demonstrated theoretically for the vacuum [26] and the buffer gas cells [23–25]. Our previous studies have shown that the evolution of the states of the atoms passing through laser beams of different profiles is governed by distinct physical processes [17, 18]. Consequently, line-shapes of EIT resonances obtained from various segments of the laser beam cross-section reflect these differences. It is expected that line-shapes of EIT resonances obtained by detecting whole laser beams of different profiles should also present distinct properties. However, there are no detailed investigations of this kind for vacuum alkali-metal vapour cells. In this work we confirm that the mentioned difference in physical processes significantly affects the overall EIT resonance line-shapes. Besides the results of [17, 18], here we take into account relative amplitudes of EIT resonances from various segments of the laser beam cross-section. The goal of this work is to show how laser intensity affects: (a) differences between the whole beam EIT resonances that are obtained using two laser profiles, (b) contribution of EIT resonances from different parts of the laser beam cross-section to the whole beam EIT and

(c) necessity of using a realistic laser beam profile in calculations for proper modelling of experimental results.

The present study is concerned with the radial intensity distribution effects of the laser beam on Zeeman EIT line-shapes in ^{87}Rb contained in a vacuum cell. The study was performed using the Hanle technique. EIT resonances are due to Zeeman coherences developed in the $F_g = 2$ hyperfine level of ^{87}Rb by using resonant laser light that couples the $F_g = 2$ level to the excited hyperfine level $F_e = 1$. We have investigated the dependence of the EIT line-widths and amplitudes on the laser beam profile for a wide range of laser intensities, 0.1–4 mW cm^{-2}. Experimental results are compared with the results of the theoretical model that calculates the density matrix elements by taking into account all of the Rb atomic levels (with Zeeman sublevels) that are resonantly coupled by the laser light.

2. Experiment

The Zeeman EIT experiment employs a single laser whose radiation frequency and polarization are stable and well controlled. Essential for Zeeman EIT measurements is the elimination of laboratory stray magnetic fields, and creation of a variable, homogeneous magnetic field over the entire volume of the Rb cell, directed along the axis of the cell. For the present studies, a careful control of the laser diameter and radial distribution of laser radiation is also necessary. A schematic of the experiment is given in figure 1. We used the extended cavity diode laser whose frequency is stabilized to the $F_g = 2 \rightarrow F_e = 1$ transition of the D$_1$ line in
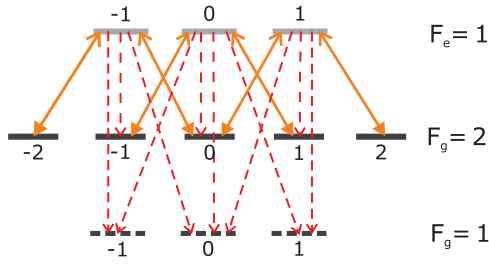
Figure 2. Zeeman sublevels scheme in ^{87}Rb at the D_1 line. The solid lines denote coupling with σ^+ and σ^- components of the linearly polarized laser light. Dashed lines represent spontaneous emission.

^{87}Rb, where F_g and F_e represent the angular momenta of the ground- and excited-state hyperfine levels, respectively. The stabilization scheme is based on the Doppler-free dichroic atomic vapour laser locktechnique [30, 31]. The laser beam is linearly polarized.

The laser beam with Gaussian radial intensity dependence, and 3 mm diameter (measured at $1/e^2$ of the peak intensity), is obtained by the single-mode optical fibre, beam collimator and beam expander. For the Π distribution of the laser beam intensity along its radius, the laser beam behind the fibre is first expanded to about 20 mm, and then the circular diaphragm of 3 mm in diameter is placed over the central part of the laser beam. We used thin foil with a 3 mm hole to obtain the Π profile of laser radiation over the entire length of the Rb cell. The laser beam profile, measured with the commercial beam profilometer, which we consider as the Π radial profile, is given in figures 1(b) and (c), at different distances from the aperture (3 and 30 cm, respectively). In the experiment, this aperture is at the entrance cell window. Laser beam intensity is controlled by the variable neutral density filter. The vacuum Rb vapour cell is 5 cm long and 25 mm in diameter, and is held at room temperature.

The solenoid surrounding the Rb cell produces the magnetic field for the Hanle experiment in the range of $\pm 100\,\mu$T. In order to minimize the stray magnetic fields in the interaction volume, the solenoid and cell are placed inside the triple layered μ-metal. Intensity of the transmitted laser light, as a function of the magnetic field, is detected by the large area photo diode and recorded by the storage oscilloscope. With the small aperture (0.5 mm in diameter) placed in front of the photo diode (with 10 mm in diameter), which we can move along the laser diameter, we were able to obtain EIT resonances only from a small cylindrical segment of the well collimated laser beam.

3. Theoretical model

Zeeman EIT resonances were calculated for the D_1 line transition between hyperfine levels of ^{87}Rb coupled by a linearly polarized laser. The energy level diagram given in figure 2 shows hyperfine levels either coupled to the laser light or populated due to spontaneous emission. The quantization axis is chosen to be parallel to the external magnetic field. The complete magnetic sublevels structure of the transition $F_g = 2 \to F_e = 1$ is considered in the calculations. The theoretical model is based on time-dependent optical Bloch equations for

the density matrix of a moving atom assuming purely radiative relaxation. Equations for density matrix elements related to the ground level $F_g = 1$ are excluded since that level is not coupled by the laser. For additional details about the resulting equations please refer to [18, 26]. It is assumed that after colliding with cell walls, atoms reset into an internal state with equally populated ground magnetic sublevels. Between collisions with cell walls, rubidium atoms interact only with the axially oriented homogeneous magnetic field and spatially dependent laser electric field. Collisions among Rb atoms are negligible due to very low Rb vapour pressure at room temperature, so that an atom moves through the laser beam with constant velocity $\boldsymbol{v} = \boldsymbol{v}_\parallel + \boldsymbol{v}_\perp$, where $\boldsymbol{v}_\parallel$ and $\boldsymbol{v}_\perp$ are longitudinal and transverse velocity components, respectively, with regard to the laser propagation direction. The former affects the longitudinal direction of the atomic trajectory and Doppler shift of the laser frequency seen by a moving atom, while the latter determines the transverse direction of the trajectory and the interaction time. The dependence of the laser intensity on the radial distance r for a Gaussian and Π-shaped profile were modelled using the following equations

$$
\begin{aligned}
I_{\text{Gauss}}(r) &= 2\bar{I}\exp\left(-2\,r^2/r_0^2\right), \\
I_\Pi(r) &= \bar{I}a(1 + \text{erf}(p(r_0 - r)))^2
\end{aligned}
\tag{1}
$$

where r_0 is the beam radius, $\bar{I}$ is the beam intensity (total laser power divided by $r_0^2\pi$), a is the normalization constant and p is a positive parameter affecting the steepness of the profile near $r = r_0$. In our calculations we neglect longitudinal changes of the beam profile compared to transverse ones so that only the transverse direction of the trajectory matters. From the reference frame of the moving atom, the electric field varies and the rate of variation depends only on $\boldsymbol{v}_\perp$. Assume that the transverse projection of the atomic trajectory is given by $\boldsymbol{r}_\perp(t) = \boldsymbol{r}_{0\perp} + \boldsymbol{v}_\perp t$, where $\boldsymbol{r}_{0\perp}$ is the perpendicular component of the atom position vector at $t = 0$. The temporal variation of the laser intensity seen by the atom is given by

$$
I(t) \equiv I(\boldsymbol{r}_\perp(t)) = I(\boldsymbol{r}_{0\perp} + \boldsymbol{v}_\perp t),
\tag{2}
$$

representing the spatial laser intensity variation along the trajectory of the atom in the laboratory frame. Additionally, due to the cylindrical symmetry of the beam profile, spatial dependence becomes purely radial dependence.

The observed resonances in EIT experiments are a probabilistic average of the contributions of many individual, mutually non-interacting atoms. Rb atoms traverse the laser beam at different trajectories with different velocities. Maxwell–Boltzmann velocity distribution, diversity of atomic trajectories, the custom cylindrical symmetric radial profile of the laser electric field, effects of the laser propagation along the cell and induced atomic polarization of the Rb vapour are treated similarly as in [18, 26]. The cell temperature was set to room temperature as in the experiment.

4. Results and discussion

In this section we compare EIT resonances obtained with two laser beam profiles in vacuum Rb gas cells. Previous comparisons between the EIT resonances obtained with
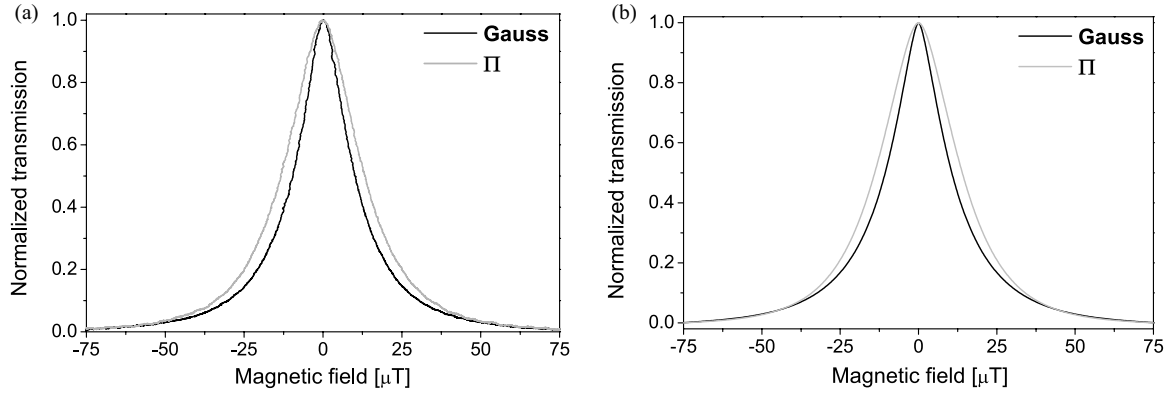
Figure 3. (a) Experimental and (b) theoretical Zeeman EIT resonances obtained by Gaussian and Π laser beam profiles. Laser intensity is 4 mW cm^{-2} and the laser beam diameter is 3 mm for both profiles.
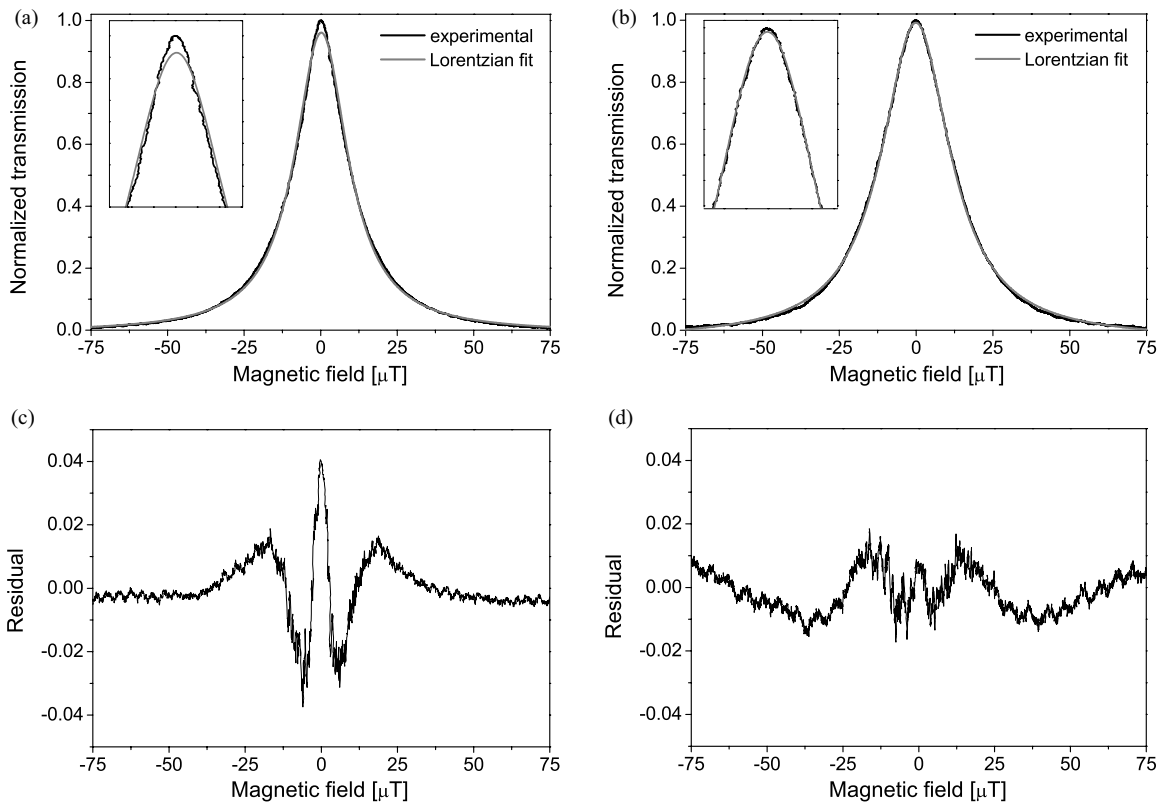

Figure 4. Experimental Zeeman EIT resonances and their Lorentzian fits for the (a) Gaussian and (b) Π laser beam profile. The resonances are obtained under the same conditions like in figure 3(a). Insets show the resonances in the vicinity of their peaks. Residuals, obtained as the difference between the raw data and the corresponding fit, for Gaussian and Π profiles are given in (c) and (d), respectively.

Gaussian and Π laser beam profiles were performed for alkali atoms in buffer gas cells [23–25]. It was calculated, assuming motionless atoms, that EIT line-shapes obtained with a Π laser beam profile are pure Lorentzian. It was also found that the resonances line-shapes are narrower for the Gaussian than for the Π laser beam profile [25]. On the other hand, analysis of the effects of the laser beam shape on EIT in vacuum Rb cells was treated only theoretically [26].

Our EIT resonances were obtained by measuring and calculating the laser transmission as a function of the scanning longitudinal magnetic field, for the Gaussian and the Π laser radial profiles, and for the laser intensity range 0.1–4 mW cm^{-2}. The laser is locked to the $F_g = 2 \rightarrow F_e = 1$ transition of the ^{87}Rb D$_1$ line. Figure 3 shows measured

and calculated resonances for two laser profiles at the laser intensity of 4 mW cm^{-2}. The EIT line-widths and amplitudes, shown and discussed below, were extracted from resonances like these in figure 3, normalized at their maximum values. As seen in figure 3, EIT resonance obtained with the Gaussian laser beam is narrower than the one obtained with the Π laser beam.

If the relaxation of atomic coherences is determined by the radiative decay or by atomic collisions, the line-shapes of the magneto-optical resonances are Lorentzian [16, 23–25, 32]. Experimental resonances and their Lorentzian fits, for the two laser beam profiles, are given in figures 4(a) and (b). It is apparent from these figures, and from residuals between the data and the fits, given in figures 4(c) and (d), that the
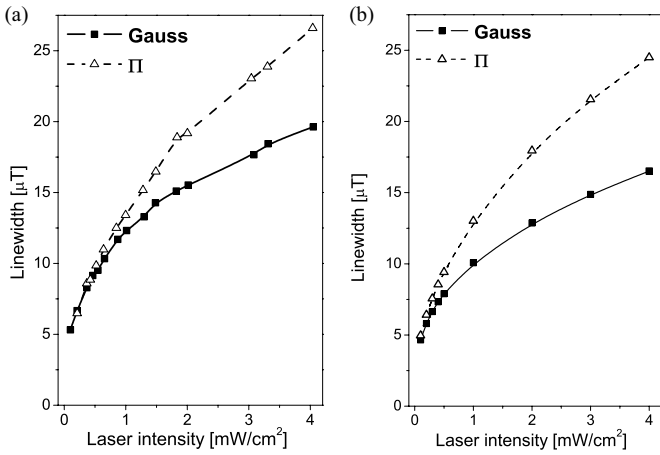
(a)

(b)

Figure 5. Intensity dependence of (a) experimental and (b) theoretical line-widths of Zeeman EIT resonances for Gaussian and Π laser beam profiles. The beam diameter is 3 mm in both cases. The curves are to guide the eye.

Lorentzian function can better fit the resonance with the Π laser beam profile than with the Gaussian profile. This is particularly the case in the vicinity of a resonance peak, as shown in the insets of figures 4(a) and (b). Corresponding *R*-square factors, representing the fit goodness, are $R_{Gauss} = 0.998\,71$ and $R_{\Pi} = 0.999\,341$. These differences between the two profiles remain for all laser intensities.

Figure 4 shows that in an effusive regime of the vacuum cell, the Gaussian laser beam profile gives the EIT line-shape that is narrower in the vicinity of the resonance peak than pure Lorentzian. This is in accordance with the previous results [16] and could be attributed to the time of flight and Ramsey-like narrowing during the free atomic passage through the Gaussian laser beam [17]. In buffer gas cells and diffusive regimes, non-Lorentzian shape (similar to figure 4(a)) is also observed due to the Ramsey effect. However, in buffer gas cells, the Ramsey type narrowing occurs because coherently prepared atoms, after leaving the laser beam and spending time outside of the beam, come back into the laser beam [28]. Line-shapes of the EIT resonances obtained with the Π laser beam profile are Lorentzian. In the case of the Π laser beam profile, laser intensity is constant during the atomic passage through the

beam and there is no Ramsey-like narrowing like in the case of the Gaussian beam [17]. In figure 5 we present variations of EIT line-widths with the laser intensity for the two laser beam profiles. As the laser intensity increases the difference between the corresponding EIT line-widths also increases. Theoretical results show very good agreement with the experiment, both qualitatively and quantitatively. For the entire range of laser intensities EIT line-width increases nonlinearly with intensity, but the slope decreases at higher laser powers. This increase in line-width is due to power broadening. For the range of laser intensities as in this work, analytical results, based on the three-level atomic system, predicted square root dependence on laser intensity [21]. What we have observed in the vacuum gas cell is different from line-width dependence on laser intensity in buffer gas cells where the linear dependence of line-width on the laser intensity is reported [25, 33–35].

Without entering into details of the atom–laser interaction for particular laser beam profile, one can give a qualitative argument as to why a Π-shaped laser beam yields broader resonances than the Gaussian laser beam. In vacuum cells Rb atoms traverse a laser beam without collisions and along straight lines. During the transit through the laser beam, the atomic state is influenced by both the laser electric field and the external magnetic field. The laser electric field prepares the atoms into a dark state determined by the laser polarization. In such a state, absorption probability of the laser light is minimal—a manifestation of EIT. The external magnetic field introduces oscillations of the atomic Zeeman ground-state coherences at the corresponding Larmor frequencies, and also degrades the dark state. At low laser intensities, the influence of the magnetic field is more significant, and the dark atomic state degrades more easily. The omnichanging electric field of the Gaussian laser beam decreases the robustness of the dark state with respect to the external magnetic field. If the dark state is more robust, the transmission decreases more slowly with the magnetic field. Therefore, greater robustness of the EIT with respect to the external magnetic field requires a larger magnetic field to halve the peak transmission and hence yields larger EIT line-widths for the Π-shaped beam than for the Gaussian beam.

Differences in robustness of dark atomic states for the two beam profiles are illustrated in figure 6. We present
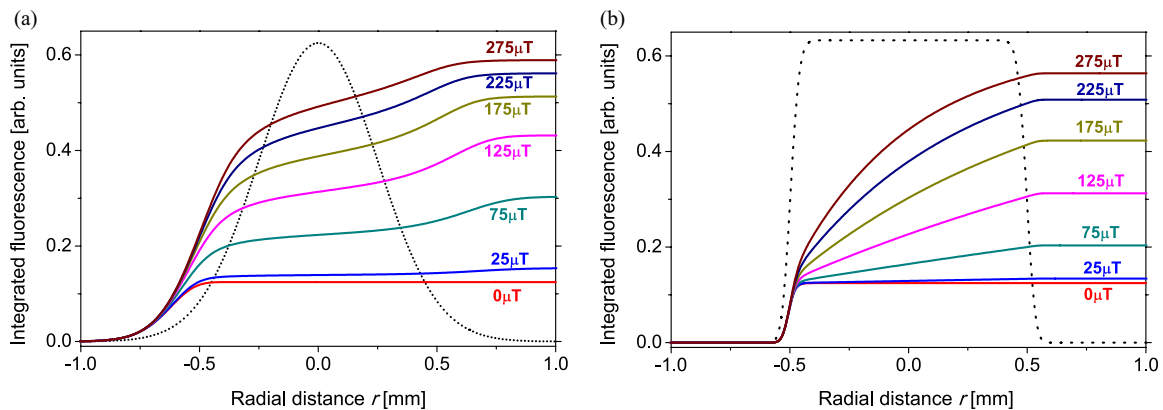
(a)

(b)

Figure 6. Integrated fluorescence along the atomic trajectory during the atomic passage through (a) Gaussian and (b) Π laser beam at different magnetic fields (given by numbers below each curve). Laser intensity is 4 mW cm^{-2} and radial atomic velocity 180 m s^{-1}.
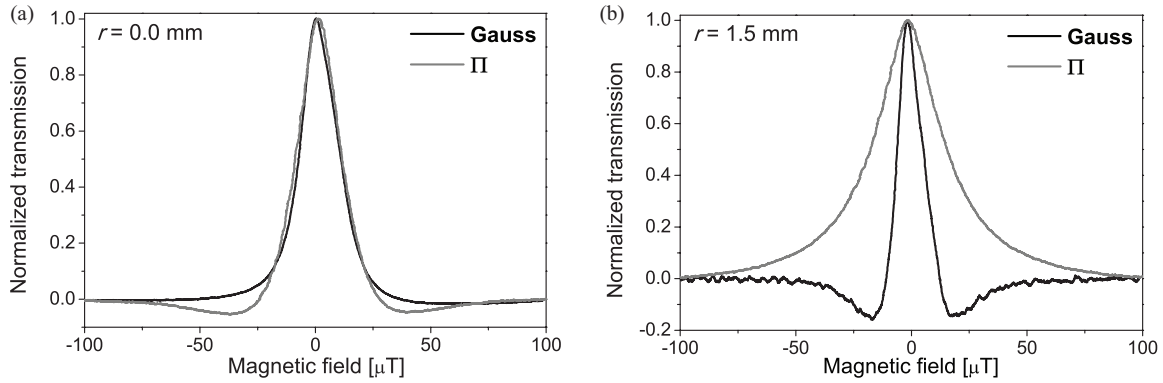
Figure 7. Experimental EIT obtained from only a small circular portion (0.5 mm in diameter) of the laser beam transmitted through the Rb cell when this portion is (a) on the beam axis ($r = 0.0$ mm) and (b) near the beam edge ($r = 1.5$ mm).

fluorescence calculated from the total population of excited Zeeman sublevels of the $F_e = 1$ hyperfine level, integrated along the atomic trajectory that passes through the beam centre, for several values of the external magnetic field. We assume that atom enters the laser beam from the left side with a radial atomic velocity of 180 m s^{-1}, which is the most probable in room temperature Rb vapour. From the curves corresponding to the same magnetic fields, it is apparent that the integrated atomic fluorescence, at the exit of an atom from the laser beam, has increased more for the Gaussian profile than for the Π profile.

In figure 7 we show the EIT obtained by detecting only a portion of the laser beam, defined by (movable) aperture placed in front of the large area photo diode (see section 2 for details). This aperture is centred on the beam axis ($r = 0.0$ mm) for the resonances in figure 7(a), and is near the beam edge ($r = 1.5$ mm) for data in figure 7(b). The EIT resonances obtained near the centre of the laser beam are very similar for two laser beam profiles. A large difference exists between EIT measured with the aperture near the beam edges of these two beam profiles. The Gaussian laser beam produces much narrower Zeeman EIT resonances near its edge than the Π-shaped beam.

Further understanding of what causes different EIT linewidths with two laser beam profiles can be obtained from measurements and calculations of EIT amplitudes at various distances from the beam axis, presented in figures 8(a)–(d). Results are given for two laser beam profiles and for two laser intensities. Amplitudes of EIT resonances are increasing with the distance from the beam axis for both beam profiles, which is more pronounced at higher laser intensities. Amplitudes are the highest in the beam segments that have a high geometrical contribution to the total laser beam cross-section. As seen in figure 7, these are also the segments where the resonances for the Gaussian beam are much narrower than for the Π beam profile. Thus, the results of figures 7 and 8 show that the outer parts of the laser beam cross-section are primarily responsible for the observed differences between EIT line-widths obtained with the two laser beam profiles. Physical mechanisms leading to such differences are explained in detail in [17, 18].

Next, we show the behaviour of the EIT amplitudes obtained with the entire Gaussian and Π laser beams. In
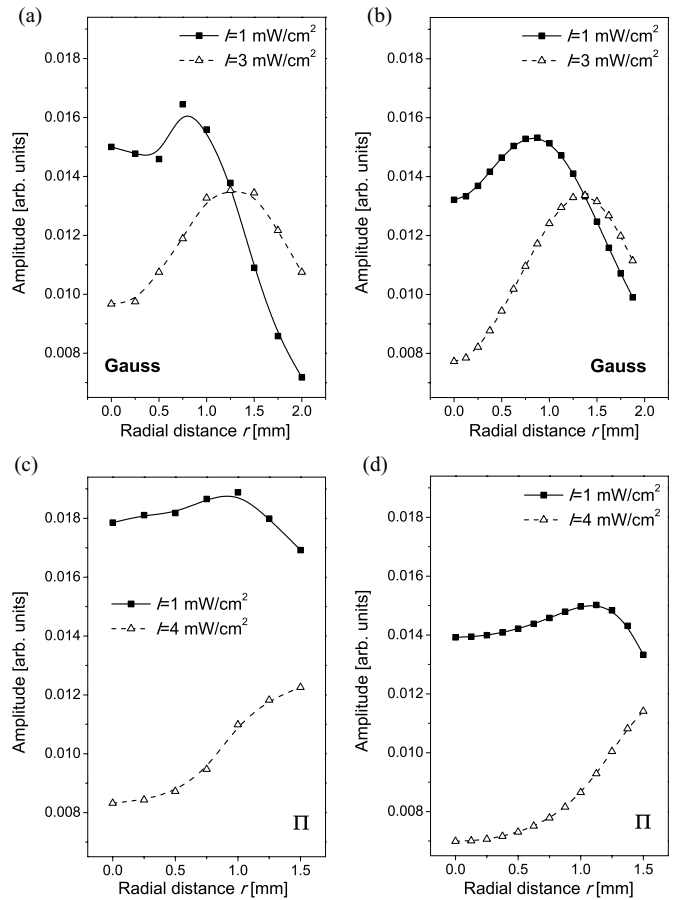

Figure 8. Experimental (a) and (c), and theoretical (b) and (d) amplitudes of the Zeeman EIT resonances obtained at different positions of small aperture along the laser beam radius for the two laser beam profiles.

figure 9 we present measured and calculated EIT amplitudes as a function of the laser intensity. As seen in figure 9, there are no essential differences between EIT amplitudes obtained with the two laser beams. At lower intensities EIT amplitudes show a steep, nearly linear increase with intensity, like in buffer gas cells [36]. The decrease in EIT amplitudes above $\sim$1 mW cm^{-2} is caused by the increase of the population loss due to optical pumping to the $F_g = 1$ hyperfine level of the Rb ground state, which is not coupled by the laser. Indeed, when the re-pumper
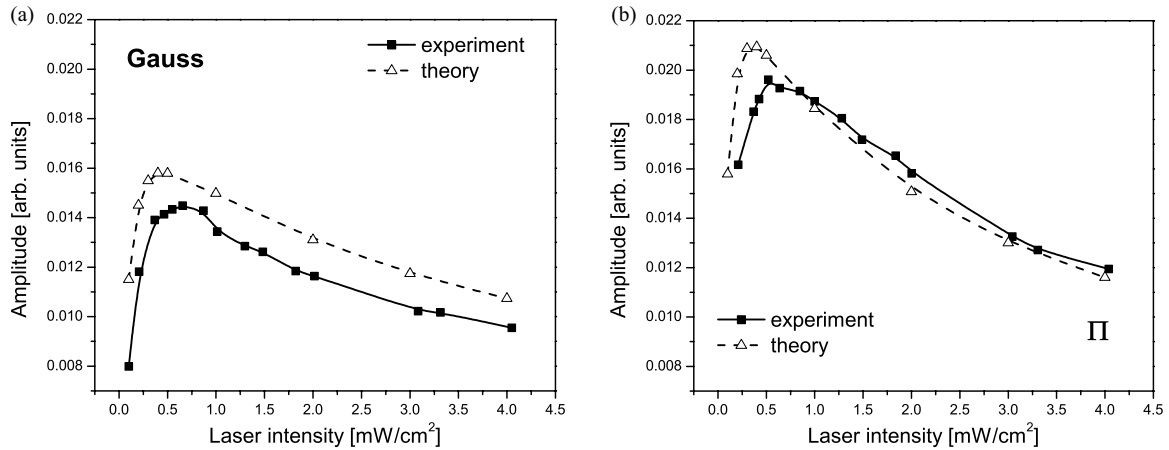
Figure 9. Experimental (solid lines) and theoretical (dashed lines) intensity dependence of Zeeman EIT amplitudes for Gaussian (a) and Π laser beam profile (b). The curves are to guide the eye.

is used to bring the population back to $F_g = 2$ as in [37], the contrast of the amplitudes increases considerably. Figures 9(a) and (b) also show good agreement between experiment and theory.

5. Conclusion

We have demonstrated substantial differences between Zeeman EIT line-shapes and line-widths obtained using two laser radial intensity profiles: Gaussian profile—frequently used in experiments, and Π-shaped laser radial distribution—common in theoretical calculations. Our work is concerned with the effects of these two laser radial profiles on EIT, generated in the Hanle configuration by laser coupling $F_g = 2 \rightarrow F_e = 1$ hyperfine levels in ^{87}Rb atoms in vacuum gas cells. We have shown theoretically and confirmed experimentally the different line-shapes of EIT resonances: those obtained with Π laser beam are very well approximated with Lorentzian, while the Gaussian laser beam profile gives non-Lorentzian Zeeman EIT resonances. EIT resonances are wider for the Π laser beam than for the Gaussian laser beam profile and this difference becomes larger as the laser intensity increases. The study is performed for laser intensities up to 4 mW cm^{-2}. We have shown that major differences in line-widths between two laser profiles are in the regions near the rim of the laser beams. The differences in line-shapes are attributed to different physical processes that Rb atoms undergo during the interaction with the two laser beam profiles. In the wings of the Gaussian laser beam, a Ramsey-like effect can reshape EIT resonances with respect to those near the laser beam centre, as shown in [16, 17]. For the Π profile, optical pumping to the uncoupled ground level dominantly influences the line-shape [18]. The theory demonstrates that the atomic dark state is more sensitive to magnetic field when the atoms are traversing the Gaussian laser beam than when passing through a constant intensity field of the Π laser beam. Larger sensitivity of the atomic dark state to magnetic field variation implies narrower Zeeman EIT line-shapes. The increase of EIT line-widths with the laser intensity is square-root-like for both profiles. Amplitudes of the EIT increase linearly for a laser intensity

up to 0.8 mW cm^{-2} for both profiles and decrease at higher intensities due to pumping to the $F_g = 1$ hyperfine level of ^{87}Rb. Observed dependence of line-widths and amplitudes of the EIT with the laser intensity in vacuum gas cells is different from previous results in buffer gas cells.

References

[1] Alzetta G, Gozzini A, Moi L and Orriolis G 1976 *Nuovo Cimento* B **36** 5–20
[2] Arimondo E 1996 *Prog. Opt.* **35** 257–354
[3] Fleischhauer M, Imamoğlu A and Marangos J P 2005 *Rev. Mod. Phys.* **77** 633–73
[4] Phillips D F, Fleischhauer A, Mair A, Walsworth R L and Lukin M D 2001 *Phys. Rev. Lett.* **86** 783–6
[5] Scully M O, Zhu S Y and Gavrielides A 1989 *Phys. Rev. Lett.* **62** 2813–6
[6] Harris S E, Field J E and Imamoğlu A 1990 *Phys. Rev. Lett.* **64** 1107–10
[7] Schmidt H and Imamoğlu A 1996 *Opt. Lett.* **21** 1936–8
[8] Knappe S, Shah V, Schwindt P D, Holberg L, Kitching J, Liew L A and Moreland J 2004 *Appl. Phys. Lett.* **85** 1460–2
[9] Affolderbach C, Andreeva C, Cartaleva S, Karaulanov T, Mileti G and Slavov D 2005 *Appl. Phys.* B **80** 841–8
[10] Fleischhauer M, Matsko A B and Scully M O 2000 *Phys. Rev.* A **62** 013808
[11] Belfi J, Bevilacqua G, Biancalana V, Cartaleva S, Dancheva Y and Moi L 2007 *J. Opt. Soc. Am.* B **24** 2357–62
[12] Dupont-Roc J, Haroche S and Cohen-Tannoudji C 1969 *Phys. Lett.* **28** 638–9
[13] Haroche S and Cohen-Tannoudji C 1970 *Phys. Rev. Lett.* **24** 974–8
[14] Weis A, Wurster J and Kanorsky S I 1993 *J. Opt. Soc. Am.* B **10** 716–24
[15] Kanorsky S I, Weis A, Wurster J and Hänsch T W 1993 *Phys. Rev.* A **47** 1220–6
[16] Pfleghaar E, Wurster J, Kanorsky S I and Weis A 1993 *Opt. Commun.* **99** 303–8

[17] Krmpot A J, Ćuk S M, Nikolić S N, Radonjić M, Slavov D G and Jelenković B M 2009 *Opt. Express* **17** 22491–8

[18] Krmpot A J, Radonjić M, Ćuk S M, Nikolić S N, Grujić Z D and Jelenković B M 2011 *Phys. Rev. A* **84** 043844

[19] Korsunsky E A, Maichen W and Windholz L 1997 *Phys. Rev. A* **56** 3908

[20] Li L, Peng X, Liu C, Guo H and Chen X 2004 *J. Phys. B: At. Mol. Opt. Phys.* **37** 1873–8

[21] Javan A, Kocharovskaya O, Lee H and Scully M O 2002 *Phys. Rev. A* **66** 013805

[22] Ye C Y and Zibrov A S 2002 *Phys. Rev. A* **65** 023806

[23] Levi F, Godone A, Vanier J, Micalizio S and Modugno G 2000 *Eur. Phys. J. D* **12** 53–9

[24] Gilles H, Cheron B, Emile O, Bretenaker F and Le Floch A 2001 *Phys. Rev. Lett.* **86** 1175–8

[25] Taïchenachev A V, Tumaikin A M, Yudin V I, Stahler M, Wynands R, Kitching J and Hollberg L 2004 *Phys. Rev. A* **69** 024501

[26] Radonjić M, Arsenović D, Grujić Z and Jelenković B M 2009 *Phys. Rev. A* **79** 023805

[27] Anupriya J, Ram N and Pattabiraman M 2010 *Phys. Rev. A* **81** 043804

[28] Xiao Y, Novikova I, Phillips D F and Walsworth R L 2008 *Opt. Express* **16** 14128–41

[29] Xiao Y, Novikova I, Phillips D F and Walsworth R L 2006 *Phys. Rev. Lett.* **96** 043601

[30] Petelski T, Fattori M, Lamporesi G, Stuhler J and Tino G M 2003 *Eur. Phys. J. D* **22** 279–83

[31] Wasik G, Gawlik W, Zachorowski J and Zawadzki W 2002 *Appl. Phys. B* **75** 613–9

[32] Castagna N and Weis A 2011 *Phys. Rev. A* **84** 053421

[33] Erhard M and Helm H 2001 *Phys. Rev. A* **63** 043813

[34] Sautenkov V A, Kash M M, Velichansky V L and Welch G R 1999 *Laser Phys.* **9** 889–93 www.maik.ru/full/lasphys/99/4/lasphys4_99p889full.pdf

[35] Figueroa E, Vewinger F, Appel J and Lvovsky A I 2006 *Opt. Lett.* **31** 2625–7

[36] Knappe S, Wynands R, Kitching J, Robinson H G and Hollberg L 2001 *J. Opt. Soc. Am. B* **18** 1545–53

[37] Kazakov G, Mosets I, Rozhdestvensky Yu, Mileti G, Delporte J and Matisov B 2005 *Eur. Phys. J. D* **35** 445–8

Field-programmable gate array based arbitrary signal generator and oscilloscope for use in slow light and storage of light experiments

Stanko N. Nikolić, Viktor Batić, Bratimir Panić, and Branislav M. Jelenković

Field-programmable gate array based arbitrary signal generator and oscilloscope for use in slow light and storage of light experiments

Stanko N. Nikolić,[1,a)] Viktor Batić,[2] Bratimir Panić,[1] and Branislav M. Jelenković[1]
[1]*Institute of Physics, University of Belgrade, Pregrevica 118, 11080 Belgrade, Serbia*
[2]*Custom Electronics Shack, Belgrade, Serbia*

We present a field-programmable gate array (FPGA) based device that simultaneously generates two arbitrary analog voltage signals with the maximum sample rate of 1.25 MHz and acquires two analog voltage signals with the maximum sample rate of 2.5 MHz. All signals are synchronized with internal FPGA clock. The personal computer application developed for controlling and communicating with FPGA chip provides the shaping of the output signals by mathematical expressions and real-time monitoring of the input signals. The main advantages of FPGA based digital-to-analog and analog-to-digital cards are high speed, rapid reconfigurability, friendly user interface, and low cost. We use this module in slow light and storage of light experiments performed in Rb buffer gas cell. © 2013 AIP Publishing LLC. [http://dx.doi.org/10.1063/1.4811147]

I. INTRODUCTION

In many physics experiments, it is of utmost importance to quickly and accurately generate arbitrary pulses of laser light and measure changes in their shapes and amplitudes upon transmission through different media. Media with electromagnetically induced transparency (EIT) are of special interest since EIT allows for a fine control of the pulse propagation. Electromagnetically induced transparency[1] is a phenomenon characterized by a narrow transmission resonance of a signal light field resonant to a particular atomic transition. EIT can develop in different media, and therefore its origin can be quite different. While EIT in photonic crystals[2] and metamaterials,[3] is a purely classical phenomena, EIT in hot and cold atomic vapors is a quantum coherent effect.[4] The latter type of EIT is a manifestation of coherent population trapping (CPT),[5] or the "dark" state. This refers to a superposition of the two lower levels, coupled by the control and the signal laser fields in Raman resonance to the same upper level. This configuration is known as Λ atomic scheme, leading to the formation of the quantum state not coupled by the signal laser light. Atoms are quickly pumped into the "dark" state, and transmission peak is generated. EIT thus renders the otherwise opaque medium transparent. If the two lower levels are Zeeman sublevels of a given atomic state, one can use different polarization components of a single laser beam for the signal and the control fields. Such EIT is called Zeeman EIT.

Within a narrow spectral band of an EIT resonance, reduced light absorption is accompanied by extremely high dispersion of the index of refraction, $dn/d\omega$. This in turn leads to slow light phenomenon[6] which is a synonym for reduced group velocity of light pulses given by the following expression:

$$v_g = \frac{c}{n + \omega(dn/d\omega)}. \tag{1}$$

Due to strong control over absorption and dispersion of the laser light, the light pulses slowed to only 17 m/s are obtained in media with coherent EIT.[7] In addition, in the strong coherent interaction of light and atomic states, and by smoothly turning the control field off, photonic excitation can be adiabatically mapped into a purely atomic excitation. This atomic excitation can reversibly be restored back to an optical excitation when the control field is turned back on, thus completing the process known as storage of light.[8,9] The storage memory efficiency ξ is defined[10] as probability of retrieving an incoming single photon after storage in an ensemble with EIT

$$\xi = \frac{\int_{\tau}^{\tau+T} |E_{out}(t)|^2 dt}{\int_{-T}^{0} |E_{in}(t)|^2 dt}, \tag{2}$$

where E, T, and τ correspond to electric field, pulse duration, and storage time, respectively. The maximal storage time is determined by the decoherence rate.

Applications of slow light and storage of light effects in the fields of quantum memory, quantum information, and quantum repeaters[4,11–13] require that fractional pulse delay, defined as a ratio of the pulse delay to its duration, should be $\gtrsim 1$. It is necessary to experiment with different waveforms of the control and signal fields in order to exceed this limit.[10,14–19] Several time dependent processes in atomic EIT in buffer gas cells are known to affect the width of EIT, and therefore delay of a light pulse. It was shown[20,21] that diffusion of the coherently prepared atoms out from the laser beam and, after multiple collisions with a buffer gas atoms, coming back into the laser field, narrows the profile of EIT resonance into sub-Lorentzian. This can be beneficial for longer pulse delay and storage efficiency if the atomic coherence evolution time, between the two separated excitation pulses of the Ramsey method,[22] is precisely timed. Enhancing the slow

---

a)Electronic mail: stankon@ipb.ac.rs

probe signal through its interference with transient pulses (precursors)[23] requires precise timing of multiple pulses, and frequent changes of the time sequence. Implementation of quantum protocols with series of pulses for the control of light pulses propagation through several separate EIT media, also needs complex time protocol. We investigate the influence of Ramsey effect on slow light and stored light properties in Rb buffer gas cell.

Main advantages of the FPGA based electronics for use in such applications are low cost and high speed operation enabled by massive parallel architecture. Laser locking circuit[24] performed by the FPGA showed nice benefits of alternative locking schemes. FPGA based servo controller with lock-in amplifier,[25] reconfigurable scanning probe/optical microscope,[26] and fast measurement and control system for the superconducting cavity of a flash free electron laser[27] have been also shown in the past.

We demonstrate below that the application of the FPGA based device linked with analog electronic circuit and a personal computer (PC) application with a graphical user interface (GUI), brings useful and quick control over many parameters in slow light and storage of light experiments. Pulse waveforms and their number in the sequence of pulses, precise timing between pulse formation and detection, and optimization of the control laser intensity can be quickly and conveniently controlled with FPGA. The role of FPGA is to synchronize all time events in the device and to simultaneously send data to the two digital-to-analog converters (DAC) and receive the data from the two analog-to-digital converters (ADC). In addition, FPGA takes care of storing all input and output data samples in the external memory. Usefulness of FPGA is demonstrated through measurements of dependencies of the group velocity of light pulses and of the storage efficiencies on the shape, intensity, and duration of both the signal and the control laser fields. This is performed by efficient control of the laser intensity and polarization and by numerical analysis of the input signals from the photodetectors. Components on the analog electronic circuit provide power supply as well as offsetting and amplifying of the input and the output voltage signals. PC application enables the user to make arbitrary output signals and to monitor and record the input signals in the graphical form in real-time with additional slow light analysis. Since FPGA and PC application communicate and exchange the data over time through universal serial bus (USB) connection, we can say that arbitrary signal generator and simple form of digital oscilloscope are realized in a single device. FPGA immediately responds to all software parameters that can be easily changed using the mouse and the keyboard. The speed of generating and acquiring voltage samples using DAC and ADC chips is independent of the speed of the attached computer.

In the final stage of preparing this paper, we noticed the work of Bowler *et al.*[28] in which authors developed FPGA based arbitrary waveform generator for controlling the trapped ions. However, there are differences between their and our device. We also created a custom signal generator but through embedded mathematical expressions in GUI. We additionally developed real time monitoring of the input signals together with slow light analysis.

II. FPGA OPERATION

The FPGA board we use is commercial Digilent Nexys-2 1200k board that houses a Spartan 3E-1200 FPGA chip, together with additional input and output headers. The FPGA master clock runs at 50 MHz. However, the reduced 25 MHz clock is used in our digital design.

In the slow light experiment, we produce a sequence of custom shaped light pulses by applying voltage pulses to the Pockels cell. Typically, the duration of the light pulses is in the range from $10\,\mu s$ to several ms. This imposes the lower limit to the DAC time resolution to $\sim 1\,\mu s$. On the other hand, since the typical delay of a slow light pulse is $\Delta t_{delay} \geq 5\,\mu s$, the ADC time resolution less than $1\,\mu s$ is acceptable in our measurements. We introduce the signal called *ActionType* in our FPGA program to indicate the real time commands for the FPGA chip.

The first task is to program the FPGA so that the two DAC chips continuously generate periodic signals of the same duration T_{DAC}. Each DAC signal is determined by the total number of samples $N_{DAC} \leq 2000$, the array of samples and the sampling time $\Delta t_{DAC} \geq 800$ ns. The FPGA thus needs 4000 or less 12-bit numbers for both converters and the usage of 16 MB of external memory (RAM) organized in 16-bits units is necessary.[29] At the beginning, both DAC arrays generated by the PC application, are transferred to the RAM (*ActionType* = 1 or 2). Upon receiving the samples, continuous generation of the output signals starts (*ActionType* = 3).

The second FPGA task is to receive the data from the ADC chips with a sampling time Δt_{ADC} over the time interval $[T_a, T_b] \subseteq [0, T_{DAC}]$ (T_a and T_b are integer multiplies of Δt_{DAC}), and store the values in the RAM with the total number of samples $N_{ADC} \leq 10\,000$. FPGA needs at least 4 clock cycles (period of 80 ns) to perform a single read/write procedure over chosen RAM unit. Therefore, the key requirement is to organize the four RAM procedures:

- reading a data sample for DAC1
- reading a data sample for DAC2
- writing a data sample from ADC1
- writing a data sample from ADC2,

so they never overlap in time. This limits the ADC sampling time to $\Delta t_{ADC}^{min} = 4 \times 80$ ns $= 320$ ns. The following algorithm takes care about these requirements. After the start of a digital-to-analog conversion, at the time $n \cdot \Delta t_{ADC}$ ($n \in \mathbb{N}$), FPGA takes 24 bits of data from both ADC chips. The readout data from the ADC1 are written to RAM, and after four clock cycles the same procedure is applied for the ADC2 value. When both writing procedures are completed, FPGA can read new DAC samples from RAM. The third step is to ensure that no readings from ADC chips will occur while the readings of the next output samples are in progress. In this way, after completion of one DAC period, N_{ADC} input samples are stored in the memory and FPGA has to transfer them to the computer. While transfer is in progress, no ADC reading is performed. However, DAC chips work continuously as needed in the experiment. Once the data are transferred to PC, the FPGA starts receiving and writing the ADC bits again at the same memory locations. The FPGA algorithm
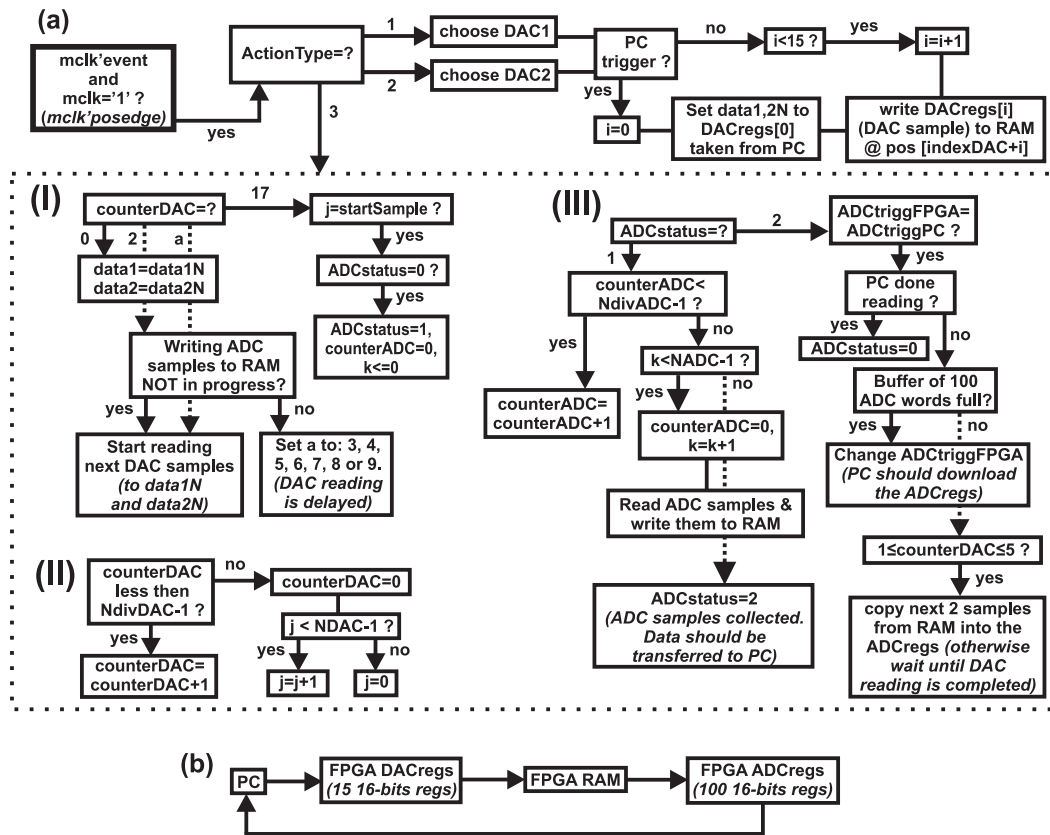
FIG. 1. (a) The simplified FPGA program algorithm and (b) the block diagram showing how the data between the PC and the FPGA board are exchanged. The explanation of all FPGA signals and registers are provided in the supplementary material.[31] Note that the blocks (I), (II), and (III) in (a) are all run in parallel by the FPGA chip.

for handling required procedures is schematically given in Fig. 1(a).

The exchange of the data between the PC and the FPGA is indirectly realized through FPGA registers as shown in Fig. 1(b). On the FPGA side, the communication is realized through slightly amended VHDL design (RegRdWr) of enhanced parallel port (EPP) protocol.[30] This module serves as the interface between the FPGA and the on-board USB controller. It has access to the FPGA registers that store the values of operating parameters which can be set up and changed by the user. We modify the original source code to extend the numbers of single byte registers to maximum value of 256. The organization of these registers is as follows: 23 bytes are related to the FPGA operating parameters for its program control, 30 bytes (15 words) are used for the multiple transfer of the two DACs data samples into the FPGA RAM of the Nexys-2 board, while other 200 bytes (100 words) are used as an intermediary memory buffer when both ADC data are transferred from the external FPGA memory to the PC. Three registers are spare.

III. ANALOG ELECTRONIC CIRCUIT

For generating analog voltage signals, Digilent PmodDA2 module containing two National Semiconductor DAC121S101 digital-to-analog converters were used. The PmodDA2 is connected to the eighth 6-pin peripheral connector of the Nexys-2 board. Both DAC chips share the same input clock pin enabling the user to generate two synchronous but independent output voltage signals in the range from 0 to 3.28 V. The DAC input is a 12-bit number between 0 and 4095. The data bits are transferred by the serial digital interface. The output voltages are driven to the amplifying and offsetting stages and, depending on the state of the DAC jumpers, may be in the following ranges: (0, 3.28) V, (0, 11) V, and (−7, 11) V. Both output impedances are 50 Ω. Analog-to-digital conversion of the input voltage signals is performed with the two Analog Devices AD9224 chips. Both input impedances are 1 MΩ. Input voltages may be in the ranges (−4.5, 0) V, (−11.5, 0) V, and (−7, +7) V depending on the ADC jumpers which define the amplification and the offset of the input signals. ADC 12-bits output data are transferred to the FPGA by parallel digital interface. The maximum sample rate is 40 MHz although we used effectively 2.5 MHz for each conversion, due to external memory issue as discussed in Sec. II. The ADC chips are connected to other seven 6-pin peripheral connectors of the FPGA board. The general schematic of the analog electronic circuit is presented in Fig. 2 (full schematic is provided in the supplementary material[31]). The photograph of the device is shown in Fig. 3 together with marks of the main elements.

IV. USER INTERFACE

The role of the PC application is to communicate with Digilent board in order to send data to and receive data from
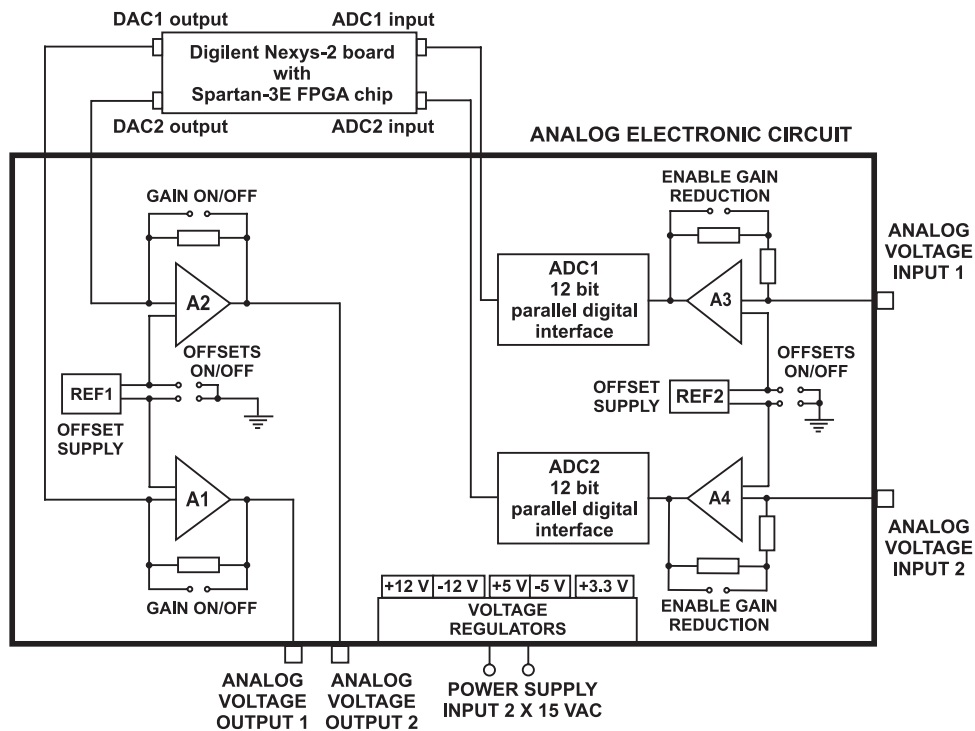
FIG. 2. The simplified scheme of the analog electronic circuit attached to the FPGA board. The circuit contains the power supply unit, the voltage regulators, the ADC chips, and the amplifying and offsetting stages for both input and output voltages.

the FPGA chip. Also, the program allows the user to set up the arbitrary output signals by using mathematical expressions, and to monitor and analyze the input signals in real-time. The PC application developed in Borland C++ Builder 6 consists of the main menu and three tabsheets.

To establish the PC side of the communication between the user interface program and the FPGA registers, the DPCUTIL library provided by Digilent is used. This library contains C++ functions that enable sending and receiving bytes to and from the registers on the FPGA. The FPGA board power supply, transfer of programmable bit files from the PC,

and full communication between the PC and the FPGA registers are realized through a single USB port.

At the start of the program, the user connects to the FPGA using the first option from the main menu. The next step is to indicate the hardware settings of both DAC and ADC jumpers states. The application is then capable of sending correct numbers to the DAC chips in order to generate desired outputs and to convert the ADC numbers to voltage values at the inputs. After completion of these initial tasks, the user can specify the number of samples for the DAC and the ADC chips. The user is required to enter the period T_{DAC} of both output
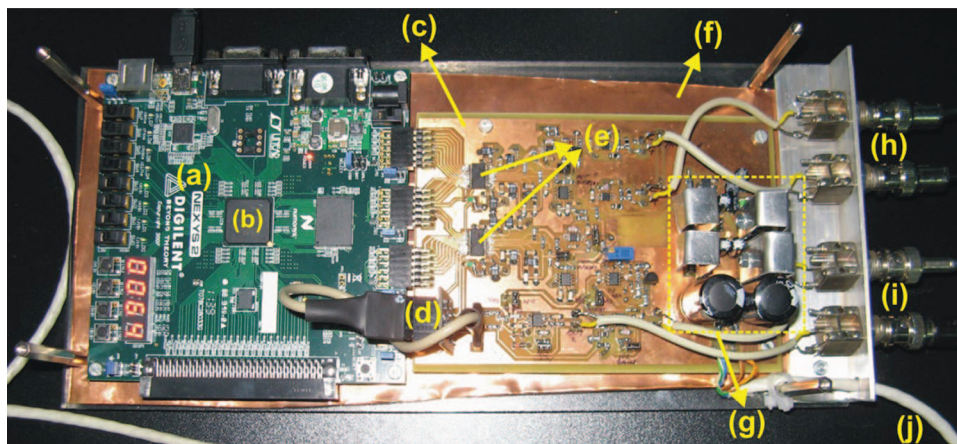

FIG. 3. The device photograph: (a) Digilent Nexys-2 board, (b) Spartan 3E-1200 FPGA chip, (c) printed circuit board, (d) two DAC chips, (e) two ADC chips, (f) the copper plate for grounding the board, (g) voltage regulators from 15 V AC down to +3.3 V, ±5 V, and ±12 V DC, (h) BNC connectors for the two analog voltage inputs, (i) BNC connectors for the two analog voltage outputs, and (j) 15 V AC power supply of the board.

signals which can be divided into several shorter time intervals $T_1, T_2, \ldots, T_n$ ($n \leq 10$). The idea is to shape voltage signals in each time interval (typical time sequence in our slow light experiment consists of voltage pulse during T_1, and zero voltage value during T_2, with the overall duration $T_{DAC} = T_1 + T_2$). Further, the user have to specify whether the time T_{DAC} is fixed so that flexible time parameter $T_n = T_{DAC} - T_1 - \ldots - T_{n-1}$ is changed accordingly. Otherwise, the overall signal duration is $T_1 + T_2 + \ldots + T_n$. Besides these time parameters, the user may specify other parameters relevant for the experiment. We developed the algorithm that calculates the real value of a multi-line string expression. Therefore, user can enter mathematical expressions in the two edit controls, for waveform shaping of both output signals. Formulae can include predefined parameters, independent time variable t, and several of the most frequent mathematical functions. After this step, the user needs to enter numerical values of all parameters. The time interval T_{DAC} is then divided into N_{DAC} time points $t_i = i \cdot T_{DAC}/N_{DAC}$ at which output voltages $V_{DAC1}(t_i)$ and $V_{DAC2}(t_i)$ are calculated after successful compilation of both expressions. Corresponding unsigned 16-bit numbers as inputs to the DAC chips are displayed in the first tabsheet table and then sent to the FPGA. Each parameter value can be quickly changed using keyboard. The software immediately calculates new output voltages and resends the data to the FPGA. There are also options to save and load configuration files containing formulae and parameters' names and values. DAC chips controls are placed on the first tabsheet of the program.

We use the polling operation to gather ADC data from the FPGA external memory. Program checks the FPGA status every 5 ms and if the memory buffer is fully loaded with the input data, the FPGA transfers packets of 100 words into its registers. From the registers data are sent to the PC. This procedure is being repeated until all the data are transferred to the computer. Real-time monitoring of the input signals is performed by using integrated graphic functions in Borland C++ Builder. In this way, a simple digital oscilloscope is realized. Upon receiving new data, the program clears, piece-by-piece, the old graphs in both channels and draws plots with the new data. At any time, user can monitor raw or averaged signals, and change the voltage scales and offsets. These settings are easily performed by the use of mouse and keyboard. Frequently in the experiments, only fractions of the input signals are of interest. Therefore, we enable the user to indicate time interval $[T_a, T_b]$ over which the ADC chips will sample the data either by using track bars or by typing formulae for T_a and T_b. Since the useful time interval is effectively reduced in this way, higher time resolution and increased acquisition speed are achieved. Controls for the ADC chips are placed on the second tabsheet of the program.

We also added the option of dynamic slow light analysis. When the user double-clicks on the scope (or presses F2), program calculates time and voltage coordinates at the given point, time delay of the slow pulse, and corresponding group velocity. These results are recorded for any set of parameters' values and are written in the grid on the third tabsheet of the program. The user can also export all input and slow light data into textual files.

V. SOURCE CODE

The VHDL source code for the FPGA chip and C++ source code for the user interface application are provided in the supplementary material.[31] We used Xilinx Webpack ISE 14.1 and Borland C++ Builder 6 compilers. The compiled WINDOWS executable and FPGA bit files are also provided.
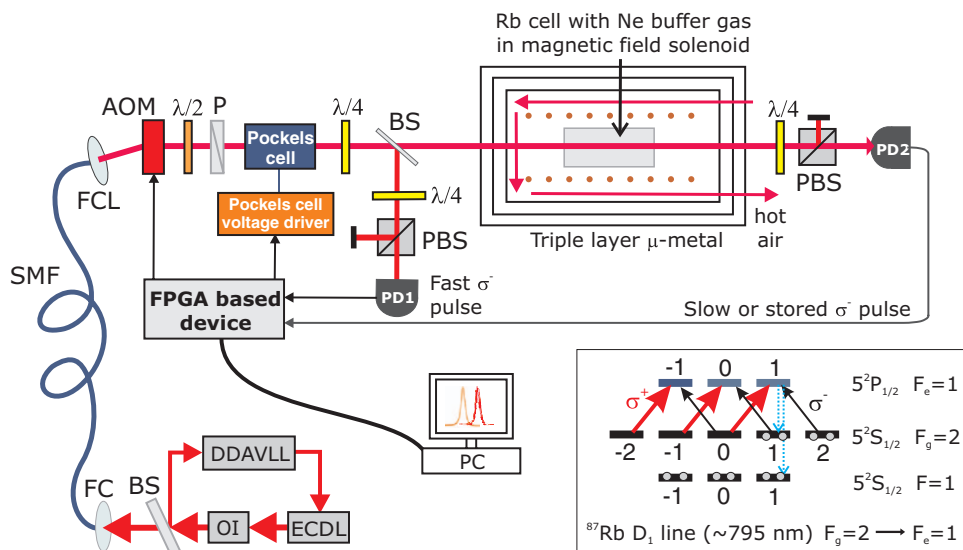

FIG. 4. Experimental setup and the atomic transition used in the experiment. ECDL: external cavity diode laser; OI: optical isolator; DDAVLL: Doppler-free dichroic atomic vapor laser lock; BS: beam splitter; FC: fiber coupler; SMF: single-mode fiber; FCL: fiber collimator; AOM: acousto-optic modulator; P: polarizer; PBS: polarizing beamsplitter; PD: large area photodetector. Output voltage signals from FPGA device control the AOM and the Pockels cell, while signals from the two photodetectors are input signals to the FPGA device.

VI. PERFORMANCE IN THE SLOW LIGHT AND THE STORAGE OF LIGHT EXPERIMENTS

The setup for slow light and storage of light experiments is shown in Fig. 4. Our home-built external cavity diode laser uses semiconductor laser diode (Eagleyard Photonics EYP-RWE-0790-04000-0750-SOT01-0000). The diode is powered by a low noise current supply and temperature controller (Thorlabs ITC102). After passing through the optical isolator (Isowave I-80-T4-L), the laser beam is frequency locked to the hyperfine $F_g = 2 \rightarrow F_e = 1$ transition of the D_1 line in ^{87}Rb by using the Doppler-free dichroic atomic vapor laser lock (DDAVLL) method.[32,33] The laser beam is introduced by the fiber coupler (Newport F-916, MV-10X, FPH-CA4) to a single mode fiber (Oz optics SMJ-3A3A-852-5/125-3-1). After the fiber, the laser beam passes through AOM (Isomet 1206C) and the diffraction maximum of -1 order is used in the experiment. AOM is used as a fast optical switch, to turn the laser beam on and off. The driver of the AOM (Isomet 530-C) has modulation pin which enables the amplitude control of the RF wave passing through the crystal and hence the control of the selected diffraction maximum power. The output voltage from the FPGA device controls the power of the first AOM diffraction maximum: $V_{DAC1} = 0$ V gives $P_{laser} = 0$ and $V_{DAC1} = 3.28$ V gives maximal P_{laser} value. Linear laser beam polarization is adjusted with polarizer (Thorlabs GTH5-B). We use Pockels cell with temperature stabilized x-cut MgO:LiNbO$_3$ crystal (produced by Castech) as the birefringent element to rotate the polarization of the linearly polarized laser light. Pockels cell and $\lambda/4$ plate (Thorlabs WPQ05M-780) are used to set the polarization of the laser beam before entering the Rb cell. With no voltage applied to the Pockels cell, a pure σ^+ polarization of the laser beam is obtained behind the Pockels cell and the $\lambda/4$ plate. By applying a voltage U to the LiNbO$_3$ crystal, the phase difference Γ between the two orthogonal components of a linearly polarized laser beam is induced due to Pockels effect.[34] Using the Jones vectors representation of the polarization states, it can be easily derived that the relative power of the σ^- pulse is

$$P_{\sigma^-}/P_{laser} = \sin^2 \frac{\Gamma}{2} = \sin^2 \frac{C \cdot U}{2}. \tag{3}$$

The parameter $C = 7.6 \times 10^{-3}$ V^{-1} from the above equation is the calibration constant of the crystal. If one wants to obtain a weak and time dependent σ^- polarization component of a laser beam $\eta(t) = P_{\sigma^-}(t)/P_{laser}$ ($\eta \lesssim 30$ %), voltages up to 150 V should be applied to the crystal. We use the home-made high-speed high-voltage amplifier, with amplification of $G = 22.1$. Output analog voltage V_{DAC2} up to 7 V from the FPGA device serves as input to the amplifier, and the amplified signal is applied to the Pockels cell. According to Eq. (3), the output voltage from the FPGA device is

$$V_{DAC2}(t) = \frac{2}{C \cdot G} \arcsin \sqrt{\eta(t)}. \tag{4}$$

In our experiments, we produce the pulses of σ^- polarized light with the Gaussian profile. This pulse propagates together with the strong σ^+ component of the laser beam through the Rb cell containing a natural abundance of Rb isotopes and 30 Torr of Ne buffer gas. The cell is 8 cm long and has a 25 mm diameter. It is placed in a plastic box and heated to $\sim$82 $^{\circ}$C by hot air circulating around the cell. The Rb cell is placed in the solenoid for producing the longitudinal magnetic field and is shielded by the triple layer μ-metal which reduces the stray magnetic fields below 10 nT. Because of the presence of the strong σ^+ field, the resonant σ^- pulse can freely propagate through the otherwise opaque medium due to EIT effect, but with a substantially reduced group velocity. In order to extract only σ^- polarization from the laser beam, we use detection system consisting of a $\lambda/4$ plate followed by a PBS (Thorlabs PBS102) and a home-made photodetector with the large area photodiode (IHTM Belgrade FD80N). The two detection systems are placed before and after the Rb cell so the fast and the slow σ^- polarization pulses, previously split from a single laser beam with a beam splitter (Thorlabs EBS2), can be measured. We use the FPGA device to gather signals from the two photodetectors. These input data are written to the external FPGA memory for the purpose of real-time monitoring and slow light analysis.

We perform the slow light measurements in the two configurations. In the first one, the power of AOM diffraction maximum is kept constant over time, while the Pockels cell generates single Gaussian-shaped σ^- polarization pulse for one DAC period. In the second configuration, we investigate the Ramsey effect on slow light propagation, i.e., the influence of repeated interaction of σ^- pulses with coherently prepared atoms in the dark state on the fractional time delay of the σ^- pulse. We first prepare Rb atoms into the dark state with a weak σ^- pulse of constant intensity (Π-shaped) over the time T_1. Then, we turn the laser beam off by the AOM for the time T_2 to enable a free time evolution of the dark state. Next, we synchronously turn the laser beam back on and generate a weak Gaussian-shaped σ^- pulse of duration T_3 with relative peak power η. We keep pure σ^+ polarization of a laser beam for a long time T_4 to "reset" and optically pump the atoms back in the ground state. Output signals from the FPGA device, in both configurations, control both the AOM and the Pockels cell and have the same overall duration $T_{DAC} = T_1 + T_2 + T_3 + T_4$. According to Eq. (4), output voltages are tailored by following mathematical expressions edited in the PC application:

$$
\begin{aligned}
V_{DAC1}(t) = {}& 3.28 \cdot \text{sgn}(t) \cdot \text{sgn1}(T_1 - t) \\
& + \text{Ctrl1} \cdot \text{sgn}(t - T_1) \cdot \text{sgn1}(T_1 + T_2 - t) \\
& + 3.28 \cdot \text{sgn}(t - T_1 - T_2) \cdot \text{sgn1}(T_1 + T_2 + T_3 - t) \\
& + 3.28 \cdot \text{sgn}(t - T_1 - T_2 - T_3) \\
& \cdot \text{sgn1}(T_1 + T_2 + T_3 + T_4 - t), \\
V_{DAC2}(t) = {}& \text{Ctrl2} \cdot \frac{2}{C \cdot G} \arcsin \sqrt{\eta} \cdot \text{sgn}(t) \cdot \text{sgn1}(T_1 - t) \\
& + 0.00 \cdot \text{sgn}(t - T_1) \cdot \text{sgn1}(T_1 + T_2 - t) \\
& + \frac{2}{C \cdot G} \arcsin \sqrt{\eta} e^{-35 \cdot (t - T_1 - T_2 - T_3/2)^2 / T_3^2} \\
& \cdot \text{sgn}(t - T_1 - T_2) \cdot \text{sgn1}(T_1 + T_2 + T_3 - t) \\
& + 0.00 \cdot \text{sgn}(t - T_1 - T_2 - T_3) \\
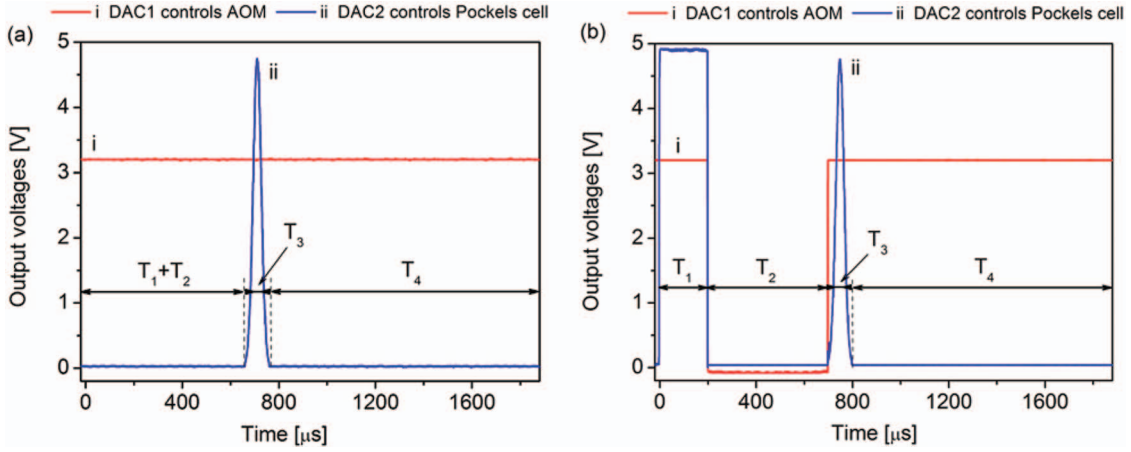& \cdot \text{sgn1}(T_1 + T_2 + T_3 + T_4 - t),
\end{aligned} \tag{5}
$$

FIG. 5. Two output DAC signals from the FPGA device that control the AOM and the Pockels cell in the slow light experiment: (a) single Gaussian σ^- light pulse of duration T_3 with AOM turned on all the time, and (b) preparation Π-shaped σ^- light pulse of duration T_1 followed by the AOM turned off during time T_2 and Gaussian σ^- light pulse of duration T_3.

where $\mathrm{sgn}(t)$ and $\mathrm{sgn}1(t)$ denote signum functions ($\mathrm{sgn}(t) = 1$ for $t \geq 0$ and $\mathrm{sgn}(t) = 0$ otherwise, while $\mathrm{sgn}1(t) = 1$ for $t > 0$ and $\mathrm{sgn}1(t) = 0$ otherwise) and serve as mathematical analogs to if-statements in programming practice. The above expressions use control parameters Ctrl1 and Ctrl2 thus covering both experimental configurations: the first one is obtained for Ctrl1 = 3.28 and Ctrl2 = 0.00, and the second one for Ctrl1 = 0.00 and Ctrl2 = 1.00. Output signals from the FPGA device which control AOM and the Pockels cell are shown in Fig. 5. The longitudinal magnetic field is $\sim 1 \ \mu$T in both configurations. Signals from the two photodetectors measuring fast (reference) and slow σ^- light pulses are inputs to the FPGA device and are shown in Fig. 6. In the first configuration, the light pulse is delayed for $\Delta t = 12.5 \ \mu$s and the group velocity is $v_g = 6.4$ km/s with a large absorption within the cell. In the second configuration, the time delay is shorter ($\Delta t = 8.24 \ \mu$s and $v_g = 9.7$ km/s) but the transparency is substantially enhanced.

In the storage of light experiment, we have two similar configurations like in the experiment with the slow light. In the first configuration, a single Gaussian-shaped σ^- polarization pulse of duration $T_3 + T_4$ is generated and the AOM is smoothly turned off at a peak of the pulse to ensure that the

most of the energy of slowed pulse is within the cell. The laser beam is kept off for the storage time $\tau = T_4 + T_5$ after which the light is turned back on. In the second configuration, the preparation Π-shaped σ^- pulse of length T_1 is applied to the Pockels cell, after which the AOM turns the laser off for the time T_2. After the time $T_1 + T_2$, both output signals have the same waveforms as in the first configuration. Output voltages are tailored by the following mathematical expressions:

$$V_{DAC1}(t) = 3.28 \cdot \mathrm{sgn}(t) \cdot \mathrm{sgn}1(T_1 - t)$$
$$+ \mathrm{Ctrl1} \cdot \mathrm{sgn}(t - T_1) \cdot \mathrm{sgn}1(T_1 + T_2 - t)$$
$$+ 3.28 \cdot \mathrm{sgn}(t - T_1 - T_2) \cdot \mathrm{sgn}1(T_1 + T_2 + T_3 - t)$$
$$+ 0.00 \cdot \mathrm{sgn}(t - T_1 - T_2 - T_3)$$
$$\cdot \mathrm{sgn}1(T_1 + T_2 + T_3 + T_4 + T_5 - t)$$
$$+ 3.28 \cdot \mathrm{sgn}(t - T_1 - T_2 - T_3 - T_4 - T_5)$$
$$\cdot \mathrm{sgn}1(T_1 + T_2 + T_3 + T_4 + T_5 + T_6 - t),$$
$$(6)$$
$$V_{DAC2}(t) = \mathrm{Ctrl2} \cdot \frac{2}{C \cdot G} \arcsin \sqrt{\eta} \cdot \mathrm{sgn}(t) \cdot \mathrm{sgn}1(T_1 - t)$$
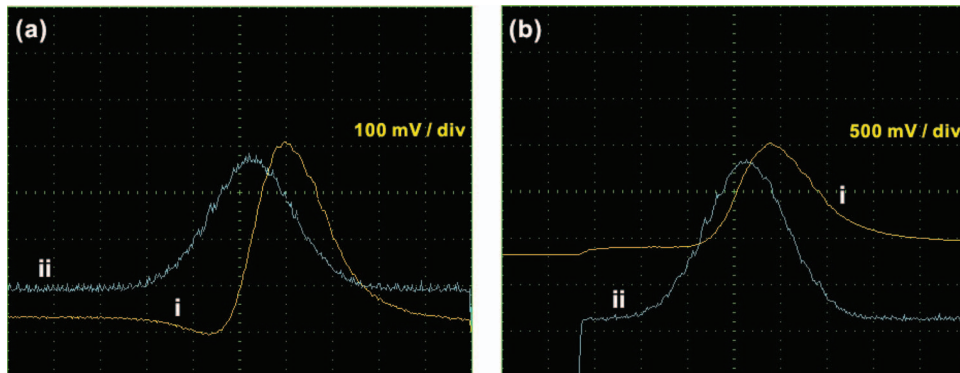$$+ 0.00 \cdot \mathrm{sgn}(t - T_1) \cdot \mathrm{sgn}1(T_1 + T_2 - t)$$

FIG. 6. Screenshots of real-time monitoring of the two photodetectors' signals that measure slow (i) and fast (ii) σ^- light pulses: (a) no preparation pulse with the AOM turned on all the time, (b) preparation Π-shaped σ^- light pulse followed by the AOM turned off and Gaussian-shaped σ^- pulse. Parameters' values: $T_{DAC} = 2$ ms, $T_1 = 200 \ \mu$s, $T_2 = 500 \ \mu$s, $T_3 = 100 \ \mu$s, $\eta = 0.15$, and $P_{laser} = 1.3$ mW. Note the different voltage scalings for curves (i) in (a) and (b).
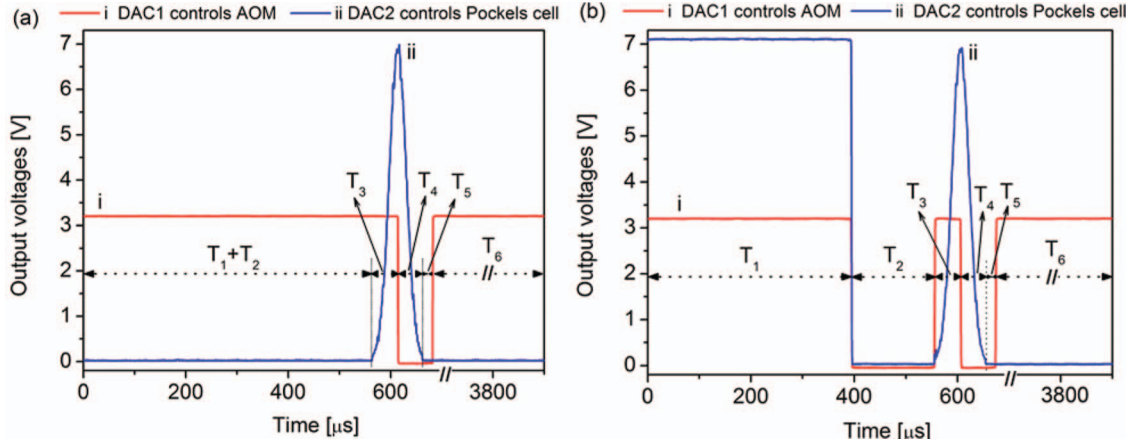
FIG. 7. Two output DAC signals from the FPGA device that control the AOM and the Pockels cell in the storage of light experiment: (a) single Gaussian-shaped σ^- light pulse of duration $T_3 + T_4$ with AOM turned off for the storage time $T_4 + T_5$, and (b) preparation Π-shaped σ^- light pulse of duration T_1 followed by the AOM turned off during the time T_2 prior to the storage of light signals' conditioning.

$$+ \frac{2}{C \cdot G} \arcsin \sqrt{\eta} e^{-35 \cdot (t - T_1 - T_2 - \frac{T_3 + T_4}{2})^2 / (T_3 + T_4)^2}$$

$$\cdot \operatorname{sgn}(t - T_1 - T_2) \cdot \operatorname{sgn1}(T_1 + T_2 + T_3 + T_4 - t)$$

$$+ 0.00 \cdot \operatorname{sgn}(t - T_1 - T_2 - T_3 - T_4)$$

$$\cdot \operatorname{sgn1}(T_1 + T_2 + T_3 + T_4 + T_5 + T_6 - t).$$

Note that in both Eqs. (5) and (6) some addends are multiplied with zero to indicate the time intervals over which the zero voltages are required in the experiment. Output signals from the FPGA device which control the AOM and the Pockels cell are shown in Fig. 7. The longitudinal magnetic field is $\sim 1 \, \mu$T in both configurations. Signals from the two photodetectors measuring fast and stored σ^- light pulses are shown in Fig. 8. Light storage efficiencies obtained in two experimental configurations are $\xi_1 = 14.5\%$ and $\xi_2 = 20\%$. Enhanced storage efficiency of a σ^- polarization pulse in the second configuration is due to higher transparency of resonant laser light, i.e., combined effects of preparation pulse and free evolution of the dark state in Rb atoms. This technique, known as Ramsey technique, improves the storage of light efficiency and will be investigated in more detail in our forthcoming work.

VII. CONCLUSION

We described the FPGA based device, consisting of an arbitrary signal generator and a simple digital oscilloscope. This device synchronously generates two analog voltage signals and acquires two analog voltage signals. Analog electronic circuit connected to the FPGA provides the desired offsetting and amplifying of both input and output voltages. All input and output data are written in the external memory of the FPGA board. The PC application which communicates and exchanges the data with the FPGA, enables the user to model waveforms of output signals through mathematical expressions including predefined parameters, time variable, and most frequent built-in mathematical functions. Quick and easy change of any parameter or formula is immediately sent to the FPGA. Simultaneously, the FPGA records the data from the inputs and right after completion, sends them to the PC application, which presents the data in a graphical form. This real-time monitoring may be further adjusted by the user, so the raw or averaged data over different time and voltage intervals could be monitored and analyzed. The detailed schematic of the analog electronic circuit, as well as VHDL source code for the FPGA chip and Borland C++ Builder code for a graphical user interface are available in the supplementary material.[31] We demonstrate effectiveness of the FPGA device
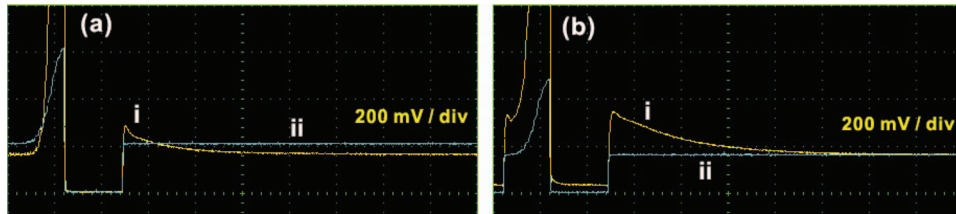

FIG. 8. Screenshots of real-time monitoring of the two photodetectors' signals that measure slow (i) and fast (ii) σ^- light pulses: (a) no preparation pulse with the AOM turned on all the time, (b) preparation Π-shaped σ^- light pulse followed by the AOM turned off and Gaussian σ^- pulse. Parameters' values: $T_{DAC} = 4$ ms, $T_1 = 400 \, \mu$s, $T_2 = 160 \, \mu$s, $T_3 = 50 \, \mu$s, $T_4 = 50 \, \mu$s, $T_5 = 20 \, \mu$s, $\eta = 0.30$, and $P_{laser} = 1.7$ mW.

in the slow light and the storage of light experiments. Outputs of the device control the AOM and the Pockels cell. In the first configuration of both experiments, we measure the propagation of a single Gaussian-shaped polarization pulse through the Rb cell. In the second configuration, prior to Gaussian-shaped pulse, we generate Π-shaped preparation pulse followed by the free evolution of the coherently prepared atoms. The signals from the two photodetectors that measure fast and slow light pulses are inputs to the FPGA device. Monitoring of the input signals showed us that enhanced transparency and storage efficiency could be obtained in the second configuration due to repeated interaction of the coherently prepared atoms with the laser light.

ACKNOWLEDGMENTS

[1] K. J. Boller, A. Imamoğlu, and S. E. Harris, Phys. Rev. Lett. **66**, 2593 (1991).
[2] T. F. Krauss, J. Phys. D: Appl. Phys. **40**, 2666 (2007).
[3] H. Xu, Y. Lu, Y. Lee, and B. S. Ham, Opt. Express **18**, 17736 (2010).
[4] M. Fleischhauer, A. Imamoğlu, and J. P. Marangos, Rev. Mod. Phys. **77**, 633 (2005).
[5] E. Arimondo, Prog. Opt. **35**, 257 (1996).
[6] J. B. Khurgin and R. S. Tucker, *Slow Light Science and Applications* (CRC Press, 2009).
[7] L. V. Hau, S. E. Harris, Z. Dutton, and C. H. Behroozi, Nature (London) **397**, 594 (1999).
[8] D. F. Phillips, A. Fleischhauer, A. Mair, R. L. Walsworth, and M. D. Lukin, Phys. Rev. Lett. **86**, 783 (2001).
[9] M. Fleischhauer and M. D. Lukin, Phys. Rev. Lett. **84**, 5094 (2000).
[10] I. Novikova, R. L. Walsworth, and Y. Xiao, Laser Photonics Rev. **6**, 333 (2012).
[11] M. D. Lukin, Rev. Mod. Phys. **75**, 457 (2003).
[12] A. B. Matsko, O. Kocharovskaya, Y. Rostovtsev, G. R. Welch, A. S. Zibrov, and M. O. Scully, Adv. At., Mol., Opt. Phys. **46**, 191 (2001).
[13] L. M. Duan, M. D. Lukin, J. I. Cirak, and P. Zoler, Nature (London) **414**, 413 (2001).
[14] A. V. Gorshkov, A. André, M. Fleischhauer, A. S. Sørensen, and M. D. Lukin, Phys. Rev. Lett. **98**, 123601 (2007).
[15] I. Novikova, A. V. Gorshkov, D. F. Phillips, A. S. Sørensen, M. D. Lukin, and R. L. Walsworth, Phys. Rev. Lett. **98**, 243602 (2007).
[16] A. V. Gorshkov, A. André, M. D. Lukin, and A. S. Sørensen, Phys. Rev. A **76**, 033804 (2007).
[17] A. V. Gorshkov, A. André, M. D. Lukin, and A. S. Sørensen, Phys. Rev. A **76**, 033805 (2007).
[18] A. V. Gorshkov, A. André, M. D. Lukin, and A. S. Sørensen, Phys. Rev. A **76**, 033806 (2007).
[19] A. V. Gorshkov, T. Calarco, M. D. Lukin, and A. S. Sørensen, Phys. Rev. A **77**, 043806 (2008).
[20] Y. Xiao, I. Novikova, D. F. Phillips, and R. L. Walsworth, Phys. Rev. Lett. **96**, 043601 (2006).
[21] Y. Xiao, I. Novikova, D. F. Phillips, and R. L. Walsworth, Opt. Express **16**, 14128 (2008).
[22] N. F. Ramsey, *Molecular Beams* (Oxford University Press, 1956).
[23] H. Jeong and S. Du, Opt. Lett. **35**, 124 (2010).
[24] A. Schwettmann, J. Sedlacek, and J. P. Shaffer, Rev. Sci. Instrum. **82**, 103103 (2011).
[25] G. Yang, J. F. Barry, E. S. Shuman, M. H. Steinecker, and D. DeMille, JINST **7**, P10026 (2012).
[26] D. B. Nowak, A. J. Lawrence, Z. K. Dzegede, J. C. Hiester, C. Kim, and E. J. Sánchez, Rev. Sci. Instrum. **82**, 103701 (2011).
[27] K. T. Pozniak, Meas. Sci. Technol. **18**, 2336 (2007).
[28] R. Bowler, U. Warring, J. W. Britton, B. C. Sawyer, and J. Amini, Rev. Sci. Instrum. **84**, 033108 (2013).
[29] R. E. Haskell and D. M. Hanna, *Digital Design Using Digilent FPGA Boards VHDL/Active-HDL Edition* (LBE Books, Rochester Hills, MI, 2009).
[30] See discussion and material at http://www.makestuff.eu/wordpress/nexys2-nexus-part-1-the-epp-emulator about VHDL design of enhanced parallel port protocol for Digilent Nexys-2 board.
[31] See supplementary material at http://dx.doi.org/10.1063/1.4811147 for the schematic of the analog electronic circuit and complete VHDL and C++ source code of our FPGA based arbitrary signal generator and digital oscilloscope.
[32] G. Wasik, W. Gawlik, J. Zachorowski, and W. Zawadzki, Appl. Phys. B **75**, 613 (2002).
[33] T. Petelski, M. Fattori, G. Lamporesi, J. Stuhler, and G. M. Tino, Eur. Phys. J. D **22**, 279 (2003).
[34] B. E. A. Saleh and M. C. Teich, *Fundamentals of Photonics* (John Wiley & Sons, Inc., Hoboken, NJ, 2007).

Effects of a laser beam profile on Zeeman electromagnetically induced transparency in the Rb buffer gas cell

S N Nikolić, M Radonjić, A J Krmpot, N M Lučić, B V Zlatković and B M Jelenković

Institute of Physics, University of Belgrade, Pregrevica 118, 11080 Belgrade, Serbia

E-mail: stankon@ipb.ac.rs

Abstract

Electromagnetically induced transparency (EIT) due to Zeeman coherences in the Rb buffer gas cell is studied for different laser beam profiles, laser beam radii and intensities from 0.1 to 10 mW cm^{-2}. EIT line shapes can be approximated by the Lorentzian for wide Gaussian laser beam (6.5 mm in diameter) if laser intensity is weak and for a Π laser beam profile of the same diameter. Line shapes of EIT become non-Lorentzian for the Gaussian laser beam if it is narrow (1.3 mm in diameter) or if it has a higher intensity. EIT amplitudes and linewidths, for both laser beam profiles of the same diameter, have very similar behaviour regarding laser intensity and Rb cell temperature. EIT amplitudes are maximal at a certain laser beam intensity and this intensity is higher for narrower laser beams. The EIT linewidth estimated at zero laser intensity is about 50 nT or 0.7 kHz, which refers to 1.5 ms relaxation times of Zeeman coherences in ^{87}Rb atoms in our buffer gas cell. Blocking of the centre of the wide Gaussian laser beam in front of the photo detector yields Lorentzian profiles with a much better contrast to the linewidth ratio for EIT at higher intensities, above $\sim$2 mW cm^{-2}.

(Some figures may appear in colour only in the online journal)

1. Introduction

Electromagnetically induced transparency (EIT) [1], a narrow resonance in the transmission of a laser beam through coherent media, is essential for subjects like slow and stored light [2], lasing without inversion [3], frequency mixing [4], Kerr nonlinearities [5] etc. Interest in EIT is due to the development of important devices based on EIT, such as atomic frequency standards [6] and magnetometers [7]. For such applications, the EIT linewidth is the most important resonance parameter. The narrow sub-natural Zeeman EIT resonances (EIT resonances for short) examined in this paper are attributed to the long-lived ground state Zeeman coherence. The same phenomenon was first known as the ground state Hanle effect, named by Dupont-Roc [8, 9]. The effect was later related to linear dichroism [10, 11]. In the past decade, the ground state Hanle effect has been reinterpreted in terms of EIT [12] or Zeeman EIT [13, 14]. Sub-natural EIT resonances are closely related to magneto-optical rotation (NMOR) of

linearly polarized light, first studied in [15]. Similar to EIT, ultra-narrow NMOR resonances [15, 16] have found useful applications as a very sensitive technique for measuring weak magnetic fields. Recently, correlations of intensity fluctuations have been studied in NMOR experiments and reported in [17, 18]. More on magneto-optical effects, EIT and NMOR can be found in [11, 19] and references therein.

For some applications and experiments, the EIT line shape is of the highest interest, for instance in the storage of light in atomic ensembles. The product of the pulse delay and pulse broadening, which is the figure of merit in such experiments, depends not only on the steepness of the EIT resonance but also on its shape [20]. The behaviour of the EIT line shape in terms of the experimental parameters is thus of great scientific and practical importance. The EIT line shape in alkali vapours contained in gas cells is altered from the fundamental Lorentzian shape of atomic resonances by many factors. The way these factors affect the EIT depends on the type of gas cell. In vacuum cells, a thermal motion of atoms affects the shape of

the EIT through a transit time effect and Doppler broadening. While these factors prevail at a lower laser power, the power broadening determines the linewidths at laser powers near saturation levels. The behaviour of the EIT as a function of the laser beam diameter [21], optical depth [22], laser intensity [23, 24] and laser beam profile [25–28] was investigated. When alkali atoms are in a cell with buffer gas atoms, the interaction time of the alkali atoms with the laser beam is considerably increased. The linewidths, controlled here by the ground state relaxation time and the laser power, are reduced by several orders of magnitude due to the Dicke effect [29]. Linewidths as narrow as 30 Hz were obtained [30]. A non-Lorentzian line shape of the EIT, with the narrower central part of the line than in a pure Lorentzian, obtained in buffer gas cells for laser beams of small diameter, was explained by the diffusion of atoms out and then back to the laser beam. Such repeated atom–light interaction effectively enables Ramsey induced narrowing and non-Lorentzian line shape for the EIT [31, 32]. Theoretical study of a simple Λ scheme, with two ground state hyperfine levels as two lower levels, has shown that, under the assumption of immovable alkali atoms in the buffer gas, such non-Lorentzian line shape for large diameter laser beams is due to the contribution from atoms in the wings of the laser Gaussian profile [25]. Since EIT resonance contrast and linewidth depend on the cell temperature, one has to find the optimum operating temperature for achieving the maximum line contrast and the minimum linewidth. Cell temperature affects the hyperfine coherences differently to the Zeeman coherences. For the former, it is found that linewidths for the same laser intensity are narrower as the cell temperature increases. The linewidth of EIT resonances due to Zeeman coherences on the other hand, are nearly independent of the cell temperature [33].

The dependence of EIT line shapes and linewidths in buffer gas cells on the laser intensity was studied both theoretically and experimentally. Theoretical models are mainly based on a three level atomic system which allows analytic [25] and perturbative solutions [34]. Numerical modelling of an EIT in the buffer gas cell that takes into account velocity changing collisions of Rb atoms due to their thermal motion, explains the elimination of Doppler shifts and the strong Dicke-type narrowing of EIT resonances [30].

In [25], the effects of the laser intensity radial profile on the linewidth and contrast were investigated. Several experiments confirm a general trend found in the models that the linewidth for a hyperfine configuration increases linearly with the intensity, for lower laser intensities [30, 35] and nonlinearly at higher laser intensities, above the saturation limit [25]. Theoretical studies of the EIT line shapes are mainly done assuming a Π radial intensity profile of laser radiation. Experiments, on the other hand, use Gaussian or Gaussian-like laser beams profiles. The discrepancies observed between a calculated [23] and measured [24] linewidth dependence on laser intensity for hyperfine EIT might be due to the different radial laser beam intensity profiles. Few papers dealing with the issues of different laser beam profiles and EIT in buffer gas [25] and vacuum cells [26], have shown theoretically that the radial intensity profile significantly affects the EIT

line shape. Most studies dealing with EIT line shapes and their dependences on the laser intensity and beam diameter, as well as on the buffer gas temperature, are for a pump–probe hyperfine configuration. There are no such studies for Zeeman EIT in a Hanle configuration.

This work investigates the behaviour of the Zeeman EIT resonances in the buffer gas cell for different laser beam radial profiles and diameters. We use the Hanle configuration in which a single, linearly polarized laser beam is resonant to the $F_g = 2 \rightarrow F_e = 1$ hyperfine transitions of the D_1 line of ^{87}Rb. The detuning of σ^+ and σ^- components of the laser beam was done by scanning the external magnetic field around zero. We obtain EIT resonances by measuring the laser transmission as a function of the applied magnetic field. The two laser beam radial profiles, Gaussian (1.3 and 6.5 mm in diameter) and Π profile (6.5 mm in diameter), were used in our study. We have also studied the EIT detected in the wings of the wide Gaussian laser beam. Thus, in this work we were able to test previously suggested effects of laser beam profiles on the EIT. According to [25, 27, 28] the line shape of the EIT is different for Gaussian and Π radial laser intensity profiles, with the former typically giving non-Lorentzian EIT resonance. Theoretical work in [25] for the three level Λ atomic scheme, shows that, when the atomic diffusion is neglected and for the same laser intensity and diameter, EIT resonances are wider and have larger amplitudes for a Π-shaped beam than for a Gaussian beam.

We develop a theoretical model based on self-consistent Maxwell–Bloch equations for the evolution of the Rb ensemble density matrix and the laser electric field in the Rb vapour. The model takes into account the collisions of Rb atoms with Ne as the buffer gas atoms through the diffusion of the Rb atoms and total depolarization of the Rb excited state. Collisional relaxation of the Rb ground state is treated using separate relaxation constants for populations and coherences. It is assumed that collisional broadening enables the approximation of the motionless atoms for longitudinal velocities. An arbitrary incident radial laser beam profile is supplied as a boundary condition for the electric field.

2. Theory and theoretical results

The starting point in calculating Zeeman EIT resonances related to the D_1 line transition $F_g = 2 \rightarrow F_e = 1$ in ^{87}Rb contained in the buffer gas cell are optical Bloch equations (OBEs) for the Rb density matrix $\hat{\rho}$.

$$\frac{\partial \hat{\rho}}{\partial t} = D\nabla^2 \hat{\rho} - \frac{\mathrm{i}}{\hbar}[\hat{H}_{\text{atom}}(B) + \hat{V}_{\text{int}}(\mathbf{r}, t), \hat{\rho}] + \left(\frac{\partial \hat{\rho}}{\partial t}\right)_{\text{SE}} + \left(\frac{\partial \hat{\rho}}{\partial t}\right)_{\text{coll}}, \quad (1)$$

where

$$\hat{H}_{\text{atom}}(B) = \sum_{j=-F_g}^{F_g} \hbar\omega_{F_g,j}(B)|F_g, j\rangle\langle F_g, j| + \sum_{F_e=1}^{2}\sum_{k=-F_e}^{F_e} \hbar\omega_{F_e,k}(B)|F_e, k\rangle\langle F_e, k|, \quad (2)$$

is the atomic Hamiltonian corresponding to ground (excited) states $|F_g, j\rangle \equiv |F_g, m_{g_j} = j\rangle$ ($|F_e, k\rangle \equiv |F_e, m_{e_k} = k\rangle$) with
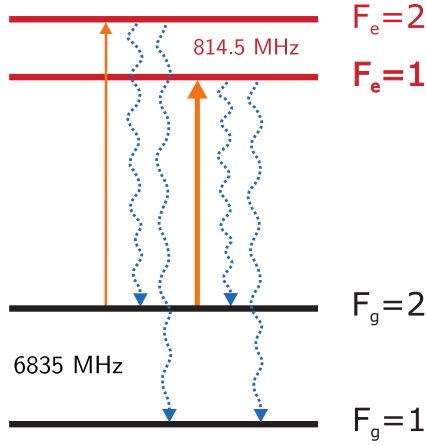
Figure 1. Energy level diagram for D_1 line transitions considered in the theoretical model. Solid lines represent transitions induced by the laser, while dotted lines correspond to possible spontaneous emission channels from excited levels. Frequency differences between adjacent hyperfine levels are shown.

Zeeman-shifted energies $\hbar\omega_{F_g,j}(B) = \hbar\omega_{F_g,0} + \mu_B g_{F_g} B m_{g_j}$ ($\hbar\omega_{F_e,k}(B) = \hbar\omega_{F_e,0} + \mu_B g_{F_e} B m_{e_k}$). μ_B is the Bohr magneton and g_{F_g} and g_{F_e} are the Landé factors for the appropriate hyperfine levels. Laser–atom interaction is given by

$$\hat{V}_{\text{int}}(\mathbf{r}, t) = -\sum_{j=-F_g}^{F_g} \sum_{F_e=1}^{2} \sum_{k=-F_e}^{F_e} \mathbf{E}(\mathbf{r}, t)$$
$$\cdot \mathbf{d}_{F_e,k}^{F_g,j} (|F_g, j\rangle\langle F_e, k| + |F_e, k\rangle\langle F_g, j|), \quad (3)$$

where $\mathbf{E}(\mathbf{r}, t)$ is the laser electric field and $\mathbf{d}_{F_e,k}^{F_g,j}$ denotes the atomic electric dipole moment $\langle F_g, j|e\hat{\mathbf{r}}|F_e, k\rangle$ for the transition between states $|F_g, j\rangle$ and $|F_e, k\rangle$. The energy level diagram given in figure 1 shows hyperfine levels either coupled to the laser light or populated due to spontaneous emission. Due to the pressure-broadening of the lines in buffer gas cells, two excited levels $F_e = 1$ and $F_e = 2$ are taken to be coupled by the laser with the ground state level $F_g = 2$. Equations related to the ground state level $F_g = 1$ are not considered since that level is not coupled by the laser.

　　Collisions with the buffer gas have several effects. First, they lead to a diffusive motion of Rb atoms that is included through the first term on the right-hand side of (1) with D as the diffusion coefficient. Second, we assume total collisional depolarization of the excited state [36, 37] with rate Γ_d, that equalizes the populations and destroys the coherences among the Zeeman excited state sublevels within each excited state manifold $F_e = 1$ and $F_e = 2$. The collisions with the buffer gas also lead to the broadening of the optical transition described by the constant Γ_c while together with the Rb–Rb collisions lead to the relaxation of the ground states that is treated by two relaxation constants, γ_p for populations and γ_c for coherences. For the buffer gas pressure of 30 Torr the collisional broadening of approximately 300–400 MHz is comparable with the Doppler width, so that the approximation of the motionless atoms is used for the longitudinal velocities.

　　In the rotating wave approximation the OBEs for the density matrix elements $\rho_{F_2,m_2}^{F_1,m_1} \equiv \langle F_1, m_1|\hat{\rho}|F_2, m_2\rangle$ of a moving atom have the form

$$\frac{\partial \rho_{F_e,k}^{F_e,j}}{\partial t} = D\nabla^2 \rho_{F_e,k}^{F_e,j} + (\mathrm{i}(\omega_{F_e,k} - \omega_{F_e,j}) - \Gamma)\rho_{F_e,k}^{F_e,j}$$
$$- \Gamma_d \left(\rho_{F_e,k}^{F_e,j} - \frac{\pi_{F_e}\delta_{jk}}{2F_e + 1} \right) + \frac{\mathrm{i}}{\hbar} \sum_{\ell=-F_g}^{F_g} \left(\tilde{\rho}_{F_g,\ell}^{F_e,j} \left(V_{F_e,k}^{F_g,\ell} \right)_+ \right.$$
$$\left. - \left(V_{F_g,\ell}^{F_e,j} \right)_- \tilde{\rho}_{F_e,k}^{F_g,\ell} \right), \quad (4a)$$

$$\frac{\partial \tilde{\rho}_{F_g,j}^{F_e,k}}{\partial t} = D\nabla^2 \rho_{F_g,j}^{F_e,k} + \left(\mathrm{i}(\omega + \omega_{F_g,j} - \omega_{F_e,k}) - \frac{\Gamma_c}{2} \right) \tilde{\rho}_{F_g,j}^{F_e,k}$$
$$+ \frac{\mathrm{i}}{\hbar} \left(\sum_{F_e=1}^{2} \sum_{m=-F_e}^{F_e} \rho_{F_e,m}^{F_e,k} \left(V_{F_g,j}^{F_e,m} \right)_- - \sum_{\ell=-F_g}^{F_g} \left(V_{F_g,\ell}^{F_e,k} \right)_- \rho_{F_g,j}^{F_g,\ell} \right), \quad (4b)$$

$$\frac{\partial \rho_{F_g,k}^{F_g,j}}{\partial t} = D\nabla^2 \rho_{F_g,k}^{F_g,j} + \mathrm{i} \left(\omega_{F_g,k} - \omega_{F_g,j} \right) \rho_{F_g,k}^{F_g,j}$$
$$- \gamma_p \delta_{jk} \left(\rho_{F_g,k}^{F_g,j} - \frac{1 - \pi_e}{n_g} \right) - \gamma_c (1 - \delta_{jk})\rho_{F_g,k}^{F_g,j}$$
$$+ \frac{\mathrm{i}}{\hbar} \sum_{F_e=1}^{2} \sum_{m=-F_e}^{F_e} \left(\tilde{\rho}_{F_e,m}^{F_g,j} \left(V_{F_g,k}^{F_e,m} \right)_- - \left(V_{F_e,m}^{F_g,j} \right)_+ \tilde{\rho}_{F_g,k}^{F_e,m} \right)$$
$$+ (-1)^{j+k} \sum_{F_e=1}^{2} (2F_e+1)\Gamma_{F_e\to F_g} \sum_{q=-1}^{1} \rho_{F_e,k+q}^{F_e,j+q} \, \mathcal{C}_q(F_e, F_g; j, k), \quad (4c)$$

where $\mathcal{C}_q(F_e, F_g; j, k)$
$$= \begin{pmatrix} F_e & 1 & F_g \\ j+q & -q & -j \end{pmatrix} \begin{pmatrix} F_e & 1 & F_g \\ k+q & -q & -k \end{pmatrix}.$$

　　Diagonal density matrix elements $\rho_{F_g,j}^{F_g,j}$ ($\rho_{F_e,k}^{F_e,k}$) are populations of $|F_g, j\rangle$ ($|F_e, k\rangle$) Zeeman sublevels, while off-diagonal elements $\rho_{F_g,k}^{F_g,j}$ ($\rho_{F_e,k}^{F_e,j}$) are appropriate Zeeman coherences between ground (excited) Zeeman sublevels. Fast oscillations of the optical coherences $\rho_{F_g,k}^{F_e,j}$ were eliminated by standard substitution $\rho_{F_g,k}^{F_e,j} = \tilde{\rho}_{F_g,k}^{F_e,j} \exp(-\mathrm{i}\omega t)$, where ω is the laser frequency in the laboratory frame. $\Gamma_{F_e\to F_g}$ is the decay rate from F_e to one F_g ground hyperfine level given by

$$\Gamma_{F_e\to F_g} = (2J_e + 1)(2F_g + 1) \begin{Bmatrix} J_g & J_e & 1 \\ F_e & F_g & I \end{Bmatrix}^2 \Gamma, \quad (5)$$

where J represents the electron angular momentum quantum numbers and $I = 3/2$ is the nuclear angular momentum of ^{87}Rb. π_{F_e} is the population of the excited level F_e, $\pi_e = \sum_{F_e=1}^{2} \pi_{F_e}$ is the total population of exited levels $F_e = 1$ and $F_e = 2$ and $n_g = 2(2I + 1)$ is the total number of substates in the ground state levels $F_g = 1$ and $F_g = 2$. Coherences among excited states belonging to different manifolds are neglected.

　　In a general case, the laser electric field is given by

$$\mathbf{E}(\mathbf{r}, t) = \mathbf{e}_x E_{0x}(\mathbf{r}, t) \cos(\omega t - \mathbf{kr})$$
$$+ \mathbf{e}_y E_{0y}(\mathbf{r}, t) \cos(\omega t - \mathbf{kr} + \varphi). \quad (6)$$

For symmetry reasons it is better to express the laser electric field in terms of the spherical basis unit vectors $\mathbf{u}_{\pm 1} = (\mp\mathbf{e}_x - \mathrm{i}\mathbf{e}_y)/\sqrt{2}$

$$\mathbf{E} = (\mathbf{u}_{+1}E_{+1,+} + \mathbf{u}_{-1}E_{-1,+}) \, \mathrm{e}^{\mathrm{i}(\omega t - \mathbf{kr})}$$
$$+ (\mathbf{u}_{+1}E_{+1,-} + \mathbf{u}_{-1}E_{-1,-}) \, \mathrm{e}^{-\mathrm{i}(\omega t - \mathbf{kr})}, \quad (7)$$

where we used the notation $E_{\pm 1,\pm} = (\mp E_{0x} + \mathrm{i} e^{\pm \mathrm{i}\varphi} E_{0y})/(2\sqrt{2})$. Terms $(V_{F_e,k}^{F_g,j})_\pm$ in OBEs (4) are of the form

$$(V_{F_e,k}^{F_g,j})_\pm = -(d_{F_e,k}^{F_g,j})_{-1} E_{-1,\pm} - (d_{F_e,k}^{F_g,j})_{+1} E_{+1,\pm}. \quad (8)$$

Here $(d_{F_e,k}^{F_g,j})_q$ is the spherical component of the electric dipole matrix element that can be calculated as

$$
\begin{aligned}
(d_{F_e,k}^{F_g,j})_q &= \langle F_g, j | \mathbf{u}_q \cdot e\hat{\mathbf{r}} | F_e, k \rangle \\
&= \langle J_g || e\hat{\mathbf{r}} || J_e \rangle (-1)^{J_g + H + j} \sqrt{(2F_g+1)(2F_e+1)(2J_g+1)} \\
&\quad \times \begin{Bmatrix} J_g & J_e & 1 \\ F_e & F_g & I \end{Bmatrix} \begin{pmatrix} F_e & 1 & F_g \\ k & q & -j \end{pmatrix},
\end{aligned} \quad (9)
$$

where $\langle J_g || e\hat{\mathbf{r}} || J_e \rangle$ is the reduced matrix element of the electric dipole operator between appropriate ground and excited states. Due to the relation $(d_{F_g,j}^{F_e,k})_q^* = (-1)^q (d_{F_e,k}^{F_g,j})_{-q}$, the terms $(V_{F_g,j}^{F_e,k})_\pm$ are completely determined by the terms $(V_{F_e,k}^{F_g,j})_\mp$.

Optical Bloch equations (4) represent a set of coupled time-dependent three-dimensional partial differential equations. We are interested in the cylindrical symmetric steady state case because the coupling laser field possesses such properties. In the magnetic field B the atomic ensemble density matrix is a function of only the radial and axial space coordinates, i.e. $\hat{\rho}(\mathbf{r}, B) \to \hat{\rho}(r, z; B)$. Also, the diffusion terms have only radial and axial derivatives, i.e. $\nabla^2 \to \nabla^2(r, z)$. For a given electric field inside the cell, OBEs can be solved with boundary conditions

$$\rho_{F_g,k}^{F_g,j}(R, z; B) = \rho_{F_g,k}^{F_g,j}(r, 0; B) = \rho_{F_g,k}^{F_g,j}(r, L; B) = \frac{\delta_{jk}}{n_g}, \quad (10)$$

with all other relevant matrix elements being set to zero. R and L are the cell radius and length, respectively.

The effects of the laser propagation along the cell and induced atomic polarization of the Rb vapour are included in the following manner. When the Rb vapour ensemble density matrix $\hat{\rho}(r, z; B)$ is known, the polarization of Rb vapour having the temperature dependent density $n(T)$ is obtained as

$$
\begin{aligned}
\mathbf{P}(r, z; B) &= n(T)\,\mathrm{Tr}(\hat{\rho}(r, z; B)\, e\hat{\mathbf{r}}) = n(T)\, \mathrm{e}^{-\mathrm{i}(\omega t - \mathbf{k}\mathbf{r})} \\
&\quad \times \sum_{j=-F_g}^{F_g} \sum_{F_e=1}^{2} \sum_{k=-F_e}^{F_e} \mathbf{d}_{F_e,k}^{F_g,j}\, \tilde{\rho}_{F_g,j}^{F_e,k}(r, z; B) + \text{c.c.},
\end{aligned} \quad (11)
$$

where $\mathbf{d}_{F_e,k}^{F_g,j} = \mathbf{e}_x((d_{F_e,k}^{F_g,j})_{-1} - (d_{F_e,k}^{F_g,j})_{+1})/\sqrt{2} + \mathrm{i}\mathbf{e}_y((d_{F_e,k}^{F_g,j})_{-1} + (d_{F_e,k}^{F_g,j})_{+1})/\sqrt{2}$. Let $\mathcal{E}(\mathbf{r}, t; B)$ and $\mathcal{P}(\mathbf{r}, t; B)$ denote complex slowly varying envelopes of the electric field and the polarization, respectively, defined by

$$\mathbf{E}(\mathbf{r}, t; B) = \mathrm{Re}(\mathcal{E}(\mathbf{r}, t; B)\, \mathrm{e}^{-\mathrm{i}(\omega t - \mathbf{k}\mathbf{r})}), \quad (12a)$$

$$\mathbf{P}(\mathbf{r}, t; B) = \mathrm{Re}(\mathcal{P}(\mathbf{r}, t; B)\, \mathrm{e}^{-\mathrm{i}(\omega t - \mathbf{k}\mathbf{r})}). \quad (12b)$$

In a steady state slowly varying envelopes are related by the propagation equation

$$\frac{\partial \mathcal{E}(r, z; B)}{\partial z} = \frac{\mathrm{i}\omega}{2\epsilon_0 c} \mathcal{P}(r, z; B), \quad (13)$$

where ϵ_0 is the vacuum dielectric constant. The laser electric field at the entrance to the Rb cell (at $z = 0$) can be an arbitrary function of the radial coordinate and it is supplied as a boundary condition. The transmitted electric field (at $z = L$) is calculated using the relations (11)–(13).

In order to obtain EIT resonances from the transmitted electric field one has to solve for the ensemble density matrix and electric field in a self-consistent way for a given magnetic field B:

(i) assume that the electric field along the cell is equal to the incident laser electric field, i.e. $\mathcal{E}(r, z; B) = \mathcal{E}_{\mathrm{in}}(r)$;

(ii) calculate the elements of the ensemble density matrix $\hat{\rho}(r, z; B)$ using steady state OBEs (4) and boundary conditions (10);

(iii) calculate the electric field inside the cell $\mathcal{E}(r, z; B)$ using (11)–(13) with $\mathcal{E}(r, 0; B) = \mathcal{E}_{\mathrm{in}}(r)$ as a boundary condition;

(iv) repeat the procedure from step (ii) until self-consistency is reached.

Numerical calculations are performed using the *DOLFIN* finite element library [38] (part of *FEniCS* project [39]) and *CBC.PDESys* package [40]. Note that the EIT resonances presented in this study are obtained after normalizing calculated or measured EIT curves to the transmission at a sufficiently large magnetic field.

In order to determine the temperature dependence of EIT resonance amplitudes, calculations are performed at temperatures of 60, 75 and 82 °C. The calculated EIT resonances for a Gaussian laser beam with $1/e^2$ diameters $d = 6.5$ mm and $d = 1.3$ mm are shown in figures 2(a) and (b). It can be seen that in this temperature range stronger resonances are obtained at higher temperatures for both beam diameters due to the increased density of Rb vapour.

In figure 3 the EIT resonances for two laser beam diameters are presented together with their Lorentzian fits. While the line shapes of the EIT curves for wider laser beams are close to Lorentzian, EIT resonances with narrower laser beams show additional narrowing in the vicinity of a zero magnetic field and certainly are non-Lorentzian. These results, both for wide and narrow Gaussian laser beams, are in agreement with [25, 31].

The EIT amplitudes and linewidths shown in figure 4 are extracted from these curves for a wide Gaussian laser beam at 82 °C and laser intensity interval 0.1–10 mW cm^{-2}. The amplitude dependence on the intensity has a maximum at $I \sim 1.1$ mW cm^{-2}. Further decrease of the amplitudes is due to the increased effect of optical pumping to the non-coupled ground state level $F_g = 1$.

3. Experiment and experimental results

Zeeman EIT experiment in the Hanle configuration needs a single laser whose frequency and polarization of radiation are stable and well controlled. Essential for Zeeman EIT measurements is also the elimination of stray magnetic fields, as well as the creation of a homogeneous magnetic field over the entire Rb cell, directed along its axis. In our experiment an additional requirement is a careful control of the laser beam diameter and radial distribution of laser radiation. The schematic of the experiment is given in figure 5.

We use the external cavity diode laser whose frequency is locked to the $F_g = 2 \to F_e = 1$ transition in ^{87}Rb with the Doppler-free dichroic atomic vapour laser lock technique [41, 42]. The Gaussian laser beam profile, whose diameter is adjusted by the periscope, is obtained by the single mode optical fibre. For achieving a Π radial intensity distribution of the laser beam we use the laser beam shaper which consists of
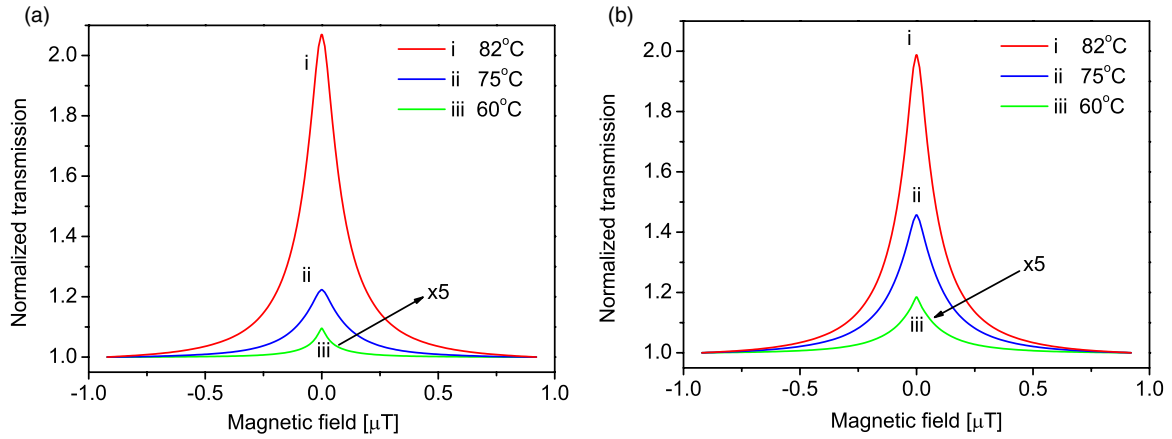
Figure 2. Theoretically obtained EIT resonances for a Gaussian laser beam of diameter (a) $d = 6.5$ mm and (b) $d = 1.3$ mm. Resonances are calculated at three temperatures: 60, 75 and 82 °C. Laser beam intensity is 1.1 mW cm^{-2}.
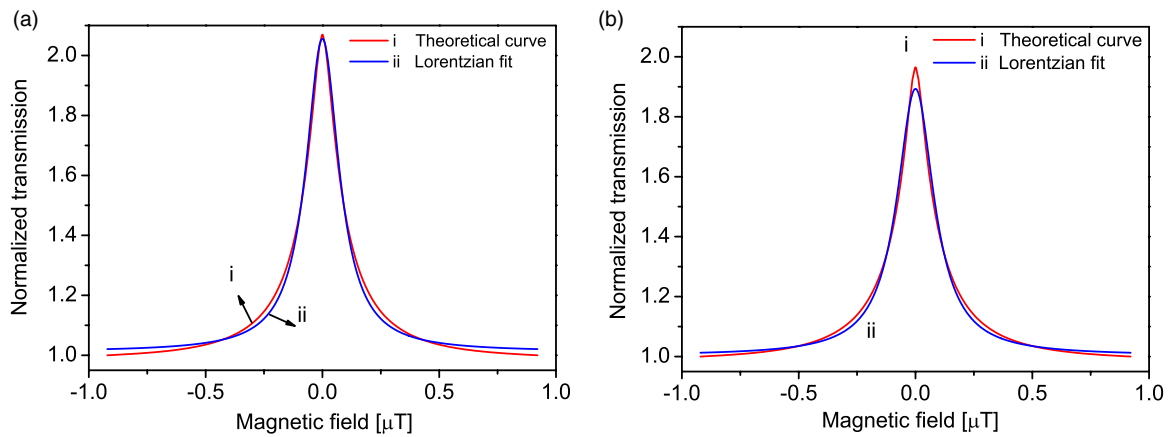

Figure 3. Theoretically obtained EIT resonances (i) and corresponding Lorentzian fits (ii) for a Gaussian laser beam of diameter (a) $d = 6.5$ mm (Adj. $R^2 = 0.997\,54$) and (b) $d = 1.3$ mm (Adj. $R^2 = 0.994\,67$). Resonances are calculated at the cell temperature of 82 °C. Laser beam intensity is 1.1 mW cm^{-2}.
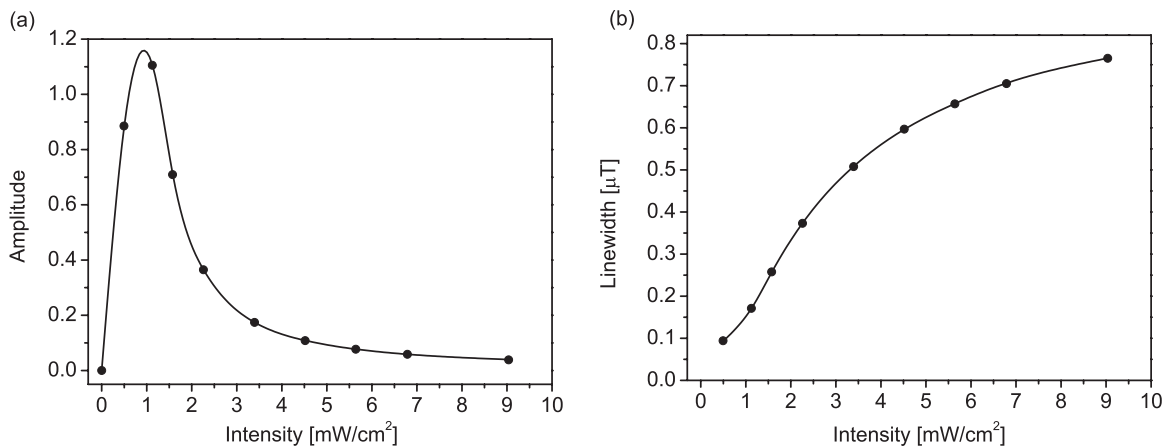

Figure 4. Calculated dependences of the EIT (a) amplitude and (b) linewidth on laser intensity for a Gaussian laser beam with a diameter of 6.5 mm at the cell temperature of 82 °C.

the beam expander, the collimator and thin foil with a 6.5 mm hole as the iris, placed over the central part of the laser beam previously expanded to approximately 20 mm in diameter. We use linearly polarized laser radiation. Linearity and orientation of the polarization is assured by the high quality polarizer and $\lambda/2$ retardation plate. Laser beam intensity is controlled by

the variable neutral density filter. The Rb glass cell, 8 cm long and 25 mm in diameter with 30 Torr of Ne buffer gas, is placed in a plastic box and heated to a certain temperature by hot air circulating around the cell. The advantage of this system in comparison with electrical heating is in elimination of the stray magnetic fields introduced by the heating current
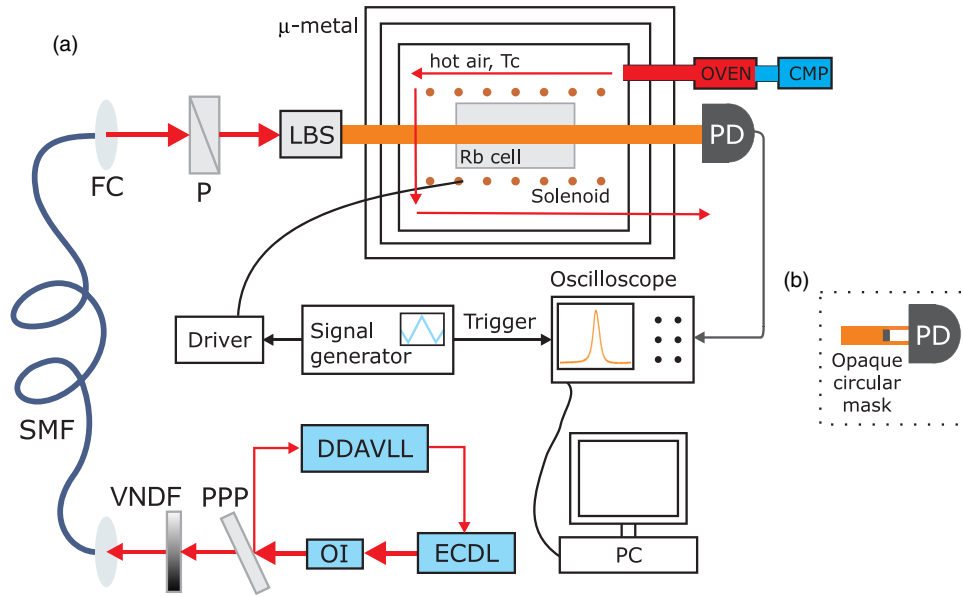
Figure 5. Experimental setup: ECDL—external cavity diode laser; OI—optical insulator; DDAVLL—Doppler-free dichroic atomic vapour laser lock; PPP—plan parallel plate; VNDF—variable neutral density filter; SMF—single-mode fibre; FC—fibre coupler; P—polarizer; LBS—laser beam shaper; PD—large area photodiode; CMP—compressor. A laser beam shaper is used to shape the diameter and the radial intensity profile of the laser beam. Detection of the whole laser beam is shown in (a). The inset in (b) presents the blockage of the laser beam centre and detection of only the outer parts of the beam.

inside μ-metal shielding. The Rb cell is shielded from external magnetic fields by the triple layer of μ-metal which reduces stray magnetic fields below 10 nT. The long solenoid around the Rb cell produces a controllable longitudinal magnetic field for the experiment in the range of $\pm 20 \mu$T. The intensity of the transmitted laser light as a function of the applied magnetic field was monitored by the photodiode and recorded by the storage oscilloscope. For measuring EIT generated only by photons from the wings of the 6.5 mm Gaussian laser beam, we put an opaque round mask of 6.0 mm in diameter, after the gas cells e.g. in front of the detector.

We present our results of the EIT line shapes, amplitudes and linewidths for various cell temperatures, laser light intensities, laser beam diameters and intensity radial profiles. We use Gaussian beams of 6.5 and 1.3 mm in $1/e^2$ diameter. We also compare these resonances with corresponding ones for a Π laser beam profile of 6.5 mm in diameter. Measurements were done in the temperature range from 50 to 82 °C and for the laser intensities 0.1–10 mW cm^{-2} for a wide Gaussian beam, 0–35 mW cm^{-2} for a narrow Gaussian beam and 0–3.5 mW cm^{-2} for a Π laser beam. It was impossible to achieve a Π laser beam profile of 1.3 mm in diameter due to the pronounced diffraction on the beam shaper aperture.

Non-Lorentzian line shapes in buffer gas cells obtained with a narrow laser beam with a diameter of the order of $\lesssim 2$ mm, were explained by diffusion induced Ramsey narrowing, due to coherently prepared atoms coming back to the laser beam after spending time in the dark [31, 32]. On the other hand, non-Lorentzian line shapes for the wide Gaussian laser beam are due to the contribution from the atoms in the wings of the beam [25]. It was demonstrated that in vacuum gas cells, repeated interactions of atoms, coherently prepared in the central parts of the beam, with the laser light in the wings

of a wide Gaussian laser beam, leads to EIT narrowing [43]. We investigated the contribution of the outer parts of the laser beam to the overall EIT formation in the buffer gas cell, by measuring the EIT resonances after blocking the central part of the well collimated laser beam just in front of the detector.

The EIT line shapes for the wide and the narrow Gaussian laser beam, are presented in figure 6, parts (a) and (b), respectively. The EIT resonances for a 6.5 mm diameter laser beam are given for two laser intensities. At a laser intensity of 1.6 mW cm^{-2} the EIT line shape (curve (i)) fits well with the Lorentzian fit (curve (ii)). Such behaviour is found for laser intensities below $\sim$5 mW cm^{-2}. However, as the laser intensity increases, the EIT line shapes are gradually different from the Lorentzian. These results are in agreement with the EIT profiles for a Gaussian laser beam [27]. The EIT resonance measured at 9.2 mW cm^{-2} is different from its Lorentzian fit, as seen from the experimental curve (iii) and its fit (iv) in figure 6(a), respectively. The non-Lorentzian EIT line shape for the wide laser beam with a Gaussian intensity profile and higher intensity could be explained in terms of unequal light intensities within different parts of the Gaussian laser beam profile [25, 27, 28]. As suggested in [25], the sharper central peak of the EIT resonance is due to the contribution of atoms illuminated by a low intensity light in the wings of the laser beam. When the overall laser intensity is higher there is enough power at the wings of the beam to enhance this effect. Conversely, when the laser intensity is small the contribution from these segments is negligible. Thus, for lower laser intensities and wide Gaussian beams, the resonance line shapes fit very well with the Lorentzian.

Resonances obtained for the narrow Gaussian laser beam of 1.3 mm in diameter, presented in figure 6(b), have non-Lorentzian line shapes and sharp central peaks regardless of
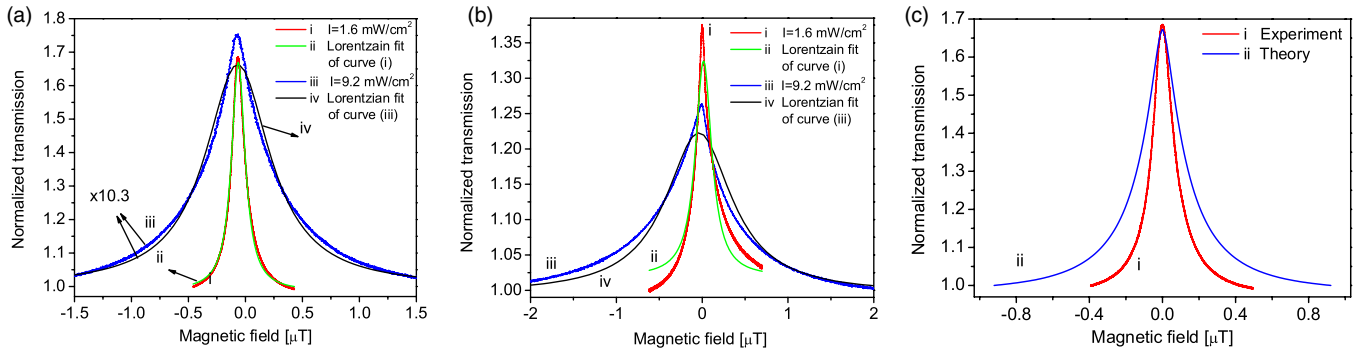
Figure 6. Measured EIT resonances for the Gaussian laser beam of diameter (a) $d = 6.5$ mm and (b) $d = 1.3$ mm. Curves (i) and (ii) are a measured EIT resonance at 1.6 mW cm^{-2} and its Lorentzian fit, respectively, while curves (iii) and (iv) correspond to the measured EIT resonance at 9.2 mW cm^{-2} and its Lorentzian fit, respectively. Note that the curves (iii) and (iv) in (a) are multiplied by 10.3 in order to present them on the same scale as curves (i) and (ii). A comparison between the measured and calculated EIT resonances (curves (i) and (ii), respectively) for a Gaussian laser beam of $d = 6.5$ mm in diameter and 1.6 mW cm^{-2} of the overall intensity is shown in (c). The cell temperature is 82 °C.

the laser intensity. The narrowing at very small magnetic fields is caused by the Ramsey effect, i.e. the diffusion of atoms out from the laser beam and then back to the interaction region as presented in [31, 32]. Non-Lorentzian line shapes for the narrow laser beam that we observed for all laser intensities, are in agreement with the diffusion induced Ramsey narrowing mechanism. Curves (ii) and (iv) in figure 6(b) are Lorentzian fits of the experimental resonances (i) and (iii) respectively, which have wider central peaks that are different from the experimental resonances. A comparison between experimentally and theoretically obtained EIT resonances for the laser beam of 6.5 mm in diameter is shown in figure 6(c). The amplitudes and line shapes of both curves (i) and (ii) are almost the same, however the linewidth of the experimental resonance is slightly narrower than its theoretical counterpart.

Resonances obtained with a Π laser beam profile of 6.5 mm in diameter have a Lorentzian line shape for all laser intensities with a similar linewidth and amplitude dependence on the laser beam intensity as for the Gaussian laser beam of the same diameter.

For the narrow Gaussian laser beam, the line shape is non-Lorentzian with a sharp central peak for all laser intensities due to diffusion induced Ramsey narrowing [31, 32]. In this case, the influence of the non-uniform beam intensity profile is marginal. A definite argument for such a conclusion could be given by a comparison with the corresponding results for the narrow Π laser beam. Unfortunately, we were not able to produce the narrow Π laser beam profile. However, indirect proof is present in [32], because there is an excellent agreement between the theory based on the narrow Π laser beam profile and the experiment with the narrow Gaussian laser beam. On the other hand, the line shape obtained with the wide Gaussian laser beam is Lorentzian for lower laser intensities. As the light intensity increases, EIT resonance line shape for the wide Gaussian laser beam becomes non-Lorentzian. Therefore, one can draw the conclusion that the diffusion induced Ramsey effect has no significant influence on the line shape for the wide Gaussian laser beam [31, 32]. Hence, non-Lorentzian line shapes at higher intensities for the wide Gaussian laser

beam are due to the non-uniform laser beam profile, in line with [25, 27, 28]. This is further supported by the fact that EIT line shapes for the wide Π profile are Lorentzian for all intensities.

The line shapes of the EIT resonances measured at the cell temperatures of 50, 60 and 75 °C are qualitatively similar to theoretical ones and those shown in figure 6. However, the EIT amplitude and linewidth dependences on laser intensity are in general different at various temperatures. Figure 7 shows the EIT amplitudes and linewidths as functions of the laser beam intensity for a wide Gaussian laser beam at four temperatures. There is a strong increase in the EIT contrast associated with a higher cell temperature, as shown in figure 7(a), with the maximum obtainable temperature of the cell achieved by hot air heating of ∼82 °C. The density of Rb atoms increases rapidly with the higher temperature, reaching ∼5 × 10^{11} cm^{-3} at 82 °C, giving stronger resonances as more atoms can undergo transition into the dark state. At even higher temperatures, radiation trapping and dark state decoherence due to Rb–Rb collisions lead to a lowering of the EIT resonances amplitudes [44, 45].

An increase of the cell temperature results in a higher optical depth, requiring a stronger light field to efficiently prepare atoms in the dark state and to obtain the peak of the laser transmission. At even larger intensities, the amplitude of the EIT resonance decreases since optical pumping into the $F_g = 1$ hyperfine state prevails coherent excitation. Indeed, when the re-pump laser is used to bring back the population to the $F_g = 2$ level, the contrast of the amplitudes increases considerably [46]. Previous analysis implies that the dependence of the EIT amplitudes on the laser intensity must possess a maximum, as shown in figure 7(a). Maximal EIT amplitude for the wide Gaussian laser beam at 82 °C is obtained for the intensity of 1.1 mW cm^{-2} which is similar to results of the theoretical model shown in figure 4(b).

While the dependence of the EIT amplitudes on the laser intensity considerably varies with the cell temperatures, the EIT linewidths have a similar dependence on the laser intensity for the whole range of cell temperatures, as shown in figure 7(b). At lower laser intensities the EIT linewidths are
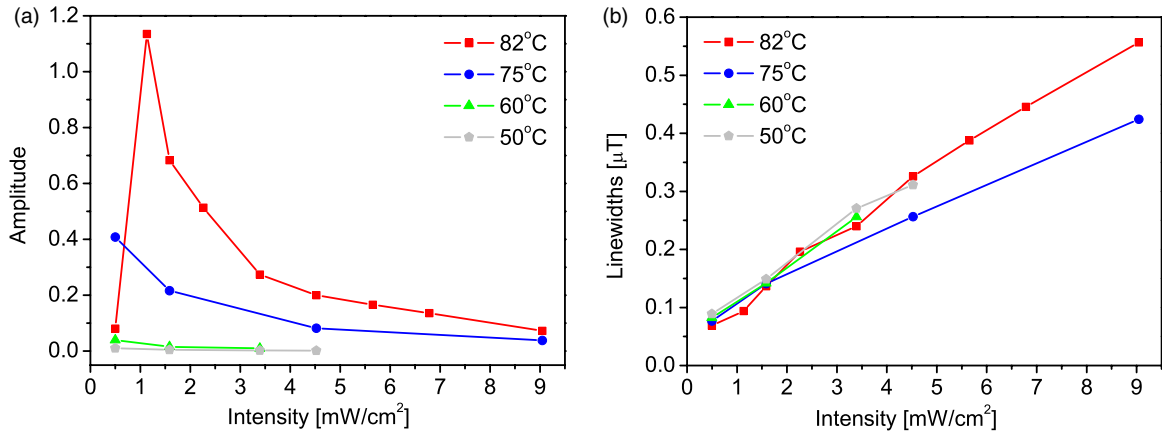
Figure 7. Experimental dependences of EIT (a) amplitudes and (b) linewidths on the overall laser intensity for a Gaussian laser beam with a diameter of 6.5 mm at four different temperatures.
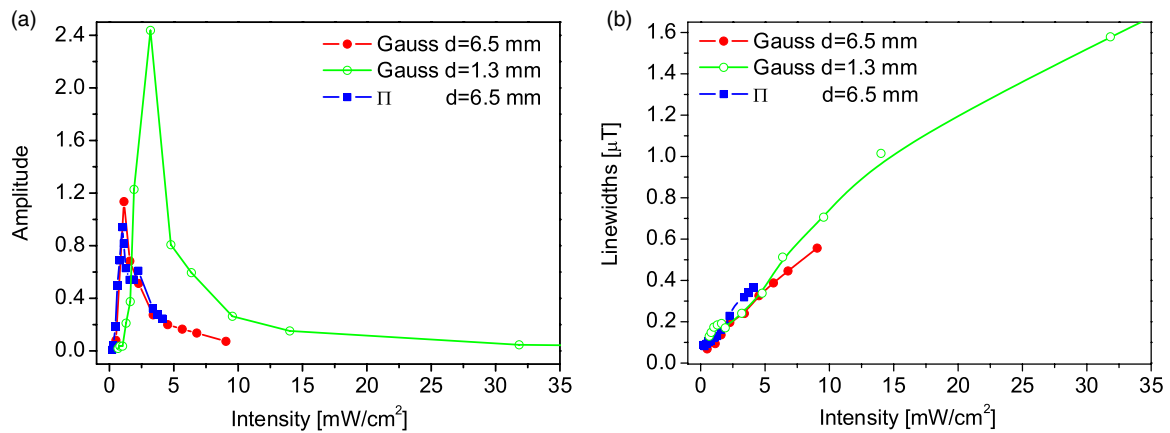

Figure 8. Experimental dependences of EIT (a) amplitudes and (b) linewidths on laser beam intensity for different laser radial profiles and diameter *d*: (i) Gaussian $d = 6.5$ mm, (ii) Π $d = 6.5$ mm and (iii) Gaussian $d = 1.3$ mm. Cell temperature is 82 °C.

independent of the cell temperature. Calculated linewidths, as a function of the laser intensity for 82 °C presented in figure 4(b), have a similar qualitative dependence as measured. These results are in agreement with [33] where a similar (non)dependence of Zeeman EIT on the cell temperature is obtained for cells with 1 and 10 Torr of Ne buffer gas. The estimated linewidth at zero laser intensity for a 6.5 mm laser beam diameter is about 50 nT or 0.7 kHz. This linewidth is an order of magnitude lower than in [33]. This reduction in linewidth could be due to the different buffer gas cells, but could also be attributed to the negligible stray magnetic fields inside the magnetic shielding achieved with hot air heating of the Rb cell.

The following results of the EIT line shapes, amplitudes and linewidths for different laser beams' radial profiles were obtained with a cell temperature of 82 °C. In figure 8 we show how the diameter of the Gaussian laser beam affects EIT amplitudes and linewidths. Amplitudes are much higher for the 1.3 mm than for the 6.5 mm beam diameter, as noted in figure 8(a). For the narrower laser beam, more non-coherent atoms can enter the laser beam and reach the intense central part. Thus, a lower off-resonant absorption is obtained for narrower than for wider Gaussian laser beams. Since we normalize the EIT resonance to the off-resonant transmission, a

stronger peak amplitude was measured for the Gaussian beam of 1.3 mm in diameter. On the other hand, EIT linewidths for both beam diameters are nearly the same (where the laser intensity ranges overlap), as given in figure 8(b). Although a narrower laser beam gives EIT line shapes with a very narrow central peak, this has an insignificant effect on EIT linewidths.

Figure 8 also presents the dependence of EIT amplitudes and linewidths on the laser intensity for a Π laser beam profile 6.5 mm in diameter. The theoretical comparisons given in [25] show that, as the laser intensity increases, resonances for the Gaussian beam get narrower and of a slightly higher amplitude than for the Π profile. Our results in figure 8 show that in the overlapping range of laser intensities there are no significant differences in EIT amplitudes for Gaussian and a Π profile of the same diameter. EIT linewidths, almost the same at a lower laser intensity, get slightly narrower for the Gaussian beam than for the Π laser beam profile. Very small differences of EIT properties obtained with the Gaussian and Π laser beam are in contrast with the strong effects of radial intensity distribution on EIT in a vacuum gas cell [47].

In order to observe EIT developed by weak laser light in the wings of the wide Gaussian laser beam, we measured transmission of the 6.5 mm Gaussian laser beam with the central part of the beam blocked by a mask 6.0 mm in
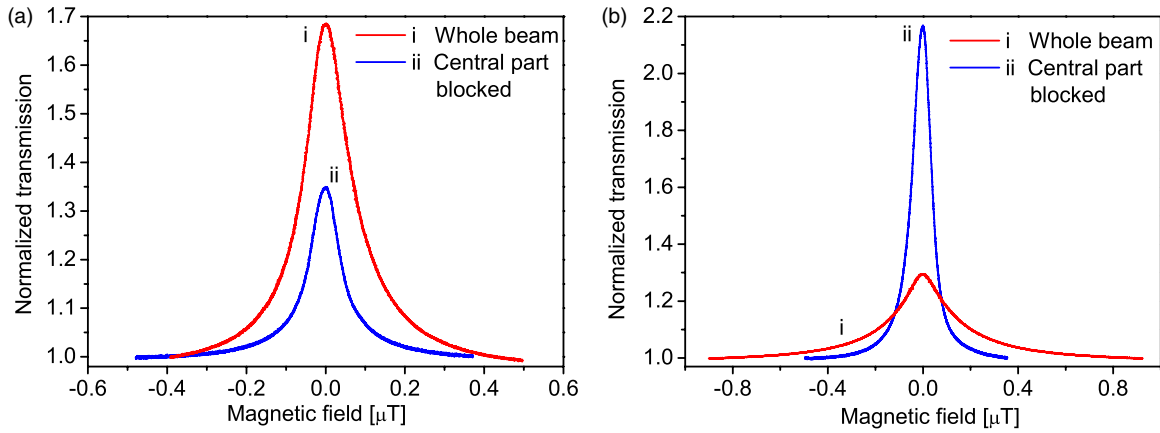
Figure 9. Measured EIT resonances for a Gaussian laser beam 6.5 mm in diameter. Marks (i) and (ii) indicate curves obtained detecting the whole beam and its outer parts only, respectively. Overall laser beam intensity is (a) 1.6 mW cm^{-2} and (b) 3.3 mW cm^{-2}.
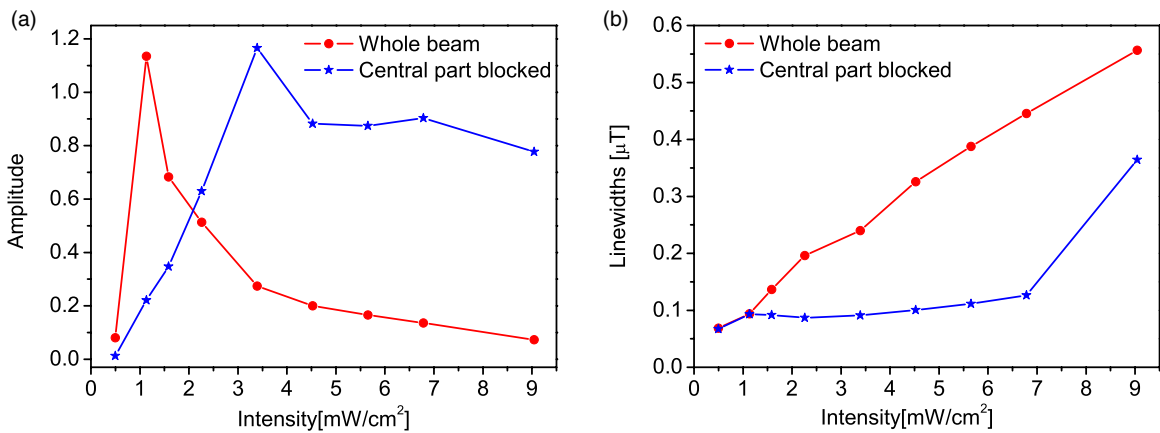

Figure 10. Experimental dependences of EIT (a) amplitudes and (b) linewidths on laser beam intensity obtained by measuring (i) the whole beam and (ii) only its outer parts. Cell temperature is 82 °C.

diameter, placed in front of the photo detector. Examples of such measurements, for two laser intensities, 1.1 and 3.3 mW cm^{-2}, are shown in figures 9(a) and (b), respectively.

EIT resonances measured by detecting the whole laser beam at lower laser intensities, have a Lorentzian line shape, in agreement with [32]. By blocking the central part of the beam, measured EIT resonances are due to the interaction of rather weak laser light in the wings of the beam with the atoms coherently prepared in the central parts of the laser beam. As we see from figure 9, the EIT resonances for the whole laser beam and for the beam whose central region is blocked, are both Lorentzian. That suggests that the diffusion-induced Ramsey effect is suppressed in this setup, likely because the atoms move mainly within the low intensity wings of the laser beam. However, we obtained interesting differences of EIT amplitudes and linewidths at different laser intensities. For the lower laser intensity, EIT resonances obtained by detecting the whole beam have a larger amplitude (figure 9(a)). As we increase the light intensity (above ∼2 mW cm^{-2}) measured resonances with the central part of the beam blocked, become more contrasted and narrower (figure 9(b)). The effect of this blocking is further investigated in figure 10 where we present dependences of EIT amplitudes and linewidths on the total intensity for these two experimental realizations.

From figure 10 we see benefits of blocking the central part of the laser beam at higher laser intensity: EIT contrast is higher and linewidths are narrower. The increase of the amplitudes is a consequence of the decreased optical pumping to the non-coupled ground state level $F_g = 1$ in the low intensity beam wings. This is in accordance with figures 4(a) and 7(a). EIT narrowing is also attributed to lower power broadening. No conclusion about the influence of Ramsey narrowing on the linewidths in figure 10 can be made due to the absence of the specific sharp central peak in the representative EIT resonances of figure 9.

4. Conclusion

We have presented experimental and theoretical results of the behaviour of Zeeman EIT resonances in a Rb buffer gas cell for different laser beam profiles, diameters and intensities. For the narrow Gaussian laser beam (1.3 mm in diameter) non-Lorentzian line shapes of EIT are obtained. The characteristic, very narrow central part of these resonances is a contribution of diffusion-induced Ramsey narrowing. We confirmed theoretical predictions that EIT resonances obtained with the wider Gaussian laser beam (6.5 mm in diameter) have different profiles at different laser intensities, a

Lorentzian-like profile for lower laser intensities and a non-Lorentzian shape with a narrower central part for higher laser intensities. In contrast to the case of the narrow laser beam, the non-Lorentzian line shape for a wider beam at higher intensities is due to the contribution of atoms from the beam's wings where the laser field is considerably lower than at the beam's centre. At lower laser beam intensities, the contribution of these segments is negligible, thus Lorentzian line shapes are obtained. Π-shaped laser beam, 6.5 mm in diameter, gives a pure Lorentzian EIT line shape.

EIT linewidths obtained either by the narrow or the wide Gaussian laser beam, for all laser intensities, are independent of the Rb temperature. The EIT with a Gaussian laser beam have the same amplitudes and are slightly narrower than those with the Π profile. About a six-fold increase in EIT contrast for higher laser intensities with a considerable decrease in linewidth was obtained simply by blocking the central part of the wide Gaussian laser beam, just in front of the photo detector. Such effects are attributed to the decreased optical pumping to the non-coupled ground state level $F_g = 1$ and reduced power broadening in the low intensity beam wings. A possible influence of the diffusion-induced Ramsey effect could not be confirmed because of the absence of a narrow peak in the EIT line shapes obtained from the beam wings.

Acknowledgments

References

[1] Fleischhauer M, Imamoğlu A and Marangos J P 2005 *Rev. Mod. Phys.* **77** 633
[2] Phillips D F, Fleischhauer A, Mair A, Walsworth R L and Lukin M D 2001 *Phys. Rev. Lett.* **86** 783
[3] Scully M O, Zhu S and Gavrielides A 1989 *Phys. Rev. Lett.* **62** 2813
[4] Harris S E, Field J E and Imamoğlu A 1990 *Phys. Rev. Lett.* **64** 1107
[5] Schmidt H and Imamoğlu A 1996 *Opt. Lett.* **21** 1936
[6] Knappe S, Shah V, Schwindt P D, Holberg L, Kitching J, Liew L A and Moreland J 2004 *Appl. Phys. Lett.* **75** 1460
[7] Fleischhauer M, Matsko A V and Scully M O 2000 *Phys. Rev.* A **62** 013808
[8] Dupont-Roc J, Haroche S and Cohen-Tannoudji C 1969 *Phys. Lett.* A **28** 638
[9] Cohen-Tannoudji C, Dupont-Roc J, Haroche S and Laloë F 1970 *Rev. Phys. Appl.* **5** 102
[10] Weis A and Karnosky S I 1992 *J. Opt. Soc. Am.* B **10** 716
[11] Budker D, Gawlik W, Kimball D F, Rochester S M, Yashchuk V V and Weis A 2002 *Rev. Mod. Phys.* **74** 1153
[12] Castagna N and Weis A 2011 *Phys. Rev.* A **84** 053421
[13] Klein M, Hohensee M, Phillips D F and Walsworth R L 2011 *Phys. Rev.* A **83** 013826
[14] Klein M J 2009 Slow and stored light in atomic vapour cells *PhD Thesis* Harvard University
[15] Gawlik W, Kowalski J, Neumann R and Trager F 1974 *Opt. Commun.* **12** 400
[16] Budker D, Yashchuk V and Zolotorev M 1998 *Phys. Rev. Lett.* **81** 5788
[17] Varzhapetyan T S, Li H, Ariunbold G O, Sautenkov V A, Rostovtsev Y V and Scully M O 2009 *Opt. Commun.* **282** 39
[18] Li H, Sautenkov V A, Varzhapetyan T S, Rostovtsev Y V and Scully M O 2008 *J. Opt. Soc. Am.* B **25** 1702
[19] Auzinsh M, Budker D and Rochester S 2010 *Optically Polarized Atoms. Understanding Light–Atom Interactions* (New York: Oxford University Press)
[20] Novikova I, Walsworth R L and Xiao Y 2012 *Laser Photon. Rev.* **6** 333
[21] Li L, Peng X, Lin C, Guo H and Chen X 2004 *J. Phys. B: At. Mol. Opt. Phys.* **37** 1873
[22] Pack M V, Camacho R M and Howell J C 2007 *Phys. Rev.* A **76** 013801
[23] Javan A, Kocharovskaya O, Lee H and Scully M O 2002 *Phys. Rev.* A **66** 013805
[24] Ye C Y and Zibrov A S 2002 *Phys. Rev.* A **65** 023806
[25] Taichenachev A V, Tumaikin A M, Yudin V I, Stahler M, Wynands R, Kitching J and Hollberg L 2004 *Phys. Rev.* A **69** 024501
[26] Radonjić M, Arsenović D, Grujić Z and Jelenković B M 2009 *Phys. Rev.* A **79** 023805
[27] Levi F, Godone A, Vanier J, Micalizio S and Modugno G 2000 *Eur. Phys. J.* D **12** 53
[28] Gilles H, Cheron B, Emile O, Bretenaker F and Floch A L 2001 *Phys. Rev. Lett.* **86** 1175
[29] Dicke R H 1748 *Phys. Rev.* **89** 472
[30] Erhard M and Helm H 2001 *Phys. Rev.* A **63** 043813
[31] Xiao Y, Novikova I, Phillips D F and Walsworth R L 2006 *Phys. Rev. Lett.* **96** 043601
[32] Xiao Y, Novikova I, Phillips D F and Walsworth R L 2008 *Opt. Express* **16** 14128
[33] Figueroa E, Vewinger F, Appel J and Lvovsky A L 2006 *Opt. Lett.* **17** 2625
[34] Vanier J, Godone A and Levi F 1998 *Phys. Rev.* A **58** 2345
[35] Novikova I, Phillips D F, Zibrov A S, Walsworth R L and Yudin V I 2006 *Opt. Lett.* **31** 2353
[36] Taichenachev A V, Yudin V I, Wynands R, Stahler M, Kitching J and Hollberg L 2003 *Phys. Rev.* A **67** 033810
[37] Failache H, Valente P, Ban G, Lorent V and Lezama A 2003 *Phys. Rev.* A **67** 043810
[38] Logg A and Wells G N 2010 *ACM Trans. Math. Softw.* **37** 20:1–20:28
[39] Logg A, Mardal K-A and Wells G N 2012 *Automated Solution of Differential Equations by the Finite Element Method (Lecture Notes in Computational Science and Engineering vol 84)* (Berlin: Springer)
[40] Mortensen M, Langtangen H P and Wells G N 2011 *Adv. Water Resources* **34** 1082
[41] Petelski T, Fattori M, Lamporesi G, Stuhler J and Tino G M 2003 *Eur. Phys. J.* D **22** 279
[42] Wasik G, Gawlik W, Zachorowski J and Zawadzki W 2002 *Appl. Phys.* B **75** 613
[43] Krmpot A J, Ćuk S M, Nikolić S N, Radonjić M, Slavov D G and Jelenković B M 2009 *Opt. Express* **17** 22491
[44] Matsko A B, Novikova I, Scully M O and Welch G R 2001 *Phys. Rev. Lett.* **87** 133601
[45] Matsko A B, Novikova I and Welch G R 2002 *J. Mod. Opt.* **49** 367
[46] Kazakov G, Masets I, Rozhdestvensky Yu, Mileti G, Delporte J and Matisov B 2005 *Eur. Phys. J.* D **35** 445
[47] Krmpot A J, Radonjić M, Ćuk S M, Nikolić S N, Grujić Z D and Jelenković B M 2011 *Phys. Rev.* A **84** 043844

The connection between electromagnetically induced transparency in the Zeeman

configuration and slow light in hot rubidium vapor

The connection between electromagnetically induced transparency in the Zeeman configuration and slow light in hot rubidium vapor

S N Nikolić, V Djokic, N M Lučić, A J Krmpot, S M Ćuk, M Radonjić and B M Jelenković

Institute of Physics, University of Belgrade, Pregrevica 118, 11080 Belgrade, Serbia

E-mail: stankon@ipb.ac.rs

Abstract

We experimentally studied Zeeman electromagnetically induced transparency (EIT) resonances and slow light propagation in hot Rb vapor. Propagation of weak σ^- polarized light pulses in the presence of stronger σ^+ polarized background through Rb vapor was realized using a single laser beam and the Pockels cell. The dependences of slow light group velocity and fractional pulse delay on the overall laser beam intensity and temporal pulse length showed that lower optical power and longer light pulses lead to improved EIT and slow light features. The connection between EIT and slow light was also investigated showing that narrower and more contrasted EIT resonances are necessary for further decreasing a group velocity.

PACS numbers: 03.65.Fd, 03.65.Sq

(Some figures may appear in colour only in the online journal)

1. Introduction

Coherent effects in Doppler broadened alkali atom vapors have been thoroughly investigated over the past decade. Coherent population trapping [1] and electromagnetically induced transparency (EIT) [2] have been observed and characterized in either the pump–probe or Zeeman configuration [3, 4]. In the latter case, EIT is based on Zeeman coherences between magnetic sublevels of a given hyperfine state of the alkali atom electronic ground state. The amplitudes and widths (full-width at half-maximum, FWHM) of the EIT resonances are limited by the average atom time-of-flight through the laser beam. To prolong the interaction time and thus the lifetime of the dark states, an inert buffer gas is added to atomic vapor in order to slow the diffusion of the coherently prepared atoms through the laser beam [5]. In such buffer gas cells, narrower EIT resonances compared to the vacuum cells and very steep dispersion of

the index of refraction are obtained. This results in low group velocities $v_g = \frac{c}{n + \omega \frac{\partial n}{\partial \omega}}$ of the light pulses or the so-called slow light phenomena [6]. We define an absolute time delay $\Delta\tau$ as the time difference between arrivals of the pulse slowed down in the Rb cell and the reference pulse. The fractional time delay η is defined as the ratio of an absolute time delay to the temporal pulse length τ_{pulse}.

In the gaseous atomic systems, ultra-low group velocities have been demonstrated experimentally in Bose–Einstein condensates [7] and thermal atomic vapor [8].

In this paper, we present the measurements of slow light in the Zeeman EIT configuration in hot Rb vapor contained in a buffer gas cell. The overall laser intensity and the temporal pulse lengths were varied in order to obtain maximal fractional delay of light pulses with minimum distortion. The dependence of the slow light effect on the EIT features [9] is also shown for our experimental setup.
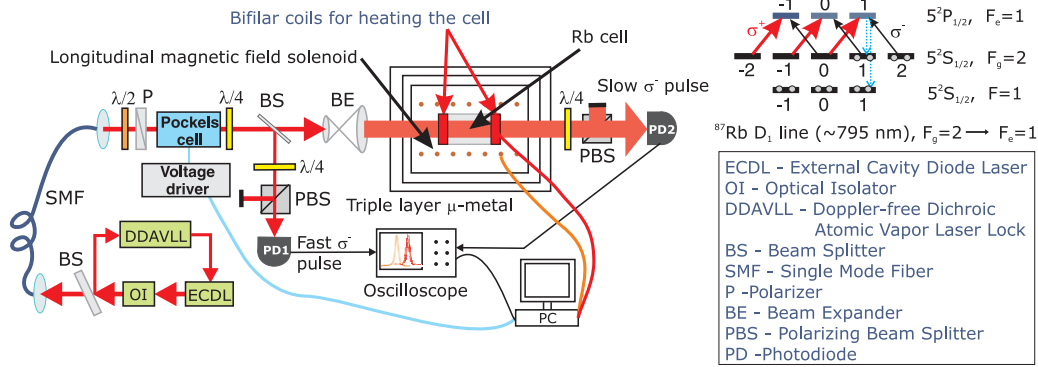
Figure 1. The experimental setup and the atomic transition used in the experiment. The computer controls the cell temperature, the external longitudinal magnetic field and the polarization pulses for the Pockels cell.
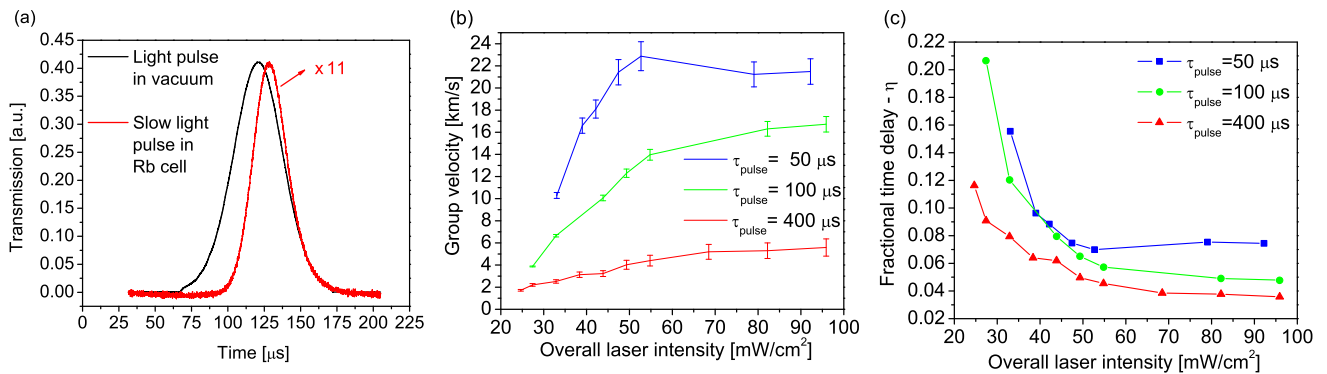

Figure 2. Experimental results of slow light. The power of the σ^- pulse in its peak is 15% of the overall laser power. (a) Black and red pulses denote reference and slow pulses, respectively. The temporal pulse length is 100 μs, the overall laser intensity is 40.5 mW cm^{-2} and the absolute time delay is 8.78 μs corresponding to a group velocity of 9.1 km s^{-1}. The dependence of (b) the group velocity and (c) the fractional time delay of σ^- pulses on the overall laser intensity for different temporal pulse lengths is shown. Blue, green and red curves show the results for pulse lengths of 50, 100 and 400 μs, respectively.

2. Experimental setup

The experimental setup is shown in figure 1. The external cavity diode laser is frequency locked to the hyperfine $F_g = 2 \rightarrow F_e = 1$ transition of the D_1 line in ^{87}Rb by using the Doppler-free dichroic atomic vapor laser lock method [10]. The laser beam passes through the 8 cm long Rb cell containing a natural abundance of Rb isotopes and filled with 30 torr of Ne buffer gas. The temperature of the cell is kept at 80 °C. The laser beam diameter is 1.4 mm. The cell is placed in the solenoid used for scanning the axial magnetic field in order to obey two-photon detuning between −400 and +400 kHz. The elliptically polarized laser beam consisting of a weak σ^- signal field and a stronger σ^+ control field is sent to the Rb cell. The Zeeman EIT resonances are obtained by measuring the transmission of σ^- light as a function of two-photon detuning. We next measure slow light propagation. By using the Pockels cell, we slightly rotate the polarization of the input light to create a weak σ^- pulse. Because of the presence of the strong σ^+ field, the resonant σ^- pulse can freely propagate through the otherwise opaque medium but with a substantially reduced group velocity.

3. Results and discussions

Experimental results of slow light propagation are presented in figure 2(a).

The group velocity is simply calculated as $v_g = L/\Delta\tau$, where L is the length of the cell and $\Delta\tau$ is absolute time delay.

The group velocity of the σ^- pulse and its fractional time delay as functions of the overall laser intensity for different temporal pulse lengths are shown in figures 2(b) and (c), respectively. The typical Zeeman EIT resonance is shown in figure 3(a).

By measuring the EIT linewidths and amplitudes at different laser intensities, the connection between slow light and EIT features could be established. In figures 3(b) and (c), we present the dependences of slow light fractional time delay on the EIT linewidth and the amplitude to linewidth ratio, respectively.

Group velocities obtained in the experiment are in the range from 1.7 km s^{-1} (overall laser intensity $I = 24.5$ mW cm^{-2} and pulse length $\tau_{pulse} = 400\,\mu$s) up to 23 km s^{-1} ($I = 52.8$ mW cm^{-2}, $\tau_{pulse} = 50\,\mu$s). Fractional pulse delays η lie in the range from 3.5 ($I = 96$ mW cm^{-2}, $\tau_{pulse} = 400\,\mu$s) up to 20.5% ($I = 27.4$ mW cm^{-2}, $\tau_{pulse} = 100\,\mu$s). The linewidths of the EIT resonances decrease from 180 down to 65 kHz as the laser intensity decreases from 110 down to 25 mW cm^{-2}. Due to the increased absorption, measurements below intensities of 20 mW cm^{-2} were not possible. Lower group velocities were obtained for narrower and more contrasted EIT lines as shown in figures 3(b) and (c).

4. Summary

We have studied the Zeeman EIT resonances and slow light propagation in hot Rb vapor and a connection between
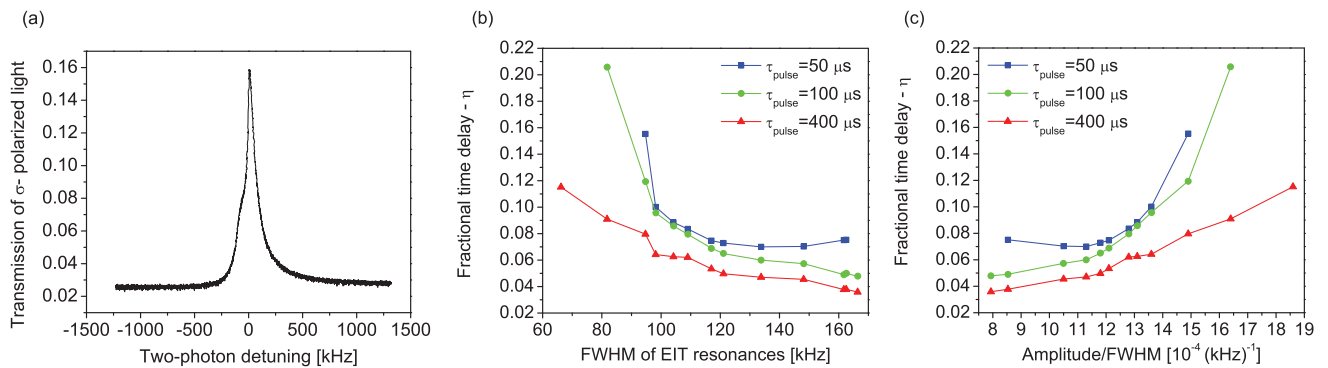
Figure 3. The connection between slow light and the EIT features. (a) The measured EIT resonance for the overall laser intensity of 40.5 mW cm^{-2}. The linewidth and amplitude of the resonance are 98 kHz and 0.13, respectively. The dependence of fractional time delay of slow light pulses on the EIT. (b) The linewidth and (c) amplitude to linewidth ratio for different temporal pulse lengths are shown. Blue, green and red curves show the results for pulse lengths of 50, 100 and 400 μs, respectively.

these coherent phenomena. We observed that decreasing the overall laser intensity leads to lower values of group velocity and fractional time delay. This is in agreement with the analysis in [2]. We also observed a strong dependence of slow light parameters on the temporal length of light pulses. Longer pulses exhibit lower group velocities. We concluded that narrower and more contrasted EIT resonances lead to improved slow light features. In forthcoming work we will investigate how to increase both the transparency of the σ^- optical field and the fractional time delay so that storage of light [11] can be achieved.

Acknowledgment

References

[1] Arimondo E 1996 Coherent population trapping in laser spectroscopy *Prog. Opt.* **35** 257–354

[2] Fleischhauer M, Imamoglu A and Marangos J P 2005 Electromagnetically induced transparency: optics in coherent media *Rev. Mod. Phys.* **77** 633–73

[3] Moruzzi G and Strumia F 1991 *The Hanle Effect and Level Crossing Spectroscopy* (New York: Plenum)

[4] Andreeva C, Cartaleva S, Dancheva Y, Biancalana V, Burchianti A, Marinelli C, Mariotti E, Moi L and Nasyrov K 2002 Coherent spectroscopy of degenerate two-level systems in Cs *Phys. Rev.* A **66** 012502 1–12

[5] Mikhailov E E, Sautenkov V A, Novikova I and Welch G R 2004 Large negative and positive delay of optical pulses in coherently prepared dense Rb vapor with buffer gas *Phys. Rev.* A **69** 063808

[6] Khurgin J B and Tucker R S 2009 *Slow Light Science and Applications* (Boca Raton, FL: CRC Press)

[7] Hau L V, Harris S E, Dutton Z and Behroozi C H 1999 Light speed reduction to 17 metres per second in an ultracold atomic gas *Nature* **397** 594–8

[8] Kash M M, Sautenkov V A, Zibrov A S, Hollberg L, Welch G R, Lukin M D, Rostovtsev Y, Fry E S and Scully M O 1999 Ultraslow group velocity and enhanced nonlinear optical effects in a coherently driven hot atomic gas *Phys. Rev. Lett.* **82** 5229–32

[9] Klein M, Hohensee M, Xiao Y, Kalra R, Phillips D F and Walsworth R L 2009 Slow-light dynamics from electromagnetically-induced-transparency spectra *Phys. Rev.* A **79** 053833

[10] Wasik G, Gawlik W, Zachorowski J and Zawadzki W 2002 Laser frequency stabilization by Doppler-free magnetic dichroism *Appl. Phys.* B **75** 613–9

[11] Phillips D F, Fleischhauer A, Mair A, Walsworth R L and Lukin M D 2001 Storage of light in atomic vapor *Phys. Rev. Lett.* **86** 783–6

Evolution of dark state of an open atomic system in constant intensity laser field

A. J. Krmpot,[*] M. Radonjić, S. M. Ćuk, S. N. Nikolić, Z. D. Grujić, and B. M. Jelenković

Institute of Physics, University of Belgrade, Pregrevica 118, RS-11080 Belgrade, Serbia

We studied experimentally and theoretically the evolution of open atomic systems in the constant intensity laser field. The study is performed by analyzing the line shapes of Hanle electromagnetically induced transparency (EIT) obtained in different segments of a laser beam cross section of constant intensity, i.e., a Π-shaped laser beam. Such Hanle EIT resonances were measured using a small movable aperture placed just in front of the photodetector, i.e., after the entire laser beam had passed through the vacuum Rb cell. The laser was locked to the open transition $F_g = 2 \rightarrow F_e = 1$ at the D_1 line of ^{87}Rb with laser intensities between 0.5 and 4 mW/cm^2. This study shows that the profile of the laser beam determines the processes governing the development of atomic states during the interaction. The resonances obtained near the beam center are narrower than those obtained near the beam edge, but the significant changes of the linewidths occur only near the beam edge, i.e., right after the atom enters the beam. The Hanle EIT resonances obtained near the beam center exhibit two pronounced minima next to the central maximum. The theoretical model reveals that the occurrence of these transmission minima is a joint effect of the preparation of atoms into the dark state and the optical pumping into the uncoupled ground level $F_g = 1$. The appearance of the transmission minima, although similar to that observed in the wings of a Gaussian beam [A. J. Krmpot *et al.*, Opt. Express **17**, 22491 (2009)], is of an entirely different nature for the Π-shaped laser beam.

I. INTRODUCTION

Coherent effects in Doppler-broadened alkali-metal-atom vapors have been intensively investigated because of numerous applications of phenomena based on such coherent effects. Coherent population trapping (CPT) [1,2], electromagnetically induced transparency (EIT) [3], and electromagnetically induced absorption (EIA) [4] have been observed and examined in either pump-probe or Hanle configurations [5,6]. All these phenomena strongly depend on the intensity of the applied laser field and consequently also on the radial profile of the intensity of the laser beam. Most often, in experiments, the radial laser beam profile is Gaussian, while theoretical models assume that the intensity of the laser field is constant across the diameter of the laser beam. The latter will be referred to throughout this paper as the Π laser beam. For the interaction of the Gaussian or Π laser beam with alkali-metal-atom vapor, the different effects such as Ramsey and Dicke narrowing, transit time, and Doppler broadening are examined either in vacuum [7,8] or in buffer gas cells [9–12] The differences in EIT line shapes for Gaussian and Π laser beams were presented in [13–15] by considering only the entire laser beam contribution without focusing on the details of laser-atom interaction within the laser beam. However, different parts of the laser beam cross section, after passing through the alkali-metal-vapor cell, carry different information about the atomic state and yield different EIT resonances [16].

In this paper we study time and space evolution of atomic states as the Rb atoms traverse the Π-shaped laser beam, i.e., electric field of nearly constant intensity. Such studies were performed by measuring EIT line shapes from different circular segments of the laser beam cross section, much smaller

than the laser beam diameter, and after the entire beam had first passed through the Rb cell. We used a Hanle configuration with the laser locked to the $F_g = 2 \rightarrow F_e = 1$ hyperfine transition of the D_1 line in the ^{87}Rb isotope in the vacuum vapor cell. Similar examinations of the EIT resonances in different segments, but for the Gaussian laser beam cross section, were performed in an effusive regime in the Rb vacuum cell [16] and in a diffusive regime in the dense ^{4}He$^+$ vapor [17]. Due to interaction with a laser electric field having different distributions in the Gaussian and Π-shaped beams, the atomic state develops differently in the presence of a small external magnetic field. Narrowing of the Hanle EIT in the wings of the Gaussian laser beam is observed and explained by the interference of the laser light and coherently prepared atoms coming from the central part of the beam [16]. Such Ramsey-type narrowing of dark-state resonances was studied also in different geometries in Refs. [18,19]. The narrowing is accompanied by the appearance of Ramsey-like transmission minima in Hanle EIT line shapes detected in the Gaussian beam wings. Therefore, it is expected that examination of EIT line shapes obtained in different segments of Π laser beam cross section should reveal some details about the transient evolution of interacting atoms. It can also help in understanding differences in linewidths and amplitudes of EIT resonances obtained using two laser beam profiles and reported in Refs. [13–15]. To our knowledge, partial Hanle EIT from different segments of the Π laser beam was not thoroughly investigated. The significance of using the Π profile is in the elimination of the effects due to transverse variation of the laser intensity, providing conditions for more direct insight into the laser-atom interaction. Experimental results of the spatial dependence of EIT line shapes along the laser beam profile are compared with the theoretical calculations. The theoretical model is based on time-dependent optical Bloch equations (OBEs) predicting the evolution of the
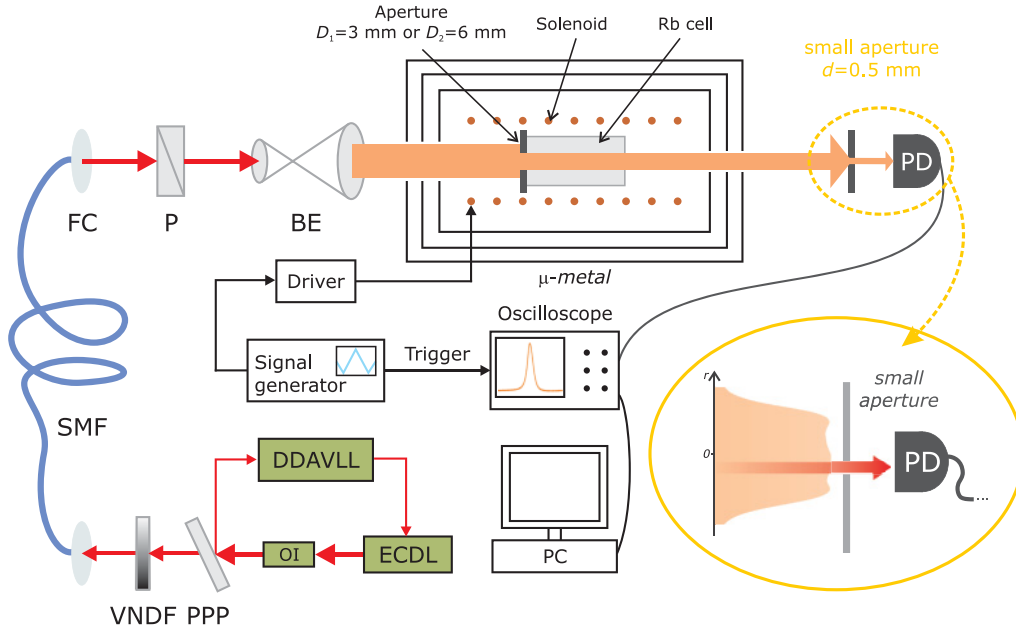
---

*krmpot@ipb.ac.rs

FIG. 1. (Color online) (a) Experimental setup: ECDL - external cavity diode laser; OI - optical isolator; DDAVLL - Doppler-free dichroic atomic vapor laser lock; VNDF - variable neutral density filter; PPP - plan parallel plate; SMF - single-mode fiber; FC - fiber collimator; P - polarizer; BE - beam expander; PD - photodiode. The aperture moved on the translation stage allows only a selected part of the laser beam to reach the detector, while the rest of the laser beam is blocked.

Zeeman sublevel populations and coherences in the laser field of profiled intensity. It unveils the influence of the optical pumping into the uncoupled ground-state hyperfine level on the obtained Hanle EIT line shapes.

II. EXPERIMENT

The experimental setup is shown in Fig. 1. The external cavity diode laser is frequency locked to the $F_g = 2 \rightarrow F_e = 1$ transition of the D_1 line in ^{87}Rb, where F_g and F_e represent the angular momenta of the ground- and excited-state hyperfine levels, respectively. Laser locking is performed in an auxiliary vacuum Rb cell using the Doppler-free dichroic atomic vapor laser lock (DDAVLL) method [20,21]. The variable neutral density filter is used for laser power adjustments. Single-mode fiber was used to provide the Gaussian laser beam. After passing through the Glan-Thompson polarizer, the laser beam becomes linearly polarized. The Π-shaped laser beam profile was obtained after expanding the Gaussian laser beam from the single-mode fiber to 20 mm in diameter and then extracting its central part using the circular aperture placed on the entrance window of the cell. After experimenting with different diameters of the expanded Gaussian laser beam, sizes of apertures, and thicknesses of the foil used for the apertures, we obtained the Π-shaped laser beam whose radial intensity profiles have the least pronounced diffraction effects as shown in Fig. 2. The beam profiles measured by the beam profiler are 3 cm [Figs. 2(a) and 2(c)] and 30 cm [Figs. 2 (b) and 2(d)] away from the 3- or 6-mm aperture on 0.1-mm-thick foil. The first profile is at a distance equal to the distance between the aperture and the midsection of the Rb cell. This profile is referred to as Π-shaped throughout the paper. We used the beam profile at 30 cm from the aperture to show

relatively small changes in the profile with distance and to justify use of the Π-shaped profile in the theoretical model. A well-collimated Π-shaped laser beam then passes through the 6-cm-long vacuum Rb cell containing a natural abundance of rubidium isotopes. The cell is placed in the solenoid used for scanning the axial magnetic field between -100 and $+100$ μT. The cell and the solenoid are placed inside the triple-layered μ-metal cylinders to eliminate Earth's and stray magnetic fields. In order to measure Hanle EIT from only small parts of the laser beam cross section, a movable aperture of 0.5 mm in diameter is placed in front of the photodiode with a large detection surface (area, 80 mm^2). "Small aperture" will henceforth refer to an 0.5-mm aperture in order to differ from the 3- or 6-mm aperture used for laser beam shaping, placed in front of the Rb cell. By moving this small aperture with the precise translation stage we allow only light from a small segment of the transmitted laser beam to reach the photodiode, after the entire beam passes through the Rb cell. The signal obtained from this photodiode while scanning the external magnetic field is recorded by the digital oscilloscope and transferred to the computer.

III. THEORETICAL MODEL

Hanle EIT resonances were calculated for the D_1 line transition $F_g = 2 \rightarrow F_e = 1$ of ^{87}Rb coupled to a linearly polarized laser in a Rb vacuum cell. The energy level diagram given in Fig. 3 shows hyperfine levels either coupled to the laser light or populated due to spontaneous emission. The quantization z axis is chosen to be parallel to the external magnetic field. The complete magnetic sublevel structure is considered in calculations. The model is based on
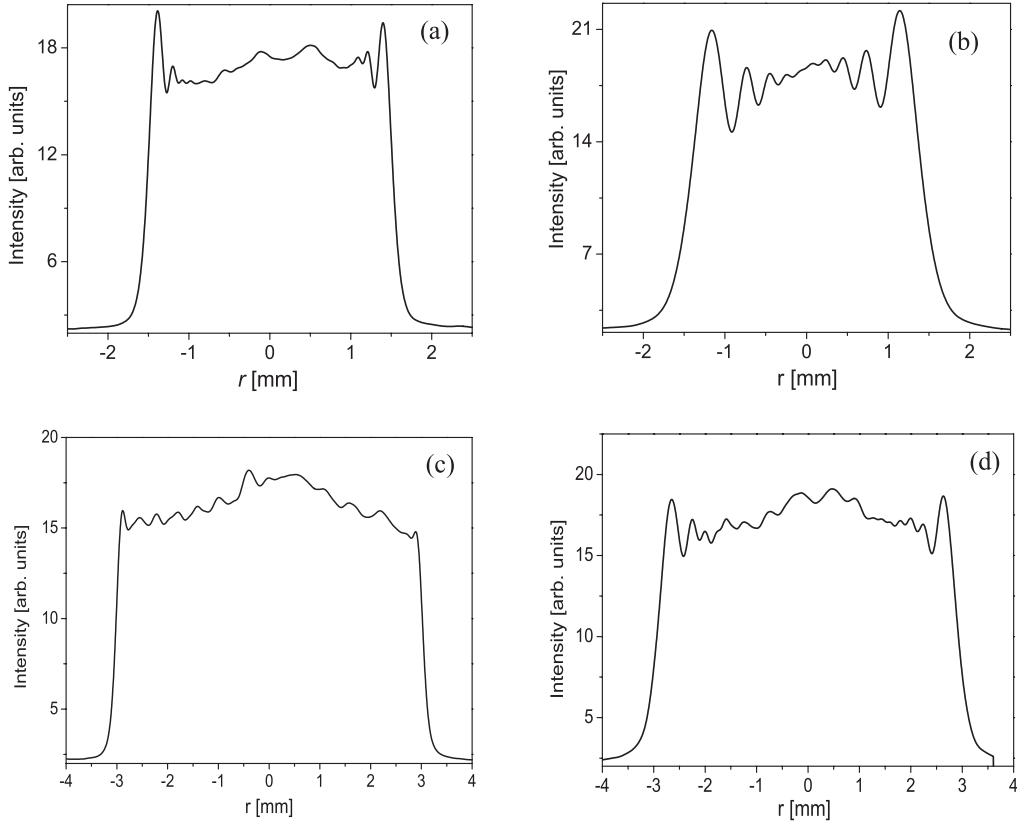
FIG. 2. Two Π-shaped beam profiles recorded by a beam profiler placed at different distances from the circular aperture: at 3 cm (a) and 30 cm (b) for the 3-mm profile, and at 3 cm (c) and 30 cm (d) for the 6-mm profile.

time-dependent optical Bloch equations for the density matrix of a moving atom,

$$\dot{\rho} = -\frac{i}{\hbar}[H_{\text{atom}}(B) + H_{\text{int}}(t), \rho] + \dot{\rho}_{\text{SE}}, \qquad (1)$$

where

$$H_{\text{atom}}(B) = \sum_j \hbar\omega_j(B)|g_j\rangle\langle g_j| + \sum_k \hbar\omega_k(B)|e_k\rangle\langle e_k| \qquad (2)$$

is the atomic Hamiltonian corresponding to ground (excited) states $|g_j\rangle \equiv |F_g, m_g = j\rangle$ ($|e_k\rangle \equiv |F_e, m_e = k\rangle$) with
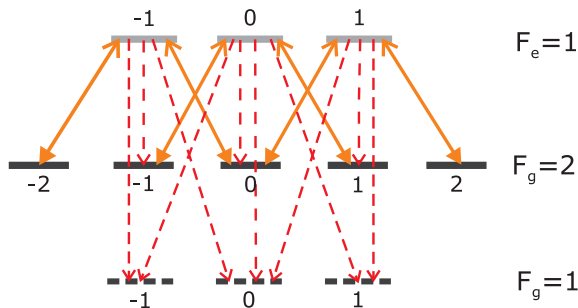

FIG. 3. (Color online) Zeeman sublevel scheme in ^{87}Rb at the D_1 line. The solid lines denote coupling with σ^+ and σ^- components of linearly polarized laser light. Dashed lines represent spontaneous emission.

Zeeman-shifted energies $\hbar\omega_j(B)$ [$\hbar\omega_k(B)$] in the external magnetic field B. Laser-atom interaction is given by

$$H_{\text{int}}(t) = -\sum_{j,k}\mathbf{E}(t)\cdot\mathbf{d}_{jk}(|g_j\rangle\langle e_k| + |e_k\rangle\langle g_j|), \qquad (3)$$

where $\mathbf{E}(t)$ is the time-dependent laser electrical field and $\mathbf{d}_{jk}$ is the atomic electric dipole moment for the transition between states $|g_j\rangle$ and $|e_k\rangle$. Spontaneous emission is included through the Lindblad-form term

$$\dot{\rho}_{\text{SE}} = \frac{\Gamma}{2}\sum_m 2A_m\rho A_m^\dagger - A_m^\dagger A_m\rho - \rho A_m^\dagger A_m, \qquad (4)$$

where $\Gamma = 2\pi \times 5.746$ MHz is the D_1 line decay rate of the excited state and A_m are operators corresponding to dipole transitions from the excited- to ground-state manifold, leading to

$$\langle e_i|\dot{\rho}_{\text{SE}}|e_j\rangle = -\Gamma\rho_{e_i e_j}, \quad \langle e_i|\dot{\rho}_{\text{SE}}|e_j\rangle = -\frac{\Gamma}{2}\rho_{e_i g_j},$$

$$\langle g_i|\dot{\rho}_{\text{SE}}|g_j\rangle = (-1)^{i+j}(2F_e+1)\Gamma_{F_e\to F_g}\sum_{q=-1}^{1}\begin{pmatrix} F_e & 1 & F_g \\ j+q & -q & -j \end{pmatrix}$$

$$\times \begin{pmatrix} F_e & 1 & F_g \\ i+q & -q & -i \end{pmatrix}\rho_{e_{i+q} e_{j+q}}. \qquad (5)$$

$\Gamma_{F_e \to F_g}$ is the decay rate from F_e to one F_g ground hyperfine level given by

$$\Gamma_{F_e \to F_g} = (2J_e + 1)(2F_g + 1) \left\{ \begin{matrix} J_g & J_e & 1 \\ F_e & F_g & I_g \end{matrix} \right\}^2 \Gamma, \qquad (6)$$

where J and I represent the electron and nuclear angular momentum quantum numbers. Equations for density matrix elements related to the $F_g = 1$ ground level are excluded since that level is not coupled by the laser. For additional details please refer to [15]. It is assumed that after colliding with cell walls, atoms reset into an internal state with equally populated ground magnetic sublevels. Between collisions with cell walls, rubidium atoms interact only with the axially oriented homogeneous magnetic field and spatially dependent laser electric field. Collisions among Rb atoms are negligible due to very low Rb vapor pressure at room temperature, so an atom moves through the laser beam with constant velocity $\mathbf{v} = \mathbf{v}_\parallel + \mathbf{v}_\perp$, where $\mathbf{v}_\parallel$ and $\mathbf{v}_\perp$ are velocity components parallel and perpendicular to laser propagation direction, respectively. The former affects the longitudinal direction of the atomic trajectory and Doppler shift of the laser frequency seen by a moving atom, while the latter determines the transverse direction of the trajectory and the interaction time. The dependence of the laser intensity on the radial distance r for a Π-shaped profile was modeled using the following equation:

$$I(r) = \bar{I} a \{1 + \text{erf}\,[p(r_0 - r)]\}^2, \qquad (7)$$

where r_0 is the beam radius, $\bar{I}$ is the beam intensity (total laser power divided by $r_0^2 \pi$), a is the normalization constant, and p is a positive parameter affecting the steepness of the profile near $r = r_0$. In our calculations we neglect longitudinal changes of the beam profile compared to transverse ones so that only the transverse direction of the trajectory matters. Therefore, we drop the explicit dependence on z of all physical quantities. From the reference frame of the moving atom, the electric field varies and the rate of variation depends only on $\mathbf{v}_\perp$. Assume that the transverse projection of the atomic trajectory is given by

$$\mathbf{r}_\perp(t) = \mathbf{r}_{0\perp} + \mathbf{v}_\perp t, \qquad (8)$$

where $\mathbf{r}_{0\perp}$ is the perpendicular component of the atom position vector at $t = 0$. The temporal variation of the laser intensity seen by the atom is given by

$$I(t) \equiv I(\mathbf{r}_\perp(t)) = I(\mathbf{r}_{0\perp} + \mathbf{v}_\perp t), \qquad (9)$$

representing the spatial laser intensity variation along the trajectory of the atom in the laboratory frame. Additionally, due to the cylindrical symmetry of the beam profile, spatial dependence becomes purely radial dependence. The observed resonances in EIT experiments are a probabilistic average of the contributions of many individual, mutually noninteracting atoms. Rb atoms traverse the laser beam at different trajectories with different velocities. Maxwell-Boltzmann velocity distribution, diversity of atomic trajectories, and custom cylindrically symmetric radial profile of the laser electric field are treated similarly as in [15]. The trajectories having different distances from the laser beam center are chosen so that the beam cross section is uniformly covered (Fig. 4). The chosen trajectories correspond to different angles ϕ defined as shown
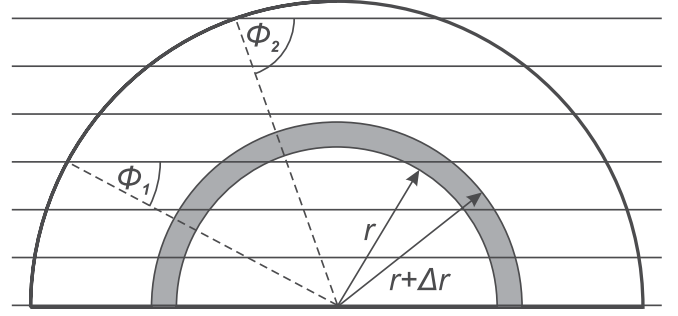

FIG. 4. Schematic of atomic trajectories chosen to cover the entire laser beam cross section (horizontal straight lines). Each trajectory defines certain angle ϕ, e.g., ϕ_1 and ϕ_2. The contribution of each segment, like the gray ring segment, is obtained by integrating the density matrix over all trajectories containing points with radial distances in the interval $(r, r + \Delta r)$.

in the Fig. 4. For a representative set of atomic velocities the atomic density matrix $\rho(B; \mathbf{v}; \mathbf{r}_\perp)$ along a given trajectory is calculated assuming constant magnetic field B during the atomic transit through the laser beam. To obtain the atomic ensemble density matrix $\rho(B; r)$ across the beam cross section for a set of radial distances r, the calculated density matrices are first averaged over the Maxwell-Boltzmann velocity distribution. Furthermore, by integrating the density matrix over all trajectories containing points with radial distances in the interval $(r, r + \Delta r)$ the contribution $\rho(B; r)$ of a certain segment of the laser beam cross section is obtained. In our case $\Delta r = 0.5$ mm corresponds to the diameter of the collecting aperture. Owing to the cylindrical symmetries of the laser beam profile and the atomic velocity distribution, the velocity-averaged density matrix will also be cylindrically symmetric. Thus, the angular integral appearing in the averaging over velocity $\mathbf{v}(\phi) = (\phi, v_\perp, v_\parallel)$ can be replaced by an angular integral over space

$$\rho(B; r) = \int_0^{2\pi} \frac{d\phi}{2\pi} \int_0^\infty dv_\perp W_\perp(v_\perp) \int_{-\infty}^\infty dv_\parallel W_\parallel(v_\parallel)$$
$$\times \rho(B; 0, v_\perp, v_\parallel; r\cos\phi, r\sin\phi), \qquad (10)$$

with the Maxwell-Boltzmann velocity distribution given by

$$W_\perp(v_\perp) = \frac{2v_\perp}{u^2} e^{-(v_\perp/u)^2}, \quad W_\parallel(v_\parallel) = \frac{1}{u\sqrt{\pi}} e^{-(v_\parallel/u)^2}, \quad (11)$$

where $u = (2k_B T/m_{\text{Rb}})^{1/2}$ is the most probable velocity of Rb atoms at temperature T.

The effects of the laser propagation along the cell and induced atomic polarization of the Rb vapor are included using the following approximations. We first compute the Rb vapor ensemble density matrix $\rho(B; r)$ and polarization $\mathbf{P}$ assuming the constant value of the electric field $\mathbf{E}$ along the z direction of laser propagation within the cell. The polarization of Rb vapor is obtained from the ensemble density matrix

$$\mathbf{P}(B; r) = n(T)\,\text{Tr}[\rho(B; r)\,e\hat{\mathbf{r}}], \qquad (12)$$

where the ^{87}Rb concentration at temperature T is given by [22]

$$\log_{10} n(T) = \log_{10}\left(0.2783 \times \frac{133.322}{k_B T}\right) - 94.0483$$
$$- 0.0377169\, T - 1961.26/T + 18.4902 \log_{10}(T).$$

(13)

Due to trace operation including dipole operator $e\hat{\mathbf{r}}$, the polarization **P** depends only on the optical coherences between the ground and the excited Zeeman sublevels. Using the computed Rb polarization, we calculate the change of the electric field due to propagation of the laser through the Rb vapor. Assuming that the change of electric field along the length L of the Rb cell is small enough, the exact relation

$$\frac{\partial \mathbf{E}(B;r,z)}{\partial z} = \frac{i\omega_0}{2\epsilon_0 c}\mathbf{P}(B;r,z)$$

(14)

in the first approximation takes the form

$$\mathbf{E}(B;r,z=L) = \mathbf{E}(B;r,z=0) + \frac{i\omega_0}{2\epsilon_0 c}\mathbf{P}(B;r)L, \quad (15)$$

where ϵ_0 is the vacuum dielectric constant and ω_0 is the laser frequency. The transmitted electric field of Eq. (15) is used in the calculations of Hanle EIT resonances. The cell temperature was set to 25 °C as in experiments.

IV. RESULTS AND DISCUSSION

Experimental and theoretical Hanle EIT resonances obtained at different positions of the small aperture along the beam diameter are presented in Figs. 5(a) and 5(b), respectively. Hereafter $r = 0$ mm refers to the center of the laser beam cross section. The beam diameter is 3 mm and overall intensity is 4 mW/cm^2. Results in Fig. 5 show significant differences in shapes, widths, and amplitudes of resonances obtained at different positions within the cross

FIG. 6. (Color online) Calculated total population $\sum \rho_{e_i e_i}$ of all Zeeman sublevels of the $F_e = 1$ excited level at different magnetic fields as a function of position along the 3-mm beam diameter of the Π-shaped laser beam. The curves corresponding to the magnetic fields 0–100 μT from the legend appear from bottom to top, respectively, at $r = -1.25$ mm. The beam intensity is 4 mW/cm^2. The atomic velocity is 180 m/s at temperature 300 K. The thin gray line represents the cross section of the laser beam with an arbitrary intensity unit. The atom enters the beam from the left.
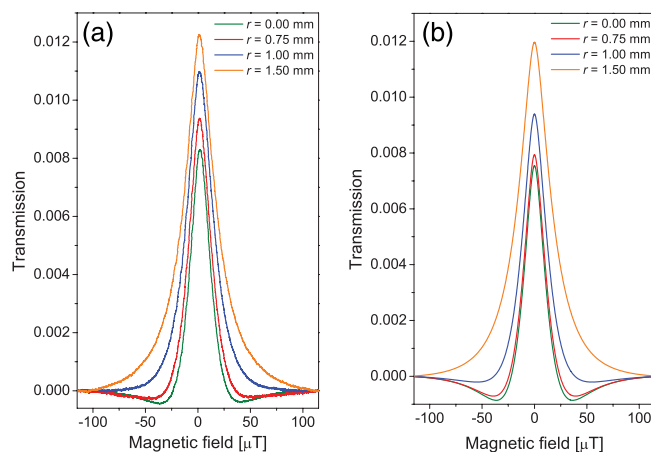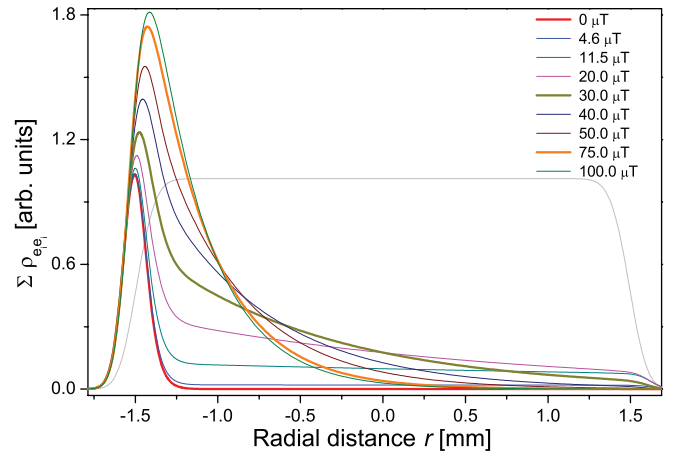

FIG. 5. (Color online) Experimental (a) and theoretical (b) Hanle EIT resonances obtained from the small segments of the Π beam cross section. Green, red, blue, and orange curves are for $r = 0$ mm, 0.75 mm, 1.0 mm and 1.5 mm, from bottom to top, respectively, where r is the radial distance of the small aperture from the beam center. The beam diameter is 3 mm and the total intensity is 4 mW/cm^2. The theoretical results were normalized to the experimental results at $r = 0$ mm.

section of the Π profiled laser beam. The Hanle EIT resonances originating from the central parts of the Π beam cross section exhibit two transmission minima next to the central maximum of the EIT resonance. Further, resonances in the center of the laser beam cross section are narrower than those originating from the outer parts of the beam. These results are reversed to the results obtained from different segments of a Gaussian laser beam cross section. In the latter case two minima appear, and the resonances are narrower, when the small aperture is placed at the wings of the Gaussian beam cross section [16].

Neglecting small intensity variations of the Π-shaped laser beam (see Fig. 2) atoms interact with a constant electric field of the laser in the presence of constant external magnetic field during the passage through the laser beam. The evolution of the atomic state under these conditions is different than in the case of the Gaussian beam. In Fig. 6 we present a calculated variation of the total population of the excited state $F_e = 1$ as a function of distance from the entrance in the laser beam (leftmost), considering atoms with the most probable radial velocity of 180 m/s at room temperature (300 K). When an atom enters the laser beam at zero magnetic field ($B = 0$), it starts to absorb photons and the population of the excited state, i.e., the sum of the populations of all excited-state Zeeman sublevels, increases (red thick line in Fig. 6). Shortly after entering the laser beam, atoms are prepared into the dark state and do not absorb photons afterward yielding maximal transmission. At small magnetic fields the preparation of atoms into the dark state is less efficient and there is certain probability for photon absorption during the entire interaction of the atom and the laser light. Thus, the excited-state population decreases less rapidly than for $B = 0$ as atoms move through the laser beam and transmission decreases. As Fig. 6 shows, the atomic total excited-state population, for atoms near the laser beam center, is largest for a magnetic field at about 30 μT (dark yellow thick

line) when transmission reaches minimum. At larger magnetic fields (e.g., 75 μT, orange thick line), pumping into the uncoupled $F_g = 1$ hyperfine level becomes considerable and transmission noticeably increases. The observed behavior of the excited-state populations and resulting laser transmission are due to the fact that the rates of pumping into the dark state and into the uncoupled level depend oppositely on the external magnetic field. Therefore, the appearance of two transmission minima at about 30 μT is a joint effect of preparation of atoms into the dark state and optical pumping into the uncoupled ground hyperfine level.

Behavior of the excited-level population at different magnetic fields explains the origin of the two symmetrically placed, with respect to the central transmission peak, transmission minima present in the Hanle EIT resonances recorded near the center of the laser beam. For a given laser intensity, atoms have to spend a certain time in the laser beam before these minima emerge in the Hanle EIT curves. It turns out that if the laser beam has a 3-mm diameter, for most atoms this shape of the EIT would only be observed in the laser beam center. If one considers a laser beam with a diameter lager than 3 mm, under the same experimental conditions (the same cell temperature, i.e., the most probable velocity, and the same laser intensity), it is expected that optical pumping would significantly affect EIT line shapes at the same distances of ~1.5 mm from the edge of the beam. Consequently, with the larger beam diameter, transmission minima should occur in the wider area around the beam center. The curves in Fig. 7 present experimental and theoretical Hanle EIT resonances obtained at different positions of the small aperture along the 6-mm diameter Π-shaped laser beam. Overall intensity is similar as before, 4 mW/cm^2. Now, transmission minima are present in Hanle EIT resonances obtained not only in the center of the laser beam, but also up to a certain distance away from the center. Moreover, the resonances obtained up to that distance
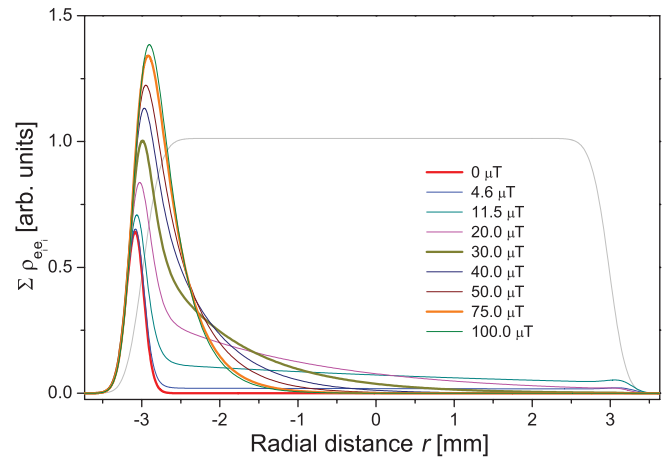
FIG. 8. (Color online) Calculated total population $\sum \rho_{e_i e_i}$ of all Zeeman sublevels of the $F_e = 1$ excited level at different magnetic fields as a function of position along the 6-mm beam diameter of Π-shaped laser beam. The curves corresponding to the magnetic fields 0–100 μT from the legend appear from bottom to top, respectively, at $r = -2.75$ mm. The beam intensity is 4 mW/cm^2 intensity. The atomic velocity is the most probable velocity at room temperature (180 m/s). The thin gray line represents the laser beam cross section profile.

are almost the same, as in the case of overlapping resonances for $r = 0$ and $r = 1$ mm in Fig. 7.

The explanation for the appearance of transmission minima in Hanle EIT line shapes in the case of a 6-mm-diameter laser beam could be made tracing the behavior of the total excited-state populations given in Fig. 8 and applying the same logic as in Fig. 6, i.e., for the 3-mm beam diameter. It is apparent from Figs. 6 and 8 that under the same experimental conditions, the distance from the beam edge where the total excited-state population at $B = 75$ μT (orange thick line) falls down to zero is the same in both cases, approximately 1.5 mm. For the 3-mm beam diameter this point coincides with the location of the beam center, while for the 6-mm-diameter beam this location is, of course, away from the beam center. Therefore for the 6-mm-diameter beam, transmission minima in Hanle EIT resonances at around $B = 30$ μT will occur as long as EIT resonances are taken from the central region of 3 mm in diameter.

To further clarify the influence of optical pumping on Hanle EIT line shapes we performed calculations by artificially closing the transition $F_g = 2 \rightarrow F_e = 1$, i.e., eliminating the optical pumping. Calculated Hanle EIT resonances, for the laser intensity of 4 mW/cm^2, are shown in Fig. 9. Obtained Hanle EIT line shapes are broader than for the open system because there is no population-loss-induced narrowing [23,24]. The absence of population loss also yields the same line shapes regardless of the distance from the beam center. There is no transmission minima in line shapes obtained at the central regions of the beam cross section. In this case, a slight increase of transmission at very large magnetic fields (~200 μT) is due to the broad single-photon Hanle background on which the EIT resonances are superimposed. Next, we investigate the influence of the overall laser intensity on line shapes of the EIT obtained in different segments of the Π-shaped laser beam. The curves in Figs. 10(a) and 10(b) are experimental
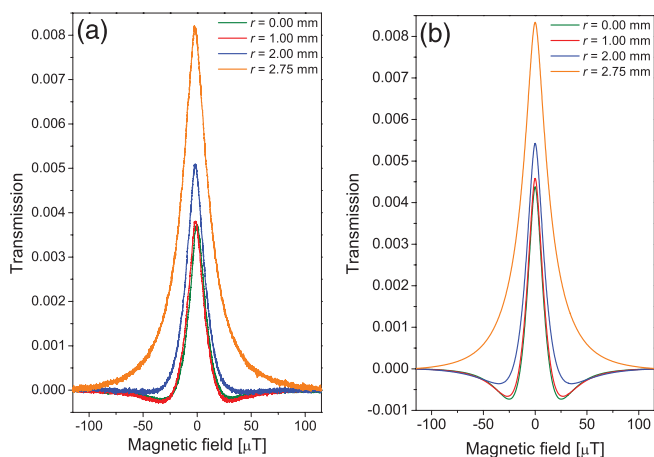

FIG. 7. (Color online) Experimental (a) and theoretical (b) Hanle EIT resonances obtained from the small segments of the Π laser beam cross section at four distances from the beam center: 0, 1.0, 2.0, and 2.75 mm (from bottom to top, respectively). The beam diameter is 6 mm and the total laser intensity is 4 mW/cm^2. The theoretical results were normalized to the experimental results at $r = 0$ mm. Note that the curves for $r = 0$ and $r = 1.0$ mm almost overlap.
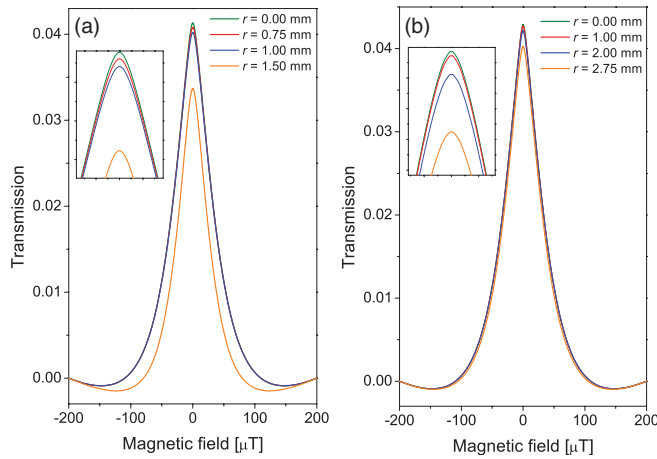
FIG. 9. (Color online) Calculated Hanle EIT resonances obtained from the small segments of the Π laser beam cross section of (a) 3 mm and (b) 6 mm diameter. It is assumed that the transition $F_g = 2 \rightarrow F_e = 1$ is closed. The resonances almost completely overlap and can be barely distinguished only near $B = 0$ (see insets). The curves corresponding to decreasing radial distances from the legends appear from bottom to top, respectively. The laser intensity is 4 mW/cm^2. Note a different scale for the magnetic field than in Figs. 5 and 7 and a broadening of resonances in the case of the closed transition.

and theoretical Hanle EIT resonances obtained for the laser intensity 0.5 mW/cm^2 at different positions of the small aperture along the beam diameter of 6 mm. At lower laser intensity, transmission minima are missing (experiment) or barely visible (theory) in the Hanle EIT profiles, because of the weak optical pumping. Since there are diffraction effects between the planes of the two apertures (see Fig. 1) the radial position of the collecting aperture does not map exactly the corresponding position in the atomic cell. This introduces some averaging that may explain why the structures are smoother in the experiments with respect to the calculations. In Fig. 10(c) we show the total excited-state populations for an atom traversing the beam with velocity 180 m/s as a function of the radial distance from the beam center at different magnetic fields. Even at a very high magnetic field (75 μT), the population is not zero as it was at high laser intensities (see Fig. 8) because optical pumping to the $F_g = 1$ level is not as efficient. In this case the transmission of the vapor will not increase at high magnetic fields and consequently there are no transmission minima at Hanle EIT resonance profiles at any position along the beam diameter.

As discussed above, EIT line shapes obtained in different parts of the Π-shaped laser beam cross section are determined by evolution of the dark states and (particularly around the beam center) by the optical pumping. On the other hand, the change of atomic coherence in the magnetic field is found to play a significant role in the line shapes obtained in parts of the Gaussian laser beam cross section [16]. Results in Figs. 11(a) and 11(b) confirm different mechanisms responsible for EIT line shapes for two radial profiles of the laser beam. Here we compare the calculated phase of the coherence, induced between the $m_F = -1$ and $m_F = 1$ Zeeman sublevels of $F_g = 2$ hyperfine level for atoms passing through the Gaussian and
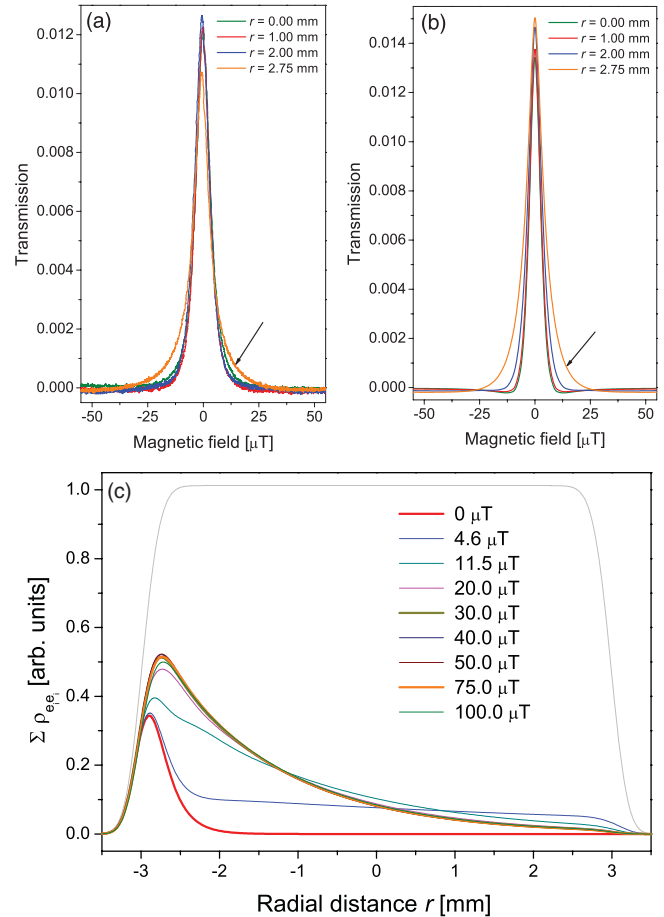

FIG. 10. (Color online) Experimental (a) and theoretical (b) Hanle EIT resonances obtained from the small segments of the Π laser beam cross section at four distances r from the beam center. The resonances are nearly identical except for the resonance obtained close to rim of the beam (pointed to with the arrow). The beam diameter is 6 mm and the total intensity is 0.5 mW/cm^2. Note that the magnetic field range is smaller than in Figs. 5 and 7. (c) Calculated total population of all Zeeman sublevels of the $F_e = 1$ excited level at different magnetic fields as a function of position along the 6-mm beam diameter of Π-shaped laser beam. The curves corresponding to the magnetic fields 0–100 μT from the legend appear from bottom to top, respectively, at $r = -2.5$ mm. The curves for $B \gtrsim 20$ μT are almost identical. The atomic velocity is the most probable velocity at room temperature (180 m/s). The thin gray line represents the laser beam cross section profile.

the Π laser beam. The magnetic field during transit time of an atom is assumed constant. The results are shown for those magnetic fields at which transmission minima appear in Hanle EIT resonances, i.e., 10 μT (30 μT) for the Gaussian (Π) laser beam. Both beams have the same average intensity. Since the laser electric field tends to keep the phase of the coherence constant while the magnetic field tends to change the phase, when both magnetic and electric field are present, the phase of atomic coherence depends on the magnitudes of these two fields. The atom is coherently prepared and the phase is kept fixed by the laser field in the central parts of the Gaussian beam. In the wings of the Gaussian beam the phase value of the same atomic coherence depends on the local laser intensity.
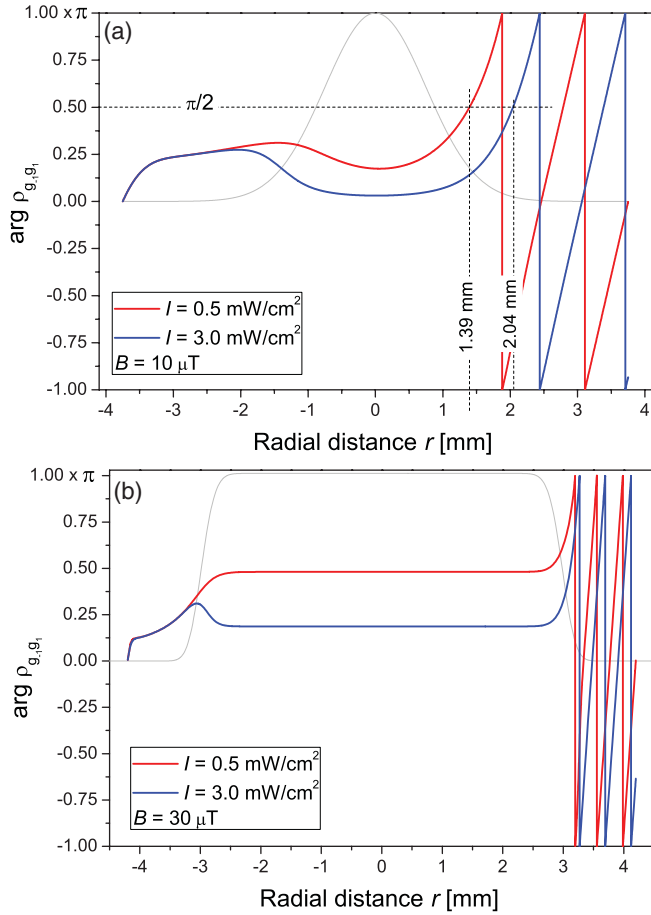
FIG. 11. (Color online) (a) Change of the argument of atomic coherence ρ_{g_{-1},g_1} during atom passage through the 3-mm-wide Gaussian laser beam at constant magnetic field. The dashed lines denote the positions along the beam radius where the Hanle EIT resonances exhibit very pronounced transmission minima. The transmission minima at the Hanle EIT resonances appear in the wings of the Gaussian beam cross section when arg ρ_{g_{-1},g_1}, i.e., the atomic phase is equal to $\pi/2$ [16]. (b) Change of the argument of atomic coherence during atom passage through the 6-mm-wide Π laser beam at constant magnetic field. It is obvious that the phase is constant during atom passage through the Π laser beam, regardless of the laser intensity. The magnetic field values of 10 μT and 30 μT for the Gaussian and Π laser beams, respectively, are chosen because the transmission minima in the Hanle EIT resonances appear exactly at those values in corresponding laser beam profiles. The beam profile is presented by the gray line.

When the atomic phase reaches $\pi/2$, i.e., the atomic state becomes bright, two transmission minima appear in Hanle EIT resonances obtained in the wings of the Gaussian laser beam [16]. In a constant and strong field of the Π-shaped laser beam, the phase of the coherence is constant across the beam and therefore it is not the change of the phase that affects the observed Hanle EIT line shapes.

Physical processes leading to line narrowing or broadening of coherent resonances were extensively studied under different experimental conditions, laser beam geometries, and cell dimensions [7–12,16,25–28]. Figures 12(a) and 12(b) show experimental and theoretical results for the dependence
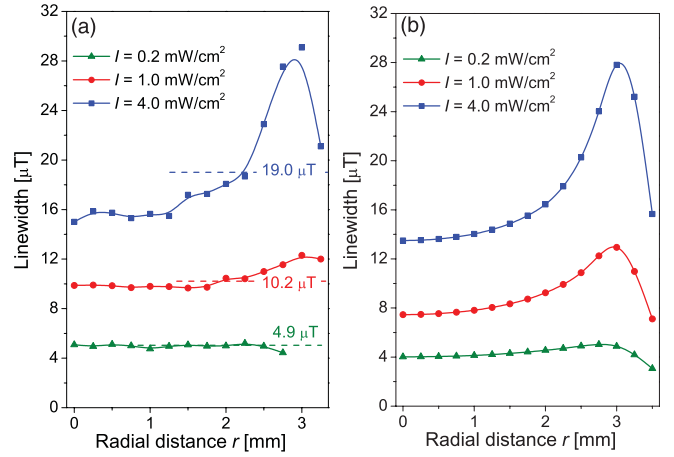

FIG. 12. (Color online) (a) Experimental and (b) theoretical Hanle EIT linewidths at different positions of small aperture along the 6-mm-diameter Π-shaped laser beam. I is the laser intensity. The dashed lines in (a) denote the Hanle EIT linewidths when the whole laser beam is detected.

of linewidths of the Hanle EIT resonances on the radial position r of the small aperture along the 6-mm diameter of the Π-shaped laser beam. The dashed lines in Fig. 12(a) denote the Hanle EIT linewidths when the whole laser beam is detected. Results are given for three different laser intensities. It is obvious that there is Hanle EIT line narrowing from the edge toward the beam center. This is population-loss-induced transit time narrowing [23,24]. As seen in Fig. 12, it is more pronounced at higher laser intensities, when most significant Hanle EIT narrowing apparently occurs in the region close to the beam edges, i.e., very soon after the atom enters the beam.

Important information about atomic evolution during interaction with the constant intensity laser field can be obtained by comparing the linewidths of the Hanle EIT resonances for central and outer regions of the Π laser beam cross section and for the whole beam, at different laser intensities. Figure 13 shows Hanle EIT linewidths versus laser intensity for (a) 3 - and (b) 6-mm beam diameters. For the 3-mm diameter Π laser beam, the linewidths are presented for resonances in the center ($r = 0$), for the resonances obtained at the outer region of the beam ($r = 1.5$ mm) and when the whole beam is detected. The resonances measured in the center of the laser beam cross section are noticeably narrower. For the 6-mm-diameter Π laser beam, besides resonances at the center ($r = 0$), at the edge ($r = 3$ mm), and for the whole beam, the linewidths of resonances obtained at $r = 1.5$ mm are also presented. The results for $r = 1.5$ mm support the discussion related to Fig. 8. It is shown that the most rapid changes of atomic state, for atoms with the most probable radial velocity, occur shortly after the atom enters the laser beam, i.e., after passing a distance of about 1.5 mm from the beam edge. Figure 13(b) shows that the resonances recorded close to the laser beam edge ($r = 3$ mm) are significantly wider than those from the inner parts of the beam ($r = 1.5$ mm and $r = 0$). In addition, an expanded laser beam (6-mm diameter) causes narrower resonances in the center of the beam cross section and also
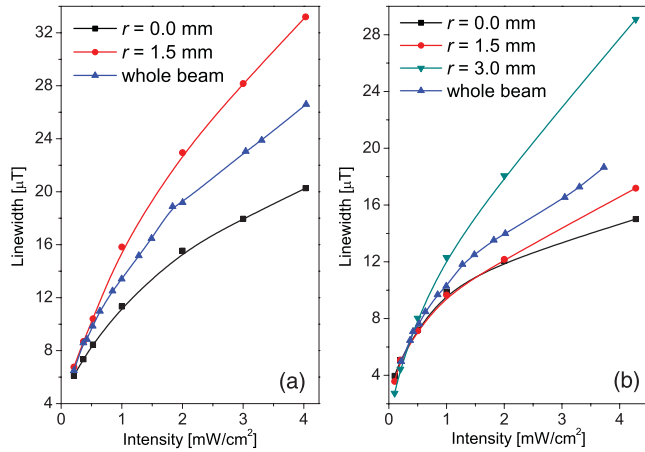
FIG. 13. (Color online) Dependence of Hanle EIT resonance linewidths from the laser intensity for the central regions of the Π laser beam cross section, the circumference region, and the whole beam. Results are shown for two laser beam diameters (a) 3 and (b) 6 mm. The results for the $r = 1.5$ mm in case of the 6-mm-diameter beam are presented for better comparison because this radius coincides with the edge of the 3-mm-diameter beam.

for the whole beam, comparing to the smaller beam diameter (3 mm).

The results from Fig. 13 show that as the diameter of the Π-shaped laser beam increases, the contribution of the Hanle EIT from the rim of the beam cross section to the whole beam resonance linewidth decreases. In other words, when increasing the laser beam diameter the whole beam resonance becomes more similar to those from the inner region of the laser beam cross section.

V. SUMMARY

We have studied the evolution of atomic states in constant magnetic and laser fields using Π-shaped laser beam resonant to the open $F_g = 2 \rightarrow F_e = 1$ transition in ^{87}Rb. This laser radial profile allows such studies to be unaffected by intensity variations of the laser electric field. Information about the transient evolution of the atomic state during the interaction with the laser beam was obtained by detailed analysis of features in line shapes of the Hanle EIT resonances from small segments of the laser beam cross section. Experimentally and theoretically these resonances were obtained by sampling the transmitted laser light at various positions of the small aperture along the radius of a well-collimated laser beam, after the entire beam had passed through the Rb cell. We have shown that considerable absorption occurs immediately after atoms enter the laser beam. At low magnetic fields this leads to the efficient preparation into a dark state and consequent evolution with low photon absorption throughout the inner region of the beam cross section. At higher magnetic fields, the initial absorption is followed by optical pumping into an uncoupled ground hyperfine level which dominates the behavior of the atomic state throughout the laser beam cross section. The appearance of transmission minima, as sidebands to the EIT resonance, in the inner regions of the laser beam is due to strong dependence of optical pumping on the magnetic field. Transmission minima were also observed for Hanle EIT resonances obtained using the Gaussian laser beam, but such EIT line shapes were only observed in the wings of the beam [16]. Their presence was attributed to the interference of the laser light in the beam wings and coherently prepared atoms coming from the central part of the beam. Thus, essentially different physical mechanisms, *optical pumping (incoherent)* in Π laser beams and *Ramsey-like effect (coherent)* in Gaussian laser beams, yield seemingly similar results, i.e., the appearance of the transmission minima in Hanle EIT line shapes. In addition, the observed narrowing of Hanle EIT resonances toward the center of the Π-shaped laser beam cross section is induced by population loss during the atomic transit through the laser beam. It is apparent that for the proper modeling of experiments and identification and understanding of dominant processes affecting the dark-state evolution within the laser beam, it is essential to take into account a real beam profile.

[1] E. Arimondo, Prog. Opt. **35**, 257 (1996).

[2] G. Alzetta, A. Gozzini, L. Moi, and G. Orriolis, Nuovo Cimento **36**, 5 (1976).

[3] S. E. Harris, J. E. Field, and A. Imamoglu, Phys. Rev. Lett. **64**, 1107 (1990).

[4] A. M. Akulshin, S. Barreiro, and A. Lezama, Phys. Rev. A **57**, 2996 (1998).

[5] G. Moruzzi and F. Strumia, *The Hanle Effect and Level Crossing Spectroscopy* (Plenum, New Yrk, 1991).

[6] C. Andreeva, S. Cartaleva, Y. Dancheva, V. Biancalana, A. Burchianti, C. Marinelli, E. Mariotti, L. Moi, and K. Nasyrov, Phys. Rev. A **66**, 012502 (2002).

[7] E. Pfleghaar, J. Wurster, S. I. Kanorsky, and A. Weis, Opt. Commun. **99**, 303 (1993).

[8] S. Knappe, M. Stähler, C. Affolderbach, A. V. Taichenachev, V. I. Yudin, and R. Wynands, Appl. Phys. B **76**, 57 (2003).

[9] Y. Xiao, I. Novikova, D. F. Phillips, and R. L. Walsworth, Phys. Rev. Lett. **96**, 043601 (2006).

[10] Y. Xiao, I. Novikova, D. F. Phillips, and R. L. Walsworth, Opt. Express **16**, 14128 (2008).

[11] O. Firstenberg, M. Shuker, R. Pugatch, D. R. Fredkin, N. Davidson, and A. Ron, Phys. Rev. A **77**, 043830 (2008).

[12] S. Mitra, M. M. Hossain, B. Ray, P. N. Ghosh, S. Cartaleva, and D. Slavov, Opt. Commun. **283**, 1500 (2010).

[13] F. Levi, A. Godone, J. Vanier, S. Micalizio, and G. Modugno, Eur. Phys. J. D **12**, 53 (2000).

[14] A. V. Taichenachev, A. M. Tumaikin, V. I. Yudin, M. Stahler, R. Wynands, J. Kitching, and L. Hollberg, Phys. Rev. A **69**, 024501 (2004).

[15] M. Radonjić, D. Arsenović, Z. Grujić, and B. M. Jelenković, Phys. Rev. A **79**, 023805 (2009).

[16] A. J. Krmpot, S. M. Ćuk, S. N. Nikolić, M. Radonjić, D. G. Slavov, and B. M. Jelenković, Opt. Express **17**, 22491 (2009).

[17] H. Gilles, B. Cheron, O. Emile, F. Bretenaker, and A. Le Floch, Phys. Rev. Lett. **86**, 1175 (2001).

[18] Z. D. Grujić, M. Mijailović, D. Arsenović, A. Kovacević, M. Nikolić, and B. M. Jelenković, Phys. Rev. A **78**, 063816 (2008).

[19] B. Schuh, S. I. Kanorsky, A. Weis, and T. W. Hänsch, Opt. Commun. **100**, 451 (1993).

[20] G. Wasik, W. Gawlik, J. Zachorowski, and W. Zawadzki, Appl. Phys. B **75**, 613 (2002).

[21] T. Petelski, M. Fattori, G. Lamporesi, J. Stuhler, and G. M. Tino, Eur. Phys. J. D **22**, 279 (2003).

[22] A. N. Nesmeyanov, *Vapor Pressure of the Chemical Elements*, edited by R. Gray (Elsevier, Amsterdam, 1963).

[23] F. Renzoni, W. Maichen, L. Windholz, and E. Arimondo, Phys. Rev. A **55**, 3710 (1997).

[24] F. Renzoni and E. Arimondo, Phys. Rev. A **58**, 4717 (1998).

[25] M. Auzinsh, R. Ferber, F. Gahbauer, A. Jarmola, L. Kalvans, A. Papoyan, and D. Sarkisyan, Phys. Rev. A **81**, 033408 (2010).

[26] D. Sarkisyan, D. Bloch, A. Papoyan, and M. Ducloy, Opt. Commun. **200**, 201 (2001).

[27] C. Andreeva, A. Atvars, M. Auzinsh, K. Blush, S. Cartaleva, L. Petrov, and D. Slavov, Phys. Rev. A **76**, 063804 (2007).

[28] E. Alipieva, S. Gateva, E. Taskova, and S. Cartaleva, Opt. Lett. **28**, 1817 (2003).

Dark Hanle resonance narrowing by blocking the central part of the Gaussian laser beam

A.J. Krmpot*, S.N. Nikolić, S.M. Ćuk, M. Radonjić, and B.M. Jelenković
Institute of Physics, University of Belgrade, Pregrevica 118, 11080 Belgrade, Serbia

ABSTRACT

We present Hanle electromagnetically induced transparency (EIT) resonances obtained from the outer parts of the Gaussian laser beam. The signal from the outer parts only was obtained by placing circular opaque masks of different diameters in the center of the laser beam just in front of the detector. The Hanle EIT resonances obtained in that way are narrower and for high laser intensities even more contrasted. Suggested explanation for the line narrowing is based on lower power broadening in the wings of the Gaussian laser beam as well as on the traversing of the coherently prepared atoms through the beam. The resonance contrast to linewidth ratio, when the central part of the beam is blocked, is higher or equal to the ratio obtained when the whole laser beam is detected, for all laser intensities used in the experiment. Due to high ratio of contrast and linewidth, resonances obtained in proposed way could be useful in frequency metrology and magnetometry.

Keywords: Hanle EIT resonances, Gaussian laser beam, metrology

1. INTRODUCTION

Coherent effects in Doppler broadened alkali atom vapor have been intensively investigated over the past decade. Coherent population trapping (CPT) [1, 2], electromagnetically induced transparency (EIT) [3], and electromagnetically induced absorption (EIA) [4] have been observed and examined in pump-probe and in Hanle configuration [5, 6]. All these phenomena strongly depend on the intensity of the applied laser field. The dependence of CPT and EIT lineshapes on the laser intensity has been extensively studied [7-9].

Typical radial laser beam profile in experiments studying CPT and EIT is Gaussian. The influence of Gaussian laser beam profile on EIT lineshapes is studied in only few papers [10-12]. However, the focus was on the overall effect of the laser beam having Gaussian profile, not on the influence of particular laser beam segments. The intensities in the center and in the wings of such beam are very different. Nevertheless, the order of magnitude lower intensity in the wings can still contribute to the coherent effects [13]. The Hanle EIT line narrowing in the wings of the Gaussian laser beam was shown in [13] and explained by transit of coherently prepared atoms through the Gaussian laser beam and by the power broadening/narrowing.

There are several papers showing the narrowing of EIT lines such as: separated, in space and/or time, laser beams tuned to Raman resonance of the atomic transitions [14], narrowing of EIT in buffer gas cells [15, 16] and cells with antireflection coatings [17]. The goal of this work is to show the proof of the principal for narrowing the Hanle EIT resonances in vacuum Rb cell and to present a simple change in relatively standard experimental setup for obtaining such narrow resonances.

In this work we study EIT resonances originating from outer parts of the Gaussian laser beam, after the whole beam passes through the Rb vapor cell. Our investigation was performed on [87]Rb atoms at D1 line in the Hanle configuration. In the experiment, the detection of the signal from the outer parts of the Gaussian beam was accomplished by placing circular opaque masks of different diameters in front of the large area photodetector. Apart from the line narrowing in the outer parts of the Gaussian laser beam the contrast of the Hanle EIT resonances could be enhanced depending on the laser intensity. The contrast to linewidth ratio of the resonances obtained in proposed way is equal or higher than in the case of the whole beam detection. Narrower and more contrasted resonances are important for applications of the CPT and EIT effects in atomic frequency standards [18] and magnetometry [19].

*krmpot@ipb.ac.rs; phone +381 11 3160 793; fax +381 11 3162 190; http://www.photonics.ipb.ac.rs/

2. EXPERIMENT

The experimental setup is shown in Fig. 1. External cavity diode laser is frequency locked to $F_g=2 \rightarrow F_e=1$ transition in ^{87}Rb, where F_g and F_e correspond to angular momentum of the ground and excited state hyperfine levels, respectively. The energy level diagram, given in the insert in Fig. 1, shows magnetic sublevels either coupled by the laser light, or populated due to spontaneous emission. Linearly polarized laser light allows for multiple Λ schemes and formation of dark states among ground Zeeman sublevels of $F_g=2$ level. The locking is performed by Doppler-free dichroic atomic vapor laser lock (DDAVLL) method using auxiliary vacuum Rb cell. The variable neutral density filter is used for the laser power adjustments. The laser beam, introduced into the single mode fiber with the collimator, provides the Gaussian beam at the exit of the fiber. After passing through the Glen-Thomson polarizer the laser beam becomes linearly polarized. The laser beam is then expanded to 3 mm in diameter. The dependence of the laser intensity on the radial distance r from the beam center is Gaussian

$$I(r) = I_0 \exp(-2r^2 / r_0^2) \tag{1}$$

where I_0 is the maximal intensity and r_0 is $1/e^2$ beam radius.

The Gaussian beam passes through 5 cm long vacuum Rb cell containing natural abundance of rubidium isotopes. The cell is placed in the solenoid used for scanning the axial magnetic field between ±300 µT. The cell and the solenoid are placed inside the triple layered µ-metal cylinder to eliminate Earth's and stray magnetic fields.

The opaque circular masks of different diameters are placed in front of the photodiode with large detection surface (area 80 mm^2). The sensitivity of the photodiode is 0.57 A/W at 780 nm and has variable transimpedance gain with nominal value of 1 MΩ (selectable between 1 kΩ and 10 MΩ). The aim of the mask is to allow only the outer part of the beam to reach the detector while the central part is blocked. The signal obtained from the photodiode while scanning the external magnetic field is recorded by the digital oscilloscope and transferred to the computer.
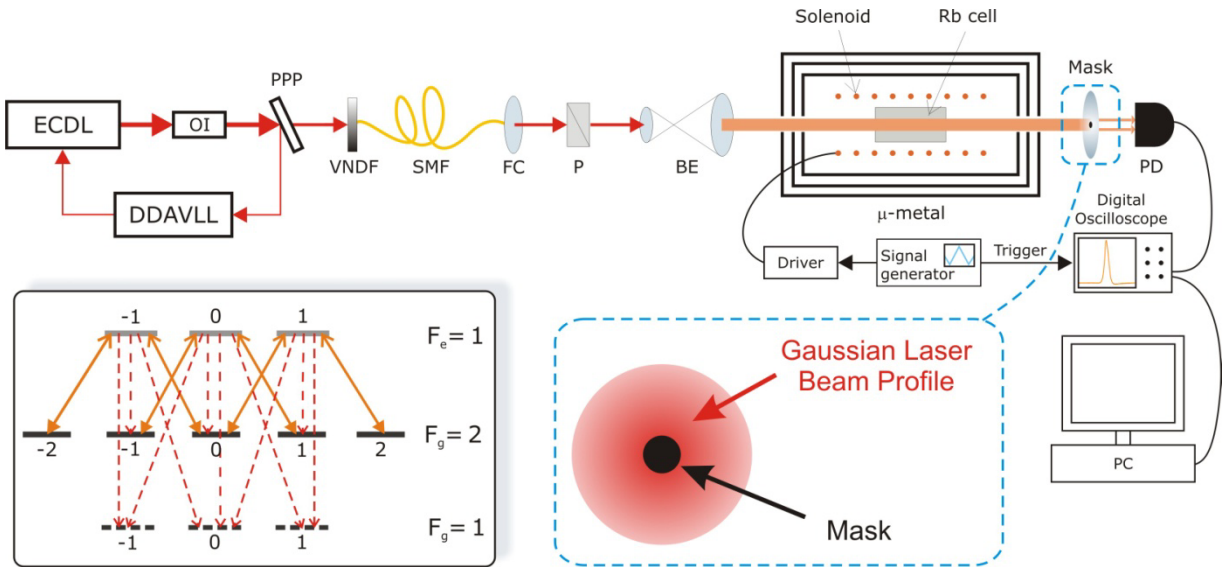

Figure 1. Experimental setup. The circular mask placed in front of the detector blocks the central part of the beam allowing only the outer part of the beam to reach the photodiode. ECDL – External cavity diode laser, OI – Optical insulator, DDAVLL – Doppler-free dichroic atomic vapor laser lock, PPP – Planparallel plate, VNDF – Variable neutral density filter, SMF – Single mode fiber, FC – Fiber collimator, P – Polarizer, BE – Beam expander, PD – Photodiode. Insert: Energy-level diagram for magnetic sublevels of the $F_g=2 \rightarrow F_e=1$ transition where solid lines represent linearly polarized laser light coupling Zeeman sublevels and dotted lines correspond to the de-excitation from excited levels.

3. RESULTS AND DISCUSSIONS

We studied Hanle EIT resonances after blocking the central part of the Gaussian beam in front of the detector. Figure 2 presents the Hanle EIT curves obtained when the mask of 2.25 mm in diameter blocks the central part of the Gaussian beam (red curve). The resonance obtained without the mask is shown by the green curve. The laser intensity in both cases was 3 mW/cm^2. It is obvious that the line obtained using the mask is narrower and has greater amplitude i.e. contrast.

The explanation for this narrowing could be given by observing the development of the atomic ground state Zeeman coherence during passage of atoms through Gaussian laser beam. The lifetime of atomic coherence is longer than the atom transit time through the laser beam. Thus, the light in the wings of the Gaussian laser beam can also "probe" the induced atomic coherence and polarization of the atom coming from central parts of the laser beam. Such "probing" leads to the line narrowing in the wings of the beam due to atomic interference with the beam i.e. a kind of Ramsey-like effect [13]. Also, due to lower intensity in the wings of the Gaussian laser beam the power broadening is significantly reduced [13, 20]. It is therefore a reasonable assumption that outer parts of the Gaussian laser beam, after passing through the alkali vapor cell, should yield narrower EIT resonances.
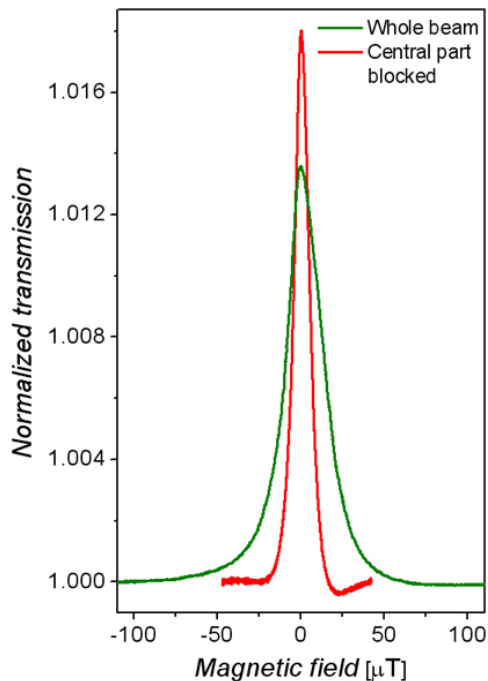

Figure 2. The experimental Hanle EIT resonances obtained when the whole beam is detected (green curve) and when the central part of the beam is blocked by using opaque circular mask of 2.25 mm in diameter placed in front of the detector. The laser intensity is 3 mW/cm^2.

In Fig. 3 (a) and (b) the dependence of the Hanle EIT linewidth and contrast on the beam intensity, with and without the mask, is shown. It is obvious that if one blocks the central part of the Gaussian laser beam, the Hanle EIT resonances will be significantly narrower for the whole laser intensities range in the experiment. Apparently, this masking effect is more prominent at higher laser intensities. At higher laser intensities masking also provides the resonances with higher contrast. One can notice that in the range of extremely low laser intensities the resonances obtained with mask are narrower but they have lower contrast in comparison with those obtained with whole beam. For many applications it is important to have narrow lines but they also should have high enough contrast in order to be useful. To resolve situation

what is get what is lost, the contrast to linewidth ratio vs. laser intensity is shown in figure 3 (c). It is obvious that only at extremely low laser intensities the ratio contrast/linewidth is comparable for the two cases, detection of whole beam and when the central part is blocked. For all other intensities detection of outer part of the beam will give resonances with much higher contrast to linewidth ratio. It is clear that using this very simple method of detection, in the worst case one can get the same contrast to linewidth ratio in comparison to whole beam detection. Otherwise this method will provide us narrower and more pronounced lines.
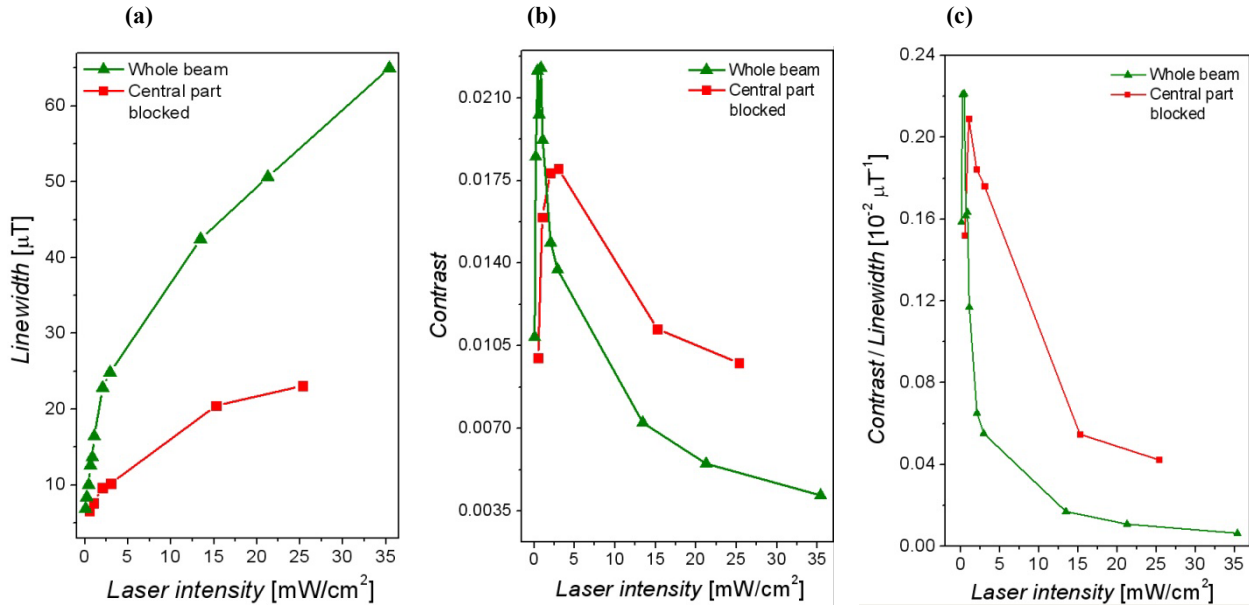

Figure 3. (a) Linewidth, (b) contrast, and (c) contrast to linewidth ratio of experimental Hanle EIT resonances versus laser intensity when the whole beam is detected (green curve) and when the central part of the beam is blocked (red curve). Circular mask diameter is 2.25 mm and the laser intensity is 3 mW/cm^2.

In the figure 4 the shapes of the Hanle EIT resonances for three different mask diameters are shown. Laser intensity was 3 mW/cm^2. It could be noticed that larger mask diameter gives narrower resonances. Quantitative confirmation for previous statement is given in figure 5 (a) where linewidths of Hanle EIT resonances vs. mask diameter are shown for three different laser intensities (0.5 mW/cm^2 , 2 mW/cm^2, and 15 mW/cm^2). Regardless of laser intensity the linewidths drops with mask diameter increment. This result is expected because it is already shown that outer parts of the Gaussian laser beam provide narrower resonances [13]. However, the effect of linewitdh decreasing while increasing the mask diameter is not so pronounced compared to the measurements when only small parts of the Gaussian laser beam are detected as in [13]. Namely, blocking the central part of the Gaussian laser beam, that gives the widest resonances, yields integral detection of the rest of the beam. Increasing the mask diameter for a certain value, one will additionally block only a small ring that will not significantly decrease the linewidth as in case when only small part of the Gaussian laser beam is detected. As a consequence of nonlinear linewidth dependence on position along the beam diameter [13] the linewidth drop in figure 5 (a) is more pronounced at higher laser intensities.

In figure 5 (b) the contrast to linewidth ratio vs. mask diameter for three different laser intensities is shown. For the low intensities (0.5 mW/cm^2 and 2 mW/cm^2) these ratios overlaps thus it is hard to say what mask diameter is optimal. At higher laser intensities (15 mW/cm^2) the situation is clear: using the mask with larger diameter for blocking the central part of the Gaussian beam will give better contrast to linewidth ratio.
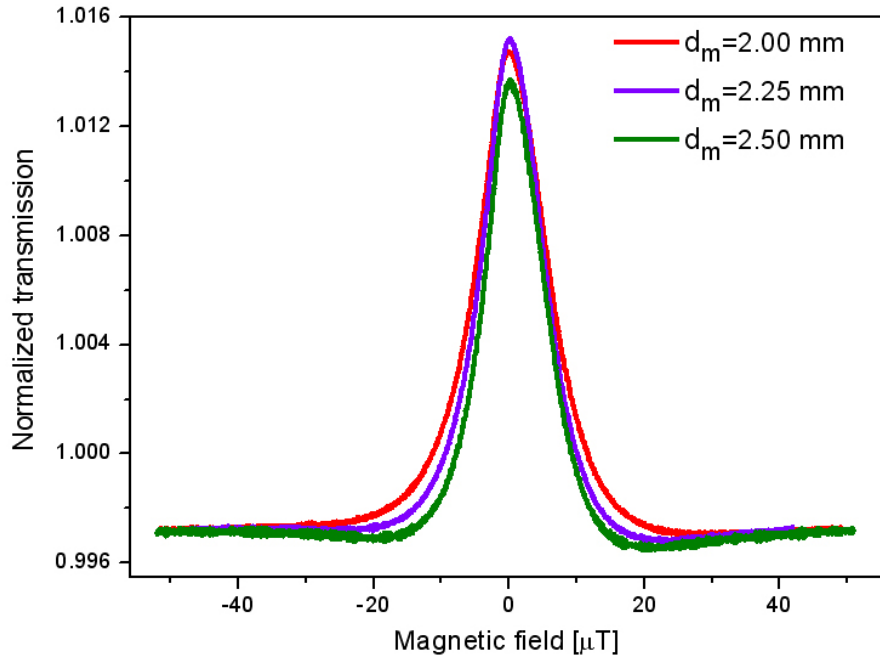
Figure 4. The experimental Hanle EIT resonances obtained by blocking the central part of the Gaussian laser beam with opaque circular masks of different diameters. The red, the violet, and the green curves correspond to masks diameters d_m of 2.00 mm, 2.25 mm and 2.50 mm, respectively. The laser intensity is 3 mW/cm^2.

Figure 5. (a) Linewidth and (b) contrast to linewidth ratio of experimental Hanle EIT resonances versus the diameter of the mask used for blocking the central part of the Gaussian laser beam. The blue, the red, and the green curves are for the laser intensities I = 15 mW/cm^2, 2 mW/cm^2, and 0.5 mW/cm^2, respectively.

4. CONCLUSION

In this work we have presented results of the Hanle EIT resonances obtained from the outer parts of the Gaussian laser beam, after the entire laser beam passes through the Rb vacuum cell. The outer parts of the laser beam were detected by placing circular opaque masks of different diameters into the center of the beam. The linewidths and contrasts of the Hanle EIT lines obtained in proposed way depend on the mask diameter used for blocking the cen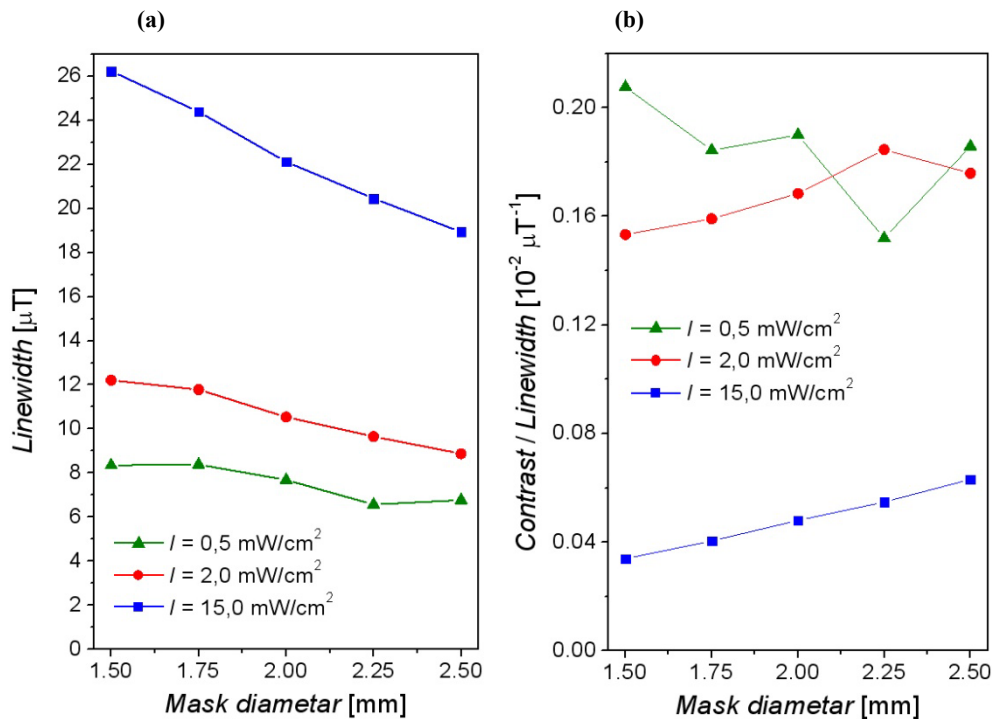tral part of the laser beam. The contrast to linewidth ratio is the same or even better for resonances obtained in the proposed way then for those obtained in common way i.e detecting the whole laser beam. The explanation for Hanle EIT lines narrowing is based on the interference between the atomic coherence carried by the coherently prepared atoms and the light in the wings of the Gaussian laser beam. This result could be of interest in applications of EIT where narrow resonances with higher contrast are of main interest e.g. atomic frequency standard and magnetometers.

ACKNOWLEDGEMENTS

REFERENCES

[1] E. Arimondo, "Coherent population trapping in laser spectroscopy," Prog. Opt. **35**, 257-354 (1996).
[2] R. Wynands, A. Nagel, "Precision spectroscopy with coherent dark states," Appl. Phys. B **68**, 1–25 (1999).
[3] M. O. Scully, and M. S. Zubairy, Quantum Optics (Cambridge University Press, Cambridge, UK, 1997).
[4] M. Akulshin, S. Barreiro, and A. Lezama, "Electromagnetically induced absorption and transparency due to resonant two-field excitation of quasidegenerate levels in Rb vapor," Phys. Rev. A **57**, 2996 (1998).
[5] Giovanni Moruzzi and Franco Strumia, "The Hanle effect and level crossing spectroscopy," (Plenum Press 1991).
[6] Andreeva, S. Cartaleva, Y. Dancheva, V. Biancalana, A. Burchianti, C. Marinelli, E. Mariotti, L. Moi, K. Nasyrov, "Coherent spectroscopy of degenerate two-level systems in Cs," Phys. Rev. A **66**, 502 (2002).
[7] Javan, O. Kocharovskaya, H. Lee, and M. O. Scully, "Narrowing of electromagnetically induced transparency resonance in a Doppler-broadened medium," Phys. Rev. A **66**, 013805 (2002).
[8] Y. Ye and A. S. Zibrov, "Width of the electromagnetically induced transparency resonance in atomic vapor," Phys. Rev. A **65**, 023806 (2002).
[9] J. Krmpot, M. M. Mijailović, B. M. Panić, D. V. Lukić, A. G. Kovacević, D. V. Pantelić, and B. M. Jelenković, "Sub-Doppler absorption narrowing in atomic vapor at two intense laser fields," Opt. Express 13(5), 1448–1456 (2005).
[10] F. Levi, A. Godone, J. Vanier, S. Micalizio, and G. Modugno, "Lineshape of dark line and maser emission profile in CPT," Eur. Phys. J. D **12**, 53 (2000).
[11] V. Taichenachev, A. M. Tumaikin, V. I. Yudin, M. Stahler, R. Wynands, J. Kitching, and L. Hollberg, "Nonliear-resonance line shapes: Dependence on the transverse intensity distribution of a light beam," Phys. Rev. A **69**, 024501 (2004).
[12] M. Radonjić, D. Arsenović, Z. Grujić, and B. M. Jelenković, "Coherent population trapping linewidths for open transitions: Cases of different transverse laser intensity distribution," Phys. Rev. A **79**, 023805 (2009).
[13] J. Krmpot, S. M. Ćuk, S. N. Nikolić, M. Radonjić, D. G. Slavov, and B. M. Jelenković, "Dark Hanle resonances from selected parts of the Gaussian laser beam at different radial distances" Opt. Express **17**, 22491-22498 (2009)
[14] Z. D. Grujić, M. Mijailović, D. Arsenović, A. Kovačević, M. Nikolić, and B. M. Jelenković, "Dark Raman resonances due to Ramsey interference in vacuum vapor cells," Phys. Rev. A **78**, 063816 (2008).
[15] Novikova, Y. Xiao, D. F. Phillips, R. L. Walsworth, "EIT and diffusion of atomic coherence," J. Mod. Opt. **52**, 2381 (2005).
[16] Y. Xiao, I. Novikova, D. F. Phillips, and R. L. Walsworth, "Diffusion-Induced Ramsey Narrowing," Phys. Rev. Lett. **96**, 043601 (2006).
[17] S. I. Kanorsky, A. Weis, and J. Skalla, "A wall-collision-induced Ramsey resonance," Appl. Phys. B **60**, S165 (1995).

[18] Affolderbach, C. Andreeva, S. Cartaleva, T. Karaulanov, G. Mileti, D. Slavov, "Light shift suppression in laser optically pumped vapour-cell atomic frequency standards," Appl Phys B **80,** 841 (2005).

[19] J. Belfi, G. Bevilacqua, V. Biancalana, S. Cartaleva, Y. Dancheva, L. Moi, "Cesium coherent population trapping magnetometer for cardiosignal detection in an unshielded environment," JOSA B **24,** 2357 (2007).

[20] H. Gilles, B. Cheron, O. Emile, F. Bretenaker, and A. Le Floch, "Rabi-Lorentzian profile of an Atomic Resonance Obtained with Gaussian Beams," Phys. Rev. Lett. 86(7), 1175–1178 (2001).

Influence of laser beam profile on electromagnetically induced absorption

S. M. Ćuk, M. Radonjić, A. J. Krmpot,[*] S. N. Nikolić, Z. D. Grujić, and B. M. Jelenković

Institute of Physics, University of Belgrade, Pregrevica 118, 11080 Belgrade, Serbia

We compared, experimentally and theoretically, Hanle electromagnetically induced absorption (EIA) obtained using Gaussian and Π-shaped laser beams 3 mm in diameter. The study was done by measuring the transmission of a laser locked to the $F_g = 2 \to F_e = 3$ transition at the D_2 line of ^{87}Rb in a vacuum cell. EIA linewidths obtained for the two laser profiles were significantly different in the range of laser intensities 1–4 mW/cm^2. EIA with the Π-shaped laser beam has a broad intensity maximum and linewidths larger than those obtained with the Gaussian beam profile. We also studied Hanle EIA by measuring the transmission of selected segments of the entire laser beam by placing a small movable aperture in front of the detector. Waveforms so obtained in Hanle EIA resonances were strongly influenced both by the radial distance of the transmitted segment from the beam center and by the radial profile of the laser beam. We show that outer regions of Gaussian beam, and central regions of the Π-shaped beam generate the narrowest lines. The different behaviors of EIA owing to different beam profiles revealed by both theory and experiment indicate the importance of the radial profile of the laser beam for proper modeling of coherent effects in alkali metal vapors.

PACS number(s): 42.50.Gy, 42.50.Nn, 42.62.Fi, 42.65.−k

I. INTRODUCTION

Coherent phenomena in Doppler broadened alkali metal atom vapors have been thoroughly examined over the past decade. Coherent population trapping (CPT) [1,2], electromagnetically induced transparency (EIT) [3], and electromagnetically induced absorption (EIA) [4,5] have been observed and analyzed in either a pump-probe or a Hanle configuration [6,7]. EIA is observed in so-called *V* atomic schemes, such that $F_g \to F_e = F_g + 1$, and $F_g > 0$, where $F_{g,e}$ are total angular momenta of the ground and excited states, respectively [8]. This phenomenon is a consequence of the transfer of coherence and the transfer of population due to spontaneous emission between the excited and the ground degenerate states [9,10]. Due to coherences developed between Zeeman sublevels, EIA could have an important role in sub-Doppler and subrecoil laser cooling mechanisms [11].

All phenomena mentioned strongly depend on the intensity of the applied laser field. Laser intensity dependence of CPT and EIT lineshapes has been studied extensively. It is shown that EIT linewidths have a linear dependence on the laser electric field at lower intensities and a linear dependence on laser intensity at higher intensities [12–14]. The EIA linewidth, in contrast, seems to have a maximum near the saturation limit [15].

The term "laser intensity" is ordinarily used in the sense of an average beam intensity (laser power divided by beam area), regardless of the laser beam profile used in the study. Since coherent phenomena are generally nonlinear, they depend strongly not only on the total beam intensity but also on the radial intensity distribution of the used laser. The typical laser beam profile used in experiments is Gaussian. Theoretical descriptions commonly assume a Π-shaped beam profile. The influence of different laser beam profiles has been studied only for EIT lineshapes in a few papers [16–18].

The goal of the present paper is to give a comparative study of the Hanle EIA resonances obtained with two radial laser beam profiles, Gaussian and Π-shaped. Our investigation was performed on ^{87}Rb vapor in a vacuum cell at the D_2 line in the Hanle configuration. This simple configuration requires only a single laser and a scanning external magnetic field, oriented parallel to the laser propagation direction. We studied EIA obtained from two beam profiles by detecting the entire 3-mm-diameter laser beam and, also, by detecting light coming from small cylindrical volumes selected by the movable 0.5-mm aperture in front of the detector. For low intensities of light passing through the aperture, the selected cylindrical volume, which we denote as quasiprobe region, plays the role of a typical probe beam. The rest of the laser beam is considered to be the pump supplying coherently prepared atoms to the quasiprobe region. Thus, we call the Hanle configuration with the movable aperture the quasiprobe Hanle configuration. Studies of EIA from selected parts of the laser beam were done by moving the aperture along the laser beam radius. Similar measurements for EIT have recently demonstrated the essential influence of different parts of the Gaussian laser beam on the overall EIT resonances, that is, on the EIT from the whole laser beam [19,20]. Our theoretical model gives the Hanle resonance lineshapes in accordance with measurements. Calculations are based on the optical Bloch equations for transient evolution of the atomic state during interaction with laser light of a profiled intensity. The effects of light propagation through polarized atomic vapor are included in the theoretical description.

II. EXPERIMENT

The experimental setup is shown in Fig. 1(a). The external-cavity diode laser is frequency locked to the $F_g = 2 \to F_e = 3$ transition at the D_2 line in ^{87}Rb, where F_g and F_e represent the angular momenta of the ground- and excited-state hyperfine levels, respectively. Laser locking is performed in an auxiliary vacuum Rb cell using the Doppler-free dichroic atomic vapor laser lock (DDAVLL) method [21]. The variable neutral density filter is used for laser power adjustments. Single-mode fiber was used to provide the Gaussian laser beam. After passing through the Glan-Thompson polarizer, the laser beam becomes linearly polarized.
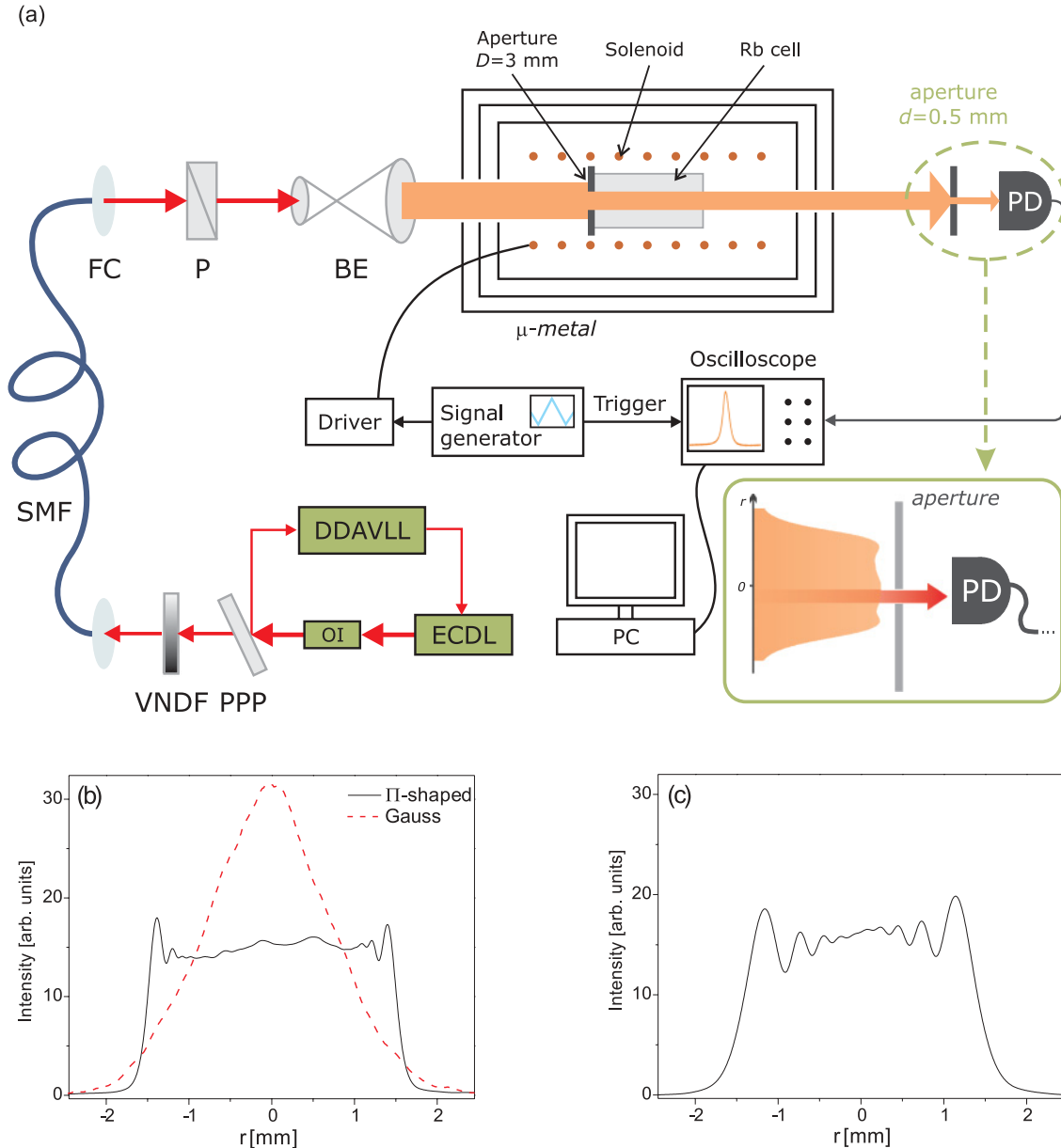
---

[*]krmpot@ipb.ac.rs

FIG. 1. (Color online) (a) Experimental setup: ECDL, external cavity diode laser; OI, optical isolator; DDAVLL, Doppler-free dichroic atomic vapor laser lock; VNDF, variable neutral density filter; SMF, single-mode fiber; FC, fiber collimator; P, polarizer; BE, beam expander; PD, photodiode. Moving the aperture on the translation stage allows only a selected part of the laser beam to reach the detector, while the rest of the laser beam is blocked. Π-shaped beam profiles were recorded by a beam profiler placed at 3 cm (b) and 30 cm (c) from the 3-mm circular aperture. (b) The dashed (red) curve is the profile of a Gaussian laser beam of the same power and diameter as the Π-shaped beam.

For experiments with the Gaussian profile, the laser beam is expanded to 3 mm in diameter. Laser beam diameters are determined from the $1/e^2$ value. The Π-shaped laser beam profile was obtained after expanding the Gaussian laser beam to 20 mm in diameter and then extracting its central part via the circular aperture placed on the entrance window of the cell. Diffraction affects the beam shape in the Rb cell and one has to settle for an approximation of the Π shape of the laser beam. After experimenting with different diameters of the expanded Gaussian laser beam, sizes of apertures, and thicknesses of the foil used for the apertures, we obtained the Π-shaped laser beam whose radial intensity profiles are given in Figs. 1(b) and 1(c). The beam profiles measured by the beam profiler are 3 and 30 cm away from the 3-mm aperture on 0.1-mm tick foil.

The first profile is at a distance equal to the distance between the aperture and the mid section of the Rb cell. This profile is referred to as Π-shaped throughout the paper. We used the beam profile at 30 cm from the aperture to show relatively small changes in the profile with distance and to justify use of the Π-shaped profile in the theoretical model. Together with the Π-shaped laser beam profile, the profile of the Gaussian laser beam is also given in Fig. 1(b). The two beams whose profiles are shown there have the same power and the same diameter.

The laser beam passes through the 6-cm-long vacuum Rb cell containing a natural abundance of rubidium isotopes. The cell is placed in the solenoid used for scanning the axial magnetic field between −50 and +50 μT. The cell and the solenoid are placed inside triple-layered μ-metal cylinders
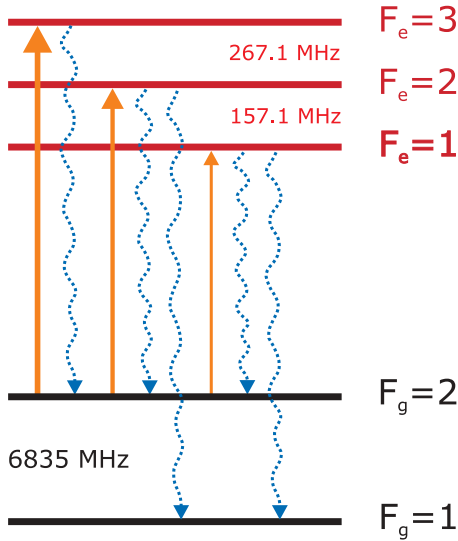
FIG. 2. (Color online) Energy level diagram for D_2 line transitions considered in the theoretical model. Solid lines represent transitions induced by the laser, while dotted lines correspond to possible spontaneous emission channels from excited levels. Frequency differences between adjacent hyperfine levels are shown.

to eliminate Earth's and stray magnetic fields. In the part of the experiment studying the effects of the laser beam profile on the intensity dependence of whole-laser-beam EIA, the entire transmitted laser beam was detected while scanning the external magnetic field.

To measure Hanle EIA from only small parts of the laser beam, a movable aperture 0.5 mm in diameter is placed in front of the large detection surface photodiode (area, 80 mm^2). By moving the aperture with the fine translation stage we allow only light from a small segment of transmitted laser beam to reach the photodiode. The signal obtained from this photodiode while scanning the external magnetic field is recorded by the digital oscilloscope and transferred to the computer.

III. THEORETICAL MODEL

Hanle EIA resonances were calculated for the D_2 line transition $F_g = 2 \rightarrow F_e = 3$ of ^{87}Rb coupled to a linearly polarized laser in a Rb vacuum cell. The energy level diagram given in Fig. 2 shows hyperfine levels either coupled to the laser light or populated due to spontaneous emission. The quantization z axis is chosen to be parallel to the external magnetic field. The complete magnetic sublevel structure is taken into account in calculations. The model is based on time-dependent optical Bloch equations for the density matrix of a moving atom,

$$\frac{d\rho}{dt} = -\frac{i}{\hbar}[H_{\text{atom}}(B) + H_{\text{int}}(t), \rho] + \left(\frac{d\rho}{dt}\right)_{\text{SE}}, \qquad (1)$$

where

$$H_{\text{atom}}(B) = \sum_j \hbar\omega_j(B)|g_j\rangle\langle g_j| + \sum_k \hbar\omega_k(B)|e_k\rangle\langle e_k| \quad (2)$$

is the atomic Hamiltonian corresponding to the ground (excited) states $|g_j\rangle$ ($|e_k\rangle$) with Zeeman-shifted energies $\hbar\omega_j(B)$ [$\hbar\omega_k(B)$] in the external magnetic field B. Laser-atom

interaction is given by

$$H_{\text{int}}(t) = -\sum_{j,k} \mathbf{E}(t) \cdot \mathbf{d}_{jk}(|g_j\rangle\langle e_k| + |e_k\rangle\langle g_j|), \qquad (3)$$

where $\mathbf{E}(t)$ is the time-dependent laser electrical field and $\mathbf{d}_{jk}$ is the atomic electric dipole moment for the transition between state $|g_j\rangle$ and state $|e_k\rangle$. Spontaneous emission is included through the Lindblad-form term,

$$\left(\frac{d\rho}{dt}\right)_{\text{SE}} = \sum_m 2\Gamma_m \rho \Gamma_m^\dagger - \Gamma_m^\dagger \Gamma_m \rho - \Gamma_m \Gamma_m^\dagger \rho, \qquad (4)$$

where Γ_m are operators corresponding to dipole transitions from the excited- to the ground-state manifold. Although the laser is frequency locked to the $F_g = 2 \rightarrow F_e = 3$ transition, owing to the Doppler broadening, the excited hyperfine levels $F_e = 2$ and $F_e = 1$ are also laser coupled and taken into consideration. Equations for density matrix elements related to the $F_g = 1$ ground level are excluded since that level is not coupled by the laser. For additional details about the resulting equations please refer to [18]. It is assumed that after colliding with cell walls, atoms reset into the internal state with equally populated ground magnetic sublevels. Between collisions with cell walls, rubidium atoms interact only with an axially oriented homogeneous magnetic field and spatially dependent laser electric field. Collisions among Rb atoms are negligible due to low Rb vapor pressure at room temperature so that an atom moves through the laser beam at a constant velocity $\mathbf{v} = \mathbf{v}_\parallel + \mathbf{v}_\perp$, where $\mathbf{v}_\parallel$ and $\mathbf{v}_\perp$ are velocity components parallel and perpendicular to the laser propagation direction, respectively. The former affects the longitudinal direction of the atomic trajectory and Doppler shift of the laser frequency seen by a moving atom, while the latter determines the transverse direction of the trajectory and the interaction time.

The dependence of the laser intensity on the radial distance r for the Gaussian profile is

$$I(r) = 2\bar{I} \exp\left(-2r^2/r_0^2\right), \qquad (5)$$

where r_0 is $1/e^2$ beam radius and $\bar{I}$ is the beam intensity (total laser power divided by $r_0^2\pi$). A Π-shaped profile of the same intensity and radius was modeled using the equation

$$I(r) = \bar{I}a \{1 + \text{erf}[p(r_0 - r)]\}^2, \qquad (6)$$

where a is the normalization constant and p is a positive parameter affecting the steepness of the profile near $r = r_0$. In our calculations we neglect longitudinal changes in the beam profile compared to transverse ones, so that only the transverse direction of the trajectory matters. Therefore, we drop the explicit dependence on z of all physical quantities. From the reference frame of the moving atom, the electric field varies and the rate of variation depends only on $\mathbf{v}_\perp$. Assume that the transverse projection of the atomic trajectory is given by $\mathbf{r}_\perp(t) = \mathbf{r}_{0\perp} + \mathbf{v}_\perp t$, where $\mathbf{r}_{0\perp}$ is the perpendicular component of the atom position vector at $t = 0$. The temporal variation of the laser intensity seen by the atom is given by

$$I(t) \equiv I(\mathbf{r}_\perp(t)) = I(\mathbf{r}_{0\perp} + \mathbf{v}_\perp t), \qquad (7)$$

representing the spatial laser intensity variation along the trajectory of the atom in the laboratory frame. Additionally, due to the cylindrical symmetry of the beam profile, spatial dependence becomes purely radial dependence.
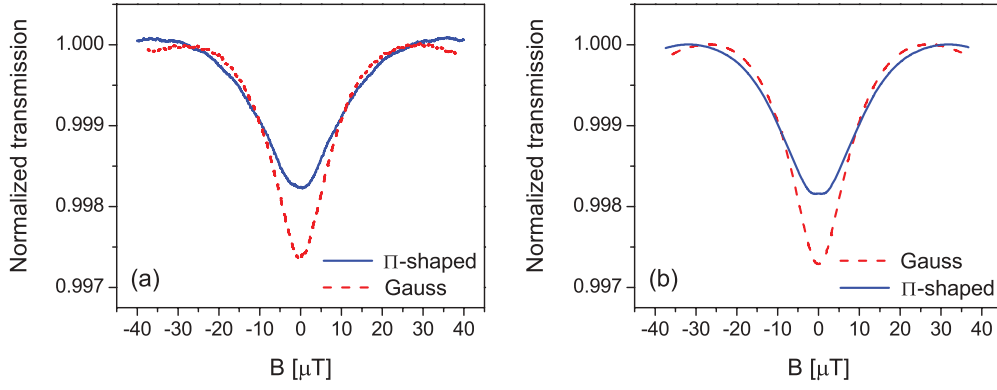
FIG. 3. (Color online) Experimental (a) and theoretical (b) Hanle EIA resonances for the Gaussian [dashed (red) curves] and Π-shaped [solid (blue) curves] beam profiles. Laser intensity is 2 mW/cm^2.

The observed resonances in EIA experiments are the probabilistic average of contributions due to many individual, mutually noninteracting atoms. Rb atoms traverse the laser beam at different paths with different velocities. The Maxwellian velocity distribution, diversity of atomic trajectories, and custom cylindrically symmetric radial profile of the laser electric field are treated similarly as in [18]. Trajectories at different distances from the laser beam center are chosen so that the beam cross section is uniformly covered. For a representative set of atomic velocities the atomic density matrix $\rho(B; \mathbf{v}; \mathbf{r}_\perp)$ along a given trajectory is calculated assuming a constant magnetic field B during the atomic transit through the laser beam. To obtain the atomic ensemble density matrix $\rho(B; r)$ across the beam cross section for a set of radial distances r, the calculated density matrices are averaged over the Maxwell-Boltzmann velocity distribution and integrated over trajectories containing points at a given radial distance r. Owing to the cylindrical symmetry of the laser beam profile and the atomic velocity distribution, the velocity-averaged density matrix will also be cylindrically symmetric. Thus, the angular integral appearing in the averaging over velocity $\mathbf{v}(\theta) = (\theta, v_\perp, v_\parallel)$ can be replaced with an angular integral over space

$$\rho(B; r) = \int_0^{2\pi} \frac{d\theta}{2\pi} \int_0^\infty dv_\perp W_\perp(v_\perp)$$
$$\times \int_{-\infty}^\infty dv_\parallel W_\parallel(v_\parallel) \rho(B; 0, v_\perp, v_\parallel; r\cos\theta, r\sin\theta),$$
$$(8)$$

with the Maxwell-Boltzmann velocity distribution given by

$$W_\perp(v_\perp) = \frac{2v_\perp}{u^2} e^{-(v_\perp/u)^2}, \qquad (9a)$$

$$W_\parallel(v_\parallel) = \frac{1}{u\sqrt{\pi}} e^{-(v_\parallel/u)^2}, \qquad (9b)$$

where $u = (2k_B T/m_{\text{Rb}})^{1/2}$ is the most probable velocity.

The effects of the laser propagation along the cell and induced atomic polarization of the Rb vapor are included using the following approximations. We first compute the Rb vapor ensemble density matrix $\rho(B; r)$ and polarization $\mathbf{P}$ assuming a constant value of the electric field $\mathbf{E}$ along the z direction of laser propagation within the cell. The polarization of Rb vapor is obtained from the ensemble density matrix,

$$\mathbf{P}(B; r) = n(T)\text{Tr}[\rho(B; r)e\hat{\mathbf{r}}], \qquad (10)$$

where the ^{87}Rb concentration at temperature T is given by [22]

$$n(T) = 0.2783 \times \frac{133.322}{k_B T}$$
$$\times 10^{-94.0483 - 0.037\,7169T - 1961.26/T + 18.4902\log_{10}(T)}. \qquad (11)$$

Due to trace operations including dipole operator $e\hat{\mathbf{r}}$, the polarization $\mathbf{P}$ depends only on the optical coherences between the ground and the excited Zeeman sublevels. Using the computed Rb polarization, we calculate the change of the electric field due to propagation of the laser through the Rb
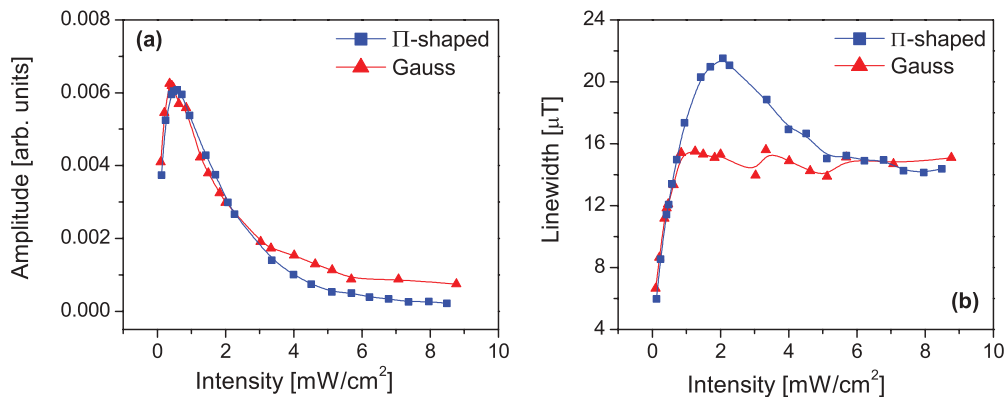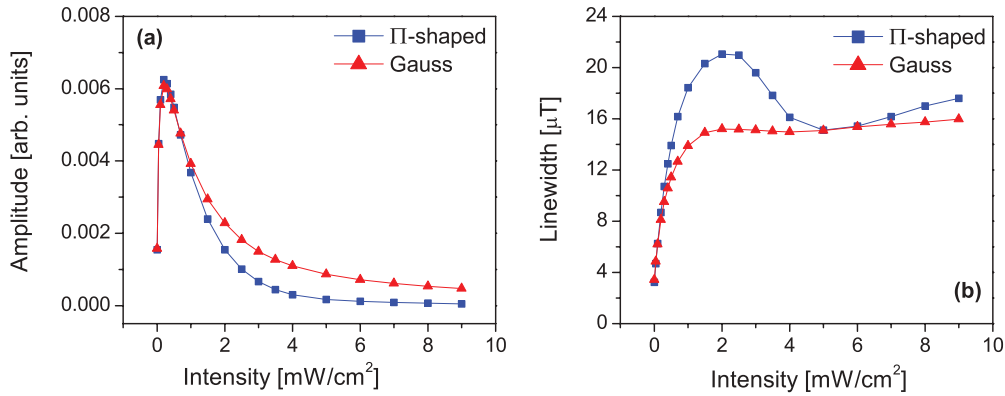

FIG. 4. (Color online) Experimental (a) amplitudes and (b) linewidths for Gaussian [(red) triangles] and Π-shaped [(blue) squares] beam profiles as a function of the laser intensity.

FIG. 5. (Color online) Theoretical (a) amplitudes and (b) linewidths for Gaussian [(red) triangles] and Π-shaped [(blue) squares] beam profiles as a function of the laser intensity.

vapor. Assuming that the change of electric field along the length L of the Rb cell is small enough, the exact relation

$$\frac{\partial \mathbf{E}(B;r,z)}{\partial z} = \frac{i\omega_0}{2\epsilon_0 c}\mathbf{P}(B;r,z) \qquad (12)$$

in the first approximation takes the form

$$\mathbf{E}(B;r,z=L) = \mathbf{E}(B;r,z=0) + \frac{i\omega_0}{2\epsilon_0 c}\mathbf{P}(B;r)L, \qquad (13)$$

where ϵ_0 is the vacuum dielectric constant and ω_0 is the laser frequency. The transmitted electric field of Eq. (13) is used in the calculations of Hanle EIA resonances. The cell temperature was set to 25°C as in experiments.

IV. RESULTS AND DISCUSSION

Figure 3 shows a comparison of Hanle EIA resonances for Gaussian and Π-shaped profiles, at a laser intensity of 2 mW/cm². The quoted laser intensity corresponds to the intensity of the whole laser beam, that is, the measured laser power at the entrance of the cell divided by the beam area. Figure 3(a) corresponds to experiment and Fig. 3(b) shows theoretical results. Key features of any resonance are amplitude and linewidth. It can be seen that for an intensity of 2 mW/cm², the Π-shaped beam profile yields resonances with

a greater linewidth. Figure 4 presents experimental, and Fig. 5 theoretical, results for the amplitudes and linewidths of EIA resonances as a function of the laser intensity, for both laser profiles. EIA amplitudes are normalized to transmitted laser intensity. In each figure we give results obtained using two radial laser beam profiles. It is shown that amplitude intensity dependencies for both profiles initially rise quite rapidly, until they reach a maximum at approximately 0.5 mW/cm². Further decrease with the laser intensity is a consequence of saturation.

Resonance linewidths obtained from the two beam profiles have different dependences on the laser intensity. For both beam profiles there is a very rapid increase at low intensities. However, the Π-shaped profile gives a pronounced maximum at about 2 mW/cm², while the Gaussian profile provides an almost-flat linewidth dependence at these and higher intensities. EIA intensity narrowing at high laser intensities, assuming a Π-shaped beam, was noted earlier, in [15]. Differences in linewidths are most notable for moderate intensities and are due to different transient dynamics of atoms passing through the laser beam. During atomic transit through the laser beam the atomic state changes due to competitive effects of the laser excitation and the external magnetic field. The laser continuously forces the atom to be "aligned" with the electric field, in which case the state of the atom relates to the appearance of EIA. The external magnetic field causes oscillations
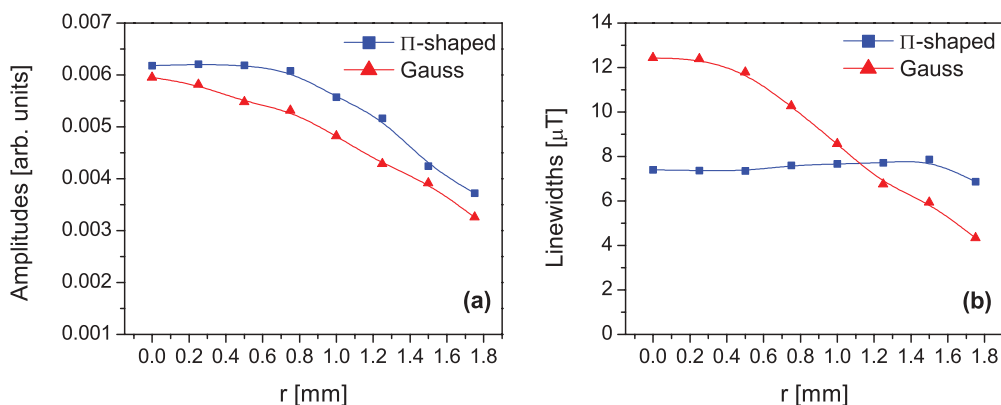

FIG. 6. (Color online) Experimental results for (a) amplitude and (b) linewidth of EIA obtained from laser beam sections at different radial distances from the laser beam center for Gaussian [(red) triangles] and Π-shaped [(blue) squares] beam profiles. Points correspond to different radial distances of the 0.5-mm aperture selecting the sections. Laser intensity is 0.2 mW/cm².
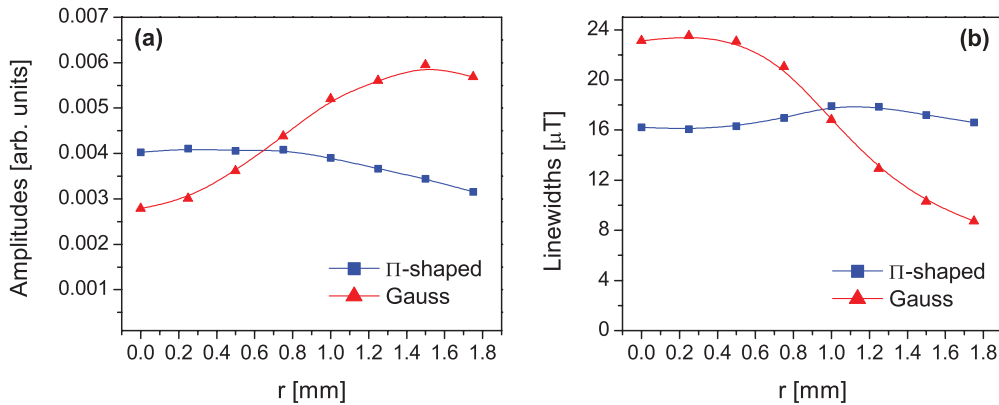
FIG. 7. (Color online) Experimental results for (a) amplitude and (b) linewidth EIA dependence on the radial position of the 0.5-mm aperture for Gaussian [(red) triangles] and Π-shaped [(blue) squares] beam profiles. Laser intensity is 1 mW/cm².

of the atomic state at the corresponding Larmor frequency. At low laser intensities, the influence of the magnetic field is more significant, so that the atomic state "aligned" with the electric field is degraded more easily. For the Gaussian laser beam, the atoms experience an omnichanging laser field, while the Π-shaped beam provides an almost-constant electric field. This difference reflects directly on the robustness of the "aligned" atomic state with respect to the external magnetic field because the spatial change in the laser field decreases the robustness by inducing an extra variation of the atomic state. Under a zero external magnetic field atoms reach an "aligned" state, and absorption reaches a maximum. A nonzero magnetic field degrades that state, reducing the absorption. If the "aligned" state is more robust, the absorption decreases less for the same magnetic field. Therefore, greater robustness of the EIA with respect to the external magnetic field requires a larger magnetic field to halve the peak absorption and hence yields larger EIA linewidths for the Π-shaped beam, compared to the Gaussian beam. When the laser intensity is high enough, differences in laser beam profile become less important, yielding very similar linewidths for both profiles.

We also studied Hanle EIA obtained by detecting transmitted light from only a part of the laser beam, as a function of the magnetic field. This was done, as explained in Sec. I, by placing a 0.5-mm aperture between the Rb cell and the detector.

We then effectively measure EIA from the cylindrical volume of the medium, which is surrounded by the same medium, illuminated by the same laser. We can regard this as a quasi probe-pump configuration, where the probe is surrounded by a copropagating pump. In such quasiprobe Hanle EIA, resonances are either because of EIA atoms coming into the probe from the surrounding pump area or because of EIA induced by the probe. Relative contributions of the probed and induced part of the observed EIA depend on the overall laser intensity, shape of the beam (Gaussian or Π-shaped), and radial distance of the quasiprobe with respect to the laser beam center.

Figures 6 and 7 present measurement results for amplitudes [Figs. 6(a) and 7(a)] and linewidths [Figs. 6(b) and 7(b)] of Hanle quasiprobe EIA resonances as a function of radial positions of the selected beam segment, at a laser intensity of 0.2 and 1 mW/cm², respectively. Figures 8 and 9 are corresponding theoretical results. While quasiprobe linewidths for the Π-shaped profile are largest at the outer parts of the laser beam, linewidths for the Gaussian laser beam are larger near the laser beam center. This can be attributed to the fact that in the region near the beam boundary, the Π-shaped profile has a higher intensity than the Gaussian. The intensity inside the Gaussian beam increases constantly toward the beam center, causing EIA resonance broadening, so the situation reverses around the radial distance where the Gaussian beam becomes more intense (note that it is two times more intense at the
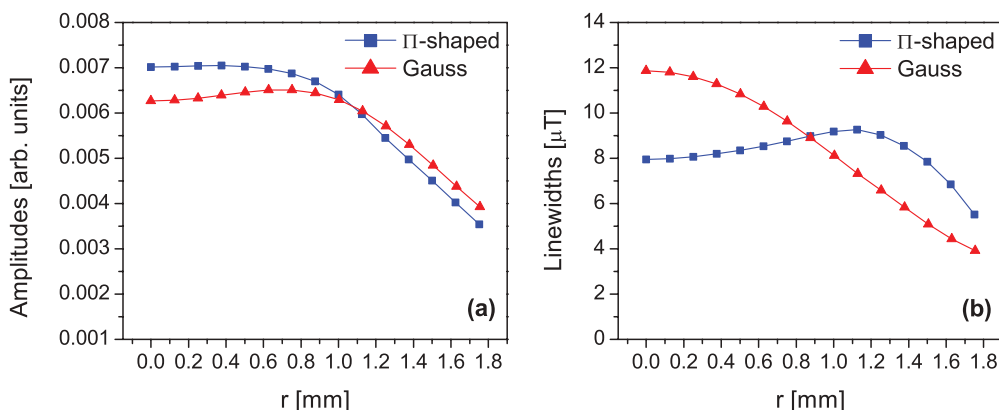

FIG. 8. (Color online) Theoretical results for (a) amplitude and (b) linewidth as a function of the radial position of the 0.5-mm aperture for Gaussian [(red) triangles] and Π-shaped [(blue) squares] beam profiles. Laser intensity is 0.2 mW/cm².
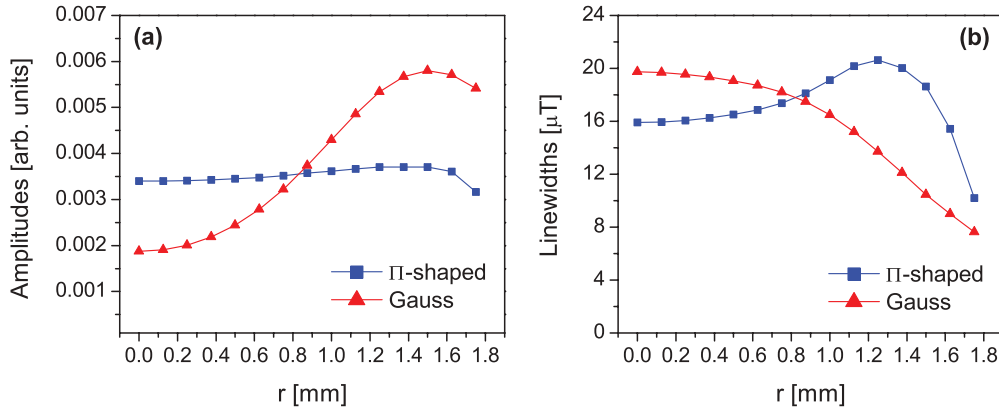
FIG. 9. (Color online) Theoretical results for (a) amplitude and (b) linewidth dependence on the radial position of the 0.5-mm aperture determining the beam segment for Gaussian [(red) triangles] and Π-shaped [(blue) squares] beam profiles. Laser intensity is 1 mW/cm^2.

center than the Π-shaped beam). Note that EIA resonances are particularly narrow in the wings of the Gaussian beam, where a very low intensity quasiprobe really probes the "aligned" EIA state of the atoms coming into the quasiprobe from the rest of the beam. At places closer to the beam center, the quasiprobe simultaneously probes and induces EIA, and eventually the induced effect dominates over probing. This leads to increased linewidths as the quasiprobe moves toward the beam center. In a Π-shaped beam, the passing atoms sense a very rapid increase in laser intensity only at the beam edge and a constant intensity inside the beam. A large variation in laser intensity causes broadening of linewidths and a resultant maximum of linewidths near the beam edge. As atoms move toward the beam center, the constant laser intensity experienced by the atoms and the longer average time of flight inside the Π-shaped beam cause the gradual narrowing of EIA resonances as the atoms move toward the beam center. In other words, the decrease in linewidths upon approaching the beam center for a Π-shaped beam is a typical time-of-flight narrowing.

Radial behavior of EIA amplitudes is notably different for two laser beam shapes at higher laser intensities, as shown in Figs. 7 and 9 for 1 mW/cm^2. Amplitudes for the Π-shaped profile do not show large variations along the beam in comparison with the Gaussian profile, where the initial rise in amplitudes turns into a significant and constant decrease. A strong laser intensity near the center of the Gaussian beam, above $\sim$1 mW/cm^2, leads to a lower amplitude in comparison to amplitudes farther from the beam center. Similar behavior, a decrease upon approaching the center, becomes present also in Π-shaped beams of a laser intensity higher than 1 mW/cm^2. This is attributed to the fact that at high intensities, the laser field dominates over the influence of the magnetic field, so that the effect of the beam profile on the EIA amplitudes becomes less pronounced.

EIA amplitudes and linewidths depend on ambient conditions, stray magnetic field, and room temperature. Effects of stray magnetic field are negligible due to shielding by the triple-layered μ-metal cylinder. The variation of room temperature from one set of measurements to the other was within $\pm1^\circ$C. These temperature variations have a negligible influence on linewidths but may result in changes in EIA amplitudes. Ambient temperature variation shifts the amplitude

radial dependencies, presented in Figs. 6(a) and 7(a), by 10%, preserving their shape.

V. SUMMARY

We studied Hanle EIA resonances at the D_2 line transition $F_g = 2 \rightarrow F_e = 3$ in ^{87}Rb using Gaussian and Π-shaped laser beams with of the same 3-mm radius. We demonstrated that the atom experiences completely different interactions depending on whether traverses one or the other profiled beam. This is shown by the Hanle EIA obtained from transmission of only one cylindrical segment of the entire laser beam. In this way we effectively measured quasiprobe EIA, surrounded by the "pump" beam, that is, by the rest of the laser beam. Since at very low laser intensities, the quasiprobe probes EIA in atoms moving toward the selected region, EIA resonances are narrower in outer regions of the Gaussian beam. At higher laser intensities the quasiprobe can also generate EIA in atoms. Thus, near the center of the Gaussian beam, EIA is widest due to higher power broadening. For a Π-shaped laser beam, the quasiprobe gives the narrowest EIA at the beam center, due to transit-time narrowing of the coherent resonance. EIA amplitudes, in the range of applied laser intensities, are lowest (highest) near the laser beam center for the Gaussian (Π-shaped) profile. Thus, outer regions of the Gaussian beam and central regions of the Π-shaped beam are the most valuable regions in the sense that they contribute the narrowest linewidths and highest amplitudes to the overall EIA. The opposite variation of quasiprobe EIA linewidths with the distance from the laser beam center for the two beam profiles makes the linewidths of whole-beam EIA less dependent on the laser beam profile. Only in the range of laser intensities 1–4 mW/cm^2 does the overall EIA with the Π-shaped laser beam have a maximum which exceeds the values obtained with the Gaussian beam that gives a flat intensity dependence.

This work has shown that it is important to take into account the real laser beam profile for proper modeling and analysis of coherent effects in alkali metal vapors. Differences in EIA linewidths obtained using two laser radial beam profiles imply that a theory with assumed Π-shaped radial dependence (common assumption in majority of models) will not produce good agreement with experiments done

usually using a Gaussian or similar beam shape. One practical consequence of these results is that detecting only the wings of the Gaussian laser beam will give narrower EIA resonances than in the case of whole-beam detection.

---

[1] E. Arimondo, Prog. Opt. **35**, 257 (1996).

[2] G. Alzetta, A. Gozzini, L. Moi, and G. Orriolis, Nuovo Cim. **36**, 5 (1976).

[3] S. E. Harris, J. E. Field, and A. Imamoglu, Phys. Rev. Lett. **64**, 1107 (1990).

[4] A. M. Akulshin, S. Barreiro, and A. Lezama, Phys. Rev. A **57**, 2996 (1998).

[5] F. Renzoni, C. Zimmermann, P. Verkerk, and E. Arimondo, J. Opt. B: Quantum Semiclass. Opt. **3**, S7 (2001).

[6] C. Andreeva, S. Cartaleva, Y. Dancheva, V. Biancalana, A. Burchianti, C. Marinelli, E. Mariotti, L. Moi, and K. Nasyrov, Phys. Rev. A **66**, 012502 (2002).

[7] G. Moruzzi and F. Strumia, *The Hanle Effect and Level Crossing Spectroscopy* (Plenum Press, New York, 1991).

[8] H. Failache, P. Valente, G. Ban, V. Lorent, and A. Lezama, Phys. Rev. A **67**, 043810 (2003).

[9] A. V. Taichenachev, A. M. Tumaikin, and V. I. Yudin, Phys. Rev. A **61**, 011802(R) (1999).

[10] C. Goren, A. D. Wilson-Gordon, M. Rosenbluh, and H. Friedmann, Phys. Rev. A **67**, 033807 (2003).

[11] J. Dalibard and C. Cohen-Tannoudji, J. Opt. Soc. Am. B **6**, 2023 (1989).

[12] A. Javan, O. Kocharovskaya, H. Lee, and M. O. Scully, Phys. Rev. A **66**, 013805 (2002).

[13] C. Y. Ye and A. S. Zibrov, Phys. Rev. A **65**, 023806 (2002).

[14] A. J. Krmpot, M. M. Mijailović, B. M. Panić, D. V. Lukić, A. G. Kovacević, D. V. Pantelić, and B. M. Jelenković, Opt. Express **13**, 1448 (2005).

[15] J. Dimitrijević, D. Arsenović, and B. M. Jelenković, Phys. Rev. A **76**, 013836 (2007).

[16] F. Levi, A. Godone, J. Vanier, S. Micalizio, and G. Modugno, Eur. Phys. J. D **12**, 53 (2000).

[17] A. V. Taichenachev, A. M. Tumaikin, V. I. Yudin, M. Stahler, R. Wynands, J. Kitching, and L. Hollberg, Phys. Rev. A **69**, 024501 (2004).

[18] M. Radonjić, D. Arsenović, Z. Grujić, and B. M. Jelenković, Phys. Rev. A **79**, 023805 (2009).

[19] H. Gilles, B. Cheron, O. Emile, F. Bretenaker, and A. Le Floch, Phys. Rev. Lett. **86**, 1175 (2001).

[20] A. J. Krmpot, S. M. Ćuk, S. N. Nikolić, M. Radonjić, D. G. Slavov, and B. M. Jelenković, Opt. Express **17**, 22491 (2009).

[21] G. Wasik, W. Gawlik, J. Zachorowski, and W. Zawadzki, Appl. Phys. B **75**, 613 (2002).

[22] A. N. Nesmeyanov, *Vapor Pressure of the Chemical Elements*, edited by R. Gray (Elsevier, Amsterdam, 1963).

Laser Beam Profile Influence on Dark Hanle Resonances in Rb Vapor

A.J. Krmpot*, S.M. Ćuk, S.N. Nikolić, M. Radonjić, Z.D. Grujić and B.M. Jelenković

Institute of Physics, Belgrade, Serbia

Influence of two different laser beam profiles, the Gaussian and the Π (top hat) profile on the resonance line widths and amplitudes in the Hanle electromagnetically induced transparency was studied. The laser beam propagates through the vacuum Rb glass cell. Studies were done at D_1 line for the open ^{87}Rb: $F_g = 2 \to F_e = 1$ transition. Hanle electromagnetically induced transparency was measured for the two beam profiles with the same total power and beam diameter and experimental results showed that Gaussian and the top hat profiles give different amplitudes and widths of the Hanle resonances. Resonances obtained from the top hat laser beam profile have lower amplitudes and higher line widths.

PACS numbers: 32.70.Jz, 42.50.Gy, 42.62.Fi, 32.30.Jc

1. Introduction

Coherent effects in the Doppler broadened alkali atom vapor have been intensively investigated over the past decade. Coherent population trapping (CPT) [1, 2], electromagnetically induced transparency (EIT) [3], and electromagnetically induced absorption (EIA) [4, 5] have been observed and examined in pump-probe and in the Hanle configuration [6]. All these effects nonlinearly depend on intensity of the applied laser field. Several papers have theoretically studied the dependence of coherent resonances on laser intensity [7–9], but most assume top hat laser beam profile due to a simplified theoretical analysis. The influence of other beam profiles, such as experimentally accessible Gaussian profile, on CPT line shape has been described only in a few papers [10–12], but there are no experimental studies dealing with the influence of the laser beam profile on the EIT line shapes.

The aim of this paper is to experimentally represent difference in line widths and amplitudes of Hanle EIT resonances for the two laser beam profiles, the Gaussian and the top hat one. Our investigation was performed on ^{87}Rb atoms at D_1 line in the vacuum cell. We presented notably different Hanle EIT resonances related to the Gaussian and the top hat profiles of the laser beam. Comparing our results with those given in [11] the significant differences between dependence of dark resonances on the laser intensity for vacuum and buffer gas cell could be observed.

2. Experiment

The experimental setup is shown in Fig. 1. External cavity diode laser is frequency locked to $F_g = 2 \to F_e = 1$

transition in ^{87}Rb by Doppler-free dichroic atomic vapor laser lock (DDAVLL) method [13] in the vacuum Rb cell. The variable neutral density filter is used for the laser power adjustments. After passing through the Glen–Thomson polarizer the laser beam becomes linearly polarized. The Gaussian beam profile with 3 mm in diameter is obtained by expanding the beam exiting the single mode fiber. For the definition of the laser beam radius we use the distance from the beam maximum where the maximal intensity drops e^2 times. For the top hat profile the Gaussian beam is further expanded to 20 mm and sent through the 3 mm aperture to extract the central part of the laser beam.
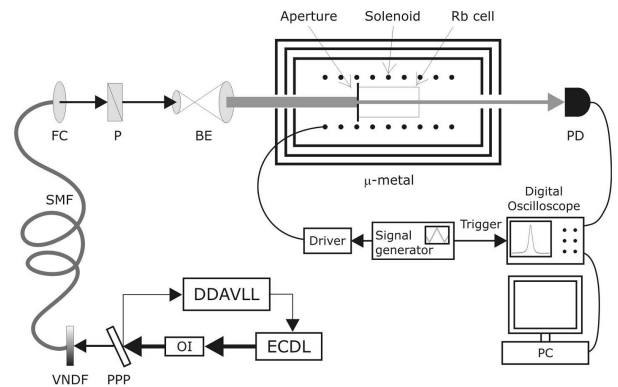
Fig. 1. Experimental setup. ECDL — external cavity diode laser, OI — optical isolator, DDAVLL — Doppler-free dichroic atomic vapor laser lock, VNDF — variable neutral density filter, SMF — single mode fiber, FC — fiber collimator, P — polarizer, BE — beam expander, PD — photodiode.

The laser beam, either Gaussian or top hat profile, passes through 5 cm long vacuum Rb cell containing nat-

* corresponding author; e-mail: krmpot@phy.bg.ac.yu

ural abundance of rubidium isotopes. The cell is placed in the solenoid used for scanning the axial magnetic field between ±3 G. The cell and the solenoid are inside the triple layered μ-metal cylinder in order to eliminate Earth's and stray magnetic fields.

The signal obtained from the photodiode, while scanning the external magnetic field, is recorded by the digital oscilloscope and transferred to the computer.

3. Results and discussion

We analyze the Hanle line shapes for the two laser beam profiles. Both the Gaussian and the top hat laser beams have the same total power P and the beam diameter d. The dependence of the intensity on the transverse distance r to the beam center can be written as

$$I(r) = I_0 f(r/r_0), \tag{1}$$

where the I_0 is the maximal intensity corresponding to $r = 0$, r_0 is the radius of the beam ($r_0 = d/2$), and $f(r/r_0)$ is a profile function ($0 < f(r/r_0) < 1$). Thus, for the top hat profile we have

$$f(r/r_0) = \begin{cases} 1, & r \leq r_0, \\ 0, & r \geq r_0, \end{cases} \tag{2}$$

and for the Gaussian profile

$$f(r/r_0) = \exp\left(-2(r/r_0)^2\right). \tag{3}$$

The Hanle EIT resonances for Gaussian and top hat laser beam profiles, at the laser intensity 1.8 mW/cm^2, are shown in Fig. 2. As could be seen, the resonance shape becomes sharper for the Gaussian profile compared to the top hat intensity distribution. This results in slightly narrower line in the case of the Gaussian beam.
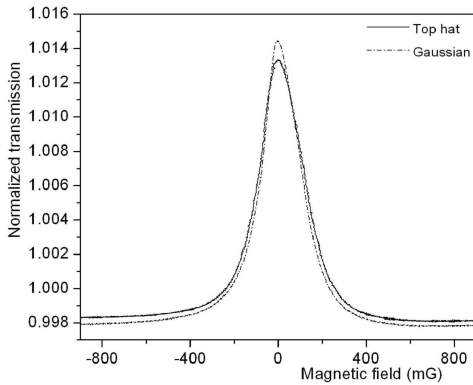

Fig. 2. Hanle EIT resonances obtained for two different laser beam profiles: Gaussian (dash dot) and top hat (solid). The beam diameter was $d = 3$ mm and the total laser intensity was $I = 1.8$ mW/cm^2.

In Fig. 3, the dependence of the Hanle EIT resonance amplitude (a) and line width (b) on the laser beam intensity is shown. According to our experimental results, for the cases of top hat (square symbol) and Gaussian (open triangle symbol) laser beam profile, the intensity dependence of resonance amplitude is nonlinear, and the amplitude is higher for the Gaussian profile in comparison with

the top hat. The amplitudes of the Hanle EIT resonances for Gaussian beam could be higher up to 12% than those for top hat profile, in the given range of laser intensities. Intensity dependences of line widths are monotonically increasing functions, with very different slopes; the EIT line widths obtained using the top hat laser beam profile are becoming wider than for the Gaussian beam up to the 18.5%, as the laser intensity increases.
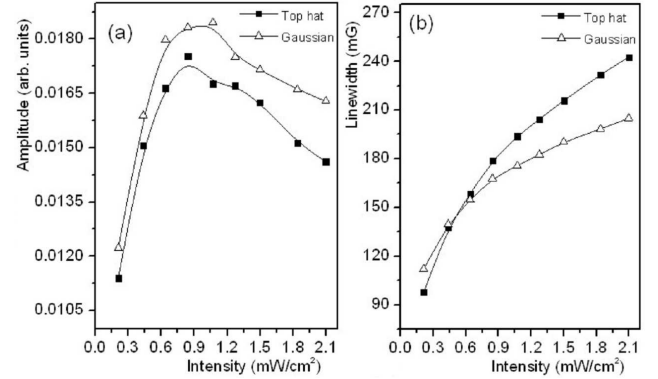

Fig. 3. Amplitude (a) and line width (b) of the Hanle EIT resonances versus laser intensity given for the Gaussian (open triangle symbol) and for the top hat laser beam profile (square symbol).

The atom experiences different excitations when enters different radial profiles of the laser intensity. For the Gaussian beam, the intensity reaches its maximal value I_0 only at the very center of the beam, while for the top hat profile this peak intensity is present all over the beam. Therefore, in the top hat beam profile all atoms see the same intensity, whereas for the Gaussian beam atoms in the outer regions are experiencing much lower laser intensity, contributing with narrower lines to the overall line shape. Top hat beam profile has significantly faster increase of light intensity at its edge, so that an atom that enters the laser beam will be promoted faster to the dark state in comparison with Gaussian profile. It is now obvious why the profile function is important when analyzing experimental dependences. However, in practice one usually calculates the field intensity as P/S, with S being the area of the light spot, without a detailed investigation of the intensity profile. Thus, for seemingly identical parameters, different experimental setups can produce different results.

When comparing our experimental results with theoretical predictions for buffer gas cell given in [11], we observe similarity in behavior of line widths versus laser intensity, i.e. Gaussian beam profile results in narrower EIT resonances than top hat profile. From Fig. 3b it could be seen that previous statement is not valid only at extremely low intensities. Concerning amplitudes of EIT lines, situation in vacuum cell is significantly different from that in a buffer gas cell. Namely, in the case of a vacuum cell Gaussian beam profile gives, particularly at higher laser intensities, higher amplitudes than top

hat profile. Situation in a buffer gas cell is vice versa, the dependence is more or less linear and Gaussian beam profile results in less intense CPT lines than top hat, over all intensities.

4. Conclusion

This study has shown that different laser beam profiles considerably influence the Hanle EIT line profiles. Assuming the same laser power and diameter for the two beam profiles, the resonances obtained from the Gaussian laser beam are narrower than those obtained with the top hat profile, particularly at higher laser intensities. This is similar to the findings in the buffered gas cells. Contrary to the results with buffered gas cells, we have found that in the vacuum gas cell amplitudes of EIT resonances are lower for the top hat laser beam profile.

References

[1] E. Arimondo, *Prog. Opt.* **35**, 257 (1996).

[2] G. Alzetta, A. Gozzini, L. Moi, G. Orriolis, *Il Nuovo Cimento* **36**, 5 (1976).

[3] S.E. Harris, J.E. Field, A. Imamoglu, *Phys. Rev. Lett.* **64**, 1107 (1990).

[4] A.M. Akulshin, S. Barreiro, A. Lezama, *Phys. Rev. A* **57**, 2996 (1998).

[5] G. Moruzzi, F. Strumia, *The Hanle effect and Level Crossing Spectroscopy*, Plenum Press, 1991.

[6] C. Andreeva, S. Cartaleva, Y. Dancheva, V. Biancalana, A. Burchianti, C. Marinelli, E. Mariotti, L. Moi, K. Nasyrov, *Phys. Rev. A* **66**, 502 (2002).

[7] A. Javan, O. Kocharovskaya, H. Lee, M.O. Scully, *Phys. Rev. A* **66**, 013805 (2002).

[8] C.Y. Ye, A.S. Zibrov, *Phys. Rev. A* **65**, 023806 (2002).

[9] A.J. Krmpot, M.M. Mijailović, B.M. Panić, D.V. Lukić, A.G. Kovačević, D.V. Pantelić, B.M. Jelenković, *Opt. Express* **13**, 1448 (2005).

[10] F. Levi, A. Godone, J. Vanier, S. Micalizio, G. Modugno, *Eur. Phys. J. D* **12**, 53 (2000).

[11] M.A.V. Taichenachev, A.M. Tumaikin, V.I. Yudin, M. Stahler, R. Wynands, J. Kitching, L. Hollberg, *Phys. Rev. A* **69**, 024501 (2004).

[12] M. Radonjić, D. Arsenović, Z. Grujić, B.M. Jelenković, *Phys. Rev. A* **79**, 023805 (2009).

[13] G. Wasik, W. Gawlik, J. Zachorowski, W. Zawadzki, *Appl. Phys. B* **75**, 613 (2002).

Dark Hanle resonances from selected segments of the Gaussian laser beam cross-section

A. J. Krmpot[1], S. M. Ćuk[1], S. N. Nikolić[1], M. Radonjić[1], D. G. Slavov[2], and B. M. Jelenković[1]

[1]*Institute of Physics, University of Belgrade, Pregrevica 118, 11080 Belgrade, Serbia*
[2]*Institute of Electronics, Bulgarian Academy of Sciences, 72 Tzarigradsko Chaussee blvd., 1784 Sofia, Bulgaria*
[*krmpot@phy.bg.ac.rs](mailto:krmpot@phy.bg.ac.rs)

Abstract: We present the Hanle EIT resonances obtained from the various segments of the Gaussian laser beam cross-section, selected by moving the small aperture (placed in front of the detector) radially along the laser beam. Significant differences in the Hanle lineshapes are observed depending on whether the central or outer parts of the Gaussian laser beam are detected. The line narrowing and two counter-sign peaks occur at outer, less intense parts of the beam. The theoretical model suggests that the EIT lineshapes in the laser wings are result of the interference of the laser light and coherently prepared atoms coming from the central part of the beam. By blocking the central part of the laser beam in front of the detector, narrower, and for high laser intensities, even more contrasted Hanle resonances are obtained.

©2009 Optical Society of America

OCIS codes: (020.1670) Coherent optical effects; (270.1670) Coherent optical effects.

References and links

1. E. Arimondo, "Coherent population trapping in laser spectroscopy," Prog. Opt. **35**, 257–354 (1996).
2. G. Alzetta, A. Gozzini, L. Moi, and G. Orriolis, "An experimental method for the observation of RF transitions and laser beat resonances in oriented Na vapour," Nuovo Cim. **36**(1), 5–20 (1976).
3. S. E. Harris, J. E. Field, and A. Imamoglu, "Nonlinear Optical Processes Using Electromagnetically Induced Transparency," Phys. Rev. Lett. **64**(10), 1107–1110 (1990).
4. A. M. Akulshin, S. Barreiro, and A. Lezama, "Electromagnetically induced absorption and transparency due to resonant two-field excitation of quasidegenerate levels in Rb vapor," Phys. Rev. A **57**(4), 2996–3002 (1998).
5. G. Moruzzi and F. Strumia, "The Hanle effect and level crossing spectroscopy," (Plenum Press 1991).
6. C. Andreeva, S. Cartaleva, Y. Dancheva, V. Biancalana, A. Burchianti, C. Marinelli, E. Mariotti, L. Moi, and K. Nasyrov, "Coherent spectroscopy of degenerate two-level systems in Cs," Phys. Rev. A **66**(1), 502 (2002).
7. A. Javan, O. Kocharovskaya, H. Lee, and M. O. Scully, "Narrowing of electromagnetically induced transparency resonance in a Doppler-broadened medium," Phys. Rev. A **66**(1), 013805 (2002).
8. C. Y. Ye, and A. S. Zibrov, "Width of the electromagnetically induced transparency resonance in atomic vapor," Phys. Rev. A **65**(2), 023806 (2002).
9. A. J. Krmpot, M. M. Mijailović, B. M. Panić, D. V. Lukić, A. G. Kovacević, D. V. Pantelić, and B. M. Jelenković, "Sub-Doppler absorption narrowing in atomic vapor at two intense laser fields," Opt. Express **13**(5), 1448–1456 (2005).
10. F. Levi, A. Godone, J. Vanier, S. Micalizio, and G. Modugno, "Lineshape of dark line and maser emission profile in CPT," Eur. Phys. J. D **12**(1), 53–59 (2000).
11. A. V. Taichenachev, A. M. Tumaikin, V. I. Yudin, M. Stahler, R. Wynands, J. Kitching, and L. Hollberg, "Nonliear-resonance line shapes: Dependence on the transverse intensity distribution of a light beam," Phys. Rev. A **69**(2), 024501 (2004).
12. M. Radonjić, D. Arsenović, Z. Grujić, and B. M. Jelenković, "Coherent population trapping linewidths for open transitions: Cases of different transverse laser intensity distribution," Phys. Rev. A **79**(2), 023805 (2009).
13. H. Gilles, B. Cheron, O. Emile, F. Bretenaker, and A. Le Floch, "Rabi-Lorentzian profile of an Atomic Resonance Obtained with Gaussian Beams," Phys. Rev. Lett. **86**(7), 1175–1178 (2001).
14. I. Novikova, Y. Xiao, D. F. Phillips, and R. L. Walsworth, "EIT and diffusion of atomic coherence," J. Mod. Opt. **52**(16), 2381–2390 (2005).
15. Y. Xiao, I. Novikova, D. F. Phillips, and R. L. Walsworth, "Diffusion-Induced Ramsey Narrowing," Phys. Rev. Lett. **96**(4), 043601 (2006).
16. S. I. Kanorsky, A. Weis, and J. Skalla, "A wall-collision-induced Ramsey resonance," Appl. Phys. B **60**, S165 (1995).
17. C. Affolderbach, C. Andreeva, S. Cartaleva, T. Karaulanov, G. Mileti, and D. Slavov, "Light shift suppression in laser optically pumped vapour-cell atomic frequency standards," Appl. Phys. B **80**(7), 841–848 (2005).

18. J. Belfi, G. Bevilacqua, V. Biancalana, S. Cartaleva, Y. Dancheva, and L. Moi, "Cesium coherent population trapping magnetometer for cardiosignal detection in an unshielded environment," J. Opt. Soc. B **24**(9), 2357 (2007).
19. G. Wasik, W. Gawlik, J. Zachorowski, and W. Zawadzki, "Laser frequency stabilization by Doppler-free magnetic dichroism," Appl. Phys. B **75**(6-7), 613–619 (2002).
20. Z. D. Grujić, M. Mijailović, D. Arsenović, A. Kovačević, M. Nikolić, and B. M. Jelenković, "Dark Raman resonances due to Ramsey interference in vacuum vapor cells," Phys. Rev. A **78**(6), 063816 (2008).

1. Introduction

Coherent effects in Doppler broadened alkali atom vapor have been intensively investigated over the past decade. Coherent population trapping (CPT) [1, 2], electromagnetically induced transparency (EIT) [3], and electromagnetically induced absorption (EIA) [4] have been observed and examined in either pump-probe and in Hanle configuration [5, 6]. All these phenomena strongly depend on the intensity of the applied laser field. The dependence of CPT and EIT lineshapes on the laser intensity has been extensively studied [7–9].

Typical radial laser beam profile in experiments studying CPT and EIT is Gaussian. The intensities in the center and in the wings of the Gaussian beam are very different. Nevertheless, the order of magnitude lower intensity in the wings can still contribute to the atomic coherent effects. The lifetime of atomic coherence is longer then the atom transit time through the laser beam. Thus, the light in the wings can "probe" the induced atomic coherence and polarization of the atom coming from central parts of the laser beam. The reversed order of events, excitation of atoms first in the wings and then in the intense central parts of the laser beam will not reveal effects of the coherently prepared state due to overwhelming effects of the photons at the center of the laser beam. It is therefore a reasonable assumption that different parts of the Gaussian laser beam, after passing through the alkali vapor cell, carry different information about the atomic coherence and should yield different EIT resonances. The influence of laser beam profiles on EIT lineshapes is studied only in few papers [10–13]. The contribution of different segments of the Gaussian laser beam to the dark resonance lineshapes in a dense ⁴He vapor was presented in Ref [13]. The results of [13] show deviation of overall resonance profile from pure Lorentzian shape attributed to observed spatial variation of lineshapes for different positions in the Gaussian beam. There are several papers showing significance of the re-excitation of atoms by separated, in space and/or time, laser beams tuned to Raman resonance of the atomic transitions. Narrowing of EIT in buffer gas cells [14, 15] and cells with antireflection coatings [16] is attributed to repeated excitation by the laser beam after the atom spends some time in 'dark', not illuminated by the laser light. The goal of this work is in part to investigate if such mechanism plays the role in observed shape of the resonance due to the light from the wings of the Gaussian laser beam.

In this work we study EIT resonances originating from different parts of the Gaussian laser beam cross-section, after the whole laser beam passes through the Rb vapor cell. Our investigation was performed on ⁸⁷Rb atoms at D1 line in the Hanle configuration. In the experiment, the detection of the signal from the specific parts of the Gaussian beam was accomplished by moving the aperture (placed between the Rb cell and the large area photo-detector) along the laser beam diameter. In the theoretical model, the Hanle resonance lineshapes were obtained by including the effects of the atomic polarization, the time evolution of the coherence, and the interaction of the atomic state with light in the wings of the Gaussian laser. The theoretical results distinguish the contribution to the EIT from atoms coming to the wings from central parts of the laser beam and from the outside of the beam. In line with these results, we were able to improve resonance linewidth and contrast of EIT resonances by blocking a small part of the central region of the laser beam by the small mask in front of the detector. Narrower and more contrasted resonances are important for applications of the CPT and EIT effects in atomic frequency standards [17] and magnetometry [18].

2. Experiment

The experimental setup is shown in Fig. 1. External cavity diode laser is frequency locked to $F_g=2 \rightarrow F_e=1$ transition in ^{87}Rb, where F_g and F_e correspond to angular momentum of the ground and excited state hyperfine levels, respectively. The energy level diagram, given in the insert in Fig. 1, shows magnetic sublevels of the hyperfine levels either coupled by the laser light, or populated due to spontaneous emission. Linearly polarized laser light allows for multiple Λ schemes and formation of dark states among ground Zeeman sublevels of $F_g=2$ level. The locking is performed by Doppler-free dichroic atomic vapor laser lock (DDAVLL) method [19] using auxiliary vacuum Rb cell. The variable neutral density filter is used for the laser power adjustments. The laser beam, introduced into the single mode fiber with the collimator, provides the Gaussian beam at the exit of the fiber. After passing through the Glen-Thomson polarizer the laser beam becomes linearly polarized. The laser beam is then expanded to 3 mm in diameter. The dependence of the laser intensity on the radial distance r from the beam center is Gaussian

$$I(r) = I_0 \exp\left(-2r^2/r_0^2\right), \qquad (1)$$

where I_0 is the maximal intensity and r_0 is $1/e^2$ beam radius.

The Gaussian beam passes through 5 cm long vacuum Rb cell containing natural abundance of rubidium isotopes. The cell is placed in the solenoid used for scanning the axial magnetic field between ±300 µT. The cell and the solenoid are placed inside the triple layered µ-metal cylinder to eliminate Earth's and stray magnetic fields.

The small movable aperture 0.5 mm in diameter is placed in front of the photodiode with large detection surface (area 80 mm^2). The sensitivity of the photodiode is 0.57 A/W at 780 nm and it has variable transimpedance gain with nominal value of 1 MΩ (selectable between 1 kΩ and 10 MΩ). By moving the aperture with the fine translation stage (0.25 mm shift per revolution) we are able to select specific parts of the Gaussian laser beam to reach the photodiode. The signal obtained from the photodiode while scanning the external magnetic field is recorded by the digital oscilloscope and transferred to the computer.

For some measurements we replaced the aperture with the circular mask to block the central part of the beam and detect only the outer parts of the beam.
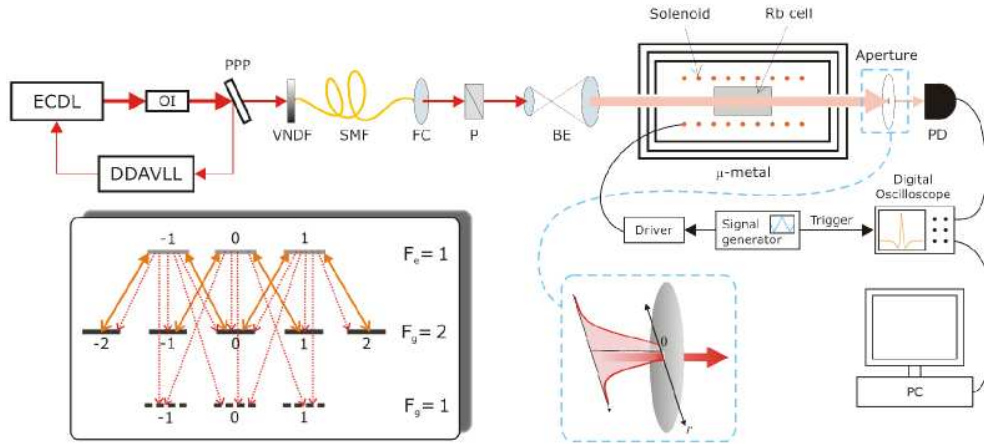

Fig. 1. Experimental setup. The aperture at translation stage allows only selected parts of the laser beam to reach detector, while the rest is blocked. ECDL – External Cavity Diode Laser, OI – Optical Isolator, DDAVLL – Doppler-free Dichroic Atomic Vapor Laser Lock, VNDF – Variable Neutral Density Filter, SMF – Single Mode Fiber, FC – Fiber Collimator, P – Polarizer, BE – Beam Expander, PD – Photodiode. Inset: The energy-level diagram for magnetic sublevels of the $F_g=2 \rightarrow F_e=1$ transition where solid lines represent linearly polarized laser light coupling Zeeman sublevels and dotted lines correspond to the de-excitation from excited levels.

3. Theoretical model

The Hanle EIT resonances were calculated for the D1 line transition $F_g=2 \rightarrow F_e=1$ of ^{87}Rb coupled by a linearly polarized laser in the Rb vacuum cell. The model is based on time dependent optical Bloch equations for the density matrix and takes into account Doppler broadening, different atomic trajectories through the laser beam, and Gaussian cylindrically symmetric radial profile of the laser electric field [12]. Rubidium atoms interact only with axially oriented homogeneous magnetic field, spatially dependent laser electric field, and cell walls. All the levels resonantly interacting with the laser light are taken into account, as well as radiative population losses to another ground state hyperfine level, $F_g=1$. After colliding with cell walls atoms reset into internal state with equally populated ground magnetic sublevels. Collisions among Rb atoms are neglected due to low Rb vapor pressure at room temperature so that the atomic trajectories through the laser beam are strait lines. For a set of atomic velocities the atomic density matrix along a given trajectory is calculated assuming constant magnetic field B during the atomic transit through the laser beam. Averaging the calculated density matrices over Maxwell-Boltzmann velocity distribution and over a collection of trajectories uniformly covering the beam cross-section, we obtain the atomic ensemble density matrix $\rho(B; r)$ across the beam for a set of radial distances r. The effects of the laser propagation along the cell and the atomic polarization of the Rb vapor are included in the following manner. Presuming that the laser intensity does not depend on the coordinate z along the laser propagation direction, we first compute the Rb vapor polarization $\mathbf{P}$ taking the constant value of the electric field $\mathbf{E}$ within the cell along the z direction. The polarization of Rb vapor of concentration n is obtained from density matrix

$$\mathbf{P}(B;r) = n \operatorname{Tr}(\rho(B;r)\, e\hat{\mathbf{r}}). \tag{2}$$

Owing to the trace operation, the polarization $\mathbf{P}$ depends only on the optical coherences between the excited and the ground Zeeman sublevels. Using the computed Rb polarization, we calculate the change of the electric field due to propagation of the laser through the Rb vapor. Assuming that the change of electric field along the length L of the Rb cell is small enough, the exact relation

$$\frac{\partial \mathbf{E}(B;r,z)}{\partial z} = \frac{i\omega_0}{2\epsilon_0 c} \mathbf{P}(B;r,z), \tag{3}$$

in the first approximation takes the form

$$\mathbf{E}(B;r,z=L) = \mathbf{E}(B;r,z=0) + \frac{i\omega_0}{2\epsilon_0 c} \mathbf{P}(B;r)L, \tag{4}$$

where ε_0 is the vacuum dielectric constant and ω_0 is the laser frequency. The transmitted electric field (Eq. (4)) is used in the calculations of Hanle EIT resonances for different segments of the Gaussian beam.

4. Results and discussion

This section presents the results of the Hanle EIT resonances obtained by sampling the small parts of the laser beam after passing through the Rb gas cell. The curves in Fig. 2(a) and (b) represent the experimental and theoretical resonances recorded for different positions of the aperture along the beam diameter, with $r = 0$ mm referring to the laser beam center. The laser intensity is 0.5 mW/cm^2. There is a good agreement between the experiment and the theory. Figure 2 reveals significant differences in shapes, widths and amplitudes of the resonances at different positions within the beam. The Hanle EIT resonances from the wings of the beam show the two counter-sign peaks at certain values of the magnetic field. We suggest that the origin of such lineshape is in interaction of photons

in the wings of the laser beam with the coherently prepared atoms coming from the central part of the Gaussian beam.
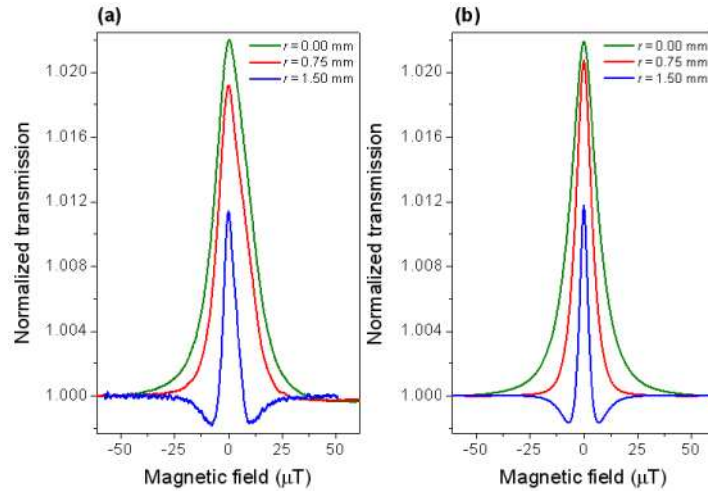

Fig. 2. Experimental (a) and theoretical (b) Hanle EIT resonances obtained from the small parts of the Gaussian beam. The green, the red and the blue curves are for $r = 0$ mm, 0.75 mm and 1.5 mm, respectively where r is the radial distance of the aperture from the beam center. The beam diameter is 3 mm and the total intensity is 0.5 mW/cm^2. Theoretical results were normalized to the experimental results such that peak values at $r = 0$ mm are equal.

During the interaction with the strong laser electric field near the center of the Gaussian beam an atom is coherently prepared into the dark state. The dark state is coherent superposition of Zeeman sublevels of $F_g=2$ ground level and is ideally non-coupled to the laser light only in the absence of external magnetic field. Zeeman sublevel populations and coherences are subjected to various relaxation processes. The transit time of the atoms through the laser beam is much shorter than the relaxation times of the ground state coherences. During the time that atom spends in the laser beam the coherences vary due to competitive effects of the laser excitation and the external magnetic field. The laser continuously forces the atomic coherence to be in-phase with the electric field. The external magnetic field causes oscillations of the coherence phase at Larmor frequency that is proportional to B. When atoms move away from the central to the outer parts of the beam (*outgoing* atoms), the oscillatory behavior prevails when the laser field is low enough. Thenceforth the phase of the atomic coherence oscillates and the atoms are cycling between dark and bright states. We name the outer section of the Gaussian beam, where this cycling occurs, *the interference region*. Aside from outgoing atoms there are also atoms coming into the interference region from the outside of the beam (*incoming* atoms). Note that the incoming atoms are not coherently prepared and do not contribute to the interference.

Consider an outgoing atom from the certain velocity class traversing the interference region along the certain trajectory. While passing through the laser beam the atom experiences nearly constant magnetic field due to its slow variation in the experiment. The phase shift of the atomic coherence at the point **r** along this trajectory depends on the value of the magnetic field B. If the coherence at **r** is in-phase with the laser electric field, the atom is in the dark state and the transparency at **r** is increased. It is clear that $B = 0$ fulfills this condition since the atom is continuously in the dark state regardless of the location in the interference region. If the magnetic field is such that the difference between the phases of the atomic coherence and the laser field equals to $\pi/2 + k\pi \ (k \in Z)$ the atom is in the bright state, and the minima of transparency at **r** occur. We denote these minima and maxima of the transparency as interference fringes. The atoms inside the cell move with different velocities and traverse different trajectories with respect to the laser beam. The averaging over the

velocity and trajectory distributions results in the lowering of the amplitude and in washing out the higher-than-first order interference fringes in the transmission signal. These considerations are supported by the results given in Fig. 3.

Figure 3 shows Hanle EIT resonances calculated by considering outgoing, incoming and both groups of atoms. The results are given for two distances from the laser beam center, $r = 1$ mm (Fig. 3(a)) and $r = 1.75$ mm (Fig. 3(b)). It is evident that only outgoing atoms are responsible for the appearance of the two sideband transmission minima. Effect of outgoing atoms on the resonance lineshape, at certain distance r, depends on the laser intensity. Results in Fig. 3 show that for 3 mW/cm^2, the contribution of outgoing atoms to Hanle EIT resonances is negligible at the distance $r = 1$ mm, while it is very strong at $r = 1.75$ mm.

The physical mechanism used in the above explanation of our results is the same as in Raman-Ramsey interference. The resulting Hanle lineshapes are similar to those obtained due to Ramsey interference in separated pump and probe laser fields in vacuum gas cells [20]. In our case, the extended low intensity wings of the Gaussian laser beam play the role of the probe beam.
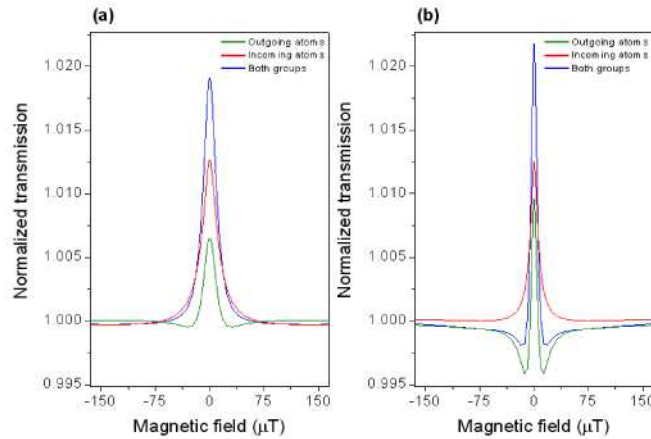

Fig. 3. Calculated contribution of outgoing (green), incoming (red) and both outgoing and incoming (blue) atoms to the Hanle EIT resonances for two distances from the laser beam center: $r = 1.00$ mm (a) and $r = 1.75$ mm (b). The total laser intensity is 3 mW/cm^2.

Figure 4 shows experimental (a) and theoretical (b) behavior of the Hanle EIT linewidths as a function of the aperture radial position. There are two reasons for narrowing of the Hanle EIT resonances in the wings of the Gaussian laser beam profile. The first is the lower power broadening in the outer parts of the laser beam. Another reason is the Ramsey-like narrowing caused by the aforementioned physical processes. The line narrowing at larger radial distances becomes more prominent as the total laser intensity increases. The dashed bars in (a) denote the linewidths of the Hanle EIT resonances for the three laser beam intensities when the whole laser beam is detected. At this point we find suitable to compare with results of Ref [13]. Lineshape Rabi power broadening corresponding to local intensities within the Gaussian beam, was also observed in [13] but without altering local resonance Lorentzian shape due to interference effects. We consider that one possible reason for the absence of the interference effects in such experiment is due to short mean free path of ^{4}He atoms. Namely, at the pressure of 1.5 Torr the mean free path of ^{4}He atoms is of the order 0.1 mm, so that ^{4}He atoms are effectively localized and do not freely traverse the 6 mm diameter laser beam. Therefore, the interference effects could not occur in the experiment performed in [13] due to frequent atom-atom collisions.

The outer, less intense, parts of the Gaussian beam, contribute with quite narrower lines to the overall Hanle EIT resonance. Thus, we studied Hanle EIT resonances after blocking the central part of the Gaussian beam in front of the detector. Figure 5(a) presents the Hanle EIT curves obtained when the mask of 2.2 mm in diameter blocks the central part of the Gaussian

beam (red curve). The resonance obtained without the mask is shown by the green curve. In Fig. 5(b) and (c) the dependence of linewidth and contrast of the EIT on the beam intensity is shown, with and without the mask. It is obvious that if one blocks the central part of the Gaussian laser beam, the Hanle EIT resonances will be significantly narrower for the range of the laser intensities used in the experiment. Apparently, this masking effect is more prominent at higher laser intensities. In cases of higher laser intensities masking provides also the resonances with higher contrast. Narrower and more pronounced resonances obtained in the proposed manner could be very useful for various applications of EIT.
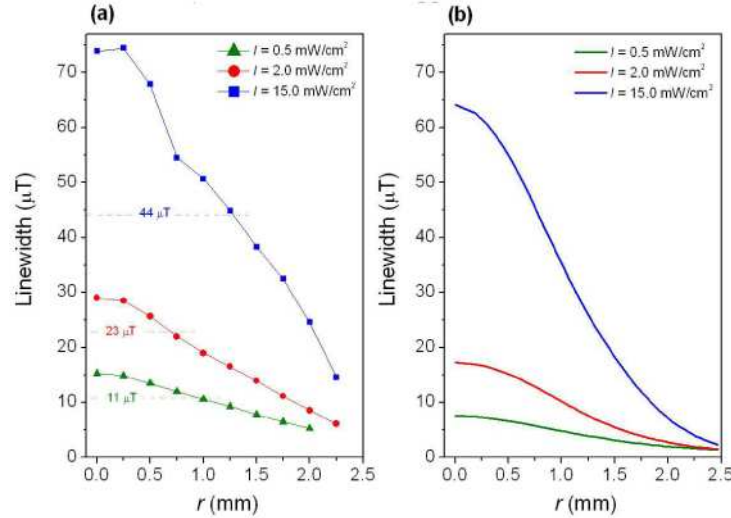

Fig. 4. Experimental (a) and theoretical (b) Hanle EIT linewidths for the different positions r of the aperture along the laser beam diameter. The blue, the red, and the green curves are for the intensities $I = 15$ mW/cm^2, 2 mW/cm^2, and 0.5 mW/cm^2, respectively. The dashed bars in (a) represent the Hanle EIT linewidths obtained by detecting the whole laser beam.
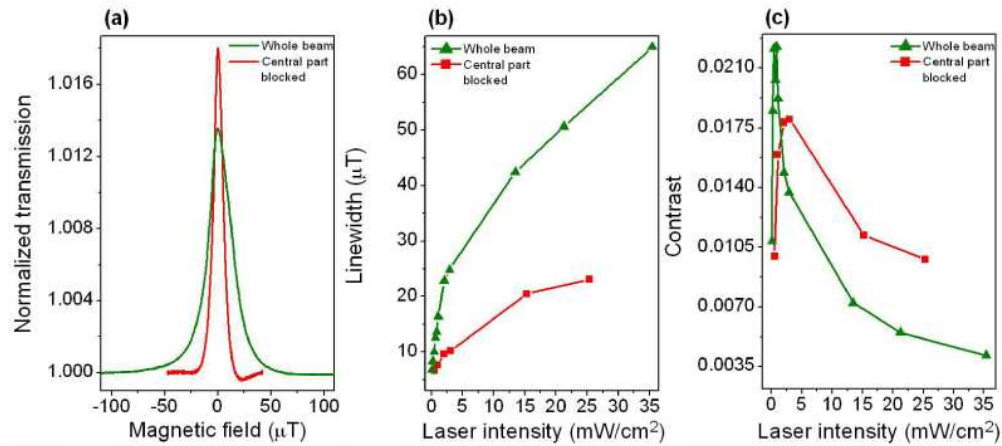
Fig. 5. (a) The experimental Hanle EIT resonances obtained when the whole beam is detected (green curve) and when the central part of the beam is blocked in front of the detector (red curve). In (b) and (c) linewidth and contrast of the EIT versus laser intensity are given for the whole beam (green) and for the beam with blocked central part (red). The central part was blocked by circular mask of diameter $d = 2.2$ mm. The laser intensity is 3 mW/cm^2.

5. Conclusion

In this work we have presented results of the Hanle EIT obtained from selected parts of the cross-section of the Gaussian laser beam, after the entire laser beam passes the Rb vacuum cell. The lineshapes, widths and contrasts of the EIT depend on the radial position of the sampled area of the laser beam. The resonances originating from the central part are different then those originated from the wings of the Gaussian. In the latter case the resonances are much narrower with two counter-sign sideband peaks. Our theoretical model reproduces the experimental EIT and explains the obtained EIT lineshapes by the interference between the atomic coherence carried by the coherently prepared atoms and the laser light in the wings of the Gaussian. The model shows that narrowing and interference features in the lineshapes are due to atoms coming from the central parts of the laser beam. These features are partially masked due to simultaneous contribution from atoms coming from the outside of the laser beam. Considerable improvement of the EIT linewidths and even contrasts is obtained by blocking the central part of the Gaussian beam in front of the photodiode and detecting only light from the wings of the laser beam. Narrowing of EIT in vacuum gas cells are of interests in EIT applications for atomic frequency standards and magnetometers.

Acknowledgements
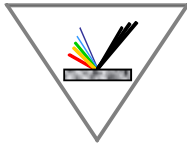
XXIII INTERNATIONAL CONFERENCE AND SCHOOL ON QUANTUM ELECTRONICS

"LASER PHYSICS AND APPLICATIONS"

23-27 September 2024, Ravda, Bulgaria

BOOK OF ABSTRACTS

[2] D. W. Coutts, D. J. W. Brown, "Production of High Average Power UV by Second-Harmonic and Sum-Frequency Generation from Copper-Vapor Lasers", IEEE Journal of Selected Topics in Quantum Electronics, 1, 3, 768-778, (1995)

[3] D. J. W. Brown, M. J. Withford, "High-average-power (15-W) 255-nm source based on second-harmonic generation of a copper laser master oscillator power amplifier system in cesium lithium borate", Optics Letters, 26, 23, 1885-1887, (2001)

P.E3

ROGUE WAVE CLUSTERS OF THE EXTENDED NONLINEAR SCHRÖDINGER EQUATIONS

Stanko N. Nikolić[1,2] and Milivoj R. Belić[2]

[1]*Institute of Physics Belgrade, University of Belgrade, Pregrevica 118,
11080 Belgrade, Serbia*
[2]*Division of Arts and Sciences, Texas A&M University at Qatar, P.O. Box 23874,
Doha, Qatar*

e-mail: stankon@ipb.ac.rs, milivoj.belic@qatar.tamu.edu

Keywords: Quintic nonlinear Schrödinger equation, Darboux transformation, Rogue wave clusters.

We analyze three types of rogue wave (RW) clusters for the quintic nonlinear Schrödinger equation (QNLSE) on a flat background. The exact QNLSE solutions are generated using the Darboux transformation (DT) scheme and they are composed of the higher-order Akhmediev breathers (ABs) and Kuznetsov-Ma solitons (KMSs) [1]. We analyze the dependence of their shapes and intensity profiles on the eigenvalues and evolution shifts in the DT scheme and on three real quintic parameters. The first type of RW clusters, characterized by the periodic array of peaks along the evolution or transverse axis, is obtained when the condition of commensurate frequencies of DT components is applied. The elliptical RW clusters are computed from the previous solution class when the first *m* evolution shifts in the DT scheme of order *n* are equal and nonzero. For both AB and KMS solutions, a periodic structure is obtained with the central RW and *m* ellipses, containing the first-order maxima that encircle the central peak. We show that RW clusters built on KMSs are significantly more vulnerable to the application of high values of QNLSE parameters, in contrast to the AB case. We next present non-periodic long-tail KMS clusters. They are characterized by the rogue wave at the origin and *n* tails above and below the central point containing the first-order KMSs. We also show that the breather-to-soliton conversion can transform the shape of RW clusters by careful adjustment of the real parts of DT eigenvalues, while remaining parameters are left unchanged.

References:
[1] S. N. Nikolić, N. B. Aleksić, M. R. Belić, "Akhmediev and Kuznetsov-Ma rogue wave clusters of the higher-order nonlinear Schrödinger equation", Opt. Quant. Electron., 56, 1182, (2024)

Rogue wave clusters of the higher-order nonlinear Schrödinger equation

Stanko N. Nikolić[1,2] and Milivoj R. Belić[2]

[1]*Institute of Physics Belgrade, University of Belgrade, Pregrevica 118, 11080 Belgrade, Serbia*

[2]*Division of Arts and Sciences, Texas A&M University at Qatar, P.O. Box 23874, Doha, Qatar*

[1]*stankon@ipb.ac.rs;* [2]*milivoj.belic@qatar.tamu.edu*

[1]ORCID ID: 0000-0002-2082-9954

ABSTRACT

We analyze three types of rogue wave (RW) clusters for the quintic nonlinear Schrödinger equation (QNLSE) on a flat background. The exact QNLSE solutions are generated using the Darboux transformation (DT) scheme and they are composed of the higher-order Akhmediev breathers (ABs) and Kuznetsov-Ma solitons (KMSs) [1]. We analyze the dependence of their shapes and intensity profiles on the eigenvalues and evolution shifts in the DT scheme and on three real quintic parameters. The first type of RW clusters, characterized by the periodic array of peaks along the evolution or transverse axis, is obtained when the condition of commensurate frequencies of DT components is applied. The elliptical RW clusters are computed from the previous solution class when the first m evolution shifts in the DT scheme of order n are equal and nonzero. For both AB and KMS solutions a periodic structure is obtained with the central RW and m ellipses, containing the first-order maxima that encircle the central peak. We show that RW clusters built on KMSs are significantly more vulnerable to the application of high values of QNLSE parameters, in contrast to the AB case. We next present non-periodic long-tail KMS clusters. They are characterized by the rogue wave at the origin and n tails above and below the central point containing the first-order KMSs. We also show that the breather-to-soliton conversion can transform the shape of RW clusters by careful adjustment of the real parts of DT eigenvalues, while remaining parameters are left unchanged.

REFERENCES

[1] Stanko N. Nikolić, Najdan B. Aleksić, Milivoj R. Belić. (2024), "Akhmediev and Kuznetsov-Ma rogue wave clusters of the higher-order nonlinear Schrödinger equation". Accepted for publication in the *Optical and Quantum Electronics*.

XI-th International Conference
"SOLITONS, COLLAPSES AND TURBULENCE:
Achievements, Developments and Perspectives"

1-5 July, 2024, Belgrade
The programme is written in Belgrade time (GMT+2)

1 Monday, 1.7.2024

	Plenary talks
09:00–09:50	**Registration**
09:50–10:00	Conference opening: Greetings
10:00–10:45	E. Kuznetsov, "Formation of magnetic filaments in convective zone of the Sun"
10:45–11:15	**Coffee break**
11:15–12:00	F. Calogero, "TBA" **(online)**
12:00–12:45	A. Mikhailov, "TBA"
12:45–14:00	**Lunch break**

	Section: Nonlinear Phenomena
14:00–14:30	L. Piterbarg, "Caustic frequency in 2D stochastic flows modeling turbulence"
14:30–15:00	N.M. Zubarev "Effect of viscosity on the self-similar growth of conic cusps on the surface of a conducting liquid in an electric field" **(online)**
15:00–15:30	V. Geogjaev, "Coupling Coefficient for 4-wave interactions: properties and asymptotics"
15:30–16:00	S. Badulin, "Self-similarity of wind-driven seas in action"
16:00–16:30	**Coffee break**
16:30–17:00	P. Pezzutto, "Reduced Hamiltonian equations for gravity waves in a big box"
17:00–17:30	V.V. Yankov, "Arnold's hierarchy of attractors and the centuries-old dispute between geometers and algebraists" **(online)**

	Section: Solitons
14:00–14:30	P. Grinevich, "Almost degenerate Riemann surfaces in the theory of rogue waves"
14:30–15:00	V. Pukhnachev, "Generelized helical flows" online
15:00–15:30	G. Grahovski, "On the N-wave hierarchy with constant boundary conditions"
15:30–16:00	A. Kamchatnov, "TBA" **(online)**
16:00–16:30	**Coffee break**
16:30–17:00	S. Dremov, "Bi-solitons on the surface of a deep fluid: an inverse scattering transform perspective based on perturbation theory"
17:00–17:30	I. Chekhovskoy, "Numerical methods for the direct and inverse Zakharov-Shabat problem"
17:30–18:00	O. Alekseev, "Universality of stochastic Laplacian growth"

2 Tuesday, 2.7.2024

	Plenary talks
09:00–09:45	S. Turitsyn, "Nonlinear photonics meets machine learning"
09:45–10:30	S. Nazarenko, "Universal scalings in stationary and evolving wave turbulence"
10:30–11:15	A. Newell, "Order parameter equations for patterns" **(online)**
11:15–11:45	**Coffee break**

	Section: Nonlinear Phenomena
11:45–12:15	P. Santini, "Periodic anomalous (rogue) waves in the $2 + 1$ dimensional Davey-Stewartson 2 equation"
12:15–12:45	A. Maluckov, "Nonlinear signatures of band topology: the role of modulation instability"

	Section: Solitons
11:45–12:15	A. Gelash, "Stochastization of condensate solitons"
12:15–12:45	D. Cevizovic, "Solitons in Flux-qubit based superconducting quantum metamaterial"

12:45–14:00	**Lunch break**

	Section: Nonlinear Phenomena
14:00–14:30	S. Vergeles, "Absorption of inertial waves by shear flow
14:30–15:00	A. Pushkarev, "Self-similarity and nonlinear resilience of wind-driven seas"
15:00–15:30	A. Kochetov, "The numerical simulations of reflection index dynamics of incident radio wave coursed by an electromagnetically driven Langmuir turbulence in a smoothly inhomogeneous plasma layer"
15:30–16:00	G. Gligorić, "Topologically protected modes in nonlinear distorted bipartite hexagonal photonic lattice"
16:00–16:30	**Coffee break**
16:30–17:00	L. Zhang, "TBA"
17:00–17:30	NM. Vucelja, "The growth rate of density inhomogeneities in weak turbulence from information theory perspective"

	Section: Solitons
14:00–14:30	V. Gerdjikov, "Riemann–Hilbert Problems, Lax Pairs and Integrable Equations"
14:30–15:00	S. Roudenko, "Soliton Stability and Stable Collapse in the NLS and KdV-type equations"
15:00–15:30	S. Nikolic, "Rogue wave clusters of the quintic nonlinear Schrodinger equation composed of Akhmediev breathers and Kuznetsov-Ma solitons"
15:30–16:00	A. Chernyavsky, "Dark-bright soliton perturbation theory for the Manakov system"
16:00–16:30	**Coffee break**
16:30–17:00	M. Lazarova, "TBA"
17:00–17:30	A. Pogrebkov, "Integrable hierarchies with negative times" **(online)**

Rogue wave clusters of the quintic nonlinear Schrödinger equation composed of Akhmediev breathers and Kuznetsov-Ma solitons

Stanko N. Nikolić[1,2], Najdan B. Aleksić[2,3], Milivoj R. Belić[2,3]

[1]*Institute of Physics Belgrade, University of Belgrade, Pregrevica 118, 11080 Belgrade, Serbia*
[2]*Division of Arts and Sciences, Texas A&M University at Qatar, P.O. Box 23874, Doha, Qatar*
[3]*Serbian Academy of Nonlinear Sciences, Kneza Mihaila 36, Belgrade, Serbia*

e-mail: stankon@ipb.ac.rs

We analyze the spatiotemporal patterns of rogue waves (RW) of the quintic nonlinear Schrödinger equation (QNLSE) in the form of multi-elliptic clusters composed of Akhmediev breathers (AB). These solutions are obtained on uniform background using the Darboux transformation (DT) scheme. We solve the eigenvalue problem of the Lax pair of order n in which the first m evolution shifts are equal, nonzero, and eigenvalue dependent, while all eigenvalues' imaginary parts are close to one. We show that AB of order $n - 2m$ appears at the origin and can be considered as central rogue wave. We show that the high-intensity narrow peak, with the complex intensity distribution in its vicinity, is enclosed by m ellipses consisting of the first-order ABs. The number of maxima on each ellipse is determined by its index and solution order.

We next present RW clusters of QNLSE composed of the Kuznetsov-Ma solitons (KMS), characterized by strong intensity narrow peaks, which are periodic along the evolution axis. These structures are calculated in DT scheme with commensurate frequencies when eigenvalues are greater than one. The second solution class exhibits a form of elliptical rogue wave clusters. Similarly to AB case, the first solution class is obtained when the first m evolution shifts in the nth order DT scheme are nonzero and equal. Here the high intensity peaks built on KMS of order n-$2m$ periodically appear along the evolution axis. The central rogue waves are enclosed by m ellipses consisting of a certain number of the first-order KMS.

Finally, we analyze the effect of three real quintic parameters (α, γ, δ), multiplying the higher-order Hirota, LPD, and quintic operators in QNLSE, on pattern and stability of AB and KMS RW clusters [1]. We show the RW clusters composed of AB/KMS in figures 1a-c and 1d-f, respectively.
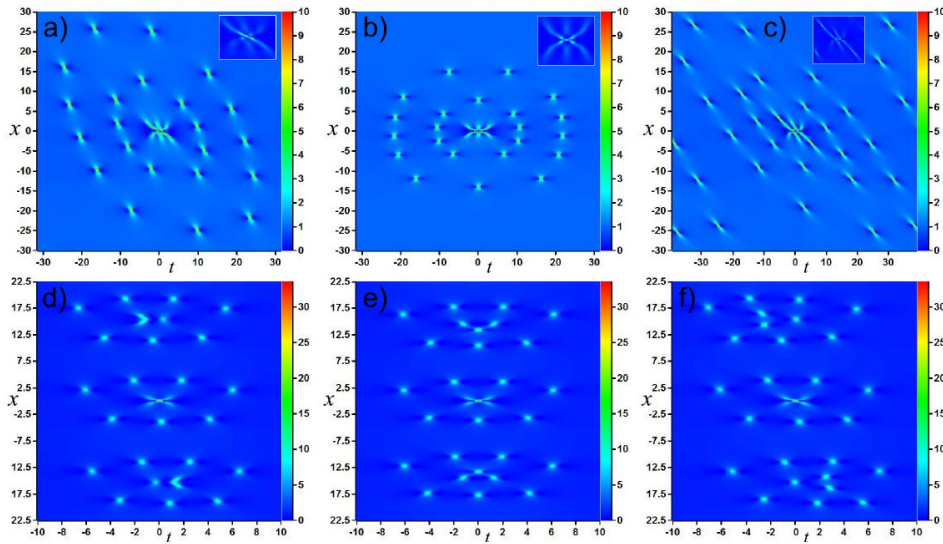

Figure 1. Intensity distributions of the multi-elliptic rogue wave clusters
built on the higher-order AB and KMS. AB clusters are calculated for quintic parameters:
(a) $\alpha = 0.07$, $\gamma = 0$, $\delta = 0$, (b) $\alpha = 0$, $\gamma = 0.07$, $\delta = 0$, and (c) $\alpha = 0$, $\gamma = 0$, $\delta = 0.035$.
KM clusters are computed when: (d) $\alpha = 0.006$, $\gamma = 0$, $\delta = 0$,
(e) $\alpha = 0$, $\gamma = 0.006$, $\delta = 0$, and (f) $\alpha = 0$, $\gamma = 0$, $\delta = 0.002$.

REFERENCES

[1] S. N. Nikolić *et al.*: *"Akhmediev and Kuznetsov-Ma rogue wave clusters of the higher-order nonlinear Schrödinger equation"*. Accepted for publication in Optical and Quantum Electronics.

Book of abstracts

IX International School and Conference on Photonics

PHOTONICA2023

with joint events:

Understanding interaction light - biological surfaces: possibility for new electronic materials and devices

&

Biological and bioinspired structures for multispectral surveillance

&

Quantum sensing integration within microfluidic Lab-on-a Chips for biomedical applications

&

Advanced Biophysical Methods for Soil Targeted Fungi-Based Biocontrol Agents

August 28 - September 01, 2023, Belgrade, Serbia

Editors

Jelena Potočnik, Maja Popović, Dušan Božanić

Vinča Institute of Nuclear Sciences – National Institute of the Republic of Serbia, University of Belgrade

Belgrade, 2023

Rogue wave clusters of the nonlinear Schrödinger equation composed of Akhmediev breathers and Kuznetsov-Ma solitons

S.N. Nikolić[1,2], S. Alwashahi[3], N.B. Aleksić[2] and M.R. Belić[2]
[1]Institute of Physics Belgrade, University of Belgrade, Pregrevica 118, 11080 Belgrade, Serbia
[2]Division of Arts and Sciences, Texas A&M University at Qatar, P.O. Box 23874, Doha, Qatar
[3]Faculty of Physics, University of Belgrade, Studentski trg 12, 11001 Belgrade, Serbia
e-mail: stankon@ipb.ac.rs

We analyze the various spatiotemporal patterns of rogue waves (RW) which may have the form of multi-elliptic clusters composed of Akhmediev breathers (AB) obtained on uniform background using the Darboux transformation (DT) scheme (Fig. 1). We solve the eigenvalue problem of the Lax pair of order n in which the first m evolution shifts are equal, nonzero, and eigenvalue dependent, while all eigenvalues' imaginary parts are close to one. We show that AB of order $n - 2m$ appears at the origin and can be considered as central rogue wave. We show that the high-intensity narrow peak, with the complex intensity distribution in its vicinity, is enclosed by m ellipses consisting of the first-order ABs. The number of maxima on each ellipse is determined by its index and solution order [1].
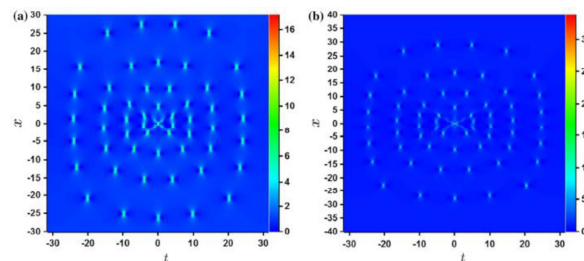

Figure 1. 2D color plots of rogue wave clusters on the uniform background having four ellipses ($m = 4$) around $n - 2m$ order rogue wave, formed at the origin of the *(x,t)* plane. The orders of DT and the Akhmediev breather representing the central peak are: (a) $n = 10$ with the second-order RW, and (b) $n = 11$ with the third-order RW.

We next show RW clusters composed of Kuznetsov-Ma solitons (KMS), characterized by strong intensity narrow peaks, which are periodic along the evolution axis [2]. These structures are calculated in DT scheme with commensurate frequencies when eigenvalues are greater than one (Fig. 2a). The second solution class exhibits a form of elliptical rogue wave clusters (MERWC). Similarly to AB case, the first solution class is obtained when the first m evolution shifts in the nth order DT scheme are nonzero and equal. Here the high intensity peaks built on KMS of order $n - 2m$ periodically appear along the evolution axis. The central rogue waves are enclosed by m ellipses consisting of a certain number of the first-order KMS (Fig. 2b).
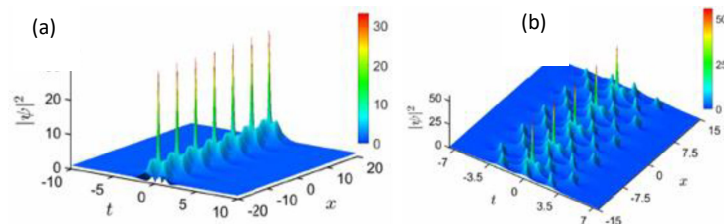

Figure 2. (a) The second-order KMS on a uniform background built from DT components with commensurate frequencies. (b) 3D intensity color plots of MERWC on the uniform background, having two ellipses (m=2) around the second-order central rogue waves (n=6).

REFERENCES
[1] S.N. Nikolić *et al.*, Nonlinear Dyn. 108, 479 (2022).
[2] S. Alwashahi *et al.*, Nonlinear Dyn. (2023), https://doi.org/10.1007/s11071-023-08480-0.

Exploring the nano-scale world using a custom-made Fluorescence Correlation Spectroscopy (FCS) instrument

J.Z. Jelić[1], M.D. Rabasović[1], S. Nikolić[1], V. Vukojević[2] and A.J. Krmpot[1]

[1]*Institute of Physics Belgrade, University of Belgrade, Belgrade, Serbia*
[2]*Department of Clinical Neuroscience, Karolinska Institutet, Nobels väg 6, 171 77 Stockholm, Sweden*
e-mail: jovana.jelic@ipb.ac.rs

Fluorescence **C**orrelation **S**pectroscopy (**FCS**) is a powerful and non-invasive technique for quantitative characterization of the concentration, mobility, and interactions of fluorescent/fluorescently labeled molecules *in vitro* and *in vivo* [1]. By exploiting the capabilities of a confocal microscope and time-correlated single photon counting (TCSPC), FCS offers high temporal resolution (sub-microsecond in commercially available systems, and down to picosecond time scale in custom-made instruments dedicated to the study of fast processes such as rotational diffusion of molecules and photon antibunching), diffraction-limited spatial resolution (≈ 200 nm) [2], as well as single-molecule sensitivity. Conventional FCS utilizes temporal autocorrelation analysis of fluctuations in recorded fluorescence signal caused by molecular motion through the small sample volume, often referred to as the focal volume (typically $0.2 - 1$ fL) [3]. FCS enables the quantitative measurement of the concentration, translational diffusion coefficient, and interactions. Furthermore, FCS can provide insights into local microenvironments, such as viscosity or pH, or about any other molecular process related to alterations in the fluorescence signal [4]. By implementing two detection channels, conventional FCS is extended to Fluorescence Cross-Correlation Spectroscopy (FCCS) [5]. In FCCS, dual-color excitation and detection enable the monitoring of interactions and dynamics of molecules that are labeled with spectrally distinct fluorophores [5].

Here, we present our custom-made FCS system and characterize its performance using Rhodamine 110 in aqueous solutions. We show that the sensitivity and effective volume size in our home-built FCS instrument are comparable to those in commercial instruments.

REFERENCES
[1] E. Haustein, P. Schwille, Annu. Rev. Biophys. Biomol. Struct. 36, 151 (2007).
[2] The bh TCSPC Handbook 9th edition, 2021 - Becker & Hickl GmbH (becker-hickl.com).
[3] V. Vukojević *et al.*, Cell. Mol. Life Sci. 62, 535 (2005).
[4] https://www.biophysics.org/Portals/0/BPSAssets/Articles/schwille.pdf.
[5] K. Bacia *et al.*, Nat. Methods 3, 83 (2006).

The rogue wave clusters of the nonlinear Schrödinger equation composed of the Kuznetsov-Ma solitons

Sarah Alwashahi[1], Najdan B. Aleksić[2], Milivoj R. Belić[2], Stanko N. Nikolić[2,3]

[1]Faculty of Physics, University of Belgrade, Studentski trg 12, 11001 Belgrade, Serbia
[2]Division of Arts and Sciences, Texas A&M University at Qatar, P.O. Box 23874 Doha, Qatar
[3]Institute of Physics Belgrade, University of Belgrade, Pregrevica 118, 11080 Belgrade, Serbia

Abstract - In this work, we investigate rogue wave (RW) clusters of different shapes, composed of the Kuznetsov-Ma solitons (KMS) from the nonlinear Schrödinger equation (NLSE) with Kerr nonlinearity [1]. We present three classes of exact higher-order solutions that are calculated on uniform background using the Darboux transformation (DT) scheme with precisely chosen parameters.

The first solution class is characterized by strong intensity narrow peaks which are periodic along the evolution when the eigenvalues in DT scheme generate KMS with commensurate frequencies (Fig. 1a). The second solution class exhibits a form of elliptical rogue wave clusters (MERWC). It is derived from the first solution class when the first m evolution shifts in the nth order DT scheme are nonzero and equal. Here the high intensity peaks built on KMS of order n-$2m$ periodically appear along the evolution axis. The central rogue waves are enclosed by m ellipses consisting of a certain number of the first-order KMS, determined by the ellipse index and the solution order (Fig. 1b). The third class of KMS clusters is obtained when purely imaginary DT eigenvalues tend to some preset offset value higher than one, while keeping the evolution shifts unchanged. The central rogue wave retains its n-$2m$ order. The n tails composed of the first-order KMS are formed above and below the central maximum (Fig. 2a). When n is even, more complicated patterns are generated, with m and m-1 loops above and below the central RW, respectively (Fig. 2b). We also compute an additional solution class on a wavy background, defined by the Jacobi elliptic dnoidal function, which display specific intensity patterns that are consistent with the background wavy perturbation.
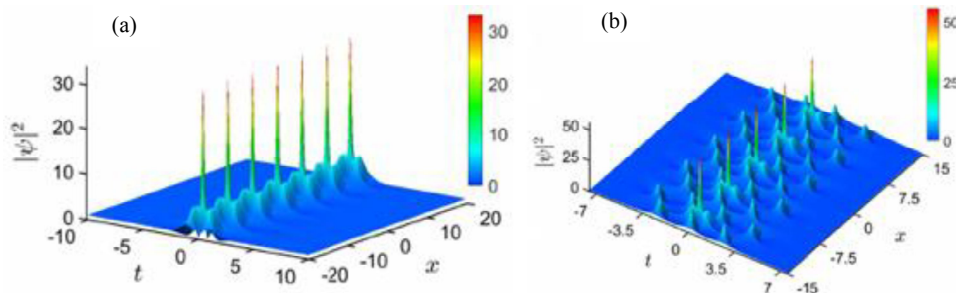
Figure 1. (a) The second-order KMS on a uniform background built from DT components with commensurate frequencies. (b) 3D intensity color plots of MERWC on the uniform background, having two ellipses (m=2) around the second-order central rogue waves (n=6).
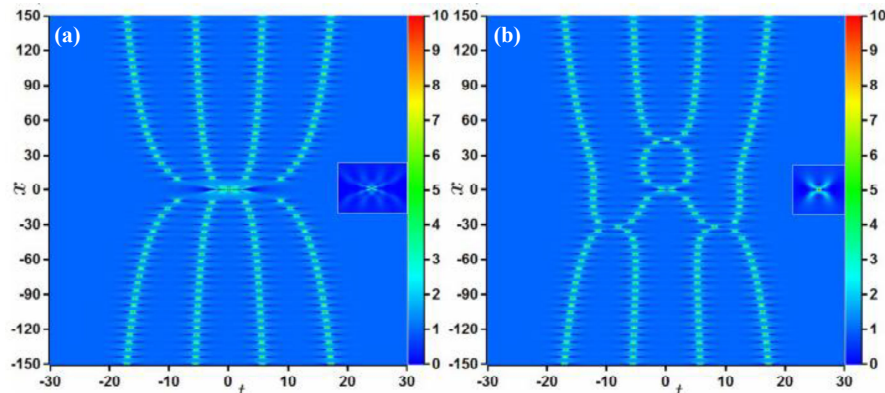

Figure 2. 2D intensity color plots of the long-tail KMS clusters on the uniform background, having one central rogue wave of the n-$2m$ order. The DT order is n=4. (a) m=0, n-$2m$=4, (b) m=1, n-$2m$=2.

References:

[1] Alwashahi S., Aleksić N.B., Belić M.R., Nikolić S.N.: *Kuznetsov-Ma rogue wave clusters of the nonlinear Schrödinger equation*. Submitted to *Nonlinear Dynamics*.
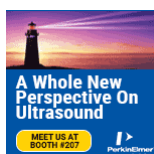
EUROPEAN MOLECULAR IMAGING MEETING
18th Annual Meeting of the European Society for Molecular Imaging

EMIM 2023 | 14th-17th March
Salzburg Congress, Austria

supported by:

(https://www.perkinelmer.com/de/)(https://www.sedecat.com/en/)(https://www.visualsonics.com/)(https://www.molecubes.com/)(https://www.trifoilimaging.com/)

≗⍟ Author Index
(/contxt_emim2023/online-program/author-index)

🏷 Keyword Index
(/contxt_emim2023/online-program/keyword-index)

☂ Chair Index
(/contxt_emim2023/online-program/chair-index)

Full text search:

| author:"Tanja" "Pajić" | ✕ (/contxt_emim2023/online-program/set-search-session) | 🔍 |

To search for a specific ID please enter the hash sign followed by the ID number (e.g. #123).

🗓 Day overview (/contxt_emim2023/online-program/day?dt=2023-03-17)

Tissue Omics & Optical Technologies

🗓
*.ics (/contxt_emim2023/online-program/session-ics?s=PW36)

Session chair: **Dale Waterhouse** (London, UK)**; Alan Race** (Unterschleißheim, Germany)

1093

Third harmonic generation imaging of live fungal cells – quantifying lipid droplets dynamics during nitrogen starvation

Tanja Pajić[1], Nataša V. Todorović[2], Miroslav Živić[1], Stanko N. Nikolić[3], Mihailo D. Rabasović[3], Andrew H. A. Clayton[4], Aleksandar J. Krmpot[3]

[1] University of Belgrade, Faculty of Biology, Institute of Physiology and Biochemistry, Belgrade, Serbia
[2] University of Belgrade, Institute for Biological Research "Siniša Stanković", National Institute of the Republic of Serbia, Belgrade, Serbia
[3] University of Belgrade, Institute of Physics Belgrade, National Institute of the Republic of Serbia, Belgrade, Serbia
[4] Swinburne University of Technology, Department of Physics and Astronomy, Optical Sciences Centre, School of Science, Computing and Engineering Technologies, Melbourne, Australia

Introduction

Studies of lipid droplet (LD) physiology in fungi are still in their infancy but their quantitation has relevance to issues in biomedicine, agriculture and industrial waste. Third Harmonic Generation (THG) microscopy is non-invasive, produces inherently confocal images and doesn't require fixation or external labeling, which make it suitable for *in vivo* LD imaging [1, 2]. We present *in vivo* and label-free imaging of LD in individual fungal cells by THG microscopy to assess the effects of nitrogen starvation. The LD quantification was performed by two image analysis techniques.

Methods

THG microscopy was applied for the first time to a filamentous fungus and our choice was the oleaginous fungus *Phycomyces blakesleeanus.* To observe the changes in LD number, the 22h old hyphae culture was divided into control and nitrogen starved groups (N-starved). A home built nonlienar microscope with Yb:KGW laser at 1040 nm (200 fs pulses, 83 MHz repetition rate) was used for THG imaging of live unstained hyphae [3]. THG signal was detected by PMT in the transmission arm after passing through a Hoya glass UV filter with the peak at 340 nm. 2D THG images of LDs (Fig. 1a) were analyzed by Image Correlation Spectroscopy (ICS) measuring spatially-correlated fluctuations [4] and software particle counting – Particle Size Analysis (PSA).

Results/Discussion

The small volume of hyphae suspension was placed between two coverslips of 170 μm thickness in order to meet the criteria for the best numerical aperture of the objective lens and for better transmission of THG signal. The high resolution of the microscopic system, the hyphae thickness (ca 10 μm) and medium transparency made it possible for the whole hyphae to be optically sectioned and a 3D model to be reconstructed (Fig. 1b and video). Since ICS was primarily developed for fluorescent images and was not used to analyze THG images, we have tested it by comparing the results to the PSA. Nitrogen starvation as expected [5] increased LD number compared to control which was confirmed by both methods and obtained results are in good agreement. The overall increase of LDs during growth without available nitrogen is found to be between 3 and 4.5 h time point, followed with the loss of population of larger-than-average LDs during prolonged starvation.

Conclusions

THG microscopy is suitable for imaging and quantification of changes in lipid droplet number, brought upon by complete removal of nitrogen, from such low density/diameter baseline. In addition, we demonstrate that the ICA is suitable for THG images, although it is primarily developed and have been mostly used for fluorescence signals so far.

Acknowledgement

Disclosure

I or one of my co-authors have **no financial interest** or **relationship** to disclose regarding the subject matter of this presentation.

References

[1]   Boyd, Robert W., 'Nonlinear Optics', Academic Press/third edition (2008)

[2]   Weigelin Bettina, Bakker Gert-Jan, Friedl Peter, 'Third harmonic generation microscopy of cells and tissue organization', Journal of Cell Science. 129, 245–255 (2016)

[3]   Pajić Tanja, Todorović Nataša V, Živić Miroslav, Nikolić Stanko N, Rabasović Mihailo D, Clayton Andrew HA, Krmpot Aleksandar J, 'Label-free third harmonic generation imaging and quantification of lipid droplets in live filamentous fungi', Scientific Reports 12, 18760 (2022)

[4]   Nohe Anja, Petersen Nils O., 'Image correlation spectroscopy', Science's STKE 2007, (417):pl7 (2007)

[5]   Li-Chi Weng, Buntora Pasaribu, I. -Ping Lin, Ching-Hsiu Tsai, Chii-Shiarng Chen, Pei-Luen Jiang, 'Nitrogen deprivation induces lipid droplet accumulation and alters fatty acid metabolism in symbiotic dinoflagellates isolated from *Aiptasia pulchella*', Scientific Reports 4, 1–8 (2014)
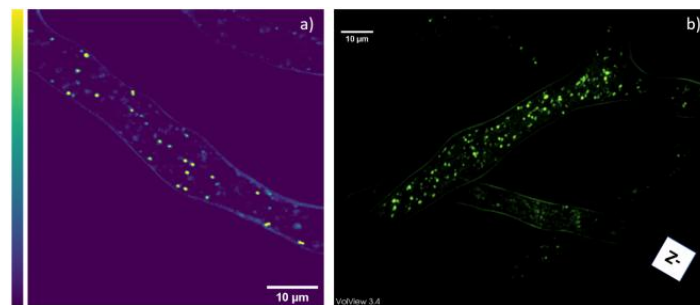
(https://www.eventclass.org/contxt_emim2023/download/media?hash=%242y%2413%24eHvP3T8Yv.2kt2MO8kldTul7f1inQRJi9h9IKlLlSfeBf%2FCpLTej6) **Figure 1. Label-free imaging of Phycomyces blakesleeanus hyphae.**

(a) one THG slice and **(b)** 3D model of 23 THG slices 0.9 µm apart. The average laser power at sample plane was 23–26 mW.

Keywords: label-free, third harmonic generation microscopy, lipid droplets, image correlation spectroscopy, filamentous fungi
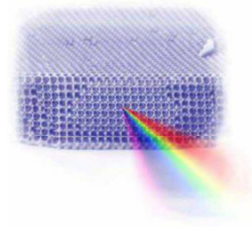
Book of Abstracts

16th Photonics Workshop

(Conference)

Fluorescence Correlation and Cross-Correlation Spectroscopy (FCS/FCCS) - versatile tool for quantitative characterization of molecular interactions *in vitro* and *in vivo*

Mihajlo D. Radmilović[1], Sho Oasa[2], Aleksandar J. Krmpot[1], Mihailo D. Rabasović[1], Jovana Jelić[1], Stanko Nikolić[1], Vladana Vukojević(1) *Institute of Physics Belgrade, University of Belgrade, Pregrevica 118, 11080 Belgrade, Serbia*

(2) *Department of Clinical Neuroscience, Karolinska Institutet, Nobels väg 6, 171 77 Stockholm, Sweden*

Contact: M.Radmilović (mihajlor@ipb.ac.rs)

Abstract. Fluorescence Correlation Spectroscopy (FCS) and Fluorescence Cross-Correlation Spectroscopy (FCCS) are quantitative, confocal laser scanning microscopy-based techniques with single-molecule sensitivity and high spatiotemporal resolution ($\approx$ 250 nm, $\approx$ 200 ns) that are widely used in molecular biophysics to quantitatively characterize molecular interactions without having to separate the free and bound fraction of molecules [1, 2]. Both techniques record fluorescence intensity fluctuations in a small volume (typically $(0.2 - 1.0) \times 10^{-15}$ l) that arise as fluorescent/fluorescently labeled molecules pass through it by free diffusion [3]. As the molecules diffuse through this volume (referred as effective volume), all additional processes that give rise to fluorescence intensity fluctuations at a shorter time scale than diffusion, such as fluorophore blinking due to single/triplet state transition, or alter the time course of fluorescence intensity fluctuations, such as binding to other molecules that slows down diffusion, can also be characterized. Quantitative information about these processes can be extracted from fluorescence intensity fluctuation time series by temporal autocorrelation analysis, and in FCCS also by temporal cross-correlation analysis, to yield information about the: concentration, diffusion (size), fraction and diffusion (size) of free/bound molecules, fraction of molecules in the triplet state and triplet-state depopulation rates [4]. Both techniques are applicable for measurements in solution and in live cells, tissue *ex vivo*, and whole organisms (*e.g.* zebrafish embryo) [5, 6].

I will introduce conventional, single-point FCS and FCCS, give examples of their applications, and discuss about their limitations. In particular, I will present recent development of our home-built FCS instrument and show using ATTO488 in solution how the sensitivity and effective volume size in our home-built FCS instrument are comparable to those in a commercial instrument. I will also discuss about future perspectives of home-built FCS instrument, giving examples of eGFP (enhanced Green Fluorescent Protein) diffusion measurements in live cells.

REFERENCES

[1] P.Schwille, *A tutorial for the Biophysics Textbook Online (BTOL).* Biophysical Society, Rockville, MD. (2002).
[2] K. Bacia, S.A. Kim, et al., (2006). *Nat. methods* **3** (2006), 83-89.
[3] R. Rigler, *Fluorescence correlation spectroscopy: theory and applications* (Vol. 65), Springer Science & Business Media, Berlin (2012).
[4] L. Yu, Y. Lei, et al., *Front. Phys.* **9** (2021) 644450.
[5]S. Oasa, S. Mikuni, et al., *Sci Rep*. **8** (2018), 7488.
[6] X.W. Ng, K. Sampath, T. Wohland *Morphogen Gradients: Methods and Protocols* (2018) 67-105.

BPU11 CONGRESS

28 August 2022 - 1 September 2022

Book of Abstracts

Editors: Antun Balaž, Goran Djordjević,
Jugoslav Karamarković, Nenad Lazarević

PT-11 / Plenary talk (virtual)

Quantitative Scanning-Free Confocal Microscopy with Single-Molecule Sensitivity and Fluorescence Lifetime Imaging for the Study of Fast Dynamic Processes in Live Cells

Authors: Stanko N. Nikolic[1]; Aleksandar J. Krmpot[1]; Sho Oasa[2]; Andrew H. A. Clayton[3]; Lars Terenius[2]; Milivoj R. Belić[4]; Rudolf Rigler[5]; Vladana Vukojevic[2]

[1] *Institute of Physics Belgrade, University of Belgrade, 11080 Belgrade, Serbia*

[2] *Karolinska Institute, Department of Clinical Neuroscience (CNS), Center for Molecular Medicine (CMM)*

[3] *Swinburne University of Technology, School of Science, Department of Physics and Astronomy*

[4] *Texas A&M University at Qatar*

[5] *Karolinska Institute, Department of Medical Biochemistry and Biophysics (MBB)*

Presenter: V. Vukojevic (`vladana.vukojevic@ki.se`)

Timing is everything in biology – biological systems exchange information by controlling the spatio-temporal behavior of biological molecules, using dynamics to encode and decode information. Dynamic changes in the concentration of biological molecules are therefore an integral part of biological networks' function and inadequate spatial distribution and temporal dynamics are characteristic of disease states.

Living cells control the concentration, spatial distribution, and temporal dynamics of biological molecules through molecular interactions and transporting processes, most notably diffusion. Through reaction-diffusion processes biomolecules are integrated in specific dynamical networks and perform specialized biological functions in the cell, such as gene expression. These networks are complex – they are made up of many constituents (different interacting molecules); they are tightly intertwined – products of one reaction are reactants in another one; and they are dynamically controlled – the rates at which biochemical transformations occur are autocatalytically regulated by molecules produced in the same biological network. Consequently, these complex networks may acquire a new quality – the capacity to self-adjust their essential variables to control their biological functions.

To understand how these dynamical networks are controlled and self-regulated, the concentration and mobility of interacting molecules – which are in addition to chemical reactivity the determinants of chemical kinetics, need to be quantitatively characterized in live cells.

To this aim, we have developed quantitative scanning-free confocal microscopy with single-molecule sensitivity, high temporal resolution (~10 μs/frame), and fluorescence lifetime imaging by integrating massively parallel fluorescence correlation spectroscopy [1] with fluorescence lifetime imaging microscopy (mpFCS/FLIM)[2].

The capacity of this method to characterize in live cells compartmentalization of molecular processes by measuring local excited-state decay *via* FLIM, and their dynamic integration by measuring diffusion/active transport using mpFCS will be discussed.

References
1. A.J. Krmpot *et al.*, Anal. Chem. **91(17)**, 11129 (2019).
2. S. Oasa, A.J. Krmpot, S.N. Nikolić *et al.* Anal. Chem. **93(35)**, 12011 (2021).

retains its degree of dispersion for one week. Therefore, this model is a suitable candidate for further research and development of a lipid-based dosage form for Alendronate sodium.

S13-BMP-200 / **Poster presentation**

Determination of spatial resolution of nonlinear laser scanning microscopy

Authors: Aleksa Dencevski[1]; Jovana Jelic[1]; Marta Bukumira[1]; Aleksandar Krmpot[1]; Ana Senkic[2]; Antonio Supina[2]; Mihailo Rabasovic[1]; Natasa Vujicic[2]; Stanko Nikolic[1]

[1] *Institute of Physics Belgrade*

[2] *Institute of Physics Zagreb*

Presenter: M. Bukumira (marta@ipb.ac.rs)

Microscope resolution is the shortest distance between two points on a sample that can be distinguished as separate entities. Due to the wave nature of light and the phenomenon of diffraction, it is fundamentally limited: even under theoretically ideal conditions and optical components, the microscope has a finite resolution.

In this paper, we determined lateral and axial resolution of a nonlinear laser scanning microscope by measuring its point spread function (PSF) in two ways: by imaging fluorescent beads using two-photon excited fluorescence (standard method), and by using monolayers of molybdenum disulfide – MoS_2 (non-standard method), obtained by chemical vapor deposition [1], which, due to the lack of central symmetry, efficiently generate second harmonic signal.

Parameters such as the numerical aperture of the objective and the excitation wavelength contribute to the resolution, so it changes depending on the current setting of the microscopic system. Measurements were performed for two different objectives and several standard excitation wavelengths, depending on the type of sample. As expected, the best resolution was obtained for the objective with the largest numerical aperture (40x 1.3) and the shortest excitation wavelength (730nm): $R_{lat} = 260nm$, $R_{ax} = 1648nm$. In addition, the values obtained by the non-standard method are closer to the theoretical values of the resolution, because the contributions of the out-of-focus signal are significantly smaller due to the two-dimensional nature of the layers. This implies that it is better to use this type of sample to determine the resolution of the microscope. The measured PSF can be further used to deconvolve the images obtained on this microscope.

Due to its properties such as large penetration depth of incident radiation and label-free imaging, as well as the possibility of obtaining 3D models, our microscope is widely used in examination of the samples of biological origin, such as: erythrocytes [2], chitinous structures [3], human colon tissue [4], collagen and dentin.

References

1. A. Senkic *et al.*, in preparation, CVD growth parameters on global and local optical properties of MoS2 monolayer
2. K. Bukara *et al.*, J. Biomed. Opt. **22**(2), 026003 (2017)
3. MD Rabasovic *et al.*, J. Biomed. Opt. **20**(1), 016010 (2015)
4. SZ Despotovic *et al.*, Sci. Rep. **10**, 6359 (2020)

S13-BMP-201 / **Poster presentation (virtual)**

Calorimetric Tracking of the Plasma and CSF Proteome in Children With Acute Lymphoblastic Leukemia

Authors: B. Antonova[1]; K. Batchvarov[2]; Yoan Dimitrov[1]; S. Abarova[1]; B. Tenchov[1]; B. Avramova[2]; M. Jordanova[2]; D. Konstantinov[2]

[1] *Medical Faculty, Medical University – Sofia, Bulgaria*

[2] *Department of Pediatric Hematology and Oncology, University Hospital "Queen Joanna", Sofia, Bulgaria*

Presenter: Y. Dimitrov (`yoandimitroff@gmail.com`)

Leukemia is the most common type of cancer found in children. It accounts for around 33% of all malignant diseases in pediatrics.

Differential scanning calorimetry DSC is a highly sensitive technique that measures temperature-induced conformation changes in proteins. As such, it is useful in measuring the exact values of concentration, conformation and interaction between proteins and other molecules and allows for observing specific insignificant changes in blood plasma and CSF (cerebrospinal fluid), related to various pathological processes. This way, plasma and CSF proteins could serve as biomarkers for the diagnosis and monitoring of the disease.

In this study we have used DSC to compare alterations in the protein thermal denaturation profiles of blood plasma and CSF, taken from children with acute lymphoblastic leukemia (ALL), with the corresponding fluids from other children in continuous remission with healthy clinical and hematological statuses, used as controls.

Here we present DSC measurements of blood plasma in children in cases with leukemic infiltration present in the bone marrow. In some cases they are about newly developed disease or relapsed one, and in other cases about Non-Hodgkin's lymphoma with secondary spread to the bone marrow and also lymphoid blast crisis

FT–01 / **Invited talk**

Challenges in supersymmetric cosmology

Author: Ignatios Antoniadis[1]

[1] *LPTHE - CNRS - Sorbonne University, Paris, France*

Presenter: I. Antoniadis (`antoniad@lpthe.jussieu.fr`)

I will discuss the problem of scale hierarchies in particle physics and cosmology and propose ways to address it. In particular I will present a framework of natural inflation within supergravity dubbed 'inflation by supersymmetry breaking'. The main idea is to identify the inflaton with the superpartner of the goldstino, in the presence of a gauged R-symmetry that may contain the R-parity of the supersymmetric Standard Model.

FT–02 / **Invited talk (virtual)**

On the nature of optical rogue waves

Authors: Milivoj R. Belić[1]; Stanko N. Nikolić[2]; Omar Ashour[3]; Najdan B. Aleksić[4]

[1] *Texas A&M University at Qatar*

[2] *Texas A&M University at Qatar; Institute of Physics Belgrade, University of Belgrade*

[3] *Department of Physics, University of California*

[4] *Institute of Physics Belgrade, University of Belgrade*

Presenter: M. Belić (`milivoj.belic@qatar.tamu.edu`)

We present rogue wave solutions to the standard cubic nonlinear Schrődinger equation that models many propagation phenomena in nonlinear optics. We propose the method of mode pruning for suppressing the modulation instability of rogue waves. We point to instances when rogue waves appear as numerical artefacts, due to inadequate numerical treatment of modulation instability and homoclinic chaos of rogue waves. In the end, we display how statistical analysis based on different numerical procedures can lead to misleading conclusions on the nature of rogue waves. Thus, we will discuss the nature of optical rogue waves in view of conflicting opinions expressed in the literature. In particular, we address three pairs of opposing suppositions on their nature: Linear vs. nonlinear [1]; random vs. deterministic [2]; and numerical vs. physical [3]. In our opinion, a short answer to the three suppositions is that rogue waves in optics are essentially nonlinear, deterministic, and physical. They are nonlinear because the major cause of rogue waves is the modulation or Benjamin-Feir instability, which by its nature is the basic nonlinear optical process. Rogue waves are deterministic because modulation instability (MI) leads to deterministic chaos; random phenomena are probabilistic and may look chaotic but are not deterministic. Rogue waves are physical because they appear in

many experiments and media, with similar statistics. Our opinion is supported by extensive numerical simulations of the nonlinear Schrődinger equation in different regimes that touch upon the aspects of all three conflicting suppositions.

Unfortunately, in numerical simulations optical rogue waves may appear fictitiously, as numerical artefacts. Different numerical algorithms represent different dynamical systems and in chaotic regimes may provide different evolution pictures for exactly the same inputs, leading – distressingly – to significantly different statistics [4]. The statistics appear similar, but the number of peaks, the maximum of intensity, and the slope of distributions, among other things, are different. Hence, in the chaos produced by modulation instability, optical rogue waves and their statistics may appear as numerical artefacts. Owing to a vague definition of rogue waves and exponential amplification of numerical errors, there are situations in which optical rogue waves may appear as linear, random, and numerical. In the very end, we demonstrate how to produce stable Talbot carpets – recurrent images of light and plasma waves – by rogue waves, for possible use in nanolithography.

References
1. F.T. Arecchi, U. Bortolozzo, A. Montina, S. Residori, "Granularity and inhomogeneity are the joint generators of optical rogue waves," Phys. Rev. Lett. 106,153901 (2011).
2. J.M. Dudley, F. Dias, M. Erkintalo, G. Genty, "Instabilities, breathers and rogue waves in optics," Nature Photonics 8, 755 (2014).
3. B.M. Herbst, M.J. Ablowitz, "Numerically induced chaos in the nonlinear Schrödinger equation," Phys. Rev. Lett. 62, 2065 (1989).
4. M.R. Belić, S.N. Nikolić, O.A. Ashour, N.B. Aleksić, "On different aspects of the optical rogue waves nature," Nonlinear Dyn. 108, 1655 (2022)

Quantum Gravity and the Swampland

Author: Emilian Dudas[1]

[1] *Ecole Polytechnique and CERN-TH, CPHT, Ecole Polytechnique 91128 Palaiseau Cedex, France*

Presenter: E. Dudas (`emilian.dudas@polytechnique.edu`)

The Swampland is defined as the set of consistent Quantum Field Theories that cannot be coupled to Quantum Gravity. The goal of the Swampland is to find or to conjecture, based on the intuition gained from String Theory, general principles that a field theory coupled to quantum gravity should respect. One example is the "gravity as the weakest force" (or "weak-gravity conjecture").

I will summarize some of the recent conjectures and their potential implications for particle physics and cosmology.

PHYSICAL CHEMISTRY 2022

16th International Conference
on Fundamental and Applied Aspects of
Physical Chemistry

Organized by
The Society of Physical Chemists of Serbia

BOOK OF ABSTRACTS

Online Event
September 26-30, 2022
Belgrade, Serbia

03-PL

EXTENDING FLUORESCENCE CORRELATION SPECTROSCOPY TO IMAGING: QUANTITATIVE SCANNING-FREE CONFOCAL MAPPING OF THE CELLULAR DYNAMICS AND LOCAL ENVIRONMENT OF MOLECULES IN LIVE CELLS

S. Oasa [1], A. J. Krmpot [2], S. N. Nikolić [2], L. Terenius [1], R. Rigler [3] and <u>V. Vukojević</u> [1]

[1] *Center for Molecular Medicine (CMM, L8:01), Department of Clinical Neuroscience (CNS), Karolinska Institute, 17176 Stockholm, Sweden (vladana.vukojevic@ki.se)*
[2] *Institute of Physics Belgrade, University of Belgrade, Pregrevica 118, 11080 Belgrade, Serbia*
[3] *Department of Medical Biochemistry and Biophysics (MBB), Karolinska Institutet, 17177 Stockholm, Sweden*

ABSTRACT
Fluorescence Correlation Spectroscopy (FCS) is an advanced, time-resolved quantitative analytical method with single-molecule sensitivity that can measure the concentration and size of molecules and characterize their interactions in solution and in live cells. However, the very same feature that gives FCS its ultimate, single-molecule sensitivity – the tiny observation volume element (OVE) that is about $(0.2 - 1.0) \times 10^{-15}$ dm^3, confers a serious limitation – restricted field of view. With the advent of new technologies [4], we have extended FCS to imaging by massively parallelizing the number of independent observation volume elements, and have integrated massively parallel FCS with Fluorescence Lifetime Imaging Microscopy (mpFCS/FLIM) to enable quantitative scanning-free confocal mapping of the cellular dynamics and local environment of molecules in live cells. In my lecture, I will present an overview of this development and give examples of important applications.
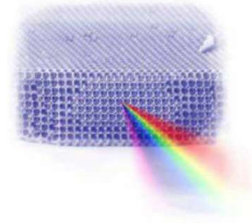
Book of Abstracts

15th Photonics Workshop

(Conference)

Characterizing red blood cells deformability by ektacytometry

Ivana Drvenica[1], Mihajlo Radmilović[2], Danica Pavlović[2], Mihailo Rabasović[2], Stanko Nikolić[2], Drenka Trivanović[1], Dušan Vučetić[3], Vesna Ilić[1], Aleksandar Krmpot[2]

(1) *Institute for Medical Research, National Institute of Republic of Serbia, University of Belgrade, Serbia, Dr. Subotica 4, POB 102, 11129 Belgrade, Serbia*

(2) *Institute of Physics Belgrade, National Institute of Republic of Serbia, University of Belgrade, Pregrevica 118, 11080 Belgrade, Serbia*

(3) *Institute for Transfusiology and Hemobiology, Military Medical Academy, Belgrade, Serbia*

Contact: I. Drvenica (ivana.drvenica@imi.bg.ac.rs)

Abstract. The erythrocytes have remarkable physico-elastic properties with an elastic modulus softer than the softest latex rubber [1]. Such feature allows them to deform from its diameter of approximately 8 μm to diameters as small as 1.5 μm in the narrowest capillaries, and consequently to perform oxygenation of the tissue [1] and help proper adhesion of white blood cells in blood flow [2] or platelets marginalization [3]. Decreased red blood cell deformability is a well-known characteristic of several disorders, such as sickle cell anemia, Plasmodium infection, iron deficiency, and hemolytic anemias, and can be conveniently measured by ektacytometry. This technique uses laser light diffraction to measure red blood cells deformability and cellular heterogeneity [4]. Since human erythrocytes possess a life span of 120 days and are under the constant influence of oxidative stress, metabolic depletion, and loss of ion gradients [1], deformability could be a biomechanical biomarker indicating presence of subtle chronic pathological states or an early sign of a disease. This study has analyzed the effects of several *in vitro* parameters on erythrocyte deformability by using RheoScan D 300 (RheoMeditech. Inc., Korea, Fig. 1). The parameters were chosen in such a way to simulate some pathological conditions and included treatment of erythrocytes by oxidative agents, changes of osmotic gradient, and erythrocytes storage and isolation from whole blood. Relevant outputs of red cells deformability include the maximum elongation index (EI Max), a quantity of the maximum deformability of erythrocytes as reaction to increasing shear stress, and shear stress ½ (SS ½), the shear stress needed for half maximal deformability.
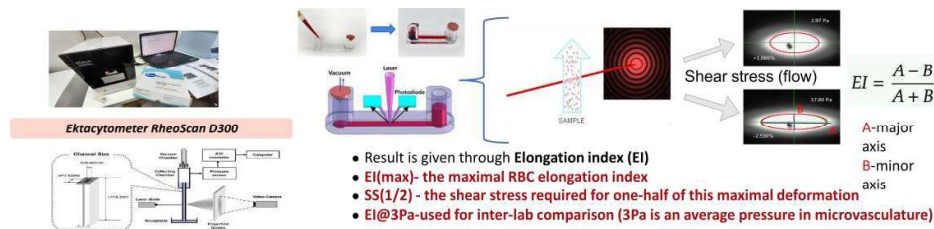
Figure 1. Schematic presentation of ektacytometer RheoScan D300 set-up and diffraction measurement of red blood cells (RBC) deformability indices-elongation index (EI) at specific shear stress (SS)

By variation of *in vitro* parameters, ektacytometry enables us to detect even those subtle differences in deformability of erythrocytes of healthy human donors induced by changes due to age, osmolarity, and type of applied oxidative stress. Since the diffraction measurement by ektacytometry is an average of all cells present in the measured sample [5], the actual usefulness of the technique for monitoring disease onset or progression through the determination of erythrocytes population deformability merits further examinations and parameters optimization.

REFERENCES

[1] R.E. Waugh, M. Narla et al., *Blood*. **79** (1992), 1351-1358.
[2] M. Gutierrez, M.B. Fish et al., *Langmuir.* **34(6)** (2018) 2363-2372.
[3] B. Czaja, M. Gutierrez et al., *PLoS Comput. Bio.l* **16(3)** (2020) e1007716.
[4] N.L. Parrow, P.C. Violet et al., *J. Vis. Exp.* **131** (2018) e56910.
[5] M. Gutierrez, M. Shamoun et al., *Sci. Rep.* **11(1)** (2021) 7909.

Two - photon microscopy as a tool for the studying erythrocyte morphology in a Diabetes mellitus type 1 patients

Mihajlo Radmilović[1], Ivana Drvenica[2], Mihailo Rabasović[1], Vesna Ilić[2], Danica Pavlović[1], Stanko Nikolić[1], Aleksandar Krmpot[1]

(1) *Institute of Physics Belgrade, Pregrevica 118, 11080 Belgrade, Serbia*

(2) *Institute for Medical Research, National Institute of Republic of Serbia, University of Belgrade, Serbia, Dr Subotica 4, POB 102, 11129 Belgrade, Serbia*

Contact: M. Radmilović (mihajlo.radmilovic@ipb.ac.rs)

Abstract.   Fluorescence emission was detected during the interaction of ultrashort laser pulses with hemoglobin (Hb) and red blood cells (RBC) [1,2]. The formation of fluorescent photoproduct was associated with the interaction of ultrashort laser pulses with Hb [3]. Here we want to present some photophysical properties of (Hb) photoproduct and to apply that knowledge for studying erythrocytes morphology in a patient with type 1 diabetes (T1DM). Diabetes mellitus (DM) represents a group of metabolic disorders characterized by hyperglycemia and insulin secretion defects [4]. Erythrocytes as a glucose-consuming cells are affected by the glucose level variation so that their morphology and function are altered [4,5]. Spatial distribution of photoproduct was measured as the change of two-photon emission signal (2PE) and reflects the position of Hb in the single RBC [6]. Our preliminary results suggest differences between healthy donor RBC Fig 1 a) and T1DM RBC Fig 1 b) in a shape and Hb distribution. Although preliminary data on T1DM RBC deformability determined by ektacytometry did not reveal any disturbance compared to normal RBC, we still assume that observed alteration in the distribution of Hb can have consequences to the RBC physiology in T1DM patients. However, further investigations are needed.
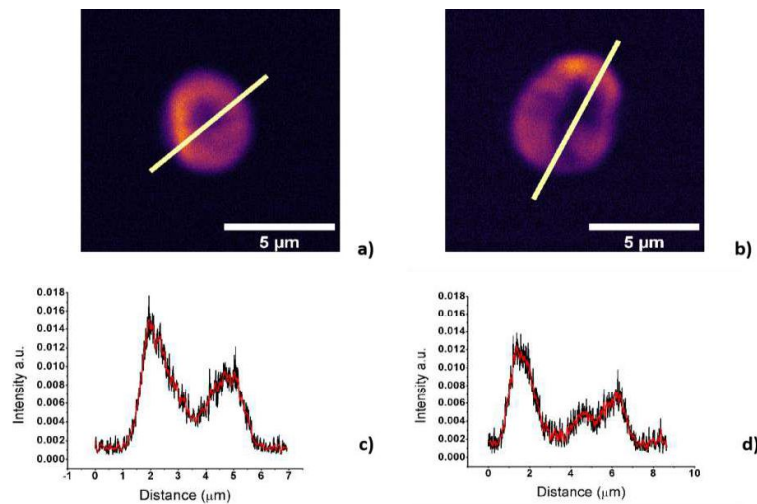
Figure 1. a) Two - photon microscopy image of RBC from a healthy donor and b) T1DM patient c) Spatial distribution of photoproduct as a change of 2PE signal through the cell diameter in a healthy donor RBC and in the d) T1DM patient. Black curve represents raw data plot and red curve are obtained using adjacent point averaging by the usage of percentile filter.

REFERENCES
[1] G. Clay et al.,*The Journal of chemical physics* 126.2 (2007), 01B609.
[2] D. Li et al., *Optics letters*, **36**(6)(2011), 834-836.
[3] E. A. Shirshin et al., *Laser Physics Letters*, **15**(7)(2018), 075604.
[4] Y. Wang et al.,*Journal of DiabetesResearch*, (2021).
[5] N. Babu et al., *Clinical Hemorheology and Microcirculation*, **31**(4) (2004), 273.
[6] K. Bukara et al.,*Journal of biomedical optics*, **22**(2) (2017), 026003.

Laser beam waveguiding capabilities of the suspension of Chlorella sorokiniana in water

Aleksander G. Kovačević[1], Tanja Pajić[2], Danica Pavlović[1], Marina Stanić[3], Marina Lekić[1], Olga Fedotova[4], Stanko N. Nikolić[1], Oleg Khasanov[4], Ryhor Rusetski[4], Najdan Aleksić[5], Branislav M. Jelenković[1]

(1) *Institute of Physics of the University of Belgrade, Pregrevica 118, 11080 Belgrade, Serbia*

(2) *Faculty of Biology of the University of Belgrade, Studentski trg 16, 11000 Belgrade, Serbia*

(3) *Institute for Multidisciplinary Research of the University of Belgrade, Bulevar Despota Stefana 142, 11060 Belgrade, Serbia*

(4) *Scientific and Practical Materials Research Centre of the National Academy of Sciences of Belarus, Minsk, Belarus*

(5) *Moscow State University of Technology "STANKIN", Vadkovskiy per. 1, 127055 Moscow, Russia*

Contact: A. Kovačević (aleksander.kovacevic@ipb.ac.rs)

Abstract. Controlled light guiding to target regions in biological and biomedical systems is important for applications like sensing and diagnosis. The penetration depth in tissues, limited due to scattering, is increased by using conventional optical waveguides, built on materials like silica glass and hard plastics. More potential for formation of biophotonic waveguides having higher biocompatibility and biodegradability have natural biomaterials, like living cells.

Strong scattering and absorption loss in cells is overcome by nonlinear effects arising during laser light propagation through suspensions of living cells, like marine bacteria [1]. Microalga *Chlorella* shows more attractiveness due to robustness, simple structure, high growth rate and ability to grow in various conditions, and its species *Chlorela sorokiniana* is most robust and most resistive to heat and intense light [2, 3].

We examined the propagation of the 532 nm CW laser beam of various powers through the suspension of freshwater green microalga *C. sorokiniana* of various concentrations. Due to nonlinear effects, like thermo-optical, scattering, optical gradient forces, the beam modified. Self-guiding and the changing of cross-section occurred for chosen parameters of power and concentration. Some of the outcomes might be of interest for applications in biophotonics and biomedicine: waveguiding, medical imaging and optimal propagation of laser beam in biological suspensions.

REFERENCES

[4] A. Bezryadina, T. Hansson, R. Gautam et al., *Phys. Rev Lett.* **119** (2017), 058101 (2017). Lj. Author, *Book title*, Publisher, New York (2018).

[5] I. Shihira, R. W. Krauss. *Chlorella. Physiology and taxonomy of forty-one isolates*, pp.1-97. Maryland: University of Maryland, College Park (1965).

[6] L. E. de-Bashan, A. Trejo et al., *Bioresource Technol.* **99** (2008), 4980–4989 (2008).

Book of abstracts
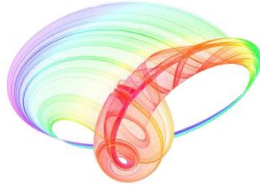
PHOTONICA2021

VIII International School and Conference on Photonics

& HEMMAGINERO workshop

23 - 27 August 2021,

Belgrade, Serbia

Editors

Mihailo Rabasović, Marina Lekić and Aleksandar Krmpot

Institute of Physics Belgrade, Serbia

Belgrade, 2021

Live-cell cartography: spatial mapping of biomolecular information by functional Fluorescence Microscopy Imaging (fFMI)

S. Oasa[1], A.J. Krmpot[2], S.N. Nikolić[2], A.H.A. Clayton[3], I.F. Tsigelny[4],
J.-P. Changeux[5], L. Terenius[1], R. Rigler[6] and V. Vukojević[1]

[1]*Department of Clinical Neuroscience (CNS), Karolinska Institutet, Stockholm Sweden*
[2]*Institute of Physics Belgrade, University of Belgrade, Belgrade, Serbia*
[3]*Optical Science Centre, Department of Physics and Astronomy, School of Science,*
Swinburne University of Technology, Melbourne, Australia
[4]*Department of Neurosciences, University of California San Diego, CA, USA*
[5]*Institut Pasteur, Department of Neuroscience, Unité Neurobiologie Intégrative des Systemés, Paris France*
[6]*Department of Medical Biochemistry and Biophysics (MBB), Karolinska Institutet, Stockholm Sweden*
e-mail:sho.oasa@ki.se

Live cells convey key information and control their vital functions *via* molecular interactions and transporting processes. Through molecular interactions and transporting processes, they precisely control, spatially and timewise, the concentration and mobility of biomolecules, and their local environment (pH, ionic strength, charge density). To understand the dynamic integration of molecular interactions through transport processes, quantitative methods with high sensitivity, spatial and temporal resolution are needed. Fluorescence microscopy- and correlation spectroscopy based methods have proven to be invaluable for this purpose, and advanced methods such as Image Correlation Spectroscopy (ICS) [1] and Single Plane Illumination Microscopy (SPIM; also called Light Sheet Microscopy)/Total Internal Reflection (TIR)-based Fluorescence Correlation Spectroscopy (SPIM-FCS/TIR-FCS) [2] have been recently developed. However, both methods, while very powerful, also have limitations. ICS is based on Confocal Laser Scanning Microscopy (CLSM), thus relying on the analysis of fluorescence signal acquired with a time lag (dwell time between pixels). In SPIM-FCS, fluorescence intensity is simultaneously read-out; but light sheet propagation may be affected by obstacles in the sample, giving rise to an uneven fluorescence excitation across the specimen. Also the observation volume elements are larger than in conventional single-point FCS due to light-sheet thickness. Finally, TIR-FCS use is limited as it only can be used to study processes at the basal plasma membrane. With this in mind, we were motivated to develop scanning-free massively parallel FCS with high spatio-temporal resolution (~240 nm and ~ 10 μs, respectively) and single-molecule sensitivity, which will allow us to quantitatively characterize fast dynamic processes and precisely measure the concentration of fluorescently-tagged biomolecules in live cells and in solution [3]. To this aim, fluorescence intensity from 256 or 1024 excitation foci generated by the diffractive optical element (DOE) are recorded by a position-matched individual single-photon avalanche detector (SPAD) in a 2D SPAD camera. Autocorrelation curves are computed from time series of fluorescence intensity fluctuation to determine the concentration (reciprocal to the amplitude of the autocorrelation curve) and diffusion time (decay time of the autocorrelation curve). Our instrument allows also Fluorescence Lifetime Imaging Microscopy (FLIM), to characterize the immediate surroundings of the fluorescent tags *via* fluorescence lifetime, and FLIM-based Förster Resonance Energy Transfer (FRET), to assess the biomolecular interaction via donor-acceptor interaction. We have applied mpFCS/FLIM to spatially map in live cells the local concentration, diffusion and local environment of a transcription factor in the cell nucleus and have characterised the effects of an allosteric inhibitor of transcription factor dimerization [4].

REFERENCES
1. Wiseman, P.W., *Image correlation spectroscopy: principles and applications.* Cold Spring Harb Protoc, 2015. **2015**(4): p. 336-48.
2. Sankaran, J., et al., *Simultaneous spatiotemporal super-resolution and multi-parametric fluorescence microscopy.* Nat Commun, 2021. **12**(1): p. 1748.
3. Krmpot, A.J., et al., *Functional Fluorescence Microscopy Imaging: Quantitative Scanning-Free Confocal Fluorescence Microscopy for the Characterization of Fast Dynamic Processes in Live Cells.* Anal Chem, 2019. **91**(17): p. 11129-11137.
4. Oasa, S., et al., *A strategy for designing allosteric modulators of transcription factor dimerization.* Proc Natl Acad Sci U S A, 2020. **117**(5): p. 2683-2686.

The nature, origin, and properties of the one- and two-dimensional optical rogue waves

S. Nikolic[1,2], S. B. A. Alwashahi[3], N. Aleksic[4], O. A. Ashour[5], S. A. Chin[6], M. Belic[2]
[1]*Institute of Physics Belgrade, University of Belgrade, Serbia*
[2]*Science program, Texas A&M University at Qatar, Doha, Qatar*
[3]*Faculty of Physics, University of Belgrade, Serbia*
[4]*Moscow State Technological University "STANKIN", Moscow, Russia*
[5]*Department of Physics, University of California, Berkeley CA 94720, USA*
[6]*Department of Physics and Astronomy, Texas A&M University, College Station TX 77843, USA*

e-mail: stankon@ipb.ac.rs

The generating mechanism of optical rogue waves (RWs) is the modulation instability (MI). It is the nonlinear optical process in which a weak perturbation of the background pump wave produces an exponential growth of higher order sidebands that constructively interfere to build RWs. We produce RWs in numerical simulations of the cubic nonlinear Schrödinger equation, Hirota, and quintic equation with noisy (or other) inputs on the flat or elliptic background [1,2].

We discuss RWs strange nature, ingrained instability, dynamic generation, and potential applications. We propose the method of mode pruning for suppressing the modulation instability of rogue waves. We further demonstrate how to produce stable Talbot carpets (two dimensional patterns) of rogue waves.

We also present statistical analysis [3] on rogue waves produced by various numerical algorithms using white noise as initial conditions.

REFERENCES
[1] S. N. Nikolic, O. A. Ashour, N. B. Aleksic, M. R. Belic, S. A. Chin, Nonlinear Dyn. **95**, 2855 (2019).
[2] S. N. Nikolic, O. A. Ashour, N. B. Aleksic, Y. Zhang, M. R. Belic, S. A. Chin, Nonlinear Dyn. **97**, 1215 (2019).
[3] S. Toenger, T. Godin, C. Billet, F. Dias, M. Erkintalo, G. Genty, J. M. Dudley, Sci. Rep. **5**, 10380 (2015).

Narrowing of laser beam propagating through biological suspension

A. Kovacevic[1], T. Pajic[2], D. Pavlovic[1], M. Stanic[3], M. Lekic[1], S. Nikolic[1], B. Jelenkovic[1]

[1] *Institute of Physics Belgrade, University of Belgrade, Pregrevica 118, 11080 Belgrade, Serbia*
[2] *Faculty of Biology, University of Belgrade, Studentski trg 16, 11000 Belgrade, Serbia*
[3] *Institute for Multidisciplinary Research, University of Belgrade, Bulevar Despota Stefana 142, 11060 Belgrade, Serbia*
e-mail:aleksander.kovacevic@ipb.ac.rs

Recent demonstration of nonlinear self-action of laser beams in suspension of biological materials, like marine bacteria and red blood cells, has been reported [1-3]. In this work, we demonstrate nonlinear optical effects of laser beam propagation through the freshwater green microalga *Chlorela sorokiniana*, cultivated in Bold basal medium with 3-fold nitrogen and vitamins (3N-BBM+V).

Chlorella sorokiniana is a species of single-celled freshwater green microalga in the division *Chlorophyta*. Its spherical or ellipsoidal cells (3 x 2 μm in small cells to 4.5 x 3.5 μm in large cells, sometimes >5 μm) divide rapidly to produce four new cells every 17 to 24 hours [4]. The non-pathogenic species has been chosen as a model organism due to its small cell dimension, rapid growth, non-mobility and non-toxicity. The algae were kept in the light chamber and the temperature was maintained at 22°C. Mid-exponential growth phase of algal culture was used for the experiments.

In the experiments, the 532 nm CW laser beam is directed to the glass cuvette that is filled either with the medium or with algae suspended in the medium. We have monitored the laser beam diameter at the entrance and exit of the cuvette, and its axial profile through entire cell length. The concentration has been determined by optical microscopy and optical density and has been varied between 10^{6} and 10^{8} cm^{-3}.

The concentration of the algae and the laser beam power affect the beam radius. Our preliminary results have shown the effect of light self-trapping, i.e., the decrease of laser diameter when the algae concentration exceeds 10^{6} cm^{-3} while laser power is above 1 W. The difference of the refractive indexes of the algae and the medium can induce optical trapping of algae, which subsequently changes the concentration of the algae within the laser beam. This in turn can explain different behavior of the beam in the medium with and without algae.

We discuss the mechanisms which led to narrowing of the beam including nonlinear effects as well as potential applications in waveguiding, medical imaging and optimal propagation of laser beam in biological suspensions.

REFERENCES
[1] A. Bezryadina, T. Hansson, R. Gautam, et al. Phys. Rev Lett. 119, 058101 (2017).
[2] R. Gautam, Y. Xiang, J. Lamstein, et al., Light: Sci. Appl. 8, 31 (2019).
[3] R. Gautam, A. Bezryadina, Y. Xiang, et al., Adv. Phys. X 5 (2020), doi: 10.1080/23746149.2020.1778526.
[4] I. Shihira, R. W. Krauss. *Chlorella*. Physiology and taxonomy of forty-one isolates, pp.1-97. Maryland: University of Maryland, College Park (1965).

NODYCON 2019

FIRST INTERNATIONAL NONLINEAR DYNAMICS CONFERENCE

Edited by
The NODYCON 2019 Program Committee
Department of Structural and Geotechnical Engineering
Sapienza University of Rome

Book of Abstracts of the First International Nonlinear Dynamics
Conference, Rome, Italy, February 17-20, 2019

Higher-order breathers, solitons and rogue waves of the quintic nonlinear Schrödinger equation

S. N. Nikolić[*,**], Najdan B. Aleksić[*,**], Omar A. Ashour[*,***], Milivoj R. Belić[*], Siu A. Chin[****]

[*] Science program, Texas A&M University at Qatar, P.O. Box 23874 Doha, Qatar

[**] Institute of Physics Belgrade, University of Belgrade, Belgrade, Serbia

[***] Department of Physics, University of California, Berkeley, Berkeley CA 94720, USA

[****] Department of Physics and Astronomy, Texas A&M University, College Station, TX 77843, USA

Abstract. We examine various solutions of the quintic nonlinear Schrödinger equation (QNLSE) on different backgrounds. We show how to use Darboux transformation (DT) to construct initial conditions for the dynamical generation of breathers, solitons and rogue waves. We provide the condition for breather-to-soliton conversion for QNLSE with the analysis of intensity profile. We present higher-order solutions of QNLSE when Jacobi elliptic functions are set as background seed solutions in DT scheme. Finally, we analyze the method for generating a new class of QNLSE solutions, called *periodic rogue waves*, which is based on the matching of the periodicity of higher-order breathers with the periodicity of the background elliptic wave.

Quintic nonlinear Schrödinger equation

The QNLSE is the extension of the nonlinear Schrödinger equation that includes all terms up to the fifth-order dispersion [1,2]:

$$i\psi_x + S[\psi] - i\alpha H[\psi] + \gamma P[\psi] - i\delta Q[\psi] = 0.$$

Here, wave function is denoted with $\psi \equiv \psi(x,t)$, the transverse variable is t and the longitudinal variable is x. Partial derivatives are denoted by subscripts. Three parameters of QNLSE are α, γ, δ and may have arbitrary real values. Operators S, H, P, and Q are:

$$S[\psi(x,t)] = \frac{1}{2}\psi_{tt} + |\psi|^2 \psi,$$

$$H[\psi(x,t)] = \psi_{ttt} + 6|\psi|^2 \psi_t,$$

$$P[\psi(x,t)] = \psi_{tttt} + 8|\psi|^2 \psi_{tt} + 6|\psi|^4 \psi + 4|\psi_t|^2 \psi + 6\psi_t^2 \psi^* + 2\psi^2 \psi_{tt}^*,$$

$$Q[\psi(x,t)] = \psi_{ttttt} + 10|\psi|^2 \psi_{ttt} + 30|\psi|^4 \psi_t + 10\psi\psi_t\psi_{tt}^* + 10\psi\psi_t^*\psi_{tt} + 20\psi^*\psi_t\psi_{tt} + 10\psi_t^2\psi_t^*.$$

Breather, solitons and rogue waves of QNLSE on uniform background

Higher-order breathers and rogue waves were firstly derived as analytical solutions for nonlinear Schrödinger equation using Darboux transformation technique [3,4]. We generalized this work to calculate exact QNLSE breathers of an arbitrary order. We extract initial condition from analytical DT solution for QNLSE [5] and then propagate it to obtain this high-intensity structure dynamically, as explain in [6,7]. For numerical integration, we use a finite difference method to calculate all derivatives with $O(h^{12})$ accuracy (h is the step size along the t-axis), and the 4th-order explicit Runge-Kutta method for the evolution of the wave function. Next, we provide analytical condition for the breather-to-soliton conversion in QNLSE and examine the transverse intensity profile of such solutions.

QNLSE solutions on elliptic background

Rogue waves in nature do not appear on a flat background. There is always a wavy background, on which under certain circumstances giant waves appear suddenly. Therefore, we examine solutions of QNLSE that are built, using DT and numerical integration, from the seed wave functions that contain Jacobi elliptic functions (JEF): cn or dn. In addition, we introduce a method for generating a new class of rogue waves, which we call the *periodic rogue waves* [8]. This method is based on the precise matching of the periodicity of higher-order breathers to the periodicity of the background elliptic wave. When these periods are matched, we obtain the array of high-intensity peaks. If slight mismatch occurs, only central peak remains in QNLSE solution.

Conclusions

The dynamical evolution of higher-order QNLSE breathers is important when the existence of such structures is questionable in the presence of modulation instability. Namely, the DT might provide analytical higher-order solutions that might not exist, owing to modulation instability, which is usually present in these solutions. Solutions on the nonuniform background represent more realistic way to describe single or periodic rogue waves in nature.

References

[1] Ankiewicz A., Kedziora D. J., Chowdury A., Bandelow U., Akhmediev N. (2016) Infinite hierarchy of nonlinear Schrödinger equations and their solutions. *Phys. Rev. E* **93**: 012206.

[2] Kedziora D. J., Ankiewicz A., Chowdury A., Akhmediev N. (2015) Integrable equations of the infinite nonlinear Schrödinger equation hierarchy with time variable coefficients. *Chaos* **25**: 103114.

[3] Kedziora D.J., Ankiewicz A., Akhmediev N. (2011) Circular rogue wave clusters. *Physical Review E* **84**: 056611.

[4] Akhmediev N., Soto-Crespo J.M., Ankiewicz A. (2009) Extreme waves that appear from nowhere: On the nature of rogue waves. *Physics Letters A* **373**: 2137.

[5] Chowdury A., Kedziora D.J., Ankiewicz A., Akhmediev N. (2014) Soliton solutions of an integrable nonlinear Schrödinger equation with quintic terms. *Physical Review E* **90**: 032922.

[6] Chin S. A., Ashour O. A., Nikolić S. N., Belić M. R. (2016) Maximal intensity higher-order Akhmediev breathers of the nonlinear Schrödinger equation and their systematic generation. *Physics Letters A* **380**: 3625.

[7] Nikolić S. N., Aleksić N. B., Ashour O. A., Belić M. R., Chin S. A. (2017) Systematic generation of higher-order solitons and breathers of the Hirota equation on different backgrounds. *Nonlinear Dynamics* **89**: 1637.

[8] Nikolić S. N., Ashour O. A., Aleksić N. B., Belić M. R., Chin S. A. (2018) Breathers, solitons and rogue waves of the quintic nonlinear Schrödinger equation on various backgrounds. Submitted to *Nonlinear Dynamics*.

Book of abstracts

PHOTONICA2015

the Fifth international school and conference on photonics

& COST actions: MP1204 and BM1205

& the Second international workshop "Control of light and matter waves propagation and localization in photonic lattices"

24 August – 28 August 2015

Belgrade, Serbia

Editors

Suzana Petrović, Goran Gligorić and Milutin Stepić

Vinča Institute of Nuclear Sciences, Belgrade, Serbia

Belgrade, 2015

Counting atoms with single-atom resolution

H. Zhang[1], R. McConnell[1], <u>S. Ćuk</u>[2], Q. Lin[1], M. H. Schleier-Smith[1],
I. D. Leroux[1] and V. Vuletić[1]

*[1]Department of Physics, MIT-Harvard Center for Ultracold Atoms, and Research Laboratory of
Electronics, Massachusetts Institute of Technology, Cambridge, Massachusetts 02139, USA*
[2]Institute of Physics, University of Belgrade, Pregrevica 118, 11080 Belgrade, Serbia
e-mail: senka@ipb.ac.rs

For hyperfine-state-selective measurements on ensembles containing 100 or more atoms, a single-atom resolution has been demonstrated [1], along with detection sensitivity that is 21 dB below the quantum projection noise limit. The demonstrated measurement resolution is expected to provide the readout capability necessary for atomic interferometry substantially below the standard quantum limit (SQL). Measurements are performed on laser-cooled ^{87}Rb atoms confined at the antinodes of a standing-wave dipole trap at 852 nm in an optical cavity. Atoms in the cavity change the refractive index of a medium and hence induce a shift of the resonance frequency of the optical resonator by an amount proportional to the atom number. In order to measure this atom-induced frequency shift, and consequently the atom number, we introduce 780-nm probe laser to the cavity and observe the dispersive Pound-Drever-Hall (PDH) signal, which detects the phase of the probe light reflected from the cavity. Resolution of the "detection system" is determined by the atom number variance extracted from a large number of repeated measurements.

REFERENCES
[1] H. Zhang et al., Phys. Rev. Lett. 109, 133603 (2012).

Connection between stationary and transient electromagnetically induced transparency and slow light in Rb buffer gas cell

S. N. Nikolić, M. Radonjić, N. M. Lučić, A. J. Krmpot and B. M. Jelenković
Institute of Physics, University of Belgrade, Belgrade, Serbia
e-mail: stankon@ipb.ac.rs

Here we report on recent progress on investigation of electromagnetically induced transparency (EIT), slow light and connection between these two phenomena in Rb buffer gas cell [1]. The EIT resonances, formed among Zeeman coherences of hyperfine state $5^2S_{1/2}$ $F_g = 2$, were studied by using a laser beam which frequency was stabilized on the hyperfine transition $F_g = 2 \rightarrow F_e = 1$ on D_1 line in ^{87}Rb isotope. The influence of the laser beam intensity, diameter (1.3 mm or 6.5 mm) and radial intensity distribution (Gaussian or Π profile) on the contrast, linewidth and line shape of EIT resonances is examined. Resonances were obtained by measuring the transmitted laser beam intensity through Rb

cell when longitudinal magnetic field was changing slowly, under the conditions of constant laser beam power and polarization. For the 1.3 mm diameter Gaussian laser beam, EIT resonances have non-Lorentzian line shapes with Ramsey narrowing of the central peak, induced by the diffusion of coherently prepared atoms in the dark, and then back to the beam. In case of a wide Gaussian beam with 6.5 mm diameter, the EIT line shape is Lorentzian when laser intensity is small, otherwise it can not be described by Lorentzian function due to contribution of the atoms in the wings of a beam. The laser beam with Π intensity profile and 6.5 mm diameter always gives Lorentzian EIT resonances.

Time development of EIT resonances was examined from σ^- transmission signal. For that purpose, two rectangular σ^- pulses separated in time were propagating through Rb cell, together with a strong σ^+ control field. The laser beam was turned off between two σ^- pulses in order to enable a free evolution of Zeeman coherences in the dark. In a repeated interaction of two σ^- pulses with Rb atoms, the Raman-Ramsey fringes were measured, both on σ^- transmission signals and temporal EIT resonances. Ramsey oscillations, appearing at the beginning of the second σ^- pulse, are dumped during pulse duration and disappear at later moments due to Zeeman decoherence. It was noticed that the linewidth of the central peak was independent on the dark time, in contrary to the fringes of higher order which got narrower when time separation between two pulses was prolonged [2].

The slow and stored σ^- pulse were measured in the Rb cell, based on stationary and temporal EIT analysis. It was experimentally ascertained that the most efficient slow light process is obtained in the medium with the most contrasted and narrowest EIT resonances. Once the optimal laser beam parameters were set, the delay of the Gaussian σ^- pulse was measured as a function of the pulse duration and laser beam intensity. The measured group velocities are in the range from 1.7 km/s to 23 km/s, while the fractional time delay is in the interval from 3.5 % to 20 % [3]. Higher transmission and higher group velocity of the Gaussian σ^- pulse were obtained when rectangular preparation pulse of the same polarization had previously prepared the dark states [4].

REFERENCES
[1] S. N. Nikolić et al., J. Phys. B 46, 075501 (2013).
[2] S. N. Nikolić et al., J. Phys. B 48, 045501 (2015).
[3] S. N. Nikolić et al., Phys. Scr. T149, 014009 (2012).
[4] S. N. Nikolić et al., Rev. Sci. Instrum. 84, 063108 (2013).

Book of abstracts
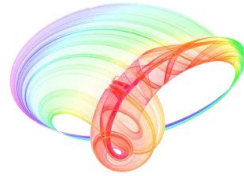
PHOTONICA2019

The Seventh International School and Conference on Photonics, 26 August – 30 August 2019, Belgrade, Serbia

& Machine Learning with Photonics Symposium (ML-Photonica 2019)

& ESUO Regional Workshop

& COST action CA16221

Editors: Milica Matijević, Marko Krstić and Petra Beličev

Belgrade, 2019

Double-periodic solutions and Talbot carpets of extended nonlinear Schrödinger equations

S. N. Nikolić[1,2], O. A. Ashour[3], N. B. Aleksić[1,2], Y. Zhang[4], M. B. Belić[2] and S. A. Chin[5]
[1]*Institute of Physics Belgrade, University of Belgrade, Serbia*
[2]*Science program, Texas A&M University at Qatar, Doha, Qatar*
[3]*Department of Physics, University of California, Berkeley, United States of America*
[4]*Key Laboratory for Physical Electronics and Devices & Shaanxi Key Lab of Information Photonic Technique, Xi'an Jiaotong University, China*
[5]*Department of Physics and Astronomy, Texas A&M University, College Station, United States of America*
e-mail: stankon@ipb.ac.rs

We present analytical and numerical double-periodic solutions of the one-dimensional nonlinear Schrödinger equation and its extended versions [1] (up to the fifth-order dispersion), in the form of Talbot carpets [2]. The breathers of different orders and rogue waves are obtained using numerical simulations, starting from the initial conditions calculated by the Darboux transformation. To suppress undesirable aspects of modulation instability leading to the homoclinic chaos, we applied Fourier modes pruning procedures. This way, we are able to preserve and maintain the twofold carpets periodicity. The novelties of our work are analytical Talbot carpets for Hirota-quintic equation and ability to obtain them dynamically by controlling the growth of the Fourier modes. In addition, the new period-matching procedure is described for periodic rogue waves [3] that can be utilized to produce Talbot carpets without mode pruning.

REFERENCES
[1] A. Ankiewicz et al., Phys. Rev. E 93, 012206 (2016).
[2] S. N. Nikolić et al., to be published in Nonlinear Dyn. *DOI:* 10.1007/s11071-019-05042-1 (2019).
[3] S. N. Nikolić et al., Nonlinear Dyn. 95, 2855 (2019).

2019 PhotonIcs & Electromagnetics Research Symposium

also known as 2019 Progress In Electromagnetics Research Symposium

(PIERS — Rome)

PIERS 2019 Rome
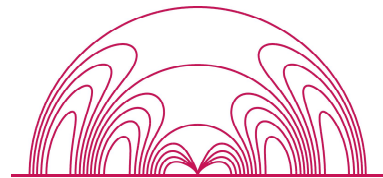
www.emacademy.org
www.piers.org

Abstracts

17–20 June 2019
Rome, ITALY

Talbot Carpets by Rogue Waves of the Extended Nonlinear Schrödinger Equation

Milivoj R. Belić[1], Stanko N. Nikolić[1,2], Omar A. Ashour[3],
Najdan B. Aleksić[2], Yiqi Zhang[4], and Siu A. Chin[5]

[1]Science Program, Texas A&M University at Qatar, Doha 23874, Qatar
[2]Institute of Physics Belgrade, Pregrevica 118, Zemun 11080, Serbia
[3]Department of Physics, University of California, Berkeley, CA 94720, USA
[4]Xi'an Jiaotong University, Xi'an 710049, China
[5]Department of Physics and Astronomy, TAMU College Station, TX 77843, USA

Abstract— We present analytical and numerical double-periodic solutions of the one-dimensional nonlinear Schrodinger equation (NLSE) and its extended versions, as self-imaging Talbot carpets. The solutions are obtained analytically using exact expressions for the rogue wave solutions of the NLSE equation. To suppress modulation instability and homoclinic chaos, numerical mode pruning procedure is invented and, when necessary, the period matching between breathers and elliptic background on which these breathers ride is applied. Such carpets can be used in nanoscale lithography.

Periodic Rogue Waves of the Extended Nonlinear Schrödinger Equation

S. N. Nikolić[1, 2], Najdan B. Aleksić[1, 2], Omar A. Ashour[1, 3], Ali Ali[1],
Milivoj R. Belić[1], and Siu A. Chin[4]

[1]Science Program, Texas A&M University at Qatar, P. O. Box 23874, Doha, Qatar
[2]Institute of Physics Belgrade, University of Belgrade, Belgrade, Serbia
[3]Department of Physics, University of California, Berkeley, Berkeley, CA 94720, USA
[4]Department of Physics and Astronomy, Texas A&M University, College Station, TX 77843, USA

Abstract— We examine various solutions of the extended nonlinear Schrödinger equation that includes all terms up to the fifth-order dispersion [1, 2]:

$$i\psi_x + S[\psi] - i\alpha H[\psi] + \gamma P[\psi] - i\delta Q[\psi] = 0.$$

This equation is called quintic nonlinear Schrödinger equation (QNLSE). The wave function is denoted with $\psi \equiv \psi(x,t)$, the spatial variable is t and the evolutional variable is x. Partial derivatives are denoted by subscripts. Three real parameters of QNLSE are α, γ, δ. Operators S, H, P, and Q are:

$$S[\psi(x,t)] = \frac{1}{2}\psi_{tt} + |\psi|^2 \psi,$$

$$H[\psi(x,t)] = \psi_{ttt} + 6 |\psi|^2 \psi_t,$$

$$P[\psi(x,t)] = \psi_{tttt} + 8 |\psi|^2 \psi_{tt} + 6 |\psi|^4 \psi + 4 |\psi_t|^2 \psi + 6\psi_t^2 \psi^* + 2\psi^2 \psi_{tt}^*,$$

$$Q[\psi(x,t)] = \psi_{ttttt} + 10 |\psi|^2 \psi_{ttt} + 30 |\psi|^4 \psi_t + 10\psi\psi_t\psi_{tt}^* + 10\psi\psi_t^*\psi_{tt} + 20\psi^*\psi_t\psi_{tt} + 10\psi_t^2\psi_t^*.$$

First, we use Darboux transformation technique (DT) [3, 4] to construct initial conditions for the dynamical generation of higher-order breathers on a flat background, which might be considered as rogue waves. However, such high intensity structures usually appear on a wavy background in nature. Therefore, we next examine solutions of QNLSE that are built on the seed wave functions containing Jacobi elliptic functions (JEF) [5]. In addition, we introduce a method for generating a new class of rogue waves, which we call the *periodic rogue waves* [6]. This method is based on the precise matching of the periodicity of higher-order breathers to the periodicity of the background elliptic wave. When these periods are matched, we obtain the array of high-intensity peaks. If slight mismatch occurs, only central peak remains in QNLSE solution.

REFERENCES

1. Ankiewicz, A., D. J. Kedziora, A. Chowdury, U. Bandelow, and N. Akhmediev, "Infinite hierarchy of nonlinear Schrödinger equations and their solutions," *Phys. Rev. E*, Vol. 93, 012206, 2016.
2. Kedziora, D. J., A. Ankiewicz, A. Chowdury, and N. Akhmediev, "Integrable equations of the infinite nonlinear Schrödinger equation hierarchy with time variable coefficients," *Chaos*, Vol. 25, 103114, 2015.
3. Kedziora, D. J., A. Ankiewicz, and N. Akhmediev, "Circular rogue wave clusters," *Physical Review E*, Vol. 84, 056611, 2011.
4. Akhmediev, N., J. M. Soto-Crespo, and A. Ankiewicz, "Extreme waves that appear from nowhere: On the nature of rogue waves," *Physics Letters A*, Vol. 373, 2137, 2009.
5. Nikolić, S. N., N. B. Aleksić, O. A. Ashour, M. R. Belić, and S. A. Chin, "Systematic generation of higher-order solitons and breathers of the Hirota equation on different backgrounds," *Nonlinear Dynamics*, Vol. 89, 1637, 2017.
6. Nikolić, S. N. O. A., Ashour, N. B. Aleksić, M. R. Belić, and S. A. Chin, "Breathers, solitons and rogue waves of the quintic nonlinear Schrödinger equation on various backgrounds," Published in *Nonlinear Dynamics*, 2018, DOI: 10.1007/s11071-018-4726-8.

Book of abstracts
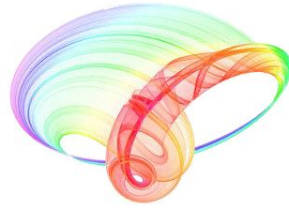
PHOTONICA2017

The Sixth International School and Conference on Photonics

& COST actions: MP1406 and MP1402

&H2020-MSCA-RISE-2015 CARDIALLY workshop

28 August – 1 September 2017

Belgrade, Serbia

Editors

Marina Lekić and Aleksandar Krmpot

Institute of Physics Belgrade, Serbia

Belgrade, 2017

Rogue waves, Talbot carpets and accelerating beams

M.R. Belic[1], S. Nikolic[1], O. Ashour[1], and Y.Q. Zhang[2]
[1]Texas A&M University at Qatar, 23874 Doha, Qatar
[2]Xi'an Jiaotong University, Xi'an 710049, China
e-mail:milivoj.belic@qatar.tamu.edu

Rogue waves are giant waves that sporadically appear and disappear in oceans and optics. Talbot carpets are elaborate recurrent images of light and plasma waves. Accelerating beams are the beams that, well, accelerate. We put the three together.

Analytical and dynamical generation of higher-order solitons and breathers of the extended nonlinear Schrödinger equation on different backgrounds

S. N. Nikolić[1,2], Najdan B. Aleksić[1,2], Omar A. Ashour[1,3], Milivoj R. Belić[1], Siu A. Chin[3]

[1]*Science program, Texas A&M University at Qatar, P.O. Box 23874 Doha, Qatar*
[2]*Institute of Physics Belgrade, University of Belgrade, Belgrade, Serbia*
[3]*Department of Physics and Astronomy, Texas A&M University, College Station, TX 77843, USA*
e-mail: stankon@ipb.ac.rs

We investigate the analytical and dynamical generation of higher-order solitons and breathers of the extended nonlinear Schrödinger equation equation (NLSE) on different backgrounds. We included the operators up to the fifth-order dispersion, called Hirota, Lakshmanan-Porsezian-Daniel (LPD), and quintic operator [1,2].

The Darboux transformation (DT) is used to construct proper initial conditions for dynamical generation of high-intensity solitons and breathers of different order on a uniform background [3,4]. We provide expressions for the Lax pair generating functions and the procedure for calculating higher-order solutions when Jacobi elliptic functions are the background seed solutions of extended NLSE. It is shown that the peak height of each soliton or breather in the nonlinear Darboux superposition adds linearly, to form the intensity maximum of the final solution. We also show that breather-to-soliton conversion can be used to produce solitons of higher amplitude and that the periodicity of Akhmediev breathers can be utilized for dynamical generation of rogue waves.

The dynamical evolution of higher-order solitons and breathers is important in the situations when the existence of such solutions is questionable in the presence of modulation instability. Namely, the DT might provide analytical higher-order solutions that might not exist, owing to modulation instability, which usually exists in these solutions.

REFERENCES
[1] A. Ankiewicz, D. J. Kedziora, A. Chowdury, U. Bandelow, N. Akhmediev, *Phys. Rev. E***93**, 012206 (2016).
[2] D. J. Kedziora, A. Ankiewicz, A. Chowdury, N. Akhmediev, *Chaos***25**, 103114 (2015).
[3] S. A. Chin, O. A. Ashour, S. N. Nikolić, M. R. Belić,*Physics Letters A***380***, 3625 (2016).
[4] S. N. Nikolić, N. B. Aleksić, O. A. Ashour, M. R. Belić,S. A. Chin, *Nonlinear Dynamics*, DOI: 10.1007/s11071-017-3540-z (2017).

Book of abstracts

PHOTONICA2015

the Fifth international school and conference on photonics

& COST actions: MP1204 and BM1205

& the Second international workshop "Control of light and matter waves propagation and localization in photonic lattices"

24 August – 28 August 2015

Belgrade, Serbia

of Colorado, Boulder, aiming to integrate photonics monolithically into processes with advanced transistors.

Moreover, just like integrating the inductor into CMOS chips at the end of 1990s revolutionized the radio design and enabled mobile revolution, the integration of silicon-photonic active and passive devices with modern CMOS transistors is greatly positioned to revolutionize a number of systems beyond computers and data-centers – sensor platforms (ultrasound, bio-screening), imaging (portable LIDAR systems), as well as the wireless communications infrastructure with photonic-assisted phase-arrays, low-phase noise signal sources and large bandwidth, high-resolution ADCs, to name a few.

REFERENCES
[1] J. S. Orcutt et al., Opt. Exp. 20, 12222 (2012).
[2] J. M. Shainline et al., Opt. Lett. 38, 2657 (2013).
[3] M. Georgas et al., "A monolithically-integrated optical transmitter and receiver in a zero-change 45nm SOI process," *IEEE Symposium on VLSI Circuits*, Honolulu (2014).
[4] C. Sun et al., IEEE Journal of Solid-State Circuits 50, 828 (2015).
[5] R. Meade et al., "Integration of Silicon Photonics in Bulk CMOS," *IEEE Symposium on VLSI Technology*, Honolulu (2014).

How Quantitative confocal fluorescence microscopy without scanning for the study of fast dynamical processes *via* massively parallel Fluorescence Correlation Spectroscopy (FCS)

Aleksandar J. Krmpot[1,2], Stanko N. Nikolić[1,2], Marco Vitali[3,4], Dimitrios K. Papadopoulos[5], Sho Oasa[6], Per Thyberg[7], Simone Tisa[8], Masataka Kinjo[6], Lennart Nilsson[9], Walter J. Gehring[10,†], Lars Terenius[1], Rudolf Rigler[1,11] and <u>Vladana Vukojević</u>[1]

[1]*Department of Clinical Neuroscience (CNS), Center for Molecular Medicine (CMM), Karolinska Institutet, 17176 Stockholm, Sweden*
[2]*Institute of Physics, University of Belgrade, 11080 Belgrade, Serbia*
[3]*Department of Chemistry, Berlin Institute of Technology, 10623 Berlin, Germany*
[4]*Omicron Energy Solutions GmbH, 12099 Berlin, Germany*
[5]*Max-Planck Institute for Molecular Cell Biology and Genetics, 01307 Dresden, Germany*
[6]*Graduate School of Life Science, Hokkaido University, Sapporo, Japan.*
[7]*AlbaNova University Center, Royal Institute of Technology, Department of Applied Physics, 106 91 Stockholm, Sweden*
[8]*Micro Photon Devices (MPD), 39100 Bolzano, Italy*
[9]*Department of Biosciences and Nutrition, Karolinska Institutet, 14183 Huddinge, Sweden*
[10]*Department of Cell Biology, Biozentrum, University of Basel, 4056 Basel, Switzerland*
[11]*Department of Medical Biochemistry and Biophysics (MBB), Karolinska Institutet, 17177 Stockholm, Sweden*
e-mail: vladana.vukojevic@ki.se

Quantitative confocal fluorescence microscopy without scanning is developed for the study of fast dynamical processes *via* massively parallel Fluorescence Correlation Spectroscopy (FCS). Simultaneous excitation of fluorescent molecules across the specimen is achieved using a Diffractive Optical Element (DOE). Fluorescence from 1024 illuminated spots is detected in a confocal arrangement by a matching matrix detector consisting of the same number of single-photon avalanche photodiodes (SPADs). Software was developed for data acquisition and fast auto- and cross-correlation analysis by parallel signal processing using a Graphic Processing Unit (GPU). Using aqueous suspension of quantum dots and live cells, we show quantitative mapping of local concentration and mobility across the specimen with a sub-millisecond temporal resolution (21 µs/frame).

Real-time measurements of intensity spatio-temporal dynamics in fiber lasers

Dmitry Churkin
Institute of Photonic Technologies, Aston University, Birmingham, UK
e-mail: d.churkin@aston.ac.uk

Physical systems with co-existence and interplay of processes featuring distinct spatio-temporal scales are found in various research areas ranging from studies of brain activity to astrophysics. Complexity of such systems makes their theoretical and experimental analysis technically and conceptually challenging. We will show that radiation of partially mode-locked fibre lasers, while being stochastic and intermittent on short time scale, exhibits periodicity and long scale correlations over slow evolution from one round trip to another. The evolution mapping of intensity autocorrelation function allows us to reveal variety of spatio-temporal coherent structures and to experimentally study their symbiotic co-existence with stochastic radiation. Our measurements of interactions of noisy pulses
over a time scale of thousands of non-linear lengths demonstrate that they have features of incoherent temporal solitons. Real-time measurements of spatio-temporal intensity dynamics are set to bring new insight into rich underlying nonlinear physics of practical active- and passive-cavity photonic systems.

Optomechanics with cold rubidium atoms

Neven Šantić[1,2], Damir Aumiler[1], Hrvoje Buljan[2] and Ticijana Ban[1]
[1]*Institute of Physics, Zagreb, Croatia*
[2]*Department of Physics, University of Zagreb, Croatia*
e-mail: ticijana@ifs.hr

Inducing mechanical action on atoms by continuous wave (cw) laser excitation has been the central topic in atomic physics for decades. Laser cooling and trapping of atoms, a

Counting atoms with single-atom resolution

H. Zhang[1], R. McConnell[1], S. Ćuk[2], Q. Lin[1], M. H. Schleier-Smith[1],
I. D. Leroux[1] and V. Vuletić[1]

[1]Department of Physics, MIT-Harvard Center for Ultracold Atoms, and Research Laboratory of Electronics, Massachusetts Institute of Technology, Cambridge, Massachusetts 02139, USA
[2]Institute of Physics, University of Belgrade, Pregrevica 118, 11080 Belgrade, Serbia
e-mail: senka@ipb.ac.rs

For hyperfine-state-selective measurements on ensembles containing 100 or more atoms, a single-atom resolution has been demonstrated [1], along with detection sensitivity that is 21 dB below the quantum projection noise limit. The demonstrated measurement resolution is expected to provide the readout capability necessary for atomic interferometry substantially below the standard quantum limit (SQL). Measurements are performed on laser-cooled ^{87}Rb atoms confined at the antinodes of a standing-wave dipole trap at 852 nm in an optical cavity. Atoms in the cavity change the refractive index of a medium and hence induce a shift of the resonance frequency of the optical resonator by an amount proportional to the atom number. In order to measure this atom-induced frequency shift, and consequently the atom number, we introduce 780-nm probe laser to the cavity and observe the dispersive Pound-Drever-Hall (PDH) signal, which detects the phase of the probe light reflected from the cavity. Resolution of the "detection system" is determined by the atom number variance extracted from a large number of repeated measurements.

REFERENCES
[1] H. Zhang et al., Phys. Rev. Lett. 109, 133603 (2012).

Connection between stationary and transient electromagnetically induced transparency and slow light in Rb buffer gas cell

S. N. Nikolić, M. Radonjić, N. M. Lučić, A. J. Krmpot and B. M. Jelenković
Institute of Physics, University of Belgrade, Belgrade, Serbia
e-mail: stankon@ipb.ac.rs

Here we report on recent progress on investigation of electromagnetically induced transparency (EIT), slow light and connection between these two phenomena in Rb buffer gas cell [1]. The EIT resonances, formed among Zeeman coherences of hyperfine state $5^2S_{1/2}$ $F_g = 2$, were studied by using a laser beam which frequency was stabilized on the hyperfine transition $F_g = 2 \rightarrow F_e = 1$ on D_1 line in ^{87}Rb isotope. The influence of the laser beam intensity, diameter (1.3 mm or 6.5 mm) and radial intensity distribution (Gaussian or Π profile) on the contrast, linewidth and line shape of EIT resonances is examined. Resonances were obtained by measuring the transmitted laser beam intensity through Rb

cell when longitudinal magnetic field was changing slowly, under the conditions of constant laser beam power and polarization. For the 1.3 mm diameter Gaussian laser beam, EIT resonances have non-Lorentzian line shapes with Ramsey narrowing of the central peak, induced by the diffusion of coherently prepared atoms in the dark, and then back to the beam. In case of a wide Gaussian beam with 6.5 mm diameter, the EIT line shape is Lorentzian when laser intensity is small, otherwise it can not be described by Lorentzian function due to contribution of the atoms in the wings of a beam. The laser beam with Π intensity profile and 6.5 mm diameter always gives Lorentzian EIT resonances.

Time development of EIT resonances was examined from σ^- transmission signal. For that purpose, two rectangular σ^- pulses separated in time were propagating through Rb cell, together with a strong σ^+ control field. The laser beam was turned off between two σ^- pulses in order to enable a free evolution of Zeeman coherences in the dark. In a repeated interaction of two σ^- pulses with Rb atoms, the Raman-Ramsey fringes were measured, both on σ^- transmission signals and temporal EIT resonances. Ramsey oscillations, appearing at the beginning of the second σ^- pulse, are dumped during pulse duration and disappear at later moments due to Zeeman decoherence. It was noticed that the linewidth of the central peak was independent on the dark time, in contrary to the fringes of higher order which got narrower when time separation between two pulses was prolonged [2].

The slow and stored σ^- pulse were measured in the Rb cell, based on stationary and temporal EIT analysis. It was experimentally ascertained that the most efficient slow light process is obtained in the medium with the most contrasted and narrowest EIT resonances. Once the optimal laser beam parameters were set, the delay of the Gaussian σ^- pulse was measured as a function of the pulse duration and laser beam intensity. The measured group velocities are in the range from 1.7 km/s to 23 km/s, while the fractional time delay is in the interval from 3.5 % to 20 % [3]. Higher transmission and higher group velocity of the Gaussian σ^- pulse were obtained when rectangular preparation pulse of the same polarization had previously prepared the dark states [4].

REFERENCES
[1] S. N. Nikolić et al., J. Phys. B 46, 075501 (2013).
[2] S. N. Nikolić et al., J. Phys. B 48, 045501 (2015).
[3] S. N. Nikolić et al., Phys. Scr. T149, 014009 (2012).
[4] S. N. Nikolić et al., Rev. Sci. Instrum. 84, 063108 (2013).